



8th INTERNATIONAL PATA Days

Blenheim, New Zealand
HANDBOOK AND PROGRAMME

13-16 November 2017

KJ Clark , P Upton, R Langridge, K Kelly, K Hammond

GNS Science Miscellaneous Series 110
November 2017

DISCLAIMER

The Institute of Geological and Nuclear Sciences Limited (GNS Science) and its funders give no warranties of any kind concerning the accuracy, completeness, timeliness or fitness for purpose of the contents of this report. GNS Science accepts no responsibility for any actions taken based on, or reliance placed on the contents of this report and GNS Science and its funders exclude to the full extent permitted by law liability for any loss, damage or expense, direct or indirect, and however caused, whether through negligence or otherwise, resulting from any person's or organisation's use of, or reliance on, the contents of this report.

BIBLIOGRAPHIC REFERENCE

Clark KJ, Upton P, Langridge R, Kelly K, Hammond K. 2017. Proceedings of the 8th International INQUA Meeting on Paleoseismology, Active Tectonics and Archeoseismology. Handbook and Programme, 13-16 November 2017. Lower Hutt (NZ): GNS Science. XX p. (GNS Science miscellaneous series 110). doi:10.21420/G2H061

CONVENORS

KJ Clark, GNS Science, PO Box 30368, Lower Hutt 5040, New Zealand
P Upton, GNS Science, PO Box 30368, Lower Hutt 5040, New Zealand
RM Langridge, GNS Science, PO Box 30368, Lower Hutt 5040, New Zealand

SCIENTIFIC COMMITTEE

Stéphane Baize, Institut de Radioprotection et de Sécurité Nucléaire (IRSN)
Kelvin Berryman, GNS Science
Kate Clark, GNS Science
Tim Dawson, California Geological Survey
Eldon Gath, Earth Consultants
Beverley Goodman, University of Haifa
Christoph Gruetzner, Friedrich Schiller University Jena
Narges Khajavi, University of Canterbury
Robert Langridge, GNS Science
Alessandro Michetti, Università degli Studi dell'Insubria
Tina Niemi, University of Missouri-Kansas City
Klaus Reicherter, RWTH Aachen University
Tom Rockwell, San Diego State University
Petra Stepánciková, Institute of Rock Structure and Mechanics, Academy of Sciences of the Czech Republic
Mark Stirling, University of Otago
Phaedra Upton, GNS Science
Neta Wechsler, Tel Aviv University
Beau Whitney, The University of Western Australia/Fugro Geoter



CONTENTS

INTRODUCTION AND PURPOSE	5
Venue Locations	5
Map of Marlborough Convention Centre	6
Map of Dodson Street Beer Garden	7
Icebreaker	8
Marlborough Convention Centre	8
Internet Access	9
Fieldtrip	9
Abstracts	9
PROGRAMME	10
POSTER PRESENTATIONS	13
ABSTRACTS	15
LIST OF PARTICIPANTS	442
PROCEEDINGS VOLUMES OF PATA DAYS	445

INTRODUCTION AND PURPOSE

Welcome to the 8th PATA Days Meeting in Blenheim, New Zealand. The GNS Science Earthquake Geology team, and our colleagues at Victoria University of Wellington, University of Canterbury and University of Otago are very pleased to welcome you all to New Zealand. The purpose of this meeting is to share new research, ideas and techniques in the fields of paleoseismology, active tectonics and archaeoseismology. We are delighted to be hosting this event in New Zealand in 2017. Several years ago, the GNS Science earthquake geology team started discussing ways in which we could commemorate the tricentenary of the AD 1717 (+/- 5 yrs!) M~8.0 Alpine fault earthquake. An international conference seemed an ideal way to gather earthquake geology expertise in New Zealand, share some of the recent work we have been undertaking on the Alpine fault and raise public awareness of the hazard posed by the Alpine fault. Alas, our plans to hold the meeting in April in Hokitika on the West Coast were well derailed by the 2016 Kaikōura earthquake. It is with some relief that we are now holding the meeting in November 2017 – our re-adjusted plans were not interrupted by another earthquake and we are still within the tercentenary year of the last great Alpine fault earthquake!

The 2016 Kaikōura earthquake demonstrates the many ways in which a large earthquake can create devastation and reshape our understanding of earthquake and tsunami hazards. One year on, main transport routes in the northern South Island are still severely disrupted, communities still isolated, and ongoing aftershocks, land instability and sediment mobilisation are constant reminders that earthquake recovery & rebuilding is a prolonged process. Amongst this are many remarkable stories of resilience and community strength. On a personal level, all earthquake geologists in New Zealand have been humbled by the generosity of landowners in allowing us access to their land for undertaking research, even in these times of severe disruption to their livelihoods. The science community has much to learn from the Kaikōura earthquake – from our underpinning understanding of how plate boundaries evolve in time and space, through to slow-slip triggering, turbidite emplacement, earthquake-induced landslide distribution, the ongoing sedimentary response as landslide debris moves downstream and communication of earthquake science in times of crisis. We hope that this meeting allows an opportunity for all to share the latest in earthquake geology research and to learn more about active tectonics in the many parts of the world from which we have all gathered. We hope you enjoy the meeting.

Kate Clark, Phaedra Upton, Rob Langridge.

Venue Locations

WORKSHOP

Marlborough Convention Centre

42A Alfred Street, Blenheim 7201

+64 3 579 5049

<https://www.marlboroughconventions.co.nz/>

ICEBREAKER

Biddy Kate's Backpackers

2 Market Street, Blenheim 7201

+64 3-578 3299

<http://www.biddykates.com/>

DINNER (DAY 4)

Dodson Street Beer Garden

1 Dodson Street, Mayfield, Blenheim 7201

+64 3 577 8348

<http://www.dodsonstreet.co.nz/>

DINNER (DAY 5)

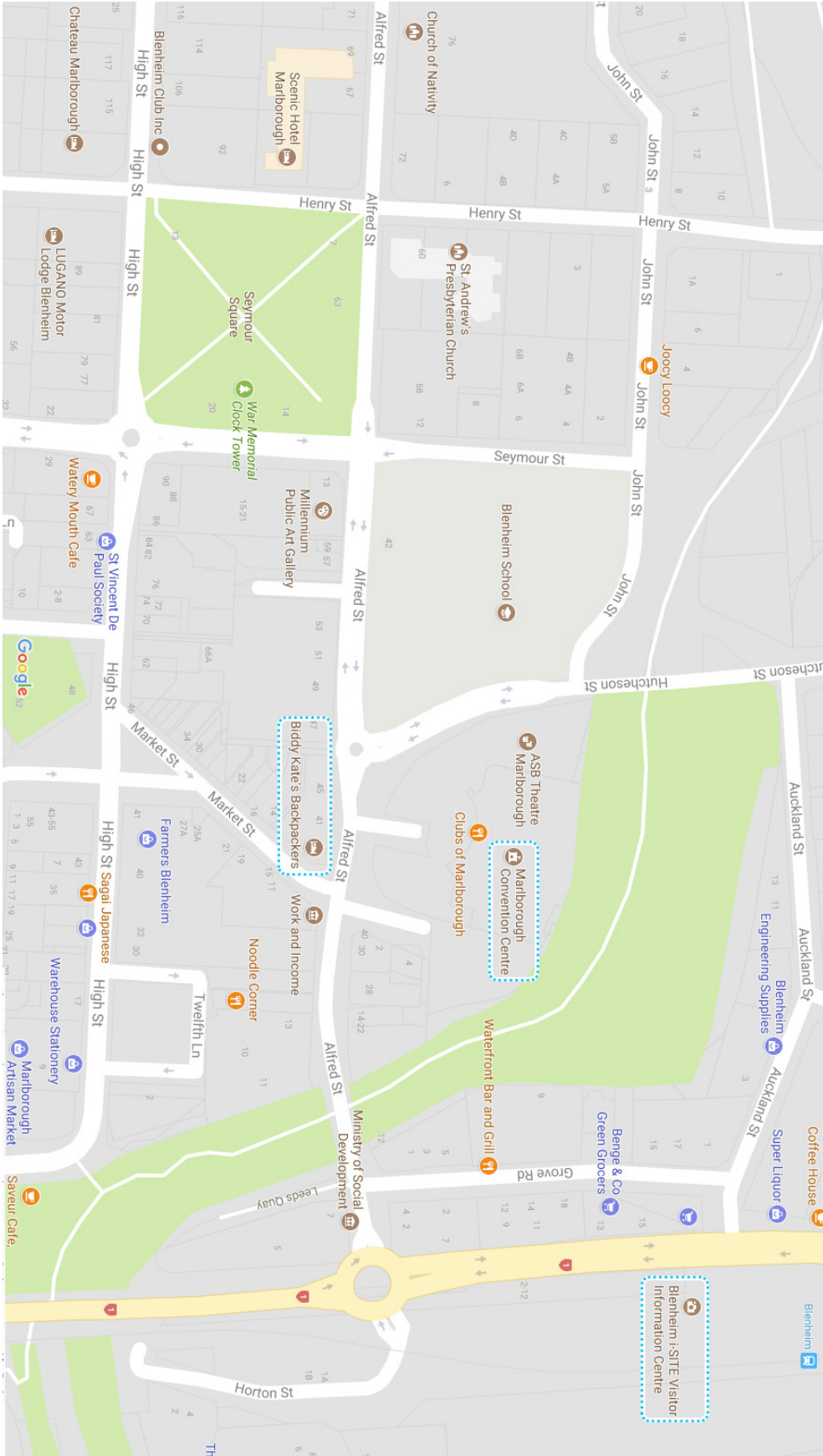
Wither Hills Winery

211 New Renwick Road, Blenheim 7272

+64 3 520 8284

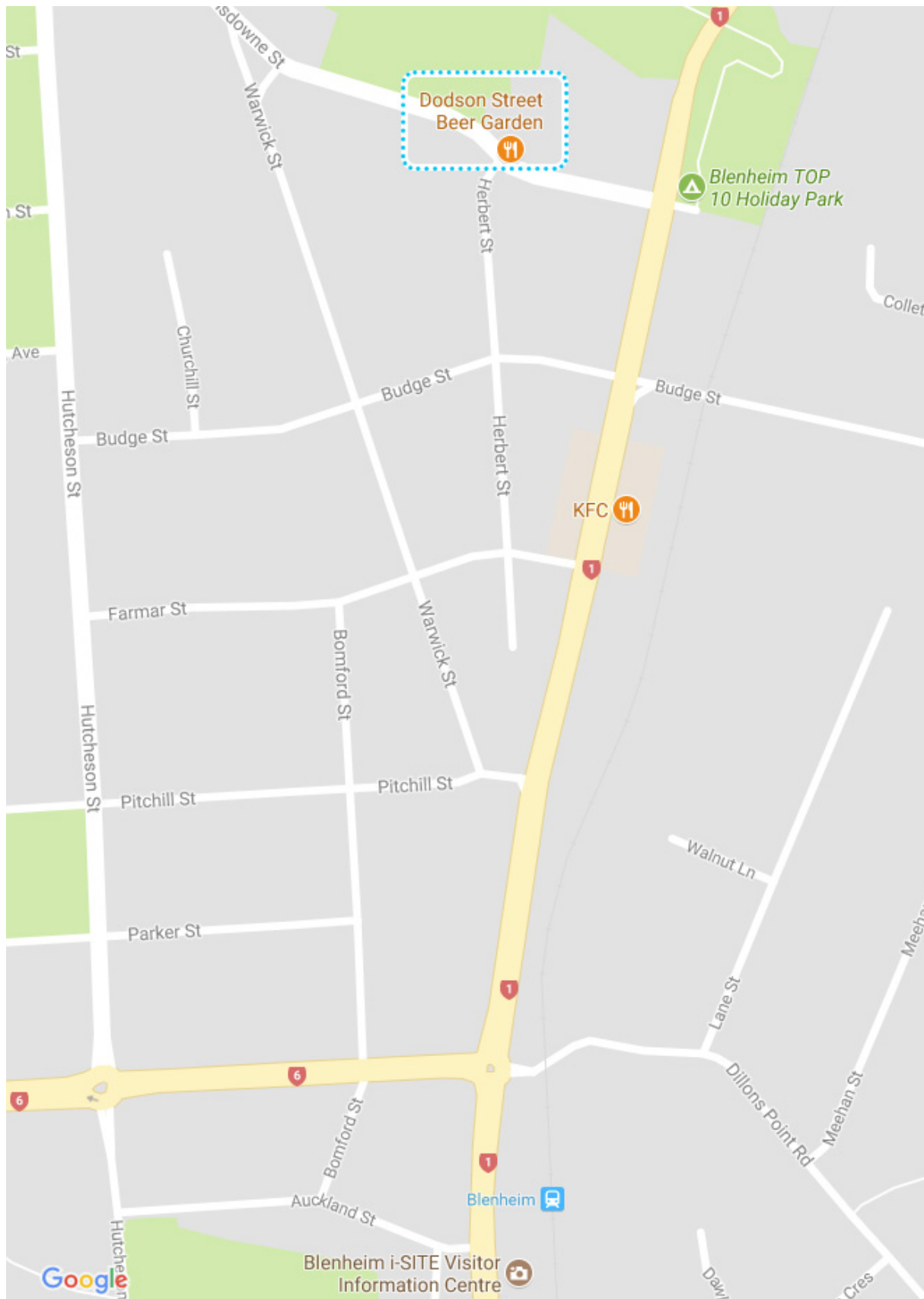
<http://witherhills.co.nz/>

Map of Marlborough Convention Centre



Map of Blenheim showing the Marlborough Convention Centre, Biddie Kate's (location of the Icebreaker) and the Visitor Information Centre.

Map of Dodson Street Beer Garden



Map showing the dinner location on Wednesday night at Dodson Street Beer Garden.

Icebreaker

Time: 6:30 - 8:00 PM

Date: 12 November 2017

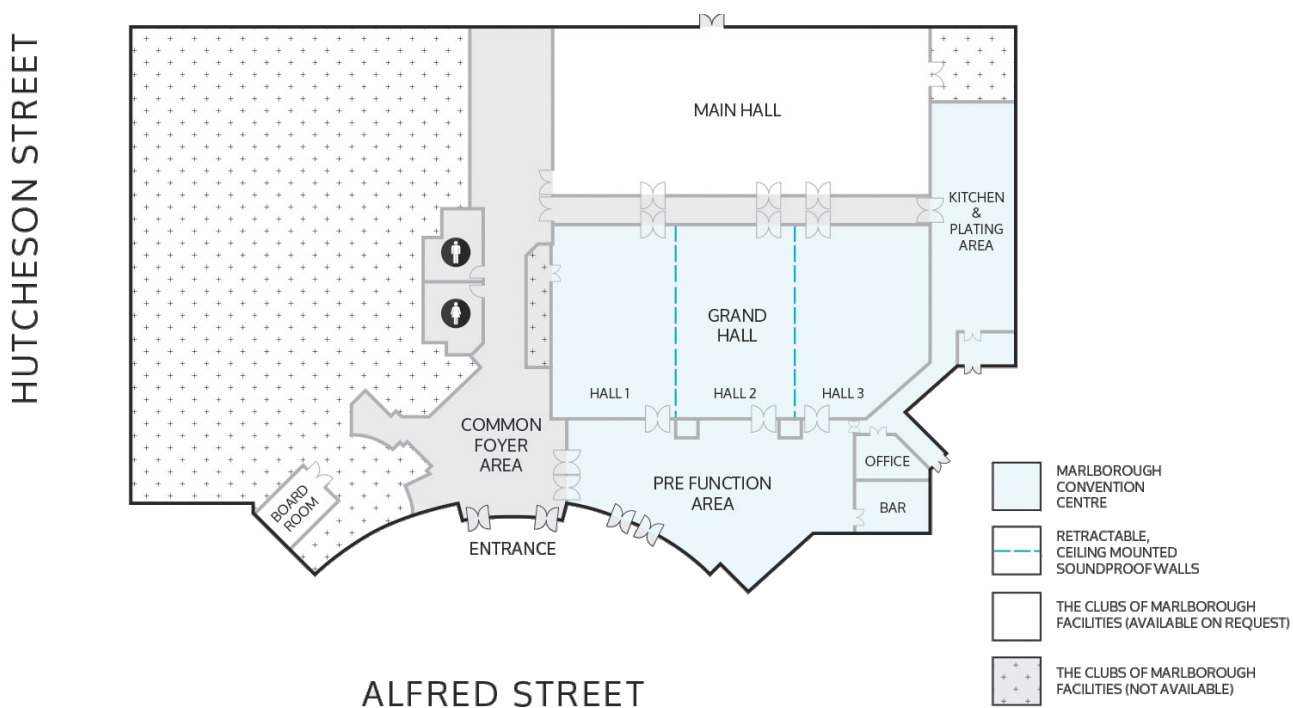
Biddy Kate's Bar, 2 Market St, Blenheim

Marlborough Convention Centre

The 2017 PATA Days meeting will be held at the Marlborough Convention Centre which located near the centre of Blenheim. Buses for the field trips will leave and return from the Marlborough Convention Centre.



FLOOR PLAN



Internet Access

During our meeting, free wireless internet access will be available. Further details on accessing this network will be provided at the venue.

For internet access during your own time please see your hotel reception or see Marlborough's FreeSpot service: <https://www.marlborough.govt.nz/our-community/how-to-access-freespot>.

Fieldtrip

For all those going on the post-conference fieldtrip. You will have been sent the information you need by email. We will be departing from the conference centre at 8:30am sharp on Friday morning.

Abstracts

<http://www.earthquakegeology.com/index.php?page=publications&s=6>

Will also be on: <https://gns.cri.nz/PATA>

PROGRAMME

Sunday, 12 November

DAY 1

6:30 PM Icebreaker

Monday, 13 November

FIELD TRIP -DAY 2

8:30 AM Field-trip departs (*All participants*)

Tuesday, 14 November

MARLBOROUGH CONVENTION CENTRE - DAY 3

8:30 AM Opening (*Kate Clark - GNS Science, Ian Simpson - CEO, GNS Science, Christoph Greutzner - Friedrich Schiller University Jena/INQUA-IFG*)

COMPLEX FAULT RUPTURES ON TRANSPRESSIONAL PLATE BOUNDARIES (TIM STAHL, RUSS VAN DISSEN)

- 9:00 AM **Kaikōura earthquake: overview of seismology, geodesy & earthquake geology** (*Pilar Villamor*)
- 9:30 AM Surface Rupture and Slip Distribution of the Kekerengu Fault during the Mw 7.8 2016 Kaikōura Earthquake (*Jesse Kearse*)
- 9:45 AM Preliminary geometry and kinematics of multiple surface ruptures during the 2016 MW 7.8 Kaikōura earthquake, North Canterbury region, New Zealand (*Narges Khajavi*)
- 10:00 AM The Hundalee Fault and the Mw7.8 2016 Kaikōura earthquake (*Mark Stirling*)
- 10:15 AM Multi-fault earthquakes with rupture complexity: how common? (*Mark Quigley*)
- 10:30AM Morning tea**
- 11:00 AM Three-dimensional coastal deformation in the Mw 7.8 Kaikōura earthquake from differential airborne lidar (*Ed Nissen*)
- 11:15 AM Surface displacement during and after the 2016 Kaikōura earthquake revealed from SAR imagery (*Teng Wang*)
- 11:30 AM High-resolution optical-image correlation for the Kaikōura earthquake, slip distribution and rupture processes (*Yann Klinger*)
- 11:45 AM The role of surface-rupturing faults in the Waiautoa microblock, Clarence valley, New Zealand, during the Mw 7.8 2016 Kaikōura Earthquake (*Rob Langridge*)
- 12:30 PM Lunch**
- 1:30 PM Castle Mountain fault, southcentral Alaska: Observations on slip partitioning from lidar and paleoseismic trenching (*Rich Koehler*)
- 1:45 PM Paleo-uplift along the Kaikōura coastline: evidence from Holocene marine terraces (*Nicola Litchfield*)
- 2:00 PM Past multi fault ruptures at the southern Hikurangi margin (*Kate Clark*)
- 2:15 PM Landslides triggered by the MW 7.8 14 November 2016 Kaikōura Earthquake, New Zealand (*Chris Massey*)

ARCHAEOSEISMOLOGY (NICOLA LITCHFIELD)

- 2:30 PM Archaeoseismology: Studying past earthquakes using archaeological data (*Tina Niemi*)
- 2:45 PM OSL Dating of Sediments Pre- and Post-dating Late Quaternary (*Manfred Frechen*)

3:00 PM Afternoon break

POSTER SESSION

- 3:30 PM 28 Posters
- Complex Fault Ruptures on Transpressional Plate Boundaries
 - Studies on Other Topics Related to Earthquakes Geology
 - Earthquake Behaviour of High Slip Strike-Slip Faults

7:00 PM - 8:30PM Public Talk

Earthquake research from New Zealand and beyond

ADVANCES IN PALEOSEISMIC TECHNIQUES (JAMIE HOWARTH)

- 8:30 AM** **Optically stimulated luminescence dating (OSL) in awkward places: what is doable in tectonically active environments**
(*Sebastian Huot*)
- 9:00 AM Sedimentary Evidence for the 2016 November M 7.8 Kaikōura Earthquake and Possible Sedimentary Evidence for Paleoearthquakes along the Hikurangi Subduction Zone (*Jason Patton*)
- 9:15 AM Paleoseismological studies on Hinagu Fault, Kumamoto, Japan (*Takashi Azuma*)
- 9:30 AM Combined high-resolution topographic analysis and paleoshoreline dating reveal spatio-temporal variability in slip rates on low-strain-rate normal faults (*Ann Egger*)
- 9:45 AM Paleoseismic Study Enhanced by U-Series Geochronology of Pedogenic Carbonate from Displaced Fluvial Gravel Deposits, Issyk-Ata Fault, Central Tien Shan, North Kyrgyzstan (*Magda Patyniak*)
- 10:00 AM Holocene deformation events in the offshore Transverse Ranges (California, USA) constrained by new high-resolution geophysical data (*Hector Perea Manera*)
- 10:15 AM Varve ages and the paleoearthquake interpretations of event horizons from three lakes, Quebec, Canada (*Greg Brooks*)
- 10:30 AM** **Morning tea**

POSTER SESSION

- 11:00 AM 30 posters
- Earthquake Geology Contributions to Seismic Hazard Analysis
- Large Earthquakes in Mountaineous Regions and Landscape Response
- Advances in Paleoseismic Techniques
- Archaeoseismology

12:45PM **Lunch**

ADVANCES (CONT.)

- 1:30 PM Slope failure - effect or trigger of tremors? Insights from geoelectrical methods, speleothem deformations dating (Tatra Mts., Carpathians) (*Maciej Mendecki*)
- 1:45 PM Soft sediment deformation structures from cave as an indicator of tremors in mountains: insights from site effects analysis (Kalacka Cave, Tatra Mts., Carpathians) (*Jacek Szczygiel*)

EARTHQUAKE GEOLOGY CONTRIBUTIONS TO SEISMIC HAZARD ANALYSIS (PILAR VILLAMOR, STEPHANE BAIZE)

- 2:00 PM** **The M7 2016 Kumamoto, Japan, Earthquake: 3D coseismic deformation from differential topography**
(*Chelsea Scott*)
- 2:30 PM Imaging the distribution of transient viscosity following the 2016 Mw 7.1 Kumamoto earthquake (*James Moore*)
- 2:45 PM Fast fault tip propagation driven by near-surface lithology: evidence from trishear inverse modeling (*Franz Livio*)
- 3:00 PM** **Afternoon break**
- 3:30 PM Tectonic Geomorphology, Late Quaternary Slip Rate, and Paleoseismology of the Whittier Fault in Southern California (*Eldon Gath*)
- 3:45 PM The new Italian seismic hazard model (*Carlo Meletti*)
- 4:00 PM Towards modelling the hazard relating to episodically slipping faults in slowly deforming regions (*Dan Clark*)
- 4:15 PM Hydrocode modeling of seismic deformation structures – assumptions and preliminary results (*Malgorzata Bronikowska*)
- 4:30 PM Earthquake history of the western Issyk-Ata Fault, Central Tien Shan, North Kyrgyzstan (*Angela Landgraf*)
- 4:45 PM INQUA - IFG Meeting
- Last year's activities, news, future PATA events, strategy. Everyone's welcome.
- 6:40 PM** **Leave for the dinner venue - Dodson St Beer Garden** (Walking distance - see the map on page X)
- 7:00 PM** **Dinner - Dodson St Beer Garden**

LARGE EARTHQUAKES IN MOUNTAINEOUS REGIONS AND LANDSCAPE RESPONSE (PHAEDRA UPTON)

- 8:30 AM** Near real-time modelling of landslide dams from the 2016 Kaikōura earthquake (*Tom Robinson*)
9:00 AM Surface rupture of the 1933 M 7.5 Diexi earthquake in eastern Tibet: implications for seismogenic tectonics (*Junjie Ren*)

EARTHQUAKE GEOLOGY CONTRIBUTIONS TO SEISMIC HAZARD ANALYSIS (PILAR VILLAMOR, STEPHANE BAIZE)

- 9:15 AM** Tectono-magmatic domains of the eastern Basin and Range, Utah, determined from paleoseismic investigations of active faults (*Tim Stahl*)
9:30 AM Paleo-liquefaction; an Alternative Tool for Seismic Hazard Assessments (*Sarah Bastin*)
9:45 AM Uplift of Fluvial Meanders at Kendeng Fold and Thrust Belt (East Java, Indonesia): Evidence of Late Quaternary Thrust Faulting (*Gayatri Marliyani*)
10:00 AM New school faults and seismic hazard, guilty (i.e. active) until proven innocent (i.e. inactive)? (*Gregory De Pascale*)
10:15 AM The AD 1755 Lisbon Earthquake-Tsunami: Modeling the seismic source from the analysis of environmental and building macroseismic data (*Pablo Silva*)
10:30 AM Morning tea

EARTHQUAKE BEHAVIOUR OF HIGH SLIP STRIKE-SLIP FAULTS (URSULA COCHRAN)

- 11:00 AM** Paleoseismology of the northern Elsinore fault in southern California (*Tom Rockwell*)
11:15 AM Geomorphic and Paleoseismic Investigation of a Prominent Secondary Strand of the San Andreas Fault in the Carrizo Plain: Implication for Rupture Complexity (*Sinan Akciz*)
11:30 AM Timing of Earthquakes during the past 800 years along the Peninsula Section of the San Andreas Fault Suggests Persistent 1906-like Behavior (*Gordon Seitz*)
11:45 AM Late Holocene Surface Rupturing on the Kekerengu fault, New Zealand (*Tim Little*)
12:00 PM Kekerengu Fault: Characterisation of fault slip rate over the last ca 30 ka, and surface rupture displacement perpendicular to strike during the 2016 Kaikōura Earthquake (*Russ Van Dissen*)
12:30 PM Lunch
12:15 PM A revised earthquake history for the North Westland segment of the Alpine Fault (*Jamie Howarth*)
1:30 PM Development of an 8000-year record of large earthquakes on the Alpine Fault, New Zealand: where to from here? (*Ursula Cochran*)
1:45 PM Along-strike variations in fault geometry and slip distribution along the Bulnay Fault, Mongolia (*Jin-Hyuck Choi*)
2:00 PM The 2007 Aysén earthquake sequence: complex faulting and seismic migration in a transpressional fault zone (*Angelo Villalobos*)
2:15 PM Late Quaternary activity of the Dangjiang fault, Central Tibetan Plateau (*Xuemeng Huang*)

EARTHQUAKE GEOLOGY GENERAL CONTRIBUTIONS (TIM DAWSON)

- 2:30 PM** Paleoseismology and Late Quaternary upper crustal deformation along active submarine faults on the continental shelf at 23°S, northern Chile (*José González-Alfaro*)
2:45 PM Assessing giant tsunamigenic subduction earthquakes in the Northern Chile Seismic Gap during the last millennia from submarine and archaeological records (*Gabriel Vargas*)
3:00 PM Afternoon break
3:30 PM Kinematics of the Area Between Palu (Elazig) and Pütürge (Malatya) on the East Anatolian Fault System in Turkey (*Mehmet Kokum*)
3:45 PM Late Quaternary activity of slow-slip intraplate Mariánské Lázně fault as revealed by trenching and shallow geophysical survey; Bohemian Massif (Czech Republic, central Europe) (*Petra Štěpančíková*)
4:00 PM Resistivity imaging of an active tectonics on examples from Central Europe (*Petr Taborik*)
4:15 PM Authentic collaboration with local communities in post-disaster reconnaissance and beyond: how to create a win-win scenario (*Kate Pedley*)
6:00 PM Bus departs for the dinner venue - Wither Hills Winery
6:15 PM Dinner - Wither Hills Winery

- 8:30 AM** Post-meeting field trip departs

POSTER PRESENTATIONS

Tuesday Posters

3:30 - 5:30 PM

COMPLEX FAULT RUPTURES ON TRANSPRESSIONAL PLATE BOUNDARIES

- Anthropogeomorphology and Paleoseismology Blend to Define the Marvast Active Fault Slip History and Potential Seismology, Central Iran (*Abolghasem Goorabi*)
- Preliminary insights of the fault geometries and kinematics along the South Leader Fault System during the Mw 7.8 Kaikōura earthquake (*Natalie Hyland*)
- Rupture patterns on the North Leader Fault System during the Mw7.8 2016 Kaikōura Earthquake (*Tabitha Bushell*)
- The effect of crustal structure on fault interactions (*Susan Ellis*)

EARTHQUAKE GEOLOGY GENERAL CONTRIBUTIONS

- An Extreme Wave Event in eastern Yucatán, Mexico: evidences of paleotsunami during the Mayan time. (*Javier Lario*)
- Exploratory use of random forest classification for characterising and predicting patterns of liquefaction ejecta (*Monica Giona Bucci*)
- Extreme soft-sediment deformation structures as palaeoseismic indicators in slurries from the Late Triassic Ordos Basin (central China) (*Tom van Loon*)
- Factors controlling the distribution of building damage in the traditional Vrissa settlement induced by the 2017 June 12, Mw 6.3 Lesvos (Northeastern Aegean Sea, Greece) earthquake (*Efthymios Lekkas*)
- First steps in assessing paleoseismic activity along the eastern boundary of the Upper Rhine Graben (*Stephane Baize*)
- From fresh tsunami deposit to paleo tsunami deposit: Preservation and disappearance of the 2011 Tohoku-Oki tsunami deposit along the Misawa coast, northern Japan (*Yuichi Nishimura*)
- Historical and paleo-tsunami deposits on the Sanriku Coast, north-east Japan (*Daisuke Ishimura*)
- Past sea level markers as accurate earthquake geological effects: pros and contras (*Teresa Bardaji*)
- Possibility of the Late Holocene uplift in Youngil Bay, the southeastern part of Korean Peninsula (*Sung-ja Choi*)
- Post-earthquake rapid assessment using Unmanned Aircraft Systems (UAS) and GIS online applications: the case of Vrissa settlement after the 2017 June 12, Mw 6.3 Lesvos (North Aegean Sea, Greece) earthquake (*Varvara Antoniou*)
- Preliminary results of a multidisciplinary investigation on a slow-moving active strike-slip fault in Korea (*Yong Sik Gihm*)
- Quaternary deformation in the Cordillera Oriental between 24°-25° SL, Central Andes (NW Argentina) (*Victor Hugo Garcia*)
- Recording Holocene paleotsunamis along the hyperarid coast of Tal-tal region in Northern Chile (*Tomas Leon*)
- Scarp erosion and burial within four years following the M7.2 2010 El Mayor-Cucapah earthquake rupture from repeat terrestrial lidar scans (*Austin Elliott*)
- Simulation of Strong Ground Motion using Seismic Data of the Earthquake Occurred on September 12th 2016, near Gyeongju, Korea (*Hak-Sung Kim*)
- Slip rate estimation from tilting of marine terraces, Kaikoura, New Zealand (*Brendan Duffy*)
- Slope movements induced by strike-slip earthquakes in Western Greece (*Spyridon Mavroulis*)
- Southern Hikurangi Margin uplift rates and tectonic implications based on new marine terrace data from the south coast of the North Island, NZ (*Dee Ninnis*)
- The Characteristics of the Gyeongju Earthquake Observed from the Eupcheon Fault Monitoring System (*Sung-il Cho*)
- Trend and policy of Quaternary fault research in Korea after 2016 Gyeongju earthquake (*Seung Ryeol Lee*)
- Valley evolution of the Biala Łądecka drainage network during late Cenozoic, Lower Silesia, Poland (*Jakub Stemberk*)
- Which sedimentary environment best preserves paleoliquefaction features? (*Peter Almond*)

EARTHQUAKE BEHAVIOUR OF HIGH SLIP STRIKE-SLIP FAULTS

- Refining the earthquake chronology of the last millennium along the Cholame segment of the San Andreas fault (*Alana Williams*)

EARTHQUAKE GEOLOGY CONTRIBUTIONS TO SEISMIC HAZARD ANALYSIS

- Anatomy of the 2016-2017 central Italy coseismic surface ruptures and their arrangement with respect to the foreseen active fault systems segmentation (*Riccardo Civico*)
- Contemporary and Paleo Liquefaction Induced Lateral Spreading in Christchurch New Zealand (*Greg De Pascale*)
- Earthquake damages associated with the 2016 ML=5.8 Gyeongju earthquake, Korea (*Kwangmin Jin*)
- Earthquake fault propagation, displacement and damages (*Young-Seog Kim*)
- Evidences of glacio-isostatic rebound in Germany and Poland – an overview of the GREBAL project (*Szymon Belzyt*)
- Fault segmentation in central Apennines: insights from trenching data (*Francesca Romana Cinti*)
- Ground response analysis during the 8 October 2005 Kashmir earthquake (Mw 7.6): implication for historical and paleoearthquake deterministic hazard assessment (*Hamid Sana*)
- Integrating faults and past earthquakes into a probabilistic seismic hazard model for peninsular Italy (*Bruno Pace*)
- Lidar and field mapping of the western Hope Fault (*Jessica Vermeer*)
- New seismicity models for updating the national Italian seismic hazard model (*Francesco Visini*)
- Preliminary study on the triggering mechanism and related faults associated with the 9.12 Gyeongju Earthquake (M=5.8), SE Korea (*Teahyung Kim*)
- Saalian earthquakes in the Ujście Basin, W Poland (*Malgorzata Pisarska-Jamroz*)
- Towards a unified and worldwide database of surface ruptures (SURE) for Fault Displacement Hazard Analyses (*Stephane Baize*)

LARGE EARTHQUAKES IN MOUNTAINOUS REGIONS AND LANDSCAPE RESPONSE

- Active faults related to the West Andean Thrust System (WATS) and coseismic mega-landslides, Central Chilean High Andes (*Jose Araya*)
- Deformation history of sackung features concentrated around the northern tip of the active Neodani Fault, central Japan (*Komura Keitaro*)
- Earthquake environmental effects induced by the 2017 June 12, Mw 6.3 Lesvos (North Aegean Sea, Greece) earthquake (*Vassiliki Alexoudi*)
- Measuring the slip-rate of the Ashgabat Fault, Turkmenistan (*Christoph Gruetzner*)
- Predicting rock failure as a function of the total stress state: An example from the western Southern Alps (*Phaedra Upton*)
- The Green Lake landslide and its implications for earthquake hazard in the southern South Island (*Tom Robinson*)

ADVANCES IN PALEOSEISMIC TECHNIQUES

- Quaternary faulting near the Utah FORGE geothermal site from high resolution topographic data and luminescence dating (*Emily Kleber*)
- Rapid RS Data Collection for Landslide Damage and Fault Rupture using UAV and Structure-From-Motion Photogrammetry following the 2016 Mw 7.8 Kaikōura Earthquake (*Katie Jones*)
- Stream channel morphology for the assessment of Quaternary fault segmentation activity along the San Ramon fault (Santiago, Chile) (*Rachel Abrahami*)
- Tsunami or Hurricane? Mapping coastal boulders and boulder fields using satellite and high-resolution drone imagery with photogrammetric techniques (*Tina Niemi*)
- Untangling Tectonic Slip from the Potentially Misleading Effects of Landform Geometry (*Austin Eliot*)
- Using the X-ray micro-computed tomography to reveal cryptic strain fabric of faulted soft sediment: outlines of a pilot study and preliminary results (*Petr Spacek*)

ARCHAEOSEISMOLOGY

- Back analysis of earthquake damage on buildings used for the detection of the basic seismological parameters of historical earthquakes: the case of the 1755 Great Lisbon earthquake (*Alexia Grampa*)
- Earthquake Archaeological Effects (EAEs) in Machupicchu. Preliminary results (*Miguel Angel Rodriguez-Pascua*)
- Lichenometric analyses of rocky fault scarps: The example of the Sencelles Fault (Balearic Islands, Spain). (*Pablo G. Silva*)
- SfM as a tool in Archaeoseismology (*Neta Wechsler*)
- The record of ancient and historic earthquakes in the archaeological site of Idanha a Vela (Central Portugal; Iberian Peninsula) (*Miguel Angel Rodriguez-Pascua*)

ABSTRACTS

Abstracts are in alphabetical order.



Stream channel morphology for the assessment of Quaternary fault segmentation activity along the San Ramon fault (Santiago, Chile)

Abrahami, Rachel (1), Vargas, Gabriel (1) Ammirati, Jean-Baptiste (1), Rebolledo, Sofia (1)

(1) Departamento de Geología, Universidad de Chile, Plaza Ercilla 803, Santiago, Chile, rabrahami@ing.uchile.cl

Abstract: The San Ramón fault is an active west-vergent thrust fault system located along the eastern border of Santiago, capital city of Chile, at the foot of the western slope of the main Andes Cordillera (Armijo et al., 2010). It is formed by N-S to NNW-striking fault segments evidenced by conspicuous Quaternary fault scarps disrupting alluvial sediments of the piedmonts units. Paleoseismological observations revealed two last large episodes with superficial rupture in the past 17–19 k.y, demonstrating active tectonic growth of the western flank of the Andes. We apply stream profile analysis as an exploratory tool in a region lacking data in order to identify the structure responsible for the seismic hazard. As preliminary results we proved the probable existence of several segments of the San Ramón fault, south and east of Santiago city.

Key words: San Ramon Fault, Santiago de Chile, Stream channel analysis, Geomorphology

INTRODUCTION

The San Ramón fault is a kilometeric crustal-scale west-vergent thrust fault system, located east of the highly populated city of Santiago at the piedmont of the main Andean Cordillera in central Chile (Fig.1). The structural system is constituted by segments of 10-15 km length, evidenced by pronounced 4 m to more than 100 m high scarps systematically located along the fault trace that affect Quaternary piedmont units, suggesting slip rate on the order of ~0.4-0.5 mm/year (Armijo et al., 2010; Rauld, 2011). Recent paleoseismological study reveals evidence of large intraplate earthquakes in the past 17–19 k.y, demonstrating active tectonic growth of the western flank

of the Andes and implying increased seismic risk for the city of Santiago (Vargas et al., 2016, 2014).

The current knowledge of the extent of the San Ramón fault is very limited. The aim of this study is to evidence news segments of the San Ramón fault using geomorphological analysis. The preliminary results show that stream profile analysis can be used as an exploratory tool to evidence probable segments of the San Ramón fault. We identified a few probable segments of the San Ramon Fault south and east of Santiago, evidenced by the presence of knickpoints and high channel steepness values.

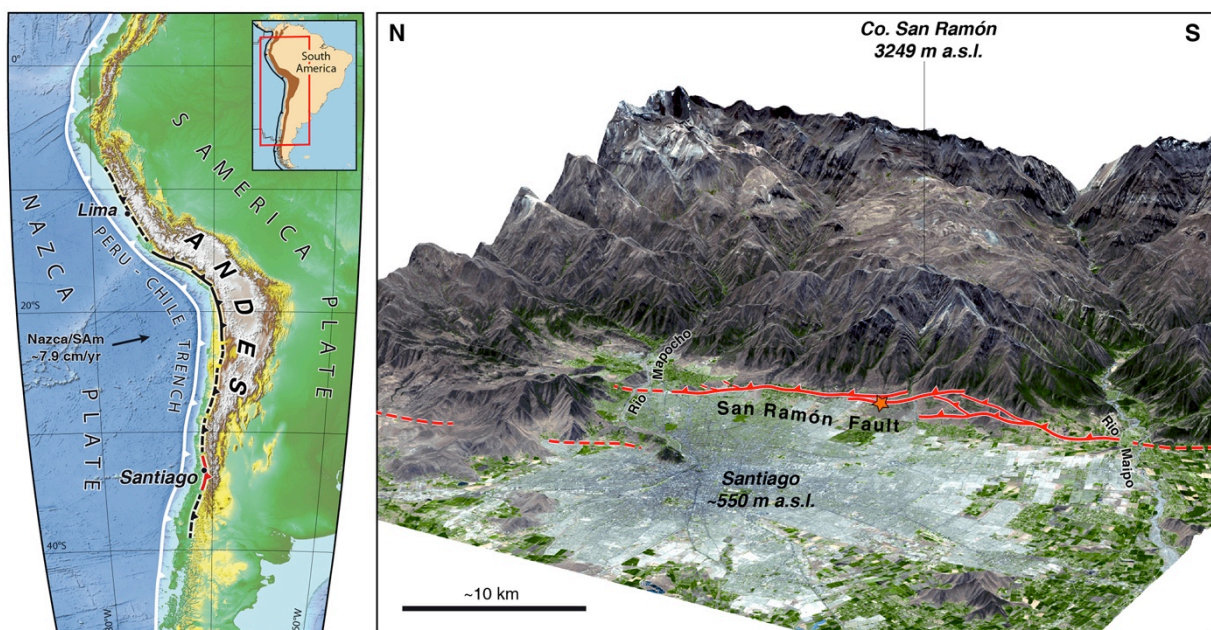


Figure 1: Tectonic and geomorphologic context of the San Ramón Fault at the eastern border of Santiago, capital city of Chile. San Ramón Fault is a part of a major tectonic system, the West Andean Thrust, located at the western border of the main Andes Cordillera (Armijo et al., 2010). Star shows the location of paleoseismological trenches excavated across a prominent young fault scarp (Vargas et al. 2014).



METHODOLOGY

Stream profile analysis

Among the geomorphic indicators, stream longitudinal profiles are considered to be very sensitive to regional tectonic uplift rates (Holbrook & Schumm, 1999; Burbank & Anderson, 2001). Steady-state rivers show concave-upward long profiles (equilibrium profile; Hack, 1957), traditionally attributed to the inverse discharge-slope relationship necessary to generate the shear stresses that entrain and move sediment (Bull, 1991). Deviation from this condition is usually indicative of a transient phase of landscape change, represented by knickpoints in the river profile. In this study we test if the stream profile analysis can evidence the presence of the fault.

The methodology used for the evaluation of the stream-profiles analysis in the study area is based on the Flint's empirical power-law equation that relates the local slope (S) to the upstream contributing drainage basin area (A):

$$S = k_s A^{-\theta}$$

where k_s is a steepness index and θ is the stream concavity. Increases in the k_s values can be related to the presence of anomalous uplift rates or a more general reduce in the erosional efficiency (Snyder et al., 2000; Kirby & Whipple, 2001; Vanlaningham, Meigs & Goldfinger, 2006). Thus for the same upstream area, the slope of a channel experiencing a high uplift rate is higher than the slope of a channel experiencing low uplift rate. Then we determined a normalized steepness index (k_{sn}) for the individual segments using a reference concavity commonly used

value in a wide range of geomorphic settings (Wobus et al., 2006, $\theta_{ref} = 0.45$).

Digital Elevation Model (DEM) and software

Quantitative topographic metrics are extracted from a DEM with a resolution of 9 m. We use the software ArcGIS together with the open source, freely accessible Stream Profiler code (Matlab) (<http://geomorphtools.geology.isu.edu/tools.htm>) for this analysis.

RESULTS AND INTERPRETATION

We present in Figure 2 the current known extent of the San Ramón fault with the results of slope, knickpoints and geographical distribution of the k_{sn} values.

In first order we can say that the current trace of the San Ramón fault matches with higher slope and channel steepness values. Increase of channel steepness values can be related to the presence of anomalous uplift rates. Moreover, all the studied streams present knickpoints around the edge of the trace of the fault. All these parameters support the existence of the trace of the San Ramón Fault east to Santiago. Thus it is possible to use this geomorphological parameter (the slope) and stream profiles analysis as exploratory tools to map fault trace in an urbanized region lacking data (e.g. GPS, datation).

In the studied area, we also observed knickpoints and high slope values, which seem to be linked to human activity such as constructions of canals or highways.

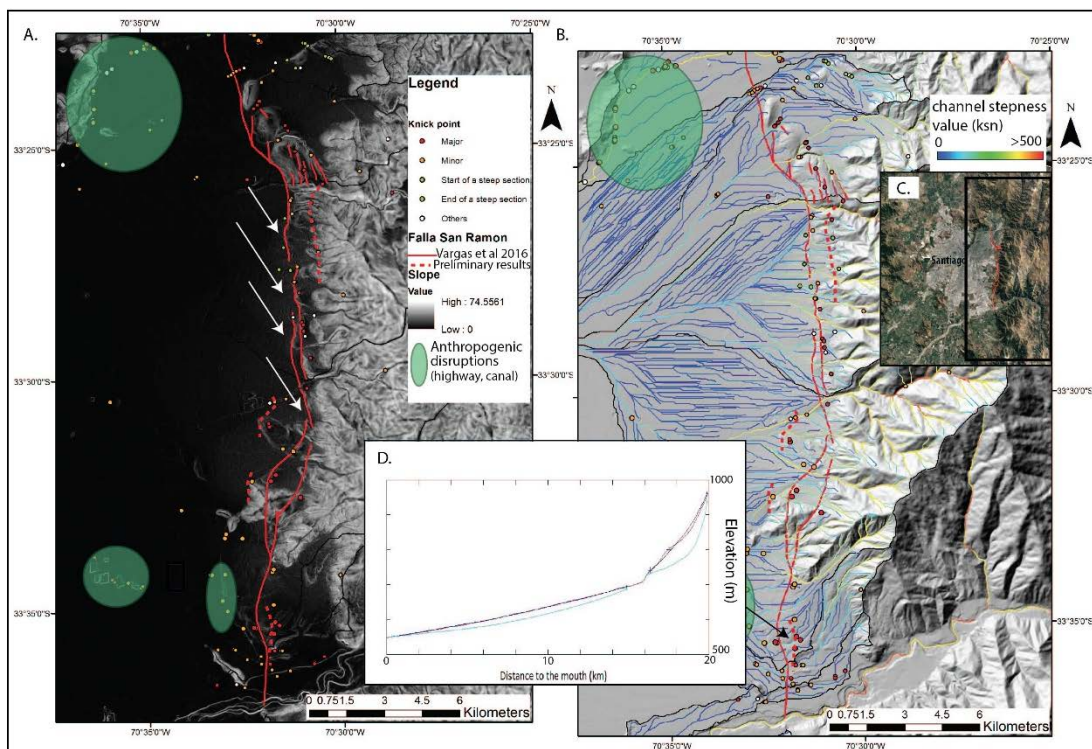


Figure 2: Slope analysis (A) and steepness channel value (B) close to the trace of the San Ramon Fault. Knickpoints are indicated by circles. Arrows (A) display the important slope along the trace of the fault. Green ellipses indicate knickpoints resulting from anthropogenic activity. (C.) Overview of the studied area. (D) An example of a stream longitudinal profile. Smoothed elevation is in pink. The dark blue lines are the profiles predicted by the regressed channel concavity. The cyan lines are for the specified reference concavity. The plusmarks along the profile indicate the locations of user-specified knickpoint positions.



In addition to the knickpoints linked to the trace of the San Ramón fault, upstream and sometimes downstream, additional knickpoints are observed (Fig.2). They are together with high channel steepness values while no change in the lithology is reported. We propose as preliminary result that they can reveal undiscovered strands of the San Ramón fault.

South of Santiago, the extent of the San Ramón fault has not been investigated yet. We used the stream profile analysis to look for any evidence, which could reveal geomorphological expressions of the fault at the surface.

High channel steepness values are identified at the mountain front in the Maipu river (Fig.3). These values may result from reduced erosional efficiency due to the presence

of Miocene Granites. Few knickpoints have been observed in the direct continuation of the current trace of the San Ramón fault. As no other knickpoints have been observed near the mountain front, we relate them to the potential ending of this segment of the fault.

Geographical distribution of the ksn values shown in Figure 3 presents high values near the mountain front. These values are linked to the change in lithology between Miocene Granite, the Tertiary Abanico Formation and the Alluvial deposits in the piedmont as well as to the change in the river regime.

However high channel steepness values are also observed in the western part of the studied area. Moreover the highest channel steepness values (purple rectangular in Figure 3 A.B. and D) are

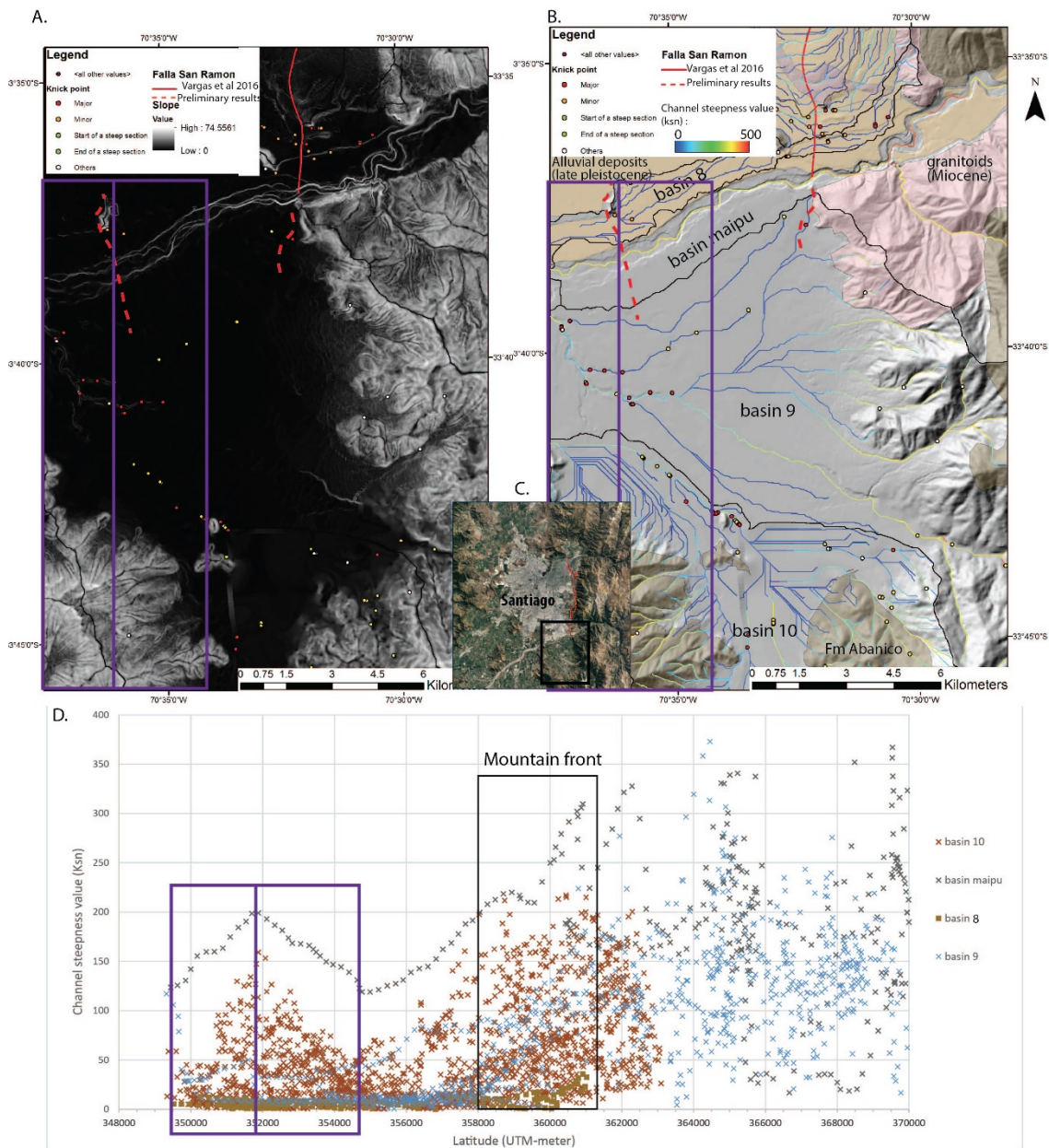


Figure 3: Slope analysis (A) and steepness channel value (B) close to the trace of the San Ramón Fault. Knickpoints are indicated by circles. (C) Overview of the studied area. (D) A graph represents the latitudinal distribution of the channel steepness values. Two peaks are observed, one around the mountain front and the second one westward.



located in almost the same latitude as the hill right north to the Maipo River. The lithology of this hill has not been described in the bibliography and must be investigated. However, we can interpret as a preliminary result that this hill may be a fault scarp. It would represent a new segment of the San Ramon fault westward of the one already described.

Regarding the northern part of the studied area (north of Santiago - Fig.4), it is hard to make any interpretation of the geomorphological changes of the stream. Indeed, this area display a lot of alluvial deposits such as terraces, which can have climatic and/or tectonic origin and can induce knickpoints. A geomorphological map of the area and field trip studies should be done.

We finally present all the results of this study in Figure 4. East of Santiago the trace of the San Ramón fault has been completed. This fault ends near the mountain front slightly south to the Maipo River.

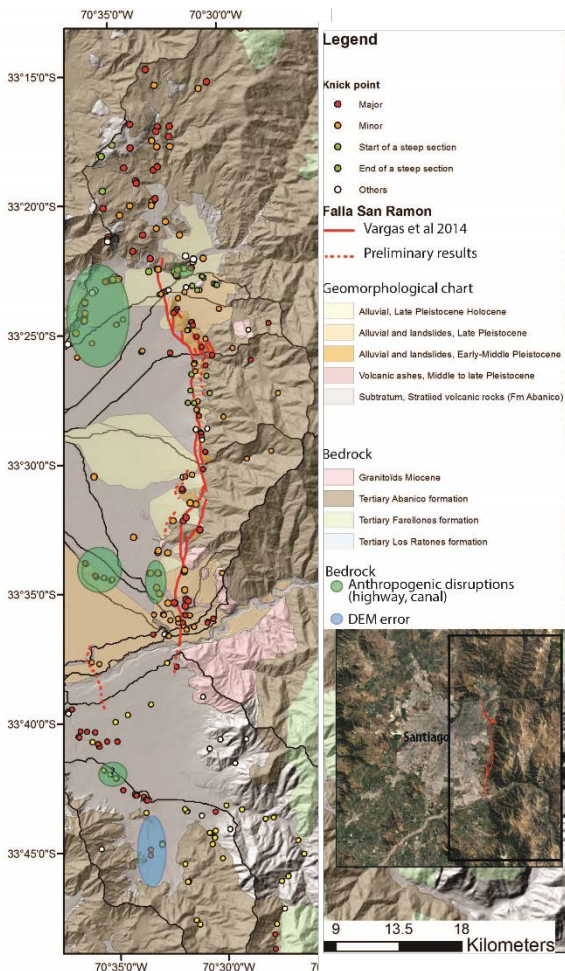


Figure 4: Geological map of the entire studied area with the trace of the San Ramón fault as mapped in the previous studies and in this study in dotted line.

Conclusion

The aim of this study was to examine the segmentation and the possible extension of the San Ramón Fault around Santiago. We showed that in a context of intensive

urbanization and without any quantitative data (e.g. differential GPS, surface dating), the study of geomorphologic parameters such as the slope or stream profile analysis brings a good first approach to reveal new fault segments and may guide future exploration. The geographical distribution of the k_{sn} values in the study area and/or the localisation of the knickpoints (Fig.4) reveal: 1) a probable segment of the fault south of Santiago, crossing the Maipo River and 2) other strands along the current San Ramón fault trace.

Acknowledgements: We acknowledge the project supporters “La Oficina Nacional de Emergencia del Ministerio del Interior” of Chile and the “Centro Sismológico Nacional” de Chile.

REFERENCES

- Armijo, R., Rauld, R., Thiele, R., Vargas, G., Campos, J., Lacassin, R., and Kausel, E., 2010, The West Andean thrust, the San Ramón fault and the seismic hazard for Santiago, Chile: *Tectonics*, v. 29, TC2007, doi:10.1029/2008TC002427.
- Bull, W.B., 1991. Geomorphic response to climatic change. *Oxford University Press*, 326p,
- Burbank, D.W. & Anderson, R.S. (2001) *Tectonic Geomorphology*, Blackwell Scientific, Oxford.
- Duvall, A., Kirby, E., & Burbank, D., 2004. Tectonic and lithologic controls on bedrock channel profiles and processes in coastal California. *Journal of geophysical research*, volume 109
- Flint, 1974. Stream gradient as a function of order, magnitude, and discharge. *Water Resource Journal*. Volume 10, Issue 5, Pages 969–973. DOI: 10.1029/WR010i005p00969
- Hack, J.T., 1957, Studies of longitudinal stream profiles in Virginia and Maryland: *U.S. Geological Survey Professional Paper 294-B*, p. 42–97.
- Holbrook, J. M. & Schumm, S.A. (1999) Geomorphic and sedimentary response of rivers to tectonic deformation: A brief review and critique of a tool for recognizing subtle epeirogenic deformation in modern and ancient settings, in Special issue on *Tectonics of Continental Interiors*. *Tectonophysics*, 305, 287-306
- Kirby, E., & Whipple, K., 2001. Quantifying differential rock-uplift rates via stream profile analysis. *Geology*. Volume 29 (5), 415-418
- Lague, D. (2014) The stream power river incision model: evidence, theory and beyond. *Earth Surf. Process. Landforms*, 39, 38–61.
- Rauld, R.A. 2011. Deformación Cortical y Peligro Sísmico Asociado a la Falla San Ramón en el Frente Cordillerano de Santiago, Chile Central (33° S). Tesis de grado para optar al grado de doctor en ciencias mención geología. Universidad de Chile, Departamento de Geología: 311 pp.
- Snyder, N., Whipple, K., Tucker, G. & Merritts, D. (2000) Landscape response to tectonic forcing: DEM analysis of stream profiles in the Mendocino triple junction region, northern California. *Geological Society of America Bulletin*, 112 (8), 1250-1263.
- Vanlaningham, S., Meigs, A. & Goldfinger, C. (2006) The effects of rock uplift and rock resistance on river morphology in a subduction zone fore-arc. *Earth Surface Processes and Landforms*, 31, 1257-1279.
- Vargas G., Rauld R., Forman S.L, Klinger Y., Rebolledo S., Rockwell T., Antinao J-L., Gosse J., Lacassin R., Armijo R., 2016. The San Ramon Fault at the eastern border of Santiago city, Chile: paleoseismological implications from the linkage between piedmont units and fluvial terraces. 7th International INQUA Meeting on *Paleoseismology, Active Tectonics and Archeoseismology (PATA)*.
- Vargas, G., Klinger, Y., Rockwell, T.K., Forman, S.L., Rebolledo, S., Baize, B., Lacassin, R., Armijo, R. 2014; Probing large intraplate earthquakes at the west flank of the Andes. *Geology*; 42 (12): 1083–1086. doi: <https://doi.org/10.1130/G35741>



Geomorphic and Paleoseismic Investigation of a Prominent Secondary Strand of the San Andreas Fault in the Carrizo Plain: Implication for Rupture Complexity

Akciz, S. (1) and Grant Ludwig, L. (2)

- (1) California State University Fullerton. sakciz@fullerton.edu
(2) University of California, Irvine

Abstract: Along one of the straightest and narrowest sections of the San Andreas Fault in the Carrizo Plain, between Wallace Creek and Bidart Fan, is a secondary fault that cuts late Holocene sedimentary deposits. We excavated two paleoseismic trenches across this fault trace to confirm prior surface rupture and investigate recency and style of deformation. Trenches revealed distinct stratigraphy which included fissures, upward termination of faults, vertical apparent offset, lateral unit thickness changes, and colluvium wedges, exposing evidence for at least five, and possibly six, surface rupturing earthquakes. Calibrated radiocarbon dates from accelerator mass spectrometer analysis of detrital charcoal indicate that these five earthquakes occurred since ~2,900 B.C. The two youngest ruptures occurred within the last 1650 years (since ~360 A.D.) with the most recent rupture presumed to have occurred in 1857. Compared to the paleoseismic record at the Bidart Fan site, which is approximately 350 m to the SW, almost all of these earthquakes (with the possible exception of the MRE) are much older, and if the record of ruptures is complete, the recurrence intervals are an order of magnitude longer than the main strand of the San Andreas (< 100 yrs vs. 900 yrs). A small ephemeral inner fan channel approximately 2 m wide and 0.5 m deep with a very sharp right-lateral bend is interpreted to have been displaced during 1857 Fort Tejon earthquake and contributed approximately 1.5 m of slip to the main displacement that occurred along the main strand. Whether this secondary strand ruptures only during large magnitude earthquakes, or earthquakes with nearby epicenters, or only during ruptures with a particular rupture directivity remain to be resolved with future investigations.



Post-earthquake rapid assessment using Unmanned Aircraft Systems (UAS) and GIS online applications: the case of Vrissa settlement after the 2017 June 12, Mw 6.3 Lesvos earthquake (North Aegean Sea, Greece)

Antoniou, Varvara (1), Andreadakis, Emmanouil (1), Mavroulis, Spyridon (1), Spyrou, Nafsika-Ioanna (1), Skourtsos, Emmanuel (1), Lekkas Efthymios (1), Carydis, Panayotis (2)

(1) Department of Dynamic Tectonic Applied Geology, Faculty of Geology and Geoenvironment, School of Sciences, National and Kapodistrian University of Athens vantoniou@geol.uoa.gr.

(2) National Technical University of Athens.

Abstract: Vrissa settlement was devastated by the Mw 6.3 earthquake generated offshore southern Lesvos. A rapid damage assessment was implemented during the first post-disaster hours. (a) Building-by-building inspection, upload of points and photos of damaged buildings to ArcGIS online platform, so that all interested agencies have access to critical information, and (b) construction of a detailed 3D model of the settlement with the use of UAS and appropriate software were performed. A point cloud, a mosaic orthophotomap, a Digital Surface Model, a Digital Terrain Model and a 3D model of the settlement were created. Objects were isolated and large trees, poles, etc. were excluded, resulting in a raster containing all building surfaces, edited manually thereafter. Damage assessment was re-run applying field observations, and editing errors of the field work. The products involve detailed topography with and without objects, vulnerability class polygons and damage grade for further processing and application of EMS-98.

Key words: drones, UAS, GIS online, earthquake, damage assessment.

INTRODUCTION

Vrissa settlement was the most affected by the Mw 6.3 earthquake generated offshore southern Lesvos (North Aegean Sea, Greece, June 12 2017). Being further inland from the epicentre than other settlements with less damage, Vrissa seemed like an impact paradox. Moreover, first reports referred to major destruction at the local scale. Thus, a rapid damage assessment with the highest possible detail was implemented during the first post-disaster hours, as follows: (a) Building-by-building inspection, upload of points and photos of damaged buildings to ArcGIS online platform, so that all interested agencies have access to critical information (<http://arcg.is/2sPnlrf>) and (b) Construction of a detailed 3D model of the settlement with the use of UAS (DJI Phantom 4 Pro) and appropriate software (Pix4D) were performed in order to capture all impacts with maximum accuracy before any intervention of competent civil protection agencies. Field observations were readily available for first remarks about damage distribution, in addition to preliminary mapping (Lekkas et al., 2017). At first sight, it was apparent that local intensity at Vrissa had a higher scale of damage than the rest of the meizoseismal area, and the earthquake was devastating for this settlement. For this reason, it was decided to study the area in the greatest possible detail, and quantify all damage so that reliable conclusions would be drawn about local intensity.

In recent years, there has been a transition of remote sensing applications for disaster management, from satellite imagery to UAV (UAS) acquired imagery, from monitoring to impact assessment, to Search and Rescue, etc. Tiered reconnaissance has been implemented as

early as in the 2003 Iran (Bam) earthquake and the Indian tsunami of 2004, for regional (Tier 1), neighbourhood (Tier 2) and per-building (Tier 3) scales (Ghosh et al., 2007). Drones, UAV or UAS (Unmanned Aircraft Systems) can be very useful for Tiers 2 and 3, because they can be rapidly deployed, explicit and fly on demand. Apart from SAR operations, and especially in the case of disaster impact assessment, UAS have become increasingly popular and effective in many case studies concerning hydro-meteorological disasters e.g. hurricanes and typhoons (Lessard-Fontaine et al., 2016), or earthquakes (Dell'Acqua & Gamba, 2012; Erdik et al., 2014) while background and thorough studies have been published (Fernandez Galarreta et al., 2015). Herewith an application of online GIS and UAS deployment was put into action for rapid damage assessment in a rather small area of a Greek island hit by an earthquake with extreme local intensity characteristics.

MATERIALS AND METHODOLOGY

Online GIS

A Geographical Information System, ArcGIS platform from ESRI Company, with both desktop and online applications, was used to accomplish this study. The creation of information layers, including existing and new data, has been performed through ArcMap v. 10.5 software ("ArcGIS for Desktop – ArcMap," n.d.). In addition, ArcGIS Online has been used for the creation of the online map (webmap) on which collected data would be presented. Finally, Collector for ArcGIS, ("ArcGIS Collector," n.d.), both compatible with Android and iOS, has been used for the data collection. This



application gives the opportunity to collect and update spatial and descriptive data through mobile devices (tablets or smartphones) on pre-set base maps. It was selected for its functional characteristics, which are of high importance in rapid assessment. During field research in Vrissa, the team uploaded locations and photos of damage to Collector for ArcGIS, which were accessible to the public and all interested parties (researchers, authorities, the press, etc.) as an ongoing update via an ESRI Story Map configured for this purpose (Figure 1).

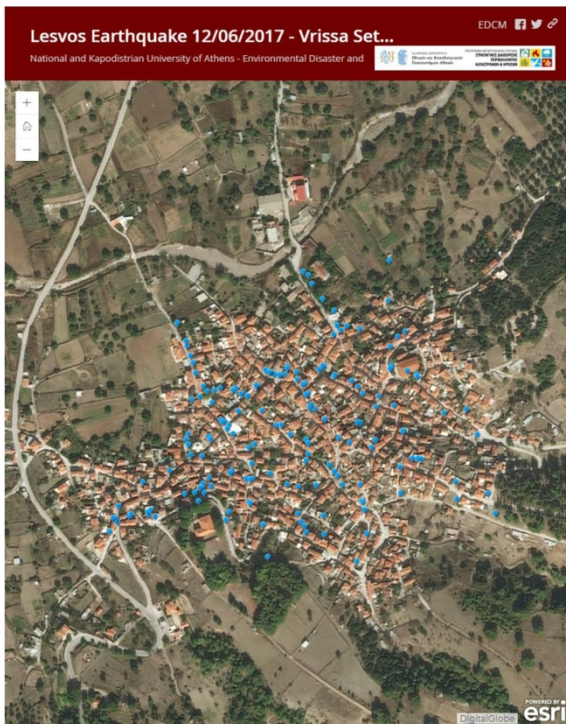


Figure 1: Through ESRI Basic Story Map collected locations of damaged buildings and respective photos and videos were made available, real time, to the public.

UAS deployment and processing of data

The type of Unmanned Aircraft System used was a Phantom 4 Pro tetracopter by DJI, deployed by the research team of the Department of Geology and Geoenvironment of the National and Kapodistrian University of Athens. Deployment took place starting the day after the earthquake, June 13th 2017 and was carried out (for Vrissa) during that day. The UAS performed two flights designed for 3D modeling, that is, scanning the area along two sets of corridors perpendicular to each other, at a height of 90m above the ground in the research area. Moreover, real-time streaming of video was transmitted via YouTube so that an overview could be obtained by interested viewers.

The flight areas were overlapping so that they would be intercalibrated (Figure 2). 440 images of Vrissa were acquired, and they were input for processing in the Pix4DMapper Pro software. Processing in Pix4D software created a point cloud, a Digital Surface Model (Figure 3), a Digital Terrain Model (Figure 4), a mosaic

orthophoto map (Figure 5) and a 3D model of the settlement. The difference between the two raster surfaces, DSM and DTM, is the recognized objects: trees, buildings, cars, etc. The settlement is a traditional village over a century old, also declared as preservable by the government. This means that architecture is uniform throughout, and buildings have a certain type and form. This uniformity essentially enables the categorization of objects into three groups, the ranges of building heights, and the shorter and taller ones. After subtracting DTM from the DSM, the resulting raster (Figure 6) contained only recognizable objects, which were then grouped into the three mentioned groups, and more specifically, building range between 2.5m and 10.7m tall, shorter and taller. In order to refine and reassess damage grades, all objects above ground surface were isolated. Then, adjusting the histogram of the objects raster, large trees, poles, etc. were excluded, resulting in a raster containing all building surfaces and some of the trees, which were then converted to polygons in ArcMap v. 10.5 and finally edited manually.



Figure 2: Camera positions during the flights of the DJI Phantom 4 Pro over Vrissa village, deployed on June 13th (the day after the earthquake).

Damage assessment was re-run on final building polygons, applying field observations, but also editing errors of the field work, revisiting the site through 3D model and with use of all footage available for any point on demand. Field observations were then assigned to the new polygons, while a review of damage grade and vulnerability class took place, using all 440 images. Once for every point of the model there is a number of images from different angles, field observations were actually supplemented by aerial observations.

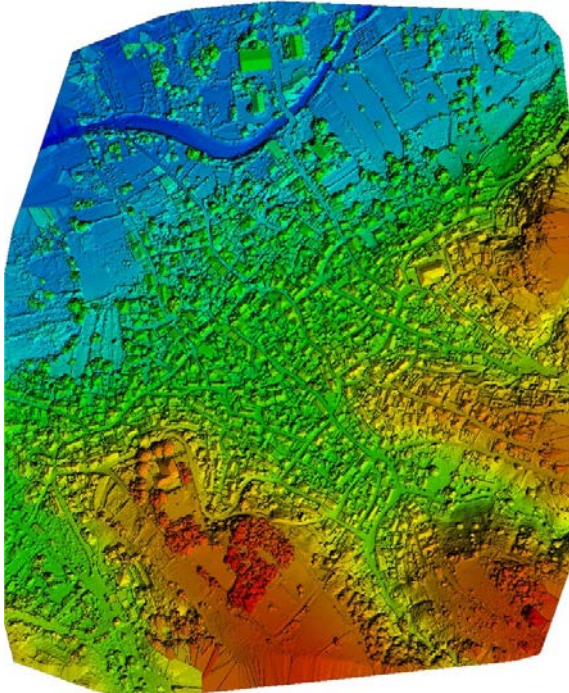


Figure 3: Digital Surface Model (processed with Pix4D Mapper Pro software).



Figure 5: Orthophoto Map (orthomosaic) processed with Pix4D Mapper Pro Soft software.

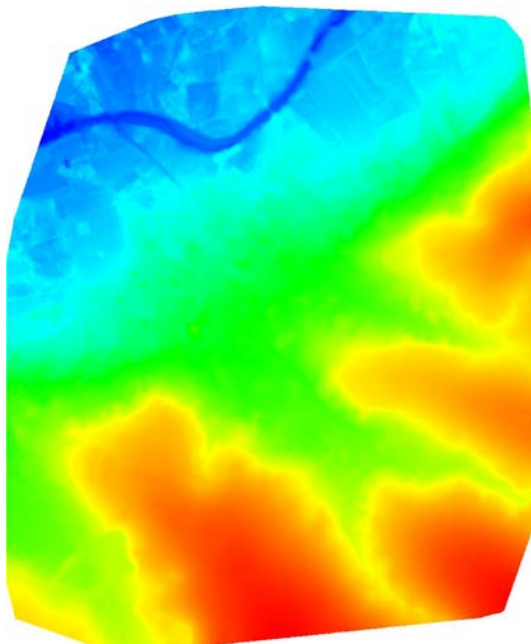


Figure 4: Digital Terrain Model (processed with Pix4D Mapper Pro software).

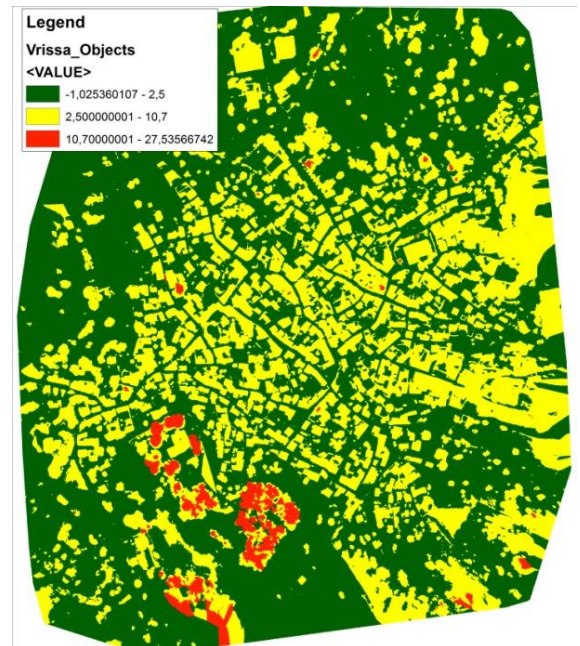


Figure 6: Classified object raster into three categories (lower than building range-green, building range-yellow and higher than building range-green).



RESULTS

The resulting damage assessment is shown in the last two figures. This detail and spatial distribution allows for calculations of damage grade percentages and classification of areas with similar statistics of damage grade, and zonal application of the EMS98 intensity scale (Grünthal, 1998) in the area. Herewith, classification of buildings according to the EMS 98 vulnerability classes is presented (Figure 7). Because the majority of buildings (>99%) belong to C Class, a map presenting damage grade of C class vulnerability buildings is shown (Figure 8). Most of the high grade damage is concentrated in the flat northwestern part of the village, consisting of loose alluvial sediments, along the terraces of the nearby river (visible at the north part of all maps). Application of EMS 98 for intensity map follows in next paper.

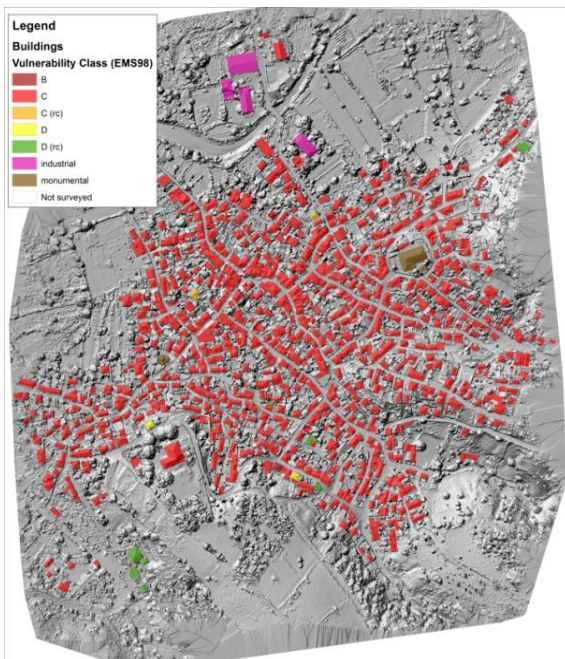


Figure 7: Final edit of building polygons, according to the EMS98 vulnerability classes.

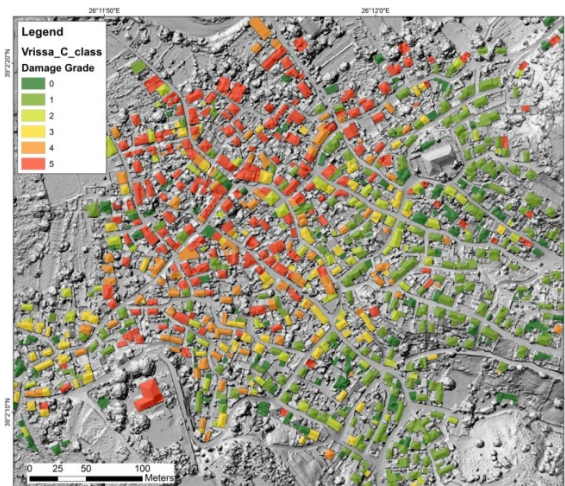


Figure 8: C Class building damages in Vrissa over the DSM hillshade.

CONCLUSIONS - DISCUSSION

Neighbourhood and building by building scale damage assessment can be made quite rapidly with the aid of online GIS and UAS. Acquisition of a detailed model of the site along with DSM, DTM, orthomosaic and numerous oblique aerial images helps rapid evaluation and savings of a lot of data immediately after the disaster, for further and more thorough processing. Depending on the equipment and the operations at the site, weather and obstruction of aerial aid can be an issue. It has to be noted that be it research or emergency operations, safety comes first, so all safety regulations must be respected, otherwise scientific and operating personnel could be put in danger. All air traffic at disaster sites must be declared, licensed and monitored by the authorities.

Acknowledgements: All equipment and funding for this work were provided by the Environmental, Disaster and Crisis Management Strategies Master's Degree Program of the Department of Geology and Geoenvironment of the National and Kapodistrian University of Athens.

REFERENCES

- ArcGIS Collector. (n.d.). Retrieved from <https://goo.gl/KoBxzn>
- ArcGIS for Desktop – ArcMap. (n.d.). Retrieved from <https://goo.gl/OPVwsG>
- Dell'Acqua, F., & Gamba, P. (2012). Remote sensing and earthquake damage assessment: Experiences, limits, and perspectives. *Proceedings of the IEEE*, 100(10), 2876–2890. <http://doi.org/10.1109/JPROC.2012.2196404>
- Erdik, M., Sesetyan, K., Denircioglu, M. B., Zulfikar, C., Hancilar, U., Tuzun, C., & Harmandar, E. (2014). Rapid Earthquake Loss Assessment After Damaging Earthquakes. In A. Ansal (Ed.), *Perspectives on European Earthquake Engineering and Seismology: Volume 1, Geotechnical, Geological and Earthquake Engineering 34* (Vol. 1, pp. 53–96). <http://doi.org/10.1007/978-3-319-07118-3>
- Fernandez Galarreta, J., Kerle, N., & Gerke, M. (2015). UAV-based urban structural damage assessment using object-based image analysis and semantic reasoning. *Natural Hazards and Earth System Sciences*, 15(6), 1087–1101. <http://doi.org/10.5194/nhess-15-1087-2015>
- Ghosh, S., Adams, B. J., Womble, J. A., Friedland, C. & Eguchi, R.T. (2007). Deployment of Remote Sensing Technology for Multi-Hazard Post-Katrina Damage Assessment. In *The 2nd International Conference on Urban Disaster Reduction*. Taipei, Taiwan. Retrieved from <https://goo.gl/iu6wfv>.
- Grünthal, G. (1998). *European Macroseismic Scale 1998 (EMS-98)* (Cahiers du Centre Européen de Géodynamique et de Séismologie European) (Vol. 15). Luxembourg.
- Lekkas, E., Voulgaris, N., Karydis, P., Tselentis, G. A., Skourtsos, E., Antoniou, V., ... Chouliaras, G. (2017). *Lesvos Earthquake Mw 6.3, June 12, 2017, Preliminary Report*. Athens.
- Lessard-Fontaine, A., Alschner, F., & Soesilo, D. (2016). *Drones in Humanitarian Action - Case Study No. 6: Rapid Damage Assessments of Tabarre and Surrounding Communities in Haiti following Hurricane Sandy*. Geneva, Switzerland. Retrieved from <https://goo.gl/sTUI5>



New evidence of active faulting in the Western flank of the Central Chilean High Andes, Metropolitan Region.

J. Araya (1), G. De Pascale (1), M. Persico (1), F. Sandoval (1), A. Serey (1), S. Sepulveda (1), M. Froude (2), D. Petley (2), W. Murphy (3)

- (1) Department of Geology, University of Chile, Santiago, Chile
(2) Department of Geography, University of Sheffield, Sheffield, UK
(3) School of Earth and Environment, University of Leeds, Leeds, UK

Abstract: The Chilean Central High Andes between 33° and 34°S is an active mountain range. At the continental intraplate zone, crustal faults are partially responsible for recent and current uplift of this orogen. These crustal structures are potential seismic sources that threaten nearby populated cities. The objective of this work is to identify active crustal faults using remote sensing and field work to further determine the potential seismic hazard for Santiago. Fault rocks such as gouge, cataclasite and breccia, as well as geomorphic features, like fault scarps and lineament have revealed previously un-identified active crustal faults in the western flank of the central Andes and also extend some previous fault traces.

Key words: Crustal faults, seismic hazard, Santiago de Chile, landslides.

INTRODUCTION

Santiago de Chile is at approx. 500 m above sea level to the west of the Andean mountain range that are up to ~ 7,000 m here in the Central High Andes. Important shallow seismicity characterized the intraplate cordilleran area (Barrientos et al., 2004). These seismic events along crustal faults contribute to the uplift of the orogenic belt and modification of the mountain relief. Unfortunately, the ground shaking related to earthquakes at shallow depths could be very dangerous and can also trigger large landslides. To reduce the associated risk of these natural disasters, the need to characterize the earthquake potential of individual faults is of importance during a seismic hazard analysis.

Numerous crustal faults are located near Santiago, but only a few were proven as active Quaternary structures (Figure 1). Lavenu and Cembrano (2008) show geological evidence south of San José de Maipo of a fault deforming a quaternary fluvial terrace of de Maipo River. Other works show that the San Ramon Fault is a reverse west verging active crustal structure just at the foothills of the Andean mountain front (e.g. Armijo et al., 2011; Rauld Plott, 2011; Vargas et al., 2014). Seismic hazard analysis demonstrated that the San Ramon Fault is an important source for geological hazards (Perez et al., 2014; Estay et al., 2016).

Although the San Ramon Fault appears to be an active structure, what other faults that may be active here? Because of the geodynamic of this subduction margin and the present day cordilleran structural style, we expect to find other structures that contribute to the present elevation and topography of the Central Andes, similar as the San Ramon Fault.

This work shows the preliminary result of a neotectonic study that present evidence of active faults as potentially seismic sources.

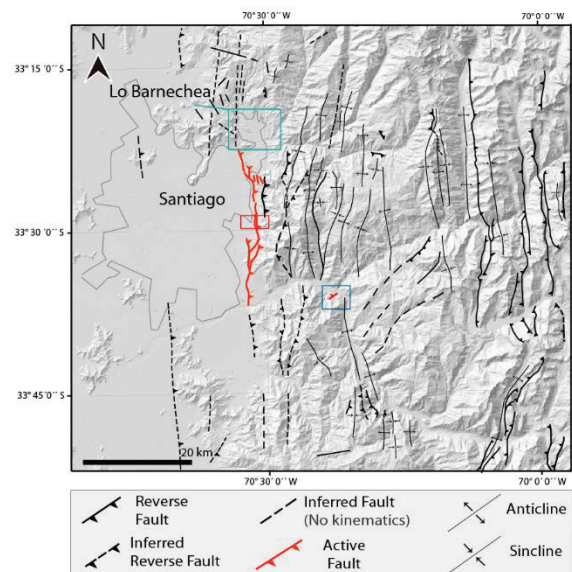


Figure 1: Compiled structure map of the Metropolitan Region. Own elaboration. Green box show Lo Barnechea, red box shows Vargas et al. (2014) trench and blue box shows Lavenu and Cembrano (2008) fault.

RESULTS

Compilation map of structures shows concentrations of reverse faults in both flanks of the Chilean Andes (Fig. 1).

Looking for a possible prolongation of the San Ramon Fault system to the north, field work in the Estero Arrayan, shows a clear 2 m wide fault zone striking 290°/70N, characterised by fault rocks including gouge, beccia, and cataclasite. This fault shows rocks of the Abanico Formation (late Eocene to early Oligocene) in both sides of the fault with different dipping beds (Fig. 2). Regional topographic expressions suggest a reverse (up to the north) mechanism for this fault. We will name this as the "El Arrayan Fault".



Figure 2: Outcrop interpretation of the fault in Lo Barnechea which shows a reverse SW verging fault (up to the North).

In Lo Barnechea, in order to investigate the surface expression of this fault, a slope map, created in ArcMap using a 12 m spatial resolution DEM from ALO SPALSAR (Fig.3), and topographic profiles in Google Earth (Fig.4), shows drastically slope changes (around 3-7°) alienated in a WNW-ESE direction. The profiles P2, P3 and P4 are located on an alluvial fan of quaternary age (Wall et al., 1999).

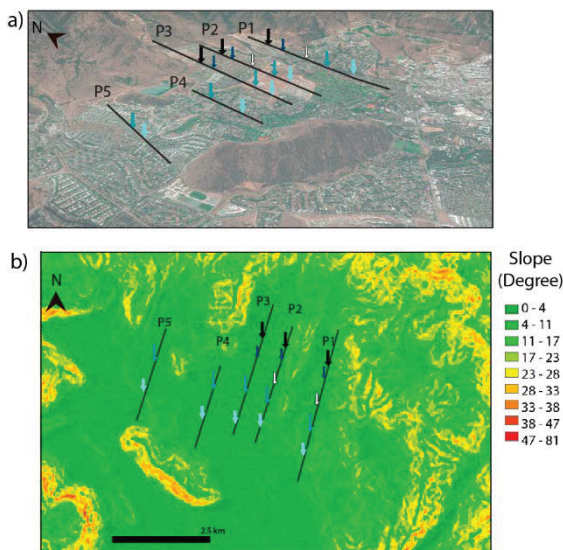


Figure 3: a) Image showing the location of the topographic profiles done in Lo Barnechea. b) Slope map of Lo Barnechea and topographic profiles. Color arrows show the slope breaks location. Alienated features are marked by arrows of the same color.

About 60 km to the north of Santiago, at the eastern limit of the Central Depression of Los Andes-San Felipe, it is possible to observe the surface expression of the Cariño Botado Fault (Troncoso, 2015; Fig 3a). New field mapping shows a west verging reverse fault with Abanico Formation bedrock thrust over Quaternary alluvium north of the Estero San Francisco, dipping 45° to the East. Gouge, breccia, and cataclasite are evidence of the fault here. 3D structural from motion (SfM) model was created by Argisoft based on drone aerial photographs, in order to better quantify the topographic features. The fault throw calculated is of about 2.5 m (Fig. 5b), based on the SfM. This model shows a 2-3 m topographic scarp aligned with the fault exposure north of the Estero San Francisco (Fig. 5c).

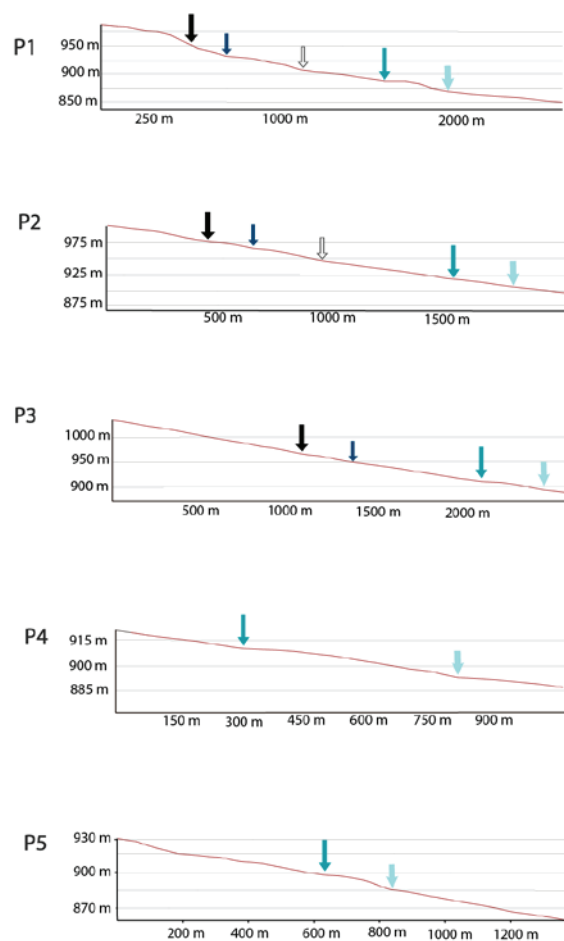


Figure 4: Detailed topographic profiles.

DISCUSSION

In Lo Barnechea the outcrop of the “El Arrayan Fault” it is along strike with the geomorphological lineaments present in the topographic profiles, suggesting a relationship between both features. The numerous slope breaks suggest that possibly more than one fault is responsible for the deformation observed, so we proposed that the drastically 3°-7° slope changes are fault scarps linked to activity of multiple splays of what should be “El Arrayan Fault system”, which has a length of at least 5 km. The quaternary age of the deformed alluvial fan evidence the recent activity.

The fault outcrop as well as the fault scarp located to the north of the northern end of the Cariño Botado Fault proposed by Troncoso (2015), suggests that the quaternary activity of the fault trace continuous to the north. Additional field work and morphometric analysis aims to better determine the full length of the fault trace.

These preliminary new results show that other faults in the region around Santiago appear to be active. The El Arrayan Fault system, as a first approximation, should be included in future seismic hazard models for Santiago because of it is located in the NE corner of the city, in particular, just beneath the Lo Barnechea, with a population of 97.230 habitants.

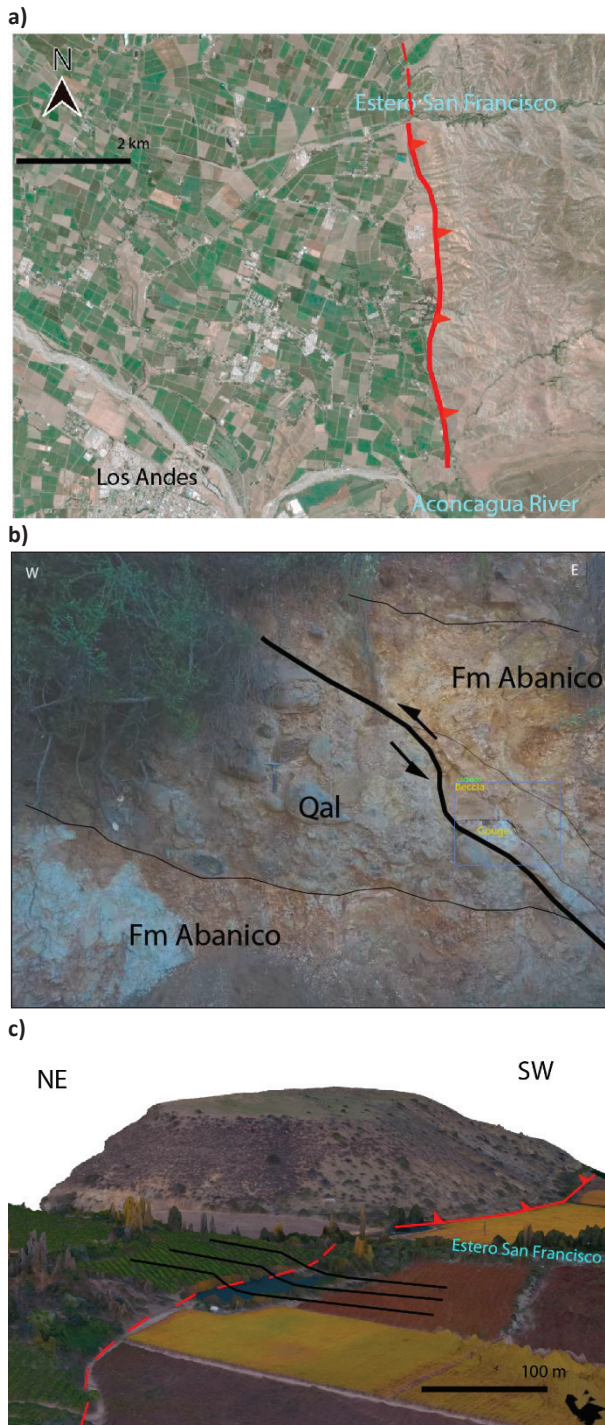


Figure 3: a) Cariño Botado fault trace near Los Andes. b) Outcrop photograph and interpretation of the Cariño Botado Fault. Photo shows overthrusting of rocks of the Abanico Formation over Quaternary alluvium (up to the east), hammer in Qal as scale. c) Sfm 3D model looking to the SE Sfm, showing the slope changes in black lines.

CONCLUSIONS

These preliminary new results show that previously unidentified faults in the region around Santiago appear to be active. The El Arrayan Fault system, as a first approximation, should be included in future seismic hazard models for the City of Santiago because of it is located in the NE corner of the city, along the range front of the Andes and an event here would be well-situated to trigger landslides that may impact people and infrastructure.

Acknowledgements: Thanks to NERC and Conicyt (Newton Fund) project NE/N000315/1 "Seismically-induced landslides in Chile: New tools for hazard assessment and disaster prevention". Thanks to Javiera Medina, Martin Mendez and Rodrigo Mardel for help in the field.

REFERENCES

- Antinao, J. L., & Gosse, J. (2009). Large rockslides in the Southern Central Andes of Chile (32–34.5 S): Tectonic control and significance for Quaternary landscape evolution. *Geomorphology*, 104(3), 117–133.
- Armijo, R., Rauld, R., Thiele, R., Vargas, G., Campos, J., Lacassin, R., & Kausel, E. (2010). The West Andean thrust, the San Ramon fault, and the seismic hazard for Santiago, Chile. *Tectonics*, 29(2).
- Barrientos, S., Vera, E., Alvarado, P., & Monfret, T. (2004). Crustal seismicity in central Chile. *Journal of South American Earth Sciences*, 16(8), 759–768.
- Estay, N. P., Yáñez, G., Carretier, S., Lira, E., & Maringue, J. (2016). Seismic hazard in low slip rate crustal faults, estimating the characteristic event and the most hazardous zone: study case San Ramón Fault, in southern Andes. *Natural Hazards and Earth System Sciences*, 16(12), 2511.
- Lavenu, A., & Cembrano, J. (2008). Deformación compresiva cuaternaria en la Cordillera Principal de Chile central (Cajón del Maipo, este de Santiago). *Revista geológica de Chile*, 35(2), 233–252.
- Pérez, A., Ruiz, J. A., Vargas, G., Rauld, R., Rebolledo, S., & Campos, J. (2014). Improving seismotectonics and seismic hazard assessment along the San Ramón Fault at the eastern border of Santiago city, Chile. *Natural Hazards*, 71(1), 243–274.
- Rauld Plott, R. A. (2011). Deformación cortical y peligro sísmico asociado a la falla San Ramón en el frente cordillerano de Santiago, Chile Central (33 S). *Tesis Doctoral, Universidad de Chile*.
- Sepúlveda, S. A., & Moreiras, S. M. (2013). Large volume Landslides in the central Andes of Chile and Argentina (32°–34°S) and related hazards. *Italian Journal of Engineering Geology and Environment - Book Series* (6).
- Troncoso, M., Pinto, L., & Vargas, G. (2015). Evidencia de neotectónica de la Falla Cariño Botado sobre la Zona de Falla Pucuro en la Provincia de Los Andes. *XIV Congreso Geológico Chileno*.
- Vargas, G., Klinger, Y., Rockwell, T. K., Forman, S. L., Rebolledo, S., Baize, S., Lacassin, R., & Armijo, R. (2014). Probing large intraplate earthquakes at the west flank of the Andes. *Geology*, 42(12), 1083–1086.
- Wall, R., Sellés, D. y Gana, P., 1999, Geología de la Hoja Santiago, área de Tiltill-Santiago, Región Metropolitana. Servicio Nacional de Geología y Minería, Mapa Geológico, v. 11.



Paleoseismological studies on Hinagu Fault, Kumamoto, Japan

Takashi AZUMA (Geological Survey of Japan/AIST)

Abstract: Geological Survey of Japan/AIST conducted paleoseismological trench surveys on the Hinagu fault zone before and after 2016 Kumamoto earthquake. Through the recent trench survey trench on the Takano-Shirahata segment, we reveal a ~15,000 years paleoearthquake history including 5 faulting events. The Recurrence interval of 3100-2800 yrs, and the long-term average uplift rate of 0.15-0.19 m/kyr were estimated. Coincidence of last events at Takaki, Yamaide, and Minamibeta suggests Takano-Shirahata segment and north of the Hinagu segment moved together at that time. We have also conducted trench and boring survey at Minamibeta area, Ogawa Town, Uki City. The latest event is estimated between 1948 to 1078 cal yBP. The average vertical displacement is about 0.4mm/yr. The latest activity of the Hinagu segment has been possibly occurred simultaneously with the adjacent Takano-Shirahata and Yatsushiro sea segment. In order to review the segmentation and simultaneous activity, it is necessary to do the field survey in the southern part of the Hinagu segment where is a blank area of field investigation.



First steps in assessing paleoseismic activity along the eastern boundary of the Upper Rhine Graben

Baize, Stéphane (1), Thomas, Jessica (2), Reicherter, Klaus (2), Seyfried, Hartmut (3)

- (1) Institut Radioprotection Sûreté Nucléaire, Seismic Hazard Division, Fontenay-Aux-Roses, FRANCE - stephane.baize@irsn.fr
- (2) RWTH, University of Aachen, GERMANY.
- (3) University of Stuttgart, GERMANY

Abstract: The Upper Rhine Graben is a large N-S structure inherited from the Oligo-Miocene extensional phase in Europe. It is now a moderately active area with steady seismicity (up to ca. M5) and strong historical events (M6.5+). To date, few studies have documented the paleoearthquake history of the structures that bound the graben, while the area encompasses critical facilities in a vulnerable region (dense population, agriculture, mining, geothermal facilities). Our project aims to fill this gap of knowledge in large and infrequent earthquakes, through a paleoseismological investigation of eastern side faults. Due to unfavourable conditions in terms of climate, low slip rates and high erosional/sedimentary rates, and human occupancy achieving this goal requires the use of a series of preliminary techniques to select appropriate trenching sites. We (will) use shallow and sub-surface geophysics (seismic reflection, electrical tomography, georadar), high-resolution LiDAR-derived DEM, shallow drilling and geological mapping. Here, we present the preliminary analysis of geophysical and geomorphological data that provide hints on potentially relevant places for future trenching (Karlsruhe, South Freiburg).

Key words: Paleoseismicity, Geomorphology, Shallow and Sub-surface geophysics, Central Europe.

INTRODUCTION

Characterizing seismic hazard at low probabilities of occurrence in moderately active areas requires information on the prehistoric earthquake recordings, beyond the duration of catalogues.

The Upper Rhine Graben (URG), and especially its southern section, has a significant network of potentially hazardous installations in a densely populated area and a vulnerable socio-economic environment (agriculture). Geological investigations are required to assess the safety of these facilities. Surprisingly, this region has rarely been investigated in terms of neotectonics and especially paleoseismicity: the most striking and successful studies were performed in the southernmost Basel region (Meghraoui et al. 2001) and along the western side of the URG (Strasbourg area: Lemeille et al., 1999; Mainz zone: Peters et al. 2005).

The primary objective of our project is to provide the first evaluation of paleoseismic activity of the fault(s) that bound the URG to the East. For this purpose, we are using complementary techniques to identify the best sites for trenching. The techniques include re-processing existing seismic lines, performing shallow geophysics, interpreting LiDAR data and geological maps, etc. Here are some of the preliminary results.

STRUCTURAL AND TECTONIC CONTEXT

Two European projects, EUCOR-URGENT (see International Journal of Earth Sciences Special Issue Volume 94, Issue 4, September 2005) and GeORG (<http://www.geopotenziale.org/>), provide geological framework, tectonic history and structure of the URG.

The URG is an inherited extensional mega-structure which formed, together with the Bresse (BG) and Limagne (LG) Grabens, the continental part of the Central European Cenozoic Rift System. Extension has stretched the crust over 5 km during the Oligo-Miocene times.

The Upper Rhine Graben provided accommodation space for deposition and preservation of Tertiary sediments (max. 5000 m in the northern part, around and north of Karlsruhe; 2500 m south of Freiburg) and is intensely sliced by post-Tertiary NNE-SSW faults. The internal parts of the URG include significant salt-bearing layers, giving rise to diapirs. Plio-Quaternary alluvial deposits are ~1000 m thick north of Karlsruhe (Mannheim), but only 250 m south of Freiburg. On the eastern side of the URG, alongside the Main Eastern Border Fault (also called Black Forest Fault in southern URG), Tertiary and Plio-Quaternary thickness maps suggest the pervasive activity of some "internal" structures, such as the Rhine River Fault. Nivière et al. (2008) proposed, based on morphological and borehole data, that this fault is active (<0.1 mm/a) and could generate M6.5+ earthquakes.

The current tectonic regime, with maximum horizontal stress striking NW-SE, imposes to the regional faults a prominent strike-slip regime, as shown by the focal mechanism (e.g. Edel et al., 2006). To date, large-scale regional GNSS network provides a maximum budget of horizontal deformation which cannot exceed 0.5 mm/y across the entire graben (Nocquet et al., 2012). The combined geodetic data (GNSS, InSAR and levelling) suggest local relative displacement in the order of 0.3 mm/y along the URG eastern border (Fuhrmann et al. 2015).



SELECTING THE RELEVANT TARGETS

To find out the right place(s) for trenches, we have to face a human-modified landscape in an active fluvial system: the Rhine River is the most powerful fluvial system of Central Europe. The sediment budget of this river changed drastically around the beginning of Quaternary when the URG started to drain the Alps (Preusser, 2008). During its most recent history (Late Pleistocene to Holocene), the valley floor was occupied by braided to meandering fluvial networks revealed in detail by high-resolution LiDAR data. Starting in the 19th century the Rhine River became progressively channelized to avoid flooding damage in this economically growing region. The combination of temperate climate, dense vegetation and low fault slip rates, however, makes localization of active faults a challenging task.

Our strategy is to develop a sound and robust pre-trenching analysis of the landscape and the graben infilling to select the appropriate site(s) where we can potentially expect the fault to cut surficial deposits. To do so, we first analyse several “industrial” seismic lines (on French and German sides) that potentially complement the European projects results. In addition, we use a very high resolution LiDAR dataset acquired by the Baden-Württemberg state, with a pixel resolution of 1 m and a vertical accuracy of 15 cm. Shallow geophysics (ground-penetrating radar (GPR), and electrical resistivity tomography (ERT), were also carried out on top of the possible fault lines inferred from seismic lines and DEM analyses.

FIRST RESULTS

Thomas et al. (2016) presented preliminary results of investigations in the Freiburg area (Denzlingen) during the 6th PATA Days in Crestone. Several geophysical anomalies were inferred, although these sub-surface deformation features have no imprint in topography. Other targets were also defined and investigated.

Karlsruhe

Figure 2 illustrates the optimal resolution of the LiDAR: besides human-made features, the LiDAR-derived DEM clearly reveals fluvial landforms. On each side of a linear scarp (a-b), the fluvial pattern is different, suggesting a braided system to the East and a single-channel system to the West. The interesting point is that the fluvial landforms are obliquely cut by a 5km long and 0.5 to 2m high scarp, suggesting a tectonic origin (which needs to be validated later-on). Alongside this recent scarp, the LiDAR-derived DEM emphasizes hanging valleys between spectacular triangular facets along the Black Forest Fault. Even if this part of the morphology might be partly inherited from the main extensional episode, we suspect that topography could have been rejuvenated during the Quaternary.

Freiburg

In the Freiburg area, we acquired three “industrial” seismic lines, two of them imaging the Rhine River fault (Figure 3). Shot in the 1980’s, we have re-processed and re-analysed them in the framework of the Project. The fault is located in the Triassic to Tertiary layers but poor sub-surface resolution prevents any sound interpretation of its occurrence in the Plio-Quaternary layer. The LiDAR-derived DEM of the area suggests vertical and horizontal offsets of several features at the surface: on Figure 4, the large Staufen alluvial fan is disrupted where the fault zone (Rhine River Fault) has been geophysically inferred (Figure 3). There also it appears that some alluvial-fan related features (such as tiny creeks and related slopes) could be displaced in the left-lateral sense. During the first months of the study, our team performed many GPR and ERT profiles across the projection lines of seismic reflection-inferred faults and across the rare scarps, to test the possible occurrence of deformation features at the ground surface (see Figures 3 and 4). However, most of the potential deformation features in the alluvial plain are buried beneath shallow sediments and could be difficult to excavate.

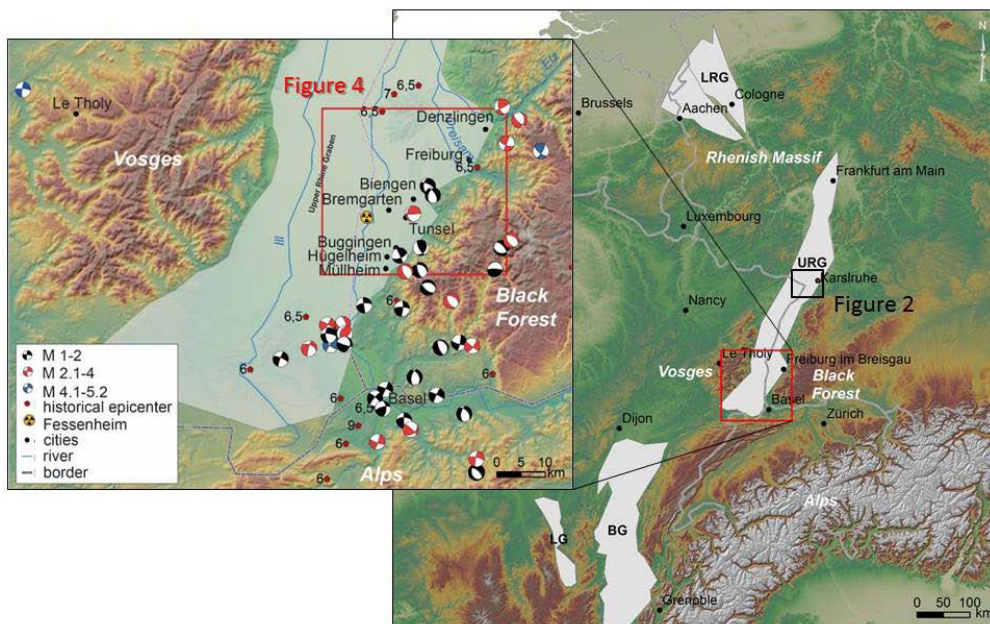


Figure 1: Location of the study area in the Central-South part of the Upper Rhine Graben (URG). This paper focuses on two specific zones of the study area, namely Karlsruhe (see text and figure 2 for more details) and Freiburg (see text and figures 3 and 4). Zoom in around Freiburg shows a set of focal mechanisms, mostly normal and strike-slip small earthquakes.



The ERT profile across the Tunsel scarp (Figure 4) highlights an anomaly at the top of the slope that could match a fault signature. In the Freiburg area, the Tunsel scarp could be the best candidate for future trenching.

CONCLUSION & FURTHER STEPS

To improve our understanding of the fault geometry from depth to the surface, we plan to reprocess other “industrial” seismic lines that were consulted at the Baden-Württemberg geological survey. A new analysis of the Plio-Quaternary horizon in the GeORG database, in cooperation with the French geological survey (BRGM), will be done to check the occurrence of other shallow “internal” faults. In cooperation with geophysicists of the University of Strasbourg, we plan to carry out light-equipment high-resolution seismic profiles where surface geology (loess) is prone to transfer seismic waves and yield sub-surface geometry. These data will complement the electrical tomography profiles in order to precisely locate the fault at depth and its shallowest tip.

The LiDAR topography is a huge source of relevant data that requires analytical time before interpreting the landscape (in terms of fluvial dynamics and neotectonics). The Tunsel area (Figure 4) is a promising site because the fault line seems to be preserved at the surface, and is a potentially good place for trenching and estimating the horizontal and vertical components of slip rate. In this same area, we will analyse the large Staufen alluvial fan and its history, through morphological analysis, geometrical reconstruction, as well as dating of landforms and associated sediments.

Acknowledgements: This study, including the PhD student grant and field work, is equally co-funded by IRSN and the University of Aachen.

REFERENCES

- Beckenbach, E., 2015. PhD Thesis, University of Stuttgart.
- Edel, J. B., et al., 2006. Seismicity wedge beneath the Upper Rhine Graben due to backwards Alpine push? *Tectonophysics* 428, 49-64.
- Fuhrmann, T. et al., 2015. Estimation of small surface displacements in the Upper Rhine Graben area from a combined analysis of PS-InSAR, levelling and GNSS data. *Geophys. J. Int.* 203, 614–631.
- Meghraoui, M., et al., 2001. Active Normal Faulting in the Upper Rhine Graben and Paleoseismic Identification of the 1356 Basel Earthquake. *Science* 293, 2070-2073.
- Nivière, B., et al., 2008. Active tectonics of the southeastern Upper Rhine Graben, Freiburg area (Germany). *Quaternary Science Reviews*, 27, 541-555.
- Nocquet, J. M., 2012. Present-day kinematics of the Mediterranean: A comprehensive overview of GPS results. *Tectonophysics* 579, 220-242.
- Peters, G., et al., 2005. Interplay between tectonic, fluvial and erosional processes along the Western Border Fault of the northern Upper Rhine Graben, Germany. *Tectonophysics* 406, 39-66.
- Preusser, F., 2008. Characterisation and evolution of the River Rhine system. *Netherlands Journal of Geosciences* 87, 7 – 19.
- Thomas, J., et al., 2016. The Southern Upper Rhine Graben: towards an active fault assessment. Extended Abstract, 7th INQUA PATA Days, Colorado, USA.

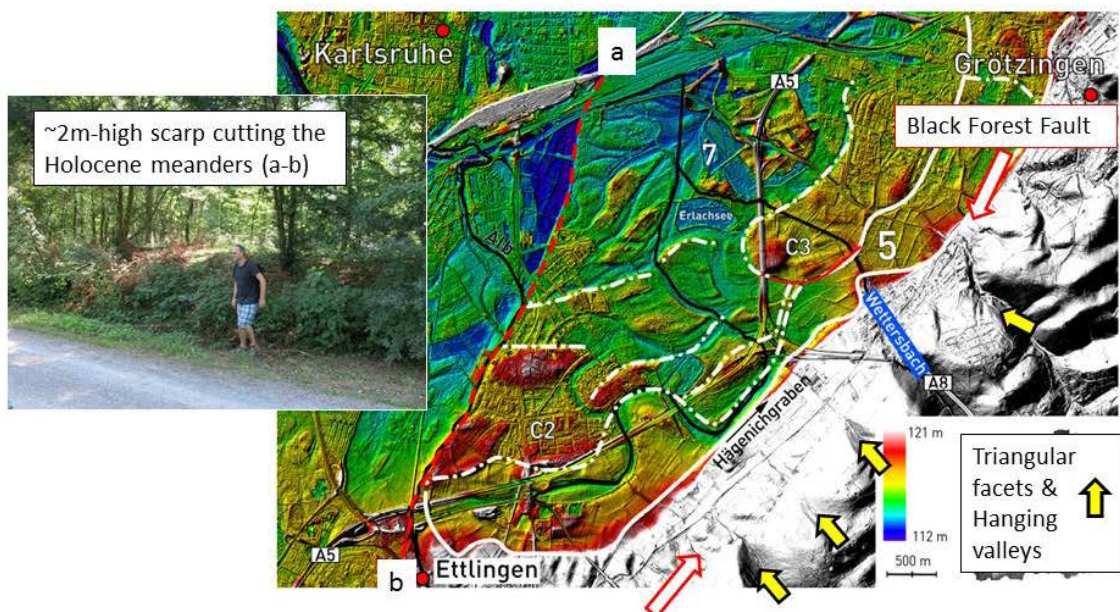
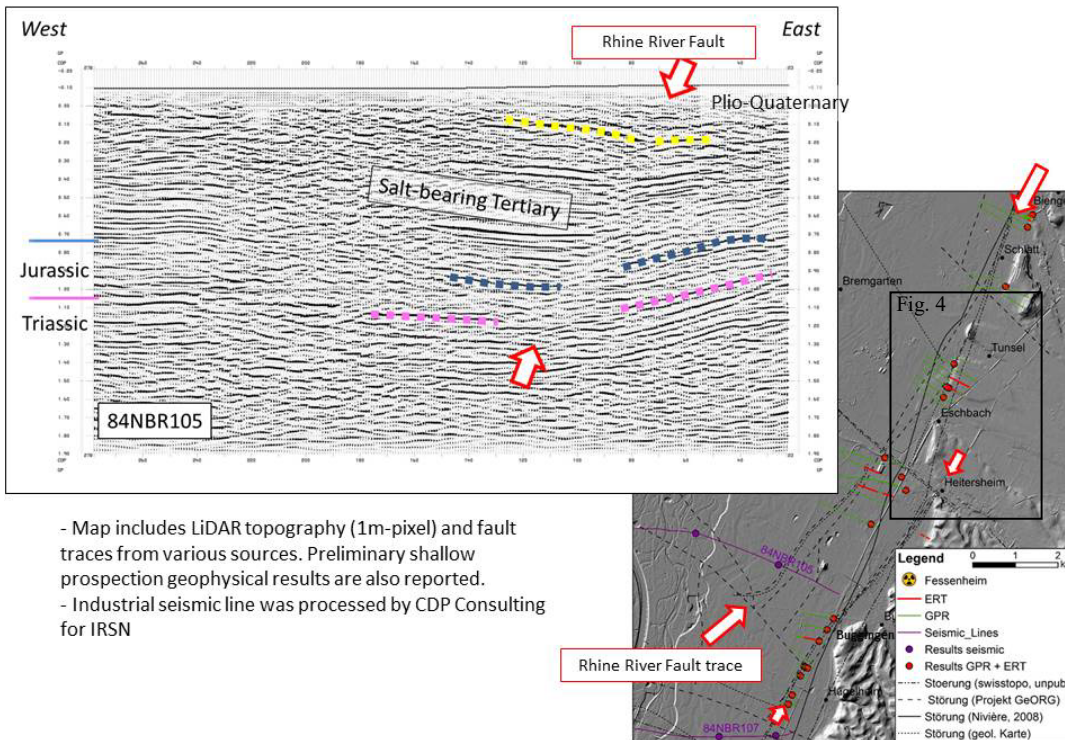


Figure 2: Nearby Karlsruhe hanging valleys along the Main Eastern Border Fault that bounds the URG to the East suggests recent activity. Several km inside the basin an outstanding 6 km long and 0.5 to 2 m high scarp (between ‘a’ and ‘b’) undercuts a Late Pleistocene valley fill (marked by white numbers and labels; figure adapted from Beckenbach, 2015). Inset shows field aspect in the northern part of the scarp.



- Map includes LiDAR topography (1m-pixel) and fault traces from various sources. Preliminary shallow prospecting geophysical results are also reported.
- Industrial seismic line was processed by CDP Consulting for IRSN

Figure 3: Example of “industrial” seismic line shot in the 1980’s, re-processed and re-analysed in the framework of the Project. This E-W section (84NBR105) intersects the Rhine River fault buried beneath the “recent” Rhine alluvium; this buried fault continues to the north and extends along the low relief escarpment in the Tunsel-Eschbach area (see figure 4). On the map, we indicate the “anomalies” inferred from deep (seismics) and shallow geophysics (ERT, GPR).

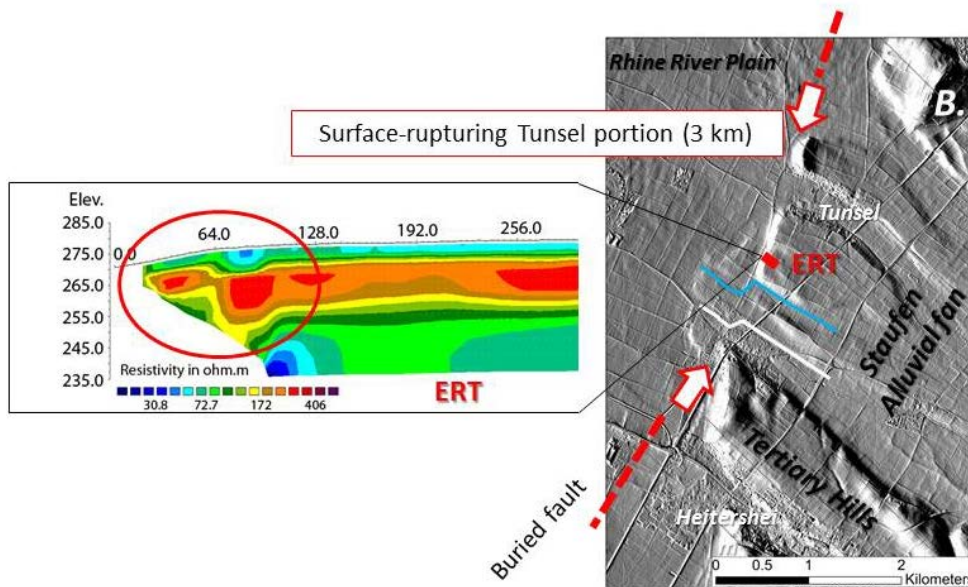


Figure 4: Detail of the Tunsel area, where the large Staufen alluvial fan is disrupted by the surface-breaking Tunsel portion of the Rhine River Fault. Several drainage features even seem to be left-laterally displaced. An ERT (electrical tomography) profile has been performed, showing an anomaly in its westernmost part (top of the slope). B.: outcrops of Jurassic limestones. DEM from 1m-pixel LiDAR data purchased to LGRB, Freiburg.



Towards a unified and worldwide database of surface ruptures (SURE) for Fault Displacement Hazard Analyses

Baize, Stéphane (1), Azuma, Takashi (2), Champenois, Johann (1, 3), Cinti, Francesca (4), Civico, Riccardo (4), Costa, Carlos (5), Dawson, Timothy (6), Elliott, Austin (7), Guerrieri, Luca (8), Klinger, Yann (3), Marti, Etienne (3), McCalpin, Jim (9), Okumura, Koji (10), Schwartz, David (11), Scotti, Oona (1), Takao, Makoto (12), Villamor, Pilar (13), Walker, Richard (7)

(1) Institut de Radioprotection et Sûreté Nucléaire - BP 17 – 92262 FONTENAY-AUX-ROSES – FRANCE. stephane.baize@irsn.fr; (2) GSI, Japan; (3) IPGP, France; (4) INGV, Italy; (5) U. San Luis, Argentina; (6) CGS, USA; (7) NERC-COMET, UK; (8) ISPRA, Italy; (9) Geo-Haz, USA; (10) U. Hirashima, Japan; (11) USGS, USA; (12) TEPCO, Japan; (13) GNS Science, New Zealand

Abstract: Fault Displacement Hazard Assessment is based on empirical relationships from historic fault ruptures. These relationships establish the likelihood of co-seismic fault displacements values, for on-fault (i.e. along the primary earthquake fault) and off-fault (i.e. distributed surface rupture off the primary rupture) displacements, for a given earthquake magnitude. These relationships are useful when trying to predict future fault displacements at, and close to an active fault, when surface rupture hazard is expected at a site (for land use planning and/or structural design of infrastructure and critical facilities located on, or close to, an active fault line). The current equations are based on sparsely populated datasets, including a limited number of mainly pre-2000 events. In 2015 an international effort started to constitute a worldwide and unified surface co-seismic displacements database (SURE) to improve further fault displacements estimations. To date, two workshops have been held and discussions on how to build such a database started. Outcomes from these discussions are: (1) the first step should be to unify the existing datasets; and (2) the future database will include recent cases which deformation have been captured and measured with modern techniques. New parameters which are relevant to properly describe the rupture will also be required. This common effort would imply a large and open community of earthquake geologists to create a free and open access database.

Key words: earthquake-related hazard, surface faulting, worldwide & unified database.

Fault Displacement Hazard Analyses (FDHA) aims to evaluate the likelihood of co-seismic surface fault displacement, for on-fault (i.e. primary/principal earthquake fault) and off-fault (i.e. distributed surface rupture off the primary rupture) displacements, for a given earthquake magnitude (Youngs et al., 2003). FDHA is based on empirical relationships from historic fault ruptures (Youngs et al., 2003; Moss and Ross, 2011; Petersen et al., 2011; Takao et al., 2013). These relationships are useful when trying to predict future fault displacements at, and close to, an active fault, when surface rupture hazard is expected at a site. In particular, these equations are useful for land use planning when new housing developments are to take place; and structural design of infrastructure and critical facilities when they have to be sited on, or close to, an active fault line (e.g., Chen & Petersen, 2011; NRC, 2012).

To date, these relationships are based on limited information from a few historical cases and on separated datasets (Youngs et al., 2003; Moss and Ross, 2011; Petersen et al., 2011; Takao et al., 2013). Earthquake geologists and practitioners have the shared opinion that the relationships need to be updated. To date, two meetings have been held (Paris, 2015, and Menlo Park, USA, 2016) to discuss future advances on FDHA with focus on the acquisition of data and development of a worldwide, publicly available, database for surface rupture data. Two main outcomes from those discussions in terms of improvements of such a database are the need for: (1) aggregating the existing datasets; and, (2) for clearly

defining the relevant parameters that should to be recorded when capturing future surface rupture data and adding it to the database.

THE AGGREGATION OF THE EXISTING DATASETS

Numerous co-seismic surface slip distributions along the seismogenic or “primary” earthquake fault exist (e.g. Lettis et al., 1997; McCalpin, 1998; Hemphill & Weldon, 1999; Wesnousky 2008; Biasi & Wesnousky 2016); however, information on “distributed” faulting off the primary rupture is only available for a few earthquakes (e.g., Pezzopane & Dawson, 1996; Petersen et al., 2011; Takao et al., 2013). In both cases, the existing datasets hold limited descriptions of the ruptures, including earthquake magnitude and sense of movement, geographic coordinates and net slip of measured locations. The surface rupture database of Pezzopane & Dawson (1996) encompasses 13 normal faulting events with some distributed faulting occurrences. The strike-slip surface rupture database from Petersen et al. (2011) contains 8 events with earthquake magnitude ranging from 6.5 to 7.6. The reverse surface rupture database compiled by Moss & Ross (2011) does not include any information on distributed ruptures; however, recent studies compiled distributed rupture information to derive regressions (Inoue et al., 2016) or fault avoidance setbacks (Boncio et al., 2017). Current FDHA regressions are robust and proven useful. However, because of the scarcity of rupture information that they are based on, we stress that aggregating databases into a uniform database (so-called SURE) and improving data



collection procedures is essential to produce revised empirical regressions in the short and long-term.

RELEVANT NEW PARAMETERS TO CHARACTERIZE SURFACE FAULTING

In addition to aggregating historical cases of existing datasets, modern cases should be implemented with additional information that describes comprehensively the surface rupture. Among the new parameters to be documented in the database, two of them will be included first: the geological nature of surficial layers and fault geometry complexity.

Surface Geology

The characteristic of the near surface geology influences the pattern of surface rupture, as exemplified by the 2010 El Mayor-Cucapah, Mexico earthquake (Teran et al., 2015). In this event, fault rupturing through basement rocks produced very narrowly localized deformation along discrete fault strands with each of fault plane accommodating large offsets. However, rupture through Quaternary gravels is more distributed by folding and/or discrete faulting on multiple strands with limited offsets. Sandbox models have further confirmed the importance of understanding the near surface material properties to predict the pattern and distribution of surface deformation at a study site. In those experimental results, the near-surface material stiffness is a crucial parameter that controls the rupture pattern and fabric (Stanton, 2013). In the database, we propose a basic classification (cover beds vs basement; basic sediment lithology) that can be very useful for predicting the type to rupture pattern and how deformation could be distributed at study site, as it would be easy to select examples from the database that are relevant to the study site. In the long term, specific regression for each near surface geology type may be developed.

Structural complexity

Discussions at the Paris and Menlo Park meeting highlighted the importance of understanding the structural pattern of a fault. By that we mean: whether the fault is represented by a main fault or several fault strands; whether the fault steps laterally to a different fault and/or there are gaps in the surface rupture; etc. This structural complexity influences, for example, the distributed faulting pattern. Distributed faulting does not have a uniform pattern and density along strike and is much more common at fault tips, step-overs, bends, and other geometric irregularities (e.g. 2010 EMC event: Fletcher et al., 2014; 2013 Balochistan event: Vallage et al., 2015). In very specific contexts such as compressional environments with flat and ramps, the “primary” surface rupture can be absent even for large magnitudes (e.g. 2015 M7.8 Nepal event: Grandin et al., 2015). In those cases, the main fault rupture does not reach the surface, but the surface can be deformed by folding. However, “distributed” ruptures could appear at the surface during such blind thrust earthquakes (e.g. 2004 and 2007 M6.5+ Chuetsu quakes, Japan), for instance with flexural slip or bending moment faulting.

To account for the different pattern that may appear in different types of fault segments, we propose to discretize segments in portions along the strike of historic surface ruptures. In this way, they can be analysed separately and be used to develop regression that are specific to the type of fault segment/section (e.g., step-over, fault termination, etc.)

IMPROVING THE CONTENT OF THE DATABASE: CONTRIBUTION OF NEW TECHNIQUES

Enriching the datasets

Modern techniques, such as SAR interferometry, LiDAR or SfM topography, have allowed the recognition of co-seismic deformation with much more detailed and with larger spatial extent for recent surface ruptures. For example, the geologist work was facilitated by the InSAR maps available during the early surface rupture mapping phase after the 2014 M6 Napa earthquake (DeLong et al., 2016). A large part of the moderate to small displacements could have been unnoticed by the field reconnaissance team without the support of satellite image analysis. The M5 26/3/2010 Pisayambo, Ecuador, earthquake rupture would not have ever been recognized without InSAR at all, in this remote and high-elevation region of the Andes (Champenois et al., 2017). Analysis of high resolution topographic maps derived from LiDAR imaging can provide accurate estimation of offsets, and a large amount of measured points along a fault, which is fundamental to appreciate the natural variability of surface faulting and to appropriately quantify uncertainties (Gold et al., 2013). Also, off-fault data is likely to be better detected in the recent and future events than previous ones (pre-INSAR and pre-LIDAR) thanks to these modern techniques.

It is possible that the improvement of detection capacity with modern techniques may attenuate the difference of surface rupture probability between Japan and western USA reported by Takao et al. (2013): these two active countries have very different morpho-climatic contexts that could largely have influenced the detection of historical surface rupture with classical mapping. Evidencing M5-6 earthquakes surface rupture is easier in southern California desert (e.g. Suarez-Vidal et al., 2007) than under the Japanese canopy. However, now with ALOS InSAR, subtle deformation features are measurable: see for instance the work of Fujiwara et al. (2016) who mapped distributed ruptures associated with the 2016 M7 Kumamoto earthquake under the Aso volcano forest.

Correlation of pre- and post-seismic optical images is another modern technique that has started to strongly support the acquisition of the earthquake-related deformation. This technique has been successfully applied to “historical” cases in California, demonstrating that a considerable part of co-seismic deformation was distributed off the major fault (Milliner et al., 2016). Klinger et al. (this issue) could map in detail the surface deformation associated with the 2016 M7.8 Kaikoura earthquake (NZ), using the sub-pixel correlator MicMac which provides reliable results especially in near-fault area.



Primary and distributed slip

Youngs et al. (2003) introduced two types of earthquake-related slip and derived two types of equations to calculate fault displacement hazard. Primary (or Principal) faulting is large and continuous slip, and represents movement along the main plane (or planes) that released seismic energy (Youngs et al., 2003). Distributed faulting is smaller, discontinuous slip, scattered over a wide zone, and that represents displacement on other faults in the soundings of the principal fault. Later on, Petersen et al. (2011) separated two kinds of off-fault slip: distributed (or secondary) slip which is “connected” to principal fault; and “non-connected” slip, which is triggered slip on distant faults. In their dataset, triggered slip is defined to have occurred beyond 2000 m from the main fault and the corresponding data were not included in their derived empirical regressions of off-fault slip with distance.

We propose that “triggered slip” should not be excluded from the surface displacement database. As stated by Petersen et al. 2011, “*adjacent faults are an important source of fault rupture hazard and should be considered in the analysis*”. Triggered slip would however be considered separately because it responds to a different process than secondary faulting. An important issue is to objectively define triggered slip, because we argue that the distance criterion is too simplistic. This crucial step still needs to be figured out.

DATABASE STRUCTURE AND CURRENT CONTENT

The SURE database contains three sections, a “displacement observation point table”; a “fault segment table” and an “earthquake table”. Displacement observation information at georeferenced points are linked to the “fault segment table” and to the causative “earthquake table” through appropriate IDs.

The displacement observation table includes basic information such as latitude, longitude, and net slip. Ideally, slip is recorded as horizontal and vertical components (with associated uncertainties), as this information will be ideal for structure design as not all faults are equally sensitive to one or other component. The table also allows for compilation of “large aperture offset”, including the discrete slip on the fault trace and the inelastic part of deformation that sometimes occurs.

The fault segment table includes primary and distributed fractures (line work) and will be stored as a polyline Shapefile. Attributes for the segment file will include ID of causative earthquake. The fault segment map (geographic distribution of surface ruptures) is an important part of table as this information is used to calculate the “rupture probability” functions for the FDHA (probability of primary slip magnitude depends on distance along the primary fault; and off-fault slip depends on distance perpendicular to the main trace).

The SURE database will include a minimal level of interpretation. However, we define fields where the author’s opinion (when existing) can be reported, as well as the compiler’s one. The database will also include the

archives of the publications, at least as an external link. The templates of the database (excel spread sheets) are available online at <http://www.earthquakegeology.com/>.

To date, forty earthquakes are included in the M5-7.9 magnitude range, including 19 cases in Japan, 13 in the USA, 2 in Mexico, 1 in New Zealand, Kazakhstan, Italy, Ecuador, Turkey and Argentina; 22 strike-slip, 9 normal and normal-oblique, 8 reverse cases. Several recent cases will soon be implemented (e.g. 2014 M6 Nagano and Napa, 2016 M6.5 Norcia).

Several recent cases will be soon integrated, including the M6.5 Norcia earthquake rupture which has been extensively mapped and measured by an international team (Open EMERGEO). Observations were compiled in a homogenous way, providing a unique dataset ready to be compiled in SURE.

FUTURE STEPS

The objective is to incorporate well-known earthquake cases described in literature and to explore the post-2000 M6+ inland earthquakes that could potentially provide relevant data. A first search in the USGS earthquake database provided a catalogue of 130 shallow M6+ onshore epicentres since 2000, most having occurred in Asia (China, Iran, Japan, Russia, Pakistan, Turkey, Kyrgyzstan, Nepal, Myanmar) and very few having reported surface rupture information. There is consequently a need for participation of Asian geologists. The search for new contributors will be one major task of the SURE working group in the next years. With the PATA Days in New Zealand, we hope to gather a large number of geologists from Oceania, but also from Asia, to consolidate the SURE database network.

The US community is currently elaborating a project to prospect funding from local stakeholders; this project aims at developing a database, models, and engineering implementation guidelines for mitigation of surface faulting hazard in the western USA. The International SURE Group should clearly take advantage of this momentum and interact through collaboration and coordination of efforts with the US Community. The International community will alongside identify support and request funding for its own activities. We plan to finalize a first version of SURE by the end of 2017 which could be available on request.

We anticipate that recent events in Oceania (e.g. 2010 and 2016 events in New Zealand, as well as 2012 and 2016 Central Australia ones) will become good candidates to populate the new database, with their field and remote sensing data. On the methodological point of view, the M7.8 November 2016 Kaikoura earthquake surface rupture will provide interesting insights on the potentiality of remote sensing techniques (e.g. optical correlation) to enrich dataset, in terms of amount and quality of data.

CONCLUSION

After the starting point of the INQUA “SURFACE” project (Baize et al., 2015), two constructive workshops (Paris,



2015 and Menlo Park, 2016) were focused on the construction of the “SURE” database for FDHA. It appears that there is broad interest worldwide to update probabilistic estimates of slip distribution during future earthquakes for engineering design of infrastructures. As well as predicting the amount of surface slip at a main fault trace, distributed deformation is a key concern, particularly for structures close to active faults (e.g., pipelines, tunnels, bridges, etc.).

The current database structure has been discussed and validated by the “SURE Group” during the workshops. Worldwide researchers are currently updating and compiling existing fault rupture data that will be incorporated into the SURE database. Following the Menlo Park meeting and the project dissemination, new fault rupture data from recent earthquakes have been or will be soon provided by some of the participants, to feed the SURE database. We will seek further participation from other scientist during the PATA Days meeting in New Zealand.

Acknowledgements: The compilation of data into and integrated dataset, which forms the SURE database, is performed in the framework of INQUA and IAEA activities. The SURE database is to date sponsored by IRSN and IPGP. The SURE Group includes the Earth scientists who provided data and/or contributed to the database definition and implementation.

REFERENCES

- Baize, S., et al., 2015. Earthquake geology of shallow crustal faults and Seismic Hazard Assessment: Challenges ahead. Extended Abstract, 6th INQUA PATA Days, Italy.
- Biasi, G., & Wesnousky, R., 2016. Steps and Gaps in Ground Ruptures: Empirical Bounds on Rupture Propagation. *Bull. Seismol. Soc. Am.* 106, 1110–1124.
- Boncio, P., et al. 2017. Width of surface rupture zone for thrust earthquakes. Implications for earthquake fault zoning. *Nat. Hazards Earth Syst. Sci. Discuss.*, doi:10.5194/nhess-2017-123.
- Champenois, J., et al. 2017. Evidences of surface rupture associated with a low magnitude (Mw5.0) shallow earthquake in the Ecuadorian Andes. *J. Geophys. Res.*, in press.
- Chen, R., Petersen, M., 2011. Probabilistic Fault Displacement Hazards for the Southern San Andreas Fault Using Scenario and Empirical Slips. *Earthquake Spectra*. 27, 293-313
- Civico, R., et al., 2017. Anatomy of the 2016-2017 central Italy coseismic surface ruptures and their arrangement with respect to the foreseen active fault systems segmentation. Extended Abstract, 8th INQUA PATA Days, New Zealand (this issue).
- DeLong, S. B., et al., 2016. Tearing the terror: Details and implications of surface rupture and deformation from the 24 August 2014 M6.0 South Napa earthquake, California. *Earth and Space Science* 3, doi:10.1002/2016EA000176.
- Fletcher, J. M., et al., 2014. Assembly of a large earthquake from a complex fault system: surface rupture kinematics of the 4 april 2010 El Mayor-Cucapah (Mexico) Mw7.2 earthquake. *Geosphere* 10, doi:10.1130/GES00933.1
- Fujiwara, S., et al., 2016. Small-displacement linear surface ruptures of the 2016 Kumamoto earthquake sequence detected by ALOS-2 SAR interferometry. *Earth, Planets and Space* 68, DOI 10.1186/s40623-016-0534-x
- Gold, R., et al., 2013. Coseismic slip variation assessed from terrestrial lidar scans of the El Mayor–Cucapah surface rupture. *Earth and Planetary Science Letters* 366, 151–162
- Grandin, R., et al., 2015. Rupture process of the Mw=7.9 2015 Gorkha earthquake (Nepal): Insights into Himalayan megathrust segmentation. *Geophys. Res. Lett.* 42, doi:10.1002/2015GL066044
- Hemphill-Haley, M. A., & Weldon, R. J. II, 1999. Estimating prehistoric earthquake magnitude from point measurements of surface rupture. *Bull. Seismol. Soc. Am.* 89, 1264–1279.
- Inoue, N., et al. 2016. Study on the Evaluation Method for Fault Displacement: Probabilistic Approach Based on Japanese Earthquake Rupture Data - Distributed fault displacements. AGU Fall Meeting, San Francisco
- Klinger et al. (2017). High-resolution optical-image correlation for the Kaikoura earthquake, slip distribution and rupture processes. Extended Abstract, 8th INQUA PATA Days, New Zealand (this issue).
- Lettis, W. R., et al. 1997. Empirical Observations Regarding Reverse Earthquakes, Blind Thrust Faults, and Quaternary Deformation: Are Blind Thrust Faults Truly Blind? *Bull. Seismol. Soc. Am.* 87, 1171–1198.
- McCalpin, J., 1998. Statistics of Paleoseismic Data, Final Technical Report, Contract 1434-HQ-96-GR-02752, National Earthquake Hazards Reduction Program, USGS, 54 pages.
- Milliner, C. W. D., et al., 2015. Quantifying near-field and off-fault deformation patterns of the 1992 Mw 7.3 Landers earthquake. *Geochem. Geophys. Geosyst.* 16, 1577–1598, doi:10.1002/2014GC005693.
- Moss, R. E. S. & Ross, Z. E., 2011. Probabilistic Fault Displacement Hazard Analysis for Reverse Faults. *Bull. Seismol. Soc. Am.* 101, 1542–1553.
- Moss, R. E. S., et al., 2013. The Impact of Material Stiffness on the Likelihood of Fault Rupture Propagating to the Ground Surface. *Seismol. Res. Lett.* 84, doi: 10.1785/0220110109.
- NRC (2012). Confirmatory Analysis of Seismic Hazard at the Diablo Canyon Power Plant from the Shoreline Fault Zone. Research Information Letter 12-01. Available at https://www.researchgate.net/publication/290393704_Confirmatory_Analysis_of_Seismic_Hazard_at_the_Diablo_Canyon_Power_Plant_from_the_Shoreline_Fault_Zone
- Petersen, M., et al., 2011. Fault Displacement Hazard for Strike-Slip Faults. *Bull. Seismol. Soc. Am.* 101, 805–825.
- Pezzopane, S. K., & Dawson, T. E., 1996. Fault displacement hazard: A summary of issues and information, In: Seismotectonic Framework and Characterization of Faulting at Yucca Mountain, Nevada, USGS Report for U.S. DOE, Yucca Mountain Project, Chapter 9, 160 pp.
- Suarez-Vidal et al., 2007. Surface Rupture of the Morelia Fault Near the Cerro Prieto Geothermal Field, Mexicali, Baja California, Mexico, during the Mw 5.4 Earthquake of 24 May 2006. *Seismol. Res. Lett.*
- Takao, M., et al., 2013. Application of Probabilistic Fault Displacement Hazard Analysis in Japan. Japan Association for Earthquake Engineering, 13.
- Teran, O. J., et al., 2015. Geologic and structural controls on rupture zone fabric: A fieldbased study of the 2010 Mw 7.2 El Mayor–Cucapah earthquake surface rupture. *Geosphere*, 11, 899–920, doi:10.1130/GES01078.1.
- Vallage, A., et al., 2015. Inelastic surface deformation during the 2013 Mw 7.7 Balochistan, Pakistan, earthquake. *Geology*, doi:10.1130/G37290.1
- Wesnousky, S. G., 2008. Displacement and Geometrical Characteristics of Earthquake Surface Ruptures: Issues and Implications for Seismic-Hazard Analysis and the Process of Earthquake Rupture. *Bull. Seismol. Soc. Am.* 98, 1609–1632
- Youngs, R. R., et al., 2003. A Methodology for Probabilistic Fault Displacement Hazard Analysis (PFDHA). *Earthquake Spectra*, 19, 191–219.



Past sea level markers as accurate recorders of earthquake geological effects: pros and cons

Bardají, T.(1); Zazo, C.(2), Goy, J.L.(3), Dabrio, C.J.(4); Lario, J.(5); Cabero, A.(6); Roquero, E.(7); Silva, P.G.(8)

- (1) Dept. de Geología, Geografía y Medio Ambiente, Universidad de Alcalá. 28805-Alcalá de Henares, Spain. teresa.bardaji@uah.es
- (2) Dept. Geología, Museo Nal. CC. Naturales, CSIC. José Gutiérrez Abascal, 6; 28002-Madrid, Spain
- (3) Dept. Geología. Universidad de Salamanca
- (4) Dept. Estratigrafía, Fac. Geología, Universidad Complutense de Madrid, 28040-Madrid, Spain.
- (5) Facultad de Ciencias, UNED. 28040-Madrid, Spain
- (6) Dept Geología, Escuela Politécnica Nacional de Ecuador. PO-Box 17-01-2759, Quito, Ecuador
- (7) Dept. Edafología, Universidad Politécnica de Madrid. 28040-Madrid, Spain
- (8) Dept. Geología, Universidad de Salamanca. Av. Hornos Caleros, 50. 05003-Ávila, Spain

Abstract: Geological indicators of former sea level can be considered an accurate tool for determining coseismic vertical displacements. However, sea level markers do not always offer the same degree of reliability. Coastal deposits or marine terraces do not mark by themselves the datum level (± 0 m). Differences in altitude amsl in present beaches can reach more than to 2 m from lower foreshore to upper backshore. Erosional features such as notches or wave-cut benches and platforms sum to their intrinsic morphological variability the difficulty in dating them. Last but not least, sea level is not a steady level either in time or in space. Models of Glacial Isostatic Adjustment support differences of several meters in sea level during former interglacials depending on the geographical location. Sea level markers are useful tools for estimating coseismic displacements if their height is compared with equivalent present sea-level markers and position of former sea is taken into account.

Key words: Sea level markers; coseismic coastal uplift/subsidence; ancient earthquakes; ESI-07 Scale.

INTRODUCTION

Coastal vertical displacement can be considered as one of the most outstanding consequences of earthquakes. Coseismic uplift/subsidence is a primary geological effect of earthquakes included in the Environmental Seismic Intensity Scale (ESI2007, Guerreri & Vittori, 2007), which in the case of coastal settings seem to be a more accurate measurement since it is compared with a reference datum. However, the quantification of these vertical movements is not always easy and precise, above all when dealing with ancient earthquakes. Differences of 1 m in height can shift seismic Intensity from IX to X, or even from VIII to X, with significant consequences in seismic hazard assessment.

Many examples from recent instrumentally-recorded earthquakes (EQs) have been described in the scientific literature, starting with the probably first reported direct measurement of 1.5-2 m uplift caused by the M_w 9.2 1964 Alaska EQ (Plafker, 1969). Many other evidences have been published since then, with different ranges of uplift or subsidence from several decimeters such as the 40-60 cm deformation caused by M_w 8.0 1985 Chile EQ, (Castilla, 1988); to several meters, as the -2.5 to 6.5 m deformation caused by the M_w 7.8 2016 Kaikoura EQ (Clark et al., 2017). Coseismic uplift of up to 2 m has been also reported for the M_w 8.8 2010 Chile EQ in the basis of biomarkers, geomarkers and other morphological features (Lario et al., 2016).

Most of these references are supported by the occurrence of living organisms that have been displaced out of their living conditions by the EQ shaking. A few good examples of these organisms are the mollusc *Balanus* sp. (M_w 9.2 1964 Alaska EQ, Plafker, 1969); grey algae *Lessonia nigrescens*

(M_w 8. 1985 Chile EQ, Castilla, 1988); coralline algae (M_w 8.1 1995 Antofagasta EQ, Ortlieb et al., 1996); coral reefs (M_w 8.1 2007 Solomon Islands EQ, Chen et al., 2017); mussel *Perumitylus purpuratus* M_w 8.8 2010 Chile EQ, Melnick et al., 2012); or the algae *Durvillaea antarctica* and *Carbophyllum maschalocarpum* and associated coralline algae (M_w 7.8 2016 Kaikoura EQ, Clark et al., 2017).

In the absence of these living organisms, coastal uplift caused by pre-instrumental, historical earthquakes has been identified by different means with a relatively high degree of confidence. Present height of fossil tubeworms allowed Hamada et al. (2016) to infer differential fault segment activity linked to an historical 1729 EQ in Japan. Historical reports and chronicles can also be considered a relatively useful tool for these determinations; such is the case of the permanent one span uplift ("palmo", 20-22 cm) reported in the Mediterranean Spanish rocky coast near Torreveja (Silva et al., 2014).

There are many examples in the scientific literature devoted to Late Quaternary uplift in seismically active regions (some examples in Ota et al., 1993; 1991; Pirazzoli et al., 1994; Chappel et al., 1996; Rust & Kershaw, 2000; Hsieh & Rau, 2009; Cundy et al., 2010; Mastronuzzi et al., 2014; Binnie et al., 2016, etc). However, many of these papers do not contemplate the need of an accurate measurement in order to infer a seismic intensity degree. The further we go back in time, the less the expected accuracy in these measurements and the less the contribution to the seismic hazard assessment. In order to make these measurements as accurate as possible, we need to know not only the height of former sea level marker but also its real departure from past sea level.



DISCUSSION

Sedimentary sea level markers

Marine terraces are usually constituted by a series of littoral deposits where the sedimentary facies can give relevant information about the paleo-datum (former sea level). Maximum and minimum height of a given marine terrace can have differences in altitude of more than 2 m. Sedimentary facies within the marine terrace can include from the lower shoreface to upper backshore, which again can mean differences of more than 2 m. So, in order to properly quantify the amount of uplift we need to know the present height of the former datum (0 m) marker. In beach environments a detailed sedimentological analyses is needed (Fig. 1) not only to quantify the uplift rates but also to differentiate coseismic vertical movements from small scale climatically-driven sea level changes, (Dabrio et al., 2011; Bardají et al., 2015).



Figure 1: Sedimentary structures depicted in a Last Interglacial coastal unit from La Marina (Alicante, Spain). Small black arrows point to different plunge steps (boundary between the foreshore and shoreface) marking different positions of sea level (taken from Dabrio et al., 2011).

In coral terraces the estimation of the sea level is more difficult because of the variable depth to which corals live. *Acropora plamata* (Fig. 2) is thought to be one of the most reliable indicator of sea level because of its shallow depth range (<1 to 5 m; Lighty et al., 1982), but this range is larger than the necessary accuracy for seismic intensity determination.

Isolated corals in the Mediterranean, such as *Cladocora caespitosa*, can also live at depths not far below sea level. However, their living range of several meters makes them useless as coseismic movement indicators.



Figure 2: In situ *Acropora palmata* trunks in Guanahacabibes peninsula, Cuba. (1.5 m amsl).

Erosional sea level markers

The utility of tidal notches as coseismic indicators has been widely proposed by many different authors (see a good synthesis in Boulton & Stewart, 2015), but has been questioned as being clear tectonic indicators but mainly climatically driven (Cooper et al., 2007). Analysis of notch morphology and genesis goes beyond the aims of this work so we will focus on its role as a coseismic indicator.

Notches are built at sea level, so its maximum concave depth marks the sea level and its width marks the amplitude of tides (Fig. 3). The problem of notches is finding dateable material, mainly when dealing with older notches.



Figure 3: Ancient notch (Holocene – MIS5a?) in Cope Basin (Murcia, Spain). Difficulty in chronology is given by the lack of datable material.

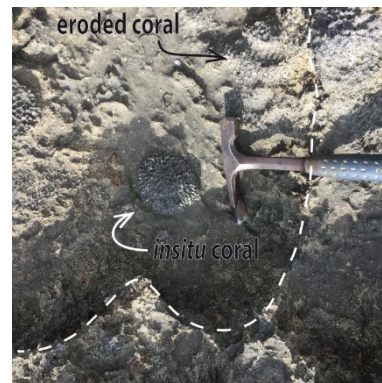


Figure 4: Small isolated coral growing into a pothole of a wavecut platform carved on a coral reef.

Wavecut platforms or benches are also a reliable sea level indicator because they are built at the base of a sea cliff by the wave action. So they represent the 0 m level. As in the case of notches, problems arise when trying to date them. In both cases, we have to find any datable material that is linked to this erosional feature with absolute certainty (Fig. 4).

Height of the former sea level

Sea level it is not a steady level either in time or in space. So, in order to use sea level markers as a geological recorder of displacement during earthquakes, we need to know how wide is the departure of the considered marker from the sea level that generated it.

Models based on glacial- and hydro-isostatic contributions in the Mediterranean (Lambeck & Purcell, 2005) points to a significant spatial variability along the Holocene (Fig. 5).

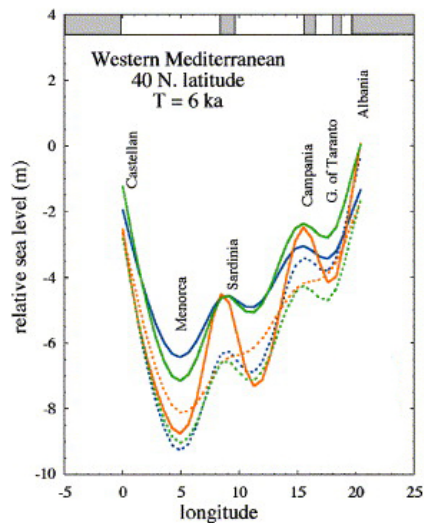


Figure 5: Predicted sea level at 6 ka in the western Mediterranean (Lambeck & Purcell, 2005).

Recently, Creveling et al. (2017) have presented a prediction model of sea level based on Glacial Isostatic Adjustment (GIA) for MIS5a and 5c, with quite different results than previously assumed. Sea level was considered to be between 15-37 m and 9-30 m below present sea level respectively, but this model points to -8.5 ± 4.6 m during MIS 5a (Fig. 6) and -9.4 ± 5.3 m during MIS5c.

Consequently, sea level must not be considered always at 0 m but global sea level distribution must be taken into account when making seismic intensity determinations.

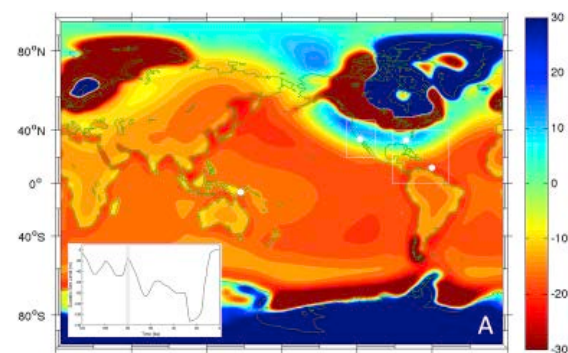


Figure 6: Predicted sea level at MIS5a (80 ka) relative to present day (color scale in m) (Creveling et al., 2017).

Acknowledgements: This work has been supported by Spanish research projects CGL15-69919-R (UAH), CGL2015-67169-P (USAL) and CGL2013-42847R (UNED), and it is a contribution to Spanish WG of IGCP639, CMP Commission of INQUA and Spanish WG QTECT-AEQUA.

REFERENCES

Bardají, T., Cabero, A., Lario, J., Zazo, C., Silva, P.G., Goy, J.L., Dabrio, C.J., 2015. Coseismic vs climatic factors in the record of relative sea level changes: an example from the Last Interglacials in SE Spain. *Quaternary Science Reviews* 113, 60-77.

- Castilla, J.J. 1988. Earthquake-Caused Coastal Uplift and Its Effects on Rocky Intertidal Kelp Communities. *Science* 242 (4877), 440-443.
- Clark, K.J., Nissen, E.K., Howarth, J.D., Hamling, I.J., Mountjoy, J.J., Ries, W.F., Jones, K., Goldstein, S., Cochran, U.A., Villamor, P., Hreinsdóttie, S., Litchfield, N.J., Mueller, C., Berryman, K., Strong, D.T., 2017. Highly variable coastal deformation in the 2016 Mw7.8 Kaikōura earthquakes reflects rupture complexity along a transpressional plate boundary. *Earth and Planetary Science Letters* (<http://dx.doi.org/10.1016/j.epsl.2017.06.48>)
- Cooper, F.J., Roberts, G.P., Underwood, C.J., 2007. A comparison of 103-105 climate stability and the formation of coastal notches. *Geophysical Research Letters* 34, L14310
- Creveling, J.R., Mitrovica, J.X., Clark, P.U., Waelbroeck, C., 2017. Predicted bound on peak global mean sea level during marine isotope stages 5a and 5c. *Quaternary Science Reviews* 163, 193-208.
- Cundy, A.B., Gaki-Papanastassiou, K., Papanastassiou, D., Maroukian, H., Frogley, M.R., Cane, T., 2010. Geological and geomorphological evidence of recent coastal uplift along a major Hellenic normal fault system (the Kamena Vourla fault zone, NW Evoikos, Greece). *Marine Geology* 271, 156-164.
- Dabrio, C.J., Zazo, C., Cabero, A., Goy, J.L., Bardají, T., Hillaire-Marcel, Cl., Gon'alez-Delgado, A., Lario, J., Silva, P.G., Borja, F., García-Blázquez, A.M. 2011. Millennial/submillennial-scale sea-level fluctuations in western Mediterranean during the second highstand of MIS 5e. *Quaternary Science Reviews* 30, 335-346.
- Guerrero, L. & Vittori, E. (Eds), 2007. *Environmental Seismic Intensity Scale ESI2007*. Memorie Descrittive. Carta Geologica d'Italia, vol. 74. Servizio Geologico d'Italia
- Hamada, M., Hiramoto, Y., Oda, M., Yamaguchi, H., 2016. Fossil tubeworms link coastal uplift of the northern Noto Peninsula to rupture of the Wajima-oki fault in AD1729. *Tectonophysics* 670, 38-47.
- Hsieh, M.L. & Rau, R.J., 2009. Late Holocene coseismic uplift on the Hua-tung coast, Eastern Taiwan: evidence from mass mortality of intertidal organisms. *Tectonophysics* 474, 595-609.
- Lambeck, K. & Purcell, A. 2005. Sea-level change in the Mediterranean Sea since the LGM: model predictions for tectonically stable areas. *Quaternary Science Reviews* 24, 1969-1988.
- Lario, J., Zazo, C., Goy, J.L., 2016. Tectonic and morphosedimentary features of the 2010 Chile earthquake and tsunamis in the Arauco Gulf and Mataquito river (Central Chile). *Geomorphology* 267, 16-24.
- Lighty, R.G., Macintyre, I.G., Stuckenrath, R., 1982. Acropora palmata reef framework: A reliable indicator of sea level in the Western Atlantic for the past 10,000 years. *Coral Reefs* 1, 125-130
- Mastroruzzi, G., Calcagnile, L., Pignatelli, C., Quarta, G., Stamatopoulos, L., Venisti, N., 2014. Late Holocene tsunamogenic coseismic uplift in Kekira Island, Greece. *Quaternary International* 332, 48-60
- Ortlieb, L., Barrientos, S., Guzmán, N., 1996. Coseismic coastal uplift and coralline algae record in northern Chile. *Quaternary Science Reviews* 15, 949-960.
- Pirazzoli, P., Stiros, S.C., Arnold, M., Laborel, J., Laborel-Deguen, F., Papageorgiou, S. 1994. Episodic uplift from holocene shorelines in the Perchora Peninsula, Corinth area, Greece. *Tectonophysics* 229, 201-109
- Plafker, G., 1969. Tectonics of the March 27, 1964, Alaska Earthquake. *U.S. Geological Survey Professional Paper* 543-I, 74 p.
- Rust, D. & Kershaw, S. 2000. Holocene tectonic uplift patterns in northeast Sicily: evidence from marine notches in coastal outcrops. *Marine Geology* 167, 105-126.
- Silva, P.G. & Rodríguez Pascua, M.A. (Eds.), 2014. Catálogo de los efectos geológicos de los terremotos en España. *Serie Riesgos Geológicos/Geotecnia IGME*, vol. 4. Instituto Geológico y Minero de España, Madrid, 350pp.



Preliminary observations of turbidite recurrence along the central and southern Hikurangi Subduction Zone: potential for paleoseismic investigations

Barnes, Philip (1), Orpin, Alan (1), Howarth, Jamie (2, 5), Patton, Jason R. (3), Lamarche, Geoffroy (1,4), Hopkins, Jenni (5) and Shipboard Science Team

(1) National Institute of Water and Atmospheric Research (Taihoro Nukurangi) 301 Evans Bay Parade, Hataitai, Wellington, 6021, New Zealand. Philip.Barnes@niwa.co.nz

(2) GNS Science (Te Pū Ao) 1 Fairway Drive, Avalon 5010 PO Box 30-368, Lower Hutt, New Zealand 5040.

(3) Humboldt State University, Dept. of Geology, Arcata, CA, USA 95521.

(4) School of Environment, University of Auckland, New Zealand

(5) Victoria University of Wellington.

Abstract: The Hikurangi margin straddles the convergent boundary between the Pacific and Australia tectonic plates. The subduction megathrust could potentially represent New Zealand's largest earthquake and tsunami source. Detailed paleoseismic records however, are sparse, and no great earthquakes ($M > 8$) have occurred on the megathrust in the historical period. In order to build long timeframe (ka) paleoseismic records, we acquired 61 sediment cores up to 5 m in length from sites on the continental margin between eastern Marlborough and Poverty Bay in 2016. The core sites targeted different sedimentary source catchments and dispersal routes, as well as relatively small basins perched on lower slope ridge crests unaffected by regional dispersal pathways. The sample sites collectively span along-strike variations in inter-seismic coupling and slow-slip. The new cores reveal successions of turbidites widely interspersed with hemipelagic sediment and volcanic ash markers. Preliminary analysis indicates turbidite emplacement since deposition of Tāupo tephra occurs on centennial timescales with recurrence intervals (RI) ranging from 170 years to 860 years, and with RI generally decreasing from south to north along the margin and with distance down distributary systems from the coast. The turbidite RIs appear comparable to coastal paleoseismic events, suggesting that the turbidite records may prove valuable paleoseismic recorders on Hikurangi Margin.

The 2016 $M_w 7.8$ Kaikōura earthquake triggered a turbidity current that emplaced a new turbidite in the Hikurangi Trough. This event presents an unprecedented opportunity to study the relations between fault source length, the spatial distribution of ground motions, turbidity current triggering and turbidite deposition for upper plate events on the margin.

Key words: Paleoseismology, Earthquakes, Hikurangi, Turbidite, Geochronology.

INTRODUCTION

In the Southwest Pacific region, the Pacific plate subducts beneath the Australia plate to form the Kermadec and Hikurangi subduction zones. Oblique convergence at the southern terminus of these megathrust faults results in strain partitioning in the forearc of the North Island and a transition from subduction to strike slip faulting in the Cook Strait region. Global positioning system (GPS) studies of current Earth deformation (years to decades) show that the megathrust fault has patches that creep slowly whilst other parts of the fault are strongly coupled inter-seismically (locked) and the potential sites of future great earthquakes (magnitude $M > 8$) (Wallace et al., 2009, 2010). The Hikurangi margin is potentially New Zealand's largest earthquake and tsunami hazard (Wallace et al., 2014; Power et al., 2016). One key question of relevance to seismic and tsunami hazard and risk in New Zealand is whether or not the Hikurangi subduction margin is capable of producing great (Magnitude $M > 8$) or giant ($M > 9$) earthquakes. If so, in what regions do they occur, and how often? Paleoseismic data are required to address these questions.

There is already a nascent paleoseismic record with which to characterize seismic hazards posed by the Hikurangi margin. The record has been derived primarily from

evidence of co-seismic coastal deformation in the form of marine terrace uplift and lagoon subsidence (Haywood et al., 2006, 2015; Wallace et al., 2014; Clark et al. 2015; and references therein). In addition, turbidite paleoseismology has been used in the New Zealand region (Pouderoux et al., 2012 a, b, 2014). These studies provided detailed offshore sedimentological observations along the northern part of the margin showing evidence for earthquakes spanning the past 16 ka, using radiometric age control and provenance of turbidite records in a series of long cores in three distinct basins.

An important unresolved question is whether other distributary systems further south preserve sedimentary records suitable for extending the turbidite paleoseismic record. Addressing this question is essential for developing a record of past Hikurangi margin earthquakes that spans the entire margin and sufficiently long timescales to capture multiple seismic cycles. Here we report on the preliminary results of a recent coring campaign that sampled discrete distributary systems along the Hikurangi margin and discuss the prospect for developing a margin-wide paleoseismic record by demonstrating synchronicity of widespread turbidites that would be consistent with strong earthquake shaking over large regions.



INQUA Focus Group Earthquake Geology and Seismic Hazards



paleoseismicity.org

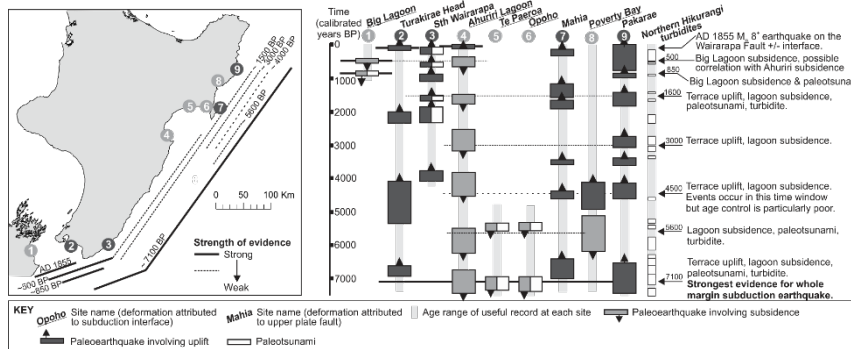
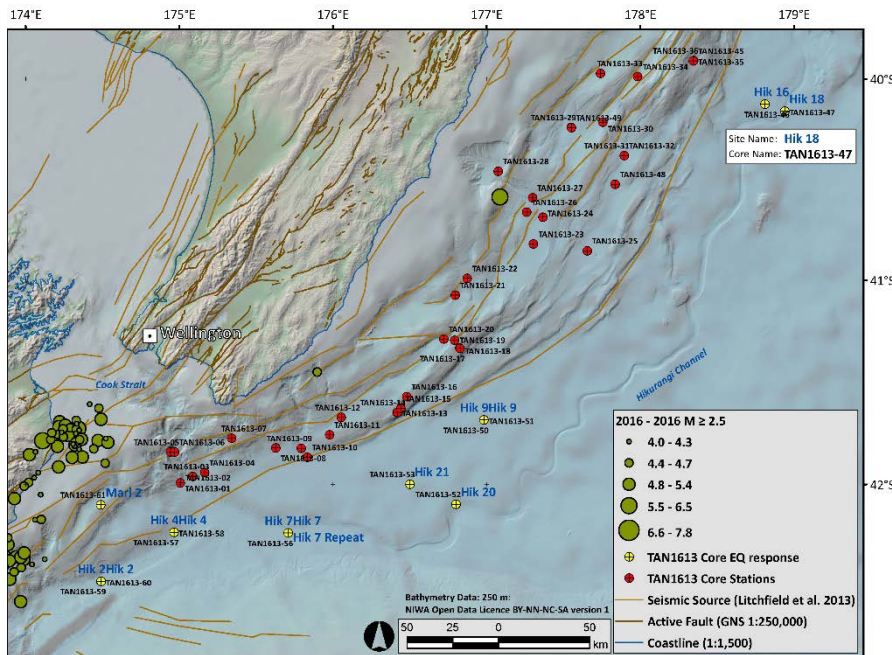


Figure 1: Upper panel, core site location map. Margin core sites are designated by red symbols, specific 2016 Mw7.8 Kaikōura earthquake response cores are designated by yellow symbols. 2016 Mw7.8 Kaikōura earthquake epicentres (USGS) are displayed as green circles. Onshore faults are from the GNS active fault database and the offshore earthquake sources are from the national seismic hazard model (Stirling et al., 2012; Litchfield et al., 2014). Lower panel, results of previous paleoseismic studies on the Hikurangi margin, derived from coastal records (Wallace et al. 2014; Clark et al. 2015) and northern (Poverty to East Cape region) margin turbidite records (Pouderoux et al., 2012 a, b).

METHODS

From 12 to 22 November 2016 the R/V Tangaroa retrieved 61 sediment cores from 12 discrete sediment distributary systems and 10 isolated slope basins from the southern and central parts of the Hikurangi margin from eastern Marlborough northwards to Poverty Bay. When combined with the distributary systems studied by Pouderoux et al. (2012 a, b, 2014) the core set spans the entire length of the Hikurangi Margin from 42.5° S to 37.0° S latitude.

We selected core sites using 30 kHz multibeam bathymetric and backscatter data, sub-bottom acoustic profiles, archived sediment samples, and results from numerical modelling of turbidity currents (Figure 1). Our rationale for selecting core sites considered issues of age control, sedimentary isolation, and geospatial relevance to historic and prehistoric fault segments (megathrust interface vs. upper-plate accretionary-prism faults). We targeted different

sedimentary source catchments and dispersal routes, as well as relatively small basins perched on lower slope ridge crests unaffected by regional dispersal pathways. The sample sites collectively span along-strike variations in inter-seismic coupling and slow-slip. Cores were retrieved using a 6 m long 7 cm diameter Kullenberg piston corer. For some sites we collected multi-cores (with four sample tubes in use) to sample the sediment water interface and the uppermost sediment with minimal disturbance.

While at sea cores were split lengthwise, digitally imaged and the lithostratigraphy described. All cores were imaged using X-Ray attenuation and magnetic susceptibility data collected at 2 cm resolution using a point sensor. Macroscopic tephra horizons were also identified visually to provide a preliminary geochronologic framework. These shipboard data provide a platform for assessing the potential of the core set for turbidite paleoseismic reconstructions along the margin. We focus on the results



from six sediment distributary systems that contain cores with a tephra inferred to be the Tāupo tephra (1718±10 CalBP), or where core-bottom radiocarbon ages provide chronologic constraint. We stress that turbidite counts and chronostratigraphic interpretations are preliminary and may change. Nonetheless, they provide valuable insights into the potential turbidite paleoseismology along the margin.

RESULTS

Cores are composed of the terrigenous-dominated sequences included layers of gravel, sand, and mud, hemipelagite, and volcanic ash. Many of these layers are turbidites, some of which may be seismogenic. An overview of the preliminary lithostratigraphy of discrete distributary systems and isolated slope basins for which some form of chronology exist are outlined below.

Cook Strait Canyon: Cores from Cook Strait Canyon are characterised by a sedimentary sequence containing up to two gravelly beds approaching 20 cm thick, overlain by interbedded hemipelagic and turbidite very fine sandy silts. Gravelly turbidites are present in cores from the canyon floor (TAN1613-06 Cook 4), a terrace perched above the canyon floor (TAN1613-05 Cook2), and at the mouth of the canyon (TAN1613-03 Cook 6). The turbidite gravels contain abundant shell fragments and clasts that are sub-rounded and have long-axis diameters up to 10 mm. The core from the canyon floor contains a sequence of three fining upward beds. Interbedded hemipelagites and silty turbidites overly the gravel bed. Cores contain up to five turbidites including the basal gravel. Four of these are above a ¹⁴C age on planktonic foraminifera of 966-755 CalBP, giving a turbidite recurrence interval (RI) of ~170 years.

Opouawe Canyon: Cores from Opouawe Canyon (TAN1613-04 Opouawe 1; TAN1613-07 Opouawe 2) are characterised by hemipelagic sequences of dark olive grey, very-fine sandy silts with abundant dark planar and convoluted colour laminations. These hemipelagites are interbedded with turbidites that have silty very fine sand bases (e.g., Figure 2). The core from the mouth of the Opouawe Canyon (Opouawe 2) contains a thin sequence of interbedded hemipelagites and turbidites (~60 cm) overlain by grey and bluish black very-fine sandy silt that has convoluted bedding and is interpreted as a debrite. In Opouawe 1, five turbidites occur above a tephra interpreted as Taupo (476.5 cm) and a ¹⁴C age on planktonic foraminifera (484.5 cm) of 1845-2087 CalBP. Based on this chronology the turbidite RI for the canyon is ~340 years.

Madden Canyon distributary system: The cores from the Madden Canyon and the Porangahau Basin are characterised by interbedded hemipelagites, silty turbidites, and sandy turbidites. Hemipelagites are composed of dark greenish to greenish grey, very-fine sandy silts, with isolated darker colour mottles and convoluted colour laminations. Turbidite morphology ranges from silty turbidites with little structure to complex sandy turbidites with multiple upward fining units at their base (e.g., Figure 2). Only in isolated instances is it possible to visually distinguish hemipelagites from the tails of silty turbidites. Three cores from the

Madden Canyon contain the inferred Tāupo tephra. There are five sandy turbidites above the tephra in TAN1613_28 MC6 from the upper canyon, and six above it in core TAN1613-27 MC5 from the canyon mouth. These sites have turbidite RI of ~340 and ~290 years, respectively. These RIs are minimums because silty turbidites are also present, but their number has not been quantified from preliminary work. TAN1613_25_MC1 from Akitio Trough in the outer Madden distributary system contains silty turbidites but none above the Tāupo tephra.

Hawkes Bay distributary system: The cores from the upper slope off southern Hawkes Bay, including Omakere Trough (TAN1613-33; HB5) and the inner Paoanui Basin (TAN1613-49; HB4), are characterised by interbedded hemipelagite, silty turbidites, and sandy turbidites. Hemipelagic sediments are characterised by dark greenish to greenish grey very-fine sandy silts that are generally massive and contain isolated convoluted colour laminations (Figure 2). Turbidites in these cores range from structurally complex sandy turbidites with multiple fining upward units to structurally simple silty turbidites (Figure 2). In contrast, the cores from the Paoanui Trough (TAN1613-34; HB6 and TAN1613-30; HB3) are dominated by hemipelagites and contain few visible turbidites. A single turbidite occurs above the inferred Tāupo tephra in TAN1613-30; HB3 suggesting a turbidite RI of 860 years at this site. A core from an un-named basin north of Akitio Trough, in the outer Hawkes Bay distributary system, is dominated by hemipelagite and contains no turbidites that can be identified visually by X-ray radiography.

Northern Slope basins: In the outer accretionary wedge off Hawkes Bay, the Rock Garden and Ritchie Ridge perched slope basins produced cores that contain hemipelagite interbedded with silty turbidites and/or tephra. Cores from the slope basin east of Rock Garden (TAN1613- 35-36; Rock1) and Ritchie Ridge each contain two silty turbidites above the inferred Tāupo tephra, providing a turbidite RI of ~860 years. Basin sites east of Ritchie Ridge (TAN1613-37 and -38, Ritchie 2; TAN1613-41, Ritchie3) contain tephra beds but no turbidites.

DISCUSSION

At sites along the margin for which preliminary chronological information is available, turbidite emplacement occurs on centennial timescales with RIs ranging from 170 years to 860 years. Rates of turbidite emplacement generally decrease from south to north along the margin and with distance down distributary systems from the coast.

Centennial scale RIs for turbidite deposition along most of the margin indicate that the records are prospective for turbidite paleoseismology. The RIs are broadly consistent with existing paleo-earthquake rates along the margin (Figure 1). For example, there have been five co-seismic coastal uplift events along the Wairarapa coast in the last 1700 years, which broadly agree with the number of turbidites observed in Opouawe and Madden canyon cores



(Clark et al., 2015, and references therein). Likewise, there have been two co-seismic uplift events at Mahia Peninsula over the last 1700 years, which agrees the two turbidites recorded above the inferred Tāupo tephra in the northern slope basin cores. In contrast, only a single turbidite is recorded above the inferred Tāupo tephra in the inner Paoanui Basin and Paoanui Trough, despite four co-seismic subsidence events over the same interval in Hawkes Bay (Haywood et al., 2006, 2015). In addition, the RI estimates from the Hawes Bay distributary system and the northern slope basins agrees with the RI for larger magnitude earthquakes presented by Pouderoux et al. (2014), even though these represent different time scales.

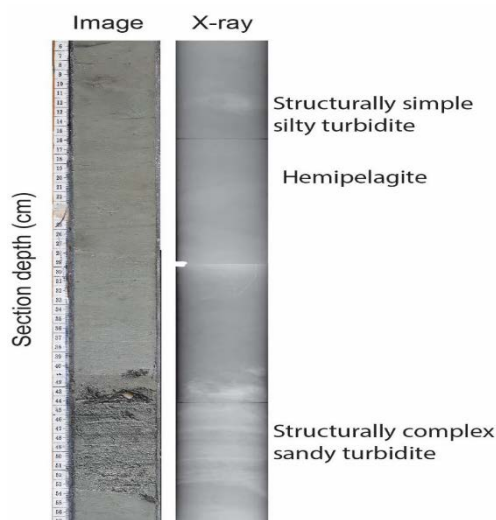


Figure 2: True colour image and X-ray radiograph showing an example of a typical sequence of interbedded hemipelagite, structurally complex sandy based turbidites and structurally simple silty turbidites. Sequence from core TAN1613-33 (HB5) from the Omakere Trough.

Reasons for the misfit between the number of paleoseismic events and turbidites may involve incompleteness in either the paleoseismic or turbidite records, earthquake hypocentre locations situated too distally to trigger turbidite emplacement, mis-identification of the Tāupo tephra, differences in the threshold to record paleoearthquake records for these different paleoseismic methods, possible non-megathrust (e.g. upper or lower plate) earthquake sources, and/or turbidite deposition by non-seismic mechanisms. Resolving these issues will require correlation of turbidites between discrete distributary systems using both the petrophysical character of turbidites and high-resolution geochronology both of which are the focus of ongoing investigations.

The relations between turbidite emplacement and the paleoseismic record also reveals one of the most significant challenges of applying turbidite paleoseismology to this margin, the high density of upper plate faults. The frequency of turbidite emplacement would be consistent with the interpretation that the cores contain a signature of both upper-plate and subduction zone earthquakes. Producing a subduction zone earthquake record on this margin however, will require the sedimentary signature of these and potentially lower plate

seismogenic sources to be unravelled. Untangling earthquakes sourced from the dense network of upper plate faults from large subduction interface events requires evidence of synchronous turbidite triggering over sufficiently large areas to eliminate upper plate fault sources. For example, great and giant earthquakes would be expected to produce strong ground shaking over very large (>200 km long) regions. Consequently, determining the relations between fault source length, the spatial distribution of ground motions, turbidity current triggering and turbidite deposition for this margin is essential (e.g., Goldfinger et al., 2012; Patton et al., 2015).

The 2016 M_w 7.8 Kaikōura earthquake presents an unprecedented opportunity to study these relations. This event occurred during the *Tangaroa* TAN1613 survey, and led to an immediate survey response by way of a suite of Hikurangi Trough channel and basin floor multicores being acquired to investigate possible turbidite emplacement (Figure 1). The cores indeed revealed a very recently emplaced, still-fluidised turbidite along the Hikurangi Trough. Mountjoy et al. (submitted) have since dated the turbidite to the earthquake using radionuclides in the Tan1613 cores, demonstrated widespread landsliding and net erosion in Kaikōura canyon, and established a recurrence for this event of about 140 years. Ongoing studies of this turbidite in parallel with our work on the paleo-turbidite records will provide an excellent analogue for the upper plate earthquakes along the Hikurangi margin.

Acknowledgements: The voyage was co-funded by the MBIE Endeavour programme 'Diagnosing peril posed by the Hikurangi subduction zone: New Zealand's largest plate boundary fault' (CONT-46722-CRFRP-GNS), and by the Marine Geological Processes and Resources programme of NIWA's Coasts & Oceans Centre.

REFERENCES

- Clark, K. J., Hayward, B. W., Cochran, U. A., Wallace, L. M., Power, W. L., and Sabaa, A. T., 2015. Evidence for Past Subduction Earthquakes at a Plate Boundary with Widespread Upper Plate Faulting: Southern Hikurangi Margin, New Zealand: BSSA, v. 105, no. 3, p. 1661-1690.
- Goldfinger, C., Nelson, C.H., Morey, A., Johnson, J.E., Gutierrez-Pastor, J., Eriksson, A.T., Karabanov, E., Patton, J., Gracia, E., Enkin, R., Dallimore, A., Dunhill, G., and Vallier, T., 2012. Turbidite Event History: Methods and Implications for Holocene Paleoseismicity of the Cascadia Subduction Zone: U.S. Geological Survey.
- Hayward, B.W., Grenfell, H.R., Sabaa, A., Carter, R., Cochran, U., Lipps, J.H., Shane, P., Morley M.S. 2006. Micropaleontological evidence of large earthquakes in the past 7200 years in southern Hawke's Bay, New Zealand. *Quaternary Science Reviews* 25, 11/12, 1186–1207.
- Hayward, B. W., Grenfell, H. R., Sabaa, A., Carter, R., Cochran, U., Lipps, J. H., Shane, P., and Morley, M. S., 2006. Micropaleontological evidence of large earthquakes in the past 7200 years in southern Hawke's Bay, New Zealand, *Quaternary Sci. Rev.* 25, nos. 11/12, 1186–1207.
- Hayward, B. W. H., Sabaa, A., Grenfell, H. R., Cochran, U., Clark, K. J., Litchfield, N. J., Wallace, L., Marden, M., and Palmer, A. 2015. Foraminiferal record of Holocene paleoearthquakes on the subsiding southwestern Poverty Bay coastline, New Zealand, *New Zeal. J. Geol. Geophys.*, doi: 10.1080/00288306.2014.992354.
- Litchfield, N.J., Van Dissen, R., Sutherland, R., Barnes, P.M., Cox, S., Norris, R., Beavan, J., Langridge, R., Villamor, P., Berryman, K.,



INQUA Focus Group Earthquake Geology and Seismic Hazards



paleoseismicity.org

- Stirling, M., Nicol, A., Nodder, S., Lamarche, G., Barrell, D.J.A., Pettinga, J.R., Little, T., Pondard, N., Mountjoy, J.J., Clark, K., 2014. A model of active faulting in New Zealand. *New Zealand Journal of Geology and Geophysics*. DOI: 10.1080/00288306.2013.854256
- Mountjoy J.J. Howarth, J., Orpin, A., Barnes, P.M., Bowden, D., Rowden, A., Schimel, A.C.G., Holden, C., Horgan, H., Nodder, S.D., Patton, J.R., Lamarche, G., Gerstenberger, M., Micallef, A., Pallentin, A., and Kane, T., Earthquakes drive large-scale submarine canyon development and sediment supply to deep ocean basins. Submitted to *Science*, Oct 2017.
- Patton, J. R., Goldfinger, C., Morey, A. E., Ikehara, K., Romsos, C., Stoner, J., Djadjadihardja, Y., Udrek, Ardhastuti, S., Gaffar, E. Z., and Viszcaino, A., 2015. A 6600 year earthquake history in the region of the 2004 Sumatra-Andaman subduction zone earthquake: *Geosphere*, v. 11, no. 6, p. 1-62.
- Pouderoux, H., Proust, J.-N., Lamarche, G., Orpin, A., and Neil, H., 2012 a. Postglacial (After 18 Ka) Deep-Sea Sedimentation Along the Hikurangi Subduction Margin (New Zealand): Characterisation, Timing and Origin of Turbidites: *Marine Geology*, v. 295-298, p. 51-76.
- Pouderoux, H., Lamarche, G., and Proust, J.-N., 2012 b. Building an 18 000-year-long paleo-earthquake record from detailed deep-sea turbidite characterisation in Poverty Bay, New Zealand: *Natural Hazards Earth System Sciences*, v. 12, p. 2077-2101.
- Pouderoux, H., Lamarche, G., Proust J.-N. 2014. Submarine paleoseismology of the northern Hikurangi subduction margin of New Zealand as deduced from turbidite record since 16 ka. *Quaternary Science Reviews*, 84, 116e131.
- Power, W. L., Wallace, L. M., Mueller, C., Henrys, S., Clark, K. J., Fry, B., Wang, X., and Williams, C., 2016. Understanding the potential for tsunami generated by earthquakes on the southern Hikurangi subduction interface: *New Zealand Journal of Geology and Geophysics*, v. 59, no. 1, p. 70-85.
- Stirling, M.W., McVerry, G., Gerstenberger, M., Litchfield, N.J., Van Dissen, R.J., Berryman, K.R., Barnes, P.M., Wallace, L., Villamor, P., Langridge, R., Lamarche, G., Nodder, S., Reyners, M., Bradley, B., Rhoades, D., Smith, W., Nicol, A., Pettinga, J., Clark, K. and Jacobs, K., 2012. National Seismic Hazard Model for New Zealand: 2010 update *Bulletin of the Seismological Society of America*, 102(4): 1514-1542. 10.1785/0120110170
- Wallace, L. M., Reyners, M., Cochran, U. A., Bannister, S., Barnes, P. M., Berryman, K., Downes, G., Eberhart-Phillips, D., Fagereng, A., Ellis, S., Nicol, A., and McCaffrey, B., 2009. Characterizing the seismogenic zone of a major plate boundary subduction thrust: Hikurangi Margin, New Zealand: *Geochemistry Geophysics Geosystems*, v. 10, no. 10.
- Wallace, L. M., Bell, R., Townend, J., Ellis, S., Bannister, S., Henrys, S., Sutherland, R., and Barnes, P. M., 2010. Subduction Systems Revealed: Studies of the Hikurangi Margin: *EOS Trans. AGU*, v. 91, no. 45.
- Wallace, L. M., Cochran, U. A., Power, W. L., and Clark, K. J., 2014. Earthquake and Tsunami Potential of the Hikurangi Subduction Thrust, New Zealand Insights from Paleoseismology, GPS, and Tsunami Modeling In *Oceanography*, v. 27, no. 2, p. 104-117.



Paleo-liquefaction; an Alternative Tool for Seismic Hazard Assessments

Bastin, Sarah (1), Green, Russell (2), Quigley, Mark (3), Bassett, Kari (4)

- (1) QuakeCoRE, University of Canterbury, Christchurch, New Zealand
- (2) Department of Civil & Environmental Engineering, Virginia Tech, Blacksburg, Virginia 24061, United States of America.
- (3) School of Earth Sciences, The University of Melbourne, Victoria 3010, Australia
- (4) Department of Geological Sciences, University of Canterbury, Christchurch 8014, New Zealand

Abstract: Liquefaction features preserved in the sub-surface provide evidence for earthquake-generated strong ground shaking exceeding threshold intensities for liquefaction. Analysis of liquefaction features preserved in the geologic record enables the approximate timing and site-specific Peak Ground Accelerations of the causative paleo-earthquake(s) to be estimated, while regional examination enables the epicentral location and magnitude to be approximated. Examination of liquefaction features formed during recent events in New Zealand provides insights into the typical morphologies and preservation potential of liquefaction features and aids the identification and interpretation of paleo-liquefaction features. Paleo-liquefaction investigations provides a fault-independent methodology by which return times of strong ground motions may be estimated for a given region, and may be employed to assess seismic hazards in areas where the distribution of active faults is uncertain, and/or many active fault sources are present.

Key words: Paleo-liquefaction, seismic hazard assessment

INTRODUCTION

Liquefaction may occur in unconsolidated and fluid-saturated sediments as earthquake-induced cyclic shearing causes the soil structure to break down and pore-water pressures to increase to the static confining pressure (Boulanger and Idriss, 2014). Liquefied sediment may be ejected to the ground surface where it typically manifests as surficial sand blows, blistering of the surface, and/or lateral spreading-induced ground surface fissuring (Obermeier et al. 2005). Surficial features are typically rapidly re-worked into surrounding deposits. Sub-surface features are likely to be present in the geologic record where host sediments are preserved and include dikes that fed the surface sand-blows, laterally injected sills, and/or other injection features (Obermeier et al., 2005). Preserved features, termed paleo-liquefaction, provide evidence for paleo-earthquakes with site-specific ground motion intensities exceeding threshold values required to trigger liquefaction. Analysis of preserved features provides a fault-independent methodology by which the timing and magnitude of historic and/or pre-historic events can be examined (e.g. Obermeier et al. 2001).

Paleo-liquefaction investigations have been employed to assess seismic hazards in areas where blind active faults are known to exist, such as the New Madrid Seismic Zone (e.g. Tuttle, 2001). Investigations typically rely on the accurate identification of liquefaction features, interpretation of their relative ages, and constraint on the shaking intensities under which liquefaction was triggered (Green et al., 2005). Ages of liquefaction features and, thus, the timing of the paleo-event may be approximated by dating bounding stratigraphy (Obermeier et al., 2005). The threshold ground motion intensity required to trigger liquefaction at a given site can be determined from site-specific geotechnical tests (e.g. Cone Penetration Tests) using simplified liquefaction triggering methodologies and assuming the earthquake

shaking must have exceeded the minimum liquefaction triggering intensity threshold (i.e. Factor of Safety against liquefaction <1 ; Boulanger and Idriss (2014)). The ground motion intensity threshold for liquefaction triggering can be quantified in terms of required magnitude-weighted peak ground acceleration ($PGA_{7.5}$), which represents the equivalent peak ground acceleration (PGA) for a M_w 7.5 event required to trigger liquefaction at a given site. The identification and dating of liquefaction features across a region, combined with minimum thresholds against liquefaction triggering enables the epicentral location and magnitude of the paleo-earthquake to be approximated (e.g. Maurer et al., 2015).

Liquefaction and associated phenomena have been reported following upwards of 13 recent and historical earthquakes in New Zealand (Fairless & Berrill, 1984; Maurer et al., 2015). Liquefaction features formed during these events are likely to be present in the sub-surface sediments. Collation of the extents of liquefaction manifestations following these events enables areas underlain by sediments with low cyclic resistances to liquefaction to be identified. These areas may be targeted to document the preservation potential of liquefaction features and/or examine the presence of paleo-liquefaction. Herein, the potential applications of paleo-liquefaction investigations as an additional tool for assessing seismic hazards are outlined using examples from recent and historical earthquakes in New Zealand.

SPATIAL DISTRIBUTIONS OF LIQUEFACTION FEATURES

Documentation of the spatial extents and morphologies of liquefaction features following recent earthquakes provides insights into the settings in which liquefaction typically manifests and the associated preservation potential. Detailed mapping of surface manifestations



following the 2010-2011 Canterbury Earthquake Sequence indicated that widespread liquefaction occurred across much of eastern Christchurch (Figure 1A; Quigley et al., 2016). Severe manifestations were observed proximal to meandering rivers and were shown by Bastin et al. (2013) to be orientated sub-parallel to the closest waterway. In addition, mapping within Blenheim following the 2016 M_w 7.8 Kaikoura earthquake indicated that liquefaction predominantly manifested to the east of the township in areas hosting shallow water-tables and underlain by young, unconsolidated fluvial deposits (Figure 1B; Stringer et al. (2017); Bastin et al., (in review)). The comparably more localized manifestations within Blenheim reflects the lower ground accelerations of the Kaikoura earthquake (~ 0.1 g; GEER (2017)) compared to the CES (~ 0.2 g; Bradley & Hughes, (2012)). The spatial distributions indicate that areas underlain by recent fluvial sediments and hosting shallow water-tables are highly susceptible to liquefaction. Similar distributions have been reported in other areas of New Zealand such as Whakatane following the 1987 Edgecumbe earthquake (Bastin et al., 2017).

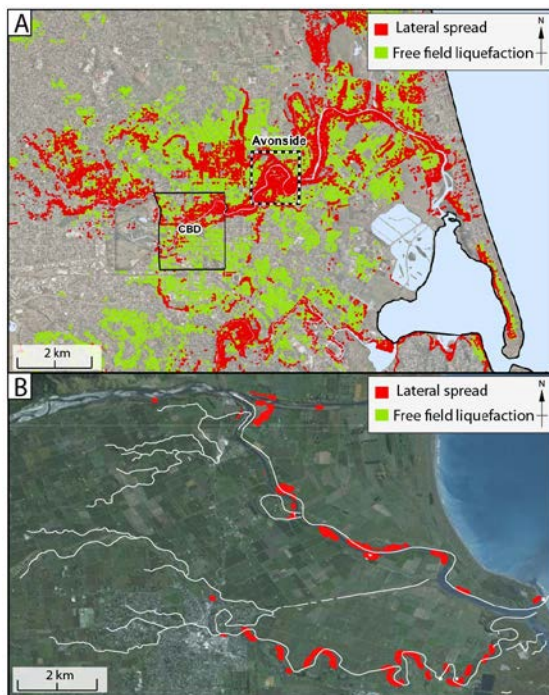


Figure 1: A) Distribution of liquefaction in Christchurch as mapped following the 2010-2011 Canterbury Earthquake Sequence. B) Distribution of liquefaction in Blenheim following the 2016 Kaikoura earthquake.

SUB-SURFACE MORPHOLOGIES OF LIQUEFACTION FEATURES

Trenching investigations undertaken in Christchurch following the 2010-2011 CES and in Blenheim following the 2016 Kaikoura earthquake indicated that the surficial liquefaction features correspond with sub-vertical and planar dikes in the sub-surface (e.g. Bastin et al. (2015); (2016); Bastin et al. (in prep)). The sub-surface liquefaction dikes were shown to be uniformly composed of grey, well

sorted fine to medium sand and cross-cut the stratigraphy from the trench floor to the surface (i.e. Figure 2; Bastin et al. (2015 and 2016)). The features generally range in width from 1 to 50 cm and increase in width with depth, indicating that they formed by the upwards flow of liquefied sediment rather than downward-propagating surface cracking (Figure 2). The sediment within the dikes lacks the oxidation and mottling developed within the surrounding stratigraphy indicating their recent emplacement. The morphologies of these features are consistent with sub-surface liquefaction features described in previous studies by Obermeier et al. (2005) and indicate that liquefaction features are typically preserved in the sub-surface as sub-vertical dikes.

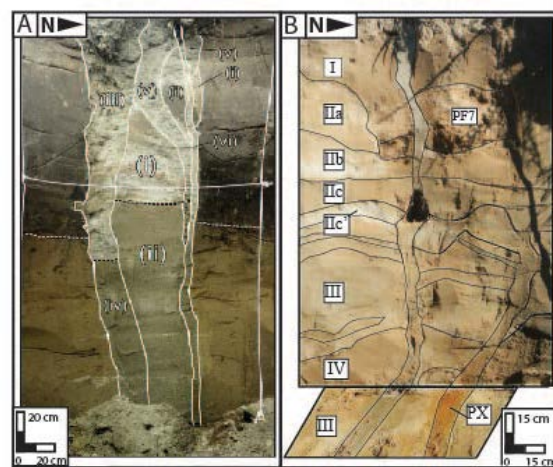


Figure 2: A) Dikey preserving evidence for four episodes of liquefaction (i-iv) as observed in eastern Christchurch (modified from Quigley et al., (2016)). B) Interpreted field photograph indicating the similar morphologies of the CES (Mx) and pre-CES (Px) dikes (modified from Bastin et al., (2015)).

Extensive trenching investigations at a site in eastern Christchurch in which upwards of 6 liquefaction triggering events are inferred throughout the CES, revealed sub-surface dikes that preserved evidence for between 1-4 episodes of liquefaction (shown in Figure 2A; Quigley et al. (2016)). Separate liquefaction events were recognized as internal dike parallel silt linings separating internal conduits and identical to those formed along the dike margins. The preservation 1-4 liquefaction-triggering events, despite the upwards of 6 events inferred for the site, indicates that the geologic record is likely to under-represent the number of liquefaction triggering earthquakes. It may therefore be difficult to discern whether a feature represents a single liquefaction-triggering event, or multiple, closely spaced events resulting from clustered earthquakes.

Identification of paleo-liquefaction

Documentation of the spatial distributions of surficial liquefaction following recent earthquakes and documentation of their preservation potential indicates that paleo-liquefaction is likely to be present in areas that have been subjected to strong ground shaking and underlain by recent fluvial sediments. Evidence of liquefaction is likely to



be preserved as sub-vertical and planar dikes orientated sub-parallel to proximal waterways.

Paleo-liquefaction investigations have recently been undertaken within Christchurch, Blenheim, Whakatane, Napier, and Hamilton to determine whether sub-surface evidence of paleo-liquefaction is present, and to ground-truth liquefaction hazard assessments. Trenching investigations were undertaken in areas underlain by sediments with low cyclic resistances to liquefaction, with trenches excavated perpendicular to river banks to enable best possible chances of intersecting features.

Sub-surface liquefaction features of consistent morphologies to those formed during the CES and 2016 Kaikoura earthquake were consistently observed during the trenching (i.e. Figure 2). Sub-vertical and planar dikes composed of mottled and oxidized, well-sorted fine to medium grained sand were identified in the trenches and cross-cut surrounding stratigraphy (example shown in Figure 2B). The mottling and oxidation developed within the features indicates their pro-longed exposure to fluctuating water tables and thus indicates emplacement during historic/ pre-historic events. Approximate timing of the paleo-earthquakes forming these features were derived from cross-cutting relationships and dating of the surrounding stratigraphy.

Paleo-liquefaction features observed in the eastern Christchurch suburb of Avonside were found to be truncated by a flood-unit at 0.7 m depth (Figure 2B; see Bastin et al. (2015) for a detailed description). Radiocarbon dating of a sample obtained from underlying stratigraphy provided a 2 σ calibrated age of 1660-1803, indicating the feature formed during an event that post-dates 1660. The feature was additionally cross-cut by an anthropogenic pit associated with an adjacent wool scouring factory, indicating the feature pre-dates closure of the factory in ca. 1905. The identification of pre-CES dikes indicates that an earthquake generating PGA in excess of the liquefaction triggering threshold occurred within Christchurch between 1660 and 1905. This is consistent with the New Zealand Seismic Hazard Model which predicts approximate return times of 50 years for PGAs of 0.11g (MMI 6-7) and 200 years for PGAs of 0.22g (MMI 7-8) for class C material (shallow soils) in the Christchurch area (Stirling et al., 2008).

Paleo-liquefaction features were additionally observed during trenching for a road construction project in Hamilton. Radiocarbon dating of material from within the trench combined with well-constrained timing of tephra deposits indicates the features formed >6,000 y BP, and likely between 6,000 – 26,500 y BP (Clayton et al., 2017).

Constraining approximate shaking intensities of the paleo-earthquakes

The identification of paleo-liquefaction provides evidence for earthquakes exceeding the threshold value required to trigger liquefaction and confirms the presence of sediments with low cyclic resistances to liquefaction. The threshold may be back-calculated from proximal CPT using the simplified liquefaction analysis methodologies and ground

motion prediction equations to produce a curve of magnitudes sufficient and insufficient to trigger liquefaction at the given site (e.g. Figure 3, and described in detail in Maurer et al. (2015)). A similar approach can be used to perform a back-analysis for a given historical event to determine the likelihood of liquefaction being triggered at a given site (see Bastin et al. (2016)). However, these methodologies require assumptions to be made on the amount of sedimentation that has occurred at the site and the likely depth to ground-water during the paleo-event. The amount of sediment overlying the paleo-liquefaction features may be back-stripped for the analysis to account for sedimentation at the site since the paleo-event however this adds additional uncertainties.

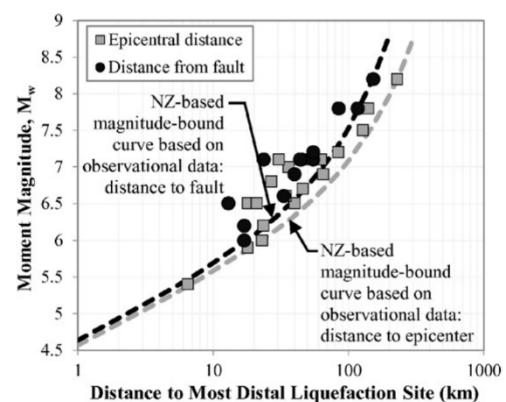


Figure 3: Example of back-calculated magnitude-bound curves comparing earthquake magnitude and distance to liquefaction as derived from New Zealand events by Maurer et al. (2015).

For example, a CPT sounding conducted at the site of paleo-liquefaction in Avonside indicates that the material at 1.6 - 2.15 m depth was potentially liquefiable ($FS < 1$) under the PGA of the Mw 7.1 September 2010 and Mw 6.2 February 2011 earthquakes. The computed minimum PGA required to liquefy this unit during these events are 0.15 g and 0.19 g respectively. The presence of pre-CES and CES liquefaction indicates the area has remained highly susceptible to liquefaction and thus it is likely that liquefaction was triggered under similar PGA for the pre-CES event. In areas where there are large uncertainties in the back-calculation, it may be assumed that the threshold most likely exceeds the global liquefaction triggering threshold of $PGA_{7.5}$ 0.09 g, as derived by Santucci de Magistris et al. (2013).

The ability to back-calculate earthquake magnitudes relies on the accurate identification of the epicentral location and associated liquefaction manifestations. The minimum magnitude may be derived using site-to-source distances utilizing curves of the distance from the epicentral location to the most distal liquefaction feature (e.g. Figure 3 and see Maurer et al. (2015)).



IMPLICATIONS AND APPLICATIONS FOR PALEO-SEISMIC HAZARD ASSESSMENTS AND INITIAL CONCLUSIONS

Analysis of paleo-liquefaction features provides an alternative, fault independent means by which return times of strong ground motions may be examined. Features are likely to be present where host sediments are preserved and provide a means by which paleo-earthquakes may be detected. Paleo-liquefaction investigations may be used to supplement paleo-seismic hazard assessments in areas where many fault sources are known to exist and/or the distribution of active faults is uncertain. The identification of paleo-liquefaction features relies on investigations to be undertaken in areas underlain by sediments with a low cyclic resistance to liquefaction and may be aided by the distributions of surface manifestations from historical events.

The distributions of liquefaction following recent and historical earthquakes in New Zealand indicate that areas underlain by recent fluvial sediments in areas hosting shallow water tables are highly susceptible to liquefaction. Examination of sub-surface features formed during recent events indicates liquefaction features typically comprise sub-vertical and planar dikes composed of fine to medium sand. Trenching in areas underlain by sediments with low cyclic resistances to liquefaction across New Zealand has revealed evidence for paleo-liquefaction preserved in the geologic record. These features provide evidence for paleo-earthquakes with site-specific ground accelerations exceeding threshold values for liquefaction and therefore may be used to make inferences on the return times of strong ground motions. Further work is required to determine approximate timing and epicentral locations of previous earthquakes generating site-specific peak ground accelerations exceeding the threshold value for liquefaction.

Acknowledgements: We thank Martitia Tuttle, Peter Almond, Pilar Villamor, for their discussions and assistance. This work was funded by an EQC Capability Fund.

REFERENCES

- Bastin, S. H., Quigley, M., Bassett, K., and Green, R. (2013). Characterization of modern and paleo-liquefaction features in eastern Christchurch, NZ, following the 2010-2011 Canterbury earthquake sequence. *Proceedings 19th NZGS Geotechnical Symposium*, Queenstown, New Zealand.
- Bastin, S., Quigley, M., and Bassett, K. (2015). Paleo-liquefaction in Christchurch, New Zealand. *GSA Bulletin*, 127(9-10):1348-1365.
- Bastin, S., Bassett, K., Quigley, M., Maurer, B., Green, R., Bradley, B., and Jacobson, D. (2016). Late Holocene liquefaction at sites of contemporary liquefaction during the 2010-2011 Canterbury earthquake sequence, New Zealand. *Bulletin of the Seismological Society of America*, 106(3): 881-903.
- Bastin, S., van Ballegooy, S., Mellsop, N., Wotherspoon, L., (2017). Liquefaction case histories from Whakatane, New Zealand as a result of the 1987 Edgecumbe Earthquake - Insights from an extensive CPT dataset and paleo-liquefaction trenching, 3rd International Conference on Performance-based Design in Earthquake Geotechnical Engineering (PBD-III) Vancouver, BC, Canada, July 16-19.
- Bastin, S., Wotherspoon, L., Ogden, M., Green, R., van Ballegooy, S., and Stringer, M. (in review). Fluvial geomorphological controls on the distribution of liquefaction in Blenheim, New Zealand following the 2016 Kaikoura Earthquake, In review for the *Bulletin of the Seismological Society of America*.
- Boulanger, R., and Idriss, I. (2014). *CPT and SPT based liquefaction triggering procedures*, Report No. UCD/CGM-14/01, Center for Geotechnical Modeling, Department of Civil and Environmental Engineering, University of California Davis, United States of America.
- Bradley, B.A., and Hughes M. (2012). Conditional peak ground accelerations in the Canterbury earthquakes for conventional liquefaction assessment. *Technical Report Prepared for the Department of Building and Housing*. April 2012. 22pp
- Clayton, P.J., Tisley, S., Bastin, S., and Green, R.A. (2017). Case study in the use of paleoliquefaction techniques to investigate liquefaction potential of Waikato soils for the Hamilton section of the Waikato expressway, *Proc. 20th NZGS Geotechnical Symposium*. Napier, New Zealand.
- Fairless, G.J., and Berrill, J.B. (1984). Liquefaction during historic earthquakes in New Zealand. *Bulletin of the New Zealand National Society for Earthquake Engineering*, 17(4): 280-291.
- GEER (2017). Geotechnical Reconnaissance of the 2016 Kaikoura, New Zealand earthquake. Report of the National Science Foundation - Sponsored Geotechnical Extreme Events Reconnaissance (GEER) Team.
- Green, R., Obermeier, S., and Olson, S. (2005). Engineering geologic and geotechnical analysis of paleoseismic shaking using liquefaction effects: field examples. *Engineering Geology*, 76: 263-293.
- Maurer, B., Green, R., Quigley, M., and Bastin, S. (2015). Development of magnitude-bound relations for paleoliquefaction analyses: New Zealand Case Study. *Engineering Geology*, 197: 253-266
- Obermeier, S. (1996). Use of liquefaction-induced features for paleoseismic analysis - an overview of how seismic liquefaction features can be distinguished from other features and how their regional distribution and properties of source sediment can be used to infer the location and strength of Holocene paleo-earthquakes. *Engineering Geology*, 44:1-76.
- Obermeier, S., Olson, S., and Green, R. (2005). Field occurrences of liquefaction-induced features: A primer for engineering geologic analysis of paleoseismic shaking. *Engineering Geology*, 76: 209-234.
- Quigley, M., Hughes, M., Bradley, B., van Ballegooy, S., Reid, C., Morgenroth, J., Horton, T., Duffy, B., and Pettinga, J. (2016). The 2010-2011 Canterbury earthquake sequence: Environmental effects, seismic triggering thresholds and geologic legacy. *Tectonophysics*, 672-673: 228-27
- Santucci de Magistris, F., Lanzano, G., Forte, G., and Fabbrocino, G. (2013). A database for PGA threshold in liquefaction occurrence. *Soil Dynamics and Earthquake Engineering*, 54: 17-19.
- Stirling, M., McVerry, G., Gerstenberger, M., Litchfield, N., Dissen, R. V., Berryman, K., Barnes, P., Wallace, L., Villamor, P., Langridge, R., Lamarche, G., Nodder, S., Reyners, M., Bradley, B., Rhoades, D., Smith, W., Nicol, A., Pettinga, J., Clark, K., and Jacobs, K. (2012). National seismic hazard model for New Zealand: 2010 update. *Bulletin of the Seismological Society of America*, 102(4): 1514-1542.
- Tuttle, M. (2001). The use of liquefaction features in paleoseismology: lessons learnt in the New Madrid Seismic Zone, Central United States. *Journal of Seismology*, 5: 361-38.



Evidence of glacio-isostatic rebound in Germany, Poland and Lithuania – an overview of the GREBAL project

Belzyt, Szymon (1), Pisarska-Jamroz, Małgorzata (Gosia) (1), Van Loon, A.J. (Tom) (2)(3), Börner, Andreas (4), Rother, Henrik (4), Bitinas, Albertas (5), Damušytė, Aldona (6), Woronko, Barbara (7)

- (1) Institute of Geology, Adam Mickiewicz University, B. Krygowski Str. 12, 61-680 Poznań, POLAND, szymon.belzyt@amu.edu.pl.
- (2) Geocom Consultants, Valle del Portet 17, 03726 Benitachell, SPAIN.
- (3) College of Earth Science and Engineering, Shandong University of Science and Technology, No.579, Qianwangang Road, 266590 Qingdao, Huangdao District, CHINA.
- (4) State Geological Survey, State Bureau for Environment, Nature Protection and Geology Mecklenburg-Vorpommern, Goldberger Str. 12, 18273 Güstrow, GERMANY.
- (5) Klaipėda University, 84 H. Manto St., Klaipėda LT-92294, LITHUANIA.
- (6) Geological Survey of Lithuania, 35 S. Konarskio St., Vilnius LT-2600, LITHUANIA.
- (7) Faculty of Geology, University of Warsaw, Żwirki i Wigury Str. 93, 02-089 Warsaw, POLAND

Abstract: *The fluctuations in the extent of the Weichselian ice sheet have induced earthquakes due to crustal rebound. These earthquakes constitute potential natural hazards for the Baltic Sea and adjacent areas. The GREBAL research project focuses on recognizing layers of unconsolidated fine-grained sediments that were deformed by earthquakes – seismites – in the southern part of the Baltic Sea Basin (north-central and eastern Europe) in the context of neotectonic activity. The seismites under study, characterized by a high concentration of soft-sediment deformation structures, are considered evidence of the glacio-isostatic rebound resulting from retreat and/or advance of the Scandinavian Ice Sheet during the Pleistocene. Our contribution presents general theses and main objectives of the GREBAL project and summarizes preliminary results of the research from eastern Germany, northern Poland and Lithuania.*

Key words: *seismites, glacio-isostatic rebound, soft-sediment deformation structures*

INTRODUCTION

A better understanding of the character of glacio-isostatic rebound during the Quaternary can deepen the insight into the behaviour of ice sheets and help to reveal the history of natural hazards, as well as to mitigate potentially negative consequences of deglaciation. The main objective of the GREBAL project (Recognition of traces left by earthquakes in Pleistocene sediments affected by glacio-isostatic rebound in the Baltic Sea Basin) is to refine the palaeoenvironmental understanding of the neotectonic history of the southern part of the Baltic Sea Basin (Germany, Poland, Lithuania, Latvia, Estonia) on the basis of reconstructions of glacio-isostatic rebound as a result of phases of retreat of the Scandinavian Ice Sheet. The area on which the project focuses is consequently located along the zone of maximum extent of the Quaternary ice sheets.

Thick ice caps exert a high pressure on the substratum, resulting in crustal subsidence during rapid ice accretion and in uplift during melting of the ice masses. The uplift of the Earth crust apparently was not gradual, but commonly shock-wise. Variations in the strain caused by a fluctuating extent of the ice cover during the Pleistocene led to rapid relaxation of accumulated stresses triggering earthquakes. The resulting shock waves could, under specific conditions, leave traces in laterally extensive layers in the form of deformed unconsolidated fine-grained sediments - seismites - characterized by a high

concentration of liquefaction-induced soft-sediment deformation structures (SSDS). To be classified as a seismite, the deformed layer must meet most of several criteria (Owen et al., 2011; Moretti & Van Loon, 2014).

North-central and eastern Europe is considered as currently low-seismicity area; yet, numerous significant earthquakes such as those near Rostock in 2001 ($M_w = 3.4$) and offshore the Kaliningrad district of Russia in 2004 ($M_w = 5.2$) have been documented during the past decades.

Within the GREBAL project, sedimentological analyses of relatively young Pleistocene seismites are used as an important tool for detailed reconstruction of the palaeoseismic activity in formerly glaciated areas. Comparison of regional analogies in the deformed layers may help to develop better criteria for the recognition of glaciation-related seismites, and to extend our knowledge concerning the formation of SSDS due to seismic shocks. These objectives are to be obtained by field investigations with emphasis on sedimentological and structural aspects, such as tracing faults in the hard-rock substratum which may have been reactivated during glaciation and/or deglaciation phases, as well as by computer modelling of seismically triggered liquefaction.

Previous research has proven the occurrence of a wide variety of SSDS triggered by earthquake-induced shocks. Fluidization-induced normal faults, ball-and-pillow structures, flame structures, sills and irregular sedimentary



intrusions, dikes and sand volcanoes were recognized within Weichselian Pleniglacial to Late Glacial alluvial-fan deposits at Oerlinghausen and Augustdorf in NW Germany (Brandes & Winsemann, 2013). The responsible shock was generated along the Osning Thrust. A combination of

liquefaction-, faulting-, and slumping-induced deformations were described from a Late Glacial glaciolacustrine succession in a cliff section on the Gnitz peninsula at the Weiße Berg site in NE Germany (Hoffmann & Reicherter, 2012, see point and photo 2 in Fig. 1).



Figure 1: General map of seismites recognized in the southern part of the Baltic Sea Basin (stars), with their relationship to the maximum ice-sheet extent. The photos show SSDS from sites(1-10).



Seismites with liquefaction- and fluidization-induced folding, collapse structures, as well as sag and load structures within Warthanian/Eemian lacustrine sediments were recognized at Siekierki in NW Poland (Van Loon & Pisarska-Jamroży, 2014, see point and photo 3 in Fig. 1). Druzhinina et al. (2017) recently proposed a paleoseismic origin of structures in Holocene deposits at Ryadino (Šešupė River Valley, Kaliningrad District, Russia), from where tongue-shaped and dome-shaped diapir-like structures were described. In the easternmost part of study area, seismites were recognized at Valmiera (Gauja river valley, NW Latvia) and Rakuti (Daugava river valley, SE Latvia, see points and photos 9-10 in Fig. 1) within Late Weichselian glaciofluvial and glaciolacustrine sands and silts (Van Loon et al., 2016).

The intraplate neotectonic activity of north-central Europe has been summarized by Brandes et al. (2015).

RESULTS

New data have recently been obtained by investigation of two unconsolidated fine-grained (muds, muddy sands and fine sands) seismites in the Dwasieden coastal cliff of Rügen Island near Sassnitz (NE Germany, see point and photo 1 in Fig. 1). These seismites have been dated as Late Weichselian, during a phase of ice advance. The abundant SSDS include (1) loading structures (load casts, flame structures, pseudonodules, ball-and-pillow structures and mud diapirs), (2) fluid-escape structures, and (3) brittle deformations (small-scale faults). The overall thickness of the deformed unit is 0.5 m and the lateral extent of the seismites is at least some 125 m. The abundant SSDS in the lower one are interpreted as having also been deformed under periglacial conditions. The observations suggest faulting phases during gradual subsidence of the Earth crust as a result of increasing ice load during ice advance.

In NW Poland, Saalian seismic activity has been recognized within a glaciolacustrine succession at Ujście (Pisarska-Jamroży et al., in review, see point and photo 4 in Fig. 1). Two layers with SSDS (load casts, flame structures and pseudonodules) induced by liquefaction and fluidization processes were recognized. The two deformed layers are believed to have been caused by seismic shocks.

Pisarska-Jamroży & Woźniak (in review, see point and photo 5 on Fig. 1) proposed a seismic trigger as the most probable cause of deformations in the Middle Pleistocene glaciolacustrine fan deposits in the Rzućewo coastal cliff in N Poland (Puck Bay). Fold structures, load structures (load casts, pseudonodules and flame structures), water-escape structures, brittle deformations (medium- and small-scale upthrusts and normal faults), and fragments of broken-up laminae are present.

The preliminary results of research in Lithuania suggest different phases of seismic activity during deglaciation phases. Deformed layers with abundant SSDS occur at Dyburiai (Minija river valley, see point and photo 6 on Fig. 1), Seredžius Slinktis (Dubysa river valley, see point and photo 7 on Fig. 1) and Liciškėnai (see point and photo 8 on Fig. 1). More detailed investigation of these sites is going on.

DISCUSSION

The preliminary results confirm that earthquakes connected with fluctuation in the extent of the Scandinavian Ice Sheet occurred as a result of rapid relaxation of accumulated stresses. The faulting may have occurred during both advance and retreat of the ice sheet. Dating of recently recognized seismites suggests faulting phases in between gradual down-pressing of the Earth crust during ice advance and multi-stage rebound.

The main challenge of the GREBAL project is to develop unambiguous criteria that allow to distinguish SSDS caused by seismicity due to post-glacial rebound from other SSDS (e.g. by gravitational processes, salt tectonics, glaciotectonics, permafrost processes). Therefore, further research will be devoted to tracing faults in the deep geological subsurface that could be reactivated during the Pleistocene, finding regional analogies in the Baltic Sea Basin, and establishing the frequency of earthquakes in combination with numerical modelling of seismically triggered liquefaction.

Acknowledgements: The GREBAL Project is financially supported by a grant from the National Science Centre, Poland, No. UMO-2015/19/B/ST10/0066.

REFERENCES

- Brandes, C. & Winsemann, J., 2013. Soft-sediment deformation structures in NW Germany caused by Late Pleistocene seismicity. *International Journal of Earth Sciences* 102, 2255–2274.
- Brandes, C., Steffen, H., Steffen, R. & Wu, P., 2015. Intraplate seismicity in northern central Europe is induced by the last glaciation. *Geology* 43, 611–614.
- Druzhinina, O., Bitinas, A., Molodkov, A. & Kolesnik T., 2017. Palaeoseismic deformations in the eastern Baltic region (Kaliningrad District of Russia). *Estonian Journal of Earth Sciences* 66, 119–129.
- Hoffmann, G. & Reicherter, K., 2012. Soft-sediment deformation of Late Pleistocene sediments along the southwestern coast of the Baltic Sea (NE Germany). *International Journal of Earth Sciences* 101, 351–363.
- Pisarska-Jamroży, M., Van Loon, A.J., Mleczak, M. & Roman, M., 2017. Saalian glacio-isostatic rebound of the Earth crust triggered enigmatic gravity flow at Ujście (W Poland), as evidenced by seismites. *Geomorphology* (in review).
- Pisarska-Jamroży, M. & Woźniak, P.P., 2017. Debris flow and glacioisostatic induced soft-sediment deformation structures in a Pleistocene glaciolacustrine fan: southern Baltic Sea coast, Poland. *Geomorphology* (in review).
- Moretti, M. & Van Loon, A.J., 2014. Restrictions to the application of “diagnostic” criteria for recognizing ancient seismites. *Journal of Palaeogeography* 3, 162–173.
- Owen, G., Moretti, M. & Alfaro, P., 2011. Recognising triggers for soft-sediment deformation: Current understanding and future directions. *Sedimentary Geology* 235, 133–140.
- Van Loon, A.J. & Pisarska-Jamroży, M., 2014. Sedimentological evidence of Pleistocene earthquakes in NW Poland induced by glacio-isostatic rebound. *Sedimentary Geology*, 300, 1–10.
- Van Loon, A.J., Pisarska-Jamroży, M., Nartišs, M., Krievāns, M. & Soms, J., 2016. Seismites resulting from high-frequency, high-magnitude earthquakes in Latvia caused by Late Glacial glacio-isostatic uplift. *Journal of Palaeogeography* 5, 363–380



Measuring the slip-rate of the Main Kopeh Dagh Fault, Turkmenistan

Bezmenov, Yevgeney (1), Begejev, Geldy (1), Carolin, Stacy (2), Grützner*, Christoph (3, 4), Jackson, James (3), Mirzin, Robert (1), Rhodes, Edward (5), Sadykov, Maksim (1), Walker, Richard (2)

- (1) Institute of Seismology, Academy of Sciences, Turkmenistan.
- (2) Dept. of Earth Sciences, Oxford University, UK.
- (3) Dept. of Earth Sciences, Cambridge University, UK.
- (4) Now at: Inst. of Geological Sciences, Friedrich Schiller University Jena, Germany. *Email: christoph.gruetzner@uni-jena.de
- (5) Dept. of Geography, Sheffield University, UK

Abstract: The relative motion between the South Caspian Basin (SCB) and its surroundings is accommodated by left-lateral fault systems in Iran, and the right-lateral Main Kopeh Dagh Fault (aka Ashgabat Fault) in Turkmenistan. Determining the rates of slip on these faults is key for understanding the motion of the SCB. However, several different tectonic models exist due to the uncertainties in the existing data. Here, we present the findings from preliminary fieldwork in Turkmenistan with the aims of (i) Providing estimates of the long-term slip-rate on the Main Kopeh Dagh Fault, (ii) Providing initial estimates of its past earthquake activity, and (iii) Better understanding the seismic hazard to the city of Ashgabat which is home to ~1 million people. We show surface evidence for a large magnitude earthquake that is not known in the historical record and we report offset geomorphic markers that will allow estimation of slip rates.

Key words: Main Kopeh Dagh Fault; Turkmenistan; South Caspian Basin; slip rate

MOTIVATION

To the east and southeast of the South Caspian Basin (SCB), shortening related to continental collision is taken up by faults in Northeastern Iran and Turkmenistan (Fig. 1A). The SCB moves as an independent block, but the direction and rates are poorly understood (Jackson et al., 2002). Attempts to measure the motion of the SCB concentrate on observations from its boundaries, as there are no GPS stations offshore and the scarcity of strong instrumentally-recorded earthquakes does not allow precise constraint on the motion from moment tensor solutions. The relative motion between the SCB and surrounding parts of Iran and Turkmenistan is accommodated by the Shahroud left-lateral fault system in Iran, and the right-lateral Main Kopeh Dagh Fault (MKDF; also known as Ashgabat Fault) in Turkmenistan. Determining the rates and directions of slip on these two faults is the key for determining the motion of the SCB, and yet there are relatively few estimates at present, and as such, several different tectonic models exist.

InSAR measurements of strain accumulation across the Shahroud fault system reveal 5-6 mm/yr of left-lateral motion being stored across the fault (Mousavi et al., 2015). This is consistent with GPS measurements of strain accumulation if the pole of rotation of the SCB is sited far from it. Similar measurements across the MKDF have large uncertainties such that the rate of strain accumulation is anywhere in the range 5-12 mm/yr (Walters et al., 2011). From existing GPS measurements in Iran it can be estimated that the slip rate of the MKDF is up to 7.5 mm/yr (right-lateral), though it is unclear how well-constrained this estimate is because the GPS stations are sited far from the fault (Mousavi et al., 2013).

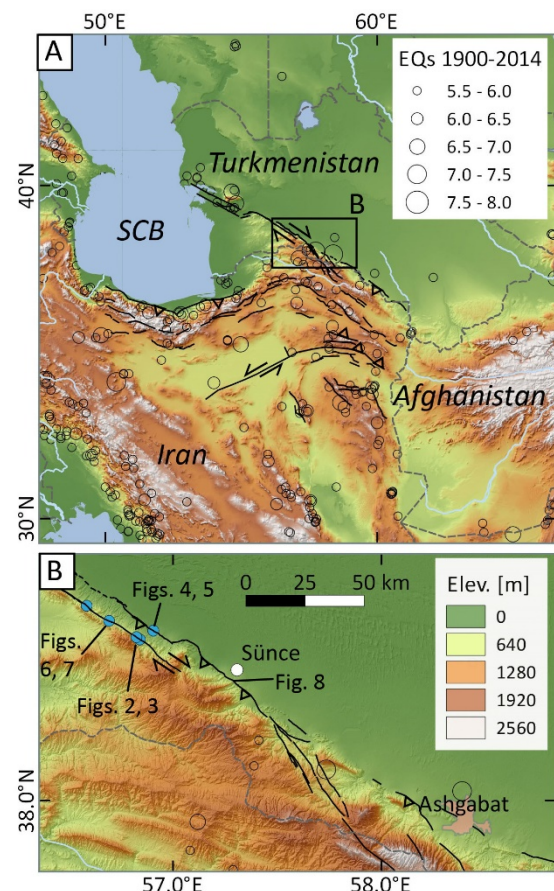


Figure 1: A) Location of the study area. Empty dots are earthquakes with $M_w > 5.5$ from the ISC-GEM database, 1900-2014 (ISC, 2014), black lines are faults from Mousavi et al. (2013) and own mapping. SCB: South Caspian Basin. Inset marks figure 1B. B) Detailed view of the study area NW of Sünce. Blue dots are field sites, active fault traces in black.



Ashgabat experienced a damaging M7.2 earthquake in 1948 (Orasymbetov et al., 1960). The rupture did not occur on the MKDF, but on the nearby Gyaur Faults (Berberian & Yeats, 2001). Apart from this, there is little information on strong earthquakes in the territory of Turkmenistan such that field investigations are necessary to understand fault activity.

In order to date the abandonment of the surfaces, we excavated pits up to 2 m deep into the alluvial fans and sampled fine-grained material for OSL/IRSL burial dating (Fig. 3). These ages combined with the measured offsets will allow us to calculate the slip-rate. All samples are currently being processed and we have no dating results yet.

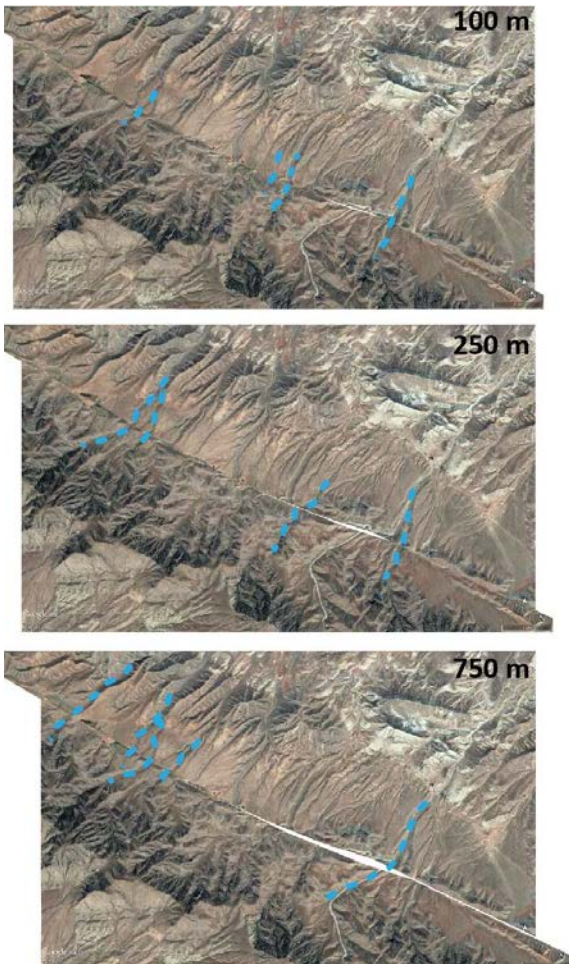


Figure 2: Different generations of offset streams incised into alluvial fans record right-lateral motion of the MKDF. Sets of streams can be restored with offsets between 100-750 m.

SLIP RATE OF THE MAIN KOPEH DAGH FAULT

In order to directly measure the fault’s slip rate and to investigate its earthquake history we conducted a first field work campaign in 2016. We concentrated on five sites to the NW of Sünce, about 150 km away from Ashgabat (Fig. 1B). Judging from the geomorphology, this region is characterised by slip partitioning: (i) A NW-SE trending strike-slip fault offsets linear and planar markers such as terraces and streams, and (ii) A thrust fault with the same strike shows vertical offsets in the youngest alluvial deposits a few kilometres further to the NE.

We analysed satellite imagery of the strike-slip fault to identify suitable targets for long-term slip rate estimates. Streams incised into alluvial fans of various ages record right-lateral offsets of up to 750 m (Fig. 2).



Figure 3: Fine-grained material from the offset alluvial fans was sampled for OSL/IRSL dating of surface abandonment.

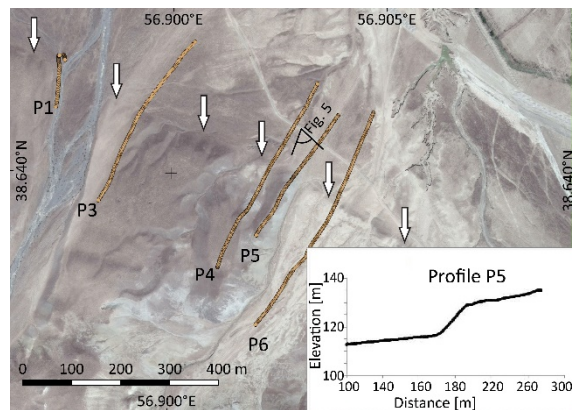


Figure 4: Offset river terraces along the mountain front, DGPS profiles are marked in orange, white arrows mark the fault, and inset shows the vertical offset recorded in profile P5.

Along the thrust fault that parallels the strike-slip fault we found river terraces with up to 10 m vertical offset (Fig. 4). We measured the vertical separation of the surfaces with differential GPS (DGPS). The terrace units include mainly coarse fluvial gravels, but also show fine-grained bands



near the surface (Fig. 5). These silty-sandy layers were sampled for OSL/IRSL dating, which is underway, and shall allow us to determine a vertical slip rate for this part of the fault. Unfortunately, no good outcrop of the fault itself was encountered, which is why we have only limited constraints on the subsurface geometry so far.



Figure 5: River terraces offset by the thrust fault, white arrows mark the fault, person (CG) encircled for scale.

EARTHQUAKE HISTORY OF THE MAIN KOPEH DAGH FAULT

In order to better understand the seismic hazard of the MKDF, as characterised by earthquake recurrence intervals, magnitudes, mechanisms, and slip per event, it is necessary to extend the earthquake catalogue by means of paleoseismic trenching.



Figure 6: An uphill-facing scarp that probably formed in a single earthquake along the strike-slip fault can be traced for several tens of kilometres. Person (RW) for scale, white arrows mark the trace of the surface rupture.

We identified a paleo-surface rupture along the strike-slip fault with more than 5 m horizontal offset that probably occurred in a single, large event. In most places we also observed a dip-slip component of the rupture that formed an uphill-facing scarp (Fig. 6). The surface rupture can be traced for several tens of kilometres and may correspond to an earthquake of $M \sim 7.5$ based on scaling relationships between offset/length and earthquake magnitude (Wells & Coppersmith, 1994). We used DGPS to create a high-resolution DEM of an area that was chosen for a more detailed study (Fig. 7).

A hand-dug trench was excavated across the fault where sediment had ponded against an uphill-facing scarp (Fig. 8). The 1.2 m deep trench revealed fine-grained sediment (fine sands and silt) juxtaposed with coarse boulders that were

surrounded by a sandy-silty matrix. Our preliminary interpretation is that a surface-rupturing earthquake offset the coarse alluvial fan material by at least 1.2 m vertically (the trench depth) and several metres horizontally as evidenced by the offset of a nearby channel. Fine-grained sediment then ponded against the scarp and filled the accommodation space, leading to the present day morphology with its flat plateau at the scarp (Fig. 8). We sampled the fine-grained material for OSL/IRSL dating, which is currently underway.

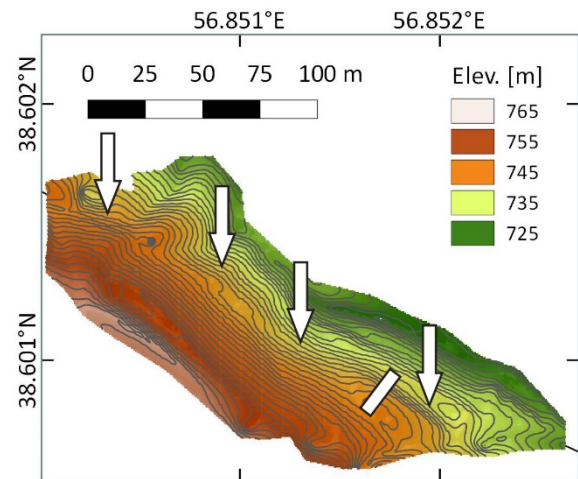


Figure 7: DGPS-derived DEM of the trench site. The DEM was computed from the DGPS point cloud by triangulation using QGIS. White arrows mark the fault trace, rectangle shows the trench site.

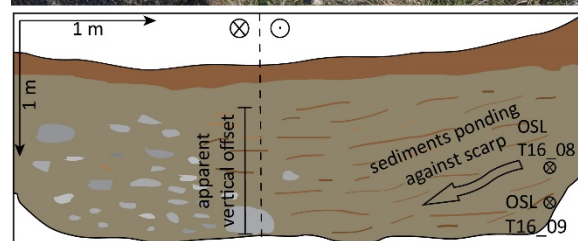


Figure 8: Trench site with the uphill-facing scarp and trench log.

Offset fluvial sediments were observed along the thrust fault near Sünce (Figs. 1, 9). In a river cutting we identified ~ 0.5 m of horizontal shortening and ~ 0.3 m of vertical offset along a thrust fault dipping $\sim 25^\circ$ to the south. The faulting affects sediments just 1.5 m above present day river level in the youngest river terrace. We sampled both the hanging wall and the footwall for OSL/IRSL and are currently waiting for the results.

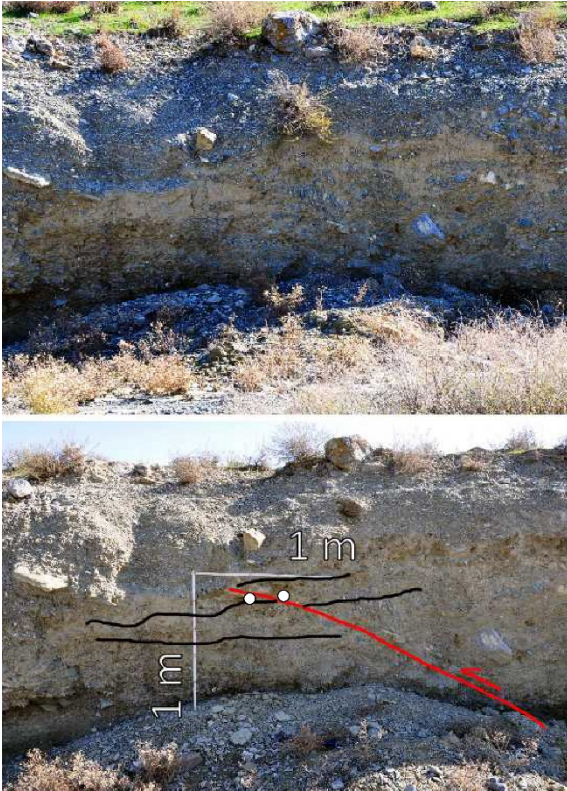


Figure 9: A thrust fault offsets the youngest layers of a river terrace near Sünce. Upper panel: The outcrop before cleaning and sampling; colours, saturation, and contrast were enhanced for better visibility. Lower panel: Annotated outcrop with the two OSL/IRSL sample locations on either side of the fault (white dots).

CONCLUSIONS

We combined remote-sensing and field observations from a field work campaign in 2016 to better understand the slip-rate and earthquake history of the MKDF in Turkmenistan. Several hundreds of metres of horizontal offsets are recoded in rivers and alluvial fans, which we sampled for OSL/IRSL dating of the fan abandonment. These data will be used to narrow down the slip rate of the fault, which will allow to better constrain the tectonic behaviour of the South Caspian Basin. We present geomorphologic and stratigraphic evidence for past surface-rupturing earthquakes. Our preliminary results will

pave the way for future, more in-depth studies and help to better understand the seismogenic behaviour of the Main Kopeh Dagh Fault. These data are urgently needed as the capital city with its ~1 million inhabitants is very close to the main fault trace and has already been devastated by an earthquake in 1948, which, however, occurred on a secondary structure.

Acknowledgements: This research was run under the Earthquakes without Frontiers project, funded by NERC and ESRC (Grant code: EwF_NE/J02001X/1_1), and within the Centre for Observation and Modelling of Earthquakes and Tectonics (COMET).

REFERENCES

- Berberian, M., & Yeats, R. S. (2001). Contribution of archaeological data to studies of earthquake history in the Iranian Plateau. *Journal of Structural Geology*, 23(2), 563-584.
- ISC (2014). International Seismological Centre, On-line Bulletin, <http://www.isc.ac.uk>, Internatl. Seismol. Cent., Thatcham, United Kingdom.
- Jackson, J., Priestley, K., Allen, M., & Berberian, M. (2002). Active tectonics of the south Caspian basin. *Geophysical Journal International*, 148(2), pp.214-245.
- Mousavi, Z., Walpersdorf, A., Walker, R. T., Tavakoli, F., Pathier, E., Nankali, H., Nilfouroushan, F., & Djamour, Y. (2013). Global Positioning System constraints on the active tectonics of NE Iran and the South Caspian region. *Earth and Planetary Science Letters*, 377, 287-298.
- Mousavi, Z., Pathier, E., Walker, R. T., Walpersdorf, A., Tavakoli, F., Nankali, H., Sedighi, M., & Doin, M. P. (2015). Interseismic deformation of the Shahroud fault system (NE Iran) from spaceborne radar interferometry measurements. *Geophysical Research Letters*, 42(14), 5753-5761.
- Orasymbetov, N. O., Serdyukov, M. M., & Shanin, S. A., (1960). The 1948 Ashgabat Earthquake (in Russian). Государственное издательство литературы по троеительству архитектуре и строительным материалам, Moscow.
- Walters, R. J., Elliott, J. R., Li, Z., & Parsons, B. (2013). Rapid strain accumulation on the Ashkabad fault (Turkmenistan) from atmosphere-corrected InSAR. *Journal of Geophysical Research: Solid Earth*, 118(7), 3674-3690.
- Wells, D. L., & Coppersmith, K. J., 1994. New empirical relationships among magnitude, rupture length, rupture width, rupture area, and surface displacement. *Bulletin of the Seismological Society of America*, 84(4), 974-1002.



Hydrocode modeling of seismite deformation structures – assumption and preliminary results

Bronikowska, M. (1) and Pisarska-Jamroży, M. (1)

(1) Institute of Geology, Adam Mickiewicz University in Poznań, Krygowski 12, 61-680 Poznań, Poland. malgorzata.bronikowska@amu.edu.pl

Abstract: Numerical modeling of the formation of soft sediments deformation structures resulted from earthquakes requires specific tools which are adopted for solving time-dependent, non-linear fluid flow problems. Existing computer codes developed mainly for modeling of seismic wave propagation, focus on seismic signals received at some distance from the wave source. Linear wave equations applied in such codes cannot face the problem of sediments movement in disturbed, non-homogenous media. In this work, we present new SSDF modeling method using shock physics hydrocode iSALE2D. The used code has been originally developed to simulate hyper velocity impact processes and is currently under the modification aimed at its adaptation for this scientific goal. Such approach allows for reconstruction of seismites spatial distribution and geometry, which makes it innovative and noteworthy.

Key words: numerical modeling, hydrocode, seismic wave

INTRODUCTION

Paleoseismological research relies on recognition of seismic deformation structures, especially their size, outer shape, and internal structure. Such deformation structures are a result of the seismic wave propagation which causes sediments to liquefy. So, there is a progressive change in the palaeoearthquakes traces left in the sediments.

About 90 percent of seismic deformation structures occur at a distance lower than 40 km from the epicenter (Galli, 2000), while most of them (related with the earthquake magnitude 5-7) are formed at a distance of about 20 km from the epicenter (Papadopoulos & Lefkopoulos, 1993). Lower magnitude earthquakes cause the sediments to liquefy only at a small distance from the epicenter.

Not all earthquakes result in liquefaction (Owen and Moretti, 2011), because liquefaction and fluidization occur only if the shock is strong enough and if the sediments are sufficiently susceptible to deformation. According to Allen (1986), Ambraseys (1988) and Galli (2000), liquefaction features are unlikely to develop in earthquakes of magnitude less than 5. The magnitude, M , of an earthquake that can cause liquefaction is at least $M = 4.5-5$ (see for instance, Rodríguez-Pascua et al., 2000).

The spatial distribution and lateral position of different sizes and types of seismic deformation structures is well established and a very useful tool allowing the reconstruction of past seismic events (Owen et al., 2011; Hoffmann & Reicherter, 2012; Moretti & Van Loon, 2014; Van Loon & Pisarska-Jamroży, 2014; Van Loon et al., 2016).

Numerical modeling of the formation of soft sediment deformation structures resulted from seismic wave

propagation requires tools adapted for computing fluid dynamics time dependent, non-linear problems. Well established method for solving such problems is hydrocode modeling – computer simulations able to model fluid flow at all speeds using conservations laws from macroscopic point of view together with equation of state for a given medium of wave propagation (Anderson, 1987).

METHODS

To investigate the formation of soft-sediment seismic deformation structures, we have used the iSALE-2D shock physics code (Wünnemann et al., 2006), which is based on the SALE hydrocode solution algorithm (Amsden et al., 1980) and has been originally developed to simulate hyper velocity impact processes. SALE was modified to include an elasto-plastic constitutive model, fragmentation models, various equations of state (EoS), and multiple materials (Melosh et al. 1992; Ivanov et al. 1997). More recent improvements include a modified strength model (Collins et al. 2004) and a porosity compaction model (Wünnemann et al., 2006; Collins et al., 2011). iSALE has been benchmarked against other hydrocodes (Pierazzo et al., 2008) and validated against experimental data (Pierazzo et al., 2008; Davison et al., 2011; Miljković et al., 2012). iSALE2D hydrocode is based on ALE (Arbitrary Lagrangian Eulerian) method, what means that the code allows material to flow through the computational mesh (Hirt et al., 1974). The code can simulate up to three different materials with various properties as strength, compaction and damage models.

The use of hydrocode modeling to study the seismites and their spatial distribution and geometry allows the precise reconstruction of the whole seismic event. Such approach has never been used in previously studies.



RESULTS

Although the work is still ongoing, we expect the following results:

1. The recognition of the soft sediment deformation structures caused by the seismic wave propagation and comparison with deformation structures obtained by Owen (1996) in experiment.
2. The recognition of spatial distribution of the soft sediment deformation structures resulted from the specific magnitude earthquake.
3. The reconstruction of the soft sediment deformation structures formation processes, i.e. the energy distribution and forces responsible for their geometry development.
4. The clarification of criteria for the soft-sediment seismic deformations diagnosis.

Acknowledgements: The GREBAL project is financially supported by a grant from the National Science Center, Poland (No. 2015/19/B/ST10/00661). We acknowledge the developers of iSALE, especially Kai Wünnemann for his substantive help.

REFERENCES

- Allen, J.R.L., 1986. Earthquake magnitude-frequency, epicentral distance, and soft-sediment deformation in sedimentary basins. *Sedimentary Geology* 46, 67–75.
- Ambraseys, N.N., 1988. Engineering seismology. *Earthquake Engineering and Structural Dynamics* 17, 1-105.
- Amsden, A., Ruppel, H. & Hirt, C., 1980. SALE: A simplified ALE computer program for fluid flow at all speeds. Los Alamos National Laboratories Report, LA-8095:101p. Los Alamos, New Mexico: LANL.
- Anderson, C. E., 1987. An overview of the theory of hydrocodes. *International Journal of Impact Engineering*, 5, 33–59.
- Collins, G., Melosh, H. & Wünnemann, K., 2011. Improvements to the epsilon-alpha porous compaction model for simulating impacts into high-porosity solar system objects. *International Journal of Impact Engineering* 38, 434–439.
- Davison, T.M., Collins, G.S., Elbeshausen, D., Wünnemann, K. & Kearley, A., 2011. Numerical modeling of oblique hypervelocity impacts on strong ductile targets. *Meteoritics & Planetary Science* 46,510–1524.
- Galli, P., 2000. New empirical relationships between magnitude and distance for liquefaction. *Tectonophysics* 324, 169–187.
- Hirt, C.W., Amsden, A.A. & Cook, J.L., 1974. An arbitrary lagrangian-eulerian computing method for all flow speed. *Journal of Computational Physics* 14, 227–253
- Hoffmann, G. & Reicherter, K., 2012. Soft-sediment deformation of Late Pleistocene sediments along the southwestern coast of the Baltic Sea (NE Germany). *International Journal of Earth Sciences* 101, 351–363.
- Ivanov, B.A., deNiem D. & Neukum, G., 1997. Implementation of dynamic strength models into 2D hydrocodes: Applications for atmospheric breakup and impact cratering. *International Journal of Impact Engineering* 20,411–430.
- Melosh, H.J., Ryan, E.V. & Asphaug, E., 1992. Dynamic fragmentation in impacts: Hydrocode simulation of laboratory impacts. *Journal of Geophysical Research* 97:14, 735–14,759.
- Miljković, K., Collins, G.S., Patel, M.R., Chapman, D. & Proud, W., 2012. High-velocity impacts in porous solar system materials. *AIP Conference Proceedings* 1426, 871–874.
- Moretti, M. & Van Loon, A.J., 2014. Restrictions to the application of “diagnostic” criteria for recognizing ancient seismites. *Journal of Palaeogeography* 3, 162–173.
- Owen, G. & Moretti, M., 2011. Identifying triggers for liquefaction-induced soft-sediment deformation in sands. *Sedimentary Geology* 235, 141–147.
- Owen, G., 1996. Experimental soft-sediment deformation: structures formed by the liquefaction of unconsolidated sands and some ancient examples. *Sedimentology* 43, 279–293.
- Owen, G., Moretti, M. & Alfaro, P., 2011. Recognising triggers for soft-sediment deformation: Current understanding and future directions. *Sedimentary Geology* 235, 133–140.
- Papadopoulos, G.A., Lefkopoulos G., 1993. Magnitude-Distance relation for liquefaction in soil from earthquakes. *Bulletin of the Seismological Society of America* 83, 925–938.
- Pierazzo E., Artemieva N., Asphaug N., Baldwin E., Cazamias E.C., Coker R., Collins G.S., Crawford D.A., Davison T., Elbeshausen D., Holsapple K.A., Housen K.R., Korycansky D.G. & Wünnemann, K., 2008. Validation of numerical codes for impact and explosion cratering: Impacts on strengthless and metal targets. *Meteoritics & Planetary Science* 43,1917–1938.
- Rodríguez-Pascua, M.A., Calvo, J.P., De Vicente, G. & Gomez-Gras, D., 2000. Soft-sediment deformation structures interpreted as seismites in lacustrine sediments of the Prebetic Zone, SE Spain, and their potential use as indicators of earthquake magnitudes during the Late Miocene. *Sedimentary Geology* 135, 117–135.
- Van Loon, A.J. & Pisarska-Jamroży, M., 2014. Sedimentological evidence of Pleistocene earthquakes in NW Poland induced by glacio-isostatic rebound. *Sedimentary Geology*, 300, 1–10.
- Van Loon, A.J., Pisarska-Jamroży, M., Nartišs, M., Krievāns, M. & Soms, J., 2016. Seismites resulting from high-frequency, high-magnitude earthquakes in Latvia caused by Late Glacial glacio-isostatic uplift. *Journal of Palaeogeography* 5, 363–380.
- Wünnemann, K., Collins, G. & Melosh, H., 2006. A strain-based porosity model for use in hydrocode simulations of impacts and implications for transient crater growth in porous targets. *Icarus* 180, 514–527.



Varve ages and the paleoearthquake interpretations of event horizons from three lakes, Quebec, Canada

Brooks, Gregory (1)

(1) Geological Survey of Canada, Natural Resources Canada, 601 Booth Street, Ottawa, Ontario, Canada, K1A0E8. Email greg.brooks@canada.ca.

Abstract: Sub-bottom acoustic profile surveys at lakes Dasserat, Duparquet, and Dufresnoy, Quebec, Canada, revealed multiple stratigraphic occurrences of subaqueous mass transport deposits (MTDs) of early Holocene age. Compiled event horizon maps range in composition from a single, isolated MTD to numerous, widespread deposits that are the product of multiple, synchronous failures. Analysis of glaciolacustrine rhythmic couplets that are interbedded between the MTDs yielded precise varve ages for the event horizons. Thirteen paleoearthquakes are interpreted from a total of 23 event horizons within the three lakes that accumulated between 9400 and 8720 ± 200 ^{14}C cal BP. The level of interpretative confidence for the paleoearthquakes varies from high to low, reflecting the weight of evidence supporting the paleoearthquake interpretations.

Key words: paleoearthquakes, mass transport deposits, varves, glacial Lake Ojibway, eastern Canada.

INTRODUCTION

Earthquake shaking can be represented stratigraphically within lake basins as event horizons composed of multiple, synchronously-aged, mass transport deposits (MTDs). A paleoearthquake interpretation is strong when multi-MTD event horizon signatures are correlated between lake basins and therefore represent a regionally synchronous occurrence that is best explained by a seismic mechanism. Developing accurate and precise chronology for the lake deposits, however, can be a challenge, particularly with studies investigating timescales extending into the mid- or early Holocene. Age uncertainty can complicate the correlation of possibly common prehistoric event horizons between lake basins.

This paper summarizes event horizon stratigraphies of MTDs from study areas at lakes Dufresnoy, Duparquet and Dasserat, situated 24 to 38 km apart in western Quebec, eastern Canada (Fig. 1). In all three lakes, the event horizons are interbedded within glaciolacustrine deposits that accumulated within glacial Lake Ojibway, which existed during regional deglaciation. Event horizon chronology is interpreted from the rhythmic couplets of the Timiskaming varve series and has annual resolution. The results of the study provide insights into the interpretation of event horizon stratigraphies that accumulated in sub-basins of a major glacial lake during regional deglaciation.

STUDY AREA

Lakes Dufresnoy, Duparquet and Dasserat are located in the Rouyn-Noranda region of western Quebec, near the Ontario-Quebec border, about 380 km northwest of Ottawa, Notario, Canada's national capital (Fig. 1). The lakes are situated within an intracratonic setting in eastern Canada and are in-line with, but situated ~180 km north of the concentrated belt of historical seismicity known as Western Quebec Seismic Zone (WQSZ; Fig.1). The 1935 Temiskaming

earthquake (M 6.1) with an epicentre located about 190 km south of the study area, is the most significant historical earthquake in the northern portion of the WQSZ.

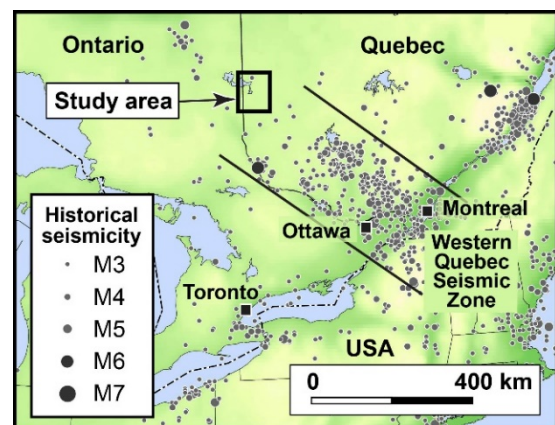


Figure 1: Map of the location of the Lake Dupaerquet, Dufresnoy and Dasserat study areas, Quebec, and historical seismicity of the Western Quebec Seismic Zone, eastern Canada (Source: Natural Resources Canada).

The study area lakes are located within the area of western Quebec-northeastern Ontario inundated by a large glacial lake that was impounded against the northerly retreating Laurentide Ice Sheet. This lake, known at different stages as lakes Barlow, Barlow-Ojibway or Ojibway, formed within the isostatically-depressed landscape between roughly 11.0 and 8.4 ^{14}C ka cal BP (Vincent and Hardy 1979; Veillette 1994; Dyke et al., 2003; Breckenridge et al., 2012). Rhythmically laminated and bedded couplets that accumulated in the glacial lake are interpreted to be annual varves. Initially compiled by Antevs (1925, 1928), the 'Timiskaming varve series' consists of about 2100 rhythmic couplets that can be correlated between different locations across the region by varve thickness patterns. Following the terminology of other studies in the area, the varves in lakes Duparquet, Dufresnoy and Dasserat are referred to as glacial Lake Ojibway deposits.

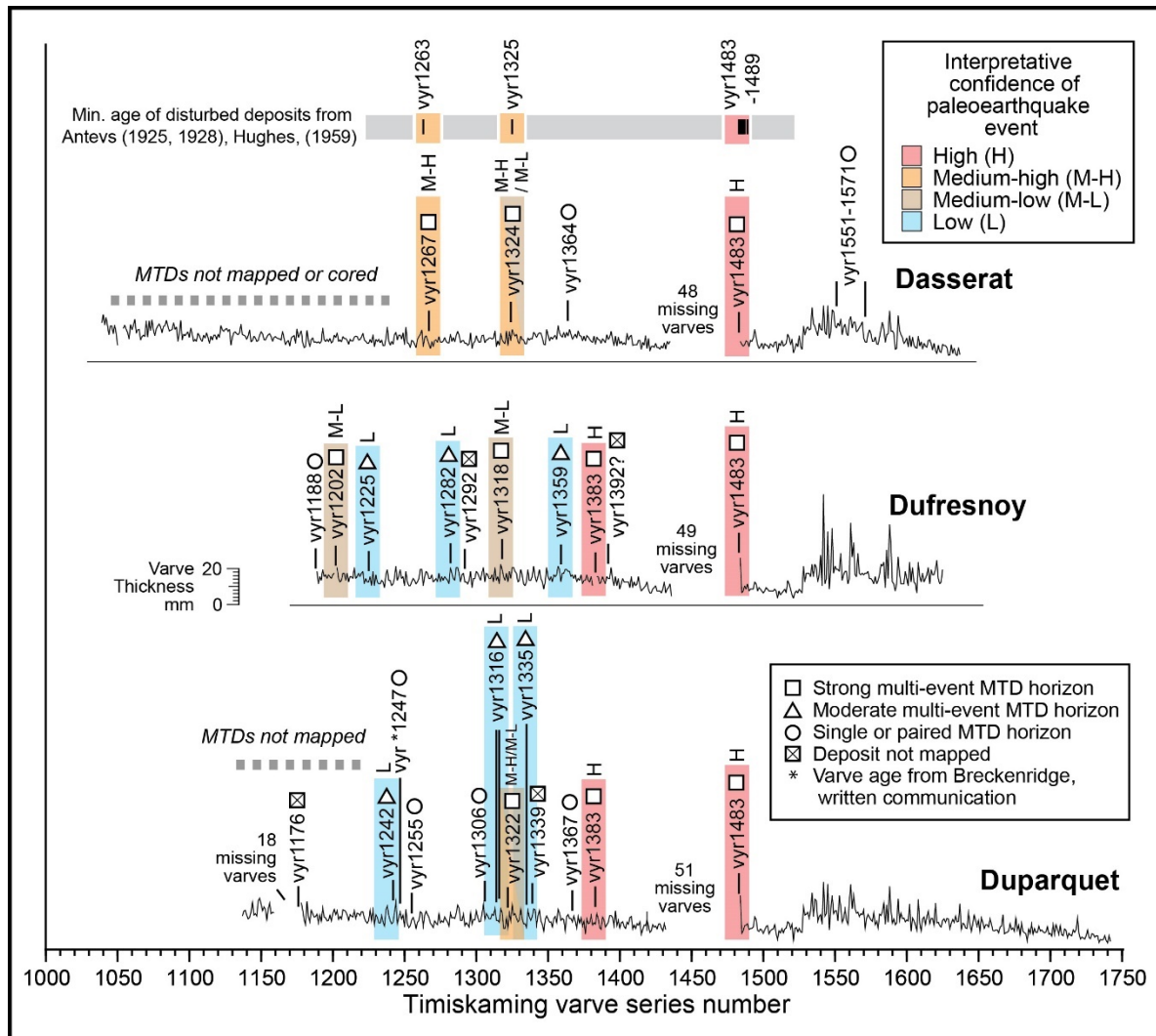


Figure 2: Diagram depicting the ages of the event horizons and unmapped mass transport deposits (MTDs) encountered in core from the Duparquet, Dufresnoy, and Dasserat study areas, superimposed on the respective varve thickness plots. Data for Lac Dasserat is from Brooks (2016a, 2016b). Varve numbering follows that of the Timiskaming varve series. Across the top of the diagram are three groupings of varve ages for disturbed glaciolacustrine deposits exposed at other locations within the glacial Lake Ojibway basin, as compiled by Brooks (2016b, his Fig. 9). The event horizons superimposed on a shaded rectangle are interpreted to represent paleoearthquakes with the level of interpretative confidence keyed by colour shading and a letter code. Unshaded event horizons and unmapped MTDs are not interpreted to represent paleoearthquakes.

RESULTS AND INTERPRETATIONS

Ten, eight and five event horizons maps were compiled for the MTDs that are interbedded within the glaciolacustrine deposits, using dense grids of sub-bottom acoustic profiles with approximately decimetre-scale resolution, at the Duparquet (64 line-km), Dufresnoy (103 line-km) and Dasserat (144 line-km) study areas, respectively. Each map depicts the MTDs interpreted to occur at a common stratigraphic level in the sub-bottom. The event horizon maps range in composition from an isolated MTD, which is the product of a single failure, to multiple MTDs that are widely distributed and coalesced in the sub-bottom and the product of numerous failures. To weight the relative differences between the event horizons, the signatures are

classified as: strong (greater than six MTDs); moderate (three to five MTDs); or single/paired (one or two MTDs). Cores recovering glaciolacustrine and mass transport deposits were collected at six, four and three sites within the Dasserat, Duparquet and three Dufresnoy study areas, respectively. Rhythmic couplet analysis yielded varve ages for the twenty-three event horizons and four unmapped MTDs, as shown on Fig. 2. The unmapped MTDs were encountered in core, but are too thin to recognize in the profile returns or too limited in extent to map. Fig. 2 also includes three groupings of varve ages representing disturbed glaciolacustrine deposits located elsewhere in the glacial Lake Ojibway basin that are reported by Antevs (1925, 1928) and Hughes (1959).



The evidence supporting a possible paleoearthquake interpretations of a given event horizon is variable, depending on: the weight of the MTD signature(s), the possible age correlation of horizons between the study areas or to a disturbed deposit(s) mentioned in the literature, and the likelihood of an aseismic mechanism explaining the triggering of the MTD(s). As regards the latter factor, Brooks (2016b) reviewed possible aseismic triggering mechanisms for event horizons at Lac Dasserat that are interbedded within deep-water glaciolacustrine deposits of glacial Lake Ojibway. He considered that grounded iceberg keels, high sedimentation rates, and wave actions possibly could account for a horizon composed of one or two MTDs, but are unlikely to cause the numerous synchronous failures associated with a strong or moderate multi-MTD event horizon. He further considered that a major, rapid drawdown of water level could trigger widespread multiple failures, but noted that there are no known drawdown events of glacial Lake Ojibway during the timespan of the Dasserat varve series. Brooks' (2016b) assessment of aseismic mechanisms is considered applicable to the event horizons of the Duparquet and Dufresnoy study areas, which were located within a similar deep-water, depositional setting of glacial Lake Ojibway and span a similar time period.

To reflect the variable evidence for the paleoearthquake interpretations, a qualitative confidence level is assigned to the interpretations in Fig. 2. A high confidence is applied to an interpretation based on strong or moderate event horizons in two or three of the study areas having identical varve ages. The medium-high confidence level is assigned to an interpretation when a strong or moderate event horizon in one of the study areas correlates closely to the age of one or more disturbed deposits mentioned in the literature. The comparison of ages is made with consideration of a ± 2 kyr uncertainty between the varve ages. A medium-low confidence is given to a horizon with a strong MTD signature that is present in only one study area and for which the wider extent is unknown. A low confidence is assigned to a horizon with a moderate MTD signature present within only one study area. An isolated single/paired MTD signature within one of the study areas is not considered to be evidence of a paleoearthquake because an aseismic mechanism could very well account for the failure(s).

The varve chronologies between the three study areas overlapped approximately between vyr1175-1625 (which is equivalent to $9395-8945 \pm 200$ ^{14}C cal BP; Fig. 2). Of the mapped event horizons over this interval, sixteen are inferred to be evidence of thirteen paleoearthquakes (Fig. 2). Two paleoearthquakes occurring in vyr1483 and vyr1383 are interpreted with high confidence, based on event horizons with identical varve ages occurring in three and two of the study areas, respectively (Fig. 2). Event horizons in the Dasserat study area that are very close to the inferred varve ages of disturbed deposits reported in the literature are interpreted to represent paleoearthquakes in vyr1324 or 1322, and vyr1263 with medium-high confidence (Fig. 2). The other nine

interpreted paleoearthquakes are based on the hypothesis that the strong (three) and moderate (six) multi-MTD signatures within a single study area are best explained by a paleoearthquake, but with medium-low or low confidence (Fig. 2). None of the seven event horizons with single/paired MTD signatures or the four unmapped MTD are considered to be indicative of a paleoearthquake, based on available data.

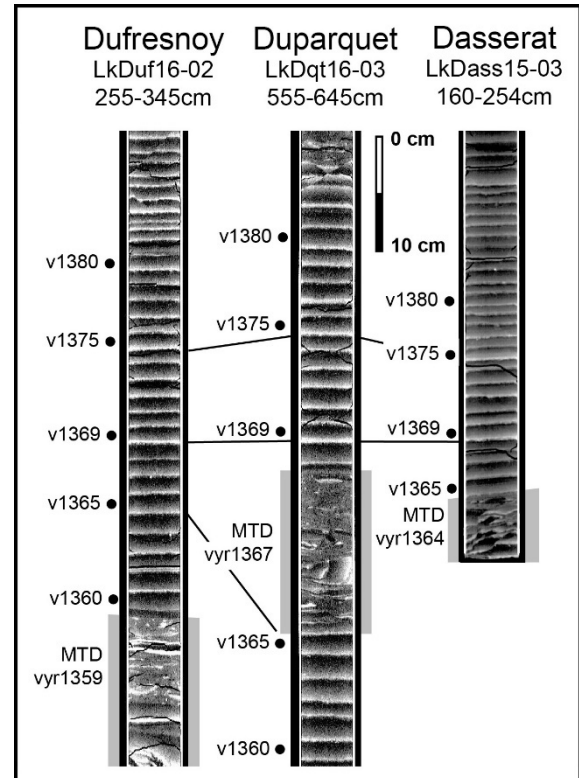


Figure 3: Illustrative radiograph images of core from the Dufresnoy, Duparquet and Dasserat study areas showing the varve sequence overlying the interpreted vyr1359, vyr1367 and vyr1364 mass transport deposits (MTDs), respectively. The varve thickness patterns support the interpretation that the MTDs occurred at distinctly separate intervals three and five varve years apart.

DISCUSSION

The paleoearthquake interpretations and the assessments of interpretative confidence are derived from the strong and moderate weightings of the event horizon signatures and, where possible, evidence supporting a geomorphic footprint extending beyond a given study area (Fig. 2). Determining the geomorphic footprint is dependent on the resolution of the varve chronology. All comparisons of event horizon varve ages between the study areas are resolved at an annual resolution, using the presence of distinctive varves in the radiograph images as a correlative guide. Thus, event horizons with age differences as low as two to five varve years are considered to represent separate mass transport depositional events between the study areas (Fig. 2). This approach creates a greater number of interpreted earthquakes in the study areas. However, it is more conservative than inferring fewer



paleoearthquakes at an implied higher interpretive confidence and greater magnitude because of wider (apparent) spatial footprints.

An example of this circumstance is demonstrated by the vyr1359 (Dufresnoy), vyr1364 (Dasserat) and vyr1367 (Duparquet) event horizons occurring at five- and three-varve-year intervals within an eight varve year span (Fig. 3). If considered to be close enough in age to indicate a common mass transport depositional event, then these event horizons could be inferred to represent a paleoearthquake at a medium-high interpretive confidence and with a spatial footprint encompassing all three study areas. However, relative to the vyr1483 paleoearthquake, in which horizons in all three study areas date to a common varve year and each exhibits a strong multi-MTD signature (Fig. 2), this probably is an incorrect interpretation. Thus, these horizons are deemed better interpreted as a paleoearthquake with low confidence (the Dufresnoy moderate MTD signature in vyr1359) and the other two horizons as representing insufficient evidence for a paleoearthquake interpretation.

CONCLUSIONS

Thirteen paleoearthquakes occurring between vyr1175-1625 (9395-8945 ± 200 ¹⁴C cal BP) are interpreted from sixteen of twenty-three mapped event horizons. None of the remaining seven event horizons with a single/paired MTD signature or the four minor, unmapped MTDs are interpreted as evidence of a paleoearthquake. The precise chronological control provided by the varves allows event horizons separated by two to five varve years to be differentiated between the study areas and interpreted as distinctly different depositional events. The presence of such closely-aged event horizons likely is impossible to recognize as separate depositional events in the post-glacial lacustrine portion of the lake deposits, since varve formation generally does not occur within Canadian Shield lakes, except in special circumstances, such as Meromictic lakes, which are uncommon. The event horizon stratigraphies from the Duparquet, Dufresnoy and

Dasserat studies areas provide insights into paleoseismic activity during deglaciation within an intracratonic tectonic setting of eastern Canada.

Acknowledgements: Comments from Hazen Russell are sincerely appreciated. I am most grateful to Alain Grenier (GSC) for assistance in the field, to K. Brewer (GSC) for logistical support, and to students Aldo Katragjini, Simon Baer, Fiona Davidson, Kevin Strauss, Katie MacDonald, Jeremie Rivest and Mitchell Jones for assistance in the field, interpreting core, and/or collecting sub-bottom acoustic profiles. This research was supported by Lands and Minerals Sector (LMS), Natural Resources Canada, and the Nuclear Waste Management Organization. This paper represents NRCan Contribution 20170117.

REFERENCES

- Antevs, E. (1925). Retreat of the last ice-sheet in eastern Canada. *Geological Survey of Canada Memoir 146*, 142 p.
- Antevs, E. (1928). *The last glaciation with reference to the retreat in northeastern North America*. American Geographical Society Research Series No. 17, New York, 292 p.
- Breckenridge, A., T.V. Lowell, J.S. Stroup, & G. Evans, (2012). A review and analysis of varve thickness records from glacial Lake Ojibway (Ontario and Quebec, Canada). *Quaternary International* 260, 43-54.
- Brooks, G.R., 2016a. A varve record of Lake Ojibway glaciolacustrine deposits from Lac Dasserat, northwestern Quebec, Canada; *Geological Survey of Canada Open File 8089*.
- Brooks, G.R., 2016b. Evidence of late glacial paleoseismicity from mass transport deposits within Lac Dasserat, northwestern Quebec, Canada. *Quaternary Research* 86, 184-199.
- Dyke, A.S., Moore, A., Roberston, L., 2003. Deglaciation of North America. *Geological Survey of Canada Open File 1574*.
- Hughes, O.L. (1959). *Surficial geology of Smooth Rock and Iroquois Falls map areas, Cochrane District, Ontario*. Department of Geology, University of Kansas, unpublished Ph.D. thesis, 190 p.
- Veillette, J.J. (1994). Evolution and paleohydrology of glacial Lakes Barlow and Ojibway. *Quaternary Science Reviews* 13, 945-971.
- Vincent, J.-S. & L. Hardy, (1979). The evolution of glacial lakes Barlow and Ojibway, Quebec and Ontario. *Geological Survey of Canada Bulletin* 316, 18 p.



Fault rupture patterns during the M_w7.8 2016 Kaikōura Earthquake in the region between the Leader and Charwell rivers, north Canterbury, New Zealand

Bushell, Tabitha (1), Nicol, Andrew (1) Fenton, Clark (1), Khajavi, Narges (1), Hyland, Natalie (1), Pettinga, Jarg (1), Pedley, Kate (1), McHale, Jess (1)

(1) Department of Geological Sciences, University of Canterbury, Private Bag 4800, Christchurch, New Zealand

Abstract: Surface rupture and slip from the M_w 7.8 2016 Kaikōura Earthquake have been mapped in the region between the Leader and Charwell rivers using field mapping and LiDAR data. The eastern Humps, north Leader and Conway-Charwell faults ruptured the ground surface in the study area. The E-NE striking 'The Humps' Fault runs along the base of the Mt Stewart range front, appears to dip steeply NW and intersects the NNW-NNE Leader Fault which itself terminates northwards at the NE striking Conway-Charwell Fault. The eastern Humps Fault is up to the NW and accommodates oblique slip with reverse and right lateral displacement. Net slip on 'The Humps' Fault is ≤ 4 m and produced ≤ 4 m uplift of the Mt Stewart range during the earthquake. The Leader Fault strikes NNW-NNE with dips ranging from $\sim 10^\circ$ west to 80° east and accommodated ≤ 4 m net slip comprising left-lateral and up-to-the-west vertical displacement. Like the Humps west of the study area, surface-rupture of the Leader Fault occurred on multiple strands. The complexity of rupture on the Leader Fault is in part due to the occurrence of bedding-parallel slip within the Cretaceous-Cenozoic sequence. Although the Mt Stewart range front is bounded by 'The Humps' Fault, in the study area neither this fault nor the Leader Fault were known to have been active before the earthquake. Fieldwork and trenching investigations are ongoing to characterise the geometry, kinematics and paleoseismic history of the mapped active faults.

Key words: Kaikōura earthquake, surface rupture, North Canterbury, New Zealand

INTRODUCTION

The Kaikōura Earthquake on 14th November 2016 produced a complex array of fault ruptures which propagated north-eastward for about 180 km from an epicentre on the Waiiau Plains in north Canterbury (Hamling et al, 2017; Litchfield et al., in review). Surface ruptures and slip of up to 12 m occurred on NE-SW striking faults in the Marlborough Fault System and the north Canterbury (tectonic) domain. Northeast-striking faults were known to be active prior to the earthquake, and include the Kekerengu Fault, 'The Humps' Fault and the Jordan Thrust. Displacement also occurred on several approximately N-S striking faults, including the Leader Fault, which were typically not known to be active before the 2016 earthquake (Litchfield et al., in review). Collectively these two main fault sets produce an interconnected fault network.

In this study we mapped the location, geometry and slip of surface rupture during the Kaikōura Earthquake for an area of ~ 400 km² between the Leader and Charwell rivers (Figure 1). The main structures that ruptured in the study area are the eastern Humps, north Leader and Conway-Charwell faults. 'The Humps' and Leader faults intersect and, for the purposes of this work, have been distinguished based on their sense of slip with the former being right-lateral and the latter left-lateral. The Conway-Charwell Fault is parallel to, and within 2 km of, the Hope Fault and it here considered to be part of the Hope Fault zone (Figure 1). These faults have been mapped using a combination of field observations (e.g., GPS surveying, bedrock mapping and tape measurements) together with interpretation of LiDAR-derived digital elevation models and orthophotos.

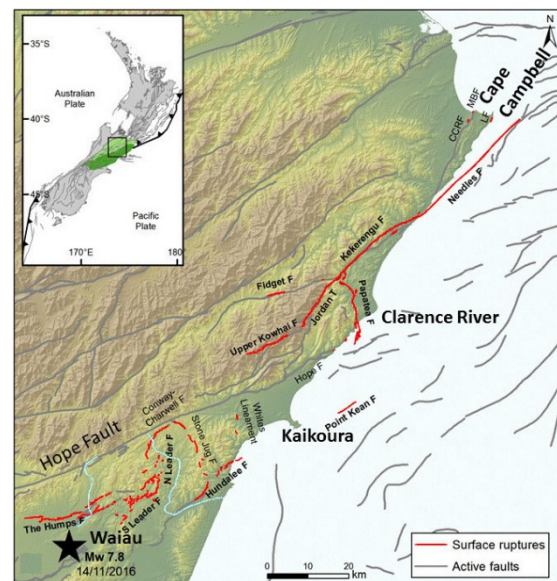


Figure 1: Preliminary map of fault surface ruptures in the 2016 Kaikōura earthquake (red lines); active faults indicated by grey lines. Approximate positions of Leader (left) and Charwell (right) rivers are indicated by light blue lines. Study area lies between these two rivers.. Figure modified from Stirling et al. (2017).

The primary objective of research is to comprehensively map the geometry and slip of surface ruptures in the study area. These data constrain the interrelationships of the surface ruptures together with helping us to understand how earthquakes produced the bedrock structure and landscape on million-year timescales. These studies will be augmented by trenching to characterise the paleoseismic histories of the faults.



DISCUSSION

Surface ruptures in the study area are complex, comprising many short (≤ 4 km) fault traces that often bifurcate with mainly strike-slip, oblique reverse or thrust displacements. The 'The Humps', Leader and Conway-Charwell faults are the primary structures in the study area.

'The Humps' Fault is the southwest-most surface rupture of the Kaikōura Earthquake. It strikes east to northeast and extends for ~ 32 km from a free tip on the western edge of the Emu Plains to its junction with the Leader Fault at the base of the Mount Stewart range in the study area (Figure 1). 'The Humps' Fault strikes at $\sim 050^\circ$ and dips steeply to the NW along the Mt Stewart range front. The primary fault trace along the base of the range partially follows the contact between Torlesse basement and overlying Miocene Greta Formation. Uplift of the range indicates vertical displacement on the fault system at depth. A maximum of 4–5 m earthquake vertical displacement has been recorded along this section of the fault.



Figure 2: Mapped fault ruptures on a LiDAR hillshade image of the study area. The Leader fault system and the continuation of the Humps around the Mt Stewart range front are marked.

Slip The Leader Fault in the study area can be divided into four parts separated by two left bends and one right bend with widths of 1–3.5 km (Figure 2). The southernmost left bend coincides with the Leader-Humps intersection south of which the main surface rupture approximately coincides with the contact between Torlesse basement and Cretaceous cover rocks which dip westwards at $\sim 10\text{--}30^\circ$. North of the fault intersection the main ruptures are contained entirely within Torlesse basement and strike

sub-parallel to basement bedding. Therefore, the geometry of the Leader Fault, both at the surface and in the sub-surface beneath Cretaceous-Cenozoic cover stratigraphy, may be controlled by the locations and geometries of planes of weakness in basement.

was transferred between intersecting faults during the earthquake. At the termination of 'The Humps' Fault oblique slip produced 3 m uplift of the Mt Stewart range in the hangingwall of the fault, which was transferred northwards onto the Leader Fault. Interaction and intersection of the main fault sets facilitated the northeast transfer of slip and potentially also propagation of the earthquake.



Figure 3: Left-lateral reverse rupture on the north Leader fault. The Doone Station. Image courtesy of Kate Pedley.

Acknowledgements: Thanks to GNS Science for use of LiDAR and orthophoto imagery, University of Canterbury and the Earthquake Commission for project funding, the landowners of Woodchester, Mendip and the Doone stations for access to their properties.

REFERENCES

- Hamling, I.J., Hreinsdóttir, S., Clark, K., Elliott, J., Liang, C., Fielding, E., Litchfield, N., Villamor, P., Wallace, L., Wright, T.J., D'Anastasio, E., Bannister, S., Burbidge, D., Denys, P., Gentle, P., Howarth, J., Mueller, C., Palmer, N., Pearson, C., Power, W., Barnes, P., Barrell, D.J.A., Van Dissen, R., Langridge, R., Little, T., Nicol, A., Pettinga, J., Rowland, J., Stirling, M., 2017. Complex multi-fault rupture during the 2016 Mw 7.8 Kaikōura earthquake, New Zealand. *Science*, DOI: 10.1126/science.aam7194 (2017).
- Litchfield N.J., Villamor P., Dissen R., Nicol A., Barnes P., Barrell D., Pettinga J., Langridge R., Little T., et al. Surface ruptures and paleoseismology of the Mw 7.8 2016 Kaikōura earthquake reveal end-member complexity. *Geology* (in review).
- Stirling, M. W., Litchfield, N. J., Villamor, P., Van Dissen, R. J., Nicol, A., Pettinga, J., ... & Mountjoy, J. (2017). The Mw7.8 2016 Kaikōura earthquake: Surface fault rupture and seismic hazard context. *Bulletin of the New Zealand Society for Earthquake Engineering*, 50(2).



Back analysis of earthquake damage on buildings used for the detection of the basic seismological parameters of historical earthquakes: the case of the 1755 Great Lisbon earthquake

Carydis, Panayotis (1), Mavroulis, Spyridon (2), Lekkas, Efthymios (2), Grampas, Alexia (2), Alexoudi, Vassiliki (2), Milios, Dimitrios (3)

(1) National Technical University of Athens

(2) Department of Dynamic Tectonic Applied Geology, Faculty of Geology and Geoenvironment, School of Sciences, National and Kapodistrian University of Athens, Panepistimiopolis, Athens 15784, Greece, smavroulis@geol.uoa.gr

(3) Decentralized Administration of Peloponnese, Western Greece and Ionian Islands - Peloponnese Waters Directorate, Tripolis, Greece

Abstract: Based on years of experience in post-earthquake inspections and on results of numerous full scale tests of structures on shaking tables, it is suggested that the basic characteristics of earthquakes (epicenter location, focal depth and seismic fault type) can be derived solely from field macroseismic observations and back analysis of building damage induced by previous earthquakes. Following this approach, important conclusions could be drawn for historical earthquakes. In the case of the 1755 Great Lisbon earthquake, macroseismic observations were derived from on-site inspection of well-preserved still-standing damaged historical buildings in Lisbon and artworks illustrating buildings damaged from this sequence. Based on damage induced by recent earthquakes, it is suggested that this damage may be attributed to a shallow near-field earthquake with a prevailing vertical component and of not so great magnitude, preceding the 1755 earthquake that caused the devastating tsunami with epicenter determined in the ocean west of Lisbon.

Key words: Building damage; vertical component; homothetic motions; historical earthquakes; Great Lisbon earthquake

INTRODUCTION

Back analysis of earthquake-induced building damage can be used for the detection of the basic seismological parameters of earthquakes due to the fact that building damage in earthquake-affected areas can reflect the distance of the affected area from the epicenter location, the focal mechanism and the type of the seismic fault (normal, reverse, strike-slip), the focal depth (shallow or deep seismic event) and the seismic intensity based on the application of macroseismic scales based on field macroseismic observations. Taking into account the response of buildings to recent earthquakes (1986 Kalamata, 1995 Aegion, 1995 Dinar, 1999 Athens, 2009 L' Aquila, 2012 Emilia Romagna, 2014 Cephalonia, 2016 Amatrice and Norcia), it is concluded that these shallow near-field events caused similar building damage (Fig. 1) that is mainly attributed to the effect of the vertical component of the earthquake ground motion (Papazoglou and Elnashai, 1996; Benedetti and Carydis, 1999; Carydis, 2004; Di Sarno et al., 2011; Carydis et al., 2012, 2017a, b).

The vertical earthquake component is quite sensitive to various ground and bed rock conditions due to its high frequency content. Moreover, it has an outstanding importance due to its high qualitative non linearity. Actually, this motion may affect the structure and/or its parts by two different and almost simultaneous mechanisms: (a) the impact and (b) the vibrational type mechanisms. The first one affects rigid bodies extended vertically like walls, columns and towers including their discontinuities, while the second one affects horizontal structures like roofs, floors, beams, cantilevers and trusses, by exciting them vertically. As regards the impact effect of the earthquake vertical component, it is extremely nonlinear above the barrier of 1.0

g ground acceleration. As regards its vibrational effect, those structures (slabs, roof, trusses, beams), whose period along the vertical axis corresponds to acceleration spectral values higher than 1.0 g, become critical for the stability of the whole structure.

One of the major effects of the vertical component is the annulment of friction mechanisms that depend on gravitational forces. Those forces are greatly reduced during some phases of the ground motion along the vertical direction. Due to this fact among others, the response of seismically isolated buildings may be adversely affected if the function of the foundations depends on friction.

Taking into account various earthquake reports on field macroseismic observations, the building damage attributed to the prevalence and the dominance of the vertical component of the ground motion during recent earthquakes in Greece and the Mediterranean are presented (Fig. 1). Based on this gathered information on earthquake-induced building damage, the basic seismological characteristics of an earthquake could be extracted based on field macroseismic characteristics in recent cases when either the available seismological data are insufficient due to lack of seismographs in the near field during the earthquake generation or the available strong motion records are not adequate in order to explain in a rational and reliable way the induced heavy damage. Moreover, the same approach could be applied in historical earthquakes characterized by lack of instrumental seismological data. In the present work, the aforementioned approach is applied to the case of the 1755 Great Lisbon earthquake sequence in order to determine its basic characteristics.



BUILDING DAMAGE FROM EARTHQUAKES INDUCED BY THE PREVAILING VERTICAL COMPONENT OF THE EARTHQUAKE GROUND MOTION

Recent shallow near-field European earthquakes caused damage and collapses that may be rather easily explained by considering the effect of vertical ground motion and can be hardly interpreted according to the horizontal one. Benedetti and Carydis (1999) presented some examples of damage to buildings caused by the 1999 Athens and 1995 Aegion earthquakes that point out the effect of the vertical component. More specifically, symmetrical buckling of longitudinal bars and loosening of stirrups in ground floor columns, compression damage at midheight of columns, bursting of over-stressed columns, throwing of infill walls away from reinforced-concrete frame as by an explosion from within, symmetrical distribution of damage around a vertical axis and other spatial homothetic motions are damage reflecting shallow near-field earthquakes with prevailing vertical component of the earthquake ground motion (Fig. 1).

Carydis (2002, 2004) demonstrated the catalytic importance of the vertical component of the earthquake ground motion on the earthquake response of structures built in epicentral regions either acting independently or in combination with the other two horizontal components of the seismic motion. Damage on reinforced-concrete (R/C) buildings and unreinforced masonry (URM) buildings with load-bearing walls caused by the destructive effect of the vertical component of the ground motion during shallow normal earthquakes in Greece and the Mediterranean is also presented and specifically include the following (Fig. 1): (a) Structures are dislodged from their foundations or toppled without damage to their structural frame due to relative deformations between stories. (b) Columns are broken as by an explosion either above their foundations or under the slab of the first storey. In many cases, lighter damage are observed along the columns at any distance from their base within the ground floor. (c) Vertical load bearing elements including columns penetrate through slabs and beams. (d) Damage is observed at the center length of beams and slabs. (e) Cantilever beams or slabs are dropped down or collapsed. Also, cantilevers may produce damages to their neighbour region due to vertical motions. (f) Masonry arched lintels are intact. (g) Partial collapse of buildings. One part is still standing and the other suffered total collapse. In most of the cases there are no partitions in the ground floor of the collapsed part. (h) Doors, paintings, radiators and other items hanging from the walls are dismantled and fall down. (i) The collapsed building are almost within their foundation plan and the remaining columns or exterior walls are vertical. (j) In rather symmetrical masonry structures, as these are the most common cases, the damage in the walls is horizontal. There are obvious traces in the roof and floors of the vertical motion and all corner cornices are fallen down. In general, damage is symmetrical to the vertical axis of the building. (k) Symmetrical distribution of damage around the vertical axis, such as the symmetrical detachment of the top four corners edges of a building with masonry load-bearing walls, which is the trademark of the prevalence and the dominance of the vertical component over the horizontal one and, as a consequence, of the macroseismic epicentral region.



Figure 1: Characteristic views of earthquake-induced building damage indicating the prevalence of the vertical component of the earthquake ground motion. (a) 1981 Alkyonides (Central Greece) earthquake: this hotel building collapsed down to the pillars without any evidence of horizontal motion. (b) 1986 Kalamata (Southwestern Peloponnese, Greece) earthquake: the roof of a church collapsed, while the exterior walls were still standing. (c, d, e) 1999 Athens (Greece) earthquake: (c) the crushing of concrete and the symmetrical buckling of bars are apparent in R/C buildings, while the vertical edges of columns are still aligned. Moreover, the glass panels remained intact. (d, e) Total vertical drop of the whole building of about 8 cm without any permanent horizontal movement or inclination. (f, g) 2014 Cephalonia (Ionian Sea, Greece) earthquakes: A two-storey R/C building suffered soft-storey failure, while the second storey remained intact. The crushing of concrete and the symmetrical buckling of bars are apparent. (h) 2009 L' Aquila (Italy) earthquake: Vertical collapse of the dome of Duomo church in L' Aquila within its foundation plan. There is not any other noticeable damage. Glass window panels are intact. (i) Impact of the vertical component of the ground motion of 2009 L' Aquila earthquake in buildings of Bazzano area. (j) An R/C building in Amatrice (Central Italy) suffered partial collapse after the 2016 Mw 6.2 Amatrice earthquake. Its remaining still-standing parts are practically undamaged. (k) The damage observed in the same R/C building was aggravated by an Mw 4.8 aftershock generated the day following the Amatrice earthquake. Spatial homothetic motions indicated the dominance of the vertical component of the earthquake ground motion.



As regards the effect of the vertical component on the seismic response of historical monumental buildings, Carydis et al. (2012) studied the influence of the vertical earthquake component and related geoscientific and engineering aspects for the 2012 Emilia Romagna earthquakes. Based on years of experience in post-earthquake investigations and on results of numerous full scale tests of structures on shaking tables, they concluded that the damage on historical monumental structures including churches might be attributed to resonance of the trusses along the vertical direction due to the vertical earthquake component in combination with the horizontal displacement of their supports due to the horizontal seismic motion. A proof of the dominance of the vertical component might be based, among others, on the response of bell towers that in the majority of the cases were not significantly damaged and on the fact that the mode of collapse is inside the ground plan of the building. Moreover, they also concluded that the incurred destruction of most of the rather modern industrial facilities started from the dislocation and collapse of their prefabricated roofing system with a mechanism similar to that of churches' roofs.

In general, the severity of the effects of the vertical component of the earthquake ground motion is almost independent of the earthquake magnitude. Intensive damage attributed to the vertical component was also observed during light and moderate earthquakes including the 1974, M 4.2 Rio, Corinth, Greece (Carydis 2002, 2004), the 1999 M 5.9 Athens, Greece (Benedetti & Carydis, 1999) and the 2002 M 4.8 Tbilisi, Georgia (Mukhadje & Timchenko, 2003) seismic events. Similar damage was also observed in strong and major earthquakes including the 1995 Mw 6.4 Aegion (Greece), 1995 Mw 6.2 Dinar (Turkey) (Benedetti and Carydis, 1999; Carydis 2002, 2004), 2009 Mw 6.3 L' Aquila (Italy) (Di Sarno et al., 2011) and the 2012 Mw 6.1 Emilia Romagna (Italy) (Carydis et al., 2012) among others.

BACK ANALYSIS OF BUILDING DAMAGE FOR DETECTING THE BASIC PARAMETERS OF RECENT EARTHQUAKES – THE 2016 AUGUST 24 AMATRICE (ITALY) EARTHQUAKE

During on-site inspection immediately after the 2016 August 24, Mw 6.2 Amatrice (Central Italy) earthquake, Carydis et al. (2017a, b) had the opportunity to observe damage induced not only by the main shock (Fig. 1j) but also by its largest aftershocks generated during the first three days of the aftershock sequence (Fig. 1k).

Bearing in mind that: (a) the soil conditions in foundations of the affected villages were neither changed nor altered, (b) the conventional dynamic parameters of buildings did not play a significant role in their seismic response against the vertical component of the earthquake ground motion, due to its impact type of loading, (c) the structures and materials have carried memories from the previous large shocks of this sequence and (d) the main shock and its largest aftershocks caused damage to buildings including spatial homothetic motions, it is concluded that: (a) the main shock and its largest aftershocks had similar focal mechanism parameters

(normal faulting), (b) the main shock and its largest aftershocks were shallow near-field seismic events, (c) the observed damage is typical of such earthquakes and (d) the vertical component of the earthquakes' ground motion has prevailed. These homothetic motions were not an isolated case, but they reached statistically significant levels.

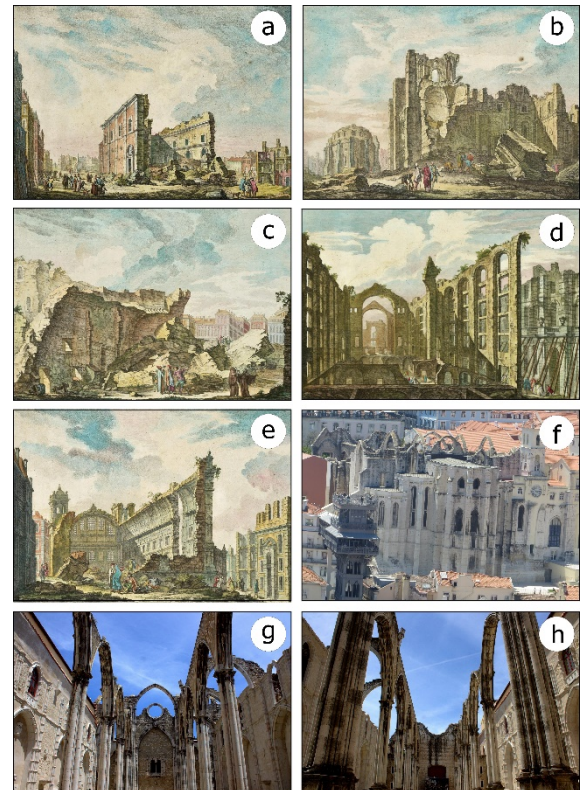


Figure 2: Engravings made by Jacques Philippe Le Bas on 1757 illustrate damage caused by the 1755 Great Lisbon earthquake to historical buildings of Lisbon: (a) St. Paul church, (b) Lisbon Cathedral, (c) St. Roch Tower, (d) Ópera do Tejo and (e) St. Nicholas Church. The roofs of the studied buildings collapsed within the foundation plan of the buildings, while the remaining exterior walls were still standing indicating the prevalence of the vertical component of the earthquake ground motion. Moreover, the observed damage is symmetrically distributed along a vertical axis. The aforementioned damage reveals that the causative earthquake is a shallow near-field earthquake with epicenter close to Lisbon, with prevailing vertical component over the horizontal movements and of magnitude lower than the 1755 Lisbon earthquake that caused the devastating tsunami with epicenter in the ocean, west of Lisbon.

BACK ANALYSIS OF BUILDING DAMAGE FOR DETECTING THE BASIC PARAMETERS OF HISTORICAL EARTHQUAKES – THE 1755 GREAT LISBON EARTHQUAKE

In the case of the 1755 Great Lisbon earthquake, field macroseismic data derived from onsite inspection of well-preserved still-standing damaged historical buildings in Lisbon city and artworks illustrating buildings that suffered damage from this sequence were used. More specifically, engravings made by Jacques Philippe Le Bas on 1757 illustrate damage caused by the 1755 Great Lisbon earthquake to historical buildings of St. Paul church (Fig. 2a), Lisbon Cathedral (Fig. 2b), St. Roch Tower (Fig. 2c),



Ópera do Tejo (Fig. 2d) and St. Nicholas Church (Fig. 2e). The roofs of the studied buildings collapsed within the building foundation plan while the remaining exterior walls were still standing. Moreover, the observed damage is symmetrically distributed along a vertical axis, also indicating the prevalence of the vertical component.

Moreover, well-preserved and still-standing historical buildings of Lisbon city that suffered damage by the 1755 Great Lisbon earthquake were also inspected. A typical example is the Carmo Convent located in the old city of Lisbon (Fig. 2f), which was ruined during the 1755 earthquake sequence. The destroyed church on the southern facade of the convent is the main trace of this sequence still visible in the old city. In comparison to the building damage illustrated in the aforementioned engravings, it is concluded that the Carmo Convent suffered collapse of its roof and upper parts of its walls within the building foundation plan (Fig. 2g, 2h), while the observed damage is symmetrically distributed along a vertical axis (Fig. 2g, 2h), also indicating the dominance of the vertical component.

Based on the aforementioned, it is suggested that this damage may be attributed to an earthquake preceding the 1755 Great Lisbon earthquake with (a) a strong vertical component, (b) its epicenter located very close to Lisbon, (c) a small focal depth and (d) of lower magnitude than the 1755 Great Lisbon earthquake that generated the devastating tsunami with epicenter in the ocean, west of Lisbon.

REFERENCES

- Benedetti, D., Carydis, P. 1999. Influence of the vertical component on damage during shallow - near field earthquakes. *European Earthquake Engineering* 3, 3-12.
- Carydis, P., Castiglioni, C., Lekkas, E., Kostaki, I., Lebesis, N., Drei, A. 2012. The Emilia Romagna, May 2012 earthquake sequence: the influence of the vertical earthquake component and related geoscientific and engineering aspects. *Ingegneria Sismica* 29, 31-58.
- Carydis, P. 2002. The vertical seismic component "The Columbus' egg in earthquake engineering". In: Proceedings of the 12th European Conference on Earthquake Engineering, 9-13 September, London, Elsevier Science Ltd, paper No. 868.
- Carydis, P. 2004. The effect of the vertical earthquake motion in near field. In: Proceedings of the 8th International Conference on Structures Under Shock and Impact, SUSI VIII, (Jones, N., Brebbia, C.A. eds.), WIT Press, 267-282.
- Carydis, P., Lekkas, E., Mavroulis, S. 2017a. Environmental effects and building damage induced by the vertical component of ground motion during the August 24, 2016 Amatrice (Central Italy) earthquake. *Geophysical Research Abstracts* 19, EGU2017-3856, EGU General Assembly 2017. Available in: <http://meetingorganizer.copernicus.org/EGU2017/EGU2017-3856-1.pdf>
- Carydis, P., Lekkas, E., Mavroulis, S. 2017b. Using structures of the August 24, 2016 Amatrice earthquake affected area as seismoscopes for assessing ground motion characteristics and parameters of the main shock and its largest aftershocks. *Geophysical Research Abstracts*, 19, EGU2017-3864, EGU General Assembly 2017. Available in: <http://meetingorganizer.copernicus.org/EGU2017/EGU2017-3864-1.pdf>

- Di Sarno, L., Elnashai, A.S., Manfredi, G. 2011. Assessment of RC columns subjected to horizontal and vertical ground motions recorded during the 2009 L'Aquila (Italy) earthquake. *Engineering Structures* 33, 1514-1535.
- Mukhadje, T., Timchenko, I. 2003. Epicentral Earthquake of April 2002, Tbilisi, Georgia: The capital in front of serious problems. In: Proceedings of the International Conference of Earthquake Engineering to Mark 40 Years from Catastrophic 1963 Skopje Earthquake and Successful City Reconstruction (SE 40 EEE), Skopje-Ohrid.
- Papazoglou, A.J., Elnashai, A.S. 1996. Analytical and field evidence of the damaging effect of vertical earthquake ground motion. *Earthquake Engineering and Structural Dynamics* 25, 1109-1137.



Characteristics of Gyeongju Earthquake Observed by the Eupcheon Fault Monitoring System in the Southeastern Part of the Korean Peninsula

Cho, Sung-II(1), Choi, Weon-Hack(1)

(1) Central Research Institute, Korea Hydro & Nuclear Power Co., Ltd. Daejeon 305-343, Korea (chosi4476@khnp.co.kr)

Abstract: The Eupcheon Fault Monitoring System, comprised of a strainmeter, seismometer, creepmeter, GPS (Global Positioning System), and groundwater meter, was installed to assess the safety of the Wolsung Nuclear Power Plant against earthquakes by monitoring the short- and long-term behavioral characteristics of the Eupcheon fault. The M_L 5.8 earthquake that occurred in Gyeongju on September 12, 2016 was the largest earthquake ever to be observed in Korea since the beginning of instrumental observations of earthquakes. The epicenter of Gyeongju earthquake was located around 27 km from the EFMS station. In this study, the fault displacement, underground stress and changes in the groundwater level recorded by the EFMS at the time of the foreshock (M_L 5.1, September 12, 2016), main shock (M_L 5.8, September 12, 2016) and aftershock (M_L 4.5, September 19, 2016) were analyzed in order to assess the safety of the Eupcheon fault against seismic events. In the case of underground stress measured by the strainmeter, abnormal changes were instantaneously observed during the foreshock, main shock and aftershock, but no cumulative stress was observed. As for the displacement of the Eupcheon fault, there are no abnormal changes caused by the earthquake that can be observed from the GPS; however, using a creepmeter, which can measure micro-displacement changes, a micro-displacement of 0.0047 mm was observed 20 minutes before the main shock. This measurement falls within the error range of ± 0.025 mm, and it is deemed that it was caused by micro vibration resulting from the foreshock, rather than a displacement of the fault. In the case of the groundwater level, it gradually increased due to a rainfall prior to the earthquake, but there were no instantaneous changes caused by the earthquake. The findings of this study show that the Eupcheon fault is a relatively stable fault that is not impacted by earthquakes occurring nearby, and confirmed the excellent utility of fault monitoring systems in analyzing the stability of a fault against earthquakes.

Key words: Gyeongju Earthquake, Eupcheon fault, Fault monitoring system

INTRODUCTION

The earthquake (M_L 5.8) occurred at around Naenam-myeon, Gyeongju, North Gyeongsang Province, South Korea on September 12, 2016 at 11:32:54 UTC (20:32:54 Korea Standard Time; GMT +9 hours), which was the largest earthquake ever recorded in the South Korea's instrumental seismic observation data. The foreshock signal of M_L 5.1 occurred 48 minutes before the main shock, and the greatest aftershock of M_L 4.5 occurred seven days after the main earthquake. About 600 aftershocks have occurred to date, and the depths of the earthquakes have been reported to be about 10 to 17 km from the surface (Kim et al., 2016). The epicenters of the Gyeongju earthquakes are located near the Yangsan fault and no earthquake-induced fault rupture has been observed so far (Fig. 1).

The Eupcheon Fault Monitoring System (EFMS), located at about 27 km from the epicenter of Gyeongju earthquake, has been operated by the Korea Hydro & Nuclear Power (KHNP) company (Fig. 1). The EFMS was installed to monitor the long-term/short-term behaviors of the Eupcheon fault and confirm the seismic safety of Wolsung nuclear power site. The Eupcheon fault is a boundary fault between the Cretaceous sedimentary rock and the Tertiary volcanic rocks, with a maximum displacement of 4.0 m, and a small scale strike and inclination of N20°E and N40°SE, respectively. In the trench survey, it was discovered that the Quaternary coastal fault was clearly cut by the Eupcheon fault, and at least two fault movements occurred during the Quaternary period.

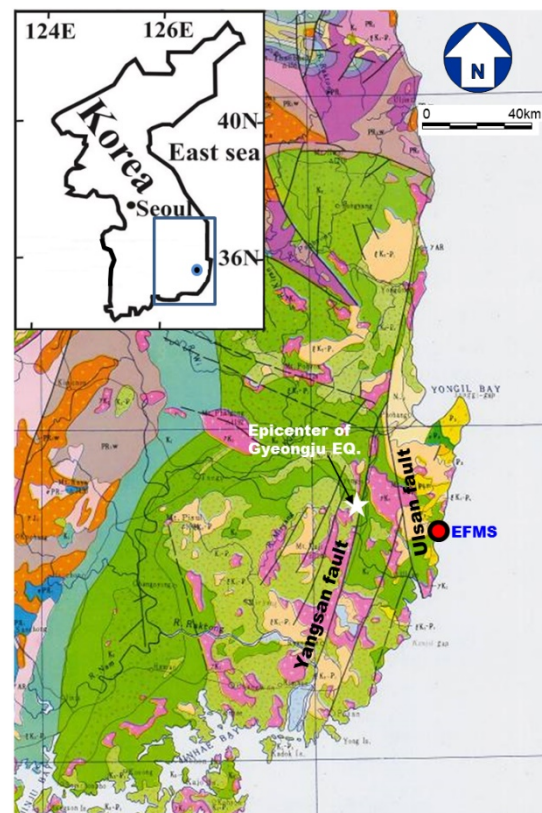


Figure 1: Geological map of the Korean Peninsula, the location of the epicenter and EFMS(modified after KIGAM, 1995).



In this study, we analyzed seismic safety of the Eupcheon fault by analyzing the changes in the underground stress, fault displacement and groundwater levels observed in the EFMS during the pre-, main and post-earthquake events.

CHARACTERISTICS OF THE EFMS

The EFMS consists of a strainmeter, seismometer, and groundwater level meter installed in boreholes of the EF01 and EF02 observatory at the upper and lower parts of the Eupcheon fault, along with a GPS added on the surface of the ground. An additional surface seismometer has been installed at the EF03 Observatory in order to improve the reliability of the seismic data. A creepmeter has also been installed at the EF04 Observatory to precisely measure the displacement of Eupcheon fault. The location and details of each instrument are shown in Fig. 2 and Table 1. The data observed from the instrument is transmitted to and stored on the server in the KHNP Central Research Institute through the wired network, and visualized through the integrated monitoring program.

The strainmeter is intended to identify the changes in the underground stress in the upper and lower parts of the Eupcheon fault caused by the seismic ground motion, and calculate the modified diameter ratio to the borehole diameter measured in the sensors installed in four directions in the borehole. The purpose of the creepmeter is to precisely measure the fine displacement of the Eupcheon fault due to the underground stress change. The displacement is measured through a 6 m nickel alloy rod and a spring sensor. The purpose of the GPS is to measure large scale displacements (over a few millimeters to several meters) caused by large scale crustal movements, along with the relative displacements of the upper and lower boundaries using a satellite. The purpose of the seismometer is to closely observe the epicenter and magnitude of the earthquake near the Eupcheon fault, and the groundwater level meter is used as a reference for the interpretation of the underground stress change by measuring the changes in the pore water pressure due to the groundwater level fluctuation around the Eupcheon fault.



Figure 2: Location of instruments of composing the fault monitoring system deployed around the Eupcheon fault.

OBSERVATION RESULTS BY THE EFMS

1. Strainmeter and Seismometer

The strainmeter data were corrected to exclude the tidal and atmospheric effects in order to extract only the effects of the earthquake. The effect of the Gyeongju earthquake was clearly observed, and the area strain at the EF02 Observatory showed a variation of 400-2600 nanostrain (Fig. 3). When the dynamic stress changes due to seismic waves, it is commonly observed from the strainmeter data, and the signal is observed for several seconds, which is very similar to the data measured by the seismometer (Fig. 4). As a result of the analysis of the strain meter data, it appears that a sudden displacement occurs simultaneously with the Gyeongju earthquake, and it returns to the original background value after the occurrence. In other words, an instant change in the stress occurred due to the Gyeongju earthquake, but the change tended to disappear over time. From this observation, it can be interpreted that the stress near the Eupcheon fault does not change before and after the earthquake, having no influence on the stability of the area.

Table 1: Specifications of measuring instruments in the EFMS

		Accuracy	Sensor Depth	Measuring Items
Strainmeter		$> 5 \times 10^{-10}$	EF01 : G.L. -153.3m EF02 : G.L. -175.4m	Strain Value
Water Level Meter	Water Level	$\pm 0.05\text{cm}$	EF01 : G.L. -25m EF02 : G.L. -20m	Groundwater Level, Temperature
	Temperature	$\pm 0.05^\circ\text{C}$		
Borehole Seismometer		62.2 V/m/s (Sensitivity)	EF01 : G.L. -145m EF02 : G.L. -155m	Seismic Wave
GPS		Horizontal : $\pm 5\text{mm}$ Vertical : $\pm 5\text{mm}$	Surface	Displacement
Surface Seismometer		2x750 V/m/s (Sensitivity)	Surface	Seismic Wave
Creepmeter	Displacement	$\pm 0.025\text{mm}$	Surface	Displacement, Temperature
	Temperature	$\pm 1^\circ\text{C}$		

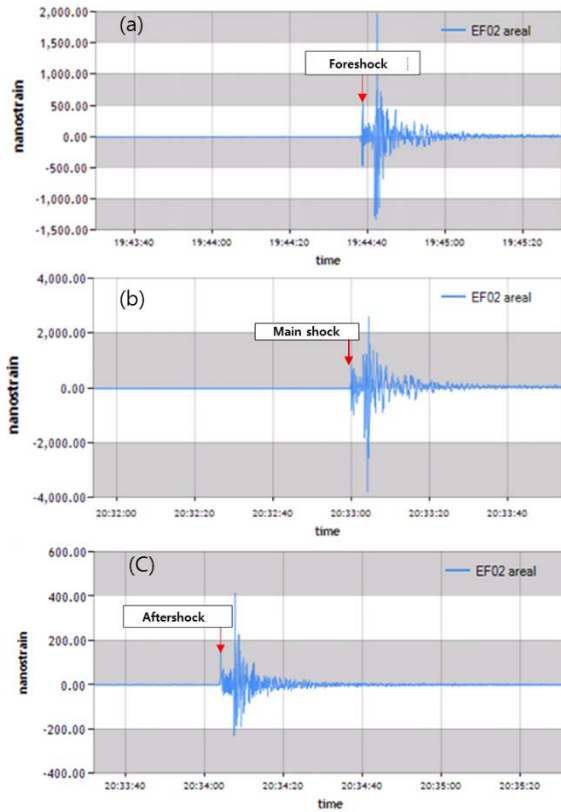


Figure 3: Strain data observed from the EF02 Observatory of EFMS. (a) Foreshock, (b) Main shock, (c) Aftershock.

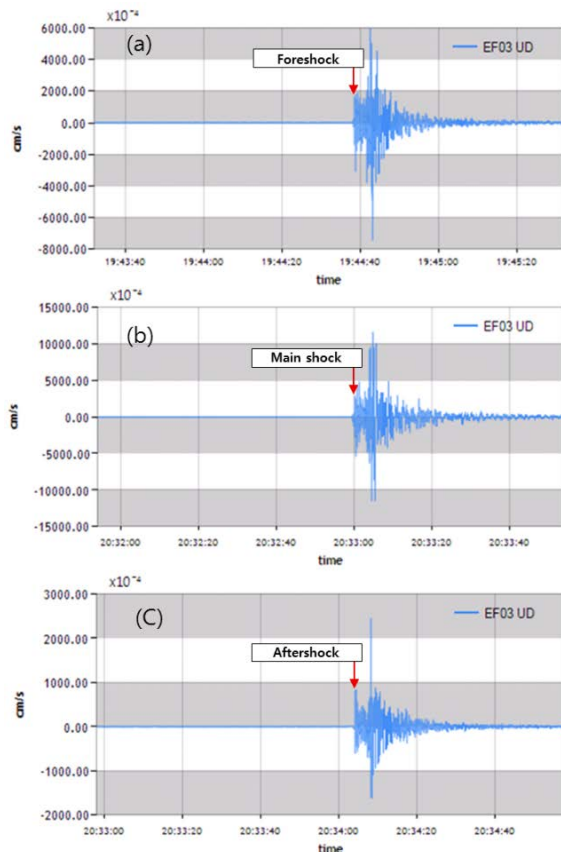


Figure 4: Seismic wave observed from the EF03 Observatory of EFMS. (a) Foreshock, (b) Main shock, (c) Aftershock.

2. GPS and Creepmeter

As for the displacement pattern of the Eupcheon fault, only the background noise due to the tidal or external influences is observed in the GPS signals, but the displacement pattern due to the Gyeongju earthquake is not observed (Fig. 5).

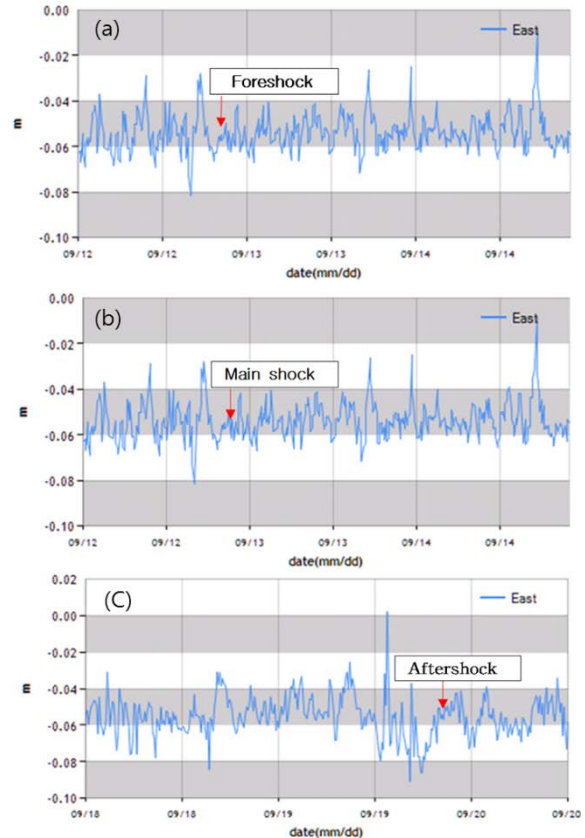


Figure 5: Relative displacements observed from the GPS of EFMS. (a) Foreshock, (b) Main shock, (c) Aftershock.

In the case of the creepmeter, a fine displacement of 0.0047 mm was observed 20 minutes before the main earthquake (Fig. 6). The measured value corresponds to the error range of ± 0.025 mm below the surface displacement measurement. It is judged to be the influence of the micro vibration due to the forward movement rather than the displacement of the fault.

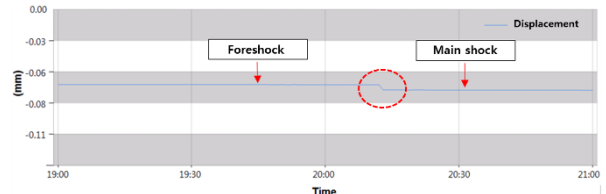


Figure 6: Displacement of Eupcheon fault observed from the creepmeter of EFMS.



3. Groundwater level meter

The groundwater level was gradually increased due to the rainfall before the earthquake, but there was no momentary change due to the earthquake (Fig. 7).

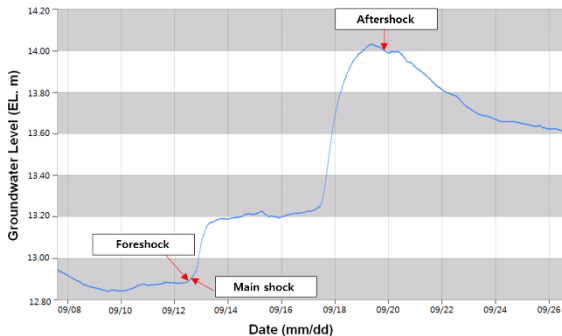


Figure 7: Groundwater level observed from the EF02 Observatory of EFMS.

DISCUSSION AND CONCLUSION

KHNP Central Research Institute has been operating the EFMS since October 2010, and the analysis of the observation data has confirmed that there is no abnormal change so far in the underground stress and fault displacement. Though the momentary changes in the underground stress is observed due to the earthquake occurred near the Eupcheon fault, accumulation of stress is not observed.

In the case of the 2011 Tohoku-oki earthquake in Japan, the change in the underground stress was observed on the EFMS strainmeter 30 minutes before the earthquake (Fig. 8), which shows the same pre-earthquake pattern as in the earthquake in Greece or Taiwan. In the case of Greece, a strainmeter, which is operated by Corinth Rift Laboratory (CRL), showed a change in the strain value at the Psathopyrgos fault, about 30 minutes before the M_L 3.5 earthquake occurred (Bernard et al., 2004). In addition, in the case of Jiasian earthquake in Taiwan, the M_L 6.4 earthquake occurred on March 4, 2010, rapid strain changes were observed in five strain gauges near the epicenter from several weeks before the earthquake (Hu et al., 2010). This indicates that the point of stress changes may be earlier than the point of occurrence of the earthquake. As a result, monitoring the change of underground stress through the EFMS can be very useful for earthquake prediction and analysis.

Through this study, it was proved that the Eupcheon fault is a relatively stable fault which is not affected by the earthquake occurring at the Yangsan fault nearby. In addition, the underground stress before the earthquake did not show a tendency to decrease or increase, and it was confirmed that the fault monitoring system could be very useful for the seismic safety analysis and the earthquake prediction study on the fault.

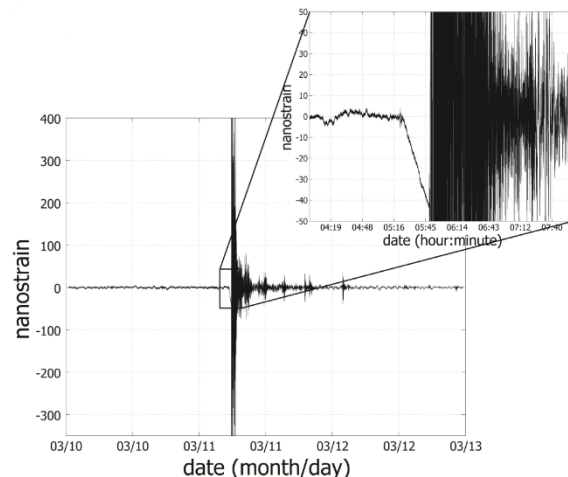


Figure 8: Strain data observed from the EFMS when the 2011 Tohoku-oki earthquake in Japan occurred.

REFERENCES

- Bernard, P., Boudin, F., Sacks, S., Linde, A., Blum, P.-A., Courtille, C., Esnault, M.-F., Castraded, H., Felekis, S., Billires, H., 2004. Continuous strain and tilt monitoring on the Trizonia island, Rift of Corinth, Greece., *C. R. Geosci.*, 336, 313-324.
- Hu, J.-C., Liu, C.-C., and Chen, C.-Y., 2010, Analysis of strain anomalies by strainmeter in Taiwan, www.gsi.ip/data/openfile/no0538/07_Hu.pdf (September 14, 2010)
- KIGAM(Korea Institute of Geoscience and Mineral Resources), 1995. Geological map in Korea (1:1,000,000).
- Kim, K-H., Kang, T-S, Rhie, J.K, Kim, Y.H., Park, Y.C., Kim, S.Y., Han, M.H., Kim, J., Park, J., Kim M., Kong, C.H., Heo, D., Lee H., Park, U., Park, H., Lee, S-J, Cho, S., Woo, J-U., Lee, S-H. and Kim, J., 2016. The 12 September 2016 Gyeongju earthquakes: 2. Temporary seismic network for monitoring aftershocks. *Geosciences Journal*, Vol. 20, No. 6, p. 753-757.



Along-strike variations in fault geometry and slip distribution along the Bulnay Fault, Mongolia

Choi, Jin-Hyuck (1), Klinger, Yann (2)

- (1) Korea Institute of Geoscience and Mineral Resources, Korea. cjh9521@kigam.re.kr.
 (2) Institut de Physique du Globe du Paris, France

Abstract: The 1905 M 8 Tsetserleg-Bulnay earthquake sequence of two earthquakes, 14 days apart, occurred on the Bulnay fault system in the northwestern part of Mongolia. A total length of ~667 km-long surface rupture, including ~338 km-long section along the main Bulnay fault, associated with this earthquake sequence has been mapped in detail using sub-metric optical satellite images 'Pleiades' with ground resolution of 0.5 m, complemented by field observations. Along-strike variations in rupture geometry, slip distribution, and off-fault damage suggest that the earthquake rupture processes are affected by geologic inheritance. Our data also indicate that the Bulnay fault consists of ~29-km-long segments that are separated by geometric discontinuities. Distribution of cumulative offsets, which represent how the fault accumulates slip over multiple surface-faulting earthquakes, show that 1) offsets potentially accompanied by the penultimate event have an almost the same distribution with the offsets from the most recent event in 1905, and 2) almost the same amounts of the offset increase on several fault segments. The results imply that the Bulnay fault might have experienced the characteristic-slip over multiple earthquakes.

Key words: earthquake rupture, slip distribution, off-fault damage, Bulnay fault, Mongolia.

THE 1905 M ≥ 8 TSETSERLEG-BULNAY EARTHQUAKES

In 1905 two large strike-slip earthquakes occurred on the Bulnay fault system, Mongolia [Fig. 1]. The magnitude M ~8 Tsetserleg earthquake occurred on July 9th at 9:40 am UT, and the M > 8 Bulnay earthquake occurred 14 days later, on July 23rd at 2:46 am UT. The two successive earthquakes together ruptured fault sections of the main Bulnay fault as well as along three other major faults: the Tsetserleg fault, the Teregtiyn fault, and the Dungen fault [Fig. 1c]. The total length of surface breaks associated with this earthquake sequence is at least 676 km. Despite the fact that the 1905 surface ruptures are well preserved up to present, it had only been mapped in detail along limited sections [Rizza et al., 2015].

In this study we use sub-metric optical satellite images 'Pleiades', complemented by two field-work campaigns, to map in detail the entire rupture zone associated with the 1905 earthquake sequence [Choi et al., in press]. Wherever it was possible, we measured any lateral offsets along the different faults studied. In total, we have collected a dataset of 654 offsets at 384 sites: at 184 sites we could measure only one offset, and at 200 sites we could measure multiple offsets. Our dataset is divided in two parts: The first part corresponds to the 1905 coseismic slip and the second part includes cumulative slip measurements. Any larger offset measured at the same site was considered as cumulative offset and ended up in the second sub-dataset. At one-offset sites, if it is different more than 50% between adjacent sites along the same fault segment we considered those unrealistic offsets as cumulative ones. Here we focus on variations of rupture geometry and both coseismic and cumulative slip distributions along the main Bulnay fault.

RUPTURE GEOMETRY & COSEISMIC SLIP DISTRIBUTION

Using detailed mapping we have been able to characterize the diversity of geometrical discontinuities along the 1905 Bulnay rupture [Fig. 2a]. These discontinuities are of two types: fault steps and fault-azimuth changes. Although steps have been recognized as potential rupture endpoints [Wesnousky, 2006], the role of fault-azimuth changes has been less considered so far. In the case of the 1905 Bulnay rupture, it appears that many geometric segments are actually defined by fault bends. These bends are on average about 6.6° and, in some cases, they extend laterally over several kilometers. In most cases, bends are coincident with local slip decreases [Fig. 2].

Based on geometrical discontinuities, including fault azimuth changes, and slip variations, we have identified 11 to 13 individual geometric segments for the 1905 Bulnay rupture [Fig. 2]. The difference of average slip between adjacent segments is ~ 1.3 m. On average the length of each segment is about 29 km with a standard deviation of 13 km, which is in the upper range of values previously proposed for strike-slip segments in continental settings [Klinger, 2010].

Numerous shorter branches can be found along the main 1905 Bulnay rupture, mostly along its eastern section [Fig. 2a]. They do not exceed 10 km in length and usually do not have significant slip. Distribution of these branches is uneven with most of the activated branches located north of the Bulnay rupture. This is interpreted as resulting from the interaction of the inherited ENE-WSW trending faults with the propagating left-lateral Bulnay rupture from west to east, which defines the northern side as the extensional side, which is more prone to branching [Poliakov et al. 2002].

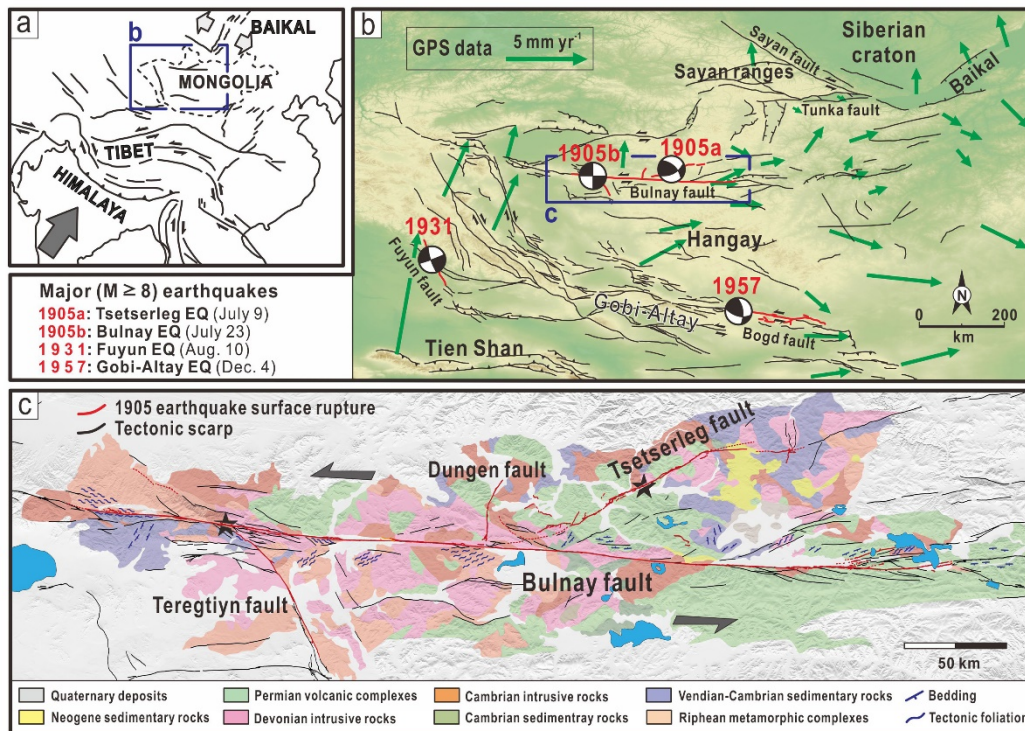


Figure 1: (a) Simplified tectonic map of the study region. (b) Tectonic setting of western Mongolia. Surface ruptures associated with major ($M \geq 8$) earthquakes during the last century are in red. Fault plane solutions constrained by first-motion solutions [Bayasgalan et al., 2005]. GPS-derived crustal motion with respect to Eurasia in green [Calais et al., 2003]. (c) Geological and structural map around the Bulnay fault system, modified from the Geological Map of Mongolia at a scale of 1:1,000,000 [Institute of Geology and Mineral Resources of the Mongolian Academy of Sciences, 1998]. Coseismic surface breaks associated with the 1905 Tsetserleg-Bulnay earthquake sequence are in red, according to mapping by Choi et al. (accepted).

One can distinguish the eastern part from the western part in the slip distribution, which join near 'Bul-E-110 km' [Fig. 2]. With exception of both ends of the rupture, each part shows a rather constant average slip, with the slip along the western part being about 2 m smaller on average than slip along the eastern part. In parallel, Figure 2b shows the general distribution of secondary faulting along the Bulnay rupture, based on our detailed mapping. Damage, which is represented by secondary ruptures and cracks, is distributed unevenly between the western and the eastern parts. Along the western part, damage is ubiquitous along the main rupture. In most places, one can find parallel ruptures and intense cracking, still visible more than a century after the event. Conversely, along the eastern part, with the exception of few short branches found close to the eastern end, deformation is highly localized along one single trace. Damage is mostly limited to boundaries of adjacent segments. Hence, we suggest that the total slip along the western and eastern parts of the 1905 Bulnay rupture is actually very similar and that the difference of slip observed along the main rupture is due to some fraction of the deformation ($\sim 21\%$ if we consider average offsets of 8.37 m and 6.64 m for the western and eastern part of the Bulnay rupture) that is accommodated by the secondary deformation.

Using the relation $M_w = 2/3 \log M_0 - 10.7$ [Hanks and Kanamori, 1979] we can compute the magnitude M_w for the 1905 Bulnay earthquake. The shear modulus is taken to be 3.0×10^{11} for average 'crustal' rocks. The average slip combined with the rupture length for the Bulnay earthquake ruptures yields a magnitude $M_w = 7.9 - 8.5$ depending on the

rupture thickness. Note that even if the inferred 1 - 2 m slip associated with off-fault damage on the western Bulnay rupture is included, the results is almost the same. This value is in good agreement with the seismic moment deduced from the body wave inversion: $M_w 8.3 - 8.5$, for the Bulnay earthquake [Schlupp and Cisternas, 2007].

CUMULATIVE SLIP DISTRIBUTION

Offsets related to the penultimate event correspond to the 2nd smallest offset minus the 1905 co-seismic offset at multiple-offsets sites. Slip distribution of the penultimate earthquake is similar to those of the most recent earthquake in 1905 [Fig. 3].

Paleoseismological studies at two sites (approximately 200 km apart) along the Bulnay fault show that the penultimate surface-faulting earthquake at each site occurred respectively 2,480 - 3,270 cal. B.P and 2,300 - 3,250 cal. B.P, suggesting that it might actually be the same earthquake [Schwartz et al., 2009; Rizza et al., 2015]. Hence, these results suggest that the Bulnay fault might at least follow a characteristic-slip pattern. At this stage the age constraints on the timing of the past earthquakes remain too weak to ensure unambiguously that the penultimate rupture was simultaneous along the entire 1905 rupture, as one could expect if the fault would behave following a characteristic earthquake pattern. In addition to the penultimate earthquake, offsets related to earlier earthquakes were estimated by geomorphic markers at a number of sites, and some of these were targeted for surface exposure dating to estimate slip-rate of the Bulnay fault.

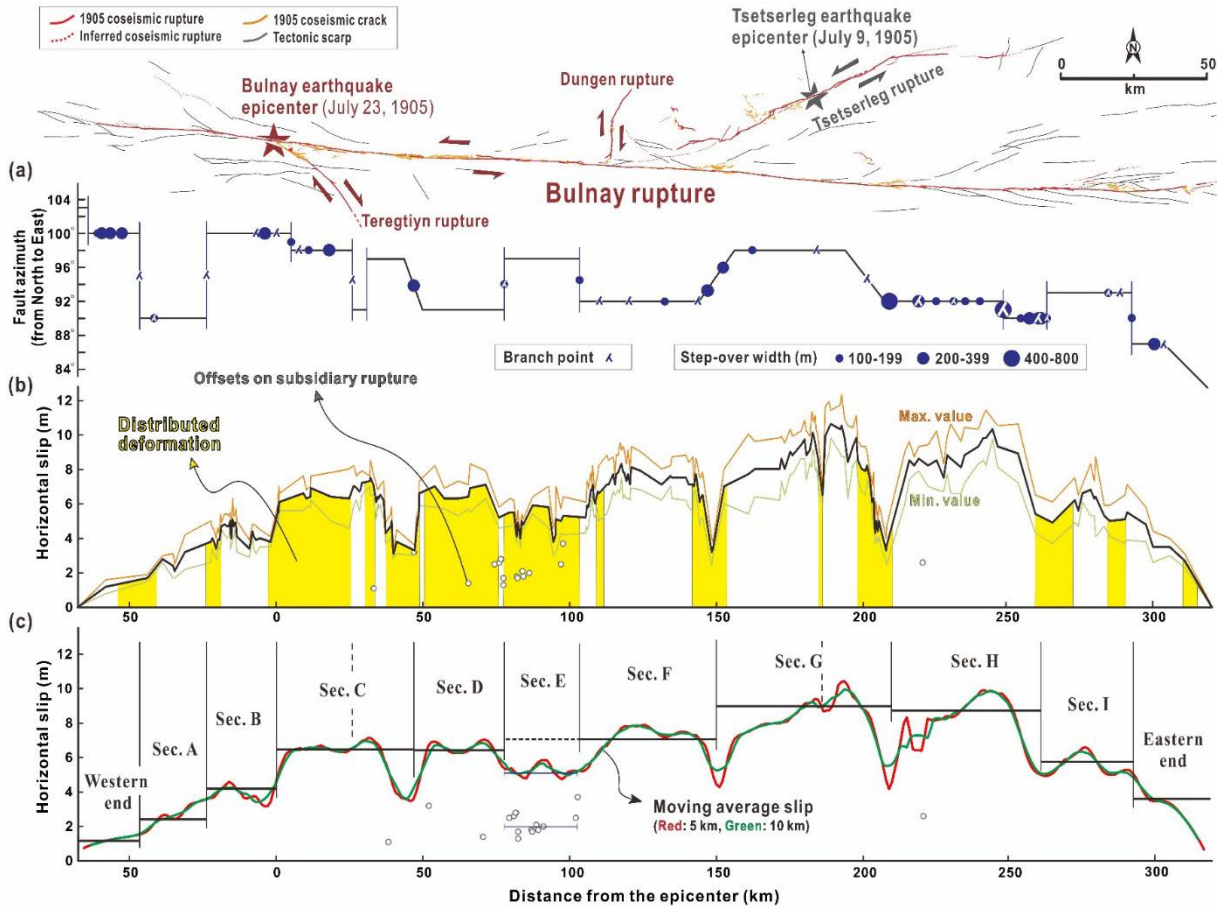


Figure 2: Segmen geometry of the 1905 Bulnay rupture, assessed based on fault discontinuities and along-fault slip variations (Choi et al., in press). (a) Geometrical features are highlighted by changes of fault azimuth as well as locations of fault steps (circles) and branch points (junctions). (b) Slip distribution including maximum and minimum values along the main rupture strand. Zones of intense distributed deformation around the main rupture are indicated in yellow. (c) The fluctuating slip distribution indicates that the Bulnay rupture consists of 11, possibly up to 13, major geometric segments that are mainly defined by changes of fault azimuth.

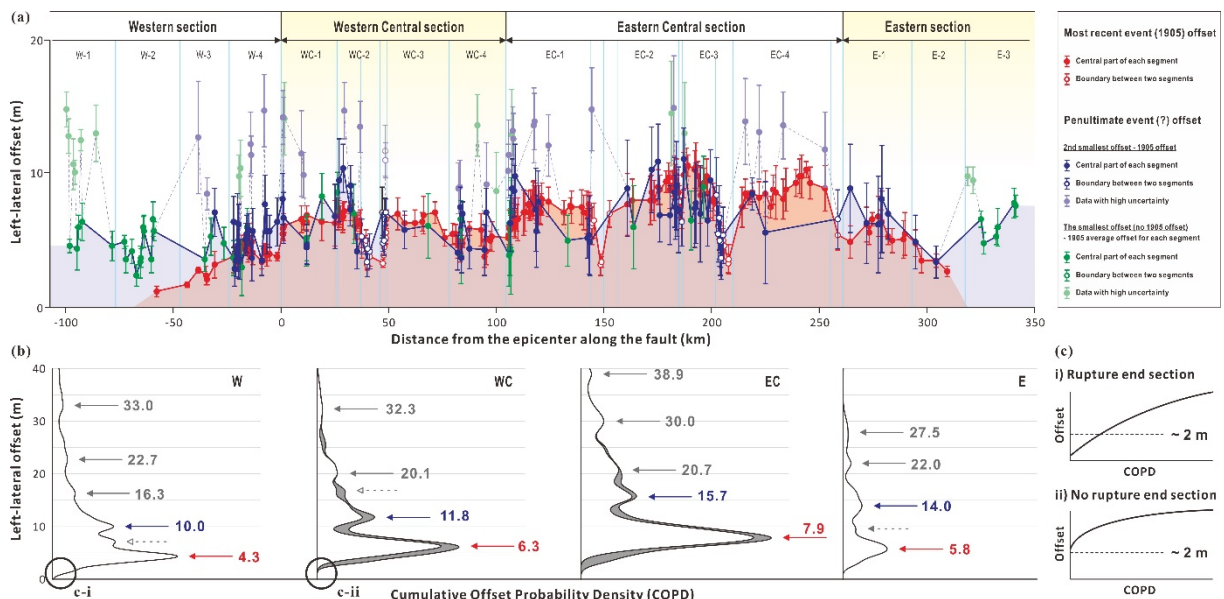


Figure 3: (a) Overlapped profiles of the last (1905) event offsets (red) and penultimate event offsets (blue) along the Bulnay Fault. Note that the penultimate event offsets were estimated by the 2nd smallest offset minus the 1905 coseismic offset at the same site. (b) Distribution of cumulative offset probability density (COPD) for each major segment. (c) Rupture end section and no rupture end section COPD profiles.



Acknowledgements: This work was supported by a grant 2017-MPSS31-006 (Research and Development of Active Fault of Korean Peninsula) from Supporting Technology Development Program for Disaster Management funded by Korean Ministry of Public Safety and Security (MPSS).

REFERENCES

- Bayasgalan, A., Jackson, J., & McKenzie, D., 2005. Lithosphere rheology and active tectonics in Mongolia: Relations between earthquake source parameters, gravity and GPS measurement. *Geophysical Journal International* 163, 1151-1179.
- Calais, E., Vergnolle, M., Sankov, V., Lukhnev, A., Miroshnitchenko, A., Amarjargal, S., & Deverchere, J., 2003. GPS measurements of crustal deformation in the Baikal-Mongolia area (1994-2002): Implications for current kinematics of Asia. *Journal of Geophysical Research* 108, B102501.
- Choi, J.-H., Klinger, Y., Ferry, M., Ritz, J.-F., Kurtz, R., Rizza, M., Bollinger, L., Davaasambuu, B., Tsend-Ayush, N., & Demberel, S., in press. Geologic inheritance and earthquake rupture processes: the 1905 $M \geq 8$ Tsetserleg-Bulnay strike-slip earthquake sequence, Mongolia. *Journal of Geophysical Research*.
- Hanks, T. C., & Kanamori, H., 1979. A moment magnitude scale. *Journal of Geophysical Research* 84, 2348-2350.
- Institute of Geology and Mineral Resources of the Mongolian Academy of Sciences (1998), The Geological Map of Mongolia at a scale of 1:1,000,000.
- Klinger, Y., 2010. Relation between continental strike-slip earthquake segmentation and thickness of the crust. *Journal of Geophysical Research* 115, B07306.
- Poliakov, A.N.B., Dmowska, R., & Rice, J.R., 2002. Dynamic shear rupture interactions with fault bends and off-axis secondary faulting. *Journal of Geophysical Research* 107(B11), 2295.
- Rizza, M., Ritz, J.-F., Prentice, C., Vassallo, R., Braucher, R., Larroque, C., Arzhannikova, A., Arzhannikov, S., Mahan, S., Massault, M., Michelot, J.-L., Todbileg, M., & ASTER Team (2015), Earthquake Geology of the Bulnay Fault (Mongolia). *Bulletin of the Seismological Society of America* 105(1), 72-93.
- Schlupp, A., & Cisternas, A., 2007. Source history of the 1905 great Mongolian earthquakes (Tsetserleg, Bulnay). *Geophysical Journal International* 169, 1115-1131.
- Schwartz, D.P., Hecker, S., Ponti, D., Stenner, H., Lund, W., & Bayasgalan, A., 2009. The July 23, 1905 Bulnay fault, Mongolia, surface rupture. *Seismological Research Letters* 80, 357.
- Wesnousky, S.G., 2006. Predicting the endpoints of earthquake ruptures. *Nature* 444(7117), 358-360.



Possibility of late Holocene uplift in Yeongil Bay, in the southeastern part of the Korean Peninsula

Choi, Sung-Ja (1), Jeon, Jeong-Soo (2)

(1) Korea Institute of Geoscience and Mineral Resources, 124 Gwahak-ro, Yusong-gu, Daejeon 34132, Korea

(2) Korea Institute of Geoscience and Mineral Resources, 124 Gwahak-ro, Yusong-gu, Daejeon 34132, Korea, jsjeon@kigam.re.kr

Abstract: Marine terraces have developed intermittently along the southeastern shore of Yeongil Bay on the Korean Peninsula. Three sea caves formed in the cliffs of the 26-m marine terrace on the headland. One of these caves is filled with > 3.4-m-thick sediments, consisting of well-sorted beach pebbles and sands, as well as disorganized ignimbrite breccia. The uppermost sediments dating to 1680–1820 AD at ca. 4 m above the present sea level may indicate a former shoreline. According to the historical earthquake catalog, the three largest earthquakes (M_w 6.2) were recorded in 1643 and 1681 AD. We concluded that the 4 m uplift of the sea cave beach sediments could be explained by the highest seismicity of the three largest historical earthquakes in the 1600s. It is believed that the main earthquake in 1681 AD resulted in reactivation of the Ocheon fault, which may have caused uplift on the Masan-ri coast of Yeongil Bay.

Key words: Marine terraces, beach sediments, 4 m above sea level, earthquakes, 1643 and 1681 AD

INTRODUCTION

The Korean Peninsula faces the sea on the east, the south, and the west. The southern and western coastlines are irregular due to subsidence (Oh, 1981), but the east is straight with emergent flights, which have developed intermittently along the coast. Choi et al. (2008) reported late Quaternary uplift on the southeastern coast of the Korean Peninsula with average long-term uplift rates ranging from 0.3 to 0.2 m/ky. Moreover, major local faulting in an intraplate regime plays an important role in raising the emergent flights of marine terraces generated by earthquakes.

the southeastern tip of the Korean Peninsula (Figures 1 and 3a). Three sea caves developed in the cliff face of the marine terrace in the study area, 26 m above sea level (asl). The caves are located at 4.5 (cave 1), 7.5 (cave 2), and 9.9 (cave 3) m asl, which could indicate their respective paleo-shoreline positions (Figure 2a). Only cave 2 was filled with sediments, consisting of > 3.4-m-thick beach deposits and a collapse ignimbrite breccia. A similar sea cave on the Masan-ri coast of Yeongil Bay was filled with horizontally bedded beach sediment. The tidal range in the Yeongil Bay area is < 0.3 m (<http://www.khoa.go.kr/>). The > 3.4-m-thick bed in the sea cave consisted of beach pebbles and an ignimbrite breccia. To understand the sediments in the cave, we attempted to discern the stratigraphic units of the cave sediment. The ages of the sediments were measured by radiocarbon dating to constrain the timing of the uplift. We compared the timing of large historical earthquakes with the calibrated age of sea cave sediments.

Tectonically, the bay is part of the southwestern edge of the pull-apart Ulleung Basin, which is part of the East Sea (the Japan Sea). Given the opening of the East Sea around 15 Ma, its closing around 12 Ma, and the middle to upper Miocene age of the sediments (Yoon and Chough, 1995; Jolivet et al., 1994; Fournier et al., 1994), the published stratigraphic and structural data (Fournier et al., 1996; Son, 2007; Kim et al., 2011) may indicate pop-up at a second-order shear fault, the Ocheon fault (OFT).

SEA CAVE SEDIMENTS

The > 3.4-m-thick sea cave deposit is divided into three units, designated as Unit-I, Unit-II, and Unit-III, in ascending order (Figure 2c). The basal Unit-I (70–80-cm-thick) consists mostly of reddish fine sands mixed with small amounts of ignimbrite clasts. The unit is characterized by matrix-supported, well-laminated textures. Some shells and charcoal fragments, as well as cherty pebbles, were observed within these sediments. The clasts, classified as andesite or ignimbrite

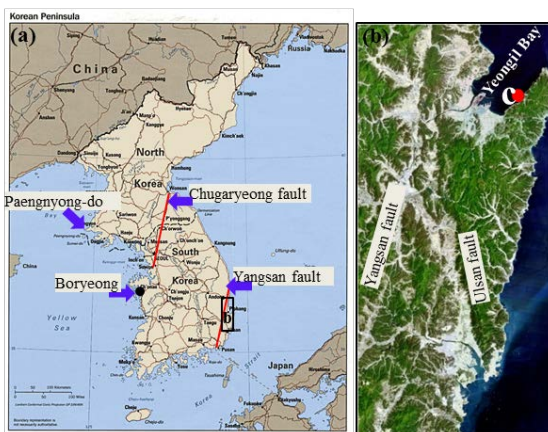


Figure 1: The study area

(<http://mapsofdallas.blogspot.kr/2009/11/map-of-korea.html>).

(a) Index map of Yeongil Bay. (b) Landsat image of the southeastern Korean Peninsula, courtesy of the Korean Ministry of Environment. The Ulsan and Yangsan faults are shown, and are located 25 and 20 km from the Masan-ri coast, respectively.

We recently investigated uplifted sea caves on the Masan-ri coast of the Korean Peninsula (Figure 1) and found potential evidence for recent earthquakes. Masan-ri village is located along the southeastern edge of Yeongil Bay, on



gravels and cobbles, showed coarsening upward. Andesite clasts were well rounded, but the ignimbrites were angular. At the upper part of Unit-I, an ignimbrite breccia layer was inserted into the laterally discontinuous laminations of the fine sands. Well-rounded and spherical black cobbles (100–200 mm) lie on the top of Unit-I.

Unit-II is characterized by milky white ignimbrite sediments (> 130-cm-thick), and by disorganized internal layers. The grain size decreased upward in Unit-II, but the oriented clasts and fine sand laminations were inclined toward the center of the sediment body, and were laterally discontinuous. The clasts and matrix were mostly derived from ignimbrite except for a few clasts consisting of well-rounded andesite pebbles.

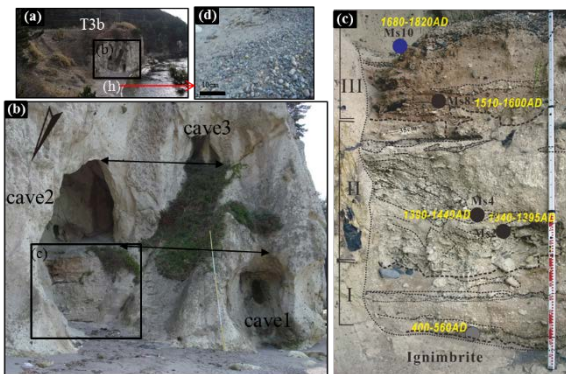


Figure 2: The sea caves in the study area. (a) Three sea caves that developed in the cliff face of the marine terrace (T3b). (b) The different elevations of the sea caves, indicating palaeoshoreline positions. (c) The 7.5-m-high sediments in one of the sea caves were divided into three units. Circles indicate the locations of carbon dating sampling sites; blue indicates shell samples, whereas black and gray indicate charcoal samples. Dating of the gray site was performed by Walter et al. (2005). (d) Modern beach pebbles.

Unit-III (> 140-cm-thick) is characterized by light brown sands and black pebbles. This unit was divided into two beds: sand and pebble. The sand bed (90-cm-thick) contained weak laminations, in which two > 10-cm-thick pebble-rich layers were intercalated and laterally discontinuous. The pebble bed overlying the sand bed was <50-cm-thick. All pebbles were well rounded, well sorted, and disc-shaped, showing imbrication.

Radiocarbon (AMS) analyses yielded calibrated ages of 1680 to 400 AD from the top to the bottom of the cave deposit. Unit I was dated to 400 to 560 AD from charcoal (Walter et al., 2005) and Unit-II of ignimbrite sediments as 1340 to 1440 AD. The upper bed was estimated as ranging from 1510 to 1820 AD.

In summary, Unit-I and Unit-III are similar, and show a different sediment composition than Unit-II. Unit-I and Unit-III consist of well-sorted sands and rounded pebbles with horizontal bedding, whereas Unit-II was mainly composed of unsorted and angular ignimbrite sand and pebbles with poor bedding. We interpreted Unit-I and Unit-III as beach sediments based on the shape of clasts,

whereas Unit-II was interpreted as breccia resulting from the collapse of the cave's roof or wall because the cave is made of pure ignimbrite.

DISCUSSION

Sea caves are inaccurate sea level indicators; however, beach sediments in the sea cave could be more reliable. We assumed that the sediments of Unit-I and Unit-III were transported by wave action, as these sediments were well sorted overall and the pebbles were well rounded and disc-shaped. The bed of Unit-III, which consists of disc-shaped pebbles, is inclined toward the sea.

According to the earthquake catalog of the Korean Peninsula, the three biggest historical earthquakes occurred in Hapcheon and Ulsan in 1643 AD and in Yangyang in 1681 AD. Historical archives describing the Yangyang earthquake report that the seawater fluctuated with a boiling sound, and retreated 60–120 m from the shore, exposing new sea bottom on the East coast of Gangweon-do (National Institute of Korean History, 2016). In addition, one significant foreshock (MMI VIII) occurred at an adjacent site 14 days before the main shock in 1681 AD. According to the historical description of this foreshock, the seawater fluctuated markedly with a boiling sound, and rock cliffs collapsed. Also, along the Yangyang and Samcheok coastlines the sea retreated to the lowest tidal levels and remained at these levels during the foreshock. The retreat of the sea may be interpreted as basement uplift caused by these earthquakes. With the seawater retreat of 60–120 m and a wave cut platform angle of 2°–3°, we can calculate an uplift of 2–6 m, correlating with the 4 m uplift recorded in the sea cave sediments.

Most historical earthquakes occurred between the 15th and 18th centuries (NEMA, 2012). The majority of Korean scientists agree that the most active periods of seismicity were in 1643 and 1681 AD. The earthquake in 1681 AD was felt all over the country and its aftershocks were recorded continuously for several months. We suggest that the Yangyang earthquakes of 1681 AD were sufficiently strong to reactivate pre-existing faults in the east coastal area, both offshore and onshore. The 1681 AD earthquakes might be the main cause of the 4 (±2)-m uplift of the sea cave sediments on the Masan-ri coast. However, the earthquake in 1643 AD could also have significantly affected the Masan-ri coast, as indicated by the young age of the sediments and the high seismicity of that period.

Vertical displacement may have resulted from movement of the OFT, because only this fault passes close to Maran-ri. A segment of the OFT with a high angle dip passing through the Masan-ri cliff containing the sea caves seems to have popped up a few meters, triggered by a strong earthquake (M_w 6.2) and foreshock in 1681 AD (Figure 3c); this was corroborated by carbon dating. However, the ~4 m uplift might be the cumulative sum of vertical displacements due to historical earthquakes since the 1600s.

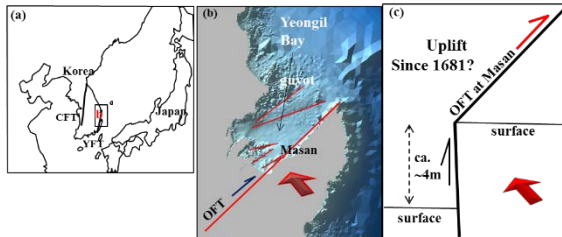


Figure 3: Locations of Masan and Yeongil Bay and a schematic diagram of the uplift. (a) Location of Yeongil Bay. CFT: Chugaryeong Fault, YFT: Yangsan Fault. (b) Fault map of Yeongil Bay showing a dextral shear fracture. The red arrow indicates an inversion of the stress field since the upper Miocene. (c) Schematic diagram showing small pop-up of a segment of the Ocheon Fault (OFT) at Masan that occurred after the 1681 AD earthquake (M_w 6.2). Black arrow: uplift, red arrow: fault sense on the surface.

Acknowledgments: This research was supported by the Basic Research Project (16-3115 and 16-3118) of the Korea Institute of Geoscience and Mineral Resources (KIGAM) funded by the Ministry of Science, ICT, and Future Planning and by the NEMA R&D Program (11-9701) funded by the Ministry of Security and Public Administration, Republic of Korea.

This paper was published in the *Journal of Asian Earth Science* (130) in 2016.

REFERENCES

- Choi, S.-J., Merritts, D.J., Ota, Y., 2008. Elevations and ages of marine terraces and late Quaternary rock uplift in southeastern Korea. *Journal of Geophysical Research* 113, B10403. DOI: 10.1029/2007JB005260.
- Fournier, M., Jolivet, L., Huchon, P., Sergeev, K.F., Ostorbin, L., 1994. Neogene strike-slip faulting in Sakhalin and the Japan Sea opening. *Journal of Solid Earth Research* 99 (B2), 2701–2725.
- Jolivet, L., Tamaki, K., Fournier, M., 1994. Japan Sea, opening history and mechanism: A synthesis. *Journal of Geophysical Research* 99, 22237–22259.
- Kim, H.J., Jou, H. T., Yoo, H.S., Kim, K.H., You, L.S., 2011. High-resolution seismic imaging of shallow geology offshore of the Korean Peninsula: Offshore Uljin. *Korean Society of Earth and Exploration Geophysicists* 14, 127–132.
- Lee, J. Han, H.-S., Han, H.-C., Kong, K.-S., Seo, Y.-K., 2010. A study on topographic features of Yeongil Bay using multibeam data. *The Korean Society of Marine Engineering* 2010, 379–383.
- National Emergency Management Agency, 2012. Active Fault Map and Seismic Hazard Map. *NEMA-Nature-2009–24*, 899 p.
- National Institute of Korean History, 2016. The Annals of the Joseon Dynasty. Retrieved on 06-29-2016 from <http://sillok.history.or.kr/main/main.do>.
- Oh, G. H., 1981. Marine terraces and their tectonic deformation on the coast of southern part of the Korean Peninsula. *Bulletin of the Department of Geography, University of Tokyo* 13, 1–61.
- Son, M., Kim, J.-S., Chong, H.-Y., Lee, Y. H., Kim, I.-S., 2007. Characteristics of the Cenozoic crustal deformation in SE Korea and their tectonic implications. *Korean Journal of Petrology* 13, 1–16.
- Walter, R.C., Merritts, D.J., Lippincott, C., Chwae, U., and Choi S., 2005. Evidence of historic earthquakes and uplift from a sea cave at the southeastern coast of Yeongil Bay. *International Conference of Active Faults*, KIGAM, Daejeon, 5–6.
- Yoon, S.H. and Chough, S.K., 1995. Regional strike slip in the eastern continental margin of Korea and its tectonic implications for the evolution of Ulleung Basin, East Sea (Sea of Japan). *Geological Society of America Bulletin* 107, 83–97.



Fault segmentation in the central Apennines: insights from trenching data

Cinti, Francesca Romana (1), Pantosti, Daniela (1), De Martini, Paolo Marco (1), Civico, Riccardo (1), Pucci, Stefano (1), Villani, Fabio (1)

(1) Istituto Nazionale di Geofisica e Vulcanologia, Rome, Italy. francesca.cinti@ingv.it

Abstract: We synthesize paleoseismic data collected from trenching in the last 30 years along the dense array of NW-SE striking, mainly normal faults accommodating the present-day regional extension of the central Apennines. Historical earthquakes and the recent seismic crisis of this portion of the Apennines occurred in a NW-SE alignment from north to south and definitively testify that we need to cope with the occurrence of multiple mainshocks close in space and time on adjacent faults and fault segments. Based on this “modern awareness” our overview aims at evaluating the role of paleoseismic data to infer possible rupture scenarios in central Apennines. We shed light on the re-assessment of the available displacement and rupture timing estimates for paleo/historical earthquakes assigned at different fault sections with the final goal to identify segments within faults systems by means of the cross-correlation of trenching data.

Key words: paleoseismology, trenching, normal fault, central Apennines, fault segmentation, earthquake surface rupture

MOTIVATION

The historical and recent $M \geq 5.5$ seismicity, including the 2016-2017 central Italy earthquake sequence, clearly document the occurrence of surface rupturing earthquakes triggering each other in a cascade fashion during days to a few years. This tectonic mechanism involves multiple faults producing complex ruptures on neighbouring faults and further stresses the need of advanced fault segmentation models for seismic hazard analysis in this portion of the Apennines.

On this basis, paleoseismic studies yield observational data on the temporal and spatial rupture characteristics of moderate to large magnitude earthquakes over multiple rupture cycles and are influent in developing models of fault behaviour and of rupture scenarios at scales of time and magnitude that may affect the territory.

DATA AND PRELIMINARY DISCUSSION

In the last 30 years, the paleoseismological community in Italy focused their efforts on the study of the numerous closely spaced active normal faults in the central Apennines (*Figure 1*). Only a few of these faults ruptured in modern time (in the last ~100 years), and their activity is mainly testified by the displacement of Late Pleistocene-Holocene deposits and landforms, and also by paleoseismic data. Although with different level of constraints, the great number of trenches supplied reliable data on the fault behaviour of many of those faults.

In this work we provide: - a synthesis of the whole set of trenching data collected so far along the major active faults of the central Apennines and - a synoptic analysis by the cross-correlation of multiple paleoseismic investigations in order to define the extent of paleo surface rupture along adjacent, parallel or stepping faults. The reconstructed paleo rupture setting from trenching data is an added essential value to the understanding whether prominent structural complexities serve as hard barriers to rupture. This latter issue is usually addressed with the long-term geologic-geomorphic approach. The recent surface faulting earthquakes in central Italy (e.g. the Mw 6.5 2016 Norcia earthquake) showed a complex surface rupture pattern, not completely reproduced in the cumulative geomorphic expression of the causative fault. This reinforces the need to use trenching data for more reliable hazard scenarios, especially for anticipating the location of surface ruptures.

The wealth of trenching data in the area, some of them reported in *Figure 1*, allows to build rupture scenarios and define fault segments. However, in some cases the uncertainties on event dating (*Figure 1*) affect the event correlation between sites along individual faults. Thus, we may not always formulate unequivocal rupture mode scenario for large event, even considering the accurate historical record. Under this light, we also target to the definition of “hot paleoseismic spots” along the known faults where the reduction of uncertainties in the earthquake chronologies would be critical to solve segmentation issues and to plan focused actions.

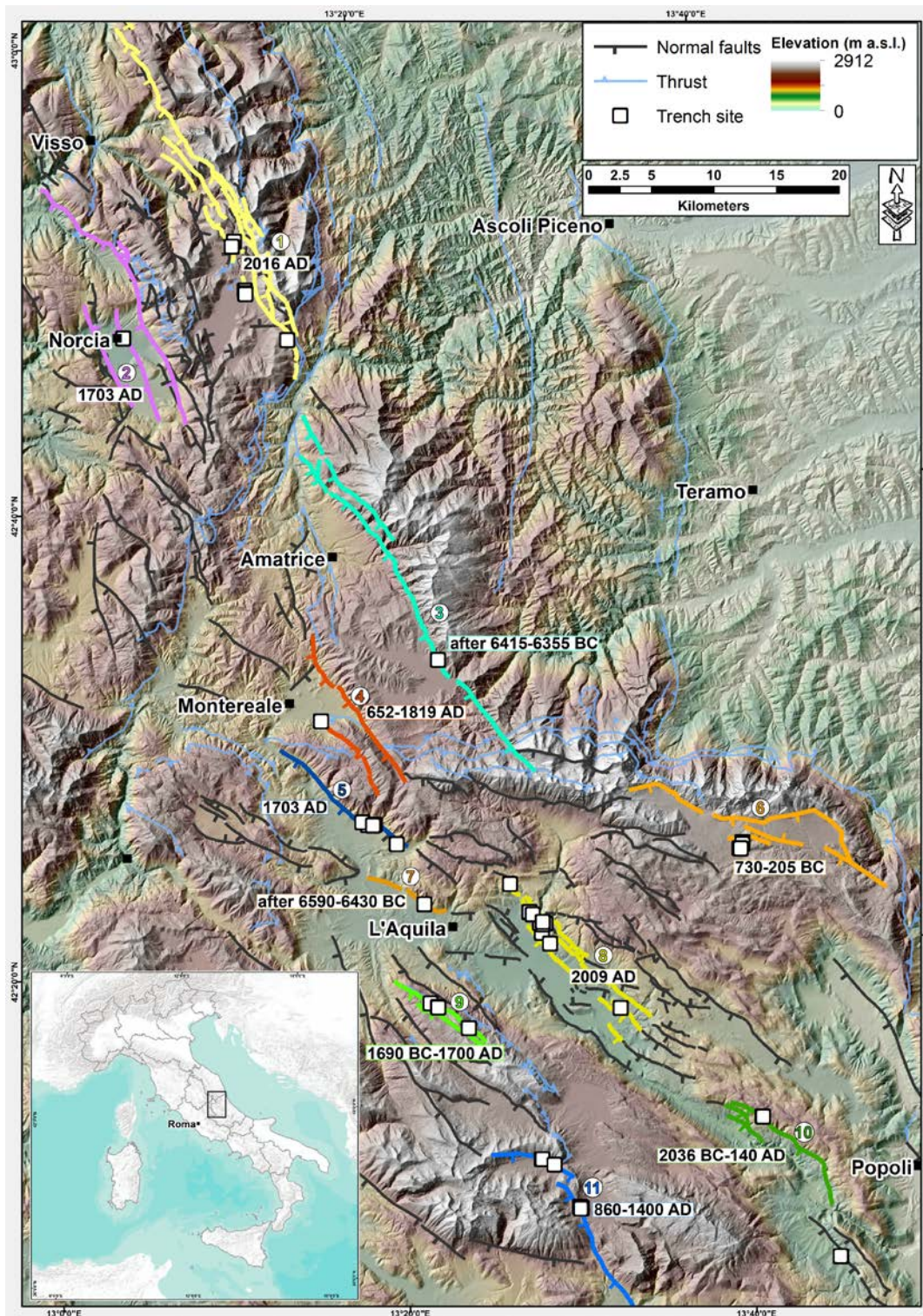


Figure 1: Overview of some paleoseismic sites (white squares) dug in the last 30 years in the central Apennines, Italy. The most recent surface faulting event assigned by Authors (see references list) based on trenching and/or coseismic observations is reported. Faults are modified after Centamore et al., 1992; Festa, 2005; Galadini and Galli, 2000 and Pierantoni et al., 2013; Pucci et al., 2015; Vezzani and Ghisetti, 1998. Numbers refer to the following faults: 1: Vettore-Bove fault system; 2: Norcia fault system; 3: Laga Mts fault system; 4: Montoreale fault system; 5: Mt. Marine fault; 6: Campo Imperatore fault; 7: Mt. Pettino fault; 8: Paganica-S. Demetrio fault system; 9: Mt. Ocre fault; 10: Media Aterno Valley fault system; 11: Ovindoli-Pezza fault.



REFERENCES

- Blumetti, A.M., Di Manna, P., Comerci, V., Guerrieri, L., Vittori, E., 2017. Paleoseismicity of the San Demetrio ne' Vestini fault (L'Aquila Basin, Central Italy): Implications for seismic hazard, *Quaternary International*, <http://dx.doi.org/10.1016/j.quaint.2016.12.039>
- Centamore, E., Adamoli, L., Berti, D., Bigi, G., Bigi, S., Casnedi, R., Cantalamessa, G., Fumanti, F., Morelli, C., Micarelli, A., Ridolfi, M., Salvucci, R., 1992. Carta geologica dei bacini della Laga e del Cellino e dei rilievi carbonatici circostanti (Marche meridionali, Lazio nord orientale, Abruzzo settentrionale), Firenze: S.E.L.C.A.
- Cinti, F.R., Civico R., Blumetti, A.M., Chiarini, E., La Posta, E., Pantosti, D., Papisodaro, F., Smedile, A., De Martini, P.M., Villani, F., Pinzi, S., Pucci, S., Brunori, C.A., 2017. First evidence for surface faulting earthquakes on the Montereale fault system (Abruzzi Apennines, central Italy), *in submission*.
- Cinti, F.R., Pantosti, D., De Martini, P.M., Pucci, S., Civico, R., Pierdominici, S., Cucci, L., Brunori, C.A., Pinzi, S., and Patera, A., 2011. Evidence for surface faulting events along the Paganica Fault prior to the April 6, 2009 L'Aquila earthquake (Central Italy), *J. Geophys. Res.* 116, B07308, doi:10.1029/2010JB007988
- Faluccci, E., Gori, S., Moro, M., Fubelli, G., Saroli, M., Chiarabba, C., Galadini, F., 2015. Implications on seismic potential assessment in tectonically active regions: Lessons from the middle Aterno valley fault system, central Italy, *Tectonophysics* 651–652, 186–198
- Festa, A., 2005. Geometrie e meccanismi di raccorciamento nel settore meridionale del Bacino marchigiano (Monte Gorzano, Appennino centrale), *Boll. Soc. Geol. It.* 44, 41-51.
- Galadini, F., & Galli, P., 2000. Active tectonics in the central Apennines (Italy) – Input data for seismic hazard assessment, *Natural Hazards* 22, 225–268.
- Galadini, F., and Galli, P., 2003. Paleoseismology of silent faults in the Central Apennines (Italy): the Mt. Vettore and Laga Mts. Faults, *Annals of Geophysics*, 46, 5, October 2003.
- Galadini, F., Galli, P., Moro, M., 2003. Paleoseismology of silent faults in the Central Apennines (Italy): the Campo Imperatore Fault (Gran Sasso Range Fault System), *Annals of Geophysics*, 46, 5, October 2003.
- Galli, P., Giaccio, B., Messina, P., Peronace, E., Zuppi G.M., 2011. Palaeoseismology of the L'Aquila faults (central Italy, 2009, Mw 6.3 earthquake): implications for active fault linkage, *Geophys. J. Int.* 187, 1119–1134.
- Galli, P., Giaccio, B., Messina, P., 2010. The 2009 central Italy earthquake seen through 0.5 Myr-long tectonic history of the L'Aquila faults system, *Quaternary Science Reviews* 29 (2010) 3768e3789.
- Galli, P., Galadini, F., Calzoni, F., 2005. Surface faulting in Norcia (central Italy): paleoseismological perspective, *Tectonophysics* 403, 117–130.
- Galli, P., Galadini, F., Moro, M., Giraudi, C., 2002. New paleoseismological data from the Gran Sasso d'Italia area (central Apennines), *Geophysical Research Letters* 29, 7, 1134, 10.1029/2001GL013292
- Gori, S., Emanuela F., Di Giulio, G., Moro, M., Saroli, M., Vassallo M., Ciampaglia, A., Di Marcantonio, P., Trotta, D., 2015. Active normal faulting and large-scale mass wasting in urban areas: the San Gregorio village case study (L'Aquila, central Italy). Methodological insight for seismic microzonation studies, G. Lollino et al. (eds.), *Engineering Geology for Society and Territory* 5, doi: 10.1007/978-3-319-09048-1_197
- Moro, M., Faluccci, E., Gori, S., Saroli, M., Galadini, F., 2016. New paleoseismic data across the Mt. Marine Fault between the 2016 Amatrice and 2009 L'Aquila seismic sequences (central Apennines), *Annals of Geophysics* 59, Fast Track 5, 2016; DOI: 10.4401/ag-7260
- Moro, M., Gori S., Faluccci, E., Saroli, M., Galadini, F., Salvi, S., 2013. Historical earthquakes and variable kinematic behaviour of the 2009 L'Aquila seismic event (central Italy) causative fault, revealed by paleoseismological investigations, *Tectonophysics* 583, 131–144.
- Moro, M., Bosi, V., Galadini, F., Galli, P., Giaccio, B., Messina, P., Sposato, A., 2002. Analisi paleosismologiche lungo la faglia del M. Marine (alta Valle dell'Aterno): risultati preliminari, *Il Quaternario Italian Journal of Quaternary Sciences* 15(2), 259-270.
- Pantosti, D., D'Addezio, G., Cinti, F.R., 1996. Paleoseismicity of the Ovindoli-Pezza fault, central Apennines, Italy: a history including a large, previously unrecorded earthquake in the Middle Ages (860–1300 A.D.), *J. Geophys. Res.* 101, 5937–5959.
- Pierantoni, P., Deiana, G., Galdenzi, S., 2013. Stratigraphic and structural features of the Sibillini Mountains (Umbria-Marche Apennines, Italy), *Italian Journal of Geosciences* 132(3): 497-520.
- Pucci, S., Villani, F., Civico, R., Pantosti, D., Del Carlo, P., Smedile, A., De Martini, P.M., Pons-Branchu, E., & Gueli, A., 2015. Quaternary geology of the Middle Aterno Valley, 2009 L'Aquila earthquake area (Abruzzi Apennines, Italy), *Journal of Maps* 11:5, 689-697, DOI: 10.1080/17445647.2014.927128.
- Salvi, S., Cinti, F.R., Colini, L., D'Addezio, G., Doumaz, F., Pettinelli, E., 2003. Investigation of the active Celano-L'Aquila Fault System, Abruzzi (central Apennines, Italy) with combined ground penetrating radar and palaeoseismic trenching, *Geophys. J. Int.* 155, 805–818.
- Vezzani, L., and Ghisetti, F., 1998. Carta Geologica dell'Abruzzo, Scala 1:100,000, S.EL.C.A., Firenze.



Towards modelling the hazard relating to episodically slipping faults in slowly deforming regions

Clark, Dan (1), Griffin, Jonathan (1), Stirling, Mark (2) & Davies, Gareth (1)

- (1) Geoscience Australia, GPO Box 378 Canberra ACT 2601, Australia. dan.clark@ga.gov.au
 (2) Department of Geology, University of Otago, PO Box 56, Dunedin 9054, New Zealand.

Abstract: We present two case studies from eastern Australia, the Cadell and Lake George faults, where late Neogene to Quaternary slip histories are deduced with variable completeness. Distinctly non-Poisson, or clustered, slip histories are revealed. When assessed together with data from other slowly deforming regions, including the Otago district of New Zealand, a linear relationship emerges between the long-term average slip rate (assessed over several seismic cycles) and the rate at which activity clusters occur. Furthermore, the rate of earthquakes within a cluster also appears to scale with long term average slip rate. Less well correlated is the rate at which a cluster decays to the background rate. That these relationships exist suggests that episodically slipping faults may be characterised and incorporated into probabilistic seismic hazard analysis (PSHA) by modelling clustered rupture behaviour as a non-homogenous Poisson process.

Key words: intraplate seismicity, clustered rupture, non-homogeneous Poisson process.

INTRODUCTION

Paleoseismological studies of Quaternary-active faults in slowly deforming regions often reveal episodic large earthquake recurrence behaviour, with active periods comprising a handful of events being separated by much longer quiescent periods (Clark *et al.*, 2012). In stable continental regions, such as Australia, this behaviour can be extreme, with quiescent periods lasting in the order of a million years or more. Such long periods of quiescence pose great challenges when attempting to reconstruct slip histories using paleoseismic techniques, and in the incorporation of these faults into PSHA. We present two case studies from eastern Australia, the Cadell and Lake George faults (Figure 1), where slip histories were deduced with variable completeness using a combination of shallow geophysics, the interrogation of high resolution topographic datasets, and traditional paleoseismological techniques. Distinctly non-Poisson slip histories are revealed, and are modelled for incorporation into PSHA.

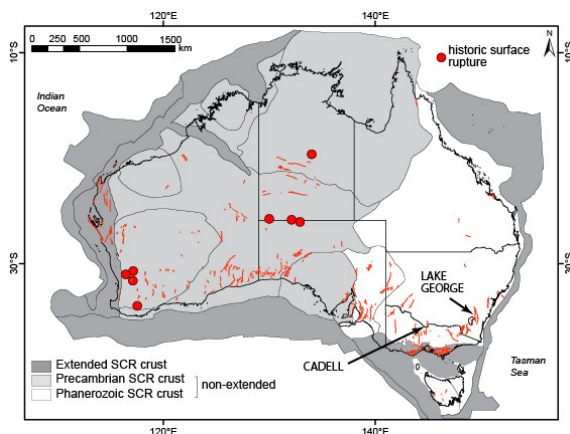


Figure 1: Neotectonic domains model for Australian intraplate crust, after Clark *et al* (2012), with neotectonic features shown.

SLIP EVOLUTION ON THE LAKE GEORGE AND CADELL FAULTS, EASTERN AUSTRALIA

The Cadell Fault, found in Phanerozoic accretionary crust in southeastern Australia, provides a record of temporally clustered morphogenic earthquakes spanning much of the Cenozoic (Clark *et al.*, 2015) (Figure 2). The slip rate, averaged over perhaps as many as five complete seismic cycles in the period 70–20 ka, is c. 0.4–0.5 mm/a, compared with an average rate of c. 0.005–0.01 mm/a over the period spanning the late Miocene to Recent. If full-length rupture of the 80 km long feature is assumed, the average recurrence for M_w 7.3–7.5 earthquake events on the Cadell Fault in the period 70–20 ka is c. 8 kyr. At least 20 kyr, and up to 32 kyr, representing more than two average seismic cycles, have lapsed since the most recent morphogenic seismic event on the fault. It might therefore be speculated that this fault has relapsed into a quiescent period. A prior active period constrained to the late Miocene to Pliocene is imaged in seismic reflection data, and involved a similar uplift amount as the most recent active period (Clark *et al.*, 2015).

The Lake George Basin formed as the result of west-dipping reverse faulting and associated fault propagation folding at the eastern margin of the Lake George Range in the interval between ca. 3.93 Ma and the present (Macphail *et al.*, 2015). Assuming that elevated gravels in the former outlet of the lake are correlative with similar lithology at the base of the basin, vertical displacement on the order of 250 m has occurred in this time interval. Three prominent angular unconformities, separating packages of approximately parallel basin strata, indicate that deformation was episodic, with 0.78 – 1.3 million years separating active periods of ~100 ka duration, involving 40–70 m of uplift on the fault. Slip rates in active periods are not well constrained, but may be >10 times the ~0.09 mm/a long-term slip rate, by analogy with the Cadell Fault. The ~75 km active length of the Lake George Fault is consistent with a M_w 7.4 characteristic earthquake (e.g. Leonard, 2010). The last active period appears to have concluded ~0.78 Ma.

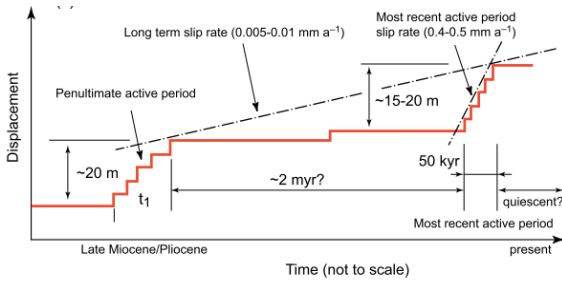


Figure 2: Slip history for the Cadell Fault, after Clark et al. (2015).

MODELLING CLUSTERED BEHAVIOUR AS A NON HOMOGENEOUS POISSON PROCESS (NHPP)

We assume that events recorded in the landscape are approximately M_{max} (i.e. not aftershocks), and that the best predictor of being in an active/quiescent phase is the time since the most recent earthquake. Further, we assume that cluster decay timescales \gg period of interest for PSHA (e.g. 50 yrs).

We perform maximum likelihood parameter estimation for a NHPP of form shown below (for methodology, see Davies et al., 2017), fitted for paleoseismic data from a range of low slip rate faults in Australia (e.g. Figure 3), New Zealand (e.g. Stirling & Anooshehpour, 2006), eastern US and Europe (e.g. Calais et al., 2016).

$$\lambda(t) = \theta_1 + \theta_2 e^{-(t-t_{last})/\theta_3}$$

This allows us to estimate the present rate of large earthquakes based upon the time elapsed since the most recent earthquake. Figure 3 shows hazard curve results for the Cadell Fault, based upon a set of events at 32, 38.5, 45, 55, 62.5, 70, 1000, 2000 and 4500 ka. Given the long time elapsed since the most recent event, the hazard is seen to be much lower than at the start of the cluster, but still twice the background rate.

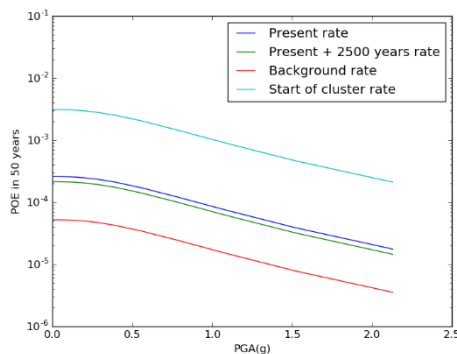


Figure 3: NHPP analysis for the Cadell Fault. $\theta_1 = 6.896e^{-7}$, $\theta_2 = 8.142e^{-5}$, $\theta_3 = 11041.6$. Hazard curves 10 km from fault.

We further assess whether the clustered model background rate (θ_1) (Figure 4), the rate within a cluster (θ_2) (Figure 5), and the timescale of expectance of further events within a cluster (θ_3) scale with long-term earthquake rate (Figure 6). Preliminary results suggest decreasing goodness of fit from $\theta_1 \rightarrow \theta_3$. Future work will include uncertainties, alternative decay models for events

in clusters, and test for dependence on tectonic regime. If this model can be developed for different neotectonic domains (e.g. Clark et al., 2012), then the hazard from a clustered fault without detailed paleoseismic data might be fully characterised by its long terms slip rate and time since the last event.

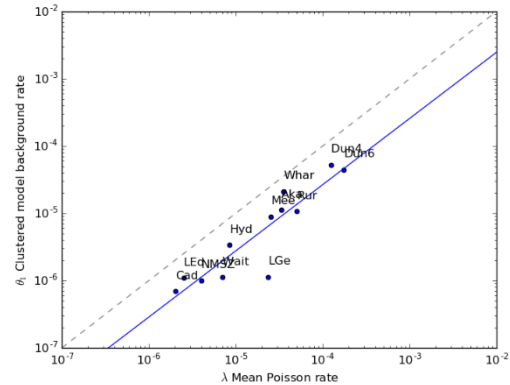


Figure 4: Rate within quiescent periods scales with long-term average rate. Cad = Cadell, LEd = Lake Edgar, Hyd = Hyden, LGe = Lake George, NMSZ = New Madrid Seismic Zone, Mee = Meers, Aka = Akatori, Whar = Wharakuri, Wait = Waitangi, Rur = Rurrand, Dun4 and Dun6 = Dunstan Fault with 4 or 6 events.

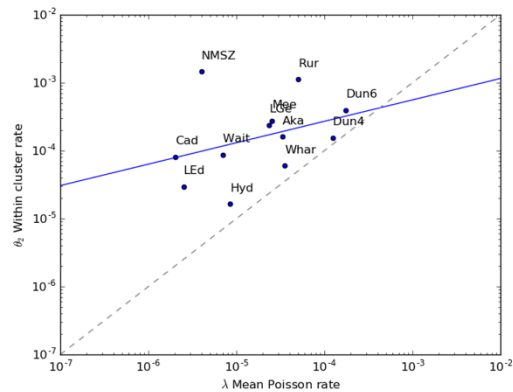


Figure 5: Rate within a cluster scales weakly with long-term average rate.

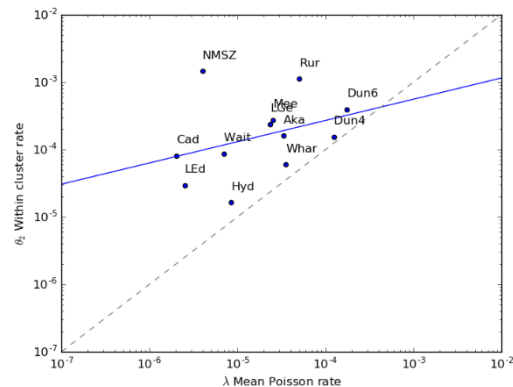


Figure 6: Cluster decay timescale scales weakly with long-term average rate.



DISCUSSION

Temporal clustering of large events in intraplate environments has been reported to be a common characteristic (e.g. Crone *et al.*, 1997; Quigley *et al.*, 2010; Clark *et al.*, 2012). The analysis presented above allows that there may be a continuum from relatively faster average long-term slip-rate intraplate faults (or even plate boundary faults?) and the slowest slip rate faults in the Australian Precambrian cratons. However, this has not been conclusively demonstrated for the low slip rate faults by paleoseismic investigation. The few studies within the non-extended Precambrian cratons (Figure 1) find evidence for one to three events in the last 100 kyr, and perhaps additional events at a time undetermined (Crone *et al.*, 1997; Crone *et al.*, 2003; Estrada, 2009; Clark *et al.*, 2011). Furthermore, all of Australia's eight historic surface ruptures occurred in the Precambrian cratons and have occurred in unexpected locations (in that recurrence could not be conclusively demonstrated). Over the last few decades, permanent and campaign GPS studies across Australia have failed to detect a tectonic deformation signal from which a strain budget could be calculated (e.g. Tregonning, 2003). Similar studies have used these observations, amongst others (e.g. Calais *et al.*, 2005), to propose that clusters of large events deplete long-lived pools of 'fossil' lithospheric strain (Calais *et al.*, 2016; Liu & Stein, 2016). It is proposed that transient changes in stress trigger this pre-strained crust, and recurrence is not required. The observation that groups of faults, together comprising a deforming region several hundred kilometres in extent, can turn 'on' and 'off' more or less simultaneously (e.g. Sandiford, 2003a; Quigley *et al.*, 2010; Clark *et al.*, 2012), is consistent with this hypothesis.

However, our data from the Cadell Fault, and particularly the Lake George Fault, comprising repeating cycles of activity and quiescence, requires recurrence of some kind, at least in Phanerozoic and probably Extended intraplate crust (Figure 1). An alternative possibility to the 'fossil stress' hypothesis is that there may be an orders of magnitude difference in the timescales of strain accumulation and seismogenic strain release in intraplate environments. Episodic rupture behaviour on the Lake George and Cadell Fault, and nearby faults in Phanerozoic crust in eastern Australia, might be controlled by their linkage into major crustal fault systems at depth (e.g. Cayley *et al.*, 2012), in apparent contrast with the style of deformation in non-extended Precambrian SCR crust. Periods of strain localization on these major crustal fault systems, effectively turning deforming regions 'on' and 'off', might still be influenced by changes in distant plate boundary forces, or stress transients.

The relationships shown in Figures 4-6, and variations in seismogenic potential between neotectonic superdomains in general (Figure 1) might relate to lithospheric thickness (cf. Mooney *et al.*, 2012). Precambrian Cratonic crust (Figure 1) is characterized by the thickest lithosphere and has the lowest seismogenic potential, despite all eight documented historic surface ruptures in Australia having occurred within this

category. Little strain accumulation is observed on individual faults and isolated single-rupture scarps are common. Where recurrence has been demonstrated, average slip rates of only a few metres per million years are indicated. In contrast, extended crust is associated with thinner lithosphere, better connection between faults, and strain localization on faults which can result in regional relief-building (Sandiford, 2003b; Sandiford, 2003a; Quigley *et al.*, 2006; Holford *et al.*, 2009; Webb *et al.*, 2011). The most active faults have accumulated several hundred metres of slip under the current crustal stress regime at rates of several tens of metres per million years. Non-extended Phanerozoic crust is typically intermediate in lithospheric thickness and seismogenic character. The more active faults have accumulated tens to a couple of hundreds of metres of slip, at rates of a few to a few tens of metres per million years (e.g. the Lake George Fault). Across all superdomains paleoseismological data suggest that the largest credible earthquakes are likely to exceed those experienced in historic times.

The recognition of a relationship between crustal type/lithospheric thickness and seismogenic potential in Australia provides a framework for assessing whether ergodic substitution (i.e. global analogue studies) might be warranted as a tool to better understand intraplate seismicity worldwide (Clark *et al.*, 2012). For example, the northern Appalachian Mountains in the northeast US are very similar in seismicity and crustal architecture (Lamontagne *et al.*, 2003) to the Flinders Ranges in South Australia (Flöttmann & Cockshell, 1996; Clark *et al.*, 2012; Balfour *et al.*, 2015). Further research is required to assess how variation in crustal stress regime, and stress magnitude, may influence faulting characteristics within different superdomains.

CONCLUSIONS

Work on characterising the seismogenic potential of the Australian intraplate crust allows for a richer understanding of variations in intraplate faulting behaviour worldwide. In general, the concept of large earthquake recurrence might only be meaningful in relation to individual faults in Phanerozoic non-extended and extended superdomains (Figure 1). However, this assertion is yet to be fully demonstrated with paleoseismic data.

Large earthquake recurrence and slip are demonstrably unevenly distributed in time. When Australian examples are assessed together with data from other slowly deforming regions, including the Otago district of New Zealand, the results suggest a linear relationship between the long-term average slip rate (assessed over several active/quiescent cycles) and the rate at which activity clusters occur (Θ_1) (Figure 4). Furthermore, the rate of earthquakes within a cluster also appears to scale with long-term average slip rate (Θ_2) (Figure 5). Less well correlated is the rate at which a cluster decays to the background rate (Θ_3) (Figure 5). That these relationships exist suggests that episodically slipping faults may be characterised and incorporated into PSHA by modelling clustered rupture behaviour as a non-homogenous Poisson process. The challenge remains to collect sufficient data to populate and validate the models.



Acknowledgements: This manuscript is published with the permission of the CEO of Geoscience Australia. An earlier version of this manuscript was improved through the thoughtful reviews of Trevor Allen and Jonathan Griffin.

REFERENCES

- Balfour, N.J., Cummins, P.R., Pilia, S. & Love, D. 2015. Localization of intraplate deformation through fluid-assisted faulting in the lower-crust: The Flinders Ranges, South Australia. *Tectonophysics*, <http://dx.doi.org/10.1016/j.tecto.2015.05.014>.
- Calais, E., Camelbeeck, T., Stein, S., Liu, M. & Craig, T.J. 2016. A New Paradigm for Large Earthquakes in Stable Continental Plate Interiors. *Geophysical Research Letters*, 10.1002/2016GL070815.
- Calais, E., Mattioli, G., DeMets, C., Nocquet, J.M. & Stein, S. 2005. Tectonic strain in plate interiors? *Nature Geoscience*, 438: E9-E10.
- Clark, D., McPherson, A. & Collins, C.D.N. 2011. Australia's seismogenic neotectonic record: a case for heterogeneous intraplate deformation. *Geoscience Australia Record*, 2011/11: 95 p.
- Clark, D., McPherson, A., Cupper, M., Collins, C.D.N. & Nelson, G. 2015. The Cadell Fault, southeastern Australia: a record of temporally clustered morphogenic seismicity in a low-strain intraplate region. In: A. Landgraf, S. Kuebler, E. Hintersburger and S. Stein (Editors), Geological Society, London, Special Publication *Seismicity, Fault Rupture and Earthquake Hazards in Slowly Deforming Regions*.
- Clark, D., McPherson, A. & Van Dissen, R. 2012. Long-term behaviour of Australian Stable Continental Region (SCR) faults. *Tectonophysics* 566-567: 1-30, <http://dx.doi.org/10.1016/j.tecto.2012.07.004>.
- Crone, A.J., de Martini, P.M., Machette, M.N., Okumura, K. & Prescott, J.R. 2003. Paleoseismicity of Two Historically Quiescent Faults in Australia: Implications for Fault Behavior in Stable Continental Regions. *Bulletin of the Seismological Society of America*, 93: 1913-1934.
- Crone, A.J., Machette, M.N. & Bowman, J.R. 1997. Episodic nature of earthquake activity in stable continental regions revealed by paleoseismicity studies of Australian and North American Quaternary faults. *Australian Journal of Earth Sciences*, 44: 203-214.
- Davies, G., Callaghan, D.P., Gravois, U., Jiang, W., Hanslow, D., Nichol, S. & Baldock, T. 2017. Improved treatment of non-stationary conditions and uncertainties in probabilistic models of storm wave climate. *Coastal Engineering*, 127: 1-19, <http://dx.doi.org/10.1016/j.coastaleng.2017.06.005>.
- Estrada, B. 2009. Neotectonic and paleoseismological studies in the southwest of Western Australia, The University of Western Australia, Perth.
- Flöttmann, T. & Cockshell, C.D. 1996. Palaeozoic basins of southern South Australia: New insights into their structural history from regional seismic data. *Australian Journal of Earth Sciences*, 43: 45-55.
- Holford, S.P., Green, P.F., Duddy, I.R., Turner, J.P., Hillis, R.R. & Stoker, M.S. 2009. Regional intraplate exhumation episodes related to plate-boundary deformation. *Geological Society of America Bulletin*, 121(11-12): 1611-1628.
- Lamontagne, M., Keating, P. & Perreault, S. 2003. Seismotectonic characteristics of the Lower St. Lawrence seismic zone, Quebec: insights from geology, magnetics, gravity, and seismics. *Canadian Journal of Earth Sciences*, 40: 317-336.
- Leonard, M. 2010. Earthquake fault scaling: self-consistent relating of rupture length, width, average displacement, and moment release. *Bulletin of the Seismological Society of America*, 100(5A): 1971-1988, DOI: 10.1785/0120090189.
- Liu, M. & Stein, S. 2016. Mid-continental earthquakes: Spatiotemporal occurrences, causes, and hazards. *Earth Science Reviews*, 10.1016/j.earscirev.2016.09.016.
- Macphail, M., Fifield, L.K., Pillans, B., Davies, M. & Hope, G. 2015. Lake George revisited: New evidence for the origin and evolution of a large closed lake, Southern Tablelands, NSW, Australia. *Australian Journal of Earth Sciences*, 10.1080/08120099.2015.1108365.
- Mooney, W.D., Ritsema, J. & Hwang, Y.K. 2012. Crustal seismicity and the earthquake catalog maximum moment magnitude (M_{cmax}) in stable continental regions (SCRs): Correlation with the seismic velocity of the lithosphere. *Earth and Planetary Science Letters*, 357-358: 78-83.
- Quigley, M.C., Clark, D. & Sandiford, M. 2010. Tectonic geomorphology of Australia. *Geological Society, London, Special Publications*, 346(1): 243-265.
- Quigley, M.C., Cupper, M.L. & Sandiford, M. 2006. Quaternary faults of south-central Australia: paleoseismicity, slip rates and origin. *Australian Journal of Earth Sciences*, 53: 285-301.
- Sandiford, M. 2003a. Geomorphic constraints on the late Neogene tectonics of the Otway Ranges. *Australian Journal of Earth Sciences*, 50: 69-80.
- Sandiford, M. 2003b. Neotectonics of southeastern Australia: linking the Quaternary faulting record with seismicity and in situ stress. In: R.R. Hillis and D. Muller (Editors), Evolution and dynamics of the Australian Plate Geological Society of Australia Special Publication, pp. 101-113.
- Stirling, M.W. & Anooshehpour, R. 2006. Constraints on Probabilistic Seismic-Hazard Models from Unstable Landform Features in New Zealand. *Bulletin of the Seismological Society of America*, 96(2): 404-414, 10.1785/0120050034.
- Tregonning, P. 2003. Is the Australian Plate deforming? A space geodetic perspective. *Geological Society of Australia Special Publication, 22 and Geological Society of America Special Publication*, 372: 41-48.
- Webb, J.A., Gardner, T.W., Kapostasy, D., Bremar, K.A. & Fabel, D. 2011. Mountain building along a passive margin: Late Neogene tectonism in southeastern Victoria, Australia. *Geomorphology*, 125: 253-262.



Assessing the evidence of past multi fault ruptures at the southern Hikurangi margin using paleoseismic records

Clark, K. J. (1), Little, T (2), Howarth, J (2), Van Dissen, R (1), Litchfield, N (1)

- (1) GNS Science, PO Box 30368, Lower Hutt, New Zealand
 (2) Victoria University of Wellington. PO Box 600, Wellington, New Zealand

Abstract: The M_w 7.8 Kaikōura earthquake, characterised by rupture of multiple upper plate faults and a part of the subduction interface, prompts reassessment of paleoseismic data to understand if synchronous crustal fault and subduction interface ruptures are a typical or atypical mode of plate motion accommodation along the very southern extent of the Hikurangi margin. Large subduction earthquakes on the southern Hikurangi margin occurred at 520 – 470 and 880 – 800 yrs BP. We compare the age ranges of these subduction earthquakes with a compilation of paleoearthquake ages on crustal faults on both sides of Cook Strait. Many of the published paleoearthquake ages pre-dated the routine use of Bayesian statistics for the analysis of radiocarbon dates so we re-evaluate some paleoearthquake ages using OxCal age models. Temporal correlations using radiocarbon-dated paleoearthquakes are hampered by decadal- to centennial-scale uncertainties intrinsic to ^{14}C measurements and calibration, and uncertainties introduced by sample proximity and relationship to the event horizon. Despite this, paleoseismic data suggests the upper plate fault-subduction interface interaction seen in 2016 has also occurred in the past, if not in a synchronous rupture then at least closely spaced in time.

Key words: southern Hikurangi margin, paleoearthquakes, paleotsunami

INTRODUCTION

The M_w 7.8 Kaikōura earthquake ruptured a complex network of crustal faults and a deep patch of the plate interface at the southern end of the Hikurangi margin (Hamling et al. 2017). Synchronous upper plate fault and subduction interface ruptures have occurred in historic times on other plate boundaries and on the Hikurangi margin. The Alaska 1964 earthquake (Plafker 1967) and 2010 Maule (Chile) earthquake (Melnick et al. 2012) saw upper plate faults rupture with the subduction interface but in these examples the splay fault rupture clearly accounted for a minor portion of the total slip. In the AD 1855 M 8.2 Wairarapa earthquake a deep portion (18 – 30 km depth) of the southern Hikurangi subduction interface may have ruptured based on historic accounts of the spatial extent of coastal deformation (Beavan and Darby 2005). However, the majority of slip occurred on the Wairarapa fault (Fig. 1a) and only a relatively minor amount could have occurred on the subduction interface. This behaviour of the deep part of the southern Hikurangi subduction interface slipping with crustal fault ruptures, now witnessed in 2 historic earthquakes, raises questions such as: (1) how and when is strain released on the shallow part of the subduction interface?; and (2) is rupture of the southern Hikurangi subduction interface always accompanied by upper plate fault rupture(s)? Here we compile paleoearthquake records from the southern Hikurangi margin and compare the timing of past crustal fault ruptures with subduction interface earthquakes.

Past subduction earthquakes on the southern Hikurangi margin
 Evidence for past subduction earthquakes on the southern Hikurangi margin is derived from studies of saltmarsh

subsidence and tsunami inundation at Big Lagoon, also called Mataora-Wairau Lagoon, 14 km east of Blenheim (Clark et al. 2015; King et al. 2017). At Big Lagoon, sudden subsidence of saltmarsh soil horizons is documented from stratigraphic and microfossil evidence (Fig. 2). The last event, recorded by ~0.25 m of subsidence, occurred at 470 – 520 yrs BP, and the penultimate event, recorded by ~0.5 m subsidence and tsunami inundation, occurred at 800 – 880 yrs BP (Clark et al. 2015). While subsidence at Big Lagoon could feasibly be caused by some nearby active crustal faults it is best-fit by rupture of the southern Hikurangi plate interface (Fig. 3). The search for evidence of older subduction earthquakes on the southern Hikurangi margin is ongoing. The ubiquity of crustal faults means many parts of the southern Hikurangi coastline have a tectonic signal dominated by upper plate faults rather than subduction earthquakes.

Historic earthquakes of the southern Hikurangi margin

The written historic period in New Zealand extends back to the early 1800's when European settlement became widespread. Since AD 1840 there have been three notable large earthquakes on the southern Hikurangi margin and Marlborough Fault System: the 1848 M 7.4 Awatere earthquake, the 1855 M 8.1 – 8.2 Wairarapa earthquake, and the 2016 M_w 7.8 Kaikōura earthquake (Fig. 1b). Of these three, the Awatere earthquake, appears to be the simplest fault rupture with a surface rupture length of 100 – 110 km (Grapes et al. 1998; Mason and Little 2006). The Wairarapa earthquake rupture was 120 km onland and up to 40 km offshore into Cook Strait (Rodgers and Little, 2006). Principally on the Wairarapa fault, where up to 18.7 m of lateral displacement occurred, the earthquake also ruptured an offshore part of the Wharekahau thrust to the south, and



probably ruptured the Alfredton fault to the north (Rodgers and Little 2006). The pattern of subsidence, recorded by historic observations, is consistent with rupture of the deep part of the subduction interface (Beavan and Darby 2005), and this deep rupture is also invoked as an explanation for the very high surface displacement for the length of the fault (Rodgers and Little 2006). The 2016 Kaikōura earthquake ruptured at least 20 crustal faults from north Canterbury to Cape Campbell (Fig. 1b), and also ruptured the deep portion of the plate interface (Hamling et al. 2017, Litchfield et al. submitted, and many papers in this volume).

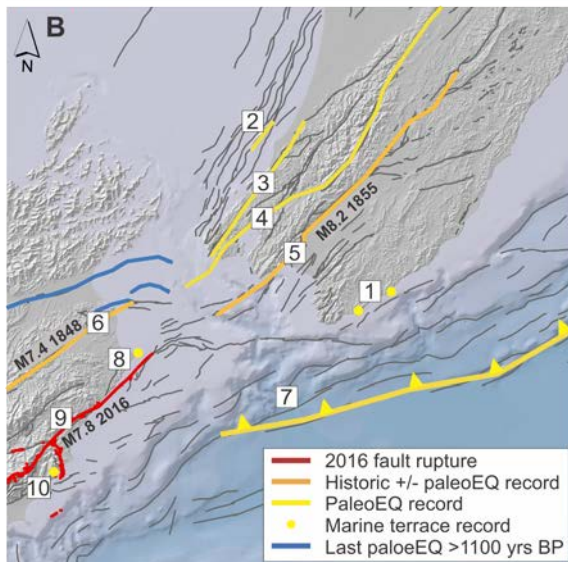
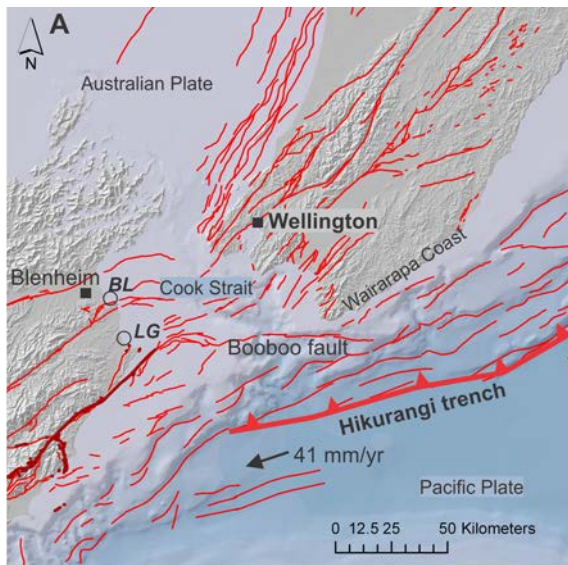


Figure 1: (a) Tectonic setting of the southern Hikurangi margin, active faults in red (onshore faults from the NZ active faults database, (Langridge et al. 2016), and offshore faults from NIWA). Dark red faults: 2016 Kaikōura earthquake ruptures. (b) Map of faults included in our compilation of historic earthquakes and paleoearthquakes, and location of marine terraces.

Past upper plate fault earthquakes on the southern Hikurangi margin

The southern Hikurangi margin is traversed by numerous active faults and paleoearthquake records spanning the past ~1200 years are known for all the high slip-rate faults, except for some offshore faults (e.g. Boo Boo fault, Fig. 1a). We have compiled the probability density functions (pdfs) for the paleoearthquakes of the past 1200 – 1500 years in Figure 4.

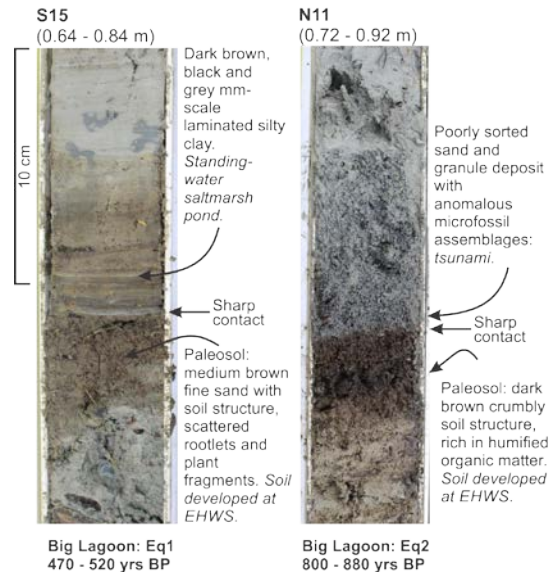


Figure 2: Stratigraphic evidence of past subduction earthquakes from Big Lagoon, figure adapted from Clark et al. (2015).

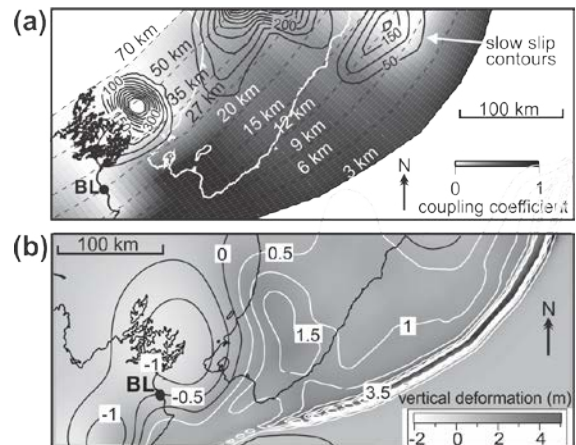


Figure 3: (a) Coupling coefficient on the southern Hikurangi subduction interface (figure modified from Wallace and Beavan 2010). (b) Upper plate deformation produced by a plausible southern Hikurangi subduction interface earthquake scenario. Here, we use elastic dislocation, half-space modelling of a subduction earthquake scenario with 500 yrs of accumulated slip based on the present-day pattern of interseismic locking shown in (a). Figure adapted from Clark et al. (2015).

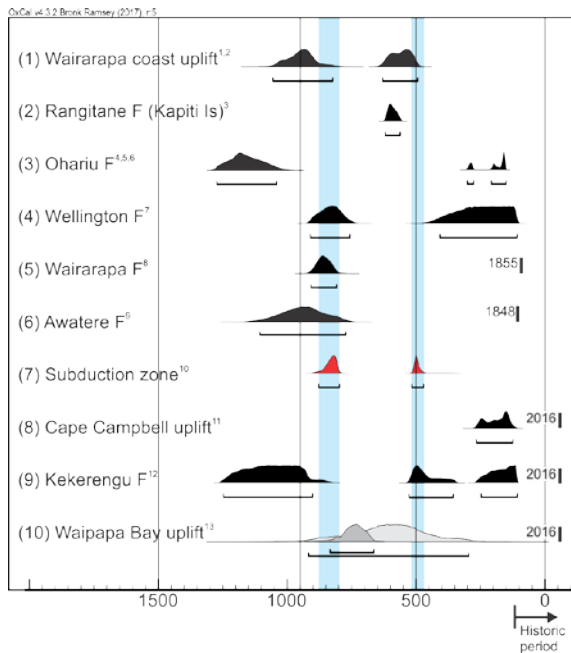


Figure 4: Probability distributions for paleoearthquakes on the subduction interface (red pdfs) and on upper plate faults of the southern Hikurangi margin (black pdfs). See Fig. 1 for locations. Subduction interface rupture age span is shaded in light blue. The grey shaded pdfs of Waipapa Bay uplift denote poorly constrained ages because the dates were obtained in the 1980s when the precision of radiocarbon dating was much lower and these ages represent only one shell from the lowest and 3rd highest terraces. Original data sources: 1: (Berryman et al. 2011); 2: (Litchfield et al. 2013); 3: (Cochran et al. 2015); 4: (Litchfield et al. 2006); 5: (Heron, Van Dissen, and Sawa 1998); 6: (Litchfield et al. 2010); 7: (Langridge et al. 2011); 8: (Little et al. 2009); 9: (Mason, Little, and Van Dissen 2006); 10: (Clark et al. 2015); 11: Litchfield et al., this volume; 12: (Little et al. in press). All terrestrial radiocarbon dates calibrated using the ShCal13 curve. Shell samples were calibrated using the Marine 13 curve, with $\Delta R = 75 \pm 46$ yrs for the Wairarapa coast (value derived from unpublished data) and $\Delta R = 3 \pm 14$ yrs for Cape Campbell and Waipapa Bay (value from McSaveney et al. 2006).

Most paleoearthquake records have been obtained from paleoseismic trenches (e.g. Wellington, Wairarapa, Awatere, Ohariu, Kekerengu faults) and some paleoearthquake ages are inferred from the coseismic uplift of Holocene marine terraces. Along the Wairarapa coast, uplift of marine terraces is primarily attributed to the offshore Paliser-Kaiwhata fault although could also be caused by the subduction interface (Berryman et al. 2011). Uplift of Cape Campbell is inferred to be caused by the Needles fault (as occurred in the 2016 Kaikōura earthquake) and uplift of Waipapa Bay is inferred to have been caused by slip on the Papatea fault (also the case in the 2016 Kaikōura earthquake). Marine terrace ages are derived from shells on the terrace and we assume the shell death dates the earthquake but acknowledge that uplift could have occurred after shell death, so the terrace ages are maximums.

Some pdfs shown in Figure 4 have been derived directly from age models presented in publications (cited in Fig. 4) but many studies pre-dated the routine use of Bayesian statistical methods for the evaluation of events

ages bounded by radiocarbon dates. For the Ohariu, Wellington, Wairarapa and Awatere faults we have recalculated the paleoearthquake ages using OxCal models (Bronk Ramsey 2009). In most cases the paleoearthquake age has not significantly changed from the published age. The Ohariu fault earthquake age shifts to an older and wider age distribution compared to the published age range of 1000 – 1050 yrs BP in (Litchfield et al. 2006).

Discussion

The assessment of multi-fault ruptures in the geological record is fraught with difficulties due to the variable thresholds for the preservation of evidence and uncertainties in paleoearthquake ages. Temporal correlations of radiocarbon-dated events are hampered by decadal- to centennial-scale uncertainties intrinsic to ¹⁴C measurements and calibration, and uncertainties introduced by sample proximity and relationship to the event horizon. Nevertheless, the evaluation of paleoseismic evidence can often firmly discount the possibility of past synchronous rupture of two or more candidate faults, and it can give us information on faults that did rupture within a certain time span. Thus, simultaneous rupture cannot be proven but it can be shown as a possibility.

Our compilation of paleoearthquake ages from the southern Hikurangi margin shows that the third most recent event of the Kekerengu fault partially overlaps (at the 95% uncertainty range) with the last rupture of the subduction interface (Fig. 4). The 95% uncertainty range on the timing of the penultimate rupture of the subduction interface overlaps partially with the age ranges of ruptures of the Wellington, Wairarapa, and Awatere faults, and with uplift of a marine terrace on the SE Wairarapa coast. Despite the age uncertainties, paleoseismic data suggests the upper plate fault-subduction interface interaction seen in 2016 has also occurred in the past, if not in a synchronous rupture then at least closely spaced in time. We also note from Figure 4 that the time period from ~550 – 800 yrs BP appears to have been relatively seismically quiescent, with only ruptures on the Rangitane fault and uplift of the SE Wairarapa coast and possibly the Waipapa Bay coast recorded.

Current research is focussing on collection of new high resolution paleotsunami, coastal deformation and turbidite records from the southern Hikurangi margin. The acquisition of more multi-proxy paleoseismic data with a focus on tight age constraints from radiocarbon dating should increase our ability to examine upper plate fault-subduction interface interactions in the past.

Acknowledgements: This research is funded by the GNS SSIF Tectonics and Structure of Zealandia research programme.



REFERENCES

- Beavan, J., and D. Darby. 2005. "Fault slip in the 1855 Wairarapa earthquake based on new and reassessed vertical motion observations: did slip occur on the subduction interface?" In *The 1855 Wairarapa Earthquake Symposium*, edited by J. Townend, R. Langridge and A. Jones, 31-41. Wellington: Greater Wellington Regional Council.
- Berryman, K, Ota Y, Miyauchi T, Hull A, Clark K, Ishibashi K, Iso N, and Litchfield N. 2011. 'Holocene Paleoseismic History of Upper-Plate Faults in the Southern Hikurangi Subduction Margin, New Zealand, Deduced from Marine Terrace Records', *Bulletin of the Seismological Society of America*, 101: 2064-87.
- Bronk Ramsey, C. 2009. 'Bayesian analysis of radiocarbon dates', *Radiocarbon*, 51: 337-60.
- Clark, K., Hayward B, Cochran U, Wallace L, Power W, and Sabaa A. 2015. 'Evidence for Past Subduction Earthquakes at a Plate Boundary with Widespread Upper Plate Faulting: Southern Hikurangi Margin, New Zealand', *Bulletin of the Seismological Society of America*, 105: 1661-90.
- Cochran, U.A., N.J. Litchfield, K.J. Clark, W.F. Ries, P. Villamor, J.D. Howarth, C. Watson, and D.T. Strong. 2015. "Improved age control for a fourteenth century earthquake and tsunami from Okupe Lagoon, Kapiti Island." In *GNS Science report 2015/28*, 37 p. + 4 appendices. Lower Hutt: GNS Science.
- Grapes, R, Little T, and Downes G. 1998. 'Rupturing of the Awatere Fault during the 1848 October 16 Marlborough earthquake, New Zealand: Historical and present day evidence', *New Zealand Journal of Geology and Geophysics*, 41: 387-99.
- Hamling, Ian J., and 28 others. 2017. 'Complex multifault rupture during the 2016 Mw 7.8 Kaikōura earthquake, New Zealand', *Science*, 356.
- Heron, D., R. Van Dissen, and M. Sawa. 1998. 'Late Quaternary movement on the Ohariu Fault, Tongue Point to MacKays Crossing, North Island, New Zealand', *New Zealand Journal of Geology and Geophysics*, 41: 419-39.
- King, D. N., J. R. Goff, C. Chagué-Goff, B. McFadgen, G. E. Jacobsen, P. Gadd, and M. Horrocks. 2017. 'Reciting the layers: Evidence for past tsunamis at Mataora-Wairau Lagoon, Aotearoa-New Zealand', *Marine Geology*, 389: 1-16.
- Langridge, R. M., W. F. Ries, N. J. Litchfield, P. Villamor, R. J. Van Dissen, D. J. A. Barrell, M. S. Rattenbury, D. W. Heron, S. Haubrock, D. B. Townsend, J. M. Lee, K. R. Berryman, A. Nicol, S. C. Cox, and M. W. Stirling. 2016. 'The New Zealand Active Faults Database', *New Zealand Journal of Geology and Geophysics*, 59: 86-96.
- Langridge R, Van Dissen R, Rhoades D, Villamor P, Little T, Litchfield N, Clark K, and Clark D. 2011. 'Five Thousand Years of Surface Ruptures on the Wellington Fault, New Zealand: Implications for Recurrence and Fault Segmentation', *Bulletin of the Seismological Society of America*, 101: 2088-107.
- Litchfield, N. J., U. A. Cochran, K. R. Berryman, B. Ansell, and K. Clark. 2013. 'Timing and amount of uplift of the youngest Holocene marine terrace along the Honeycomb Rock – Riversdale Beach coast, eastern Wairarapa', *GNS Science Report 2013/54*: 44 p. <http://www.gns.cri.nz/static/pubs/2013/SR%202013-054.pdf>.
- Litchfield, N, Van Dissen R, Heron D, and Rhoades D. 2006. 'Constraints on the timing of the three most recent surface rupture events and recurrence interval for the Ohariu Fault: Trenching results from MacKays Crossing, Wellington, New Zealand', *New Zealand Journal of Geology and Geophysics*, 49: 57-61.
- Litchfield, N., van Dissen, R., Hemphill-Haley, M., Townsend, D., & Heron, D. (2010). Post c. 300 year rupture of the Ohariu Fault in Ohariu Valley, New Zealand. *New Zealand Journal of Geology and Geophysics*, 53(1), 43-56. doi:10.1080/00288301003631780
- Litchfield, N. J., and 50 others. Submitted. Surface Fault Rupture from the Mw 7.8 2016 Kaikōura Earthquake, New Zealand, and Insights into Factors Controlling Multi-Fault Ruptures, *Bulletin of the Seismological Society of America*.
- Little, T. A., R. Van Dissen, E. Schermer, and R. Carne. 2009. 'Late Holocene surface ruptures on the southern Wairarapa fault, New Zealand: Link between earthquakes and the uplifting of beach ridges on a rocky coast', *Lithosphere*, 1: 4-28.
- Little, T. A., R. Van Dissen, J. Kears, K. Norton, A. Benson, and N. Wang. in press. 'Kekerengu fault, New Zealand: timing and size of Late Holocene surface ruptures', *Bulletin of the Seismological Society of America*.
- Mason, D., and Little T. 2006. 'Refined slip distribution and moment magnitude of the 1848 Marlborough earthquake, Awatere Fault, New Zealand', *New Zealand Journal of Geology and Geophysics*, 49: 375-82.
- Mason, D, Little T, and Van Dissen R. 2006. 'Refinements to the paleoseismic chronology of the eastern Awatere Fault from trenches near Upcot Saddle, Marlborough, New Zealand', *New Zealand Journal of Geology and Geophysics*, 49: 383-97.
- McSaveney, M., Graham, I., Begg, J., Beu, A., Hull, A., Kim, K., & Zondervan, A. (2006). Late Holocene uplift of beach ridges at Turakirae Head, south Wellington coast, New Zealand *New Zealand Journal of Geology and Geophysics*, 49, 337–358
- Melnick, D, Moreno M, Motagh M, Cisternas M, and Wesson R. 2012. 'Splay fault slip during the Mw 8.8 2010 Maule Chile earthquake', *Geology*, 40: 251-54.
- Plafker, G. 1967. 'Surface faults on Montague Island associated with the 1964 Alaska earthquake', *U.S. Geological Survey Professional Paper 543-G*: 42 p.
- Rodgers, D., and T. Little. 2006. 'World's largest coseismic strike-slip offset: The 1855 rupture of the Wairarapa Fault, New Zealand, and implications for displacement/length scaling of continental earthquakes', *Journal of Geophysical Research*, 111: doi:10.1029/2005JB004065.
- Wallace, L, and Beavan J. 2010. 'Diverse slow slip behavior at the Hikurangi subduction margin, New Zealand', *Journal of Geophysical Research*, 115: B12402.



Development of an 8000-year record of large earthquakes on the Alpine Fault: where to from here?

Cochran, Ursula (1), Clark, Kate (1), Berryman, Kelvin (1), Biasi, Glenn (2), Langridge, Robert (1), Villamor, Pilar (1), Howarth, Jamie (3), Van Dissen, Russ (1)

- (1) GNS Science, 1 Fairway Drive, Avalon, Lower Hutt, New Zealand. u.cochran@gns.cri.nz
- (2) United States Geological Survey, 525 South Wilson Avenue, Pasadena, CA91106, USA
- (3) Victoria University of Wellington, PO Box 600, Wellington, New Zealand

Abstract: We used sedimentary sequences from wetlands adjacent to the Alpine Fault in Southland, New Zealand to develop a history of surface-rupturing earthquakes. At Hokuri Creek and John O’Groats River, wetlands on the upstream but downthrown side of the Alpine Fault have recorded hydrological and sedimentological responses to earthquakes over many millennia. We used various paleoseismological techniques to identify past earthquakes and obtain age estimates. Our analyses indicate 27 surface-rupturing earthquakes occurred on the South Westland section of the fault over the last 8000 years. The coefficient of variation for the dataset (0.41) indicates quasi-regular occurrence of earthquakes. This is consistent with the structural maturity of the fault and the high proportion of plate-boundary motion it accommodates. It suggests time-dependent recurrence models are appropriate for seismic hazard estimation on this and similar faults. We explore the potential for extracting long earthquake records using similar techniques at other sites in New Zealand.

Key words: Alpine Fault; paleoseismology; recurrence behaviour; seismic hazard; surface-rupturing earthquakes

INTRODUCTION

The year 2017 marks 300 years since the last major surface-rupturing earthquake on the Alpine Fault – the transform plate boundary fault that traverses the length of the South Island in New Zealand (Fig. 1). The 1717 AD earthquake is estimated to have been of magnitude 8.1 and to have ruptured 380 km of the fault (Wells et al., 1999; De Pascale & Langridge, 2012). Impacts of this event included extensive landsliding, forest destruction, and decades of increased sedimentation in lakes, rivers and at the coast (Wells & Goff, 2007; Howarth et al., 2014). The impact of such an event today is likely to include hundreds of fatalities, thousands of injuries and billions of dollars of damage (Robinson et al., 2014). The aim of our research was to better understand the earthquake recurrence behaviour of the Alpine Fault and to improve seismic hazard estimates.

We developed long earthquake records from two sites on the South Westland section of the Alpine Fault (the southernmost onshore extent of the fault; Fig. 1). At Hokuri Creek, we studied fault-proximal outcrops from a paleo-wetland and at John O’Groats River, we collected cores from a fault-proximal wetland. At these sites, the Alpine Fault, although dominantly strike-slip, has a small component of vertical slip that causes uplift to the northwest (i.e., opposite sense to that observed on the central and North Westland sections) so drainage from mountains to the east is impeded by the fault scarp (Fig.2). Hokuri Creek and John O’Groats River have had to flow

through channels incised into scarps that rise up to 15 m above the valley floor. Therefore, coseismic movement results in offset of the channel and flooding of the valley floor on the upstream side of the fault until the new scarp is eroded or a new channel established.

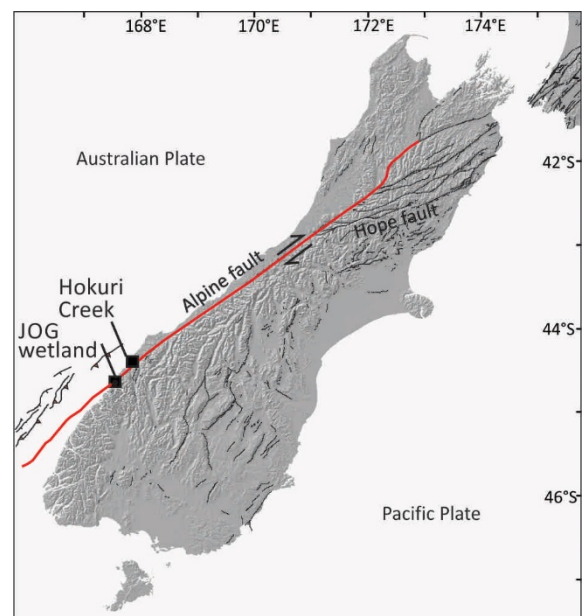


Figure 1: Map of the South Island of New Zealand showing the Alpine Fault with a bold red line, the location of study sites as black squares, and other active faults as fine black lines.



Figure 2: Photos of the study sites at Hokuri Creek (left) and John O'Groats River (right) looking northeast. The trace of the Alpine Fault is marked by arrows and the outcrops and core locations are marked by circles. The channels of both Hokuri Creek and John O'Groats River reach the upthrown scarp of the Alpine Fault and are forced to flow along the scarp to a previous outflow channel or low point across the fault. Hokuri Creek has now abandoned its old outflow channel and cut down through the wetland sequence that we studied. At John O'Groats River, the wetland is still in place ready to record the next earthquake so it acts as a modern analogue for what the Hokuri Creek study site would have looked like. These sites are about 20 km apart along the fault (Fig. 1).

This geomorphology, along with the sedimentary regime of the catchments, has resulted in preservation of millennial-scale records of past surface-rupturing earthquakes. We observed cyclic stratigraphy at both sites that consisted of peats and organic silts of an in-situ wetland being repeatedly overlain by non-organic fine sands and silts transported from the catchment.

We inferred that the wetland peats represent the interseismic period and the clastics represent the post-seismic response in the form of flooding and sediment flux from the catchment. This enabled us to identify earthquake event horizons at the major, valley-wide transitions between peat and silt. We obtained age estimates for the earthquakes by radiocarbon dating short-lived organic fractions such as seeds and leaves either side of these sedimentary transitions.

The key techniques we used to develop these earthquake records were:

- Geomorphological characterisation of the site including single event displacement measurements.
- Stratigraphic characterisation of all available outcrops and cores in both fault-parallel and fault-normal directions.
- A ground penetrating radar survey to map the continuity of units between cores at the John O'Groats River site.

- Detailed sedimentology and microfossil analysis to determine depositional environments and processes of all sediment types present.
- Ranking of peat-silt transitions according to specific criteria to determine likelihood of earthquake versus non-earthquake cause of change. Criteria included suddenness of change, amount of change in depositional environment, lateral extent and synchronicity of change across each basin.
- Radiocarbon dating immediately either side of event horizons. Earthquake age estimates and uncertainties were obtained through Bayesian statistical modelling.

DISCUSSION

We found that major, basin-wide peat-silt couplets at each site represented earthquake event horizons. We identified 22 earthquakes occurring over 7000 years at Hokuri Creek (Clark et al., 2013) and 7 earthquakes in 2000 years at John

O'Groats River (Cochran et al., 2017). Two earthquakes overlap in time between the two sites and are considered to represent the same earthquakes. Therefore, the joint record consists of 27 earthquakes over the last 8000 years (Cochran et al., 2017; Fig. 3).

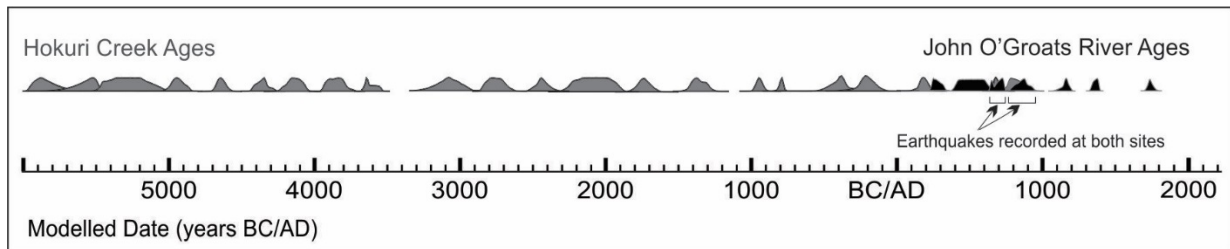


Figure 3: Ages of major, surface-rupturing earthquakes on the South Westland section of the Alpine Fault as recorded in fault-proximal wetlands at Hokuri Creek (grey curves) and John O'Groats River (black curves). Curves are the probability density functions of the modelled ages. Two earthquakes were recorded at both sites as noted by the square brackets.

The exact magnitude of events recorded at these sites is unknown. However, it appears that they must have been earthquakes large enough to break the ground surface with metre-scale oblique offset to have caused the observed flooding. Single event displacement measurements at Hokuri Creek indicated that the northwestern block of the Alpine Fault moved 7.5 ± 1 m dextrally and 1 ± 0.5 m vertically in the most recent event (Clark et al., 2013). The most recent whole-fault rupture (1717 AD) is calculated to have been a magnitude 8.1 earthquake (De Pascale & Langridge, 2012). Therefore, our dataset likely includes earthquakes in the magnitude range of high sevens to low eights – we refer to them informally as “major”. The record may be missing an occasional major earthquake, but regardless, the timeline clearly indicates relatively regular occurrence of such events (Fig. 3).

The impact of these results has been threefold. Firstly, we have demonstrated that the mature, fast-slipping, strike-slip Alpine Fault ruptures quasi-periodically (Berryman et al., 2012). The coefficient of variation for the joint dataset is 0.41 and suggests that time-dependant earthquake recurrence models are appropriate for seismic hazard estimation on this, and similar faults worldwide (Cochran et al., 2017).

Secondly, we have vastly improved the robustness of seismic hazard estimates because they are now based on 27 past earthquakes rather than the 3 or 4 that were previously known about (Biasi et al., 2015; Cochran et al., 2017). The mean recurrence interval for major earthquakes on the South Westland section of the Alpine Fault is $291 \text{ years} \pm 23 \text{ years}$ which is similar to the 300 years of elapsed time since the last major surface-rupturing earthquake.

Thirdly, knowledge of this long earthquake record and associated statistics has helped motivate earthquake preparedness in communities living along the fault and increased co-ordination efforts by civil defence and the local authorities who will be part of the response to such an event in the future.

The success of this research led us to ask in this paper, “Where to from here?” Can similar sites and techniques be used to complement other on-fault and off-fault earthquake records and contribute to much improved understanding?

The key features of the Hokuri Creek and John O'Groats River sites that made them excellent repositories of paleoseismological information are:

- A confined catchment with drainage that crosses the fault of interest.
- A vertical component of fault movement that inhibits drainage immediately after each earthquake (preferably the downstream side of the fault is upthrown coseismically).
- A catchment that produces clastic sediment in response to seismic shaking in volumes that don't overwhelm the valley.
- A sedimentary basin that accumulates sediment interseismically and incorporates organic material suitable for radiocarbon dating.

Along other parts of the Alpine Fault long (1-2 ka) earthquake records have been successfully derived from lacustrine sedimentary sequences (Howarth et al., 2012; 2014; 2015). However, there are long stretches of the fault where suitable lakes do not exist and wetland-derived records may be the best approach for improving understanding.

In addition, there are other fast-slipping faults in New Zealand for which robust seismic hazard estimates would be very beneficial for risk estimation and preparedness planning. For example, the Hope Fault (Fig. 1) slips at rates of up to 23 ± 4 mm/yr (Langridge et al., 2013) and only the last 2-3 earthquakes have been identified for the eastern, most populated Conway segment of the fault (Langridge et al., 2003). Further west up to six events have been identified including some from fault-proximal wetlands (Cowan & McGlone, 1991) and shutter basin deposits (Khajavi et al., 2016). The Hope Fault did not rupture in the M_w 7.8 Kaikōura earthquake of 2016 despite faults to the south and north of it rupturing. Will it be the source of our next major earthquake? One way of improving estimates of the probability of future rupture would be to derive longer earthquake records with high-resolution age control from fault-proximal ponds and wetlands.

Fault-proximal earthquake records such as those described here have advantages and disadvantages over more traditional on-fault and off-fault records. They are not as unequivocally tied to the fault of interest as are earthquake records derived from trenches across the fault, but they are more convincingly linked than records from distal lakes that may record events from a number of sources. They



have more continuous sedimentation and higher likelihood of containing dateable material than trenches but sedimentation is unlikely to be as continuous as lake records. We believe that fault-proximal earthquake records have an important role to play in bridging the gap between on-fault and off-fault records to improve our understanding of earthquake recurrence behaviour and seismic hazard in this country.

Acknowledgements: This research was funded by the Royal Society of New Zealand's Marsden Fund and the Natural Hazards Research Platform. The Department of Conservation permitted the fieldwork to take place. We are thankful to everyone who helped with this work including William Ries, Marcus Vandergoes, Bella Ansell, Tim Bartholomew, Daniella Pantosti, Schmuell Marco, Gillian Turner, Mark Hemphill-Haley, Nicola Litchfield, Neville Palmer, Dan Barker, Christine Prior, Lizzie Ingham, Tom Dutton, John West, Bernard Barry and Marianna Terezow.

REFERENCES

- Berryman K.R., Cochran U.A., Clark K.J., Biasi G.P., Langridge R.M., Villamor P., 2012. Major earthquakes occur regularly on an isolated plate boundary fault. *Science* 336, 1690-1693.
- Biasi G.P., Langridge R.M., Berryman K.R., Clark K.J., Cochran U.A., 2015. Maximum-Likelihood Recurrence Parameters and Conditional Probability of a Ground-Rupturing Earthquake on the Southern Alpine Fault, South Island, New Zealand. *Bulletin of the Seismological Society of America* 105(1), 94-106.
- Clark K.J., Cochran U.A., Berryman K.R., Biasi G., Langridge R., Villamor P., Bartholomew T., Litchfield N., Pantosti D., Marco S., and others, 2013. Deriving a long paleoseismic record from a shallow-water Holocene basin next to the Alpine fault, New Zealand. *Geological Society of America Bulletin* 125(5-6), 811-832.
- Cochran U.A., Clark K.J., Howarth J.D., Biasi G.P., Langridge R.M., Villamor P., Berryman K.R., Vandergoes M.J., 2017. A plate boundary earthquake record from a wetland adjacent to the Alpine Fault in New Zealand refines seismic hazard estimates. *Earth and Planetary Science Letters* 464, 175-188.
- Cowan H.A. & McGlone M.S., 1991. Late Holocene displacements and characteristic earthquakes on the Hope River segment of the Hope Fault, New Zealand. *Journal of the Royal Society of New Zealand* 21(4), 373-384.
- De Pascale G.P. & Langridge R.M. 2012. New on-fault evidence for a great earthquake in A.D. 1717, central Alpine Fault, New Zealand. *Geology* 40, 791-794.
- Howarth J.D., Fitzsimons S.J., Norris R.J., Jacobsen G.E., 2012. Lake sediments record cycles of sediment flux driven by large earthquakes on the Alpine fault, New Zealand. *Geology* 40(12), 1091-1094.
- Howarth J.D., Fitzsimons S.J., Norris R.J., Jacobsen G.E., 2014. Lake sediments record high intensity shaking that provides insight into the location and rupture length of large earthquakes on the Alpine Fault, New Zealand. *Earth and Planetary Science Letters* 403, 340-351.
- Howarth J.D., Fitzsimons S.J., Norris R.J., Langridge R., Vandergoes M.J., 2015. A 2000 yr rupture history for the Alpine Fault derived from Lake Ellery, South Island, New Zealand. *Geological Society of America Bulletin* 128(3-4), 627-643.
- Khajavi N., Langridge R.M., Quigley M.C., Smart C., Rezanejad A., Martin-Gonzalez F., 2016. Late Holocene rupture behavior and earthquake chronology on the Hope fault, New Zealand. *Geological Society of America Bulletin* 128(11/12), 1736-1761.
- Langridge R., Campbell J., Hill N., Pere V., Pope J., Pettinger J., Estrada B., Berryman K., 2003. Paleoseismology and slip rate of the Conway Segment of the Hope Fault at Greenburn Stream, South Island, New Zealand. *Annals of Geophysics* 46(5), 1119-1139.
- Langridge R.M., Almond P.C., Duncan R.P., 2013. Timing of late Holocene paleoearthquakes on the Hurunui segment of the Hope fault, implications for plate boundary strain release through South Island, New Zealand. *Geological Society of America Bulletin* 125(5-6), 756-776.
- Robinson T.R., Wilson T.R., Davies T.R.H., Orchiston C., Thompson J.R., 2014. Design and development of realistic exercise scenarios, a case study of the 2013 Civil Defence Exercise Te Ripahapa. *GNS Science Miscellaneous Series*. 113 p.
- Wells A. & Goff J., 2007. Coastal dunes in Westland, New Zealand, provide a record of paleoseismic activity on the Alpine fault. *Geology* 35(8), 731-734.
- Wells A., Yetton M.D., Duncan R.P., Stewart G.H., 1999. Prehistoric dates of the most recent Alpine fault earthquakes, New Zealand. *Geology* 27(11), 995-998.



Contemporary and Paleo Liquefaction-induced Lateral Spreading in Christchurch, New Zealand

De Pascale, Gregory (1), Bachhuber, Jeffery (2), Rathje, Ellen (3), Little, Mike (3), Almond, Peter (4), Ruegg, Christian (5), Finnemore, Mike (5)

- (1) Department of Geology, University of Chile, Plaza Ercilla 803, Santiago, Chile. snowknight@gmail.com.
- (2) Pacific Gas & Electric (PG&E), San Francisco, California.
- (3) University of Texas at Austin, Department of Earthquake Engineering, Austin, Texas.
- (4) Department of Soil Sciences, Lincoln University, Lincoln, New Zealand.
- (5) Southern Geophysical Limited, Christchurch, New Zealand.

Abstract: Earthquake triggered liquefaction and lateral spreading was widespread in Canterbury, New Zealand (NZ) during the 2010-2012 Canterbury Earthquake Sequence (CES) and led to ~\$20 Billion NZD of damage. Although the causes and timing of liquefaction during the CES are well known, the geological controls on lateral spreading are more poorly-understood. We undertook a multidisciplinary investigation funded by the National Science Foundation (NSF) and explored lateral spreading in Christchurch during the CES using image differencing displacement maps, shear wave velocity profiles, boreholes and cone penetration (CPT) soundings, and paleoseismic trenching with radiocarbon dating. Preliminary results suggest that cumulative displacements from the CES are less than those observed in our trench along faults and index beds in the subsurface, and along a key down-dropped soil, when combined with clear paleoliquefaction at the site (e.g. faulted pre-CES sand boils) suggest at least one major pre-CES lateral spreading event here.

Key words: Canterbury Earthquake Sequence, Lateral Spread, Liquefaction, Coseismic geohazards, Earthquake Geology

INTRODUCTION

Earthquake triggered liquefaction and lateral spreading was widespread in Canterbury, New Zealand during the 2010-2012 Canterbury Earthquake Sequence (CES) and led to ~\$20 Billion NZD of damage to infrastructure. The 2010-2012 CES caused widespread liquefaction over approximately half of the urban area of Christchurch (damaging nearly 60,000 homes with about 8000 properties abandoned due to being uneconomical for redevelopment; Cubrinovski and Robinson, 2016) during a number of events from Mw 5.9-7.1 (e.g. Gledhill et al., 2011; Kaiser et al., 2012). Liquefaction is well studied from the CES geological investigations (Quigley et al., 2013; Bastin et al., 2015, 2016; Villamor et al., 2016), liquefaction-induced lateral spreading, or large permanent ground displacements towards waterways, is a major coseismic geohazard although the geological and geomorphic controls of lateral spreading is poorly characterised. We undertook a multidisciplinary investigation funded by the National Science Foundation (NSF) and explored lateral spreading in the red zone of Christchurch (Figure 1), New Zealand during the CES using a number of methods.

We used image differencing displacement maps derived from WorldView-1 (pre-event) and GeoEye-1 (post-event) satellites, shear wave velocity profiles, boreholes and cone penetration (CPT) soundings, and paleoseismic trenching with radiocarbon dating. Permanent lateral ground displacements and subsequent vertical subsidence along rivers and streams progressed hundreds of metres back from the river banks, significantly exceeding expected lateral spread distances calculated from empirically-based predictive relationships. Although the causes and timing of liquefaction during the CES are well known, the geological controls on lateral spreading are more poorly-understood.



Figure 1: Google Earth image showing the “red zone” of residential Christchurch after the CES. Note that most of the area in green was once filled with homes that were damaged due to lateral spreading towards the Avon River. Note star shows approximate location of Figure 2 and the trench location.

At our Avonside Drive site (Figs. 1 and 2), where lateral spreading along the Avon River was common, the highest displacement values in the modelled displacements coincided with a house, yard, and fence with a down to the west linear vertical step in it (Fig. 2). This was coincident with highest displacements in the displacement maps. Here we trenched along the headscarp of the lateral spread. We dug and logged a 22 m long trench in order to better understand lateral spreading here.



Figure 2: Google maps street view image of a house in the Red Zone with a vertical scarp (down to the west) running under it due to lateral spreading (our trench location). House location shown in Fig. 1.

DISCUSSION

Mapping and trenching results shows the lateral spreads terminate at clear geological contacts where liquefaction susceptible sands overlap non- or less-susceptible silts and clays (Fig. 3). Because of repeated lateral spreading (pre-historic and CES) along the same down-dropped blocks (i.e. boundaries) found in our trench, these preliminary results suggest geological control on lateral spreading. Key silt lenses allowed us to track displacements across the trench (Fig. 4) in relation to surface displacements.



Figure 3: Field photograph of the Red Zone trench log floor showing extension along the headscarp of a lateral spread with infilled liquefaction-induced sand dikes. Note that the lateral spread terminated at a contact between sand and clay. Down-dropped side is behind person and uppermost sand dike is the limit of lateral spreading during the CES.

Importantly we found that cumulative displacements from the CES are less than those observed in our trench along faults and index beds (e.g. Fig. 4) in the subsurface, and along a key down-dropped young soil, when combined with clear paleoliquefaction at the site (e.g. faulted pre-CES

sand boils), and radiocarbon dating suggest a major pre-CES lateral spreading here in the last 600 years.

Importantly, although sites that are susceptible for liquefaction can be investigated via geological and geotechnical means prior to development, very limited work has been done to screen for lateral spreading hazards from a geological perspective prior to development. Repeated lateral spreading appears to have a critical geological control, with recurrence of events occurring at the contact between susceptible and non-susceptible deposits.

Thus, our preliminary results suggest that trenching investigations of lateral spreading, like commonly used for investigations to better understand “active” faults (De Pascale et al., 2017), can provide a sound basis for hazard zonation maps (e.g. liquefaction and lateral spreading), and mitigation strategies (e.g. avoidance areas or ground improvement targets) to reduce the future impact of liquefaction induced lateral spreading during earthquakes. Because preliminary data are so encouraging, more focus should be undertaken on this topic globally to better understand and plan for this important coseismic geohazard.

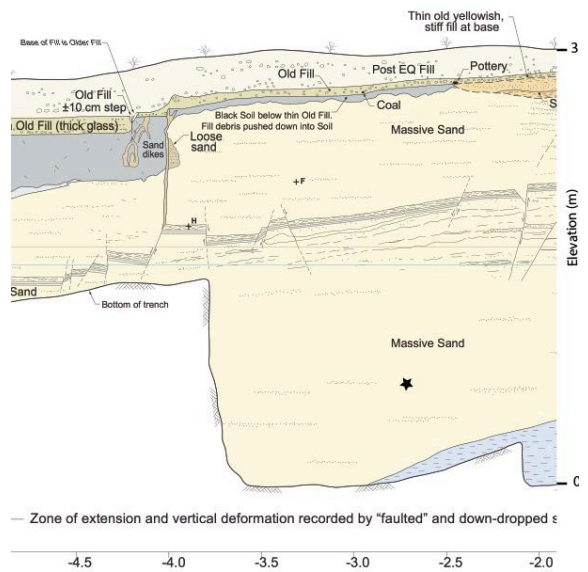


Figure 4: Portion of Red Zone NSF trench log showing down dropped silt unit in massive sand due to lateral spreading. Horizontal Scale at bottom and vertical scale in m. Star shows approximate location of radiocarbon date.

Acknowledgements: Thanks to the NSF award 1462855 (to Rathje) for supporting this work. Thanks to the Fugro professional development fund. De Pascale is supported by a Fondecyt Initiation Grant (11160038). Thanks to the Southern Geophysical Limited (SGL) professional development fund for field support. We appreciate constructive discussions in the field with Sarah Bastin and Monica Giona Bucci.



REFERENCES

- Bastin, S.H., Quigley, M.C., Bassett, K., 2015. Paleoliquefaction in Christchurch, New Zealand. *Geological Society of America Bulletin* 127 (9-10), 1348-1365.
- Bastin, S., Bassett, K., Quigley, M., Maurer, B., Green, R., Bradley, B., & Jacobson, D. 2016. Late Holocene liquefaction at sites of contemporary liquefaction during the 2010-2011 Canterbury Earthquake Sequence, New Zealand. *Bulletin of the Seismological Society of America* 106 (3), 881-903.
- Cubrinovski, M., and Robinson, K., 2016. Lateral spreading: Evidence and interpretation from the 2010–2011 Christchurch earthquakes. *Soil Dynamics and Earthquake Engineering* 91, 187-201.
- De Pascale, G.P., Araya, J., Persico, M., Sandoval, F., Sepulveda, S., Moncada, D., 2017. New school faults and seismic hazard, guilty (i.e. active) until proven innocent (i.e. inactive), *PATA DAYS 2017: 8th International Workshop on Paleoseismology, Active Tectonics and Archeoseismology*, 13th - 16th November 2017, Blenheim, New Zealand.
- Gledhill, K., Ristau, J., Reyners, M., Fry, B., Holden, C., 2011. The Darfield (Canterbury, New Zealand) Mw 7.1 earthquake of September 2010: a preliminary seismological report. *Seismological Research Letters* 82, 378–386.
- Kaiser, A., Holden, C., Beavan, J., Beetham, D., Benites, R., Celentano, A., Collett, D., Cousins, J., Cubrinovski, M., Dellow, G., Denys, P., Fielding, E., Fry, B., Gerstenberger, M., Langridge, R., Massey, C., Motagh, M., Pondard, N., McVerry, G., Ristau, J., Stirling, M., Thomas, J., Umaa, S. R., and Zhao, J., 2012. The Mw 6.2 Christchurch earthquake of February 2011: preliminary report, *New Zealand Journal of Geology and Geophysics* 55, 67–90.
- Quigley, M., Bastin, S., Bradley, B., 2013. Recurrent liquefaction in Christchurch, New Zealand, during the Canterbury earthquake sequence, *Geology* 41 (4), 419–422.
- Villamor, P., Almond, P., Tuttle, M., Giona-Bucci, M., Langridge, R., Clark, K., Ries, W., Bastin, S., Eger, A., Vandergoes, M., 2016. Liquefaction features produced by the 2010–2011 Canterbury earthquake sequence in southwest Christchurch, New Zealand and preliminary assessment of paleoliquefaction features, *Bulletin of the Seismological Society of America* 106 (4).



New school faults and seismic hazard, guilty (i.e. active) until proven innocent (i.e. inactive)?

De Pascale, Gregory (1), Araya, Jose (1), Persico, Mario (1), Sandoval, Francisca (1), Medina, Javiera (1), Sepulveda, Sergio (1), Moncada, Daniel (1)

(1) Department of Geology, University of Chile, Plaza Ercilla 803, Santiago, Chile. snowknight@gmail.com.

Abstract: Of primary importance in Seismic Hazard Assessments (SHA) is finding, mapping, and then investigating faults in order to determine if they are “active”, and thus potential seismic sources. Thus, faults are generally considered innocent (i.e. inactive) until proven guilty (i.e. active). Recent evidence demonstrates that lack of evidence of activity (or mapping) due to lack of investigation along these faults does not mean the faults are inactive. Although there are uncertainties due to mapping at various scales and definition of how long since last activity a fault is considered active, by comparing all identified faults in three regions, we find that 71% of faults in California, 24% of faults in New Zealand, and 5% of faults in Chile are considered “active”. Thus, in the best studied area (California), most of the faults are active. Thus to answer the question in the title, perhaps yes it is better to consider all faults in tectonically active zones guilty (active) until proven inactive (not guilty) and we should invest in mapping to best understand seismic sources.

Key words: Active Faults, Inactive Faults, New Zealand, California, Chile

INTRODUCTION

Of primary importance in Seismic Hazard Assessments (SHA) is finding, mapping, and then investigating faults in order to determine if they are “active” (from Cenozoic to Quaternary to Holocene in timescales), and thus potential seismic sources. Thus, faults are considered innocent (i.e. inactive) until proven guilty (i.e. active).

Perhaps this workflow works ok in slowly deforming regions, or in regions that are well mapped and investigated, but recent evidence from zones globally with rapid tectonic deformation demonstrate that oftentimes lack of evidence of activity (or lack of mapping) due to lack of investigation (or limited field observations) along these faults does not mean the faults are inactive.

Excellent mapping and compilations (i.e. databases) in New Zealand (e.g. NZ active fault database by GNS) and California (the AP Zoning maps from California Geological Survey, CGS), provide first-order indications of activity which is helpful for fault rupture avoidance. However these databases are limited to results from published papers, maps, or reports as input parameters.

Fault ruptures during the Mw 7.8 2016 Kaikoura, NZ Earthquake are telling, where a number of previously unmapped and/or formerly considered “inactive” faults ruptured over a complex fault network with 12 different fault rupturing (Fig. 1; e.g. Hamling et al., 2017). Recent fieldwork in the near the Salton Sea of Southern California demonstrates that previously unmapped major faults (e.g. the Salton Trough Fault) are important parts of the San Andreas fault system and are active (e.g. Sahakian et al., 2016). In NZ, New results from the South Westland Fault shows extensive Quaternary activity west of the Alpine Fault in Westland (e.g. De Pascale et al., 2016), with reverse ruptures and hanging wall anticlinal folding in an area without previously identified active faults (Langridge et al., 2016). In Chile, the best database of active faults (Laveanu,

2000), prior to this study, shows 31 Quaternary active faults, two of which have known slip rates.

Thus these recent examples outline the fact that we are currently learning a great deal about where active faults are (i.e. mapping and investigating), which is a primary input for seismic hazard models.

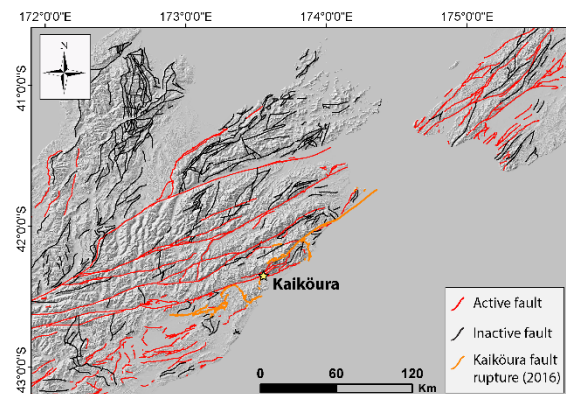


Figure 1: Map showing faults (active and inactive) and ruptures from the 2016 Kaikoura Earthquake. Note that a number of the faults that ruptured were considered “inactive” prior to this rupture (after Hamling et al., 2017). Faults are from the New Zealand Active Fault Database.

METHODS AND RESULTS

In order to better explore the frequency and distribution of faults and active faults around the Pacific Rim, we selected three regions to compare and contrast; NZ, California, and Chile. We undertook a preliminary analysis where we compiled all faults, both active and inactive in each area, based on data available from GNS (NZ), The California Geological Survey (CGS), and the Ministry of Mining and Geology of Chile (SERNAGOMIN). For California, we took the CGS fault database (Jennings and Bryant, 2010; CGS, 2010) which is divided in to color-coded and designated into one of five categories: historic (red), Holocene (orange), late



Quaternary (Qt, green), undivided Quaternary (purple), and pre-Quaternary (black). For simplicity, we divided these classes into to Pre-Qt and Qt or younger faults.

We also took each polyline from the data as a individual fault, directly from the digital Database (GIS).

For NZ we used the New Zealand Active Fault Database (e.g. Langridge et al., 2016; GNS, 2017). Here we manually counted in the database each continuous line as a individual fault, as well as the active as the inactive ones. In Chile we used two databases, the Geological Map of Chile (Sernageomin, 2002) and the Lavenu et al. (2000) paper. For Chile, each fault was manually counted in the database.

There are a number of uncertainties through the comparison of these different datasets from different sources (e.g. mapping scale, identification of fault segments/sections, and timeframe for which a fault is considered active), but even considering these uncertainties, this analysis provides new first-order insight into potential fault activity in two less-well studied regions in comparison to perhaps the gold standard for fault mapping, California. Importantly as outlined by Langridge et al. (2016), the way different mapped scales portray faults across different databases is challenging, from individual lines (10's m) to generalised lines covering large areas. This variability in characterisation certainly has an impact in comparing these datasets, the results of which are tabulated in Table 1.

By comparing all identified faults, we find that 71% of faults in California are potentially “active”, 24% of faults in New Zealand, and 5% of faults in Chile are considered “active”. Graphing these data provides important insight (Fig. 2), in particular when scaling the fault type versus size of the territory (based on km² outlined in Table 1).

	New Zealand	California	Chile
Total Faults	2265	53870	12127
Active faults	442	38645	613
Inactive faults	1823	15225	11514
Activity criteria	< 125,000 yr	Quaternary Activity	Quaternary Activity
% of active faults	24.2	71.7	5.1
Source	GNS Science	California Geological Survey (CGS)	SERNAGEOMIN
Surface Area x 1000 (km ²)	268.0	424.0	756.1

Table 1: Table showing total faults, active faults, inactive faults, activity criteria and percentage of active faults from NZ, California, and Chile. Note that NZ has a much shorter time duration for the characterisation of active faults (<125 ka), and thus if faults were defined in a binary way, Quaternary or not, will thus greatly increase the number of active faults there.

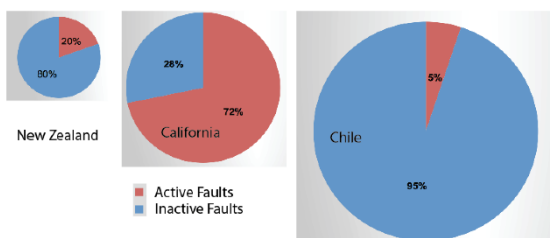


Figure 2: Pie charts showing the percentage of inactive and active faults in New Zealand, California, and Chile scaled relative to their surface area (from Table 1, with NZ being smallest and Chile being largest). Note that the tectonic rates in Chile (~ 8 cm/yr) are almost that of California (~ 4 cm/yr) and NZ (~3-4 cm/yr) combined.

DISCUSSION

More and more faults are being found globally (e.g. faults from the Canterbury Earthquake Sequence from 2010-2012) in addition to faults that were previously deemed “inactive” now being put into the active camp based on new observations. As seen in Table 1 and Figure 2, in relative terms California, although not the largest territory by surface area, has 5 times the number of mapped faults as Chile and 25 times the number of faults of NZ. Variable definitions of “active” (i.e. <125 ka) for NZ, versus Quaternary in California and Chile, make a one to one comparison between these three difficult, because certainly the number of Quaternary active faults in NZ is higher than those active in the past 125 ka. Nevertheless this provides us with important insight. With the majority of mapped faults in California being considered active, this forces the following questions: A) Are the majority of faults in NZ and Chile also active in the Quaternary? And B) and thus are the number of active faults in Chile and NZ currently underestimated?

We reiterate that the tectonic rates in Chile (~ 8 cm/yr) are almost that of California (~ 4 cm/yr) and NZ (~3-4 cm/yr) combined. If California has, a legal mandate to map active faults and a much larger population than NZ and Chile, both with much smaller populations, budgets, and number of earthquake geologists working on these problems, do NZ and Chile actually have many more active faults that should be considered as a rupture hazard and considered as seismic sources than are currently considered? It certainly appears to be the case.

A simple solution to address this uncertainty, not only in NZ and Chile, but in other rapidly deforming regions globally is as follows. In tectonically active regions like NZ, California, and Chile, if there is a fault, perhaps it should be considered active until proven inactive. If the majority of faults in California are active in the Quaternary, then they likely will also be similar in NZ and Chile, which then would mean that the number of potentially active faults in NZ and Chile are currently greatly underestimated.

The Alquist-Priolo Earthquake Fault Zoning Act in California (e.g. Hart and Bryant, 1999), the gold standard for active fault legislation globally, states that if minor faults are found within a mapped buffer zone near a known mapped active fault, then studies need to be undertaken in order to prove inactivity of these minor faults, in this case the lack of Holocene activity. In California, during seismic hazards analysis, potential unknown seismic sources are generally accounted for in the background seismicity - UCERF3 (Field et al., 2014) contains a maximum background magnitude of ~ M_w7.8 - a magnitude which accounts for most faults with unknown activity. This is excellent for a place like California with excellent mapping and decades of active fault mapping and investigations, however for places with lower resolution mapping and limited field investigations (e.g. some areas in NZ and much of Chile), perhaps adopting a guilty (active) until proven innocent first-order assessment would reduce uncertainty. Irrespective, for site-specific critical projects, most faults



are considered active until proven otherwise but for regional seismic hazard assessments, having the input of a fault database and then assuming that all of these faults are active will provide a conservative first order estimate of regional crustal seismic sources.

A similar method could be applied to all faults over large areas (e.g. NZ or Chile) where if there is a mapped fault in an area, then we assume it is a potentially active (Quaternary), with rupture hazards and potentially a source of seismic hazard, until it is proven otherwise. This proposal would of course change greatly the mapping, and would have to be used with a number of caveats, but may also reduce the risk (by perhaps limiting development along, adjacent, and crossing these faults), and also provide insight into complex ruptures connecting known active faults that were not believed possible prior to the Kaikoura event (Hamling et al., 2017).

Importantly, the best input for this new model of if a fault is present, then it is potentially active, would of course be mapping, which will be used to define locations and fault length. In places with limited mapping e.g. Chilean Patagonia, Westland, NZ and remote locations in the Sierra Nevada mountains California, additional mapping is required to define presence (or absence) of faults. If this were to be accepted as a means to better update regional seismic hazard models, then clearly the better the mapping, the better the models, and thus additional resources should be made available for basic mapping of structures (faults and folds).

Ultimately, after this preliminary analysis, we can attempt a first order answer the question in the title. Perhaps it is better to consider all faults in tectonically active zones with limited mapping and fault investigations, guilty (active) until proven inactive (not guilty). If so, we should invest additional resources for improved basic mapping to best understand presence and distribution of Quaternary structures that are perhaps seismic sources in understudied regions.

Acknowledgements: This work is supported by a Chilean Fondecyt Initiation Grant (11160038) to GDP and a NERC and Conicyt (Newton Fund) project NE/N000315/1 "Seismically-induced landslides in Chile: New tools for hazard assessment and disaster prevention". Thanks to Tim Dawson for constructive feedback on this work.

REFERENCES

- California Geological Survey, 2010, Fault Activity Map of California. <http://maps.conservation.ca.gov/cgs/fam/> Last accessed on 14 September 2017.
- De Pascale, G., Chandler-Yates, N., Dela Pena, F., Wilson, P., May, E., Twiss, A., Cheng, C., 2016. Active tectonics west of New Zealand's Alpine Fault: South Westland Fault Zone activity shows Australian Plate instability, *Geophysical Research Letters* 43 (7), 3120-3125.
- Field, E. H., R. J. Arrowsmith, G. P. Biasi, P. Bird, T. E. Dawson, K. R. Felzer, D. D. Jackson, K. M. Johnson, T. H. Jordan, C. Madden, A. J. Michael, K. R. Milner, M. T. Page, T. Parsons, P. M. Powers, B. E. Shaw, W. R. Thatcher, R. J. Weldon II, and Y. Zeng (2014) Uniform California Earthquake Rupture Forecast Version 3 (UCERF3) – The Time-Independent Model, *Bull. Seismol. Soc. Am.*, 104, 1122-1180.
- GNS 2017, Active Faults 250 k, digital database; <http://data.gns.cri.nz/af/> last accessed 17 September 2017.
- Hamling, I, and 28 others, 2017. Complex multifault rupture during the 2016 Mw 7.8 Kaikoura earthquake, New Zealand, *Science* 356 (6334).
- Hart, E., and Bryant, W. 1997. FAULT-RUPTURE HAZARD ZONES IN CALIFORNIA Alquist-Priolo Earthquake Fault Zoning Act with Index to Earthquake Fault Zones Maps, California Department of Conservation, Division of Mines and Geology, 54 p.
- Jennings, C.W., and Bryant, W.A., 2010, Fault activity map of California: California Geological Survey Geologic Data Map No. 6, map scale 1:750,000.
- Langridge, R., Ries, W., Litchfield, N., Villamor, P., Van Dissen, R., Barrell, D., Rattenbury, M., Heron, D., Haubrock, S., Townsend, D., Lee, J., Berryman, K., Nicol, A., Cox, A., Stirling, M. 2016. The New Zealand Active Faults Database, *New Zealand Journal of Geology and Geophysics* 59 (1), 86-96.
- Lavenu, A.; Thiele, R.; Machette, M.; Dart, R.; Bradley, L.; Haller, K. 2000. Maps and Database of Quaternary Faults in (ACTIVE FAULTS) Bolivia and Chile, United States Geological Survey Open-File Report 00-283): p. 50
- Sahakian, V., Kell, A., Harding, A., Driscoll, N., and Kent, G., 2016. Geophysical evidence for a San Andreas subparallel transtensional fault along the northeastern shore of the Salton Sea, *Bulletin of the Seismological Society of America* 106 (5), 1963–1978.
- Sernageomin. 2002, Mapa Geologico de Chile, Escala 1:1000000.



Slip rate estimation from tilting of marine terraces above an offshore listric thrust fault, Kaikoura, New Zealand

Duffy, Brendan (1)

(1) School of Earth Sciences, The University of Melbourne, Parkville VIC 3010, Australia. brendan.duffy@unimelb.edu.au

Abstract: Slip on an offshore fault uplifted and tilted the Kaikoura Peninsula during the 2016 Kaikoura earthquake. Analysis of a 2012, 1m Lidar DEM shows that the uplifted Kaikoura marine terraces have been progressively tilted in the same manner since 120 ka. A Monte-Carlo analysis of tilt-age relationships, based on a model of listric faulting, and using published age data and Papuan and regional sea level curves, implies that slip rates have increased from 2.3 ± 1.3 mm/yr to 4.1 ± 1.2 mm/yr since c.60 ka. Comparison of the elevation of young, uplifted beaches surrounding the peninsula, with a Late Holocene sea level curve, suggests three earthquake events (including 2016) over 3 kyr. The timing of the earthquakes implies lower Late Holocene slip rates, compared with post-60 ka slip rates; comparison of these events with paleoseismic records of the Marlborough Fault System is interpreted to suggest latest Holocene clustering of seismicity.

Key words: Kaikoura Peninsula, marine terrace, slip rates, paleoseismic.

INTRODUCTION

The Kaikoura Peninsula (Fig. 1) lies at the southern terminus of the Hikurangi subduction margin, where plate boundary deformation is progressively transferred to the upper plate faults of the Marlborough Fault System (MFS) (Little and Jones 1998). The peninsula tilted toward the west during the 2016 Kaikoura Earthquake, inferred to be the result of slip on a blind, shallow NW-dipping reverse fault (Clark et al. 2017); similar tilting is recorded by uplifted Pleistocene marine terraces (Campbell et al. 2005, Ota et al. 1996) (Fig. 2). Furthermore, the peninsula is fringed by Late Holocene beaches that have been interpreted to provide an uplift record over the last three millennia (Barrell 2015, McFadgen 1987). However, the slip rate on the underlying fault, and its variability, is not well known.

The Kaikoura Earthquake was exceedingly complex, involving a diverse range of fault types, with diverse slip rates, and across several tectonic domains (Clark et al. 2017, Hamling et al. 2017, Stirling et al. 2017). Knuepfer (1992) suggested that the faults of the MFS display episodic variations in activity over 5 ky timescales, and faults such as the Wairau, Awatere, Clarence, Hope, Kekekeno, and Porters Pass Faults had exhibited reduced slip rates over the last 3-5 kyr. To understand how these faults interact over different temporal and spatial scales, it is necessary to understand variability in the slip rates and paleoseismicity of component faults, including the fault that uplifts the Kaikoura Peninsula, and to examine patterns in the regional paleoseismicity of the MFS. Therefore, this study asks (i) what are the Late Pleistocene slip rates on the Kaikoura Peninsula Fault; (ii) how do these slip rates compare with rates calculated from uplifted Holocene beaches using the same geometry; and (iii) how do slip rate variations at the Kaikoura Peninsula relate to slip rate variability across the MFS.

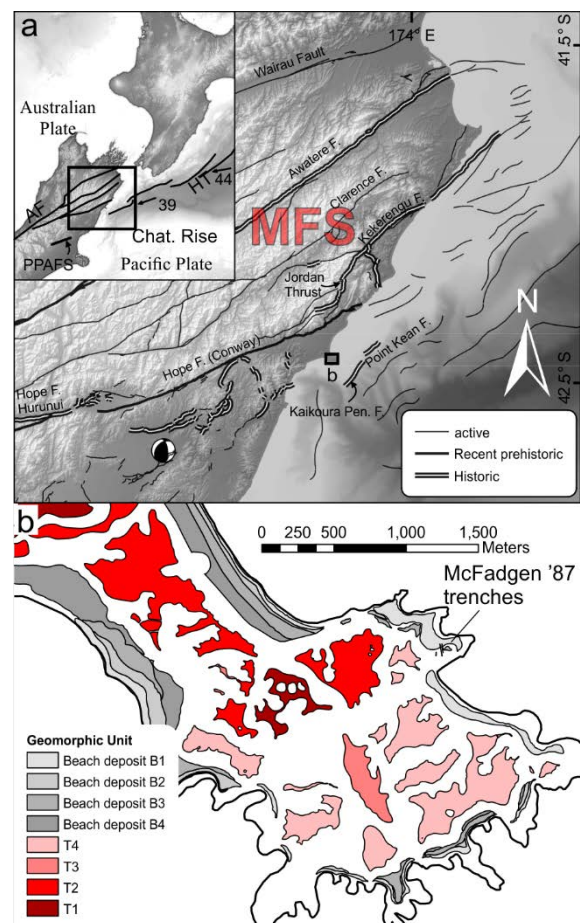


Figure 1: a) location of Kaikoura Peninsula relative to the Marlborough Fault System; Faults from NZ active faults database, and Stirling et al. (2017); b) Sketch map of the Kaikoura Peninsula, showing the distribution of Late Pleistocene terraces and Holocene beaches.

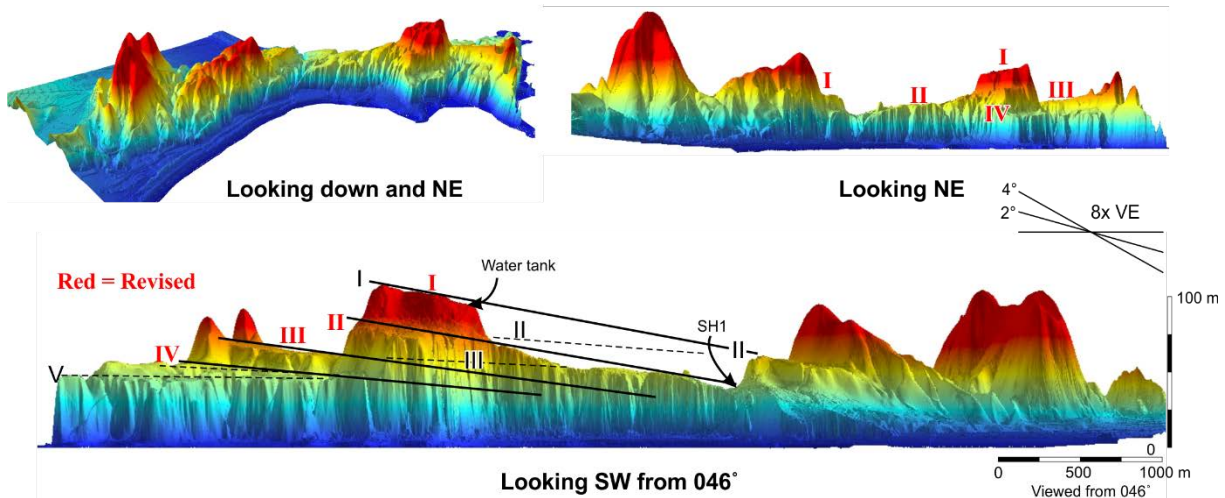


Figure 2: 1m Lidar DEM showing correlation of terraces with new correlations labelled in red, and old correlations labelled in black. DEM provided by Environment Canterbury.

METHODS

These questions are addressed here using a 2012 1 m Lidar DEM, based on the interpretation that the progressive tilt at Kaikoura Peninsula records primarily the effects of slip on an underlying listric fault of a constant radius, similar to those that mark the shelf edge further north (Barnes and Audru 1999). The tilt and Lidar elevation-at-a-point of an individual strandline depends on the thickness of cover sediments (taken from Ota et al. 1996), the amount of slip, and the relative sea level (RSL) at which the terrace formed (Fig. 3). This analysis therefore searches for terrace-highstand correlations that produce (i) close agreement of fault radius, and (ii) a close match of strandline elevation-at-a-point using a common fault radius for all terraces. The age of the highest terrace was constrained to 110 ± 20 ka based on the only existing amino-acid-racemization age (Ota et al. 1996).

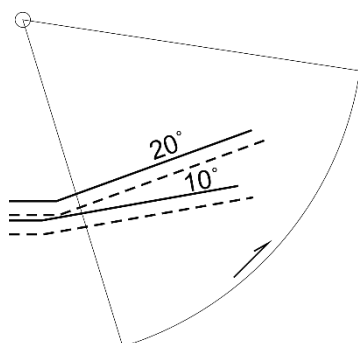


Figure 3: The elevation-at-a-point of a terrace rotating above a listric fault depends on the RSL at which it formed (compare solid and dashed lines) and the amount of slip on the underlying fault.

The slip rates were determined by relating apparent-strandline tilt and elevation, minus cover thickness, to the Papuan sea level curve (Lambeck and Chappell 2001), and to a regionally-derived sea level curve based on predominantly Southeast Australian data (Blakemore et al.

2014, Hails et al. 1984, Murray-Wallace 2002), with some constraints from Banks Peninsula, south of Kaikoura (Shulmeister et al. 1999). The regional curve provided better results and the Papuan correlations are discussed little here, although the full rationale is presently in review elsewhere. Each of the inputs into this analysis has an associated error; these errors are accounted for in a 10,000 iteration Monte Carlo simulation. All results are presented at 95% confidence interval.

RESULTS

The correlations of terraces along the peninsula are shown in Fig. 2. Four terraces are defined; a previously defined fifth terrace follows the strike of bedrock units that form resistant topography on the modern shore platform, and is not considered to be a terrace. The slip rates for all scenarios is shown in Fig. 4. The elevation and rotation of the four terraces is consistent with a 120-60 ka slip rate of 2.31 ± 1.3 mm/yr, based on the preferred regional sea-level history, followed by an increase to 4.1 ± 1.3 mm/yr since 60ka.

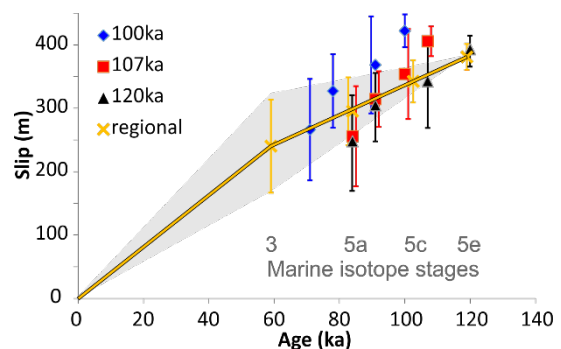


Figure 4: Summary of slip rates estimated from different sea level correlation scenarios. Grey zone highlights the slip rate history implied by the regional sea level curve. Error bars show 95% confidence interval.

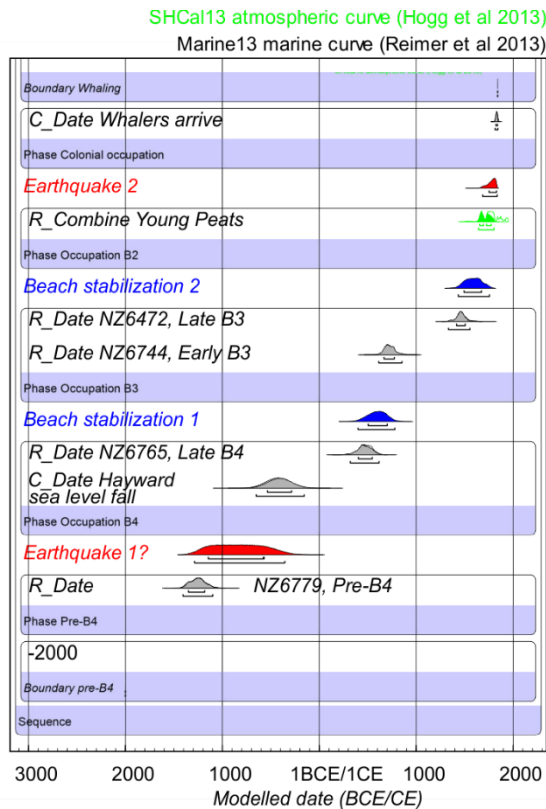


Figure 5: Oxcal model showing modelled McFadgen (1987) radiocarbon ages, with upper limits constrained by the establishment of whaling at Kaikoura in c.1840 CE. Beach stabilization 1 and 2 (blue) based on comparison of RSL change with Hayward et al.'s (2016) sea-level curve. Earthquake events (red) do not relate to documented sea level falls.

McFadgen (1987) dated several beaches and obtained uplift rates of >2 mm/yr over the latest Holocene. These rates (and Barrell's 2015 review thereof) assumed a constant Late Holocene sea level, but Hayward et al. (2016) showed that sea level has fallen over several stages from a mid-Holocene highstand, and risen markedly over the industrial period. Re-evaluation of McFadgen's (1987) radiocarbon ages within an OxCal model (Fig. 5) and comparison with Hayward et al.'s sea level curve indicate that only the first and last beach forming events (1287 to 356 BCE and 1687 to 1837 CE) are consistent with earthquake uplift, while the other two beaches are consistent in terms of magnitude and timing with Late Holocene sea-level fall. The uplift rate implied by the interval between earthquakes 1 and 2 (Fig. 5) is 0.45 ± 0.16 mm/yr, less than half the Late Pleistocene uplift rate of the peninsula. If the 0.8-1.0 m of uplift during the Kaikoura Earthquake (Clark et al. 2017) is also included, the uplift rate reaches 0.72 ± 0.17 mm/yr, which is still lower than the long-term rates and not consistent with the increased slip rate suggested by Pleistocene terrace uplift.

DISCUSSION

The paleoseismic interpretation in Fig. 6 implies two earthquakes within 500 years on the Kaikoura Peninsula Fault following a relatively quiescent period of ~ 2 kyr.

Comparing this data with records from the rest of the MFS shows that several faults, including the Kekerengu and Hope faults, display similar patterns (Fig. 6), consistent with Knuepfer's (1992) interpretation of a period of Late Holocene quiescence across much of the system. Episodicity or clustering of earthquakes is reported from both stable continental regions (Clark et al. 2012) and other plate boundaries (Dolan et al. 2007). Together with similar effects found in numerical models (Ben-Zion et al. 1999), these patterns suggest that fault systems such as the MFS and associated faults may periodically host clusters of seismic events, including the largest events on the system, and otherwise display low moment release during small to moderate earthquakes.

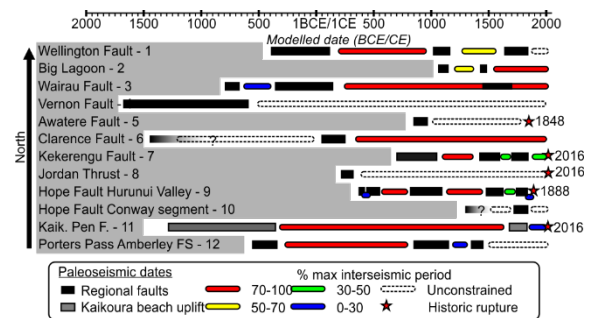


Figure 6: Compilation of regional paleoseismic ages for MFS faults, ordered from north to South. Greyed out area shows no-data. Interseismic periods are colour coded to highlight short (blue/green) versus longer (yellow/red) interseismic periods. Paleoseismic data from: 1 - Langridge et al. (2011); 2 - Clark et al. (2015); 3 - Zachariassen et al. (2006); 4 - Bartholomew et al. (2014); 5 - Mason et al. (2006); 6 - Van Dissen and Nicol (2009); 7 - Little et al. (2016); 8 - Van Dissen et al. (2006); 9 - Khajavi et al. (2016); 10 - Langridge et al. (2003); 11 - This study; 12 - Howard et al. (2005).

CONCLUSION

The Kaikoura Peninsula Fault has been uplifting and rotating the peninsula by slipping at rates that have increased from 2.3 ± 1.5 mm/yr to 4.1 ± 1.3 mm/yr since 60 ka. The age and elevation of beach ridges around the peninsula suggest Late Holocene slip rates are around half of the long term rate. Most of the Late Holocene slip seems to have occurred during two events since ~ 1800 CE. This period coincides with short recurrence interval ruptures on the Hope and Kekerengu faults in the MFS.

Acknowledgements: I thank Environment Canterbury for provision of the Lidar and Dr Nicola Litchfield for her review. Much of this work was originally started during a fixed term position at the University of Canterbury in 2014.

REFERENCES

- Barnes, P. M., and J.-C. Audru (1999). Recognition of active strike-slip faulting from high-resolution marine seismic reflection profiles: Eastern Marlborough fault system, New Zealand, Geological Society of America Bulletin 111 538-559.
- Barrell, D. (2015). General distribution and characteristics of active faults and folds in the Kaikoura District, North Canterbury, GNS Science Consultancy Report 2014/210.



INQUA Focus Group Earthquake Geology and Seismic Hazards



paleoseismicity.org

- Bartholomew, T. D., T. A. Little, K. J. Clark, R. Van Dissen, and P. M. Barnes (2014). Kinematics and paleoseismology of the Vernon Fault, Marlborough Fault System, New Zealand: Implications for contractional fault bend deformation, earthquake triggering, and the record of Hikurangi subduction earthquakes, *Tectonics* 33 1201-1218.
- Ben-Zion, Y., K. Dahmen, V. Lyakhovskiy, D. Ertas, and A. Agnon (1999). Self-driven mode switching of earthquake activity on a fault system, *Earth and Planetary Science Letters* 172 11-21.
- Blakemore, A. G., C. V. Murray-Wallace, and T. J. Lachlan (2014). First recorded evidence of subaqueously-deposited late Pleistocene interstadial (MIS 5c) coastal strata above present sea level in Australia, *Marine Geology* 355 377-383.
- Campbell, J. K., P. Tonkin, and J. D. Bradshaw (2005). Structure and Tectonics of the Kaikoura Peninsula, in *Field Trip Guides*, Geological Society of New Zealand 50 Annual Conference, Kaikoura, New Zealand. J. R. Pettinga and A. M. Wandres (Editors), Geological Society of New Zealand Misc. Publ. 119B, 111-127.
- Clark, D., A. McPherson, and R. Van Dissen (2012). Long-term behaviour of Australian stable continental region (SCR) faults, *Tectonophysics* 566 1-30.
- Clark, K. J., B. W. Hayward, U. A. Cochran, L. M. Wallace, W. L. Power, and A. T. Sabaa (2015). Evidence for Past Subduction Earthquakes at a Plate Boundary with Widespread Upper Plate Faulting: Southern Hikurangi Margin, New Zealand, *Bulletin of the Seismological Society of America*.
- Clark, K. J., E. K. Nissen, J. D. Howarth, I. J. Hamling, J. J. Mountjoy, W. F. Ries, K. Jones, S. Goldstien, U. A. Cochran, P. Villamor, S. Hreinsdóttir, N. J. Litchfield, C. Mueller, K. R. Berryman, and D. T. Strong (2017). Highly variable coastal deformation in the 2016 MW7.8 Kaikōura earthquake reflects rupture complexity along a transpressional plate boundary, *Earth and Planetary Science Letters*.
- Dolan, J. F., D. D. Bowman, and C. G. Sammis (2007). Long-range and long-term fault interactions in Southern California, *Geology* 35 855-858.
- Hails, J. R., A. P. Belperio, V. A. Gostin, and G. E. G. Sargent (1984). The submarine Quaternary stratigraphy of northern Spencer Gulf, South Australia, *Marine Geology* 61 345-372.
- Hamling, I. J., S. Hreinsdóttir, K. Clark, J. Elliott, C. Liang, E. Fielding, N. Litchfield, P. Villamor, L. Wallace, and T. J. Wright (2017). Complex multifault rupture during the 2016 Mw 7.8 Kaikōura earthquake, New Zealand, *Science*.
- Hayward, B. W., H. R. Grenfell, A. T. Sabaa, U. A. Cochran, K. J. Clark, L. Wallace, and A. S. Palmer (2016). Salt-marsh foraminiferal record of 10 large Holocene (last 7500 yr) earthquakes on a subducting plate margin, Hawkes Bay, New Zealand, *Geological Society of America Bulletin* 128 896-915.
- Howard, M., A. Nicol, J. Campbell, and J. Pettinga (2005). Holocene paleoearthquakes on the strike-slip Porters Pass Fault, Canterbury, New Zealand, *New Zealand Journal of Geology & Geophysics* 48 59-74
- Khajavi, N., R. M. Langridge, M. C. Quigley, C. Smart, A. Rezanajad, and F. Martín-González (2016). Late Holocene rupture behavior and earthquake chronology on the Hope fault, New Zealand, *GSA Bulletin* 128 1736-1761.
- Knuepfer, P. L. K. (1992). Temporal variations in latest Quaternary slip across the Australian- Pacific plate boundary, northeastern South Island, New Zealand, *Tectonics* 11 449-464.
- Lambeck, K., and J. Chappell (2001). Sea Level Change through the Last Glacial Cycle, *Science* 292 679-686.
- Langridge, R. M., J. Campbell, N. Hill, V. Pere, J. Pope, J. Pettinga, B. Estrada, and K. Berryman (2003). Paleoseismology and slip rate of the Conway Segment of the Hope Fault at Greenburn Stream, South Island, New Zealand, 2003 46.
- Langridge, R. M., R. Van Dissen, D. Rhoades, P. Villamor, T. Little, N. Litchfield, K. Clark, and D. Clark (2011). Five Thousand Years of Surface Ruptures on the Wellington Fault, New Zealand: Implications for Recurrence and Fault Segmentation, *Bulletin of the Seismological Society of America* 101 2088-2107.
- Little, T. A., and A. Jones (1998). Seven million years of strike-slip and related off-fault deformation, northeastern Marlborough fault system, South Island, New Zealand, *Tectonics* 17 285-302.
- Little, T. A., R. J. Van Dissen, K. P. Norton, J. R. Kearse, J. Whattam, and A. M. Benson (2016). Late Holocene Surface Rupturing History of the Kekerengu Fault, Marlborough Fault System, New Zealand., in *Geosciences 2016 C. Riesselman and A. Roben (Editors)*, Geoscience Society of New Zealand Miscellaneous Publication 145A, Wanaka, 46.
- Mason, D. P. M., T. A. Little, and R. J. Van Dissen (2006). Rates of active faulting during late Quaternary fluvial terrace formation at Saxton River, Awatere fault, New Zealand, *Geological Society of America Bulletin* 118 1431-1446.
- McFadgen, B. G. (1987). Beach ridges, breakers and bones: late Holocene geology and archaeology of the Fyffe site, S49/46, Kaikoura Peninsula, New Zealand, *Journal of the Royal Society of New Zealand* 17 381-394.
- Murray-Wallace, C. V. (2002). Pleistocene coastal stratigraphy, sea-level highstands and neotectonism of the southern Australian passive continental margin—a review, *Journal of Quaternary Science* 17 469-489.
- Ota, Y., B. Pillans, K. Berryman, A. Beu, T. Fujimori, T. Miyauchi, G. Berger, A. G. Beu, and F. M. Climo (1996). Pleistocene coastal terraces of Kaikoura Peninsula and the Marlborough coast, South Island, New Zealand, *New Zealand Journal of Geology and Geophysics* 39 51-73.
- Shulmeister, J., J. M. Soons, G. W. Berger, M. Harper, S. Holt, N. Moar, and J. A. Carter (1999). Environmental and sea-level changes on Banks Peninsula (Canterbury, New Zealand) through three glaciation–interglaciation cycles, *Palaeogeography, Palaeoclimatology, Palaeoecology* 152 101-127.
- Stirling, M. W., N. Litchfield, P. Villamor, R. Van Dissen, A. Nicol, J. Pettinga, P. Barnes, R. Langridge, T. Little, D. Barrell, J. Mountjoy, W. F. Ries, J. Rowland, C. Fenton, I. Hamling, C. Asher, A. Barrier, A. Benson, A. Bischoff, J. Borella, R. Carne, U. A. Cochran, M. Cockroft, S. C. Cox, G. Duke, F. Fenton, C. Gasston, C. Grimshaw, D. Hale, B. Hall, K. X. Hao, A. Hatem, M. Hemphill-Haley, D. W. Heron, J. Howarth, Z. Juniper, T. Kane, J. Kearse, Khajavi, G. Lamarche, S. Lawson, B. Lukovic, C. Madugo, J. Manousakis, S. McColl, D. Noble, K. Pedley, K. Sauer, T. Stahl, D. T. Strong, D. B. Townsend, V. Toy, M. Villeneuve, A. Wandres, J. Williams, S. Woelz, and R. Zinke (2017). The Mw7.8 2016 Kaikōura earthquake: Surface fault rupture and seismic hazard context, *Bulletin of the New Zealand Society for Earthquake Engineering* 50 73-84.
- van Dissen, R., and A. Nicol (2009). Mid-late Holocene paleoseismicity of the eastern Clarence Fault, Marlborough, New Zealand, *New Zealand Journal of Geology and Geophysics* 52 195-208.
- Van Dissen, R. J., D. G. Sutherland, R. J. Bowers, and J. L. Redwine (2006). Forest burial by large rock avalanche in Miller Stream, Seaward Kaikoura Range, New Zealand, c. 1700 years ago, *New Zealand Journal of Geology and Geophysics* 49 151-157.
- Zachariassen, J., K. Berryman, R. Langridge, C. Prentice, M. Rymmer, M. Stirling, and P. Villamor (2006). Timing of late Holocene surface rupture of the Wairau Fault, Marlborough, New Zealand, *New Zealand Journal of Geology and Geophysics* 49 159-174.



Combined high-resolution topographic analysis and paleoshoreline dating reveal spatio-temporal variability in slip rates on low-strain-rate normal faults

Egger, Anne E., Marion, Brian, Hall, Jennifer

Department of Geological Sciences, Central Washington University, 400 E. University Way, Ellensburg, WA, 98926-7418, eggera@cwu.edu

Abstract: In the northwestern Basin and Range of the western US, normal fault scarps line many of the range-fronts and pluvial lakes filled many of the valleys during the Pleistocene. Lake paleoshorelines provide a paleohorizontal datum from which to assess crustal deformation. Often these shorelines are capped by carbonate tufa. Detailed mapping of fault scarps and paleoshorelines along with radiocarbon geochronology provides insight into the distribution and timing of slip along faults, such as the Surprise Valley fault (SVF) in California and the Winter Rim fault system (WRF) in Oregon. Our analyses reveal that slip rates vary by as much as 4x along the length of the SVF over the last 25 ky, and that segments of the WRF that are optimally-oriented for activation under the prevailing stress regime have accumulated twice as much offset as non-optimally-oriented segments. Our results highlight significant spatio-temporal variability in slip rates.

Key words: normal fault, Basin and Range, lidar, surface offset, slip rate

INTRODUCTION

The northwestern Basin and Range (NWBR) of south-central Oregon, northeastern California, and northwestern Nevada (Figure 1) is a low-strain rate extensional province (Kreemer et al., 2012). The region is tectonically active (Berg and Baker, 1963; Bryant, 1990; Uhrhammer, 1991); though no large earthquakes have occurred historically, Holocene and latest Pleistocene normal fault scarps line many of the range-fronts (Figure 1). Scarps are particularly prominent along the Surprise Valley fault and the Winter Rim fault system, with smaller-offset, less continuous scarps along the Abert Rim, in the Warner Valley, and elsewhere (Figure 2). As a result of the semi-arid climate of the region, the scarps are well-preserved

and easily mapped and measured using high-resolution topographic data.

These normal fault-bound basins, while largely dry today, once hosted lakes that reached depths up to a few hundred meters. Throughout the Basin and Range, there is abundant evidence that valleys were filled with pluvial lakes approximately contemporaneous with glacial ages (e.g. Reheis et al., 2014, and references therein) (Figure 1). While Lake Bonneville and Lake Lahontan are the largest and best known of these lakes, most of the valleys in the NWBR also hosted lakes, including Lake Surprise (in Surprise Valley) and Lake Chewaucan in the Summer and Abert Lake basins (Figure 2).

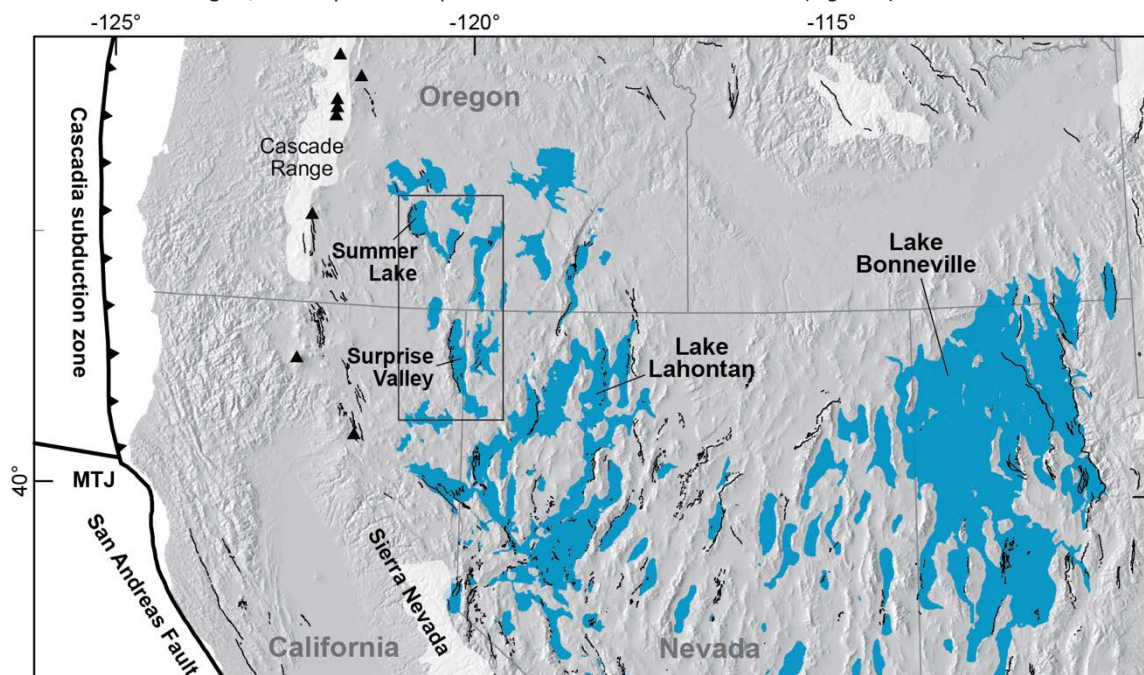


Figure 1: Map showing faults that have ruptured since 15 ka (USGS, 2006); extent of ice sheets during the Last Glacial Maximum in white, and the maximum extent of pluvial lakes in blue. Triangles indicate active volcanoes in the Cascades arc. Inset box indicates area shown in Figure 2.

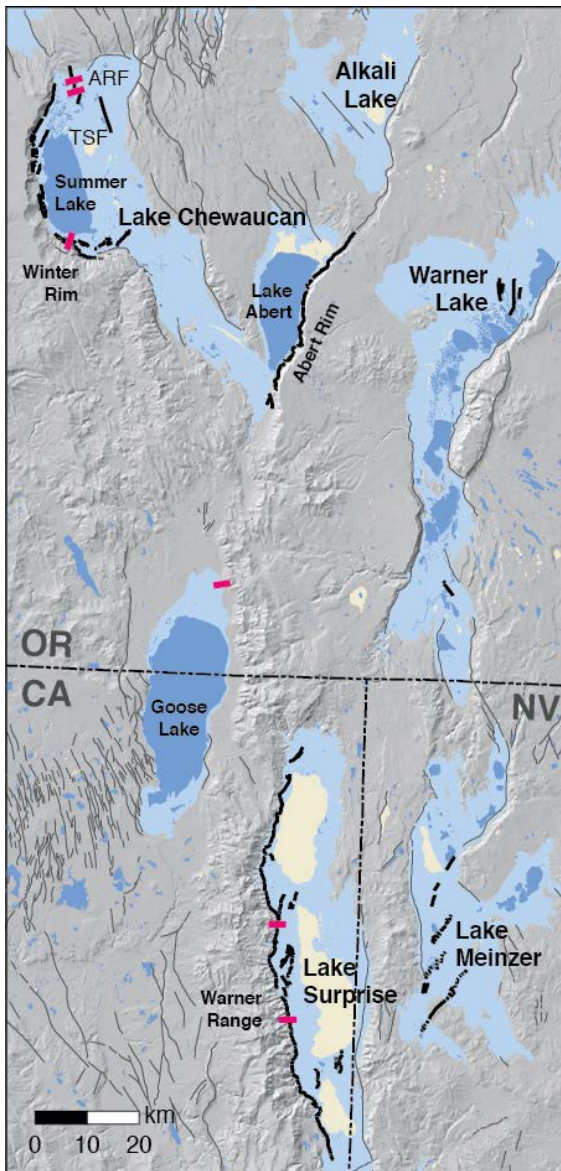


Figure 2: Map of a portion of the northwestern Basin and Range showing faults active in the last 15 ks (USGS, 2006). Pink lines indicate the locations of paleoseismic trenches mentioned in the text. Approximate extents of pluvial lakes shown in light blue, modern lakes in dark blue, and playas in tan. ARF—Ana River fault, TSF—Thousand Springs fault

Lake levels fluctuated in response to climatic changes, leaving behind a record of their fluctuations in sets of paleoshorelines that rim the basins. Paleoshoreline features include wave-formed terraces as described by Adams and Wesnousky (1998), which are primarily erosional but can also include a thin lag deposit of gravel. A continuous shoreline feature is a paleohorizontal datum recording when the pluvial lake was at that particular elevation. Significant deviation from that datum implies deformation that has occurred since shoreline formation.

Wave-formed terraces are commonly capped by carbonate tufas likely precipitated in the photic zone and record lake levels within a few meters of the lake surface (Felton et al., 2006). Thus, radiocarbon dates on these tufas can be

considered to record lake stillstands at those elevations. Precise elevations of the geomorphic features are determined and mapped using high-resolution topographic data. By obtaining ages for shorelines (ideally sets of shorelines) and comparing their elevations across major faults, we can calculate the amount and style of deformation since shoreline formation.

We analyzed high-resolution lidar data along two major fault systems: the Surprise Valley fault in California and the Winter Rim fault system in Oregon, which provided a base for detailed mapping and topographic analysis of fault scarps, paleoshorelines, and Quaternary deposits. We also collected tufa samples for radiocarbon dating from target geomorphological features. Combining the detailed measurements and spatial distribution of surface offset with the deformation of paleoshorelines provides insight into how slip rates and deformation vary over time and space both within a basin and throughout the northwestern Basin and Range.

DISCUSSION

A previous trenching study along the Surprise Valley fault (Figure 2) reveals five surface-rupturing earthquakes in the last 20 ka, with the most recent earthquake occurring 1.2 ± 0.1 ka (Personius et al., 2009). In the Summer Lake basin, a trench along the E-W-oriented Slide Mountain segment of the Winter Rim fault system (Figure 2) may indicate three surface-rupturing events prior to 2130 ± 90 yr and most likely while the most recent pluvial Lake Chewaucan was present (Pezzopane, 1993). At the north end of the basin on the Ana River fault, several trenches (Figure 2) reveal three earthquakes since ca. 15 ka, but only four in the 70 ky prior (Langridge et al., 2001; Weldon et al., 2009). All of these investigations share similar conclusions: that slip rates and earthquake recurrence intervals along these faults have varied over the late Pleistocene and Holocene.

In this study, we compared and calculated slip rates from two independent datasets in both Surprise Valley and the Summer Lake basin: (1) surface offsets across fault scarps measured through topographic profiles, and (2) elevation differences of sets of dated paleoshorelines on opposite sides of major faults.

In Surprise Valley, detailed mapping of fault scarps built on the previous work of Hedel (1980, 1984) and Bryant (1990). The extremely high (0.5 m²) resolution of the lidar data allowed for identification of subtle scarps within the valley and more precise and detailed mapping than existed previously, not only of fault scarps, but of the Pleistocene and Quaternary units they cut. Mapping indicates that scarps occur along ~64 km of the SVF (Figure 3) in Quaternary units, including older and younger fan deposits, landslides, alluvium, colluvium, and Pleistocene fan deltas. We extracted 78 topographic profiles across fault scarps; surface offset across the scarp ranges from 0.8–22.2 m (Figure 3). The smallest offsets (0.6–4.9 m) are preserved in active alluvial fans and are present along a length of ~42 km of the SVF (Figure 3); these scarps are



interpreted to record only the most recent event, which occurred 1.2 ± 0.1 ka. The measured offsets match well with estimated displacements of Personius et al. (2009) obtained through trenching.

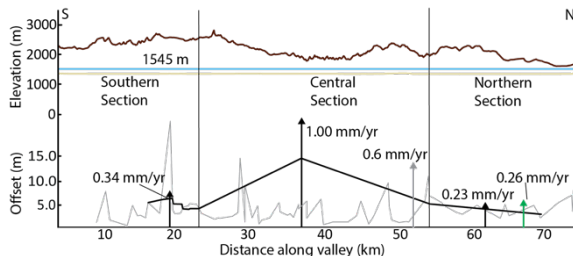


Figure 3: Slip rate distribution for SVF. N-S topographic profile along the Warner Range (brown), and Surprise Valley playa (tan). Elevation of Lake Surprise highstand at 1545 m (blue). Total offset of topographic profiles of SVF scarps (grey) and measured offset using paleoshoreline sets across the valley (black). Gray arrow: previously determined slip rate along the entire fault (Personius et al., 2009). Black arrows: slip rates calculated from paleoshoreline offsets. Green arrow: slip rate calculated from potential field modeling (Marion, 2016).

Radiocarbon ages obtained on samples of tufa collected on paleoshoreline features record the transgression of Lake Surprise to a post-LGM highstand of ~ 185 m depth at 15.98 ± 0.19 ka. Samples also record a less complete regression sequence, with the youngest dated sample of 10 ka and a lake depth of ~ 80 m; the lake had receded to the modern playa by 6-8 ka (O'Connell and Inoway, 1994)

Four out of five of the earthquakes whose timing were constrained by Personius et al. (2009) occurred after the youngest dated shoreline (<10 ka). Detailed mapping of shoreline elevations show that the heights between shorelines are consistent across the basin, even while the absolute elevation of sets of shorelines differs by as much as 13 m (Figure 3). We interpret that total elevation difference as the cumulative slip along the Surprise Valley fault since the most recent highstand.

In combination, these data allow us to show that slip rates vary by as much as 4x along the length of the 90 km-long Surprise Valley fault system over the last 25 ky, with the highest slip rates and greatest offset in the center of the fault and tapering asymmetrically both to the north and to the south (Figure 3).

In the Summer Lake basin, the Winter Rim fault system consists of two main segments (Figure 2). one trends NNW and is perpendicular to the nearly E-W extension direction as determined by structural analysis (Pezzopane and Weldon, 1993; Treerotchananon, 2009) and earthquake focal mechanisms (Crider, 2001) and thus is optimally oriented to slip in the modern tectonic setting. The other trends WSW and is nearly parallel to the extension direction, and thus we might anticipate highly oblique slip along this segment. Given the difference in orientation of the two segments, we examined each somewhat independently.

We extracted 30 topographic profiles along the ~ 30 -km length of the more-optimally-oriented Winter Ridge segment and measured scarp heights range from 1.0–56.5

m with an average height of 12.2 m. Excluding the highest value of 56.5 m, which is significantly higher than the next highest value of 35.7 m, the average scarp height is 10.7 m (Figure 4). On the oblique Slide Mountain segment, we extracted 23 profiles across multiple strands along a length of ~ 16 km, and measured scarp heights range from 1.2–27.4 m with an average height of 6.0 m. Excluding the 27.4 m measurement, the next highest value is 9.7 m and the average scarp height is 5.0 m (Figure 4).

Our results indicate that the optimally-oriented segments of the Winter Rim fault system have accumulated twice as much offset as non-optimally-oriented segments (Figure 4). The current estimate of the slip rate for the Winter Rim fault system (0.43 mm/yr) is based primarily on a paleoseismological study of the Slide Mountain segment — the segment nearly parallel to the extension direction (Figure 2) (Pezzopane, 1993). Based on our surface offset measurements, we conclude that this slip rate could be an underestimate by a factor of two for the Winter Rim segment of the fault.

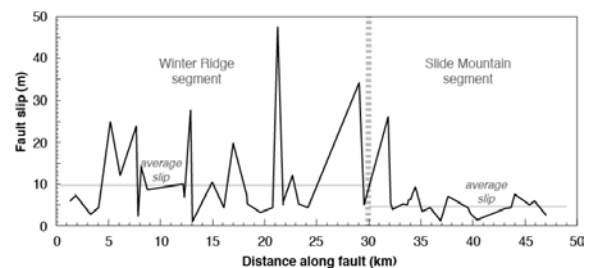


Figure 4: Graph showing fault slip measured from surface offsets along fault scarps along the length of the Winter Rim fault system. The wide dashed line represents the change in orientation that marks the transition from the Winter Ridge segment (with a strike of approximately 350°) to the Slide Mountain segment (with a strike of approximately 270°).

Lidar data and mapping also revealed the full extent of the Thousand Springs fault (Figure 2), a west-dipping normal fault antithetic to the Winter Rim segment. Nine topographic profiles across the best-constrained 8 km of the Thousand Springs fault yield a range of scarp heights from 0.9 m to 5.6 m, with an average of 1.9 m (Figure 5). Two additional profiles near the southern end of the valley have scarp heights of 5.9 m and 2.6 m; if these are part of a continuous Thousand Springs fault, the entire fault is as long as the Winter Rim segment (~ 30 km) and equally well-oriented to slip in the current stress regime. The hazard associated with slip on the Thousand Springs fault has not been assessed.

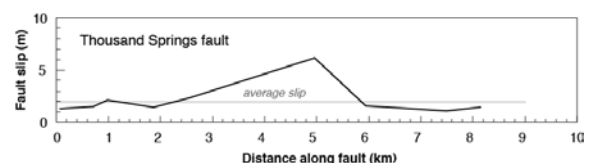


Figure 5: Graph showing fault slip measured from surface offsets along the Thousand Springs fault.

The paleoshorelines in Summer Lake are more challenging to interpret than those in Surprise Valley. The shorelines are less well-preserved, and our radiocarbon ages do not



record a clean transgression and regression sequence as in Surprise Valley. Instead, a cluster of ages 13–14 ka mark the most recent highstand with a lake depth of about 90 m, with an older and higher highstand (lake depth ~140 m) between 26 and 30 ka. In addition, we were unable to match sets of shorelines across the basin, in large part due to the presence of massive landslides along the western margin (Badger and Watters, 2004).

In both basins, we compared our lake-level hydrographs with published paleoseismic records. In both cases, it appears that earthquake frequency increased during the period of rapid lake-level regression (ca. 13–8 ka)—in other words, earthquakes occurred more frequently while the local stress regime was in rapid flux. This correlation is seen throughout the northwestern Basin and Range (Egger et al., in review). Recent modeling suggests that variations in slip rates of faults beneath and near Lake Bonneville and Lake Lahontan (*Figure 1*) were caused by changes in differential stress due to transgression and regression of the pluvial lakes (Hempel et al., 2010; Karow and Hempel, 2010). Our results suggest that similar processes may be operating even in lake basins much smaller than Bonneville.

Acknowledgements: Funding for lidar data collection in Surprise Valley was from NASA ROSES Grant 10-UAS10-0021. Funding to collect samples in Summer Lake was provided by the National Earthquake Hazards Reduction Program (NEHRP) of the USGS, grant G14AS00036. Brian Marion was supported in part by a fellowship from the School Graduate Studies and Research at Central Washington University. We'd like to thank Daniel Ibarra for his help in collecting and analyzing carbonate tufa samples.

REFERENCES

- Adams, K. D., and Wesnousky, S. G., 1998, Shoreline processes and the age of the Lake Lahontan highstand in the Jessup embayment, Nevada: *GSA Bulletin*, v.110, no.10, p.1318-1332. doi: 10.1130/0016-7606(1998)110<1318:SPATAO>2.3.CO;2
- Badger, T. C., and Watters, R. J., 2004, Gigantic seismogenic landslides of Summer Lake basin, south-central Oregon: *Geological Society of America Bulletin*, v. 116, no. 5-6, p. 687-697. doi: 10.1130/b25333.1
- Berg, J. W. J., and Baker, C. D., 1963, Oregon earthquakes, 1841 through 1958: *Bulletin of the Seismological Society of America*, v. 53, no. 1, p. 95-108.
- Bryant, W. A., 1990, Surprise Valley and related faults, Lassen and Modoc counties.
- Crider, J.G., 2001, Oblique slip and the geometry of normal-fault linkage: mechanics and a case study from the Basin and Range in Oregon: *Journal of Structural Geology*, v. 23, p. 1997–2009
- Egger, A. E., Weldon, R. J., Langridge, R. M., Ibarra, D. E., Marion, B., and Hall, J., in review, The influence of pluvial lake cycles on earthquake recurrence in the northwestern Basin and Range, USA, in Starratt, S. W., and Rosen, M. R., eds., *From Saline to Freshwater: The Diversity of Western Lakes in Space and Time*: Boulder, CO, Geological Society of America.
- Felton, A., Jewell, P. W., Chan, M., and Currey, D., 2006, Controls of Tufa Development in Pleistocene Lake Bonneville, Utah: *The Journal of Geology*, v. 114, no. 3, p. 377-389. doi: 10.1086/501218
- Hempel, A., Hetzel, R., and Maniatis, G., 2010, Response of faults to climate-driven changes in ice and water volumes on Earth's surface: *Philosophical Transactions of the Royal Society of London A: Mathematical, Physical and Engineering Sciences*, v. 368, no. 1919, p. 2501-2517. doi: 10.1098/rsta.2010.0031
- Hedel, C. W., 1980, Late Quaternary faulting in western Surprise Valley, Modoc County, California [M.S. Master's]: San Jose State University, 142 p.
- , 1984, Maps showing geomorphic and geologic evidence for late Quaternary displacement along the Surprise Valley and associated faults, Modoc County, California: U. S. Geological Survey, scale 1:62,500.
- Karow, T., and Hempel, A., 2010, Slip rate variations on faults in the Basin-and-Range Province caused by regression of Late Pleistocene Lake Bonneville and Lake Lahontan: *International Journal of Earth Sciences*, v. 99, no. 8, p. 1941-1953. doi: 10.1007/s00531-009-0496-3
- Kreemer, C., Hammond, W. C., Blewitt, G., Holland, A. A., and Bennett, R. A., 2012, A Geodetic Strain Rate Model for the Pacific-North American Plate Boundary, Western United States, Volume M178: Reno, NV, Nevada Bureau of Mines and Geology, p. 1.
- Langridge, R. M., Pezzopane, S. K., and Weldon, R. J., 2001, Slip rate, recurrence intervals and paleoearthquakes for the Ana River Fault, central Oregon, in Negrini, R., Pezzopane, S. K., and Badger, T. C., eds., *Quaternary Studies near Summer Lake, Oregon*, Friends of the Pleistocene, p. 126.
- Marion, Brian, 2016, Spatiotemporal Slip Rate Variations Along Surprise Valley Fault in Relation to Pleistocene Pluvial Lakes, MS Thesis, Central Washington University
- O'Connell, J. F., and Inoway, C. M., 1994, Surprise Valley Projectile Points and Their Chronological Implications: *Journal of California and Great Basin Anthropology*, v. 16, no. 2, p. 162-198.
- Personius, S. F., Crone, A. J., Machette, M. N., Mahan, S. A., and Lidke, D. J., 2009, Moderate rates of late Quaternary slip along the northwestern margin of the Basin and Range Province, Surprise Valley fault, northeastern California: *Journal of Geophysical Research*, v. 114, no. B09405, p. 17. doi: 10.1029/2008jb006164
- Pezzopane, S. K., 1993, Active faults and earthquake ground motions in Oregon, PhD thesis: University of Oregon, 250 p.
- Pezzopane, S. K., and Weldon, R. J., II, 1993, Tectonic role of active faulting in central Oregon: *Tectonics*, v. 12, no. 5, p. 1140-1169. doi: 10.1029/92tc02950
- Reheis, M. C., Adams, K. D., Oviatt, C. G., and Bacon, S. N., 2014, Pluvial lakes in the Great Basin of the western United States—a view from the outcrop: *Quaternary Science Reviews*, v. 97, p. 33-57. doi: http://dx.doi.org/10.1016/j.quascirev.2014.04.012
- Treerotchananon, A., 2009, Extension between major faults, central Oregon Basin and Range [M.S. thesis]: University of Oregon, 71 p.
- Uhrhammer, R. A., 1991, Northern California seismicity, in Slemmons, D. B., Engdahl, E. R., Zoback, M. D., and Blackwell, D. D., eds., *Neotectonics of North America*, Volume 1: Boulder, CO, Geological Society of America, p. 99-106.
- U.S. Geological Survey, 2006, Quaternary fault and fold database for the United States
- Weldon, R. J., Langridge, R. M., Pezzopane, S. K., and Weldon, E., 2009, An earthquake cluster followed the drying of Pleistocene Lake Chewaucan, central Oregon Basin and Range: *Geological Society of America Abstracts with Programs*, v. 41, no. 7, p. 456.



Scarp erosion and burial within four years following the M7.2 2010 El Mayor-Cucapah earthquake rupture from repeat terrestrial lidar scans

Elliott, Austin (1), Oskin, Michael (2), Gold, Peter (3), Hinojosa-Corona, Alejandro (4)

- (1) University of Oxford, Department of Earth Sciences. ajelliott@ucdavis.edu.
- (2) University of California Davis, Department of Earth and Planetary Sciences.
- (3) University of Texas Jackson School of Earth Sciences.
- (4) Centro de Investigacion Cientifica y de Educacion Superior de Baja, Mexico.

Abstract: We document the spatial and temporal distribution of scarp erosion and burial over a 3.5-yr span following the 4 April, 2010 M_w 7.2 El Mayor-Cucapah (EMC) earthquake in northern Baja, Mexico, measuring topographic change from repeat, centimeter-scale terrestrial lidar scanning (TLS) surveys. Our analysis reveals emplacement mechanisms of common paleoseismic markers and informs the interpretation of discontinuous or eroded offset features. These observations capture the rapid timing of stratigraphic rupture markers, and show the varying preservation timescales for geomorphic offsets due to surface rupture.

Key words: earthquake rupture, scarp erosion, drainage analysis, terrestrial lidar, high resolution topography

INTRODUCTION

On 4 April, 2010, at 15:40 local time (UTC -7), a M_w 7.2 earthquake initiated on a SE-dipping normal fault in the northern Gulf of California rift, then propagated bilaterally along a network of oblique right-normal faults (Wei et al., 2011; Uchide et al., 2013). It ruptured 60 km southward along a fault buried beneath the thick sediments of the Colorado River Delta, and 70 km northward along a complex network of bedrock faults that overlie an east-dipping detachment fault which controls the whole system (Oskin et al., 2012; Fletcher et al., 2014; Teran et al., 2015; Fletcher et al., 2016). Extensive surface ruptures revealed a network of shallow faults that produced complex near-field deformation, accommodating region-scale oblique extension (Fletcher et al., 2014; Teran et al., 2015). This surface rupture was the first to be fully imaged before and after the event using high resolution topographic datasets, and thus provided a detailed view of the coseismic deformation field which has been used to inform our understanding of earthquake mechanics and regional crustal kinematics (Oskin et al., 2012; Fletcher et al., 2016; Barišín et al., 2015; Zhou et al., 2016).

In addition to the unprecedented insight into coseismic surface deformation, the EMC earthquake abruptly produced a step-function offset in the landscape, offering a rare chance to track geomorphic response to a simple, discrete perturbation (Arrowsmith et al., 1994). We have documented and analysed these changes using repeat ground-based topographic surveys of the ruptures (Gold et al., 2013).

In the days after the earthquake we conducted ground-based lidar surveys which targeted four distinct substrates of the rupture: bedrock, alluvial fan conglomerate, fluvial sand, and aeolian silt, in order to capture the geometries of the scarps and their subsequent degradation in these different environments.

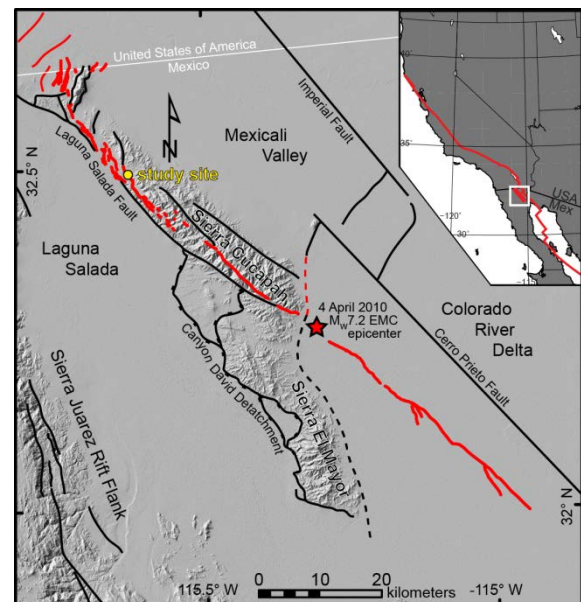


Figure 1: Location & setting of the 4 April 2010 El Mayor-Cucapah earthquake. The event initiated with a M_w 6.8 normal-faulting sub-event on a N-striking, E-dipping fault, and then propagated bilaterally for 100 km along a complex array of >6 oblique right-normal faults embedded within the system of major right-lateral and extensional faults controlling the transition zone between the San Andreas transform system and the Gulf of California rift.

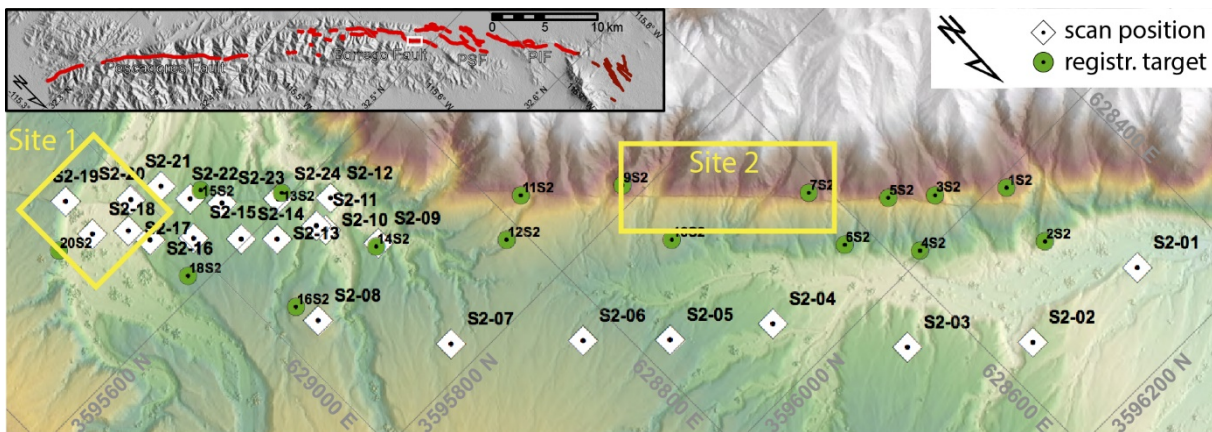


Figure 2: Overview map of scan sites described here; Map centered at 32.492°N 115.630°E and rotated 135° CW for display. Site 1—the uphill facing scarp on an alluvial fan—is shown in Figure 5, and Site 2—the hillslope scarp—is shown in Figure 4. Note difference in scan layout between the sub-horizontal, rough alluvial fan surface (left), and the oblique vantage of the bedrock hillslope site (right) which required far fewer scan setups to adequately capture. Basemap is 25-cm DEM & hillshade from post-earthquake airborne lidar survey.

METHODS

We collected TLS surveys 12 days, 1 year, and 3.5 years after the earthquake at four ~250 m-long reaches of the surface rupture. Initial ground-based lidar surveys, within two weeks of the earthquake, targeted four distinct substrates of the rupture. Fault geometry, fault zone width, and both geomorphic processes and rates are each expected to vary among these different lithologies. Both sites documented here (Figure 2) lie along a kilometer-long reach of the Borrego Fault, a steeply (89°) east-dipping oblique right-lateral/normal fault within the Cucapah range, containing the maximum measured offsets from this earthquake (3.44 m, Fletcher et al., 2014).

Capturing localized erosion of a fault scarp requires extremely accurate collocation of sequential scans. Initially poor regional GPS coverage (during 2010 and 2011 scans) and coseismic backslip corrections by NOAA's Horizontal Time-Dependent Positioning (HTDP) system resulted in relatively high errors (25-150 cm) among our GPS-measured network of tiepoints at each site. To accurately collocate t-lidar point clouds from different years, we aligned later surveys with earlier ones using an iterative closest point (ICP) matching algorithm, and were inspected using *LidarViewer* in the 3D immersive visualization facility KeckCAVES (Gold et al., 2013; Kreylos et al., 2013).

RESULTS AND DISCUSSION

Site 2 – Downhill-facing Bedrock Scarp

Our Site 2 (sites were named in the order chosen and surveyed; Gold et al., 2013) covers a 250-m reach of the Borrego fault where it runs along a steep bedrock hillslope marked in some places by paleoscarps in shallow alluvium and colluvium. Here the exposed free-face reveals ~20 cm of chemically weathered granitic grus overlying more intact granite which is in places exposed where a 5-cm thick sliver of fault gouge has been removed (Figure 3). Thus the substrate here is faulted granitic bedrock overlain by a shallow soil composed of the same local lithology, but weathered.



Figure 3: Before-and-after photographs of an eroded reach of the Borrego fault captured in 2010 (above) and in 2013 (below). Note extensive vertical rilling of scarp free-face, and removal of striated gouge. Intense scarp-crest erosion is further enhanced by relative incompetence of weathered grus compared to bedrock below.

Within the first year, extremely little erosion was documented, but sediment transport was sufficient to fill fault zone fissures. Narrow chutes were eroded where streams crossed downhill-facing scarps (Figure 3). The first year's difference maps verify that common paleoseismic age brackets (fissure-fill deposits) are reliably formed within <1 year following an earthquake, even in this hyper-arid environment.



During the second year, heavy rainstorms dramatically eroded the scarp (Figure 4). Here, the bedrock scarp has been pervasively eroded headward by >10 cm, and up to 2 m, with higher rates of headward erosion in the upper ~20 cm of soil than in the bedrock exposed in the free-face below. The free-face itself has been largely removed, with little of the striated gouge remaining. The original slip surface here is only preserved along a ~4 m reach of the fault adjacent to the largest drainage (Figure 4). Significantly, this portion of the bedrock scarp is oriented with a dip direction perpendicular to the local hillslope direction, protecting it from erosion. These TLS datasets document three modes of scarp erosion: 1) rapid (>1 m yr⁻¹) headward retreat in active channels, 2) pervasive rilling and minor headward retreat along hillslope reaches, and 3) limited erosion, i.e., preservation, on channel margins, where hillslope aspect is parallel to fault strike. This counterintuitively suggests that channel margins may be the most likely places to preserve fault scarps on downhill-facing scarps.

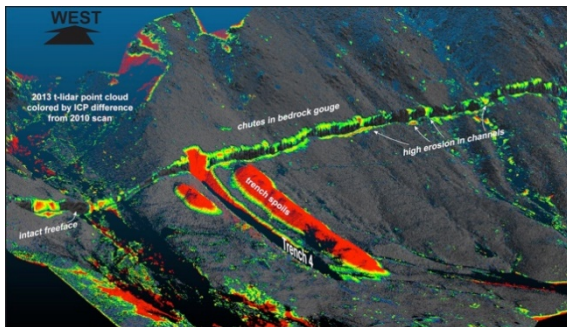


Figure 4: Oblique view of bedrock hillslope scarp point cloud, colored by ICP distance between 2011 and 2013 point clouds. Paleoseismic trench and spoils dominate the survey, but scarp crest degradation and deposition at the base are the main natural changes. Note absence of scarp-crest degradation adjacent to large channels, where scarp strike is parallel to hillslope direction, noted as “intact free-face”.

Site 1 – Uphill-facing Alluvial Fan Scarp

To the southeast of Site 2, a major channel drains westward through the range uplifted by the Borrego Fault, locally reversing the drainage direction across the fault (Figure 2). Here, a complex of abandoned alluvial fans surrounds the modern stream channel, which is a coarse sandy wash. The older among these exhibit a paleoscarp where the 2010 rupture offsets them, but otherwise the modern rupture of the Borrego Fault is the only tectonic disruption, uplifting the downstream sides of these fans and downdropping their upstream reaches.

On these uphill facing scarps, mass wasting was the dominant erosive mechanism, leading to highly asymmetrical scarp profiles. Localized blocks toppled from the upthrown side of the fault, but upon deposition on the downthrown side crumbled into diffuse mounds at the angle of repose and spread more evenly as a colluvial wedge. Sharp crests in broken desert pavement were softened mildly by minor diffusive processes, i.e., rainsplash. Where this uphill-facing scarp blocks active stream channels, height differencing reveals 20-70 cm of upstream aggradation by ponding and delta progradation, and 80 cm of downstream erosion due to overtopping of the scarp by floodwaters (Figure 5).

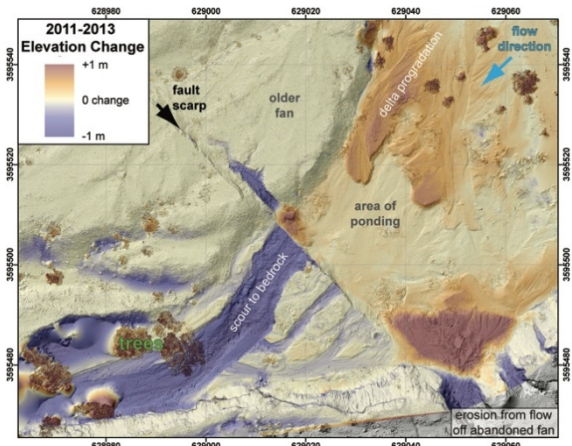


Figure 5: Topographic difference map showing geomorphic changes to the arroyo dammed by the uphill-facing 2010 scarp. Underlying hillshade image is of 5-cm DEM from most recent (Nov. 2013) t-lidar scans. Coordinates in UTM zone 11N.

The uphill-facing scarps induce a major change to the hydrology and ecology of the site by impeding streamflow. Evidence of ponding upstream is ubiquitous, spurring growth of broad-leaved plants and drowning or burying desert shrubs. Although dry and caked with cracked mud upon our visit, various animal tracks and excavations attested to heavy use of this area as a source of water throughout and beyond its final days of evaporation.

Downstream, the watershed is deprived of normal surface flows, and rare overtopping (after the stream has deposited its fine material upstream of the new natural dam) has resulted in the thorough scouring of the sand and gravel from above the bedrock strath, often undermining or carrying away vegetation from the channel.

Significantly, deep channels have been incised parallel to the fault along the base of the scarp, especially where deflected streamflow crosses the knickpoints formed by abandoned terrace risers. Even the modest flows collected in the small watersheds atop an abandoned alluvial fan remnant are sufficient to incise into these risers where they intersect the fault. This situation is particularly problematic because this type of flow will preferentially erase horizontal piercing lines where they intersect the fault. Our documentation of this phenomenon presents a cautionary example of the processes that drive uncertainty in measuring horizontal riser offsets.

CONCLUSION

Documenting two intervals of geomorphic change in the immediate aftermath of a fault rupture highlights that erosive processes which are modeled diffusively over long timespans are highly temporally episodic and spatially heterogeneous in the short term—importantly, during the time span in which they operate at their highest rates. These observations guide predictions of fault scarp morphology and preservation potential, which may aid in identifying paleoseismic markers in the hunt for earthquakes elsewhere.



Acknowledgements: This work was supported by the Southern California Earthquake Center. We thank both Eric Cowgill and UNAVCO for the use of lidar scanning instruments and GPS receivers. Richard Styron, Michael Taylor, Ed Nissen, and Kendra Johnson joined us in deploying surveys over the years, as well as undergraduate and graduate students from both UCLA and CICESE who provided indispensable field help.

REFERENCES

- Arrowsmith, J. R., & Rhodes, D. D. (1994). Original forms and initial modifications of the Galway Lake Road scarp formed along the Emerson fault during the 28 June 1992 Landers, California, earthquake. *Bulletin of the Seismological Society of America*, 84(3), 511–527.
- Barišić, I., Hinojosa-Corona, A., & Parsons, B. E. (2015). Co-seismic vertical displacements from a single post-seismic lidar DEM: Example from the 2010 El Mayor-Cucapah earthquake. *Geophysical Journal International*, 202(1), 328–346. doi:10.1093/gji/ggv139
- Fletcher, J. M., Teran, O. O. J., Rockwell, T. K. T., Oskin, M. E., Hudnut, K. W., Mueller, K. J., Spelz, R. M., Akçiz, S. O., Masana, E., Faneros, G., Fielding, E. J., LePrince, S., Morelan, A. E., Stock, J., Lynch, D. K., Elliott, A. J., Gold, P. O., Liu-Zeng, J., González-ortega, A., Hinojosa-Corona, A., González-García, J. (2014). Assembly of a large earthquake from a complex fault system: Surface rupture kinematics of the 4 April 2010 El Mayor–Cucapah (Mexico) Mw 7.2 earthquake. *Geosphere*, 10(4), 797–817. doi:10.1130/GES00933.1
- Fletcher, J. M., Oskin, M. E., Teran, O. J. (2016). The role of a keystone fault in triggering the complex El Mayor – Cucapah earthquake rupture. *Nature*, 9(3918). doi:10.1038/NGEO2660
- Gold, P. O., Oskin, M. E., Elliott, A. J., Hinojosa-Corona, A., Taylor, M. H., Kreylos, O., & Cowgill, E. (2013). Coseismic slip variation assessed from terrestrial lidar scans of the El Mayor–Cucapah surface rupture. *Earth and Planetary Science Letters*, 366, 151–162. doi:10.1016/j.epsl.2013.01.040
- Kreylos, O., Oskin, M. E., Cowgill, E., Gold, P. O., Elliott, A. J., & Kellogg, L. H. (2013). Point-based computing on scanned terrain with LidarViewer. *Geosphere*, 9(3), 546–556. doi:10.1130/GES00705.1
- Oskin, M. E., Arrowsmith, J. R., Hinojosa-Corona, A., Elliott, A. J., Fletcher, J. M., Fielding, E. J., Gold, P. O., González-García, J., Hudnut, K. W., Liu-Zeng, J., Teran, O. J. (2012). Near-Field Deformation from the El Mayor-Cucapah Earthquake Revealed by Differential LIDAR. *Science*, 335(February), 702–705.
- Teran, O. J., Fletcher, J. M., Oskin, M. E., Rockwell, T. K., Hudnut, K. W., Spelz, R. M., Akçiz, S., Hernandez-Flores, A. P., Morelan, A. E. (2015). Geologic and structural controls on rupture zone fabric: A field-based study of the 2010 Mw 7.2 El Mayor–Cucapah earthquake surface rupture. *Geosphere*, 11(3), 899–920. doi:10.1130/GES01078.1
- Zhou, Y., Walker, R. T., Elliott, J. R., & Parsons, B. (2016). Mapping 3D fault geometry in earthquakes using high-resolution topography: Examples from the 2010 El Mayor-Cucapah (Mexico) and 2013 Balochistan (Pakistan) earthquakes. *Geophysical Research Letters*, 43(7), 3134–3142. doi:10.1002/2016GL067899



The effect of lower crustal structure on stress loading around faults

Ellis, Susan (1), Williams, Charles (2), Van Dissen, Russ (2), Langridge, Rob (2), Prior, Dave (3), Cross, Andy (4), Hamling, Ian (2)

- (1) GNS Science, Lower Hutt. S.ellis@gns.cri.nz.
- (2) GNS Science, Lower Hutt.
- (3) University of Otago, Dunedin.
- (4) Washington University St Louis, USA.

Abstract: Faults are not long, planar features rupturing an elastic half-space, but instead complex, messy and intersecting zones of damage and strain localization within heterogeneous lithosphere. At both large and small scales, fault displacement and interactions between faults will be influenced by the inherited crustal structure at greater depths. We demonstrate some of these effects using numerical models informed by fault structure in the South Island of New Zealand. We show how weak regions such as a subduction interface or lower crustal mylonite zone can help load stresses onto brittle faults in the upper crust. Such regions also play a role in the communication and static stress interactions between fault networks. Complex fault interactions can occur as a response to inherited lithospheric discontinuities within the basement and mid-crust.

Key words: faults, strain, localization, lithosphere, geodynamic models.

INTRODUCTION

The recent M_w 7.8 Kaikōura earthquake in the South Island of New Zealand has highlighted the effects of complex interactions between multiple fault segments underlain by a strong lower crustal slab (Hamling et al., 2017; Stirling et al., 2017). Yet even simpler fault systems - including the Alpine Fault along the west coast of the South Island of New Zealand - are subject to complex stress states (e.g., Upton et al., 2016; Ellis et al., 2006; 2017). Tectonic inheritance can exert an important control on the manner in which crust localizes, including the distribution of upper crustal faults, their style of deformation, and how stress is transferred between brittle upper crust and ductile lower crust (Ellis et al., 2006).

The static stress changes following a major earthquake are generally estimated by computing the stress change from fault dislocation in an elastic half-space (King et al., 1994). While dynamic stress triggering may play an important role in an earthquake sequence such as the Kaikōura earthquake (e.g., Kaiser et al., 2017), a fault must also possess sufficient static stress to fail. The present-day stress magnitudes along hazardous faults in the South Island of New Zealand are poorly known. While faults are ultimately loaded by the far-field convergence between tectonic plates, they may also be locally loaded by stress perturbations from surrounding fault ruptures, and from slow ductile deformation in the underlying crust. Understanding the role of these different loading factors is critical for improvements to estimates of stress in the lithosphere and to synthetic seismicity models (e.g., Robinson & Benites, 1995; Pollitz, 2016).

Here, we explore and review some of the fundamental effects that pre-existing structure has on stress loading of faults. We show that the degree of localization beneath a fault (e.g., from thermal weakening and/or development of mylonitic fabric) can have an important effect on the magnitude of stress loading between seismic events.

STRESS CYCLING AROUND A FAULT- EFFECT OF LOWER CRUSTAL STRUCTURE

The finite-element code SULEC (Buiter & Ellis, 2012) is used to model the stress cycling around a crustal fault. The numerical model setup is shown in *Figure 1*. Previous stress cycling models of this kind have been conducted using the Abaqus Standard finite element software (Ellis et al., 2004, 2006; Nüchter & Ellis, 2010).

The model domain is 150 km wide and 30 km deep and includes a "fault" that dips at 45° and extends from the surface ($y=0$) to the bottom of the domain ($y=-30$ km). The crust is prescribed an elasto-visco-plastic rheology, with a shear modulus $G=40$ GPa, coefficient of internal friction 0.75, cohesion 1 MPa, and ductile flow based on the dislocation creep quartzite flow-law from Hirth et al. (2001). Frictional plasticity obeys Coulomb yield when effective deviatoric stress reaches the yield stress.

The fault is modelled as a thin (200 m wide) zone that, most of the time, has the same properties as surrounding crust (yellow line, *Fig. 1*). Its frictional strength is lowered every 300 years to simulate the static effects of dynamic fault weakening during an earthquake, by changing the friction coefficient to 0.12 (from 0.75). This weakening is imposed all the way along the yellow line in *Fig. 1* to the base of the crust. However, owing to the effects of ductile creep which relaxes stress at high temperatures, the fault only slips down to about 8-10 km (e.g., Ellis et al., 2006; Nüchter & Ellis, 2010) (solid part of yellow line). In the intervening 300 years, the crust is loaded by applying a horizontal velocity of 1 cm yr^{-1} and an out-of-plane velocity of 3 cm yr^{-1} at the right-hand boundary, while the left-hand boundary is held fixed. A small flux of material ($1/3$ of the incoming flux at the side) is prescribed to leave the base as shown on *Fig. 1*.

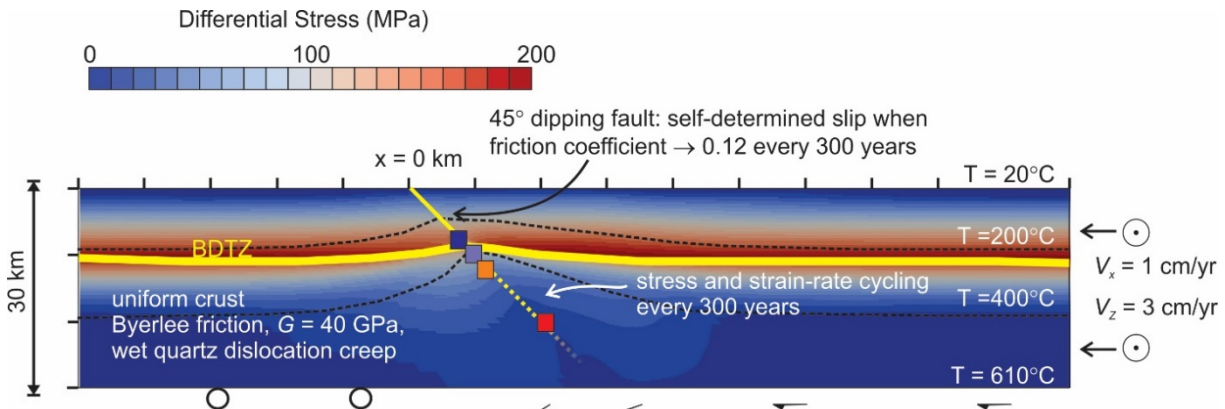


Figure 1. End of the setup phase (lasting 20 kyr) of a numerical model showing differential stress (colour contours) and temperature contours as indicated (dotted black line). The thin yellow line marks the location of the imposed “fault” weakening which has friction coefficient reduced to 0.12 every 300 years, while the thick yellow line indicates location of steady-state brittle-ductile transition (BDTZ) as predicted by the model. Loading from the transpressive boundary conditions has allowed stress to build up in the mid-crust, while at greater depths, stresses have been relieved by ductile creep. The coloured boxes refer to locations plotted in Figure 2.

The thermal conditions in the model were based on the inferred Alpine Fault temperature-depth profile from Cross et al. (2015). Away from the fault, we assumed a linear geothermal gradient with a bottom boundary temperature of 610°C at $y = -30$ km and 20°C at the surface. These conditions created a perturbed geothermal field in the vicinity of the fault as shown in Fig. 1.

We first benchmarked the SULEC stress cycling technique against equivalent models previously published using the Abaqus software (Nüchter et al., 2010). We verified that slip amounts, stress changes, and strain-rates were similar. The model required an initial period in which stresses are “spun up” (Ellis et al., 2004; Hetland and Hager, 2006); i.e. the crust is elastically loaded by applying the boundary conditions, which imposes a net stress state of transpression. This “spin up” period was 10 kyr with the fault locked; 10 kyr with the fault slipping (friction coefficient lowered to 0.12); and 300 years with the fault locked, before imposing the first seismic step. We analyse stresses during a seismic step and subsequent interseismic step after 4 complete cycles, to ensure that the model has settled into a self-similar behaviour (e.g., Nüchter et al., 2010) (Figure 2).

The model shown in Fig. 1, 2 and 3a illustrates stress cycling of ~ 14 MPa in the uppermost crust near the fault, and greater than 30 MPa in the ductile lower crust- where the fault no longer ruptures, as it does not have sufficient stress surrounding it to drive fault slip (cf. Fig. 1). A large component of the stress cycling around the fault is driven by localized creeping beneath the fault, which loads the stresses around the brittle part of the fault during the interseismic period (Fig. 3c, blue shaded regions). In contrast, a model in which the geotherm is uniform with depth and is not perturbed below the fault experiences reduced stress cycling, and the brittle part of the fault, which slips during each seismic cycle, extends to greater depths (Fig. 3b). The change in loading mechanism can be clearly seen in Fig. 4. The case without thermal weakening along the fault (Fig. 4b) has only a small amount of lower crustal creep, so that fault is reloaded laterally after a

seismic slip event, rather than from below. The uniform geotherm model experiences less than half as much stress drop and recovery in the upper crust in comparison to the localized creeping case (Fig. 3c)

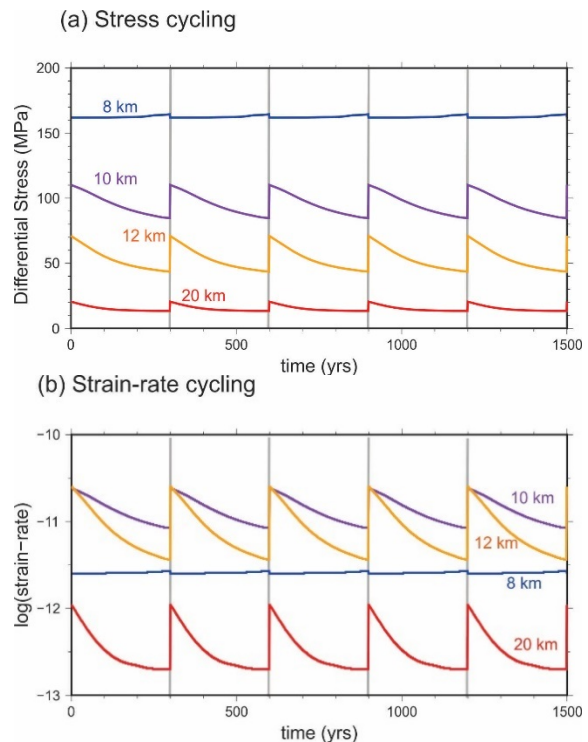
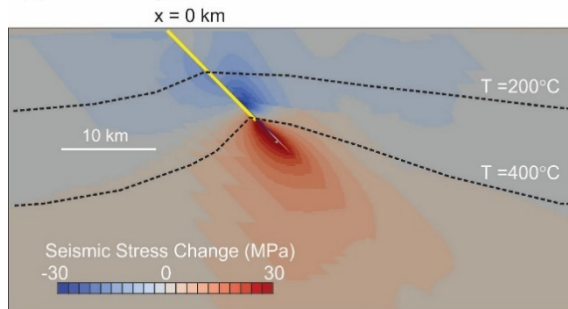


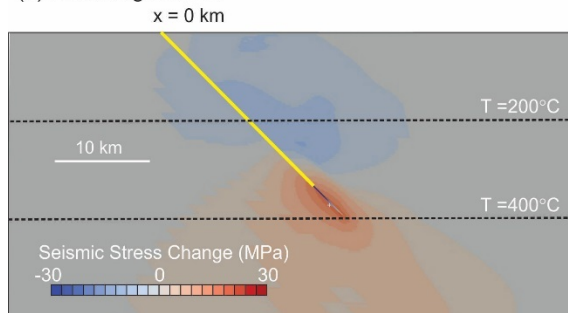
Figure 2. (a) Stress and (b) strain-rate cycling of the numerical model at 4 different depths in crust near the fault as indicated on figure 1. Regular seismic cycles of 300 years duration are imposed by lowering fault strength for a short time. Note that dynamic stress effects (during the earthquake) are not included. In the uppermost (brittle) crust, a stress drop accompanies motion along the fault (300, 600, 900, 1200 years on x-axis, figure 2a), while at greater depths, stresses increase as lower crust is loaded by fault motion above it. Strain-rates in the mid and lower crust decay in a non-linear fashion with time after each seismic event.



(a) Perturbed geotherm: weak ductile zone beneath fault



(b) Uniform geotherm



(c) Stress change along fault

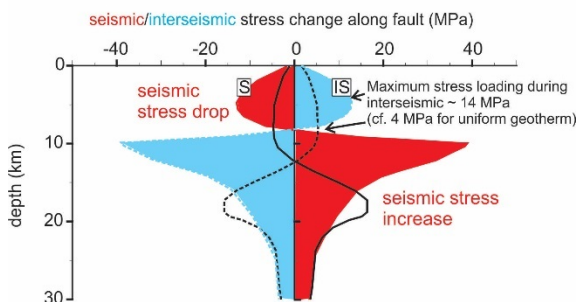
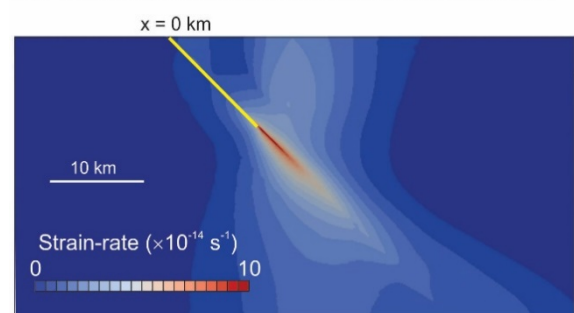


Figure 3. (a) Contour plot of the stress change during a typical seismic step in the model where the brittle part of the fault releases stress in the upper crust and loads the lower (ductile) crust. The yellow line shows the part of the imposed fault plane that experiences brittle failure (this is self-determined in the model). (b) Contour plot of the seismic stress change for a model that is the same as (a) but does not have a perturbed geotherm. In this case, much less ductile weakening and localization is present beneath the fault. Stress cycling is reduced in both upper and lower crust. (c) The seismic (red) and interseismic (blue) stress changes along the fault plane for the case with an elevated geotherm beneath the fault. For comparison, the stress profiles for the case with a uniform geotherm (corresponding to Fig. 3b) are also shown (solid and dashed black lines representing seismic and interseismic stress changes, respectively).

The comparison discussed above considers the effect of different amounts of localization in the ductile lower crust beneath a major fault. Weak ductile lower crust may also be reduced by subduction of a strong slab to depth. To test the effect that this has on ductile flow and stress reloading beneath a fault, we added a strong, brittle layer underthrusting the fault to the model with uniform geothermal gradient shown in Fig. 4b. This results in enhanced shearing along the top of the slab (Fig. 5), but only where ductile crust is present. The enhanced shearing at the top of the slab transfers deformation up-dip to a secondary (prescribed) fault that dips steeply to a depth of ca. 20 km.

(a) Perturbed geotherm: weak ductile zone beneath fault



(b) Uniform geotherm

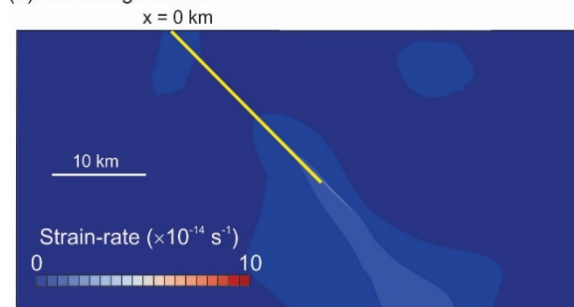


Figure 4. (a) Strain-rate in the middle of the interseismic period for the model shown in Fig. 1, 2, and 3a with a perturbed geotherm leading to ductile weakening below the brittle part of the fault plane. Localised strain accumulates beneath the brittle fault and above the lower tip of the brittle fault. (b) Strain-rate for the case with a uniform geotherm and less ductile weakening below the fault (Fig. 3b).

DISCUSSION

The model experiments are obviously simplified compared with stress cycling associated with earthquake sequences observed in the real world. Nevertheless, they do illustrate some basic features of a brittle fault embedded within a continental crustal layer which can creep at elevated temperatures, typically found at depths > 15-20 km. The model results suggest that faults underlain by thermally-perturbed low-strength ductile shear zones (e.g., as found in a sheared and uplifting mylonites) build up stress faster and experience greater stress cycling over seismic timescales compared to faults that are underlain by more homogeneous ductile crust. They are loaded by creeping from below as well as laterally by far-field tectonics.

A subducted slab can cut off ductile flow at depth, and concentrate flow instead along the top of the slab. This occurs whether or not the slab is overlain by a weak frictional interface, at depths where material is ductilely creeping rather than failing by brittle mechanics. The shear zone at the top of the slab can help transfer stress and deformation up-dip to secondary faults.

Figures 3 and 4 helps illustrate how the weak ductile mylonite zone beneath the Alpine Fault helps to load it and allows stresses and strain-rates to cycle on seismic timescales. The relative contribution of lateral stress loading of a fault vs. loading from localized creeping at greater depths is an important factor to consider when prescribing tectonic loading of faults in synthetic seismicity models.

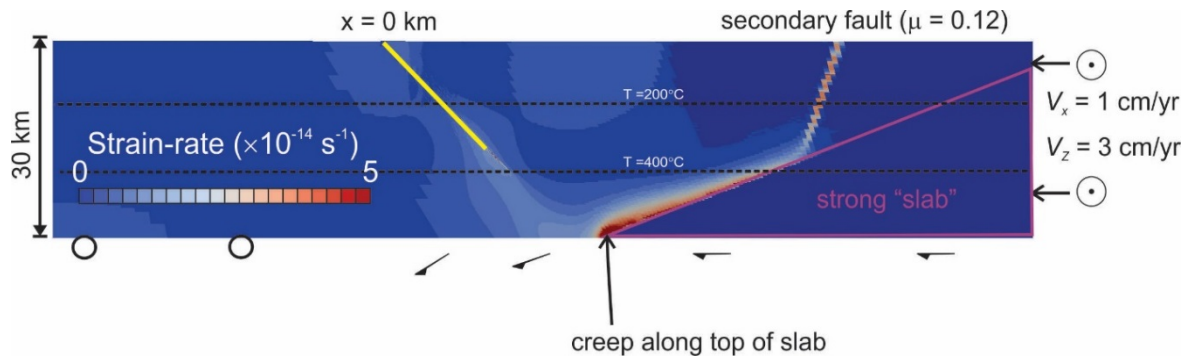


Figure 5. Strain-rate for a model that includes a strong, brittle wedge representing a subducting slab, which prevents ductile flow near the base of the crust. A secondary fault is also imposed with a low coefficient of friction, although this fault remains unlocked during the seismic cycle of the main fault (yellow dipping line).

Acknowledgements: This project was supported by Public Research Funding from the Government of New Zealand.

REFERENCES

- Buiter, S. & Ellis, S., 2012. SULEC: Benchmarking a new ALE finite-element code. In *EGU General Assembly Conference Abstracts* 14, p. 7528.
- Cross, A.J., Kidder, S. & Prior, D.J., 2015. Using microstructures and TitaniQ thermobarometry of quartz sheared around garnet porphyroclasts to evaluate microstructural evolution and constrain an Alpine Fault Zone geotherm. *Journal of Structural Geology*, 75, 17-31.
- Ellis, S. & Stöckhert, B., 2004. Imposed strain localization in the lower crust on seismic timescales. *Earth, Planets and Space*, 56, 1103-1109.
- Ellis, S., Beavan, J., Eberhart-Phillips, D. & Stöckhert, B., 2006. Simplified models of the Alpine Fault seismic cycle: stress transfer in the mid-crust. *Geophysical Journal International*, 166, 386-402.
- Ellis, S., Van Dissen, R., Eberhart-Phillips, D., Reyners, M., Dolan, J.F. & Nicol, A., 2017. Detecting hazardous New Zealand faults at depth using seismic velocity gradients. *Earth and Planetary Science Letters*, 463, 333-343.
- Hamling, I.J., Hreinsdóttir, S., Clark, K., Elliott, J., Liang, C., Fielding, E., Litchfield, N., Villamor, P., Wallace, L., Wright, T.J. & D'Anastasio, E., 2017. Complex multifault rupture during the 2016 Mw 7.8 Kaikōura earthquake, New Zealand. *Science* 356 10.1126/science.aam7194.
- Hetland, E.A. & Hager, B.H., 2006. Interseismic strain accumulation: Spin-up, cycle invariance, and irregular rupture sequences. *Geochemistry, Geophysics, Geosystems*, 7(5).
- Hirth, G., Teyssier, C. & Dunlap, J.W., 2001. An evaluation of quartzite flow laws based on comparisons between experimentally and naturally deformed rocks. *International Journal of Earth Sciences*, 90(1), 77-87.
- Kaiser, A., Balfour, N., Fry, B., Holden, C., Litchfield, N., Gerstenberger, M., D'Anastasio, E., Horspool, N., McVerry, G., Ristau, J. & Bannister, S., 2017. The 2016 Kaikōura, New Zealand, Earthquake: Preliminary Seismological Report. *Seismological Research Letters* 88(3), 727-739.
- King, G.C., Stein, R.S. & Lin, J., 1994. Static stress changes and the triggering of earthquakes. *Bulletin of the Seismological Society of America*, 84(3), 935-953.
- Nüchter, J.A. & Ellis, S., 2010. Complex states of stress during the normal faulting seismic cycle: Role of midcrustal postseismic creep. *Journal of Geophysical Research: Solid Earth*, 115(B12).
- Pollitz, F.F., 2016. A Note on Adding Viscoelasticity to Earthquake Simulators, *Bulletin of the Seismological Society of America*, DOI: 10.1785/0120160192.
- Robinson, R. & Benites, R., 1995. Synthetic seismicity models of multiple interacting faults. *Journal of Geophysical Research: Solid Earth*, 100(B9), 18229-18238.
- Stirling, M.W., Litchfield, N.J., Villamor, P., Van Dissen, R.J., Nicol, A., Pettinga, J., Barnes, P., Langridge, R.M., Little, T., Barrell, D.J.A. & Mountjoy, J., 2017. The Mw7.8 2016 Kaikōura earthquake: surface fault rupture and seismic hazard context. *Bulletin of the New Zealand Society for Earthquake Engineering* 50(2).
- Upton, P., Song, B. R., & Koons, P.O., 2016. Topographic controls on the stress state, shallow fault structure and strain partitioning, Alpine Fault, Whataroa, New Zealand, *American Geophysical Union, Fall General Assembly 2016*, abstract #EP53B-0932.



OSL Dating of Sediments Pre- and Post-dating Late Quaternary Earthquakes

Manfred Frechen

(1) Leibniz Institute for Applied Geophysics (LIAG), Section Geochronology, Stilleweg 2, 30655 Hannover, Germany
Manfred.Frechen@liag-hannover.de

Abstract: A reliable chronology is mandatory to reconstruct the timing of earthquakes of the past. Luminescence dating has significantly improved over the past 15 years and proved to be a useful tool to determine reliable deposition ages of terrestrial sediments for the time span ranging from a few years to several hundred thousand years. Furthermore, luminescence dating is the method of choice when organic matter is not available for radiocarbon dating or extending the dating limit of the latter method. In this presentation we will give a state of the art of optical stimulated luminescence dating and its application in relation to Late Quaternary earthquakes, especially in the Lower Rhine Valley in NW Europe including the Bree fault Scarp and the Peel Boundary Fault in Belgium and the Netherlands, respectively. We revisited previous study sites Vanneste et al. 2001; Frechen et al. 2001; Frechen & van den Berg 2002) to study and improve the precision and timing of the Late glacial and/or Holocene earthquake events by applying quartz OSL and thus avoiding the problems of anomalous fading and minimizing the problem of insufficient bleaching in those latter studies.

REFERENCES

- Frechen, M., Vanneste, K., Verbeeck, K., Paulissen, E., Camelbeeck, T. (2001): The deposition history of the coversands along the Bree Fault Escarpment, NE Belgium.- Netherlands Journal of Geosciences, 80: 171-185.
- Frechen, M., van den Berg, M.W. (2002): The coversands and timing of Late Quaternary earthquake events along the Peel Boundary Fault in the Netherlands.- Netherlands Journal of Geosciences, 81: 61-70.
- Vanneste, K., Verbeeck, K., Camelbeeck, T., Paulissen, E., Megraoui, M., Renardy, F., Jongmanns, D., Frechen, M. (2001): Surface-rupturing history of the Bree fault scarp, Roer Valley graben: Evidence for six events since the late Pleistocene.- Journal of Seismology, 5: 329-359.



Quaternary deformation in the Cordillera Oriental between 24°-25° SL, Central Andes (NW Argentina)

García, Víctor Hugo (1,2,3)

- (1) Adjunct Researcher, LATE Andes SA (Geomap-CONICET), Las Moreras 510 (4401) Vaqueros, Salta, Argentina. Email: victorg76@gmail.com
(2) Postdoctoral Fellow, Fundação CAPES, Ministério da Educação, Brazil.
(3) Guest Researcher, Institut für Erd- und Umweltwissenschaften, Universität Potsdam, Germany.

Abstract: NW Argentina is part of the Central Andes, an active subduction orogen enhancing reactivation of older structures and growth of new ones. The seismic record (historical and instrumental) shows frequent shallow crustal events including destructive ones, giving to the region the status of high seismic risk. In this paper, I provide an updated synthesis on the characterization of Quaternary structures found in the middle-eastern portion of Cordillera Oriental geological province. Some growth folds and fault scarps show evidence of Upper Pleistocene to Holocene activity and moderate deformation rates. These facts remark the strategic necessity of improving the investigation on Quaternary deformation in order to get extra tools for the seismic hazard assessment of this densely populated region.

Key words: Neotectonics, seismogenic structures, seismic hazard, Central Andes

INTRODUCTION

Tectonic setting

The Cordillera Oriental is part of the retrowedge of the Central Andes (Fig. 1a). It can be described as a thick-skinned fold and thrust belt characterized by N-S to NNE thrust sheets exhuming the basement of the region (Mon & Salfity, 1995; Monaldi et al., 1996; Carrera & Muñoz, 2008). The analysis of growth strata and cooling ages in apatites have determined the onset of the compressive deformation in its W border as late Eocene (Carrapa et al., 2011; Pearson et al., 2013; del Papa et al., 2013). Thermochronological analysis on synorogenic deposits preserved between the thrust sheets allow to some Authors to propose a progressive propagation of the deformation towards the foreland (Carrapa et al., 2011). Recently, Pearson et al. (2013) presented AHe cooling ages for the basement cores that indicate more complex migration patterns, with fast pulses of propagation towards the foreland followed by events of backthrusting towards the hinterland. García et al. (2013a) reached similar conclusions by analysing the stratigraphy and neotectonics of the N sector of the Lerma valley (Fig. 1a). These complex patterns are variable along different segments of the orogen and could be partially controlled by reactivation of previous structures (normal faults/previous heterogeneities). Regarding the traces of Quaternary deformation, they are not concentrated in a single orogenic front, rather are distributed (as the shallow crustal seismicity) along more than 200 km wide region, supporting the hypothesis of complex patterns of neotectonic activity (Fig. 1a).

Stratigraphic synthesis

The stratigraphy of the neotectonic basement can be divided in four sequences: 1) Late Proterozoic to Early

Cambrian low grade metamorphic rocks of the Puncoviscana Formation (Turner & Mon, 1979); 2) Early Paleozoic marine sedimentary rocks (Turner & Mon, 1979); 3) Cretaceous-Paleogene continental strata with conglomerates, sandstones, mudstones and limestones of the Salta Group rift sequence (Marquillas et al., 2005); and 4) synorogenic Neogene to early Pleistocene strata composed of reddish sandstones and mudstones, and brownish conglomerates interbedded with mudstones of the Guanaco and Piquete Formations respectively (Gebhard et al., 1974). The Quaternary deposits are mainly composed by alluvial coarse conglomerates and fan conglomerates and terraced fluvial conglomerates and sandstones. In many sectors, these deposits unconformably overlain the upper section of the synorogenic deposits. Fluvial terraces of the easternmost valleys of Cordillera Oriental (Lerma and Humahuaca valleys) were dated by several researchers using OSL and CRN. The obtained ages range between 35 and 118 ka, (Robinson et al., 2005; García et al., 2013b; Schlidgen et al., 2016).

Seismicity

The historical record of seismicity in the region starts with the Esteco earthquake in 1692 (MMI=IX, 13 fatalities). Other important events were the following: Salta 1844 (MMI=VII); Jujuy 1863 (MMI=VIII); Orán 1871 (MMI=VIII); Salta-Bolivia 1887 (MMI=IX); Salta 1908 (MMI=VII); La Poma 1930 (MMI=VIII); Salta 1948 (MMI=IX); Salta 1959 (MMI=VIII); Jujuy 1973 (MMI=VII). Shallow earthquakes with magnitudes close to 6 hit NW Argentina in the last years, some causing material damage and fatalities (Campo Quijano 2010, M=6.1 and El Galpón 2015, M=5.9) (INPRES, 2017).



QUATERNARY STRUCTURES

Due, in part, by these last events, the efforts to identify and characterize the Quaternary deformation of this region have been increased during the last decade. The characterization of the structures more studied of this segment of the Cordillera Oriental is presented in the next sections.

Lomas de Medeiros

These low relief hills are located in the northernmost part of the Lerma valley, in the NW extreme of Salta city, and represent the southern tip of the structural trend of the Vaqueros-La Caldera ranges (Fig. 1b). Scarce outcrops of the Piquete Formation appears in some deep creeks and along the Vaqueros river, always unconformably overlain by fluvial conglomerates of middle to late Pleistocene. The dips measured in this unit allow to reconstruct a N-S asymmetrical anticline with east vergence. The forelimb dips 60° E and the backlimb dips as much as 30° W. In the backlimb, the dips decreases progressively towards the western extreme of the fold (García et al., 2013a). A palinspastic reconstruction of the structure allows to model it as a fault-propagation fold with a blind thrust that dips 30° W and a decollement level located in the interface between the basement and the Neogene synorogenic deposits. The decreasing pattern of dips in the backlimb have been interpreted as evidence of syntectonic sedimentation in the upper section of the Piquete Formation since ca. 2-3 Ma (García et al., 2013a).

The coarse conglomerates that unconformably cover the Piquete Formation are disposed in a series of six strath terraces no more than 10 m thick. The regional geomorphological correlation of these deposits indicates that they should had been formed between ca. 300 and 50 ka (García et al., 2013a). Topographic profiles of the terraces projected transverse to the fold axis show that the terraces are folded and that the amplitude is progressively higher for the older ones. Uplift rates of up to 0.7 mm/a have been calculated for the last ca. 50 ka taking into account the estimated age for the younger terrace.

Lomas de Carabajal

The Lomas de Carabajal are a series of low hills of NW-SE trending and 10 km length located on the western border of the Lerma valley, close to the confluence between Rosario and Manzano rivers (Fig. 1b). As in Lomas de Medeiros, the Piquete Formation crops out occasionally in deep creeks and is unconformably overlain by fluvial conglomerates of middle to late Pleistocene age. Given the dips measured in Piquete Formation, García et al. (2013b) characterizes the structure as a series of subparallel and short wavelength (<1 km) N-S anticlines and synclines showing an *en-echelon* arrangement in a map view.

Five strath terraces (T1-T5) has been identified in the SE extreme of the hills. These terraces are gently folded and composed by 5 to 15 m of fluvial coarse conglomerates of middle to late Pleistocene age. The oldest terrace could be as old as ca. 300 Ka following the applied criteria for Lomas

de Medeiros. The T5 terrace level is particularly well exposed along the Manzano river creek that cuts the hills in the NW sector. The poorly stratified coarse conglomerates that crops out there allow to identified up to three gentle growth anticlines, whose amplitudes reach as much as 20 meters. A little hill (Loma de la Usina) is recognized a dozen hundred meters upstream Manzano river from the NW border of the Lomas de Carabajal (Fig. 1b). It is conformed by the T5 materials, have 10 m of altitude relative to the riverbed and can be described as an NW-SE asymmetric anticline with SW vergence, with several meter to centimeter scale reverse faults cutting and folding the poorly developed stratification. A silty bed of more than 50 centimeter thick has been dated in both sectors by OSL giving ages between $30,1 \pm 2,1$ ka and $39,8 \pm 2,9$ ka. Consequently, uplift rates ranging from 0.50 to 0.66 mm/a can be estimated for the T5 terrace taking into account the folds maximum structural relief of 20 meters (García et al., 2013b). The youngest terrace over the Manzano river (T6) has rich organic matter sediment close to its top yielding ¹⁴C (AMS) Holocene ages. A 2.5 meters high NW-SE scarp (SE continuation of Loma de la Usina structure) is disrupting this terrace indicating an moderate uplift rates for recent times (García et al. in preparation). A reactivation of the entire Lomas de Carabajal structure could trigger a Mw 6.3 event (Wells & Coppersmith, 1994).

Sierra de Los Alisos

Los Alisos range is located just to the south of San Salvador de Jujuy city, in the bajada of Eastern Cordillera. It comprises a series of low relief hills with NNW trend whose extension reach 20 km (Fig. 1b). The topographic relief do not exceed 200 m and progressively decreases to the S. Miocene to early Pleistocene synorogenic strata crop outs in their hillslopes delineating a west verging asymmetrical fault-propagation fold. A tuff interbedded in the subvertical Piquete Formation at the frontal limb has been dated in 4.50 ± 0.13 Ma (U-Pb LA-ICP-MS in zircons). Growth strata geometries are interpreted in the upper section of the same unit at the backlimb, indicating that the growing of the structure starts after ca. 4 Ma. A blind fault dipping 30° ESE, with a decollement level located at the interface between the basement and the synorogenic strata, is interpreted as the responsible of the deformation (García et al., 2017a).

Middle to late Pleistocene conglomeratic alluvial and fluvial terraces unconformably overlain the synorogenic strata (T1-T4). The relation between the oldest terrace (T1) and the synorogenic strata is particularly well preserved in the southernmost creek that cuts the hills. The ephemeral stream running there is disproportionately small comparing to the size of the valley and the big boulders that compose the T1 deposit. It allows to interpret that the Los Morados river had been the responsible of the generation of this creek and later it was diverted southward by the progressive growth of the anticline (Fig. 1b). The three younger terraces (T2-T4) are preserved at the northern extreme of the hills, where is San Salvador de Jujuy city. Topographic profiles of the terraces, following a transversal trend respect the fold axis, show that they are folded with the same structural pattern than the anticline. The amplitude is progressively



higher in the older terraces, reaching up to 61 meters in T1. Uplift rates of 0.20 mm/a for the last 300 ka and 0.48 mm/a for the last 50 ka are obtained by correlation of the terraces with the Lerma valley ones (T1 ~300 ka; T2 ~150 ka; T3 ~100 ka; T4 ~50 ka). An earthquake of Mw ~6.5 could strike the region if the entire surface of the fault ruptures during an event (Wells & Coppersmith, 1994).

DISCUSSION

The Quaternary structures briefly described here are aligned along N-S wide valleys at around 65.5°W that correspond with main tectonic structures in the crust and where two big province capital cities are located. The slip rates derived from the deformation measured in geomorphological markers characterize this sector of the Cordillera Oriental as a region with moderate activity rate sensu Slemmons & De Polo (1986). In some cases, Holocene activity has been confirmed pushing the bar higher and challenging the efforts to better constrain the recent history of these potentially seismogenic structures.

The existence of seismicity and evidence of Quaternary deformation toward both the E and the W highlights that there is not an unique orogenic front in this segment of the Central Andes rather it is distributed over a region more than 200 km wide (García et al., 2017b). This pattern of deformation could be related both with subcritical orogenic wedge conditions and/or controlled by previous heterogeneities (Pearson et al., 2013).

In this framework, the multiplicity of potential seismogenic sources in such a populated region (close to 2 MM inhabitants) and the lack of detailed studies aimed to establish their paleoseismological behavior, represents a challenge for the development of new and multidisciplinary approaches in order to improve the knowledge of the active tectonics in NW Argentina.

Acknowledgements: Field studies were funded by CONICET-IDEA project “Estructuras cuaternarias y caracterización del riesgo y peligrosidad sísmica en la provincia de Salta”. The author would like to acknowledge to the International Research Training Group IGK2018 STRATEGy (DFG) and INQUA for their financial support to take part of this symposium.

REFERENCES

- Carrapa, B., Bywater-Reyes, S., DeCelles, P., Mortimer, E. & Gehrels, G.E., 2011. Late Eocene-Pliocene basin evolution in the Eastern Cordillera of northwestern Argentina (25°–26°S): regional implications for Andean orogenic wedge development. *Basin Research* 23: 1-20.
- Carrera, N. & Muñoz, J.A., 2008. Thrusting evolution in the southern Cordillera Oriental (northern Argentine Andes): Constraints from growth strata. *Tectonophysics* 459, 107-122.
- del Papa, C., Hongn, F., Powell, J., Payrola, P., Do Campo, M., Strecker, M.R., Petrinovic, I., Schmitt, A.K., & Pereyra, R., 2013. Middle Eocene-Oligocene broken-foreland evolution in the Andean Calchaqui Valley, NW Argentina: insights from stratigraphic, structural and provenance studies. *Basin Research* 25: 574-593, doi: 10.1111/br.12018.
- García, V.H., Hongn, F. & Cristallini, E.O. 2013a. Late Miocene to recent morphotectonic evolution and potential seismic hazard of the northern Lerma valley: clues from Lomas de Medeiros, Cordillera Oriental, NW Argentina. *Tectonophysics* 608, 1238-1253, DOI: 10.1016/j.tecto.2013.06.021.
- García, V., Robinson, R., Hongn, F., Cristallini, E., Yagupsky, D., Winocur, D. & Vera, D., 2013b. Late Quaternary uplift rate of Lomas de Carabajal, Lerma valley, Cordillera Oriental, NW Argentina. Insights from structural analysis and OSL dating. *4th International INQUA Meeting on Paleoseismology, Active Tectonics and Archeoseismology*. Aachen (Germany).
- García, V., Hongn, F., Pingel, H. & Strecker, M., 2017a. Estructura y neotectónica de la sierra de los Alisos, provincia de Jujuy. *XX Congreso Geológico Argentino*, Actas ST2, Tucumán.
- García, V.H., Casa, A., Hongn, F., Figueroa, S., Aranda, G., Escalante L., Montero, C., Yamín, M., Amengual, R. & Aramayo, A., 2017b. Deformación cuaternaria. In: *Relatorio del XX Congreso Geológico Argentino* (Murua, C., Grosse, P., eds.). Tucumán, Argentina.
- Gebhard, J.A., Giudici, A.R. & Oliver, J.O., 1974. Geología de la comarca entre el río Juramento y el arroyo Las Tortugas, provincias de Salta y Jujuy, República Argentina. *Revista de la Asociación Geológica Argentina* 29(3), 359-375.
- INPRES, 2017. *Historical earthquakes in Argentina*. <http://contenidos.inpres.gov.ar/sismologia/historicos>.
- Marquillas, R.A., del Papa, C. & Sabino, I.F., 2005. Sedimentary aspects and paleoenvironmental evolution of a rift basin: Salta Group (Cretaceous–Paleogene), northwestern Argentina. *International Journal of Earth Sciences* 94, 94–113. <http://dx.doi.org/10.1007/s00531-004-0443-2>.
- Mon, R. & Salfity, J., 1995. Tectonic evolution of the Andes of northern Argentina. In: *Petroleum basins of South America* (Tankard, A., Suárez Soruco, R & Welsink, H. eds.). American Association Petroleum Geologist Memoir 62, 269-283.
- Monaldi, C., González, R. & Salfity, J., 1996. Thrust fronts in the Lerma valley (Salta, Argentina) during the Piquete Formation deposition (Pliocene-Pleistocene). *3rd International Symposium on Andean Geodynamics*, Extended Abstracts, 447-450. St. Malo, France.
- Pearson, D.M., Kapp, P., DeCelles, P.G., Reiners, P.W., Gehrels, G.E., Ducea, M.N. & Pullen, A., 2013. Influence of pre-Andean crustal structure on Cenozoic thrust belt kinematics and shortening magnitude: Northwestern Argentina. *Geosphere* 9(6), 1766-1782.
- Robinson, R.A.J., Spencer, J.Q.G., Strecker, M.R., Richter, A. & Alonso, R.N., 2005. Luminescence dating of alluvial fans in intramontane basins of NW Argentina. In: *Alluvial Fans: Geomorphology, Sedimentology, Dynamics* (Harvey, A.M., Mather, A.E. & Stokes, M., eds.), 153–168, London.
- Schildgen, T.F., Robinson, R.A.J., Savi, S., Phillips, W.M., Spencer, J.Q.G., Bookhagen, B., Scherler, D., Tofelde, S., Alonso, R.N., Kubik, P.W., Binnie, S.A. & Strecker, M.R. 2016. Landscape response to late Pleistocene climate change in NW Argentina: Sediment flux modulated by basin geometry and connectivity. *Journal of Geophysical Research* (ES) 121(2), 392-414.
- Slemmons, D. B. & de Polo, C. M. 1986. Evaluation of active faulting and associated hazard. In: *Active Tectonics* (Wallace, R.E., ed.). National Academy Press, Washington, 45–62.
- Turner, J.C.M. & Mon, R. 1979. Cordillera Oriental. *II Simposio de Geología Regional Argentina*. Academia Nacional de Ciencias de Córdoba, 1, 57–94.
- Wells, D.L. & Coppersmith, K.J., 1994. New empirical relationships among magnitude, rupture length, rupture width, rupture area, and surface displacement. *Bulletin of the Seismological Society of America* 84, 974-1002.

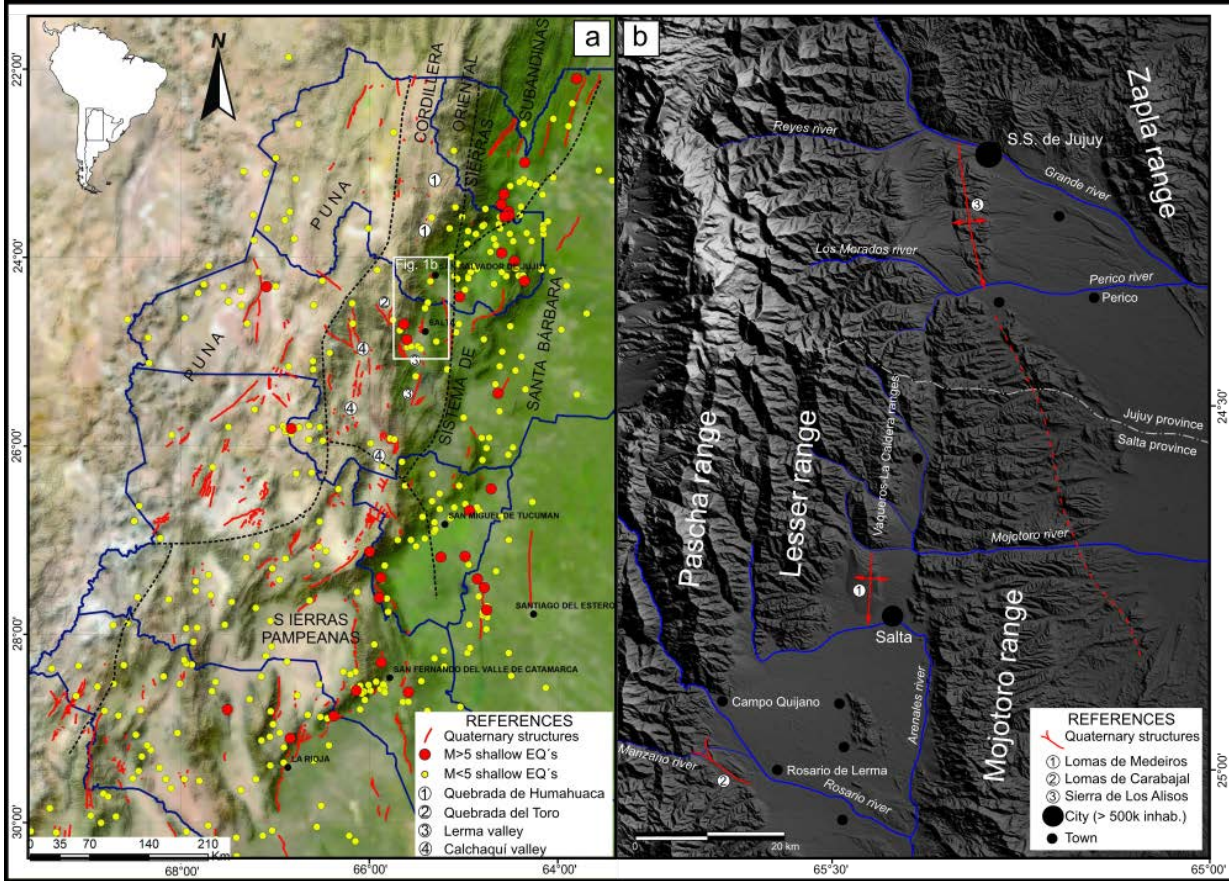


Figure 1: a) Location of the studied area in the framework of the geological provinces of NW Argentina. Quaternary structures and shallow seismicity are also indicated (modified from Garcia et al., 2017b). b) Detailed location map with the Quaternary structures described in the text.



Tectonic Geomorphology, Late Quaternary Slip Rate, and Paleoseismology of the Whittier Fault in Southern California

Gath, Eldon (1), Gonzalez, Tania (1), Rockwell, Tom (2)

- (1) Earth Consultants International, Santa Ana, California USA. gath@earthconsultants.com.
 (2) San Diego State University, San Diego, California USA.

Abstract: The 40-km long Whittier fault bounds the southern margin of the Puente Hills in the eastern Los Angeles Basin, right-laterally deflecting all fault-crossing stream channels. This fault accommodates the westward extrusion of the basin due to the oblique northwesterly convergence of the Santa Ana Mountains with the north-vergent Puente Hills thrust, lying south of the San Gabriel Mountains. The Whittier fault began as a Miocene normal fault, but geomorphic reconstructions of the deformed fluvial system and dating of a suite of fill terraces indicates that it has reactivated as a right-lateral strike-slip fault. 3-D trenching of the fault within the Olinda oil field exposed seven late Quaternary alluvial channels, with increasing displacement with age from a main feeder channel. Three of the channel deposits were radiocarbon dated: one channel (10,600 BP) is displaced 11 m, another (14,700 BP) 18 m, and the oldest channel (17,700–19,000 BP), 27 m. These yield a minimum displacement rate of 1–1.5 mm/yr, as there is a second, geomorphically similar and parallel fault trace. If both strands transfer similar amounts of slip, as suggested by their geomorphology, then we estimate a dextral slip rate of 2.5–3.0 mm/yr for the entire Whittier fault zone. Stratigraphic relationships permitted the interpretation of at least five surface offsets between <10 ka and >19 ka, yielding a recurrence interval of ≥ 2 –2.5 ka. Studies about 3 and 8 km farther southeast constrained the MRE to between 1,400–2,200 BP, and the penultimate event to $\sim 3,400$ BP. Given that our results indicate the Whittier fault has one of the highest slip rates in the Los Angeles basin, and that it may have accumulated as much as 4–5 m of potential slip since its last surface rupture, it could be one of the most dangerous structures in the greater Los Angeles region.

Key words: Tectonic geomorphology, Paleoseismology, Whittier fault

INTRODUCTION

The Whittier fault is a major structural element of the eastern Los Angeles basin that forms the northwesternmost 40-km-long segment of the Elsinore fault zone between the Santa Ana and San Gabriel rivers. As such, the Whittier fault is accommodating neotectonic strain from the Gulf of California transform system directly into the Los Angeles (LA) metropolitan area (Figure 1). The fault strikes about N70° W and dips from 65° to 80° to the northeast, forming a structural contact between the Miocene Puente Formation to the north, and the Plio-Pleistocene Fernando and La Habra formations to the south (Durham and Yerkes, 1964; Yerkes, 1972; Tan et al., 1984). The north dip of the fault places older rocks structurally over younger rocks. This relationship, combined with the elevated Puente Hills to the north, has led many workers to assume that the Whittier fault has a large component of reverse slip (Bjorklund and Burke, 2002; Davis et al., 1989). The amount and sense of slip, however, has been the source of some controversy and is addressed in this paper.

TECTONIC GEOMORPHOLOGY

The geomorphology along the Whittier fault is profoundly indicative of right-lateral faulting. All major fault-crossing streams are right-laterally deflected where they cross the Whittier fault (Fig 2). Hill (1954) recognized that all of the deflections were oriented in a right lateral (RL) sense, not randomly left and right as would be expected from erosion alone, leading him to conclude that active

tectonics was the most likely cause. The abundance of small offsets associated with small streams and canyons (Fig. 3) and larger displacements of the major canyons support a tectonic interpretation, as does the observation that the deflections are generally up the regional stream gradient. This leads to the conclusion that the predominant sense of slip on the Whittier fault during the late Quaternary has been RL strike-slip.

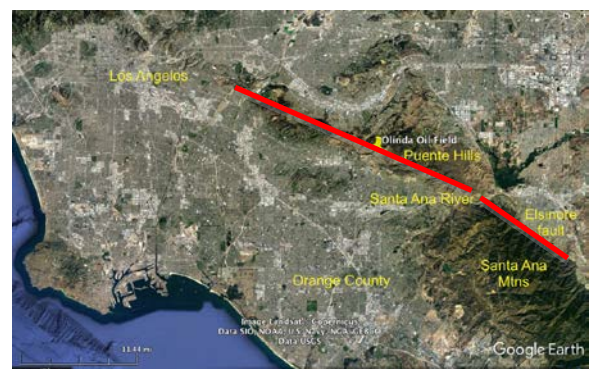


Figure 1: Index map of eastern Los Angeles basin, showing the Whittier and Elsinore faults, and the Olinda oil field study site.

As part of the tectonic geomorphic mapping, 130 stream deflections were measured directly from stereo aerial photographs, supplemented with field measurements (Fig. 4). The largest drainages (Tonner, Carbon, and La Mirada) have the greatest amount of right deflection at nearly 1700 meters. The major tributary canyons to the



Santa Ana River have all been deflected 400 ± 50 meters, also in a right lateral sense. The smallest gully offsets observed were 4 and 8 meters (Fig. 3) but there are clear groupings of deflection amounts (Fig. 4). These deflections strongly correlate with drainage basin area; larger drainages are deflected more than smaller ones, a correlation that supports the tectonic interpretation for the channel deformations.



Figure 2: Vertical DEM of the Puente Hills showing the pronounced deflections of the streams where they cross the Whittier fault (opposing red arrows). Right-lateral displacement by repeated earthquakes has offset every fault-crossing stream. Olinda Creek trenching site shown by red circle



Figure 3: Photo from the Olinda Oil Field showing an 8-meter right-lateral offset of a small drainage swale (arrows). The fault location (dashed red line) was confirmed by trench excavations off both sides of the photo.

SLIP RATE

Two strands of the Whittier fault are well expressed in the landscape across the Olinda Oil Field in the eastern LA Basin. Both fault strands were exposed in stream bank cuts with the southern fault dipping to the north and the northern fault dipping to the south, forming a positive flower structure (Fig. 5). Both faults displayed reverse separation placing Miocene Puente Formation over late Pleistocene channel bank colluvium.

A 3-D trenching pattern was employed to expose and measure laterally displaced channel deposits south of the fault. A total of 14 trenches were excavated, with ten of the trenches situated in a dense array oriented both parallel and normal to the fault (Fig. 6). The fault-parallel trenches were emplaced to intercept the margins of buried stream channels and obtain piercing lines across the fault, measured from the feeder channel margin on the north side of the fault.

Many of the trenches were enlarged by hand to ensure continuity of the stratigraphy, and to minimize data loss from over-digging a trench. A Wild TC-2000 Total Station surveying system was used to map stratigraphic markers, major fault splays, and charcoal-sample collection locations within the three-3-D framework of the trench locations.

Figure 6 shows thinly stratified alluvial sediments in apparent reverse contact with bedrock of the Puente Formation. The main trace of the southern fault contained a well-developed shear fabric between the bedrock and the alluvium. The alluvial sequence was divided into seven primary stratigraphic units (A-G) based on abrupt lithologic changes for the deeper units (E-G), and on intercalated alluvial and colluvial channel-margin wedges for the higher units (A-D). Most of the units contained chunks of detrital charcoal that were collected for radiocarbon dating.



Figure 4: Sorted plot of measured stream deflections across the Whittier fault.



Figure 5: Olinda Creek paleoseismic trenching location showing some of the trenches that were excavated perpendicular to the fault to locate the fault and define the channel margin stratigraphy. Fault-parallel trenches were excavated later. The two strands of the fault (dashed red lines) form both sides of a positive flower structure. Blue arrows show the ± 30 meter offset of Olinda Creek across the southern (left) fault trace, and the similar offset across the central (right) fault strand. Oil field operations straightened the stream channel.

The channel margins south of the fault were defined by the intersection of the most westerly occurrence of channel sands and associated colluvial deposits of the channel wall slope. The closely spaced trenching pattern and the stratigraphic resolution allowed the margins to be defined within about 0.5 m. The four channel margins on the southwestern side of the fault (Units A, B, C, & D) served as piercing points to measure the amount of lateral slip across the fault (Fig. 7). Similar margins for Units E, F, and G exceeded our westernmost trenching limits, but were constrained to 32-35 m by the Puente Formation outcrops (Fig. 7).

The fluvial system is fed from a primary feeder channel on the north side of the fault and all channels are progressively offset to the west. Although channels B and C appear to be reversed downstream, they are in correct stratigraphic order at the fault. Measuring from the westernmost margin of the feeder channel, Channels A through D are progressively offset from 11.2 ± 0.5 to 27 ± 1 meters, with the error being 1/2 the width of the 1-m trench width. Although well constrained to the west the offsets are

minimum values due to the uncertain position of the feeder channel at the time the displaced channels were active.

Radiocarbon ages were obtained from three of the channel deposits (Table 1) and, along with the measured channel margin offsets, these ages were used to calculate slip rates. As these are all minimum offsets, we prefer the longer-term RL slip rate of 1.5 mm/yr for this southern strand of the fault.

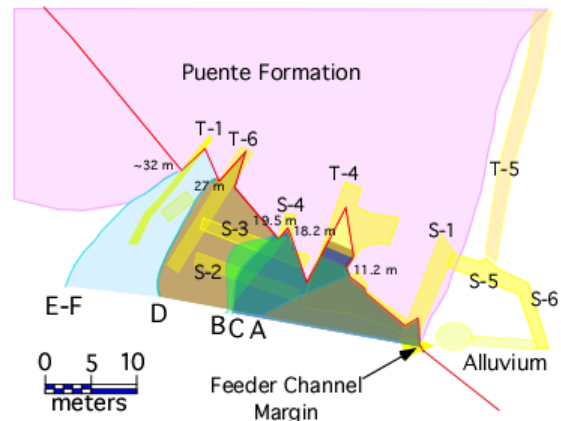


Figure 7: Map of Olinda Creek trenching site showing trenches, channel margins, and the Whittier fault. The system is fed from a primary feeder channel on the north side (top) of the fault and all channels are progressively offset to the west. North is to the top.

Channel	Median Age (years BP)	Minimum Offset (m)	Minimum Slip Rate (mm/yr)
A	$10,650 \pm 240$	11.2 ± 0.5	1.1 ± 0.1
B	$14,270 \pm 535$	18.2 ± 0.5	1.3 ± 0.1
C	N/A	19.5 ± 0.5	N/A
D	$17,700 \pm 250$	27.0 ± 1.0	1.5 ± 0.1
G	20,000-24,000	32-35	1.5 ± 0.2

Table 1: Summary of slip rate calculations for the three radiocarbon dated piercing-point channels. Age of Channel G deposits is estimated based on regional Pleistocene river incisions during the last glacial maximum.

Due to its similar geomorphic expression, but somewhat smaller channel deflections, we infer that the northern strand of the fault has a similar although slightly lower slip rate, yielding a value of 2.5-3.0 mm/yr as the preferred late-Pleistocene slip rate for the Whittier fault.



Figure 6: Composite photomosaic log of Trench 4 showing the alluvial stratigraphy of Olinda Creek in apparent reverse separation fault contact with the Puente Formation (right). The darker layers in the alluvium are colluvium, the lighter units are alluvium.



PALEOSEISMOLOGY

Because the fault was bound by bedrock on the north side, events were impossible to discern at the main fault trace, but the upwardly flowering nature of the fault within the bedrock (Fig. 6) would imply multiple surface-rupturing events. The events that we were able to interpret involved smaller, secondary fault offsets, branching from the main fault into the alluvial sediments. Figure 7 shows two such minor faults that allowed us to interpret two separate events.



Figure 7: Photo from Trench 4 showing two of the events interpreted within the alluvial stratigraphy. The three thin dark layers are charcoal-rich burn horizons.

Event 1 branches from the main fault near the lower right corner of Figure 7. This rupture affects the alluvial deposits up to the prominent dark layer, which may be warped but is clearly not displaced; the fault does not propagate above it. Event 2 branches from the main fault higher in the section, truncates the dark layer overlying the earlier rupture and is in turn capped by a prominent sand layer just off the top of the photo. Table 2 provides a discussion of the event chronology.

CONCLUSIONS

Geomorphic strip mapping and 3D trenching of the Whittier fault have demonstrated that it is an active, right-lateral, strike-slip fault. All streams are right-laterally deflected where they cross the fault, and larger streams are deflected more than smaller streams. Three-dimensional trenching of the fault in Olinda Creek has yielded a minimum late-Pleistocene slip rate of 1.5 ± 0.1 mm/yr on one of two geomorphically similar fault strands, for a preferred total rate of 2.5-3.0 mm/yr. Based on measured channel separations, the vertical component of offset is less than 10% of the horizontal.

The paleoearthquake sequence is incompletely resolved, but appears to indicate a 1500-2000 year recurrence interval, implying large events with potentially 4+ meter displacements. The last event on the Whittier fault occurred between 2100 and 1600 BP (Patterson and Rockwell, 1993), so there is at least 4 meters of accumulated strain. From all the data collected, and our interpretation of them, we conclude that the Whittier fault is one of the most dangerous structures in the Los Angeles Basin.

Event	Age Est.	Units	Explanation
EQ-7+	19-24 ka	E & F	Units E&F vertically offset by 1 m; 0.5 m greater offset than Unit D. This could be along-channel gradient differences, but interpreted as tectonic.
EQ-6+	17-19 ka	D, E, & F	Unit D is vertically offset only 0.5 m. Fault rupture is truncated by other Unit D strata.
EQ-5+	15-17 ka	C & D	Unit D beds overlying EQ-4 are offset. Rupture dies out within Unit C channel sands, and is sharply truncated by Unit B strata. Unit C is laterally displaced ~1.0 m more than Unit B, indicating event likely occurred during Unit C.
EQ-4+	10-14 ka	B	Unit B is offset. Unit A overlies the rupture.
EQ-3+	<10 ka	A	Unit A is displaced along the main trace of the fault. Multiple events missing.
Penultimate	2.2 – 3.9 ka		Offset channel sediments at Fig Creek.
MRE	2.2 – 1.6 ka		Based on displaced sediments at Bee Creek and an unfaulted colluvial deposit in Fig Creek.

Table 2: Proposed chronology of earthquake events. Based strictly on the Olinda study, we interpret a minimum of five events in about 10,000 years on the Whittier fault. The MRE and penultimate events come from two studies about 2 and 8 km, respectively, east of this Olinda site (Patterson and Rockwell, 1993).

Acknowledgements: Acknowledgement is made to Santa Fe Energy Company for access to the Olinda oil field for the trenching program. Thanks to so many for generous contributions of their time in the field, assisting with trenching, logging and surveying. This work was supported by Southern California Earthquake Center (SCEC) grants, and by USGS Contract No. 14-08-0001-G1696 to Gath.

REFERENCES

- Bjorklund, T. and Burke, K., 2002, Four-dimensional analysis of the inversion of a half-graben to form the Whittier fault-fold system of the Los Angeles basin. *J. Struct Geol* 24, 1369-1387.
- Davis, T.L., Namson, J., and Yerkes, R.F., 1989, A cross section of the Los Angeles area: seismically active fold and thrust belt, the 1987 Whittier Narrows earthquake, and earthquake hazard, *J. of Geophysical Research* 94, B7, 9644-9664.
- Durham, D.L. and Yerkes, R.F., 1964, Geology and oil resources of the eastern Puente Hills area, southern California: USGS Professional Paper 420-B, 62 p.
- Hill, M.L., 1954, Tectonics of faulting in southern California, in Jahns, R.H. (ed.), *Geology of southern California*: CDMG Bulletin 176, Ch. 4, 5-14.
- Patterson, A. C. and T. K. Rockwell (1993). Paleoseismology of the Whittier fault based on 3-dimensional trenching at Olinda Oil Field, Orange County, southern California (abs), *Geol. Soc. Am.* 25, no. 5, 131.
- Tan, S.S., Miller, R.V., and Evans, J.R., 1984, Environmental Geology of Parts of the La Habra, Yorba Linda and Prado Dam Quadrangles, Orange County, California: CDMG Open-file Report 84-24-LA, 113p.
- Yerkes, R.F., 1972, Geology and oil resources of the western Puente Hills area, southern California: USGS Professional Paper 420-C, 63 p.



Sedimentological features of Holocene gravel deposits: Implications for tectonic uplift in the southwestern Korean Peninsula (Yellow Sea)

Yong Sik Gihm, Sung-Ja Choi, You Bong Kim, Seung-Ik, Park

(1) Geology Division, Korea Institute of Geoscience and Mineral Resources (KIGAM), naress@kigam.re.kr

Abstract: Holocene gravel deposits located in southwestern coastline in the Korean Peninsula occur on the Cretaceous basement 2.5 to 3 m high above the mean water level. We analysed the sedimentological features of the gravel deposits using cm-scale stratigraphic logs as well as radiocarbon (AMS) analysis. We interpreted them as the Holocene beach deposits on the basis of seaward imbrication of disc-shaped clasts, clast-supported fabric, and abundance in rounded and well sorted gravels. The calibrated radiocarbon AMS age is estimated 2160 ± 30 BP. According to previous researches, since the beginning of the Holocene, the sea level rose rapidly and reached the present sea level at 6 ka. Thus, occurrence of the raised Holocene deposits along the coastline can result from tectonic uplift following the deposition. Future research, such as collecting age data, finding tectonic signature, and interpretation of cause of tectonic uplift, are needed to strengthen the interpretation.

Key words: Beach, Uplift, Sea level, Depositional

INTRODUCTION AND PHYSIOGRAPHIC SETTINGS

The Korean Peninsula is located in the far eastern part of Eurasian Plate and is generally regarded as intraplate, stable tectonic settings. But, ENE compression induced by combined effects of subduction of the Pacific Plate and collision of the Indian Plate beneath the Eurasian Plate resulted in moderate earthquakes along the NE-SW trending, Quaternary faults (e.g. Yangsan, Ulsan faults) in the Korean Peninsula (Choi & Jeon, 2016 and references therein). In addition, uplift of the eastern part of the Korean Peninsula has given rise to a series of Quaternary marine terraces along the coastlines. In contrast to the eastern coastline, geomorphic and geologic features related with the tectonic uplift are rare along the western coastline. Recently, we have found and sedimentologically analysed the raised Holocene deposits. With combination of future analysis, such as detailed age dating and tectonic stress, this study will improve the understanding of tectonic uplift in western part of the Korean Peninsula.

The study area is located in southwestern part of the Korean Peninsula, where numerous islands are scattered on the Yellow Sea (Fig. 1). Geologically, the study area is composed mostly of the Cretaceous volcanic rocks (e.g. tuff, rhyolite) that are underlain unconformably by the Jurassic granite and the Precambrian schist. The volcanic rocks are intruded by the Cretaceous granite porphyry with minor feldspar and quartz porphyry (Fig. 1; Choi et al., 2016). The volcanic rocks are unconformably covered by the Quaternary aeolian sand dunes and alluvium (Fig. 1, Choi et al., 2016). By reclaiming land from sea, some neighboring islands are connected to each other.

Coastlines of the study area are characterized by rocky coasts or cliffs that are commonly bounded on the seaward side by wave-cut platform and tidal flats. According to tidal records in the Mokpo station of Korea hydrographic and oceanography agency (KHOA), the tide is semidiurnal, and its range is mesotidal to macrotidal (Fig. 2; KHOA, 2017). Wave

data are also recorded by three buoys of Korea metrological agency (KMA, 2010 to present) around the study area, and average significant wave height is < 0.5 m with periodicity of 7s to 9s (Fig. 1; KMA, 2017). Although the wave height increases up to 2 m during winter season by northwesterly winds, the high wave only lasts one to two days. Also, even typhoon-induced, storm waves are not exceeded over 2 m during summer season (KMA, 2017). This is because the study area is partly exposed to open sea (Fig. 1).

The Holocene deposits in the study area occur on the Cretaceous basement in the embayment of rocky coastlines or cliffs. The Holocene deposits are composed of gravels of tuff and rhyolite as well as feldspar porphyry. There is no available coarse-grained sediment source adjacent to the study area. The gravels are thought to originate from wave erosion of rocky coast and cliff, which is well consistent with identical composition of the gravels to the Cretaceous basement.

SEDIMENTOLOGICAL FEATURES OF THE HOLOCENE DEPOSITS

The Holocene deposits occur unconformably on the Cretaceous basements (Fig. 2). The interface between them is sharp and gently inclined seawards (1°). The Holocene deposits are composed of well bedded, subrounded to rounded gravels; however, shapes and size of the gravels are variable. Based on morphology and caliber of gravels and depositional features, including clast imbrication, grain supported fabric, and sorting degree, we classify the Holocene deposits into four units (Unit-1 to -4; Fig. 2). Unit-1 is made up of angular to rounded cobble to boulder clasts (Fig 3a). The clasts show coarse-tail normal grading and clast-supported fabric (Fig. 2). Spherical and rod-shaped pebbles are also found in the voids. Unit-2 is composed mostly of pebble to cobble sized, spherical and rod-shaped clasts (Fig. 3b). Some blade-shaped clasts are found, and their a-b plane is inclined seaward (Fig. 3b). Unit-2 shows clast-supported fabric, and the voids infilled with well sorted very coarse sand with fine pebbles (Fig. 2). Near the boundary with the overlying pebbles



and cobbles (Unit-4) which is characterized by poor sorting and matrix(muddy sand)-supported fabric, the voids are filled with a muddy sand matrix. In YG-3, Unit-2 is interbedded with sand-rich layers, forming crude planar stratifications (Fig. 3c).

Unit-3 occurs only in YG-1 and is intercalated with Unit-4 (Fig. 2). Unit-2 is < 0.5 m thick and consists of moderately to well sorted pebble and cobble clasts (Figs 2 and 3d). The clasts are generally blade-shaped, and a-b plane of the clasts is plunged seaward (Fig. 4d). The clasts are framework-supported, and the space between the clasts is

filled with muddy sand. In YG-1, internal erosional surfaces are developed (Fig. 3e).

Unit-4 is laterally discontinuous and is dominated by angular to subangular pebble to cobble clasts, and some boulders are scattered (Fig. 2). The clasts are poorly sorted and disorganized, which is supported by muddy sand matrix. Plant fragments are abundant in the matrix (Fig. 3e). Unit-4 is decimeters thick and is entirely massive. The carbonized plant fragments have been dated using radiocarbon (AMS) analysis, and calibrated age is 2160±30 BP.

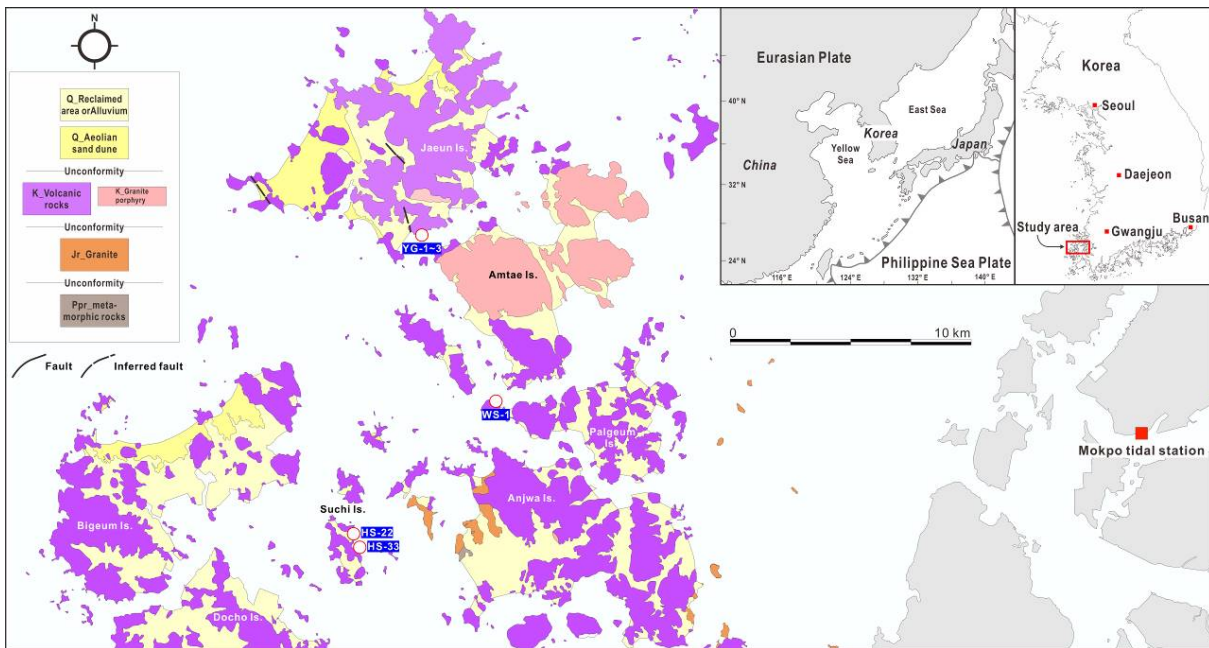


Figure 1. Geological map of the study area with tectonic outline in the foreast Eurasina Plate (inset) (Ppr: Precambrian, Jr: Jurassic, K:Cretaceous, Q: Quaternary).

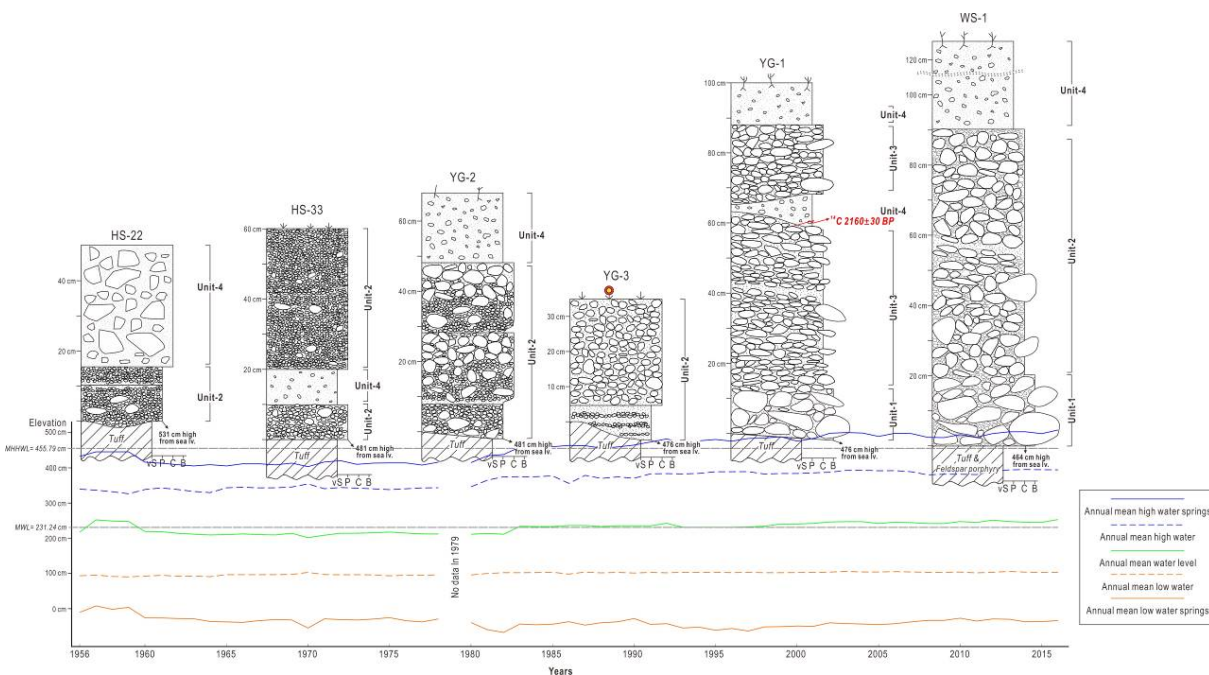


Figure 2. Stratigraphic logs of the Holocene deposits with tidal ranges recorded in the Mokpo tidal station.



Unit-1 to -3 of the Holocene deposits are interpreted herein as gravel beach deposits on the basis of seaward inclination of the blade-shaped pebble and cobble, framework- or clast-supported fabric, and abundance in moderately to well sorted, rounded to subrounded clasts (Bluck, 1967, 1999; 2011; Orford, 1977; Massari and Parea, 1988; Postma and Nemec, 1990; Hayes et al., 2010). The gently, seaward dipping interface between the Holocene deposits and the underlying basement is also inferred to form as a result of wave abrasion of the basement on intertidal to subtidal zone. This suggests accumulation of the gravel deposits on wave-cut platform (Bird, 2008). Unit-1 in the Holocene deposits is interpreted to be as lag deposits covering the wave-cut platform. The angular to subangular boulder clasts would derive from erosion from nearby rock cliff that fell on wave-cut platform. Their subangular edge is presumably due to low wave regime in the study area and/or insufficient time for abrasion, resulted from subsequent deposition of the overlying sediments. Spherical and rod-shaped pebbles and cobbles that interbedded with sand-rich layers of Unit-2 resemble an infill zone of Bluck (1967). The plentiful of the spherical and rod-shaped clasts are attributed to their higher pivotability than that of disc-shaped clasts, hence easily reworked by returning waves during relatively long-lasting, fair weather conditions (Buscombe and Masselink, 2006; Hayes et al., 2010). The sand-rich layers in YG-3 correspond to sand runs. Seaward-dipping, framework-supported, disc-shaped clasts indicate that Unit-3 is an imbricated disc-zone of Bluck (1967). The imbrication resulted from resistance of disc-shaped pebble and cobble clasts against backwash, and the framework-supported fabric is attributed to selective removal of fine-grained, spherical and rod-shaped particles (Bluck, 1967). Infilling of muddy sand in YG-1 is thought to be the products of infiltration of the matrix from the overlying Unit-4. The internal erosional surfaces are inferred to form by erosion by storm waves, followed by oblique deposition of disc-shaped clasts on the erosional surface (Massari and Parea, 1988). Poor sorting and abundant plant fragments suggest formation of Unit-4 without hydraulic wave segregation. The matrix supported fabric, lateral discontinuity, and massive features indicate that Unit-4 was deposited by *en masse* freezing of mass flows (e.g. debris flows or slumps; Nemec, 1990). The mass flows would result from slope instability of nearby mountains.

Alternatively, it is plausible that the Holocene deposits are regarded as the modern highest storm berms or tsunami deposits. However, the highest storm berms are unlikely, because the Holocene deposits are vertically exposure on the basement, in excess of the angle of repose of the gravels (40-45°). Furthermore, the shapes and size of the Holocene deposits are differ from storm berms that are composed mainly of disc-shaped cobble without imbrication (a large disc zone of Bluck (1967)). Tsunami deposits are also implausible, since the Holocene deposits do not show depositional features of tsunamite, such as significant erosional surface, bidirectional imbrication (resulted from inflows and backflows), grading patterns, and organic-rich layers (Fujino et al., 2007). In addition, the Holocene deposits occur only along the modern coastlines and cannot be traced landwards beyond the coastlines.

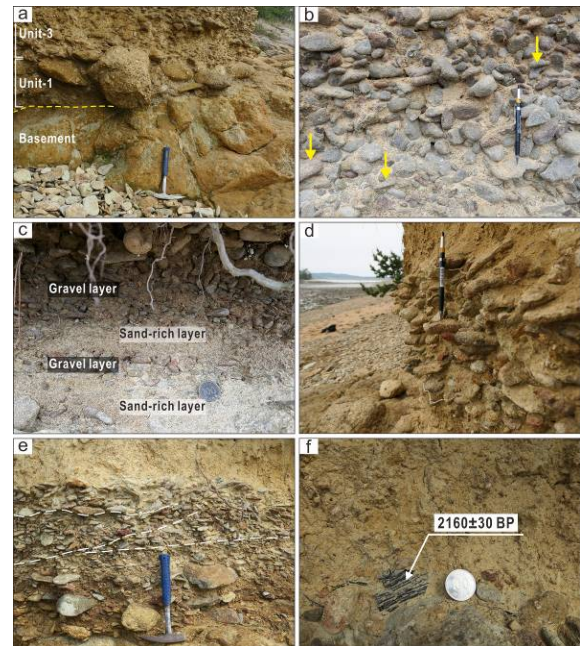


Figure 3. Photographs of the Holocene deposits in the study area. (a) Unit-1 composed of cobble and boulder frameworks on the Cretaceous basement. (b) Unit-2 made up of spherical and rounded clasts with seaward-imbricated, disc-shaped clasts (arrows). (c) Alternating layers of the gravel and sand-rich layer in Unit-2. (d) Seaward imbrication of the blade-shaped clasts in Unit-3. (e) Internal erosional surfaces (dashed lines) in Unit-3. (f) Plant fragment with C^{14} dating results of Unit-3.

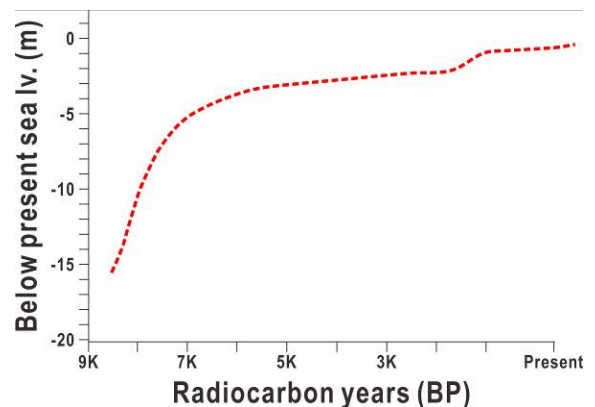


Figure 4. Sea level curve in the western coastline of the Korean Peninsula (after Lee & Chang, 2015).

SHORELINE RETREAT? OR TECTONIC UPLIFT?

Previous discussions suggest that the deposits are the Holocene beach deposits. The high stratigraphic position compared to modern shoreline resulted either from a drop of sea level or from uplift of shoreline. However, according to studies of the Holocene sea level curve (Lee & Chang, 2015 and references therein), the sea level are raised rapidly (10 mm/yr) by marine transgression since the beginning of the Holocene. At 6Ka, the rates of the sea level rise decelerates as low as 1 mm/year and approximately reached the present sea level. Thus, the Holocene deposits can be formed by tectonic uplift, likewise raised marine terrace along the eastern coastlines of the Korean Peninsula. Future



researches, such as age dating, seismic data related to tectonic uplift, tectonic outline in the western coastlines as well as sedimentological features associated with ground motion (soft-sediment deformation structures) are necessary to reveal the tectonic motion in the southwestern part of the Korean Peninsula.

Acknowledgements: This study is supported by a project "Research and Development of Active fault of Korea Peninsula (2017-MPSS31-006)" funded by Ministry of the Interior and Safety.

REFERENCES

- Bird, E., 2008. Coastal Geomorphology: an introduction. John Wiley & Sons, England, 411 p.
- Bluck, B.J., 1967. Sedimentation of beach gravels: examples from South Wales. *J. Sediment. Petrol.* 37, 128-156.
- Bluck, B.J., 1999. Clast assemblages, bed-forms and structure in gravel beaches. *Trans. R. Soc. Edinb. Earth Sci.* 89, 291-332.
- Bluck, B.J., 2011. Structure of gravel beaches and their relationship to tidal range. *Sedimentology* 58, 994-1006.
- Buscombe, D. & Masselink, G., 2006. Concepts in gravel beach dynamics. *Earth Sci. Rev.* 79, 33-52.
- Choi, K.H. & Seong, Y.B., 2014. The rock coast of Korea. In: *Rock Coast Geomorphology: A Global Synthesis* (Kennedy, D.M., Stephenson, W.J., Naylor, L.A. eds). The Geological Society, London, 203–224.
- Choi, S-J. & Jeon, S-S., 2016. Possibility of the Late Holocene uplift in the southeastern coast of Yeongil Bay, Korean Peninsula: Evidence from an exposed sea cave. *J. Asian Earth Sci.* 130, 256-264.
- Choi, S-J., Kim, Y. B., & Gihm, Y.S., 2016. Geological report of the Bungye, Jaeundo, Bigeumdo, and Gijwado Sheets, institute, Korea Institute of Geoscience and Mineralogy Resources (KIGAM). Daejeon, Korea.
- Fujino, S., Masuda, F., Tagomori, S., & Matsumoto, D., 2006. Structure and depositional processes of a gravelly tsunami deposit in a shallow marine setting: Lower Cretaceous Miyako Group, Japan. *Sediment. Geol.* 187, 127-138.
- Hayes, M.O., Michel, J., & Betenbaugh, D.V., 2010. The intermittently exposed, coarse-grained gravel beaches of Prince William Sound, Alaska: comparison with open ocean gravel beaches. *J. Coast. Res.* 26, 4–30.
- KHOA, 2017. http://www.khoa.go.kr/koofs/kor/webzine/bookstand.do?pub_type=1&paging=1, August, 8th, 2017
- KMA, 2017. <https://data.kma.go.kr/data/sea/selectFargoBuoyRltmList.do?pgmNo=55>, August, 3rd, 2017.
- Lee, E. & Chang, 2015. Holocene Sea Level Changes in the Eastern Yellow Sea: A Brief Review using Proxy Records and Measurement Data. *J. Korean. Earth Sci. Soc.* 36, 520-532. (Korean with English abstract)
- Massari, F. & Parea, G.C., 1988. Progradation of gravel beach sequences in a moderate to high-energy, microtidal marine environment. *Sedimentology* 35, 881-913.
- Nemec, W., 1990. Aspect of sediment movement on step delta slope. In: *Coarse Grained Deltas* (Colella, A., Prior, D.B. eds). IAS Special Publication, Blackwell Science, Oxford, pp. 29-74.
- Orford, J.D., 1977. A proposed mechanism for storm beach sedimentation. *Earth Surf. Process. Landf.* 2, 381-400.
- Postma, G. & Nemec, W., 1990. Regressive and transgressive sequences in a raised Holocene gravelly beach, southwestern Crete. *Sedimentology* 37, 907-920.
- Saito, Y., Yang, Z., & Hori, K., 2001. The Huanghe (Yellow River) and Changjiang (Yangtze River) deltas: a review on their characteristics, evolution and sediment discharge during the Holocene. *Geomorphology* 41, 219-231.



Which sedimentary environment best preserves paleoliquefaction features?

M. Giona Bucci (1), P. Almond (1), P. Villamor (2), M. Tuttle (3), M. Stringer (4), C. Smith (1), W. Ries (2), J. Bourgeois (5), R. Loame (6), J. Howarth (7), M. Watson (8)

- (1) Lincoln University, Soil Science Department, P O Box 85084, Lincoln, Christchurch, New Zealand. peter.almond@lincoln.ac.nz
- (2) GNS Science, P O Box 12345, Lower Hutt, New Zealand.
- (3) M. Tuttle & Associates, PO Box 345, Georgetown, ME 04548 USA
- (4) University of Canterbury, PO Box 4800, Christchurch 8140 New Zealand
- (5) University of Washington, College of the environment 1492 NE Boat St., Seattle, WA 98105
- (6) Waikato University, PO Box 3105, Hamilton 3240, New Zealand
- (7) Victoria University of Wellington, School of Geography, Environment and Earth Sciences, New Zealand
- (8) ScanTec, Geophysical Consultants, Ltd, PO Box 999, Whangarei, New Zealand

Abstract: We investigated the sedimentary architecture of alluvial and coastal environments affected by the 2010-2011 liquefaction events, with the aim of understanding why specific geomorphic elements are most prone to liquefaction. In the alluvial setting, we found that where liquefaction occurred, the inclined contacts of beds in the paleochannel and point bar deposits provided preferential flow paths for the liquefied material to travel to the surface. In the coastal dune environment, we found that since liquefaction source layers were close to the surface (<1 m) and the overlying soil is cohesionless, water escape during liquefaction caused fluidization and extreme disruption of the overlying soil profile. This makes investigation of paleoliquefaction features in the coastal setting particularly challenging. In contrast, the alluvial environment is the best setting for targeting paleoliquefaction features because the sediment characteristics, and regular sediment deposition provide for preservation and stratigraphic bracketing of paleoliquefaction features.

Key words: liquefaction, paleoliquefaction, alluvial and coastal environment, fluidization, liquefaction source layer

INTRODUCTION

Evidence of paleoliquefaction features in the soil profile provides information about the occurrence of past earthquakes ($M_w > 5$). Therefore, targeting sites that best preserve paleoliquefaction features is important for improving the paleoseismic record and better constraining seismic hazard assessments. Several studies have analysed the higher liquefaction susceptibility of alluvial, deltaic and coastal environments (e.g. Amick et al., 1990; Holzer et al., 2010; Holzer, 1998; Tinsley et al., 1998; Tuttle, 1999; Youd and Hoose, 1977; Youd and Perkins, 1978; Ziony, 1985). Recently, in the aftermath of the Canterbury Earthquake Sequence (CES) many studies were undertaken to investigate the liquefaction susceptibility of the alluvial environment, since it was the setting most affected by liquefaction (Almond et al., 2012; Bastin et al., 2015; Brackley et al., 2012; Quigley et al., 2013; Townsend et al., 2016; Villamor et al., 2016; 2014). In terms of prevalence of liquefaction, the alluvial environment was followed by the coastal setting which has only recently become the focus of detailed study (Giona Bucci et al., 2017a). Research interests related to the coastal setting of Christchurch have arisen also because some areas liquefied in all events, including the Valentine's Day event, while others areas did not (CGD0200, 2013). The study of the liquefaction features in the coastal setting of Christchurch provides an opportunity to examine the contrasting sedimentary architecture between coastal and alluvial environments, in order to better understand the potential for preservation of paleoliquefaction features. Our conclusions highlight the different factors influencing

liquefaction susceptibility, ground failure and formation of liquefaction features, and effects on soil stratigraphy in the two targeted environments.

STUDY SITES AND METHODS

In the coastal area of Christchurch, three sites were selected: Wainoni and QEII Parks in the urban area of Christchurch, and Featherston Avenue Reserve site, near Kaiapoi ~20 km north of Christchurch (Figure 1). In the alluvial setting, two sites were selected along the Halswell River floodplain (Figure 2, ~18 km southwest of Christchurch). The Hardwick and Marchand sites are characterized by a paleochannel buried by a crevasse splay and point bar deposits, respectively (Tuttle et al., 2017; Villamor et al., 2016). At all sites, we conducted a GPR survey (2D and/or 3D), excavated and logged trenches, retrieved hand piston cores and vibracores, collected grain size samples and organic material for dating.

RESULTS AND DISCUSSION

Style of liquefaction features

In the alluvial environment we found that liquefaction ejecta appeared aligned along paleochannel edges (at Hardwick site) and along point bar deposits (at Marchand site) (Tuttle et al., 2017; Villamor et al., 2016). In contrast, the liquefaction features of the coastal setting appeared randomly scattered, with a rounded shape, and mainly associated with interdune depressions where the water table was especially shallow (Giona Bucci et al., 2017a).

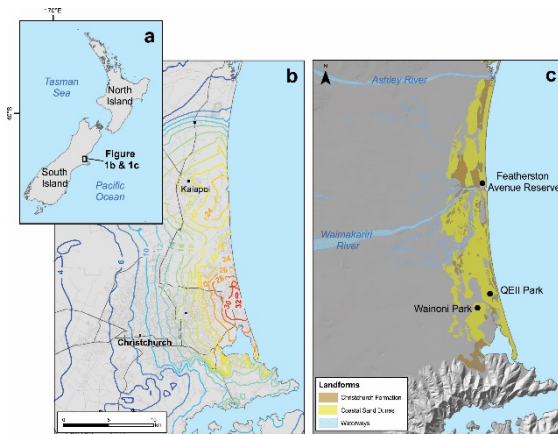


Figure 1: Location of coastal sites in Christchurch.

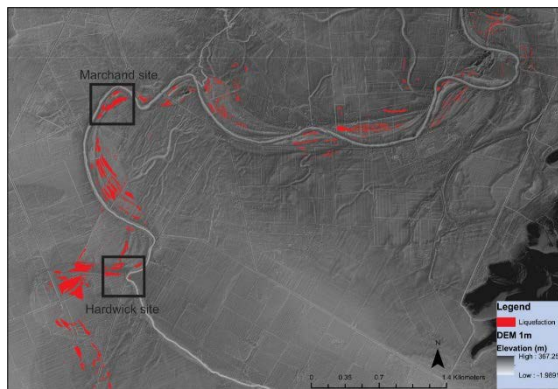


Figure 2: Alluvial sites along the Halswell River, ~18 km southwest of Christchurch.

Sedimentary characteristics

Grain size analysis from the Hardwick and Marchand sites showed that liquefiable sand underlay most of the alluvial floodplain (Villamor et al., 2016; 2014). However, the liquefaction source layers for ejecta were specifically identified as the sandy paleochannel deposits (at Hardwick site) and the point bar sediment (at Marchand site). In particular at Hardwick site, the use of grain size analysis, cross section stratigraphy and CPT (Cone Penetration Tests) (see for more details Giona Bucci et al., 2017, in review; Villamor et al., 2016) allowed us to identify that contacts of channel-fill and point bar deposits, characterized by sub-inclined surfaces facilitated movement of the liquefied sediment upwards, as shown in Figure 3. These findings are in agreement with previous research (Tuttle and Barstow, 1996), and with centrifuge experiments (Dobry and Abdoun, 2001; Dobry and Liu, 1994).

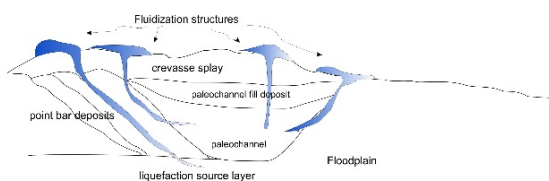


Figure 3: Model of the liquefaction features and fluidization pathways occurring in the alluvial environment (readapted from Giona Bucci et al., 2017, in review). The paleochannel deposits were the liquefaction source layers in this alluvial setting, while crevasse splay and paleochannel-fill deposit constitute the

overlying layer or top-stratum through which dikes were injected and on which sand blows or volcanoes were deposited. Clasts of the top-stratum can be entrained in the escaping slurry of water and sediment but otherwise does not fluidize as occurs into the coastal setting, see text for more details.

The investigation of the coastal environment showed that the coastal dune sediment is characterized by a shallower water table, well sorted and contains few fines. The absence of fines reduces the cohesion and plasticity of the sediment and enhances liquefaction susceptibility. Together, the shallow water table and sediment characteristics meant that liquefaction occurred within 1 m of the surface. Furthermore, the generally cohesionless nature of the overlying soil made it prone to the effects of fluidisation as water was ejected from the liquefied material beneath. This combination of phenomena (near-surface liquefaction and fluidisation) led to a unique suite of features in the soil including A horizon splitting, A-horizon foundering, pillow-like features and collapse features (for more details see Giona Bucci, 2017; Giona Bucci et al., 2017b). The severe disturbance of the soil profile made separate liquefaction events of the CES impossible to discriminate and presumably obscured any evidence of older (paleo) liquefaction events (Figure 4).

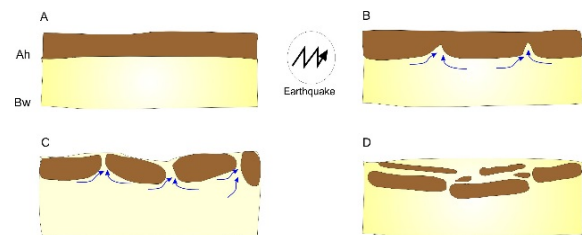


Figure 4 Generalized and simplified model of the liquefaction and fluidization occurring in the coastal setting. A) Soil horizons of the coastal setting before the earthquake; B) during the earthquake the cyclic seismic load causes the liquefaction of the Bw horizon. Liquefaction causes the Bw horizon to lose strength, therefore the Ah horizon founders or sinks into liquefied Bw sediment, forming depressions in the ground surface. As large pieces or clasts of Ah horizon founder, the liquefied sediment of the Bw horizon flows around the edges of the clasts forming 'cusps' type of features; C) some cusps extend between the clasts, forming pipes (dikes) that concentrate the flow of the slurry of water and entrained sediment, likely leading to an increase of velocity. The venting of the sediment from the pipes on the ground surface forms sand blows that fill the surface depression. D) The former Ah horizon has foundered into the liquefied and fluidized Bw horizon and this has also caused the A horizon to split up (A horizon splitting).

Topographic effect

Another aspect observed during our research is related to the concentration of liquefaction features on particular landforms such as the crevasse splay (at Hardwick site) and on the point bar ridges (at Marchand site). This could have been influenced by a topographic effect. At Hardwick site, it was not possible to excavate trenches and/or collect CPT tests south of the Hardwick property where liquefaction features were not observed and thus test our hypothesis that liquefaction features are spatially correlated with the crevasse splay and not just the underlying channel and point-bar deposits. However, the detailed sedimentary



architecture explored by Villamor et al (2016; 2014) and Giona Bucci et al. (2017, in review) provides two possible explanations: 1) the southern portion of the paleomeander was not in hydraulic connectivity with the modern active portion of the meander (Samadder-Ratan et al., 2011), therefore the sediment was not (entirely) saturated and it could not liquefy; 2) the crevasse splay is characterized by a concave profile topography and a slightly higher elevation. These two factors, taken together might have concentrated earthquake-related shear stress (Giona Bucci, 2017; Martel, 2016; Moon et al., 2017) and thus caused cracking, which facilitated surface evidence of liquefaction features.

Which sedimentary environment best preserves paleoliquefaction features?

This research brought to light that the coastal dune environment, particularly young dune deposits, are very susceptible to liquefaction and likely to result in surface manifestations of liquefaction due to the well-sorted nature of the sandy sediment and to the very shallow water table near the shoreline. As a result, fluidization process (water escape features, sensu Owen, 1987; 1996) affect the overlying soil causing severe disruption of the soil stratigraphy. Therefore, in a highly susceptible environment multiple liquefaction events are likely overprinted, hindering the ability to identify individual paleoliquefaction events. The lower frequency of deposition in the coastal dune environment is also less favourable to stratigraphic bracketing of paleoliquefaction features. Only at one of our coastal sites (Wainoni Park) we were able to identify paleoliquefaction features (AD 1730-1803 Giona Bucci, 2017) since the dunes were older (starting to form at least 1000 years ago) and the water table deeper (~1.50 m below the surface).

In conclusion, the alluvial setting is considered a better place than coastal dune setting for investigating paleoliquefaction features, for the following reasons: 1) the alluvial stratigraphy is characterized by sandy channel and point-bar deposits that are prone to liquefaction overlain by silty and clayey channel-fill and overbank deposits that are not prone to liquefaction and therefore likely to preserve sand dikes and sand blows ; 2) the higher frequency of sediment deposition of a floodplain will allow bracketing of liquefaction injection and ejections, forming cross cutting relations; and 3) floodplains have a higher content of organic material that can be dated. However, if the aim of the investigation is to confirm that earthquake-induced liquefaction has occurred in the past and not to establish the timing of paleoearthquakes, the coastal dune environment may provide a higher likelihood of success since it tends to contain sediment that is especially susceptible to liquefaction.

REFERENCES

Almond, P., Villamor, P., Tuttle, M., Langridge, R., Clark, K., Eger, A., Bastin, S., Quigley, M., Barker, P., and Vandergoes, M., Liquefaction induced by the 2010-2011 Canterbury earthquake sequence and implications from recently discovered

- paleoliquefaction features, in Proceedings GSA Annual meeting, 4-7 November Charlotte North Carolina, 2012.
- Amick, D., Gelinis, R., Maurath, G., Cannon, R., Moore, D., Billington, E., and Kempainen, H., 1990, Paleoliquefaction features along the Atlantic Seaboard: Division of Engineering Office of Nuclear Regulatory Research U.S Nuclear Regulatory Commission Washington DC 20555 NRC FIN D1682.
- Bastin, S., Quigley, M., and Bassett, K., 2015, Paleoliquefaction in Eastern Christchurch, New Zealand: Geological Society of America Bulletin v. 127, no. 9-10, p. 1348-1365.
- Brockley, H. L., Almond, P., Barrell, D. J., Begg, J., Berryman, K., Christensen, S., Dellow, G., Fraser, J., Grant, H., Harwood, N., Irwin, M., Jacka, M., Jones, K., Lee, J., McCahon, I., McMorran, T., Scott, D., and Townsend, D., 2012, Review of liquefaction hazard information in eastern Canterbury, including Christchurch City and parts of Selwyn, Waimakariri and Hurunui Districts: GNS Science Consultancy Report 2012/218, 99p.
- CGD0200, 2013, Liquefaction interpreted from Aerial Photography.
- Dobry, R., and Abdoun, T., Recent studies on seismic centrifuge modeling of liquefaction and its effects on deep foundations, in Proceedings International Conference on recent advances in geotechnical earthquake engineering and soil dynamics, Missouri, Mar 26th-Mar 31th 2001, Scholars'Mine.
- Dobry, R., and Liu, L., Centrifuge modelling of soil liquefaction, in Proceedings Earthquake Engineering, Tenth World Conference, Balkema, Rotterdam, 1994.
- Giona Bucci, M., 2017, Lessons learned from liquefaction of the Canterbury Earthquake Sequence (2010-2011) to inform paleoliquefaction studies [PhD Lincoln University, 320 p.
- Giona Bucci, M., Almond, P., Villamor, P., Ries, W., Smith, C., and Tuttle, M., 2017a, When the earth blisters: exploring recurrent liquefaction features in the coastal system of Christchurch, New Zealand: Terra Nova, v. 29, p. 162-172.
- Giona Bucci, M., Almond, P., Villamor, P., Tuttle, T., Stringer, M., Smith, C., Ries, W., Bourgeois, J., Loame, R., Howarth, J., and Watson, M., 2017b, Controls on patterns of liquefaction in a coastal dune environment, in prep.
- Giona Bucci, M., Villamor, P., Almond, P., Tuttle, M., Ries, W., Smith, C., Hodge, M., and Watson, M., 2017, in review, Associations between sediment architecture and liquefaction susceptibility in fluvial settings: the 2010-2011 Canterbury Earthquake Sequence, New Zealand: Engineering Geology.
- Holzer, T. L., Noce, T. E., and Bennett, M. J., 2010, Liquefaction Probability Curves for Surficial Geologic Deposits: Environmental & Engineering Geoscience, v. XVII, no. 1, p. 1-21.
- Holzer, T. L. c., 1998, The Loma Prieta, California, Earthquake of October 17, 1989-Liquefaction: United States Geological Survey.
- Martel, S. J., 2016, Effects of small-amplitude periodic topography on combined stresses due to gravity and tectonics: International Journal of Rock Mechanics and Mining Sciences, v. 89, p. 1-13.
- Moon, S., Perron, J. T., Martel, S. J., Holbrook, W. S., and St. Clair, J., 2017, A model of three-dimensional topographic stresses with implications for bedrock fractures, surface processes and landscape evolution Journal of Geophysical Research.
- Owen, G., 1987, Deformation Processes in unconsolidated sands.
- , 1996, Experimental soft-sediment deformation: structures formed by the liquefaction of unconsolidated sands and some ancient examples.: Sedimentology, v. 43, p. 279-293.
- Quigley, M. C., Bastin, S., and Bradley, B. A., 2013, Recurrent liquefaction in Christchurch, New Zealand, during the Canterbury earthquake sequence Geology, v. 41 No 4, p. 419-422.
- Samadder-Ratan, K., Kumar, S., and Gupta-Ravi, P., 2011, Paleochannels and their potential for artificial groundwater recharge in the western Ganga plains: Journal of Hydrology, v. 400, no. 1, p. 154-164.



INQUA Focus Group Earthquake Geology and Seismic Hazards



paleoseismicity.org

- Tinsley, J. C., Egan, J. A., Kayen, R. E., Bennet, M. J., Kropp, A., and Holzer, T. L., 1998, Appendix: Maps and descriptions of liquefaction and associated effects in Holzer, T.L.; ed.; The Loma Prieta, California, Earthquake of October 17 1989.
- Townsend, D., Lee, J., Strong, D., Jongesen, R., Smith Lyttle, B., Ashraf, S., Rosser, B., Perring, N., Cubrinovski, M., Taylor, M., Hughes, M., Wilson, T., Almond, P., Jacka, M., McCahon, I., and Christensen, S., 2016, Mapping surface liquefaction caused by the September 2010 and February 2011 Canterbury earthquakes- a digital dataset: *New Zealand Journal of Geology and Geophysics*, v. 59, no. 4, p. 496-513.
- Tuttle, M., and Barstow, N., 1996, Liquefaction-related ground failure: a case study in the New Madrid Seismic Zone, Central United States: *Bulletin of the Seismological Society of America*, v. 86 No3, p. 636-645.
- Tuttle, M. P., 1999, Late Holocene earthquakes and their implications for earthquake potential of the New Madrid seismic zone, central United States [PhD: University of Maryland, 247 p.
- Tuttle, M. P., Villamor, P., Almond, P., Bastin, S., Giona Bucci, M., Langdrige, R., Clark, K., and Hardwick, C., 2017 Liquefaction induced by the 2010-2011 Canterbury, New Zealand, Earthquake Sequence and Lessons Learned for the Study of Paleoliquefaction features: *Seismological Research Letters*, v. 88, no. 4.
- Villamor, P., Almond, P., Tuttle, M. P., Giona Bucci, M., Langridge, R. M., Clark, K., Ries, W., Bastin, S. H., Eger, A., Vandergoes, M., Quigley, M. C., Barker, P., Martin, F., and Howarth, J., 2016, Liquefaction features produced by the 2010-2011 Canterbury earthquake sequence in southwest Christchurch, New Zealand and preliminary assessment of paleoliquefaction features: *Bulletin of Seismological Society of America* v. 106, no. 4.
- Villamor, P., Giona Bucci, M., Almond, P., Tuttle, M., Langridge, R., Clark, K., Ries, W., Vandergoes, M., Barker, P., Martin, F., Bastin, S., Watson, M., Howarth, J., and Quigley, M., 2014, Exploring Methods to assess paleoliquefaction in the Canterbury area: GNS Science consultancy report 2014/183.
- Youd, T. L., and Hoose, S. N., 1977, *Proceedings of the Sixth World Conference on Earthquake Engineering: Indian Society of Earthquake Technology*, v. III, p. 2189-2194.
- Youd, T. L., and Perkins, D. M., 1978, Mapping liquefaction-induced ground failure potential: *Journal of geotechnical engineering division*, v. 104, no. 4, p. 433-446.
- Ziony, I. J. c., 1985, *Evaluating Earthquake Hazards in the Los Angeles Region- An Earth-Science Perspective*



Exploratory use of random forest classification for characterising and predicting patterns of liquefaction ejecta

Giona Bucci, M (1), Almond, P (1), Villamor, P (2), Case, B (3), Hodge, M (4)

- (1) Lincoln University, Soil Science Department, PO Box 85084, Lincoln, Christchurch. Monica.GionaBucci@lincolnuni.ac.nz
- (2) GNS Science, PO Box 12345, Lower Hutt.
- (3) Auckland University of Technology, 55 Wellesley Street East, Auckland Central.
- (4) UN. Statistical Institute for Asia and Pacific

Abstract: We carried out a random forest analysis (Machine Learning Technique) to characterise the pattern of ejecta on the Halswell River floodplain with the aim of applying this knowledge to predict the location of paleoliquefaction on similar landforms. We hypothesised that patterns of liquefaction ejecta had both subsurface controls related to sedimentary architecture, and surface controls influenced by 1) stress fields engendered by topography, and 2) the nature of the crust. Here we focus on possible surface controls. Both factors 1 and 2 are influenced by geomorphic characteristics, which we used an ensemble of micro-topographic parameters (elevation, slope, plan and profile curvature) to capture. Hence, if our hypothesis is correct we expect to find systematic relationships between ejecta presence/absence and microtopographic characteristics. Our random forest classifier appeared capable of recognising different landforms, and predicting liquefaction ejecta in a way consistent with the pattern at our training area.

INTRODUCTION

Liquefaction occurs in low lying areas of young Holocene sediment (<2000 years old) near waterways, where sandy or sandy silt sediment is water saturated, and near seismogenic sources that can cause a ground shaking of $PGA > 0.090 g$ (Santucci de Magistris et al., 2013). More specifically, liquefaction *surface manifestation* (ejecta) appear to be controlled by the local presence of (i) liquefiable sediment, (ii) a shallow water table (e.g. perched water table or confined and semiconfined aquifers) and (iii) by the existence of pathways (cracks or weaknesses) that the fluidised sediment can use to gain access to the surface (Giona Bucci et al., 2017, in review).

Landforms have specific morphological characteristics and are associated with characteristic sediment types (e.g. point bars or crevasse splays in a fluvial environment). Consequently, the liquefaction susceptibility of subsurface sediment, or the strength of surface crusts will be characterized by a specific geomorphology that may be identified by unique combinations of topographic attributes. Some studies also inferred that landforms' geometries determine surface gravitational stresses (Caputo, 2005), which may predispose certain parts of the land surface to tensional strain (via brittle failure and cracking) once a subsurface layer liquefies and loses shear strength. The latter is most strongly expressed in lateral spreading where free faces already exist, but is also hypothesised to occur where more gentle topographic variation prevails and not necessarily in proximity to free faces. In other words, the landforms' geometry, inferred by microtopographic parameters plays a critical role in the liquefaction surface manifestation.

It is hypothesised that microtopographic parameters derived by LiDAR DEM have predicative power with respect to the location of liquefaction ejecta. The aim of this

research is to assess whether it is possible to adopt a novel approach based on a Machine Learning scheme, in particular the Random Forest algorithm (Breiman, 2001, 2004), to objectively formalise the relationships between liquefaction ejecta presence or absence and microtopographic parameters. If statistically significant relationships exist, the microtopographic parameters may provide a basis for better discriminating potential areas where liquefaction ejecta will occur under a given ground shaking in the future, or where paleoliquefaction may have occurred as a result of past earthquakes.

To achieve this aim the following objectives are established:

- 1) Understand the correlation between liquefaction manifestation and micro-topographic parameters. By using the CES (Canterbury Earthquake Sequence) liquefaction surface manifestation mapping in conjunction with a high resolution DEM derived from LIDAR. Machine Learning Techniques are used to derive a new classification that links specific microtopographic parameters with liquefaction surface manifestation;
- 2) Understand whether the microtopographic parameters can accurately predict the liquefaction surface manifestation, and what is the sensitiveness of the classifier;
- 3) Apply the classification issued in a new area outside the Canterbury Region where there is no modern evidence of liquefaction features. The Manawatu River Basin was chosen as a target area to apply the algorithm. This area was selected because it has high liquefaction susceptibility (it has also historically liquefied, see Beetham et al., 2011) and has similar geomorphic expression to the machine learning CES training sites used.



METHOD

Machine Learning is a set of data mining techniques used in discovering structural patterns within a dataset. In particular, machine learning is useful for datasets where non-linear relationships cannot be solved by using basic regression methods (Hastie et al., 2009; Witten et al., 2011).

One of the techniques that belong to the Machine Learning ensemble is Random Forest. The Random Forest grows many decision trees. Decision trees are a style of representation characterized by nodes and leaves, where each node splits an attribute into two subsets. After a large number of trees is generated, the most popular class is chosen by the algorithm (Breiman, 2001). This procedure has been demonstrated to be an effective tool for predictions¹ and an accurate classifier (Breiman, 2001). A training dataset is used in the random forest procedure to enable the algorithm to learn the classification. Then a confusion matrix output provides an evaluation of how well the classifier has learnt and what will be the performance of the classifier on the testing dataset. Once the model validation is carried out, the method is applied to a new area where its purpose is to predict certain behaviour (in this case surface manifestation of liquefaction).

The data used in this study were obtained from precise digital elevation models (DEMs) for the three study sites (two Canterbury training sites, Hardwick and Marchand, and one application site in Manawatu region) and re-sampled at 10-15-20 m resolution, and from detailed maps of surface manifestation of liquefaction. The relevant micro-topographic parameters for the analysis presented here were derived from the DEM and are: elevation, slope (measured in percent rise), profile and plan curvature, by using the Surface analysis toolset in ArcGIS 10.2. These micro-topographic parameters are characterized by a relationship among themselves (the curvature is the second derivative of the surface) but also with the presence or absence of liquefaction; the latter extracted from the detailed liquefaction maps.

RESULTS AND DISCUSSION

Topographic predictors and the random forest model

Examples of decision trees obtained using the Hardwick and Marchand sites as training datasets are shown in Figures 1 and 2, respectively.

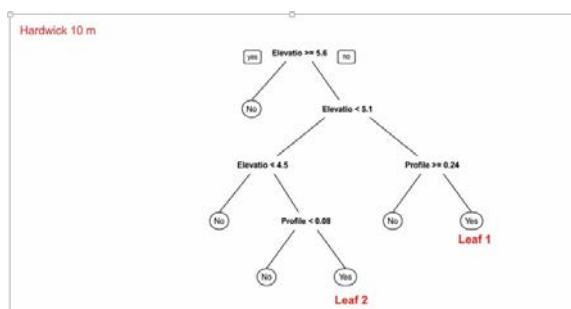


Figure 1: Decision tree from Hardwick site issued at 10m resolution.

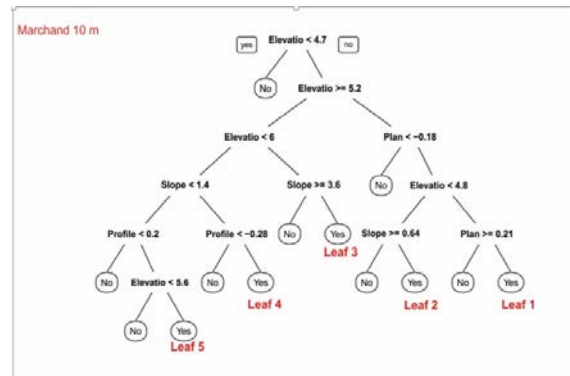


Figure 2: Decision tree from Marchand site issued at 10 m resolution.

At both sites it appears that Elevation is the most important variable determining liquefaction manifestation, followed by Slope and Profile curvature. Plan Curvature appears to have a minor role. The difference in resolution (10-15-20 m pixel resolution) does not seem to affect the sensitivity of the classifier, and the micro topographic variables appear in the same order across all the model resolutions.

The model is expected to perform well: the ROC value (receiver operating characteristics) for all the trees is in the range of 0.95-0.99 indicating the model has a very high accuracy, corroborated also by the confusion matrix.

Qualitatively, the classifier at 10 m resolution is the most geomorphically plausible predictor of liquefaction surface manifestation. All the leaves predict ejecta on alluvial geomorphic features known for being liquefaction susceptible (scroll bars and more in general inner meander bend) (Holzer et al., 2010). The testing of the classifier at 15 and 20 m resolution revealed generally the predictions were plausible but there was a small proportion of implausible predictions.

Application of Random Forest technique to predict sites of surface manifestation of liquefaction in the Manawatu River catchment

The detailed geomorphology of the chosen Manawatu River meander is shown in Figure 3. A geomorphic map was constructed for the meander with the purpose of showing the geomorphic association of the predicted liquefaction ejecta. Figure 4 shows the application of the classifier to the Manawatu River at 10 m resolution.

The random forest classifier predicts the scroll bar and natural levee landforms as sites susceptible to liquefy and be affected by surface ejecta, in line with the most recent literature (Alessio et al., 2013; Bastin et al., 2015; Civico et al., 2015; Tuttle, 2001; Villamor et al., 2016; Wotherspoon et al., 2012) and our findings (Giona Bucci et al., 2017, in review). In contrast, the abandoned paleochannels are never identified as potential locations for liquefaction surface manifestation at any of the topographic resolutions employed. From a sedimentology perspective,

¹ In Theorem 1.2 explained in Breiman (2001) it is demonstrated that the random forests do not overfit as more trees are added, due to the Law of Large numbers.



abandoned meanders are characterized by clay-rich sediment (clay-plug, see reference Ricci-Lucchi, 1980), which notably reduces the liquefaction susceptibility. From a topographic perspective the paleochannels are characterized by a much lower elevation and a general concave shape at the surface (positive values for profile curvature and negative values for plan curvature), a potentially more stable surface form (Talebi et al., 2008) less susceptible to cracking and thus less prone to allow sediment to come up at the surface. However, the ostensible plausibility of the results is not enough to definitively prove that the model is robust and that it can be used for predicting where liquefaction ejecta will occur, or have occurred in the past.

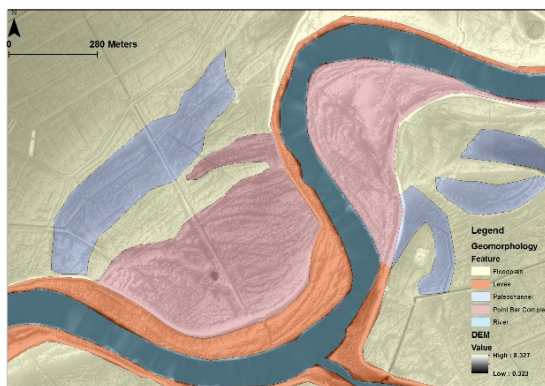


Figure 3: Geomorphic map of the Manawatu River (North Island, New Zealand).

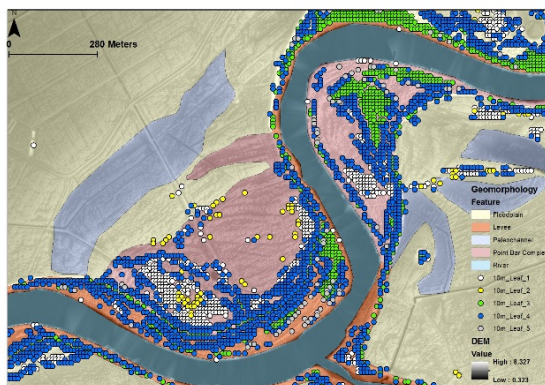


Figure 4: Application of the Classifier at 10 m resolution to the Manawatu meander.

All the predicted liquefaction ejecta are centred along the natural levee and in the inner meander belt of the river, in particular within the point bar area characterized by higher elevation.

Although several aspects of the classifier need further improvement, the use of the random forest algorithm suggests an association between the micro topographic attributes and liquefaction ejecta exists. The results represent correlation not causation, and it may be that the direct controls on the spatial pattern of liquefaction ejecta are the availability of liquefiable sediment at an appropriate depth, water table conditions and the nature of the surface soils. Nonetheless, the findings are consistent with the

hypothesis that surface gravitational stresses control paths for liquefaction ejection (Caputo, 2005), leading some parts of the landform to show greater liquefaction surface manifestation than others. In a 2-D modelling study of topographic influences on subsurface stress fields Martel et al. (2016) showed that pure gravitational stresses related to topography lead to horizontally oriented compressive stresses on ridges and horizontally oriented tensional stresses in valley bottoms in landscapes of low relief. This may suggest that liquefaction-induced loss of subsurface shear strength could lead to a propensity for cracking and ejection of sediment in the low elevation parts of the landscape. However, these authors also show that where tectonic compressional forces dominate gravitational forces the pattern of tensional and compressive stresses change. Under this condition ridges become zones of vertical tension, while valleys become compressive. An outcome could be the formation of sheeting cracking planes subparallel to the land surface over the ridge, the latter potentially forming sediment flow pathways (dikes). Moon et al. (2017) extended this kind of modelling work to three dimensions and showed that the shape and thickness of the subsurface zone prone to fracturing was dependent on firstly, the ratio of tectonic to gravitational stresses and, secondly, the curvature of the overlying topography; more highly curved parts of the landscape had thicker zones of fracturing, and those zones were thickest near ridges and thinnest under valleys. Although these studies assumed isotropic rock masses and constant tectonic stresses they suggest possible important interactions between topography and imposed external stresses that could provide insights into subsurface fracturing patterns relevant to understanding how liquefied sediment vents to the surface. The appropriateness of the analogies drawn here to cyclical earthquake stresses remains an open question that would require rigorous geomechanical modelling outside the scope of the present research to answer.

Limits of the random forest algorithm to predict the liquefaction ejecta

One of the limitations of this random forest application is the use of only four attributes (elevation, slope, profile and plan curvature) for predicting the surface manifestation of liquefaction. In our application of random forests, PGA (peak ground acceleration), water table, and distance from the epicentre are not considered as predictors for the model because these variables were either unknown (e.g. water table) or essentially invariant over the small study area (P.G.A., distance from epicentre). In order to test more parameters as predictors of liquefaction ejecta we suggest the selection of a wider study area over which PGA values, along with other derived predictors (shear wave velocity, shear modulus and differences in sedimentary settings) would vary and hence be potentially suitable as predictors for the classifier.

SUMMARY

In summary, the Random Forest classifier applied to microtopographic parameters shows potential for being used in an automated prediction of liquefaction surface



manifestation. Tests of the Random Forest algorithm have identified specific geomorphic features as liquefaction prone areas. However, the study does not systematically succeed in identifying these sites, or over-predicts liquefaction occurrence. This new method provides insights into the topographic conditions sufficient for occurrence of liquefaction ejecta. Therefore, it will support (but not replace) other important tools such as geomorphic mapping and subsurface geological, geotechnical and groundwater models for locating study sites for paleoliquefaction investigations.

REFERENCES

- Alessio, G., Alfonsi, L., Brunori, C. A., Burrato, P., Casula, G., Cinti, F. R., Civico, R., Colini, L., Cucci, L., De Martini, P. M., Falucci, E., Galadini, F., Gaudiosi, G., Gori, S., Mariucci, M. T., Montone, P., Moro, M., Nappi, R., Nardi, A., Nave, A., and Pantosti, D., 2013, Liquefaction phenomena associated with the Emilia earthquake sequence of May–June 2012 (Northern Italy): *Natural Hazards and Earth System Sciences*, v. 13, p. 935–947.
- Bastin, S., Quigley, M., and Bassett, K., 2015, Paleoliquefaction in Eastern Christchurch, New Zealand: *Geological Society of America Bulletin* v. 127, no. 9-10, p. 1348-1365.
- Beetham, D., Begg, J., Barker, P., Levick, S., and Beetham, J., 2011, Assessment of liquefaction and related ground failure hazards in Palmerston North, New Zealand: *GNS Science consultancy report 2011/108*, v. July 2011.
- Breiman, L., 2001, Random Forests: *Machine Learning*, v. 45, p. 5-32.
- Caputo, R., 2004, Consistency for a simple model of Random Forest: *University of California*.
- Caputo, R., 2005, Stress variability and brittle tectonic structures: *Earth-Science Reviews*, v. 70, no. 1-2, p. 103-127.
- Civico, R., Brunori, C. A., De Martini, P. M., Pucci, S., Cinti, F. R., and Pantosti, D., 2015, Liquefaction susceptibility assessment in fluvial plains using airborne lidar: the case of the 2012 Emilia earthquake sequence area (Italy): *Natural Hazards and Earth System Sciences*, v. 15, p. 2473-2483.
- Giona Bucci, M., Villamor, P., Almond, P., Tuttle, M., Ries, W., Smith, C., Hodge, M., and Watson, M., 2017, in review, Associations between sediment architecture and liquefaction susceptibility in fluvial settings: the 2010-2011 Canterbury Earthquake Sequence, New Zealand: *Engineering Geology*.
- Hastie, T., Tibshirani, R., and Friedman, J., 2009 *The elements of statistical learning. Data mining, Inferences, and Prediction: Second edition*
- Holzer, T. L., Noce, T. E., and Bennett, M. J., 2010, *Liquefaction Probability Curves for Surficial Geologic Deposits: Environmental & Engineering Geoscience*, v. XVII, no. 1, p. 1-21.
- Martel, S. J., 2016, Effects of small-amplitude periodic topography on combined stresses due to gravity and tectonics: *International Journal of Rock Mechanics and Mining Sciences*, v. 89, p. 1-13.
- Moon, S., Perron, J. T., Martel, S. J., Holbrook, W. S., and St. Clair, J., 2017, A model of three-dimensional topographic stresses with implications for bedrock fractures, surface processes and landscape evolution *Journal of Geophysical Research*.
- Ricci-Lucchi, F., 1980, *Sedimentologia CLUEB*, 1980 548 p.
- Santucci de Magistris, F., Lanzano, G., Forte, G., and Fabbrocino, G., 2013, A database for PGA threshold in liquefaction occurrence: *Soil Dynamics and Earthquake Engineering*, v. 54, no. 0, p. 17-19.
- Talebi, A., Troch, P. A., and Uijlenhoet, R., 2008, A steady-state analytical slope stability model for complex hillslopes: *Hydrological Processes*, v. 22, no. 4, p. 546-553.
- Tuttle, M., 2001, The use of liquefaction features in paleoseismology : lessons learned in the New Madrid Seismic Zone, central United States: *Journal of Seismology* v. 5, p. 361-380.
- Villamor, P., Almond, P., Tuttle, M. P., Giona Bucci, M., Langridge, R. M., Clark, K., Ries, W., Bastin, S. H., Eger, A., Vandergoes, M., Quigley, M. C., Barker, P., Martin, F., and Howarth, J., 2016, Liquefaction features produced by the 2010-2011 Canterbury earthquake sequence in southwest Christchurch, New Zealand and preliminary assessment of paleoliquefaction features: *Bulletin of Seismological Society of America* v. 106, no. 4.
- Witten, I. H., Ffrank, E., and Hall, M. A., 2011, *Data mining: practical machine learning tools and techniques. Third edition.*
- Wotherspoon, M. L., Pender, M. J., and Orense, P. R., 2012, Relationship between observed liquefaction at Kaiapoi following the 2010 Darfield earthquake and former channels of the Waimakariri River: *Engineering Geology*, v. 125, p. 45-55.



Paleoseismology and Late Quaternary upper crustal deformation along active submarine faults on the continental shelf at 23°S, northern Chile

José González-Alfaro (1), Gabriel Vargas (1), Gabriel González (2), Bonvalot Sylvain(3), Germinal Gabalda (3), Gabriel Álvarez (4), Felipe Leyton (5), Byron Huerta (4), Javiera Valdenegro (4)

(1) Departamento de Geología, Facultad de Ciencias Físicas y Matemáticas, Universidad de Chile, Plaza Ercilla 803, Santiago, Chile., Chile.
Email: josgonal@uchile.cl.

(2) Departamento de Ciencias Geológicas, Centro Nacional de Investigación para la Gestión Integrada de Desastres Naturales (Cigiden), Universidad, Católica Del Norte, Avenida Angamos 0610, Antofagasta, Chile.

(3) GET/UMR5563 (UPS, CNRS, IRD, CNES); Obs. Midi-Pyrénées, Université P. Sabatier, Toulouse, France.

(4) Departamento de Ingeniería en Geomensura y Geomática, Facultad de Ingeniería, Universidad de Antofagasta, Avenida Universidad de Antofagasta, 02800, Antofagasta, Chile.

(5) Centro Sismológico Nacional, Universidad de Chile, Blanco Encalada 2002, Santiago, Chile.

Abstract: *The forearc region of the Central Andes is characterized by active faults. Nevertheless, the submarine cartography and activity of these faults are almost unknown. Here, we report late Pleistocene-Holocene surface deformation and active submarine normal faulting on the continental shelf of the northern Mejillones Peninsula. Through differential GPS data and submarine subbottom profiles we characterized the deformation of the hanging wall of the Mejillones Fault system. At the tip point of the northern submarine fault branch of this system, we observed an overlapping transition zone characterized by large submarine landslides and vertical accumulated fault scarp offsets (>300 m height). Similar features were identified hundred kilometers to the north (Iquique and Pisagua areas), which we interpreted as evidence of normal faulting associated to the great N Chile Coastal Scarp. We conclude that submarine active faults play an important constructive role contributing to coastal relief.*

Key words: *Late Quaternary, upper crustal deformation, submarine faults, neotectonics, paleoseismology*

INTRODUCTION

The landscape of the Central Andes forearc evidence several geomorphologic features, with a high grade of preservation, linked to upper crustal deformation owing to the null erosion rates which are characteristics for the hyper-arid Atacama Desert. This positions the Atacama Desert as an excellent place to study Late Quaternary surface deformation linked to both subduction and intraplate fault earthquakes (González et al., 2003; Vargas et al., 2011; Loveless et al., 2009; Cortés et al., 2012; Baker et al., 2013). Nevertheless, there is not sufficient research about the characterization and potential seismic hazard of the upper intraplate faults. Previous works evidenced slip rates of 0.1-0.6 m/ka with recurrences of thousands of years (Vargas et al., 2011; Cortés et al., 2012; Vargas et al., 2014). The latter could be considered unessential for the Chilean active margin, because subduction earthquakes $>M_w7.0$ have recurrences of tens of years, and usually caused localized damage to infrastructure and few human losses, even when the events have been of large magnitude (e.g. 2010 $M_w8.8$ Maule, 2014 $M_w8.2$ Iquique and 2015 $M_w8.4$ Illapel earthquakes). However, it is widely known that intraplate fault earthquakes are characterized by shallow depths and high Peak Ground Acceleration (PGA) close to the rupture. Over the past 10 years, the improvement of the Chilean geodetic network, confirmed that Chile had experienced important earthquakes ($M_w>6.0$) linked to shallow intraplate faults. All of them related to submarine faults (Fariás et al., 2011; González et al., 2015) that

remained unknown until the occurrence of the main shock. The 2007 $M_w6.2$ Puerto Aysén earthquake was the most devastating instrumentally recorded upper intraplate earthquake. This event triggered an aerial landslide into the sea causing a tsunami that killed 3 people and left 10 others missing (Vargas et al., 2013). To this day, shallow intraplate fault mapping and associated seismic hazard assessments is still very poor.

In this work, we use subbottom seismic profiles, differential Global Position System (GPS) tracks, trigonometric topographic profiles and PGA estimations, to characterize the Mejillones Fault (MF). This fault appears to have seismic potential for a $M_w\sim7.0$, likely accompanied with severe PGA intensities. The MF trace has been mapped offshore from the N Mejillones Peninsula (MP), where it clearly affects the continental shelf, to Punta Yayas, where it overlaps another normal fault (Figure 1) likely linked to the Great Northern Chile Coastal Scarp (GNCCS) evolution.

METHODS

We acquired submarine data using subbottom profilers Bathy 2000 (12 kHz) and Bathy 2010 (3.5 kHz) to characterize the bathymetry, sedimentary infill, geomorphology and structures of the Mejillones Bay seabed (Figure 1). Those campaigns included data from hundreds of kilometers northward the MP, off coast of both Iquique and Pisagua (Figure 3).

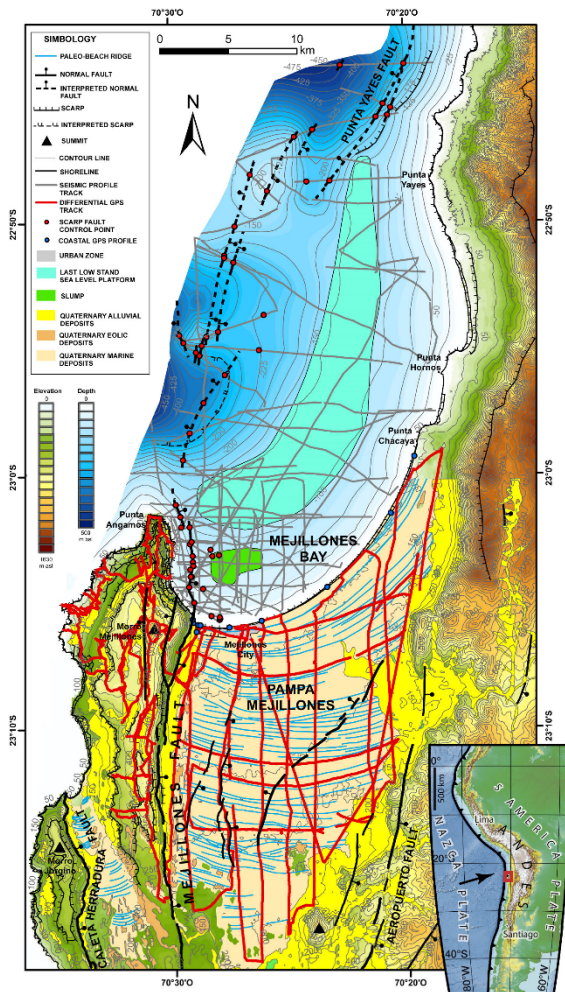


Figure 1: Map of the Northern Mejillones Peninsula showing geomorphological and structural features present in the study area as well as the GPS and seismic reflection data acquisition profiles.

In the inland area, GPS measurements in both Morro Mejillones and Pampa Mejillones areas (Figure 1) allowed to determinate precise heights of the geomorphic features, and to estimate surface tilting. The GPS data were corrected to take into account the local ellipsoid, which has been previously estimated for northern MP. In addition, we realized trigonometric topographic profiles perpendicular to the Mejillones Bay's coastal scarp between Punta Chacaya and Mejillones city (Figure 1), including sea level average and GPS positioning observations.

Taking both bathymetric and topographic data, we performed a kriging interpolation yielding a high resolution Digital Elevation Model (DEM) in order to quantify slope and tilting directions of the surface.

To estimate the PGA of an earthquake occurring at MF, we considered a normal fault, dipping 75°E with a fault plane extending down to 15-20 km depth. The ShakeMap shows two worst possible scenarios: a seismic rupture encompassing the conspicuous MF trace from the southern Pampa Mejillones to Punta Angamos and another one, from the southern Pampa Mejillones to Punta Yayas (Figures 1, 2). The latter considered the activation of all segments.

RESULTS

Offshore northern MP, we observe the submarine continuity of the MF at the western Mejillones Bay (Figure 1). The fault trace is conspicuous until Punta Angamos. From Punta Angamos to Punta Yayas, the MF is subdivided in NNE-oriented segments. The normal faults are deforming the Mejillones Bay sedimentary infill through both fragile and ductile structures, highlighting kilometric syncline fold as well as a N-S, west dipping homocline fold located between Mejillones Bay and Punta Yayas that follow roughly the -100 m contour line. Within the substrate, we identified an angular unconformity between the Neogene and Holocene deposits. Much of this surface is interpreted as the Last Low Stand Sea Level platform (LLSSL; Figure 1), which is tilting to the NW. In addition, we identified slump deposits lying at the centre of the Mejillones Bay at the E side of the MF (Figure 1). Further north, the Punta Yayas Fault (PYF) corresponds to a W- dipping normal fault which develops large accrued vertical scarp offsets (~300 m) with associated submarine landslides, as seen in the seismic profiles (Figure 3).

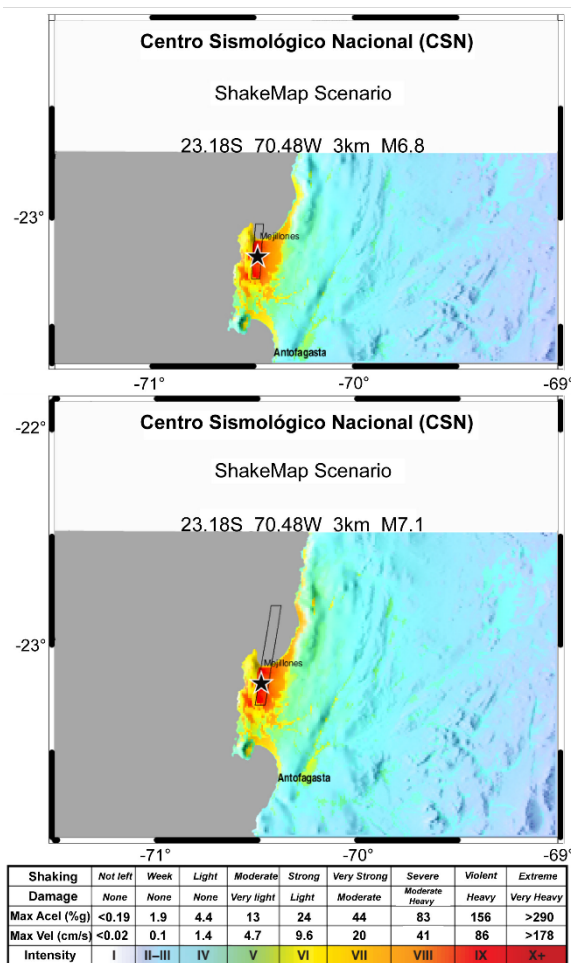


Figure 2: ShakeMaps of the two possible worst scenarios for the Mejillones Fault. The intensity color scale is based on Worden et al. (2010).



In the inland area, we determined that the steeper slopes in the W direction are in the northern Pampa Mejillones than the southern part; and the steeper slopes in the N direction are in the eastern Pampa Mejillones than western part. Nevertheless, the steepest slopes are in NW direction, which are located from the centre to the NE Pampa Mejillones. The erosion rates are considered null for this area, so it is not expected important changes in the surface slopes over the time.

In the ShakeMap scenarios the hanging wall (Pampa Mejillones) is the block which undergoes higher intensities than the footwall (Figure 2). The first scenario considers a rupture along 29 km with a hypocentre of 3 km depth, and a maximum expected magnitude of M_w 6.8. The second scenario considers a rupture along 52 km with a hypocentre of 3 km depth, and a maximum expected magnitude of M_w 7.1 (Figure 2). The accelerations in Pampa Mejillones are very strong to severe, and might generate an enormous damage to the Mejillones city infrastructure, including an important industrial district which provides service and energy to the national copper mining (the mega-sea port, thermoelectrics and mining factories).

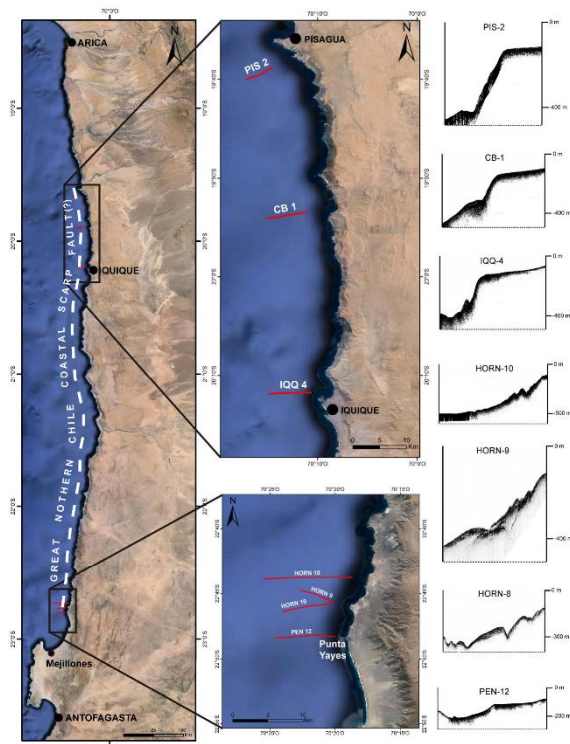


Figure 3: Distribution of the subbottom seismic profiles where we recognized the large normal fault associated to the GNCCS evolution. The profiles show vertical offsets on the order of 300 m. From N to S, note that the vertical offsets of the GNCCS fault scarps decrease approaching at Punta Yayas. The GNCCS fault has no submarine expression to the S of this locality.

DISCUSSION

According to the ShakeMap scenarios (Figure 2), the MF is an active normal fault (Vargas et al., 2005; Vargas et al., 2011, Cortés et al., 2012) with a high seismic hazard

potential. Normal faults located on the continental margin could be affected by changes in Coulomb stress triggered by large subduction earthquakes, as occurred during the M_w 7 Pichilemu seismic sequence (M_w 7), days after the M_w 8.8 2010 Maule earthquake main shock (Fariás et al., 2011). The MP proximity to the subduction trench is potentially a hazardous location considering that it is located at the S edge of the major N Chile seismic gap, which triggered an $M \sim 8.8$ earthquake in 1877. The activation of intraplate faults, located on the active margin following subduction earthquakes, has been empirically evidenced for large global events, such as the M_w 9.3 2004 Sumatra-Andaman and the M_w 9.0 2011 Tohoku-Oki earthquakes.

The Holocene substrate of the Mejillones Bay presents several slump deposits, highlighting a large slump occurred close to the MF (Figure 1). The large Holocene slump has a radiocarbon age of 3000-2300 BP (Vargas et al., 2005) and a volume of roughly $6.05 \times 10^6 \text{ m}^3$. One smaller slump deposit (3% the size of the bigger one) has a radiocarbon age of 1754-1789 AD (Vargas et al., 2005) and it could be linked to the 1768 $M_s > 7.7$ subduction earthquake which affected the MP area (Comte & Pardo, 1991). Considering these observations, we relate the occurrence of the large slump with the last large MF $M_w \sim 7$ earthquake. The latter is corroborated from the 2007 ESI scale (Michetti, et al., 2007) for which slope movements of $\sim 10^6 \text{ m}^3$ are correlated with intensities of IX-X and our intensities for Mejillones Bay are about IX (Fig. 2).

From the bathymetric and topographic data interpretations, we determinate that the surface deformation observed in both Mejillones Bay and Pampa Mejillones is linked to the activity of the MF for at least 400 ka. This age corresponds to the oldest paleo-beach ridge located at the southern Pampa Mejillones (Ortlieb et al., 1996). The NW slopes in Pampa Mejillones could be indicating a high slip rate of the fault in the Mejillones Bay area. This is supported by direct geomorphological evidence of the MF scarp, which increases in height to the N indicating a scissor geometry. This hypothesis is strengthened by gravimetric observations showing a thick sedimentary infill ($\sim 1 \text{ km}$) on the substrate of the Mejillones Bay (Castillo, 2008). The submarine fault segments could be a primitive stage of the fragile surface deformation of the MF to the N. The submarine faults are cutting and deforming Holocene deposits, so these are active.

The slope direction of the erosion surface assigned to the LSSL platform ($\sim 20 \text{ ka}$) is contradictory to the interpretation of a highest slip rate of the MF in Mejillones Bay area. The inner edge of the LSSL platform is located at shallower depths in its S part than in the N part. This may be indicating that other processes are affecting the area, perhaps related to regional uplifting which would outpace the MF activity or the proximity of the northern LSSL platform to the PYF overlapping (Figure 1).

At Punta Yayas, the overlapping between the MF system and the PYF shows a structural complexity. Similar faults to PYF are recognized offshore Iquique and Pisagua (Figure 3). These faults are located 5-10 km from the coastline and



they are associated to large submarine landslides indicating continental shelf collapse. The idea of a great fault that controls the GNCCS evolution was proposed by Armijo & Thiele (1990). Recent geophysical data (e.g., Contreras-Reyes et al., 2012) research supports this idea. We propose that Punta Yayas marks an important transition zone between a large normal fault that would control the GNCCS evolution and the local deformation of the MF submarine segments linked to the MP evolution. This transition zone would be likely related to changes in the slab mechanical properties.

CONCLUSION

The active MF is potentially represents severe seismic hazard that could generate devastating earthquakes and possible tsunamis in the area. The presence of an important structural overlapping at Punta Yayas can be the upper crustal response of changes in mechanical properties of the subduction interface. The geomorphological features linked to these structures demonstrate that active submarine faults play an important role contributing to the construction of coastal relief.

Acknowledgements: This work was funded through the financial contributions made by the FONDECYT projects N° 1085117 and 1140846. Thanks to J.B. Ammirati for his contribution to the improvement of the English writing of this extended abstract.

REFERENCES

- Armijo, R., & Thiele, R., 1990. Active faulting in northern Chile: ramp stacking and lateral decoupling along a subduction plate boundary? *Earth and Planetary Science Letters* 98, 40-61.
- Baker, A., Allmendinger, R. W., Owen, L. A., & Rech, J. A., 2013. Permanent deformation caused by subduction earthquakes in northern Chile. *Nature Geoscience* 6, 492-496.
- Comte, D., & Pardo, M., 1991. Reappraisal of great historical earthquakes in the northern Chile and southern Peru seismic gaps. *Natural Hazards* 4 (1), 23-44.
- Contreras-Reyes, E., Jara, J., Grevemeyer, I., Ruiz, S., & Carrizo, D., 2012. Abrupt change in the dip of the subducting plate beneath north Chile. *Nature Geoscience* 5, 342-345.
- Cortés, J., González, G., Binnie, S., Ruth, R., Freeman, S., & Vargas, G., 2012. Paleoseismology of the Mejillones Fault, northern Chile: insights from cosmogenic ¹⁰Be and optically stimulated luminescence determinations. *Tectonics* 31, 21 p.
- Castillo, C., 2008. Modelamiento geológico-gravimétrico de la anomalía isostática residual en el Hemigraben de Mejillones, Región de Antofagasta, Chile. Memoria de Título (Unpublished), Universidad Católica del Norte, Departamento de Ciencias Geológicas.
- Fariás, M., Comte, D., Roecker, S., Carrizo, D., & Pardo, M., 2011. Crustal extensional faulting triggered by the 2010 Chilean earthquake: The Pichilemu Seismic Sequence. *Tectonics* 30 (6), TC6010.
- González, G., Cembrano, J., Carrizo, D., Macci, A., Schneider, H., 2003. The link between forearc tectonics and Pliocene-Quaternary deformation of the Coastal Cordillera, northern Chile. *Journal of South American Earth Sciences* 16 (5), 321-342.
- González, G., Salazar, P., Loveless, J. P., Allmendinger, R. W., Aron, F., & Shrivastava, M., 2015. Upper plate reverse fault reactivation and the unclamping of the megathrust during the 2014 northern Chile earthquake sequence. *Geology* 43, 671-674.
- Michetti, A. M., Esposito, E. et al. 2007. Intensita` scale ESI 2007. In: Guerrieri, L. & Vittori, E. (eds), *Memorie Descrittive Carta Geologica d'Italia*, 74, Servizio Geologico d'Italia, Dipartimento Difesa del Suolo, APAT, Rome, 53 p.
- Loveless, J. P., Allmendinger, R. W., Pritchard, M. E., Garroway, J. L., & González, G., 2009. Surface cracks record long-term seismic segmentation of the Andean margin. *Geology* 37, 23-26.
- Ortlieb, L., Zazo, C., Goy, J., Hillaire-Marcel, C., Ghaleb, B. & Cournoyer, L., 1996. Coastal deformation and sea-level changes in the northern Chile subduction area (23°S) during the last 330 ky. *Quaternary Science Reviews* 15, 819-831.
- Vargas, G., Ortlieb, L., Chapron, E., Valdés, J., & Marquardt, C., 2005. Paleoseismic inferences from a high-resolution marine sedimentary record in northern Chile (23° S). *Tectonophysics* 399, 381-398.
- Vargas, G., Palacios, C., Reich, M., Luo, S., Shen, C-C., González, G., & Wu, Y-C., 2011. U-series dating of co-seismic gypsum and submarine paleoseismology of active faults in Northern Chile (23°S). *Tectonophysics* 497, 34-44.
- Vargas, G., Rebolledo, S., Sepúlveda, S. A., Lahsen, A., Thiele, R., Townley, B., Padilla, C., Rauld, R., Herrera, M. J., & Lara, M., 2013. Submarine earthquake rupture, active faulting and volcanism along the major Liquiñe-Ofqui Fault Zone and implications for seismic hazard assessment in the Patagonian Andes. *Andean Geology* 40 (1), 141-171.
- Vargas, G., C. Palacios, M. Reich, S. Luo, C. Shen, G. González & Y. Wu, 2011a. U-series dating of co-seismic gypsum and submarine paleoseismology of active faults in Northern Chile (23°S). *Andean Geology* 38 (1), 219-238.
- Worden, C.B., Wald, D. J., Allen, T.I., Lin, K. W., Garcia, D., & Cua, G., (2010). A revised ground-motion and intensity interpolation scheme for ShakeMap. *Bulletin of Seismological Society of America* 100(6), 3083-3096.



Anthropogeomorphology and Paleoseismology Blend to Define the Marvast Active Fault Slip History and Potential Seismology, Central Iran

Goorabi, Abolghasem (1)

(1) Abolghasem Goorabi, Faculty of Geography, University of Tehran, Enqlab Avenue, Tehran, Iran. goorabi@ut.ac.ir

Abstract: We first describe the late Holocene slip history of the Marvast active fault, in central Iran, by combining geomorphology investigations with paleoseismological evidences. Although the Marvast fault system did not produced earthquakes larger than 4.5(Mb) yet, but there is abundant evidence for tectonic activity. We opened a trench across the Marvast fault trace. Despite the lack of large instrumental earthquakes (1900-2017) related to this fault, all geomorphology and paleoseismology evidence implies that the Marvast fault has had significant vertical and horizontal movements in the Holocene. Qanats are one of the oldest human phenomena (about 1000 years) in the region. The Marvast fault has displaced and destroyed them during the last 1000 years. The reconstruction of the interplay between theses human phenomena of the site (Qanats) and the geomorphic evidence, permitted us to gain reliable chronological data for constraining the fault slip history in the last 1000 yr. Our results show that this fault has been activated in the Quaternary.

Key words: Marvast fault; Paleoseismology; Active faulting; Central Iran.

INTRODUCTION

The Iranian plateau extends over a number of continental fragments welded together along suture zones of oceanic character (Nadimi, 2007). Due to the Arabian–Eurasian collision (Berberian and King, 1981) and their dynamics (Vernant et al., 2004), the Iranian territory may be considered as one of the most tectonically active regions of the world. The Central Iranian interior plateau (herein referred to as Central Iran) consists of five major crustal domains from east to west (the Lut, Tabass, Kalmard, Poshtabadam and Yazd blocks, respectively). It is characterized by strike-slip faulting on long faults (Berberian, 1976) (e.g., Dehshir, Anar, Dorouneh, Nayband, Nehbandan, Bam, Sabzevar, Kuhbanan, etc) (Figure 1).

All faults with present-day and Holocene offsets or other manifestations of activity during the last 10,000 years have been defined as active faults (Allen, 1975). However, since it is hard in many regions to differentiate the Holocene geological features from those of the Late Pleistocene, we consider it necessary to extend the time interval accepted as characteristic for active faults to 100,000 years, i.e. Holocene and Late Pleistocene.

Several studies have been carried out on active faults of Central Iran (Berberian, 1981; Berberian et al., 2001; Meyer and Dortz, 2007; Tchalenko and Berberian, 1975), especially in its eastern parts (Bachmanov et al., 2004; Walker and Jackson, 2004; Walker et al., 2003). The activity of faults has caused a long series of large damaging earthquakes, many of them occurring within the 20-21th century in the Central Iran. There have been roughly 126,000 deaths attributed to 14 earthquakes of magnitude ~7.0 (about one M7 earthquake every seven years), and 51 earthquakes of 6.0-6.9 (about one every

two years) that took place in Iran since 1900. During this period, nine cities were devastated (about one city every ten years) (Berberian, 2014).

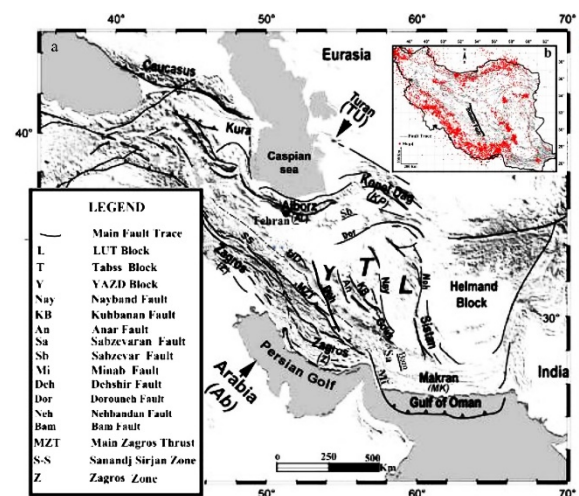


Figure 1: (a) Simplified topographic (derived from SRTM90) and tectonic map of Iran and its surroundings, with simplified main active fault traces. Deh refers to location of the Dehshir and Marvast fault. (Goorabi, 2009) (b) Distribution of earthquakes in Iran (1900–2017, USGS).

The Marvast fault is a segment (about 100 km) of the Dehshir strike-slip fault zone (overall, 400 km). Dehshir fault zone is located at the westernmost of Central Iran (Goorabi, 2009) (Figure 1 a and Figure 2). Based on historical (Ambraseys and Melville, 2005; Berberian and Yeats, 1999) and instrumental earthquake data (Figure 1 b, USGS) the Marvast fault has not had large earthquakes ($M_b \geq 4.5$) and is commonly seen as an area with potential of low seismicity (Figure 1 b). Notwithstanding, the Marvast fault hosts geomorphic evidence of Quaternary activity.



Material and Methods

We utilized Landsat ETM+, ASTER, IRS, DEMs and SRTM-30&90-m imageries, Google Earth, detailed maps of drainage systems, and fieldwork to identify and interpret the geomorphic evidence associated with Quaternary landforms along the Marvast fault.

The large Dehshir strike-slip fault zone cuts the main part of the Iranian plateau (Figure 1 a). It is orientated NNW–SSE between 29.5°N and 32.5°N. The Dehshir fault zone is segmented into several linear sections from NW to SE (Goorabi, 2009): The first section runs N170°, is about 75 km long, and cuts the eastern part of Central Iran between Ardestan playa (north) to Gavkhoni playa (south). This section of of the Dehshir fault zone has been named locally Nain fault (Alai-Mahabadi and Foudazi, 2004) (Figure 2, see 1).

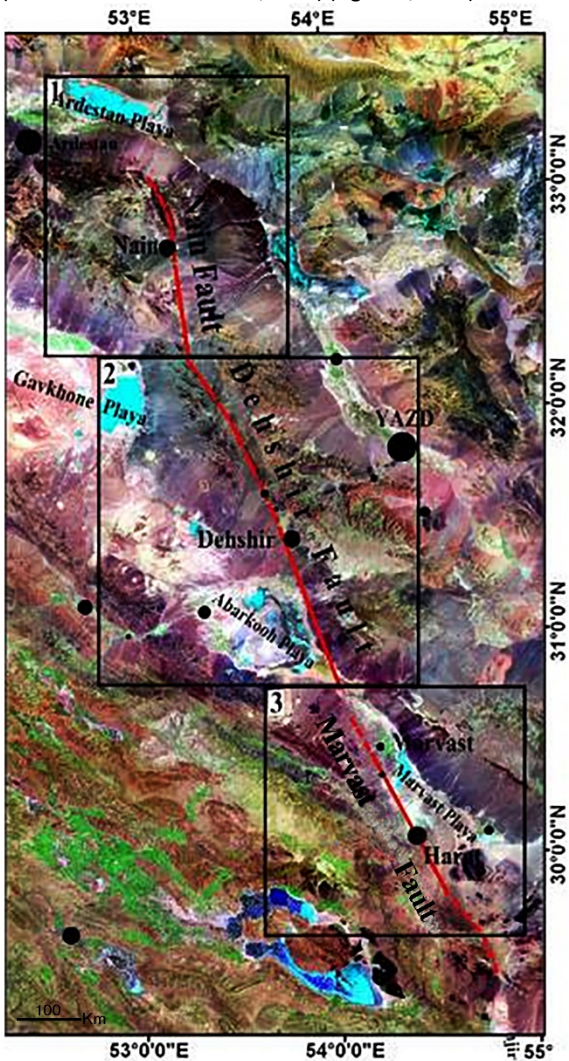


Figure 2: Imagery of the study area showing the major sections of the Dehshir fault zone and the Marvast Fault.

The next segment runs N160° and is 200 km long. It starts north of Dehshir and cuts ponded lakes, marshes, and Quaternary salt flats, and finally ends SE of Abarkooh playa (Figure 2, see 2). This section has been named locally Dehshir

fault (Rowshan Ravan et al., 2004). The third segment strikes N154°. It is 100 km long and begins at the Abrkooch-Marvast playas, ending south of Harat. The local name of this segment is Marvast fault (Goorabi, 2009) (Figure 2, see 3). Finally, the fourth section, locally named Cheshmeh Anjir fault (Rowshan Ravan et al., 2004), terminates in the east of the Main Zagros Thrust (MZT) (Berberian, 1981; Meyer et al., 2006) (Figure 1 and Figure 2). In this study, we focused on the Marvast segment (Figure 2, see 2), which cuts Holocene landforms and Qanats.

RESULTS

We compare our study area with recent research and dating of Quaternary landforms in Central Iran (Fattahi, 2010; Fattahi et al., 2006, 2007; Nazari et al., 2009; Regard et al., 2006) and suggest that the landforms deformed by the Marvast Fault are Holocene in age. Tectonically deformed Qanats are not older than 1000 years.

Quaternary faulting along the Marvast Fault

Along the Marvast fault we observe displaced landforms, deflected and deformed drainage, and deformed Holocene alluvium. The fault can be traced by offset channels, spring lines, and linear valleys (Figure 3). In addition to the horizontal component of faulting, vertical component has created remarkable fault scarps along the Marvast fault (Figure 5). The combination of these two components coincident with Holocene faulting of Marvast fault in some parts(hanging block) along it extreme erosion occurred faster than the adjacent region (footwall block), This process has produced longitudinal depressions along the fault trace, incised alluvial fans (rillwashes), and many small sub-basins on the hanging wall block in alluvium (Figure 3).

The Quaternary terrace of Marvast river hosts linear geomorphic elements that cross the fault and thus can be used as piercing points. These include channel axes, channel margins, and depositional levees (ridges). We measured the offset of the Marvast river terrace and found about 1000 m horizontal displacement since the Early Quaternary (Figure 4). Therefore, the fault slip rate is about 0.5 mm/yr during the Quaternary.

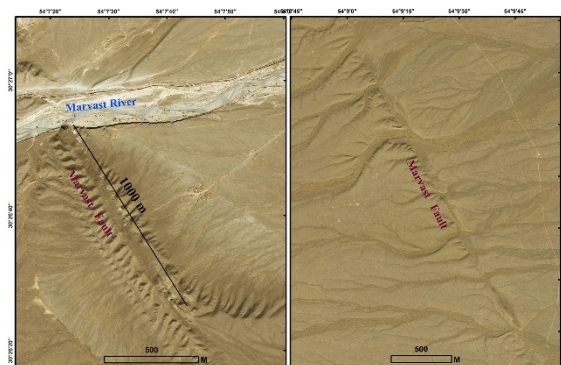


Figure 3: Evidence of neotectonics along the Marvast strike-slip fault west of Marvast city. The early Quaternary terrace of Marvast River has been displaced by about 1000 m.



The youngest Marvast river terrace hosts similar linear markers. 30 m offset were found in Holocene landforms, hence, the slip rate is about 3.0 mm/yr in the Holocene.

Qanats are still in use in many parts of Central Iran. This water irrigation system was developed by the Persians in the 6th Century BC, and is a hand-dug subterranean conduit with a gentle gradient that brings water from the aquifer to the oases in arid lowlands. In the study area, several Qanats are offset across the Marvast fault (Figure 5 and 5). A maximum age of about 4000 years is assumed for Qanats in Iran (Berberian, 2014). However, in the Marvast area, Qanats are likely to be much younger than 4000 years, and may indicate a higher rate of slip. In the study area, the entrances of Qanats are usually drilled into the hanging wall block of fault. Therefore, most farms are located on the foot wall of Marvast fault. Fault scarps in this area range between 20-60 m (c, Figure 5) Indeed, the Marvast faulting, and its uplifted aquifer, provide the main source of water for agricultural purposes, and together indicate the reason for the location of the oasis and its agriculture in the Marvast area (Figure 5).

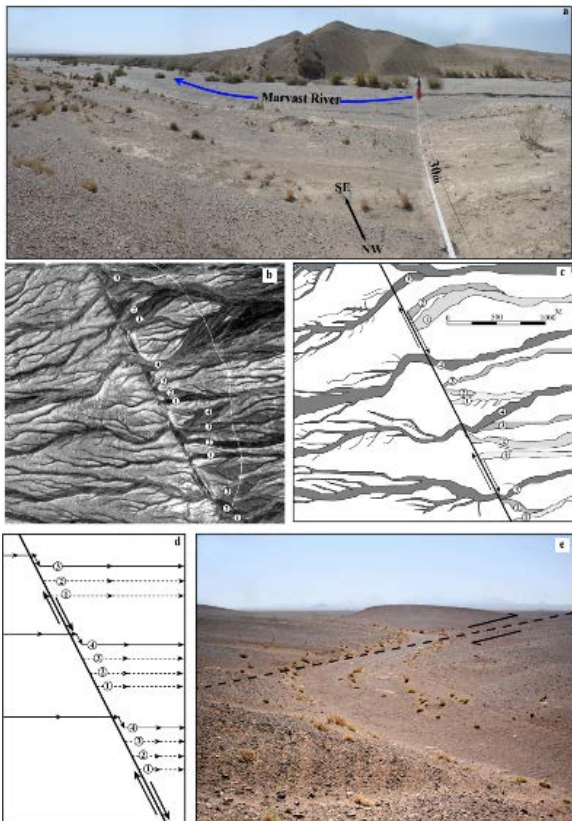


Figure 4: (a) 30 m offset in the Holocene Marvast river terrace. (b) Deflected rillwashes on the Marvast alluvial fan in IRS P5 imagery (2.5 m resolution). (c) Schematic diagram of deflected drainages caused by motion on the Marvast-Harat fault. The present-day drainages are marked by numbers 3, 4 in every ravine course. (d) Reconstruction of the drainage network. (e) Field photo showing one of the drainage offset.

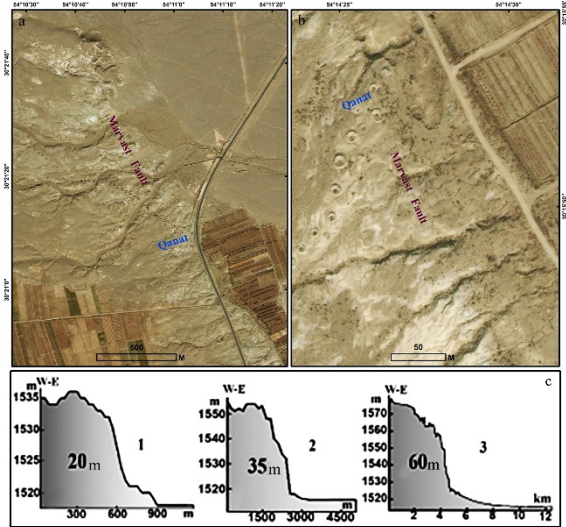


Figure 5: The shafts of Qanats are displaced across the Marvast fault (a and b). c show W-E topographic profiles across Marvast fault.

The lines of the Qanats are shown in Figure 6. Some of them are deflected to the south a few meters west of the frontal escarpment, caused by right-lateral strike-slip faulting (Figure 6).

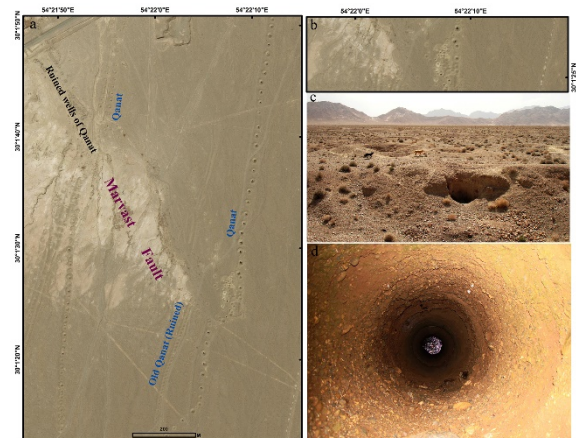


Figure 6: (a) and (b) Several generations of Qanats indicate repeated disruption to water flow. (c and d) Shafts (wells) of a Qanat dug in alluvial sediment.

The water table appears to change in height across the fault, being ~20-60 m (almost equal to fault scarp high, see c at the Figure 5) underground to the east of the fault trace, but deeper in the qanats. The fault may form a barrier to the flow of water or may separate sediments of differing permeability. Some researchers (Yazdi and Khaneiki, 2016) also state that some qanat tunnels have been dug along the fault trace itself, presumably to maximize the flow of water by tapping the elevated water table along the fault. We conclude that Holocene activity on the Marvast fault is documented by uplift and offset of ancient Qanats.



Figure 7: Evidence of active faulting in man-made structures. (a) Road damage, (b) uplifting and erosion of the hanging wall of the Marvast fault, (c) the destruction of water wells and Qanats

CONCLUSIONS

This study attempts to clarify the Late Pleistocene–Present deformation along the Marvast fault and to analyse the occurrence of recent tectonic activity. Indicators for active faulting are preserved in Quaternary landforms. The morphology of several landforms is strongly influenced by active faulting. All data show that the Marvast fault is a very active fault with a Holocene slip rate of 3 mm/yr and a Quaternary slip rate of 0.5 mm/yr.

Acknowledgements: The author is grateful to the staff of the Geological Survey of Iran (GSI) for all the kind help and the logistic organization of fieldwork. I also acknowledge the Department of Geography, University of Tehran, for providing the facilities.

REFERENCES

- Alai-Mahabadi, S., and Foudazi, M. (2004). Nain Geology Map (Tehran: Geological Surveying of Iran).
- Allen, C.R. (1975). Geological Criteria for Evaluating Seismicity. *Geol. Soc. Am. Bull.* 86, 1041–1057.
- Ambraseys, N.N., and Melville, C.P. (2005). *A History of Persian Earthquakes* (Cambridge University Press).
- Bachmanov, D., Trifonov, V., Hessami, K., Kozhurin, A., Ivanova, T., Rogozhin, E., Hademi, M., and Jamali, F. (2004). Active faults in the Zagros and central Iran. *Act. Faults East. Hemisphere* 380, 221–241.
- Berberian, M. (1976). *Seismotectonic Map of Iran* (Tehran: Geological Survey of Iran).
- Berberian, M. (1981). Active faulting and tectonics of Iran. *Geodyn. Ser.* 3, 33–69.
- Berberian, M. (2014). *Earthquakes and Coseismic Surface Faulting on the Iranian Plateau, Volume 17* (Amsterdam: Elsevier).
- Berberian, M., and King, G.C.P. (1981). Towards a paleogeography and tectonic evolution of Iran. *Can. J. Earth Sci.* 18, 210–265.
- Berberian, M., and Yeats, R.S. (1999). Patterns of historical earthquake rupture in the Iranian Plateau. *Bull. Seismol. Soc. Am.* 89, 120–139.
- Berberian, M., Jackson, J.A., Fielding, E., Parsons, B.E., Priestley, K., Qorashi, M., Talebian, M., Walker, R., Wright, T.J., and Baker, C. (2001). The 1998 March 14 Fandoqa earthquake (Mw 6.6) in Kerman province, southeast Iran: re-rupture of the 1981 Sirch earthquake fault, triggering of slip on adjacent thrusts and the active tectonics of the Gowk fault zone. *Geophys. J. Int.* 146, 371–398.
- Fattahi, M. (2010). Refining the OSL age of the last earthquake on the Dhesir fault, Central Iran. *Quat. Geochronol.* 5, 286–292.
- Fattahi, M., Walker, R., Hollingsworth, J., Bahroudi, A., Nazari, H., Talebian, M., Armitage, S., and Stokes, S. (2006). Holocene slip-rate on the Sabzevar thrust fault, NE Iran, determined using optically stimulated luminescence (OSL). *Earth Planet. Sci. Lett.* 245, 673–684.
- Fattahi, M., Walker, R.T., Khatib, M.M., Dolati, A., and Bahroudi, A. (2007). Slip-rate estimate and past earthquakes on the Doruneh fault, eastern Iran. *Geophys. J. Int.* 168, 691–709.
- Goorabi, A. (2009). Effect of Neotectonics on Evolution of Quaternary landforms in Central Iran (Case Study on Dehshir and Anar Faults). University Of Tehran.
- Meyer, B., and Dortz, K.L. (2007). Strike-slip kinematics in Central and Eastern Iran: Estimating fault slip-rates averaged over the Holocene. *Tectonics* 26, 20 PP.
- Meyer, Mouthereau, F., Lacombe, O., and Agard, P. (2006). Evidence of Quaternary activity along the Deshir Fault: implication for the Tertiary tectonics of Central Iran. *Geophys. J. Int.* 164, 192–201.
- Nadimi, A. (2007). Evolution of the Central Iranian basement. *Precambrian Cont. Growth Tectonism* 12, 324–333.
- Nazari, H., Fattahi, M., Meyer, B., Sébrier, M., Talebian, M., Foroutan, M., Le Dortz, K., Bateman, M.D., and Ghorashi, M. (2009). First evidence for large earthquakes on the Deshir Fault, Central Iran Plateau. *Terra Nova* 21, 417–426.
- Regard, V., Bellier, O., Braucher, R., Gasse, F., Bourlès, D., Mercier, J., Thomas, J.-C., Abbassi, M.R., Shabanian, E., and Soleymani, S. (2006). ¹⁰Be dating of alluvial deposits from Southeastern Iran (the Hormoz Strait area). *Palaeogeogr. Palaeoclimatol. Palaeoecol.* 242, 36–53.
- Rowshan Ravan, J., Eshraghi, S., and Sabzehei, M. (2004). *Chahak Geology Map* (Tehran: Geological Surveying of Iran).
- Tchalenko, J.S., and Berberian, M. (1975). Dasht-e Bayaz Fault, Iran: Earthquake and Earlier Related Structures in Bed Rock. *Geol. Soc. Am. Bull.* 86, 703–709.
- Vernant, P., Nilforoushan, F., Hatzfeld, D., Abbassi, M.R., Vigny, C., Masson, F., Nankali, H., Martinod, J., Ashtiani, A., Bayer, R., et al. (2004). Present-day crustal deformation and plate kinematics in the Middle East constrained by GPS measurements in Iran and northern Oman. *Geophys. J. Int.* 157, 381–398.
- Walker, R., and Jackson, J. (2004). Active tectonics and late Cenozoic strain distribution in central and eastern Iran. *Tectonics* 23, 24 PP.
- Walker, R., Jackson, J., and Baker, C. (2003). Surface expression of thrust faulting in eastern Iran: source parameters and surface deformation of the 1978 Tabas and 1968 Ferdows earthquake sequences. *Geophys. J. Int.* 152, 749–765.
- Yazdi, A.A.S., and Khaneiki, M.L. (2016). *Qanat Knowledge: Construction and Maintenance* (Springer).



Review of Existing On-Fault Paleoseismic Data for the North Westland Section of the Alpine Fault

Howarth, Jamie (1), Langridge, Rob (2), Fitzsimons, Sean (3)

- (1) Victoria University of Wellington, Wellington, New Zealand. Jamie.Howarth@vuw.ac.nz
 (2) Active Landscapes Dept., GNS Science, PO Box 30-368, Lower Hutt, New Zealand.
 (3) University of Otago, Dunedin, New Zealand

Abstract: The plate boundary Alpine Fault is one of New Zealand's largest sources of seismic hazard. Despite this the earthquake history of its North Westland section remains poorly defined. It has been hypothesised that the most recent earthquake (MRE) on the section occurred in ~1620 A.D. and ruptured ~250 km of the North Westland and Central sections of the fault but new paleoseismic data from lake sediments has raised questions about the extent of this rupture. We re-evaluate chronologies from fault trenches on the North Westland section using the current ^{14}C calibration curve and Bayesian age modelling to integrate radiocarbon and stratigraphic constraints. The revised chronologies are not consistent with a ~1620 age for the MRE on the North Westland section and suggest a complex rupture history over the last 500 years. The evaluation demonstrates the need for further on-fault and off-fault investigation to constrain the timing and extent of recent earthquakes on North Westland section.

Key words: Alpine Fault, paleoseismology, earthquakes, chronology

INTRODUCTION

The Alpine Fault is an 850 km long transform plate boundary fault that strikes the length of the South Island of New Zealand (Norris and Cooper, 2001). In the central South Island the fault accommodates up to 80% of the 39 mm.yr⁻¹ of plate motion between the Pacific and Australian plates, making it one of the South Island's largest sources of seismic hazard (Sutherland et al., 2007). No large earthquakes have occurred on the fault during the 150 year period of written records. Paleoseismic data from on-fault trenches, dendrochronology, and lake records indicate that ~380 km of the fault last ruptured in 1717 A.D. in an estimated Mw 8.1 earthquake (De Pascale and Langridge, 2012; Howarth et al., 2016a; Wells et al., 1999). Long records (>10 events) of paleo-earthquakes have also been developed for the South Westland and Central sections of the fault from near fault swamps and lake records (Cochran et al., 2017; Howarth et al. 2012; 2014; 2016; Figure 1). By comparison, the earthquake history of

the North Westland section remains poorly constrained despite a high density of on-fault paleoseismic sites.

On-fault records with poor age control have been correlated with precisely dated evidence for landscape disturbance (using dendrochronology) to infer that the North Westland section of the Alpine Fault last ruptured in ~1620 A.D. (Sutherland et al., 2007; Yetton, 1998). The ~1620 A.D. earthquake is thought to have ruptured ~250 km of the Alpine Fault's North Westland and Central sections (Figure 1). This paradigm has persisted for the last 20 years but requires further scrutiny because the timing of this event does not agree well with precisely dated paleo-earthquake histories derived from lake records (Howarth et al., 2012; Howarth et al., 2014; Howarth et al., 2016b). Here we review on-fault paleoseismic data for the North Westland section and update trench chronologies using Bayesian age modelling to re-examine ~1620 A.D. earthquake.

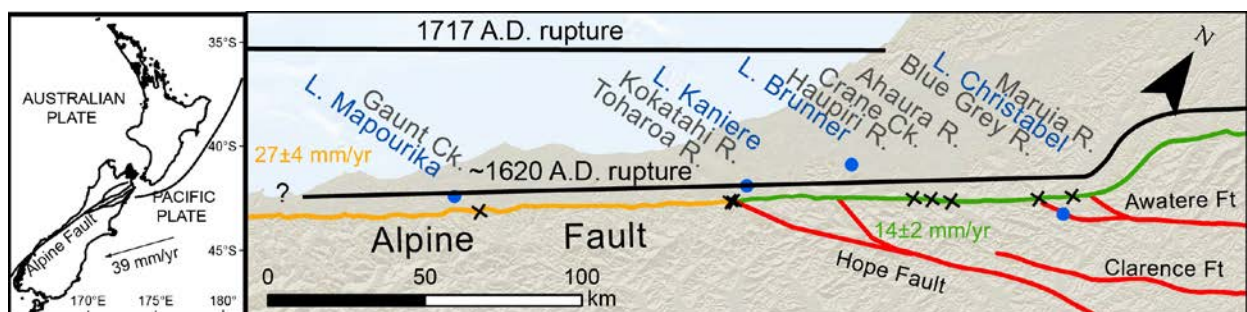


Figure 1: Tectonic setting (left) and the Central (yellow) and North Westland (green) sections of the Alpine Fault in the South Island, New Zealand (right). The Alpine Fault last ruptured in 1717 A.D. in a Mw8.1 earthquake but the timing and extent of the penultimate event on the North Westland section remains poorly defined. It has been widely accepted that the most recent earthquake (MRE) to rupture the entire North Westland section occurred in 1620 A.D. Blue circles = lake paleoseismic sites; crosses = on-fault trench paleoseismic sites.



REVIEW OF TRENCH SITE CHRONOLOGIES

Between the Maruia and the Toaroha rivers there are eight sites where paleoseismic trenches have been excavated across the fault. These trenches provide evidence of the last 1-2 ruptures of the fault section and sparse, though important, constraint on the timing of the events from radiocarbon dates (Yetton, 1998; Yetton et al., 1998; Yetton, 2002; Yetton and Wells, 2010). A summary and re-evaluation of the results of these trench investigations is timely because many were conducted in the late 1990s and since then there have been significant advances in methodologies for treating radiocarbon ages. In particular, developments in the Southern Hemisphere calibration curve (ShCal13; Hogg et al., 2013) have superseded the convention to report conventional radiocarbon ages (CRA) less than 200 yr BP as modern. With the new calibration curve these young ages contain useful information that can be extracted. The chronology from the trench sites is evaluated below and updated using the current calibration curve and Bayesian statistical approaches for integrating ¹⁴C dates and information on their stratigraphic position. We use the Sequence prior in OxCal 4.3 to integrate numerical age information and stratigraphic constraints to produce earthquake chronologies (Lienkaemper and Ramsey, 2009). Earthquake ages are reported as 95% highest probability density function range (95% HPDF).

Maruia River: At Maruia River a single multi-arm trench was excavated across the surface trace of the Alpine Fault (Yetton, 2002). The trench was located in the tread of the most recently abandoned terrace of the Maruia River that hosts a channel offset by 1.3 m ± 1 m across the Alpine Fault trace. The trench shows evidence of the last

rupture at this site. Unfortunately, the CRAs that bound the rupture are on fragments of charcoal that have obviously been reworked. Charcoal from deposits at the base of channel fill from an un-faulted channel provided a CRA of 805 ± 49 yr BP (Wk9623), while charcoal from faulted gravely, sandy silt has ages of 477 ± 58 yr BP (Wk9325) and 609 ± 57 yr BP (Wk9326). As the charcoal was extracted from sediment that experienced fluvial reworking and has an unknown residence time within the catchment before deposition, the youngest CRA (Wk9325) provides a crude maximum for the most recent earthquake (MRE) of sometime after 1625 - 1399 A.D.

Blue Grey River: Constraints on the timing of the last surface rupture were produced from a hand-dug trench across the active trace near the track to Lake Christabel (Yetton, 2002). The trench contains stratigraphic evidence of the MRE, which also offset channels that cross the fault by an average of 1 m ± 0.3 m. The offset is inferred to be the displacement caused by the last rupture (Yetton, 2002). The age of the rupture is bounded by a CRA of 281 ± 56 yr BP (Wk10000) from branch fragments trapped in the shear zone, and a CRA of 219 ± 57 yr BP (Wk10001) from charcoal within colluvium immediately overlying the upper terminations of the fault strands. An additional constraint comes from the lack of documented historical rupture of the Alpine Fault since 1840 A.D. The modelled age for the most recent rupture was 1843 - 1567 A.D. (Figure 2).

Ahaura River: A single trench at Ahaura River was excavated across the westernmost of two Alpine Fault surface traces, immediately south of Coates Creek (Yetton et al., 1998). Faulted overbank silts are overlain by silty, sandy, angular, fine schist gravels that are

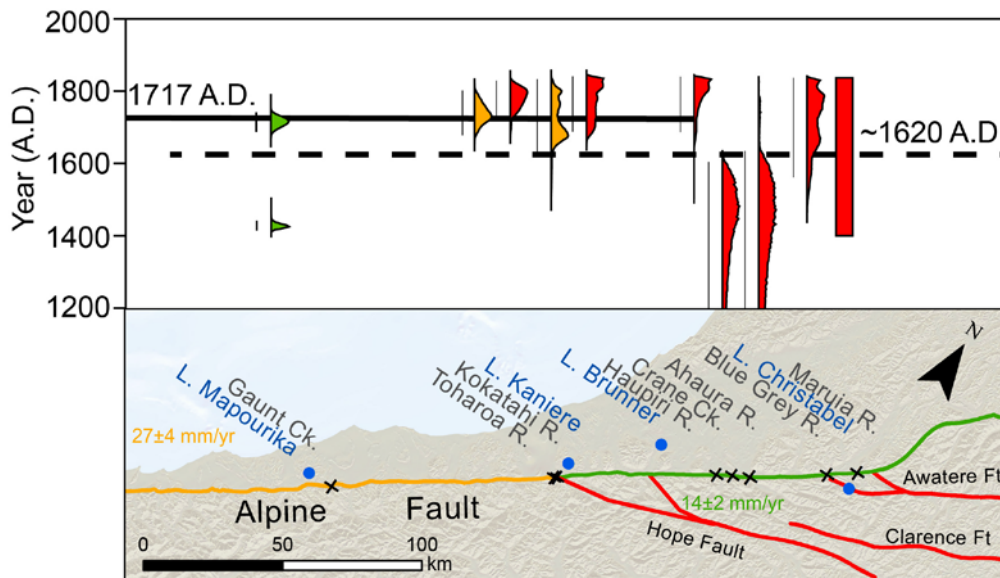


Figure 2: Space and time diagram showing the most recent earthquake (red) and penultimate (yellow) earthquake age probability density functions (PDFs) derived from the Bayesian age modelling of trench stratigraphy and ¹⁴C dates. Green age PDFs = MRE and penultimate MM9 shaking on the central section recorded in fault proximal lake records



interpreted as post seismic creek aggradation. A CRA of 380 ± 60 yr BP (Wk5378) from a small branch located at the base of the angular schist gravels provides a minimum age for the last rupture at this site. Branches from near the base of an unleached brown peat with minor sand and schist gravel produced a CRA of 127 ± 48 yr BP (Wk5528). Bayesian age modelling of this sequence provides an age for the last event of 802-1642 A.D.

Crane Creek: A single trench was hand-dug across a fault furrow that Yetton et al. (1998) infer as the youngest surface trace of the Alpine Fault, immediately south of Crane Creek. The trench records the stratigraphic evidence of the rupture that generated the fault furrow. A shear zone is overlain by silty sand with fine schist gravel and Yetton et al. (1998) infer that it is scarp-derived colluvium. Two CRAs from twigs within the colluvium provide ages of 380 ± 25 yr BP (Wk5263) and 360 ± 50 yr BP (Wk54489). These ages immediately post-date the rupture recorded in the trench. Yetton et al. (1998) infer that this rupture presents the last event on the Alpine Fault at this location. The timing of the event is further constrained by the presence of a small landslide from the fault scarp that buries the trenched fault furrow and is not faulted, indicating that it post-dates the rupture that formed the furrow. Ring counts from trees growing on the landslide demonstrate that this fault trace has not ruptured in the last ~300 years (Yetton et al., 1998). Based on this evidence the last rupture of the Alpine Fault at this location was in 1601-1110 A.D. (Figure 2).

Hauptiri River: A hand-dug pit was located across the only surface trace of the Alpine Fault immediately north of the Hauptiri River, where the toe of a small landslide from the fault scarp has been offset from the scarp by 5 m - 6 m (Yetton et al., 1998). The trench stratigraphy reveals sheared gravels that are overlain by un-faulted scarp derived colluvium, which in turn is overlain by brown peat. Yetton et al. (1998) infer that this sequence records the last rupture of the Alpine Fault. CRAs of 210 ± 50 yr BP (Wk5529) from twigs and leaves trapped within the shear, and 134 ± 46 yr BP (Wk5379) from twigs and small branches from the base of the colluvium, provide bounding age constraint for the most recent rupture at this location. The modelled age for the last rupture at Hauptiri River is 1843-1689 A.D (Figure 2).

Kokatahi River: On the northern bank of the Kokatahi River the Alpine Fault has two recent surface traces that were both trenched by Yetton et al. (1998). The trench stratigraphies are similar to those at Toaroha River and are characterised by alluviums, overbank silts, and colluviums. Both trenches record shear that relates to at least the last two ruptures at this location. Maximum age constraint for the timing of the penultimate earthquake is derived from two CRAs from Kokatahi 1 trench extracted from deposits faulted by two ruptures. The first is a CRA of 490 ± 40 yr BP (Wk 5470) from a *M. umbellata* log that had sapwood removed by river abrasion and was extracted from flood channel sands and the second is a CRA of 120 ± 40 yr BP (Wk 5471) from a *D. dacrydiodes*

root that had its upper termination sheared and was in growth position within the flood channel sands. Maximum age constraint for the most recent rupture is provided by a CRA from the Kokatahi 2 trench of 220 ± 40 yr BP (Wk5473) from a piece of decayed *M. umbellata* branch extracted from a soil breccia interpreted to have formed as a product of liquefaction during the MRE. Minimum age constraint for the latest rupture is provided by a CRA of 93 ± 40 yr BP (Wk5469) from a small stump in growth position that was buried by flood channel sands that are inferred by Yetton et al. (1998) to postdate the last rupture. The modelled ages for the last two earthquakes at Kokatahi River are 1845-1703 A.D. and 1814-1684 A.D. (Figure 2).

Toharoa River: Two trenches were excavated across the surface trace of the frontal thrust of the Alpine Fault at the Toharoa River (Yetton et al. 1998). The stratigraphy of the Toharoa 1 trench is characterised by sequences of alluvium, overbank silts, colluvium and buried soils that have been sheared in at least two ruptures. Temporal constraint on the timing of these ruptures comes from both trenches. A CRA of 250 ± 50 yr BP (Wk5511) from root material within fluvial sands that was faulted by the shear caused by the penultimate rupture provides a maximum age for the most recent two ruptures. A branch extracted from scarp-derived colluvium that is faulted by a shear that reaches the surface provided a CRA of 166 ± 42 yr BP (Wk5512) and post-dates the penultimate rupture while pre-dating the most recent earthquake. Wood and charcoal collected from near the ground surface (Wk 5510) provided a post-1950 A.D. age. When modelled, the stratigraphic sequence and calibrated CRAs return ages of 1841-1687 A.D. for the most recent rupture and 1833-1624 A.D. for the penultimate rupture (Figure 2). Only the MRE is constrained by CRAs in the Toharoa 2 trench. The modelled age for this event is 1844-1696 A.D., which is consistent with the event chronology for Toharoa 1 (Figure 2).

CONCLUSIONS

The review of existing on-fault paleoseismic data from trenches on the North Westland section of the Alpine Fault reveals the possibility that the MRE on this section occurred more recently than the 1717 A.D. great earthquake. Four out of seven trench sites contain evidence that is consistent with a post-1717 A.D. rupture, one provides inconclusive evidence, and two sites seem to preclude post-1717 A.D. rupture. The reanalysed chronologies do not support a MRE that involved a ~250 km long rupture of the fault in ~1620 A.D. and point instead to complex rupture behaviour on this section of the fault over the last 500 years. There is obviously a need for further on-fault and off-fault investigations to constrain the timing of the MRE on this section. Future studies must involve excavations across all active traces in sedimentary environments that facilitate accurate dating of earthquakes.



REFERENCES

- Cochran, U. A. et al., 2017, A plate boundary earthquake record from a wetland adjacent to the Alpine fault in New Zealand refines hazard estimates: *Earth and Planetary Science Letters*, v. 464, p. 175-188.
- De Pascale, G. P., and Langridge, R. M., 2012, New on-fault evidence for a great earthquake in AD 1717, central Alpine fault, New Zealand: *Geology*, v. 40, no. 9, p. 791-794.
- Hogg, A. G. et al., 2013, SHCal13 Southern Hemisphere Calibration, 0–50,000 Years cal BP, 2013.
- Howarth, J. D., Fitzsimons, S. J., Norris, R. J., and Jacobsen, G. E., 2012, Lake sediments record cycles of sediment flux driven by large earthquakes on the Alpine fault, New Zealand: *Geology*, v. 40, no. 12, p. 1091-1094.
- Howarth, J. D., Fitzsimons, S. J., Norris, R. J., and Jacobsen, G. E., 2014, Lake sediments record high intensity shaking that provides insight into the location and rupture length of large earthquakes on the Alpine Fault, New Zealand: *Earth and Planetary Science Letters*, v. 403, p. 340-351.
- Howarth, J. D., Fitzsimons, S. J., Norris, R. J., Langridge, R., and Vandergoes, M. J., 2016a, A 2000 yr rupture history for the Alpine fault derived from Lake Ellery, South Island, New Zealand: *Geological Society of America Bulletin*, v. 128, no. 3-4, p. 627-643.
- Lienkaemper, J. J., and Ramsey, C. B., 2009, OxCal: Versatile Tool for Developing Paleoequake Chronologies, *A Primer: Seismological Research Letters*, v. 80, no. 3, p. 431-434.
- Norris, R. J., and Cooper, A. F., 2001, Late Quaternary slip rates and slip partitioning on the Alpine Fault, New Zealand: *Journal of Structural Geology*, v. 23, no. 2-3, p. 507-520.
- Sutherland, R. et al., 2007, Do Great Earthquakes Occur on the Alpine Fault in Central South Island, New Zealand?, *A Continental Plate Boundary: Tectonics at South Island, New Zealand*, American Geophysical Union, p. 235-251.
- Wells, A. et al., 1999, Prehistoric dates of the most recent Alpine fault earthquakes, New Zealand: *Geology*, v. 27, no. 11, p. 995-998.
- Yetton, M. D., 1998, Progress in understanding the paleoseismicity of the central and northern Alpine Fault, Westland, New Zealand: *New Zealand Journal of Geology and Geophysics*, v. 41, no. 4, p. 475-483.
- Yetton, M., and Wells, A., 2010, Earthquake rupture history of the Alpine Fault over the last 500 years, in Williams, A.L., Pinches, G.M., Chin, C.Y., McMorrin, T.J., and Massey, C.I., eds., *Geologically Active: Proceedings of 11th International Association for Engineering Geology and the Environment Congress*, Auckland, September 2010: Boca Raton, CRC Press, p. 881–891.
- Yetton, M.D., 2002, Paleoseismic investigation of the north and west Wairau sections of the Alpine Fault, South Island, New Zealand. EQC Research Report 99/353, Wellington.
- Yetton, M.D., et al., 1998, The probabilities and consequences of the next Alpine Fault earthquake. EQC Research Report 95/193, Wellington. (Bold 9 pts. two lines after acknowledgements or final conclusions)



Late Quaternary activity of the Dangjiang fault, Central Tibetan Plateau

Xuemeng Huang, Wu Jiwen, Xie Furen

(1) The Institute of Crustal Dynamics, China Earthquake Administration

Abstract: The left-lateral strike-slip Dangjiang fault, which strikes NWW and extends over a length of 180km, is located at the westernmost of the Ganzi-Yushu fault zone between Bayan Har block and Qiangtang block in the central-eastern Tibetan Plateau. Due to the remoteness and high altitude, the late Quaternary activity of the Dangjiang segment is poorly understood compared with other segments within the Ganzi-Yushu Fault system. Based on the interpretation of remote sensing images and field investigations, this fault has a clear geomorphic expression which is characterized by prominent surface rupture zone, fault scarp and systematically offset gullies, fluvial terraces and alluvial fans along strike. We identified an 85km-long surface rupture zone produced by most recent large seismic event (1738 earthquake) with a maximum 5m of co-seismic displacement based on the offset of gullies on the alluvial fan surface, this earthquake might be of moment magnitude 7.5 according to relative empirical equations. The late Quaternary left lateral slip rate of this fault was estimated to be about 6.7~7.8mm/a according to typical gullies and alluvial offset and corresponding ages. The result is consistent with those obtained from long-term geological evidence and GPS derived estimates. This slip rate combined with the maximum co-seismic displacement of 5m estimates the recurrence interval of such great earthquake (M 7.5) is about 640~750a. This study provides basic data for the seismic hazard assessment of the Ganzi-Yushu fault in central Tibetan Plateau.

This research was supported by the China Earthquake Administration Research Fund (No. DZJ2016-18) and the National Natural Science Foundation of China (No. 41602222).



Optically stimulated luminescence dating (OSL) in awkward places: what is doable in tectonically active environments

Huot, Sebastien (1)

(1) Illinois State Geological Survey, Prairie Research Institute, University of Illinois at Urbana-Champaign. shuot@illinois.edu

Abstract: Luminescence (OSL) dating is a technique able to measure the time elapsed since the last exposure to sunlight, hence the burial age of sediment. It has a wide range of application in geology. A key obstacle for dating, here, is an effect called < partial bleaching >. At < time zero >, when the sediment is for the last time eroded, transported and buried, the luminescence age of this sediment has to be zero. If not, then the calculated age for a buried sediment will appear as too old, older than what should be expected. This is an issue that will be explained during the presentation. It will also offer brief examples taken from seismic areas.



Preliminary insights into the fault geometries and kinematics of surface rupture along the South Leader Fault during the Mw 7.8 Kaikoura earthquake

Hyland, Natalie (1), Nicol, Andrew (1) Fenton, Clark (1), Narges Khajavi (1) Pettinga, Jarg (1) Bushell, Tabitha (1)

(1) Department of Geological Sciences, University of Canterbury, Private Bag 4800, Christchurch, New Zealand

Abstract: The south Leader Fault (SLF) is a newly documented active structure that ruptured the surface during the Mw 7.8 Kaikoura earthquake. The Leader Fault is a NNE trending oblique left lateral thrust that links the predominantly right lateral 'The Humps' and Conway-Charwell faults. The present research uses LiDAR at 0.5 m resolution and field mapping to determine the factors controlling the surface geometries and kinematics of the south Leader Fault ruptures at the ground surface. The SLF zone is up to 2km wide and comprises a series of echelon NE-striking thrusts linked by near-vertical N-S striking faults. The thrusts are upthrown to the west by up to 1 m and dip 35-45°. Thrust slip surfaces are parallel with Cretaceous-Cenozoic bedding and may reflect flexural slip folding. By contrast, the northerly striking faults dip steeply (65° west- 85° east), and accommodate up to 3m of oblique left lateral displacement at the ground surface and displace Cenozoic bedding. Some of the SLF has been mapped in bedrock, although none were known to be active prior to the earthquake or have a strong topographic expression. The complexity of fault rupture and the width of the fault zone appears to reflect the occurrence of faulting and folding at the ground surface during the earthquake.

Key words: Kaikoura Earthquake, North Canterbury, Fault Kinematics, Fault Geometries, Transpressive Structures

INTRODUCTION

The November 14th Mw 7.8 Kaikoura earthquake ruptured at least 14 faults of varying orientations, ages, geometries, kinematics, and total displacements (Hamling et al., 2017; Litchfield et al., 2017; unpublished data). The earthquake nucleated near the township of Waiau propagated to the northeast and produced slip on a complex network of faults in both the North Canterbury Domain (NCD) and Marlborough Fault System (MFS). The MFS and NCD are accommodating transpressive deformation in response to oblique convergence of the Pacific and Australian plates (Nicol et al., 2017). The Leader Fault, which is in the NCD, is predominantly a left-lateral oblique thrust that has a general strike of NNE and links 'The Humps' and Conway-Charwell faults. The southern part of the Leader Fault (SLF) is the focus of this study (Figure 1).

While there are other well documented transpressive structures in an overall-all strike-slip zone (i.e. California, Mongolia), the detailed geometries, surface expressions and slip within the SLF remains largely unexplained by international models. Historically, events that ruptured complex fault networks (The El Mayor Cucupah Earthquake; Gonzalez-Ortega et al. 2010; Fletcher et al., 2016) produced larger ruptures and displacements than would be expected for a single isolated fault. To improve our understanding of events that may rupture multiple faults, it is necessary to determine the main factors that influence the geometry, kinematics, and slip distribution for any given surface rupture.

The primary objective of this research at present is to analyse the slip, geometries, and kinematics of the SLF gathered from field work offset measurements, RTK

surveying and bedrock mapping) and terrestrial LiDAR at 0.5 m resolution. These data will be used to produce a kinematic model of the SLF which accounts for both the local complexities and regional tectonics. The results will be compared to and conditioned by international studies in transpressional settings.

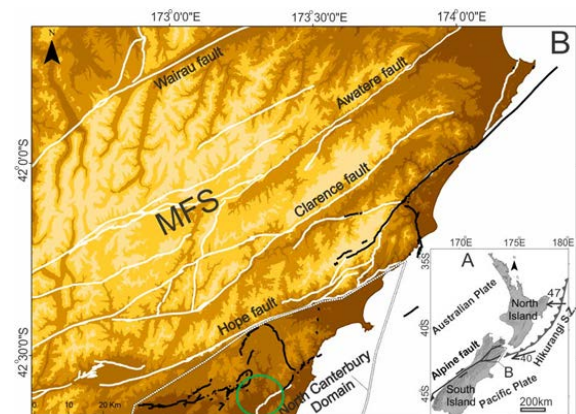


Figure 1: A) The Plate Boundary and motion vectors of New Zealand, DeMets et al., 1994. B) Digital elevation model depicting the position of the South Leader Fault (green circle) within the geological setting of the Mw 7.8 Kaikoura earthquake, where active faults are white lines and black lines are ruptures resulting from the Kaikoura Earthquake.

DISCUSSION

The Leader Fault is primarily left-lateral reverse with an overall NNE strike. The fault zone has an end-to-end strike length of ~22 km from a free tip in the south to its intersection with the Conway-Charwell Fault in the north. The SLF forms a complex zone up to ~3 km wide with strike



varying through 180° and dips from 60° east to 25° west along the fault. Prior to the earthquake it had been mapped as a bedrock fault forming a Torlesse basement to Greta Siltstone Formation contact and also within the Greta Siltstone (Warren, 1993; Rattenbury et al., 2006). The fault was neither mapped in Torlesse basement nor mapped as active before the earthquake and, at the time of writing, no active fault scarps have been mapped which pre-dated the earthquake.

The SLF comprises faults striking NE and dipping at shallow angles (20-40°) to the northwest interspersed with parts of the fault that strike to the north and dip steeply (e.g., >60°; Figure 2). Shallow dipping parts of the fault have irregular rupture-trace geometries which, in part, reflect the interplay between the low fault dips and topography. These shallow faults are often located at the contact between basement and Cretaceous-Cenozoic cover rocks and/or at the base of the Greta Siltstone Formation. They appear to accommodate bedding-parallel slip, perhaps associated with flexural-slip folding of the Cretaceous-Cenozoic sequence. The steep north-striking parts of the SLF are generally contained within the Miocene Greta Siltstone Formation.



Figure 2: The Waiiau Wall of Woodchester: a ~3m vertical displacement (Photo by Dr. Kate Pedely).

Slip on the SLF during the earthquake increased in a non-linear fashion northwards from the southern tip of the fault. Over the southern 4 km of the fault, maximum vertical and horizontal slip was 1m and 0.7m, respectively, upthrown to the west. Where strike slip is observed on these southern traces it is left lateral, although there are limited exposures where horizontal displacements can be accurately measured. To the north, the SLF is characterized by much larger displacements, where a maximum vertical and horizontal displacement are 3.4m and 2.5m, respectively. At the Waiiau Wall locality (Figure 2), the faults displace the Miocene Greta Siltstone Formation and slip is close to its maximum in the study area.

The complexity of fault rupture and the width of the fault zone was unexpected. Our ability to map this complexity has been aided by a lack of vegetation in the study area and the availability of LiDAR-derived DEM. In the absence of these data and after several hundred years of surface processes (e.g., erosion/burial) many of the surface

ruptures would be undetectable. In the study area the complexity of surface ruptures appears to reflect a number of factors, including the occurrence of faulting and folding (associated with flexural slip) at the ground surface during the earthquake.

Acknowledgements: Thanks to GNS Science for use of LiDAR and orthophoto imagery, and The University of Canterbury and the Earthquake Commission for funding of this project. To the landowners of Woodchester, David and Rebekah Kelly, for their continued tolerance, generosity and resilience in the face of hardship, to Paul Ashwell and Andrea Barrier for their help and comradery in the field, and to my advisory team; Andy Nicol, Clark Fenton, Narges Khajavi, and Jarg Pettinga for their guidance, support, humour, and expertise.

REFERENCES

- DeMets, C., Gordon, R.G., Argus, D.F., Stein, S., 1994. Effect of recent revisions to the geomagnetic reversal time scale on estimates of current plate motions. *Geophysical Research Letters* 21, 2191-2194.
- Fletcher, J.M., Oskin, M.E., and Teran O.J., 2016. The role of a keystone fault in triggering the complex El Mayor-Cucapah earthquake rupture. *Nature Geoscience*, 9(4), pp.303-307
- Gonzalez-Ortega, A., Y. Fialko, D. Sandwell, F. A. Nava-Pichardo, J. Fletcher, J. Gonzalez-Garcia, B. Lipovsky, M. Floyd, and G. Funning (2014), El Mayor-Cucapah (Mw7.2) earthquake: Early near-field postseismic deformation from InSAR and GPS observations, *Journal of Geophysical Research: Solid Earth*, 119(2), 1482–1497, doi:10.1002/2013jb010193.
- Hamling, I.J., Hreinsdóttir, S., Clark, K., Elliott, J., Liang, C., Fielding, E., Litchfield, N., Villamor, P., Wallace, L., Wright, T.J., D'Anastasio, E., Bannister, S., Burbidge, D., Denys, P., Gentle, P., Howarth, J., Mueller, C., Palmer, N., Pearson, C., Power, W., Barnes, P., Barrell, D.J.A., Van Dissen, R., Langridge, R., Little, T., Nicol, A., Pettinga, J., Rowland, J., Stirling, M., 2017. Complex multi-fault rupture during the 2016 Mw 7.8 Kaikōura earthquake, New Zealand. *Science*, DOI: 10.1126/science.aam7194 (2017).
- Litchfield N.J., Villamor P., Dissen R., Nicol A., Barnes P., Barrell D., Pettinga J., Langridge R., Little T., et al. Surface ruptures and paleoseismology of the Mw 7.8 2016 Kaikōura earthquake reveal end-member complexity. *Geology* (in review).
- Nicol, A., Seebeck, H., Wallace, L., 2017. Quaternary tectonics of New Zealand. In: Schulmeister, J., (ed) *Atlantis Advances in Quaternary Science: Landscape and Quaternary Environmental Change in New Zealand*, Atlantis Press, p. 1-34, DOI: 10.2991/978-94-6239-237-3_1.
- Stirling, M.W., Litchfield, N.J., Villamor, P., Van Dissen, R.J., Nicol, A., Pettinga, J., Barnes, P., Langridge, R.M., Little, T., Barrell, D.J.A., Mountjoy, J., Ries, W.F., Rowland, J., Fenton, C., Hamling, I., Asher, C., Barrier, A., Benson, A., Bischoff, A., Borella, J., Carne, R., Cochran, U.A., Cockroft, M., Cox, S.C., Fenton, F., Gasston, C., Grimshaw, C., Hale, D., Hall, B., Hao, K., Hatem, A., Hemphill-Haley, M., Heron, D.W., Howarth, J., Juniper, Z., Kane, T., Kearse, J., Khakavi, N., Lamarche, G., Lawson, S., Lukovic, B., Madugo, C., Manousakis, I., McColl, S., Noble, D., Pedley, K., Sauer, K., Stahl, T., Strong, T., Townsend, D.B., Toy, V., Villeneuve, M., Wandres, A., Williams, J., Woelz, S., Zinke R., 2017. The Mw 7.8 2016 Kaikōura earthquake: Surface fault rupture, and seismic hazard context. *Bulletin of the New Zealand Society for Earthquake Engineering* 50(2)(June 2017), 73-84.



Historical and paleo-tsunami deposits on the Sanriku Coast, northeast Japan

Ishimura, Daisuke (1)

(1) Department of Geography, Tokyo Metropolitan University. ishimura@tmu.ac.jp.

Abstract: After the 2011 Tohoku-oki earthquake and tsunami, the significance of tsunami deposit research was elevated, and tsunami deposit surveys were increased worldwide. The 2011 Tohoku-oki tsunami was investigated from various research viewpoints, and valuable information about the 2011 tsunami and its deposits was obtained. However, the long-term tsunami history along the Pacific coast in the Tohoku region (Sanriku Coast) before the 2011 event was not well known. Thus, paleo-tsunami deposit surveys have been conducted at several sites along the Sanriku Coast since 2012. Based on these surveys, long-term tsunami history was revealed and paleo-tsunami frequency and magnitude was estimated. Information regarding these events is significant not only for revealing the mechanism of tsunami generation but also for assessing the tsunami and earthquake hazard and risks along the Pacific coast of northeast Japan.

Key words: the 2011 Tohoku-oki earthquake, tsunami deposits, paleo-tsunami history, Sanriku Coast, Tohoku region.

INTRODUCTION

The Sanriku Coast (Fig. 1), a part of the Pacific coast in the Tohoku region, has been known for large and frequent tsunami disasters over the last hundred years (e.g., the 1960 Chile tsunami, the 1933 Showa Sanriku tsunami, and the 1896 Meiji Sanriku tsunami). However, the scale of the huge and devastating Tohoku-oki earthquake and tsunami in 2011 was unexpected. Before the 2011 event, there was insufficient information on long tsunami history (on the order of 10^3 years), and this area was considered inappropriate for finding tsunami deposits owing to its geomorphological characteristics (ria coast with a narrow coastal lowland) and recent artificial modification.

After the 2011 event, information on historical and paleo-tsunami history was considered increasingly necessary to evaluate earthquake and tsunami hazards and to mitigate risks; therefore, tsunami deposit surveys were conducted more commonly worldwide. Along the Sanriku Coast, historical and paleo-tsunami deposits were found by Ishimura & Miyauchi (2015, 2017) and Ishimura (2017) and by other researchers (Goto et al., 2015; Takada et al., 2016). However, long-term tsunami history was not well known, and the known tsunami deposits were not correlated to remote areas (e.g., Hokkaido and Sendai). In this paper, the author shows results of tsunami deposit surveys and presents conclusions on tsunami history, frequency and magnitude along the Sanriku Coast.

KOYADORI, CENTRAL SANRIKU COAST

In Koyadori (Fig. 1), a trench survey, drilling survey, and Handy Geoslicer survey were conducted (Ishimura & Miyauchi, 2015; Ishimura et al., 2014, 2015). In the Koyadori trench (12 m long, 3 m wide, and 2 m deep), 11 historical and paleo-tsunami deposits (E1–E11 deposits) were found in the marsh sediments dated from ca. 4000 cal. BP (Fig. 2). They are traceable in the trench, and the E1–E4 deposits, particularly, were widely distributed in the Koyadori lowland according to the Handy Geoslicer survey (Ishimura et al., 2015). Recently,

Ishimura (2017) re-examined the ages of the tsunami deposits to obtain a reliable correlation with historical tsunamis and to reveal the accurate ages of paleo-tsunami deposits using radiocarbon dating and other radiometric methods (^{137}Cs and excess ^{210}Pb). The new analysis provided reliable ages for 10 historical and paleo-tsunami deposits. Several tsunami deposits may be correlated with those of Takada et al. (2016), which conducted a tsunami deposit survey along the entire Sanriku Coast. The average recurrence interval of historical and paleo-tsunamis in the last 4 ka is 350–390 years, and each recurrence interval between the E4 and E11 deposits is similar despite the fact that the tsunami deposits exhibit different characteristics. In Koyadori, far-field tsunamis (e.g., the 1960 Chile tsunami) were not expected according to observation and topography (5 m high beach ridge), and thus, tsunami deposits at this site are more likely to reflect the near-field tsunami history and frequency. Therefore, the Koyadori site can be considered a type location for the near-field tsunami history along the Sanriku Coast and may enable us to compare the ages and frequency of tsunami deposits in other Pacific coast areas (e.g., Hokkaido and Sendai).

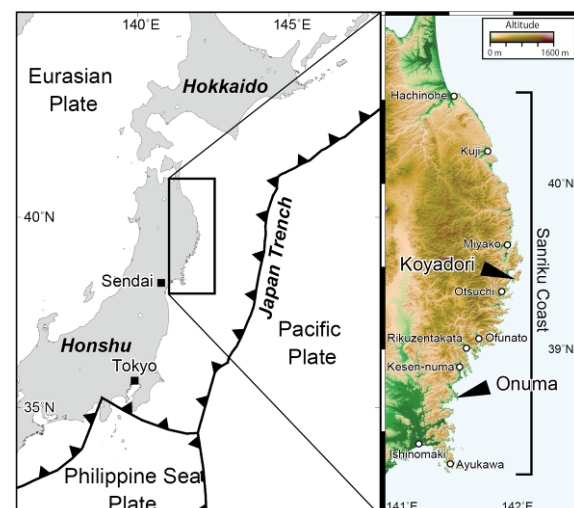


Figure 1: Tectonic setting and topography around the Sanriku Coast.

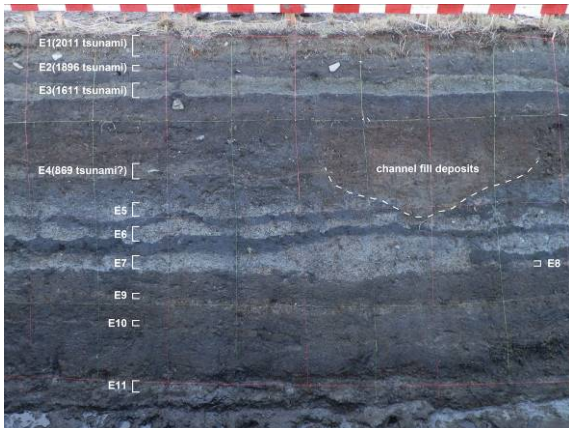


Figure 2: Photograph of a trench wall at Koyadori. The grid size is 50 cm.

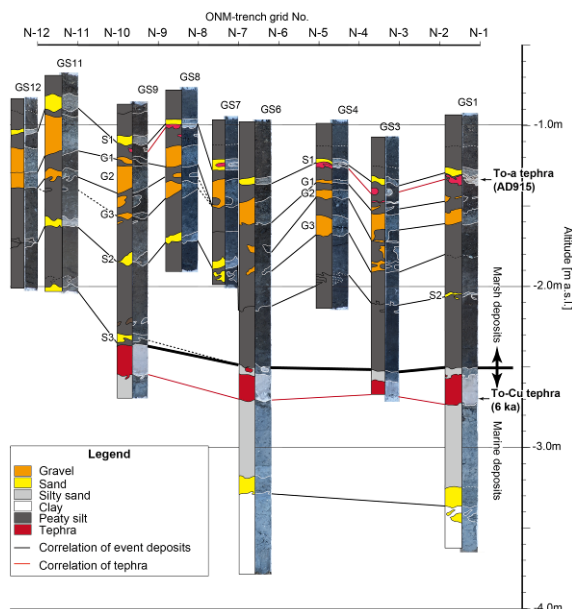


Figure 3: Handy Geoslicer cores from the trench floor at Onuma. This is modified after Ishimura and Miyauchi (2017).

ONUMA, SOUTHERN SANRIKU COAST

In Onuma (Fig. 1), a trench survey, drilling survey, and Handy Geoslicer survey were conducted (Ishimura & Miyauchi, 2017). At this site, the first wave of the 2011 Tohoku-oki tsunami passed over a hill from the north coast and inundated Onuma. Subsequently, another tsunami wave inundated Onuma again from the south coast. In the Onuma trench (13 m long, 3 m wide, and 2 m deep), only the 2011 tsunami deposits were found owing to thick artificial deposits. Therefore, the Handy Geoslicer survey was conducted on the trench bottom to observe deeper sediments. They found six tsunami deposits (S1–S3 and G1–G3 deposits) and two tephra (To-a (AD915) and To-Cu (6 ka); Machida and Arai, 2003) in the Handy Geoslicer cores (Fig. 3). The tsunami deposits were dated at 690–1040 BP (S1), 2240–3310 BP (G1), 3320–3630 BP (G2), 3620–4060 BP (G3), 4030–4400 BP (S2), and 4440–5570 BP (S3). Tsunami deposits were divided into two types (sandy (S1–S3) and gravelly (G1–G3) tsunami deposits). Ishimura & Miyauchi (2017) noticed the differences in beach

conditions along the north and south coasts and interpreted that the sandy tsunami deposits were composed of beach ridge and sand dune deposits from the south coast and that the gravelly tsunami deposits were composed of beach gravel deposits from the north coast. Next, they estimated the heights of the paleo-tsunamis as 5–10 m for sandy tsunami deposits and >10 m for gravelly tsunami deposits based on sources of the tsunami deposits and behavior of the 2011 tsunami (Fig. 4). They additionally demonstrated the use of paleo-environmental reconstruction, based on macro- and micro-fossil analysis, to evaluate the preservation potential and accommodation space available for tsunami deposits using long drilled cores.

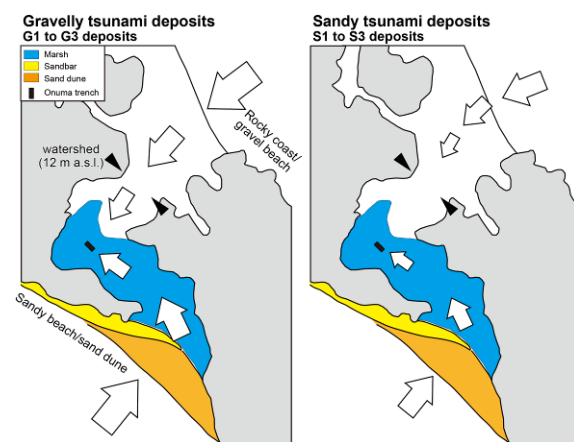


Figure 4: Schematic illustrations of two types of tsunami processes. Arrows indicate tsunami direction and relative flow speed. This is modified after Ishimura and Miyauchi (2017).

CONCLUSIONS

The author identified tsunami deposits and established tsunami histories at two sites on the Sanriku Coast. At Koyadori, the 11 historical and paleo-tsunami deposits since ca. 4 cal. kyr BP were identified, indicating high-frequent tsunami occurrence. At Onuma, the 6 tsunami deposits from 1 to 6 cal. kyr BP were found and their deduced sources enabled us to estimate the height of paleo-tsunamis. The author’s and other researchers’ exhaustive tsunami deposit research along the Sanriku Coast after the 2011 event revealed many distinguishable underground tsunami deposits and appropriate sites for tsunami deposit surveys along the coast, which was earlier regarded as inappropriate for tsunami deposit research. All the researchers since 2011 considered the topography and behavior of the 2011 event to determine study sites. Therefore, site selection is one of the most important considerations for finding and distinguishing tsunami deposits. Moreover, the preservation potential and availability of accommodation space are also important for assessing the reliability of the number of tsunami deposits. Comprehensive approaches are necessary for obtaining objective evidence. New problems such as the criteria for correlating tsunami deposits in remote areas and for evaluating their ages will be considered in future studies. The present and future problems related to tsunami deposit research need to be overcome to better understand the hazards and risks tsunamis pose.



INQUA Focus Group Earthquake Geology and Seismic Hazard



paleoseismicity.org

Acknowledgements: I would like to thank the Prof. Takahiro Miyauchi for giving me an opportunity to study tsunami deposits along the Sanriku Coast. This study was part of “Geophysical and geological studies of earthquakes and tsunamis for off-Tohoku district, Japan” and was supported by the Ministry of Education, Culture, Sports, Science, and Technology, Japan. This work was partially supported by Intramural Research Grant for Special Project Researches from International Research Institute of Disaster Science, Tohoku University, and JSPS KAKENHI Grant Number 26882001.

REFERENCES

- Ishimura, D., 2017. Re-examination of the age of historical and paleo-tsunami deposits at Koyadori on the Sanriku Coast, Northeast Japan. *Geoscience Letters*, 4, 11. DOI: 10.1186/s40562-017-0077-4.
- Ishimura, D., & Miyauchi, T., 2015. Historical and paleo-tsunami deposits during the last 4000 years and their correlations with historical tsunami events in Koyadori on the Sanriku Coast, northeastern Japan. *Progress in Earth and Planetary Science*, 2, 16. DOI: 10.1186/s40645-015-0047-4.
- Ishimura, D., & Miyauchi, T., 2017. Holocene environmental changes and paleo-tsunami history in Onuma on the southern part of the Sanriku Coast, northeast Japan. *Marine Geology*, 386, 126–139.
- Ishimura, D., et al., 2014. Characteristics of tephra interbedded with the Holocene sediments in the Sanriku Coast, northeast Japan. *Journal of Geography*, 123, 671–697 (in Japanese with English abstract).
- Ishimura, D., et al., 2015. Continuity of tsunami deposits and their correlations based on close interval Handy Geoslicer survey: case study of Koyadori, Yamada Town, Iwate Prefecture, northeast Japan. *Active Fault Research*, 43, 53–60 (in Japanese with English abstract).
- Goto, T., Satake, K., Sugai, T., Ishibe, T., Harada, T., & Murotani, S., 2015. Historical tsunami and storm deposits during the last five centuries on the Sanriku coast, Japan. *Marine Geology*, 367, 105–117.
- Machida, H., & Arai, F., 2003. Atlas of Tephra in and Around Japan [Revised Edition]. University of Tokyo Press, Tokyo (in Japanese).
- Takada, K., Shishikura, M., Imai, K., Ebina, Y., Goto, K., Koshiya, S., Yamamoto, H., Igarashi, A., Ichihara, T., Kinoshita, H., Ikeda, T., & River Division Department of prefectural Land Development, Iwate Prefecture Government, 2016. Distribution and ages of tsunami deposits along the Pacific Coast of the Iwate Prefecture. *Annual report on active fault and paleoearthquake researches*, 16, 1–52 (in Japanese with English abstract).



Earthquake damages associated with the 2016 $M_L=5.8$ Gyeongju earthquake, Korea

Jin, Kwangmin (1), Kim, Young-Seog (2), Lee, Jinhyun (2)

(1) Climate Change Mitigation and Sustainability Division, Korea Institute of Geoscience and Mineral Resources (KIGAM), Korea.
maxgarion@kigam.re.kr

(2) Dept. of Earth & Environmental Sciences, Pukyong National University.

Abstract: Recently, an earthquake of $M_L=5.8$ hit Gyeongju area on September 12, 2016, which is the largest instrumentally recorded earthquake in South Korea. Some buildings and houses in villages around the epicentre were severely damaged, providing an opportunity to evaluate the potential hazards and character of destruction that occurs to buildings of specific construction and materials, known underlying foundation properties (sediment or bedrock character) and instrumentally recorded parameters (magnitude, epicentre, depth) of the causal earthquake event. During this study, damaged buildings and houses were investigated, described and recorded with the aim to characterize the damage and determine related controlling factors. The distribution of damaged buildings was found to be relatively scattered rather than concentrated around the epicenter. This may be related to the focal depth, which was about 14–16 km deep. The overall area of influence was within 17 km radius from the epicentre, suggesting that the area influenced by ground motion is almost the same as the focal depth, which is concentrated. The damaged buildings have different damage patterns depending on their building structures, material property and seismic design. In one small village, we found wholly different degrees of damages for buildings and houses. After an electrical resistivity survey to assess the local geologic conditions, it was shown that the more heavily damaged area corresponded with construction on unconsolidated alluvium. This information will be useful for the construction code of reinforcement design and earthquake hazard studies.

Key words: Gyeongju earthquake, earthquake damage, focal depth, damaged building, local geologic condition

INTRODUCTION

In recent decades large earthquakes have caused major loss-of-life and extreme property damage worldwide, and projected population growth combined with urbanisation suggest this trend will continue (Wisner et al., 2008; EM-DAT, The International Disaster Database, 2011; Doocy et al., 2013). The Korea Peninsula is commonly considered to be tectonically stable compared to neighbouring Japan and Taiwan because it is located within the Eurasian intracontinental region (e.g. Kim et al. 2004). However, more than 60 potentially active Quaternary faults have been reported along the Yangsan and Ulsan faults in southeast Korea (Fig. 1). 94 historical earthquakes recorded above magnitude of 5 around Gyeongju were reported in historical records (e.g. *Samguksagi*, *Koryeosa*, etc.). Recently, an earthquake ($M_L=5.8$) hit the Gyeongju area, which is the largest earthquake since the onset of modern instrumental recording in South Korea. Many buildings and houses were damaged during the event (Kim et al., 2017).

In this study, we investigated the damage patterns of the buildings to understand controlling factors associated with earthquake hazards, such as relationship between damage distribution and focal depth, difference of damage patterns on building structures, and local soil and geologic conditions. Although it is difficult to estimate the exact relationship between earthquake damages and any certain controlling factor, it will provide useful information for preparing for future earthquake events.

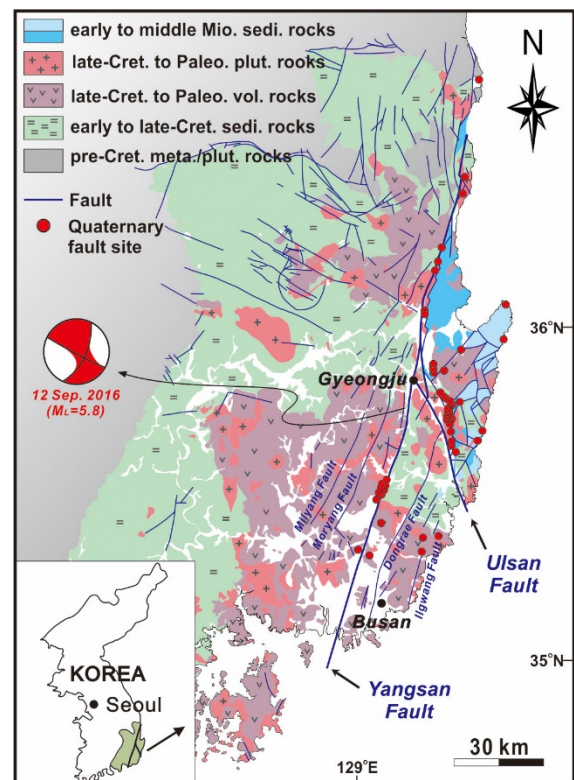


Figure 1: Geologic and structural map of the study area (modified from Chough and Sohn, 2010). Red dots indicate the Quaternary fault sites. Fault plane solution for the 2016 Gyeongju earthquake ($M_L=5.8$) constrained by first-motion solution.



DISTRIBUTION OF THE 2016 GYEONGJU EARTHQUAKE DAMAGES

Generally, the focal depth affects the amount of shaking during an earthquake event (Keller and DeVecchio, 2016). Seismic waves from deep earthquakes should travel a greater distance to the surface, losing some of their energy along the way. It means that shallower focal depth events will correspond to more intense shaking while deeper focal depths should result in less shaking. While deeper earthquakes may be less damaging, they are felt for a greater distance. For example, in 2016 a strong earthquake (M=6.2) with a shallow focal depth (4.0-9.6 km), hit Pescara del Tronto, Italy, killing many people and destroying a number of buildings (Masi et al., 2016). A bigger earthquake (M=6.8), hit Bagan, Myanmar the same year with a deeper focal depth (~85 km). The earthquake resulted in lower relative loss-of-life and property damage despite its larger magnitude (Zaw et al., 2017).

Many buildings and houses were severely damaged during the 2016 Gyeongju earthquake in villages around the epicenter (Fig. 2). Some big cities, located around the Gyeongju, were also affected by the earthquake. However, the distribution of damaged buildings is relatively scattered rather than concentrated around the epicenter (Fig. 2). The serious ground motion and associated damages effected by the earthquake are mainly concentrated within 17 km radius area from the epicenter (Fig. 2). It indicates that the distribution of damages associated with the 9.12 Gyeongju earthquake may be closely related to the focal depth. Furthermore, according to media reports, when the earthquake occurred, it was felt nearly everywhere in Korea, and some reports were received from China and Japan.

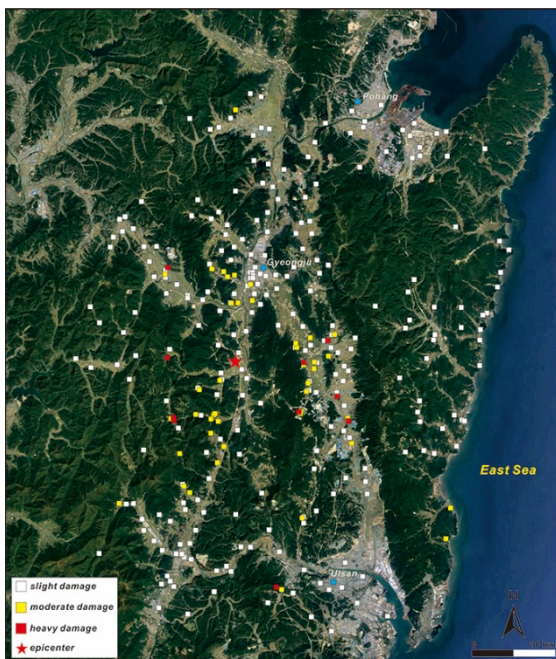


Figure 2: Distribution map of damaged buildings and houses associated with the 9.12 Gyeongju earthquake.

DAMAGE PATTERNS OF BUILDINGS AND HOUSES DEPENDING ON THEIR BUILDING STRUCTURES

Field investigations of damaged buildings and houses following an earthquake is one of the most fundamental activities completed to enhance earthquake protection strategies (Okada and Takai, 2000). We carried out field investigation on destroyed buildings and houses after the 9.12 Gyeongju earthquake around the epicenter. The types of buildings and houses were divided into categories based on their building structures, such as reinforced concrete frame buildings, reinforced concrete confined masonry, unreinforced and unconfined masonry, vernacular and historical constructions.

Reinforced concrete frame buildings had the least damage from the earthquake. Buildings constructed in this manner consisted of schools, hospitals, government buildings, hotels, and business buildings. There are many historical heritage and traditionally constructed buildings and houses, because Gyeongju is the old capital city of Silla Dynasty (57 BC – 935 AD). Some buildings have been maintained for over 1000 years. For this reason, Gyeongju is one of the most famous tourist cities in South Korea. Most of severe damages occurred on unreinforced and unconfined masonry, vernacular, and traditional construction (Fig. 3). In particular, wooden frame houses with lightweight roof tiles and fences built out of stone and mud (Fig. 4) were the most vulnerable to the earthquake shaking. This indicates that the different amount of damages and damage patterns are strongly dependent on the building structures, materials, and seismic design.



Figure 3: Damages associated with unreinforced and unconfined masonry constructions of old styled houses by the 9.12 Gyeongju earthquake ($M_L=5.8$).



Figure 4: Damages of lightweight roof tiles with mud and stone fence with mud by the 9.12 Gyeongju earthquake ($M_L=5.8$).

DAMAGED BUILDINGS AND HOUSES DEPENDING ON LOCAL SOIL AND GEOLOGICAL CONDITIONS

In general, local soil and geological conditions can cause changes in the amplitudes, spectral content, duration of strong earthquake ground motion, and ultimately the resulting damage to man-made structures (Trifunac, 2016). During the field investigation on damage patterns of buildings and houses, we found wholly different damage intensities depending on the specific location in a small village, Bandong Village (Fig. 5). Although the buildings have even similar building structures and materials, the damages are entirely different between the northern (Fig. 5a, c, e, g) and southern (Fig. 5b, d, f, h) areas in the village. The damages are more serious in the southern area than in the northern area.



Figure 5: Damage patterns in a small village, Bandong Village, by the 9.12 Gyeongju earthquake ($M_L=5.8$). Photographs show wholly different damage intensities even with similar building structures and materials.

To identify the causes, we carried out electrical resistivity surveys across the village's alluvium surface. Two lines (Line A and Line B) were set up with a length of 280 m in northern and southern areas, respectively (Fig. 6a). Based on the exploration result, the depth of the alluvium in the northern and southern parts is different (Fig. 6b). The depth of the alluvium along the Line A is about 5-20 m, whereas it is about 15-50 m along the Line B. The alluvium along the Line B is twice as deep than the alluvium deposits along Line A (Fig. 6b). Therefore, it indicates that local soil and geological conditions changed the amplitudes and duration of earthquake motion, causing different damages to man-made buildings.

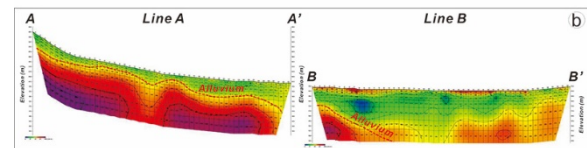


Figure 6: The electrical resistivity exploration on the alluvium in the Bandong Village. (a) Location map of designed exploration lines. (b) The exploration result of the two lines. It shows the difference of alluvium thickness.

DISCUSSION

Historical records on earthquake in Korea exist from 2 AD to the present, and can be classified according to three historical time periods; 1) Three Kingdoms (18 BC – 918 AD), 2) Koryeo Dynasty (918 – 1392 AD), and 3) Choseon Dynasty (1392 – 1911 AD). In particular, 105 earthquakes recorded in the period of Three Kingdoms, most of these earthquakes were concentrated on the capital cities of the Three Kingdoms such as Guknaeseong, Pyeongyang, Hansan, Booyeo, and Gyeongju. This result may partly attribute to relatively systematic reporting and recording system in old capital cities. The Gyeongju city was the capital city of the Silla Dynasty (Three Kingdoms) during the period of almost 1,000 years. Thus, it contains many historical heritage sites and a well organized reporting and recording system. According to historical records, the city experienced many large earthquakes resulting in extensive damage to the heritage sites of the Silla Dynasty. Recently, an archaeoseismological studies have been reported on the historical heritages in Gyeongju area (Jin et al., 2009, 2011). However, it is unique scientific study on historical heritages associated earthquake events. Therefore, additionally intensive studies on the historical heritages must be conducted focusing on the archaeoseismic evidences potentially documented in Gyeongju area.



According to historical records, large earthquake events occurred around the Gyeongju and neighbouring cities. However, surface ruptures or faults corresponding with large earthquakes have not been reported in Gyeongju area. Hence, intensive paleoseismological investigation for the active faults triggered large historical earthquakes should be studied in or around Gyeongju city.

CONCLUSION

During the 2016 Gyeongju earthquake, a lot of buildings and houses were severely damaged. We found several characteristics of damages and related controlling factors to the damages throughout the detailed investigation on damaged buildings.

Firstly, broadly scattered damaged buildings and houses may be related with the relative deep focal depth of the earthquake. Secondly, the strongly different damage patterns are dependent on their building structures, materials, seismic design, and etc. Thirdly, it is well known that local soil and geological conditions can cause severe damages to man-made buildings changing the amplitudes and durations of earthquake ground motion.

Although we think these points are the main controlling factors to the earthquake damages by the 2016 Gyeongju earthquake, probably there are some other factors to be considered. Finally, this information will be helpful for future earthquake hazard assessment and anti-earthquake design.

Acknowledgements: This study was supported by a part of the project titled "Development of nationwide geoenvironmental maps for HLW geological disposal (17-3424)" funded by the Ministry of Science and ICT, Korea.

REFERENCES

Chough, S.K., & Sohn, Y.K., 2010. Tectonic and sedimentary evolution of a Cretaceous continental arc-backarc system in the Korean peninsula: New view. *Earth-Science Reviews* 101, 225-249.

- Doocy, S., Daniels, A., Packer, C., Dick, A., & Kirsch, T.D., 2013. The Human Impact of Earthquakes: a Historical Review of Events 1980-2009 and Systematic Literature Review. *PLoS Current*, 5, ecurrents.dis.67bd14fe457f1db0b5433a8ee20fb833.
- EM-DAT, The International Disaster Database, 2011. Retrieved Mar 3, 2011 and July 28, 2011 from www.emdat.be/
- Jin, K., Lee, M., & Kim, Y.-S., 2009. Geological study on the collapse of a carved stone Buddha statue in Yeolam valley of Namsan, Gyeongju, Korea. *Journal of the Geological Society of Korea* 42, 79-94 (in Korean with English abstract).
- Jin, K., Lee, M., Kim, Y.-S., & Choi, J.-H., 2011. Archaeoseismological studies on historical heritages sites in the Gyeongju area, SE Korea. *Quaternary International* 242, 158-170.
- Kim, Y.-S., Kim, T., Kyung, J.B., Cho, C.S., Choi, J.-H., & Choi, C.U., 2017. Preliminary study on rupture mechanism of the 9.12 Gyeongju Earthquake. *Journal of the Geological Society of Korea* 53, 407-422 (in Korean with English abstract).
- Kim, Y.-S., Park, J.Y., Kim, J.H., Shin, H.C., & Sanderson, D.J., 2004. Thrust geometries in unconsolidated Quaternary sediments and evolution of the Eupcheon Fault, southeast Korea. *The Island Arc* 13, 403-415.
- Keller, E.A., & DeVecchio, D.E., 2016. *Natural Hazards (4th edition)*. Routledge. London and New York. 574 p.
- Masi, A., Santarsiero, G., Chiauzzi, L., Gallipoli, M.R., Piscitelli, S., Vignola, L., Bellanova, J., Calamita, G., Perrone, A., Lizza, C., & Grimaz, S., 2016. Different damage observed in the villages of Pescara del Tronto and Vezzano after the M 6.0 August 24, 2016 Central Italy earthquake and site effects analysis. *Annals of Geophysics* 59, 1-12.
- Okada, S., & Takai, N., 2000. Classifications of structural types and damage patterns of buildings for earthquake field investigation. In: *12th World Conference on Earthquake Engineering*, Auckland, New Zealand.
- Trifunac, M.D., 2016. Site conditions and earthquake ground motion-A review. *Soil Dynamics and Earthquake Engineering* 90, 88-100.
- Wisner, B., Blaikie, P., Cannon, T., & Davis, I., 2008. *At Risk: Natural hazards, people's vulnerability and disasters (2nd Edition)*. Routledge. New York. 275p.
- Zaw, S.H., Ornthammarath, T., & Poovarodom, N., 2017. Seismic reconnaissance and observed damage after the Mw 6.8, 24 August 2016 Chauk (Central Myanmar) earthquake. *Journal of Earthquake Engineering* (in press).



Surprisingly high post-glacial fault slip rates in a slow deforming area: the case of the Culoz fault system (French Jura Mountains)

Jomard, Hervé (1), De La Taille, Camille (1,2,3), Crouzet, Christian (2,3), Jouanne, François (2,3), Beck, Christian (2,3)

- (1) Institut de Radioprotection et de Sûreté Nucléaire, BERSIN, 92260 Fontenay aux Roses, France,
 (2) Institut des Sciences de la Terre, Université de Savoie, 73376 Le Bourget du Lac, France
 (3) CNRS, ISTerre, 73376 Le Bourget du Lac, France

Abstract: The north-western Alps foreland (Jura Mountains) is considered as still experiencing distal effects of the Alpine collision, resulting in a moderate but significant seismicity. This study focuses on the Culoz strike slip fault, developing from the Jura Mountains to the West, to the Chautagne swamp and through Lake Le Bourget to the East. Because erosion and anthropogenic activities erased most of the potential geological markers of quaternary deformations on land, we used high resolution seismic imaging to detect and characterize active faulting in the Quaternary sediments of the Bourget post-glacial Lake. The well-stratified character of the lake infill is locally disturbed by tectonic deformations associated with the activity of the left lateral Culoz fault as well as gravity reworking. Taking into account the age of the sediments (based on core samples), a quantification of the observed deformations together with the analysis of a well preserved outcrop on land, attest for fault slip-rates ranging from 0.055 to 3.11 mm/yr, the latter being surprisingly high in comparison with what we know elsewhere in France. A comparison with core-drills obtained in the neighboring lakes (Beck, 2009) allows us to envisage a non-stable seismic activity along the fault through time, and to propose a dominant control of the deglaciation on the observed fault slip-rates.

Key words: Jura Mountains, fault slip rate, Culoz fault, earthquake recurrence.

INTRODUCTION

The north-western Alps foreland and the Jura Mountains (Fig. 1) are classically considered to register moderate deformations induced by the anticlockwise rotation of the Adria microplate relative to stable Eurasia (Biju-Duval et al., 1977; Vigny et al, 2002; Nocquet et al., 2012). In addition to this kinematics, the fast disappearance of the Last Glacial Maximum (LGM) glacial cover and the mass transfer following the LGM may have significantly enhanced seismicity and gravity instabilities through unloading effects (Beck et al., 1996; Vernant et al., 2013).

Because erosion and anthropogenic activities erased most of the potential geological markers of Quaternary deformations on land, we used high resolution seismic imaging to detect and quantify active faulting in the Quaternary sediments of the Bourget post-glacial Lake, located along the eastern tip of the Culoz strike slip fault (De La Taille et al., 2015). The obtained data are analysed in the light of previous works describing the sedimentological infill of both Le Bourget and nearby Annecy Lakes (Van Resbergen et al., 1999, Chapron, 1999; Beck, 2009).

NEOTECTONIC SETTINGS

In southern Jura, the tectonic activity appears concentrated along NW–SE left lateral strike slip faults, such as the Culoz Fault and the Vuache Fault (Figure 1). The Culoz Fault extends from the internal Jura to the west (Figure 1) to the Chautagne swamp and Lake Le Bourget to the East. Historical earthquakes are known in the vicinity of this fault, in particular the one that occurred in February 1822 (Figure 1 and 2), with an epicentral intensity of VII–VIII (Vogt and Godefroy, 1979). Concerning Lake Le

Bourget, the Culoz fault locally influences the lake sediments by either in-situ disturbances or reworking events (see Beck, 2009). In particular, several circular depressions with concentric steps have been observed with sonar survey; they are 15 to 20 m wide, 1 to 2 m deep and affect up to 4.5 m of sediments. As they are close to the main known historical earthquake and affect the most recent unconsolidated sediments, they have been interpreted as “collapse craters”, which are common features related to massive and sudden fluid escape during seismic shaking (Chapron, 1999; Ledoux et al., 2010).

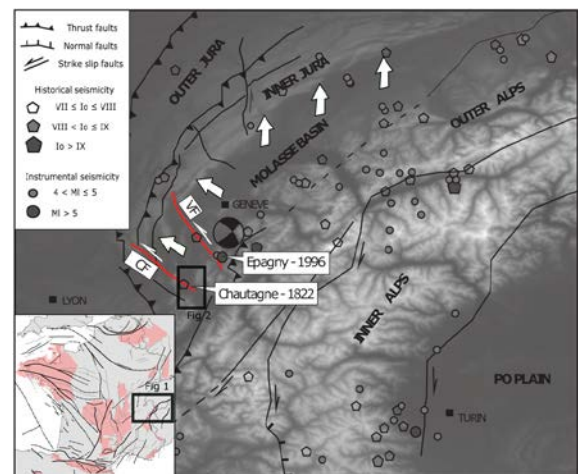


Figure 1: Localisation of the Culoz and the Vuache left lateral strike slip faults (CF and VF, respectively) in the Alpine context. Main historic (SisFrance catalog) and instrumental (CEA/LDG catalog) seismic events are plotted. The focal mechanism related to the 1996 Epagny event is also reported. Inset shows the study site in France. White arrows indicate the orientation of the maximum horizontal stresses in the Jura Mountains (from Becker et al., 2000).

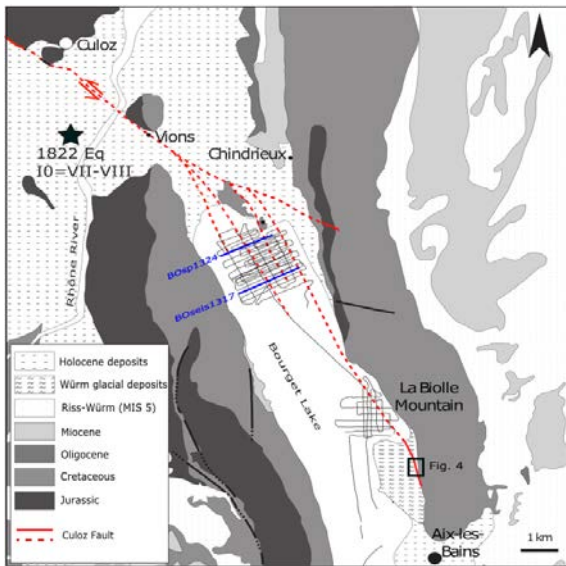


Figure 2: Eastern termination of the Culoz fault as inferred from off-shore geophysics and on-shore data (De La Taille et al., 2015). The black star represents the epicentral location of the 1822 earthquake as reported in the Sisfrance database. Location of figure 4 is reported on the map as well as the location of the seismic profiles presented in Figure 3.

DATA ACQUISITION AND RESULTS

A seismic survey was performed to image the suspected subaqueous (“offshore”) prolongation of the Culoz fault. The orientation of the navigation plan (Figure 2) was carried out based on land data, electrical resistivity tomography results, as well as on previous work on Lake Le Bourget. Two types of reflection-seismic sources were used, CENTIPED sparker (1.3 kHz frequency, 37-75 cm resolution, ≈200 m penetration) and Seistec boomer (2.5 kHz frequency, 10-20 cm resolution, ≈40 m penetration).

High resolution seismic profiles in Lake Le Bourget show that the seismic signature of the Culoz fault is characteristic of strike-slip faulting negative (flower structure, Figure 3). Surficial fractures affect different paleo-surfaces of the lake infill, reaching locally the lake floor (Figure 3), and indicating a persistence of pre-LGM active tectonics.

The most recent deformed sedimentary unit (in pink, figure 3) consists of a sheet drape of low amplitude continuous reflections corresponding to the actual lake sedimentation (biological activity with little fluvial influences) since 11,500 cal. BP. (Van Rensbergen et al., 1999). This stratified unit was then used to quantify slip rates along the fault based on vertical offsets and well constrained sedimentation rates (Figure 3). Indeed, since we do not have a direct view of the actual fault kinematics in offshore data we propose, in order to derive a range of possible Holocene slip rates, a hypothesis base on inland observed slickensides measured onto Mesozoic limestones, assuming that the measured pitch has been constant since Mio–Pliocene shortening times ($10^{\circ} \pm 5$). This last point is strengthened by the discovery of an outcrop (Figure 4) in which interglacial sediments (≈50 ky) are faulted and show slickensides that are coherent with the long term kinematics of the fault.

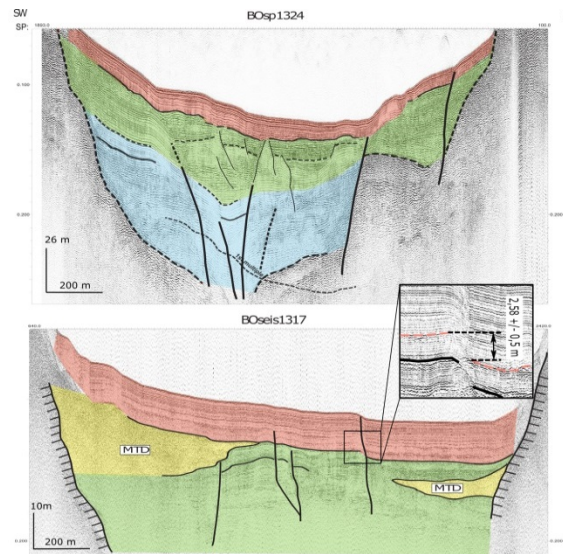


Figure 3: Interpreted seismic reflection profiles across northern Lake Le Bourget (location on Figure 2). Top: fault strands of the Culoz fault affecting different sedimentary layers (De La Taille et al., 2015). Bottom: most recent surface ruptures affecting the Holocen (pink layer). Zoom presenting where vertical deformations have been quantified.

Results are reported in Table 1, with slip rates ranging from 0.22 ± 0.01 mm/yr in case of pure vertical deformations, up to 1.9 ± 1.21 mm/yr when considering a major horizontal component.

Rake	Xv (m)	Total slip (m)	Time (years)	Slip-rate
Vertical	2.58 ± 0.5	Min=2.08 Max=3.08	11,500 ± 150	Min=0.21mm/yr Max=0.23mm/yr
10 ± 5°	2.58 ± 0.5	Min=8.03 Max=35.3	11,500 ± 150	Min=0.69mm/yr Max=3.11mm/yr

Table 1: Calculated possible fault slip-rates using offshore data.

The only exposed outcrop highlighting recent faulted sediments allows making a comparison with the results obtained offshore (Figure 4). It consists in a succession of gravels, clays and sands, deposited along a polished limestone surface. These sediments contain well preserved vegetal remnants, used for C14 dating (age > 45.1 ky). In parallel, massive sand layers were sampled for OSL dating (43.2 ± 4.8 ky).

The sediments are clearly affected by faulting, with a vertical displacement of 2.70 ± 0.05 m. Sub-horizontal slickensides can be observed with a pitch of $15 \pm 5^{\circ}$, but without clear evidences of slip direction. However, both fault direction (N175°) and strike-slip component are coherent with active faulting as observed in the lake along the Culoz fault.

We therefore calculated a range of fault slip rates as performed from offshore results. Results are reported in Table 2, with slip rates ranging from 0.058 ± 0.03 mm/yr (pure vertical deformations), and up to 0.25 ± 0.9 mm/yr when considering the observed slickensides.



Rake	Xv (m)	Total slip (m)	Time (years)	Slip-rate
Vertical	2.70 ± 0.05	Min=2.65 Max=2.75	Min=45,100 Max=48,000	Min=0.055mm/yr Max=0.061mm/yr
15 ± 5°	2.70 ± 0.05	Min=7.75 Max=15.83	Min=45,100 Max=48,000	Min=0.16mm/yr Max=0.35mm/yr

Table 2: Calculated possible fault slip-rates using on-shore data.



Figure 4: Fault outcrop at the southeastern tip of the Culoz fault. Interstadial sediments (MIS III) are faulted and vertically displaced by 2.7 meters. A pitch of $15 \pm 5^\circ$ was measured but without clear evidence of motion direction. OSL (White circle, 1 – sample BRI4) as well as C14 (White star, 2 – sample BRI2) dating's provide ages constraints ranging from 45 to 53 ky.

DISCUSSION

In the Jura Mountains, evidences of active faulting were observed and described along the Culoz fault system. From the collected datasets, we calculated a wide range of possible fault slip-rates that we will discuss hereafter.

Comparing the data obtained offshore and on land, we observe very similar vertical fault displacements. However, because of different ages obtained on the deformed sediments, the inferred slip rates differ by at least one order of magnitude. Different hypotheses may be drawn from these observations:

- (1) Different behavior of earthquake rupture at surface: in order to reconcile observations performed on land and offshore, we may argue that slip rates derived from strike-slip faulting onshore are coherent with those derived from vertical deformations offshore. This may be explained by very different rheological answers to strike slip faulting between consolidated and unconsolidated sediments;
- (2) Slip rates may be non-stationary through time. For instance, in case of punctual enhanced earthquake activity, fault slip rates may be coherent between our two observations despite highlighting very different ages;

- (3) Our observations concern different fault segments at different places along the fault. In this case it may be difficult to simply reconcile these observations.

In comparison with what is known in metropolitan France, slip rates obtained along the Culoz fault (except for the lowest ones inferred on land, which are probably not reliable) will at least be among the highest ones ever described (Jomard et al., 2017), and possibly even faster if we consider offshore strike-slip scenarios. As an example, along the neighboring Vuache fault (VF, Figure 1), Baize et al., (2011) proposed horizontal slip rates ranging from 0.15 to 0.28 mm/yr based on long term morphological markers. In comparison, such evidences are not as clear along the Culoz fault, which may attest of a lower long term slip rate. Hence, one should explain the evidence for these surprisingly high slip rates and figure out what kind of processes may be at work.

First of all, non-tectonic processes may lead to deformations similar to earthquake-related ones. This can for example be the case after gravitational reworking of sediments, or by glaciotectonism. Even if it is not possible to completely rule out these hypotheses, both evidences of strike-slip faulting and their coherence along the fault militates in favor of a tectonic origin. In this case, data obtained by Beck et al. (1996) and discussed by Beck (2009) provide an alternative solution, keeping alive the seismic origin of the deformations, but their origin may at least partly be climatic.

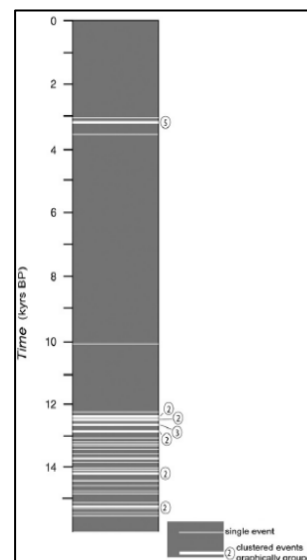


Figure 5: Time distribution of the sedimentary “events” observed in the CLIMASILAC core (from Beck, 2009) performed in the Annecy Lake.

In a long core (43 m) performed in the neighboring Annecy Lake, the observation of an important decrease in earthquake-related reworking events (about 42 silty-sandy turbidites and grain flows, Beck et al., 1996, 2009 – Figure 5) suggests a diminution of seismic activity through time after the pre-Holocene maximum. This observation could be interpreted as the strain decrease through time due to an unloading effect linked to ice melting and mass transfer following the last deglaciation. Then, if the earthquake



activity during the deglaciation was larger than today, we can propose the existence of a time dependent postglacial deformation along the Culoz fault, leading to the surprisingly high slip rates we inferred.

Acknowledgements: Camille de La Taille Ph.D fellowship was supported by a grant from the Assemblée des Pays de Savoie and IRSN. Data acquisition has been supported by a grant from Labex OSUG@2020 (Investissements d'avenir — ANR10 LABX56) and by ISTERre laboratory for financial support. The authors thank Marc De Batist for giving us the possibility to provide the expertise and the logistics of the Renard Centre of Marine Geology (GhentUniversity) for seismic imaging.

REFERENCES

- Baize, S., Cushing, M., Lemeille, F., Gelis, C., Texier, D., Nicoud, G., Schwenninger, J.-L., 2011. Contribution to the seismic hazard assessment of a slow active fault, the Vuache fault in the southern Molasse basin (France). *Bull. Soc. Geol. Fr.* 182 (4), 347–365.
- Beck, C., 2009. Late Quaternary lacustrine paleo-seismic archives in north-western Alps: examples of earthquake-origin assessment of sedimentary disturbances. *Earth Sci. Rev.* 96, 327–344.
- Beck, C., Manalt, F., Chapron, E., Van Rensbergen, P., De Batist, M., 1996. Enhanced seismicity in the early post-glacial period; evidence from the post-Würm sediments of Lake Annecy, northwestern Alps. *J. Geodyn.* 22 (1/2), 155–171.
- Becker, A., 2000. The Jura Mountains—an active foreland fold-and-thrust belt?. *Tectonophysics*, 321(4), 381-406.
- Biju-Duval, B., Dercourt, J., Le Pichon, X., 1977. From the tethys Ocean to the Mediterranean seas: a plate tectonic model of the evolution of the western Alpine systems. In: Biju-Duval, B., Montadert, L. (Eds.), *Internat. Symp. Struct. History of the Mediterranean Basins, Split (Yugoslavia)*, 1976. Technip, Paris, pp. 143–164.
- Chapron, E., 1999. Contrôles climatique et sismo-tectonique de la sédimentation lacustre dans l'avant-pays Alpin (Lac du Bourget) durant le Quaternaire récent (PhD thesis), *Géologie Alpine Mémoire Hors Série 30*. Université de Grenoble, France (258 pp.).
- De La Taille, C., Jouanne, F., Crouzet, C., Beck, C., Jomard, H., De Rycker, K., & Van Daele, M., 2015. Impact of active faulting on the post LGM infill of Le Bourget Lake (western Alps, France). *Tectonophysics*, 664, 31-49.
- Jomard, H., Cushing, M.E., Palumbo, L., Baize, S., David, C., Chartier, T. 2017. Transposing an active fault database into a seismic hazard fault model for nuclear facilities – Part 1: Building a database of potentially active faults (B DFA) for metropolitan France. *Nat. Hazards Earth Syst. Sci.*, 17, 1–12, 2017
- Ledoux, G., Lajeunesse, P., Chapron, E., St-Onge, G., 2010. Multibeam bathymetry investigations of mass movements in Lake Le Bourget (NW Alps, France) using a portable platform. In: Mosher, D.C., et al. (Eds.), *Submarine Mass Movements and Their Consequences. Advances in Natural and Technological Hazards Research* 28, pp. 423–434.
- Nocquet, J.-M., 2012. Present-day kinematics of the Mediterranean: a comprehensive overview of GPS results. *Tectonophysics* 579, 220–242.
- Van Rensbergen, P., De Batist, M., Beck, C., Chapron, E., 1999. High-resolution seismic stratigraphy of glacial to interglacial fill of a deep glacigenic lake: Lake Le Bourget, northwestern Alps, France. *Sediment. Geol.* 128, 99–129.
- Vernant, P., Hivert, F., Chéry, J., Steer, P., Cattin, R., Rigo, A., 2013. Erosion-induced isostatic rebound triggers extension in low convergent mountain ranges. *Geology* 41, 467 – 470. <http://dx.doi.org/10.1130/G33942.1>.
- Vigny, C., Chéry, J., Duquesnoy, T., Jouanne, F., Ammann, J., Anzidei, M., Avouac, J.-P., Barlier, F., Bayer, R., Briole, P., Calais, E., Cotton, F., Duquenne, F., Feigl, K., Flouzat, M., Gamond, J.-F., Geiger, A., Harmel, A., Kasser, M., Laplanche, M., Le Pape, M., Martinod, J., Ménard, G., Meyer, B., Ruegg, J.-C., Scheubel, J.-M., Scotti, O., Vidal, G., 2002. GPS network monitors the Western Alps' deformation over a five-year period: 1993–1998. *J. Geod.* 76 (2), 63–76.
- Vogt, J., Godefroy, P., 1979. Le tremblement de terre du 19 février 1822 (Bugey-Savoie). *Éléments de discussion*. Technical Report, BRGM.



Rapid RS Data Collection for Landslide Damage and Fault Rupture using UAV and Structure-From-Motion Photogrammetry following the 2016 Mw 7.8 Kaikōura Earthquake

Jones, Katie (1), Lawson, Steve (2), Asher, Cameron (2), Manousakis, John (3), Clark, Kate (1), Archibald, Garth (1), Ries, William (1), Massey, Chris (1)

- (1) GNS Science, P O Box 30368, Lower Hutt 5040, New Zealand. Email: katie.jones@gns.cri.nz
- (2) GNS Science, Private Bag 2000, Taupo 3352, New Zealand
- (3) Elxis Group, 7-9 Dimitressa Street, GR 11528, Athens, Greece

Abstract: Following the 14 November 2016 Mw 7.8 Kaikōura earthquake six landslide dams on the Conway, Hapuku, Leader, Linton, Medway, Stanton and Towy Rivers were flown with an unmanned aerial vehicle, along with short sections of the Kekerengu and Papatea faults. Images were collected to generate high resolution, small scale topographic digital surface models and red-green-blue encoded point cloud datasets for 3D viewing. Rapid post-event imagery capture means ephemeral features are recorded at relatively low-cost for subsequent detailed geomorphological mapping applications. Collective xyz ground control point accuracy was typically in the order of 0.2 m and as flying height dictates ground sample distance, this varied over the high relief terrain resulting in digital surface models and orthomosaic datasets with a pixel resolution of less than 1 m.

Key words: UAV, Digital Surface Model, Structure from motion, Kaikōura earthquake

INTRODUCTION

The acquisition of remotely sensed high resolution topographic data has been transformed considerably over the past decade by new technology and geospatial processing platforms. Unmanned aerial vehicles (UAVs) equipped with compact digital cameras can be deployed quickly and at low cost to collect high resolution images, and post processing with accurate ground control generates cm-scale orthophotos and digital surface models (DSM) suitable for detailed geomorphological mapping applications.

Following the 14 November 2016 Mw 7.8 Kaikōura earthquake surface rupture was identified on at least 21 faults extending over 150 km and significant landslide damage was observed across the North Canterbury and Marlborough regions of the South Island, New Zealand. 196 landslide dams were identified, and several significant dams which posed a risk to downstream communities were closely monitored until failure. Six of these landslide dams, on the Conway, Hapuku, Leader, Linton, Medway, Stanton and Towy Rivers (Figures 3-9), were flown with an UAV between 1 - 14 December 2016. Similarly, short sections (up to 1.3 km) of the Kekerengu and Papatea faults were flown between 20 November and 2 December 2016. Such rapid acquisition of post-event imagery means ephemeral features were chronicled for later analysis at relatively low cost.

STRUCTURE FROM MOTION

Advances in photogrammetric image processing combined with computer vision have resulted in a technique known as Structure from Motion (SfM) (Westoby et al. 2012). Detailed 3D models can be generated from overlapping multi-view photography using SfM algorithms. Compared to traditional photogrammetry, which relies on aerial

photography with 60%/30% forward/lateral overlap, and on nadir view angle, SfM integrates multi-position, multi-scale and multi-angle photographs with 80-90% overlap.

Following the 2016 Kaikōura earthquake airborne digital photographs were acquired using the small fixed sensor DJI Phantom 4 and the UAV flight path was recorded by the on-board GPS. Ground control points (GCPs) were surveyed at most sites to improve output accuracy. Photographs were captured using a combination of manual, semi-automated and autonomous grid modes, depending on the terrain. Due to limited access at some sites in narrow high-sided valleys, and a capped flying height of 120 m above the take off point, using a pre-programmed flying grid to cover the AOI was not always possible. Instead, at these sites the Phantom 4 was flown by the controller around the boundary of the feature of interest then automatically flown within this user defined boundary. Additional photos in hard to reach spots were acquired by manual UAV flight. Due to the inaccessibility of Linton landslide dam, two thirds of the photos were captured with a handheld digital camera from a helicopter. This often-irregular image pattern capture introduced errors in later SfM processing.

SfM processing was undertaken using the commercial software package Agisoft PhotoScan Professional version 1.3.2 (Agisoft). A more detailed description of the SfM procedure and commonly used parameters are described by Agisoft (2017), Javernick et al. (2014) and Ouédraogo (2014). Photos were aligned in Agisoft with pair pre-selection based on the photo GPS coordinate as stored in the JPEG EXIF headers. This feature was disabled for the Linton landslide site as the hand-held photos were not GPS encoded.



The GCP markers were identified in the individual photographs within Agisoft and real time kinematic (RTK) GPS coordinates were added to the markers. With added GCPs the bundle adjustment was recalculated with estimated accuracy settings of the camera GCP set to 10 m and the ground GCP set to 0.005 cm. Residuals for the GCPs were calculated as an initial indication of the geometric accuracy of the models. Optimization using RTK measured GCP markers reduced the collective root-mean-square error (RMSE) from tens of metres to centimetre scale accuracy. The accuracy of the digital surface model was assessed with XYZ residuals for the GCP markers, calculated in Agisoft as part of the bundle adjustment and model generation process (Table 1).

The RMSE can be misleading as to output quality, as it was defined primarily by the distance of the photographs to the ground, regular overlap between adjacent frames, and disbursement of the GCP markers.

Table 1. Agisoft SfM point cloud GCP accuracy and output resolution for the landslide dam sites.

AOI	Ground Resolution	GCP	Pre / Post RMSE	DSM / Ortho Resolution
Conway	3.7 cm/pix	10	12.51m / 2.90 cm	12m / 3 cm
Hapuku	4.08 cm/pix	4	34.06 m / 2.97 cm	14 cm / 4 cm
Leader	4.68 cm/pix	9	35.83 m / 16.10 cm	16 cm / 4cm
Linton	3.26 cm/pix	4	7.32 / 1.18 cm	30 cm / 7.5cm
Medway	4.68 cm/pix	0	N/A	21 cm / 5cm
Stanton	3.2 cm/pix	3	25.80 / 50.34 cm	11 cm / 3cm
Towy	5.13 cm/pix	12	62.59 / 31.17 cm	16 cm / 4cm

Flying height dictates the ground sample distance (GSD), and this varied over the mix of high to low relief terrain resulting in DSM and orthophoto datasets with a pixel resolution of < 1 m. A polygonal mesh model based on the dense cloud data converts the point cloud to a triangulated surface, and orthomosaics were generated by correcting the individual photographs for relief distortions and projecting them onto a planimetric surface with a real-world coordinate system (for this study, New Zealand Transverse Mercator 2000).

DIGITAL TOPOGRAPHY RESULTS – LANDSLIDES AND FAULT RUPURE

The SfM Agisoft processing created high resolution, detailed models for each AOI. A selection of SfM results are shown in figures 1 to 4. The outputs of these models were used for various purposes. Simple visual inspection of slope failures, dam extents and water levels was possible in the 3D textured mesh. The 2D DSM and orthomosaics were used in ArcGIS for measurements, modelling and high-resolution mapping.

UAV capture of fault ruptures in key locations allowed the recording of fault offsets before they were removed or fixed by landowners. Compared to LiDAR, the UAV-derived DSMs of fault rupture have far greater detail which is useful for mapping fine-scale fault fissures and fractures (Figure 2). However, for the measurement of several > m-scale landform offsets, the UAV-derived and LiDAR-derived models are of equivalent utility with LiDAR having the advantage of the removal of vegetation, although there are examples of vegetation lines providing useful offset markers.

The landslide dam surveys were useful to complete the coverage where terrestrial laser scanning (TLS) extent was discrete and limited to the more accessible areas for scanner line-of-sight and set up. Again, rapid capture meant the landslide dammed features were recorded before further rainfall raised the dammed water level and the dam breached or a channel was eroded to create an outlet as many of the smaller dams were quickly drained.

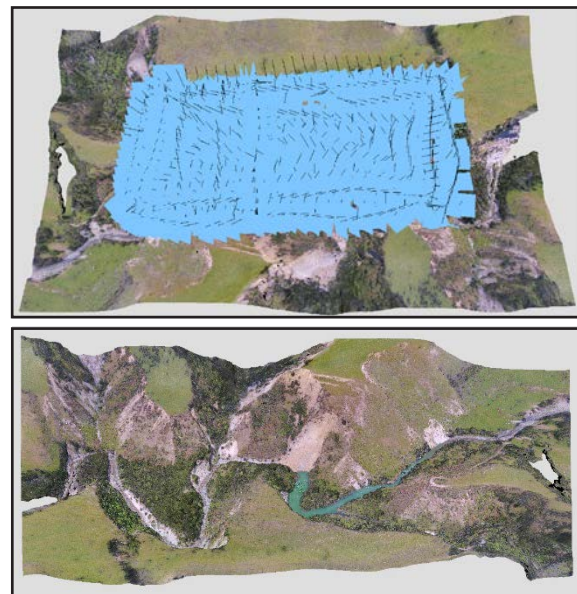
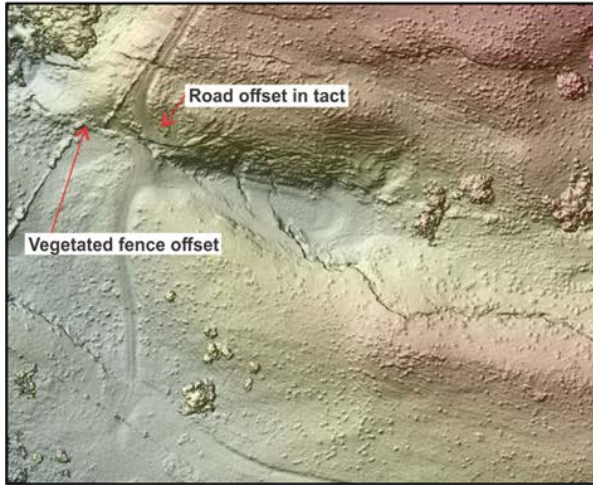


Figure 1. The regular and overlapping photo coverage (top) resulted in an impressive 3D SfM model of Medway landslide dam, shown as a textured point cloud (bottom), however the utility of the model was limited by the absence of GCPs to correct the poor Phantom 4 inbuilt GPS, resulting in an estimated offset of ~20 m in XYZ directions.

Accessibility and topographic restrictions in many valleys blocked by large landslides meant less-than-optimal UAV photograph capture and limited distribution of GCPs; this has resulted in DSMs with higher uncertainties. A key issue in field data acquisition, particularly on the fault ruptures, were inexperienced users of the RTK-GPS meaning GCPs were not recorded properly at some sites or the site was flown before GCP markers were laid so were not captured for later identification. This rendered the resulting DSMs of limited use for offset measurement (Figure 1).



UAV-derived DSMs



Lidar DTMs/ 0.3 m aerial image

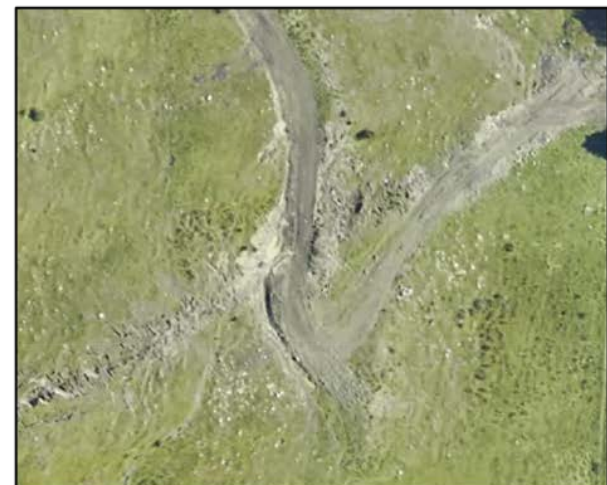
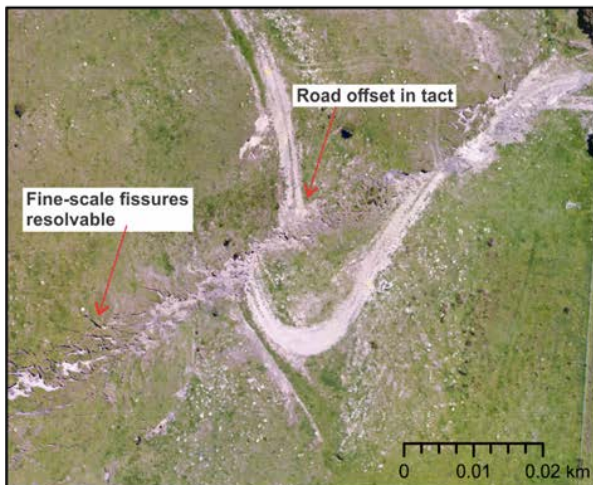
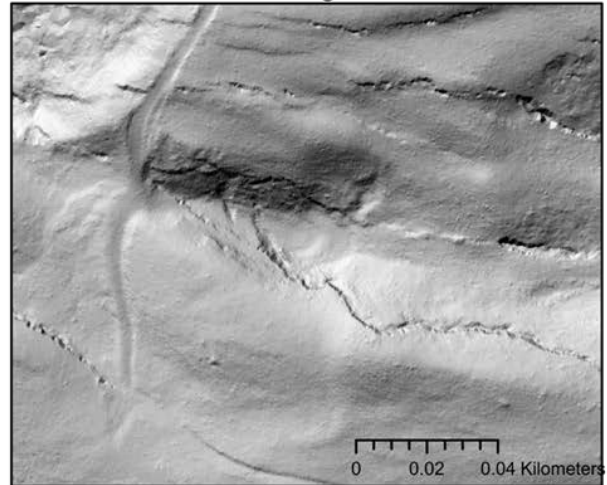


Figure 2. Comparison of the SfM DSM (left panel: top) and orthomosaic (bottom) compared to the LiDAR datasets (right) for the Kekerengu Fault rupture. LiDAR was captured between 3/12/2016 and 6/1/2017.



Figure 3. (left) The SfM textured mesh model of the Hapuku landslide dam. Figure 4. (above) close up of the Hapuku dam material showing the surface detail and size of individual boulders.



Best practice for accuracy assessment is the use of two sets of clearly visible reference markers (GCPs) randomly placed around the AOI with accurate XYZ. Where the distribution of these points is irregular, or limited in spatial coverage, the accuracy away from the GCP marker points is unknown in the final exported datasets. Using two sets of GCP markers means one set of GCPs can be used for the SfM adjustment process and the second independent set is useful for accuracy assessment of output datasets.

LIMITATIONS OF UAV DERIVED OUTPUTS

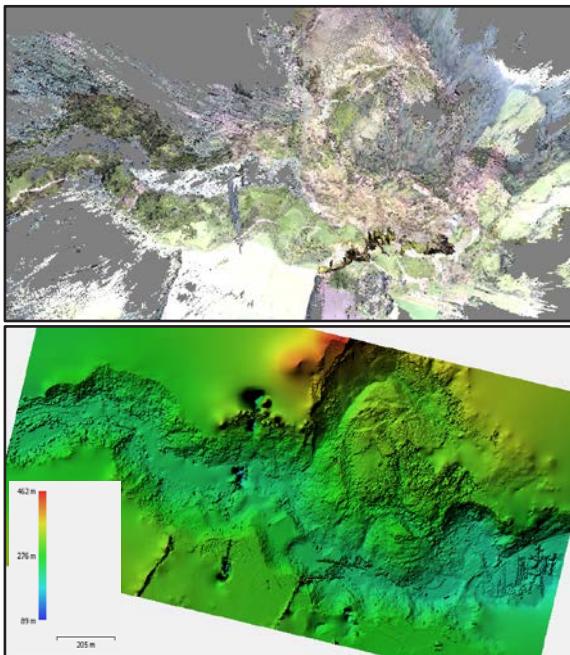


Figure 5. Leader landslide toe from the SfM textured dense point cloud. Note the random surfaces floating in space, and holes in the water surface (river channel). Issues included mismatching between photos due to overlapping at vastly different scales and orientations, in addition to reflection off the water surface on a sunny day. However, the resulting DSM is still of useful quality to identify key landslide features.

Features not visible due to shadow, or hidden by dense vegetation, are not resolvable by the UAV-derived DSMs. Unlike LiDAR or TLS, the SfM 3D point cloud cannot be stripped of vegetation to create a bare earth model or expose shallow bathymetry. Any features covered by vegetation or low overhanging features remain concealed. However, DSMs could be created faster and at more frequent intervals than LiDAR, and with larger coverage than TLS collection, and such DSMs are potentially very useful for assessing failure likelihood of landslide dams.

In addition, using the SfM models for differencing to estimate failure size is problematic as the headscarp mapping is incomplete to the large size of many of the failures, with the scar beyond the 120 m max flying height when take-off is from dam level to comply with Civil Aviation Authority of New Zealand rules. Vegetation coverage is also included in these surfaces, so the representation is not the true failure surface, and holes

occur in the models due to mismatching errors between poor resolution photos.

Different illumination conditions during image acquisition are a source of matching error, including direction of solar illumination and shadowing, changes in diffuse light under overcast conditions, or direct sunlight resulting in bright or over exposed image quality. Differences in vegetation and ground conditions (e.g. tree tops moving in windy conditions) causing image blur, and wet surfaces reflecting light (e.g. river channels) cause the final point cloud dataset to have offset points above the main surface, or floating surfaces radially positioned as various offset angles to the real ground surface (Figure 5). Hence, the output is only as good as the input photos, and only dense and close coverage will result in a realistic high resolution dataset.

SUMMARY

UAV collection of photographs to create high-resolution DSMs was a fast and cost-efficient method of attaining topographic data following the Kaikōura earthquake. Ephemeral features were recorded before the earthquake damage was remedied anthropogenically or further altered by natural processes. Quick assessments of landslide scar size, volume of displacement material, dam extent, and fault offset are all possible but measurements are only worthwhile when using RTK GCPs to quantify accurate scaling of the digital surfaces. Lack of GCP markers for some of the Kaikōura sites limited the derived output use from the impressive models results in essentially unmeasurable fault offsets and landslide failures. Quick, cheap and easily repeatable UAV surveys are also an excellent tool for mapping the long term downstream impact of large slope failures on the sediment transportation and storage networks within the fluvial system.

Acknowledgements: This research was partially funded by the Natural Hazards Research Platform Kaikōura earthquake response funding and the GNS Science Direct Crown Funding Minerals, Urban and Regional Geology Programme.

REFERENCES

- Agisoft (2017) – Agisoft PhotoScan User Manual: Professional Edition. Version 1.3.
 url: http://www.agisoft.com/pdf/photoscan-pro_1_3_en.pdf
- Javernick L., Brasington J., Caruso B., 2014. Modelling the topography of shallow braided rivers using structure-from-motion photogrammetry. *Geomorphology* 213, 166-182.
- Ouédraogo, M.M., Degré, A., Debouche, C., Lisein, J., 2014. The evaluation of unmanned aerial system-based photogrammetry and terrestrial laser scanning to generate DEMs of agricultural watersheds. *Geomorphology*, 214, 339-355.
- Westoby, M.J., Brasington, J., Galsler, N.F., Hambrey, M.J., Reynolds, J.M., 2012. 'Structure-from-Motion' photogrammetry: A low cost, effective tool for geoscience applications. *Geomorphology*, 179:300-314.



Surface Rupture and Slip Distribution of the Kekerengu, Needles, Jordan Thrust, Upper Kowhai and Manakau Faults during the M_w 7.8 2016 Kaikōura Earthquake

Kearse, Jesse (1), Little, Tim (1), Van Dissen, Russ (2) Barnes, Phil (3) Langridge, Rob (2) Mountjoy, Joshu (3) Ries, Will (2) Villamor, Pilar (2) Clark, Kate (2) Benson, Adrian (1) Hill, Matt (2) Hemp-Hill Haley, Mark (4) Lamache, Geoffroy (3,5)

- (1) School of Geography, Environment and Earth Sciences, P.O. Box 600, Victoria University of Wellington. Email: Jesse@kearse.co.nz
- (2) Active Landscapes, GNS Science, Lower Hutt, New Zealand.
- (3) National Institute of Water and Atmospheric Research, Wellington, New Zealand
- (4) Humboldt State University, California, U.S.A.
- (5) Dept. of Earth Sciences, University of Auckland, New Zealand

Abstract: The M_w 7.8 2016 Kaikōura earthquake provided an insightful opportunity to evaluate in detail variations in rupture morphology and slip distribution along an 83 km long rupture - incorporating the offshore Needles, and onshore Kekerengu, Jordan, Upper Kowhai and Manakau faults. On the dextral-reverse Needles fault, multibeam bathymetric and high-resolution seismic reflection data image a throw of the seabed of up to 3.5±0.2 m. Onshore, we surveyed >100 displaced cultural and natural features in the field, and using airborne LiDAR data interpolated to 20-cm grids. Maximum dextral displacements were ~12 m, one of the largest five coseismic surface rupture displacements so far observed globally. Mean dextral slip was 6±1 m. We surveyed long, once linear, fence lines that cross at high angles and span completely the rupture zone. In some locations, for example in nascent bedrock fault zones, total lateral surface displacement is distributed across a deformation zone up to 122 m wide, measured perpendicular to strike; whereas, elsewhere it is focused in a zone <6 m wide.

Key words: 2016 Kaikoura earthquake, Surface Rupture, Kekerengu fault, Needles Fault, Jordan Thrust

INTRODUCTION

the 14th November 2016 M_w 7.8 Kaikōura earthquake involved surface rupture on >20 faults, which together formed the most complex pattern of co-seismic surface faulting observed to date (Hamling et al., 2017; Kaiser et al., 2017; Clark et al., 2017; Litchfield et al., 2017). Surface rupture in this event occurred on two spatially-distinct fault domains, separated by >13 km across the largely unruptured Hope fault (Sterling et al., 2017; Litchfield et al., 2017) (Fig. 1). Despite the overall complexity of this event, faults within the northern domain broke the surface as a straight and near continuous, 83 km-long zone of ground surface and seabed rupture, comprising the longest, through-going component of the Kaikōura earthquake (Fig. 1). From SW-NE, these northern domain faults are: the Manakau, Upper Kowhai, Jordan thrust, Kekerengu and Needles (Fig. 1). Slip on these faults was mostly dextral-reverse, and co-seismic displacements reached a maximum on the Kekerengu fault of ~12 m - one of the top five co-seismic surface displacement magnitudes so far observed globally (Rogers & Little, 2006; Wesnousky, 2008; Gold et al., 2015 Zinke et al., 2014; Lin et al., 2001; 2007; Baljinyam, 1993; Sieh, 1978).

A primary goal of this study is to characterise the distribution of horizontal and vertical displacement along the above-mentioned 83 km, onshore-offshore rupture. We document the distribution and accumulation of dextral slip at the surface as a function of across-strike distance, using the surveyed post-earthquake shape of 15 once-straight fence lines that crossed the entire deformation zone of the Kekerengu fault. We also demonstrate that the Jordan thrust—a range-front thrust fault responsible for

rapid Holocene uplift rates—slipped during this event with a normal sense of displacement, despite both sides of fault experiencing uplift relative to sea-level.

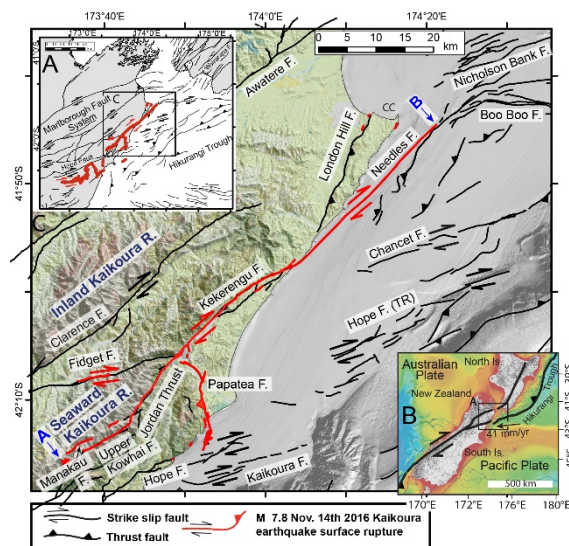


Figure 1: Map of co-seismic surface rupture on faults within the northern domain, during the Kaikoura earthquake (red lines). Inset A shows all surface ruptures during the Kaikoura earthquake (red lines). Inset B shows the plate boundary setting of New Zealand.

These northern domain faults are part of the Marlborough Fault System (MFS), a zone of active dextral-slip faulting that transfers Pacific-Australia plate motion (40 mm/y) between the Hikurangi subduction zone to the northeast and the Alpine fault to the southwest (Fig. 1b). The MFS is underlain at 30-50 km depth by the southern end of the Hikurangi subduction interface (Eberhard-Phillips and Bannister, 2010).



METHODOLOGY

Onshore analysis was based primarily on field surveys of 81 cultural and natural piercing lines that had been co-seismically displaced across the surface fault rupture. Field survey equipment was Real-time-Kinematic GPS—where skyview was abundant—and total station theodolite and tape measurement where it was not. Secondly, by landform matching in a GIS environment, LiDAR data that had been flown along the length of rupture in early 2017, and for which ground returns were gridded at 20 cm, was used by us to acquire an additional 31 displacement measurements. Offset features included—in order of decreasing relative abundance—fence lines, river channels, rills, levees or gully margins; farm tracks (4WD roads), landslide margins, individual trees or roots split by the fault (and matched), small spurs, animal tracks, beach dunes, State Highway (SH 1), the main trunk railway line, and a previously back-filled paleoseismic trench (Little et al., this volume). Marine reconnaissance on the Needles fault rupture was carried out in two surveys led by NIWA. The first survey included the collection by the *Tangaroa* vessel of Kongsberg EM302 30 kHz multibeam bathymetry, backscatter sonar and TOPAS PS18 sub-bottom profiles along the northern section of the Needles fault, in water depths >30 m. A second near-shore survey using the *Ikatere* vessel, along the southern ~20 km of the Needles fault collected Kongsberg EM2040 300 kHz multibeam bathymetry.

CO-SEISMIC SLIP DISTRIBUTION – HORIZONTAL

The along-strike distribution of dextral surface fault rupture slip is presented in Figure 2, extending 83 km from the southwestern extent of the Manakau and Upper Kowhai faults to the northeastern extent of seabed rupture of the Needles fault. Note that in Figure 2, where multiple strands of the Kekerengu fault overlap, dextral displacement has been summed across all the strands (Manakau, Jordan Thrust, Kekerengu and Tinline Downs). The onshore part of the strike-slip envelope defines a semi-bell shape (Fig. 2b). Southwest of site 138, on the Upper Kowhai and Manakau faults, displacement was difficult to accurately quantify due to inaccessibility issues, lack of LiDAR coverage on the Manakau fault and a paucity of piercing points with which to measure displacement. Here we assume a northeast to southwest linear decrease in dextral slip. On the Jordan Thrust, between sites 138-118, dextral slip rises linearly (~0.6 m/km) to 2 ± 0.5 m (Fig. 2b). At its northern tip, the Jordan Thrust overlaps the Kekerengu fault, and here the two faults share 7.1 ± 0.5 m of dextral slip, each accommodating ~3.5 m (sites 115 and 116, Fig. 2b). Within the relatively flat, central 9 km of the slip envelope—between sites 78-20—dextral slip averages ~10 m (Fig. 2a). This section includes the maximum observed dextral-slip of 11.8 ± 0.3 m at Ben More Stream (site 25), and 8 additional sites where slip is >10.5 m. In the area to the northeast of the central slip high, between sites 16-5 strike-slip is 8-9 m. No lateral offsets could be measured along the 30 km-long rupture of the offshore Needles fault (only vertical ones) because of the absence of suitable markers on the flat seabed.

A discontinuity in horizontal slip gradient is located across the intersection of the Papatea fault surface rupture with the greater Kekerengu fault (Figs. 1 and 2b). Across this zone of fault intersection, in a southwest direction—between sites 100-107—slip drops from ~10 m to 7.3 ± 0.2 m. This drop in dextral-slip on the “greater” Kekerengu fault zone is an expectable result of the observed uplift, shortening and reverse-sinistral slip on the Papatea fault that intersects it to the east (Hamling et al., 2017; Langridge et al., in prep).

Co-seismic Slip Distribution – Vertical

The along-strike distribution of vertical surface fault rupture displacement is presented in Figure 6c. Between sites 110-5 (Fig. 2c), throw is a largely up-to-the-northwest and reverse, with magnitudes averaging ~1.5 m, and locally exceeding 2 m. By contrast, from the southwest tip of the rupture to site 117, throw is up-to-the-southeast and has normal sense. Magnitudes here are highly variable and between 0.5 – 3.6 m. This reversal in sense of throw straddles the Papatea fault intersection (Figs 1 and 2c). InSAR data show that during the earthquake, the northwest-dipping Jordan Thrust was uplifted on its northwest side by 2-3 m and on its southeast side by 5-6 m. (Hamling et al., 2017)—in other words the sense of dip-slip on the Jordan fault during the Kaikōura Earthquake was normal rather than reverse. Considered on a longer time frame, however, the steep topographic flank of the Kaikōura Ranges across the trace of the Jordan fault indicates that this fault usually (previously) slips with an oblique-reverse sense (Van Dissen and Yeats, 1991).

Along the 2 km stretch of rupture at the coast (sites 14-6, Fig. 2c), differential LiDAR data reveal that both sides of the fault subsided by up to 2.5 ± 0.2 m (relative to sea-level) during the earthquake (Clark et al., 2017). Here the fault maintained a northwest dip and had an up-to-the-southeast oblique-normal sense of throw, which was between $1.2-2.2 \pm 0.2$ m. Moving northeast towards the coast, where the fault crosses a coastal field of sand dunes (sites 7-5), throw on the fault reverts from up-to-the-southeast (1.75 ± 0.2 m, probably normal) to up-to-the-northwest (1.2 ± 0.2 m, probably reverse). Site 6 records the “hinge point” of this transition because at this site there is locally no relief across the fault trace.

The vertical throw envelope along the Needles fault has a bell-shape along the southern 20 km of the trace (Fig. 2c). The maximum throw of 3.5 m occurs about 11 km along the fault (Fig. 2c).

This is extremely consistent with similar maximum measurements of coastal uplift, incorporating field observations, as well as pre- and post-earthquake differencing using LiDAR and radar datasets (Clark et al., 2017). The compatibility of the marine scarp measurements and the nearby coastal uplift data support our interpretation that the marine surface trace is entirely the result of co-seismic rupture associated with the November 14th 2016 Kaikōura Earthquake.

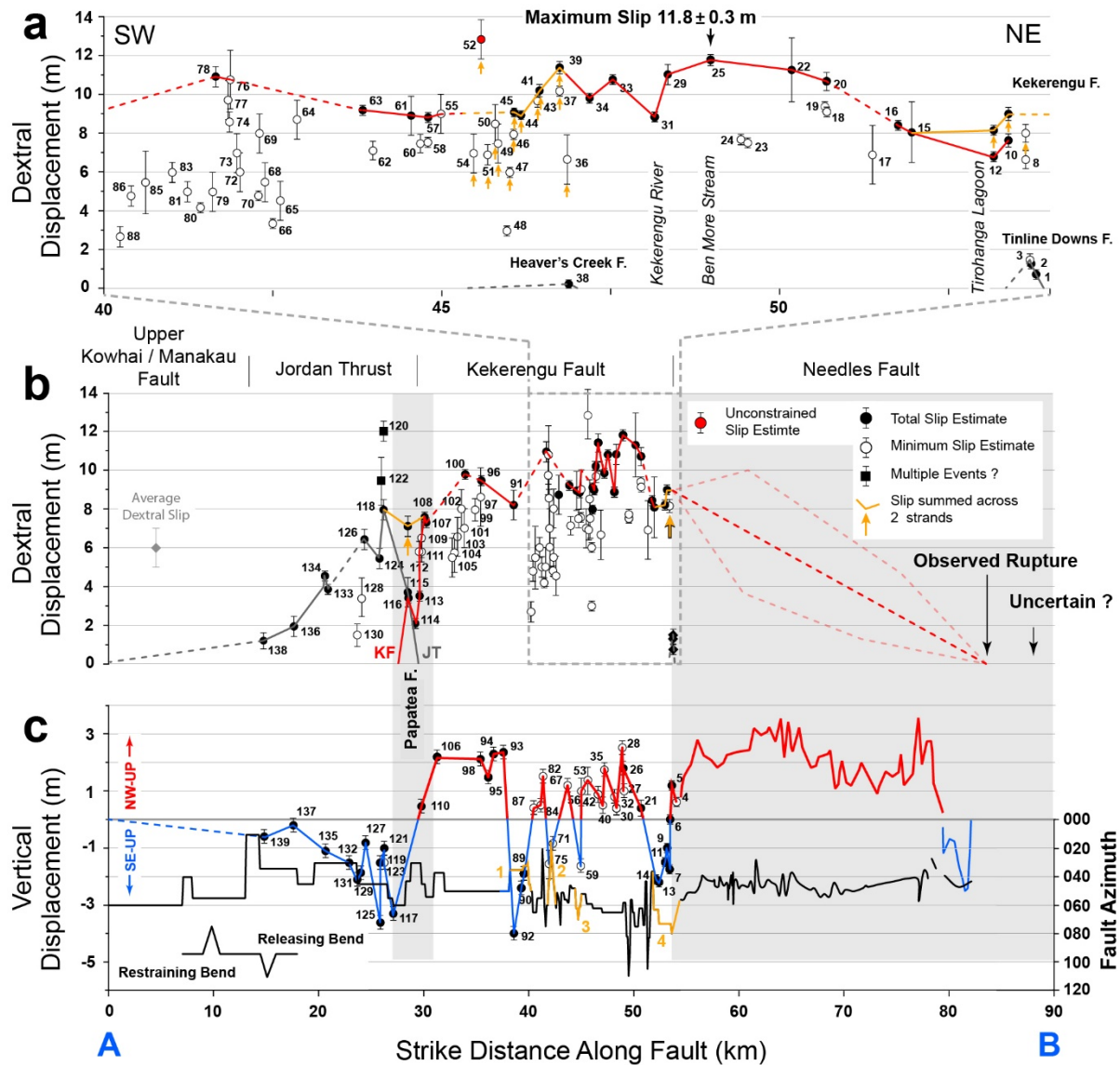


Figure 2: Dextral and vertical displacement distribution along the length of the northern domain of surface rupturing. A: Enlarged view of the central high in dextral displacement, including the maximum dextral slip of 11.8 ± 0.3 m at site 25. Orange curves denote sections of the Kekerengu fault where slip has been summed across the Heaver's Creek and Tinline downs faults. Grey curve relates to slip on the Manakau, Upper Kowhai and Jordan Thrust faults, red curve relates to slip on the Kekerengu fault. Papatea fault intersection and Needles fault are highlighted in with vertical grey bars. Bold dashed red line on the Needles fault represents the curve used to estimate average slip, pink dashed lines above and below refer to the curves used to place error bounds on this estimation. C: Vertical displacement distribution. Red curve is up-to-the-northwest throw, blue curve is up-to-the-southeast throw. Black curve illustrates changes in fault azimuth.

CO-SEISMIC SLIP DISTRIBUTION – ACROSS STRIKE

On average, most dextral slip (80%) was accommodated within the central 43% of the ground deformation zone. As inferred from deflection of the otherwise linear fences, the overall width of this deformation zone ranged between 13 – 112 m and averaged ~50 m. On average, 40-90% of the total dextral-slip magnitude was accommodated in a step-like slip discontinuity across the central ~5 m of the deformation zone, with the remaining displacement accommodated across a more diffuse, distributed shear gradient extending to the outer margins of the deformation zone. Where the

total width of deformation was 30 m or less ($n=4$), 80% of the dextral slip was distributed across the central 25% of the deformation zone (<7.5 m wide). Here, displacement gradients were highest, with finite shear strains between 0.7-3.3. Elsewhere, where total deformation widths were >30 m ($n=9$) mean finite shear strains were between 0.07-0.4. In a case of widely distributed slip (mean finite shear strain = 0.07), 8.1 m of dextral slip was nearly evenly distributed across the 112 m total width of deformation formed in hard limestone bedrock that we infer to be deforming by extension fracturing and vertical-axis rotation of bedrock strips. A notable feature of displacement at this



site is that the fence was cut by only two extensional fissures, across which there is no significant discontinuity in displacement. The remaining ≥ 7.5 m of displacement was accommodated without any obvious rupturing at the ground surface. This suggests that along the Kekerengu fault during the 2016 rupture, shear strains in excess of about 0.1 were needed before recognizable discrete shears formed on the ground surface.

DISCUSSION/CONCLUSION

We have documented ground surface and seabed fault rupture along the longest and most continuous component on the 2016 M_w 7.8 Kaikōura earthquake. This comprised 53 km of onshore fault rupture and at least 30 km of seabed rupture on the Needles fault, extending offshore of southeast of Cape Campbell (Fig. 1). This event was the first time a co-seismic surface rupture was surveyed both onshore and offshore immediately following the causative event. Our analysis of co-seismic horizontal and vertical displacements and rupture morphology along the 83 km length of the northern domain of surface fault rupture indicates earthquake ruptured with a mean dextral-slip of 6 ± 1 m, and a dextral slip maximum of 11.8 ± 0.3 m. For the rupture length, these slip magnitudes are unusually large compared to a global catalogue of other large magnitude strike-slip earthquakes. The elastic dislocation model of Hamling et al. (2017) supports our conclusion that the high slip to length ratio may reflect a deeply penetrating rupture. On average, 80% of the total strike-slip displacement at a site is distributed across the central 43% of the total rupture deformation width.

Acknowledgements: This study was (part) funded by the New Zealand Earthquake Commission (EQC).

REFERENCES

- Baljinnyam, I. (Ed.). (1993). Ruptures of major earthquakes and active deformation in Mongolia and its surroundings, *Geol. Soc. Am.* Vol. 181.
- Clark, K. J., Nissen, E. K., Howarth, J. D., Hamling, I. J., Mountjoy, J. J., Ries, W. F., et al., (2017). Highly variable coastal deformation in the 2016 M_w 7.8 Kaikōura earthquake reflects rupture complexity along a transpressional plate boundary. *Earth Planetary Sci. Lett.* **474** 334-344.
- Eberhart-Phillips, D., & Bannister, S. (2010). 3-D imaging of Marlborough, New Zealand, subducted plate and strike-slip fault systems. *Geophys. J. Int.* **182** 73-96.
- Gold, R. D., Reitman, N. G., Briggs, R. W., Barnhart, W. D., Hayes, G. P., & Wilson, E. (2015). On-and off-fault deformation associated with the September 2013 M_w 7.7 Balochistan earthquake: implications for geologic slip rate measurements, *Tectonophysics*, **660** 65-78
- Hamling, I. J., Hreinsdóttir, S., Clark, K., Elliott, J., Liang, C., Fielding, E., et al (2017). Complex multifault rupture during the 2016 M_w 7.8 Kaikōura earthquake, New Zealand. *Science*, **356**(6334), eaam7194.
- Kaiser, A., Balfour, N., Fry, B., Holden, C., Litchfield, N., Gerstenberger, M., et al (2017). The 2016 Kaikōura, New Zealand, Earthquake: Preliminary Seismological Report, *Seismol. Res. Lett.*, **88** 727-739.
- Langridge, R., Ries, W., Rowland, J., Villamor, P., Kears, J., Little, T., et al., (2017). The role of surface-rupturing faults in the Waiatua microblock, Clarence valley, New Zealand, during the M_w 7.8 2016 Kaikōura Earthquake. *Proceeding from the 8th International INQUA Meeting on Paleoseismology, Active Tectonics and Archeoseismology, November 2017*.
- Lin, A., Ouchi, T., Chen, A., & Maruyama, T. (2001). Co-seismic displacements, folding and shortening structures along the Chelungpu surface rupture zone occurred during the 1999 Chi-Chi (Taiwan) earthquake, *Tectonophysics*, **330** 225-244.
- Lin, A., & Nishikawa, M. (2007). Coseismic lateral offsets of surface rupture zone produced by the 2001 M_w 7.8 Kunlun earthquake, Tibet from the IKONOS and QuickBird imagery. *International Journal of Remote Sensing*, **28**(11), 2431-2445.
- Litchfield, N. J., Villamor, P., Van Dissen, R. J., Nicol, A., Pettinga, J. Barnes, P., et al., in review, Insights into the complexity of fault rupture during a single earthquake, *Geology*.
- Litchfield, N. J., Van Dissen, R. J., Hornblow, S., Quigley, M. C., & Archibald, G. C. (2014). Detailed analysis of Greendale Fault ground surface rupture displacements and geometries. *GNS Science Report 2013/18*
- Little, T. A., Van Dissen, R., Kears, J., Norton, K., Ningsheng, W., *this volume* Kekerengu fault, New Zealand: timing and size of Late Holocene surface ruptures, *Bull. Seismol. Soc. Am.*
- Rodgers, D. W., and T. A. Little (2006). World's largest coseismic strike-slip offset: The 1855 rupture of the Wairarapa Fault, New Zealand, and implications for displacement/length scaling of continental earthquakes, *J. Geophys. Res. B. Solid Earth Planets* **111**, no. B12.
- Sieh, K. E. (1978). Slip along the San Andreas fault associated with the great 1857 earthquake, *Bull. Seismol. Soc. Am.* **68** 1421-1448.
- Stirling, Mark W., N. J. Litchfield, P. Villamor, R. J. Van Dissen, A. Nicol, J. Pettinga, P. Barnes et al, (2017) The M_w 7.8 2016 Kaikōura earthquake: Surface fault rupture and seismic hazard context, *Bull. New Zeal. Soc. Earthquake Eng.* **50** 73-84.
- Van Dissen, R., & Yeats, R. S. (1991). Hope fault, Jordan thrust, and uplift of the seaward Kaikoura Range, New Zealand. *Geology*, **19** 393-396.
- Van Dissen, R., Hornblow, S., Quigley, M., Litchfield, N., Villamor, P., Nicol, A., et al., (2013). Towards the development of design curves for characterising distributed strike-slip surface fault rupture displacement: An example from the 4 September, 2010, Greendale Fault rupture, New Zealand. In *Proceedings of the 19th NZGS (New Zealand Geotechnical Society) Geotechnical Symposium, Queenstown, New Zealand* 20-23.
- Wesnousky, S. G. (2008). Displacement and geometrical characteristics of earthquake surface ruptures: Issues and implications for seismic-hazard analysis and the process of earthquake rupture. *Bull. Seism. Soc. of Am.* **98** 1609-1632.
- Zinke, R., Hollingsworth, J., & Dolan, J. F. (2014). Surface slip and off-fault deformation patterns in the 2013 M_w 7.7 Balochistan, Pakistan earthquake: Implications for controls on the distribution of near-surface coseismic slip, *G-cubed*, **15**(12) 5034-50



Deformation history of sacking features concentrated around the northern tip of the active Neodani fault, central Japan

Keitaro Komura (1)*, Heitaro Kaneda (1), Shintaro Kashihara (1), Tomohiro Nishio (2), Satoru Kojima (3)

- (1) Chiba University. (komukeit@chiba-u.jp)
- (2) Japan Atomic Energy Agency Tono Geoscience Center.
- (3) Gifu University.
- * Central Research Institute of Electric Power Industry

Abstract: Recent high-resolution airborne LiDAR revealed that many sacking features are concentrated around the northern tip of the active Neodani fault, central Japan. These features are hidden under forest canopies, and thus high-precision dating of slope deformation episodes would be possible by radiocarbon dating. In order to examine the relationship between the fault activity and the formation/growth of the sacking features, we conducted hand corings and pit excavations at two sites out of the many sacking depressions found adjacent to the Neodani fault. Our results revealed that the sacking scarps experienced multiple growth events after ~5 ka and the latest event might have occurred simultaneously with the 1891 Nobi earthquake, suggesting that local earthquakes from adjacent active faults are important trigger of formation and growth of those sacking features. We suggest that detailed study of selected sacking features adjacent to an active fault may contribute to reconstruct local paleoseismic history.

Key words: Sacking feature, Active fault, LiDAR, Pit excavation

INTRODUCTION

Uphill-facing scarps and linear depressions are often recognized on and around mountain ridges, which are generally interpreted to be gravitational features and called sacking or sagging features (Zischinsky, 1966). In earthquake-prone regions, a relationship between the origin of sacking features and earthquakes has been often discussed (e.g. Beck, 1968) and co-seismic formation and/or growth of sacking features have been reported around the world (e.g. Ponti & Wells, 1991). Trenching excavations for sacking features have also been attempted mainly in alpine areas after the pioneering work of McCalpin et al (1995). However, a relationship between sacking features and paleoearthquakes is not well understood primarily because of general lack of datable materials in alpine landscape.

Recent high-resolution LiDAR data revealed that numerous sacking features were hidden under forest canopies in the 1,000-1,500-m-high Etsumi Mountains, central Japan (Kaneda & Kono, 2015). In particular, anomalously concentrated sacking depressions were found adjacent to the northern tip of the active Neodani fault (Figure -1). Those sacking depressions are most probably filled with peaty sediments with abundant in-situ organic materials, which would be a big advantage over similar studies in alpine areas. We thus conducted hand corings and pit excavations at some of those dammed-up sacking depressions (Figure -2) to discuss the relationship between sacking features and paleoearthquake.

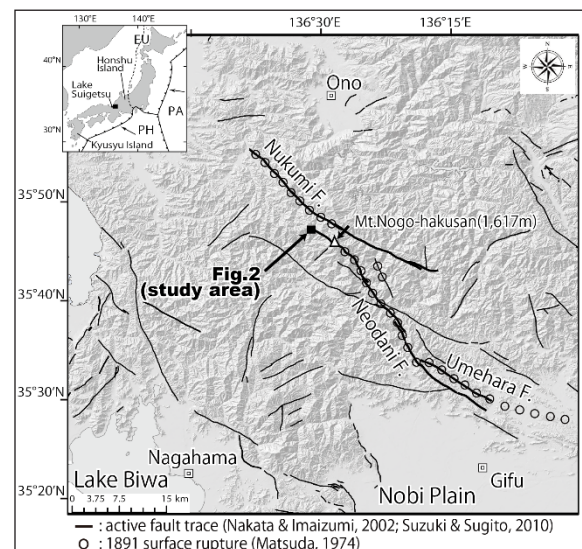


Figure 1: Topography and active fault traces in the Etsumi Mountains. Surface rupture traces of the 1891 Nobi Eq. (Matsuda, 1974) are also shown by open circles. Abbreviations are Eurasian plate, EU; Pacific plate, PA; and Philippine Sea plate, PH.



STUDY AREA

A number of NW-SE trending active left-lateral faults comprise the Nobi active fault system in the Etsumi Mountains (Matsuda, 1974). The Nukumi, Neodani and Umehara faults of this system ruptured in the 1891 Nobi earthquake (Figure -1), which is the largest inland earthquake (Mw:7.5) ever recorded in the Japanese written history (Usami, 2003). Our study area is located ~600 m southwest of the northernmost Neodani fault, where W- to WNW-trending and 2-5-m-high sackung scarps have formed many small dammed-up depressions (Figure -2). Out of those depressions, we have targeted two sackung depressions (Sites A and B) that were dammed up by the same sharp scarp (Scarp A; Figure -2).

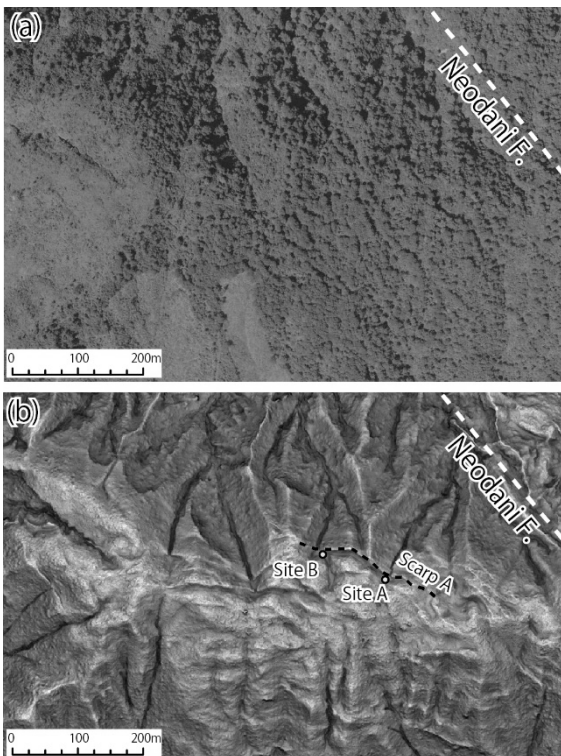


Figure 2: (a) Aerial photograph of our study area. See Fig.1 for location. (b) Red Relief Image Map of the same area based on 0.5 m and 1.0 m LiDAR DEMs. This image is produced by patent-protected (but open to academic use) DEM visualization method of Asia Air Survey Co., Ltd (Japanese Patent No.3670274 and No.4272146).

METHODS AND RESULTS

We conducted eleven hand corings (down to ~2.5 m deep) and three hand-excavated pits (down to ~1.7 m deep) at the target sackung depressions (Figure -2). Our investigation revealed that the sackung depressions are filled with peat and lacustrine clay sediments, which show various degree of deformation after their deposition. At least three growth events of Scarp A are inferred to have occurred after ~5 ka based on radiocarbon ages from seeds, leaves and twigs collected from the peat. Especially, the timing of the latest growth event was consistent with the 1891 Nobi earthquake.

DISCUSSION

Paleoseismic studies on the Neodani fault have revealed that three earthquakes, including the 1891 Nobi earthquake, occurred after ~7 ka (Awata et al., 1999; Tanaka et al., 2017), which appear to be correlated to the growth events identified in our study area and imply a probable simultaneity of sackung scarp growth and paleoearthquakes. Seismic shaking from the adjacent active fault may thus be an important trigger of formation/growth of sackung features.

We suggest that detailed geochronology of off-fault sackung features may contribute to reconstruct local paleoseismic history, although further investigation is required in our study area and elsewhere for deeper understanding of triggers and controls of sackung features around active faults.

Acknowledgements: We thank Tsutomu Inoue, Naoya Iwamoto, Hoshikazu Hayashi, Souta Takagi and Masaya Okabe for their field support and Takahiro Miyauchi and Daisuke Ishimura for helpful discussions. This work funded by Grant-in-Aid for Scientific Research (24700945) by Japan Society for the Promotion of Science (JSPS).

REFERENCES

- Awata, Y., Kariya, Y., and Okumura, K., 1999. Segmentation of the surface ruptures associated with the 1891 Nobi earthquake, central Honshu, Japan, based on the paleoseismic investigations, in Interim Report number EQ/99/3, Geological Survey of Japan, Tsukuba, 115–130 (in Japanese with English abstract).
- Beck, A.C., 1967. Gravity faulting as a mechanism of topographic adjustment, *New Zealand Journal of Geology and Geophysics*, 11 : 1, 191-199.
- Kaneda, H., and Kono, T., 2015. Seismic impact on long-term gravitational slope deformation. XIX INQUA 2015 in Nagoya, T15-01.
- Matsuda, T., 1974. Surface Faults Associated with Nobi (Mino-Owari) Earthquake of 1891, 13. *Special Bulletin Earthquake Research Institute, University of Tokyo, Japan*, pp. 85–126 (in Japanese with English abstract).
- McCalpin, J.P., and Irvine, J.R., 1995. Sackungen at the Aspen Highlands Ski Area, Pitkin County, Colorado, *Environmental and Engineering Geoscience*, 1, 3, 277-290.
- Nakata, T. and Imaizumi, T., (Eds), 2002. *Digital Active Fault Map of Japan*, University of Tokyo Press, Tokyo (in Japanese).
- Ponti, D.J., and Wells, R.E., 1991. Off-fault ground ruptures in the Santa Cruz Mountains, California: Ridge-top spreading versus tectonic extension during the 1989 Loma Prieta earthquake, *Bulletin Seismological Society of America*, 81, 5, 1480-1510.
- Suzuki, Y., and Sugito, N., (Ed.), 2010, 1:25,000 Gifu Active fault map, Gifu Prefecture, 138p.
- Tanaka, T., Kaneda, H., and Inoue, T., 2017, Tectonic geomorphology and paleoseismology of the northern Neodani fault around Mt. Nogo-Hakusan, central Japan. *JpGU-AGU Joint Meeting 2017, SSS12-P14*.
- Usami, T., 2003. *Materials for Comprehensive List of Destructive Earthquakes in Japan, [416]-2001, Latest Edition*, Univ. Tokyo Press, Tokyo (in Japanese).
- Zischinsky, U., 1966. On the deformation of high slopes. *International Society of Rock Mechanism, 1st Congress, Proceedings*, 2, 179-185.



Preliminary geometry and kinematics of multiple surface ruptures during the 2016 M_w 7.8 Kaikōura earthquake, North Canterbury region, New Zealand

Khajavi, Narges (1), Nicol, Andrew (1) Fenton, Clark (1), Pettinga, Jarg (1), Stahl, Tim (1), Hyland, Natalie (1), Bushell, Tabitha (1), Pedley, Kate (1), McColl, Sam (2), Noble, Duncan (1)

- (1) Department of Geological Sciences, University of Canterbury, Private Bag 4800, Christchurch, New Zealand
 (2) College of Sciences, Massey University, Private Bag 11222, Palmerston North, New Zealand

Abstract: The M_w 7.8 Kaikōura earthquake produced a surface rupture of ~200 km across the northern South Island of New Zealand. This study was conducted in an area of ~600 km² in the epicentral region where the surface rupture is comprised of two main non-coplanar sets of faults that trend E-NE and NNE-NW with mainly steep dips (60°-80°). Analysis of the surface rupture using field and LiDAR data provides new information on the dimensions, geometries and kinematics of these faults. The more northerly trending fault set is sub-parallel to basement bedding and accommodated maximum oblique left-lateral reverse slip of ~1 and ~5 m for the Stone Jug and Leader faults, respectively. The E-NE striking Conway-Charwell and The Humps faults exhibit right-lateral to oblique reverse slip of up to ~2 and ~5 m, respectively. The faults form a hard-linked system of transpressional structures along this portion of the plate boundary which is dominated by kinematics consistent with oblique subduction. The intersections of the main fault sets facilitated the propagation of the earthquake and transfer of slip northwards across this portion of the plate boundary zone.

Key words: Kaikōura earthquake, surface rupture, North Canterbury, New Zealand

INTRODUCTION

Historical earthquakes can provide key information about the earthquake and tectonic processes that shape plate boundaries (e.g., Sieh et al., 1993; Fariás et al., 2010). The M_w 7.8 Kaikōura earthquake ruptured at least 14 faults (~200 km of surface rupture) (Fig. 1) across the New Zealand-Australian plate boundary zone on the northern South Island of New Zealand, and was recorded by both remote and terrestrial datasets (e.g., Hamlin et al., 2017; Litchfield et al., 2017). The earthquake produced geologically synchronous slip of up to ~12 m (Hamlin et al., 2017) on faults within the mainly strike-slip Marlborough Fault System (MFS), which accommodates most (≥80%) of the relative plate motion (Fig. 1). Further south in the transpressional North Canterbury Domain (NCD) the earthquake ruptured faults with Late Quaternary slip rates <2 mm/yr and regional shortening rates 2-3 mm/yr (e.g., Nicol et al., 1994; Litchfield et al., 2014, 2017). Many aspects of the earthquake were unexpected including the number and geometric complexity of the faults, and the propagation of the rupture obliquely across the plate boundary which resulted in slip on faults with variable slip rates and in different tectonic domains.

To better understand the factors that contributed to the complexity of the earthquake, we present a preliminary analysis of the geometry and kinematics of the faults that ruptured during the Kaikōura earthquake in the epicentral area. The study area covers ~600 km² and is located in the NCD immediately south of the Hope Fault. In the study area, the earthquake ruptured a network of faults producing a total length of mapped traces of ~140 km (mapping is ongoing and both the number and total length of these traces may increase). The majority of these

surface ruptures form along four primary faults or fault zones that are here referred to as The Humps, Leader, Conway-Charwell and Stone Jug faults, which are the primary focus of this paper (Figs. 2). Analysis of the surface rupture from field mapping and LiDAR data provides new information on the dimensions, geometries and kinematics of these faults.

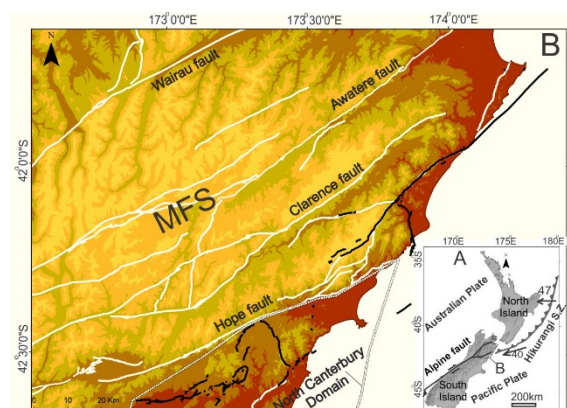


Figure 1: Tectonic setting of the November 14 M_w 7.8 Kaikōura earthquake. A) New Zealand plate boundary setting with relative plate boundary motion vectors (DeMets et al., 1994). B) Digital elevation model of the Northern South Island showing active faults (white lines), the location of the Marlborough Fault System (MFS; between the Wairau and Hope faults), and the faults that ruptured in the 2016 Kaikōura Earthquake (black lines). Location of the North Canterbury domain is also shown on B.



Figure 2: Mapped traces of the faults that ruptured during the Kaikōura earthquake (white lines) within the study area; north of the NCD. Leader and southern sections of the Stone Jug faults were not known to be active prior to the Kaikōura earthquake. The Hundalee Fault was not studied in this research.

DISCUSSION

In the NCD, the faults that ruptured during the earthquake comprise two main non-coplanar sets that trend E-NE and NNE-NW with mainly steep dips (60° - 80°). The more northerly trending faults which were largely unknown prior to the earthquake, accommodated predominantly left-lateral reverse slip (Leader and Stone Jug faults). East to northeast trending faults (The Humps and Conway-Charwell faults) accrued right-lateral (east) to oblique reverse (northeast) slip. Detailed field mapping shows that the oblique Humps faults strike 87° in the west, 65° where it crosses the Leader River, and 54° at its termination against the Leader fault. The oblique Conway-Charwell faults strike 42° at the intersection with the Leader fault, and 54° towards NE.

Fault scarp heights and lateral displacements of cultural features such as fences and roads have been widely observed and indicate that oblique slip was common. The earthquake produced maximum oblique slip of ~ 5 m on the Humps and Leader faults, ~ 2 m on the Conway-Charwell fault and ~ 1 m on the Stone Jug fault (see selected field photos showing the scarp heights and lateral offsets along fences (Figs. 3). The relative components of strike slip and dip slip are strongly dependent on fault strike. Along The Humps fault, for example, slip was mainly right lateral at its western end where it strikes approximately east-west (i.e. sub-parallel to the relative plate motion vector) and oblique reverse right lateral at its eastern end where it strikes northeast.

Slip is transferred between the main faults which intersect each other at the ground surface. For example, at the eastern termination of The Humps Fault zone, right-lateral reverse slip was transferred northwards onto the Leader Fault zone producing up to ~ 3 m of uplift at the northern end of the Mt Stewart range in the hangingwall of the Leader Fault (Fig. 2). Slip transfer at fault intersections is often achieved by a distributed network of smaller faults.



Figure 3: Selected field photos showing scarp heights and lateral offsets along Leader, Conway-Charwell, The Humps and Stone Jug faults. Photos: Kate Pedley, Narges Khajavi, and Clark Fenton.



CONCLUSIONS

The faults form a hard-linked system of transpressional structures along this portion of the plate boundary which is dominated by kinematics consistent with oblique subduction. In the study area, the relative plate motion is accommodated by an array of northerly striking left-lateral reverse to reverse left-lateral and E-NE right-lateral to reverse right-lateral faults. Northerly striking faults accommodate distributed bookshelf-shear, and can also terminate at, E-NE striking faults in a predominantly transpressional regime. The intersections of the main fault sets facilitated the propagation of the earthquake and transfer of slip northwards across this portion of the plate boundary zone.

Acknowledgements: We thank the Institute of the Geological and Nuclear Science (GNS) for providing LiDAR data, and the Department of Geological Sciences, University of Canterbury, and the New Zealand Earthquake Commission (EQC) for funding this research. The landowners of the Waiau region, Emu Plain, Woodchester, Mendip, Doone, and Conway Downs are thanked for permission to access the study area. We thank Virginia Toy, Matt Cockcroft, Anekant Wanders, Chris Grimshaw, Josh Borrella, Andrea Barrier and Alan Bischoff for assisting with fieldwork and data collection.

REFERENCES

- DeMets, C., Gordon, R.G., Argus, D.F., Stein, S., 1994. Effect of recent revisions to the geomagnetic reversal time scale on estimates of current plate motions. *Geophysical Research Letters* 21, 2191-2194.
- Fariás, M., Vargas, G., Tassara, A., Carretier, S., Baize, S., Melnick, D., Bataille, K., 2010. Land-level changes produced by the Mw 8.8 2010 Chilean earthquake. *Science* 329, 916.
- Hamling, I.J., Hreinsdóttir, S., Clark, K., Elliott, J., Liang, C., Fielding, E., Litchfield, N., Villamor, P., Wallace, L., Wright, T.J., D'Anastasio, E., Bannister, S., Burbidge, D., Denys, P., Gentle, P., Howarth, J., Mueller, C., Palmer, N., Pearson, C., Power, W., Barnes, P., Barrell, D.J.A., Van Dissen, R., Langridge, R., Little, T., Nicol, A., Pettinga, J., Rowland, J., Stirling, M., 2017. Complex multi-fault rupture during the 2016 Mw 7.8 Kaikōura earthquake, New Zealand. *Science*, DOI: 10.1126/science.aam7194 (2017).
- Litchfield, N.J., Van Dissen, R., Sutherland, R., Barnes, P.M., Cox, S.C., Norris, R., Beavan, J., Langridge, R., Villamor, P., Berryman, K., Stirling, M., Nicol, A., Nodder, S., Lamarche, G., Barrell, D.J.A., Pettinga, J.R., Little, T., Pondard, N., Mountjoy, J.J., Clark, K., 2014. A model of active faulting in New Zealand. *New Zealand Journal of Geology & Geophysics* 57 (1), 32-56, doi: 10.1080/00288306.2013.854256.
- Litchfield N.J., Villamor P., Dissen R., Nicol A., Barnes P., Barrell D., Pettinga J., Langridge R., Little T., et al. In review. Surface ruptures and paleoseismology of the Mw 7.8 2016 Kaikōura earthquake reveal end-member complexity. *Geology*.
- Nicol, A., Alloway, B.V., Tonkin, P.J. 1994. Rates of deformation, uplift and landscape development associated with active folding in the Waipara area of North Canterbury, New Zealand. *Tectonics* 13, 1321-1344.
- Sieh, K., Jones, L., Hauksson, E., Hudnut, K., Eberhart-Phillips, D., Heaton, T., Hough, S., Hutton, K., Kanamori, H., Lilje, A. and Lindvall, S., 1993. Near-field investigations of the Landers earthquake sequence, April to July 1992. *SCIENCE-NEW YORK THEN WASHINGTON-*, 260, pp.171-171.



Simulation of Strong Ground Motion using Seismic Data of the Earthquake that Occurred on September 12th 2016, near Gyeongju, Korea

Kim, Hak-Sung (1), Park, Dong-Hee (1), Choi, Weon-Hack (1)

(1) Central Research Institute, Korea Hydro and Nuclear Power Co., Ltd., 70, 1312 Beon-gil, Yuseong-daero, Yuseong-gu, Daejeon, 34101, Korea. haksung.kim@khnp.co.kr.

Abstract: The seismic data of large earthquake is required for the reliable ground motion prediction which is an essential part of seismic hazard analysis. In Korea, however, large earthquake data is limited because the Korean peninsula is located in the low seismicity zone. Therefore, ground motions induced by the large earthquake should be hypothetically generated using the small earthquake data. Meanwhile, earthquakes of moment magnitude (M_w) 5.5 occurred on September 12th 2016, near Gyeongju, Korea. This is the largest earthquake ever occurred in Korea since measurement began in 1905, and high-quality ground motion data were measured by seismic monitoring network of Korea. In this study, M_w 6.5 earthquakes are simulated from the seismic data of 2016 Gyeongju earthquake using the empirical Green's function method based on a scaling law of fault parameters and the omega-squared source spectra. The results of this study can be used for the seismic hazard assessment and seismic damage evaluation of important infrastructures (e.g., nuclear power plants, transmission towers, and dams) in Korea.

Key words: Gyeongju Earthquake, Ground motion prediction, Seismic waveform, Green's function.

INTRODUCTION

The seismic data of large earthquakes (i.e., moment magnitude 6.0 and greater) is required for the reliable ground motion prediction which is an essential part of seismic hazard analysis and seismic design. In Korea, however, there is no large earthquake data because the Korean peninsula is located in a low seismicity zone while the maximum magnitude of historical earthquake has been considered as 6.2-6.7 (Lee and Yang, 2006; KIGAM, 2012). Therefore, ground motion induced by large earthquakes should be estimated using observed seismic data of small earthquakes.

The empirical Green's function method is the one of the most effective semi-empirical methods for simulating strong ground motions using observed seismic data. The empirical Green's function is based on the assumption that ground motions induced by earthquakes can be characterized with three elements: (1) seismic source (i.e., faults), (2) seismic wave propagation paths, and (3) site effects (i.e., local ground response, basin effects, and effect of surface topography). It is very difficult to describe seismic wave propagation paths and site effects for a site because there is a great epistemic uncertainty induced by complicated geological structures and geophysical properties (e.g., heterogeneity and anisotropy) of realistic media. Semi-empirical approach using similarly relations between small and large earthquakes for closely located seismic sources can overcome these difficulties. Ground motions of a common site induced by closely located earthquakes share the same seismic wave propagation path and site effects. Therefore, a ground motion recording at a common site can be synthesized using smaller earthquake data for closely located seismic sources because common wave propagation path and site effects can be ignored (Bakum and Bufe, 1975). This approach is considered as an empirical Green's function (Hartzell, 1978). In this study, Empirical Green's function

method formulated by Irikura and Kamae (1994) was used. Irikura's technique is based on two similarity relations between the small and large earthquakes. One is the scaling relation of source parameters such as fault dimensions, slip, and slip duration (Kanamori and Anderson, 1975) and the other is the scaling relation of omega-squared source spectra (Aki, 1967). The ground motion for a large earthquake is synthesized by summing the observed data of small earthquakes with corrections for the difference in the slip velocity time function between the small and large earthquakes scaling laws. Figure 1 shows the schematic drawing of empirical Green's function method formulated by Irikura and Kamae (1994).

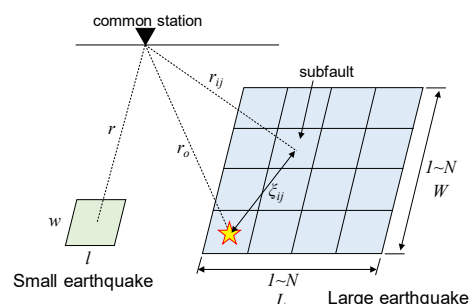


Figure 1: Schematic diagram of the empirical Green's function method. $L \times W$ and $l \times w$ are fault dimensions of large and small earthquakes, respectively. Meanwhile, N is defined to be $N = L/l = W/w$ (after Irikura and Kamae, 1994).

The sum of observed data of small earthquakes can be expressed as:

$$U(t) = \sum_{i=1}^N \sum_{j=1}^N \frac{r}{r_{ij}} F(t) * (C \cdot u(t)), \quad (1)$$

where r is the hypocentral distance from the observation point, r_{ij} is the distance from the observation point to the subfault (refer to Figure 1), $U(t)$ is the simulated ground



motion for the large earthquake, $u(t)$ is the observed ground motion the small earthquake, C is the ratio of stress drop between small and large earthquake, N is the ratio of fault dimension between small and large earthquake, and $F(t)$ is the filtering function to adjust the difference in the slip velocity time functions between the small and large earthquakes (Irikura, 1986; Irikura et al., 1997).

SOURCE CHARACTERISTICS

A strike-slip earthquake with moment magnitude (M_w) of 5.5 occurred in the south-eastern part of the Korean peninsula on September 12th 2016 (Hereinafter, called 2016 Gyeongju earthquake after nearby historic city, Gyeongju). Figure 2 shows the epicenter and moment tensor solution of the 2016 Gyeongju earthquake. The main shock of 2016 Gyeongju earthquake was the largest earthquake that ever occurred in Korea since measurements began in 1905. The source characteristics of the 2016 Gyeongju earthquake used in this study are summarized in the table 1.

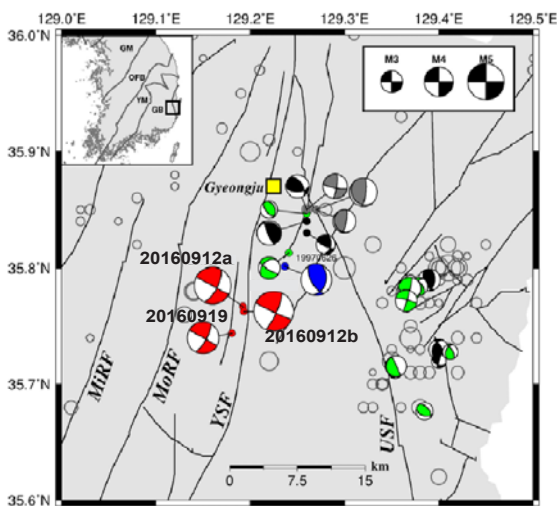


Figure 2: Epicenter and focal mechanism of 2016 Gyeongju earthquakes (drawn by Kim et al. (2016)). Red beach balls with the date labeled show the source mechanisms of the 2016 Gyeongju earthquake ('20160912a' for MW 5.1 earthquake, '20160912b' for MW 5.5 earthquake, and '20160919' for MW 4.4 earthquake). Other colored beach balls show past earthquakes in the region (Kim et al., 2016).

Table 1: Source characteristics of 2016 Gyeongju earthquake used in this study.

Parameter	Value
Origin time	16/09/12, 11:32:54.80
Epicenter	129.19°E, 35.76°N
Focal depth ¹	14.2 km
Moment magnitude	5.5
Stress drop	127 bar
Moment tensor solution ¹	115/86/12, 24/78/176

¹: Kim et al., 2016

PARAMETERS FOR SIMULATING GROUND MOTIONS

High-quality ground motion data were acquired by Korean Integrated Seismic System (KISS), seismic sensor network of Korea Hydro and Nuclear Power (KHNP) and Korea Institute of Nuclear Safety (KINS). In this study, seismic data of the 2016 Gyeongju earthquake observed at KINS seismic monitoring station of Wolsung nuclear power plant site (KINS WSN station) was selected as Green's function (i.e., subfault event). KINS WSN station is 27 km away from epicentre of 2016 Gyeongju earthquake. Figure 3 and 4 shows the location of KINS WSN station, and observed seismic data of 2016 Gyeongju earthquake at KINS WSN station, respectively. Parameter for simulating ground motions in this study are summarized in Table 2.

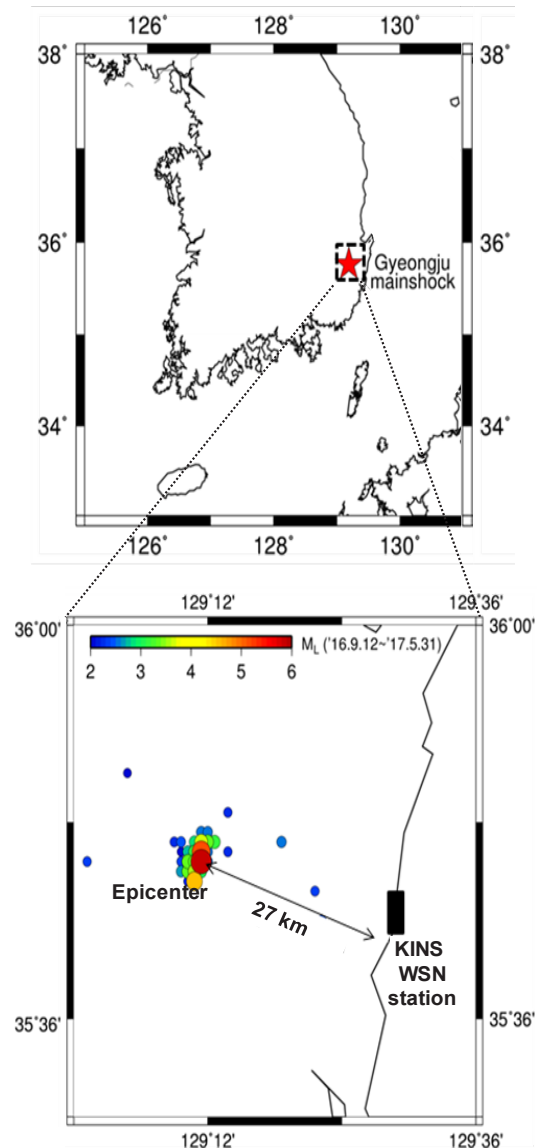


Figure 3: The location of KINS WSN station and the epicenter of the 2016 Gyeongju Earthquake. The location and device information of KINS WSN station is available at <http://emc.kins.re.kr/USERIF/OSVI/NclrEqOsvi.aspx>

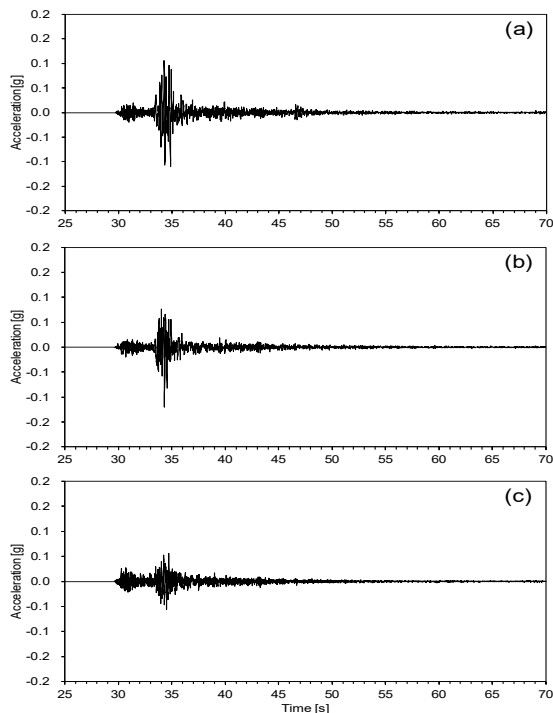


Figure 4: The observed ground motion of 2016 Gyeongju earthquake at KINS WSN station (a) North-South component, (b) East-West component, (c) Vertical component. The data is available at <http://emc.kins.re.kr/USERIF/MESR/SeimDataView.aspx?SEQ=1474>.

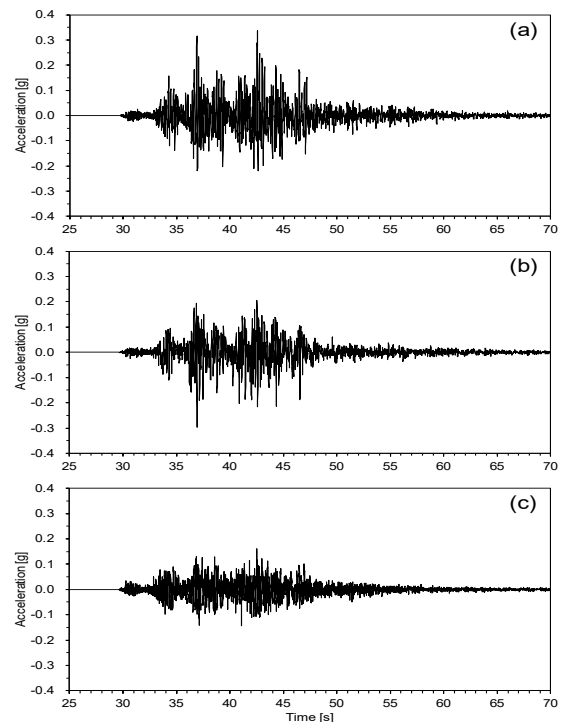


Figure 5: An example of simulated ground motion of M_w 6.5 hypothetical earthquake at KINS WSN station (a) North-South component, (b) East-West component, (c) Vertical component.

Table 2: Input parameter for simulation

Parameter	Value
S-wave velocity	3.5 km/sec
Rupture velocity	2.7 km/sec
Rise time of subfault	0.1 s
N (number of subfault)	9
C (stress drop ratio)	1.24
Epicentral distance	27 km

RESULTS AND DISCUSSION

Figure 5 shows an example of simulated ground motion of M_w 6.5 hypothetical earthquake at KINS WSN station. The peak ground acceleration of simulated results is 0.33 g. The strong ground motion can be estimated more precisely if additional information of fault geometry is obtained using analysis on aftershock distribution. The estimated ground motions can be used as the reference data for seismic hazard assessment and seismic damage evaluation of important infrastructures (e.g., nuclear power plants, transmission towers, and dams) in Korea. Also, the ground motion estimation techniques can be used for the development of attenuation relation.

REFERENCES

- Aki, K., 1967. Scaling law of seismic spectrum, *Journal of Geophysical Research* 72, 1217-1231.
- Bakun, W. H. and Bufe, C. G., 1975. Shear-wave attenuation along the San Andreas Fault zone in Central California, *Bulletin of the Seismological Society of America* 65, 439-460.
- Hartzell, S. H., 1978. Earthquake aftershocks as Green's functions, *Geophysical Research Letters* 5, 1-4.
- Irikura, K., 1986. Prediction of strong acceleration motions using empirical Green's function, *the proceeding of 7th Japan Earthquake Engineering Symposium*, 151-156.
- Irikura, K. and Kamae, K., 1994. Estimation of strong ground motion in broad-frequency band based on a seismic source scaling model and an empirical Green's function technique, *Annali di Geofisica* 37, 1721-1743.
- Irikura, K., Kagawa, T., and Sekiguchi, H., 1997. Revision of the empirical Green's function method by Irikura (1986), *Programme and abstracts, Seismological Society of Japan 2*, B25 (in Japanese).
- Kanamori, H. and Anderson, D.L., 1975. Theoretical basis of some empirical relations in seismology, *Bulletin of the Seismological Society of America* 65, 1073-1095.
- Kim, Y. H., Rhie, J. K., Kang, T. S., Kim, K.H., Kim, M., Lee, S.J., 2016. The 12 September 2016 Gyeongju earthquakes: 1. Observation and remaining questions, *Geosciences Journal* 20(6), 747-752.
- KIGAM (Korea Institute of Geoscience and Mineral Resources), 2012. Final report of project 'Active fault map and seismic hazard map', publication code: NEMA-자연-2009-24 (in Korean).
- Lee, K.H., and Yang, W.S., (2006), "Historical seismicity of Korea", *Bulletin Seismological Society of America*, Vol. 96, pp. 846-855.



Preliminary study on the triggering mechanism and related faults associated with the 9.12 Gyeongju Earthquake (M=5.8), SE Korea

*Kim, Taehyung, Kim, Young-Seog**

Pukyong National University (#416, B-14, 45 Yongsoro, Namgu, Busan, S.Korea). ysk7909@pknu.ac.kr

Abstract: The 9.12 Gyeongju Earthquake (ML=5.8) was followed by hundreds of aftershocks around Gyeongju, Korea. The focal mechanism of the main shock indicates $027^{\circ}/76^{\circ}$ of dextral strike-slip fault plane. There are many N-S to NNE-SSW trending lineaments, including the Yangsan fault (YSF) and the Deokcheon fault (DCF), which were recognized on the LiDAR image. The two major faults (YSF and DCF) are geometrically linked by several NE-SW trending lineaments. We identified that many of the NE-SW trending lineaments have evidences of faults based on field observation. Furthermore, almost all of the seismic events were concentrated in a narrow quadrangle area with a NE-SW trend between YSF and DCF. This geometry is similar to the reported examples of right bending/stepping linkage zone of two strike-slip faults. This result is well matched with previous studies associated with aftershock clustering and fault damage zones.

Key words: Gyeongju Earthquake, aftershock cluster, rupture mechanism, Yangsan Fault, damage zone

INTRODUCTION

The biggest instrumental seismic event in South Korea ($M_L=5.8$) occurred in Gyeongju City on 12th September, 2016. The 9.12 Gyeongju Earthquake was followed by hundreds of small to medium scale aftershocks around the Naenam-myeon, Gyeongju City. This earthquake is a shock to the Korean people who believed that the Korean peninsula is a safe place from earthquakes. It was a wakeup call for them to consider the importance of earthquake studies of the active faults.

Earthquakes generally occur by sudden slip along a fault to release cumulated stress on a specific fault or a fault system. A fault is activated when the accumulated tectonic stress overcomes the frictional strength of the rock body (Reid, 1910; Scholz, 2002). The recurrence cycle of the earthquake and its characteristics such as magnitude and slip rate is affected by tectonic setting and rock properties. Thus, it is important to trace pre-existing active faults to understand fault behaviours associated with seismic events, because the reactivation of pre-existing geological structures is easier than the formation of new structures. Based on this concept, we investigated pre-existing faults around the epicentral area through LiDAR imagery and field observation.

GEOLOGICAL SETTING

Almost all of the fore/aftershocks including the main shock ($M_L=5.8$) are located around the Hwagok reservoir in Gyeongju. Basement rocks in the study area are Cretaceous sedimentary rocks, which were later intruded by Cretaceous and Paleogene igneous rocks (Fig. 1).

The Cretaceous Daegu formation is composed of red, grey and greenish shale and sandstone. Some of this formation in contact with the granite is metamorphosed to hornfels. According to Kim et al. (1971), major faults were generally

believed to be post-granite intrusion, and their trend is roughly $N10^{\circ}-20^{\circ}E$. Epicenters of the 9.12 earthquake and related aftershocks are mainly concentrated in the Naenam-myeon area, located around the junction between the Yangsan fault (YSF) and Ulsan fault (USF). The geometry of the intersection between the YSF and USF is similar to the suggested λ -fault system (Du and Aydin, 1995) and reported small-scale λ -fault system (Kim et al., 2000; Han et al., 2009).

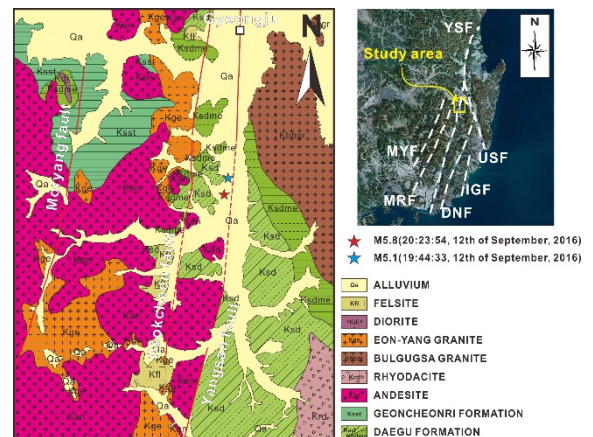


Figure 1: Geological map of the study area and its location, modified from Kim et al., (1971). Lineaments are multiple deformed strike-slip fault system and called 'Yangsan fault system'(YSF: Yangsan fault, MYF: Milyang fault, MRF: Moryang fault, DNF: Dongnae fault, IGF: Ilgwang fault, USF: Ulsan fault).

Several historical earthquakes have been reported around this area (Jin et al., 2011), and recently, more than 40 Quaternary faults have been interpreted around the YSF and USF system (Lee et al., 2016). Therefore, this area is a historically and paleoseismologically active area in Korea. A subsidiary sub-parallel fault to the YSF was already recognized in the western part of the fault, but the name was not given and the activity has not been studied.

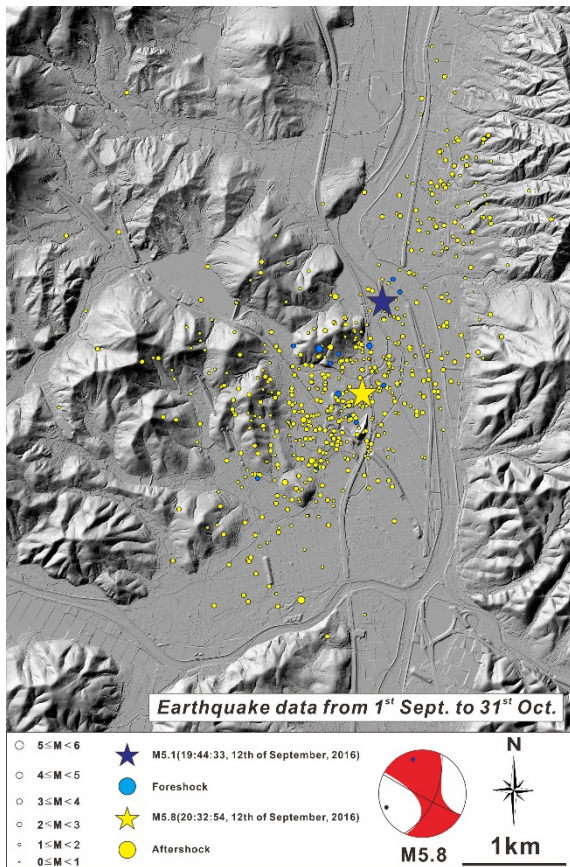


Figure 2: Fore/aftershock distribution on the LiDAR image

FORE/AFTERSHOCK DISTRIBUTION

The distribution of the main shock and related aftershocks of the 9.12 earthquake is concentrated between the Yangsan fault and the subsidiary Deokcheon fault (DCF; Fig. 2). It may indicate that the rupture of the related fault in depth is confined within this area. Furthermore, the aftershock distribution area is consistent with a previously reported fault linkage model (e.g. Kim et al., 2004).

Based on the previous earthquake mechanism study (Sibson, 1989), aftershocks generally cluster in regions where mean stress has been reduced by slip on the main shock rupture. The concentrations of aftershocks in dilational fault jogs and bends, and immediately outside contractional jogs may support this idea. Our aftershock data from 9.12 Gyeongju earthquake is consistent with this previous study.

LINEAMENT ANALYSIS BASED ON LIDAR IMAGES AND FIELD OBSERVATION

LiDAR is a very powerful tool to get valuable DEM data even in high vegetation areas like Korea. We constructed hill-shade images from the DEM based on high resolution LiDAR data for a lineament analysis. A lineament is a useful linear feature in a landscape, because it is an expression of an underlying geological structure such as a fault (O'Leary et al., 1976).

A suite of N-S, NNW-SSE, NNE-SSW, and NE-SW trending lineaments are recognized around the study area (Fig. 3). The main feature of the lineaments is the N-S to NNE-SSW trending major lineaments parallel to the main YSF and the subsidiary DCF, which are geometrically linked by several NE-SW trending connecting lineaments (Fig. 3). This geometry is very similar to the suggested linkage model of fault damage zones (Kim et al., 2004) and the aftershock distribution is consistent with the previous examples reported by Sibson (1989).

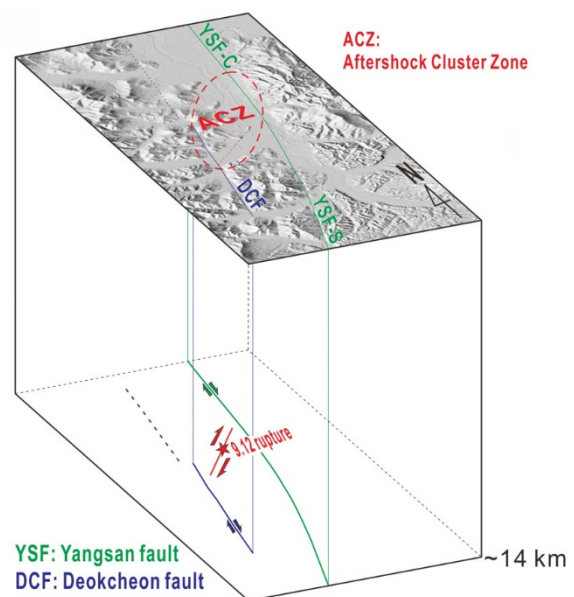


Figure 3: A schematic model of rupture mechanism of the 9.12 Gyeongju earthquake. The earthquake rupture occurred along a subsidiary fault in the fault damage zone around the YSF (modified from Kim et al., 2017).

CONCLUSION

The 9.12 Gyeongju earthquake ($M_L=5.8$) occurred in 2016 was the biggest instrumental seismic record on the Korean peninsula. We investigated exposed faults around the epicentral area of the 9.12 Gyeongju earthquake. Based on the LiDAR images and fieldwork, we have preliminary concluded that the 9.12 earthquake rupture occurred at depth along a subsidiary fault located in the linking damage zone between the main YSF and its subsidiary fault (DCF).

Acknowledgements: This research was supported by grant 2017-MPSS31-006 from Supporting Technology Development Program for Disaster Management funded by the Korean Ministry of Public Safety and Security (MPSS) and the evaluation of fault activity and probabilistic seismic hazard analysis around the Wolsung nuclear power plant sites, Korean Hydro & Nuclear Power Co., Ltd (Grant No :A16IP55) and BK21 plus Project of the Graduate School of Earth Environmental Hazard System.



REFERENCES

- Du, Y., Aydin, A., 1995, Shear fracture patterns and connectivity at geometric complexities along strike-slip faults. *Journal of Geophysical Research* 100, 18093-18102.
- Han, S. -R., Park, J., Kim, Y. -S., 2009, Evolution modeling of the Yangsan-Ulsan fault system with stress changes. *Journal of the Geological Society of Korea* 45, 361-377 (in Korean with English abstract).
- Jin, K., Lee, M., Kim, Y.-S. & Choi, J.-H., 2011, Archaeoseismological studies on historical heritage sites in the Gyeongju area, SE Korea. *Quaternary International*, 242(1), 158-170.
- Kim, N. J., Kwon, Y. I., and Jin, M. S., 1971, Explanatory text of the geological map of Moryang sheet 1: 50,000. Geological Survey of Korea.
- Kim, Y. -S., Andrew, J. R., Sanderson, D. J., 2000, Damage zones around strike-slip fault systems and strike-slip fault evolution, Cracking Haven, southwest England, *Geoscience Journal* 4, 53-72.
- Kim, Y.-S., Peacock, D. C. P. & Sanderson, D. J., 2004, Fault damage zones. *Journal of Structural Geology* 26, 503-517.
- Kim, Y. -S., Kim, T., Kyung, J. B., Cho, C. S., Choi, J. -H., Choi, C. U., 2017, Preliminary study on rupture mechanism of the 9.12 Gyeongju earthquake. *Journal of the Geological Society of Korea*, 53(3), p.407-422.
- Lee, J., Rezaei, S., Hong, Y., Choi, J.-H., Choi, J.-H., Choi, W.-H., Rhee, K.-W. and Kim, Y.-S., 2015, Quaternary fault analysis through a trench investigation on the northern extension of the Yangsan fault at Dangu-ri, Gyungju-si, Gyeongsangbuk-do. *Journal of the Geological Society of Korea*, 51(5), 471-485 (in Korean with English abstract).
- O'Leary, D. W., Friedman, J. D., and Pohn, H. A., 1976, Lineament, linear, lineation: Some proposed new standards for old terms. *Geological Society of America Bulletin*, v. 87, p.1463-1469.
- Reid, H. F., 1910, The mechanics of the earthquake. In: Lawson, A. C. (chairman), Vol. II of the California earthquake of April 18, 1906: Report of the state earthquake investigation commission. Carnegie Institution of Washington Publication 87 (reprinted in 1969).
- Scholz, C. H., 2002, *The Mechanics of Earthquakes and Faulting* (2nd ED.), Cambridge University Press, Cambridge, United Kingdom.
- Sibson, R. H., 1989, Earthquake faulting as a structural process. *Journal of Structural Geology*, 11(1/2), 1-14.



Earthquake fault propagation, displacement and damages

Kim, Young-Seog (1), Jin, Kwangmin (2), Choi, Jin-Hyuck (2), Sambit Prasanajit Naik (1)

- (1) Dept. of Earth & Environmental Sciences, Pukyong National University. ysk7909@pknu.ac.kr.
 (2) Korea Institute of Geoscience and Mineral Resources

Abstract: Although it is not easy to understand and predict earthquake damage patterns, several examples associated with earthquake damage show the importance of earthquake surface ruptures and fault damage zones as well as seismic shaking. The characteristics of earthquake fault (rupture) propagation, which is recorded as along-fault slip (or displacement) distribution, can provide us very useful information related to earthquake wave or energy propagation. Therefore, we could interpret the earthquake behavior from the patterns of slip and fault damages along earthquake ruptures. Earthquake damages also depend on the position along or around the faults including hanging wall and footwall of the faults. We also could consider several other factors such as the conditions of ground foundation including consolidation, the depth of hypocenter, distance and location related to the epicenter.

Key words: Earthquake fault, rupture propagation, displacement, damage

INTRODUCTION

Although it is not easy to understand the intensities and patterns of earthquake damages, it is an important issue in earthquake hazard assessments and earthquake mitigation studies. If we could understand the relationship between earthquake damages and their controlling factors, we could greatly reduce the casualties as well as the costs by earthquakes.

Especially, this is very important to site selection of critical facilities such as nuclear power plants and waste disposal sites. Although our knowledge is not enough to completely understand this issue, recently we got great progress from the studies of surface rupture, slip (displacement), earthquake propagation, and fault damage patterns (e.g. Sibson, 1989; Kim et al., 2003, 2004; Kim and Sanderson, 2005; Choi et al., 2012).

IMPORTANCE OF SURFACE RUPTURE AND FAULT DAMAGE ZONES

Strong earthquakes (over M6) commonly produce surface ruptures, which is the one of the most serious effects by earthquakes. As shown in the Figure 1, most of the houses along the surface ruptures are completely demolished. However, other houses just several tens of meters away from the surface ruptures are slightly damaged. It means that understanding and predicting the precise position of surface ruptures are very important to estimate earthquake hazards. Most of co-seismic surface ruptures are results of reactivation of the pre-existing active faults. Thus, tracing pre-existing active faults is an important task.

The most recently suggested classification divides fault damage zones into three main categories depending on concern and plane of description; *cross-fault damage*, *along-fault damage* and *around-tip damage* (Fig. 2). Cross-fault damage (densely fractured rocks across a fault plane) is generally used to describe large scale faults across the fault zone, while along-fault damage (volume of deformed wall

rocks developed along a fault trace) is relatively useful to describe small or medium scale faults along the fault trace. Around-tip damage (various damages depend around the 3D fault tips) is very useful to describe fault evolution, propagation, and fault tip modes (Kim et al., 2003, 2004).



Figure 1: Surface ruptures related with the 1999 Mw7.6 Chi-Chi earthquake, Taiwan. Most of the houses on the surface ruptures are completely destroyed while other houses are not seriously damaged.

However, an earthquake fault is composed of complicated structures including damage zones and branch faults, not a simple planar structure. Recently, fault zone architectures are classified in detail to understand the characteristics of faults (Caine et al, 1996; Kim et al., 2003, 2004; Choi et al., 2016).

Fault damage zones are very important concept to understand and describe deformations around faults. Especially, the importance has well been reported from natural fault systems (Kim et al., 2003, 2004). Serious damages are observed especially at tip and linkage damage zones, which can produce high density of secondary faults and fractures. These damage zones are unsuitable locations for critical sites, but could be high potential sites for fluid flow such as ore or oil. Therefore, if we have strong background and knowledge on fault damage zones, it could be very useful for exploration of natural resources and site selection of critical facilities.

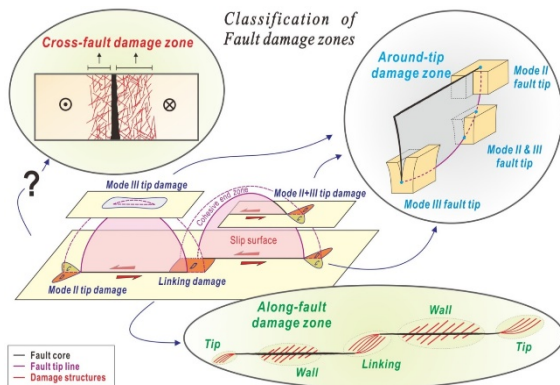


Figure 2: Conceptual models of fault and related damage zones (from Choi et al., 2016). Fault damage zones are classified in detail to properly describe.

IMPORTANCE OF FAULT GEOMETRY AND LINKAGE

Fault geometry and linkage is another important point to earthquake hazards. Several examples are reported from earthquakes and natural faults. The 2016 M7.3 Kumamoto Earthquake is an ideal example of merging fault system (Fig. 3).

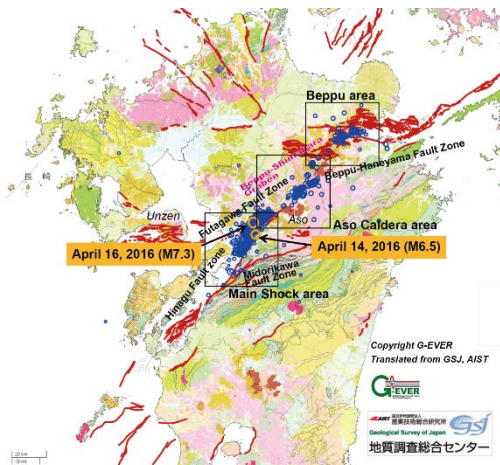


Figure 3: Surface ruptures and locations of two main earthquakes and related minor earthquakes of the 2016 M7.3 Kumamoto Earthquake, Japan.

Two successive earthquakes and related minor earthquake epicentres (foreshocks and aftershocks) are mainly concentrated at the merging point of the two faults (Futagawa Fault and Hinagu Fault). It means that the intersection between the two faults may affect to earthquake triggering. This type of non-parallel fault merging is described as λ-fault (Du and Aydin, 1995) and similar examples with higher damages have been reported (Kim et al., 2000).

Fault linkage (e.g. Peacock, 1991) is an importance process/mechanism of fault growth and evolution. At early stages, small fault segments grow themselves and gradually interact with each other from soft-linked to hard-linked to be a single fault. However, the behaviour of the overstep zone between the two segments is wholly different depending on slip sense and stepping direction, producing extensional or contractional overstep zones

(Kim et al., 2004). These zones can produce a wide range of fracture patterns that depend on the nature of the interaction between the two fault segments.

The fault linkage patterns have been reported from several earthquake surface ruptures (e.g. Jin and Kim, 2010; Choi et al., 2012). It could be very useful to predict fault section involving future potential earthquake ruptures, especially when the ruptures are partly activated from the linking system (Fig. 4).

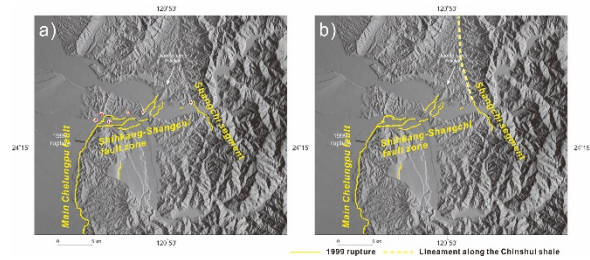


Figure 4: Surface ruptures related with the 1999 Mw7.6 Chi-Chi earthquake, Taiwan and future potential ruptures based on the linking fault model (from Jin and Kim, 2010).

DISPLACEMENT PATTERNS AND SLIP COMPENSATION

Displacement or slip patterns along faults or surface ruptures are one of the key parameters to understand fault behaviour. The along-fault slip distribution is variable depending on several factors such as segmentation, linking stage, propagation direction and others.

If we measure both components of slip (vertical and horizontal), we could get some more information. At some linkage parts, slip compensation is visible between the two components (Choi et al., 2012), while we could not find this phenomena at other linkage parts. It depends on the evolution stage between two segments and stepping direction. For example, along a strike-slip fault, if vertical displacement increases as horizontal displacement decreases, it may indicate barrier overstep zones. This also could be helpful to understand earthquake hazards and mechanical changes along active faults.

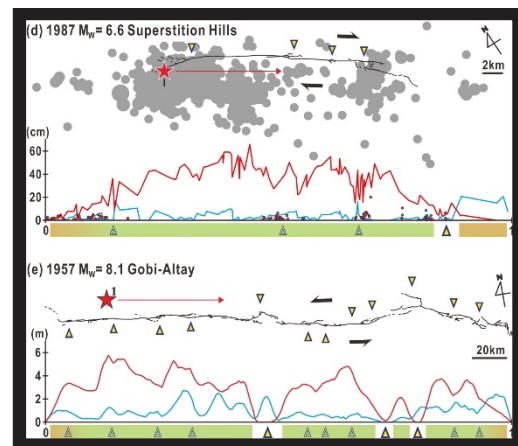


Figure 5: Displacement patterns along the two surface ruptures related with the 1987 Mw6.6 Superstition Hills Earthquake, California and the 1957 Mw8.1 Gobi-Altay Earthquake, Mongolia. Two slip components are seperately measured and plotted, which show slip compensation at some parts (from Choi et al., 2012).



DAMAGE DIFFERENCES BETWEEN HANGING WALL AND FOOTWALL

Differences in fracture density and damage between hanging wall and footwall of dip-slip faults have well been reported (e.g. Riley et al., 2011). It is well observed on several exposed outcrops showing clear difference between them with higher density of fractures in the hanging wall (Fig. 6). The difference in fracture density may result in color and weathering changes due to different fluid flow characteristics.



Figure 6: An outcrop photo showing fracture density and damage difference between hanging wall (highly fractured) and footwall on a vertical section of a dip-slip fault.

Earthquake damage difference between hanging wall and footwall can also appear obviously (Fig. 7). This may be related to not only the damage difference but also earthquake wave propagation. Epicenter is located on the hanging wall and the accumulated stress is released through hanging wall, because hanging wall is usually mobile block located above hypocenter.

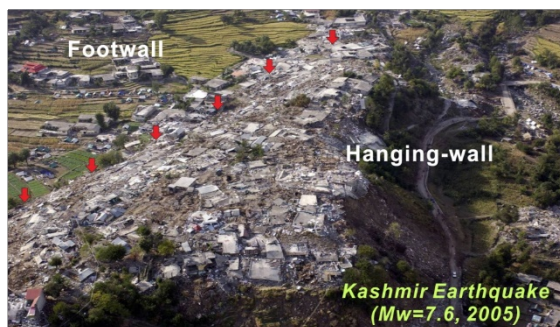


Figure 7: Earthquake damage difference between hanging wall and footwall by the 2005 Mw7.6 Kashmir Earthquake, Pakistan. It clearly shows damage difference across the fault, which is interpreted as a result from damage zone and seismic wave differences.

DISCUSSION

The intensity of earthquake damage (e.g. building damage) associated with a certain magnitude is very variable, which is depending on seismic property, geologic condition, building structure, distance from surface rupture or hypocenter, and etc. However, fault damage zone or permanent deformation is a very important issue, because the released stress is so high and we cannot avoid this damage by reinforcement design. It is mainly related with

surface ruptures (Fig. 1) and it should be carefully considered for site selection of critical facilities (Fig. 8). Therefore, tracing active faults is very important to predict future potential surface ruptures. Moreover, the width of damage zones or *respect distance* (Munier et al., 1997) has been considered as an important factor to estimate earthquake hazards.

However, the permanent deformation is closely related with 3D fault zone properties, which is a very complicate structure related with segmentation, geometry, slip sense, amount of slip, stepping, hanging wall and footwall, and etc. The components combined can produce various damage patterns. Therefore, it is very important to understand damage patterns and damage formation concept, because surface ruptures, aftershock clusters and damages are asymmetric and concentrated at some local areas around faults and affected by several factors. Thus, these are also probably related to rupture propagation and fault geometry. Therefore, the study on earthquake propagation and damage zone is a very important issue for earthquake hazard analysis.

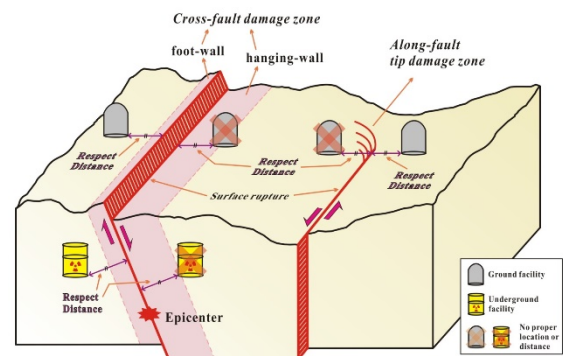


Figure 8: Surface rupture, respect distance and fault damage zone should be considered to select proper sites for important facilities.

CONCLUSION

Earthquake damage patterns show the importance of earthquake surface ruptures and fault damage zones as well as seismic shaking. Slip (or displacement) distribution along the surface rupture can provide us very useful information related with earthquake wave or energy propagation.

Earthquake damages also depend on the position along or around the faults including hanging wall and footwall. We could consider several other factors such as the conditions of geological media, the depth of hypocenter, distance and location from the epicenter.

Especially, permanent damages are very variable strongly depending on asymmetric fault geometries and surface ruptures. Therefore, tracing active faults and estimating respect distance (the expected deformation zone across the fault) are important. However, because damage zones are not symmetric, we should consider 3D fault damage patterns, fault geometry, segmentation, stepping, and slip sense. The careful consideration of these factors could be helpful to proper estimation of



earthquake hazards. This knowledge could be very useful to site selection of critical facilities such as nuclear power plants and waste disposal sites.

Acknowledgements: This research was supported by a grant (2017-MPSS31-006) from Supporting Technology Development Program for Disaster Management funded by Korean Ministry of Public Safety and Security (MPSS).

REFERENCES

- Caine, J.S., 1996. Fault zone architecture and permeability structure. *Geological Society of America*, 1025-1028.
- Choi, J.-H., Jin, K., Enkhbayar, D., Davvasambuu, B., Bayasgalan, A., & Kim, Y.-S., 2012. Rupture propagation inferred from damage patterns, slip distribution, and segmentation of the 1957 Mw 8.1 Gobi-Altay earthquake rupture along the Bogd fault, Mongolia. *Journal of Geophysical Research* 117, B12401, doi:10.1029/2011JB008676.
- Choi, J.-H., Edwards, P., Ko, K.T., & Kim, Y.-S., 2016. Definition and classification of fault damage zones: A review and a new methodological approach. *Earth-Science Reviews* 152, 70–87.
- Du, Y., & Aydin, A., 1995. Elastic stress relaxation: A mechanism for opposite sense of secondary faulting with respect to a major fault. *Tectonophysics* 257, 175-188.
- Jin, K., & Kim, Y.-S., 2010. Review and new interpretation for the propagation characteristics associated with the 1999 Chi-Chi earthquake faulting event. *Island Arc* 19, 659–675.
- Kim, Y.-S., Andrews, J.R., & Sanderson, D.J., 2000. Damage zones around strike-slip fault systems and strike-slip fault evolution, Crackington Haven, southwest England. *Geosciences Journal* 4, 53 – 72.
- Kim, Y.-S., Peacock, D.C.P., & Sanderson, D.J., 2003. Mesoscale strike-slip faults and damage zones at Marsalforn, Gozo Island, Malta. *Journal of Structural Geology* 25, 793–812.
- Kim, Y.-S., Peacock, D.C.P., & Sanderson, D.J., 2004. Fault damage zones. *Journal of Structural Geology* 26, 503–517.
- Kim, Y.-S., & Sanderson, D.J., 2005. The relationship between displacement and length of faults: a review *Earth-Science Reviews*. *Earth-Science Reviews* 68, 317-334.
- Munier, R., Sandstedt, H., & Niland, L., 1997. Förslag till principiella utformningar av förvar enligt KBS-3 för Aberg, Beberg och Ceberg.
- Peacock, D.C.P., 1991. Displacements, segment linkage and relay ramps in normal fault zones. *Journal of Structural Geology* 13, 721-733.
- Riley, P., Tikoff, B., & Murray, A.B., 2011. Quantification of fracture networks in non-layered, massive rock using synthetic and natural data sets. *Tectonophysics* 505, 44-56.



Preliminary assessment of Quaternary faulting based on high resolution topographic data near the FORGE geothermal site, Mineral Mountains, Utah, USA

Kleber, Emily (1), Kirby, Stefan (1), Hiscock, Adam (1), and Bowman, Steve (1)

(1) Utah Geological Survey, 1594 W. North Temple, Suite 3110, Salt Lake City, UT, 84114-6100, USA. ekleber@utah.gov

Abstract: The Great Basin area of the Basin and Range Province (USA) has geothermal systems that have been developed for power generation. Roosevelt Hot Springs is located on the western flank of the Mineral Mountains—a north-south-trending range of intermediate to felsic plutonic rocks and young rhyolite flows in southwestern Utah, USA. The Mineral Mountains do not have a range-front normal fault that is typical of most Basin and Range mountains. Two Quaternary normal-fault systems form a series of scarps that cut aggrading alluvial fans from the western flank of the Mineral Mountains. North to south, these include the Opal Mound fault and the Mineral Mountains West (MMW) faults. Using airborne lidar data, we performed detailed surficial-geologic mapping and fault scarp morphometric analysis along strike. Results indicate that the surface expression of these faults may have been affected during the Quaternary by the presence of subsurface circulating magmatically heated geothermal fluids.

Key words: Normal faulting, Great Basin, Sevier Desert, geothermal, lidar

INTRODUCTION

The characteristics of surface-rupturing normal faults are critical to understanding seismic hazard in the Great Basin, Basin and Range Province, western USA (Fig. 1). The Basin and Range Province is a region of east-west extension covering a majority of the southwestern United States. It consists of north-south-striking, range-bounding normal faults that define a series of bedrock horst blocks and corresponding basins. Basin and Range extension began in the early Miocene (ca. 17.5 Ma) and continues today (Dickinson, 2006). Within the Great Basin, geothermal systems are common. Most developed hydrothermal systems are fault controlled (Faulds et al., 2011). In the Sevier Desert of southwestern Utah, several geothermal systems may have magmatic sources (Faulds et al., 2011). Recent work investigating late Quaternary faulting in the Sevier Desert indicates that geodetic rates are best explained by narrow magma-assisted rifting (Stahl and Niemi, 2017).

The Roosevelt Hot Springs, located 350 km south of Salt Lake City, Utah, is a magmatic heat source geothermal system that currently generates up to 35 Mwe of gross power at the Blundell Power Plant (Simmons et al., 2016) (Fig. 2). Roosevelt Hot Springs is on the western flank of the Mineral Mountains, a 45-km-long north-south-trending mountain range consisting primarily of late Oligocene to late Miocene intrusive rocks (Nielson et al., 1986). Unlike most fault-bounded ranges of the Basin and Range (Fig. 1), the Mineral Mountains have no obvious surface expression of a range-front fault and active fans grade up to 4 km into bedrock embayments (Fig. 2).

West of the Mineral Mountains, the Utah FORGE (Frontier Observatory for Research in Geothermal Energy) site (Fig. 1, Fig. 2) is being considered for a competitive U.S.

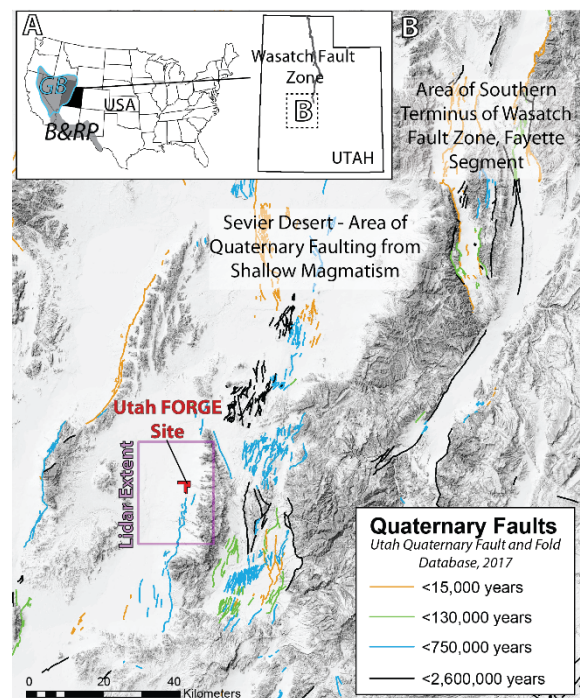


Figure 1: (A) Overview of location relative to the Great Basin (GB), Range Province (B&RP), and the Wasatch fault zone in Utah. (B) Regional Quaternary faults near the Utah FORGE site. The area is characterized by the southern terminus of the active Wasatch fault zone (WFZ), and Quaternary faulting driven by shallow magmatism in the Sevier Desert (Stahl and Niemi, 2017).

Department of Energy grant to improve drilling technologies and techniques for developing enhanced geothermal systems using deep well fracturing techniques to break-up hot dry rock, developing permeability, and circulating water to produce geothermal energy (www.forgeutah.com). In 2016, 0.5 m airborne lidar (light detection and ranging) data were collected along the western flank of the Mineral Mountains and adjoining basin floor (Fig. 1) to better



characterize surface faulting and Quaternary deposits. These data are crucial to understand surface features that indicate the presence and relative activity of basement faults and fractures. This information is critical to potentially developing deep (2 – 3 km) enhanced geothermal systems (EGS) at the Utah FORGE project site (Fig. 2).

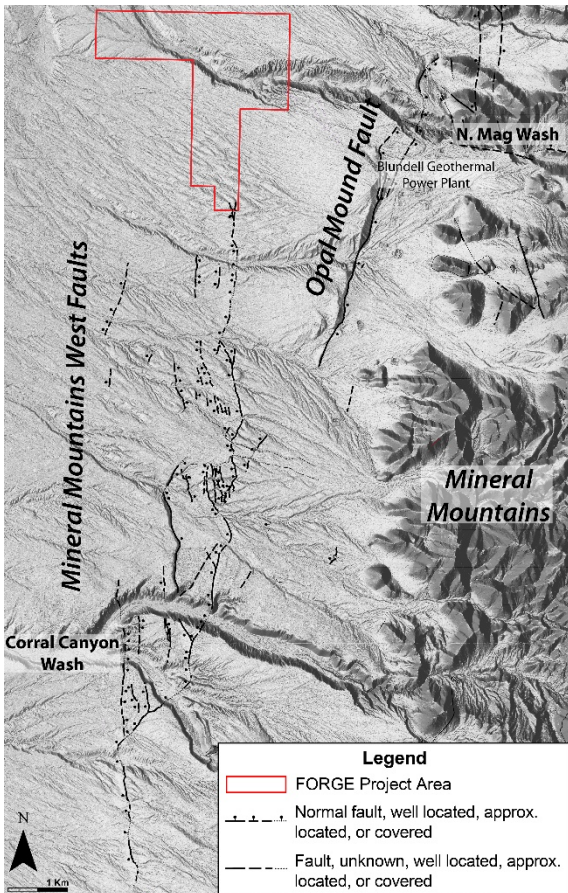


Figure 2: Half-meter slope-shade image derived from lidar of the fault systems around Roosevelt Hot Springs. The east-dipping Opal Mound fault is considered a hydrologic barrier to geothermal fluid flow. The northern extent of the MMW faults is a graben system, initiating 8 km south of the FORGE project area. The graben has internal horsts and grabens, with some discontinuous faults outside of the surface expression of the main graben.

The Quaternary surfaces west of the Mineral Mountains range front consist of a series of west-aggrading alluvial fans of various ages. These fans are derived from Quaternary extrusive rhyolite, felsic to mafic Tertiary plutonic rock, and Precambrian gneissic rocks exposed in the Mineral Mountains (Simmons et al., 2016). Alluvial fan material proximal to the Opal Mound fault has been partially cemented by siliceous sinter deposits associated with the Roosevelt Hot Springs geothermal system (Lynne et al., 2005). Additionally, the high-stand shoreline of pre-historic Lake Bonneville cuts alluvial fan deposits 7 km west of the range front. Two dominant high-angle normal fault systems are apparent from offset Quaternary alluvial fans: (1) the east-dipping Opal Mound fault (7 km long, mean scarp height: 11 m) capped by extensive opaline and siliceous sinter deposits, and (2) the northern 12 km of the MMW faults, with an 8-km-long graben that varies in width from ~700 to 1200 m with internal horst

and graben blocks (mean scarp height: 3.5 m) (Fig. 2). The east-dipping Opal Mound fault is ~600 meters from the range front south of N. Mag wash, and 500 to 100 meters from the range front north of N. Mag wash (Fig. 2).

The morphology of normal fault scarps in alluvium within the Basin and Range can be used to get a morphologic age (Wallace, 1977; Bucknam and Anderson, 1979; Hanks and Andrews, 1989). When an earthquake on a steeply dipping normal fault creates surface rupture, the surface is split into upper and lower offset surfaces and a fault scarp free face. As the free face is exposed to surface processes, colluvial and alluvial processes degrade the scarp, decreasing the scarp slope, and create a convex and concave slope at the top and bottom of the slope, respectively (Wallace, 1977). High resolution topographic data can be used to quickly and accurately measure topographic profiles of scarps and thus can be used to determine the morphologic age of fault scarps (Hilley et al., 2010; Brunori et al., 2013; Zielke et al., 2015).

To better constrain faulting history, we mapped the Quaternary faults and performed morphometric analysis of relevant fault scarps along strike of the Opal Mound and MMW faults. Alluvial fans that have been faulted by the Opal Mound and MMW graben faults are currently being mapped in detail to determine a relative history of deposition. Using scarp profile analysis, we show that the two fault systems have different morphologies along strike. The Opal Mound fault is highly geothermally influenced in its uncharacteristic fault height-to-length ratio and deposition of siliceous sinter along the fault length. The MMW faults and graben decrease in fault scarp height and slope at the fault terminus. The first-order normal fault scarp morphologies of the Opal Mound and MMW faults are not similar to tectonic faults in the Basin and Range Province.

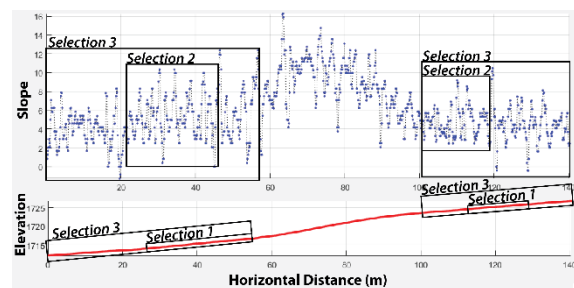


Figure 3: GUI interface from Scarp Offset script (DuRoss, in prep.) showing selections of points for three iterations of three fault scarp measurements. The top chart is slope vs. horizontal distance and the bottom is elevation vs. horizontal distance.

METHODS

In February of 2017, the Utah Geological Survey (UGS) received ~520 km² of high resolution lidar point cloud data and a 0.5-m bare-earth digital elevation model (DEM) of the Milford Valley and adjoining Mineral Mountains. We created derivative models and products from the DEM, including slope maps (0° – 33°), hillshade models from several sun angles, slope and aspect maps, and elevation contours. To compare fault scarp morphologies along strike, we generated elevation profiles from a 0.5-m lidar



DEM in Global Mapper v.14. Using a slope map, we collected topographic profiles perpendicular to fault scarps with sufficient length to ensure complete capture of undeformed alluvial fan surfaces on the hanging wall and footwall of the faults (Fig. 2; Fig. 3).

We used Scarp Offset (v4g) (DuRoss, in prep.) in MatLab (v. R2017a) to analyze the fault scarp profiles. This script uses a graphical interface displaying elevation versus distance and slope versus distance to allow the user to select the upper and lower bounds (i.e., fault offset surfaces) and the fault scarp slope (Fig. 3). The script produces multiple measurements of the scarp to determine a preferred, mean, or midpoint offset value for the scarp and a minimum-maximum range. For this analysis, three measurement iterations were taken for each fault scarp profile based on (1) the topographic profile, (2) slope change, and (3) utilizing all the profile data, except for the fault scarp (Fig. 3). The value used in each scarp height and scarp slope measurement is the mean value of these three measurements (Fig. 4).

RESULTS

For this study, we analyzed the northern 12 km of the ~35 km MMW fault system. The west-dipping single-strand fault system splays northward into an 8-km-long graben

just south of Coral Canyon wash (Fig. 2). Fault scarp heights for the 12 km fault length range from 0.3 to 12.3 m (average: 3.2 m) and scarp slopes range from 3° to 16° (average: 6.5°). Within the graben, east-dipping scarps have an average height and slope of 3.18 m and 5°, respectively, and west-dipping faults have an average height and slope of 3.16 m and 7°, respectively. Both east- and west-dipping graben scarps increase in height and slope south of the FORGE area.

Opal Mound and MMW fault scarps have been affected by surface processes over time. The Opal Mound scarp is cut by two significant drainages: the N. Mag wash and a smaller wash south of the Blundell power plant (Fig. 2). Post-Lake Bonneville high-stand (< 18 ka) alluvial deposits locally cover MMW faults and are not displaced (Fig. 2). Our mapping shows that fault scarps are scant north of the FORGE site.

Previous work on the Opal Mound fault characterized the siliceous sinter deposited from the interaction of faulting on the Opal Mound fault and circulating siliceous geothermal fluids over time (Lynne et al., 2005). A paleoseismic trench from another previous study of the Opal Mound fault revealed extensive siliceous sinter deposits and a 10-m shear zone with cemented shear fabrics and fault offsets of 5 – 33 cm (Brogan and Bucknam, 1981).

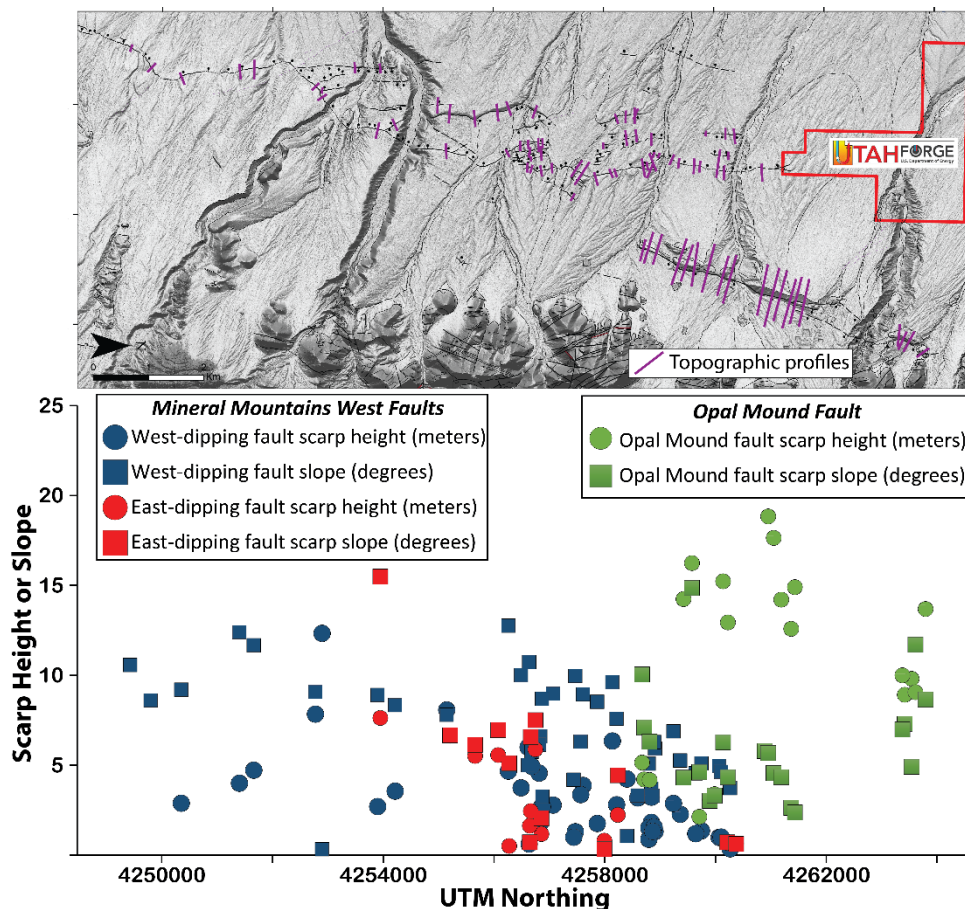


Figure 4: Slope-shade image of the western Mineral Mountains showing location and extent of fault-scarp elevation profiles. Graph shows fault scarp height and slope along strike of the MMW faults and the Opal Mound fault.



DISCUSSION

Results from the first phase of fault characterization indicate that Quaternary faulting along the base of the western Mineral Mountains is strongly influenced by geothermal activity. This is particularly apparent for the Opal Mound fault. The Opal Mound fault's maximum scarp height (18 m) is anomalously large for its short length (7 km). Abundant siliceous sinter deposits mapped along the Opal Mound fault have likely influenced differential erosion along the fault. The scarp heights measured along the Opal Mound fault represent both fault offset and sinter deposition and are thus unreliable for traditional estimations of earthquake magnitude given fault length and scarp height (e.g., Wells and Coppersmith, 1994).

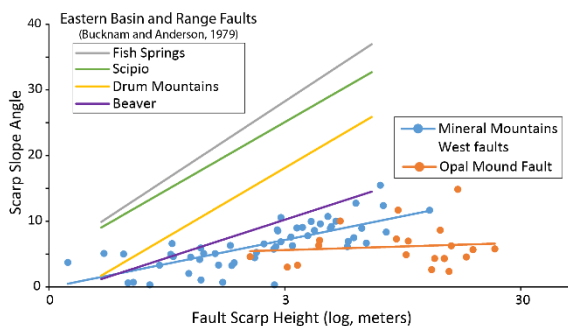


Figure 5: Scarp height (log) plotted against scarp slope angle with a logarithmic regression. Regression functions from other Basin and Range faults reported in Bucknam and Anderson (1979).

Temperature data derived from local deep geothermal wells show conductive temperature gradients below 2 km depth and temperatures > 200°C west of the Opal Mound fault (Allis et al., 2016). The connection between the Quaternary movement of MMW faults and presence of geothermal fluids in hot basement rocks is suspicious and requires further investigation. In comparing the Opal Mound and MMW faults to other faults of the eastern Basin and Range, scarp slopes are not as steep for a given scarp height (Fig. 5). This could potentially be due to less activity in the Quaternary. However, the presence of circulating geothermal fluids from magmatic intrusions interacting with basement faults, especially the Opal Mound fault, required further examination before Quaternary fault activity can be determined.

Future work includes luminescence dating of the faulted alluvial fans to determine the age of these deposits. The burial ages of quartz and feldspar sand in offset fans will give maximum ages for fan surface abandonment, where applicable. Additionally, these ages will be used in scarp degradation modeling to better constrain the morphologic age of faults scarps to better understand their activity in the Quaternary.

Acknowledgements: This work was funded by the U.S. Department of Energy (DE-EE0006732) and the Utah Geological Survey. Thanks to John Bartley, Bob Biek, Tyler Knudsen, Brendon Quirk, and Tammy Rittenour. More info at www.forgeutah.com.

REFERENCES

- Allis, R., Moore, J., Davatzes, N., Gwynn, M., Hardwick, C., Kirby, S., McLennan, J., Potter, S., and Simmons, S., 2016, EGS Concept Testing and Development at the Milford, Utah FORGE Site. *GRC Transactions*, 13 p.
- Brogan, G., and Birkhahn, P., 1981, Faults and occurrence of geothermal anomalies: USGS final report.
- Brunori, C.A., Civico, R., Cinti, F.R. and Ventura, G., 2013, Characterization of active fault scarps from lidar data: a case study from Central Apennines (Italy). *International Journal of Geographical Information Science*, v. 27, p. 1405 – 1416, doi: 10.1080/13658816.2012.684385
- Bucknam, R.C., and Anderson, R.E., 1979, Estimation of fault-scarp ages from a scarp-height - slope-angle relationship. *Geology*, v. 7, p. 11–14.
- Dickinson, W.R., 2006, Geotectonic evolution of the Great Basin. *Geosphere*, v. 2, p. 353–368, doi: 10.1130/GES00054.1.
- DuRoss, C., in prep., Scarp Offset v4g, MATLAB script.
- Faulds, J.E., Hinz, N.H., Coolbaugh, M.F., Cashman, P.H., Kratt, C., Dering, G., Edwards, J., Mayhew, B., and McLachlan, H., 2011, Assessment of favorable structural settings of geothermal systems in the Great Basin, Western USA. *GRC Transactions*, v. 35.
- Hanks, T.C., and Andrews, D.J., 1989, Effect of Far-Field Slope on Morphologic Dating of Scarplike Landforms. *Journal of Geophysical Research*, v. 94, p. 565–573.
- Hilley, G.E., DeLong, S., Prentice, C., Blisniuk, K. and Arrowsmith, J.R., 2010, Morphologic dating of fault scarps using airborne laser swath mapping (ALSM) data. *Geophysical Research Letters*, v. 37(4).
- Lynne, B.Y., Campbell, K.A., Moore, J.N., and Browne, P.R.L., 2005, Diagenesis of 1900-year-old siliceous sinter (opal-A to quartz) at Opal Mound, Roosevelt Hot Springs, Utah, USA: *Sedimentary Geology*, v. 179, p. 249–278.
- Nielson, D.L., Evans, S.H., and Sibbett, B.S., 1986, Magmatic, structural, and hydrothermal evolution of the Mineral Mountains intrusive complex, Utah (USA).: *Geological Society of America Bulletin*, v. 97, p. 765–777.
- Simmons, S., Kirby, S., Jones, C., Moore, J., Allis, R., Brandt, A., and Nash, G., 2016, The Geology, geochemistry, and geohydrology of the FORGE Deep Well Site, Milford, Utah. *GRC Transactions*, 10 p.
- Stahl, T., and Niemi, N.A., 2017, Late Quaternary faulting in the Sevier Desert driven by magmatism: *Scientific Reports*, v. 7, p. 44372, doi: 10.1038/srep44372.
- Wallace, R.E., 1977, Profiles and ages of young fault scarps, north-central Nevada. *Geological Society of America Bulletin*, v. 88, p. 1267–1281.
- Wells, D.L. and Coppersmith, K.J., 1994. New empirical relationships among magnitude, rupture length, rupture width, rupture area, and surface displacement. *Bulletin of the Seismological Society of America*, 84(4), p.974–1002.
- Zielke, O., Klinger, Y., and Arrowsmith, J.R., 2015, Fault slip and earthquake recurrence along strike-slip faults - Contributions of high-resolution geomorphic data: *Tectonophysics*, v. 638, p. 43–62, doi: 10.1016/j.tecto.2014.11.004



High-resolution optical-image correlation for the Kaikoura earthquake, slip distribution and rupture processes

Klinger, Yann (1), Champenois, Johann (1), Delorme, Arthur (1), Okubo, Kurama (2), Vallage, Amaury (1), Bhat, Harsha (2), Baize, Stephane (3)

- (1) Institut de Physique du Globe de Paris – CNRS, 1 rue Jussieu, F-75005 Paris, France. klinger@ipgp.fr
(2) Ecole Normale Supérieure, 24 rue Lhomond, F-75005 Paris, France.
(3) IRSN, 31 avenue de la division Leclerc, F-92260 Fontenay-aux-Roses, France.

Abstract: The Mw 7.8, 2016 Kaikoura earthquake is a stunning example of multi-stranded rupture. A large variety of faults have been activated, including thrust faults and strike-slip faults. As on-shore ruptures are often located in pasture or wilderness areas with limited piercing lines straddling ruptures, determining surface-slip distribution for the different fault segments is difficult. Here, applying optical correlation techniques to high-resolution satellite images (Sentinel2, Spot6 and Pleiades) we are able to derive horizontal displacement field with a resolution of about 2 meters in the direct vicinity of the main surface ruptures. Such high resolution provides insight into slip variation correlated with variation of the rupture geometry and off-fault damage. Eventually, combining these results with dynamic rupture models, we can explore different rupture scenarios at the junction between the Papatea, the Jordan thrust and the Kekerengu faults.

Key words: surface rupture, co-seismic displacement, fault geometry, rupture process.

On the 14th of November 2016, the Mw 7.8 Kaikoura earthquake ruptured a series of faults in the northern part of the South Island in New Zealand. The rupture involved some displacement on a blind thrust fault, which is described as being the southern end of the Hikurangi megathrust (i. g. Duputel and Rivera, 2017), and displacement on several crustal faults that are part of the Marlborough fault zone (Hamling et al., 2017). Many of these crustal faults did rupture the surface with displacement that could reach several metres, dominated by strike-slip motion with a secondary component of thrusting. Some ruptures were also located off-shore, which are not yet well documented.

Although complex ruptures involving several parallel strands with slip-partitioning or branching are not unusual in continental settings (e.g. Klinger et al., 2005; Xu et al., 2009; Choi et al., 2017), the Kaikoura rupture represents an extreme case with at least 15 different faults that did rupture almost simultaneously (Stirling et al., 2017). Although the dominant direction of the crustal faults that ruptured is SW-NE, accommodating right-lateral strike-slip motion, in several places, such as the North Leader fault or the Papatea fault, displacement took place along faults oriented SE-NW to N-S. The orientation of these faults promotes compressional motion in addition to left-lateral displacement.

Because the rupture is complex and the instrumental coverage is limited, deciphering the details of the rupture history remains difficult. Remote sensing techniques using radar data are limited in resolution and could saturate at close distances from the surface rupture (Hamling et al., 2017). Seismological data, because of the limited number of strong motion instruments at short distance, are also limited in resolving details of the rupture process (Duputel and Rivera., 2017; Kaiser et al., 2017; Zhang et al., 2017).

Indeed, recent earthquake surface-rupture studies have shown that details of the surface rupture geometry and slip distribution can be useful to get some insights in large-magnitude earthquakes (Vallage et al., 2016; Rockwell & Klinger, 2013; Klinger et al., 2017; Choi et al., 2015). Despite remarkable fieldwork of many New Zealand scientists, detailed slip distribution remains difficult to establish for the several fault sections activated during the Kaikoura earthquake. One reason is that a large part of the land affected by surface ruptures is remote, mostly through farm-lands and wilderness areas, some forested. Hence, obvious piercing lines to measure reliable horizontal offsets are not so numerous. A second reason is that in many places, in addition to the dominant strike-slip motion, is a variable amount of dip-slip motion. Often, the direct effect of such dip-slip component is to make the surface expression of the rupture more complex and potentially to distribute deformation over a wider area, as it has already been documented for other earthquakes (Vallage et al., 2015).

To cope with these difficulties, we used optical correlation technics with high-resolution satellite images. Unlike previous studies that used images with decametric pixel size (Hollingsworth et al., 2017; Käab et al., 2017; Girod et al., 2017), we focused our processing on images with metric pixel size, which gives us access to full fault geometry details. In the next sections, we present briefly the data and the methodology that we used to image in details horizontal displacements along the Jordan Thrust Fault, the Papatea fault and the Kekerengu fault. Then we present preliminary maps of amplitude displacement and variability of direction of displacement. We also point to some specific characteristics of the deformation field that could inform us on possible rupture scenarios.



The correlation of our different sets of optical satellite images has been processed with the free software package MicMac (Rosu et al., 2014; Rupnik et al., 2016). We processed two specific sets of images. One set of images is formed by ESA Sentinel-2A images that were acquired on April 9th, 2016 and on December 15th, 2016. The Sentinel-2A images are multi-spectral images, acquiring information on 13 channels, with a ground resolution ranging between 10 m and 60 m, depending on the channel. The three channels in the visible spectrum, blue, green and red-near infrared, have a resolution of 10 m. Although the Sentinel-2A images are not very high resolution and therefore might not bring much additional information compared to what was already published, processing the Sentinel-2A data proved useful at least in one aspect: the maximum width of the Sentinel-2A images is 290 km. Even if one part of the image is actually imaging the sea, this kind of image allows imaging at once a large portion of ground, including some part that can be assumed with no significant displacement. This is used to fine tune the image processing and to limit uncorrected defects due to satellite attitude issues. Eventually, from these images it was possible to produce a co-seismic horizontal-displacement field with a resolution of 10 m over the entire area of rupture.

Our second set of images is composed on one hand of a stereo-pair of CNES SPOT6 images acquired before the Kaikoura earthquake, in May 2014. These images are panchromatic images with a ground resolution at nadir of 1.8 m. On the other hand, we used a tri-stereo acquisition from the CNES Pleiades satellite. These images were acquired in January 2017. These images are panchromatic images with a ground resolution at nadir of 50 cm. A major difficulty with such images is that the acquisition width is more limited and it might be difficult to have zero-deformation zone inside the image. For both the SPOT6 and the Pleiades images, first we computed a DEM of the area that was latter used to orthorectify the different images. Eventually, we had 2 orthorectified SPOT6 images and 3 orthorectified Pleiades images focused on the main deformation zone of the Kaikoura event. The Pleiades images were downsampled to 1.8m using a near-neighborhood scheme to be of similar resolution as the SPOT6 images. Eventually, using the MicMac package the images were correlated to produce 1.8 m resolution horizontal displacement maps in E-W and N-S directions. Ramp artifact and sensor correction were removed, in part using the Sentinel-2A correlation as a reference.

Figure 1 shows the horizontal displacement amplitude map centered on the junction between the Jordan Thrust fault, the Kekerengu fault and the Papatea fault. Figure 2 shows the continuation of the same map towards the North, along the Kekerengu fault. The small vectors on top of the amplitude map indicate the direction of motion. Although these maps are still preliminary, some observations can be made. In the northern part of the Kekerengu fault (Fig. 2) it is very clear that the dominant displacement is right-lateral strike-slip, parallel to the fault. Profiles across the fault zone in this section indicate displacement on the order of 6 to 10 m, in agreement with field measurements (Stirling et al.,

2017). A component of shortening that becomes more important as one moves southward is visible from the progressive orientation of the slip vector. This is particularly visible in the northern part of Fig. 1 and in its continuation in the southern part of Fig. 2. The shortening component is dominant along the Papatea fault, where the eastern block is clearly moving westward. The wedge in-between the Papatea fault and the Jordan Thrust fault is moving southward, consistently with left-lateral motion along the Papatea fault and right-lateral motion along the Jordan Thrust fault, as shown in Hamling et al. (2017).

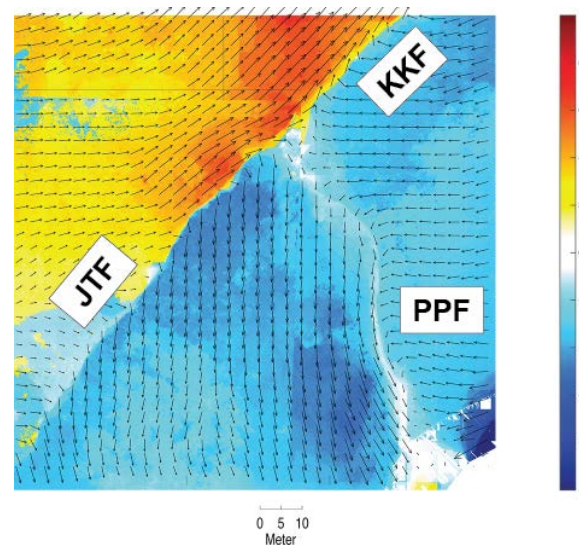


Figure 1: Amplitude image of horizontal displacement at the triple-junction between Jordan Thrust fault (JTF), Kekerengu fault (KKF) and Papatea fault (PPF). Negative values towards SW. Arrows show direction of motion.

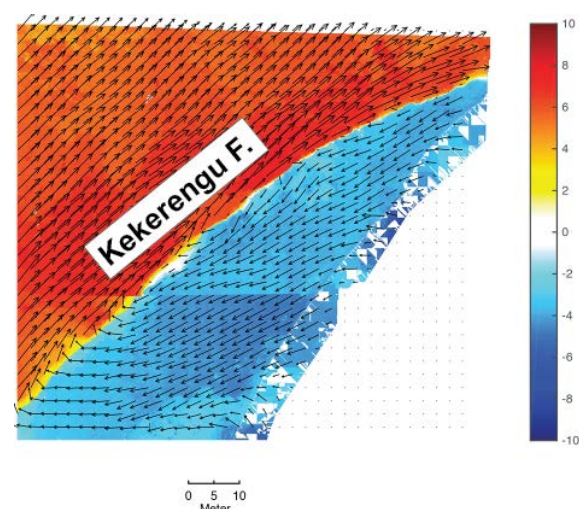


Figure 2: Amplitude image of horizontal displacement along the northern section of the Kekerengu fault. Negative values towards SW. Arrows show direction of motion.

A feature revealed by the high-resolution correlation is the distribution of the deformation along the Kekerengu fault. Following the rupture southward, Figs. 1 and 2 show that the rupture goes from a very sharp localized rupture in the North to a more distributed rupture. The distributed deformation zone is characterized by the widening yellow



ribbon along the Kekerengu fault towards the triple-junction. This distributed section ends abruptly as one passes the triple-junction and the rupture becomes highly localized again along the Jordan Thrust fault. Hence, we interpret the existence of the distributed deformation zone as a direct effect of the triple junction. Actually, a similar pattern can be seen along the Papatea fault where deformation becomes more distributed as ones get closer to the triple junction (the length of the slip vector shows distributed slip). At the same place, in the inner corner between the Papatea fault and the Kekerengu fault, the direction of displacement becomes messy, which characterize an area of large damage. Another zone of distributed deformation can be recognized at the southern end of the Papatea fault. There, locally amount of deformation decreases in the fault zone, which characterizes distributed deformation. In that case, it is consistent with the existence of multiple faults traces mapped at the toe of the Papatea range (Clark et al., 2017). Because these fault strands accommodate mostly vertical motion they are more difficult to see them in our displacement maps, which are more sensible to horizontal motion.

Eventually, based on the pattern of deformation we can evidence from high-resolution horizontal deformation maps, we could question rupture processes during the Kaikoura rupture. Our new displacement maps show that in general displacement is highly localized along faults, but except when one gets closer to the triple junction. Close to the triple junction, both the Papatea fault and the Kekerengu fault display more distributed deformation. Significant damage could be mapped in the inner corner between these two faults. Conversely, the inner corner between the Jordan Thrust fault and the Papatea fault does not display any specific indication of damage or distributed deformation. Such dissymmetry in the pattern of deformation relative to position of the different faults forming the triple junction could be indicative of the way rupture propagated during the Kaikoura earthquake. Seismological data show that during the Kaikoura earthquake, the rupture initiated in the South and then propagated northward. The second major burst of seismic moment release corresponds to the activation of the thrust fault associated to Hikurangi megathrust. Then the next major seismic moment release is associated with slip north of the thrust patch, around the Kekerengu fault, although details of fault activation are not known yet. Hence, based on distribution of damage, we suggest that following the activation of slip on the thrust fault, the Papatea fault might have been activated first with rupture propagating north-westward towards the triple junction. At the triple junction, the rupture would jump on the Kekerengu fault to propagate mainly northward, although some slip would also be triggered on the Jordan thrust fault. Damage in the inner corner between the Papatea and the Kekerengu faults would results from part of the rupture shortcutting the triple junction. Dynamic rupture propagation models favor such scenario as they show that it would be almost impossible for a rupture propagating northward on the Jordan Thrust fault to branch backward on the Papatea, considering the regional stress conditions. An alternative

scenario that cannot be ruled out at the moment would be simultaneous rupture on different fault sections, although it would not explain the specific distribution of damage.

Acknowledgements: Access to images was possible through ESA CEOS_seismic project and through CNES ISIS program. Development of MicMac project is partly funded by TOSCA CNES project.

REFERENCES

- Choi, J.-H., Klinger Y., Ferry M., Ritz J.F., Kurtz R., Rizza M., Bollinger L., Davaasambuu B., Tsend-Ayush N., & Demberel S., in-press 2017., Geologic inheritance and earthquake rupture processes: the 1905 M ≥ 8 Tsetserleg-Bulnay strike-slip earthquake sequence, Mongolia, *J. Geophys. Res.*
- Clark, K., E. Nissen, J. Howarth, I. Hamling, J. Mountjoy, W. Ries, K. Jones, S. Goldstien, U. Cochran, & P. Villamor, in-press 2017. Highly variable coastal deformation in the 2016 M W 7.8 Kaikōura earthquake reflects rupture complexity along a transpressional plate boundary, *Earth and Planetary Science Letters.*
- Duputel, Z., & L. Rivera, 2017. Long-period analysis of the 2016 Kaikoura earthquake, *Phys. Earth. Planet. Inter.*, 265, 62-66.
- Girod, L., C. Nuth, A. Käbb, R. McNabb, and O. Galland, 2017. MMASTER: Improved ASTER DEMs for Elevation Change Monitoring, *Remote Sensing*, 9(7), 704.
- Hamling, I. J., S. Hreinsdóttir, K. Clark, J. Elliott, C. Liang, E. Fielding, N. Litchfield, P. Villamor, L. Wallace, & T. J. Wright, 2017. Complex multifault rupture during the 2016 Mw 7.8 Kaikōura earthquake, New Zealand, *Science*, 356(6334), eaam7194.
- Hollingsworth, J., L. Ye, & J. P. Avouac, 2017. Dynamically triggered slip on a splay fault in the Mw 7.8, 2016 Kaikoura (New Zealand) earthquake, *Geophysical Research Letters*, 44(8), 3517-3525.
- Käbb, A., B. Altena, & J. Mascaro, 2017. Coseismic displacements of the 14 November 2016 MW7.8 Kaikoura, New Zealand, earthquake using an optical cubesat constellation, *Nat. Hazards Earth Syst. Sci. Discuss.*
- Kaiser, A., N. Balfour, B. Fry, C. Holden, N. Litchfield, M. Gerstenberger, E. D'Anastasio, N. Horspool, G. McVerry, & J. Ristau, 2017. The 2016 Kaikōura, New Zealand, Earthquake: Preliminary Seismological Report, *Seismological Research Letters*, 88(3), 727-739.
- Klinger, Y., J. H. Choi, & A. Vallage, 2017. Fault branching and long-term earthquake rupture scenario for strike-slip earthquakes, in *Fault Zone Dynamic Processes: Evolution of Fault Properties During Seismic Rupture*, edited by M. Thomas, H. Bhat and T. Mitchel, pp. 217-228, AGU Monograph.
- Klinger, Y., X. W. Xu, P. Tapponnier, J. Van der Woerd, C. Lasserre, & G. King, 2005. High-resolution satellite imagery mapping of the surface rupture and slip distribution of the MW 7.8, 14 November 2001 Kokoxili Earthquake, Kunlun Fault, northern Tibet, China, *Bull. Seis. Soc. Am.*, 95(5), 1970-1987.
- Rockwell, T. K., & Y. Klinger, 2013. Surface rupture and slip distribution of the 1940 Imperial Valley earthquake, Imperial Fault, Southern California: Implications for rupture segmentation and dynamics, *Bull. Seis. Soc. Am.*, 103(2A), 629-640.
- Rosu, A.-M., M. Pierrot-Deseilligny, A. Delorme, R. Binet, & Y. Klinger, 2015. Measurement of ground displacement from optical satellite image correlation using the free open-source software MicMac, *ISPRS Journal of Photogrammetry and Remote Sensing*, 100, 48-59.
- Rupnik, E., M. Pierrot-Deseilligny, A. Delorme, & Y. Klinger, 2016. Refined Satellite Image Orientation in the Free Open-Source



INQUA Focus Group Earthquake Geology and Seismic Hazards



paleoseismicity.org

Photogrammetric Tools Apero/micmac, ISPRS Annals of the Photogrammetry, *Remote Sensing and Spatial Information Sciences*, 3(1).

- Stirling M, Litchfield N, Villamor P, Van Dissen R, Nicol A, Pettinga J, Barnes P, Langridge R, Little T, Barrell D, Moun-tjoy J, Ries W, Rowland J, Fenton C, Hamling I, Asher C, Barrier A, Benson A, Bischoff A, Borella, Carne R, Cochran U, Cockroft M, Cox S, Duke G, Fenton F, Gasston C, Grimshaw C, Hale D, Hall B, Hao K, Hatem A, Hemphill- Haley M, Heron D, Howarth J, Juniper Z, Kane T, Kears J, Khajavi N, Lamarche G, Lawson S, Lukovic B, Madugo C, Manousakis I, McColl S, Noble D, Pedley K, Sauer K, Stahl T, Strong D, Townsend D, Toy V, Villeneuve M, Wandres A, Williams J, Woelz S, and Zinke R (2017). "The Mw7.8 2016 Kaikura earthquake: Surface fault rupture and seismic hazard context". *Bulletin of the New Zealand Society for Earthquake Engineering*, 50(2): 73–84.
- Vallage, A., Y. Klinger, R. Grandin, H. S. Bhat, & M. Pierrot-Deseilligny, 2015. Inelastic surface deformation during the

2013 Mw7.7 Balochistan, Pakistan, earthquake, *Geology*, 43(12), 1079-1082, doi:10.1130/G37290.1.

- Vallage, A., Y. Klinger, R. Lacassin, A. Delorme, & M. Pierrot-Deseilligny, 2016. Geological structures control on earthquake ruptures: The M(w)7.7, 2013, Balochistan earthquake, Pakistan, *Geophysical Research Letters*, 43(19), 10155-10163, doi:10.1002/2016gl070418.
- Xu, X., X. Wen, G. Yu, G. Chen, Y. Klinger, J. Hubbard, & J. Shaw, 2009. Co-seismic reverse- and oblique-slip surface faulting generated by the 2008 Mw 7.9 Wenshuan earthquake, China, *Geology*, 37(6), 515 - 518, doi:10.1130/G25462A.1.
- Zhang, H., K. D. Koper, K. Pankow, & Z. Ge, 2017. Imaging the 2016 MW 7.8 Kaikoura, New Zealand Earthquake with Teleseismic P Waves: A Cascading Rupture Across Multiple Faults, *Geophysical Research Letters*, 44, 4790 - 4798, doi:10.1002/2017GL073461.



Castle Mountain fault, southcentral Alaska: Observations on slip partitioning from lidar and paleoseismic trenching

Koehler, Rich

University of Nevada, Reno, Nevada Bureau of Mines and Geology, 1664 N. Virginia St., MS 178, Reno, NV 89557. rkoehler@unr.edu

Abstract: The Castle Mountain fault extends across the northern Alaska Aleutian subduction zone forearc and accommodates a component of the 55 mm/yr of convergence between the Pacific and North American plates. Lidar and field based mapping indicates that the trace of the fault is characterized by hanging-wall grabens, south-facing scarps, and folded surfaces, consistent with high-angle reverse faulting. Left-stepping en echelon scarps superimposed on larger scarps suggest a component of right-lateral deformation however lateral offsets of geomorphic markers remain elusive. Trench observations indicate thickness differences of stratigraphic units across fault strands and the presence of a soil (~12,000 cal. yr BP) that buries fault strands associated with the penultimate event and is folded and displaced by the most recent event. The observations suggest that earthquakes along the fault are characterized by recurrence of 1000's of years and partitioned vertical and lateral slip, however reverse displacement is the dominant component.

Key words: Alaska forearc, earthquake timing, slip partitioning.

INTRODUCTION

The Castle Mountain fault (CMF) in southcentral Alaska extends from the southern front of the Talkeetna Mountains on the east to west of Mount Susitna, and represents the structural boundary between the Cook Inlet forearc basin on the south and the Susitna basin on the north (figure 1). In this area, subduction of the Pacific plate beneath North America (~55 mm/yr) has caused right-transpressional deformation across southern Alaska, counter-clockwise rotation of the crust (generally north of the CMF), and the development of folds within Cook Inlet south of the CMF. The CMF has a regional orientation of 240° and poses a significant surface fault rupture hazard to the Susitna lowland and strong ground motion hazard to the city of Anchorage. The U.S. National Seismic Hazards map considers the fault capable of generating an earthquake with a maximum magnitude of M_{max} 7.1 based primarily on smoothed seismicity and limited paleoseismic data (Wesson et al., 2007).

Interpretation of geophysical data from the Susitna lowland indicates late Tertiary, north-side-up, dip-slip movement of at least 0.5 km and development of a 4-km-wide anticline (Haeussler et al., 2000). Bedrock mapping to the east indicates post-Paleocene lateral slip of ~14 km (Fuchs, 1980; Kelly, 1963). Evidence for active deformation includes a well-defined ~60-km-long topographic scarp that is readily identifiable by distinct vegetation lineaments in the Susitna lowland (figure 2) and the occurrence of two moderate historic earthquakes in 1983 (Mw5.7, Lahr et al., 1986) and 1996 (M4.6) along the base of the Talkeetna Mountains (figure 1).

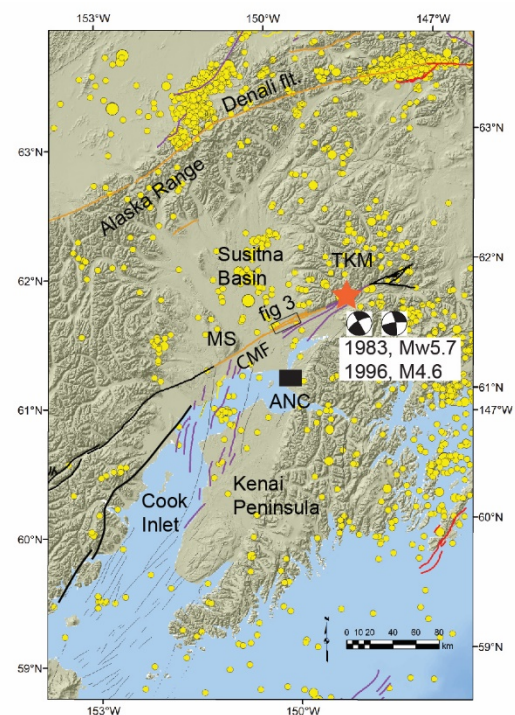


Figure 1: Shaded relief map of south-central Alaska, showing the location of the CMF and Denali faults. Circles show shallow crustal seismicity of $M > 3$ from 1980 through 2011. Star shows general location of historic earthquakes along the CMF. MS, Mount Susitna; TKM, Talkeetna Mountains; Anc, Anchorage. Faults from Koehler (2013) with colors indicating relative activity including: red, historic; orange, Latest Pleistocene to Holocene; yellow, latest Quaternary; purple, Quaternary; black, suspicious.



Previous paleoseismic investigations (figure 3) report conflicting results regarding the style and rate of Quaternary deformation. Detterman et al. (1974) dated a buried soil exposed in a trench excavated across a 2.1-m-high scarp east of the Little Susitna River and implied an $1,860 \pm 250$ yr BP age for the most recent event. At this locality, the fault dips 75° north. Detterman et al. (1974) also suggested possible right-lateral displacements of 3.6 to 7 m. Trenching studies by Haeussler et al. (2002) suggest thrust motion along the fault and the occurrence of four late Holocene earthquakes in the last 2,700 years with an average repeat time of ~ 700 years. A late Pleistocene-Holocene right-lateral slip rate of 2–3 mm/yr was estimated by Willis et al. (2007) based on lateral offset of 36 m measured on an inferred post-glacial channel margin. Thus, motivated by these conflicting data, a series of lidar geomorphic mapping and paleoseismic trenching investigations were conducted. Here, I present observations from these studies that shed light on the style of deformation and the number of latest Pleistocene-Holocene earthquakes. The results have important implications to the estimation of fault rupture parameters for infrastructure design and seismic hazards assessments for southern Alaska.



Figure 2: View West of the Castle Mountain fault. The fault is clearly expressed as a distinct vegetation lineament characterized by large deciduous trees growing along the uplifted North side of the fault and stunted black spruce growing south of the fault. Mount Susitna in the background.

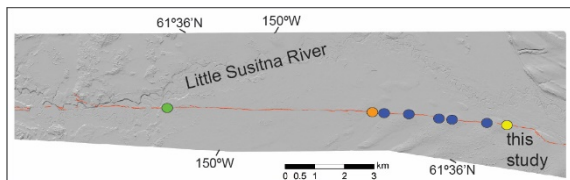


Figure 3: Lidar hillshade showing previous paleoseismic studies along the Castle Mountain fault. Green, Detterman et al., 1974; orange, Willis et al., 2007; blue, Haeussler et al., 2002; yellow, this study. Location shown on Figure 1.

RESULTS AND DISCUSSION

Surficial-geologic mapping was performed across ~ 40 km of the Susitna lowland to independently evaluate the results of previous paleoseismic investigations and to better characterize faulted deposits and fault rupture parameters. The mapping indicates that the fault is characterized by three relatively straight, well-expressed

and clearly defined traces that gradually change strike from east to west from 242° to 236° . These traces are separated by two ~ 1 -km-wide bands trending $\sim 270^\circ$ including one where the Little Susitna River crosses the fault and another in the vicinity of Fish Creek. In some areas, the scarp is confined to a narrow zone less than several meters. However, much of the fault trace is characterized by wide zones (25–150 m) of left-stepping en echelon surface scarps oblique to the trace of the fault and left stepping grabens up to 400 m north of the main scarp (figure 4). In the vicinity of steps in the surface trace, the fault trace lacks a well-defined scarp and is characterized by a broad anticline associated with a gentle south-facing slope north of the fault indicating that the fault may have a shallow dip and be blind in those areas.

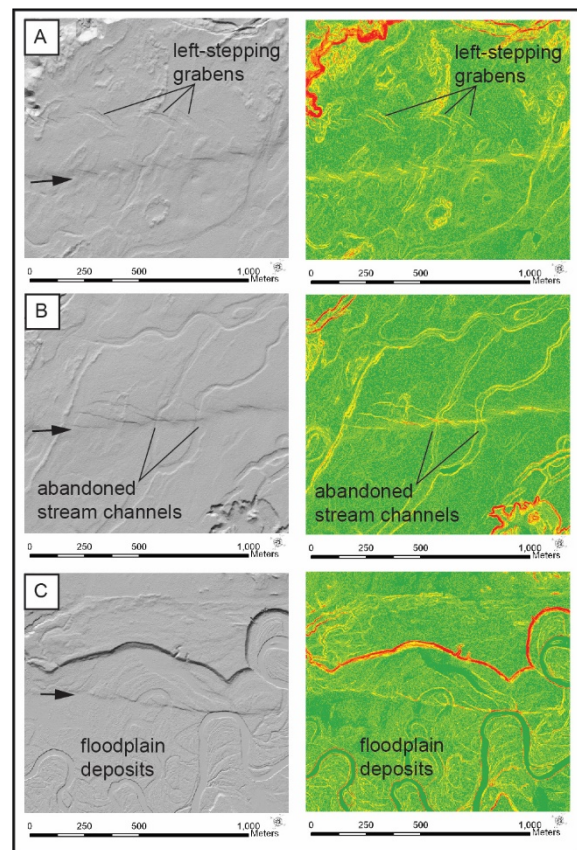


Figure 4: Lidar hillshade images and corresponding slope maps illustrating scarp morphology. A) Left-stepping en echelon scarps superimposed on larger south-facing scarp and left-stepping grabens north of the main fault. B) Wide zone of anastomosing scarps and abandoned early Holocene stream channels that are vertically offset. C) Displaced oxbow lakes and floodplain deposits of the Little Susitna River. Black arrow indicates location of the CMF in each image.

Offset late Elmendorf (14–15 ka) glacial and Holocene deposits including glacial drift, sandy fan deltas, outwash plains, grounding-line moraines, stream terraces, and oxbow lakes (Koehler et al., 2012) provide observations that bear on the style and amount of displacement (figures 5 and 6). Vertical displacements across these deposits vary in height from ~ 0.5 to 5 m. Larger scarps are typically a composite of several overlapping smaller scarps. These



smaller scarps maintain a consistent morphology across the entire lowland and likely represent the topographic expression of the most recent event. All of these scarps are consistently south-facing.

Numerous abandoned channels, stabilized sand dunes, and terrace margins oriented orthogonal to the scarp are vertically offset, and show relatively little lateral displacement (figure 4b). Based on the lidar and field surveys, geomorphic features typical of strike-slip faults are absent. In particular, sag ponds, pressure ridges, oppositely facing scarps, linear valleys and troughs, and offset streams are not present. It is possible that glacial advances removed all evidence of late Pleistocene lateral offsets and that the Holocene features present on the Susitna lowland are too young and subtle to preserve evidence of lateral displacement. Although inspection of lidar hillshades and field exposures did not reveal evidence of lateral displacement, it is acknowledged that lateral offset of up to a meter may not be recognizable due to the curvilinear pattern of geomorphic features where they cross the fault. Sand dune offsets of 3.6-7 m reported by Detterman et al. (1974) could not be independently verified. The cumulative surficial geomorphic observations across the Susitna lowland strongly suggests that the dominant sense of displacement in the Holocene has been reverse, with a permissible albeit lesser component of right-lateral strike-slip.

Two trenches (CMF-1 and CMF-2) were excavated approximately 5 km west of the Parks Highway in the Little Susitna River valley (figure 5). The purpose of the trenching was to assess the number of displacement events and better characterize rupture parameters including the dip of the fault in the shallow subsurface and style of deformation. The trenches were excavated across an ~1-m-high south-facing scarp that cuts flood deposits inset into a late Elmdorf (14-15 ka) grounding-line moraine. The margin of the grounding-line moraine does not exhibit any appreciable lateral displacement (figure 5).

Both trenches exposed interbedded layers of well-sorted sand and poorly sorted pebble-cobble gravels that postdate the grounding-line moraine (figure 6). These strata are cut by a 1- to 2-m-wide fault zone. Folded strata north of the fault zone indicate that the total zone of deformation is distributed over a 4-m-wide zone. Stratigraphic and structural relations exposed in the trenches provide evidence for at least two earthquakes in latest Pleistocene/Holocene time (figure 6). The most recent event is associated with several anastomosing subvertical fault traces that break the surface and form the scarp. A small graben or depression is present south of the main scarp and is bound by a second set of faults that dip 47° to 70° north. These faults are buried by a subtle soil and overbank sand deposit, providing evidence for the penultimate earthquake. Radiocarbon analyses of charcoal from within the buried soil indicate that the penultimate earthquake occurred prior to about 12,000 cal yr BP. Drag folding, discreet vertical offsets, stratigraphic juxtapositions, and thickness changes across individual

fault traces are consistent with both vertical and lateral displacement. Although facies and thickness changes of the thin fluvial deposits make correlation of stratigraphic units difficult, the gross stratigraphic packages are generally consistent across the fault zone, suggesting that the dominant mechanism of deformation is vertical displacement and hanging-wall folding. Lateral juxtapositions of stratigraphy across some faults indicate a small component of lateral displacement.

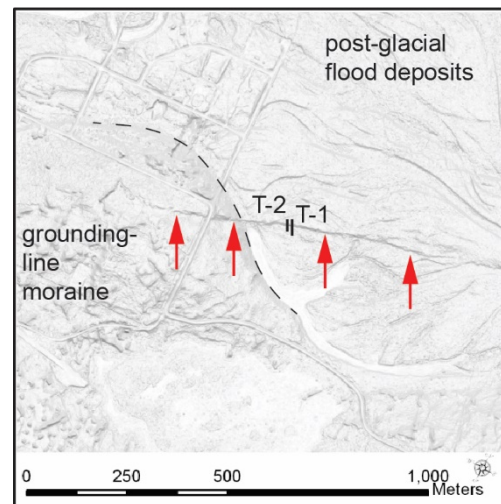


Figure 5: Lidar hillshade of the Castle Mountain fault trench Site. Fault extends along arrow tips. Dashed black line is the margin of the late Elmdorf grounding-line moraine and shows negligible lateral offset.

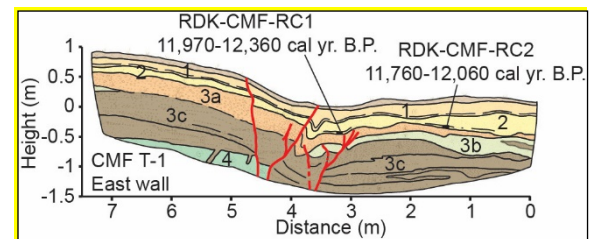


Figure 6: Stratigraphic log of the east wall of Castle Mountain fault trench CMF T-1. Unit 4, Sand, indurated (glacio-fluvial); Unit 3c, interbedded sand, gravel, and pebbly sand (fluvial); Unit 3b, sand, fine-grained (fluvial); Unit 3a, sand, fine-grained (fluvial); Unit 2, sand, fine-grained (fluvial); Unit 1, silt and very fine-grained sand (loess). Roots and modern peat mat comprise the upper unit.

CONCLUSION

Based on the mapping of scarp and fault zone morphology, rupture trace geometry, and continuity of geomorphic features across the fault, earthquakes along the Castle Mountain fault are best characterized by oblique reverse faulting above a north-dipping fault. The grabens north of the fault are the product of folding and extension (bending moment deformation) in the crest of an anticline developing in the hanging wall of a reverse fault consistent with the Tertiary anticline geophysically imaged at depth. The left-stepping en echelon pattern of scarps and grabens on the surface and stratigraphic juxtapositions in the trenches permit a small oblique component of right-lateral slip. The



oblique motion may be related to a combination of counter-clockwise rotation of south-central Alaska, oblique subduction along the Alaska-Aleutian subduction zone, and geodetically observed westward motion of the Kenai Peninsula (Snay et al., 2013; Fletcher, 2002). The fault scarp morphology along the CMF is similar to other historic oblique ruptures including the 1980 El Asnam and 1988 Spitak, Armenia earthquakes (Philip and Meghraoui, 1983; Philip et al., 1992). These similarities include stepping en echelon scarps superimposed on vertical scarps and grabens on the hanging wall and provide additional support for the partitioning of slip along the CMF between vertical and right-lateral strike-slip components.

The observations on the style and amount of slip differ from the view of Willis et al., (2007) in terms of the amount of lateral displacement. The previously reported slip rate of 3 mm/yr is likely too fast and may be closer to the long-term bedrock rate of <0.3 mm/yr that can be inferred from the offsets reported by Fuchs (1980). The trenching results indicate the occurrence of at least 2 latest Pleistocene-Holocene events, an apparent lesser number of events than the four events in the last 2700 years previously reported by Haeussler et al. (2002). If true, the two events in the latest Pleistocene documented here suggest recurrence intervals of several thousand years. However, it is acknowledged that additional unrecognized Holocene events may have only been expressed by subtle folding at the site and that additional studies are necessary to resolve the apparent discrepancy in the number of Holocene events.

Continuous clearly expressed Holocene fault scarps extend from the Parks Highway westward to the Susitna River. Observations from reconnaissance and proprietary industry studies indicate that Holocene scarps may extend several tens of kilometres west of the Susitna River. Thus, previous estimates of M_{max} may underestimate the maximum earthquake potential of the Castle Mountain fault. Additional studies focused on better bracketing the ages of paleoearthquakes and defining the western extent of Holocene scarps are needed to refine recurrence estimates along the Castle Mountain fault and to better characterize seismic hazards in southcentral Alaska.

Acknowledgements: The Author wishes to thank the Alaska Gasline Development Corporation for providing the funding for lidar acquisition and field studies. Field assistance from Dick Reger, Alex Gould, Ellie Spangler, Trent Hubbard, Rachel Frohman, Tony Crone and Gary Carver is greatly appreciated.

REFERENCES

- Detterman, R.L., Plafker, G., Hudson, T., Tysdal, R.G., and Pavoni, N., 1974, Surface geology and Holocene breaks along the Susitna segment of the Castle Mountain fault, Alaska: U.S. Geological Survey Miscellaneous Field Studies Map 618, 1 sheet, scale 1:24,000.
- Fletcher, H.J., 2002, Crustal deformation in Alaska measured using the Global Positioning System: Fairbanks, AK, University of Alaska Fairbanks Ph.D. thesis, 135 p.
- Fuchs, W.A., 1980, Tertiary tectonic history of the Castle Mountain fault-Caribou fault system in the Talkeetna Mountains, Alaska: Salt Lake City, University of Utah, Ph.D. dissertation, 152 p.
- Haeussler, P.J., Bruhn, R.L., and Pratt, T.L., 2000, Potential seismic hazards and tectonics of the upper Cook Inlet basin, Alaska, based on analysis of Pliocene and younger deformation: Geological Society of America Bulletin, v. 112, no. 9, p. 1,414-1,429.
- Haeussler, P.J., Best, T.C., and Waythomas, C.F., 2002, Paleoseismology at high latitudes-Seismic disturbance of upper Quaternary deposits along the Castle Mountain fault near Houston, Alaska: Geological Society of America Bulletin, v. 114, no. 10, p. 1,296-1,310, 1 sheet.
- Kelly, T.E., 1963, Geology and hydrocarbons in Cook Inlet basin, Alaska: American Association of Petroleum Geologists Memoir, v. 2, p. 278-296.
- Koehler, R.D., 2013, Alaska's Quaternary faults and folds (QFF): Digital Data Series DDS 3, Alaska Division of Geological & Geophysical Surveys, Fairbanks, AK, USA.
- Koehler, R.D., Reger, R.D., and Frohman, R.A., 2012, The Castle Mountain fault, south-central Alaska: New lidar-based observations on the sense of slip, Eos Trans., AGU, Fall Meet. Suppl., Abstract #S53D-2530.
- Lahr, J.C., Page, R.A., Stephens, C.D., and Fogleman, K.A., 1986, Sutton, Alaska, earthquake of 1984-Evidence for activity on the Talkeetna segment of the Castle Mountain fault system: Bulletin of the Seismological Society of America, v. 76, no. 4, p. 967-983.
- Philip, H. and Meghraoui, M., 1983, Structural analysis and interpretation of the surface deformations of the El Asnam earthquake of October 10, 1980, Tectonics, vol. 2, no. 1, p.p. 17-49.
- Philip, H., Rogozhin, E., Cisternas, A., Bousquet, J.C., Borisov, B., and Karakhanian, A., 1992, The Armenian earthquake of 1988 December 7: faulting and folding, neotectonics and palaeoseismicity, Geophysical Journal International, v. 110, pp. 141-158.
- Snay, R.A., Freymueller, F.T., and Pearson, C., 2013, Crustal motion models developed for Version 3.2 of the horizontal time-dependent positioning utility, Journal of Applied Geodesy, vol. 7, pp. 173-190.
- Wesson, R.L., Boyd, O.S., Mueller, C.S., Bufe, C.G., Frankel, A.D., and Petersen, M.D., 2007, Revision of time-independent probabilistic seismic hazard maps for Alaska, U.S. Geological Survey Open-File Report 2007-1043, 33 p.
- Willis, J.B., Haeussler, P.J., Bruhn, R.L., and Willis, G.C., 2007, Holocene slip rate for the western segment of the Castle Mountain fault, Alaska: Bulletin of the Seismological Society of America, v. 97, no. 3, p. 1,019-1,024.



Kinematics of the area between Palu (Elazığ) and Pütürge (Malatya) on the East Anatolian Fault System in Turkey

Kokum, Mehmet(1), Inceoz, Murat(2)

- (1) Department of Geological Engineering of Fırat University, Elazığ, Turkey. Email: mkokum@firat.edu.tr
 (2) Department of Geological Engineering of Fırat University, Elazığ, Turkey.

Abstract: The sinistral East Anatolian Fault System (EAFS) is the second most active strike slip fault zone after the North Anatolian Fault System (NAFS) in Turkey. In this paper, we reveal complex fault geometry of the related area by studying geomorphic features, field work and instrumental period earthquakes. This study presents a kinematic analysis (paleostress) based on fault-slip data in the area between Palu (Elazığ) and Pütürge (Malatya) on the EAFS. Results show that σ_1 (maximum principal stress) and σ_3 (minimum principal stress) are generally sub-horizontal and σ_2 (intermediate principal stress) is sub-vertical, which is characterized by NE-SW compression with major strike-slip system.

Key words: East Anatolian Fault System (EAFS), Kinematic analysis.

INTRODUCTION

Turkey is located near the centre of the Alpine-Himalaya system. The East Anatolian region is under compression with the collision of the Arabian and African plates at the south and Eurasian plate at the north (Figure 1). Significant deformations on both the Anatolian and the Arabian (indenter) plates due to collision have occurred and are still continuing. Large scale faults such as the EAFS (East Anatolian Fault System), NAFS (North Anatolian Fault System) and NEAFS (Northeast Anatolian Fault System) and many other small-scale faults have developed on the Anatolian plate are examples of these deformation structures. For this reason, the EAFS is classified as an indent-linked transcurrent strike-slip fault related to the collision according to the classification made by Sylvester (1988). The EAFS forms a triple junction with the NAFS in Karlıova (Bingöl) at the northeast, and forms another triple junction with the Dead Sea Fault System (DFS) in Amik (Antakya) in the southwest. The EAFS, a left lateral (sinistral) strike slip fault, is about 580 km in length and although the strike direction of the EAFS changes in some places, it mostly follows the N60°E direction. In this work, an area about 120 km long extending from Palu in the north to Pütürge in the south was studied along the EAFS. We aimed to reveal deformation mechanism of the area on the EAFS by collecting and analysing fault slip data.



Figure 1: Tectonic map of Turkey showing the plate motion along the major faults. Study area is marked in red on the EAFS.

METHODS

The aim of kinematic analysis (paleostress inversion) is to build past and present behaviour of the faults using fault slip data (Angelier, 1994). The method is based on the hypothesis that the slip occurs parallel to the maximum resolved shear stress along an optimally orientated plane of weakness (Wallace 1951; Bott 1959).

The sense of slip on the fault plane is obtained from slickenside lineation and mineral steps. The data that are used for the inversion are the fault plane, slickenside orientation and the sense of movement derived from kinematic indicators and mineral steps on each fault plane (Figure 2).

In the paleostress inversion, the maximum shear stress direction is determined by calculating the axes of the stress ellipsoid by using the shape factor ($\Phi = \sigma_2 - \sigma_3 / \sigma_1 - \sigma_3$). In which σ_1 , σ_2 and σ_3 correspond to maximum, intermediate and minimum principal stress magnitudes, respectively. In this study, we have performed the numerical method improved by Angelier (1988).



Figure 2: Example of fault slip data at sinistral strike-slip fault plane in the study area (Figure 4, Site B).

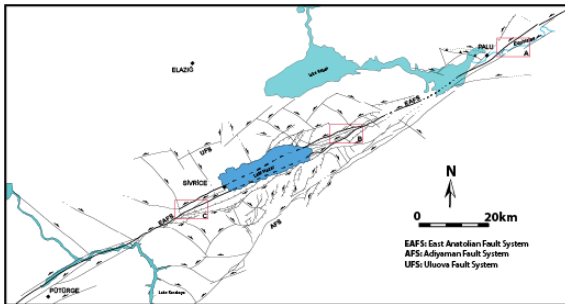


Figure 3: Tectonic map and sample locations of study area (modified from Aksoy et al., 2007).

RESULTS

Twenty measurements were performed to the north of the Palu from Eocene aged limestone (Figure 3, Site A). The stress tensors were obtained from the fault population: the inversion after Angelier (1994) (Figure 4) gives the maximum principal stress axis (σ_1): 236/05, the intermediate principal stress axis (σ_2): 039/85, the minimum principal stress axis (σ_3): 145/01; with stress ratio (R): 0.165. The tensor belongs to transpressive regime. It indicates NE–SW compression and NW–SE extension. This tensor produced the NE trending sinistral strike-slip faults with their conjugate NW trending dextral strike slip faults.

The second fault population with thirty measurements from northeast of the Lake Hazar (Figure 3, Site B) from basin infill deposits based on the inversion after Angelier (1994) the maximum principal stress axis (σ_1): 070/69, the intermediate principal stress axis (σ_2): 227/19, the minimum principal stress axis (σ_3): 320/08; with stress ratio (R): 0.408. The tensor belongs to pure extensive regime. It indicates NW–SE extension. This tensor produced the NW and SE trending normal faults (Figure 4).

Fifteen fault-slip data were carried out in an area located in the southwest of the Lake Hazar near Pütürge (Figure 3, Site C). The stress tensors were obtained from the fault slip data: the inversion after Angelier (1994) (Figure 4) gives the maximum principal stress axis (σ_1): 024/49, the intermediate principal stress axis (σ_2): 191/40, the minimum principal stress axis (σ_3): 286/06; with stress ratio (R): 0.724. The tensor belongs to pure extensive regime. It indicates NW–SE extension. This tensor produced the NE trending sinistral strike-slip faults with their conjugate NW trending dextral strike slip faults.

DISCUSSION

The data collected from the field, there are two different tectonic tensor (transpressive and pure extensive regime) along the EAFS. The inversion based on Angelier (1994) indicates that the intermediate principal stress axis (σ_2) and the maximum principal stress axis (σ_1) are sub-vertical. This situation can be explained as the changed in the tectonic regime through tectonic history. Extensional structures, e.g., NW–SE trending normal faults and

compressional structures like NE–SW trending folds were also formed in the study area. North of Lake Hazar the EAFS geometry is considered to be a negative flower structure (Aksoy et al., 2007). It is quite common to have both these extensional and compressional structures in the major strike-slip systems.



Figure 4: Normal faults developed within the basin infill north of the Lake Hazar.

CONCLUSION

In this study, the complex geometry of the EAFS has been revealed and mapped. Based on preliminary results of paleostress inversion on EAFS has displayed at least two different tectonic regimes length according to strike changes.

Sixty-five measurements were performed and inversion suggest that these stress tensors may be responsible for the formation of the NE–SW sinistral and NW–SE dextral strike slip faults as well as local NW–SE normal faults in the study area.

Acknowledgements: This work is supported by FUBAP (Firat University Scientific Research Projects Unit), (Project No: MF-1642). We would like to thank FUBAP for its financial support.

REFERENCES

- Angelier, J. 1988. Tector: Determination of stress tensor using fault slip data set. Quantitative Tectonics, University Pierre and Marie Curie, Paris.
- Angelier, J. 1994. Fault slip analysis and paleostress reconstruction. In Hancock, P. (ed): continental deformation. Pp: 53–100, Pergamon Press Oxford.
- Aksoy, E., Inceöz, M. & Koçylğit, A. 2007. Lake Hazar basin: a negative flower structure on the East Anatolian fault system (EAFS), SE Türkiye. Turkish Journal of Earth Sciences 16, 319–338.
- Bott, M. P. H. 1959. The mechanics of oblique-slip faulting. Geological Magazine, 96, 109–117.
- Sylvester A.G. - 1988. Strike-slip faults. Geological Society of America Bulletin 100 (11), 1666–1703.
- Wallace, R. E. 1951. Geometry of shearing stress and relation to faulting. Journal of Geology, 69, 118–130.



Earthquake history of the western Issyk-Ata Fault, Central Tien Shan, North Kyrgyzstan

Landgraf, Angela (1,2), Patyniak, Magda (1), Dzhumabaeva, Atyrgul (3), Abdrakhmatov, Kanatbek (3), Arrowsmith, J Ramón (4), Korup, Oliver (1) Strecker, Manfred R. (1)

- (1) University of Potsdam, Institute of Earth and Environmental Science, K.-Liebknecht Str. 24-25, D-14476 Golm, Germany
landgraf@geo.uni-potsdam.de
- (2) Nagra (National Cooperative for the Disposal of Radioactive Waste), Hardstrasse 73, Postfach 280, 5430 Wettingen, Switzerland
- (3) Institute of Seismology, National Academy of Science of Kyrgyzstan, Asanbay 52-1, 720060 Bishkek, Kyrgyzstan
- (4) School of Earth and Space Exploration, Arizona State University, Tempe, Arizona, USA

Abstract: Correlating paleoearthquakes along faults is crucial to understand the earthquake recurrence pattern and to assess potential earthquake hazard. We present data from four trenches at three sites along the western Issyk Ata Fault, a 120-km-long thrust bounding the northern Kyrgyz Tien Shan. A part of this fault has ruptured during the 1885 AD Belovodskoe event (M6.9). Two trenches in the epicentral area of this rupture revealed the most recent event to represent the Belovodskoe earthquake. The penultimate earthquake occurred here probably around 1.9 ± 0.3 cal ka BP. 12 km east, earthquakes ruptured at 10.5 ± 1.1 cal ka BP, 5.6 ± 1.0 cal ka BP, and $\sim 630 \pm 100$ cal a BP. Yet 13 km farther east the MRE postdates 685 ± 30 cal a BP. Thus, in the recent past, Issyk-Ata Fault segments ruptured diachronously and only along certain portions with respect to the entire fault length.

Key words: Paleoearthquakes, Thrusting, Issyk Ata Fault, Tien Shan, Kyrgyzstan

INTRODUCTION

Fault slip distributions, earthquake timing, maximum magnitude, and recurrence intervals are important parameters to assess the hazard potential of a fault. Similarly, the understanding of the associated fault-rupture or earthquake model relies on multiple paleoseismic records along the fault (Biasi and Weldon, 2006). But even at fast-slipping plate-boundary faults with sufficient paleoseismic data, correlating paleoearthquakes along strike is not unambiguous because of uncertainties in age determination and stratigraphic relationships (e.g., Weldon et al., 2004, 2005).

In low-strain areas, however, uncertainties are even higher, because long recurrence times in the order of thousands of years decrease the preservation of landscape-evidence of faulting (e.g., Landgraf et al., 2017). In compressional environments, yet another drawback might emanate from range-bounding positions of active thrust faults, which cut through alluvial fans and provide mainly coarse-grained stratigraphy that is difficult to date. Thrust faulting furthermore often exhibits near-surface complexities that directly translate into the trench stratigraphy and complexity in interpretation. Typical examples, observed in unconsolidated sediment, are fault migration into the hanging wall or footwall over time, as well as duplexing, folding or roll-over of hanging-wall strata into sub-horizontal positions. Additionally, large cumulative dip-slip offsets of strong events often limit the discovery to a few past events because of logistic requirements, thus hampering our understanding of active thrust faults and their rupture behavior.

One of such faults posing an inherent seismic hazard to the Kyrgyz capital Bishkek is the Issyk Ata Fault, a 120-km-long thrust, bounding the northern Kyrgyz Tien Shan. During an earthquake sequence of five large-magnitude earthquakes (M 6.9-8) that ruptured the northern Tien Shan between 1885 and 1938 (e.g., Kalmetieva et al., 2009), apparently only the westernmost Issyk-Ata fault segment broke in the Belovodskoe event (1885, M6.9). The central and eastern Issyk-Ata Fault, however, did not rupture, leaving a 200-km-long gap in the east-west distribution of faulting during this sequence (Fig. 1A+B).

This observation highlights the need for a better understanding of the paleoearthquakes and rupture behaviour of the Issyk Ata fault. We have analysed the geomorphology and excavated four trenches at three sites along the western and central-western part of the fault. Here, we present the first integrative summary of the earthquake history from these data.

PREVIOUS STUDIES

The oldest earthquake record that later was associated with the Issyk Ata Fault is the Ignatiev (1886) report on the 1885 Belovodskoe event. In that paper, which is based on eyewitness information, he describes that the majority of damage, including an about 20-km-long open crack, occurred between the Aksu and Sokuluk rivers (see Fig. 1B). Additional cracks were observed discontinuously eastward towards the Ala-Archa river valley (Fig. 1B). Peer-reviewed studies of paleoseismicity along the Issyk Ata fault so far are rare. Thompson (2001) documented a trench at the western fault branch, where he inferred four surface-rupturing events since terrace formation between 13 to 15 kyr ago. Presumably, the last two earthquakes



occurred within the past 2.3 to 2.7 cal kyr BP, including the 1885 event. A few trench logs or sketches with limited age control can be found in Russian literature and local institutional compilations (e.g., Chedia et al., 2000, Omuraliev and Omuraliev, 2004). Dzhumabaeva et al. (2015) presented a review of these data, including a calibration of therein-published radiocarbon results to assess if earthquakes along the Issyk Ata fault have clustered in time similarly to the 150-yr-old recent earthquake sequence. They argue that at least four strong earthquakes occurred along the fault within the past 5000 years with a possible cluster between 2-2.5 kyr. However, the uncertainty in age control of the paleoevents exceeds the age range of the recent clustered events. Recently, Smekalin et al. (2016) show illustrations of additional trenches along this fault (Fig. 1B) in an attempt to localize the 1885 rupture extent. Also, these authors used previously published radiocarbon results together with their own data. Based on the relatively narrow age range, but without direct age control, Smekalin et al. (2016) argue for the same earthquake that ruptured the Issyk Ata Fault between 887–1533 cal. yrs BC at least to an extent of 36 km between Sokuluk and Kok Dzhar (Fig. 1B). Our own studies challenge this assumption: Patyniak et al. (2017) show three surface-rupturing earthquakes that occurred diachronously at 10.5 ± 1.1 cal ka B., 5.6 ± 1.0 cal ka BP, and $\sim 630 \pm 100$ cal a BP at Belek, which is located between above-mentioned sites (Fig. 1B). Here, we additionally present our new data from two further sites (Asylbash and Dzhal) that help deciphering the earthquake history of the western Issyk Ata Fault (Fig. 1B).

EARTHQUAKE HISTORY OF THE WESTERN ISSYK ATA FAULT

The fault-scarp geomorphology of these sites was mapped and interpreted using high-resolution imagery to provide a detailed characterization of the rupture zone. At each location the scarp around the trench sites was mapped using a LEICA differential GPS system and the data were interpolated into high-resolution digital elevation models (~ 1 m/pixel; DEM). From these DEMs, we subsequently calculated scarp-perpendicular profiles to determine cumulative vertical fault offsets. Scarp heights roughly agree within uncertainties.

Trenching was performed at three sites (from east to west, Fig. 1B): Dzhal, Belek (Patyniak et al., 2017), and Asylbash. – Age control of the trench stratigraphy was based on radiocarbon methods and infrared stimulated luminescence (IRSL). At Asylbash, we opened two trenches along the same scarp that were 120 m apart. The trenches were 18-m and 22-m-long. The trench at Dzhal with a length of 19 m has been excavated across an undisturbed scarp that showed about 5.5 m vertical offset. The scarp uplifts an alluvial terrace. An abandoned channel produced a hanging valley with an offset of about 3.8 m, and a small inset terrace east of the trench location is offset by about 0.5 m, indicating a succession of at least three sudden uplift events, given the full scarp height.

At all sites, late Pleistocene and Holocene faulting has cut alluvial surfaces of similar degree of surface roughness and incision. Repeated faulting was accompanied by syntectonic loess deposition against the growing fault scarp, filling paleo-topography.

We observe an alluvial clast deposit that builds the hanging wall and the thrust contact against an aeolian loess deposit in the footwall. Within the exposure of our trenches, we did not find a similar clast deposit in the footwall. At one location (Asylbash) we have been able to date the alluvial sedimentation with IRSL to 18.4 ka. This age is in concordance with a late sedimentation age of 17.3 ± 4.3 ka at a similar alluvial fan at Panfilovkoe, about 50 km west of Asylbash (Landgraf et al., 2016). Similarly concordant, this sedimentation age predates exposure ages of 14.8 ka at Panfilovkoe and the 13.5 to 15.5 kyr terrace ages east of Bishkek that have been correlated to the fan surface at Asylbash earlier (Thompson, 2001). Within this age range, it is thus reasonable to assume a glaciofluvial origin for the boulders that have been transported into the foreland after the Last Glacial Maximum (LGM).

Loess sedimentation must have started immediately afterwards as documented with one age at 15.9 cal. ka BP (Asylbash). Our age distribution and the lack of paleosoils within the stratigraphic sequence suggest a more or less continuous or repeated loess sedimentation until about 6.5 cal. ka BP, as the majority of snails from these units date between 9.5 and 6.5 cal. kyrs BP. Interestingly, the age range and loess thickness vary between the three sites. The growing, N-facing fault scarps seem to provide an efficient sediment trap for the S-transported loess. Similarly, at these positions it might be largely sheltered from N-directed wind deflation. Further faulting progressively increases the stratigraphic separation, as diffusive scarp degradation removes the loess from the hanging wall, which further thickens at the footwall. The magnitude of this process differs at the three sites and might reflect the scarp-type and thus the underlying fault geometry: the shallower the scarp slope, the more loess is preserved in the hanging wall. The fault geometry as visible in these trenches resembles a hanging-wall-collapse or simple thrust scarp.

The strong clast-silt-contrast seems to have guided the surface rupture. This is not only true at the base of the alluvial sequence, but even for the frontal thrust of a duplex visible in Asylbash-T2. Here, a scarp-parallel channel has been deformed and incorporated in the thrusting.

Probabilistic modelling of the stratigraphic chronology with OxCal (Bronk Ramsey, 2013) revealed the most recent event (MRE) in the Asylbash trenches at the epicentral area of the 1885 rupture consistently at 273 ± 168 and 316 ± 172 cal a BP, respectively, which we interpret to represent the Belovodskoe event. The penultimate earthquake occurred here probably around 1.9 ± 0.3 cal ka BP. In contrast, at Belek, 12 km to the east, earthquakes ruptured at 10.5 ± 1.1 cal ka BP, 5.6 ± 1.0 cal ka BP, and $\sim 630 \pm 100$ cal a BP (Patyniak et al., 2017). Yet 13 km farther east (Dzhal), faulting during the MRE ruptured soil layers dating to 804 ±



54 and 685 ± 30 cal a BP. We infer that this event corresponds to the youngest event observed at Belek, providing a minimum surface rupture length of 13 km. Unfortunately, older events cannot be differentiated unambiguously.

DISCUSSION & CONCLUSION

Our observations support the notion that at least in the recent past, the Issyk-Ata Fault ruptured only certain portions with respect to the entire fault length. Apparently, the earthquake timing did not overlap between the Asylbash and Belek sites for the past two events, respectively. Combined with the fact that even the interevent times differ between the sites, this might indicate an efficient segment boundary that could limit future ruptures. One could speculate that the Sokuluk river valley itself mimics the segment boundary. There is a clear break in the topographic expression at the fault location (Fig. 1B). The diachronous earthquake timing also excludes a through-going surface rupture between Sokuluk (Asylbash) and Kok Dzhaz about 2.5 ka ago, as assumed by Smekalin et al. (2016). However, this does not exclude that a rupture across the supposed segment boundary or even along the entire fault length could occur at other times. Results from earthquake simulations (e.g., Zielke and Arrowsmith, 2008) have shown that bimodal rupture behaviour with frequent small to intermediate and infrequent large-magnitude events (incomplete and full rupture respectively) might explain observed differences in rupture extent. The offsets, observed for the respective events (Patyniak et al., 2017 and also in this study, but not shown) can be associated to paleomagnitudes between 6.8 and 7.1, thus similar to the 1885 earthquake. The segment-wise, diachronous faulting along the Issyk Ata Fault and within the active fault systems that comprise the northern Tien Shan might resemble the conceptual model of Liu et al., 2011, where earthquake activity migrates between faults, and some faults become seismically quiet for periods of time, while others take over the activity. Such model has been proposed for continental interiors, but the northern Tien Shan as a diffuse plate boundary region seems to behave in a similar way.

The diachronous ruptures, observed at the western and central-western Issyk Ata Fault might also explain the east-west large gap within the earthquake sequence of the late 19th/early 20th century. The MRE at Belek and Dzhaz occurred only $\sim 630 \pm 100$ cal a BP (Patyniak et al., 2017). Similarly, the central and eastern portions of the faults could have experienced earthquakes that are not yet in the record, but that have released stresses affecting subsequent event timing along portions of the fault zone. With general recurrence intervals of several thousand years (Landgraf et al., 2016, Patyniak et al., 2017), these segments could be in any stage of strain accumulation. Interestingly, although an historic earthquake record for Kyrgyzstan has been compiled (e.g., Kalmetieva et al., 2009), not much is known for medieval and older times. The previous cultural center of Balasagun (near present day Kant, Fig. 1B, e.g., Kalmetieva et al., 2009) might have been destroyed by an earthquake

around 1475 AD; its surface trace and evidence has yet to be found. The MRE at Belek and Dzhaz, although located further east, might be a valid candidate.

Acknowledgements: This work was funded by the Volkswagen Foundation Germany. Authors wish to thank the radiocarbon laboratory in Poznan/Poland for dating the samples. Frank Preusser is thanked for analysing the IRSL samples.

REFERENCES

- Biasi, G. P., and R. J. Weldon II (2006), *Bull. Seismol. Soc. Am.*, 96(5), 1612–1623.
- Bronk Ramsey, C. (2013), *OxCal 4.2*, Web Interface Build No. 78, Oxford Univ., Oxford, U. K.
- Chediya O.K., Abdрахmatov K.E., Lemzin I.N., Michel G. & Mikhailev V., 2000. Issyk Ata, North Tien Shan Fault in the Holocene. *Journal of Earthquake Prediction Research*, 8, 379–386.
- Dzhumabaeva, A., Abdрахmatov, K.; Landgraf, A., & Rosenwinkel, S., 2015. Temporary clustering of strong earthquakes or lack of data?, *Geophysical Research Abstracts*, Vol. 17, EGU2015-13940
- Ignatiev, I. V. (1886), Earthquakes in Tokmak district in 1885 [in Russian], *Isvestia Russ. Geogr. Soc.*, 22, 1–14.
- Kalmetieva, Z.A., Mikolaichuk, A.V., Moldobekov, B.D., Meleshko, A.V., Jantaev, M.M., & Zubovich, A.V., 2009. Atlas of Earthquakes in Kyrgyzstan, ECHO, UNISDR, and CAIAG, pg. 233.
- Landgraf, A., A. Dzhumabaeva, K. E. Abdрахmatov, M. R. Strecker, E. A. Macaulay, JR. Arrowsmith, H. Sudhaus, F. Preusser, G. Rugel, and S. Merchel, 2016. Repeated large-magnitude earthquakes in a tectonically active, low-strain continental interior: The northern Tien Shan, Kyrgyzstan, *J. Geophys. Res.* 121, doi:10.1002/2015JB012714.
- Landgraf, A., Kübler, S., Hintersberger, E. & Stein, S., 2017. Active tectonics, earthquakes, and paleoseismicity in slowly deforming continents. In: *Seismicity, Fault Rupture and Earthquake Hazards in Slowly Deforming Regions* (Landgraf, A., Kübler, S., Hintersberger, E., and Stein, S., eds.), Geological Society of London, Special Publications (432), <http://doi.org/10.1144/SP432.13>.
- Liu, M., Stein, S., & Wang, H., 2011. 2000 years of migrating earthquakes in North China: How earthquakes in midcontinents differ from those at plate boundaries. *Lithosphere*, 3(2), 128-132.
- Omuraliev M., Omuralieva A. , 2004. Late Cenozoic Tectonics of the Tien-Shan. Kyrgyzstan, Central Asia. Bishkek, 166p
- Patyniak, M., Landgraf, A., Dzhumabaeva, A., Abdрахmatov, K.E., Rosenwinkel, S., Korup, O., Preusser, F., Fohlmeister, J., Arrowsmith, JR. & Strecker, M.R., 2017. Paleoseismic Record of Three Holocene Earthquakes Rupturing the Issyk-Ata Fault near Bishkek, North Kyrgyzstan, accepted for publication in BSSA
- Smekalin, O. P., Imaev, V. S., Korzhenkov, A. M., & Chipizubov, A. V., 2016. Paleoseismological investigations in the pleistoseismal zone of the 1885 Belovodskoe earthquake, North Tien Shan. *Seismic Instruments*, 52 (4), 279-289.
- Thompson, S. C., 2001. *Active tectonics in the central Tien Shan, Kyrgyz Republic*, PhD thesis, Univ. of Washington, Wash.
- Thompson S.C., Weldon R.J., Rubin C.M., Abdрахmatov R., Molnar P, and Berger G.W., 2002. Late Quaternary slip rates across the central Tien Shan, Kyrgyzstan, Central Asia. *Journal of Geophysical Research*, 107 (B9)
- Weldon, R., Scharer, K., Fumal, T., & Biasi, G., 2004. Wrightwood and the earthquake cycle: What a long recurrence record tells us about how faults work. *GSA today*, 14 (9), 4-10.
- Weldon, R. J., Fumal, T. E., Biasi, G. P., & Scharer, K. M., 2005. Past and future earthquakes on the San Andreas fault. *Science*, 308(5724), 966-967.
- Zielke, O., & Arrowsmith, J. R. (2008). Depth variation of coseismic stress drop explains bimodal earthquake magnitude-frequency distribution. *Geophysical Research Letters*, 35(24).

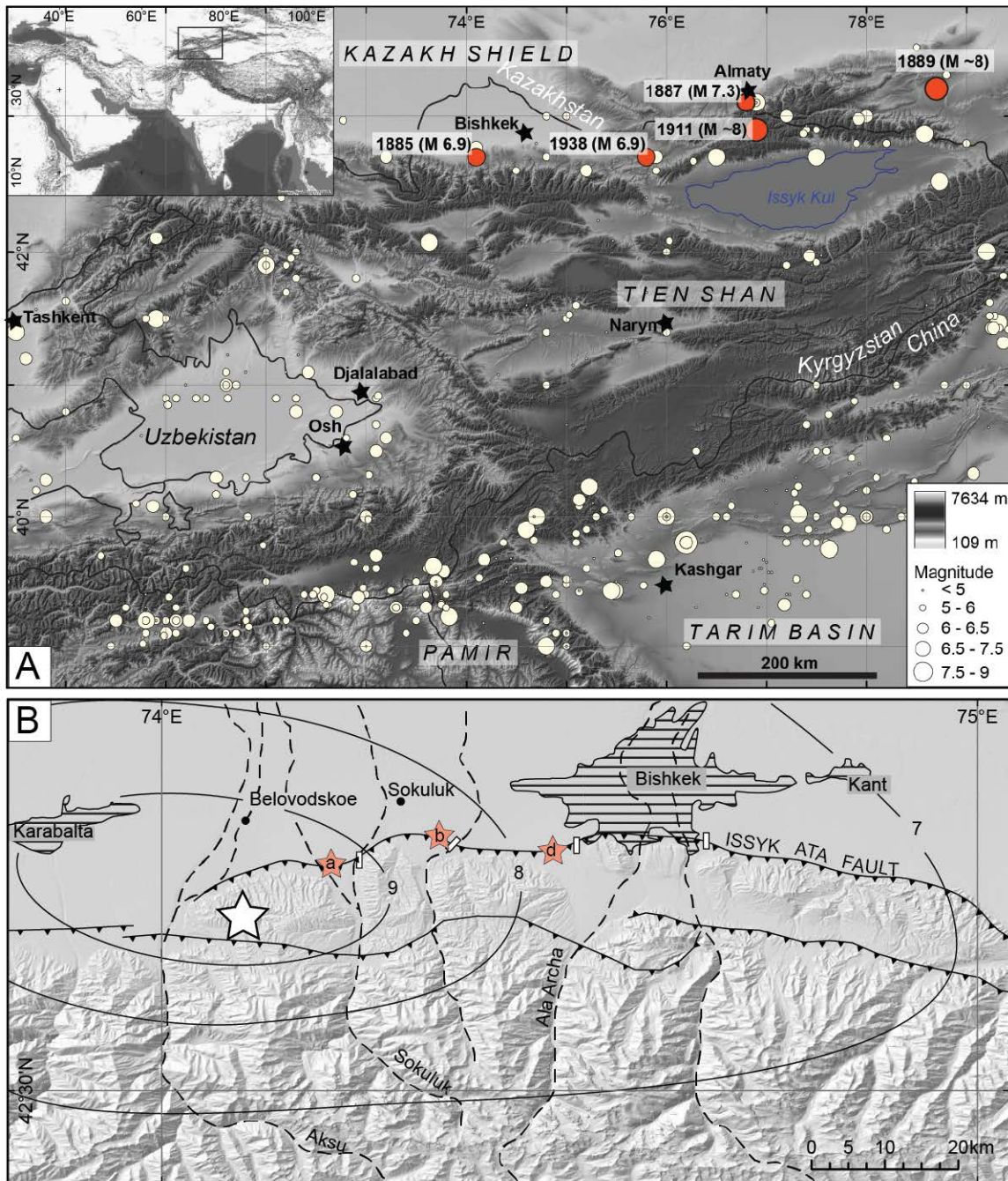


Figure 1: The study area within its tectonic and geographic framework (after Landgraf et al., 2016). (A) Digital elevation model (SRTM) of Kyrgyzstan. Major geographic features and major cities are labeled. Overlain are historical earthquakes (Kalmetieva et al., 2009). Note the series of strong events along the northern rim of the Tien Shan at the turn of the 19th/20th century (highlighted in red). The study areas are located in the wider epicentral area of the 1885 earthquake. Inset shows position of figure (box) in an Asian-Eurasian framework. (B) Overview of the central Kyrgyz Range. Overlain are active faults after Thompson et al. (2002), as well as isoseismals (Intensities VII to IX) related to the 1885 Belovodskoe earthquake (epicenter marked by white star) after Kalmetieva et al. (2009). Shaded pattern marks villages and towns, small red stars are assigned to our trench locations: (a) Asylbash, (b) Belek, (d) Dzhal. White rectangles are study sites correlated in Smekalin et al. (2016), from west to east: Sokuluk, Kuzul-Tuu, Dzhal & Kok-Dzhar.



The role of surface-rupturing faults in the Waiautoa microblock, Clarence valley, New Zealand, during the M_w 7.8 2016 Kaikōura Earthquake

Langridge, Robert (1), Ries, William (1), Rowland, Julie (2), Villamor, Pilar (1), Kearsse, Jesse (3), Little, Timothy (3), Nissen, Edwin (4), Madugo, Chris (5), Litchfield, Nicola (1), Gasston, Caleb (2), Hall, Brendon (2), Canva, Albane (2), Hatem, Alex (6), Zinke, Robert (6).

- (1) Active Landscapes Dept., GNS Science, PO Box 30-368, Lower Hutt, New Zealand. Email: r.langridge@gns.cri.nz; w.ries@gns.cri.nz
 (2) Dept. of Earth Sciences, University of Auckland, New Zealand
 (3) Dept. of Earth Sciences, Victoria University of Wellington, Wellington, New Zealand
 (4) School of Earth and Ocean Sciences, Victoria University, British Columbia, Canada
 (5) Pacific Gas and Electric, Kensington, California USA.
 (6) Dept. of Earth Sciences, University of Southern California, Los Angeles, California, USA

Abstract: The M_w 7.8 Kaikōura Earthquake has presented an opportunity to study the scale of earthquake deformation from regional-scale, to individual block and micro-block tectonics. The 2.5 km² 'Waiautoa microblock' refers to the high-angle fault intersection area between the co-seismic ruptures of the Jordan, Kekerengu, Papatea, and Waiautoa faults in the Clarence valley. Detailed field observations and post-earthquake LiDAR mapping indicate that these faults intersect in a complex, triangular fashion. The Jordan Thrust (dextral-normal in 2016) overlaps the dextral-reverse Kekerengu Fault near George Stream. In this same area, ruptures of the reverse-sinistral Papatea Fault almost intersect the Jordan Thrust. To close the triangle, the reverse-sinistral Waiautoa Fault is inferred to link the Papatea with the Kekerengu Fault. Assessment of piercing line markers indicates that co-seismic surface slip increases to the NE of George Stream, and is largely conserved along the length of the Waiautoa microblock as the Jordan, Kekerengu and Waiautoa faults share and exchange 7-9 m of surface slip. Summed co-seismic surface slip within the Waiautoa microblock is sub-equal to co-seismic surface slip on the Kekerengu Fault northeast of the microblock, suggesting that this zone of complexity promoted the continuation of surface rupture.

Key words: Waiautoa Fault, Papatea Fault, 2016 Kaikoura earthquake, transpression.

INTRODUCTION

The 14 November 2016 (local time) M_w 7.8 Kaikōura earthquake, New Zealand is one of the largest, high-slip onshore earthquakes to have occurred in recent times (Hamling et al., 2017; Kaiser et al., 2017; Stirling et al., 2017). Surface rupture occurred on at least 14 named faults between Waiiau in north Canterbury and offshore of Cape Campbell, Marlborough over c. 160 km (Fig. 1). The pattern of surface faulting is highly complex both at the full scale of the rupture and at smaller scales where individual faults or fault segments interact with adjoining faults. This paper documents an important complexity near the centre of the Kaikōura earthquake rupture zone where 5 distinct faults – the Jordan, Kekerengu, Papatea, Fidget and Waiautoa faults - join and overlap one another in three dimensions.

The Kaikōura earthquake occurred in the central part of the Australia-Pacific plate boundary through New Zealand in the northeastern South Island. This region is characterized by plate convergence rates of c. 37-40 mm/yr and a progression from compression in the southwest, to transpression and strike-slip motion in the northeast, across a transitional plate boundary setting where the leading edge of the Pacific plate subducts beneath the New Zealand margin (e.g. Wallace et al., 2012). Fault rupture during the Kaikōura earthquake began in the North Canterbury Domain and propagated into the Marlborough Fault System (MFS) (Litchfield et al., 2014;

Langridge et al., 2016a) (Fig. 1). The vast majority of seismic energy and surface slip was released during the second half of the earthquake sequence when rupture of the northern faults within the MFS, initiated and propagated slip to the northeast (e.g. Kaiser et al., 2017).

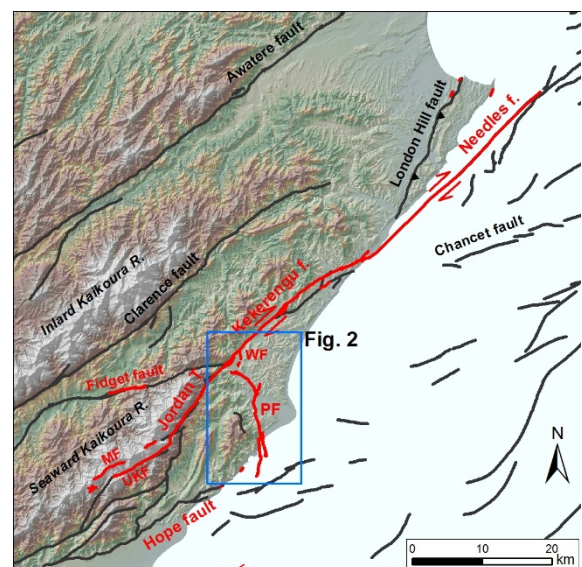


Figure 1: Map of the northern surface fault ruptures (red lines) in the 2016 M_w 7.8 Kaikōura Earthquake. Blue box indicates Fig. 2 highlighting the Papatea Fault (PF) and Waiautoa Fault (WF). See text for other abbreviations.



This paper describes the 'Waiautoa microblock' where five of the major northern faults join and overlap one another and where both proximity of individual fault ruptures and the partitioning of slip from one to another can be measured and documented. Understanding how faults and fault zones within the upper crust interact at the km-scale, with respect to the shape and size of fault stepovers and bends is of great relevance for considering the seismic hazard posed by integrated fault networks (Wesnousky, 2008; Barka and Kadinsky-Cade, 2002).

METHODOLOGY

Following the Kaikōura earthquake, we collected field observations where fault surface rupture was recognized and accessible, and undertook helicopter reconnaissance of sites in remote areas where landing was difficult or impractical. We employed a variety of techniques to measure surface slip including tape measure, sighting of scarp heights, real-time kinematic (RTK-GPS), total station, and UAV (drone) surveys. Offsets were recorded on cultural features including fencelines, roads, and planted treelines, and geomorphic features such as stream channels, risers and scree deposits. Due to the possibility of offsets being destroyed by bad weather and/or farm reparations and the slow availability of some airborne datasets, the faults were mapped and surveyed as quickly as was practical on the ground soon after the earthquake. In early 2017 we received aerial orthomosaics and in mid-2017 post-earthquake LiDAR coverage of most of the earthquake rupture zone. In some cases, such as along the coast and up the Clarence valley, pre-earthquake LiDAR surveys existed (Langridge et al., 2016b). In these cases, we developed Differential LiDAR (D-LiDAR) models of the ground surface change (Clark et al., 2017; Nissen et al., this volume). Field and GIS data were collated to produce surface rupture maps, slip vectors and slip distributions for individual faults (Jordan, Kekerengu, Papatea, Fidget and Waiautoa) within 10 km of the Waiautoa microblock area.

MAJOR FAULT RUPTURES ASSOCIATED WITH THE WAIAUTOA MICROBLOCK AREA

Papatea Fault - The Papatea Fault, which extends from offshore in Waipapa Bay to George Stream (Fig. 2), was recognised as an important NNW-striking bedrock, and possibly active, fault prior to the Kaikōura earthquake (Barrell, 2015; Rattenbury et al., 2006). Papatea fault ruptures have a variable strike along the mapped length of the fault. They are commonly reverse-sinistral in sense with a maximum (near-field) net slip of 7.4 ± 0.6 m. D-LiDAR profiles are consistent with InSAR results that suggest the Papatea Block (i.e. the block bounded by the Papatea, Jordan and Hope faults) moved vertically by 8-10 m (and by several m to the south) (Hamling et al., 2017). Offsets on the Papatea Fault are locally sinistral-reverse with up to 6 m of net slip at the coast across two distinct fault strands (Clark et al., 2017). Near the northern end of the fault, an impressive N-striking reverse-sinistral rupture scarp bends to the NW into a splaying, distributed zone of sinistral-normal faulting and monoclinial ruptures within

the hangingwall. The main reverse-sinistral trace is progressively concealed in George Stream (Fig. 3).

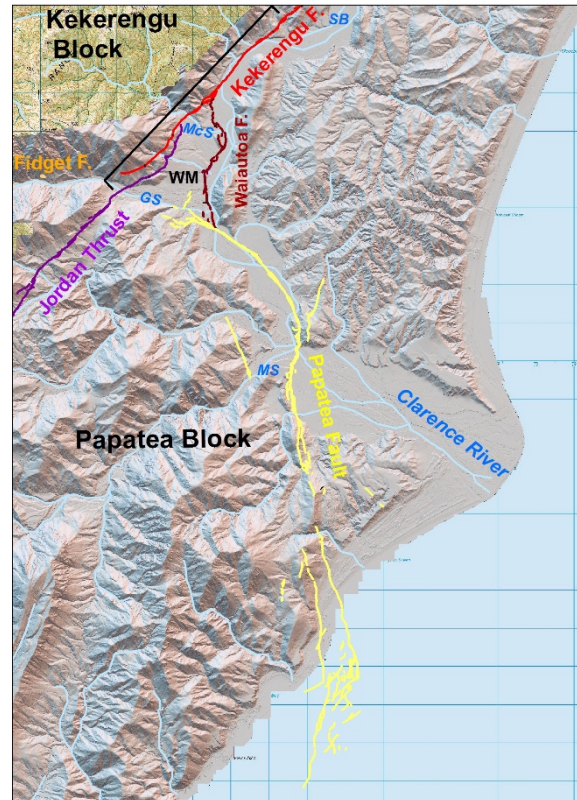


Figure 2: 2016 co-seismic surface rupture of the Papatea Fault (yellow) and ruptures of the Jordan (purple), Kekerengu (red) and Waiautoa (brick) faults in the vicinity of the Waiautoa microblock (WM). George (GS), Miller (MS) and Mclean (McS) streams and Shag Bend (SB) are labelled. Black line marks Fig. 4 slip-section.

Jordan Thrust - The Jordan Thrust is an important, northeast-striking, high-slip rate plate boundary fault that links the Kekerengu with the Hope Fault to the southwest (Van Dissen and Yeats, 1991). Following the earthquake, helicopter reconnaissance and limited ground observations indicated that only the northern half of this fault (as mapped) had surface rupture. Farther inland, parts of the Upper Kowhai Fault (UKF) and Manakau Fault (MF) within the Seaward Kaikōura Range also displayed surface rupture. The northern half of the Jordan Thrust typically displayed dextral-normal (uphill-facing) surface rupture with 3-4 m dextral slip near Miller Stream and up to 6-8 m at George Stream. Northeast of this point, the Jordan Thrust overlapped with rupture on the Kekerengu Fault. While dextral-normal motion was observed the long-term motion for this fault is of transpression, therefore, we entertain the possibility of a blind component of reverse motion on the Jordan fault.

Kekerengu Fault - The northeast-striking Kekerengu Fault represents the longest onland rupture (c. 28 km) and largest recorder of slip (up to 11.8 m dextral) during the Kaikōura earthquake sequence (Hamling et al., 2017; Stirling et al., 2017; Kearse et al., this volume). The southern half of the fault occurs from George Stream north along the Clarence River valley. Northeast of the river, the fault traverses



farmland out to the Marlborough coast. While the highest offsets in 2016 were documented in the north, the southern half of the fault consistently produced surface ruptures with 9-11 m of dextral slip in the floor of the Clarence River and across the Shag Bend area. South of Shag Bend there is an apparent drop in the magnitude of slip toward Waiautoa Station and McLean Stream, where there is c. 6 m of dextral slip. South of McLean Stream, surface rupture associated with the Kekerengu Fault is dextral-normal in sense and coincides with pre-existing geomorphology within the range front (Fig. 3). Where it could be measured the slip between McLean Stream and George Stream decreased from c. 6 to 2 m and effectively to zero where the fault bends to the southwest to become the Fidget Fault.

Waiautoa Fault - The north-striking Waiautoa Fault is a short (3.4 km) reverse-sinistral slip fault that ruptured during the Kaikōura earthquake with slip up to c. 1 m. The presence of the Waiautoa Fault is coincident with the course of the Clarence River and Tertiary bedrock structure. In the north, the fault splays from the Kekerengu Fault and is characterized by reverse-slip rolls, thrusts and folds that generally follow pre-existing topography such as risers and alluvial fans. The fault proceeds south toward the Waiautoa homestead, where a reverse-slip rupture with 20-40 cm up-to-the-west motion is mapped across McLean stream in LiDAR images. The Waiautoa Fault is projected to the south according to the presence of surface ruptures and ridge-crest extension, toward the Clarence River bridge. Abutments of the bridge appear to be offset sinistrally by c. 1 m.

THE WAIAUTOA MICROBLOCK – INTERPRETATION

Careful mapping and surveying has allowed for the connection and correlation of the five mapped faults whose junction area form a 2.5 km² triangular area - the Waiautoa microblock. The Fidget Fault bends from an ENE to NE strike to merge with the Kekerengu Fault at the SW corner of the microblock. Minor to zero surface rupture slip on the Fidget Fault evolves abruptly into full surface rupture of the Kekerengu Fault with slip increasing from c. 6 to 10-12 m dextral in the northeast beyond the Waiautoa microblock. Multi-metre dextral slip on the Jordan Thrust reaches a peak at the southwestern end of the microblock at George Stream. To the north, rupture of the Jordan Thrust continues immediately east of, and overlapping with, the Kekerengu Fault, converging from an across-strike width of 350 m between surface ruptures to an observed minimum of <100 m (Fig. 3). In this overlap zone, there is a trade-off or sharing of fault slip between the Jordan and Kekerengu faults. For example, at the southern part of this overlap at George Knob a single long fence line crosses both faults with 3.2 ± 0.4 m dextral slip on the former and 3.4 ± 0.4 m on the latter (Fig. 4). Toward the northern convergence of the Jordan-Kekerengu fault overlap, the Jordan Thrust appears more and more to be a thrust fault that partners the Kekerengu Fault.

The Papatea Fault almost certainly extends to the southwest corner of the Waiautoa microblock, though there is a lack of visible surface slip over c. 1.4 km between

the northwest end of rupture on the Papatea Fault and the Jordan Thrust at George Stream. Similarly, despite a lack of continuous rupture or exposure, we infer that the Waiautoa Fault forms a link between the Kekerengu and Papatea faults and forms the eastern boundary of the Waiautoa microblock. The translation of slip off the Papatea Fault near its northern end and increased slip on the Kekerengu Fault north of Waiautoa Station both equate with a slip and kinematic transfer from these faults onto the Waiautoa Fault.



Figure 3: View to the northeast at George Stream, which is impounded by dextral-normal slip on the Jordan Thrust, and cuts a swath through the native forest. The overlapping rupture of the Kekerengu Fault is upslope to the left of this photo.

DISCUSSION

Observations

Mapping using a variety of tools indicates that the Waiautoa microblock forms a kinematic complexity at the southern end of the Jordan-Kekerengu-Needles rupture set within the 2016 Kaikōura earthquake sequence. This 2.5 km² fault junction area has accommodated the transpressional strain release of five distinct faults or fault segments in a single earthquake, dominated by dextral slip, but including reverse and sinistral motion. These five faults yield slip vectors consistent with the northeast to eastward kinematic motion across faults (relative to the coast and plate boundary). Rupture through this complexity (microblock) heralded the 2nd half of the complex Kaikōura earthquake sequence with the highest slips and strongest ground motions; thus the complexity did not act to inhibit rupture, rather it was central to a burst of fault ruptures, the timings of which can only be deduced from seismology (Kaiser et al., 2017; Duputel and Rivera, 2017). Simplified slip distributions (Fig. 4) indicate that 7-11 m of slip consistently passes into, or out of, the Waiautoa microblock area, thus either: 1) slip is: essentially conserved at a first order across the microblock, or 2) rupture energy (and therefore slip) grew out of the basin to reach a peak on the northern end of the Kekerengu Fault.

Implications

We can learn a lot about rupture process from 3rd order complexities involved in such complex earthquake ruptures. For example:



1) faults can join with hard or soft linkages in 3-D both in a mappable sense and in an individual earthquake rupture. The result of this is that it is important to map faults at the scale to which it is relevant, i.e. if a fault is being mapped for a critical facility or structure, such as a city, dam or nuclear facility, then the detail and the complexity that need to be considered are greater (e.g. Petersen et al., 2010). This paper highlights that because the Kaikōura ruptures have often been mapped at a scale of 1:1000, then far more complexity and a greater array of structures can be observed. This is also true for faults that can be mapped using airborne LiDAR and other digital datasets (e.g. Barth et al., 2012).

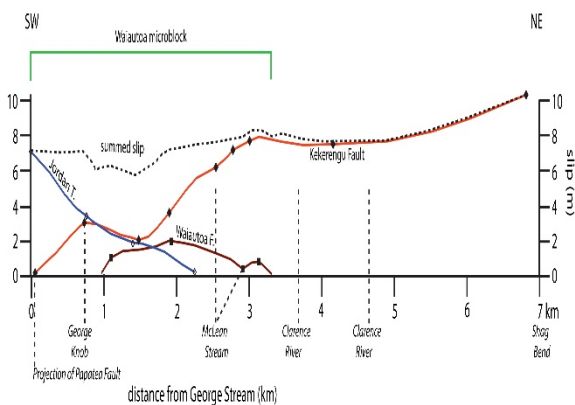


Figure 4: Simplified slip distribution across the Waiataoa microblock summing motion from the Jordan, Kekerengu and Waiataoa faults. Slip profile projected normal to Kekerengu Fault and includes dextral and reverse motion (see black line on Fig. 2).

2) faults can communicate in 3-D to effectively 'share' slip across a complexity. In the context of the Waiataoa Basin, the Jordan and Kekerengu faults overlap one another to share slip, while the Kekerengu and Papatea faults accommodate the complex transition from dextral-reverse to reverse-sinistral motion via the reverse-sinistral slip Waiataoa Fault.

3) small transpressive complexities such as the Waiataoa microblock may not be rupture inhibitors, but rather rupture promoters, or 'kickers'. Rupture of faults surrounding the Waiataoa microblock were involved in kicking off the 2nd half of the Kaikōura earthquake sequence. When such features are mapped for seismic source or hazard purposes they should not necessarily be considered as a structural complexity that will halt through-going fault rupture.

4) finally, along with the long histories of bedrock and geomorphic fault offsets on individual faults of the MFS (Freund, 1971), the Waiataoa microblock must be considered a long-lived geomorphic and kinematic feature as it is responsible for developing secondary topography and controls both the short term passage of the Clarence River, and its long-term history, sitting at the southern end of a 12 km deflection of this important river.

Acknowledgements: We wish to thank those agencies that funded post-earthquake mapping efforts including GeoNet, NSF, MBIE and GEER. This paper was reviewed by Phaedra Upton.

REFERENCES

- Barka, A., Kadinsky-Cade, K. (1988). Strike-slip fault geometry in Turkey and its influence on earthquake activity. *Tectonophysics* 7: 663-684.
- Barrell, D.J.A. (2015). General distribution and characteristics of active faults and folds in the Kaikōura District, North Canterbury. GNS Science Consultancy Report 2014/210. 59 p.
- Barth, N.C., Toy, V.G., Langridge, R.M., and Norris, R.J. (2012). Scale dependence of oblique plate boundary partitioning: new insights from LiDAR, central Alpine Fault, New Zealand: *Lithosphere* 4: 435-448.
- Clark, K.J. and 14 others (2017). Highly variable coastal deformation in the 2016 M_w 7.8 Kaikōura earthquake reflects rupture complexity along a transpressional plate boundary. *Earth and Plan. Science Lett.*: doi: 10.1016/j.epsl.2017.06.048.
- Duputel, Z., Rivera, L. (2017). Long-period analysis of the 2016 Kaikōura earthquake. *Physics of the Earth and Planetary Interiors* 265: 62–66.
- Freund, R. (1971). The Hope Fault: A strike-slip fault in New Zealand. *New Zealand Geological Survey Bulletin* 86: 49 p.
- Hamling, I.J.; and 28 others. 2017 Complex multifault rupture during the 2016 M_w 7.8 Kaikōura earthquake, New Zealand. *Science*, 356 (6334): doi: 10.1126/science.aam7194.
- Kaiser, A.E.; and 25 others (2017). The 2016 Kaikōura, New Zealand, earthquake: preliminary seismological report. *Seismol. Res. Letters*, 88(3): 1-13; doi: 10.1785/0220170018.
- Kearse, J. and 11 others (2017). Surface rupture and slip distribution of the Kekerengu Fault during the M_w 7.8 2016 Kaikōura Earthquake. (this volume)
- Langridge RM, and 14 others (2016a). The New Zealand Active Faults Database. *New Zealand Journal of Geology and Geophysics* 59 (1): doi:10.1080/00288306.2015.1112818.
- Langridge, R.M.; Ries, W.F.; Barth, N.; Howarth, J.D.; Quigley, M.; Farrier, T. (2016b). Assembling lidar swaths along the South Island plate boundary, New Zealand: the South Island 'b4' project. 4 p. IN: McCalpin, J.P.; Gruetner, C. (eds.) *Proceedings of the 7th International Workshop on Paleoseismology, Active Tectonics and Archeoseismology ("PATA Days")*, Crestone, Colorado, USA. Crestone, Colo.
- Litchfield, N.J. and 19 others 2014. A model of active faulting in New Zealand. *N.Z. J. Geol. Geophys.* 57: 32-56.
- Nissen, E., Raghu Malireddi, S., Clark, K., Hamling, I., Langridge, R., Ries, W., Tagliasacchi, A. (2017). Three-dimensional coastal deformation in the M_w 7.8 Kaikōura earthquake from differential airborne lidar. (this volume).
- Petersen, M.D., Dawson, T.E., Chen, R., Cao, T., Wills, C.J., Schwartz, D.P., Frankel, A.D. (2017). Fault displacement hazard for strike-slip faults. *Bull. Seismol. Soc. America* 101: 805-825.
- Rattenbury, M.S., Townsend, D.B., Johnston, M.R. (compilers) (2006). *Geology of the Kaikōura area*. Inst. of Geological & Nuclear Sciences 1:250,000 geological map 13. 1 sheet + 70 p.
- Stirling, M.W. and 56 others (2017). The M_w 7.8 Kaikōura earthquake: surface fault rupture and seismic hazard context. *Bull. N. Z. Society for Earthquake Engineering*, 50(2): 73-84.
- Stirling, M.W. and 19 others, 2012. *National Seismic Hazard Model for New Zealand: 2010 Update*: *Bull. Seismological Soc. America*, v. 102, p. 1514-1542, doi: 10.1785/0120110170.
- Van Dissen, R.; Yeats, R. S. (1991). Hope fault, Jordan thrust, and uplift of the Seaward Kaikōura Range, New Zealand. *Geology* 19: 393-396.
- Wallace, L.M. and 8 others (2012). The kinematics of a transition from subduction to strike-slip: An example from the central New Zealand plate boundary. *Journal of Geophysical Research*, 117, B02405, doi:10.1029/2004JB003241.
- Wesnously, S.G. (2008). Displacement and geometrical characteristics of earthquake surface ruptures: Issues and implications for seismic-hazard analysis and the process of earthquake rupture. *Bull. Seismol. Soc. America* 98: 1609-16.



An Extreme Wave Event in eastern Yucatán, Mexico: evidence of a paleotsunami event during the Mayan times

Lario, Javier (1), Spencer, Chris, (2), Bardají, Teresa (3), Marchante, Ángel (4), Garduño-Monroy, Víctor Hugo (5), Macias, Jorge (6), Ortega, Sergio (7)

- (1) Facultad de Ciencias, UNED, Spain. javier.lario@ccia.uned.es
 (2) Geography and Environmental Management, University of the West of England, UK
 (3) Departamento de Geología, Geografía y Medio Ambiente, Universidad de Alcalá, Spain.
 (4) Grupo de Investigación TARHA, Universidad de las Palmas de Gran Canaria, Spain.
 (5) Departamento de Geología y Mineralogía, Universidad Michoacana de San Nicolás de Hidalgo, México.
 (6) Depto. de A.M., E. e I.O. y Matemática Aplicada, Facultad de Ciencias, University of Málaga, Spain.
 (7) Laboratorio de Métodos Numéricos, SCAI, University of Málaga, Spain.

Abstract: The Yucatán Peninsula, Mexico, has typically been considered a tectonically stable region without significant seismic activity, in contrast, the region is one that is regularly affected by hurricanes. A detailed survey of ca. 100 km of the eastern Yucatan and Cozumel coast identified the presence of ridges containing boulders measuring >1 m, with up to three ridges at some locations. The ridges reach five metres in height and their origin is associated with Extreme Wave Event (EWE) activity. Previously modelled tsunami waves from known seismically active zones in the region (Muertos Thrust Belt and South Caribbean Deformed Belt) are not of sufficient at the Yucatan peninsula to have produced the boulder ridges recorded in this study. The occurrence of hurricanes in this region is more common, but two of the most destructive (Hurricane Gilbert 1988 and Hurricane Wilma 2005) produced coastal waves too small to have created the ridges recorded here. In this paper a new tsunami model has been generated that indicates a tsunami event may have caused the EWE that resulted in the deposition of the boulders ridges.

Key words: Extreme Wave Event, tsunami, boulders, archeoseismology, paleoseismology.

INTRODUCTION

The Yucatan Peninsula of Mexico is a carbonate platform comprised of Eocene-age limestone in the interior, with off-lapping sequences to a Quaternary coastline (Weidie, 1985). The present-day coastline is incised into the Pleistocene shelf margin, reef, and back-reef limestones, which were deposited during the last interglacial sea level highstand (marine isotope stage -MIS 5). The Pleistocene deposits extend inland for some 10 km and form the most recent of a sequence of accreted carbonate units at least 12 m thick (Ward, 1985).

The Peninsula is considered to have been tectonically stable since the late Pleistocene (Szabo et al., 1978), also supported by the lack of recorded historical seismicity (Marquez-Azua et al., 2004).

A detailed survey of ca. 100 km of the eastern Yucatan coast (Quintana Roo and Cozumel Island) identified the presence of beach ridges containing boulders measuring >1 m, up to three ridges at some locations (Figure 1).

The ridges reach five meters in height and their origin is inferred to be associated to Extreme Wave Event (EWE) activity, either tsunamis (not recorded in the area) or hurricanes (frequent in the area). These boulder ridges were recently partially described by Shaw & Benson (2015) and associated to a tsunami event, but no evidence of the tsunami source was provided.

BOULDER RIDGES

There are two main sectors of the boulder ridge that were studied in detail: the coast in Quintana Roo between Playa del Carmen and Caleta Tankah and the eastern coast of Cozumel Island (Figure 1).

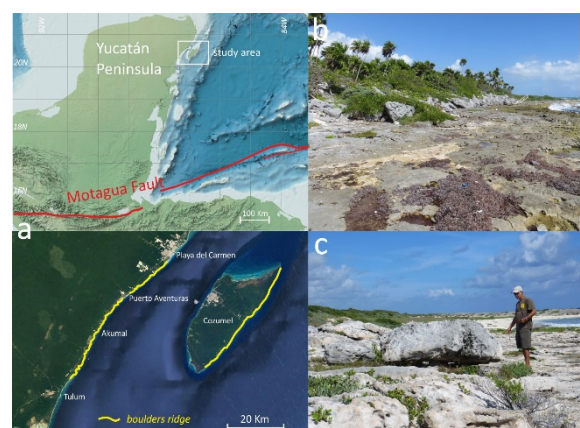


Figure 1; a) Location map of the boulders ridges; b) Boulders ridge at Punta Venado. c) Boulders at eastern Cozumel.

The ridges are composed of accumulations of coral reef boulders, most of them imbricated, individual boulders are more than 1 m length and the ridges reach heights of 5 m. A greater accumulation of boulders is recorded along more rocky sections of the coastline, rocky platforms and capes whilst in caletas (karstic bays) the boulder ridges are absent instead a ridge of sand and reef pebbles and



cobbles is present. Typically, the boulders are from joint bounded blocks (JBB) in the late Pleistocene platforms near msl. At some of the sites a second smaller ridge exists overlapping the main one, the smaller ridge composed mainly of pebbles and cobbles.

More than 100 boulders have been measured (a, b and c dimensions, height, distance to sea and main lithology) and photographed for photo restitution. The blocks and boulders represent heterogeneous reef-rock and consist of varying percentages of several different lithofacies. The bulk density of similar deposits has been determined to be between 2.07-2.40 g/cm³ by Engel & May (2012).

Table 1 presents data from the main boulders representative of the ridge (by weight, volume and height). The application of different approaches to calculate the wave heights inferred from the boulder record show that the minimum wave height for the displacement ranges from 2.5 to 2.9 m for a tsunami (Ht) and from 10.5 to 11.5 m for a severe storm (Hs) using formulas for a JBB scenario by Engel & May (2012). The submerged scenario of Nott (2003) produces ranges from 2.0 to 2.4 m (Ht) and from 8.0 to 9.8 m (Hs).

Boulder	t	JBB Ht	JBB Hs	Sub. Ht	Sub. Hs
BPM6	1.39	1.77	7.06	0.50	1.99
BPM9	8.35	2.55	10.21	1.64	6.54
BPM10	5.66	1.91	7.64	1.06	4.26
BA12	1.70	2.00	8.02	0.35	1.41
BN1	1.59	1.79	7.16	0.39	1.57
BN5	1.38	1.81	7.25	0.51	2.03
BCZ3	0.40	0.45	1.81	1.69	6.77
BCZ4	0.61	0.76	3.05	1.09	4.34
BCZ6	8.03	1.96	7.83	1.85	7.42
BCZ7	4.06	2.86	11.45	0.61	2.43
BCZ8	1.27	0.72	2.86	2.44	9.76
BPA1	1.73	2.08	8.30	0.29	1.15
BPA2	2.20	2.27	9.07	0.51	2.03
BPA3	1.47	1.84	7.35	0.33	1.34
BPA5	1.69	2.12	8.49	0.29	1.14
BPA9	2.34	2.39	9.54	0.30	1.20
BPA10	5.15	2.58	10.31	0.73	2.91
BPA11	2.36	1.69	6.78	0.68	2.73
BAK3	1.89	2.00	8.02	0.35	1.42
BAK4	1.42	2.08	8.30	0.34	1.35
BAK6	1.35	2.05	8.21	0.35	1.41
BKAN4	4.85	1.67	6.68	1.55	6.20
BKAN9	2.74	1.22	4.87	2.02	8.09
BKAN10	4.69	2.39	9.54	0.71	2.83

Table 1: Tsunami wave height (Ht) and storm wave height (Hs) calculate for each boulder in each scenario (JBB: Join-bounded blocks; Sub.: Submerged blocks). Weight in toons (t).

TSUNAMIS VS. HURRAICINE ORIGIN

As has been outlined, the Yucatan Peninsula has been considered to be a tectonically stable area since the late Pleistocene. Tsunami catalogues in the Caribbean area show no recorded events for the Quintana Roo coast (compiled in Engel et al., 2016). The tsunami waves that could be produced by earthquakes from known seismically

active zones in the region (Muertos Thrust Belt and South Caribbean Deformed Belt) would not have been sufficient at the Yucatan peninsula to have produced the boulder ridges recorded in this study. Models of tsunami propagation in the Caribbean (Engel et al., 2016) show that a tsunami generated by a Mw 7.99 earthquake from the Muertos Thrust Belt (MTB) cannot reach the Yucatan coast. However, a tsunami generated by a Mw 8.8 earthquake generated in South Caribbean Deformed Belt (SCBD) can reach the north-eastern Yucatan coast with a wave height <1.0 m, thus not sufficient to produce the ridges discussed in this study.

The occurrence of hurricanes in this region is more common, two of the most destructive produced 6-8 m high waves at the coast and inundation up to 5 km inland (Hurricane Gilbert, 1988), and 8 m high waves at the coast (Hurricane Wilma, 2005), but those coastal waves are still too small to have produced the ridges recorded here.

In order to locate a seismic source capable of generating a tsunami wave of sufficient size to reach the eastern coast of Yucatan and thus, corroborate a tsunami origin for the boulder ridges, a new model has been generated. The USGS Earthquake catalogue records an earthquake of Mw 7.3 offshore of Honduras in 2009 associated with the Motagua fault (Figure 2), showing that there is an active structure capable of generating significant seismic events in the region.

A model of a tsunami generated by a seismic event from the Motagua fault has been generated simulating an earthquake Mw 7.6, 19 km depth with a 110 length and 26 km width rupture area. The numerical code used is Tsunami-HySEA, this is a GPU-based shallow water code, developed by the EDANYA Group (University of Málaga) and extensively benchmarked for tsunami simulations (Macías et al., 2017). For the numerical simulation, a two-way nested mesh technique (as in Macías et al., 2016) is used. The global mesh that covers all the computational domain has a resolution of 15 arc sec (~450m). Then six nested meshes, with an enhanced resolution of 0.9375 arc sec (~28 m) are used in the coastal strip to better assess tsunami wave height in this region.

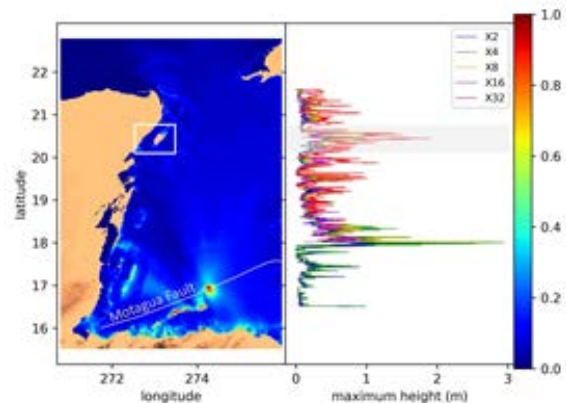


Figure 2. Model of a tsunami generated by an earthquake Mw 7.6 along Motagua fault.



Results at x32 resolution show that a wave height > 2.0 m would be generated in the studied area (Figure 2). Therefore, it is reasonable to assign the main boulder ridge to a tsunami generated by an earthquake $M_w > 7.5$ offshore in the eastern Caribbean sector of Motagua fault. The smaller ridge overlapping the main boulder ridge was generated by the Hurricane Wilma in 2005 (witness's communication), demonstrating that destructive Hurricanes do not have sufficient energy in this area to generate the large boulders ridges recorded.

TSUNAMI AGE AND PALEOSEISMIC IMPLICATIONS

In some places within the region, it is possible observe Mayan buildings constructed over and therefore post-dating the boulder ridges, for example in the Xcaret complex or Punta Chile (SW XpuHa). Despite the different phases of construction, these remains are Costa oriental in style (Eastern coast), meaning post classic Maya period, between 900-1521 AD (Andrews and Andrews, 1975; Covarrubias and Rojas, pers.comm.). Shaw & Benson (2015) recorded peat deposits beneath and so pre-dating the main boulder ridge near Akumal. These were dated using C14 to ~471 AD suggesting that the tsunami event took place between ca.500-800 AD, during the late Classic period. It is remarkable that there is no evidence of settlements prior to the post-classic period in this coastal area, and it may be that any small settlements that did exist were affected and covered by the tsunami deposits.

The confirmation of a likely tsunami event with a potential surge of an $M_w > 7.5$ earthquake on the Motagua fault implies that even if a long recurrence interval exists, destructive tsunami episodes can reach the eastern Yucatan coast. Despite the belief that the area has been tectonically stable since the late Pleistocene this study founded more evidences of seismic activity during Mayan times, such as archeoseismological features located in Mayan sites (tilted walls, "antiseismic" fabric...), evidence of seismic events in submerged caves systems (tilted speleothems, collapses and orientated speleothems...) as well as faults affecting the late Pleistocene and Holocene reef deposits (eastern Cozumel), that still under study.

CONCLUSIONS

A semi-continuous boulder ridge up to 5 m a.s.l, has been observed on the eastern coast of the Yucatan Peninsula and Cozumel island, generated by an Extreme Wave Event. The application of different approaches demonstrates that waves of between 2.0-2.9 m (in the case of tsunami origin) and between 8.0-11.5 m (in the case of Hurricane origin) would need to be generated to result in the accumulation of these boulders. Most of the possible tsunami source areas located in East Caribbean are not capable of generating a tsunami that would reach the Yucatan coast. However, as demonstrated through model simulation in this study, the Motagua Fault section located in the SW

Caribbean basin can generate a tsunami with waves of between 2.0-3.0 m high at the eastern Yucatan coast, resulting from an earthquake of $>M_w 7.5$.

This and other evidence demonstrates the occurrence of seismic activity during late Pleistocene and Holocene in the Eastern Yucatan Peninsula and surrounding areas illustrating the necessity to review all mitigation protocols in this area related to seismic and tsunami hazards.

Acknowledgements: Financial support by Spanish government projects CGL2013-42847-R and CGL2015-69919-R and SIMURISK (MTM2015-70490-C2-1-R). The GPU and multi-GPU computations have been performed at the Unit of Numerical Methods (UNM) of the Research Support Central Services (SCAI) of the University of Malaga. It is a contribution to the IGCP Project 639 "Sea Level Change from Minutes to Millennia".

REFERENCES

- Andrews, E.W., & Andrews, A.P, 1975. A preliminary study of the ruins of Xcaret, Mexico, with notes on other archaeological remains on the central east coast of the Yucatan Peninsula. Middle American Research Institute, Publication 40, Tulane University, New Orleans.
- Engel, M., & May, S.M., 2012. Bonaire's boulder fields revisited: evidence for Holocene tsunami impact on the Leeward Antilles. *Quaternary Science Reviews* 54, 126-141.
- Engel, M., Oetjen, J., May, S.M. & Brückner, H., 2016. Tsunami deposits of the Caribbean – Towards an improved coastal hazard assessment. *Earth-Science Reviews* 163, 260-296.
- Macías, J., Castro, M.J., Ortega, S., Escalante, C., & González-Vida, J.M., 2017. Performance benchmarking of Tsunami-HySEA model for NTHMP's inundation mapping activities. *Pure and Applied Geophysics* 174, 3147–3183.
- Macías, J., Mercado, A., González-Vida, J.M., Ortega, S., & Castro, M.J., 2016. Comparison and numerical performance of Tsunami-HySEA and MOST models for LANTEX 2013 scenario. Impact assessment on Puerto Rico coasts. *Pure and Applied Geophysics* 173, 3973–3997.
- Marquez-Azua, B., Cabral-Cano, E., Correa-Mora, F., & DeMets, C., 2004. A model for Mexican neotectonics based on nationwide GPS measurements, 1993–2001. *Geofísica Internacional* 43, 319–330.
- Nott, J., (2003). Waves, coastal boulder deposits and the importance of the pretransport setting. *Earth Planet. Sci. Lett.* (210), 269-276.
- Shaw, C.E., & Benson, L., 2015. Possible Tsunami Deposits on the Caribbean Coast of the Yucatán Peninsula. *Journal of Coastal Research* 31, 1306-1316.
- Szabo, B.J., Ward, W.C., Weidie, A.E., & Brady, M.J., 1978. Age and magnitude of the late Pleistocene sea-level rise on the eastern Yucatan Peninsula. *Geology* 6, 713–715.
- Ward, W.C., 1985. Quaternary geology of the northeastern Yucatan Peninsula. In: *Geology and hydrogeology of the Yucatan and quaternary geology of the Northeastern Yucatan Peninsula*. (Ward, W.C., Weidie, A.E., & Back, W. eds). New Orleans Geological Society, 23-53.
- Weidie, A.E., 1985. Geology of the Yucatan Platform. In: *Geology and hydrogeology of the Yucatan and quaternary geology of the Northeastern Yucatan Peninsula* (Ward, W.C., Weidie, A.E., & Back, W. eds). New Orleans Geological Society, 1–19.



Trend and policy of Quaternary fault research in Korea after 2016 Gyeongju earthquake

Seung Ryeol Lee (1), Jin-Hyuck Choi (1)

(1) Geology Division, Korea Institute of Geoscience and Mineral Resources (KIGAM), Daejeon 34132, Korea. leesr@kigam.re.kr

Abstract: The Gyeongju earthquake ($M_L = 5.8$) that occurred on 12th September, 2016 ranks as the largest earthquake ever instrumentally recorded in mainland of Korea. It shocked the government as well as the public, because they have never considered earthquakes as serious natural hazard in Korea. The Gyeongju earthquake has been interpreted to occur as a result of reactivation of the central part of the Yangsan fault system (YFS). The genetic connection between the Gyeongju earthquake and the YFS immediately raised the necessity of nationwide survey and evaluation of potential active faults in Korea. For this purpose the government made a new R&D program of active fault research jointly operated by several government departments. Here, we introduce the general outline of Korea's new active fault R&D program. Through this introduction and advertisement we look forward to international cooperation with research groups with experiences in advanced research techniques for surveying active faults.

Key words: Quaternary fault, South Korea, Gyeongju earthquake, Yangsan fault system.

INTRODUCTION

On 12th September 2016 the biggest ($M_L = 5.8$) instrumental earthquake occurred in near Gyeongju city and about 600 aftershock events continued for at least 6 months around the epicenter area. The earthquake, named the Gyeongju earthquake, shocked the Korean government as well as the public and has completely changed the common belief that the Korean Peninsula is tectonically stable and is quite a safe from severe earthquake hazard. After the Gyeongju earthquake, there are increasing concerns about future earthquakes in society. These concerns include worrying about safety of nuclear power plants that are concentrated near the epicenter of the earthquake.

The Gyeongju earthquake occurred in the vicinity of the Yangsan Fault System (YFS) (Fig. 1). The YFS has been suspected to be seismologically active for a long time (Lee & Na, 1983), which is clearly confirmed by the Gyeongju earthquake. As genetic connection between the Gyeongju earthquake and the YFS has been manifested, the government was forced to make new R&D programs to investigate and evaluate potential active faults in Korea as follow-up measures against the Gyeongju earthquake last year. The new R&D program is launched as a joint program operated by several government departments. Here we introduce the general outline of Korea's new active fault R&D program. In particular, we focus on the role and research plan of Korea Institute of Geoscience and Mineral Resources (KIGAM) which, as Korea's sole geological survey, is granted a role in the advanced technical development of active fault research in Korea. The main purpose of attending this meeting is to advertise Korea's new active fault R&D program to active fault research groups worldwide. Through this opportunity we look forward to international cooperation with research groups with experiences in advanced research techniques for surveying active faults, which is critical to fulfil the KIGAM's role within Korea's new active fault R&D program.

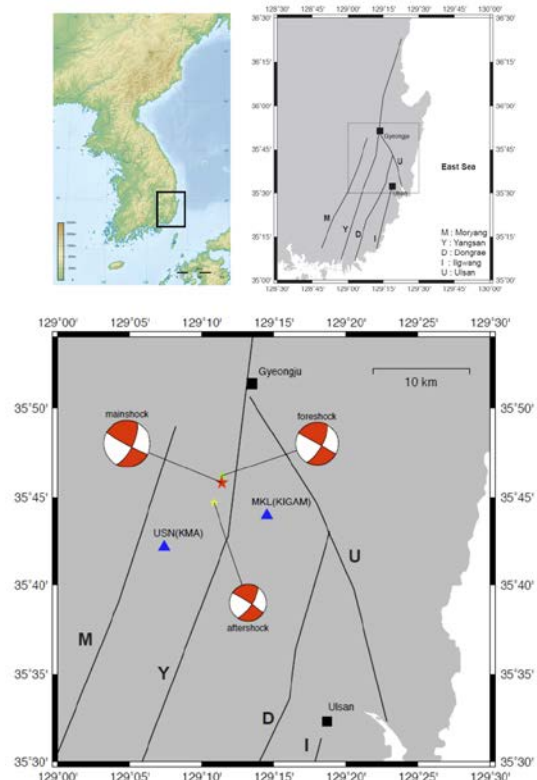


Figure 1: Map of Korean Peninsula (upper left) where the rectangle is enlarged to show the locations of the main fault traces of the Yangsan fault system (upper right). The rectangle area is further enlarged to show the Gyeongju earthquake sequence (bottom). Moment tensor solutions for all three events are presented. (modified after Lee & Song, 2016). Abbreviations: M, Moryong fault; Y, Yangsan fault; D, Dongrae fault; I, Ilgwang fault; and U, Ulsan fault.



OVERVIEW OF THE GYEONGJU EARTHQUAKE

A sequence of moderate-sized earthquakes with local magnitudes (M_L) 5.1 and 5.8 occurred on September 12, 2016 near the city of Gyeongju (Fig. 1). The largest aftershock of M_L 4.5 occurred one week later, and about 600 aftershock events continued for at least 6 months around the epicenter area. The focal depth of the earthquakes is about 15 km and the earthquakes occurred on a NNE-directed, right-lateral strike-slip faulting parallel to the strike of the Yangsan fault (Lee & Song, 2016). Kim et al. (2017) interpreted that the earthquake occurred on a subsidiary fault in the western damage zone of the Yangsan fault near epicenter (Kim et al., 2017).

A MULTI-DEPARTMENT, JOINT R&D PROGRAM OF ACTIVE FAULT RESEARCH IN KOREA

In the past most of active fault studies were conducted to provide basic site information needed for constructing nuclear power plants. Since seismic hazard was not considered serious, even though several active faults were found, it was used to establish the design basis for the construction of the nuclear power plant. However, after the Gyeongju earthquake, the government and the public have raised concerns about the possibility of a reduction or concealment of the previously surveyed results of active faults, and requested a transparent, impartial disclosure of the future research results of active faults. Therefore, a new active fault research program is designed to meet these requirements as well as to prevent duplicate investments.

A multi-department, joint R&D program of active fault research is supervised by a Joint Project Agency (tentative designation) and consists of three individual projects supported by Ministry of Public Safety and Security (MPSS), Nuclear Safety and Security Commission (NSSC), and Ministry of Science, ICT and Future Planning (MSIP) (Fig. 2). The project originally proposed by Korea Meteorological Administration (KMA) was excluded from the program because it does not deal with active fault but plans to study regional shallow and deep crustal structures of the Korean Peninsula.

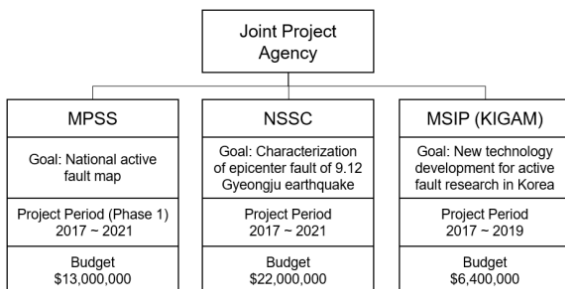


Figure 2: Organization of a multi-department, joint R&D program of active fault research, which shows the participating government departments, main goal, project period and presumed budget.

The main purpose of the project supported by MPSS is to make a nationwide active fault map (Fig. 2). This project consists of 5 phases, each of which is composed of 5 years. The surveys of the first phase (2017 – 2021) will mainly cover the south-eastern area of the Korean Peninsula, where most of the potential active faults are located, including the YFS. It takes an approximate budget of \$13 Million. Recurrence interval of faulting events in Korea is assumed to be quite long (approximately in the range of 7 - 10 ka) (Kyung, 2010). Therefore, paleoseismological approach will be largely applied to investigate active faults in Korea.

NSSC is a supervisory authority for nuclear power plants in Korea. The public as well as the government are worried about safety of nuclear power plants after the Gyeongju earthquake, and requested reliable re-evaluation on the seismic design of the plants. The main goal of the project supported by NSSC is to characterize the epicenter fault that caused the Gyeongju earthquake in order to reassess seismic design of existing nuclear power plants (Fig. 2). Because the focal depths of the Gyeongju earthquake are about 15 km, this project will take 5 years (2017 – 2021) and aims to build up a microearthquake monitoring system in order to characterize the epicenter fault of the Gyeongju earthquake. It will also try to image deep crustal structure around the epicenter using magnetotellurics (MT) survey. It takes an approximate budget of \$22 Million.

MSIP is a ministry responsible for science and technology R&Ds in Korea, and defines a mission for new technology development for active fault research to KIGAM. The budget is approximately \$6.4 Million for the 3 year (2017 – 2019) project. KIGAM’s role and research activity is explained in the next section.

ACTIVE FAULT RESEARCH OF KIGAM

The active faults in Korea have been known to be characterized by slow slip rates (ca. 0.1 – 0.06 m/ka) and long recurrence interval (ca. 7 – 15 ka) (Kyung, 2010). In addition, most of the historic and instrumental earthquakes are small to moderate-sized in magnitude, which leaves no significant evidence for surface ruptures (Kyung, 2010). These features make it very difficult to find a good outcrop for paleoseismological investigation. Even when a proper site is found, it is usually located on private property, and it is hard to get permission for trench work.

Despite of these challenging obstacles and problems, KIGAM, as the only geological survey in Korea, undertakes the assignment given by the government to develop new scientific technology for improving the level of research of active faults in Korea. In this project, first of all, KIGAM focuses on developing scientific techniques to detect and trace buried faults in the central part of the Yangsan fault. Modern image analysis (e.g., LiDAR) is applied for regional and local geomorphic analysis. 3D image analysis using drone is also applied to get detailed geomorphic features on a local scale. Preliminary analysis of LiDAR images succeeded to identify several sites with apparent surficial



displacements of 17 – 250 m. Geologic and geophysical investigations are now undertaken at those sites for trench works. Geophysical (e.g., electrical resistivity survey, shallow seismic survey, GPR) and borehole techniques are combined with traditional geologic, geomorphic and quaternary mapping techniques in order to detect and trace the buried active faults. Advanced methods of quaternary geochronology are developed to guarantee reliable age constraints on fault activity. All of the information acquired from these scientific techniques are realized in the form of 'thematic map of faults'. International cooperation with research groups with experience in advanced research techniques for surveying active faults is actively planned to raise the research level of active faults in Korea.

Acknowledgements: This work was supported by a grant 2017-MPSS31-006 (Research and Development of Active Fault of Korean Peninsula) from Supporting Technology Development Program for Disaster Management funded by Korean Ministry of Public Safety and Security (MPSS).

REFERENCES

- Kim, Y.-S., Kim, T., Kyung, J.B., Cho, C.S., Choi, J.-H., & Choi, C.U., 2017. Preliminary study on rupture mechanism of the 9.12 Gyeongju earthquake. *Journal of the Geological Society of Korea*, 53 (3), 407-422 (in Korean with English abstract).
- Kyung, J.B., 2010. Paleoseismological study and evaluation of maximum earthquake magnitude along the Yangsan and Ulsan fault zones in the southeastern part of Korea. *Jigu-Mulli-wa-Mulli-Tamsa*, 13 (3), 187-197 (in Korean with English abstract).
- Lee, K., & Na, S.H., 1983. A study of microearthquake activity of the Yangsan fault. *The Journal of the Geological Society of Korea* 19 (3), 127-135.
- Lee, K., & Song, S.G., 2016. A Preliminary Study on the Gyeongju Earthquakes. *Proceedings of National Academ of Science, Korea*, 55 (2), 25-39.



Earthquake environmental effects induced by the 2017 June 12, Mw 6.3 Lesvos (North Aegean Sea, Greece) earthquake

Lekkas, Efthymios, Mavroulis, Spyridon, Skourtsos, Emmanuel, Andreadakis, Emmanouil, Antoniou, Varvara Kranis, Charalambos, Soukis, Konstantinos, Lozios, Stylianos, Alexoudi, Vassiliki

Department of Dynamic Tectonic Applied Geology, Faculty of Geology and Geoenvironment, School of Sciences, National and Kapodistrian University of Athens, Panepistimiopolis, Athens 15784, Greece, smavroulis@geol.uoa.gr

Abstract: On June 12, 2017 an Mw 6.3 earthquake struck Lesvos Island (Northeastern Aegean, Greece). Its epicenter is located offshore southeastern Lesvos at depth of about 13 km. The main shock was generated by a NW-SE striking and SW-dipping normal fault that constitutes the northern margin of the offshore Lesvos basin. It caused extensive secondary environmental effects. Ground cracks were observed along the main tectonic structure of the affected area, the onshore active NW-SE striking and SW-dipping Polichnitos fault as well as close to river banks and the coastline occurred southeast of the worst affected area. Slope movements included landslides, rockfalls and rockslides. A small tsunami generated offshore southeastern Lesvos is attributed either to sea bed displacement or more probably to submarine landslides. The size of total affected area based on the generated EEE was around 100 km² corresponding to a VIII_{ESI-07} epicentral intensity.

Key words: Lesvos; Greece; Earthquake environmental effects; Seismic intensity; ESI 2007 scale.

INTRODUCTION

On June 12, 2017 (12:28 GMT) a strong earthquake struck Lesvos Island (Northeastern Aegean, Greece) (Fig. 1). It was estimated to be Mw 6.3 (Papadimitriou et al., 2017). It was predominantly felt on Lesvos Island and throughout the North Aegean Islands and western Turkey. It claimed the life of a woman due to building collapse and 15 injured due to collapsing buildings and falling debris. The southeastern part of Lesvos suffered the most by the earthquake in its natural environment, building stock and infrastructures.

Based on the preliminary seismological data provided by the University of Athens (Papadimitriou et al., 2017), the earthquake epicentre is located offshore southeastern Lesvos (Fig. 1). The main shock is located at depth of about 13 km and the fault plane solutions demonstrated a NW-SE striking and SW-dipping normal fault that constitutes the northern margin of the offshore Lesvos basin (Fig. 1).

The 2017 Lesvos earthquake induced extensive secondary earthquake environmental effects (EEE) comprising ground cracks, slope movements and tsunami waves.

GEOLOGICAL AND SEISMOTECTONIC SETTING

The eastern Lesvos comprises alpine rocks, including a lower unit of Upper Paleozoic to Triassic schists and marbles, underlying tectonically large ultrabasic masses (Lesvos ophiolites) (Hecht, 1972, 1974a, b, c; Pe-Piper, 1978; Katsikatsos et al., 1982; Pe-Piper & Piper, 1993). As regards more recent formations, continental sedimentation occurred during Pleistocene in the coastal region of Vatera located in southeastern Lesvos (Fig. 1), when a relatively thick sequence of conglomerates and clays was deposited.

The main active faults of Lesvos are the Gavathas, Skala Eressos, Kalloni - Agia Paraskevi, Polichnitos - Plomari, Agios Isidoros - Cape Magiras and Geras Gulf fault zones (Chatzipetros et al., 2013) (Fig. 1). The main active fault of the affected area is the Polichnitos - Plomari fault. The NW-SE striking and SW-dipping Polichnitos - Plomari fault is about 13.5 km (Fig. 1), defines the long linear series of hills in the areas between Polichnitos and Plomari (Fig. 1) and is associated with the thermal activity of the Polichnitos geothermal field (Günther et al., 1977). Its footwall is composed of ophiolites, schists and marbles, while its hanging wall consists of Pleistocene and Holocene deposits (Hecht, 1972, 1974c).

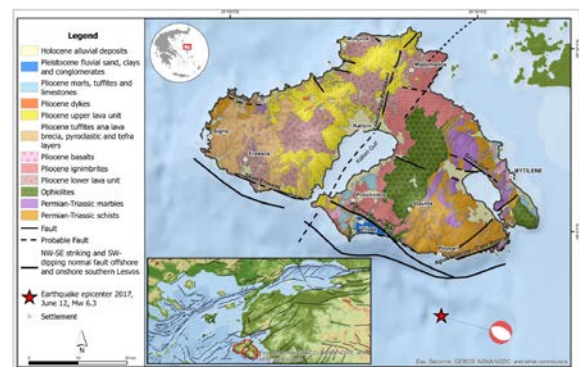


Figure 1: The 2017 Lesvos (Northeastern Aegean Sea, Greece) earthquake was generated offshore southeastern Lesvos by a NW-SE striking and SW-dipping normal fault that constitutes the northern margin of the offshore Lesvos basin located southwards of the island.

Based on the historic and instrumentally recorded seismicity of Lesvos, it is concluded that the island has been repeatedly struck by earthquakes from 1383 to present with magnitudes varying from 6.2 to 7.4 and seismic intensities of up to X (Papazachos & Papazachou, 2003; Taxeidis 2003; Ambraseys 2009) with significant



effects to the local population, the natural environment and the building stock. It is not the first time that the southeastern Lesvos is the worst affected by an earthquake. Similar distribution of seismic intensities were also reported after the 1845 (October 11, $M=6.8$, $I_{MAX}=X$), 1867 (March 7, $M=7.0$, $I_{MAX}=X$), 1953 (March 18, $M=7.4$, $I_{MAX}=IX+$) and 1981 (December 19, $M=7.2$, $I_{MAX}=VIII$) (Fig. 2).

Based on historical seismicity data (Papazachos & Papazachou, 2003; Taxeidis, 2003; Ambraseys, 2009) and the distribution of seismic intensities of historical and instrumentally recorded earthquakes in Lesvos wider area, it is concluded that the highest seismic intensities have undoubtedly been observed in the southeastern Lesvos (Fig. 2). On the contrary, the southwestern part of Lesvos has suffered low seismic intensities (Fig. 2).

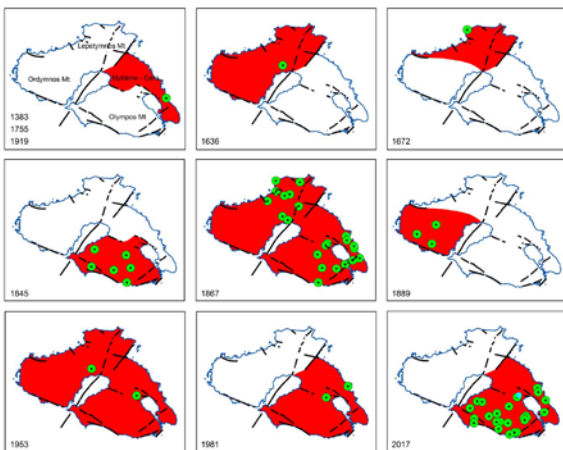


Figure 2: Areas with high contrasts in seismic intensities during large earthquakes in Lesvos. The maximum intensities have undoubtedly been observed in the southern and eastern part of Lesvos during the 1845, 1867, 1953 and 1981 earthquakes (data from Papazachos & Papazachou, 2003; Taxeidis, 2003; Ambraseys, 2009).

EARTHQUAKE ENVIRONMENTAL EFFECTS

Ground cracks

NW-SE ($N310^\circ$) striking ground cracks were observed disrupting the embankment of a provincial road close and parallel to the Polichnitos fault (Fig. 3, 4a). They were 50 meters long and 1 cm wide (Fig. 4b). However, tectonic surface deformation (uplift or subsidence) and associated structures were not detected on both sides of the cracks. However, large fragment of tectonic breccia were detached from fault surfaces formed on ophiolites and scree were detached from slopes and rolled down towards the rural road, while already existing joints in ophiolites were widened.

Ground cracks were also observed close to Agia Katerina area and parallel to the banks of Almyropotamos River (Fig. 3, 4c) with length of about 5 m and width of 1 cm as well as in Vatera coastal area close and parallel to the coastline with length of 10 m and width of 1 cm (Fig. 3, 4d) disrupting the asphalt pavement in both cases. Displacement was also not detected on both sides of the cracks in Agia Katerina and Vatera sites.



Figure 3: Environmental effects induced by the 2017 Lesvos earthquake including ground cracks, slope movements and tsunami wave.



Figure 4: Ground cracks (a) close and almost parallel to Polichnitos fault, (b) on the road close to the coastline in Vatera coastal area, (c) on the road close and almost parallel to banks of the Almyropotamos River. All sites are located in the hanging wall of the Polichnitos fault, close to the worst affected area of Vrissa and are considered as secondary EEE.

Slope movements

The 2017 Lesvos earthquake induced slope movements included mainly landslides, rockfalls and rockslides. They were observed in several sites of the earthquake-affected area including Palaeochori (Fig. 5a-b), Agios Isidoros (Fig. 5c-d) and Akrasi (Fig. 5e) sites as well as along the road leading from Plomari to Melinda (Fig. 5f, g, h). They resulted in partial damage to the road network including cracks and craters in the asphalt pavement and deformation of road protection barriers as boulders bounced across the roads, damage to adjacent building structures and related facilities (Fig. 5h) and temporary or permanent traffic disruption.



The aforementioned slope movements are attributed to: (a) pre-existing instability conditions formed in geotechnically unstable areas and landslide zones, (b) presence of active faults forming intense relief with high and abrupt slopes and scarps, as well as (c) suitable geometry of beds and discontinuities dipping towards the free face of slopes.

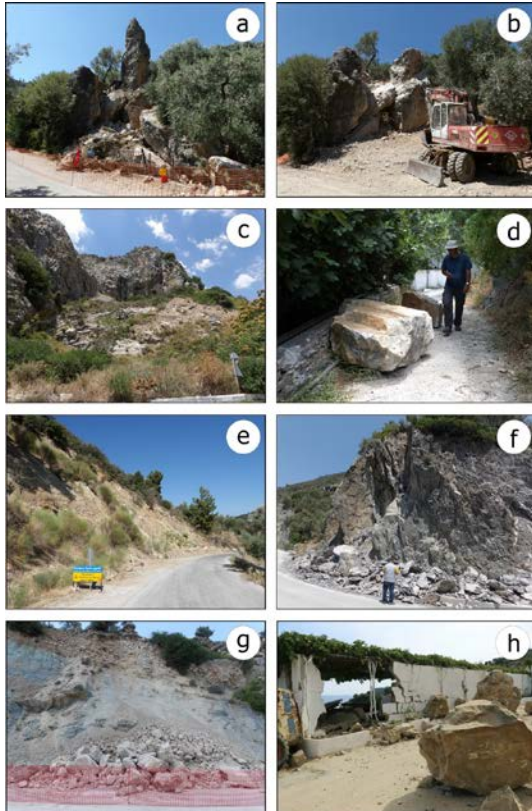


Figure 5: Slope movements were induced by the 2017 Lesvos earthquake in the following areas: (a-b) Palaeochori, few hours after the earthquake (a) and the same site a month later (b), (c-d) Agios Isidoros, (e) Akrasi, (f, g, h) along the road from Plomari to Melinta, resulting in damage to the road network, temporary traffic disruption and destruction of adjacent buildings and facilities.

Tsunami waves

After the earthquake, a small tsunami was generated offshore southeastern Lesvos and was reported by residents in the coastal area of Plomari and mainly in Plomari port (Fig. 3). It is characterized as a small tsunami of peak-to-peak amplitude of ~30 cm (Papadopoulos et al., 2017). The same wave of less amplitude was observed in Foca (Turkey). Preliminary analysis of various tide-gauge stations in the Aegean Sea area showed disturbances with amplitudes of few cm which may be due to the aforementioned tsunami (Papadopoulos et al., 2017).

ENVIRONMENTAL SEISMIC INTENSITY 2007 (ESI 2007)

The Environmental Seismic Intensity 2007 (ESI 2007) scale allows an assessment of seismic intensity based solely on primary and secondary EEE (Michetti et al., 2007). Primary EEE are directly linked to the earthquake energy and particularly to the surface expression of the causative seismic fault and include surface faulting and

permanent ground dislocation induced by tectonic uplift and tectonic subsidence, while secondary EEE are caused by the ground shaking and include hydrological anomalies, anomalous waves/tsunamis, ground cracks, slope movements, trees shaking, liquefaction phenomena, dust clouds and jumping stones (Michetti et al., 2007). Based on the provided guidelines by Michetti et al. (2007) updated by Audemard et al. (2015) the epicentral intensity (I_0) and the local intensities can be assessed. Surface faulting parameters such as the surface rupture length and the maximum surface displacement can be used to assess the epicentral intensity (I_0), while the dimensions and the areal distribution of secondary EEE occurred in different sites are used to assess the local intensities.

The secondary EEE induced by the 2017 Lesvos earthquake and their spatial distribution were considered appropriate for the application of the ESI 2007 scale based on the guidelines developed by Michetti et al. (2007) and the evaluation of the epicentral intensity (I_0) and local intensities occurred in different sites. The total area distribution of secondary EEE has been used for assessing epicentral intensity (I_0). The size of total affected area was around 100 km² corresponding to an intensity VIII_{ESI-07}.

VI_{ESI-07} intensity is assigned to all sites with observed ground cracks (Fig. 6) based on their dimensions including length varying from 5 to 50 m and width of up to 1 cm.

VI_{ESI-07} intensity is assigned to Plomari coastal area (Fig. 6) based on the peak-to-peak amplitude (~30 cm) of the reported tsunami.

As regards the sites with earthquake induced slope movements, based on the volume of the mobilized material, V_{ESI-07} intensity is assigned to Palaeochori, Plomari, Akrasi and Agios Isidoros sites. V-VI_{ESI-07} intensity is assigned along the road from Plomari to Melinta (Fig. 6).



Figure 6: ESI 2007 Seismic intensities assigned to sites with environmental effects induced by the 2017 Lesvos earthquake.



CONCLUSIONS

The June 12, 2017 Mw 6.2 Lesvos earthquake induced secondary EEE in the southeastern part of the island. Ground cracks were observed close to the main onshore active fault of the affected area, close and parallel to river banks and the southern coastline of the most affected area and attributed to the ground shaking and the pre-existing instability conditions formed close to river banks and the coastline.

Slope movements were observed in various sites of the affected area along pre-existing geotechnically unstable zones characterized by frequent generation of slope failures even before the earthquake, which acted as a triggering mechanism.

Tsunami was reported in Plomari port and attributed probably to offshore landslides close to the epicentral area.

Based on the application of the ESI 2007 scale, seismic intensities vary from V to VI taking into account the dimensions of the recorded EEE.

Acknowledgements: All funding for this work were provided by the Environmental, Disaster and Crisis Management Strategies Masters Degree Program of the Department of Geology and Geoenvironment of the National and Kapodistrian University of Athens.

REFERENCES

- Ambraseys, N., 2009. *Earthquakes in the Mediterranean and Middle East: a multidisciplinary study of seismicity up to 1900*. Cambridge University Press. 947 p.
- Audemard, F., Azuma, T., Baiocco, F., Baize, S., Blumetti, A.M., Brustia, E., Clague, J., Comerci, V., Esposito, E., Guerrieri, L., Gurpinar, A., Grützner, C., Jin, K., Kim, Y.S., Kopsachilis, V., Lucarini, M., McCalpin, J., Michetti, A.M., Mohammadioun, B., Morner, N.A., Okumura, K., Ota, Y., Papathanassiou, G., Pavlides, S., Perez Lopez, R., Porfido, S., Reicherter, K., Rodriguez Pascua, M.A., Roghazin, E., Scaramella, A., Serva, L., Silva, P.G., Sintubin, M., Tatevossian, R., Vittori, E. 2015. *Earthquake environmental effect for seismic hazard assessment: the ESI intensity scale and the EEE catalogue*. Mem. Carta geologica d'Italia, 97 p.
- Chatzipetros, A., Kiratzi, A., Sboras, S., Zouros, N., Pavlides, S. 2013. Active faulting in the north-eastern Aegean Sea Islands. *Tectonophysics* 597-598, 106-122.
- Günther, R., Kappelmeyer, O., Kronberg, P. 1977. Zur prospektion auf geothermale anomalien, erfahrungen einer modelluntersuchung in Polichnitos, Lesbos (Griechenland). *Geologische Rundschau* 66, 10-33.
- Hecht, J. 1972. Geological map of Greece, Plomari-Mytilini sheet. Institute of Geology and Mineral Exploration of Greece scale 1:50.000.
- Hecht, J. 1974a. Geological Map of Greece (1:50.000), Lesbos Island, Sheet «Methymna», IGME.
- Hecht, J. 1974b. Geological map of Greece, Eressos sheet. Institute of Geology and Mineral Exploration of Greece scale 1:50.000.
- Hecht, J. 1974c. Geological map of Greece, Polichnitos sheet. Institute of Geology and Mineral Exploration of Greece scale 1:50.000.
- Katsikatsos, G., Mataragas, D., Migiros, G., Triandafyllou, E. 1982. Geological study of Lesbos island. Special Report, IGME.
- Michetti, A.M., Esposito E, Guerrieri L, Porfido S, Serva L, Tatevossian R, Vittori, E., Audemard, F., Azuma, T., Clague, J., Comerci, V., Gurpinar, A., McCalpin, J., Mohammadioun, B., Morner, N.A., Ota, Y., Roghazin, E. 2007. *Intensity Scale ESI 2007*. In: Mem. Descr. Carta Geol. d' Italia., Vol. 74, Servizio Geologico d'Italia - Dipartimento Difesa del Suolo, APAT, (Guerrieri, L., Vittori, E. eds.) Rome, Italy.
- Papadimitriou, P., Tselentis, G.-A., Voulgaris, N., Kouskouna, V., Lagios, E., Kassaras, I., Kaviris, G., Pavlou, K., Sakkas, V., Moumoulidou, A., Karakonstantis, A., Kapetanidis, V., Sakkas, G., Kazantzidou, D., Aspiotis, T., Fountoulakis, I., Millas, C., Spingos, I., Lekkas, E., Antoniou, V., Mavroulis, S., Skourtsos, E., Andreadakis, E. 2017. Preliminary report on the Lesvos 12 June 2017 Mw=6.3 earthquake. Euro-Med Seismological Centre (EMSC). Available in: https://www.emsc.eu/Files/news/Earthquakes_reports/lesvos_report_nkua_v5.pdf
- Papadopoulos, G.A., Agalos, A., Charalampakis, M., Novikova, T., Triantafyllou, I., Yalciner, A. 2017. The Lesvos Isl. strong (Mw6.3) earthquake of 12 June 2017, its rupture process and the associated small tsunami. In: Safe Athens 2017, New Technologies at the Civil Protection Service, 28-30 June 2017, Athens, Greece, p. 76. Available in: <http://safeathens.gr/files/Safe%20Athens%20program-final.pdf>
- Papazachos, B.C., Papazachou, C.B. 2003. *The earthquakes of Greece*. Ziti Publ., Thessaloniki, Greece, 286 p. (in Greek).
- Pe-Piper, G. 1978. Cainozoic Volcanic Rocks of Lesbos Island. Ph.D. Thesis. University of Patras, Greece. 365 p.
- Pe-Piper, G., Piper, D.J.W. 1993. Revised stratigraphy of the Miocene volcanic rocks of Lesbos, Greece. *Neues Jahrbuch Geologie und Palaeontologie Munchen* 2, 97-110.
- Taxeidis, K. 2003. Study of Historical Seismicity of the Eastern Aegean Islands. PhD thesis, National and Kapodistrian University of Athens, Greece. 301 p. Available in: <http://macroseismology.geol.uoa.gr/studies/TAXE003.pdf>



Factors controlling the distribution of building damage in the traditional Vrissa settlement induced by the 2017 June 12, Mw 6.3 Lesvos (Northeastern Aegean Sea, Greece) earthquake

Lekkas, Efthymios (1), Carydis, Panayotis (2), Skourtsos, Emmanouel (1), Mavroulis, Spyridon (1), Andreadakis, Emmanouel (1), Antoniou, Varvara (1), Spyrou, Nafsika-Ioanna (1)

- (1) Department of Dynamic Tectonic Applied Geology, Faculty of Geology and Geoenvironment, School of Sciences, National and Kapodistrian University of Athens, Panepistimiopolis, Athens 15784, Greece, smavroulis@geol.uoa.gr
 (2) National and Technical University of Athens

Abstract: On June 12, 2017 an Mw 6.3 earthquake struck the southeastern part of Lesvos Island (Northeastern Aegean Sea, Greece). Damage was localized in Vrissa area, in the western part of the affected area. Based on this damage distribution and on the fact that Vrissa is located inland further from the epicenter than other settlements with less damage, an earthquake impact paradox raised. In order to interpret this paradox, a field macroseismic survey was conducted. It is concluded that very heavy structural damage was observed in the western part of Vrissa, while its eastern part remained intact. The geological and geomorphological setting along with the building characteristics have been identified as factors controlling the spatial distribution of building damage. Specifically, highly vulnerable old structures founded on alluvial deposits and on slopes in an area bounded by significant faults in combination with probable directivity phenomena resulted in destruction.

Key words: macroseismic survey; vulnerability class; damage grade; historical buildings; landslides

INTRODUCTION

On June 12, 2017 (12:28 GMT), an Mw 6.3 earthquake struck Lesvos Island (Northeastern Aegean, Greece) (Fig. 1). It caused a fatality, 15 injured, extensive earthquake environmental effects and building damage throughout the southeastern part of Lesvos. Its epicenter was located offshore southeastern Lesvos along an offshore NW-SE striking and SW-dipping normal fault as it is shown by the provided focal mechanisms and the spatial distribution of the aftershock sequence (Fig. 1).

Building damage induced by the earthquake was localized in the western part of the affected area and more specifically in the wider area of the traditional settlement of Vrissa. It suffered most damage to its building stock, while less damage was observed in other villages in the southern part of Lesvos (Fig. 1). Minor damage was also reported from other localities of Chios Island located southwards as well as from localities of western Turkey.

Taking into account the spatial distribution of damage induced by the 2017 Lesvos earthquake in the southeastern part of the island (Fig. 1) and the fact that Vrissa is located inland, further from the epicenter than other settlements with less damage (e.g. Plomari, Vatera etc), Vrissa seemed like an earthquake impact paradox. Moreover, the first reports, apart from the earthquake effects on human health, referred to total or near total collapses of many buildings throughout the village. In order to interpret this paradox, an immediate damage assessment was implemented, with the highest possible detail including not only typical methods but also modern and innovative techniques. The early included on-site building-by-building inspection and the late comprised modern and innovative techniques comprising Unmanned Aircraft Systems (UAS) and GIS online

applications adjusted to the field macroseismic survey are described in detail by Antoniou et al. (this volume). Moreover, the factors controlling damage and seismic intensities distribution throughout the settlement are herein presented and analyzed.

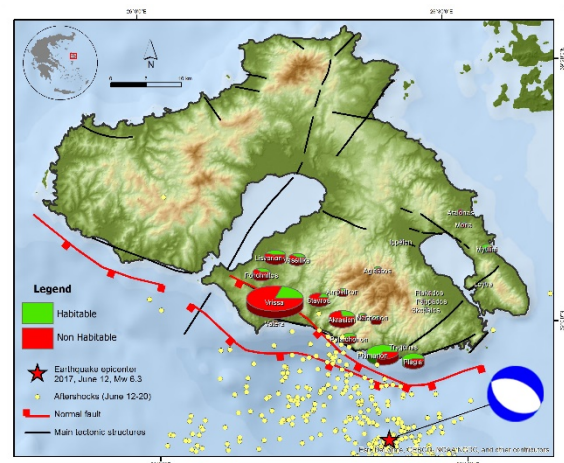


Figure 1: The 2017 Lesvos (Northeastern Aegean Sea, Greece) earthquake was generated offshore southeastern Lesvos by a NW-SE striking and SW-dipping normal fault that constitutes the northern margin of the offshore Lesvos basin located southwards of the island.

GEOLOGY AND GEOMORPHOLOGY OF VRISSA

Vrissa area is located in the hangingwall of Polichnitos-Plomari fault (Fig. 2), which constitutes the main tectonic structure of the affected area. It is a 13.5 km long NW-SE striking and SW-dipping normal fault controlling the long linear series of hills in the areas between Polichnitos and Plomari (Chatzipetros et al. 2013) and is associated with the thermal activity of the Polichnitos geothermal field



(Günther et al. 1977). Its footwall is composed of ophiolites, schists and marbles, while its hangingwall comprises Pleistocene and Holocene deposits (Fig. 2) (Hecht, 1972, 1974). As regards the geological setting of the settlement of Vrissa, its western part is founded on Holocene alluvial deposits comprising gray and red clays, sands and gravels, while its eastern part is founded on Pleistocene deposits including fluvial sand, clays and conglomerates with thickness of about 100 m (Fig. 2, 3) (Hecht 1972).

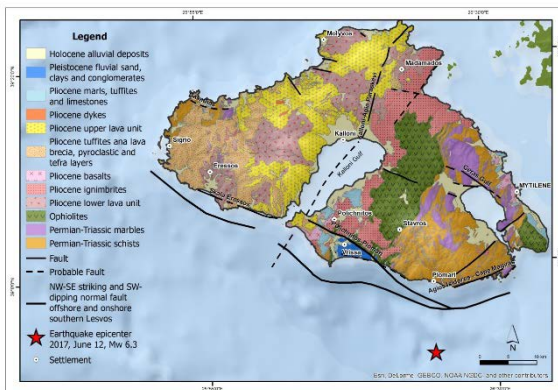


Figure 2: Geological map of Lesvos Island. Vrissa is located in the hangingwall of Polichnitos-Plomary fault.

As regards the geomorphology of Vrissa area, its western part composed of Holocene alluvial deposits comprises a flat lowland area with elevation varying from 40 to 50 m (Fig. 3). It is formed in the junction of several NW-SE trending streams flowing from SE to NW and depositing gray and red clays, sands and gravels. In contrast, the eastern part of Vrissa composed of Pleistocene formations comprises an area with intense relief with elevation varying from 50 to 100 m and larger slopes (55-195%) observed along the stream valleys (Fig. 3).

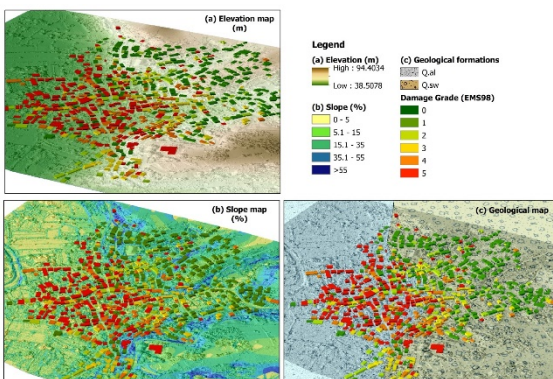


Figure 3: (a) Elevation map of Vrissa. (b) Slope map of Vrissa (values %). (c) Geological map of the broader area of Vrissa based on Hecht (1972). Geology consists of: Q.al - Holocene alluvial deposits, Q.sw - Pleistocene scree, talus cones, torrential deposits and landslide material and Pl.k.m - Pliocene marl, tuffite and limestone (marly and argillaceous clastic sediments, pelite and paleosols). (d) Damage grade map based on the classification of building damage according to the European Macroseismic Scale 1998 (EMS-98) provided by Grünthal (1998).

DOMINANT BUILDING TYPES OF VRISSA

Based on the on-site building-by-building inspection, the dominant building types in Vrissa are: (a) masonry buildings, (b) reinforced-concrete (R/C) buildings, and special structures including (c) monumental and (d) industrial structures (Fig. 4).

The first category includes 1- to 3-storey masonry buildings with load-bearing walls (Fig. 4a). They can be further classified depending on the construction material of the masonry, which can be composed of (a) massive stones, (b) manufactured stone units, (c) mixed materials including massive stones, manufactured stone units, handmade solid clay bricks, perforated bricks and concrete blocks. These materials are bound by different types of mortar including mainly clay and lime mortars in the old structures and cement mortars in more recent ones. The main characteristic of the masonry buildings is the fact that their construction is dated back to the late 19th and the early 20th century. Consequently, they are at the end of their conventional life cycle and face up probable decay problems affecting the mechanical properties of their elements and their structural response during an earthquake. A special category of traditional masonry residential buildings was detected and characterized by anti-seismic construction (Fig. 4b). They have constructed with dual structural system comprising autonomous masonry walls and timber frames with extensive “X” bracing (Fig. 4b). During an earthquake, these frames could guarantee the stability of the roof in case of a partial collapse of the masonry structure. It has been also observed in Eressos settlement in the western part of Lesvos and in Bergama in the western coast of Turkey and thoroughly described and analyzed by Karydis (2008).

The second category include R/C buildings with R/C frame composed of horizontal elements (beams) and vertical elements (columns) connected by rigid joints as well as infill walls (Fig. 4c). They are recent structures built during the last decades according to strict anti-seismic regulations and specifications and belong to the vulnerability class D. The third category include masonry monumental structures such as churches (Fig. 4d) and schools (Fig. 4e). Unfortunately, these structures are systematically altered and face up decay problems attributed to the old construction age and the inappropriate and inadequate preservation methods. The fourth category includes industrial buildings including masonry production structures and their masonry chimneys (Fig. 4f). They are still standing, although their static compliance is gradually reduced through the years.

Based on the fact that (a) since 1889 no strong earthquake struck Lesvos until 2017 and (b) Vrissa is a traditional settlement of Lesvos, described as a preserved settlement according to the Governmental Gazette of Hellenic Republic, the majority of buildings include masonry structures belonging to the vulnerability class C, while the minority comprises very few R/C buildings belonging to the vulnerability class D (Fig. 5a).

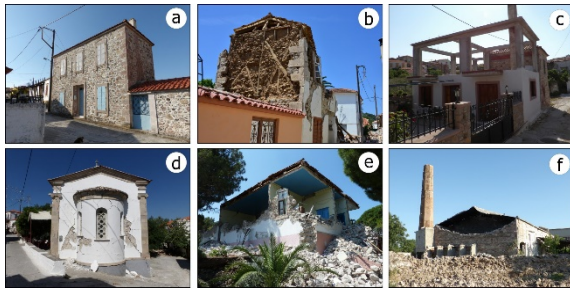


Figure 4: Dominant building types in Vrissa. (a) masonry building with load bearing walls, (b) masonry residential building with dual structural system, (c) residential building with reinforced concrete frame, (d) masonry monumental structure (church), (e) masonry school building and (f) masonry industrial building with masonry chimney.

DISTRIBUTION OF BUILDING DAMAGE IN VRISSA

The stone masonry buildings suffered the most by the 2017 Lesvos earthquake. They sustained (a) damage grade 1 comprising hairline cracks in the load-bearing masonry walls, (b) damage grade 2 including cracks in many walls, detachment of small pieces of places from the walls and partial collapse of chimneys, (c) damage grade 3 comprising large and extensive cracking of all masonry load-bearing walls, detachment of large pieces of plaster in all load-bearing walls, dislocation and fall of roof tiles, detachment of the roof from the rest of the structure and fall of gables, (d) damage grade 4 including heavy structural failure of roofs and floors and (e) damage grade 5 of partial and total collapse based on the EMS-98 (Grünthal, 1998). From the earthquake engineering point of view, the damage observed in this dominant type of structures is attributed mainly to their old construction age and their high vulnerability taking into account the fact that their construction is dated back to the late 19th or the early 20th century.

The special structures including temples, post-byzantine structures, museums, schools and industrial buildings with masonry load-bearing walls suffered similar damage with the masonry residential buildings. More specifically, temples suffered damage comprising cracks in most of the masonry walls and in other parts such the dome, the columns, the aisles, the apse and the gable. Post-byzantine structures suffered the aforementioned damage as well as partial collapse of the walls.

Industrial buildings suffered partial collapse of the perimeter masonry walls and damage of the masonry chimneys on the verge of collapse. Schools suffered fall of the gable above the entrance and partial collapse of the load-bearing masonry walls.

All R/C buildings constructed during the last decades showed good performance during the 2017 Lesvos earthquake since none of them suffered heavy structural damage. R/C buildings suffered only non-structural damage including cracks in the infill walls, detachment of large pieces of plaster from the infill walls and detachment of the infill walls from the surrounding R/C frame (damage

grade varying from 1 to 2 based on the EMS-98). However, some free standing elements sensitive to base accelerations were dislocated and damaged.

Based on the observed damage grades and the damage distribution in Vrissa, it is concluded that its northwestern part is the worst affected characterized by damage grades 4 and 5 including partial structural failure of roofs, floors and walls as well as total or near total collapse respectively (Fig. 5b). 47.2% of the surveyed buildings of vulnerability class C suffered damage grade 5, 18.1% damage grade 4, 12.7% damage grade 3, 8.0% damage grade 2 and 13.3% damage grade 1.

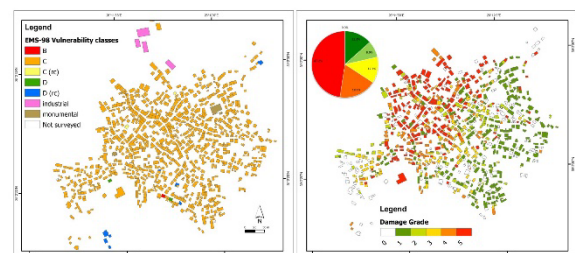


Figure 5: (a-left) Map of the buildings' vulnerability in Vrissa settlement based on the field macroseismic observations and the EMS-98. A percentage of 99.38% of the buildings are of vulnerability class C. (b-right) Damage grades map for Vrissa settlement.

CONCLUSIONS

The very heavy structural damage was observed in the western part of Vrissa, while its eastern part remained relatively intact. Taking into account the geological and tectonic structure, the geomorphological setting and the field macroseismic observations on the type, vulnerability and damage grades of buildings, it is concluded that the worst affected part of Vrissa is founded on Holocene alluvial deposits comprising gray and red clays, sands and gravels, while the slightly affected part is founded on Pleistocene deposits including fluvial sands, clays and conglomerates with thickness of about 100 m. Moreover, the groundwater level in the alluvial deposits was high resulting in reduction of (a) the absorption of the vertical (P) waves, (b) the strength and the stiffness of the soils due to the fact that the water acts as lubricant reducing friction and increasing mobility of deposits and (c) the generation of the S waves due to saturated deposits. All the aforementioned facts led to large differences in seismic intensities between the two parts of Vrissa comprising different geological and geomorphological setting.

Apart from the worst affected western part of Vrissa founded on alluvial deposits, very heavy structural damage including partial or total collapses was also observed in isolated areas in its southwestern intact part. The most characteristic "damage islet" has been detected around the partially collapsed elementary school of Vrissa. It is characterized by partial or total collapse of masonry buildings of old construction age and high vulnerability as well as by damage to infrastructures and more specifically to the road and electricity networks. The aforementioned



damage is attributed to the generation of landslides along a geotechnically unstable zone detected south of the elementary school of Vrissa and characterized by relatively steeper slopes (Fig. 6). A landslide was generated southeast of the school resulting in destruction of the road network and tilting and collapse of electricity pillars (Fig. 6). Another landslide was observed in the southern part of the school resulting in hairline cracks to a masonry perimeter wall located in the westward prolongation of the crown cracks, partial collapse of a retaining wall supporting the school's playground and severe damage to a warehouse adjacent to the unstable and mobilized slope inside the school's yard (Fig. 6). It is significant to note that this is not the first time that landslides have been generated in the same site. Evidences of generation of similar phenomena (creep and slow crack growth) were detected on an adjacent perimeter wall that suffered cracks and were repeatedly restored with the use of concrete.

- Grünthal, G. (ed) 1998. European Macroseismic Scale 1998 (EMS-98) (Cahiers du Centre Européen de Géodynamique et de Séismologie European) (Vol. 15). Luxembourg.
- Günther, R., Kappelmeyer, O., Kronberg, P. 1977. Zur prospektion auf geothermale anomalien, erfahrungen einer modelluntersuchung in Polichnitos, Lesbos (Griechenland). *Geologische Rundschau* 66, 10-33.
- Hecht, J. 1972. Geological map of Greece, Plomari-Mytilini sheet. Institute of Geology and Mineral Exploration of Greece scale 1:50.000.
- Hecht, J. 1974. Geological map of Greece, Polichnitos sheet. Institute of Geology and Mineral Exploration of Greece scale 1:50.000.
- Karydis, N. 2008. Traditional antiseismic structure in the Eastern Aegean: The case of Eressos and Pergamon. In: 3rd Panhellenic Conference on Earthquake Engineering & Seismology, 5-7 November 2008.



Figure 6: (a) Pleistocene deposits with large dip angle in the area east of the elementary school of Vrissa. (b) Landslides affecting road and electricity pillars, (c) landslide and crown cracks resulting in destruction of an adjacent warehouse (d).

Acknowledgements: All funding for this work were provided by the Environmental, Disaster and Crisis Management Strategies Masters Degree Program of the Department of Geology and Geoenvironment of the National and Kapodistrian University of Athens.

REFERENCES

- Antoniou, A., Andreadakis, E., Mavroulis, S., Spyrou, N.-I., Skourtsos, E., Lekkas, E., Carydis, P. (2017). Post-earthquake rapid assessment using Unmanned Aircraft Systems (UAS) and GIS online applications: the case of Vrissa settlement after the 2017 June 12, Mw 6.3 Lesbos earthquake (North Aegean Sea, Greece). In: 8th International INQUA Meeting on Paleoseismology, Active Tectonics and Archeoseismology (PATA), 13 – 16 November, 2017, New Zealand.
- Chatzipetros, A., Kiratzi, A., Sboras, S., Zouros, N., Pavlides, S. 2013. Active faulting in the north-eastern Aegean Sea Islands. *Tectonophysics* 597-598, 106-122.



Recording Holocene paleotsunamis along the hyperarid coast of Taltal region in Northern Chile

Tomás León (1), Gabriel Vargas (1), Diego Salazar (2), James Goff (3), Jean Louis Rajot (4)

- (1) Departamento de Geología, Facultad de Ciencias Físicas y Matemáticas, Universidad de Chile, Plaza Ercilla 803, Santiago, Chile. tleon@ing.uchile.cl, gvargas@ing.uchile.cl
- (2) Departamento de Antropología, Universidad de Chile, Ignacio Carrera Pinto 1045, Piso 2, Ñuñoa, Santiago, Chile.
- (3) School of Biological, Earth and Environmental Sciences, University of New South Wales, Sydney 2052, Australia.
- (4) Centre National de la Recherche Scientifique-Retired.

Abstract: The Chilean coast is subjected to strong subduction earthquakes and giant tsunamis. Nevertheless reports recording paleotsunamis along the hyperarid coast of Northern Chile are almost non-existent. This investigation focuses on the Taltal bay area, within the major seismic gap of Northern Chile where the last giant tsunamigenic earthquake -Mw8.8- occurred in 1877. Two trenches were dug at archaeological sites, both of which exhibit anomalous layers of reworked material. Selected samples were subjected to multiproxy analyses and we were able to identify at least 4 Holocene paleotsunami deposits. All had erosional basal contacts, fined upwards and inland, and also became thinner with increasing distance from the sea. In addition, we also observed and recorded large waterworn boulders most likely indicative of tsunami inundation. We discuss the discrimination between paleotsunami deposits and other kinds of catastrophic events such as debris flows and storms along this rocky coast in this world's most hyperarid environment.

Key words: Chile, Holocene, Paleotsunamis, Taltal, Trench.

INTRODUCTION

Chile is located in a highly seismic area because the Nazca plate is subducting under the South American plate with a convergence rate of 6.8 cm/yr (Figure 1(a)), subjecting the coastal area to strong earthquakes and giant tsunamis. Scientific research on historical and paleotsunamis records has been mostly concentrated along the central-southern region (Cisternas et al., 2005; Ely et al., 2014) owing to the environment being more favorable to the preservation of deposits thus allowing their clear identification usually in wetland areas. While steep cliffs and a narrow coastal plain control the northern landscape, blocking deposition in many cases. Coastal areas are not only affected by tsunamis, but also by storms, tidal waves and debris flow, hampering deposits preservation and identification. This research article seeks to contribute scientific knowledge about the hyperarid coast of Northern Chile where reports recording paleotsunamis are almost non-existent. This investigation focuses on "Isla Blanca Bay" south of Taltal. An area located within the major seismic gap of Northern Chile where the last giant tsunamigenic earthquake – Mw8.8- occurred in 1877, affecting an area from Arica to Caldera (Monge, 1993). Two locations were studied, one 7 km south along the coast from the city where the coast has a N-S trend, and the other 17 km south from Taltal, where the coast is trending W-E.

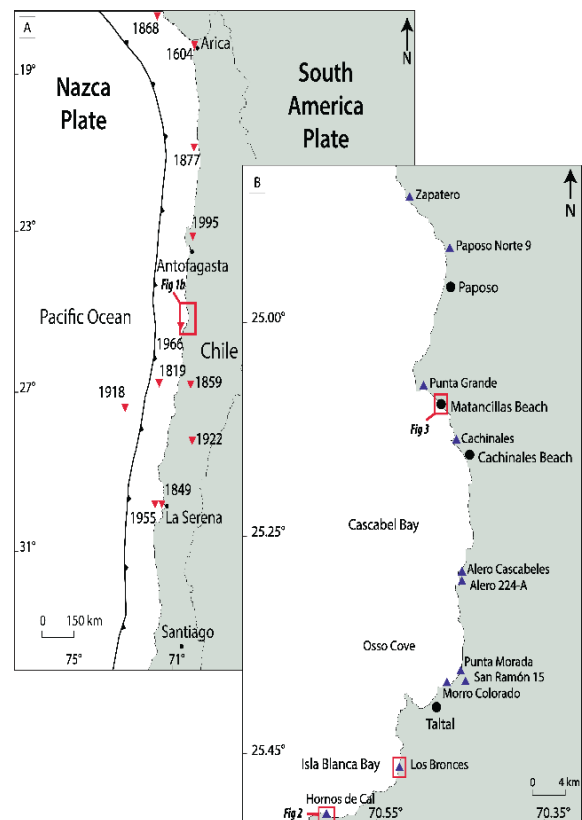


Figure 1. Location maps A) Study area and historic tsunamis. B) Trench locations and principle archaeological sites.



As some authors point out, tsunami deposit identification can be difficult and so applying multiproxy techniques to better understand a deposit's genesis is important (Chagué-Goff et al., 2011). To do this, sediments were analyzed using sedimentology, stratigraphy and geomorphology, looking for evidence to identify late Holocene tsunami deposits related to archaeological occupation (Figure 1 (b)). Since sea level stabilized around 6000 years ago (Pirazzoli, 1991), coasts became favorable places for human settlement, allowing for numerous coastal occupation sites to be established along Taltal bay and the surrounding areas (Salazar et al., 2015). Like today, these sites are likely to have been affected by catastrophic events such as tsunamis in the past, making it important to better understand these earlier events.

Methods and materials

In order to describe the landscape components, high definition photogrammetry has been used with Phantom 4 Pro drone, these pictures were processed using the Agisoft Photoscan Professional software producing Digital elevation models (DEM), orthophotographies and a 3D model. After digging several test trenches along the coast, two were dug at "Los Bronces" and "Hornos de cal" Holocene archaeological sites. The Los Bronces trench was located at 8 meters above sea level and 85 m from the coast. It was 1.2 m deep and 1.9 m wide. The Hornos de cal trench was located 95 m from coast and 11 m.a.s.l., it was 1.1 m deep and 1.8 m wide. Both had well preserved sedimentary records due to the surrounding rock outcrops protecting them from reworking by floods. Different layers were identified and described using stratigraphic and sedimentological criteria, samples were also taken from each layer. Manual sieving and laser grain size analysis using Malvern Mastersizer 2000 were applied to these samples. Results were processed using GRADISTAT 8.0 software (Blott & Pye, 2001) and X-ray fluorescence analyses were also carried out to identify chemical elements suggesting deep marine sediment transportation to the coast. Sediment texture was studied using a stereoscopic microscope and organic material was also studied to differentiate between anthropogenic and natural sources. Radiocarbon analysis is also being carried out on shell and charcoal samples.

RESULTS AND DISCUSSION

Los Bronces Trench

At Los Bronces there are 3 medium sand layers identifiable along the entire trench profile and considered to be tsunamis deposits. The first layer (event 1) is located from 75 to 84 cm deep, the second one (event 2) between 71 and 73 cm and the last one (event 3), located from 45 to 55 cm. They have a sharp lower contact, become thinner landward and exhibit normal grading in general with a few cases of inverse grading zones. Many articles emphasize the normal grading of tsunamis deposits (J. Goff et al.,

2001; Nichol et al., 2007), which is produced by decreasing velocity as the wave moves inland (Morton et al., 2007). Nevertheless inverse grading may occur when there are fine but heavy sediments at the base of the tsunami flow; these particles deposit faster with coarser and lighter sediments deposited above (Jaffe et al., 2012; Moore et al., 2011; Morton et al., 2008). When this occurs, a normal grading layer is expected over them, as in layers from events 1 and 3. Overall deposits fine upwards within each layer (Goff et al., 2012). The rounding of particles is higher in these layers compared to the other deposits above and below them, supporting the inference of the inland transport of sea-rounded sediments. A common feature in these layers is the presence of intact and broken shells which in some cases also show flow direction. Chemical element analysis shows a relative increase in Ca and Sr, related to carbonates from marine shells and microfossils, and often used to support a tsunami interpretation for a deposit (Goff et al., 2004; Nichol et al., 2010). There are also increases in Ti and Fe associated with heavy minerals – these are used as indicators of high energy deposits (Goff et al., 2010; Nichol et al., 2007). Organic material analysis shows the presence of limpets (*Scurria parasitica*) and sea snails (*Tegula*). These species were not used as food by the ancient humans in the area (Guzmán et al., 1998) supporting the interpretation that these layers were produced naturally and do not have an anthropogenic origin. Regarding the events chronology, the Los Bronces archaeological site dates from the III Archaic phase, 7500 to 5500 BP (Salazar et al., 2015), and thus some of these events may be from at least 7500 years ago. Ongoing radiocarbon analysis will help to confirm their age.

Hornos de Cal Trench

The geologic log shows fragmented and complete shells in a gray sand layer. The shells are orientated in a manner indicating a flow direction from the sea. This layer gets thinner inland, shows a sharp lower contact and rests between anthropogenic layers (Figure 2). All these criteria may be indicative of a tsunami deposit (Goff et al., 2011). This layer was also found during inland archaeological digging showing the same stratigraphic depth as in Hornos de Cal between 25 and 50 cm, with a 15 cm average thickness. Granulometric analysis shows the relative size decreasing inland. Although grain size is not a tsunami discriminant feature, since it depends on the sediment source (e.g. Dawson & Stewart, 2007; Goff et al., 2012), this size difference, on the tsunami deposit, may be explained by the finer sediments being contributed from a sea flow to the coast, supported by these decreasing sorting. Samples show positive skewness (fine skewed) and a very platykurtic curve indicating a different source compared to the rest of layers. The sediment texture shows a better sphericity and roundness than the surrounding layers, and a flat discoidal shape probably produced by particles being moved up and down during wave swash and backwash.

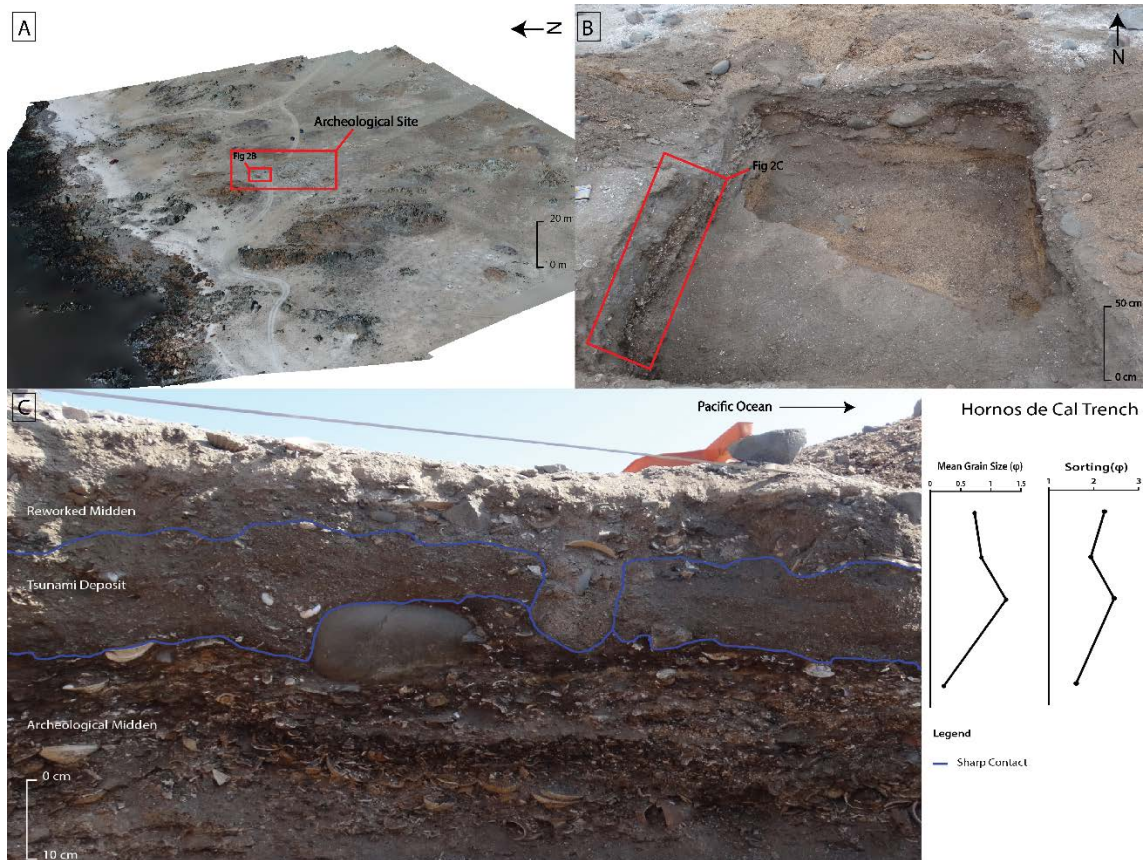


Figure 2: Tsunami deposit in archeological site. A) 3D Model of the area. B) Hornos de Cal Trench. C) Stratigraphic profile.

In contrast to the Los Bronces trench, organic material in this layer shows edible fauna such as sea urchin and *Chiton curangist*, and inedible material such as *Scurria parasitica* and *Tegula*, there were also some signs of stone knapping. This mixing of material within the deposit is caused by the reworking of pre-existing midden during tsunami inundation. The chemical analyses did not show clear indications of marine inundation with only a notable increase in Ca most likely reflecting the incorporation of midden material into the deposit.

Finally, to the south of the study area, large boulder deposits were identified. They had been moved inland several meters. This is similar to Matancillas beach (Figure 3), where numerous boulders are located more than 100 m. from the coast. Many authors have shown that tsunamis are capable of transporting large boulders a considerable distance inland (e.g. Goto et al., 2010, 2012; Piscitelli et al., 2016) and it is likely that these are linked with the finer sediment deposits reported from the trenches.

CONCLUSIONS

Through this multiproxy study, including chemical, sedimentological, geomorphological, and archaeological analyses, we were able to identify at least 4 Holocene paleotsunami deposits. The presence of large boulders at or near the coast can also be related to tsunami

inundation. It is known that historical tsunamis have affected this coast but these deposits reported here are considerably older. Ongoing radiocarbon analysis will help determine the age of these events and provide more information about past tsunamis affecting the northern Chile coast.

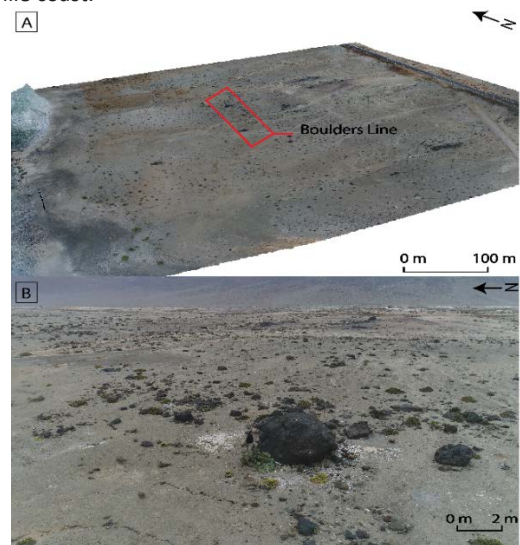


Figure 3: A) Boulders line in Matancillas beach. B) Example of big boulders.



Acknowledgements: Funding for this study was provided through FONDECYT 1161547 and 1151203. We thank the anonymous reviewers for their comments and help on this article edition.

REFERENCES

- Blott, S. J., & Pye, K. (2001). Gradistat: A grain size distribution and statistics package for the analysis of unconsolidated sediments. *Earth Surface Processes and Landforms*, 26(11), 1237–1248, doi: 10.1002/esp.261.
- Chagué-Goff, C., Schneider, J. L., Goff, J. R., Dominey-Howes, D., & Strotz, L. (2011). Expanding the proxy toolkit to help identify past events - Lessons from the 2004 Indian Ocean Tsunami and the 2009 South Pacific Tsunami. *Earth-Science Reviews*, 107(1–2), 107–122, doi: 10.1016/j.earscirev.2011.03.007.
- Cisternas, M., Atwater, B. F., Torrejón, F., Sawai, Y., Machuca, G., Lagos, M., Eipert, A., Youlton, C., Salgado, I., Kamataki, T., Shishikura, M., Rajendran, C., Malik, J., Rizal, Y. & Husni, M. (2005). Predecessors of the giant 1960 Chile earthquake. *Nature*, 437(7057), 404–407, doi: 10.1038/nature03943.
- Dawson, A. G., & Stewart, I. (2007). Tsunami deposits in the geological record. *Sedimentary Geology*, 200(3–4), 166–183, doi: 10.1016/j.sedgeo.2007.01.002.
- Ely, L. L., Cisternas, M., Wesson, R. L., & Dura, T. (2014). Five centuries of tsunamis and land-level changes in the overlapping rupture area of the 1960 and 2010 Chilean earthquakes. *Geology*, 42(11), 995–998, doi:10.1130/G35830.1
- Goff, J., Chagué-Goff, C., & Nichol, S. (2001). Palaeotsunami deposits: A New Zealand perspective. *Sedimentary Geology*, 143(1–2), 1–6.
- Goff, J. R., Wells, A., Chagué-Goff, C., Nichol, S. L., & Devoy, R. J. N. (2004). The elusive AD 1826 tsunami, South Westland, New Zealand. *New Zealand Geographer* 60(2), 28–39.
- Goff, J., Nichol, S., & Kennedy, D. (2010). Development of a palaeotsunami database for New Zealand. *Natural Hazards*, 54(2), 193–208, doi: 10.1007/s11069-009-9461-5.
- Goff, J., Lamarche, G., Pelletier, B., Chagué-Goff, C., & Strotz, L. (2011). Predecessors to the 2009 South Pacific tsunami in the Wallis and Futuna archipelago. *Earth-Science Reviews* 107, 91–106, doi:10.1016/j.earscirev.2010.11.003.
- Goff, J., Chagué-Goff, C., Nichol, S., Jaffe, B., & Dominey-Howes, D. (2012). Progress in palaeotsunami research. *Sedimentary Geology* 243–244, 70–88, doi:10.1016/j.sedgeo.2011.11.002.
- Goto, K., Kawana, T., & Imamura, F. (2010). Historical and geological evidence of boulders deposited by tsunamis, southern Ryukyu Islands, Japan. *Earth-Science Reviews*, 102(1–2), 77–99, doi:10.1016/j.earscirev.2010.06.005.
- Goto, K., Nishimura, Y., Sugawara, D., & Fujino, S. (2012). The Japanese tsunami deposit researches. *The Journal of the Geological Society of Japan*, 118(7), 431–436, doi: 10.5575/geosoc.2012.0042.
- Guzmán, N., Saá, S., & Ortlieb, L. (1998). Catálogo descriptivo de los moluscos litorales (Gastropoda y Pelecypoda) de la zona de Antofagasta, 23 S (Chile). *Estud. Oceanol*, 17, 17–86.
- Jaffe, B. E., Goto, K., Sugawara, D., Richmond, B. M., Fujino, S., & Nishimura, Y. (2012). Flow speed estimated by inverse modeling of sandy tsunami deposits: Results from the 11 March 2011 tsunami on the coastal plain near the Sendai Airport, Honshu, Japan. *Sedimentary Geology*, 282, 90–109, .
- Monge, J., (1993). Estudios de riesgo de tsunami en costas chilenas. Jornadas chilenas de Sismología en ingeniería antisísmica, V.2., Santiago, Chile, pp. 3–22.
- Moore, A., Goff, J., McAdoo, B. G., Fritz, H. M., Gusman, A., Kalligeris, N., ... Synolakis, C. E. (2011). Sedimentary Deposits from the 17 July 2006 Western Java Tsunami, Indonesia: Use of Grain Size Analyses to Assess Tsunami Flow Depth, Speed, and Traction Carpet Characteristics. *Pure and Applied Geophysics*, 168(11), 1951–1961, doi: 10.1007/s00024-011-0280-8.
- Morton, R. A., Gelfenbaum, G., & Jaffe, B. E. (2007). Physical criteria for distinguishing sandy tsunami and storm deposits using modern examples. *Sedimentary Geology*, 200(3–4), 184–207, doi:10.1016/j.sedgeo.2007.01.003.
- Morton, R. A., Goff, J. R., & Nichol, S. L. (2008). Hydrodynamic implications of textural trends in sand deposits of the 2004 tsunami in Sri Lanka. *Sedimentary Geology* 207, 56–64, doi:10.1016/j.sedgeo.2008.03.008
- Nichol, S. L., Goff, J. R., Devoy, R. J. N., Chagué-goff, C., Hayward, B., & James, I. (2007). Lagoon subsidence and tsunami on the West Coast of New Zealand. *Sedimentary Geology* 200, 248–262, doi:10.1016/j.sedgeo.2007.01.019
- Nichol, S. L., Chagué-Goff, C., Goff, J. R., Horrocks, M., McFadgen, B. G., & Strotz, L. C. (2010). Geomorphology and accommodation space as limiting factors on tsunami deposition: Chatham Island, southwest Pacific Ocean. *Sedimentary Geology*, 229(1–2), 41–52. doi:10.1016/j.sedgeo.2010.06.001
- Pirazzoli, P. A. (1991). *World Atlas of Holocene sea-level changes*, 300 pp, Elsevier Oceanographic Series, Amsterdam, Netherlands.
- Piscitelli, A., Milella, M., Hippolyte, J. C., Shah-Hosseini, M., Morhange, C., & Mastronuzzi, G. (2016). Numerical approach to the study of coastal boulders: The case of Martigues, Marseille, France. *Quaternary International*, 439, 52–64.
- Salazar, D., Figueroa, V., Andrade, P., Salinas, H., Olguín, L., Power, X., Rebolledo, S., Parra, S., Orellana, H. & Urrea, J. (2015). Cronología Y Organización Económica De Las Poblaciones Arcaicas De La Costa De Taltal. *Estudios Atacameños*, 50, 07–46, doi: 10.4067/S0718-10432015000100002.



Holocene marine terraces record long-term uplift along the Kaikōura coastline

Litchfield, Nicola (1), Clark, Kate (1), Miyauchi, Takahiro (2), Berryman, Kelvin (1), Barrell, David (13), Brown, Len (4), Ota, Yoko (5), Fujimori, Takatoshi (6)

- (1) GNS Science, PO Box 30 358, Lower Hutt 5040, New Zealand. n.litchfield@gns.cri.nz
- (2) Department of Earth Sciences, Chiba University, 1-33 Yayoi-cho, Inage-ku, Chiba 263-8522, Japan.
- (3) GNS Science, Private Bag 1930, Dunedin 9054, New Zealand.
- (4) 13 Munbilla Close, Mountain Creek, Queensland 4557, Australia.
- (5) 2-11-13-201 Minami-senzoku, Ota-ku, Tokyo 145-0063, Japan.
- (6) Keio Futsubu School, 1-45-1 Hiyoshi-honcho, Kohoku-ku, Yokohama 223-0062, Kanagawa, Japan.

Abstract: The 2016 M_w 7.8 Kaikōura Earthquake caused vertical deformation along ~110 km of the Kaikōura coast, much of which is characterised by Pleistocene and Holocene marine terraces. The Holocene marine terrace data is largely unpublished, and this paper presents reconnaissance mapping and radiocarbon dating results, and compares these with the 2016 coseismic vertical deformation and paleoearthquake ages for the Kekerengu Fault. The distribution of coseismic and paleo-deformation broadly coincide except for the area between the Kekerengu and Papatea faults and in the Kaikōura Plain, suggesting uplift mechanisms other than the faults that ruptured in 2016 operate over long timescales. Terrace ages from the Cape Campbell coast broadly match paleoearthquake ages from the Kekerengu Fault, suggesting it generally ruptures with the Needles Fault. Ages from Waipapa Bay and Kaikōura Peninsula may be the first paleoearthquake ages for the Papatea Fault and a blind fault offshore of Kaikōura Peninsula, respectively.

Key words: 2016 Kaikōura Earthquake, marine terrace, coastal uplift, radiocarbon age, paleoseismology

INTRODUCTION

The 14 November 2016 M_w 7.8 Kaikōura Earthquake caused vertical deformation of over ~110 km of the Kaikōura coast, northeastern South Island, New Zealand (Clark et al., 2017; Figure 1). The deformation was highly variable, reflecting the complexity of fault ruptures, but was not unprecedented, as much of the coast is characterised by Holocene and Pleistocene marine terraces (Duckmanton, 1974; McFadgen, 1997; Ota et al., 1996). Reconnaissance mapping and radiocarbon dating of the Holocene marine terraces and examination of water bore logs was undertaken by several of the co-authors in the late 1980's and early 1990's but has largely remained unpublished. This paper summarises that data, as well as other existing data and two new radiocarbon ages. We briefly compare the terrace distribution and ages with the Kaikōura Earthquake coastal deformation and fault paleoearthquake records.

HOLOCENE MARINE TERRACE DATA

Flights of up to 7 Holocene marine terraces have been mapped at a number of localities between Mussel Point and Kaikōura Peninsula (Figure 1). The terraces were originally mapped using 1940's aerial photographs and more recently using a 1 m-pixel LiDAR Digital Elevation Model. Radiocarbon samples (Table 1) were collected from natural marine terrace exposures and the Hawthorne Road drill-hole, and the majority of the marine terrace sample elevations were surveyed with a total station. The results are briefly discussed below, from north to south.

Mussel Point and Cape Campbell

Two Holocene marine terraces are mapped at Mussel Point (~3.6 and 3 m amsl) and four at Cape Campbell (~15, ≤7, 5.8 and 3.5 m amsl). The older (1989, pre-AMS) ages from the lowest terrace at each site overlap, but new (2017, AMS) ages from the lowest terrace at Cape Campbell are younger than the Mussel Point age (Table 1). The ages for the second-highest terrace at each site overlap, and the age for the third-highest terrace at Cape Campbell is slightly older.

Cape Campbell to the Kekerengu Fault

Holocene marine terraces are intermittently preserved south of Cape Campbell, with three terraces mapped at Chancet Rocks (~11, 10.2 and 6.5 m amsl) and four at Mirza Creek (~13-15, 10-13, 6-8 and 5 m amsl) and Wharanui (~18, 14, 8, 4 m amsl). The ages obtained from the lowest terrace at Chancet Rocks and Mirza Creek overlap, as does an age obtained from a single terrace at Long Point, and the lowest terrace at Cape Campbell and Mussel Point (Table 1). The age obtained from the lowest terrace at Wharanui is older, however. The second-highest terrace at Wharanui has a radiocarbon age older than any of the material dated from the Cape Campbell terraces. A wood sample from valley infill sediment adjacent to the Flaxbourne River is much older, consistent with an estuarine or fluvial post-transgressive sequence (e.g., Ota et al., 1988, 1995; Litchfield and Clark, 2015).

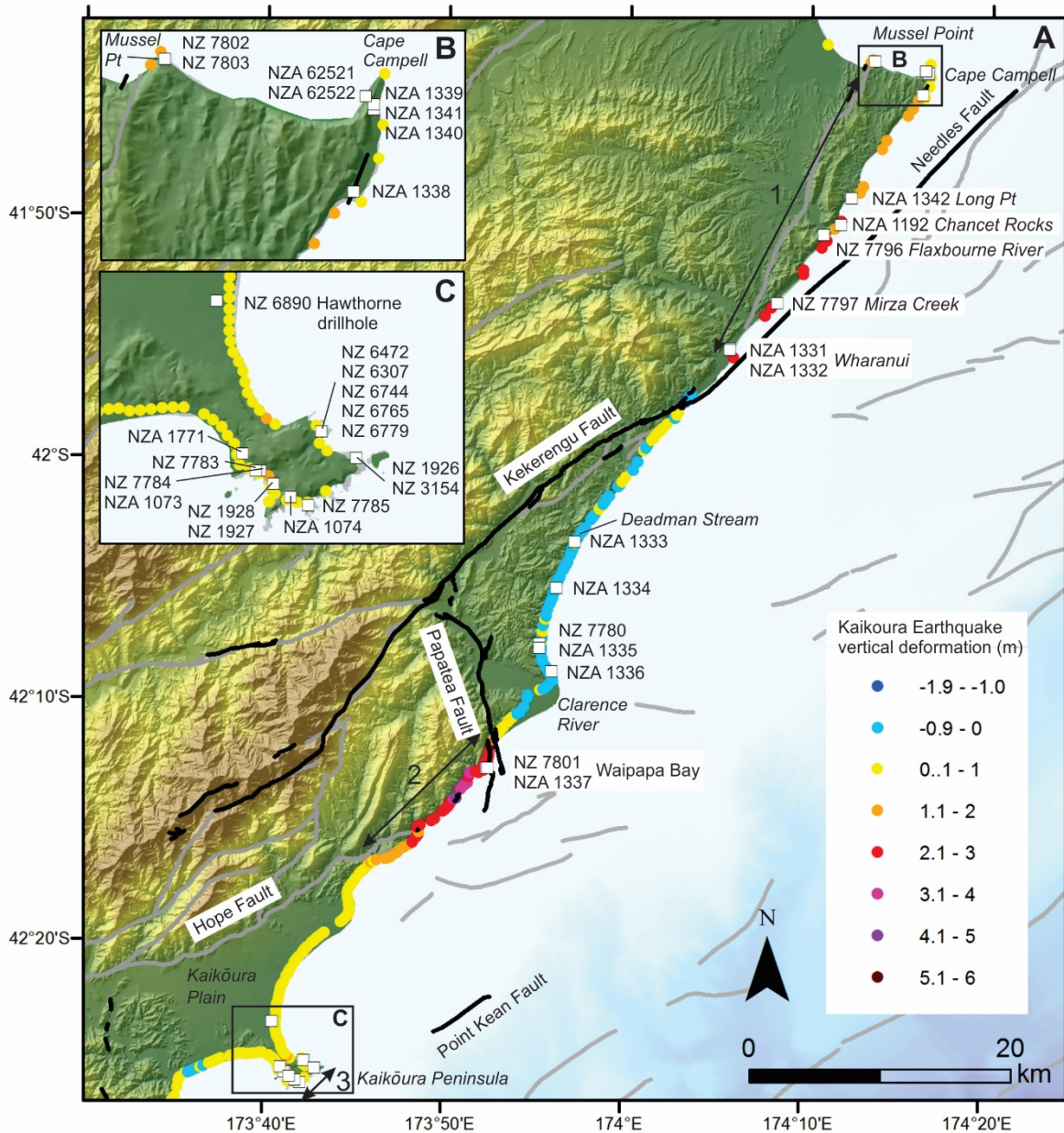


Figure 1: Holocene marine terrace dating sites and 2016 Kaikōura Earthquake vertical coastal deformation (Clark et al., 2017). The sites are labelled with the Rafter Radiocarbon Laboratory numbers (A is AMS). 1-3 are areas where 2016 Kaikōura Earthquake and long-term uplift coincide.

Kekerengu Fault to the Papatea Fault

Up to seven Holocene marine terraces are mapped between Deadman Stream and the Clarence River, with the highest at ~15 m amsl and the lowest at 4 m amsl. Four ages obtained from the lowest terrace overlap with one another and with the ages from the lowest terraces farther north (Table 1). An older age was obtained from a terrace at ~7.5 m amsl, which overlaps with the age of the lowest terrace at Wharanui.

Waipapa Bay

Three terraces are mapped on the south side of the Papatea Fault at Waipapa Bay, with elevations at ~6 m, 4 m and 3 m amsl. Radiocarbon ages were obtained from the lowest and third-highest terraces and appear to be different from the terrace ages from elsewhere (Table 1).

Kaikōura Plain

The Kaikōura Plain was mainly swamp and marsh before being drained towards the end of the 1800s and has no clear marine terraces. A groundwater test bore drilled at Hawthorne Road reached bedrock (Tertiary siltstone and sandstone) at 41 m bgs, and is overlain by beach gravel, fluvial gravel, and swamp deposits (Brown, 1988). A late Holocene age was obtained from wood at the base of the swamp deposits (Table 1), but ages from shells within the beach deposits (not included in Table 1) were beyond radiocarbon dating limits and the shells may be reworked (e.g., from the Pleistocene marine terraces). The available evidence is thus equivocal for long-term uplift or subsidence of the Plain.



Table 1: Holocene terrace and drillhole radiocarbon ages. All samples were dated at Rafter Radiocarbon Lab.

NZ no.	Sample type	Reported CRA (yr BP)	Updated CRA (yr BP) ¹	Age (Cal. yr BP) ²	Sample height (m amsl)	Terrace	Data source
7802	Shell	1065 ± 34	1027 ± 36	660-530	3.6	Highest (Ms ₁)	1
7803	Shell	772 ± 34	733 ± 35	460-290	3.0	Lowest (Ms ₂)	1
A 62521	Shell	585 ± 26		290-130	2.9 ³	Lowest (C ₄)	2
A 62522	Shell	586 ± 26		290-130	2.6 ³	Lowest (C ₄)	2
A 1339	Shell	1780 ± 150	1780 ± 217	1830-890	6.0	Third highest (C ₂)	1
A 1340	Shell	1120 ± 64	1120 ± 170	1040-410	5.5	Second highest (C ₃)	1
A 1341	Shell	636 ± 54	636 ± 166	500-0	3.0	Lowest (C ₄)	1
A 1338	Shell	1400 ± 67	1400 ± 171	1280-640	5.5	Third highest (C ₂)	1
A 1342	Shell	622 ± 70	622 ± 172	500-0	3.0	Single	1
A 1192	Shell	686 ± 74	686 ± 177	560-0	6.0	Lowest	1
7796	Wood	7430 ± 50	7421 ± 58	8000-7740	c. 1	Valley infill	1
7797	Shell	639 ± 60	626 ± 54	420-140	5.4	Lowest (M ₄)	1
A 1331	Shell	3710 ± 120	3709 ± 200	4180-3130	8.0	Second highest (WH ₃)	1
A 1332	Shell	1424 ± 93	1424 ± 186	1330-630	4.5	Lowest (WH ₄)	1
A 1333	Shell	1295 ± 87	1295 ± 183	1210-540	7.5		1
A 1334	Shell	521 ± 86	521 ± 182	450-0	4.0		1
7800	Wood	180 ± 60		280-0	4.2	Lowest (P ₇)	1
A 1335	Shell	626 ± 58	627 ± 168	500-0	3.0	Lowest (P ₇)	1
A 1336	Shell	547 ± 68	547 ± 171	460-0	4.0	Lowest (P ₇)	1
7801	Shell	1230 ± 30	1225 ± 30	870-680	4.5	Third highest (W ₁)	1
A 1337	Shell	1034 ± 66	1034 ± 171	920-310	3.5	Lowest (W ₃)	1
6890	Wood	1705 ± 65		1720-1410	-13.0	Hawthorne Road drillhole	1
6472	Shell	535 ± 43	871 ± 40	550-420	1.9	Second highest (C)	3
6307	Shell	1315 ± 65	1651 ± 58	1310-1060	1.3	Below second highest (C)	3
6744	Shell	1340 ± 35	1676 ± 29	1290-1170	2.1	Third highest (D)	3
6765	Shell	1595 ± 40	1932 ± 34	1570-1370	2.9	Fourth highest (E)	3
6779	Shell	3020 ± 40	3354 ± 27	3540-3360	3.1	Foreshore inland of fourth highest (E)	3
1926	Peat	300 ± 60		490-140	0.5	Lowest	4
3154	Peat	150 ± 50		280-0		Lowest	4
7785	Shell	1030 ± 60	1029 ± 57	680-510	6.0	Single	1
A 1074	Shell	1670 ± 71	1670 ± 173	1600-860	4.3	Sea cave	1
1928	Shell	290 ± 40	598 ± 40	330-90	0.5	Lowest	4
1927	Wood	160 ± 60		280-0	1.0	Lowest	4
7784	Shell	726 ± 47	726 ± 54	470-270	3.0	Second highest	1
A 1073	Shell	1486 ± 60	1486 ± 168	1340-690	1.5	Lowest	1
7783	Shell	1476 ± 36	1445 ± 37	1090-900	4.0	Third highest	1
A 1171	Charcoal	537 ± 64		640-330	5.8	Third highest?	1

¹ Recalculated relative to the OxI standard as per Stuiver and Polach (1977).² Shell ages were calibrated using MARINE13 (Reimer et al., 2013) and the closest available (Turakirae Head, Wellington) regional delta R of 3 ± 14 years (McSaveney et al., 2006). Wood and peat ages were calibrated using SHCAL13 (Hogg et al., 2013). All are quoted with 2σ uncertainties.³ Pre-earthquake height, calculated by removing 0.5 m of Kaikōura Earthquake uplift, for comparison purposes.⁴ 1 Miyauchi et al. (unpubl.), 2 Litchfield and Clark (unpubl.), 3 McFadgen (1987), 4 Duckmanton (1974).



Kaikōura Peninsula

At least four Holocene marine terraces have been mapped at Kaikōura Peninsula, at heights ranging from ~6 to 0.5 m amsl. The ages do not match particularly well between sites, but the youngest terrace is generally <500 cal. yr BP. The ages may suggest four uplift events in the last 1570 or 3540 years.

DISCUSSION AND CONCLUSIONS

Paleo and coseismic deformation comparison

The distribution of Holocene marine terraces coincides with some areas of coastal uplift during the Kaikōura Earthquake (areas 1-3 on Figure 1). However, the majority of the coastline between the Papatea Fault and the Kekerengu Fault underwent coseismic subsidence in 2016, whereas the presence of up to seven emergent terraces suggests long-term uplift. This may suggest an additional uplift mechanism for the coast between the Kekerengu and Papatea faults, such as the submarine portion of the Hope Fault, or possibly the Hikurangi subduction interface. The Kaikōura Plain was uplifted up to 1 m in the Kaikōura Earthquake, whereas the evidence for long-term deformation is equivocal. It is possible the plain is a hinge zone between the uplift of the Kaikōura Peninsula and the downthrown side of the Hope Fault.

Terrace ages and paleoearthquakes

With the notable exception of Wharanui, the ages of the terraces in area 1 broadly match the timing of the three most recent events on the Kekerengu Fault (Little et al., 2017 - this volume). This is best shown by the two new (2017, AMS) ages for the lowest terrace at Cape Campbell (290-130 cal. yr BP), which closely matches the timing of the most recent event on the Kekerengu Fault (250-110 cal. yr BP). If all these events are coincident, then this suggests that the Kekerengu and Needles faults generally rupture together, and may in fact be a single fault.

As noted earlier, the Waipapa Bay terrace ages appear to be different from the ages elsewhere. This may support them being the result of previous Papatea Fault earthquakes, which are currently undated.

The uplift of Kaikōura Peninsula in the Kaikōura Earthquake is inferred to be from a blind shallow-dipping fault with a tip southeast of the Peninsula (Clark et al., 2017). This interpretation is consistent with the northwest-tilt of the Pleistocene marine terraces and the Kaikōura Peninsula Fault inferred by Barrell (2015). If this is the sole cause of the long-term uplift, then the relatively young Holocene terrace ages may constrain the most recent paleoearthquake ages for that fault.

Future work

There is only one radiocarbon age from the majority of the Holocene marine terraces and most have broad uncertainties. Higher resolution dating is therefore a priority. The delta R value used (3 ± 14 years) to calibrate the radiocarbon ages is from the southern North Island, and a local value should be obtained. Further analysis

should also be undertaken on the well-logs from the Kaikōura Plain to resolve any long-term deformation.

Acknowledgements: The Miyauchi et al. (unpubl.) data was funded by the Japanese Ministry of Science, Education and Culture (Project no. 0141040) and DSIR Geology and Geophysics. The new work and write-up was funded by GeoNet Kaikōura Earthquake Response and GNS Science SSIF funding.

REFERENCES

- Barrell, D.J.A. 2015. *General distribution and characteristics of active faults and folds in the Kaikōura District, North Canterbury*. GNS Science Consultancy Report 2014/210. 59 p.
- Brown, L.J. 1988. Water well data, geohydrology and Quaternary geology, southern Marlborough, *New Zealand Geological Survey Report* 111.
- Clark, K., and 13 others 2017. Highly variable coastal deformation in the 2016 Mw7.8 Kaikōura earthquake reflects rupture complexity along a transpressional plate boundary. *Earth and Planetary Science Letters* DOI: 10.1016/j.epsl.2017.06.048.
- Duckmanton, N.M., 1974. *The shore platforms of the Kaikōura Peninsula*. Unpublished MA Thesis, University of Canterbury. 136 p.
- Hogg, A.G., Hua, Q., Blackwell, P.G., Niu, M., Buck, C.E., Guilderson, T.P., Heaton, T.J., Palmer, J.G., Reimer, P.J., Reimer, R.W., Turney, C.S.M., & Zimmerman, S.R.H., 2013. SHCAL13 Southern Hemisphere Calibration, 0–50,000 years Cal. BP. *Radiocarbon* 55, 1889–1903.
- Litchfield, N., & Clark, K.J. 2015. Fluvial terrace formation in the lower Awheha and Pahaoa River valleys, New Zealand: implications for tectonic and sea-level controls on river behaviour. *Geomorphology* 231, 212–228.
- Little, T.A., Van Dissen, R.J., Kears, J.R., Norton, K.P., Benson, A.M., & Ningsheng, W. 2017. Kekerengu fault, New Zealand: timing and size of Late Holocene surface ruptures. PATA Days 2017.
- McFadgen, B.G. 1987. Beach ridges, breakers and bones: late Holocene geology and archaeology of the Fyffe site, S49/46, Kaikōura Peninsula, New Zealand. *Journal of the Royal Society of New Zealand* 17, 381–394.
- McSaveney, M.J., Graham, I.J., Begg, J.A., Beu, A.G., Hull, A.G., Kim, K., Zondervan, A., 2006. Late Holocene uplift of beach ridges at Turakirarae Head, south Wellington coast, New Zealand. *New Zealand Journal of Geology and Geophysics* 49, 337–358.
- Ota, Y., Berryman, K.R., Hull, A.G., Miyauchi, T., & Iso, N. 1988. Age and height distribution of Holocene transgressive deposits in eastern North Island, New Zealand. *Palaeogeography, Palaeoclimatology, Palaeoecology* 68, 135–151.
- Ota, Y., Brown, L.J., Berryman, K.R., Fujimori, T., & Miyauchi, T. 1995. Vertical tectonic movement in northeastern Marlborough: stratigraphic, radiocarbon, and palaeoecological data from Holocene estuaries. *New Zealand Journal of Geology and Geophysics* 38, 269–282.
- Ota, Y., Pillans, B., Berryman, K., Beu, A., Fujimori, T., Miyauchi, T., & Berger, G., 1996. Pleistocene coastal terraces of Kaikōura Peninsula and the Marlborough coast, South Island, New Zealand. *New Zealand Journal of Geology and Geophysics* 39, 51–73.
- Reimer, P.J., and 29 others 2013. INTCAL13 and MARINE13 radiocarbon age calibration curves 0–50,000 years Cal. BP. *Radiocarbon* 55, 1869–1887.
- Stuiver, M., & Polach, H.A., 1977. Discussion of reporting of ^{14}C data. *Radiocarbon* 19, 355–363.



Late Holocene Surface Ruptures Inferred for the Kekerengu fault, New Zealand

Little, Tim (1), Van Dissen, Russ (2), Kearsse, Jesse (1), Norton, Kevin (1), Benson, Adrian (1), Wang, Ningsheng (1)

(1) School of Geography, Environment & Earth Sciences, Victoria University of Wellington, P.O. Box 600, Wellington, New Zealand. Timothy.little@vuw.ac.nz.

(2) Active Landscapes Group, GNS Science, P.O. Box 30368, Lower Hutt, New Zealand

Abstract: We excavated three trenches across the Kekerengu fault 10 months prior to those trenches being offset in the Mw 7.8 Kaikoura earthquake. Paleoequakes occurred at 249-108, 528-356, and 1249-903, cal yrs. B.P. Our data indicate a mean recurrence interval (RI) for the Kekerengu fault of 376 ± 32 yrs (1σ). This is within error of that of the Hope fault; moreover, using the ~ 9 m single-event displacement (SED) for the Kekerengu fault at the trench sites in 2016, and assuming a CoV of 0.5 to this estimate of SED at a point, our RI implies a dextral slip-rate of 24 ± 12 mm/yr (1σ), which overlaps with the Hope fault. Our data supports the hypothesis that slip on the Hope fault is mostly transferred northward onto the Jordan-Kekerengu-Needles fault to reach within 60 km of Wellington, rather than extending ENE along the offshore Hope fault. Since AD 1855, the Kekerengu and Wairarapa faults have ruptured >200 km of plate boundary with unusually large surface slips.

Key words: 2016 Kaikoura Earthquake, Kekerengu Fault, Paleoseismology

INTRODUCTION

The November 2016, Mw 7.8 Kaikoura earthquake ruptured many faults within a ~ 180 km long, NE-SW trending swath in NE South Island, New Zealand (Hamling et al., 2017, Kaiser et al., 2017, Litchfield et al., in review). In contrast to the complexity that characterized ruptures to the south, to the north of the Hope fault, the Kekerengu fault—together with its SW extensions the Jordan Thrust, Upper Kowhai fault and Manakau fault, and its NE offshore extension, the Needles fault—broke as a single, nearly continuous dextral-slip fault over a distance of ~ 90 km (Fig. 1). Displacements of >8 m were widespread, and locally slip reached nearly 12 m—the latter being one of the largest known surface displacements measured globally (Kearsse et al., this volume).

Our goal was to extend the record of seismic activity on the Kekerengu fault into the past. Measuring the tempo of major earthquakes on the Kekerengu fault would contribute to our understanding of the role of this fault in accommodating Pacific-Australia plate motion through central New Zealand. The Kekerengu fault is part of the Marlborough Fault System (MFS), a zone of active dextral-slip faulting that transfers Pacific-Australia plate motion between the Hikurangi subduction zone to the NE, and the Alpine fault to the SW (Figs. 1 and 2). Near Cook Strait between the North and South Islands of New Zealand, plate motion (Pacific relative to Australia) is ~ 40 mm/yr and trends WSW. Most slip on the Alpine fault is known to transfer northeastwards onto the Hope fault. Earthquakes on the Hope fault are known to occur at an average recurrence of 180 - 300 years (Langridge et al., 2003; Khajavi, 2016). The locus of plate motion beyond the onland Hope fault is less certain. Does slip extend ENE and offshore along the continuation of the Hope fault,

eventually to link with the Hikurangi margin? Or does slip step NE onto the Jordan and Kekerengu faults on the eastern flank of the Seaward Kaikoura Ranges before heading offshore farther north in Cook Strait? If the first scenario is correct, the pace of earthquake activity on the Kekerengu fault is predicted to be slow; if the second is correct, it should be fast (approximately on par with the Hope fault).

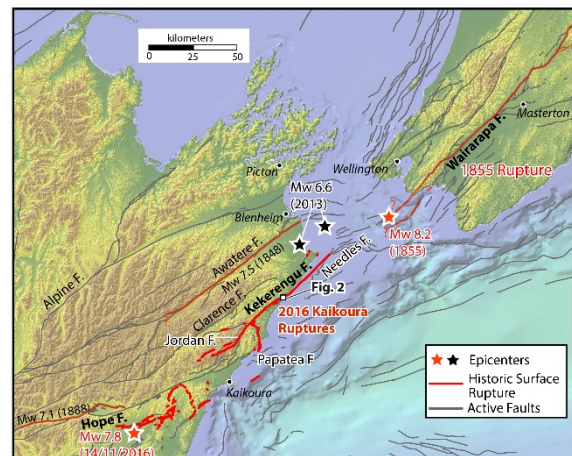


Figure 1: Location of the Kekerengu, Needles, Jordan, and Papatea faults in relation to other ruptures during the 16 November, 2016, Mw 7.8 Kaikoura earthquake (bold traces) and to other historic earthquakes, (after Barnes et al., 2008; Litchfield et al., in review).

TRENCHING RESULTS

Three fault trenches were excavated across prominent, topographically expressed traces of the Kekerengu fault on grass-covered hills near its intersection with its southern splay, the Heaven's Creek fault (Fig. 2). The eastern part of the Kekerengu fault is marked as a linear fault furrow that contains a string of small pull-apart basins. The basins are bounded by oblique-normal faults



on one or both sides. Trench 1 was excavated perpendicular to a 2-3 m-deep furrow enclosing a swampy depression. After it had been backfilled and ten months after its excavation, the trench was ruptured by the 2016 earthquake and displaced dextrally by ~9 m across a prominent moletrack (Fig. 3). Trench 2 was excavated across a similar furrow about 800 m along strike to the SW of Trench 1, but this fault strand did not rupture during the 2016 earthquake. Trench 3 was located about 40 m upslope and to the north of Trench 2 along a trace that did rupture in 2016. Because of length limits for this abstract, we here discuss logged relationships of a part of only Trench 1 (Fig. 4).

them, units “g,” “o,” “m,” and “ml” consist of silty clay or clayey silt, and were probably largely reworked from loess. The lenses were deposited in a swamp or pond that developed in the central ~2 m of the swampy topographic furrow. Seven samples from this trench were submitted for radiocarbon analysis from the fine-grained units infilling the synclinal depression along the axis of the topographic fault furrow. The syncline becomes incrementally tighter down-section. Crosscutting relationships and radiocarbon ages record three deformational increments that we attribute to a sequence of paleoearthquakes (E1, E2 and E3) that took place after ~1800 cal. yrs. B.P. Deformation during each increment included not only slip on faults, but also repeated deepening of the axial syncline. During each earthquake, minor extension across the central fault zone caused the depression to gravitationally collapse, leading to an incremental deepening of the sag basin and to angular discordances developing between the layers. In the subsequent interseismic period, the rejuvenated sag basin was partially infilled with undeformed peat or silt, thus reducing the amplitude of the syncline upward towards the surface. Using Oxcal 4.2.3 (Bronk Ramsey et al., 2013), we modeled event ages using the seven radiocarbon ages, the stratigraphic order of the dated samples, and historical constraints (i.e., no earthquake post A.D. 1840), which yields estimated ages of earthquakes as follows: E0, Kaikoura earthquake (A.D. 2016, -67 cal. yrs. B.P.); E1, 249-108 cal. yrs. B.P.; E2, 528-356 cal. yrs. B.P.; and E3, 1630-778, cal. yrs. B.P. Data from Trench 3 (not shown here) was used to narrow the age estimate of E3 to 1249-902 cal. yrs. B.P., and to identify an older event (E4), which is not robustly dated.

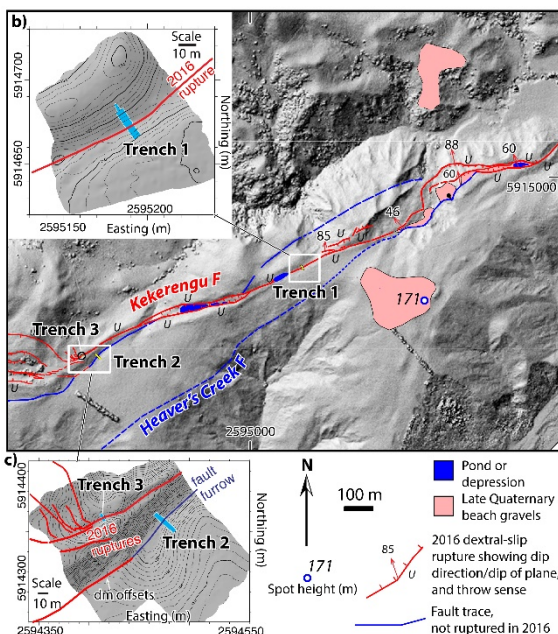


Figure 2: a) Map of active fault traces near the trenches. See Fig. 1 for location. Coordinates (in meters) are in New Zealand Map Grid. b and c) RTK-GPS derived topographic maps of trench sites 1, 2 and 3. Contour interval 50 cm.



Figure 3: Drone photograph (J. Thompson, GNS Science) of Trench 1 on 19 November, 2016, looking SW. People on left provide a scale. Dextral-slip is ~9 m.

The trench traversed a fault furrow (Figs. 2b, 3). Within a meter of the surface, several synclinal lenses of clayey silt or peat (units “uc”, “lp”, “mp” and “up”) are either cut by faults and/or have been deposited across them. Below

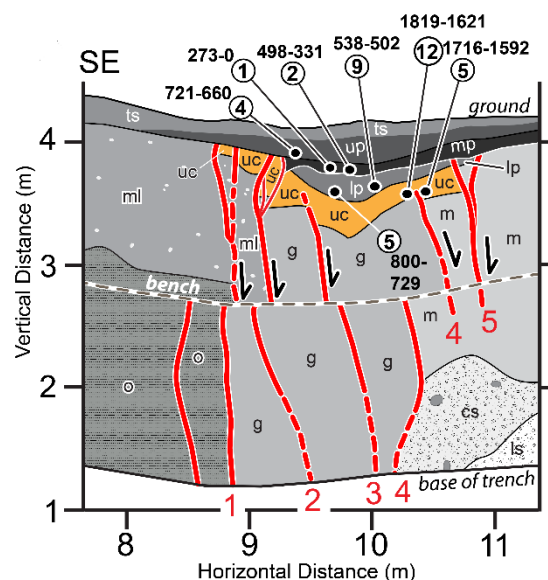


Figure 4: Detail of an upper part of the SW wall of Trench 1, showing mapped units, faults, and ¹⁴C samples and ages (displayed in cal. yrs. B.P. at 95% confidence). Units: “ml,” clayey silt; “o,” olive clay; “g,” grey clay; “m,” silty clay; “uc,” clayey silt; “lp,” organic silt-peat; “mp,” peat; “up,” organic silt-peat; “ts,” topsoil; “cs,” clayey silt; “ls,” limestone breccia (intepreted as landslide deposit).



DISCUSSION AND CONCLUSIONS

Including the 2016 earthquake, the sequence derived from an analysis of the data from our three trenches (Little et al., in review) includes at least four well-dated earthquakes in the past ~1200 years. On the basis of the last four events (three interseismic periods), we have estimated a mean recurrence interval for the Kekerengu fault (322-438 years at 95% confidence or 376 ± 32 yrs. at $\pm 1\sigma$). This result is within error of that evaluated for the Hurunui segment of the Hope fault (298 ± 98 years), where six well-resolved events have occurred since ~1600 cal. yrs. B.P. (Khajavi et al., 2016).

The timings of the youngest three paleoearthquakes on the Kekerengu fault are each within error (Fig. 5) of the youngest three paleoearthquakes on the Hope fault (Hurunui and Conway segments, Khajavi et al., 2016, Langridge et al., 2003). For example, both the Kekerengu and Hope faults experienced earthquakes in the immediate prehistoric period at <225 cal yrs B.P. This apparent temporal correlation suggests either that earthquakes took place on the adjacent Hope and Kekerengu faults at intervals that were smaller than radiocarbon dating can resolve—perhaps as a result of static stress triggering; or that the two faults ruptured together during single earthquakes. The 2016 Kaikoura earthquake involved a cascade of ruptures on many faults over a distance of ~180 km (Kaiser et al., 2017)—thus the idea of coeval rupturing on these two major faults seems plausible, especially as they intersect one another (via the Jordan thrust and upper Kowhai fault). On the other hand, the Kekerengu fault ruptured in its entirety during the 2016 earthquake, yet the Hope fault did not rupture on the surface except along a <1 km-long coastal trace that slipped dextrally by ~15 cm. Litchfield et al. (in review) argue that the 2016 earthquake cannot be “typical”, as it involved coeval rupturing on faults having discordant long-term recurrence intervals; for example, ~300-400 yrs on Kekerengu fault, ~3100 yrs on the Hundalee fault, and ~13000 yrs on the Humps fault.

The similar mean earthquake recurrence intervals of the Hope and Kekerengu faults supports the model of plate boundary slip in the South Island being transferred northward from the Hope fault predominantly onto the Jordan-Kekerengu-Needles fault system (Van Dissen & Yeats, 1991). During the 2016 earthquake, the eastern, near-coastal part of the Kekerengu fault near our trenches slipped dextrally by 9.13 ± 0.4 m (Kearse et al., this volume, and manuscript in review). If this magnitude of single event displacement (SED) is representative of the eastern section of the Kekerengu fault (and here we attribute a coefficient of variation of 0.5 to this estimate of mean single-event displacement at a point after Hecker et al., 2013) then our derived recurrence interval of 376 ± 32 yrs (1σ) for this section implies a slip rate of 24 ± 12 mm/yr (1σ). The estimate is within error of a preliminary late Quaternary slip-rate for the Kekerengu fault determined by Van Dissen et al. (2016), based on the dextral offset of late Quaternary fluvial terraces (23 ± 3 mm/yr), and both are similar to the

Late Quaternary slip rate on the Hope fault (Conway segment), which is 23 ± 4 mm/yr (1σ) (Langridge et al., 2003, 2010). While the SED derived slip rate is speculative, the data support the model of predominantly northward slip transfer from the Hope fault onto to the Jordan-Kekerengu-Needles fault system.

Northward routing of plate boundary deformation onto the offshore Needles fault in Cook Strait positions an active fault with a short recurrence interval (RI) and large Single Event Displacement (SED) to within ~60 km of Wellington City—much closer than if most of plate boundary motion went offshore along the Hope fault ~100-150 km distance from Wellington. The current National Seismic Hazard Model for New Zealand (Stirling et al., 2012) focuses slip and earthquake hazard on the Kekerengu-Needles fault system, attributing fewer earthquakes and less slip to the offshore Hope system. So our study supports key assumptions that are encoded into the National Seismic Hazard Model for New Zealand.

Another relationship highlighted by this study is the efficacy by which earthquakes during the last ca. 160 years have ruptured the plate boundary in central New Zealand (Fig. 1). For example, the 1855 and 2016 earthquakes jointly combined to generate over 300 km of surface fault rupture, with very large dextral displacements (up to ~18 m on the Wairarapa fault in 1855, and up to ~12 m on the Kekerengu fault in 2016). The Wairarapa and Kekerengu ruptures are, respectively, the largest, and one of the top-several largest earthquake surface displacements thus far recognized globally. Rodgers & Little (2006) argued that the large displacement (and especially the large displacement to length ratio) of the Wairarapa fault rupture reflects its unusually large down-dip extent and low aspect ratio, such that the rupture may have reached—and perhaps co-ruptured with—the subduction interface in 1855. Similarly, Hamling et al.’s (2017), elastic dislocation modeling of coseismic deformation in the 2016 earthquake requires the rupture of the Kekerengu fault to have slipped dextrally by up to ~20 m, and to have extended down to at least ~25 km depth. The combined Wairarapa and Kekerengu-Needles faults thus accommodate a large fraction of plate boundary slip traversing Cook Strait.

Finally, the penultimate earthquake on the Kekerengu fault (E1) preceded the 1855 earthquake on the Wairarapa fault by <144 years and perhaps by only a few decades (Fig. 5). Similarly, Event E3 on the Kekerengu fault, at 1249-903 cal. yrs. B.P., probably closely predated the penultimate earthquake on the Wairarapa fault at 920–800 cal. yrs. B.P. (Little et al., 2009). These relationships suggest possible stress triggering between the Kekerengu-Needles and Wairarapa faults, which are separated by <50 km across Cook Strait and occur along-strike of one another (Fig. 1).

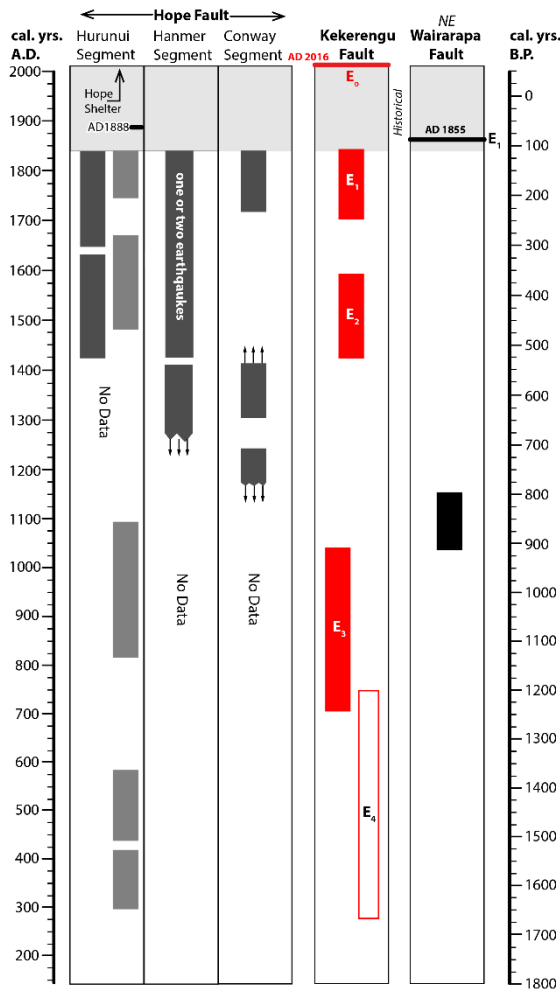


Figure 5: Space-time plot of late Holocene earthquake ruptures inferred from historic and paleoseismic data on selected sections of the Hope fault (compilation of Langridge et al., 2013, also Khajavi et al., 2016); the Kekerengu fault (Little et al., in review); and the Wairarapa Fault (Little et al., 2009).

Acknowledgements: This work was funded by Natural Hazards Research Platform grant 2015-NHRP-VUW-01, and by the 2015 Victoria University of Wellington, Student Summer Scholarship Scheme. We thank Tom Rockwell for reviewing the paper.

REFERENCES

- Barnes, P.M., Pondard, N., Lamarche, G., Mountjoy, J., Van Dissen, R., Litchfield, N., 2008. It's Our Fault: Active faults and earthquake sources in Cook Strait. *National Institute of Water & Atmospheric Research Client Report* WLG2008-56.
- Bronk Ramsey, C., 2013. *OxCal Program*, v. 4.1.7. Oxford, UK, Radiocarbon Accelerator Unit, University of Oxford <https://c14.arch.ox.ac.uk/oxcal.html>.
- Hamling, I. J., Hreinsdóttir, S., Clark, K., Elliott, J., Liang, C., Fielding, E., Litchfield, N., Villamor, P., Wallace, L., Wright, T. J., et al., 2017. Complex multi-fault rupture during the 2016 Mw 7.8

Kaikōura earthquake, New Zealand. *Science*, doi: 10.1126/science.aam7194.

Hecker, S., Abrahamson, N.A., Wooddell, K.E. 2013. Variability of displacement at a point: Implications for earthquake-size distribution and rupture hazard on faults. *Bulletin Seismological Society of America* 103, 651-674.

Kaiser, A., Balfour, N., Fry, B., Holden, C., Litchfield, N., Gerstenberger, et al., 2017, The Kaikōura (New Zealand) earthquake: preliminary seismological report. *Seismological Research Letters* 88, doi:10.1785/0220170018.

Kearse, J., Little, T. Van Dissen, R., Barnes, P., Mountjoy, J., Ries, W., Langridge, R., Villamor, P., Benson, A., Hill, M., Hemphill-Haley, M., Lamarche, G., this volume. Surface Rupture and Slip distribution of the Kekerengu Fault during the Mw 7.8 2016 Kaikōura Earthquake. In: *8th International INQUA Meeting on Paleoseismology, Active Tectonics and Archeoseismology (PATA)*, 13 – 16 November, 2017, New Zealand, pages.

Khajavi, N., Langridge, L.M., Quigley, M.C., Smart, C., Rezanejad, A., Martin-Gonzalez, F., 2016. Late Holocene rupture behaviour and earthquake chronology on the Hope Fault, *Geological Society of America Bulletin* 128, 1736-1761.

Langridge, R.M., Almond, P.C., Duncan, R.P., 2013. Timing of Holocene paleoearthquakes on the Hurunui segment of the Hope fault: Implications for plate boundary strain release through South Island, New Zealand, *Geological Society of America Bulletin* 125, 756-775.

Langridge, R.M., Campbell, J.K., Hill, J.K., Pere, V., Pope, J., Pettinga, J.R., Estrada, B., Berryman, K.R., 2003. Paleoseismology and slip rate of the Conway Segment of the Hope Fault at Greenburn Stream, South Island, New Zealand. *Annals in Geophysics* 46, 1119-1139.

Langridge, L.M., Villamor, P., Basili, R., Almond, P.C., Martinez-Diaz, J.J., Conora, C., 2010. Revised slip rates for the Alpine fault at Inchbonnie: Implications for plate boundary kinematics of S. Island, New Zealand. *Lithosphere* 2 139-152.

Litchfield, N. J., Villamor, P., Van Dissen, R. J., Nicol, A., Pettinga, J. Barnes, P., et al., in review. Large and complex, multiple surface fault ruptures in the 2016 Mw 7.8 Kaikōura Earthquake, *Geology*.

Little, T. A., Van Dissen, R., Kearse, J., Norton, K., Benson, A., and Wang, N., in review. Kekerengu fault, New Zealand: timing and size of Late Holocene surface ruptures. *Bulletin of the Seismological Society of America*.

Little, T.A., Van Dissen, R., Schermer, E., Carne, R., 2009. Late Holocene surface ruptures on the southern Wairarapa fault, New Zealand: Link between earthquakes and the uplifting of beach ridges on a rocky coast, *Lithosphere* 1, 1-23.

Rodgers, D.W., Little, T. A., 2006. World's largest co-seismic strike-slip offset: The 1855 rupture of the Wairarapa Fault, New Zealand, and implications for displacement/length scaling of continental earthquakes. *Journal of Geophysical Research* 111, B12408, doi:12410.11029/12005JB004065.

Stirling, M. W., McVerry, G. H., Gerstenberger, M. C., Litchfield, N. J., Van Dissen, R. J., Berryman, K. R., Barnes, P., Wallace, L. M., Villamor, P., Langridge, R. M., et al., 2012. National seismic hazard model for New Zealand: 2010 update, *Bulletin Seismological Society of America* 102, 1514-1542.

Van Dissen, and R., Yeats, 1991. Hope fault, Jordan thrust, and uplift of the Seaward Kaikōura Range, New Zealand, *Geology* 19, 393-396.

Van Dissen, R.J., et al., 2016, Late Quaternary dextral slip rate of the Kekerengu Fault: New Zealand's third fastest on-land fault: New Zealand GeoSciences Society Conference (Wanaka, New Zealand). *GeoSciences Society of New Zealand, Miscellaneous Publication* 142A.



Fast fault tip propagation driven by near-surface lithology: evidence from trishear inverse modeling

Franz Livio (1), Chiara Frigerio (1), M. Francesca Ferrario (1) and Alessandro M. Michetti (1)

(1) Università degli Studi dell'Insubria, via Valleggio, 11 22100 – Como (ITALY).

Abstract: The assessment of potential for surface faulting (i.e., Fault Displacement Hazard Assessment – FDHA) has gained an increasing interest in recent years due to recent strong earthquakes that caused widespread and well-documented surface rupture. Near-surface geology (i.e., lithology; sub-cropping bedrock versus a thick cover of quaternary sediments) has obviously a significant control in promoting or inhibiting surface faulting, as also observed during some well-documented earthquake ruptures (i.e., the 2016 M_w 7.2 El-Mayor eq.; the 2016 M_w 6 South Napa event, and the 2016 - 2017 M_w 5.9- 6.6 Central Italy seismic sequence). Fault differential behaviour is expressed in kinematic models (e.g., trishear model) as “Propagation/Slip Ratio” (P/S) which is considered as the amount of upward propagation of the fault tip per unit of slip. Here, we show some preliminary results on the kinematic inverse modelling of a fault propagation fold at Monte Netto hill (Capriano del Colle, BS, Northern Italy). At this site, we demonstrate that shallow stratigraphy can significantly change the potential of surface faulting from an upward propagating fault. In the upper ca. 50 m, the studied structure affects fluvial pre-growth strata and a sequence of fluvial and aeolian syn-growth sediments. Trishear kinematic restoration of the main fault plane and associated fold allows to perform a grid search over the parameters regulating fault growth and propagation. Our preliminary results indicate a two-stage growth history characterized by variable P/S values, slowing down from 7 to ca. 3. Stratigraphic data (i.e., several deep and shallower boreholes) show that a ca. 50 m-thick sequence of channel facies alluvial deposits is present beneath the section, overlaid by a fine-grained overbank sequence. We interpret the higher P/S value (i.e., 7) as due to the presence of the underlying clast-supported sediments. These promoted brittle fracturing rather than plastic and distributed deformation.

Key words: surface faulting; trishear kinematic modelling; FDHA

INTRODUCTION

The assessment of potential for surface faulting (i.e., Fault Displacement Hazard Assessment – FDHA) has gained an increasing interest in recent years due to recent strong earthquakes that caused widespread and well-documented primary and secondary rupture of the ground surface (e.g., the 2010 M_w 7.2 Baja California eq.; the 2010 M_w 7.1 Darfield and the 2016 M_w 7.8 Kaikoura earthquakes in New Zealand, the 2014 M_w 6 South Napa eq.; the 2016 M_w 7 Kumamoto earthquakes in Japan; and the 2016 M_w 5.9 - 6.6 Central Italy earthquake sequence, Fletcher and Spelz, 2009; Elliott et al., 2012; Floyd et al., 2016; Shirahama et al 2016; Livio et al. 2016; Pucci et al. 2016 Quigley et al 2016; Hamling et al. 2017;).

Present models of FDHA (e.g., ANSI/ANS-2.30, 2015) consider the probability of ground rupture and the amount of expected average slip as primarily controlled by the maximum expected magnitude and, in the case of distributed faulting, as a function of the distance from the primary fault. Nevertheless, we indicate that other parameters controlling the potential for surface faulting should be considered.

As mentioned in previous studies (Teran et al. 2015; Floyd et al. 2016; Livio et al., 2016), near-surface geology (i.e., lithology; overburden thickness; fluid

saturation of sediments) has a significant control on promoting or inhibiting surface faulting. Appropriate modelling and weighting of these parameters could significantly enhance the prediction power of the present FDHA models.

Trishear kinematic models depend solely on an area balancing assumption, although they resume well the geometries predicted by more complicated mechanical models (Cardozo et al. 2003). Kinematic models have the significant advantage of not implying the characteristics of the faulted rocks/sediments. such a complex interaction of geotechnical and rheological parameters is synthetically expressed in trishear deformation as “Propagation/Slip Ratio” (P/S) which is considered as the amount of upward propagation of the fault tip per unit of slip (Williams and Chapman, 1983). This is the most effective parameter in controlling the final fold geometry predicted by trishear models (Allmendinger & Shaw, 2000). For example, at lower P/S, larger strain cumulates in the triangular zone in front of the propagating fault, which results in a tighter fold.

Here, we show some preliminary results on the trishear inverse modelling of a break-through fault propagation fold, where it appears that the local stratigraphy plays a major role in promoting or inhibiting upward fault tip propagation.

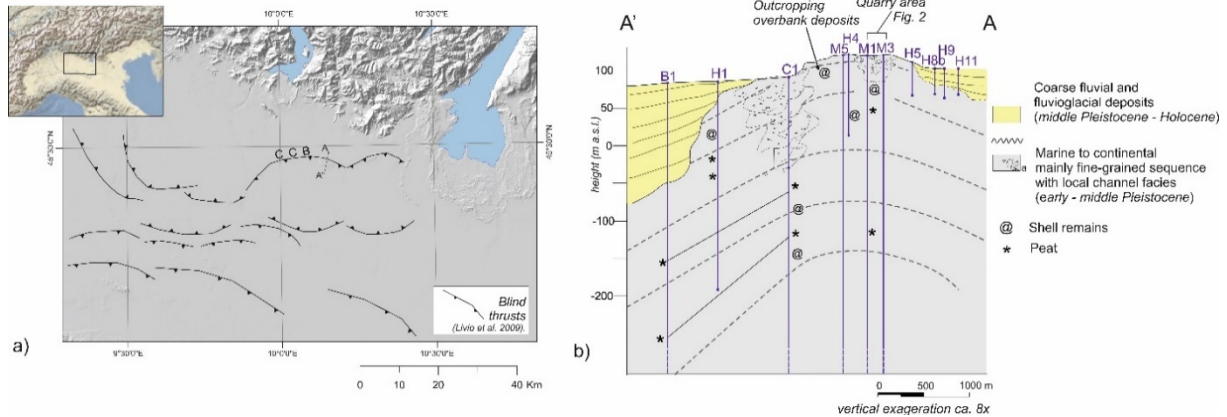


Figure 1: a) structural setting of the study area: a, shows the location of the study site on the Capriano del Colle backthrust (CCB) within the southern alps buried thrusts belt; b) detailed geological cross-section across the Monte Netto hill with borehole data.

STUDY SITE

Monte Netto hill, Italy, is located at the northern margin of the Po Plain foredeep, along an array of E-W trending thin-skinned blind thrusts (Fig. 1). Study site is located on top of a small isolated hill, at the structural culmination of CCB anticline: a north-verging fault-propagation fold (Fig. 1). Late Pleistocene to Holocene surface folding and faulting at meter-scale has been described in quarry area (Livio et al. 2009; 2014). In 2016, new excavations exposed a thrust fault zone, confirming previous interpretations and

offering the opportunity to investigate fault geometry and characteristics. The ca. 6 m-wide fault zone, cutting through a fluvial and overlying syn-growth loess-paleosol sequence, is composed by tens of discrete closely spaced reverse and thrust fault traces, striking ca. 290° (Fig. 2). Kinematic indicators point to a pure dip-slip thrust.

The fault has already been mapped as active (e.g., ITHACA, <https://goo.gl/fHFvwj> and DISS 3.2.0 <http://diss.rm.ingv.it/diss/>).

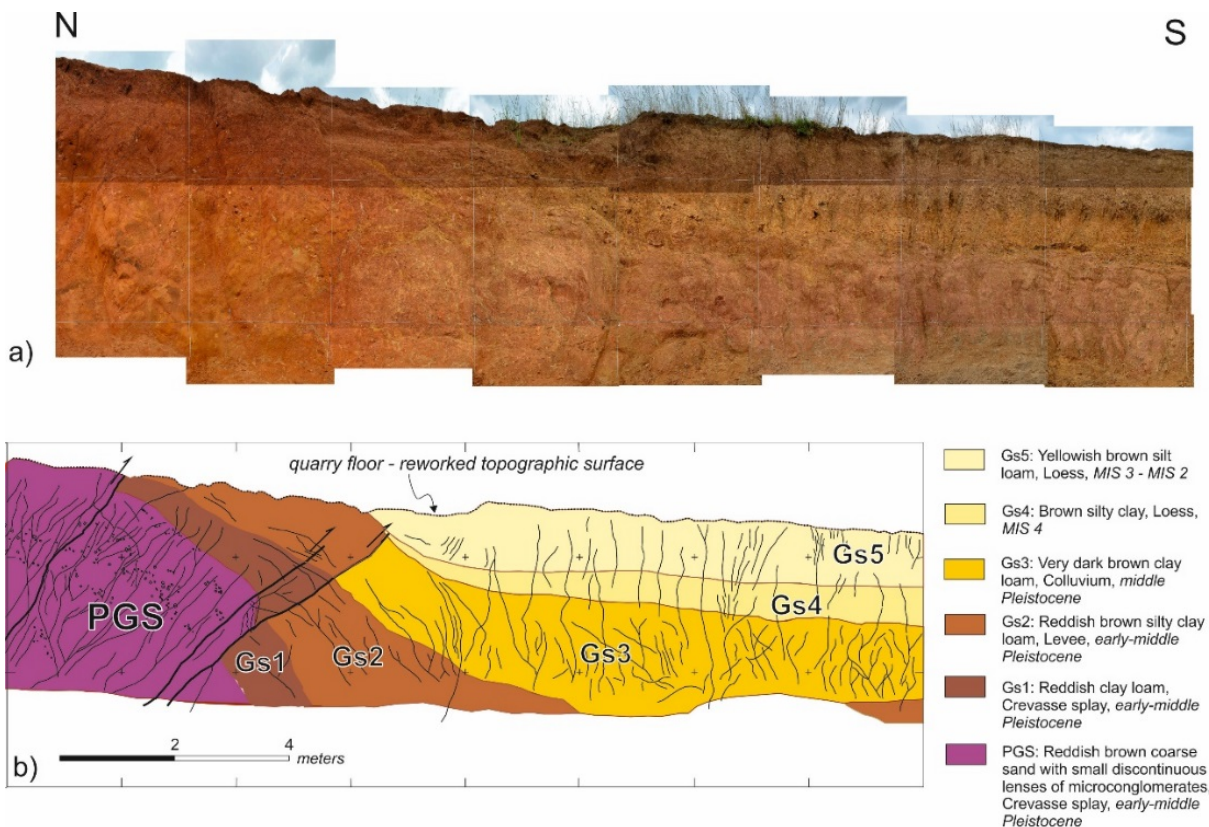


Figure 1: Analysed section outcropping in the Monte Netto quarry area. PGS, pre-growth strata; Gs1 to 5: growth strata.



There is no clear earthquake record on the fault. However, the site lies in the epicentral area of the destructive Dec. 25, 1222 earthquake (I₀ IX MCS; Guidoboni and Comastri, 2005).

RESULTS AND DISCUSSION

Trishear kinematic restoration of the break-through thrust according to a trishear model (Erslev, 1991) allowed to perform a grid search over the parameters regulating fault growth and propagation (i.e., fault slip, trishear angle, ramp angle, tip line position and P/S). We chose the most appropriate combination of parameters as that restoring a reference horizon to an original horizontal position and minimizing a statistical fitness score (chi-squared value). The restoration of the model was done according to best fit results. However, precise unfolding the anticline resulted in poor restoration of fault cutoffs. Conversely, precise retrodeformation of fault cutoffs obtained by lowering the P/S value, produced undesirable fold restoration (Fig. 3). Our results suggest that the total slip of 13 m was cumulated through a two-stage evolution; the fault propagated faster (P/S = 7) through deeper stratigraphic units and slower through shallower stratigraphic units (P/S ca. 3).

Stratigraphic data collected from a set of deep and shallow boreholes (fig. 1) show a 50 m-thick sequence of channel *facies* alluvial deposits overlaid by clay-rich silts and sands beneath the study site. We thus interpret that the modelled switch in the P/S value during fault growth is primarily due to shallow lithological variations beneath the site. Clast-supported channel sediments promoted brittle fracturing rather than plastic and distributed deformation. Vertical and lateral changes of lithological units would thus result in derived changes in the potential for surface faulting across the same fault. Our results provide new insights into fault displacement hazard assessment.

Moreover, these results have significant implications in paleoseismic investigations which are mainly based on the analysis of the on-fault displacements at the ground surface. Slow propagating faults can accommodate distributed deformation at surface rather than discrete faulting. Therefore, it is possible that we miss some paleoevents if careful analysis of horizon's geometry is lacking during paleoseismological trenching. To better assess the fault related hazards, an integrated approach is recommended including high resolution topographic surveys (e.g., terrestrial and airborne LiDAR, close-range photogrammetry, and total station topographic data).

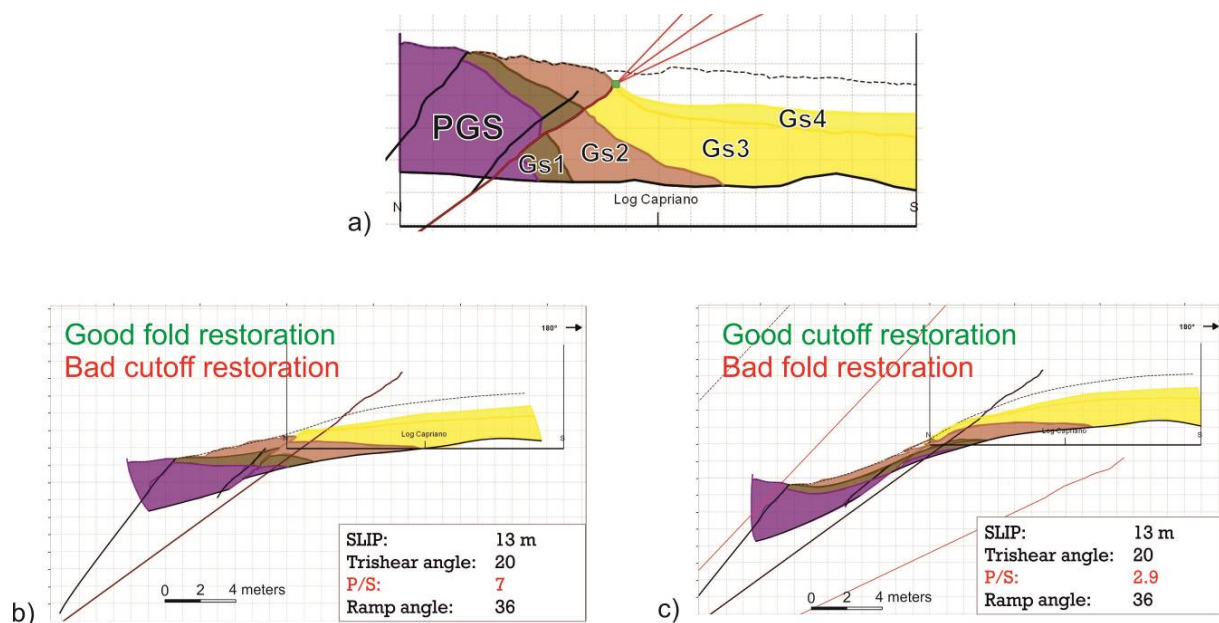


Figure 3: a) schematic restoration through trishear kinematic modeling: note the fault strand, in red and the associated trishear triangle at the fault tip; b) retrodeformation using the parameters obtained through the inverse grid search approach: fault cutoff has not been appropriately restored; c) retrodeformation obtained using the P/S value measured at outcrop (i.e., ca. 3): fold is not appropriately restored.



REFERENCES

- Allmendinger, R. W. and Shaw, J. H. (2000). Estimation of fault propagation distance from fold shape: Implications for earthquake hazard assessment. *Geology*, 28(12), 1099–1102.
- ANSI/ANS-2.30, 2015. Criteria for Assessing Tectonic Surface Fault Rupture and Deformation at Nuclear Facilities. Published by the American Nuclear Society.
- Capriano del Colle Municipality (2004). Studio geologico del territorio comunale – REPORT.
- Cardozo, N., K. Bhalla, A. T. Zehnder and R.W. Allmendinger (2003), Mechanical models of fault propagation folds and comparison to the trishear kinematic model, *Journal of Structural Geology*, 25(1), 1–18.
- Elliott, J. R., Nissen, E. K., England, P. C., Jackson, J. A., Lamb, S., Li, Z., Oehlers, M. and Parsons, B. (2012). Slip in the 2010–2011 Canterbury earthquakes, New Zealand. *Journal of Geophysical Research: Solid Earth*, 117(B3).
- Erslev, E. A. (1991). Trishear fault-propagation folding: *Geology*, 19(6), 617–620.
- Fletcher, J.M., and R.M., Spelz (2009), Patterns of Quaternary deformation and rupture propagation associated with an active low-angle normal fault, Laguna Salada, Mexico: Evidence of a rolling hinge?, *Geosphere*, v. 5, p. 385–407, doi:10.1130/GES00206.1.
- Floyd, M., Walters, R., Elliot, J., Funning, G., Svarc, J. L., Murray, J. R., Hooper, A.J., Larsen, Y., Marinkovic, P., Bürgmann, R., Johanson, I. and Wright, T. (2016). Rupture and afterslip of the 2014 South Napa earthquake reveal spatial variations in fault friction related to lithology. *Geophysical Research Letters*, 43(13), 6808–6816.
- Guidoboni, E. and Comastri, A. (editors), 2005. Catalogue of earthquakes and tsunamis in the Mediterranean area from the 11th to the 15th century. vol. II, INGV Istituto Nazionale di Geofisica e Vulcanologia & SGA Storia Geofisica e Ambiente S.r.l., Bologna, 950 p.
- Hamling, I. J., Hreinsdóttir, S., Clark, K., Elliott, J., Liang, C., Fielding, E., Litchfield, N., Villamor, P., Wallace, L., Wright T., D'Anastasio, E., Bannister, S., Burbidge, D., Denys, P., Gentle, P., Howarth, J., Mueller, C., Palmer N., Pearson, C., Power, W., Bernes, P., Barrel, D., Van Dissen, R., Langridge, R., Tittle, T., Nicol, A., Pettinga, J., Rowland, J. And Stirling M. (2017). Complex multifault rupture during the 2016 Mw 7.8 Kaikōura earthquake, New Zealand. *Science*, 356(6334), eaam7194.
- Livio, F. A., Berlusconi, A., Michetti, A. M., Sileo, G., Zerboni, A., Trombino, L., Cremaschi, M., Mueller, K., Vittori, E., Carcano, C. and Rogledi, S. (2009). Active fault-related folding in the epicentral area of the December 25, 1222 (I₀= IX MCS) Brescia earthquake (Northern Italy): seismotectonic implications. *Tectonophysics*, 476(1), 320–335.
- Livio, F. A., Berlusconi, A., Zerboni, A., Trombino, L., Sileo, G., Michetti, A. M., Rodnicht, H. and Spötl, C. (2014). Progressive offset and surface deformation along a seismogenic blind thrust in the Po Plain foredeep (Southern Alps, Northern Italy). *Journal of Geophysical Research: Solid Earth*, 119(10), 7701–7721.
- Livio, F., Michetti, A., Vittori, E., Gregory, L., Wedmore, L., Piccardi, L., Tondi, E., Roberts, G., W.G., C., Blumetti, A., Bonadeo, L., Brunamonte, F., Commerci, V., Di Manna, P., Ferrario, M., Walker, J., Frigerio, C., Fumanti, F., Guerrieri, L., Iezzi, F., Leoni, G., McCaffrey, K., Mildon, Z., Phillips, R., Rhodes, E., Walters, R., and Wilkinson, M. (2016). Surface faulting during the August 24, 2016, central Italy earthquake (Mw 6.0): preliminary results. *Annals of Geophysics*, 59. doi:http://dx.doi.org/10.4401/ag-7197.
- Pucci, S., De Martini, P. M., Civico, R., Villani, F., Nappi, R., Ricci, T., Azzaro, R., Brunori, C.A., Caciagli, M., Cinti F.R., Sapia, V. De Ritis, R., Mazzarini, F., Tarquini, S., Gaudiosi, G., Nave, R., Alessio, G., Smedile, A., Alfonsi, L., Cucci, L. and Pantosti, D. (2017). Coseismic ruptures of the 24 August 2016, Mw 6.0 Amatrice earthquake (central Italy). *Geophysical Research Letters*, 44(5), 2138–2147.
- Quigley, M. C., Hughes, M. W., Bradley, B. A., van Ballegooy, S., Reid, C., Morgenroth, J., Horton, T., Duffy, B. & Pettinga, J. R. (2016). The 2010–2011 Canterbury earthquake sequence: Environmental effects, seismic triggering thresholds and geologic legacy. *Tectonophysics*, 672, 228–274.
- Shirahama, Y., Yoshimi, M., Awata, Y., Maruyama, T., Azuma, T., Miyashita, Y., Mori, H., Takeda, N., Ochi, T., Oktsubo M., Asahina D. & Otsubo, M. (2016). Characteristics of the surface ruptures associated with the 2016 Kumamoto earthquake sequence, central Kyushu, Japan. *Earth, Planets and Space*, 68(1), 191.
- Teran, O.J., Fletcher, J.M., Oskin, M.E., Rockwell, T.K., Hudnut, K.W., Spelz, R.M., Akciz, S.O., Hernandez-Flores, A.P., and Morelan, A.E. (2015). Geologic and structural controls on rupture zone fabric: A field-based study of the 2010 Mw 7.2 El Mayor–Cuapah earthquake surface rupture: *Geosphere*, v. 11, no. 3, p. 899–920, doi:10.1130/GES01078.1.
- Williams, G., and Chapman, T. (1983). Strains developed in the hangingwalls of thrusts due to their slip/propagation rate; a dislocation model: *Journal of Structural Geology*, 5(6), 563–571.



Surface displacements in the 2016 Kaikoura earthquake derived from multi-scale optical data

Mackenzie, David (1), Elliott, John (2), Rhodes, Ed (3), Lamb, Simon (4), Parsons, Barry (1)

(1) University of Oxford, Oxford, UK, david.mackenzie@earth.ox.ac.uk

(2) University of Leeds, Leeds, UK

(3) University of Sheffield, Sheffield, UK

(4) Victoria University, Wellington, NZ

Abstract: The November 14th MW 7.8 Kaikoura Earthquake ruptured a complex array of faults in the South Island of New Zealand. We use high resolution stereo and tri-stereo optical satellite data, medium resolution satellite imagery and aerial photomosaics to directly construct a 3D displacement field for the earthquake without many of the biases/ambiguities of InSAR. Complementing the space-based photogrammetric DEMs, we collected photographs for structure-from-motion DEMs in a narrow corridor along three of the primary surface traces. Such high-resolution surveys provide independent constraints on surface slip at a variety of scales. Our multi-resolution approach demonstrates the utility of optical imaging, photogrammetry, and image and elevation model correlation, to rapidly document surface deformation at a broad range of scales following a large earthquake. We use our derived displacement field to investigate the link between earthquakes, the tectonic setting and the long-term evolution of the landscape.

Key words: 3D displacement field, Surface faulting, Slip geometry, Photogrammetry, Image correlation.

INTRODUCTION

On November 14th the South Island of New Zealand was struck by a M_w 7.8 earthquake causing extensive damage throughout the Kaikoura, Marlborough, Hurunui and Wellington districts. InSAR, GPS and seismological data suggest a complicated, multi-segment rupture through a large array of faults, most but not all previously mapped as active [Hamling *et al.*, 2017; Hollingsworth *et al.*, 2017; Kaiser *et al.*, 2017]. This earthquake therefore joins a suite of earthquakes in recent years which have ruptured complex series of linked faults, previously unanticipated in seismic hazard models [e.g. Wei *et al.*, 2011; Elliott *et al.*, 2012].

The 2016 Kaikoura earthquake presents an opportunity to study the interaction between fault segments in a dense network of faults. The variety of styles of faulting observed in the earthquake also presents difficulties in linking the behaviour of faults in individual earthquakes to long-term fault displacements and mountain building.

InSAR data provides precise constraints on the far field displacement for the Kaikoura earthquake, but the majority of the near-field region decorrelates due to very steep displacement gradients and ground damage [Hamling *et al.*, 2017]. ALOS2 L-band interferograms maintain coherence over the southern faults (South of Kaikoura), but loose coherence to the north. Sentinel 1 C-band interferograms are incoherent through the majority of the near field, region. Offset tracking by amplitude cross correlation of the SAR images can be used to partially complete the displacement map, but the resolution is much diminished, especially in the along-track (azimuth) direction. Thus it can only provide good constraint on the range-component of motion (i.e. in the

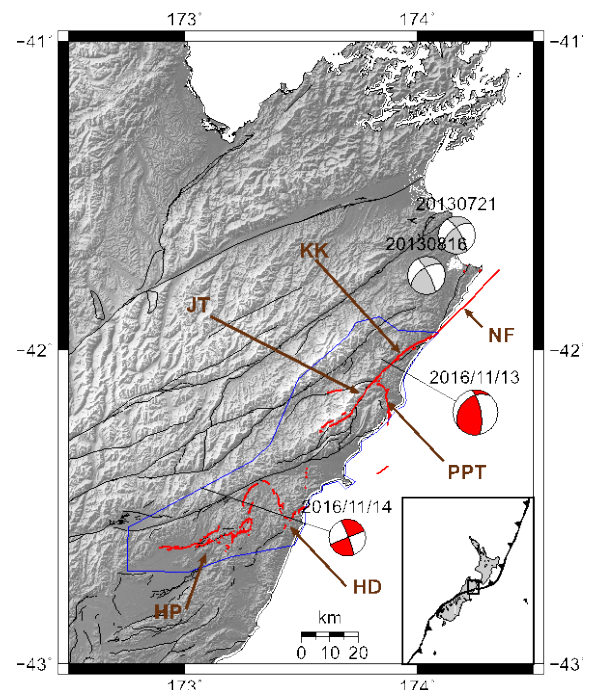


Figure 1: Epicentral region of the 2016 Kaikoura earthquake. Black lines show the NZ active fault database [Langridge *et al.*, 2016], while red shows the mapped surface ruptures. The blue polygon indicates the extents of the Pleiades dataset. Focal mechanism (GCMT, Ekström *et al.*, 2012) for the mainshock and largest aftershock are shown in red, and the mechanisms for the Cook Strait/Seddon Earthquake sequence are shown in grey. Fault labels: KK – Kekerengu Fault, PPT – Papatea Fault, NF – Needles Fault, HD – Hundalee Fault, HU – Humps Fault.

satellite line-of-sight). In addition to SAR, cross-correlation of Landsat 8 optical imagery has been used to image the horizontal surface displacements, but is also limited by the imaging resolution (15 m), such that the smallest



resolvable displacements are ~1m [Hollingsworth *et al.*, 2017]. Here, we complement previous studies with a study of the near-field domain using high and very high resolution satellite (70 cm and 2.5 m) and aerial (30 cm) imagery to construct a 3D displacement field.

METHODS

We extract a 3D displacement field for the earthquake by combining a variety of optical datasets to form and estimate independent of the SAR and InSAR datasets. The pre- and post-earthquake datasets are outlined in table 1. The primary post-earthquake dataset is 70cm resolution tri-stereo Pleiades data (17 overlapping tiles, outline in Figure 1). Prior to the earthquake, there is a 30 cm resolution aerial photo orthomosaic (Environment Canterbury & LINZ) and a series of SPOT6 stereo acquisitions (same footprint as the Pleiades data).

The post-earthquake Pleiades data are used to generate a Digital Surface Model (DSM) and ortho imagery using the ERDAS Imagine Photogrammetry Suite, with a joint bundle adjustment refinement of the RPC parameters and a correlation window of 7 px. Similarly, the SPOT6 data are used to generate a pre-earthquake DSM (at a resolution of 5 m), however these data were mostly acquired during winter time with deep shadows on the south facing slopes and poor dynamic range due to snow-capped peaks. As a result the pre-earthquake elevation model is poor and contains holes in its coverage.

To generate the 3D displacement field, we use COSI-CORR toolbox [Leprince *et al.*, 2007] to estimate a horizontal displacement field between the aerial orthomosaic and Pleiades orthoimagery. The large displacements (>8 m) relative to the image pixel size (0.7 m) necessitates using a large sampling window. Smaller windows resulted in poor signal-to-noise ratios. Using the COSI-CORR denoising routine (Non-local means) and median filtering we generate a smoothed horizontal displacement field preserving fault discontinuities. We then retro-deform the post-earthquake elevation pointcloud, re-grid it and difference it with the pre-earthquake elevation data to estimate a vertical displacement field.

The displacements derived from the image-correlation and DSM-differencing are also compared to estimates from smaller-scale structure-from-motion DSMs generated at key field sites. The images were acquired by helicopter and DJI Phantom 4 pro drone and the DSMs were generated using the Agisoft Photoscan package.

RESULTS

Figure 2 shows the preliminary results for the horizontal displacement field and DSM differencing around the region of the Papatea, Kekerengu and Jordan Thrust intersection where large surface offsets were observed in the field and InSAR displacements.

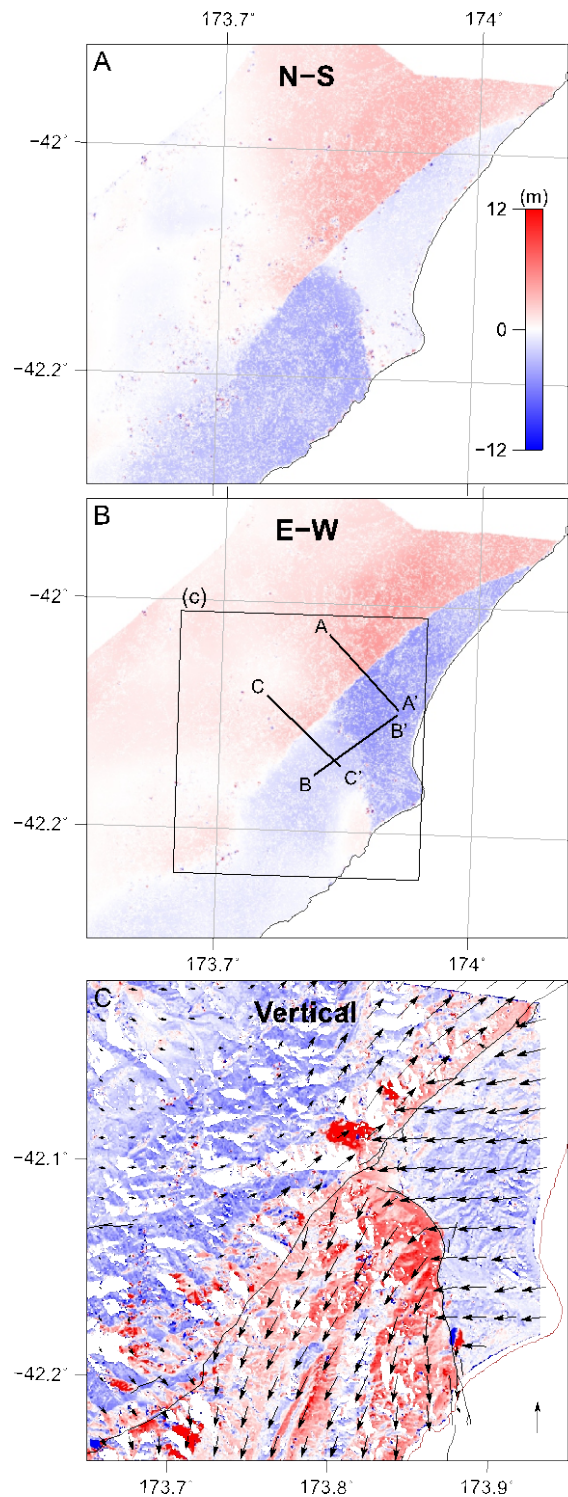


Figure 2: Displacement field for the northern faults. A: East-west displacements. B: North-south displacements. Also shown are the lines of the profiles in Figure 4. C: Vertical displacement field with a subsampled vector field showing the horizontal components overlaid. Colour scale is consistent for all components.

The horizontal field shows a level of detail far in excess of what was possible in the SAR datasets – allowing us to directly interrogate the shortening/extensional and lateral components of slip on each fault. Several important observations can be made: The Jordan thrust, Kekerengu



Fault and Papatea Fault (locations in Figure 1) all show a negative divergence at the scales observed here (>200 m), both the Kekerengu and Jordan's faults show right-lateral displacements up to ~10 m, while the Papatea fault shows left-lateral displacements of up to ~5-6 m (Figure 3).

The vertical displacement field is much less well resolved here, primarily due to the noise and holes in the pre-earthquake DSM. A remnant of topography due to mis-registration is also – poorer in the regions of steeper topography present (failure to account fully for horizontal displacements leads to an apparent vertical difference due to the advection of the topography). The broad trends are visible however, with uplift of up to ~6-10 m in the Papatea block and mild uplift in the hangingwall of the Kekerengu fault.

Analysis of the remainder of the dataset (along faults south of Kaikoura) is still in progress, and further refinement of the vertical differencing is needed to unambiguously estimate the vertical displacements in regions of steep topography.

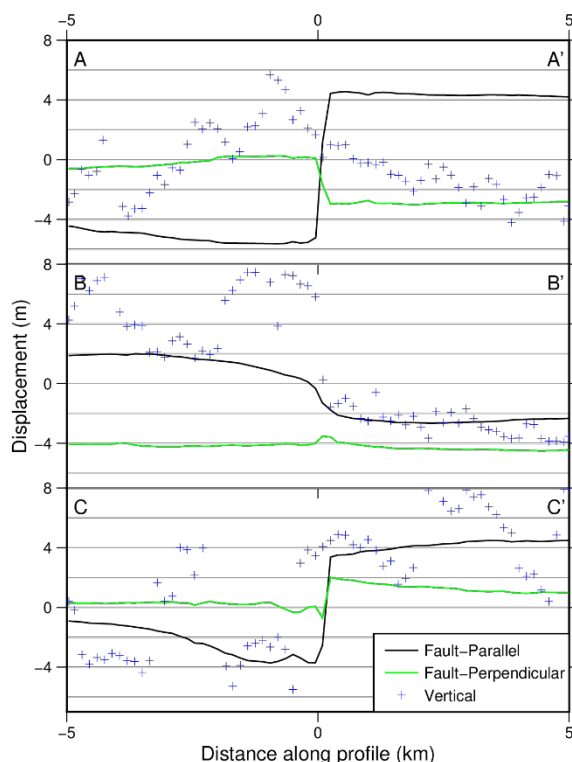


Figure 3: Three profiles through the displacement field (locations in Figure 2). Horizontal displacements have been projected on to fault-parallel and fault-perpendicular components at each profile. A positive change with positive distance along profile indicates right-lateral and extensional displacements respectively.

DISCUSSION

In general these observations agree with our field observations and those of others [Stirling *et al.*, 2017], with left-lateral oblique reverse displacements along the Papatea fault and primarily right-lateral (with minor reverse component) displacements along the Kekerengu fault.

When compared to long-term landscape morphology however, the displacements on the Jordan's Thrust appear to be opposite the sense of motion indicated on the mapped fault (blind-reverse, *Van Dissen and Yeats*, 1991). The optical displacement field shows extension of up to ~1-2 m across the fault at the northern end. We also observe normal scarps at the surface.

At the Papatea fault, we have observed vertical offset of ~8 m, and a left lateral offset of ~4 m and shortening of <50 cm. This implies an abnormally steep dip of >60° for a primarily dip-slip fault.

The normal-oblique slip on the Jordan's thrust are consistent with anelastic deformation in a restraining bend as suggested by *Hamling et al.*, 2017. We also note that at least the lateral component of slip appears relatively distributed at the northern section of the Papatea fault; approximately half of the left-lateral slip is accommodated over a wavelength of ~3 km into the hangingwall. This suggests some variation of the fault geometry in the uppermost few km – this gradient is particularly visible in the N-S component (Figure 2A), and is indicative of a more linear fault at depth despite the relatively sinuous surface trace. The vertical component of the displacement needs further refinement in order to establish whether the vertical slip is also distributed.

CONCLUSIONS

We have estimated a 3-component surface displacement field for the northern faults involved in the 2016 M_w 7.8 Kaikoura earthquake, New Zealand. In the near-field region the largest surface displacements are well resolved, showing that this technique is a useful complement to InSAR which is entirely decorrelated. This will be instrumental in resolving the kinematics of the Papatea fault block and slip in the uppermost crust.

Acknowledgements: This work was supported by funding from the UK Natural Environment Research Council (NERC) through the Looking Inside the Continents (LiCS) project (NE/K011006/1), and the Centre for the Observation and Modelling of Earthquakes, Volcanoes and Tectonics (COMET, COME30001, <http://comet.nerc.ac.uk>). We thank James Hollingsworth and Francois Ayoub for help and advice with image correlation, and Yu Zhou for advice on DEM differencing.

REFERENCES

- Van Dissen, R., and R. S. Yeats (1991), Hope Fault, Jordan Thrust, and uplift of the Seaward Kaikoura Range, New Zealand, *Geology*, 19(4), 393–396, doi:10.1130/0091-7613(1991)019<0393:HFJTAU>2.3.CO;2.
- Ekström, G., M. Nettles, and A. M. Dziewoński (2012), The global CMT project 2004–2010: Centroid-moment tensors for 13,017 earthquakes, *Phys. Earth Planet. Inter.*, 200–201, doi:10.1016/j.pepi.2012.04.002.
- Elliott, J. R., E. K. Nissen, P. C. England, J. A. Jackson, S. Lamb, Z. Li, M. Oehlers, and B. Parsons (2012), Slip in the 2010–2011 Canterbury earthquakes, New Zealand, *J. Geophys. Res. Solid Earth*, 117(B03401), doi:10.1029/2011JB008868.
- Hamling, I. J. *et al.* (2017), Complex multifault rupture during the 2016 M_w 7.8 Kaikōura earthquake, New Zealand, *Science* (80–



INQUA Focus Group Earthquake Geology and Seismic Hazards



paleoseismicity.org

-), 356(6334), eaam7194, doi:10.1126/science.aam7194.
- Hollingsworth, J., L. Ye, and J.-P. Avouac (2017), Dynamically triggered slip on a splay fault in the M w 7.8, 2016 Kaikoura (New Zealand) earthquake, *Geophys. Res. Lett.*, 44(8), 3517–3525, doi:10.1002/2016GL072228.
- Kaiser, A. et al. (2017), The 2016 Kaikōura, New Zealand, Earthquake: Preliminary Seismological Report, *Seismol. Res. Lett.*, 88(3), 727–739, doi:10.1785/0220170018.
- Langridge, R. M. et al. (2016), The New Zealand Active Faults Database, *New Zeal. J. Geol. Geophys.*, 59(1), 86–96, doi:10.1080/00288306.2015.1112818.
- Leprince, S., S. Barbot, F. Ayoub, and J.-P. Avouac (2007), Automatic and Precise Orthorectification, Coregistration, and Subpixel Correlation of Satellite Images, Application to Ground Deformation Measurements, *IEEE Trans. Geosci. Remote Sens.*, 45(6), 1529–1558, doi:10.1109/TGRS.2006.888937.
- Stirling, M. W. et al. (2017), The Mw7. 8 2016 Kaikōura earthquake: Surface fault rupture and seismic hazard context, *Bull. New Zeal. Soc. Earthq. Eng.*, 50(2), 73–84.
- Wei, S. et al. (2011), Superficial simplicity of the 2010 El Mayor–Cucapah earthquake of Baja California in Mexico, *Nat. Geosci.*, 4(9), 615–618, doi:10.1038/ngeo1213.



Untangling Tectonic Slip from the Potentially Misleading Effects of Landform Geometry

Mackenzie, David (1), Elliott, Austin (1)

(1) University of Oxford, Oxford, UK, david.mackenzie@earth.ox.ac.uk

Abstract: We present a new three-dimensional (3D) approach to the analysis of fault scarps using high-resolution elevation models. Advances in topographic measurement techniques [e.g., lidar (light detection and ranging) and photogrammetric techniques] have allowed extensive measurement of single earthquake and cumulative scarps to draw conclusions about along-strike slip variation and fault slip history. The resulting slip distributions are almost always variable and noisy, but the cause is often unclear. We first present the results of sensitivity analysis to demonstrate significant apparent noise due to varying terrain and fault and measurement geometry (topographic slope attitude, fault dip and slip obliquity). We show, with a case study on the Hoshab fault, Pakistan, that oblique slip can have a significant effect on the measured apparent slip.

Individual planar geomorphic markers only constrain one component of the full 3D slip vector. We use the variation in apparent offset with marker geometry to constrain the slip vector in 3D. Combining multiple offset measurements along strike, we show that determining the slip vector is reduced to a simple linear formulation. We test our method using a terrestrial lidar data set from the ruptures on the Borrego fault from the 2010 El Mayor–Cucapah earthquake (Baja California, Mexico). Combining 22 observations, we estimate a throw of 1.56 ± 0.02 m and a lateral slip of 1.9 ± 0.3 m. The vertical slip estimate agrees well with previous studies, but the lateral slip is significantly smaller. In regions of steep varied topography or with oblique slip, our method will give enhanced slip resolution while standard methods will give biased estimates.

This study is published (open access) at: <http://geosphere.geoscienceworld.org/content/early/2017/06/20/GES01386.1>



Uplift of Fluvial Meanders at Kendeng Fold and Thrust Belt (East Java, Indonesia): Evidence of Late Quaternary Thrust Faulting

Marliyani, Gayatri (1), Helmi, Hurien (2), Pramumijoyo, Subagyo (1), Arrowsmith, Ramon (3)

- (1) Geological Engineering Department, Universitas Gadjah Mada, Yogyakarta, Indonesia. gayatri.marliyani@ugm.ac.id
- (2) Geological Engineering Department, Sekolah Tinggi Teknologi Nasional, Yogyakarta, Indonesia.
- (3) School of Earth and Space Exploration, Arizona State University, Tempe, United States of America.

Abstract: Deformation in the back-arc region of Java, Indonesia forms the 200 km-long prominent topography of Kendeng fold and thrust belt which cuts through the heavily populated region of East-Central Java. Small-but-frequent earthquakes occur within proximity of this feature but the fault zone has yet to be classified as active and was not considered as a significant threat to the region. We identified an abandoned meander along the south-flowing Kabuh River that crosses one of the E-W trending folds, a few kilometers to the west of Kabuh town in East Java. The distinctly separated abandoned meander bend is located 3 meters above the adjacent active bedrock-incised channel, suggesting recent uplift. We estimate the uplift rate that may reflecting slip along the fault. We mapped the extent of the abandoned meander and excavated several shallow pits to identify the elevation of the paleochannel bottom. We collected 19 charcoal samples from various depths of the pits for 14C analysis. We surveyed the topography of the site using a total station. Additionally, we acquired aerial photos using a drone and created a high resolution digital elevation model of the site using photogrammetry. The 14C samples yield most dates ranging from 215 to 130BP. A sample taken from the oldest stratigraphy of the channel fill is 1680-1764 cal AD. With an elevation difference of 3 m, the date suggests an uplift rate of at least 10 mm/yr. Our result suggests that Kendeng thrust fault is actively deforming. Although the deformation of Kabuh strand, as suggested by this study is relatively slow, additional other strands along this 200km-long thrust fault may also be active and large earthquakes may occur. Further investigation along the thrust is needed to constrain the slip distribution along the fault and to assess the seismic hazards of the region.

Key words: Kendeng fold and thrust, fluvial meander, Quaternary uplift, thrust fault, active fault

INTRODUCTION

Java is part of a volcanic arc complex in the Sunda-Banda subduction system. The arc consists of (landward): fore-arc basins, active volcanic arc and back arc fold-and-thrust belt. This configuration is especially profound in the central and eastern part of Java.

The actively subducting Indian plate to the Eurasian causes an extensive deformation in Java that are associated with earthquakes. Although the deformation is evidenced in the geomorphic, geologic, and geodetic data (Hamilton, 1979; Koulali et al., 2014; Visser, 1922; Whichmann, 1918; De Genevraye and Samuel, 1972), there are only few studies that have quantified the deformation. The limited mapping of the region has likely led to an underestimate of hazard in the region.

In the back-arc region of East-Central Java, a 200 km-long prominent topography of Kendeng fold and thrust belt cuts through the heavily populated region. This fold and thrust belt is an example of a thin-skinned fold-and-thrust belt as a result from the distant push from the converging plate. Small-but-frequent earthquakes occur within proximity of this feature. However, the fault zone has yet to be classified as active and was not considered as a significant threat to the region.

During our active fault mapping campaign in 2012, we identified an abandoned meander along the south-flowing Kabuh River that crosses one of the E-W trending folds within Kendeng fold and thrust fault zone (Figure 1 and 2). It is located a few kilometres to the west of Kabuh town in East Java. The fold is characterized by a gently double plunging E-W striking axis. The distinctly separated abandoned meander bend is located 3 meters above the adjacent active bedrock-incised channel, suggesting recent uplift. We quantify the uplift rate by combining detailed topography mapping and radiocarbon dating of the abandoned-channel fill. This study provides an important contribution to the limited data of the long-term rate of deformation in Java crucial to improve the seismic hazard analysis of the area.

RESULTS AND DISCUSSION

We mapped the extent of the abandoned meander using surface geological and geomorphological mapping techniques. We excavated three shallow pits within the meander-fill (KBH 1, KBH 3, and KBH 4, Figure 3, Figure 4) to determine the bedrock elevation of the meander channels. In addition, we also excavate two other shallow pits in the terraces (KBH 2 and KBH 5, Figure 3). We collected 19 charcoal samples from various depths of the pits for 14C analysis. The radiocarbon analysis was done at the W. M. Keck Carbon Cycle Accelerator



Mass Spectrometry Laboratory at the University of California, Irvine.

To obtain detailed topography data for the site, we use a total station with a local georeferenced point. In addition, we acquired aerial photos using a drone and created a high resolution digital elevation model of the site using photogrammetry. The photogrammetry techniques provide a high resolution data up to centimetre resolution.

The surface of the palaeo-meander channels is horizontal. At the surface, the meander is filled with distinctively finer sediment than their surroundings. Dates taken from the meander fills yield most dates ranging from 215 to 130BP. A sample taken from the lowest stratigraphic unit in KBH 1 (Figure 5) dates the channel fill to 1680-1764 cal AD. The ages however, only represent the time when the meanders were abandoned and filled. It is not necessarily coincidence with the time of deformation. We assume that the abandonment of the meander was caused by the tectonic uplift along the Kendeng fold.

The elevation difference between the active channel and the paleochannel bottom is 3 m, which reflects the magnitude of vertical offset of the uplift events. The dates of our samples constrain the possible timing of the events. Assuming the vertical offset is a result of cumulative uplift events, we calculate the long-term rate of vertical separation of ~10 mm/yr. The number reflects a minimum estimate, as our calculation does not take into account regional subsidence and sedimentation rate. Nevertheless, our result suggests that Kendeng thrust fault is actively deforming.

Although the deformation of Kabuh strand, as suggested by this study is relatively slow, other strands along this 200 km-long thrust fault may also be active and large earthquakes may occur. Further investigation along the thrust is needed to constrain the slip distribution along the fault and to assess the seismic hazards of the region.

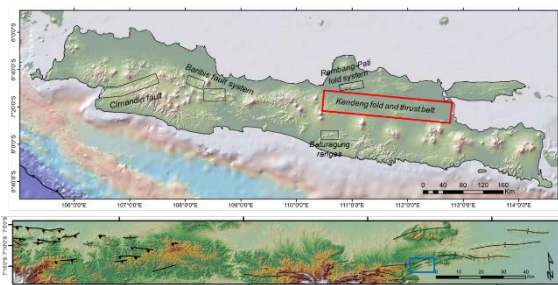


Figure 1: Map overlain on Global Multi-Resolution Topography (GMRT) data show the locations of the Kendeng and fold thrust (red quadrangle) and Kabuh site, the structures in the lower figure are adopted from Marliyani (2016). Blue box in the lower figure show the area of Figure 2.



Figure 2: The enlarge image of the blue box area of Figure A1. The Kabuh River (blue dashed line) flows across an anticline. The abandoned meander is located at ~3m above the active channel, some uplifted river terraces were also identified.

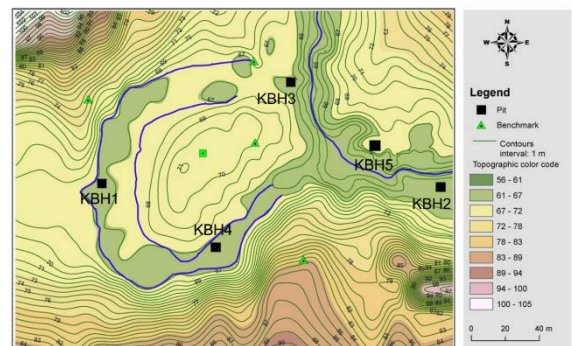


Figure 3: Contour map of the site generated using total station with local coordinate system indicate the location of the test pits excavated at this site (black squares). Green squares indicate the location of the survey station, green triangles are the benchmarks. Further processing is necessary to georeferencing the data into global coordinate system. Thick blue lines delineate the extent of the abandoned meander.



Figure 4: Photographs of the KBH-1 (left) and KBH 3 (right) pits that were excavated at Kabuh site. The pits were excavated and logged manually. Rapid logging was necessary to avoid flooding due to the shallow water table. Refer to Figure 3 for location.

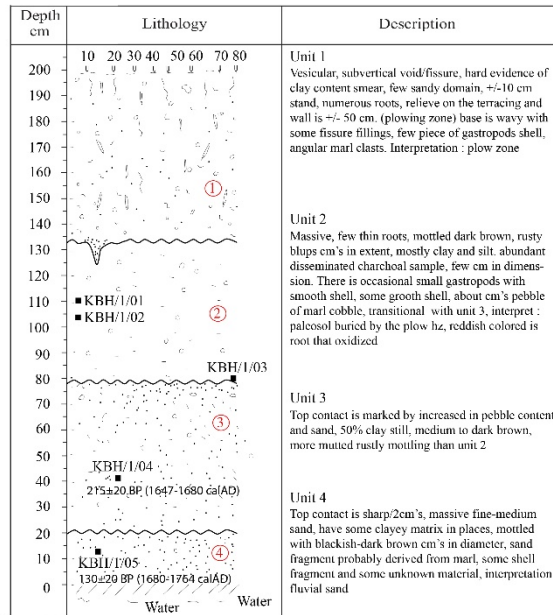


Figure 5: Log of KBH1 pit showing the typical sediment of the meander fill. Black squares indicate locations of radiocarbon samples. The radiocarbon dates is stratigraphically inconsistent, we use the youngest date taken from the oldest stratigraphic unit to estimate the age of the channel abandonment (1680-1764 calAD). Refer to Figure 3 for location.

Acknowledgements: We would like to thank the office of forestry and plantation of Jombang regency for allowing us to access the Kabuh site. This research was supported by funding from Geological Engineering Department, Universitas Gadjah Mada and the Schlumberger Foundation: Faculty for the Future.

REFERENCES

- De Genevraye, P. and Samuel, L., 1972. Geology of the Kendeng Zone (Central & East Java), 1st Annual Convention Proceedings, 1972, Pages 17-30.
- Hamilton, W., 1979, Tectonic of The Indonesian Region, USA, U.S. Geological Survey.
- Koulali, A., McClusky, S., Susilo, S., Leonard, Y., Cummins, P., Meilano, I., Efendi, J., and Wijanarto, A. B., 2016, *The kinematics of crustal deformation in Java from GPS observations: implications for fault slip partitioning*: Earth and Planetary Science Letter, v. In Press.
- Marliyani, G.I., 2016. *Neotectonics of Java, Indonesia: Crustal deformation in the overriding plate of an orthogonal subduction system*. Arizona State University.
- Visser, S. W., 1922, *Inland and Submarine epicentra of Sumatra and Java earthquakes: Koninklijk Magnetisch en Meteorologisch Observatorium te Batavia*, v. Verhandelingen no.9, p. 1-14.
- Wichmann, A., 1918, *Die Erdbeben des Indischen Archipels bis zum Jahre 1857: Verhandlungen der Koninklijke Akademie van Wetenschappen te Amsterdam (Tweede Sectie)*, Deel XX. No. 4.



Slope movements induced by strike-slip earthquakes in Western Greece

Mavroulis, Spyridon, Lekkas, Efthymios, Skourtsos, Emmanuel, Danamos, Georgios

Department of Dynamic Tectonic Applied Geology, Faculty of Geology and Geoenvironment, School of Sciences, National and Kapodistrian University of Athens, Panepistimiopolis, Athens 15784, Greece, smavroulis@geol.uoa.gr

Abstract: Over the last decade, four large earthquakes have occurred in Western Greece: the June 8, 2008 Mw=6.4 Andravida, the January 26 and February 3, 2014 Mw=6.0 Cephalonia and the November 17, 2015 Mw=6.4 Lefkas earthquakes. They were all generated by NE-SW striking dextral strike-slip faults with significant reverse component. They also induced extensive environmental effects including slope movements classified into landslides, rockfalls, rockslides and rock toppling failures. They affected various lithologies (clays, silts, sands, conglomerates, limestones, clastic sequences) in alpine and post-alpine formations. Based on field data, the recorded phenomena were highly concentrated in specific zones associated with lithology, tectonic structure and geomorphology. Taking into account that NW Peloponnese and Ionian Islands are among the most tectonically and seismically active areas, these phenomena are characterized as structurally controlled. Their distribution also supports earlier studies suggesting that they are concentrated in specific zones associated with bedrock geology, geomorphology, topography, and human factors.

Key words: Earthquake-induced landslides; rockfalls; strike-slip earthquakes; Peloponnese; Ionian Islands

INTRODUCTION

Earthquake-induced slope movements have recently drawn increasing attention from researchers of various scientific fields including tectonics, geomorphology, natural hazards, geographic information system (GIS) and remote sensing among others. Damage from earthquake-induced slope movements were documented from 1789 B.C. in China and 373 or 372 B.C. in Greece (Papadopoulos & Plessa, 2000; Zhou et al., 2016). They have claimed thousands of people's lives and caused large economic losses especially in mountainous areas, where damage and fatalities induced by the earthquake-induced landslides are larger than those caused by the earthquake itself (Keefer, 1984). During the last decades, various studies on earthquake-induced slope movements have been carried out.

Compiling of a detailed and comprehensive inventory and spatial distribution analyses of earthquake-induced slope movements are important in understanding which areas are most susceptible to this kind of failure in future earthquakes (Xu & Xu, 2016). Detailed co-seismic landslide inventories are also essential and important to landslides hazard assessment, topography evolution of the earthquake areas, controlling of active fault on landslide spatial distribution patterns, as well as inversion of earthquake-associated features (Xu and Xu, 2016). Moreover, this data represents a useful and reliable tool for assessing seismic intensity of significant earthquakes and furthermore for seismic hazard assessment in earthquake prone areas as earthquake-induced slope movements can be used as highly diagnostic elements in macroseismic intensity scales, including the Environmental Seismic Intensity 2007 (ESI-07) scale among others.

Landslide inventory maps can be produced using different techniques such as detailed field investigation,

digitalization of historic landslide inventory, visual interpretation of aerial photos, pc-aided supervised or unsupervised interpretation of remote sensing images (Qiao et al., 2013). Field investigation provides more detailed and intuitive landslide information, while photo interpretation method greatly enhances the efficiency of landslide inventory preparation and has become popular since the 1970s (Scaioni et al., 2014).

The aim of this study is to present the slope movements induced by the largest earthquakes in Western Greece during the last decade and study the factors controlling their generation and their spatial distribution. These slope movements were observed and recorded during emergency field reconnaissance of the earthquake-affected areas conducted immediately after each earthquake by members of the Department of Dynamic Tectonic and Applied Geology of the Faculty of Geology and Geoenvironment (NKUA) in order to obtain the firsthand information of the earthquake-triggered slope movements. Such information would be also important for earthquake rescue and subsequent scientific studies of coseismic slope movements.

THE LARGEST EARTHQUAKES IN WESTERN GREECE DURING THE LAST DECADE

Western Greece has recently experienced the destructive impact of four strong earthquakes, namely the June 8, 2008 Mw 6.4 Andravida (Northwestern Peloponnese) earthquake, the January 26 and the February 3, 2014 Mw 6.0 Cephalonia (Ionian Sea) earthquakes and the November 17, 2015 Mw 6.4 Lefkas (Ionian Sea) earthquake.

The most common characteristic of all four events is that they were generated by the activation of NNE-SSW to NE-SW strike-slip faults based on their moment tensor



solutions and the spatial distribution of their aftershock sequences derived from national and international seismological institutes and observatories. These tectonic structures have significantly affected the geodynamic setting of Western Greece and have played a decisive role in the evolution of the Northwestern Peloponnese and the Ionian Islands. Another similarity of these events is that they all have had extensive impact on the natural environment including generation of many secondary earthquake environmental effects such as ground cracks, slope movements, liquefaction phenomena and hydrological anomalies (Mavroulis et al., 2010, 2013; Lekkas & Mavroulis, 2015, 2016; Lekkas et al., 2016).

SLOPE MOVEMENTS INDUCED BY THE 2008 ANDRAVIDA (NORTHWESTERN PELOPONNESE) EARTHQUAKE

Slope movements induced by the 2008 Andravida earthquake were observed in 8 localities over a wide area NW Peloponnese (Fig. 1). The minimum distance of occurrence from the epicenter of the main shock was of 5.91 km, while the maximum was 24.4 km. They are classified as landslides (6 from 8 total cases) of formations consisting of alternations of marls, clays, silts, sands with consolidated or non-consolidated conglomerates along bedding planes and joints dipping towards the free face of road slopes and along active fault zones as well as rockfalls (2) along steep mountain slopes and active faults (Fig. 2). The volume of the mobilized geological material did not exceed 10m³, indicating a V_{ESI-07} intensity. The affected formations were alpine comprising Upper Cretaceous limestones of Gavrovo and Paxoi geotectonic units and Palaeocene-Middle Eocene limestones of Tripolis geotectonic unit as well as post-alpine deposits including Upper Pliocene-Pleistocene alternations of marls, clays, silts, sands with consolidated or non-consolidated conglomerates were affected by the aforementioned slope movements (Fig. 2). As regards their geotechnical characteristics, these lithologies can be further classified into (a) Quaternary loose deposits with mixed phases, (b) fractured formations with secondary loosening due to dense fracturing of beds and (c) highly tectonized formations, disintegrated into large or small fragments or their decomposition into powder.

As regards the factors controlling the generation and the spatial distribution of these slope movements, they were due to: (a) the strong ground shaking, (b) the presence of geological formations with mechanical characteristics that make formations susceptible to failure, (c) the strong heterogeneity and the rapid change of the mechanical characteristics in the different horizons both vertically and horizontally resulting in non-uniform and anisotropic mechanical behavior of formations, (d) the intense and multiple fracturing, erosion and weathering contributing to the decreased cohesion along steep mountain slopes as well as (e) the intense tectonic deformation along active fault zones resulting in a dense net of discontinuities and sectors of decreased cohesion and formations loosening.

SLOPE MOVEMENTS INDUCED BY THE 2014 CEPHALONIA (IONIAN SEA) EARTHQUAKES

Slope movements induced by the two strong earthquakes occurred in 2014 at Cephalonia were observed in 21 localities in the western part of the island (Fig. 1). The minimum and maximum distances of occurrence from the epicenters was 3.13 and 20.92 km respectively for the first earthquake and 1.57 and 16.59 km respectively for the second one. They are classified as landslides (3), rockfalls (2), while the majority of them (16) comprise mixed types of slope failures including rotational slides or slumps, translational slides, rockfalls and rock toppling failures (Fig. 2). The volume of the mobilized geological material varied from 1m³ in small rockfalls to larger than 10³m³ in mixed type phenomena indicating intensities ranging from V_{ESI-07} to VII_{ESI-07}. The affected formations were alpine formations including Middle Miocene-Early Pliocene clay-clastic sequence with marls, clays, mudstones and Triassic-Middle Miocene limestones of the Paxoi geotectonic unit as well as more recent deposits comprising Middle Pleistocene scree and Pliocene-Calabrian marls (Fig. 2).

The main factors controlling the generation of these slope movements were the particularly complex geotechnical regime and pre-existing instability conditions along geotechnically unstable zones characterized by fractured and brecciated rock mass, suitable geometry of beds and discontinuities, high and steep slopes and scarps. The intense tectonic uplift plays a decisive role in the development of instability conditions since it increases the inclination and the height of slopes. This tectonic deformation resulting in considerable uplift and intense incision have formed an area with adverse relief characterized by steep slopes, large morphological discontinuities, straight and deep thalwegs, which in combination with the lithological anisotropy of alpine formations and post-alpine deposits and the erosion and weathering processes contribute to decreased cohesion along steep slopes and scarps. All these endogenic and exogenic processes make the affected areas highly susceptible to the generation of slope movements and the early 2014 Cephalonia earthquakes act as triggering mechanisms for the generation of the aforementioned phenomena.

SLOPE MOVEMENTS INDUCED BY THE 2015 LEFKAS (IONIAN SEA) EARTHQUAKE

Slope movements induced by the 2015 Lefkas earthquakes were observed in 15 localities in the western part of the island (Fig. 1). The minimum and maximum distances of occurrence from the epicenter of the main shock was 1.09 and 17.39 km respectively. They are classified into landslides (7), rockfalls (4), mixed type phenomena comprising rockfalls and landslides (3) and mixed type phenomena comprising landslides, rockfalls and rockslides (1) (Fig. 2). The volume of the mobilized geological material varied from 10³ m³ in relatively small phenomena to 10⁵-10⁶ m³ in large landslides, indicating intensities varying from VI_{ESI-07} to VIII_{ESI-07}. The most affected lithologies were



in Alpine formations, especially Middle Miocene-Early Pliocene clay-clastic sequence with marls, clays and mudstones and Triassic-Middle Miocene limestones of the Paxoi geotectonic unit as well as recent deposits comprising Middle Pleistocene scree and Pliocene-Clabrian marls (Fig. 2). Most of them remained active for a long time after the main earthquake mainly due to the recently established instability conditions and the ongoing aftershock sequence including earthquakes with magnitude equal to or larger than 4.0 and epicenters determined close to the western part of the island.

The coastal slopes of the western part of Lefkas suffered the most by the 2015 earthquake due to the combination of the following parameters: (a) The tectonic structure of the western coastal part of Lefkas, which is characterized by active faults that play decisive role in the formation and the evolution of the island. Along with a dense net of joints, they additionally form a geotechnically unstable region characterized by high and steep slopes and scarps, highly fractured, brecciated and almost powdered limestones with secondary welding and extensive semi-cohesive scree with limestone breccia and red-clay filled fractures as well as suitable geometry of beds and discontinuities; (b) The lithological heterogeneity and the mechanical anisotropy of the alpine and post-alpine formations; (c) The exogenic processes comprising repeated cycles of mechanical, chemical and organic weathering and fluvial, marine and aeolian erosion contribute to the decreased cohesion and formations loosening along the steep coastal slopes of the affected area. For example, sea waves erode the base of the almost vertical slopes forming steep limestone cliffs, caves and overhangs and creating conditions favorable for slope movements. The probability for the generation of slope movements increases during earthquakes.

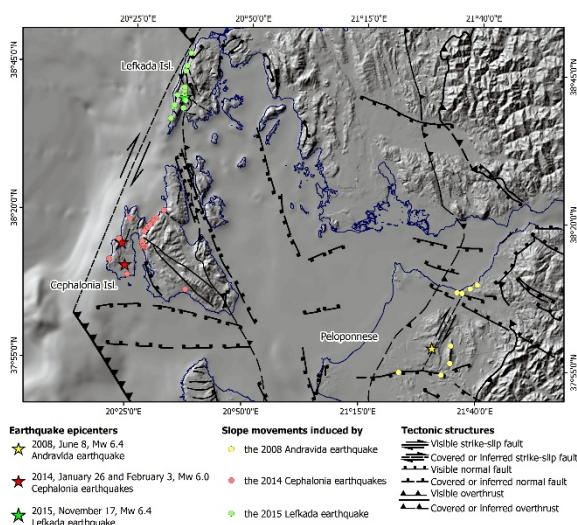


Figure 1: Spatial distribution of slope movements induced by the largest earthquakes in Western Greece during the last decade.

These phenomena can be considered as well predictable, because they occur repeatedly at the same places when earthquakes hit the island. In fact, slope movements including rockfalls and landslides were generated in

western Lefkas during the 1783, 1885, 1914, 1948 and 2003 earthquakes (Margaris et al. 2003; Lekkas et al. 2004; Papanthassiou & Pavlides, 2007; Rondoyanni et al. 2012).

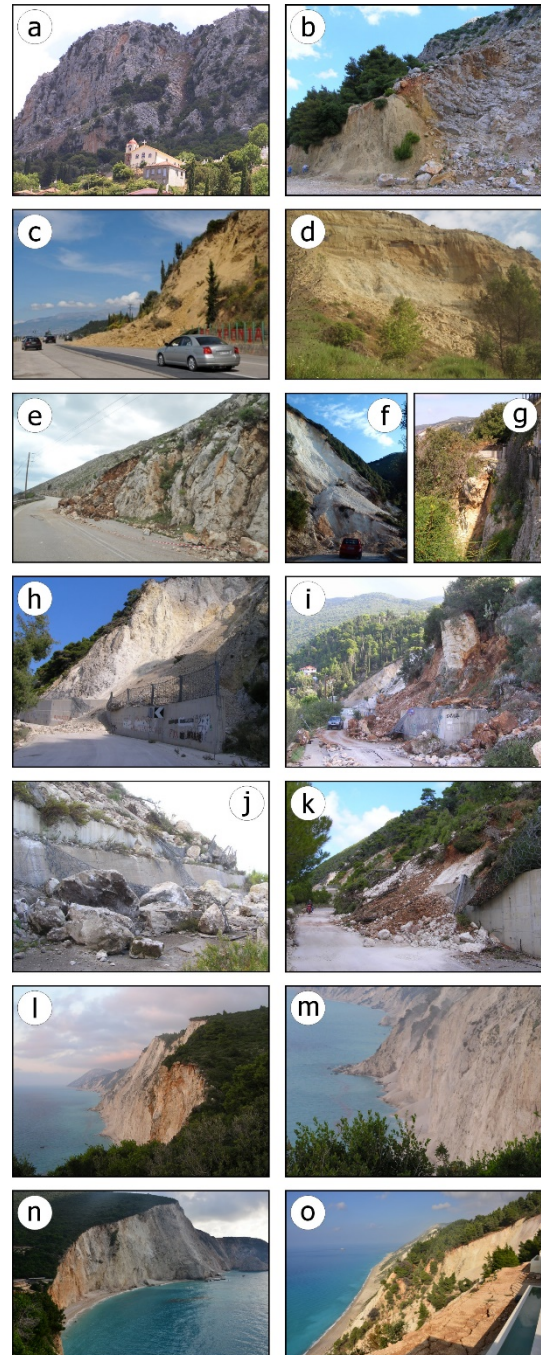


Figure 2: Slope movements in Western Greece induced by the 2008 Andravida earthquake (a-d), the 2014 Cephalonia earthquakes (e-g) and the 2015 Lefkada earthquake (h-o). (a) rock toppling failures of limestones, (b) rockfalls of limestone blocks, (c) landslide and failure of road slopes, (d) sliding of formation consisting of alternations of various lithologies, (e) rockfalls occurred in limestone blocks, (f) landslide of Triassic-Middle Miocene limestones and the Middle Miocene-Early Pliocene clay-clastic sequence of Paxoi unit, (g) landslide and rockfalls of Triassic-Middle Miocene limestones of Paxoi unit, (h-k) landslides and rockfalls of disintegrated and almost powdered limestones of Paxoi unit, (l-o) mixed types of slope failures including landslides, rockfalls and rockslides.



IMPACT OF THE EARTHQUAKE-INDUCED SLOPE MOVEMENTS IN WESTERN GREECE

Partial damage to the road network including cracks and craters in the asphalt pavement and deformation of road protection barriers as boulders bounced across the street, damage to adjacent building structures and related facilities and temporary or permanent traffic disruption were mainly caused by the studied earthquakes generated in Western Greece.

Unfortunately, rockfalls during the 2015 Lefkas earthquake claimed a life, when loose limestone blocks were detached from steep limestone slopes, rolled down and slammed into a residential building.

CONCLUSIONS

This study supports the view that earthquake-induced slope movements are highly concentrated in specific zones associated with the lithology, tectonic structure, geomorphology, topography and human presence. Taking into account that NW Peloponnese and Ionian Islands are among the most tectonically and seismically active areas and that these slope movements are mainly observed along active and probably active tectonic structures, these phenomena could be characterized as structurally controlled. Their distribution supports earlier studies of earthquake-triggered landslides, which suggests that although earthquake-triggered landslides are abundant throughout an extensive area from the epicentre, they are concentrated in specific zones associated with the bedrock geology, geomorphology, topography, and human factors (Keefer, 1984; Rodriguez et al., 1999). These criteria should be used therefore for mapping landslide susceptibility in the study area, and produce suitable hazard maps.

REFERENCES

- Keefer, D.K. 1984. Landslides caused by earthquakes. *Geol. Soc. Am. Bull.*, 95, 406-421.
- Lekkas, E., Danamos, G., Lozios, S., Skourtsos, E., Verykiou, E. 2004. The geographic distribution of landslides of Lefkas earthquake (August 14 2003) and factors affecting their generation. In: *Proceedings of the 10th International Congress of the Greek Geological Society, Extended Abstracts* 130-131.
- Lekkas, E., Mavroulis, S., Alexoudi, V. 2016. Field observations of the 2015 (November 17, mw 6.4) Lefkas (Ionian Sea, Western Greece) earthquake impact on natural environment and building stock of Lefkas Island. *Bulletin of the Geological Society of Greece*, 48, 499-510.
- Lekkas, E.L., Mavroulis, S.D. 2015. Earthquake environmental effects and ESI 2007 seismic intensities of the early 2014 Cephalonia (Ionian Sea, western Greece) earthquakes (January 26 and February 3, Mw 6.0). *Natural Hazards* 78, 1517-1544.
- Margaris, B., Papaioannou, C., Theodulidis, N., Savvaidis, A., Anastasiadis, A., Klimis, N., Makra, K., Demosthenous, M., Karakostas, C., Lekidis, V., Makarios, T., Salonikios, T., Sous, I., Carydis, P., Lekkas, E., Lozios, S., Skourtsos, E., Danamos, G. 2003. Preliminary Observations on the August 14, 2003 Lefkada Island (Western Greece) Earthquake, EERI Special Earthquake Report, Nov. 2003. (Joint report by Institute of Engineering Seismology and Earthquake Engineering, National Technical University of Athens and University of Athens), 1-12.
- Mavroulis, S., Fountoulis, I., Lekkas, E. 2010. Environmental effects caused by the Andravida (08-06-2008, $M_L=6.5$, NW Peloponnese, Greece) earthquake. In: Williams, A., Pinches, G., Chin, C., McMorran, T., Massey, C. (Eds.), *Geologically Active: 11th IAG Congress*. Taylor & Francis Group, Auckland, New Zealand, pp. 451-459.
- Mavroulis, S., Fountoulis, I., Skourtsos, E., Lekkas, E., Papanikolaou, I. 2013. Seismic intensity assignments for the 2008 Andravida (NW Peloponnese, Greece) strike-slip event (June 8, Mw=6.4) based on the application of the Environmental Seismic Intensity scale (ESI 2007) and the European Macroseismic scale (EMS-98). Geological structure, active tectonics, earthquake environmental effects and damage pattern. *Annals of Geophysics* 56, 6, S0681; doi:10.4401/ag-6239.
- Papadopoulos, G.A., Plessa, A. 2000. Magnitude-distance relations for earthquake-induced landslides in Greece. *Engineering Geology*, 58, 377-386.
- Papathanassiou, G., Pavlides, S. 2007. Using the INQUA scale for the assessment of intensity: Case study of the 2003 Lefkada (Ionian Islands), Greece earthquake. *Quaternary International* 173-174, 4-14.
- Qiao, G., Lu, P., Scaioni, M., Xu, S., Tong, X., Feng, T., Wu, H., Chen, W., Tian, Y., Wang, W., Li, R. 2013. Landslide investigation with remote sensing and sensor network: from susceptibility mapping and scaled-down simulation towards in situ sensor network design. *Remote Sensing*, 5, 4319-4346.
- Rodriguez, C.E., Bommer, J.J., Chandler, R.J. 1999. Earthquake induced landslides: 1980-1997. *Soil Dynamics Earthquake Engineering* 18, 325-346.
- Rondoyanni, Th., Sakellariou, M., Baskoutas, J., Christodoulou, N. 2012. Evaluation of active faulting and earthquake secondary effects in Lefkas Island, Ionian Sea, Greece: an overview. *Natural Hazards* 61, 843-860.
- Scaioni, M., Longoni, L., Melillo, V., Papini, M. 2014. Remote sensing for landslide investigations: An overview of recent achievements and perspectives. *Remote Sensing* 6, 9600-9652.
- Xu, C., Xu, X. 2016. Statistical analysis of landslides caused by the Mw 6.9 Yushu, China, earthquake of April 14, 2010. *Natural Hazards* 72, 871-893. DOI 10.1007/s11069-014-1038-2
- Zhou, S., Chen, G., and Fang, L. 2016. Distribution Pattern of Landslides Triggered by the 2014 Ludian Earthquake of China: Implications for Regional Threshold Topography and the Seismogenic Fault Identification. *ISPRS International Journal of Geo-Information* 5, 46, <https://doi.org/10.3390/ijgi5040046>, 2016.



The new Italian seismic hazard model

Meletti, Carlo (1), Marzocchi, Warner (1), Albarello, Dario (2), D'Amico, Vera (1), Luzi, Lucia (1), Martinelli, Francesco (1), Pace, Bruno (3), Pignone, Maurizio (1), Rovida, Andrea (1), Visini, Francesco (1), and the MPS16 Working Group

- (1) Istituto Nazionale di Geofisica e Vulcanologia, Centro di Pericolosità Sismica, Italy
- (2) Università degli Studi di Siena, Italy
- (3) Università degli Studi di Chieti-Pescara, Italy

Abstract: In 2015, the Seismic Hazard Centre (CPS) of the Istituto Nazionale di Geofisica e Vulcanologia (INGV) was commissioned to engage and coordinate the national community with the aim of elaborating a new reference seismic hazard model, which is expected to be released in mid 2018. CPS outlined a roadmap to describe the main features of this complex endeavour, including the different scientific tasks, milestones and timelines. The scientific tasks focus their work on i) improving the quality and the accuracy of the input data (e.g. historical seismic catalogue, seismotectonic zonation, etc.); ii) building new earthquake rate models based on these new input data, iii) selecting the most proper ground motion prediction equations, iv) testing the overall seismic hazard model as well as each component; v) combining the results of the statistical testing phase and the outcome of an expert's elicitation session to assign a weight to each component of the final seismic hazard model. The new seismic hazard model is based on an innovative coherent probabilistic framework, which allows a proper description of the aleatory variability and epistemic uncertainty, and the validation of the seismic hazard model. Here, we describe the progress made to date up to now, the comparison between the new and the official national model, and finally we discuss the scientific aspects that have the most significant impact on the new picture of PSHA in Italy.

Key words: Italy, Seismic Hazard, Building Code.

INTRODUCTION

In 2004-2006 a new seismic hazard model for Italy (MPS04; <http://zonesismiche.mi.ingv.it>) was released; it was based on the most recent data, approaches, and available software tools. At that time, it was considered one of the most advanced models in Europe, and, for the first time in Italy, it was possible to define the seismic code on the uniform hazard spectra assessed on a regular 5 km spaced grid over the whole national territory. Previously, the territory was classified into 4 seismic categories, each one described by a single response spectrum. Interestingly, the new building code based on MPS04 was not mandatory until 2009, a few months after the Mw6.1 L'Aquila earthquake.

In the following years, the update of MPS04 was not considered a priority, since the professional engineers needed time to become familiar with the proper application of the new EuroCode 8 building code.

In 2013, a new seismic hazard model for Europe (the European SHARE hazard model, <http://www.share-eu.org/>) was delivered, which showed marked increases of peak ground acceleration (PGA) at a level of probability of exceedance of 10% in 50 years with respect to MPS04 (Meletti et al., 2014). These differences were somewhat surprising because SHARE and MPS04 used very similar area source models (Meletti et al., 2008) and historical seismic catalogue. A detailed investigation showed that the use of more recent ground-motion prediction equations (GMPE) in SHARE explains the largest discrepancies between SHARE and MPS04 (Meletti et al., 2014).

Besides the developments of these new GMPEs, during the last ten years many new data became available, and the computational codes were significantly improved. Therefore, in 2015 the Italian scientific community led by the Seismic Hazard Centre (Centro Pericolosità Sismica – CPS hereafter) of the National Institute of Geophysics and Volcanology (Istituto Nazionale di Geofisica e Vulcanologia – INGV hereafter) proposed the building of a new national seismic hazard model that could be used to revise the design spectra for the building code. This proposal was funded by the Italian government through the Department of Civil Protection (Dipartimento di Protezione Civile, DPC hereafter), and it is still ongoing mostly because of the continuous and intense interaction with the review panel (namely the High Risks Commission of the Italian Civil Protection Department; <http://www.protezionecivile.gov.it/jcms/en/home.wp>).

DISCUSSION

From the beginning of 2015, DPC has been funding CPS to build a new seismic hazard model, which is aimed to replace MPS04 (MPS Working Group, 2004; Stucchi et al., 2011). Since the beginning, CPS and DPC representatives agreed on fixing some key constraints that must be honoured in building a seismic hazard model for practical purposes.

These points, which basically aim to guarantee a broad participation and both scientific and non-scientific consensus, can be summarized as follows: (i) use of international standards according to the state of the art in Probabilistic Seismic Hazard Assessment (PSHA) (e.g. SHAAC, 1993 and Woessner et al., 2015); (ii) open and transparent procedures



that guarantee completely reproducible outcomes; (iii) use of formats that have to be approved by the decision makers; (iv) the involvement of the whole Italian scientific community in proposing data, models and approaches; (v) a full and coherent exploration and representation of the epistemic uncertainty in the final seismic hazard model; (vi) the implementation of a robust testing phase, and of an elicitation session with national and international independent experts, in order to check the reliability of each component of the seismic hazard model.

Concerning the point (iii) above, CPS representatives and the national earthquake engineering community discussed the most proper outcomes of the new seismic hazard model for the building code purpose. Specifically, the time-independent model has to consider only declustered seismicity (in order to maintain a coherence with the past); the model has to cover the whole national territory, the reference soil is rock ($V_{s30} > 800\text{m/s}$); the hazard has to be expressed in terms of PGA, PGV, PGD, spectral acceleration, velocity, displacement, macroseismic intensity; the spectral ordinates have to be in the range between 0.05 and 4 seconds, and the return periods from 30 to 5000 years.

The project for the new seismic hazard model has been organized into 6 tasks, each one of them led by 2 coordinators. All the coordinators, together with 4 external experts on seismic hazard, form Task 1 ("Project coordination") which is in charge of evaluating any aspect of the project, and checking the effective interaction among the researchers. The other tasks are: "Input Data", "Seismicity models", "GMPEs", "Computation and rendering", "Testing phase".

Task 2 "Input Data" is in charge of selecting all the useful basic data for the project, in order to have a common dataset of information. Within this task, many deliverables have already been met; probably the most important one is the new historical earthquake catalogue that updated the previous versions. This catalogue, named CPTI15 (<http://emidius.mi.ingv.it/CPTI15>), contains more than 4500 records, from 1000 AD to 2014, that have been compiled with homogeneous criteria for location and magnitude of each event; for the pre-instrumental period, the moment magnitude has been assessed on the basis of the distribution of macroseismic intensities, now available for every earthquake on Italian territory. The catalogue was then declustered with the Gardner and Knopoff (1974) algorithm and its time-interval completeness was also defined according both an historical and a statistical approach. The choice of exploiting this declustering technique is arbitrary but it is the best way to obtain a Poisson time-distribution for the mainshocks.

Other types of data have been released or updated, such as: the catalogue of focal mechanisms and moment tensors, the GPS velocity solution for the Mediterranean area, the DISS database of seismogenic sources capable of $M_w \geq 5.5$ earthquakes, the flat file of accelerometric

recordings for $M_w \geq 4.0$ earthquakes that represents the reference information for the tasks "GMPEs" and "Testing Phase".

The main goal of Task 3 "Seismicity models" is to provide a set of seismicity models that have been proposed independently by different groups of researchers. The Task's 3 coordinators must ensure the compatibility of these models with the OpenQuake engine platform (Pagani et al., 2014), and the coherence of the outcomes (all of the models have to provide forecasts of the same quantity). Besides these activities, this task acts as a link between the groups of modellers and Task 2 that furnish common databases.

Each earthquake rate model has to be reproducible; this means that modellers have to clearly explain how the model is built and which data have been used. Moreover, modellers have to explore the epistemic uncertainty related to their model, i.e., how the model outcome varies as a function of the variability of the parameters of the model itself. This step is crucial to estimate an overall epistemic uncertainty of the final model, which includes the uncertainty of each model and the uncertainty among models.

Task 3 collected 12 models that cover the national scale and 1 specific model for the Mt. Etna volcanic area. The 12 models were grouped according to the (main) typology of seismogenic sources: areas (5 models), faults (2 models) and points (5 models).

Task 4 "GMPEs" aims at identifying the most proper GMPEs to be used for the new seismic hazard map. A first selection of the many GMPEs in literature has been performed taking into account the following basic requirements: i) the GMPEs should uniformly cover the Italian territory and surrounding areas (with the exception of volcanic zones); ii) rocky soil conditions and flat topography have to be considered (although hazard maps for different soil classes could also be released); iii) the hazard has to be estimated in terms of peak ground acceleration, velocity and displacement (PGA, PGV, PGD), response spectra in acceleration, velocity and displacement (if PGD or the velocity and displacement spectra are not available, they are derived by integration from PGA and acceleration response spectra, respectively), macroseismic intensity and possible additional parameters, such as Housner or Arias intensity; iv) horizontal motion has to be represented by the geometrical mean of the horizontal components; v) GMPEs have to estimate 12 spectral periods, in the range 0.05-4 seconds.

The forecasting performance of each GMPE was evaluated through the comparison with accelerometric records available in the Italian (itaca.mi.ingv.it; Luzi et al., 2008; Pacor et al., 2011) and European (esm.mi.ingv.it; ESM Working Group, 2015) strong-motion databases and with Italian macroseismic data (DBMI15; <http://emidius.mi.ingv.it/DBMI15>). In this way, each GMPE was ranked according to different specific metrics, so that the best performing GMPEs could be identified. The ranking procedure was established in collaboration with the task 6 "Testing phase".



This selection procedure allows us to identify a set of GMPEs to use for the new seismic hazard model, among the GMPEs that have been calibrated for Italy (e.g., Bindi et al., 2011), for the European region (Douglas et al., 2014), and among the NGA-West2 models (Bozorgnia et al., 2014), that were developed for the latest seismic hazard maps of United States by the USGS (Petersen et al., 2014). The decision to select the best GMPEs for different classes of GMPEs is due to the need to consider GMPEs that may be suitable for the different Italian geodynamic contexts. A similar analysis was also carried out for the macroseismic intensity prediction equations (IPE).

Task 5 “Computation and Rendering” uses the code OpenQuake (www.openquake.org; Pagani et al., 2014) because of several reasons: it is free and it is open source, so everyone can reproduce the outcomes and verify how the code works. Moreover, since OpenQuake is developed by GEM (www.globalquakemodel.org), it is possible to interact with the developer team to modify or integrate the code, as well as to ask for the development of new dedicated functions. No less important, OpenQuake guarantees rapid assistance for problems concerning the elaboration or installation issues. One of the main goals of Task 5 is to disseminate the outcomes of the seismic hazard model in the form of graphs, tables, maps and through both paper and electronic tools. The previous experience gained in disseminating the outcomes of the previous MPS04 model was very positive and successful (Martinelli and Meletti, 2008): specifically, a webGIS application allows any user to view hazard maps, hazard curves and uniform hazard spectra. For the new seismic hazard model, the hazard will be disseminated by developing an analogous web tool, with new and extended features, which allow the users to receive more information with additional formats.

Task 6 “Testing phase” is an important and innovative aspect of the project. In common practice, the reliability of a seismic hazard model is based on the consensus of the scientific community on the model's outcomes. A more objective approach is based on testing the seismic hazard model, or its components such as the earthquake rate models and the GMPEs, using the available data. Despite the obvious importance of this step if we want to keep seismic hazard in a scientific domain, there is not yet a commonly accepted framework for testing seismic hazard models, and only a few approaches based on different assumptions have been proposed. The role of subjective expert opinion, the heterogeneous probabilistic approaches used to build the models, and the scarcity of independent data for evaluation make this issue extremely challenging, both from a theoretical and a practical point of view.

In Task 6 we adopt the probabilistic framework introduced by Marzocchi and Jordan (2014), which allows a meaningful testing and validation of a seismic hazard model, properly accounting for the epistemic

uncertainty. (We defer to this paper and references therein for a detailed discussion on this topic). As far as long-term seismic hazard models are concerned, seismologists cannot usually evaluate models using independent data. Some efforts in this direction are ongoing, but with some limitations (e.g. Mak et al., 2014). Most of the time, as for the new seismic hazard model, only past data, which have been used more or less directly to build the hazard model, can be used for testing. Hence, instead of using the term validation, we prefer to use the less ambitious term “consistency” of the model's output with data. In other words, the model should describe the data that have been used to build the model. Specifically, the main goal of Task 6 is to test the consistency of the new seismic hazard model, as well as of its components, i.e., the seismicity rate models and the GMPEs.

A second goal of Task 6 is to score the models. Specifically, we compare different models that form the new seismic hazard model to rank them according to their retrospective forecasting (hereafter past-casting) performances; we named this procedure “scoring”. All hazard models, and every single component have been scored according to few pre-selected specific metrics. The goal of scoring is to facilitate the merging of models in a final seismic hazard assessment; in fact, the final weight of each component of the hazard model is assigned according to its scoring, and the outcomes of an experts' elicitation session with independent national and international experts.

To sum up, the testing of the new seismic hazard model consists of 4 different phases. In testing phase 1, we evaluate the consistency of the final hazard model using the past accelerometric data that are available in Italy, properly accounting for the epistemic uncertainty. In testing phase 2, we test the new seismic hazard model in terms of macroseismic intensity. We compare the outcomes of the model with the intensity observations that occurred in the last centuries. In testing phase 3, we test every single seismicity rate model for consistency, comparing the rates with the seismicity that has been observed in the last centuries (taken from the CPTI15 catalogue). In testing phase 4, we provide a quantitative score for each model based on the comparison of their past casting. This score could be useful to establish the weight of each model, but we underline that scoring a model is entirely based on data analysis, while establishing weights could require more subjective assessment, for instance, when the dataset used for scoring is not particularly large. The scoring is applied to the set of final hazard models as well as to single components such as the seismicity rate models and the GMPEs, using the databases described in the previous testing phases.

CONCLUSIONS

The Italian scientific community is soon to release a new seismic hazard model for Italy. This effort began in 2015 and to date has involved more than 150 researchers. With respect to the previous model, we have taken advantage of the significant updates of several input data, such as the historical seismic catalogue, and of a richer set of models for earthquake rates and GMPEs. The new seismic hazard model



also contains some important novelties, such as a new probabilistic framework that allows the validation of the model and a proper and coherent description of the epistemic uncertainty. We have also introduced a strong testing phase, which allows a more objective evaluation of the hazard model and of its components. Last but not least, the final model is going to be fully transparent and reproducible. This will facilitate any later evaluation of the model by independent groups of researchers.

REFERENCES

- Bindi, D., Pacor, F., Luzi, L., Puglia, R., Massa, M., Ameri, G. & Paolucci, R., 2011. Ground motion prediction equations derived from the Italian strong motion database. *Bulletin of Earthquake Engineering* 9 (6), 1899-1920, doi:10.1007/s10518-011-9313-z.
- Bozorgnia, Y., Abrahamson, N.A., Al Atik, L., Ancheta, T.D., Atkinson, G.M., Baker, J.W., Baltay, A., Boore, D.M., Campbell, K.W., Chiou, B.S.-J., Darragh, R., Day, S., Donahue, J., Graves, R.W., Gregor, N., Hanks, T., Idriss, I.M., Kamai, R., Kishida, T., Kottke, A., Mahin, S.A., Rezaeian, S., Rowshandel, B., Seyhan, E., Shahi, S., Shantz, T., Silva, W., Spudich, P., Stewart, J.P., Watson-Lamprey, J., Wooddell, K. & Youngs, R., 2014. NGA-West2 Research Project. *Earthquake Spectra* 30 (3), 973-987, doi:10.1193/072113EQS209M.
- Douglas, J., Akkar, S., Ameri, G., Bard, P.Y., Bindi, D., Bommer, J.J., Bora, S.S., Cotton, F., Derras, B., Hermkes, M., Kuehn, N.M., Luzi, L., Massa, M., Pacor, F., Riggelsen, C., Sandikkaya, M.A., Scherbaum, F., Stafford, P.J. & Traversa, P., 2014. Comparisons among the five ground-motion models developed using RESORCE for the prediction of response spectral accelerations due to earthquakes in Europe and the Middle East. *Bulletin of Earthquake Engineering* 12 (1), 341-358, doi:10.1007/s10518-013-9522-8.
- ESM working group, 2015. Engineering strong-motion database, version 1.0, doi: 10.13127/ESM.
- Gardner, J.K. & Knopoff, L., 1974. Is the sequence of earthquakes in southern California, with 836 aftershocks removed, Poissonian? *Bulletin of the Seismological Society of America* 64, 1363–1367.
- Luzi, L., Hailemichael, S., Bindi, D., Pacor, F., Mele, F. & Sabetta, F., 2008. ITACA (Italian ACcelerometric Archive): a web portal for the dissemination of Italian strong-motion data. *Seismological Research Letters* 79 (5), 716-722, doi: 10.1785/gssrl.79.5.716.
- Mak, S., Clements, R.A. & Schorlemmer, D., 2014. The Statistical Power of Testing Probabilistic Seismic-Hazard Assessments. *Seismological Research Letters* 85, 781-783.
- Martinelli, F. & Meletti, C., 2008. A webgis application for rendering seismic hazard data in Italy. *Seismological Research Letters* 79 (1), 68-78. DOI: 10.1785/gssrl.79.1.68
- Marzocchi, W. & Jordan, T.H., 2014. Testing for ontological errors in probabilistic forecasting models of natural systems. *Proceedings of the National Academy of Science* 111 (33), 11973-11978.
- Meletti, C., Galadini, F., Valensise, G., Stucchi, M., Basili, R., Barba, S., Vannucci, G. & Boschi, E., 2008. A seismic source model for the seismic hazard assessment of the Italian territory. *Tectonophysics* 450 (1), 85-108. DOI:10.1016/j.tecto.2008.01.003.
- Meletti, C., Rovida, A., D'Amico, V. & Stucchi, M., 2014. Modelli di pericolosità sismica per l'area italiana: "MPS04-S1" e "SHARE". *Progettazione Sismica* 5 (1), 15-25. Doi: 10.7414/PS.5.1.15-25
- MPS Working Group, 2004. Redazione della mappa di pericolosità sismica prevista dall'Ordinanza PCM del 20 marzo 2003 n. 3274, All. 1. Rapporto conclusivo per il Dipartimento della Protezione Civile, aprile 2004, Istituto Nazionale di Geofisica e Vulcanologia (INGV), Milano-Roma, 163 pp., <http://zonesismiche.mi.ingv.it/>
- Pacor, F., Paolucci, R., Luzi, L., Sabetta, F., Spinelli, A., Gorini, A., Nicoletti, M., Marcucci, S., Filippi, L. & Dolce, M., 2011. Overview of the Italian strong motion database ITACA 1.0. *Bulletin of Earthquake Engineering* 9 (6), 1723-1739, doi: 10.1007/s10518-011-9327-6.
- Pagani, M., Monelli, D., Weatherill, G., Danciu, L., Crowley, H., Silva, V., Henshaw, P., Butler, L., Nastasi, M., Panzeri, L., Simionato, M. & Viganò, D., 2014. OpenQuake Engine: an open hazard (and risk) software for the Global Earthquake Model. *Seismological Research Letters* 85, 692-702.
- Petersen, M.D., Moschetti, M.P., Powers, P.M., Mueller, C.S., Haller, K.M., Frankel, A.D., Zeng, Y., Rezaeian, S., Harmsen, S.C., Boyd, O.S., Field, N., Chen, R., Rukstales, K.S., Luco, N., Wheeler, R.L., Williams, R.A. & Olsen, A.H., 2014. Documentation for the 2014 update of the United States national seismic hazard maps. *U.S. Geological Survey Open-File Report 2014-1091*, 243 p., <http://dx.doi.org/10.333/ofr20141091>.
- SSHAC (Senior Seismic Hazard Analysis Committee), 1997. Recommendations for probabilistic seismic hazard analysis: guidance on uncertainties and use of experts. *Report NUREG-CR-6372*, U.S. Nuclear Regulatory Commission, Washington D.C..
- Stucchi, M., Meletti, C., Montaldo, V., Crowley, H., Calvi, G.M. & Boschi, E., 2011. Seismic hazard assessment (2003-2009) for the Italian building code. *Bulletin of the Seismological Society of America*, 101, 1885-1911.
- Woessner, J., Danciu, L., Giardini, D., Crowley, H., Cotton, F., Grünthal, G., Valensise, G., Arvidsson, R., Basili, R., Demircioglu, M.B., Hiemer, S., Meletti, C., Musson, R., Rovida, A., Sesetyan, K., Stucchi, M. & the SHARE consortium, 2015. The 2013 European seismic hazard model: key components and results. *Bulletin of Earthquake Engineering*, 13, 3553-3596.



Slope failure - effect or trigger of tremors? Insights from geoelectrical methods and dating of speleothem deformation, Tatra Mountains, Carpathians

Mendecki, M.^{1*}, Szczygieł, J.¹, Glazer, M.¹, Hercman, H.², Wróblewski, W.³

¹Faculty of Earth Sciences, University of Silesia, Będzińska 60, 41-200 Sosnowiec, Poland; *Corresponding author: maciej.mendecki@us.edu.pl

²Institute of Geological Sciences, Polish Academy of Sciences, Twarda 51/55, 00-818 Warszawa, Poland

³Institute Of Geological Sciences, Jagiellonian University, Gronostajowa 3a, 30-387 Kraków, Poland

Abstract: Tectonic studies of the Kalacka Cave, Tatra Mts., indicates the presence of faults that have been active during the Quaternary. Soft sediment deformation within clastic deposits infilling a sump located near the faults also supports the occurrence of ground shaking in the region during the Quaternary. The main objective of this study was to confirm the recent activity on the documented faults through multidisciplinary investigations (tectonic, sedimentological, geophysical, radiometric and palaeomagnetic) in the Kalacka Cave and its vicinity. A damaged flowstone was sampled from one of the faults and a pre-damage and- and post-damage layer of calcite were dated using the U-series method, this indicated the age of the flowstone disturbance was $281 \text{ ka} \pm 6$.

Geological mapping of the Kalacka Turnia peak area was undertaken and two resistivity cross-sections were obtained in order to better understand the near surface geology of the Kalacka Cave and correlations between faults on the surface terrain and in the cave. The geophysical survey profiles were composed of two parallel 300 m and 200 m- lines. On the first 300 m profile the Induced Polarization method was applied to find chargeable areas that can indicate a fracture systems filled with water.

The presence of well-preserved scarps, connected with the faults in the cave and the high resistivity anomalies 60 m below surface demonstrate faulting caused by debuttrressing. The slope deformation was initiated at least $281 \text{ ka} \pm 6 \text{ ka}$ and the most significant downslope movements probably took place during the last interglacial. Moreover, presence of soft sediment deformation in the cave suggest that slope failure had a violent character and triggered ground shaking.



Imaging the distribution of transient viscosity following the 2016 Mw 7.1 Kumamoto earthquake

*Moore, James Daniel Paul (1), Hang, Yu (2), Tang, Chi-Hsien(3), Wang, Teng (1), Barbot, Sylvain (1), Peng, Dongju (1), Masuti, Sagar (1), Dauwels Justin (2), Hsu, Ya-Ju Hsu (3), Lambert, Valere (4), Nanjundia, Priyamvada (1), Wei, Shengji (1), Lindsey, Eric (1), Feng, Lujia (1), Shibazaki, Bunichiro (5).

* earth@jamesdpmoore.com

- (1) Earth Observatory of Singapore, Nanyang Technological University.
- (2) School of Electrical & Electronic Engineering, Nanyang Technological University.
- (3) Institute of Earth Sciences Academia Sinica, Taipei, Taiwan.
- (4) California Institute of Technology.
- (5) International Institute of Seismology and Earthquake Engineering, Building Research Institute, Japan.

Abstract: The deformation of mantle and crustal rocks in response to stress plays a crucial role in the distribution of seismic and volcanic hazards, controlling tectonic processes ranging from continental drift to earthquake triggering. However, the spatial variation of these dynamic properties is poorly understood as they are difficult to measure. We exploit the large stress perturbation incurred by the 2016 earthquake sequence in Kumamoto, Japan to directly image localized and distributed deformation. The earthquakes illuminated distinct regions of low effective viscosity in the lower crust, notably beneath the Mt Aso and Mt Kuju volcanos, surrounded by larger scale variations of viscosity across the back-arc. This study demonstrates a new potential for geodesy to directly probe rock rheology in situ across many spatial and temporal scales.

Key words: Kumamoto, Rheology, Geodesy, Viscoelasticity, Postseismic.

Postseismic studies of geodetic data following large earthquakes indicate a wide range of mechanisms contribute to the observed deformation and stress relaxation. Both on-fault afterslip and off-fault viscoelastic relaxation can contribute to the postseismic transient phase of the earthquake cycle. One problem with these (quasi-) dynamic models is that there is a wide range of parameter space to be investigated, with each parameter pair possessing their own tradeoffs. This becomes especially problematic when trying to model both on-fault and off-fault deformation simultaneously. Here, we draw insight from postseismic geodetic observations following the 2016 Mw 7.0 Kumamoto earthquake by utilizing a novel inversion technique.

We present a novel approach to invert for on-fault and off-fault deformation simultaneously using analytical Green's functions for distributed deformation at depth (Barbot, Moore and Lambert., 2016) and on-fault deformation (Okada 1985, Nikkhoo and Walter 2015). Using these Green's functions, we jointly invert InSAR images and GEONET GPS time series following the Kumamoto earthquakes for afterslip and lower-crustal viscoelastic flow.

The calculated strain-rates in the lower crust are directly converted to effective viscosities and we investigate the implications of the effective viscosity structure within an outlier-sensitive Bayesian statistical framework to estimate in-situ parameters, such as temperature. Using our new method, we are able to interrogate the transient deformation in the first few months of the postseismic deformation to obtain these parameters.

The postseismic deformation at Kumamoto brings new insights into the distribution of brittle and ductile crustal processes beneath Japan and can be used to infer lower crustal properties.

Following the work presented in Moore et. al. (2017) we extend the study over the 18months following the earthquake sequence and draw comparisons with the inelastic strain distributions in Kyushu presented in Matsumoto et. al. (2016), Fig. 1 and 2.

Acknowledgements: This research was supported by the National Research Foundation (NRF) of Singapore under the NRF Fellowship scheme (National Research Fellow Award NRF-NRFF2013-04), the Earth Observatory of Singapore under the Research Centres of Excellence initiative, and the Singapore Ministry of Education (Tier 2 project ARC5/14). We also thank Y. Ito for supporting access to the GEONET data. Data used in this study are stored at the Earth Observatory of Singapore and are freely available upon request.

REFERENCES

- Moore, J. D. P., Hang, Y., Tang, C., Wang, T., Barbot, S., Peng, D., Masuti, S., Dauwels J., Hsu, Y., Lambert, V., Nanjundia, P., Wei, S., Lindsey, E., Feng, L., Shibazaki, B. Imaging the distribution of transient viscosity after the 2016 Mw 7.1 Kumamoto earthquake. *Science* **356**, 163–167 (2017).
- Barbot, S. D., Moore, J. D. P., Lambert, V., Displacements and Stress Associated with Distributed Anelastic Deformation in a Half Space. *Bull. Seismol. Soc. Am.* **107**(2), 10.1785/0120160237 (2017).
- Okada, Y., Surface deformation due to shear and tensile faults in a half-space. *Bull. Seismol. Soc. Am.*, **75**, 1135–1154 (1985).
- Matsumoto S., Nishimura, T., Ohkura, T. *Earth, Planets and Space* **68:207** DOI 10.1186/s40623-016-0584-0 (2016)

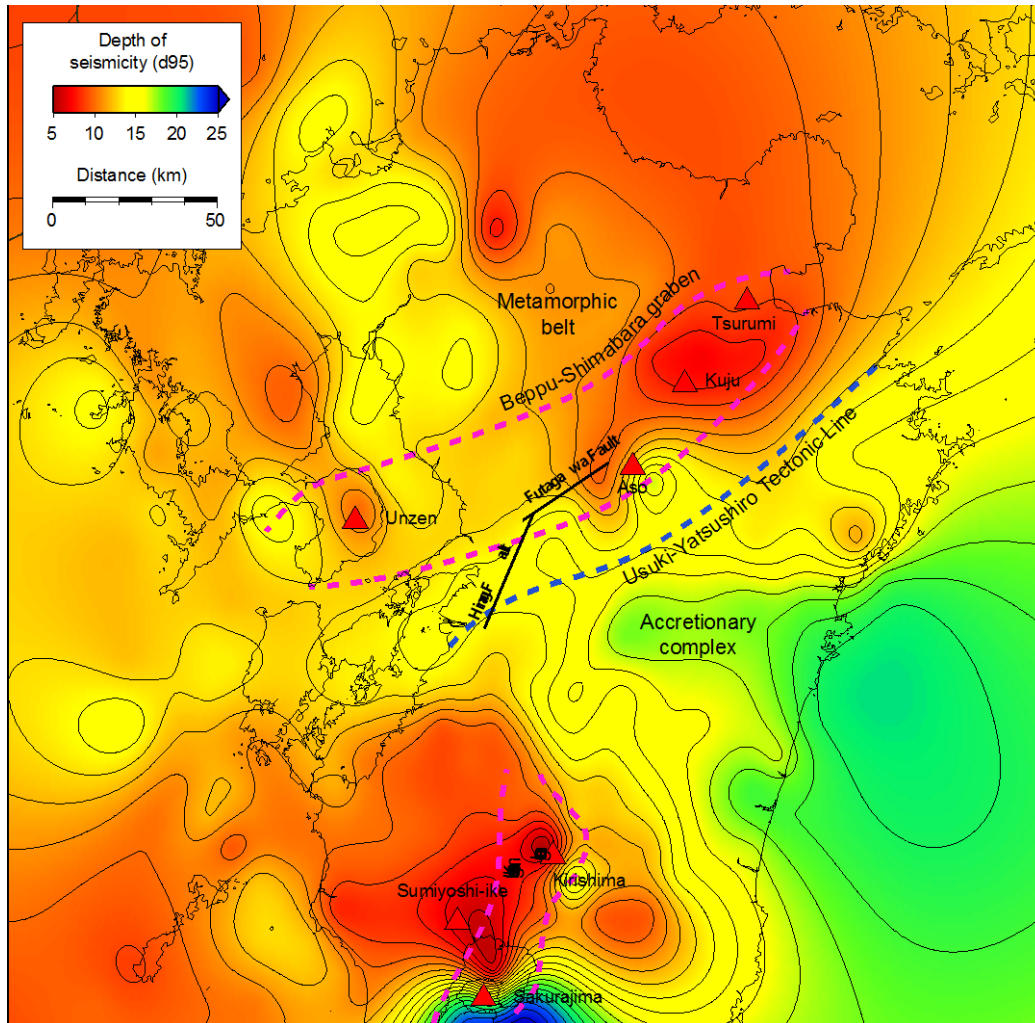


Figure 1: Depth distribution of the Kyushu island earthquakes, January 1993 to July 2013, showing the deeper (d95) limits of studied events. Red triangles denote active volcanoes.

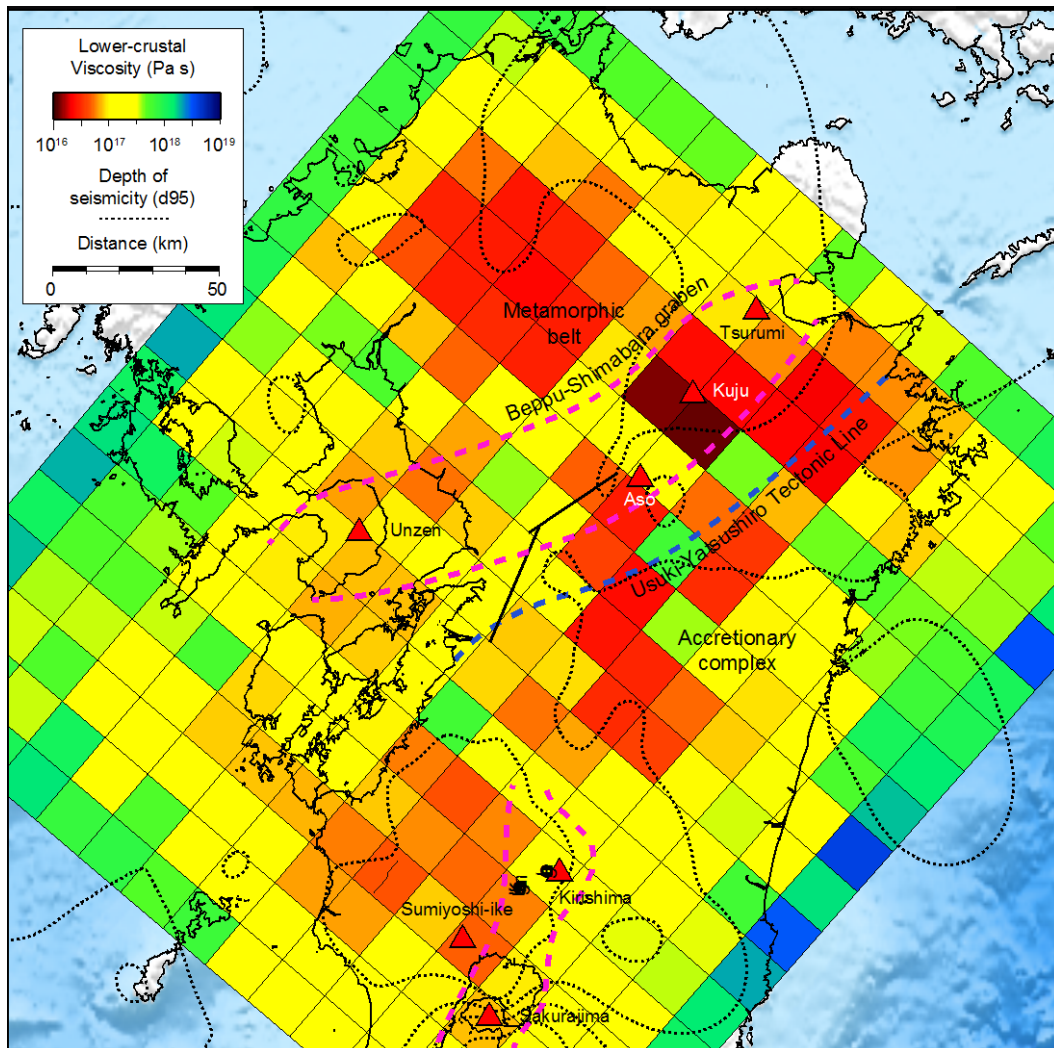


Figure 2: Transient viscosity of the lower crust with volcanoes marked in red triangles, the Hinagu and Futagawa faults in black, modified from Moore et. al. (2017). The regions of low viscosity follow the pattern of coseismic stress change modulated by the distribution of arc volcanism and plutonic bodies in Kyushu, with noticeable low-viscosity anomalies beneath Mount Aso and Mount Kuju. 5km contours of the depth of seismicity, d_{95} (Fig. 1), superimposed as a dashed line.



Archaeoseismology: Studying past earthquakes using archaeological data

Niemi, Tina M. (1), Sintubin, M. (2), Altunel, E. (3), Stewart, I. (4)

- (1) University of Missouri-Kansas City, Department of Geosciences, Flarsheim Hall 420, 5110 Rockhill Road, Kansas City, MO 64110 USA
email niemit@umkc.edu
- (2) Katholieke Universiteit Leuven, Department of Earth & Environmental Sciences, Celestijnenlaan 200E, 3001 Leuven, Belgium
email manuel.sintubin@ees.kuleuven.be
- (3) Eskişehir Osmangazi Üniversitesi, Department of Geological Engineering, 26480 Eskişehir, Turkey
email ealtunel@ogu.edu.tr
- (4) University of Plymouth, School of Earth, Ocean & Environmental Sciences, Plymouth PL4 8AA, U.K.
email iain.stewart@plymouth.ac.uk

Abstract: Earthquakes have disrupted human societies throughout history and prehistory. Whereas hunter-gatherer cultures may have been relatively little affected by seismic events, the built environment of sedentary societies is quite vulnerable to collapse of structures by earthquake-induced ground motion. Understanding the severity and frequency of past earthquakes is important for understanding the history, consequences, and responses of past societies to these seismic disasters, as well as the hazards posed to modern populations. Ambraseys (1971, 1973) was one of the first to advocate the modern use of archaeological data to help define a region's earthquake history and other seismic hazards. Deciphering and dating evidence of earthquake damage at archaeological sites is the goal of the modern field of "archaeoseismology"—a term first coined in the paper by Karcz and Kafri (1978). The field of archaeoseismology investigates both earthquake collapse horizons within archaeological stratigraphic contexts and damaged extant buildings and structures. Many archaeologists have documented "destruction horizons," —i.e., stratigraphic layers that show signs of fire, instantaneous destruction, or massive structural collapse with evidence of smashed, in situ vessels and other artifacts on living surfaces, toppled masonry, or other catastrophic building failures interpreted as earthquake damage. Earthquake damage is, however, difficult to differentiate from other causes of building failures, including static collapse due to lack of maintenance, disrepair, or warfare, slumping or gravitational sliding, foundation subsidence, and other geotechnical issues. Understanding the tectonic, geologic, and geomorphic setting of an archaeological site has long been recognized as fundamental to understanding archaeoseismic evidence. Recent advances in the field include developing means to quantify a earthquake intensity scale for seismic damage at archaeological site, detailed mapping of damage to extant archaeological structures, and the use of numerical modeling to calculate ground motion that created the structural failures. Archaeoseismology is rapidly developing as a multidisciplinary research field where qualitative observations and quantitative data can yield valuable seismic parameters of ancient earthquakes.



Tsunami or Hurricane? Mapping coastal boulders and boulder fields using satellite and high-resolution drone imagery with photogrammetric techniques

Niemi, Tina M.

University of Missouri-Kansas City, Department of Geosciences, Flarsheim Hall 420, 5110 Rockhill Road, Kansas City, MO 64110 USA
email niemit@umkc.edu

Abstract: High-energy marine inundation events like hurricanes and tsunamis have the ability to move large boulders and create boulder ridges and boulder fields along rocky coastlines. The transport mechanism of megaboulders, defined as a clast with a long axis greater than 4 m (Terry and Goff, 2014), is not well understood. Determining the run-up height, areal extent of flooding, and direction of transport of boulders moved along coasts from modern events will help to quantify the parameters of boulder movement and help to determine the origin of some enigmatic boulder deposits (i.e. hurricane vs. tsunami). We report here on a monitoring program of boulders along several rocky shorelines on a small island, San Salvador, located on the windward, southeast side of the Bahamian archipelago. The Bahamas are subject to frequent category >4 hurricanes. We use field observations since 2005, satellite imagery, and high-resolution photographs from a kite-mounted camera and a DJI Phantom 3 advanced drone to monitor boulder movement in recent hurricanes. Before and after imagery allow us to determine how boulders have moved. Our data show that a 16-tonne boulder was lifted up a 2-m-high cliff and deposited inland in the category 4 Hurricane Francis in 2004. We also document that even category 1 hurricanes can move large boulders by sliding. Large boulders available for transport are created by erosional retreat of the shoreline. Deep water close to shore and localized coves along the shoreline appear to focus wave energy and increase the transport potential of very large boulders. Wave equations that attest to discern between storm and tsunami mechanisms for boulder movement do not appear to be accurate. Our data corroborate other studies that have shown that storms rather than tsunamis have moved very large boulders, but the upper limit for the size of boulders capable of being transported by a storm surge or rogue wave in contrast to a tsunami is still not known.



Southern Hikurangi Margin uplift rates and tectonic implications, based on new marine terrace data from the southern North Island, New Zealand

Ninis, Dee (1), Little, Tim (1), Litchfield, Nicola (2)

- (1) Victoria University of Wellington, Kelburn, Wellington, New Zealand. dee.ninis@src.com.au.
(2) GNS Science, PO Box 30 358, Lower Hutt 5040, New Zealand.

Abstract: Tectonic uplift of the southern Hikurangi Margin is recorded by Pleistocene marine terraces preserved along the south coast of the North Island of New Zealand. We employ optically stimulated luminescence (OSL) analysis of overlying deposits, and strandline elevations, to quantify uplift across the margin. The highest uplift rate, 1.67 ± 0.08 mm/yr, is recorded by the easternmost terrace, ~40 km from the Hikurangi Trough. Uplift decreases monotonically towards the west, to 0.15 ± 0.03 mm/yr ~70 km from the trough. The long wavelength of uplift suggests that deep-seated processes, most likely subduction of the buoyant Hikurangi Plateau and permanent co-seismic uplift resulting from repeated megathrust earthquakes, are responsible for the vertical deformation across this region. At distances >70 km from the trough, terraces are vertically offset across the major upper plate faults, suggesting that these structures contribute to enhanced uplift rates, while overall uplift is possibly related to sediment underplating.

Key words: Hikurangi margin, marine terrace, uplift rates.

INTRODUCTION

At the southern Hikurangi Margin, the subduction interface between the Australian and Pacific plates, beneath the southern North Island of New Zealand, is 'locked' (e.g. Reyners, 1998; Darby & Beavan, 2001; Wallace et al., 2004; 2012). It has previously been estimated that sudden slip on this locked portion of the interface could result in a subduction megathrust earthquake of M_w 8.0-8.5 or larger (Reyners, 1998; Wallace et al., 2009). Historically, however, no significant ($>M_w$ 7.2) subduction earthquake has occurred at the southern Hikurangi Margin (Wallace et al., 2009), and the hazard from subduction earthquakes to this region, which includes New Zealand's capital city of Wellington, remains largely unknown.

Patterns of tectonic deformation at subduction margins can provide insight into underlying subduction processes, including megathrust earthquakes (e.g. Bradley & Griggs, 1976; Ghani, 1978; Muhs et al., 1990; Machare & Ortlieb, 1992; Berryman, 1993; Ota et al., 1996). With the objective to provide insight into the relationship of permanent vertical deformation to subduction processes at the southern end of the Hikurangi Margin, we provide a new evaluation of the age and distribution of the flights of late Pleistocene marine terraces preserved along the south coast of the North Island (Fig. 1). Such geomorphic features, when constrained by absolute dating, provide a valuable set of data with which to quantify tectonic uplift (e.g. Zazo et al., 2003; Pedoja et al., 2006; Wilson et al., 2007; Matsu'ura et al., 2009; Saillard et al., 2011).

We employ OSL analysis to obtain absolute ages for the Pleistocene terraces preserved on the south coast of the North Island, many for the first time. Shore platform elevations are accurately measured for the first time using

Global Navigational Satellite Systems (GNSS) surveying. We use the surveyed data points (latitude, longitude, elevation) to construct a plane of best fit to represent the shore platforms and determine their attitudes where they are preserved along the coast. Because the ancient shorelines are now obscured by covered deposits, we use the calculated shore platform attitudes to reconstruct strandline elevations. These strandline elevations, corrected for sea level during their formative highstands, have been used to quantify rates of uplift across the southern Hikurangi Margin.

RESULTS & DISCUSSION

Seven different-age Pleistocene terraces are preserved along the south coast of the North Island, the most extensive forming during sea level highstands of Marine Isotope Stages (MIS) 5a (~82 ka), 5c (~96 ka), 5e (~123 ka) and 7a (~196 ka). The terraces are most continuously preserved within the forearc region of the Hikurangi Margin, which spans a distance of ~70 km from the Hikurangi Trough.

The highest uplift rate of 1.67 ± 0.08 mm/yr is recorded by the easternmost preserved terrace, near Cape Palliser, ~40 km from the trough (Fig. 1, Fig. 2). Here, the MIS 5e terrace is tilted by 2.5-2.9° towards the west. At Washpool, the uplift rate determined from the younger MIS 5a terrace preserved locally is 1.25 ± 0.08 mm/yr. Moreover, the MIS 5a terrace at Washpool is also tilted less than the older terraces on this coast, with a dip of 1.5° towards the west. The lowest rate of uplift, <0.2 mm/yr, is observed at Wharekauhau, ~70 km from the trough. Overall, in the Hikurangi Forearc, uplift monotonically decreases away from the trough, despite the fact that uplift rates have been determined from different-aged terraces along this coast, and terraces are tilted towards the west, with older

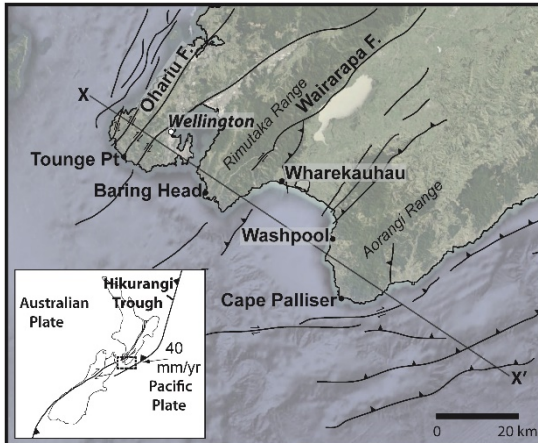


Figure 1: Lower North Island of New Zealand, showing the major active faults (Barnes et al., 1998; Barnes & Audru, 1999; Begg & Johnston, 2000; GNS Science Active Faults Database - <http://data.gns.cri.nz/af/>) and field sites of this investigation. Cross section of X-X' profile is shown in Fig. 2. Background satellite image from Digital Globe/ TerraMetrics (Google Earth) 2016. Inset – Tectonic setting of New Zealand.

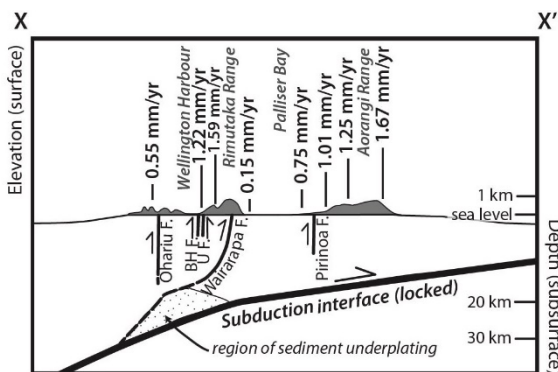


Figure 2: Schematic cross section X-X' across southern North Island, showing representative topography (exaggerated), uplift rates and locations of faults observed to offset the Pleistocene marine terraces; 'BH F.' is Baring Head Fault, 'U F.' is un-named fault at Baring Head. Figure modified after Little et al. (2009) and updated using data from Begg & Johnston (2000), Henrys et al. (2013) and Williams et al. (2013). Subsurface Wairarapa Fault location and region of sediment underplating from Henrys et al. (2013).

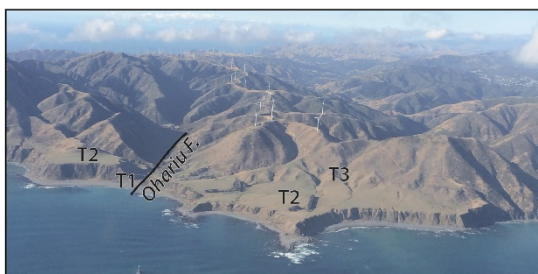


Figure 3: Pleistocene marine terraces preserved at Tongue Point, west of Wellington (see Fig. 1 for location). Three terraces are preserved at this site. The main, coastal most terrace here T2, formed during MIS 5e (~123 ka) ago. A hummocky strip is all that remains of an older, terrace, T3. Remnants of the youngest terrace, T1, are not easily viewed in this photograph. Terraces are vertically offset, uplifted to the west (right side of fault in this image) by the Ohariu Fault. View looking towards the north.

terraces exhibiting the most tilting. This ~30 km long pattern of uplift within the forearc suggests that deep-seated processes are the main contributors to permanent vertical deformation, the most likely contenders being subduction of the buoyant Hikurangi Plateau and permanent uplift resulting from repeated megathrust earthquakes.

The marine terraces are vertically offset across upper plate faults, most notably in the Axial Ranges, at a distance of >70 km from the Hikurangi Trough. The uplift rate at Baring Head, west and on the upthrown side of the Wairarapa Fault, is as much as 1.59 mm/yr. At Tongue Point (Fig. 3), where the Ohariu Fault offsets the marine terraces preserved there, uplift calculated from the western, upthrown side of the fault is 0.55 ± 0.04 mm/yr, whereas uplift calculated from the downthrown side is 0.16 ± 0.04 mm/yr (see Fig. 2). These vertical offsets suggest that at this distance, the major active upper plate faults contribute to enhanced uplift rates on the upthrown sides of the faults. However, because this entire region is elevated overall, uplift here also likely has a deeper source, and is possibly related to the sediment underplating previously identified beneath this region (Henrys et al., 2013).

Acknowledgements: We thank the Frank Evison Research Scholarship in Geophysics and the Earthquake Commission for funding to undertake this research.

REFERENCES

Barnes, P. M., Mercier de Lepinay, B., Collot, J.-Y., Delteil, J. and Audru, J.-C., 1998. Strain partitioning in the transition area between oblique subduction and continental collision, Hikurangi margin, New Zealand. *Tectonics*, 17, 534-557.

Barnes, P. M., and Audru, J. C., 1999. Quaternary faulting in the offshore Flaxbourne and Wairarapa basins, southern Cook Strait, New Zealand. *New Zealand Journal of Geology and Geophysics*, 42(3), 349-367.

Begg, J.G. and Johnston, M.R., 2000. Geology of the Wellington area. 1: 250 000 Geological map 10. Institute of Geological and Nuclear Sciences, Lower Hutt, New Zealand.

Berryman, K., 1993. Age, height, and deformation of Holocene marine terraces at Mahia Peninsula, Hikurangi subduction margin, New Zealand. *Tectonics* 12(6), 1347-1364.

Bradley, W. C., and Griggs, G. B., 1976. Form, genesis, and deformation of central California wave-cut platforms. *Geological Society of America Bulletin* 87(3), 433-449.

Darby, D. and Beavan, J., 2001. Evidence from GPS measurements for contemporary interplate coupling on the southern Hikurangi subduction thrust and for partitioning of strain in the upper plate, *Journal of Geophysical Research* 106, (12), 30881-30891.

Ghani, M. A., 1978. Late Cenozoic vertical crustal movements in the southern North Island, New Zealand. *New Zealand Journal of Geology and Geophysics* 21(1).

Henrys, S., Wech, A., Sutherland, R., Stern, T., Savage, M., Sato, H., Mochizuki, K., Iwasaki, T., Okaya, D., Seward, A. and Tozer, B., 2013. SAHKE geophysical transect reveals crustal and subduction zone structure at the southern Hikurangi margin, New Zealand. *Geochemistry, Geophysics, Geosystems* 14(7), 2063-2083.

Little, T.A., Van Dissen, R., Schermer, E. and Carne, R., 2009. Late Holocene surface ruptures on the southern Wairarapa fault,



- New Zealand: Link between earthquakes and the uplifting of beach ridges on a rocky coast. *Lithosphere* 1(1), 4-28.
- Macharé, J. and Ortlieb, L., 1992. Plio-Quaternary vertical motions and the subduction of the Nazca Ridge, central coast of Peru. *Tectonophysics* 205(1-3), 97-108.
- Matsu'ura, T., Furusawa, A. and Saomoto, H., 2009. Long-term and short-term vertical velocity profiles across the forearc in the NE Japan subduction zone. *Quaternary Research* 71(2), 227-238.
- Muhs, D. R., Kelsey, H. M., Miller, G. H., Kennedy, G. L., Whelan, J. F., & McInelly, G. W., 1990. Age estimates and uplift rates for late pleistocene marine terraces' Southern Oregon portion of the Cascadia forearc. *Journal of Geophysical Research* 95(B5) 6685-6698.
- Ota, Y., Pillans, B., Berryman, K., Beu, A., Fujimori, T., Miyauchi, T. Berger, G., Beu, A. G. & Climo, F. M., 1996. Pleistocene coastal terraces of Kaikoura Peninsula and the Marlborough coast, South Island, New Zealand. *New Zealand Journal of Geology and Geophysics* 39(1) 51-73.
- Pedoja, K., Ortlieb, L., Dumont, J. F., Lamothe, M., Ghaleb, B., Auclair, M., & Labrousse, B., 2006. Quaternary coastal uplift along the Talara Arc (Ecuador, Northern Peru) from new marine terrace data. *Marine Geology* 228(1), 73-91.
- Reyners, M., 1998. Plate coupling and the hazard of large subduction thrust earthquakes at the Hikurangi subduction zone, New Zealand. *New Zealand Journal of Geology and Geophysics* 41, 343-354.
- Saillard, M., Hall, S. R., Audin, L., Farber, D. L., Regard, V., & Hérail, G., 2011. Andean coastal uplift and active tectonics in southern Peru: 10 Be surface exposure dating of differentially uplifted marine terrace sequences (San Juan de Marcona, ~ 15.4 S). *Geomorphology*, 128(3), 178-190.
- Wallace, L.M., Beavan, J., McCaffrey, R. and Darby, D., 2004. Subduction zone coupling and tectonic block rotations in the North Island, New Zealand. *Journal of Geophysical Research: Solid Earth* 109(B12).
- Wallace, L.M., Reyners, M., Cochran, U., Bannister, S., Barnes, P.M., Berryman, K., Downes, G., Eberhart-Phillips, D., Fagereng, A., Ellis, S. and Nicol, A., 2009. Characterizing the seismogenic zone of a major plate boundary subduction thrust: Hikurangi Margin, New Zealand. *Geochemistry, Geophysics, Geosystems* 10(10).
- Wallace, L. M., Barnes, P., Beavan, J., Van Dissen, R. J., Litchfield, N. J., Mountjoy, J., Langridge, R. M., Lamarche, G., and Pondard, H., 2012. The kinematics of a transition from subduction to strike-slip: an example from the central New Zealand plate boundary, *Journal of Geophysical Research: Solid Earth* doi: 10.1029/2011JB008640.
- Williams, C.A., Eberhart-Phillips, D., Bannister, S., Barker, D.H., Henrys, S., Reyners, M. and Sutherland, R., 2013. Revised interface geometry for the Hikurangi subduction zone, New Zealand. *Seismological Research Letters*, 84(6), 1066-1073.
- Wilson, K.J., N.J. Litchfield, K.R. Berryman & T.A. Little, 2007: Distribution, age, and uplift patterns of Pleistocene marine terraces of the northern Raukumara Peninsula, North Island, New Zealand. *New Zealand Journal of Geology and Geophysics*, 50: 181-191.
- Zazo, C., Goy, J. L., Dabrio, C. J., Bardají, T., Hillaire-Marcel, C., Ghaleb, B, Gonzalez-Delgado, J-A. & Soler, V., 2003. Pleistocene raised marine terraces of the Spanish Mediterranean and Atlantic coasts: records of coastal uplift, sea-level highstands and climate changes. *Marine Geology* 194(1), 103-133.



From fresh tsunami deposit to paleotsunami deposit: Preservation and disappearance of the 2011 Tohoku-Oki tsunami deposit along the Misawa coast, northern Japan

Nishimura, Yuichi (1)

(1) Institute of Seismology and Volcanology, Hokkaido University, N10W8, Sapporo, Hokkaido, Japan. Email: yns@sci.hokudai.ac.jp

Abstract: A coastal forest in Misawa, northern Japan, is a place where sandy deposits laid down by the 2011 Tohoku tsunami are well preserved in the natural environment. We reviewed this sediment in 2016 when it was covered with soil. The deposits were preserved especially well in the undamaged coastal forest. Most of the sites near the inundation limit within the residential area, were undetectable in 2016. On average, the inland limit for tracing the deposits reduced 14% in distance and 21% in elevation over 5 years. The coastal forest of Misawa is a place where researchers can continue to study the tsunami traces under weathering, and it is highly likely to become a worldwide type locality for studying paleotsunami deposits. The remaining tsunami deposits are valuable objects that should be effectively and sustainably utilized not only in research but also in disaster prevention and education.

Key words: Tsunami deposit, Preservation potential, Coastal forest, Disaster archive.

INTRODUCTION

Tsunami deposits are persuasive evidence for past large tsunamigenic earthquakes. They have been used to construct recurrence intervals and to estimate the largest possible event in a certain area. However, little attention has been paid to the possibility that such traces may disappear or become undetectable over the years, although post-depositional changes to tsunami sediment has been inferred to be significant in some studies (Szczeniński, 2012; Spiske et al., 2013). The disappearance of the trace can be caused by human activity and occurs in the natural environment. The 2011 Tohoku-Oki tsunami deposits provide an opportunity not only to study the formation process of the deposit but also to observe their weathering and subsequent processes.

We investigated the preservation and disappearance of tsunami deposits that formed in the 2011 Tohoku-Oki tsunami along the Misawa coast, Aomori Prefecture, northern Japan, where the 2011 tsunami height was 5 to 10 m above mean sea level and the inundation distance is 200-500m. Figure 1 shows our study area, and Figure 2 shows views of the tsunami affected area taken in April 2011 and in September 2016.

PRESERVATION AND DISAPPEARANCE OF THE TSUNAMI DEPOSITS

How the tsunami deposits are influenced

Nakamura et al. (2012) described the thickness, facies, and structure of the sandy tsunami deposits at 13 profiles along the Misawa coast in April 2011, less than one month after the tsunami. In September 2016, we revisited all the sites studied by Nakamura et al. (2012) and found that the deposits were still preserved at 68 sites (50% of all sites). The deposits were well preserved especially in the undamaged coastal forest, where the deposits have been

covered with newly developed soil and their thicknesses are not changed significantly (figure 3). Meanwhile, at the seaside forest where trees were knocked over or heavily damaged by the tsunami, they were removed during the reconstruction process and new planting has started, and there the 2011 tsunami deposits have disappeared. At most of the sites near the inundation limit within residential areas, the deposits were undetectable in 2016, because of human activity and weathering by rain and wind. Weathering has progressed even in the process of deposits being buried by new soil formation.



Figure 1: Location of our observation profiles along the Misawa coast, Aomori prefecture, Japan. The coast has a sandy beach and coastal forest. The forest was developed to provide protection from wind-blown sand and tsunami disasters about one hundred years ago. The 2011 tsunami destroyed the seaward parts of forest and inundated across the forest in some places.



Figure 2: View of traces of the 2011 tsunami near the coast (A, D), in the coastal forest (B, E), and near the inundation boundary. A, B and C were taken in April 2011, and D, E and F were in September 2016.

Preservation states of the deposits

Thirteen observation profiles studied by Nakamura et al. (2012) and re-examined by us are shown in Figure 1. Each profile is 230 to 550 m long and has 3 to 22 excavation sites (in total 137). Figure 4 shows the features of preservation and disappearance of the deposits for all profiles and sites.



Figure 3: The 2011 sandy deposits preserved in the coastal forest. The sand layers were well preserved in the dark mid-forest (A). In contrast, deposits were significantly disturbed by plant growth where there were numerous grasses growing (B).

The thickness of the sandy deposits in 2011 and 2016 and the tsunami inundation limits are also plotted. Our results are summarized in Figure 5. We found preservation state of the tsunami deposit increased from the coast to the forest and suddenly decreased in the residential area. This is because of reconstruction near the coast and high preservation potential in the forest. Note that about half of thin deposits (less than 2 cm) even in 2011 were detectable in 2016.

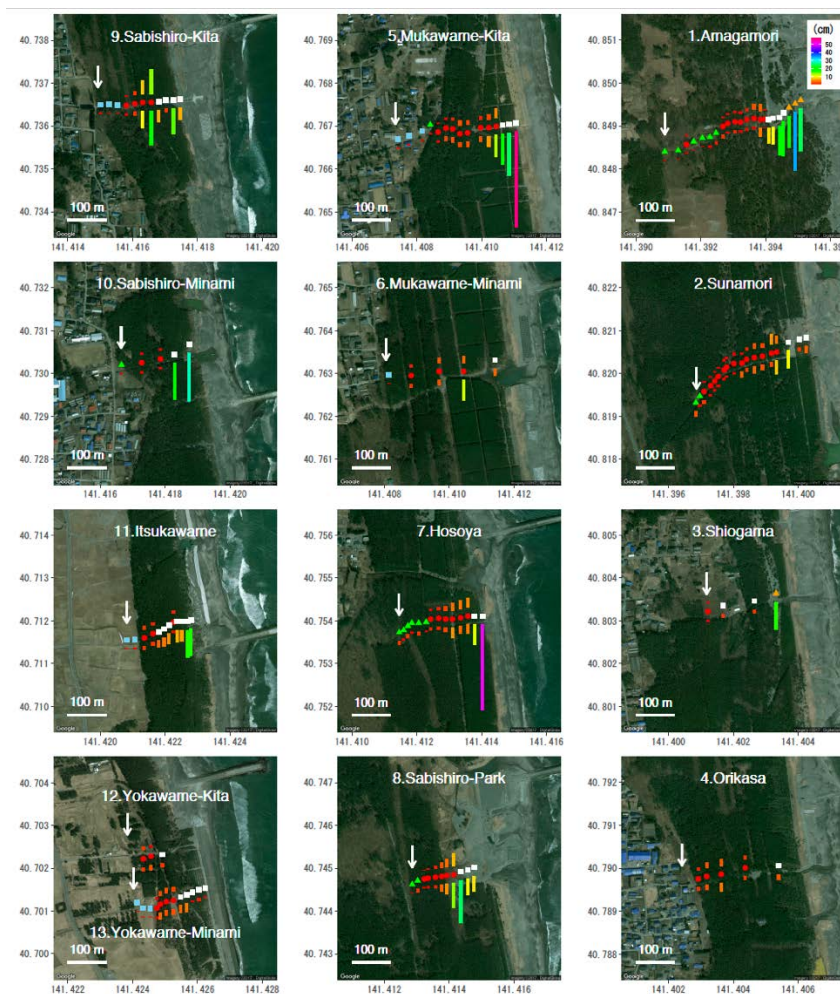


Figure 4: Preservation and disappearance of the 2011 tsunami deposits at 137 observation sites on 13 profiles. Color bars show thickness of the tsunami deposits observed in 2011 (lower) and in 2016 (upper) at survey points on the 13 profiles by Nakamura et al. (2012). Red circles are sites where the deposits are identifiable after 5 years. White and blue rectangles are sites where the deposits were removed by human activity. Green triangles are sites where the deposits were not identified in spite of having been in the natural environment. White arrows indicate the tsunami inundation limits

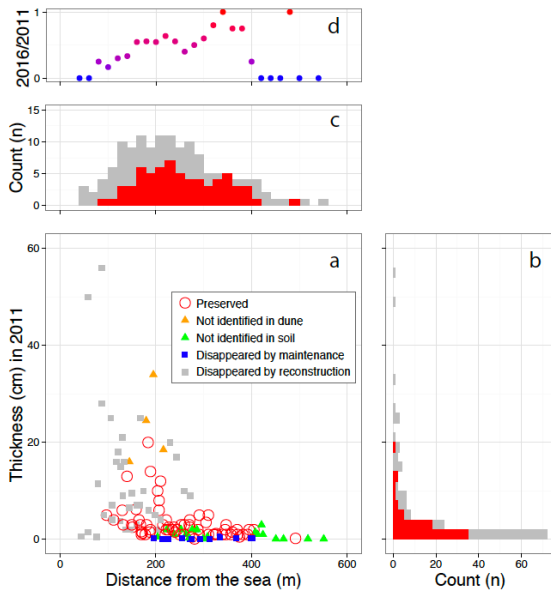


Figure 5: Preservation and disappearance of the deposits as related to their original thickness and distance from the sea as obtained in 2011 by Nakamura et al., 2012 (a). In histograms (b & c), gray bars are for all counts and red are for those preserved. Preservation state is also shown at the top of the figure (d). The vertical axis is the ratio to the all of the preserved. The color continuously changes from 1 (red) to 0 (blue).

INUNDATION BOUNDARY VS TRACE BOUNDARY

In 2011, Nakamura et al. (2012) traced the tsunami deposits up to the tsunami inundation limits for 4 profiles of the 13 profiles. However, in 2016, the deposits near the boundary for these 4 profiles were not detectable even though 3 of them were in the forest and not expected to have been disturbed by human activity. It may be because the thin and fine deposits were blown away by wind while on the ground surface or scattered in the soil during plant growth. Of the other 9 profiles, there were only 3 of them for which we could trace the deposits in 2016 up to the 2011 boundary. Figure 6 shows inundation limits of the tsunami, deposition limits in 2011 and those in 2016 for each profile. Inland limits of the deposits thicker than 2cm were also plotted, supposing only thick deposits remain detectable in the future. On average, the inland limit for tracing the deposits reduced 14% in distance and 21% in elevation. This information could be useful for evaluating tsunami inundation based on deposit distribution for historical or prehistorical events.

TSUNAMI DEPOSITS AS DISASTER ARCHIVES

The Misawa coast is a valuable place not only to study the formation process of the 2011 tsunami deposits but also to examine their preservation potential and weathering in the natural environment. Therefore, the coastal forest in Misawa is highly likely to become a useful type locality for studying paleotsunami deposits.

The remaining tsunami deposits can be considered a disaster archive that should be effectively and sustainably utilized for societal benefit. This could include, for example, not only research, but also excursions for the local people and displays of deposit peals in public facilities to promote disaster prevention education.

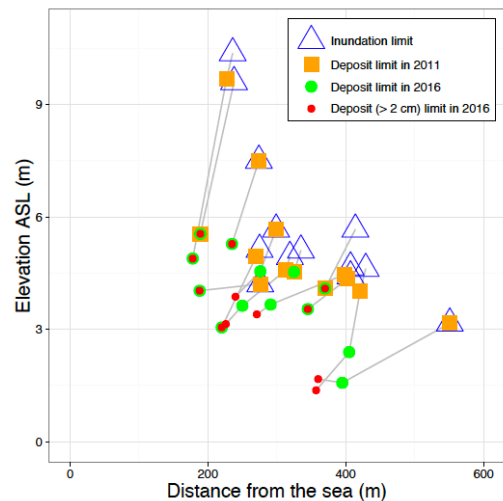


Figure 6: Inundation limits of the 2011 tsunami, inland limits of the deposit distribution observed in 2011 and in 2016 for each profile. Inland limits of the deposits thicker than 2cm were also plotted.

REFERENCES

Nakamura, Y., Nishimura, Y., & Putra, P. S., 2012. Local variation of inundation, sedimentary characteristics, and mineral assemblages of the 2011 Tohoku-oki tsunami on the Misawa coast, Aomori, Japan. *Sedimentary Geology* 282, 216-227.

Spiske, M., Piepenbreier, J., Benavente, C., & Bahlburg, H., 2013. Preservation potential of tsunami deposits on arid siliciclastic coasts. *Earth-Science Reviews* 126, 58-73.

Szczuciński, W., 2012. The post-depositional changes of the onshore 2004 tsunami deposits on the Andaman Sea coast of Thailand. *Natural Hazards* 60(1), 115-133.



Three-dimensional coastal deformation in the M_w 7.8 Kaikōura earthquake from differential airborne lidar

Nissen, Edwin (1), Malireddi, Sri Raghu (2), Clark, Kate (3), Hamling, Ian (3), Langridge, Robert (3), Ries, William (3), and Tagliasacchi, Andrea (2)

- (1) School of Earth and Ocean Sciences, University of Victoria, Victoria BC, Canada. enissen@uvic.ca.
(2) Department of Computer Science, University of Victoria, Victoria BC, Canada
(3) GNS Science, PO Box 30368, Lower Hutt 5040, New Zealand

Abstract: We investigate coastal deformation in the 2016 M_w 7.8 Kaikōura earthquake by differencing airborne lidar topography data surveyed in 2012 and late 2016. The 90 km-long, 1 km-wide strip of lidar double-coverage crosses coastal outcrops of the Hundalee, Hope, Papatea and Kekerengu faults, and also extends inland for several kilometers along the Papatea fault. We compute the three-dimensional coseismic surface displacement field using new adaptations of the Iterative Closest Point algorithm. Resulting surface displacements are in good agreement with independent measurements, but with better spatial coverage (over field and GPS data) and improved coherence (over InSAR). We observe multiple-wavelength signals related to oblique rupture of shallow upper plate faults, off-fault deformation, and possibly slip on the underlying plate interface. The complex coastal uplift pattern should prompt reassessment of coastal paleoseismic and marine terrace records that may not have considered multiple-fault ruptures of this type.

Key words: Lidar, coseismic surface deformation, Kaikōura earthquake

INTRODUCTION

The 13 November 2016 M_w 7.8 Kaikōura (New Zealand) earthquake cascaded across a fractured array of onshore and offshore reverse, strike-slip and oblique-slip faults within the Marlborough Fault System (Hamling *et al.*, 2017). At least twenty distinct faults are known to have slipped coseismically (Stirling *et al.*, 2017), making this one of the most complicated earthquakes on record globally. These faults mark the transition between westward subduction of Pacific oceanic lithosphere beneath the North Island, and continental strike-slip along the Alpine Fault in the South Island (Wallace *et al.*, 2012). The Kaikōura earthquake therefore offers insights both into the rupture process of a major, multi-segmented earthquake and into the regional fault kinematics.

The Kaikōura earthquake was well-recorded by field surveys (Clark *et al.*, 2017; Stirling *et al.*, 2017), by satellite optical sub-pixel correlation (Hollingsworth *et al.*, 2017; Kääb *et al.*, 2017) and InSAR (Hamling *et al.*, 2017), and by regional and teleseismic seismometers (Bai *et al.*, 2017; Duputel & Rivera, 2017; Kaiser *et al.*, 2017; Zhang *et al.*, 2017). However, due in part to the complexity of the surface deformation and seismic wave fields, the relative importance of the constitutive faults and their geometries at depth remain uncertain. In particular, the presence or absence of coseismic slip on the southernmost Hikurangi subduction megathrust has been subject to much debate (e.g. Bai *et al.*, 2017; Furlong & Herman, 2017; Hamling *et al.*, 2017; Clark *et al.*, 2017). Whether or not rupture segments with disconnected surface traces are linked at depth is of general importance for understanding of how earthquakes propagate and terminate (e.g. Wesnousky, 2006; Nissen *et al.*, 2016). This question is of fundamental significance to the field of paleoseismology, since it informs how to interpret overlapping paleo-earthquake ages from trench sites on neighbouring but distinct faults.

The aim of this project is to provide additional constraints on source faulting in the Kaikōura earthquake using paired airborne lidar surveys undertaken in 2012, four years before the earthquake, and in late 2016, during the weeks after it. By mapping topography at a finer (sub-meter) spatial resolution than coseismic slip (up to several meters in this earthquake), lidar has the potential for revealing details of the earthquake that satellite-based imaging may have overlooked. However, to our knowledge this is only the seventh earthquake globally, and the first coastal event, to be captured (to any extent) with “before” and “after” lidar topography, and methodologies for differencing high-resolution topographic datasets are still in a nascent phase (e.g. Leprince *et al.*, 2011; Borsa & Minster, 2012; Oskin *et al.*, 2012; Nissen *et al.*, 2012). An additional motivation of ours is therefore to use the Kaikōura earthquake as a test case for improving the ways in which repeat topography data are analyzed.

METHODS

The Kaikōura coastline was mapped with airborne lidar in July 2012 and again in the weeks following the earthquake, providing a narrow (ca. 0.5 – 4 km), ca. 90 km-long coastal strip of repeat, sub-meter resolution topography. Details of the two surveys are provided in Clark *et al.* (2017). In this updated analysis, we additionally exploit newly-available lidar double coverage inland of the coastline along the lower Clarence River valley, capturing much of the Papatea fault rupture.

We applied two complementary approaches to mapping the surface deformation. Initially, we were most interested in deciphering the vertical component of deformation. The most convenient method for doing so is to subtract digital elevation models of the 2012 lidar survey from those of the 2016 survey (a “DEM of Difference”). This is also the most computationally-manageable approach – since it relies



only upon regularly-gridded (rasterized) data – and furthermore it can be undertaken at close to the full resolution of the lidar data. However, a key limitation is that lateral motions are neglected; raw elevation changes are influenced by horizontal displacement magnitude and azimuth, slope aspect and angle, and topographic roughness, all of which can obscure the true vertical deformation signal (Oskin *et al.*, 2012; Duffy *et al.*, 2013).

However, restricting the calculations to flat, smooth parts of the topography greatly reduces such biasing, such that the simple elevation change closely resembles the true vertical displacement (Clark *et al.*, 2017). Therefore, we restricted the DoD calculations to areas with slopes of $<5^\circ$. Because our focus is on coseismic displacements, rather than erosional or depositional processes, we also removed riverbeds, beaches and landslides from the analysis. Finally, we also found that applying an additional cut-off in surface area further enhanced the signal-to-noise, reducing localized scatter in elevation changes to typically ca. 1 m for areas of $<10 \text{ m}^2$, and ca. 0.5 m for larger areas of $<2000 \text{ m}^2$.

In the second approach, we compute the three-dimensional coseismic surface displacement field through local registrations (alignments) of the 2012 and 2016 lidar point clouds. This has the obvious advantage of accounting fully, and equitably, for the three components of the deformation field, but comes at the expense of spatial resolution, since the datasets must be correlated over an area that greatly exceeds the raw lidar point spacing. Working well with irregular point clouds, this approach is truest to the original data but also challenging computationally.

Various algorithms have been proposed to determine three-dimensional deformation from repeat topographic data (Leprince *et al.*, 2011; Borsa & Minster, 2012; Nissen *et al.*, 2012; Zhang *et al.*, 2015; Moya *et al.*, 2017). We develop and apply our own adaptation of the Iterative Closest Point (ICP) point cloud registration algorithm (Besl & McKay, 1992; Chen & Medioni, 1992), building upon previous work by Nissen *et al.* (2012, 2014) and Glennie *et al.* (2014). The pre- and post-earthquake point clouds are first filtered to remove vegetation and building laser returns, and then split into overlapping square cells. Each pre-earthquake cell is then aligned with its equivalent post-event cell by minimizing closest neighbour distances, through an iterative sequence of rigid body translations along and rotations about the x (North-South), y (East-West) and z (up-down) coordinate axes. For each pair of cells, the summed translation over all iterations defines the local coseismic surface displacement; repeated across the entire scene, the displacement field is mapped.

We explored various implementations of ICP, including point-to-point and point-to-plane varieties as well as a new “sparse ICP” approach that iteratively re-weights the point clouds to lend greater prominence to those points which held more influence during the previous iteration (Bouaziz *et al.*, 2013). The iterative re-weighting acts to reduce the

influence of outlier points, which can otherwise potentially lead regular ICP towards local, rather than global, minima in the registration misfit. After trial and error, we find that 50 m-wide cells provide the best balance of high spatial resolution and displacement robustness. However, we also implement a “sliding window” option that allows additional densification of the displacement field.

Our ICP approach is implemented within a single MATLAB script and requires no other dependencies, and is available upon request to the authors.

RESULTS

Elevation change results are plotted on a SW – NE-oriented line of projection that approximately parallels the Kaikōura coastline (Figure 1a, reproduced from Clark *et al.*, 2017). We discuss the elevation change profile at length in Clark *et al.* (2017), and provide only a brief summary of our observations below.

Several interesting trends are apparent. Abrupt vertical offsets related to slip on the Hundalee fault (Figure 1b) and the double-stranded Papatea fault (Figure 1d) are clear, though we observe no such displacement across the Hope fault. Broader (ca. 10 km length scale) swells of uplift northeast of the Hundalee fault and southwest of the Papatea fault are probably related to slip at depth on these faults. Highly localized (200 – 400 m length scale) subsidence of up to ca. 3 m around the Kekerengu fault is harder to interpret, as it occurs on both sides of the fault (Figure 1a). This may be related to bulk material processes such as fault zone dilatancy rather than elastic slip on the Kekerengu fault, which would give rise to a much broader displacement pattern.

A broad swell of uplift is observed from ca. 4 km south to ca. 16 km north of the Kaikōura Peninsula (Figure 1a), and the peninsula itself appears to have been tilted slightly towards the NW (Figure 1c). These signals do not appear related to any of the faults that cross the area of lidar double coverage, and marine surveying indicates that the Hundalee fault rupture probably terminates south of the peninsula (Clark *et al.*, 2017). The signal appears too abrupt to be explained by slip on the subduction interface, which is at ca. 19 km depth in this area. We tentatively ascribe this deformation to slip on an offshore reverse fault that strikes SW and dips ca. 35° beneath Kaikōura peninsula. Slip on this structure may be responsible for the ca. 2 m sea level draw-down observed on a tide gauge at Kaikōura over ca. 24 minutes after the earthquake.

An example of our three-dimensional deformation measurements is shown in Figure 2, from along a section of the Papatea fault rupture in the Clarence River valley.

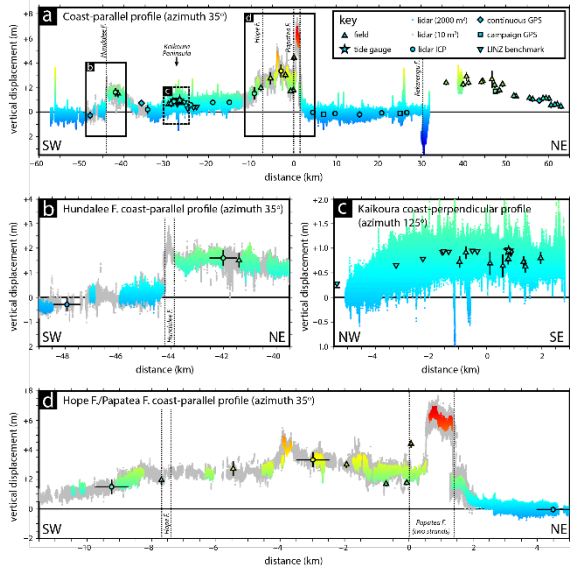


Figure 1: reproduced from Clark *et al.* (2017). (a) Elevation changes projected onto a 35°-trending straight line which parallels the Kaikōura coastline. The profile is centered ($x = 0$) at the Papatea fault and vertical dashed lines mark locations of major faults at the coastline. Vertical bars show 95% confidence bounds on field coastal uplift measurements and GPS-derived vertical displacements (the latter are barely visible at this scale). Coloured points represent elevation changes calculated from overlapping surface areas $>2000 \text{ m}^2$; the grey points represent surface areas $>10 \text{ m}^2$. (b) Detail across the Hundalee fault. (c) Coastline-perpendicular uplift profile (azimuth 125°, projection center at Kaikōura township) showing tilting across the Kaikōura Peninsula. (d) Detail across the Hope and Papatea faults.

Spurious ICP results, caused by changes to internal cell topography such as along the Clarence River, have been filtered from the figure. Work towards reproducing the full displacement field is ongoing, reflecting in part the computational challenge of manipulating very large point cloud datasets (hundreds of gigabytes).

Left-lateral and vertical offsets across the Papatea rupture are clearly resolved in the displacement field. A parallel strand of faulting around ca. 1 km west of the Papatea fault can also be observed, upthrown to the east and with a small left-lateral component. Furthermore, *absolute* motions of the two sides of the Papatea fault can be determined. The block west of it moved several meters southwards and upwards, whereas the block east of it remained relatively stationary, moving only a little towards the west (in good agreement with coarser-resolution SAR pixel offset results; Hamling *et al.*, 2017).

Displacement vectors appear remarkably consistent even around the highly-sinuous trace of the rupture. This implies that the slip vector is quite constant even as the style of faulting changes around the fault bends. In the northwest part of the scene, the NW-SE-trending scarp accommodates left-lateral strike-slip with very little fault-normal motion (despite the clear vertical offset). In the southeast part of the scene, the N-S-trending scarp accommodates roughly equal amounts of left-lateral strike-slip and shortening.

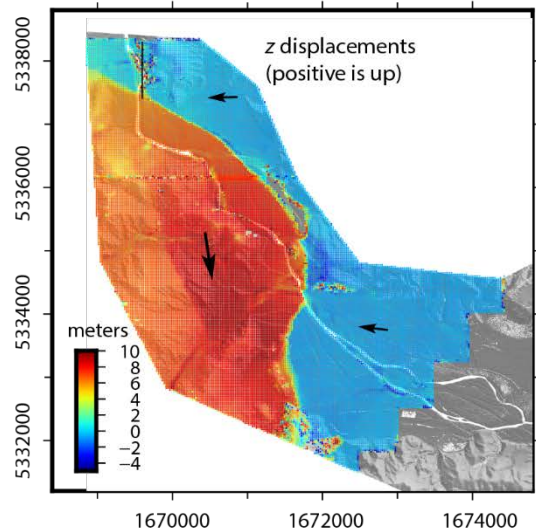
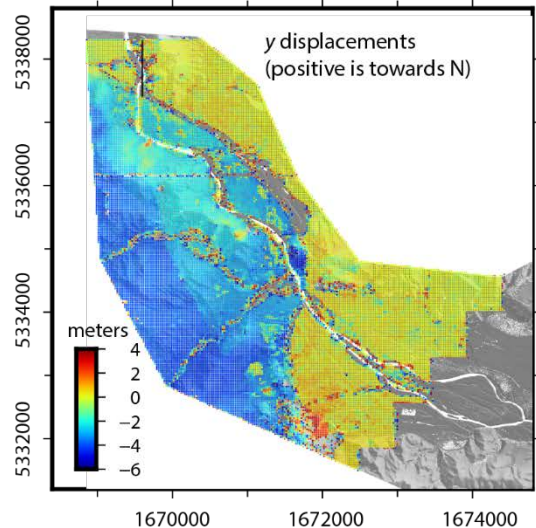
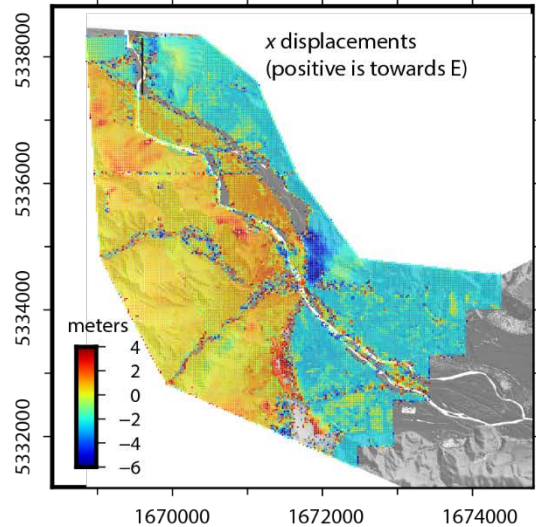


Figure 2: ICP results from part of the Papatea fault, using a cell size of 50 m, a slide of 25 m, and point-to-plane ICP. The panels show E-W, N-S and up-down displacements, respectively. The general sense of the horizontal motions is shown on the final panel by black arrows. Coordinates are given in meters in the NZTM2000 coordinate system.



Acknowledgements: We thank Land Information New Zealand, New Zealand Transport Authority, Environment Canterbury, Marlborough District Council, Aerial Surveys Ltd and AAM NZ Ltd for providing excellent lidar data. The 2012 lidar data (<http://dx.doi.org/10.5069/G98C9T67>) and derived products are hosted and disseminated by the OpenTopography Facility (<http://www.opentopography.org/>) with support from the US National Science Foundation under NSF Awards #1226353 and #1225810. E.N. and S.R.M. were supported by the Natural Sciences and Engineering Research Council of Canada (NSERC) through Discovery Grant #2017-04029.

REFERENCES

- Bai, Y., Lay, T., Cheung, K. F., & Ye, L., 2017. Two regions of seafloor deformation generated the tsunami for the 13 November 2016, Kaikoura, New Zealand earthquake. *Geophysical Research Letters* 44, 6597–6606.
- Besl, P. J., & McKay, N. D., 1992. A method for registration of 3-D shapes. *IEEE Transactions on Pattern Analysis and Machine Intelligence* 14 (2), 239-256.
- Borsa, A., & Minster, J. B., 2012. Rapid Determination of near-fault earthquake deformation using differential LiDAR. *Bulletin of the Seismological Society of America* 102 (4), 1335-1347.
- Bouaziz, S., Tagliasacchi, A., & Pauly, M., 2013. Sparse Iterative Closest Point. *Computer Graphics Forum* 32, 113–123.
- Chen, Y., & Medioni, G., 1992. Object modelling by registration of multiple range images. *Image and Vision Computing* 10 (3), 145-155.
- Clark, K. J., Nissen, E. K., Howarth, J. D., Hamling, I. J., Mountjoy, J. J., Ries, W. F., Hreinsdóttir, S., Litchfield, N. J., Mueller, C., Berryman, K. R., & Strong, D. T., 2017. Highly variable coastal deformation in the 2016 M_w 7.8 Kaikōura earthquake reflects rupture complexity along a transpressional plate boundary. *Earth and Planetary Science Letters* 474, 334-344.
- Duffy, B., Quigley, M., Barrell, D. J., Van Dissen, R., Stahl, T., Leprince, S., McInnes, C., & Bilderback, E., 2013. Fault kinematics and surface deformation across a releasing bend during the 2010 M_w 7.1 Darfield, New Zealand, earthquake revealed by differential LiDAR and cadastral surveying. *Geological Society of America Bulletin* 125 (3-4), 420-431.
- Duputel, Z., & Rivera, L., 2017. Long-period analysis of the 2016 Kaikoura earthquake. *Physics of the Earth and Planetary Interiors* 265, 62-66.
- Fielding, E. J., Lundgren, P. R., Bürgmann, R., & Funning, G. J., 2009. Shallow fault-zone dilatancy recovery after the 2003 Bam earthquake in Iran. *Nature* 458 (7234), 64-68.
- Furlong, K. P., & Herman, M., 2017. Reconciling the Deformational Dichotomy of the 2016 M_w 7.8 Kaikoura NZ Earthquake. *Geophysical Research Letters* 44, 6788–6791.
- Glennie, C. L., Hinojosa-Corona, A., Nissen, E., Kusari, A., Oskin, M. E., Arrowsmith, J. R., & Borsa, A., 2014. Optimization of legacy lidar data sets for measuring near-field earthquake displacements. *Geophysical Research Letters* 41 (10), 3494-3501.
- Hamling, I. J., Hreinsdóttir, S., Clark, K., Elliott, J., Liang, C., Fielding, E., Litchfield, N., Villamor, P., Wallace, L., Wright, T. J., D'Anastasio, E., Bannister, S., Burbidge, D., Denys, P., Gentle, P., Howarth, J., Mueller, C., Palmer, N., Pearson, C., Power, W., Barnes, P., Barrell, D. J. A., Van Dissen, R., Langridge, R., Little, T., Nicol, A., Pettinga, J., Rowland, J., & Stirling, M., 2017. Complex multifault rupture during the 2016 M_w 7.8 Kaikōura earthquake, New Zealand. *Science* 356 (6334), eaam7194.
- Hollingsworth, J., Ye, L., & Avouac, J. P., 2017. Dynamically triggered slip on a splay fault in the M_w 7.8, 2016 Kaikoura (New Zealand) earthquake. *Geophysical Research Letters* 44, 3517-3525.
- Kääb, A., Altena, B., & Mascaro, J., 2017. Coseismic displacements of the 14 November 2016 M_w 7.8 Kaikoura, New Zealand, earthquake using the Planet optical cubesat constellation. *Natural Hazards and Earth System Sciences* 17, 627-639.
- Kaiser, A., Balfour, N., Fry, B., Holden, C., Litchfield, N., Gerstenberger, M., D'Anastasio, E., Horspool, N., McVerry, G., Ristau, J., Bannister, S., Christophersen, A., Clark, K., Power, W., Rhoades, D., Massey, C., Hamling, I., Wallace, L., Mountjoy, J., Kaneko, Y., Benites, R., Van Houtte, C., Dellow, S., Wotherspoon, L., Elwood, K., Gledhill K., & Bannister, S., 2017. The 2016 Kaikōura, New Zealand, Earthquake: Preliminary Seismological Report. *Seismological Research Letters* 88 (3), 727-739.
- Leprince, S., Hudnut, K. W., Akciz, S. O., Hinojosa-Corona, A., & Fletcher, J. M., 2011. Surface rupture and slip variation induced by the 2010 El Mayor–Cucapah earthquake, Baja California, quantified using COSI-Corr analysis on pre-and post-earthquake lidar acquisitions. *American Geophysical Union Fall Meeting*, EP41A-0596.
- Moya, L., Yamazaki, F., Liu, W., & Chiba, T., 2017. Calculation of coseismic displacement from lidar data in the 2016 Kumamoto, Japan, earthquake. *Natural Hazards and Earth System Sciences* 17 (1), 143-156.
- Nissen, E., Krishnan, A. K., Arrowsmith, J. R., & Saripalli, S., 2012. Three-dimensional surface displacements and rotations from differencing pre-and post-earthquake LIDAR point clouds. *Geophysical Research Letters* 39, L16301.
- Nissen, E., Maruyama, T., Arrowsmith, J. R., Elliott, J. R., Krishnan, A. K., Oskin, M. E., & Saripalli, S., 2014. Coseismic fault zone deformation revealed with differential LiDAR: Examples from Japanese M_w ~7 intraplate earthquakes. *Earth and Planetary Science Letters* 405, 244-256.
- Nissen, E., Elliott, J. R., Sloan, R. A., Craig, T. J., Funning, G. J., Hutko, A., Parsons, B. E., & Wright, T. J., 2016. Limitations of rupture forecasting exposed by instantaneously triggered earthquake doublet. *Nature Geoscience* 9 (4), 330-336.
- Oskin, M. E., Arrowsmith, J. R., Corona, A. H., Elliott, A. J., Fletcher, J. M., Fielding, E. J., Gold, P. O., Gonzalez Garcia, J. J., Hudnut, K. W., Liu-Zeng, J., & Teran, O. J., 2012. Near-field deformation from the El Mayor–Cucapah earthquake revealed by differential LIDAR. *Science* 335 (6069), 702-705.
- Stirling, M. W., and fifty-seven others, 2017. The M_w 7.8 2016 Kaikōura earthquake: Surface fault rupture and seismic hazard context. *Bulletin of the New Zealand Society for Earthquake Engineering* 50 (2), 73-84.
- Wallace, L. M., Barnes, P., Beavan, J., Van Dissen, R., Litchfield, N., Mountjoy, J., Langridge, R., Lamarche, G., & Pondard, N., 2012. The kinematics of a transition from subduction to strike-slip: An example from the central New Zealand plate boundary. *Journal of Geophysical Research: Solid Earth* 117, B02405.
- Wesnousky, S. G., 2006. Predicting the endpoints of earthquake ruptures. *Nature* 444 (7117), 358-260.
- Zhang, X., Glennie, C., & Kusari, A., 2015. Change detection from differential airborne LiDAR using a weighted anisotropic iterative closest point algorithm. *IEEE Journal of Selected Topics in Applied Earth Observations and Remote Sensing* 8 (7), 3338-3346.
- Zhang, H., Koper, K. D., Pankow, K., & Ge, Z., 2017. Imaging the 2016 M_w 7.8 Kaikoura, New Zealand Earthquake with Teleseismic P Waves: A Cascading Rupture Across Multiple Faults. *Geophysical Research Letters* 44, 4790–4798.



Paleoseismic Study Enhanced by U-Series Geochronology of Pedogenic Carbonate from Displaced Fluvial Gravel Deposits, Issyk-Ata Fault, Central Tien Shan, North Kyrgyzstan

Patyniak, Magda (1), Landgraf, Angela (1), Dzhumabaeva, Atyrgul (2), Abdrakhmatov, Kanatbek (2), Fohlmeister, Jens (1,4), Rosenwinkel, Swenja (1), Korup, Oliver (1), Preusser, Frank (3), Arrowsmith, Ramón J. (5) and Strecker, Manfred R. (1)

- (1) Institute of Earth and Environmental Sciences, University of Potsdam, K.-Liebknecht Str. 24-25, D-14476 Golm, Germany. Email: patyniak@uni-potsdam.de
- (2) Institute of Seismology, National Academy of Science of Kyrgyzstan, Bishkek, Kyrgyzstan
- (3) Institute of Earth and Environmental Sciences, University of Freiburg, Freiburg, Germany
- (4) Helmholtz Centre Potsdam, GFZ German Research Centre for Geosciences, Potsdam, Germany
- (5) School of Earth and Space Exploration, Arizona State University, Tempe, AZ, USA

Abstract: The evaluation of thrust paleoearthquakes and associated fault scarps is often hampered by the size of their cumulative scarps and interaction with sedimentary processes during interseismic periods. Paired with areas undergoing low strain accumulation with long recurrence intervals and environments, which provide limited datable material, an event chronology becomes even more difficult to develop. In our trenching study in alluvial fans in the semiarid Tien Shan, we used radiocarbon and IRSL dating, and complemented that by dating pedogenic carbonate coating with the U-series method to improve age information on seismogenic deformation on longer timescales. In addition, if these are cross-checked with radiocarbon ages, U-series ages might also highlight potential reservoir effects in pedogenic carbonate ages. Besides numeric ages, carbonate coating on clast undersides provide relative age constraints based on the relation between their orientations and seismic deformation, further improving the earthquake age models.

Key words: Pedogenic Carbonate, Geochronology, Paleoseismology, Issyk-Ata Fault, Tien Shan

INTRODUCTION

The improvement of quality and quantity of potential earthquake maps in continental seismic zones relies on a combination of instrumental records with extended archives of historic earthquakes, and data derived from paleoseismological studies. The reliability of the latter depends on structural interpretation combined with relative and absolute geochronology. However, a meaningful age model is often hampered by the poor availability and quality of datable material. This is especially the case in semiarid regions, where grass dominated vegetation leads to a lack of organics for radiocarbon based dating. Further, if alluvial and fluvial deposits characterize those areas, optical stimulated luminescence (OSL) dating is often limited due to insufficient grain sizes and/or abundance of quartz.

Here we present the application of pedogenic carbonate coatings on clast undersides as an additional relative time constraint and for absolute age control through U-series dating to complement established methods like OSL and radiocarbon dating.

STUDY AREA

The Issyk-Ata fault defines the northern most deformation front of the Kyrgyz Range in the northern Central Tien Shan (Figure 1). The south-dipping fault with reverse to thrust sense of motion has an approximate extend of 120 km in the east-west direction (Abdrakhmatov, 1988; Chediya et al., 1998; Thompson et al., 2002; Bullen et al., 2003; Macaulay et al., 2014).

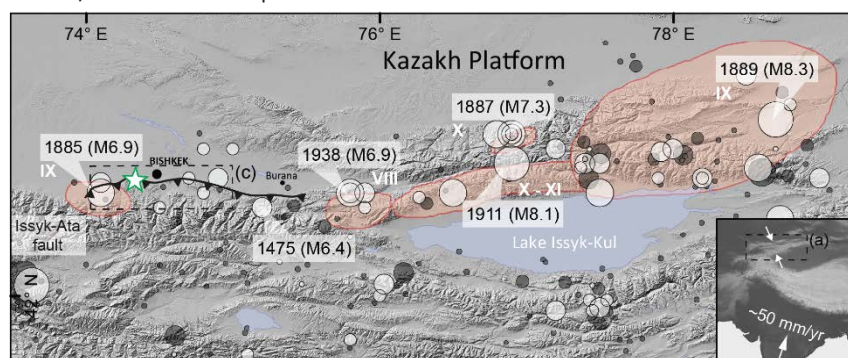


Figure 1: Seismological overview of the Northern Tien Shan with the location of the trenching study indicated by the green star. Circles include historic (light) and instrumental (dark) earthquakes (ComCat, USGS). The earthquake sequence that affected that area in the 19th to 20th century is labeled with year and magnitude. Red polygons indicate areas of associated earthquake intensities (MSK64 scale). Single intensities are labeled by white roman numerals. (modified after Patyniak et al. 2017).



INQUA Focus Group Earthquake Geology and Seismic Hazards



paleoseismicity.org

The western most tip of the Issyk-Ata fault ruptured in A.D. 1885 (Belovodskoe; $M = 6.9$), initiating a remarkable sequence of large-magnitude earthquakes ($M > 6.9$) that affected the Northern Tien Shan at the turn of the 19th to the 20th century (e.g., Bogdanovich et al., 1914; Kalmetieva et al., 2009; Kulikova and Krüger, 2015). However, almost the entire eastward extend of the fault was left unruptured during this ~50-year long sequence.

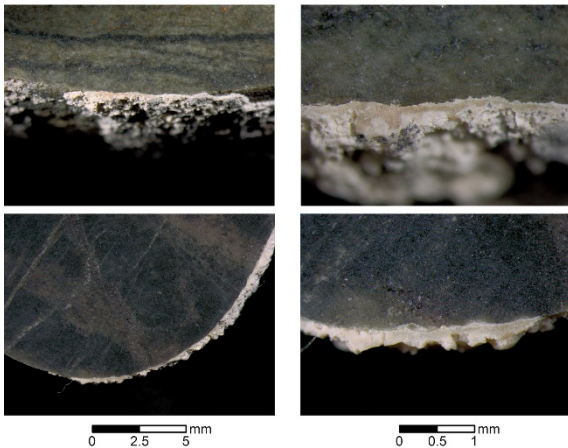


Figure 2: Close-up images of polished cross-sections of two sample clasts and carbonate coating on their undersides. Left column with a 10x and right column with 40x magnification. (modified after Patyniak et al. 2017)

The Belek site is located ~20 km NE of the potential Belovodskoe earthquake epicenter and ~25 km SW of Bishkek, the capital city of Kyrgyzstan (Figure 1). At this site, the prominent scarp of the Issyk-Ata fault can be traced for roughly 1 km in east-west direction. The fault displays a distinct north-facing fault scarp cutting through

an alluvial fan constituting Upper Pleistocene and Holocene deposits (Burg et al., 2004) and intersecting a part of the northern margin of the Kyrgyz Range.

GEOCHRONOLOGY

Key units pre- or postdating interpreted surface rupturing features from both trench walls were sampled to provide a representative range of maximum and minimum ages to provide a chronological earthquake history of the Belek site. For sediment deposition ages, we dated fine-grained material using IRSL dating. Further, we applied radiocarbon dating on organic material incorporated into the sediments. Finally, as additional method we applied the U-series dating on pedogenic carbonate coating from clast undersides as representatives of phases of stable soil formation conditions.

We used carbonate coatings of four pebble samples with a thickness ranging between 0.1 – 0.4 mm (Figure 2). The pre-preparation included a mechanical removing of the full amount of each coating that was subsequently leached in a weak acid. U and Th were separated following the method described in Douville et al. (2010). Isotopic measurements were conducted using MC-ICP-MS (Thermo Fisher Neptune/Finnigan Neptune) at the Institute of Environmental Physics at Heidelberg University. More information about the instrumentation and measurement protocols is provided in Arps et al. (in review).

By using OxCal radiocarbon calibration and v4.2 analysis software (Bronk Ramsey, 2013) with the IntCal13 calibration curve for ¹⁴C (Reimer et al., 2013) we computed probability density functions (PDF) representing the age of the rupture events based on all obtained ages.

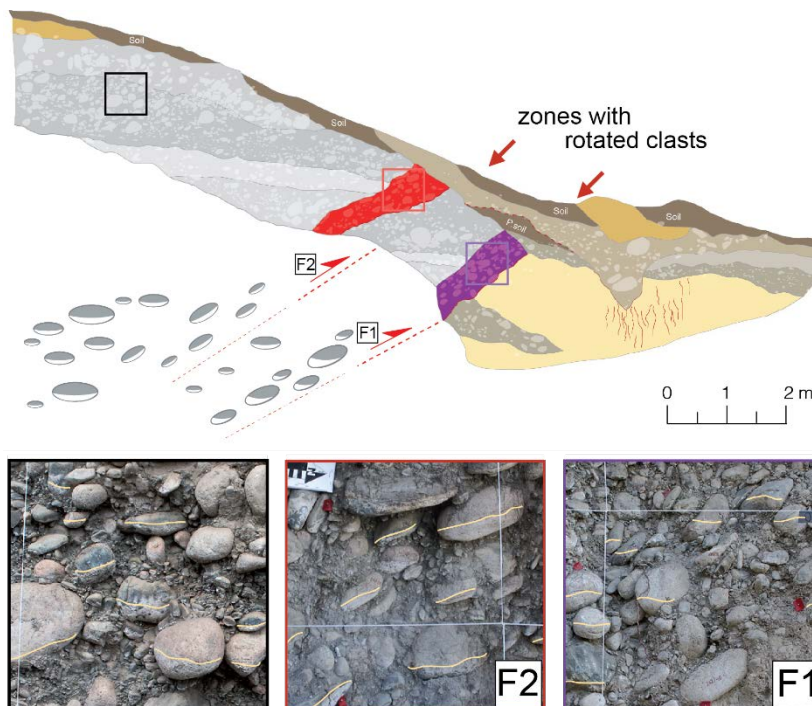


Figure 3: Above: Trench log of the west wall including a sketch of clast orientation and associated orientation of carbonate coatings in different zones throughout the hanging wall. Below: Close up into the defined zones with the carbonate coating orientation on clast undersides outlined in yellow.



PALEOSEISMOLOGY AT THE BELEK SITE

The trench was excavated with dimensions of 18 x 2.5 x 2 m (length x width x depth) perpendicular to the fault scarp, which has a height of 8 m and a total vertical offset of 6.8 m.

Trench Stratigraphy

The exposed strata are mainly composed of alluvial and fluvial gravel and boulders in the hanging wall south of the fault zone. They can be distinguished by two separated zones of rotated clasts with respect to the surrounding material, which are subparallel to the fault strands (Figure 3). In the unconsolidated gravel deposits, distinct carbonate-rich horizons with different stages of carbonate accumulation can be observed throughout several units. Within these units and in the fault zones, we note clasts that are coated with carbonated coating on their undersides. The footwall in turn predominantly shows a massive loess unit that is intersected and overlain by a succession of coarse colluvial and finer wash deposits.

Evidence for Earthquakes

The up-thrust sense of the hanging wall is reflected by one distinct carbonate cemented unit that was used as an offset marker. To determine the number of earthquakes that affected this site, we focused on the wedge shaped and colluvial deposits representing the direct link to surface rupturing seismic events. Based on these and the two fault zones we count at least three earthquakes. The carbonate coatings show different orientations between non-faulted and faulted zones that can be separated into three different styles: (1) non-faulted strata in the hanging wall with horizontally oriented coatings, (2) fault zone F1 with rotated clasts but horizontally oriented coatings, and (3) fault zone F2 with rotated clasts and carbonate coating (Figure 3; black, purple and red box).

Timing of past earthquakes

The interplay of the orientation of the clasts and the carbonate coating was used to build our interpretation for relative timing between the three events as follows: (1) the horizontally oriented carbonate coatings on the undersides of clasts define carbonate cementation in the original, undisturbed stratigraphic context; (2) therefore, rotated clasts with horizontally oriented carbonate coating imply that the rupture along this fault strand happened before the carbonate coating; (3) rotated clasts with non-horizontal carbonate coatings indicate rupture after carbonate precipitation. Combining this information with the colluvial package relative positions, we inferred that at least two earthquakes ruptured along F1 before faulting apparently migrated southward into the hanging wall, rupturing along F2 at least one more time. Further, all earthquakes that ruptured along F1 must be older than the precipitation age of the carbonate coatings.

The probabilistic timing and associated uncertainties of the inferred earthquakes were modeled by combining the minimum and maximum ages in OxCal, resulting in earthquake timing before 10.5 ± 1.1 cal ka BP (EQ1), in the range of 5.6 ± 1.0 cal ka BP (EQ2), and at about 626 ± 95 cal ka BP (EQ3).

DISCUSSION

Excavation across the Belek fault scarp reveals two shear zones that are clearly distinguishable by two areas of rotated clasts. The pedogenic carbonate coatings underneath those clasts provided relative ages of the two fault zones and allowed a conclusion of fault propagation into the hanging wall, a common phenomenon observed in other cumulative thrust-fault systems (e.g., Tsukuda et al., 1993; Yeats et al., 1997; McCalpin, 2009).

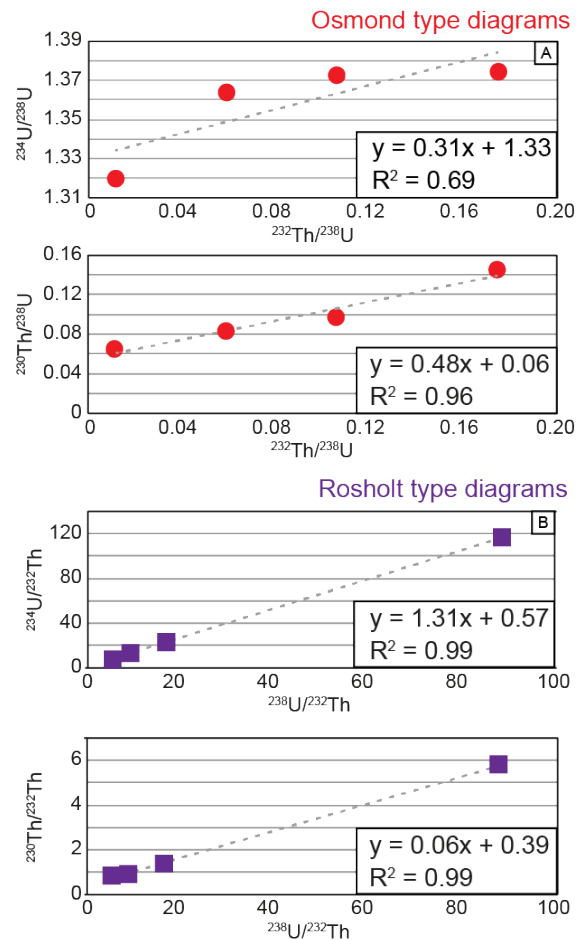


Figure 4: Osmond (A) and Rosholt (B) type diagrams of U and Th isotope analysis. The y-axis intercept of the Osmond plots gives the $^{234}\text{U}/^{238}\text{U}$ and $^{230}\text{Th}/^{238}\text{U}$ isotope ratios of the detrital-free carbonate phase. Both isotope ratios are determined by the slopes of the lines in the Rosholt-type diagrams. In all plots the four samples span a large range and fit well on straight lines. The linear regressions are shown. (modified after Patyniak et al. 2017)

For U-series dating we used four carbonate samples. U-series disequilibrium age determination is made through single sample correction methods, where the detrital U and Th contribution are subtracted from individual

measurements. All four sample showed a high amount of U (6-9 ng/g), but three of the four also showed large detrital inputs, manifested in the high ^{232}Th concentration (1-3 ng/g). Consequently, only one sample with a sufficiently low ^{232}Th content enabled an age calculation. All other resulted in large age error and thus ages are not provided.



INQUA Focus Group Earthquake Geology and Seismic Hazards



paleoseismicity.org

To solve the problem, whether the age of this one sample is representing a real age or not, we calculated isochrones to determine the timing. The fact that all four clasts with carbonate coatings were sampled in the same location next to each other allows us to assume that the carbonate formed at roughly the same time. If this is the case and the source of detritus is the same for all coatings, then all the samples should form straight lines in appropriate U and Th isotope ratio plots. The y-intercepts of Osmond-type diagrams ($^{232}\text{Th}/^{238}\text{U}$ vs. $^{230}\text{Th}/^{238}\text{U}$ and $^{232}\text{Th}/^{238}\text{U}$ vs. $^{234}\text{U}/^{238}\text{U}$) or the slopes of Rosholt-type diagrams ($^{230}\text{Th}/^{232}\text{Th}$ vs. $^{238}\text{U}/^{232}\text{Th}$ and $^{234}\text{U}/^{232}\text{Th}$ vs. $^{238}\text{U}/^{232}\text{Th}$) can be used to determine the ($^{230}\text{Th}/^{238}\text{U}$) and ($^{234}\text{U}/^{238}\text{U}$) ratios of detritus-free carbonate (Osmond et al., 1970; Rosholt, 1976). As shown in figure 4, the results of both types of plots do show a high correlation and thus provide precise ratios of $^{230}\text{Th}/^{238}\text{U}$ and $^{234}\text{U}/^{238}\text{U}$. Therefore, we assume that the resulting ages are similar to each other with respect to errors and correlate with the age determined for sample T2e-3.

To provide unambiguous data for earthquake age modeling and well-constrained PDFs, and to avoid broadly shaped PDFs, a large number of overlapping maximum- and minimum-limiting ages is needed (Lienkaemper and Williams, 2007; Lienkaemper and Ramsey, 2009; DuRoss et al., 2011). This was accomplished by combining different chronometers, which in addition showed consistencies in the ages of units on both walls and within the same units across sample materials and dating methods, further resulting in correct stratigraphic order.

CONCLUSIONS

Here, we performed a stratigraphic and structural analysis of a paleoseismic trench at the Belek site along the Issyk-Ata fault in the Northern Tien Shan. In addition to reliable IRSL and radiocarbon dating, we further dated pedogenic carbonates to produce a probabilistic paleoseismic history. We distinguish at least three surface-rupturing paleoearthquakes. Interestingly, the 1885 A.D. Belovodskoe ($M = 6.9$) earthquake that ruptured along the westernmost part of the Issyk-Ata fault, approximately 20 km west of our study site, could not be identified in our trench.

The complementary dating method by means of Th/U disequilibrium dating was successfully applied to date several secondary precipitated carbonates such as stalagmites, corals or travertines. The calculation of isochrones enabled us to determine the timing of the building of the carbonate coating despite large detrital inputs in three out of the four samples.

Besides the absolute ages derived from all three dating methods, we used the orientation of the carbonate coating as a relative time constraint. This not only reinforced the event chronology, but also confirmed our absolute age control.

Acknowledgements: The Volkswagen Foundation (Germany) provided funding for this study. We would like to acknowledge Andrea Schröder-Ritzrau, René Eichstädter, and Norbert Frank for conducting U-Th isotope analyses of the carbonate crusts and providing helpful advice and assistance. Further, we would like to thank T. Goslar from the Radiocarbon Laboratory (Poznan, Poland) for analyzing our radiocarbon samples.

REFERENCES

- Abdrakhmatov, K.Y. (1988). Quaternary Tectonics of the Chu Basin (in Russian), 120 pp. Ilim Bishkek Kyrg.
- Bogdanovich, K.I., Kark, I.M., Korol'kov, B.Y., and Mushketov, D.I. (1914). Earthquake in Northern district of Tien-Shan, 22 December 1910 (4 January 1911). *Geol. Comm. New Ser.* 89.
- Bronk Ramsey, C. (2013). OxCal 4.2. Web Interface Build.
- Bullen, M.E., Burbank, D.W., and Garver, J.I. (2003). Building the northern Tien Shan: Integrated thermal, structural, and topographic constraints. *J. Geol.* 111, 149–165.
- Burg, J.P., Mikolaichuk, A., and Apayarov, F. (2004). Digital geological map of the Kyrgyz range and Chu Basin transitional zone, SNSF, Project No 7KSPJ065518.
- Chediya, O.K., Abdrakhmatov, K.Y., Lemzin, I.H., Mihel, G., and Mikhailev, V. (1998). Seismotectonic characterization of the Issyk Ata fault. *Bishkek Inst. Nauk Kyrg.* 58–69.
- DuRoss, C.B., Personius, S.F., Crone, A.J., Olig, S.S., and Lund, W.R. (2011). Integration of paleoseismic data from multiple sites to develop an objective earthquake chronology: Application to the Weber segment of the Wasatch fault zone, Utah. *Bull. Seismol. Soc. Am.* 101, 2765–2781.
- Kalmetieva, Z.A., Mikolaichuk, A.V., Moldobekov, B.D., Meleshko, A.V., Jantaev, M.M., Zubovich, A.V., and Havenith, H.B. (2009). Atlas of earthquakes in Kyrgyzstan. Cent.-Asian Inst. Appl. Geosci. U. N. Int. Strategy Disaster Reduct. Secr. Off. Cent. Asia Bishkek 75.
- Kulikova, G., and Krüger, F. (2015). Source process of the 1911 M8.0 Chon-Kemin earthquake: investigation results by analogue seismic records. *Geophys. J. Int.* 201, 1891–1911.
- Lienkaemper, J.J., and Ramsey, C.B. (2009). OxCal: Versatile tool for developing paleoearthquake chronologies—A primer. *Seismol. Res. Lett.* 80, 431–434.
- Lienkaemper, J.J., and Williams, P.L. (2007). A record of large earthquakes on the southern Hayward fault for the past 1800 years. *Bull. Seismol. Soc. Am.* 97, 1803–1819.
- Macaulay, E.A., Sobel, E.R., Mikolaichuk, A., Kohn, B., and Stuart, F.M. (2014). Cenozoic deformation and exhumation history of the Central Kyrgyz Tien Shan. *Tectonics* 33, 135–165.
- McCalpin, J.P. (2009). Paleoseismology (Academic press).
- Osmond, J.K., May, J.P., and Tanner, W.F. (1970). Age of the Cape Kennedy Barrier-and-Lagoon Complex. *J. Geophys. Res.* 75, 469–479.
- Reimer, P.J., Bard, E., Bayliss, A., Beck, J.W., Blackwell, P.G., Bronk Ramsey, C., Buck, C.E., Cheng, H., Edwards, R.L., Friedrich, M., et al. (2013). IntCal13 and Marine13 radiocarbon age calibration curves 0–50,000 years cal BP.
- Rosholt, J.N. (1976). $^{230}\text{Th}/^{234}\text{U}$ dating of travertine and caliche rinds. In *Geological Society of America Abstracts with Programs*, p. 1076.
- Thompson, S.C., Weldon, R.J., Rubin, C.M., Abdrakhmatov, K., Molnar, P., and Berger, G.W. (2002). Late Quaternary slip rates across the central Tien Shan, Kyrgyzstan, central Asia. *J. Geophys. Res. Solid Earth* 107.
- Tsukuda, E., Awata, Y., Yamazaki, H., Sugiyama, Y., Shimokawa, K., and Mizuno, K. (1993). Explanatory text of the strip map of the Atera Fault system, scale 1: 25,000. In *Tectonic Map Series* (7), (Geol. Surv. Japan), p. 39.
- Yeats, R.S., Sieh, K.E., and Allen, C.R. (1997). The geology of earthquakes (Oxford University Press New York).



Authentic collaboration with local communities in post-disaster reconnaissance and beyond: how to create a win-win scenario.

Pedley, Katherine L. ¹

(1) Department of Geological Sciences, University of Canterbury, P.O Box 4800, Christchurch. 8140, New Zealand.
Email: kate.pedley@canterbury.ac.nz

Abstract: Geological research in the immediate aftermath of the 2016 Kaikōura Earthquake, New Zealand, was necessary due to the importance and perishability of field data. It also reflects a real desire on the part of researchers to contribute not only to immediate scientific understanding but also to the societal recovery effort by enhancing knowledge of the event for the benefit of affected communities, civil defence organizations and regional and national decision makers. This commitment to outreach and engagement is consistent with the recent IAPG statement of Geoethics. More immediately, it was informed by experience of the 2010-2011 Canterbury Earthquake sequence. After that earlier disaster, intense interactions between researchers and various response agencies as well as local communities informed the development and dissemination of a set of ethical guidelines for researchers immediately following the Mw7.8 14 November 2016 Kaikōura Earthquake. In this presentation, I argue that ethical engagement of this kind is the key to gathering high quality research data immediately after the event. Creating trusting and mutually respectful, mutually beneficial relationships is also vital to ongoing engagement to facilitate further “in depth” research in collaboration with communities.

Key words: Kaikōura earthquake, surface rupture, ethics, community engagement, New Zealand

INTRODUCTION

A balance of opportunities and risks

After the Mw7.8 14 November 2016 Kaikōura Earthquake time was of the essence in gathering data on the physical features that resulted. The bulk of fault ruptures in the Waiau region in North Canterbury following the Kaikōura Earthquake are situated in highly erodible marine siltstone. A wet autumn and winter and the everyday needs of the rural community resulted in rapid deterioration of field evidence, as locals worked to restore crucial lifelines (i.e. water supply, roads and fences), farm infrastructure (e.g. woolsheds, milking sheds) and livelihoods (e.g. ploughing fields for winter crops Fig 1a, reducing fault-scarp hazard to stock Fig 1b). Acquiring perishable data as quickly as possible is vital to understanding the complexities of fault rupture geometries and associated features, particularly with the multiple ruptures that characterised the Kaikōura Earthquake (e.g. Hamlin et al. 2017, Stirling et al. 2017).



Figure 1a (above): Before (left) and after (right) of a flattened out fault scarp on the Leader River terraces, ready for winter crop planting, Woodchester Station. In the before image, Duncan Noble from the UC Waiau fault rupture team surveys the scarp with GPS. Figure 1b (below): UC Science Outreach coordinator Tamsin Laird with landowner Rebekah Kelly (right) of Woodchester Station watching a digger flattening out one of the fault ruptures on her farm to reduce hazard to stock after workers repaired ruptured stock water supply lines. All images by the author.



It has been well established, however, that research pressure can pose significant risks to the local community following a hazard event. Interactions with community members can exacerbate stress, put additional pressure on scarce resources, and interfere with emergency operations (IAVCEI 1999; Citraningtyas 2010, Beaven et al. 2016).

In New Zealand, the physical science response to the 2010-2011 Canterbury Earthquake sequence was very much focused on science advice to emergency support organizations and decision makers. For example, scientists were meeting with the mayor and politicians on a daily, often hourly basis. This also included a very heavy demand from media for information and required a large team of people to service the many needs at the Emergency Centre while others were out gathering field data.

Additional research pressure specifically following the 22nd February 2011 Christchurch Earthquake (Beaven et al, 2016; Beaven et al, 2017) was such that in the initial days following the Kaikōura Earthquake the National Hazards



Research Platform distributed a 1 page guideline (New Zealand NHRP, 2016) for all research parties involved which set out guidelines for appropriate interactions with communities during a hazard event. In research response to the Kaikoura Earthquake sequence, our coordinating organization, the Institute of Geological and Nuclear Sciences Ltd. (GNS) disseminated these guidelines to all field teams.

NHRP (2016) outlines that “Decisions and actions should not benefit the decider/actor at the expense of others, increase harm to others, or violate human rights (Werhane 1999)”. Additionally, the “beneficence principle” as outlined in the NHRP guiding principles specifically requires that “research does no harm AND also provides benefits to those it directly impacts”.

Despite promotion of NHRP (2016) guiding principles, some instances were reported in relation to the Kaikōura Earthquake event where external research teams did not follow these guidelines, with a corresponding negative response from local community members and landowners.

DISCUSSION

Why should we put ethical principles into action?

While these principles are an important first official step, they are not enough in themselves; it’s necessary to go further to really generate win-win post-disaster research outcomes, which benefit researchers and local communities alike. Creating trusting and mutually respectful relationships with landowners and local communities is vital to the quality and effectiveness of data gathered, immediately after the event, but more importantly for ongoing access to facilitate further “in depth” research.

Our University of Canterbury (UC) fault rupture mapping team based our research in the Waiau region of North Canterbury, working outwards from the epicentral region of the earthquake, located in the alluvial plains and hill country near Waiau township. When our team first arrived into the area in the days following the event it became clear very quickly that the emergency focus was on the region of Kaikōura and that Waiau district residents were largely supporting themselves as a community. Many of our UC team (including the author) suffered our own stressful traumatic experiences and losses during the Canterbury Earthquake sequence 2010-2011 and aftermath, which certainly had a very conscious impact on our approach to locals, particularly as we often found ourselves in the role of first “science” responders. First and foremost, our initial task in the Waiau region was therefore to devote as much time as was needed in order to listen to their experiences and observations. This provided the additional benefit of landowners drawing our attention to some impacts on their properties away from the main rupture traces.

Because trusted relationships with landowners have been built, there is a real willingness on the part of the locals to assist our research team. Landowners have been very supportive of our research students undertaking projects

and have offered to vary some key farm practices so that we can gather perishable data, telling and showing us changes in their landscape that they (with their detailed knowledge and understanding of their land) have noticed, especially features that we as (“expert”) outsiders may have missed. At the fundamental level, without the landowners’ willingness to assist, we would have no ongoing access to the land in order to collect field data and ground truth remote sensing models.

On top of data gathering for our research, our UC team has been able to provide support to locals through a variety of platforms. As research got under way our role expanded into providing expert geological context and insight in relation to impacts on infrastructure in order to facilitate landowners’ negotiations with insurance, EQC and other relevant parties. Our presentations to local communities on why this event had happened have also been crucial in encouraging locals and scientists to discuss what they were going through and how it has affected them. Education about earthquakes as a process of plate tectonics, and how they could protect themselves, has been very well received by the community in helping them demystify the processes; one of the key sources of anxiety. There has been an overall sense of appreciation from the community as to how research can help benefit them in future by adding to engineering design solutions, hazard mitigation and disaster planning.

CONCLUSION

Following ethical guidelines during post-disaster reconnaissance facilitates engagement with the affected communities, which is the key to gathering high quality research data immediately after the event. Creating trusting and mutually respectful relationships is additionally vital to ongoing engagement to facilitate further “in depth” research in collaboration with communities for the benefit of all parties.

Acknowledgements: *A sincere thank you to those who offered their advice, support and edits towards this article – Sarah Beaven, Deirdre Hart, Tim Davies, and Jarg Pettinga. Thank you to my fellow Waiau UC fault rupture mapping team members. And lastly, and most of all, sincere thanks to all the landowners and local communities of the Waiau region, particularly Rebekah and Dave Kelly of Woodchester Station.*

REFERENCES

- Beaven, S., Wilson, T., Johnston, L., Johnston, D. and Smith, R. (2017) Role of Boundary Organization after a Disaster: New Zealand’s Natural Hazards Research Platform and the 2010-2011 Canterbury Earthquake Sequence. *Natural Hazards Review* 18(2).
- Beaven, S., Wilson, T., Johnston, L., Johnston, D. and Smith, R. (2016) Research engagement after disasters: Research coordination before, during, and after the 2011-2012 Canterbury Earthquake Sequence, New Zealand. *Earthquake Spectra* 32(2): 713-735.
- Citrangtyas, T., MacDonald, E., & Herrman, H. (2010). A Second Tsunami? The Ethics of Coming into Communities following Disaster. *Asian Bioethics Review*, 2(2), 108–123.



INQUA Focus Group Earthquake Geology and Seismic Hazards



paleoseismicity.org

- Di Capua G., Peppoloni S. and Bobrowsky P. (2016). Cape Town Statement on Geoethics. With the contributions of Bilham N., Bohle M., Clay A., Lopera E.H., Mogk D. IAPG - International Association for Promoting Geoethics. Online available: <http://www.geoethics.org/ctsg>.
- Hamling, I.J., Hreinsdóttir, S., Clark, K., Elliott, J., Liang, C., Fielding, E., Litchfield, N., Villamor, P., Wallace, L., Wright, T.J., D'Anastasio, E., Bannister, S., Burbidge, D., Denys, P., Gentle, P., Howarth, J., Mueller, C., Palmer, N., Pearson, C., Power, W., Barnes, P., Barrell, D.J.A., Van Dissen, R., Langridge, R., Little, T., Nicol, A., Pettinga, J., Rowland, J., Stirling, M., 2017. Complex multi-fault rupture during the 2016 Mw 7.8 Kaikōura earthquake, New Zealand. *Science*, DOI: 10.1126/science.aam7194 (2017).
- IAVCEI Subcommittee for Crisis Protocols (Newhall C, Aramaki S, Barberi F, Blong R, Calvache M, Cheminee J-L, Punongbayan R, Siebe C, Simkin T, Sparks RSJ, Tjetjep W) (1999) Professional conduct of scientists during volcanic crises. *Bull Volcanol* 60:323–334.
- New Zealand NHRP, Resilience to Nature's Challenge and Quakecore research programmes 18/11/2016
- Quarantelli, E.L. (1997) 'The Disaster Center field studies of organized behavior in the crisis time period of disasters', *International Journal of Mass Emergencies and Disasters*, 15(1), 47–69.
- Stallings, R.A. (2007) 'Methodological issues', in H. Rodríguez, E.L. Quarantelli & R.R. Dynes (eds.), *Handbook of disaster research*, pp. 55–83, Springer, New York.
- Stirling, M.W., N. J. Litchfield, P. Villamor, R. J. Van Dissen, A. Nicol, J. Pettinga, P. Barnes, R. M. Langridge, T. Little, D. J. A. Barrell, J. Mountjoy, W. F. Ries, J. Rowland, C. Fenton, I. Hamling, C. Asher, A. Barrier, A. Benson, A. Bischoff, J. Borella, R. Carne, U. A. Cochran, M. Cockroft, S. C. Cox, G. Duke, F. Fenton, C. Gasston, C. Grimshaw, D. Hale, B. Hall, K. X. Hao, A. Hatem, M. Hemphill-Haley, D. W. Heron, J. Howarth, Z. Juniper, T. Kane, J. Kearse, N. Khajavi, G. Lamarche, S. Lawson, B. Lukovic, C. Madugo, J. Manousakis, S. McColl, D. Noble, K. Pedley, K. Sauer, T. Stahl, D. T. Strong, D. B. Townsend, V. Toy, M. Villeneuve, A. Wandres, J. Williams, S. Woelz and R. Zinke (2017). THE MW7.8 2016 KAIKŌURA EARTHQUAKE: SURFACE FAULT RUPTURE AND SEISMIC HAZARD CONTEXT. *Bulletin of the New Zealand Society for Earthquake Engineering*, Vol. 50, No. 2.
- Werhane, P. H. (1991). Engineers and management: The challenge of the challenger incident. *Journal of Business Ethics*, 10(8), 605–616.



Holocene deformation events in the offshore Transverse Ranges (California, USA) constrained by new high-resolution geophysical data

Perea, Hector (1,2), Ucarukus, Gülsen (3), Driscoll, Neal (1), Kent, Graham (4), Levy, Yuval (5), Rockwell, Thomas (5)

- (1) Geosciences Research Division, Scripps Institution of Oceanography, 9500 Gilman Drive, University of California, San Diego, San Diego, California 92124, USA. hperea@ucsd.edu
- (2) Institut de Ciències del Mar, Consejo Superior de Investigaciones Científicas, Psg. Marítim de la Barceloneta, 37-49, 08003 Barcelona, Spain. hperea@icm.csic.es
- (3) Geological Engineering Department, Istanbul Technical University, Maslak, 34469 Istanbul, Turkey.
- (4) Nevada Seismological Laboratory/0174, University of Nevada, Reno, Reno, Nevada 89557, USA.
- (5) Department of Geological Sciences, San Diego State University, 5500 Campanile Drive, San Diego, California 92182, USA.

Abstract: *The Transverse Ranges (Southern California, USA) accommodate the contraction resulting from a regional restraining bend in the San Andreas Fault to form a fold-and-thrust belt system. The southern boundary of this system corresponds to the E-W trending Ventura basin, which is filled by more than 5 km of Pleistocene sediment and is shortening at about 7-10 mm/yr. Although the different thrusts and folds are fairly well known in the onshore areas of the basin, there is still uncertainty about their continuation in the offshore. The analysis of new high-resolution seismic data (chirp) and its combination with existing geophysical information has allowed us to map and characterize the active geological structures in the offshore. In addition, we have also identified 3 to 5 fold growth sequences associated with tectonic deformation events (e.g. earthquakes) in different thrust-related anticlines. This information may help us to determine the deformation history in the basin.*

Key words: *Active faults; Thrust and fold belt; Submarine paleoseismology; Fold growth sequences; Ventura Basin.*

The Sumatra 2004 and the Tohoku 2011 earthquakes and related tsunamis, which caused tens of thousands of deaths and extensive and severe damage, have shown the importance of studying and characterizing submarine faults to mitigate their hazard. In Southern California, the Transverse Ranges are characterized by the presence of E-W trending thrust faults and related anticlines that bound the Santa Barbara Channel and Ventura Basin (e.g., Sedlock and Hamilton, 1991; Yerkes et al., 1987). Although the different thrusts and folds are fairly well known in the onshore areas, there is still uncertainty about their continuation in the offshore. The aim of the present work is to better characterize the active geological structures in the offshore Ventura Basin by the analysis of new high-resolution and existing seismic data, making emphasis on the deformation history of the main thrust faults systems.

The Transverse Ranges zone has gone through different tectonic phases related to the evolution of the western Pacific-North America plate boundary during the last 25 Ma (e.g., Nicholson et al., 1994; Sedlock and Hamilton, 1991). Sometime during the last ca. 2-5 Ma the region started to go through a N-S compression resulting from the formation of a regional restraining bend in the San Andreas Fault to form an E-W trending *fold-and-thrust* belt system, the Transverse Ranges (e.g., Nicholson et al., 1994; Yerkes et al., 1987). The analysis of GPS data shows a north-south convergence across the Ventura Basin at 7–10 mm/yr (e.g., Marshall et al., 2013).

The western Transverse Ranges are crossed by the eastward striking Ventura sedimentary basins and its offshore extension, the Santa Barbara Channel (Fig. 1),

which are filled by more than 5 km of Pleistocene sediment (e.g., Huftile and Yeats, 1995; Rockwell et al., 2016; Yerkes et al., 1987). A series of folds and thrusts bound the basin. To the south, the main structure is the Oak Ridge anticline, which is associated with a reverse fault that dips to the south and continues towards the offshore and has an average slip rate of 5 mm/yr (e.g., Huftile and Yeats, 1995; Sorlien et al., 2000; Yerkes et al., 1987). To the north, there is a series of E-W anticlines verging south and associated with reverse faults dipping to the north. The main ones are the San Cayetano, the Pitas Point, the Ventura-Avenue anticline and the Red Mountain, which have average slip rates between 2 and 6 mm/yr (Hubbard et al., 2014; Huftile and Yeats, 1995; Rockwell, 1988; Yeats et al., 1987; Yerkes et al., 1987).

The analyzed high-resolution seismic dataset (Fig. 1) involved twenty-seven newly acquired profiles with the SIO chirp and mini-sparker and chirp profiles available from the USGS (Sliter et al., 2008). The SIO chirp profiles have decametric vertical resolution, 30-50 m of subbottom penetration and cover two different areas in the Santa Barbara Channel. In the area between Rincon Point and Santa Barbara, sixteen profiles were acquired beginning or ending close to the coastline and approximately perpendicular to it, with lengths between 5 and 10 km, and four perpendicular and crossing the previous ones to tie seismostratigraphic units across the area. Another five profiles were acquired close to the Pitas Point, all of which trend NW-SE and are each around 4.5 km in length. The USGS profiles have coarse resolution and are in some cases of poor quality. They were used to better correlate the main geologic structures and horizons along the basin.

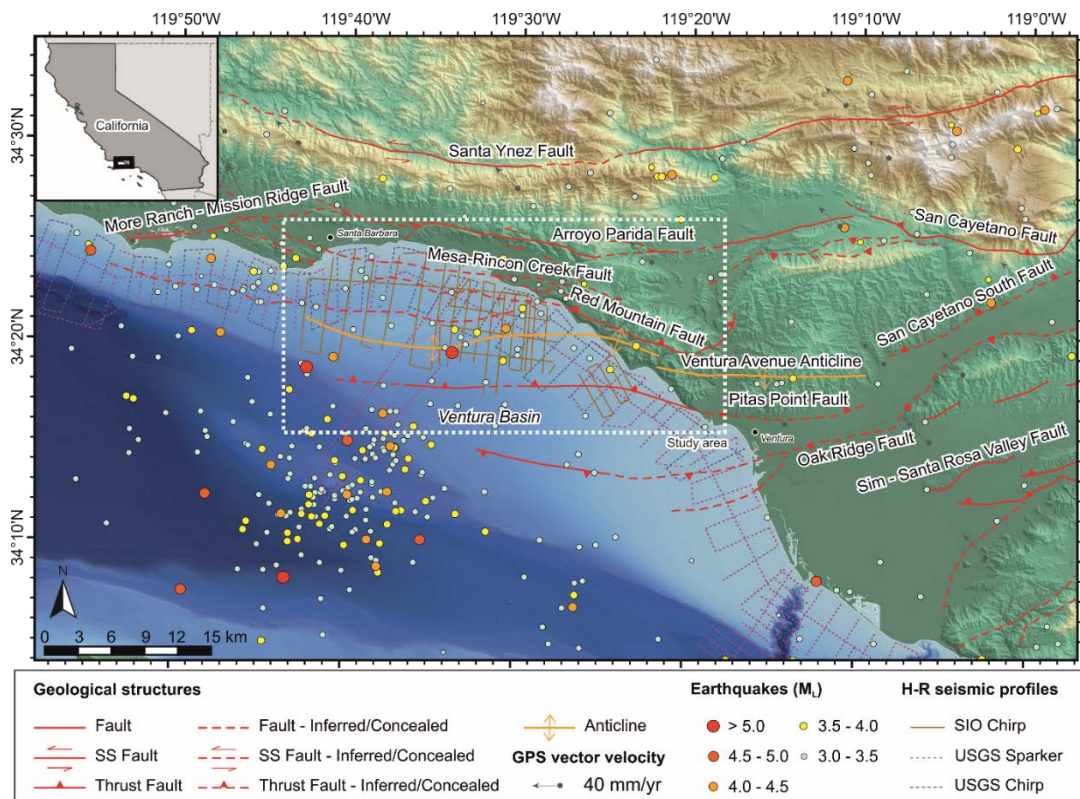


Figure 1: Map showing the relief model of the area around the Ventura basin showing the location of the different high-resolution seismic profiles used in this study, the main active faults in the area (Jennings and Bryant, 2010), the seismicity between 1933 and 2017 (Hutton et al., 2010) and the GPS vector velocities (UNAVCO). The white dotted rectangle localizes the study area. Inset: Location of the main map in the State of California (US).

In the SIO chirp profiles, we have identified two different seismostratigraphic units separated by a regional erosional unconformity, which corresponds to a transgressive surface (LGTS) associated to the Last Glacial Maximum and subsequent sea level rise. The LGTS developed over the Pleistocene units at 10-8 ka BP. This unconformity has been identified in almost all the seismic profiles, with the exception of those located close to Ventura, where the Holocene unit is thicker and the multiple is shallow. Usually, the unconformity corresponds to a reflector of high amplitude and low frequency that is rather continuous and planar. Nevertheless, in some regions, the LGTS has been apparently uplifted and folded. We interpret this deformation as probably related activity on blind thrust and backthrust faults. Below the LGTS, the Early to Late Pleistocene units are commonly not very well imaged. However, in different areas, we observe the presence of well-developed folds (anticlines and synclines) and high-angle dipping reflectors. In some places, these dipping reflectors produce irregularities on the LGTS that indicate that they correspond to hard sedimentary layers. These irregularities in the seafloor are also observed in places where the LGTS has been uplifted. Above the LGTS, there is the Holocene seismostratigraphic unit, which presents an irregular distribution and thickness. Usually, it is located in the lower zones of the basin and attains its maximum thickness close to Ventura. In some of the seismic profiles localized in the northern and central part of the basin, two different Holocene units have been

differentiated. The lower is a progradational unit characterized by downward dipping reflectors in the direction of progradation that show high amplitude and low frequency. Usually, these reflectors downlap over the LGTS but in some places they are parallel to it. On top of the progradational unit, there is an aggradational unit. It shows continuous and parallel reflectors with medium to high amplitude and high frequency.

Based on the identification and correlation of faults and folds (anticlines and synclines) affecting the Pleistocene units and the LGTS in the different profiles, we have been able to tie them to the main fault systems identified onshore, the Pitas Point, the Red Mountain and the Mesa Rincon Creek faults, and to the Ventura-Avenue anticline. Furthermore, we have interpreted different deformation events (i.e. earthquakes) related to some of these faults due to the recognition of anticline scarps, growth strata sequences, onlap unconformities and erosion surfaces in the Holocene strata (Fig. 2).

The Pitas Point fault clearly continues towards the west in the offshore. The fault is blind and shows a monocline geometry verging to the south (Fig. 3), and is mapped for approximately 18 km in our seismic data. Nevertheless, towards the west, this monocline becomes subtle and just deforms deeper Holocene reflectors. This may suggest either that the fault does not extend very far west into the basin, which contrasts with previous interpretations (e.g., Hubbard et al., 2014; Jennings and Bryant, 2010; Rockwell

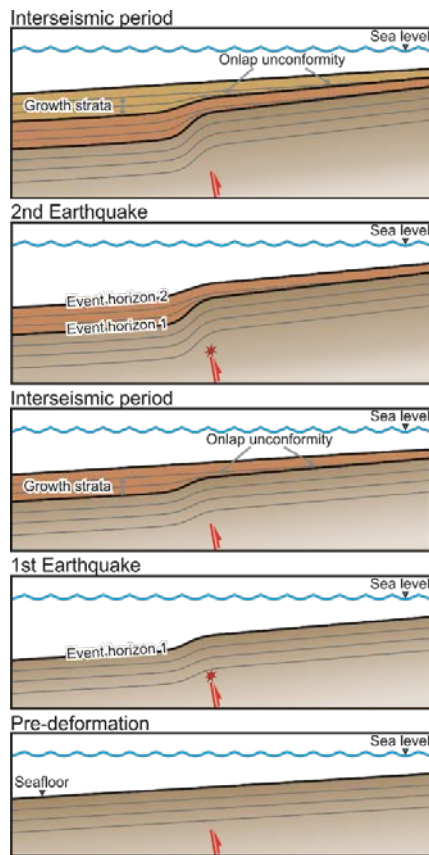


Figure 2: Sketch showing the formation of an anticline scarp related to a blind thrust fault due to the occurrence of different earthquakes and the later development of growth strata sequences and onlap unconformities during the interseismic period. The event horizon corresponds to the last reflectors/sediments folded by the earthquake and on which the upper reflectors/sediments onlap.

et al., 2016), or that the sedimentary rate during the Holocene has been much higher in the inner basin than the folding rate, softening the deformation. On the Pitas Point fault, we have found probable evidence of the three most recent Holocene events (Fig. 3). Events 1 and 2 are based on the observation of growth strata sequences in the downthrown block and onlap on the upthrown block. In the case of event 3 we have recognized onlaps on the upthrown block, but due to signal wipe out (gas) there is no evidence of growth strata, even though the unit may thicken towards the SE. Rockwell et al. (2016) analyzed the marine terraces in the Pitas Point found evidence for four large uplift events during the past 7000 yr. We have not found evidence for a fourth event in the seismic profiles. However, since we have not been able to identify the LGTS because it is either masked by the seismic multiple or by wipe out related to gas presence, we cannot discard an older event than those identified.

The Red Mountain fault. In the central part of the basin, there is an important uplift of the LGTS, between Rincon Point and Santa Barbara. We relate this deformation to a high amplitude anticline, which trends E-W in the western part of the basin and changes to NE-SW towards the East and to NNE-SSW close to Rincon Point. This large anticline

may be related to the main blind thrust dipping to the north and a shallower blind backthrust dipping to the south. Even though these observations point to this anticline being the offshore continuation of the Red-Mountain fault system, the different trends close to Rincon Point between various structures makes it difficult to establish their connection and a more detailed structural analysis of the area is needed. Based on similar observations on the seismic profiles than those made for the Pitas Point fault, and on the presence of different erosional surfaces, we have found evidence for four deformation events related to the southern flank of the anticline, even though evidence for one of them is weak. There is also evidence of the two younger events on the northern flank.

The Mesa-Rincon Creek fault that is mapped in the onshore areas has been correlated with a deformation zone (faults and folds) observed in the offshore between Carpinteria and Santa Barbara. Associated with this system, we have recognized an area where the LGTS dips strongly towards the north, just at the base of the shelf, providing a lot of space for sediment accumulation. We suggest that this area may correspond to a subsidence zone related to the loading produced by the emplacement of the Mesa-Rincon Creek thrust. The deformation associated with this fault system is revealed by the presence of different units that onlap ones towards the others due to a folding process. We have identified up to five different deformation events. However, close to Santa Barbara the LGTS is difficult to differentiate and, thus, we have not certainty whether the oldest of these events occurred during the Holocene or is older.

The Ventura-Avenue Anticline continues west in the offshore and gently folds the sediments above the LGTS. However, it seems that farther west, this anticline may have become inactive during the Holocene since it does not appear to deform the LGTS, even though the anticline is clearly identified in the Pleistocene units. We suggest that the Red Mountain fault has been the main structure absorbing the deformation in the area between Carpinteria and Santa Barbara during the Holocene since the observed lack of activity in the Ventura-Avenue Anticline occurs in the zone where it goes parallel and approaches the Red Mountain fault. In a profile west of Rincon Point, we have found evidence of at least three events above the LGTS related to the activity of the Ventura-Avenue Anticline. However, due to signal wipe out (gas) there is no evidence for a fourth event as reported from the onshore Holocene marine terraces (Rockwell et al., 2016).

The identification of different zones where the LGTS shows evidence of Holocene deformation in the new high-resolution SIO chirp profiles and their correlation between them and with the onshore structures allows mapping the offshore Holocene active structures between Santa Barbara and Ventura. Moreover, we have found evidence of 3 to 5 Holocene deformation events (i.e. earthquakes) associated with the main active systems. The identification

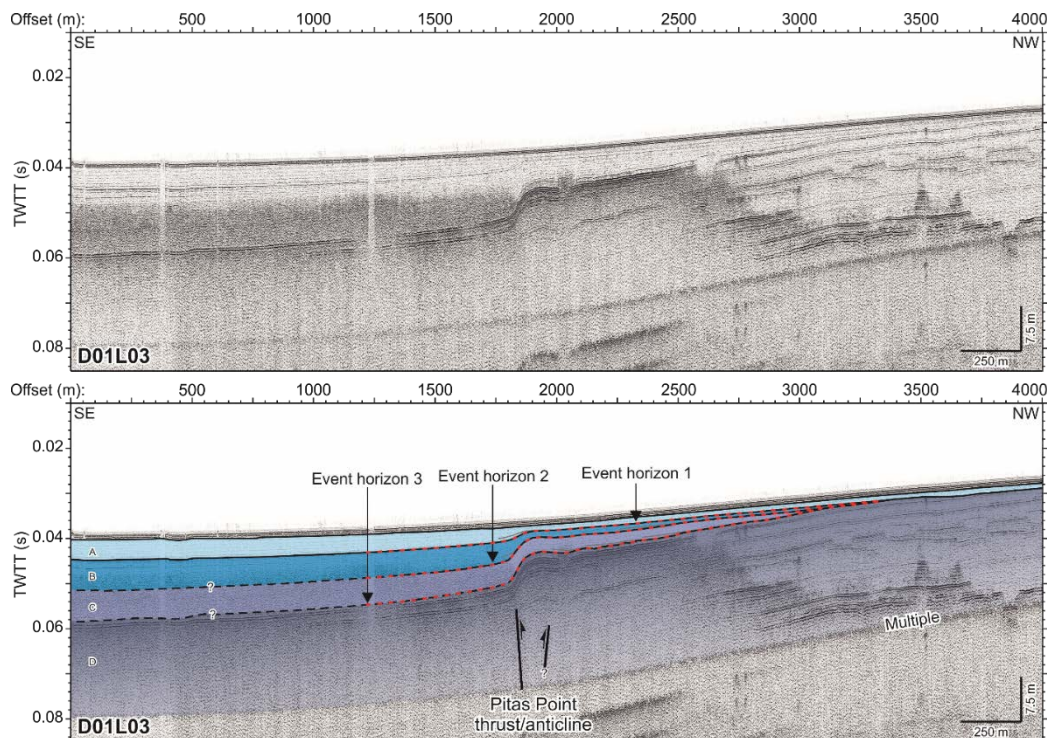


Figure 3: High-resolution SIO CHIRP profile acquired across the Pitias Point thrust fault close to the eastern margin of the study area and its interpretation. Letters A, B, C and D identify different seismostratigraphic units. The Last Glacial Transgressive Surface may be located some milliseconds below the multiple. Accordingly, these units may be Holocene in age. The black thick and dashed lines correspond to the boundary and inferred boundary between the different units. Red dashed lines identify the different horizon events identified in this profile. Above each of these horizons different onlap unconformities (gray lines) has been recognized, as well as growth strata sequences in units A and B. Each event horizon is associated with the occurrence of an earthquake.

of a similar number of events in the different systems could point to event triggering, where the occurrence of one event triggers the next one in close faults and close in time, or to the simultaneous rupture of all the segments during just one event. Both hypotheses have different implications for the seismic hazard in the area and to select between them it will be necessary to date the events.

Acknowledgments: This research has received funding from the SCEC (award #12026) and from the European Union's Horizon 2020 research and innovation programme under grant agreement No H2020-MSCA-IF-2014 657769.

REFERENCES

- Hubbard, J., Shaw, J.H., Dolan, J., Pratt, T.L., McAuliffe, L., Rockwell, T.K., 2014. Structure and Seismic Hazard of the Ventura Avenue Anticline and Ventura Fault, California: Prospect for Large, Multisegment Ruptures in the Western Transverse Ranges. *BSSA* 104, 1070–1087.
- Huftile, G.J., Yeats, R.S., 1995. Convergence rates across a displacement transfer zone in the western Transverse Ranges, Ventura basin, California. *JGR Solid Earth* 100, 2043–2067.
- Hutton, K., Woessner, J., Hauksson, E., 2010. Earthquake Monitoring in Southern California for Seventy-Seven Years (1932–2008). *BSSA* 100, 423–446.
- Jennings, C.W., Bryant, W.A., 2010. Fault activity map of California - Data Map No. 6 (map scale 1:750,000).
- Marshall, S.T., Funning, G.J., Owen, S.E., 2013. Fault slip rates and interseismic deformation in the western Transverse Ranges, California. *JGR Solid Earth* 118, 4511–4534.
- Nicholson, C., Sorlien, C.C., Atwater, T., Crowell, J.C., Luyendyk, B.P., 1994. Microplate capture, rotation of the western Transverse Ranges, and initiation of the San Andreas transform as a low-angle fault system. *Geology* 22, 491.
- Rockwell, T.K., 1988. Neotectonics of the San Cayetano fault, Transverse Ranges, California. *GSA Bull.* 100, 500–513.
- Rockwell, T.K., Clark, K., Gamble, L., Oskin, M.E., Haaker, E.C., Kennedy, G.L., 2016. Large Transverse Range Earthquakes Cause Coastal Uplift near Ventura, Southern California. *BSSA* 106, 2706–2720.
- Sedlock, R.L., Hamilton, D.H., 1991. Late Cenozoic tectonic evolution of southwestern California. *JGR* 96, 2325.
- Sliter, R.W., Triezenberg, P.J., Hart, P.E., Draut, A.E., Normark, W.R., Conrad, J.E., 2008. USGS Open-File Report 2008-1246: High-Resolution Chirp and Mini-Sparker Seismic-Reflection Data From the Southern California Continental Shelf—Gaviota to Mugu Canyon.
- Sorlien, C.C., Gratier, J.-P., Luyendyk, B.P., Hornafius, J.S., Hopps, T.E., 2000. Map restoration of folded and faulted late Cenozoic strata across the Oak Ridge fault, onshore and offshore Ventura basin, California. *GSA Bull.* 112, 1080–1090.
- Yeats, R.S., Lee, W.H.K., Yerkes, R.F., 1987. Geology and seismicity of the eastern Red Mountain fault, Ventura County, in: *Recent Reverse Faulting in the Transverse Ranges, California*. USGS Professional Paper 1339. pp. 161–168.
- Yerkes, R.F., Sarna-Wojcicki, A.M., Lajoie, K.R., 1987. Geology and Quaternary deformation of the Ventura area, in: *Recent Reverse Faulting in the Transverse Ranges, California*. USGS Professional Paper 1339. pp. 169–178.



Saalian earthquakes in the Ujście Basin, W Poland

Pisarska-Jamroży, Małgorzata (1), Van Loon, Antonius Johannes (Tom) (2, 3), Mleczak, Mateusz (1), and Roman, Małgorzata (4)

- (1) Institute of Geology, Adam Mickiewicz University, B. Krygowskiego Str. 12; 61-680 Poznań, POLAND; E-mail: pisanka@amu.edu.pl
(2) Geocom Consultants, Valle del Portet 17, 03726 Benitachell, SPAIN
(3) College of Earth Science and Engineering, Shandong University of Science and Technology, No. 579, Qianwangang Road, 266590 Qingdao, Huangdao District, CHINA
(4) Department of Geomorphology and Palaeogeography, University of Łódź, Narutowicza 88, 90-139 Łódź, POLAND

Abstract: A sand layer of 0.5 m thickness in the middle part of a sandy Saalian glaciolacustrine succession near Ujście (W Poland) contains two levels with abundant soft-sediment deformation structures (SSDS). The grain size of the deformed levels is the same as that of the under- and overlying undeformed layers: coarse silt and very fine-grained sand with admixtures of clay, commonly in the form of alternating laminae. The lateral extent of the levels with SSDS is significant: at least 350 m (the whole extent of the outcrop). The two SSDS levels are interbedded between sediments that do not show any significant SSDS. The occurrence of two deformed levels indicates that some deformation process was repeated. This suggests that the liquefaction required for the formation of these SSDS was most probably induced by a trigger that was repeated so quickly that no significant amount of sediment could accumulate in the meantime.

Key words: glacio-isostatic rebound, seismites, soft-sediment clasts, gravity-flow deposits, Pleistocene

INTRODUCTION

The study site (53°02'40"N and 16°41'41"E) is an active sand quarry, located 2 km SW from the town of Ujście (W Poland, Fig. 1). The succession at Ujście (Fig. 2) contains mainly silty sands, with intercalated beds of silty sand and gravelly sand. The succession under study is interpreted as glaciofluvial at its base, gradually changing into glaciolacustrine in its middle part and glacial (basal till) in its top part (Chmal, 2006). The glaciolacustrine sediments comprise two levels with abundant soft-sediment deformation structures (SSDS) that differ from common SSDS.

The objective of the present contribution is to identify the trigger mechanism responsible for the two levels with these enigmatic soft-sediment deformation structures.

THE SEDIMENTARY SUCCESSION

The lower part of the Ujście succession consists of horizontally-laminated sands (lithofacies Sh), at least 9 m thick (the base is not exposed), which contain a small admixture of silt. The laminae are slightly (2-4°) inclined southwards, south-westwards and westwards.

The middle part of the succession consists mainly of ripple-cross-laminated silty sands, sandy silts and silts (lithofacies SFr, FFr, Fr). Some horizontally laminated silty sands (lithofacies SFh) also occur. Two levels in this middle part are exceptional, because they are strongly deformed.

The upper part of the succession consists of a massive diamicton (lithofacies Dm) that represents a basal till from the Wartanian stadial of the Saalian glaciation (MIS 6).

THE DEFORMED LEVELS

A sand layer of 0.5 m thick in the middle part of the succession is exceptional because of three reasons: (1) it contains two levels with abundant soft-sediment deformation structures, a lower one (level SSDS-S1) and an upper one (SSDS-S2); (2) the grain size of the deformed levels is the same as that of the undeformed under- and overlying sands: coarse silt (31-63 μm) and very fine-grained sand (63-125 μm) with admixtures of clay (<3.9 μm), commonly in the form of alternating laminae; (3) the lateral extent of the levels with SSDS is significant: at least 350 m.



Figure 1: Location of the study area

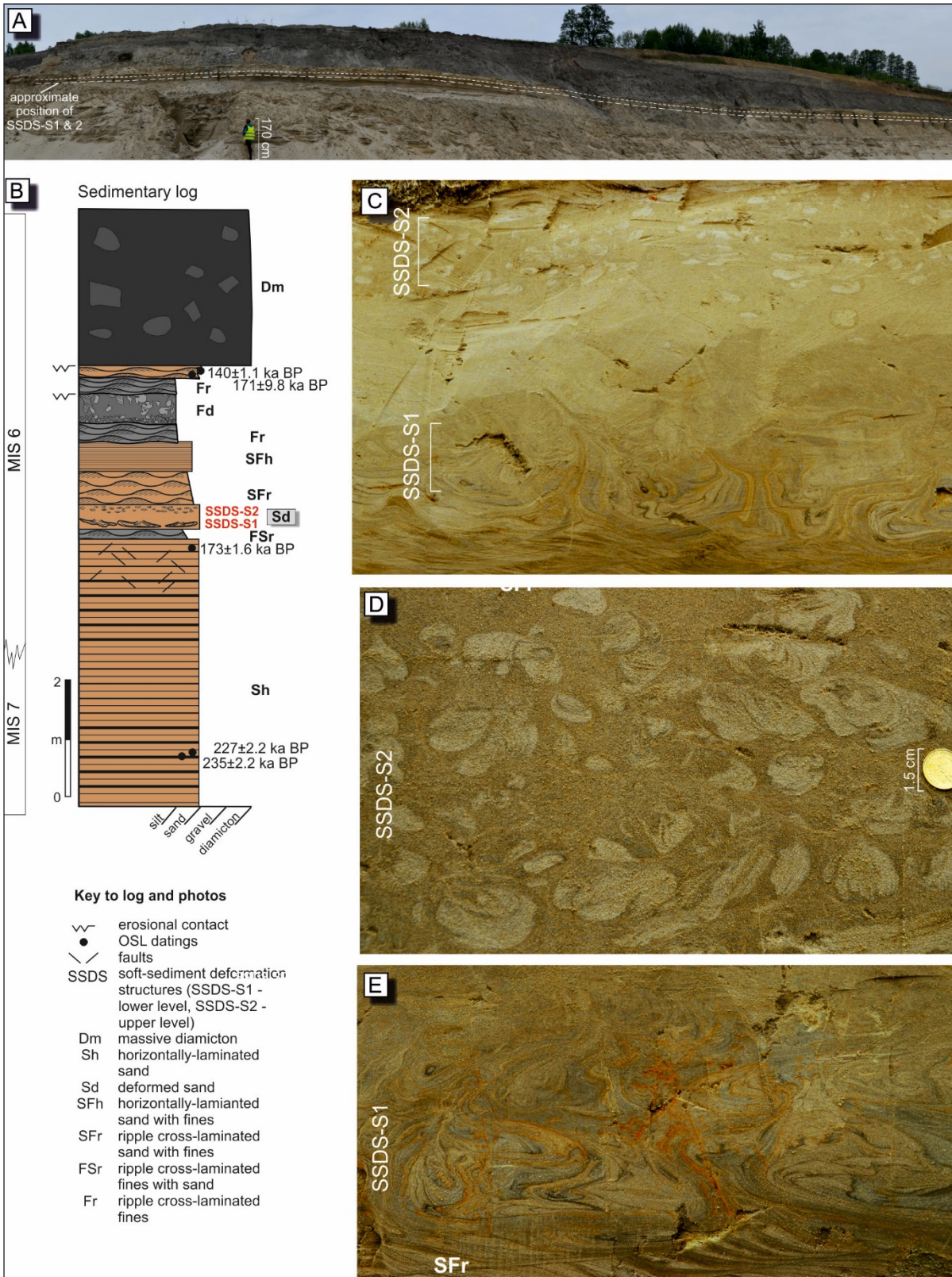


Figure 2: The sedimentary succession at Ujście. A.: Position of the two levels with SSDS. B: Sedimentary log with lithofacies. C: The two deformed levels: SSDS-S1 and SSDS-S2. D: Pseudonodules in SSDS-S2. E: Load and flame structures in the lower deformed level. Composite load casts indicating several phases of load casting.



Descriptions

The lower level (SSDS-S1)

The lower level, which is about 20 cm thick, is deformed over its total exposed length (Fig. 2). Most of the SSDS are complex, sometimes even chaotic; most of them are load casts and genetically related flame structures. Most load casts are 5–20 cm wide in cross-section, and they occur at several heights, commonly deforming each other. The flame structures are up to 7 cm high and 0.5–2 cm wide; they are frequently bent at their tops, sometimes to a more or less horizontal position. They consist of coarse silt with some very fine-grained sand and minor admixtures of clay; they are intruded into the host sediment that consists of sandy silt.

The upper level (SSDS-S2)

The upper deformed level, of which the thickness varies from 10 to 20 cm (Fig. 2), differs from the lower level because the deformations consist exclusively of pseudonodules. The kidney- and oval-shaped pseudonodules are composed mainly of sandy silt; they are 0.5–7 cm wide, and 0.5–3.5 cm high in cross-section.

Interpretation

The presence of two deformed levels (with different deformation characteristics) separated by an undeformed level with essentially identical granulometrical characteristics indicates that some deformation process acted at least twice. The presence of load casts that affect each other is additional evidence that several deformation phases must have taken place. This indicates that the liquefaction required for the origination of these SSDS was most probably induced by a trigger that was several times repeated so quickly after each other that no distinguishable amount of sediment could accumulate during the time-span in which repeated shocks occurred that caused new load casts to affect older ones.

TRIGGER MECHANISM

Owen (1992) and Moretti et al. (1999) showed experimentally that particularly load casts and associated structures (such as flame structures) are easily formed as a result of shocks such as those that are induced by earthquakes. This is understandable, as the seismically induced shock waves that are responsible for the development of SSDS in water-saturated, unconsolidated sediments in the uppermost decimetres of a sedimentary succession are Raleigh waves, which result in alternations of pressure and tension within the sediment, thus facilitating sinking of material into the underlying layer, even if there is hardly any difference in density (see Rossetti, 1999).

In the lower level (SSDS-S1), the flame structures that are bent to a more or less horizontal position indicate that the loading process continued (or started again) after earlier generations of load casts had formed. The final morphologies of the load structures consequently vary in size and shape. The tendency of the pseudonodules in the upper level to be concentrated at a specific level suggests

that this level, too, has been affected by several phases of loading. The overlying younger deposits are undeformed (see SFr lithofacies). Loading is facilitated by reversed density gradients, but the development of load casts can take place only if the layer under the parent layer of the load casts or pseudonodules becomes liquefied (Moretti & Ronchi, 2011). Liquefaction requires that the sediment involved is fully water-saturated, but it needs a trigger (Allen, 1982; Owen, 1987, 1995; Jones and Omoto, 2000). Seismically-induced liquefaction processes are commonly connected with seismic shocks with a magnitude of $M > 5$ (Ambraseys, 1988). The effects are mainly located within a maximum distance from the epicentre of 40 km (more than 90% of recent seismic events: Galli, 2000). Earthquakes with a lower magnitude ($M < 5$) may also trigger liquefaction, but only in an area closer to the epicentre, even < 20 km (Papadopoulos & Lefkopoulos, 1993).

In the case of the Ujście deposits, the nearest fault that may have become re-activated as a result of postglacial glacio-isostatic crustal rebound occurs at a distance of only 12 km (Fig. 3). The likely occurrence of earthquakes sheds also light on the possible trigger of the gravity flows that resulted in a breccia complex. Earthquake-induced shocks are well-known triggers of such flows, as can be deduced from both field data and experiments (e.g. Takahashi et al., 2014; Pouderoux et al., 2015; Chen et al., 2017).

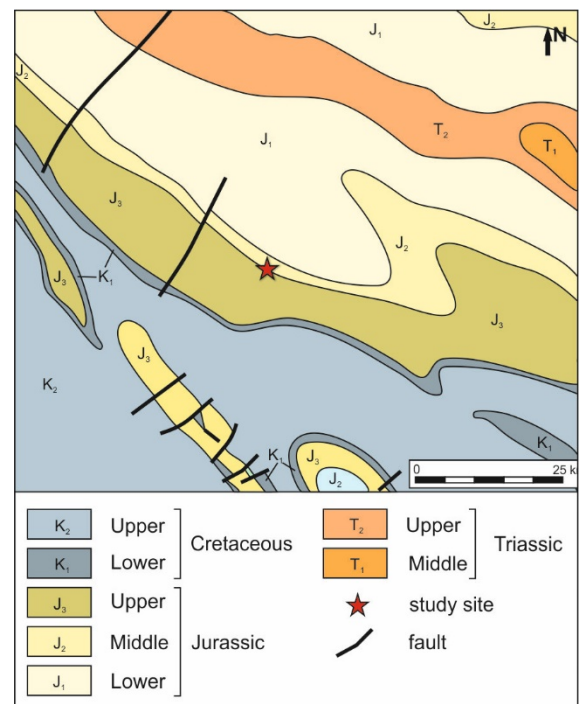


Figure 3: Pre-Paleogene map of the study site, showing faults in the Mesozoic, some of which may have been reactivated by Pleistocene post-glacial rebound of the earth crust.

The two deformed levels might consequently be considered as seismites, caused by successive earthquakes that were separated by a phase of quiet sedimentation. SSDS-1 must have been formed by several earthquakes that triggered seismic shocks so (geologically) quickly after



each other that no undisturbed sediments could accumulate in the meantime. Whether this also holds for SSDS-2 cannot be determined with sufficient certainty, but it cannot be excluded either. Comparable seismites of late Saalian age have been described earlier from NW Poland (Van Loon & Pisarska-Jamroży, 2014); late Weichselian seismites in Latvia have also been ascribed to postglacial glacio-isostatic rebound of the earth crust (Van Loon et al., 2016).

Acknowledgements: We thank Leszek Grochal and Janusz Hegyi from Ardagh Glass in Ujście for permission to carry out our sedimentological study in the Ujście quarry. We thank Dominika 385 Nowak for field assistance. Przemek Szymura performed the granulometric analyses, and Michał Jankowiak prepared the thin sections. The GREBAL project is financially supported by a grant from the National Science Centre, Poland (No. 2015/19/B/ST10/00661).

REFERENCES

- Allen, J.R.L., 1982. Sedimentary Structures: Their Character and Physical Basis. *Developments in Sedimentology* 30B, Elsevier (Amsterdam), 633 pp.
- Ambraseys, N., 1988. Engineering seismology. *Earthquake Engineering and Structural Dynamics* 17, 1–105.
- Chen, Y.-T., Su, C.C., Lu, Y.W. & Cheng, Y., 2017. Across-canyon movement of earthquake-induced sediment gravity flow offshore southwestern Taiwan. *Geophysical Research Abstracts* 19, EGU2017-5402.
- Chmal, R., 2006. Objasnienia do Szczegółowej Mapy Geologicznej w skali 1 : 50 000. Arkusz Piła [Explanations to the Detailed Geological Map of Poland, scale 1 : 50 000. Sheet Piła]. Polish Geological Institute, Warszawa. (in Polish).
- Galli, P., 2000. New empirical relationships between magnitude and distance for liquefaction. *Tectonophysics* 324, 169–187.
- Jones, A.P. & Omoto, K., 2000. Towards establishing criteria for identifying trigger mechanisms for soft-sediment deformation: a case study of Late Pleistocene lacustrine sands and clays, Onikobe and Nakayamadaira Basins, northeastern Japan. *Sedimentology* 47, 1211–1226.
- Moretti, M., Alfaro, P., Caselles, O. & Canas, J.A., 1999. Modelling seismites with a digital shaking table. *Tectonophysics* 304, 369–383.
- Moretti, M. & Ronchi, A., 2011. Liquefaction features interpreted as seismites in the Pleistocene fluvio-lacustrine deposits of the Neuquén Basin (northern Patagonia). *Sedimentary Geology* 235, 200–209.
- Owen, G., 1987. Deformation processes in unconsolidated sands. In: Jones, M.E. & Preston, R.M.F. (Eds.), *Deformation of Sediments and Sedimentary Rocks*. Geological Society Special Publications 29, pp. 11–24.
- Owen, G., 1992. A shaking table for experiments on soft-sediment deformation. *Journal of Sedimentary Petrology* 62, 733–734.
- Owen, G., 1995. Soft-sediment deformation in Upper Proterozoic sandstones (Applecross Formation) at Torridon, northwest Scotland. *Journal of Sedimentary Research* A65, 495–504.
- Papadopoulos, G.A. & Lefkopoulos, G., 1993. Magnitude-distance relation for liquefaction in soil from earthquakes. *Bulletin of the Seismological Society of America* 83, 925–938.
- Pouderoux, H., Proust, J.N. & Lamarche, G., 2015. On the use of deep-sea gravity-flow deposits to unravel seismic hazard: turbidite paleoseismology of the northern Hikurangi subduction margin of New Zealand. *Abstracts 15 Congrès Français de Sédimentologie (Chambéry, France)*, 340. Association des Sédimentologues Français.
- Reineck, H.E. & Singh, I.B., 1986. *Depositional Sedimentary Environments*. Springer-Verlag (Berlin, Heidelberg, New York), 551 pp.
- Rossetti, D.F., 1999. Soft-sediment deformation structures in late Albian to Cenomanian deposits, San Luis Basin, northern Brazil: evidence for paleoseismicity. *Sedimentology* 46, 1065–1081.
- Takahashi, H., Sassa, S. & Morikawa, Y., 2014. Centrifuge modelling of earthquake-induced submarine landslide and its gravity flow transition. In: Gaudin, C. & White, D. (Eds.), *Physical Modelling in Geotectonics*. Taylor & Francis Group (London), pp. 1009–1015.
- Van Loon, A.J. & Pisarska-Jamroży, M., 2014. Sedimentological evidence of Pleistocene earthquakes in NW Poland induced by glacio-isostatic rebound. *Sedimentary Geology* 300, 1–10.
- Van Loon, A.J., Pisarska-Jamroży, M., Nartišs, Krievāns, M. & Soms, J., 2016. Seismites resulting from high-frequency, high-magnitude earthquakes in Latvia caused by Late Glacial glacio-isostatic uplift. *Journal of Palaeogeography* 5, 363–380.



Anatomy of the 2016-2017 central Italy coseismic surface ruptures and their arrangement with respect to the foreseen active fault systems segmentation

Pucci, Stefano (1), Villani, Fabio (1), Civico, Riccardo (1), De Martini, Paolo Marco (1), Del Rio, Luca (2), Cinti, Francesca Romana (1), Pantosti, Daniela (1)

- (1) Istituto Nazionale di Geofisica e Vulcanologia, Italy. riccardo.civico@ingv.it.
 (2) Università degli Studi di Roma "La Sapienza", Italy.

Abstract: In 2016-2017 a series of moderate to large earthquakes struck central Italy producing severe damage and resulting in 299 casualties. The complex seismic sequence depicts a multiple activation of the Mt. Vettore-Mt. Bove (VBFS) and the Laga Mts. fault systems, considered in literature independent segments connoting a seismic gap between two recent seismic sequences: the 1997-1998 Colfiorito and the 2009 L'Aquila. We mapped in detail the normal-faulting coseismic surface ruptures following three mainshocks, for a total length of 5.2 km, ≈ 10 km and ≈ 25 km, respectively. We recorded with an unprecedented detail geometric and kinematic characteristics of the ruptures along the activated VBFS. Moreover, we built serial geologic cross-sections to reconstruct the net offset distribution of the activated fault system. Then, we compared the coseismic and the long-term geologic and morphologic expressions to: test a cause-effect relationship between faulting and tectonic landforms and evaluate "ex post" the segmentation hypothesis.

Key words: earthquake, coseismic ruptures, segment boundary, Apennines.

INTRODUCTION

Central Italy was recently hit by a seismic sequence causing 299 fatalities and >20,000 homeless, with widespread destruction affecting small towns like Amatrice, Visso and Norcia (Figure 1). The sequence initiated on 24 August 2016 with an Mw 6.0 earthquake that was followed by several M>5 shocks, like the 26 October Mw 5.9 event close to Visso, and culminated on 30 October with an Mw 6.5 earthquake located near Norcia. This is the strongest Italian seismic event since the 1980 M_s 6.9 Irpinia earthquake (Westaway and Jackson, 1987; Bernard and Zollo, 1989). On January 2017, other five M>5 earthquakes occurred at the southern part of the ca. 50 km-long activated crustal volume (Gruppo di Lavoro INGV sul Terremoto in centro Italia, 2017). This seismic sequence appears to fill the main seismic gaps of the central Apennines highlighted by geological and paleoseismological studies and located between the recent 1997 Colfiorito and 2009 L'Aquila events (Galadini and Galli, 2003; Boncio et al., 2004).

The study area has undergone a complex history of multi-phased contractional and extensional deformation: (1) pre-orogenic Jurassic extension, responsible for the fragmentation of the regional carbonate platform in deep pelagic basins and shallow-water structural highs separated by major tectonic structures (Ciarapica & Passeri, 2002; Butler et al., 2006); (2) late Miocene-early Pliocene NE-verging compression, which produced the fold-and-thrust belt (e.g. Barchi et al., 1998a; Vezzani et al., 2010); (3) post-orogenic, NE-directed late Pliocene-Quaternary extension, which dissected the axial zone of the belt and is responsible for the present-day seismogenic activity (Lavecchia et al., 1994; Barchi et al., 1998b; Cavinato and De Celles, 1999).

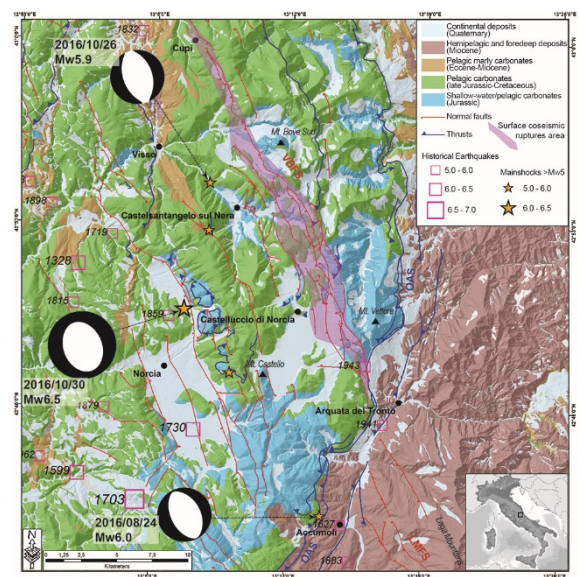


Figure 1: Geological map of the study area (modified from 1:10,000-scale cartography of Regione Umbria and Marche). TDMT focal mechanism of the mainshocks are reported (<http://cnt.rm.ingv.it/>).

In fact, seismological data indicate normal-faulting sources consistent with the current extensional regime affecting the chain axis (1.5-3 mm/yr extension rates; D'Agostino et al., 2014). The mainshocks nucleated at about 8-9 km depth on the deep portion of two important NW-trending and SW-dipping Quaternary normal fault-systems, namely the Mt. Vettore - Mt. Bove (VBFS) and the Laga Mts. (LMFS) faults. Based on geologic and paleoseismic evidence, those faults were previously considered active, 25-30 km-long seismogenic structures with an independent behavior, and separated by crustal-scale structural barriers (Boncio et al., 2004; Galadini and Messina, 2001; Galadini and Galli, 2003). However, the inversion models of geodetic and seismological



data of the mainshocks revealed an unexpected rupture complexity, being generated by both partial and quasi-simultaneous activation of different sections of the VBFS and LMFS, in some cases rupturing repeatedly the same location (Tinti et al., 2016; Cheloni et al., 2017). The 30 October Mw 6.5 Norcia earthquake, in particular, was unexpected due to its considerable size within the already activated portion of the VBFS, the exceptional high peak slip values inferred from inversion of strong motion and GPS data (up to 3 m), and the clear breaking of an asperity previously broken by the 24 August Amatrice earthquake.

The seismic sequence caused an impressive system of surface ruptures, rare for the Italian territory, running for a total length of about 30 km along the VBFS (Civico et al., 2017) (Figure 1).

The 24 August Mw 6.0 earthquake caused ~5.0 km-long, extensional coseismic ground breaks with centimeter-scale displacements along the southern section of the VBFS and no surface breakages were mapped on the LMFS segment (EMERGEO Working Group, 2016; Pucci et al., 2017).

The 26 October Mw 5.9 earthquake caused ~7.0 km-long, discontinuous extensional coseismic ground breaks with centimeter-scale displacements along the northern section of the VBFS (Civico et al., 2017).

The 30 October Mw 6.5 main shock produced coseismic surface ruptures extending for more than 25 km along several synthetic and antithetic fault splays of the VBFS.

This study examines the along-strike coseismic slip and slip vectors distribution observed in the context of the net geologic offsets and geomorphic expression of the disrupted slopes with respect to their depositional and erosive processes.

Our aim is to compare the coseismic surface ruptures with the long-term geologic and morphologic expressions to test a cause-effect relationship between faulting and tectonic landforms. This is to test the segmentation hypothesis by looking for evidence on the surface of a repeating pattern of complexity, possibly similar to that expressed by the 2016-

2017 seismic sequence, as well as to examine if the observed coseismic segmentation is due to permanent or non permanent rupture boundaries at geometrical and geological discontinuities along the fault system.

METHODS

As part of the EMERGEO Working Group of the Istituto Nazionale di Geofisica e Vulcanologia, we performed a detailed and extensive survey of the fault rupture. Comprehensive mapping of the extent and the geometric characteristics of the surface ruptures in this mountainous and difficult to access region was facilitated by oblique photographs (more than 11,000 digital images) and Structure-from-Motion (SfM) photogrammetry (Westoby et al., 2012), taken from helicopter flights. After the 30 October Mw 6.5 mainshock, thanks to the collaborative effort of the Open EMERGEO Working Group (Civico et al., 2017), we were able to collect >7,000 observation points, containing >5000 surface offset values: such numbers represent the event as one of the best documented cases of surface faulting earthquakes worldwide. We provide a thorough description of the surface ruptures in terms of geometry, structural architecture, displacement distribution and kinematics. In fact, we collected hundreds of kinematic indicators of coseismic slip, based on the offset morphologic markers and lineations on bedrock fault planes.

We expanded and complemented our analyses by constructing 1:10,000-scale geological longitudinal and cross-sections through the VBFS (Figures 2 and 18, respectively) based on updated maps (Regione Umbria - geo.umbriaterritorio.it/umbriageo/atlante/; Regione Marche - www.ambiente.marche.it/Territorio; Centamore et al., 1992; Pierantoni et al., 2013) and we reconstructed the net offset distribution of the activated fault system, as a result of the contribution of the different parallel fault splays (Figure 2).

Furthermore, we plotted the cumulative morphologic throws along the activated fault splays by means of 10m-resolution DEM (Tarquini et al., 2007) and, locally, by high-resolution DEMs obtained through Structure-from-Motion photogrammetry.

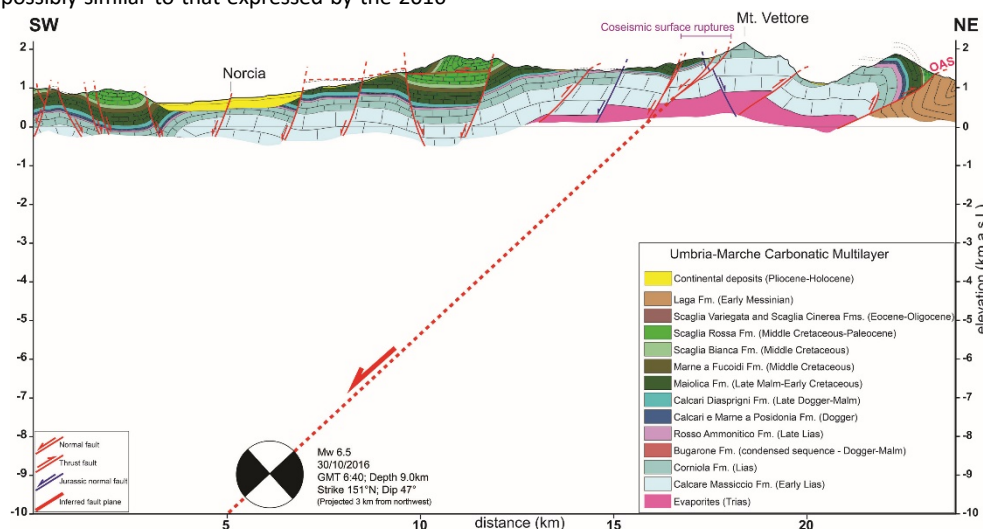


Figure 2: Example of geological cross-section. TDMT focal mechanism of the Mw 6.5 mainshock and inferred deep fault plane are reported.



DISCUSSION

Notably, the 30 October coseismic surface ruptures re-ruptured completely the southern section of the VBFS that ruptured during the 24 August earthquake and partly re-ruptured the northern section of the VBFS that ruptured during the 26 October earthquake (Figure 3).

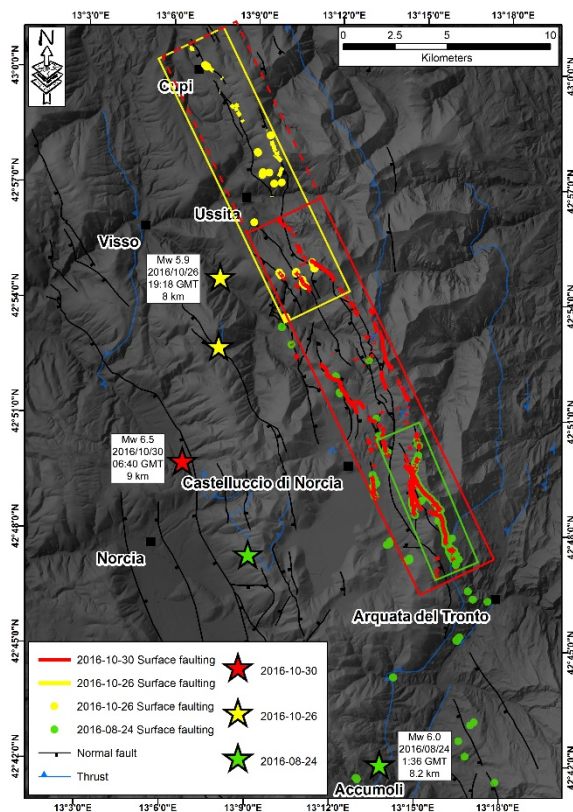


Figure 3: Map of the surface faulting distribution for earthquakes in the 2016 sequence.

The surface ruptures trend with an average N155° strike and consistent kinematics, with mainly SW-side-down motion along the base of a preexisting, SW dipping active normal faults, which exhibit a long-term geomorphologic and geologic expressions (e.g.: ~20m high Quaternary fault scarp and >500 m of net offset, respectively, along the Cordone del Vettore fault, at the southern termination of the VBFS). In some cases, the coseismic slip occurred on small variably-oriented fault planes, inherited from the Jurassic extensional phase. Kinematic indicators of coseismic slip point out a consistent almost pure dip-slip kinematics of the fault blocks, with a subtle component of left-lateral slip on the SW-dipping planes, and subordinate right-lateral movement on the antithetic NE-dipping ruptures. Also, the direction of the coseismic slip vectors are comparable with that of the exhumed normal fault strands, showing stepping relationships and several underlapping regions. The width of the overall near-fault coseismic deformation zone widens in the central and southernmost sectors of the VBFS, being ~3.5 km in the Mt. Porche sector, and ~2.5 km in the Castelluccio sector. We found a complex slip distribution of the 30 October ruptures, with an average value of about 0.3 m and a ~2 km-long zone

of concentrated vertical displacement >1 m, displaying local throw exceeding 2.3 m along the Cordone del Vettore fault, coincident with the 24 August throw maxima.

In general, the 30 October event dominates the coseismic slip distribution sum of the three events (i.e. the average net displacement is four times that of both the 24 August and of the 26 October events). As a whole, it describes an asymmetric bell-shaped curve, with a larger slip gradient along the southern section of the VBFS.

The surface slip heterogeneity displays a remarkable similarity with the complex slip distribution inferred from kinematic inversion of strong motion data, thus suggesting a link between deep slip patches and local surface slip peaks. In fact, the overlapping 30 October and 24 August near-fault surface coseismic displacements differ by one order of magnitude, consistent with the estimates of slip from the seismological data.

The distribution of the aggregate long-term displacement observed by means of the geologic cross-sections along the main Quaternary splays helps to constrain the geometry of the complex VBFS, characterized by an asymmetric bell-shaped curve of the $d-x$ profile (i.e. displacement-length) which displays some similarity with the coseismic one, but distinct from the LMFS segment.

The asymmetric $d-x$ profile is discussed in terms of possible interaction between the VBFS and LMFS and/or presence of a major crustal structural complexity inherited from the previous tectonic phases (i.e. the Olevano-Antrdoco-Sibillini thrust - OAS) may hamper lateral fault growth while favoring growth only by slip accumulation producing a displacement gradient that increases at the fault system tip (Peacock & Sanderson, 1996; Peacock, 2002). This comparison relates the slip events to finite displacement on faults and corroborates the existing models for the long term accumulation of displacement on faults.

We then provide a reconstruction of the 2016 rupture pattern, both at surface and depth, as representative of the VBFS behavior, and a discussion on the fault system boundaries persistence as well as on the significance of the repeated surface faulting at the same location.

Acknowledgements: We thank the Italian Civil Protection Department for the logistics and funding. We are grateful to Corpo Nazionale dei Vigili del Fuoco (National Fire Corps) and Corpo Forestale dello Stato (State Forestry Corp) for the support on the aerial surveys; we also thank Corpo Nazionale Soccorso Alpino e Speleologico (Mountain rescue) for the logistic support.

REFERENCES

- Barchi, M., DeFeyter, A., Magnani, B., Minelli, G., Piali, G., & Sotera, B., 1998a. The structural style of the Umbria-Marche fold and thrust belt. *Memorie della Società Geologica Italiana* 52, 557-578.
- Barchi, M., DeFeyter, A., Magnani, M., Minelli, G., Piali, G., & Sotera, B., 1998b. Extensional tectonics in the Northern Apennines (Italy): evidence from the CROP03 deep seismic reflection line. *Memorie della Società Geologica Italiana* 52, 528-538.



- Bernard, P., & Zollo A., 1989. The Irpinia (Italy) 1980 earthquake: Detailed analysis of a complex normal faulting. *J. Geophys. Res.* 94(B2), 1631–1647, doi: 10.1029/JB094iB02p01631.
- Boncio, P., Lavecchia, G., & Pace, B., 2004. Defining a model of 3D seismogenic sources for Seismic Hazard Assessment applications: the case of central Apennines (Italy). *Journal of Seismology* 8(3), 407-425.
- Butler, R. W., Tavarnelli, E., & Grasso, M., 2006. Structural inheritance in mountain belts: an Alpine–Apennine perspective. *Journal of Structural Geology* 28(11), 1893-1908.
- Cavinato, G. P., & De Celles, P. G., 1999. Extensional basins in the tectonically bimodal central Apennines fold-thrust belt, Italy: response to corner flow above a subducting slab in retrograde motion. *Geology* 27 (10), 955-958.
- Centamore, E., Adamoli L., Berti D., Bigi S., Casnedi R., Cantalamessa G., Fumanti F., Morelli C., Micarelli A., Micarelli A., Ridolfi M., Salvucci R., Chiochini M., Mancinelli A., & Potetti M., 1992. Carta geologica dei bacini della Laga e del Cellino e dei rilievi carbonatici circostanti in: *Studi Geologici Camerti, Vol. Spec* (Università degli Studi, Dipartimento di Scienze della Terra eds). SELCA, Firenze.
- Cheloni, D., De Novellis, V., Albano, M., Antonioli, A., Anzidei, M., Atzori, S., Avallone, A., Bignami, C., Bonano, M., Calcaterra, S., et al., 2017. Geodetic model of the 2016 Central Italy earthquake sequence inferred from InSAR and GPS data. *Geophys. Res. Lett.* 44, 6778–6787. doi: 10.1002/2017GL073580.
- Ciarapica, G., & Passeri, L., 2002. The palaeogeographic duality of the Apennines. *Bollettino della Società Geologica Italiana* 121 (1), 67-75.
- Civico R., Pucci S., Villani F., Pizzimenti L., De Martini P.M., Nappi R. & the Open EMERGEO Working Group, 2017. Surface ruptures following the 30 October 2016 Mw 6.5 Norcia earthquake, central Italy, *Journal of Maps*, submitted.
- D’Agostino, N., 2014. Complete seismic release of tectonic strain and earthquake recurrence in the Apennines (Italy). *Geophys. Res. Lett.* 41, 1155–1162, doi: 10.1002/2014GL059230.
- EMERGEO, W. G., Pucci, S., De Martini, P. M., Civico, R., Nappi, R., Ricci, T., Villani, F., Brunori, C.A., Caciagli, M., Sapia, V., Cinti, F.R., et al., 2016. Coseismic effects of the 2016 Amatrice seismic sequence: first geological results. *Annals of Geophysics* 59, doi: 10.4401/ag-7195.
- Galadini, F., & Messina, P., 2001. Plio-Quaternary changes of the normal fault architecture in the central Apennines (Italy). *Geodinamica Acta* 14(6), 321-344.
- Galadini, F., & Galli, P., 2003. Paleoseismology of silent faults in the Central Apennines (Italy): the Mt. Vettore and Laga Mts. faults. *Annals of Geophysics* 46 (5), 815-836.
- Gruppo di Lavoro INGV sul Terremoto in centro Italia, 2017. Relazione sullo stato delle conoscenze sulla sequenza sismica in centro Italia 2016-2017 (aggiornamento al 2 febbraio 2017) (Istituto Nazionale di Geofisica eds). Roma, Italy, doi: 10.5281/zenodo.267984
- Lavecchia, G., Brozzetti, F., Barchi, M.R., Keller, J.V.A., & Menichetti, M., 1994. Seismotectonic zoning in east-central Italy deduced from the analysis of the Neogene to present deformations and related stress fields. *Geological Society of America Bulletin* 106, 1107-1120.
- Peacock, D. C. P., 2002. Propagation, interaction and linkage in normal fault systems. *Earth-Science Reviews* 58 (1), 121-142.
- Peacock, D. C. P., & Sanderson, D. J., 1996. Effects of propagation rate on displacement variations along faults. *Journal of Structural Geology* 18 (2-3), 311-320.
- Pierantoni, P., Deiana, G., & Galdenzi, S., 2013. Stratigraphic and structural features of the Sibillini mountains (Umbria-Marche Apennines, Italy). *Italian Journal of Geosciences* 132 (3), 497-520.
- Pucci, S., De Martini, P. M., Civico, R., Villani, F., Nappi, R., Ricci, T., Brunori, C. A., Caciagli, M., Cinti, F. R., Sapia, V., De Ritis, R., Mazzarini, F., Tarquini, S., Gaudiosi, G., Nave, R., Alessio, G., Smedile, A., Alfonsi, L., Cucci, L., & Pantosti, D., 2017. Coseismic ruptures of the 24 August 2016, Mw 6.0 Amatrice earthquake (central Italy). *Geophys. Res. Lett.* 44, 2138–2147, doi:10.1002/2016GL071859.
- Tarquini, S., Isola, I., Favalli, M., Mazzarini, F., Bisson, M., Pareschi, M. T., & Boschi, E., 2007. Tinality/01: A new triangular irregular network of Italy. *Annals of Geophysics* 50, 407–425. doi: 10.4401/ag-4424.
- Tinti, E., Scognamiglio, L., Michelini, A., & Cocco, M., 2016. Slip heterogeneity and directivity of the ML 6.0, 2016, Amatrice earthquake estimated with rapid finite-fault inversion. *Geophys. Res. Lett.* 43, 10745–10752, doi: 10.1002/2016GL071263.
- Vezzani, L., Festa, A., & Ghisetti, F. C., 2010. Geology and tectonic evolution of the Central-Southern Apennines, Italy. *Geological Society of America Special Papers* 469, 1-58.
- Westaway, R., & Jackson, J., 1987. The earthquake of the 1980 November 23 in Campania-Basilicata (southern Italy). *Geophys. J. Int.* 90 (2), 375-443. doi: 10.1111/j.1365-246X.1987.tb00733.x.
- Westoby, M.J., Brasington, J., Glasser, N.F., Hambrey, M.J., & Reynolds, J.M., 2012. ‘Structure-from-Motion’ photogrammetry: A low-cost, effective tool for geoscience applications. *Geomorphology* 179, 300-314, doi: 10.1016/j.geomorph.2012.08.021.



Multi-fault earthquakes with kinematic and geometric rupture complexity: how common?

Quigley, Mark (1,2), Mohammadi, Hiwa (1), Jiménez, Abigail (3) Duffy, Brendan (1)

(1) School of Earth Sciences, The University of Melbourne, Parkville VIC 3010, Australia

(2) Department of Geological Sciences, University of Canterbury, New Zealand

(3) Departamento de Química y Física, Universidad de Almería, Carretera de Sacramento s/n, Almería, Spain

Abstract: We examine 257 finite-fault rupture models for 135 moment magnitude (M_w) 4.1 to 8.1 continental earthquakes to estimate how many source faults ruptured in each earthquake. We use fault geometries and rupture kinematic criteria to estimate fault populations. The minimum observed M_w for multi-fault rupture is 6.0. Approximately ~37% of the 135 earthquakes investigated were sourced from multi-fault ruptures. Upper-bounds and variance of fault rupture populations increase with increasing M_w . Fault rupture populations show no dependency on strain rate or proximity to plate boundaries. Coulomb stress modelling provides useful insights into why many earthquakes exhibit complex multi-fault rupture characteristics, and how this influences earthquake M_w maximum estimations and shapes of earthquake frequency-magnitude distributions. The 2016 M_w 7.8 Kaikoura earthquake is amongst the most complex multi-fault earthquakes ever recorded.

Key words: multi-fault earthquakes, rupture complexity, earthquake catalogues

INTRODUCTION

Many continental earthquakes, including the 2016 M_w 7.8 Kaikoura and 2010 M_w 7.1 Darfield earthquakes, are sourced from the concurrent rupture of multiple faults with different orientations, rupture kinematics, and source M_w contributions (e.g., Hamling et al., 2017; Beavan et al., 2012). Here we ask, *how globally common are multi-fault earthquake ruptures, and why do they occur?*

To address these questions, we must first distinguish a “single earthquake” emanating from a spatiotemporally defined source from multiple earthquakes separated in time and / or space. Temporal gaps in seismic moment release rate exceeding 20 seconds are interpreted as distinct earthquakes (≤ 20 second gaps are interpreted as a single earthquake). Fault ruptures with the most proximal subsurface rupture termini exceeding 10 km apart are classified as distinct earthquakes (≤ 10 km gaps are interpreted as a single earthquake source). These criteria allow us to distinguish a defined multi-fault earthquake from multiple fault ruptures (multiple earthquakes) with intervening non-rupturing periods indicated by moment release rate gaps that may be 10s of seconds or hours apart, such as the 1986 Tennant Creek (Bowman 1992) and 2010-2011 Canterbury earthquake sequences (Quigley et al., 2016) and (ii) dynamically-triggered earthquakes on distal fault systems that occur quasi-instantaneously with the mainshock but that are not structurally or kinematically linked to the mainshock source fault(s) (Nissen et al., 2016).

We define a distinct “fault” using two different sets of criteria that incorporate structural and kinematic components of the rupture source. A *geometrically distinct* fault deviates at its termini by ≥ 20 degrees in strike and / or ≥ 20 degrees in dip from the termini of its nearest neighbouring faults. A *kinematically distinct* fault is

distinguished by abrupt changes of ≥ 30 degrees in the slip vector (rake and / or azimuth) from neighbouring faults. We also count the number of distinct slip patches (i.e., asperities) with minimum slip values ≥ 1 m that taper outwards to encircling low slip domains in the source models, although we do not explicitly consider these in the fault population analyses presented herein

We first downloaded 197 seismic source models for 92 different earthquakes from the SRCmod Catalogue (<http://equake-rc.info/SRCMOD/>) (Mai and Thingbaijam, 2014) from June 1 to August 1, 2017. All original publication sources were consulted to confirm the reliability of the source models in the database. A further 60 source models for 43 different earthquakes were obtained using Google Scholar and Scopus searches for “earthquake source model” over the same time interval. Earthquake dates are between April 1906 and June 2017 and corresponding source models were published between 1982 and 2017. For earthquakes where multiple source models and fault populations exist, we selected a preferred model based on the perceived quality and quantity of data used to derive the source model. Models were typically given the higher preference if they included InSAR, GPS and near-source seismicity data (e.g., strong ground motion data) that allowed rupture complexity to be investigated in higher fidelity than models where teleseismic data was the primary input. Our dataset should be viewed as preliminary; we are continuously searching for missing events and additional source models to gain further clarity on this topic.

DISCUSSION

Reported fault populations for individual earthquakes and for the overall catalogue typically exceed fault populations that can be distinguished kinematically and geometrically (Figure 1). The upper-bound for the number of reported faults in the catalogue seems to increase with increasing



year of publication (Figure 2). This could relate to the emergence and increasing utility of new technologies (e.g., InSAR) that enabled multi-fault earthquake ruptures to be better identified, or it could relate to changes in the abundance of multi-fault earthquakes. The first use of InSAR to identify fault ruptures (Massonnet et al., 1993 – not pictured in Figure 2) led to increasing utility of this technique; many post-2000 multi-fault earthquake models in the catalogue were developed using InSAR (Figure 2). The low relative abundance of $M_w > 7$ earthquakes in the early (pre-2000) part of the catalogue (Figure 3) prohibits us from directly evaluating whether the apparent increase in upper bounds of fault populations reflects the increasing population of large earthquakes for which rupture models were published, and / or an increased occurrence of multi-fault earthquakes.

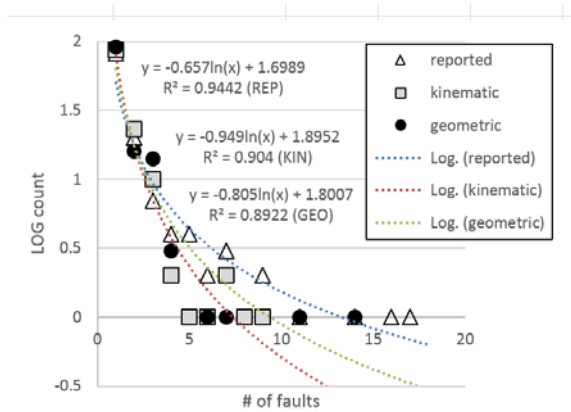


Figure 1: Number of distinct faults (LOG count of preferred value) for 128 earthquakes as reported in literature (REP), distinguished kinematically (KIN), and distinguished geometrically (GEO).

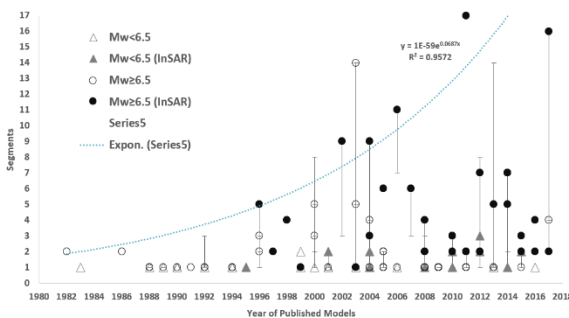


Figure 2: Number of reported faults ('segments') versus published year of preferred source model. Dotted line denotes exponential fit through six earthquakes with largest segment populations.

The smallest M_w multi-fault earthquake based on either kinematic or geometric criteria is 6.0 (Figure 4,5). This could reflect a reduced ability to resolve multi-fault earthquake ruptures at lower M_w and/or an increased likelihood that lower M_w earthquakes are confined to single fault sources. The upper range of fault populations increases with increasing M_w (Figures 4,5). Approximately 37% of the 135 earthquakes investigated were sourced from multi-fault ruptures. The number of earthquake source faults does not correlate clearly with strain rate (Figure 6) or distance from plate boundary (Figure 7).

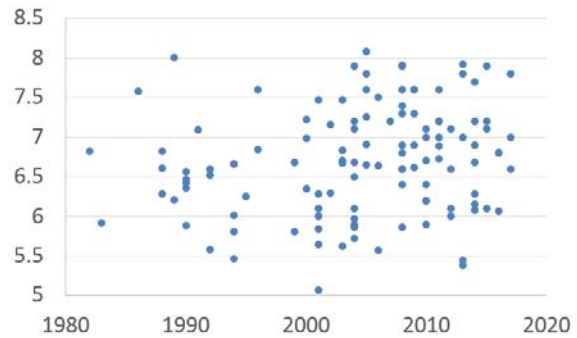


Figure 3: Earthquake M_w (y axis) versus publication year of preferred source model (x axis).

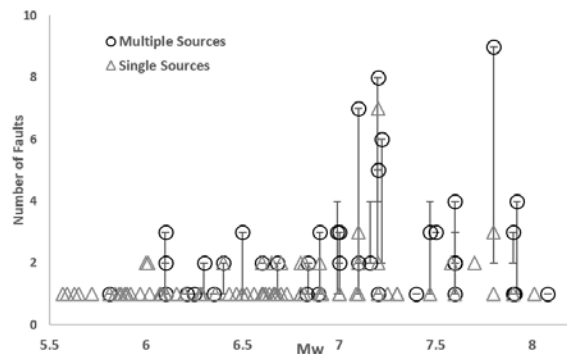


Figure 4: Kinematically-distinguished fault populations versus earthquake M_w .

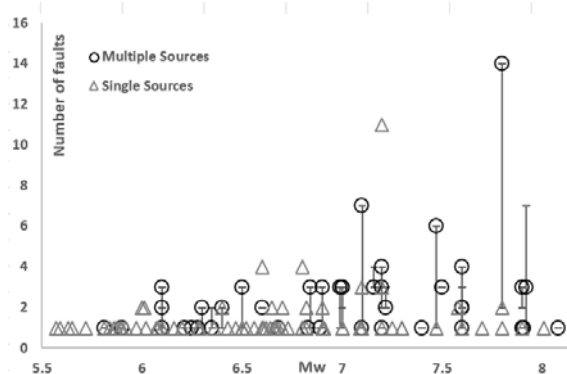


Figure 5: Geometrically-distinguished fault populations versus earthquake M_w .

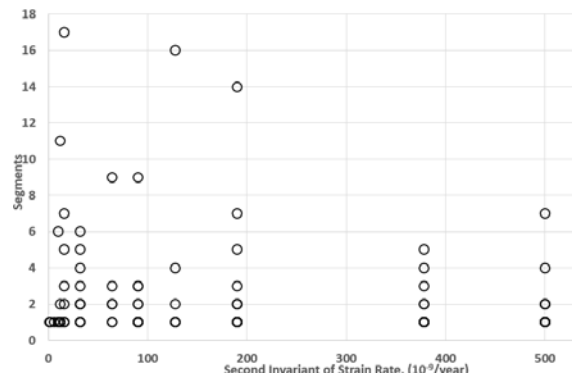


Figure 6: Strain rate versus reported fault segments

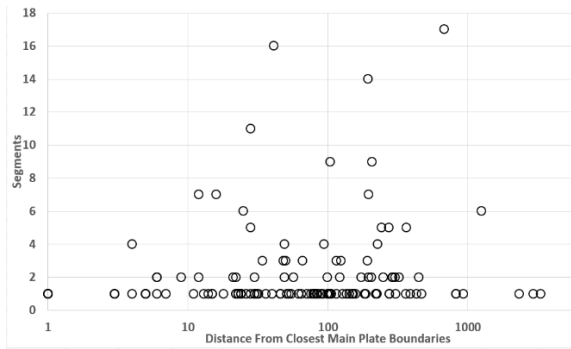


Figure 7: Distance from plate boundary versus reported fault segments.

Our Coulomb stress modelling (Figure 8) of the source faults for the Darfield earthquake (from Beavan et al., 2012) reveals one reason why multi-fault earthquakes are common; static stress changes exerted on receiver faults following mainshock rupture (top panel) exceed rupture triggering thresholds, and these ruptures in turn trigger rupture on other adjacent faults (bottom panel), encouraging the rupture to cascade across the network.

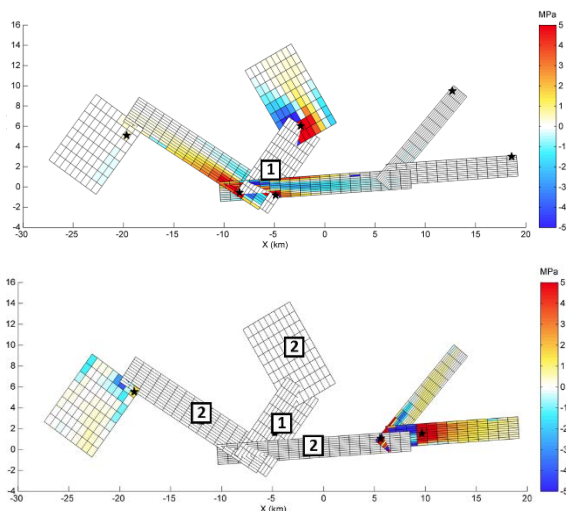


Figure 8: Coulomb stress modelling of the Darfield earthquake. Fault (1) denotes hypocentral source fault rupture. Faults (2) are receiver faults that rupture immediately after fault (1) due to imposed static stresses. Combined ruptures of (1) and (2) cause large positive static stress changes on the remaining faults, enabling rupture spreading across the entire fault network.

Multi-fault earthquakes result in an amalgamated M_w that exceeds the M_w of any contributing individual source fault (Figure 9). The maximum M_w of the fault system similarly exceeds the maximum M_w of any one contributing source. The shape of the Gutenberg-Richter frequency- M_w distribution is strongly influenced by multi-fault earthquakes. If the G-R b value derived from fits to lower M_w events is projected to higher magnitudes, the multi-fault earthquake scenario results in lower-than-expected M_w populations in the M_w ranges of the individual source faults, whereas the source de-aggregated M_w overpopulates this M_w range.

The 2016 M_w 7.8 Kaikoura earthquake is perhaps the most kinematically and geometrically complex earthquake ever recorded (Hamling et al., 2017). However, aspects of this earthquake such as the ~25 km gap between adjacent ruptures (Kaiser et al., 2017) and possible dynamic triggering (Hollinsworth et al., 2017) raise complications on how this earthquake should be divided into distinct events with different fault populations. This remains a focus of further research. Other complex multi-fault earthquakes include the 2010 M_w 7.1 El Mayor-Cucupah, 2010 M_w 7.1 Darfield, 1997 M_w 7.2 Zirkuh (East Iran), and 1992 M_w 7.2 Landers earthquakes.

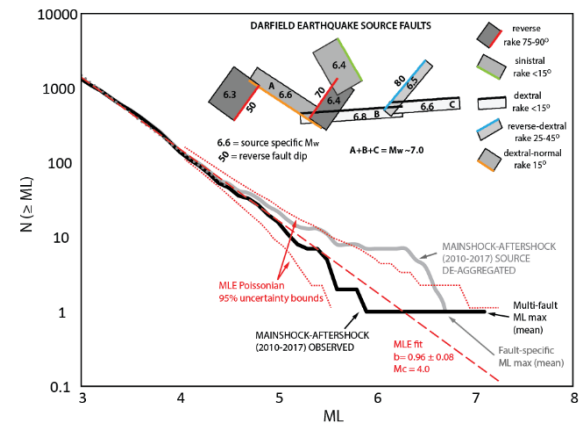


Figure 9: Geometrically-distinguished fault populations versus earthquake M_w .

REFERENCES

- Bowman, J. R., 1992. The 1988 Tennant Creek, Northern Territory, earthquakes: A synthesis. *Australian Journal of Earth Sciences*, 39(5), 651-669.
- Hamling, I.J., and 28 others, 2017. Complex multifault rupture during the 2016 M_w 7.8 Kaikōura earthquake, New Zealand. *Science*, 356(6334), p.eaam7194.
- Hollinsworth, J., Ye, L., & Avouac, J. P., 2017. Dynamically triggered slip on a splay fault in the M_w 7.8, 2016 Kaikōura (New Zealand) earthquake. *Geophysical Research Letters*, 44(8), 3517-3525.
- Kaiser, A., and 23 others, 2017. The 2016 Kaikōura, New Zealand, Earthquake: Preliminary Seismological Report. *Seismological Research Letters*, 88(3), 727-739.
- Mai, P.M. and Thingbaijam, K.K.S., 2014. SRCMOD: An online database of finite-fault rupture models. *Seismological Research Letters*, 85(6), pp.1348-1357.
- Massonnet, D., Rossi, M., Carmona, C., Adragna, F., Peltzer, G., Feigl, K. and Rabaute, T., 1993. The displacement field of the Landers earthquake mapped by radar interferometry. *Nature*, 364(6433), pp.138-142.
- Nissen, E. K., Elliott, J. R., R. A. Sloan, T. J. Craig, G. J. Funning, A. Hutko, B. E. Parsons & T. J. Wright, 2016. Dynamic triggering of an earthquake doublet exposes limitations to rupture forecasting. *Nature Geoscience*, doi:10.1038/NGEO2653
- Quigley, M.C., Hughes, M.W., Bradley, B.A., van Ballegooy, S., Reid, C., Morgenroth, J., Horton, T., Duffy, B. and Pettinga, J.R., 2016. The 2010–2011 Canterbury earthquake sequence: Environmental effects, seismic triggering thresholds and geologic legacy. *Tectonophysics*, 672, pp.228-274.



Surface rupture of the 1933 M 7.5 Diexi earthquake in eastern Tibet: implications for seismogenic tectonics

Junjie Ren (1), Xiwei Xu (2), Shimin Zhang (1), Robert S. Yeats (3), Jiawei Chen (1), Ailan Zhu (4), Shao Liu (5)

- (1) Key Laboratory of Crustal Dynamics, Institute of Crustal Dynamics, China Earthquake Administration, Beijing 100085, China
Email: renjunjie@gmail.com.
- (2) National Center for Active Fault Studies, Institute of Geology, China Earthquake Administration, Beijing 100029, China
- (3) College of Earth, Ocean, and Atmospheric Sciences, Oregon State University, Corvallis, OR 97331, USA
- (4) Shanghai Earthquake Administration, Shanghai 201203, China
- (5) Sichuan Earthquake Administration, Chengdu 610044, China

Abstract: The 1933 M 7.5 Diexi earthquake is another catastrophic event with the loss of over 10,000 lives in eastern Tibet, comparable to the 2008 Wenchuan Mw 7.9 earthquake. Because of its unknown surface rupture, the seismogenic tectonics of the 1933 earthquake remains controversial. We collected unpublished reports, literature, and old photos associated with the 1933 earthquake, and conducted field investigations based on high-resolution imagery. Combined with paleoseismological analysis, radiocarbon dating, and relocated earthquakes, our results demonstrate that the source of the 1933 earthquake is the northwest-trending Songpinggou fault. This quake produced a > 30 km long normal-fault surface rupture with the coseismic maximum offset of ~1.6-1.7 m, suggesting a moment magnitude (Mw) ~6.8. The Songpinggou fault has an average vertical slip rate of ~0.27 mm/yr, and may obey a characteristic slip model with a recurrence interval of ~6700 yrs. The normal surface rupture probably formed in response to the growth of the reactivated Mesozoic anticlines above the deep-seated Songpinggou blind reverse faults. We infer that the reactivated Mesozoic structures between the strike-slip and boundary faults may also take a role in strain partitioning of eastern Tibet. This study contributes to a larger understanding of tectonics of large earthquakes in a compressional setting and strain partitioning in eastern Tibet.

Key words: Tip- left. Diexi earthquake, surface rupture, eastern Tibet, Minjiang fault, Songpinggou fault

Large earthquakes can provide insights for understanding transformation from elastic strain accumulation to permanent tectonic deformation in the deforming crust (Klinger et al., 2006; Lin et al., 2016). The resultant surface rupture gives direct evidence to deformation pattern, movement state, and faulting process (Fletcher et al., 2014; Jayangondaperumal et al., 2017). Therefore, the investigation of surface rupture is one of the priorities when a large earthquake occurs (Xu et al., 2009).

The Tibetan Plateau is one of the most tectonically active regions in the world. The rapid, ongoing collision between the Indian and Eurasian plates has resulted in the eastward extrusion of the Plateau (Molnar and Tapponnier, 1975; Peltzer and Saucier, 1996; Tapponnier and Molnar, 1977; Zhang et al., 2004), and generated the uplift of eastern Tibet, characterized by strong tectonic compression and amounts of reverse faults and folds, accompanied by high seismicity (Burchfiel et al., 1995; Hubbard and Shaw, 2009) (Figure 1). Especially, the 2008 Wenchuan earthquake (Mw 7.9) ruptured this area and caused the loss of many thousands of lives and large property damage. This quake produced a ~300-km long surface rupture along the Longmen Shan fault zone, a northeast-trending thrust with a right-lateral component (Xu et al., 2009; Zhang et al., 2010). The 1933 Diexi M 7.5 earthquake is another catastrophic 20th century event with the loss of over 10,000 lives in eastern Tibet (China Earthquake Administration, 1999). It destroyed Diexi Town, an important ancient town in western Sichuan Province; the

resultant huge landslides blocked the Minjiang River and formed several dammed lakes along the upper reach of Minjiang trunk stream and its main tributary, the Songpinggou River, in the epicentral area. Two months later, the breakout of dammed lakes killed at least 2,500 from the Maoxian, Wenchuan, to Guanxian (Dujiangyan) counties along the middle and lower reaches of the Minjiang River (Tang et al., 1983).

However, the 1933 Diexi earthquake occurred during the Chinese Civil War. The society was so chaotic that no detailed field investigation took place. It remains a matter of debate over the source of this earthquake. Different scholars and institutes gave different isoseismal contours trending east-west (Chang, 1938), northwest (Tang et al., 1983), and north-south (China Earthquake Administration, 1999) that resulted in three different interpretations for the causative fault of the 1933 earthquake: the east-west-trending normal Canling Mountain, the northwest-trending left-lateral Songpinggou, and the north-south Minjiang faults. Because the Minjiang fault is close to the epicenter, it has been considered to be the most likely candidate (Chen et al., 1994) and has been used in numerous models of seismic hazard analysis (e.g. Wang et al., 2010).

However, due to a lack of surface rupture along the Minjiang fault, Zhang et al. (2016) proposed a buried north-south-striking west-dipping ramp-type thrust at a depth of ~10-15 km beneath the Minjiang River. Although focal mechanisms of this earthquake appear to support strike slip



on the Minjiang fault, a lack of local seismic stations result in such poor constraints of fault plane solution that similar data, by two different institutes, produced opposite senses of strike slip (Wang and Shen, 2011) (Figure 2). With the current dearth of direct geologic evidence; finding the surface rupture of the 1933 Diexi earthquake is the key to its source fault and seismogenic tectonics.

In this study, we collected all of the available literature and photos related to the 1933 Diexi earthquake and conducted extensive field investigations based on the imagery. We found fault exposures from some road cuts and a fault scarp on alluvial landforms along the Songpinggou River, to verify the existence of the Songpinggou fault (Figure 2). Real Time Kinematic (RTK) GPS and drone photography with the resolution of several centimeters are used to survey the offsets. Radiocarbon dating is used to constrain the age of the displaced units. Combined with relocated earthquakes around the epicentral area, we then discuss the relationship of the Songpinggou fault and the 1933 Diexi earthquake, as well as its tectonic implications in eastern Tibet. This study contributes to an understanding of seismogenic tectonics of large earthquakes in a transpressional setting in eastern Tibet.

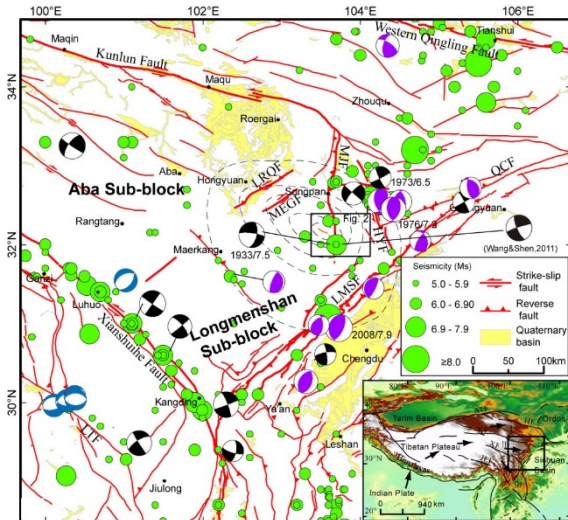


Figure 1: Active faults and seismicity in eastern Tibet. Seismic data include instrumentally recorded earthquakes (China Earthquake Networks Center, <http://www.csnmc.ac.cn>) and historical catalogue (China Earthquake Administration 1999a; b). Fault data are adapted after Xu et al. (2009) and Ren et al. (2013a). Focal mechanism data are from Global CMT Catalog (<http://www.globalcmt.org>): Blue- normal, black – strike-slip, and purple- reverse. Date lines are isoseismal data adapted from Tang et al. (1983). Inset map shows major boundary faults and blocks of the Tibetan Plateau. Black arrows indicate block motion direction according to GPS data (Gan et al. 2007). I, Qaidam-Qilian block; II, Bayan Har block; III, Sichuan-Yunnan block. Abbreviations for active faults: ATF, Altyn Tagh fault; HF, Haiyuan fault; HYF, Huya fault; JLF, Jiali fault; KF, Kunlun fault; LMSF, Longmen Shan fault; LRQF, Longriqiu fault; LTF, Litang fault; MEGF, Maoergai fault; MJF, Minjiang fault; QCF, Qingchuan fault; RF, Red River fault.

Based on the obtained data and field observations and radiocarbon dating, we made the following paleoseismic conclusions: (1) The source of the 1933 M7.5 Diexi earthquake is the northwest-trending Songpinggou fault. It

generated an > 30 km long normal-faulting surface rupture with the maximum coseismic offset of ~1.6-1.7 m. Its moment magnitude (M_w) would be ~6.8, with a vertical slip rate of ~0.25 mm/yr and may obey a characteristic slip model with a recurrence interval of ~6700 yrs. (2) The normal-faulting Songpinggou rupture in the 1933 Diexi earthquake probably formed in response to the growth of the reactivated Mesozoic anticlines above the deep-seated Songpinggou blind reverse faults. (3) Large numbers of Mesozoic structural zones between the strike-slip and boundary faults may take a role in strain partitioning of eastern Tibet.

Acknowledgements: This work was jointly supported by the Public Service Funds for Earthquake Studies (201408023), National Science Foundation of China (41572193), Institute of Crustal Dynamics, China Earthquake Administration Research Fund (ZDJ2017-24). I am grateful to an anonymous reviewer for detailed comments.

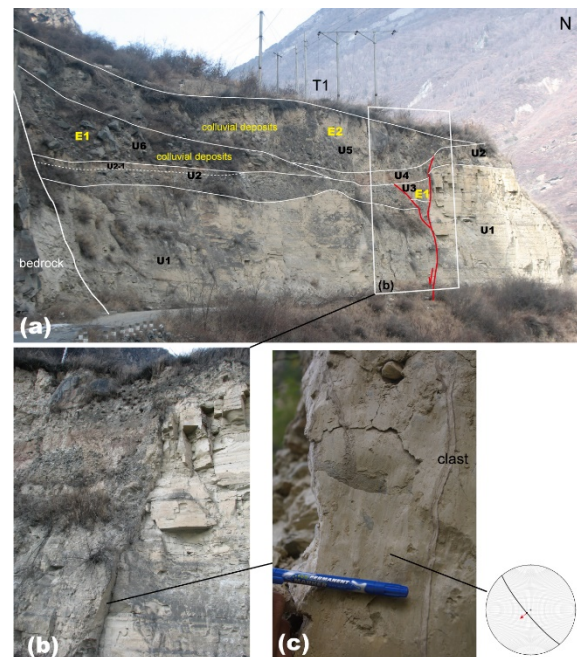


Figure 2. Displaced terrace with the base of the lake deposits in a road cut west of Diexi Lake. Photo (a) shows displaced alluvial gravel. E1, E2, colluvium. Photo (b) indicates smooth fault plane. Photo (c) is the striations on the fault plane and clasts in the fault zone, showing normal slip. The structural datum is plotted by using Rick Allmendinger's Faultkin program.

REFERENCES

- Silva, P.G., Rodríguez-Pascua, M.A., Pérez-López, R., Giner-Robles, J.L., Lario, J., Bardaji, T., Goy, J.L., & Zazo, C., 2009. Geological and archaeological record of the 1504 AD Carmona earthquake (Guadalquivir Basin, South Spain): a review after Bonsor, 1918. In: *Archaeoseismology and Palaeoseismology in the Alpine-Himalayan Collisional Zone* (Pérez-López, R., Grützner, C., Lario, J., Reicherter, K., Silva, P.G. eds). Baelo Claudia, Spain, 139-142.
- Hinzen, K.-G., Schreiber, S., & Yerli, B., 2010. The Lycian Sarcophagus of Arttumpara, Pinara (Turkey) -Testing Seismogenic and Anthropogenic Damage Scenarios. *Bulletin of the Seismological Society of America* 100 (6), 3148-3164.



- Nur, A., & Burgess, D., 2008. *Apocalypse: Earthquakes, Archaeology and the Wrath of God*. Princeton University Press. Princeton and Oxford. 309 p.
- Stiros, S., 1988b. Archaeology, a tool to study active tectonics – The Aegean as a case study. *Eos, Transactions, American Geophysical Union* 13, 1636-1639.
- Burchfiel, B., Zhiliang, C., Yupinc, L., Royden, L., 1995. Tectonics of the Longmen Shan and adjacent regions, central China. *International Geology Review*, 37(8): 661-735.
- Chang, L., 1938. Investigation report on Diexi earthquake of Sichuan. *Geological Review*, 3(3): 251-291.
- Chen, S.F., Wilson, C., Deng, Q.D., Zhao, X.L., Zhi, L.L., 1994. Active faulting and block movement associated with large earthquakes in the Min Shan and Longmen Mountains, northeastern Tibetan Plateau. *Journal of Geophysical Research: Solid Earth*, 99(B12): 24025-24038.
- China Earthquake Administration, 1999. *Recent Earthquake catalog of China (1912-1990, Ms≥4.7)* (in Chinese). Chinese Sciences and Technology Press, Beijing.
- Fletcher, J.M. et al., 2014. Assembly of a large earthquake from a complex fault system: Surface rupture kinematics of the 4 April 2010 El Mayor–Cucapah (Mexico) Mw 7.2 earthquake. *Geosphere*, 10(4): 797-827.
- Hubbard, J., Shaw, J.H., 2009. Uplift of the Longmen Shan and Tibetan plateau, and the 2008 Wenchuan (M = 7.9) earthquake. *Nature*, 458(7235): 194-197.
- Jayangondaperumal, R. et al., 2017. Great earthquake surface ruptures along backthrust of the Janauri anticline, NW Himalaya. *Journal of Asian Earth Sciences*, 133: 89-101.
- Klinger, Y., Michel, R., King, G., 2006. Evidence for an earthquake barrier model from Mw~ 7.8 Kokoxili (Tibet) earthquake slip-distribution. *Earth and Planetary Science Letters*, 242(3): 354-364.
- Lin, A. et al., 2016. Coseismic rupturing stopped by Aso volcano during the 2016 Mw 7.1 Kumamoto earthquake, Japan. *Science*, 354(6314): 869-874.
- Molnar, P., Tapponnier, P., 1975. Cenozoic tectonics of Asia: effects of a continental collision. *Science*, 189(4201): 419-426.
- Peltzer, G., Saucier, F., 1996. Present-day kinematics of Asia derived from geologic fault rates. *J. Geophys. Res.*, 101(B12): 27943-27956.
- Tang, R., Liu, S., Jiang, N., 1983. *The 1933 Diexi Earthquake* (in Chinese). Sichuan Scientific and Technological Press, Chengdu, 69 pp.
- Tapponnier, P., Molnar, P., 1977. Active faulting and tectonics in China. *Journal of Geophysical Research*, 82(20): 2905-2930.
- Wang, H., Liu, M., Shen, X., Liu, J., 2010. Balance of seismic moment in the Songpan-Ganze region, eastern Tibet: Implications for the 2008 Great Wenchuan earthquake. *Tectonophysics*, 491(1): 154-164.
- Wang, K., Shen, Z., 2011. Location and focal mechanism of the 1933 Diexi earthquake and its associated regional tectonics. *Acta seismologica sinica*, 33(5): 557-567 (in Chinese).
- Xu, X. et al., 2009. Coseismic reverse-and oblique-slip surface faulting generated by the 2008 Mw 7.9 Wenchuan earthquake, China. *Geology*, 37(6): 515-518.
- Zhang, P. et al., 2004. Continuous deformation of the Tibetan Plateau from global positioning system data. *Geology*, 32(9): 809-812.
- Zhang, P., Wen, X., Shen, Z.K., Chen, J., 2010. Oblique, high-angle, listric-reverse faulting and associated development of strain: The Wenchuan earthquake of May 12, 2008, Sichuan, China. *Annu. Rev. Earth Planet. Sci.*, 38: 353-382.
- Zhang, Y., Li, J., Li, H., Li, J., 2016. Reinvestigation on Seismogenic Structure of the 1933 Diexi Ms 7.5 Earthquake, Eastern Margin of the Xizang(Tibetan) Plateau. *Geological Review*, 62(2): 267-276.



The Green Lake landslide and its implications for earthquake hazard in the southern South Island

Robinson, Thomas (1), Davies, Tim (2)

(1) Department of Geography, Durham University, Durham, UK. tom.robinson@durham.ac.uk

(2) Department of Geological Sciences, University of Canterbury, Christchurch, NZ.

Abstract: The Green Lake landslide in southern Fiordland is one of the largest on Earth and is thought to have been seismically-triggered by shaking of at least MM 9. It has previously been assumed that this landslide resulted from an earthquake on the Alpine Fault, which produces $M_w \sim 8.0$ earthquakes every ~ 300 years. However, New Zealand-specific attenuation relationships suggest that such an earthquake is unable to produce sufficiently strong shaking at Green Lake. Thus, the Green Lake landslide was either triggered by a different earthquake, by weaker shaking, or was not seismically-triggered. Here, we show that the only plausible scenario capable of generating MM 9 shaking at Green Lake is an $M_w \sim 7.5$ earthquake on the nearby Hauroko Fault. The activity of this fault is relatively unknown and such an earthquake would cause MM 9 shaking in Te Anau and MM 8 in Tuatapere. It may therefore be an important consideration for earthquake hazard in the region.

Key words: Green Lake landslide, earthquake hazard, Alpine Fault, Hauroko Fault, seismically-triggered landslides

INTRODUCTION

Giant ($> 1 \text{ km}^3$) sub-aerial landslides are rare, with only a small number of examples known globally (Korup et al. 2007). While they can be triggered by a number of different factors, the majority are thought to result from strong ground shaking associated with earthquakes (Hancox & Perrin, 2009). Prehistoric examples therefore present an off-fault record of past ground shaking that can be used to assess the paleoseismic history of nearby faults (e.g. De Pascale et al., 2014; Howarth et al., 2014).

In New Zealand, the largest identified landslide is the Green Lake landslide deposit in southern Fiordland (Figure 1), which covers an area of $\sim 45 \text{ km}^2$ and has an estimated volume of $\sim 27 \text{ km}^3$ (Hancox & Perrin, 2009). This landslide was first identified by Whitehouse (1983) and subsequently described in detail by Hancox & Perrin (1994; 2009), but relatively little further work has been published on the deposit. Stability analysis of the slope has suggested that the catastrophic collapse was triggered by at least Modified Mercalli (MM) intensity 9 ground shaking, although long-duration MM 8 shaking may also have resulted in failure (Hancox & Perrin, 2009). The Green Lake deposit therefore provides compelling evidence that this region of Fiordland has previously suffered violent shaking and may therefore experience similar shaking in the future.

Hancox & Perrin (2009) suggested that this shaking resulted from an $M_w 7.5+$ earthquake on the Alpine Fault, $> 80 \text{ km}$ north of the deposit (Figure 1). This fault has been shown to cause $M_w \sim 8.0$ earthquakes regularly, with average return periods of 290-330 years (Berryman et al., 2012; Cochran et al., 2017). At least 30 other large ($> 10^6 \text{ m}^3$) prehistoric landslide deposits in the region are also thought to have resulted from previous Alpine Fault earthquakes due to their proximity to the fault (Figure 1). Nevertheless, given the distance between the Green Lake

deposit and the Alpine Fault, it seems questionable that an earthquake on this fault could generate sufficiently strong shaking to initiate failure. Instead, the Green Lake deposit may provide evidence of a large prehistoric earthquake on a different fault. Identifying the most likely source is therefore important for assessing earthquake hazard in the region.

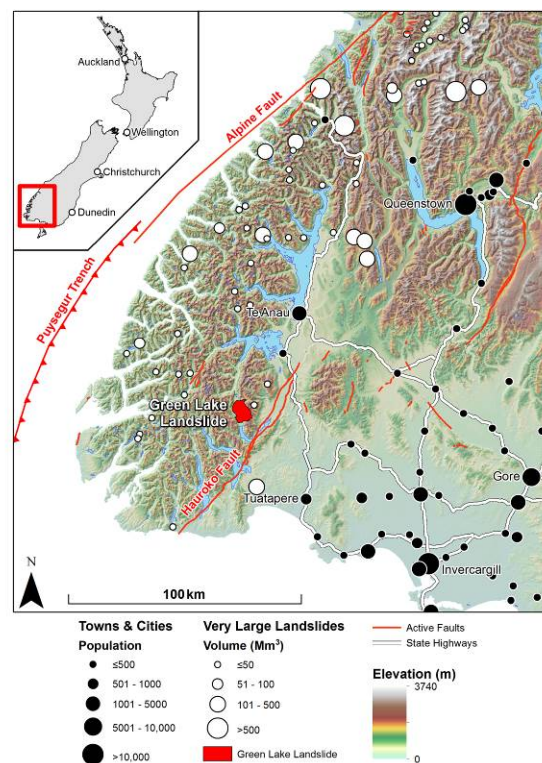


Figure 1: Location of the Green Lake landslide in southern Fiordland in comparison to other very large landslide deposits, known active faults, and towns and cities.



OBJECTIVE & METHODS

This study aims to identify the most likely earthquake scenario capable of triggering the Green Lake landslide, by modelling a series of different earthquakes on known faults in the region. Ground shaking is modelled using New Zealand-specific attenuation relationships from Dowrick & Rhoades (2005), with scenario earthquakes devised for mapped active faults from the GNS Science Active Fault database (<http://data.gns.cri.nz/af/>) based on known and inferred fault parameters. A discussion of the implications for earthquake hazard in the region is provided based on the results.

RESULTS

Four potential earthquake scenarios with the capability of producing MM 9+ shaking are considered (Figure 2).

The first is an earthquake on the Alpine Fault, suggested by Hancox & Perrin (2009) to be the trigger for the Green Lake landslide. Despite no historically recorded earthquake on this fault, several paleoseismic studies have identified numerous previous ruptures dating back to at least 8 ka. As well as being shown to rupture regularly, the fault is thought to be relatively uni-modal, with little variation in rupture style between individual earthquakes (Berryman et al., 2012; Howarth et al., 2012; 2014). These typically involve surface ruptures of at least 300 km between Charles Sound and Lake Kaniere and displacements of ~8 m horizontally and ~2 m vertically. Combined with estimated fault locking depths of ~12 km (Beaven et al., 2010), this corresponds to earthquakes with $M_w \sim 8.0$.

While such an earthquake is capable of producing MM 9+ shaking near to the fault rupture, it only generates MM 7 shaking at Green Lake (Figure 2a). This is insufficient even considering the potential for failure resulting from weaker (MM 8), long-duration shaking, and therefore we conclude that an earthquake on the Alpine Fault cannot have been responsible for the Green Lake landslide.

While the Alpine Fault forms the onshore boundary between the Australian and Pacific plates, offshore the boundary is the Puysegur Trench, which accommodates eastward subduction of the Australian Plate beneath the southern South Island (Figure 1). This fault has been responsible for some of New Zealand's largest historically recorded earthquakes, including an M_w 7.2 in 2003 and an M_w 7.8 in 2009 (Hancox et al., 2003; Fry et al., 2010). However, despite the 2003 earthquake generating MM 9 shaking in its epicentral region, neither was able to generate sufficiently strong shaking at distances sufficient to reach Green Lake. This suggests if an earthquake on this subduction zone is responsible it must be larger than M_w 7.8.

We therefore model two different magnitude earthquakes on the Puysegur Trench: M_w 8.0 and M_w 8.5 (Figure 2b & c). The 2009 earthquake suggests that the Puysegur Trench is able to sustain earthquakes up to M_w 8.0; however, no evidence for larger earthquakes on this fault has been

identified. Nevertheless, recent earthquakes on subduction zones globally have highlighted that these faults are able to sustain giant earthquakes with $M_w > 9.0$, and M_w 8.6 earthquakes have previously been considered on the Puysegur Trench as part of national seismic hazard studies (Stirling et al., 2012). We therefore model an M_w 8.5 earthquake to represent a conservative upper estimate for earthquakes on this fault.

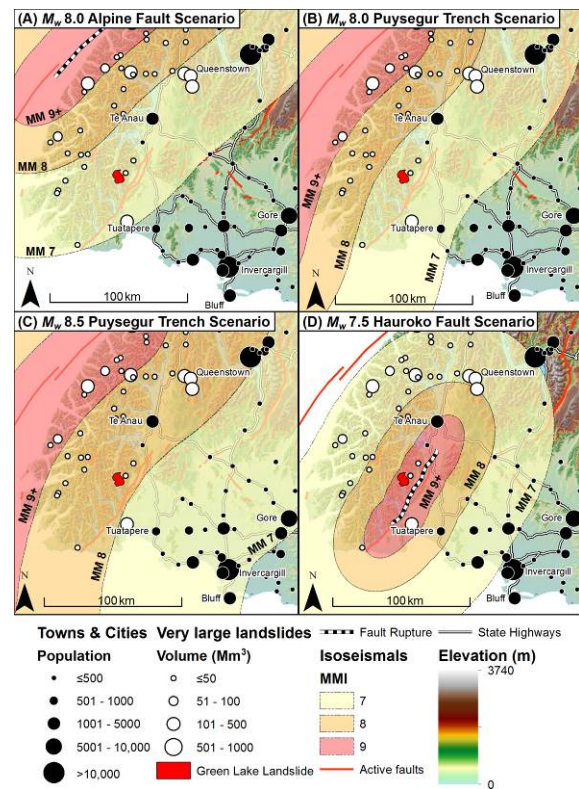


Figure 2: Ground shaking from four different earthquake scenarios in southern Fiordland in relation to the Green Lake landslide deposit. (A) M_w 8.0 earthquake on the Alpine Fault; (B) M_w 8.0 earthquake on the Puysegur Trench; (C) M_w 8.5 earthquake on the Puysegur Trench; (D) M_w 7.5 earthquake on the Hauroko Fault. Only the scenario on the Hauroko Fault is able to produce sufficient shaking at Green Lake to trigger failure.

Assuming both scenarios on the Puysegur Trench rupture a fault patch between 5 km and 40 km depth, both are unable to produce MM 9+ shaking at Green Lake (Figure 2). As with the Alpine Fault scenario, an M_w 8.0 Puysegur Trench earthquake is only capable of MM 7 shaking at Green Lake and therefore cannot be responsible. In comparison, an M_w 8.5 earthquake would produce MM 8 shaking at Green Lake, and therefore could be responsible if failure was triggered by long-duration shaking, but does not reach the MM 9+ considered most likely by Hancox & Perrin (2009).

The final scenario considers rupture of the Hauroko Fault, which is located <20 km east of the Green Lake landslide at its closest point (Figure 1). This fault runs for ~100 km south-west from Lake Manapouri to the southern coast. The activity of the fault is relatively poorly understood however, it is inferred to accommodate dextral motion and



to have sustained Cenozoic movement, thus being considered 'active'. Assuming this fault is capable of sustaining earthquakes and, like the Alpine Fault, is locked to at least a depth of ~12 km, we suggest a plausible maximum magnitude earthquake on this fault could be as large as M_w 7.5. Previous earthquakes on unknown or poorly known faults in New Zealand have exceeded M_w 7.0, with the recent M_w 7.8 earthquake in Kaikōura rupturing multiple previously unknown faults (Hamling et al., 2017). An M_w 7.5 earthquake on the Hauroko Fault would therefore not be surprising.

This scenario is the only one of the four modelled capable of producing MM 9+ shaking at Green Lake (Figure 2d). Thus, despite being the smallest earthquake and the only scenario not on the main plate boundary, an M_w ~7.5 earthquake on the Hauroko Fault presents the only feasible scenario of those modelled to have caused the Green Lake landslide.

DISCUSSION

In summary, while the Green Lake landslide is thought to have been seismically-triggered, the source of the ground shaking has previously been incorrectly assumed to have originated from an earthquake on the Alpine Fault. Here, we have shown, using New Zealand-specific attenuation relationships, that a rupture of the Alpine Fault cannot be the cause for this giant landslide. Consequently, this leaves only three alternative options:

- i. Failure resulted from weaker shaking than modelled stability analysis suggests;
- ii. Failure was not seismically-triggered; or
- iii. Failure resulted from an earthquake on a different fault.

The stability analysis undertaken by Hancox & Perrin (2009) is appropriate and based on well-founded assumptions on the pre-slide topography and strength conditions. Further, we note that previous historic large landslides in New Zealand have resulted from MM 8-9 shaking, and most pre-historic large landslides cluster near to the Alpine Fault and Puysegur Trench (Figure 1) where such shaking recurs at least every ~300 years. Given this and the extreme size of the Green Lake landslide, it seems unlikely that seismically-triggered failure would result from shaking less than MM 8 and we therefore do not consider option (i) a viable explanation.

While heavy rainfall in New Zealand has been responsible for numerous landslides, the majority of these are relatively small in volume compared to the Green Lake deposit (Hancox & Wright, 2005). Despite numerous predisposing factors at the site making the slope susceptible to collapse, the previous stability analysis clearly shows the slope was statically stable and required some external perturbation to initiate failure. Hancox & Perrin (2009) modelled the effect of changes in groundwater on the slope stability and showed that only changes > 100 m were sufficient to induce collapse. Such large-scale changes are unlikely to result from heavy

rainfall; although the area has high annual rainfall, the changes in weather needed to cause such a change in groundwater are dramatic and we therefore consider option (ii) to be implausible, although we cannot discount it entirely.

The only remaining explanation for the collapse of the Green Lake landslide is therefore option (iii); an alternative earthquake not on the Alpine Fault. While we have shown that an M_w ~7.5 earthquake on the Hauroko Fault is a potential candidate, our analysis is not comprehensive and various alternative scenarios remain untested. For instance, an earthquake on an as yet unidentified fault (or series of faults) in the vicinity of the deposit could also explain the collapse, as may a much larger (M_w 9.0+) earthquake on the Puysegur Trench. However, without clear evidence for either of these alternatives it is difficult to assess their plausibility.

Notably, another large (> 10⁷ m³) landslide deposit west of Tuatapere also lies in the MM 9 shaking zone of the Hauroko Fault scenario (Figure 2d). While stability analysis of this landslide has not been undertaken, its location provides further circumstantial evidence for previous large ruptures on the Hauroko Fault.

If the Hauroko Fault is responsible for the Green Lake landslide, this is likely to have important implications for future earthquake hazard in the region. Presently, earthquake hazard for southern Fiordland is thought to primarily relate to the Puysegur Trench and Alpine Fault (Stirling et al., 2012). However, an M_w ~7.5 earthquake on or near the Hauroko Fault could cause widespread impacts throughout the region. Notably, this scenario produces stronger shaking than any of the other scenarios considered for the townships of Te Anau, Manapouri, and Tuatapere, as well as providing another possible source of MM 7+ shaking for Queenstown (Figure 2). For townships west of Invercargill and Gore, only an M_w ~8.5 earthquake on the Puysegur Trench is able to produce stronger shaking than the Hauroko Fault scenario. The Hauroko Fault may therefore present one of, if not the, largest earthquake hazard to communities in the southern South Island.

The Hauroko Fault is presently considered to have a nominal recurrence interval of 5000-10,000 years. While a definitive date for the Green Lake landslide has not been established, the relatively unmodified deposit suggests failure occurred after deglaciation ~14 ka ago. Debutressing may therefore have contributed to failure, although is unlikely to have been the sole triggering factor. Dating of sediments from an infilled landslide dammed lake provide a lower age limit of ~11.5 ka (Hancox & Perrin, 2009) suggesting this event may have occurred between 12-13 ka ago. If the assumed recurrence interval for the Hauroko Fault is accurate, this suggests the fault is late in its seismic cycle, or that a more recent earthquake on this fault has subsequently occurred. If the latter is true, evidence of this may be found from paleoseismic studies of the fault or from dating of the large landslide west of Tuatapere.



Finally, the Green Lake landslide is between 1 and 2 orders of magnitude larger than other landslides in the region. This gigantic landslide occurred in a region of only moderate relief and unexceptional seismicity and lithology's. Further, as we have shown, the collapse of this deposit may have been triggered by a relatively moderate earthquake on a non-plate boundary fault. It is important, therefore, for further work to understand why the Green Lake landslide was so large, and to ascertain whether moderate earthquakes in moderate relief could trigger exceptionally large landslides in the future.

CONCLUSIONS

The giant Green Lake landslide provides substantial evidence that the surrounding region has previously experienced shaking intensities of at least MM 9. While previously thought to have resulted from an Alpine Fault earthquake, we have shown that such an event cannot produce sufficiently strong shaking at the site. The only known fault thought to be capable of generating earthquakes with sufficient shaking in the region is the Hauroko Fault, which is currently poorly understood. An $M_w \sim 7.5$ earthquake on the Hauroko Fault would explain the Green Lake landslide, and a similar future rupture would generate MM 9+ shaking in Te Anau and MM 8 shaking in Tuatapere. Estimated dates for the Green Lake landslide are at the upper end of the Hauroko Fault's assumed recurrence interval, suggesting the fault may be late in its seismic cycle. Paleoseismic studies of the fault are likely to yield important information on its past as well as providing crucial data on the earthquake hazard posed to the surrounding region. The Green Lake landslide is therefore an important example of how off-fault evidence for past earthquakes can be used to identify gaps in our knowledge of fault histories and thus improve understanding of future seismic hazard.

Acknowledgements: The authors would like to thank Louisa Hall and Jean Echard for their help and support in the field as well as preliminary discussions on the manuscript. This work was partly supported by University of Canterbury and by the DIFeREns2 (2014-2019) COFUND scheme supported by the European Union's Seventh Framework Programme (grant number 609412).

REFERENCES

- Beavan, J., Denys, P., Denham, M., Hager, B., Herring, T., & Molnar, P., 2010. Distribution of present-day vertical deformation across the Southern Alps, New Zealand, from 10 years of GPS data. *Geophysical Research Letters* 37, 7-11.
- Berryman, K.R., Cochran, U.A., Clark, K.J., Biasi, G.P., Langridge, R.M., & Villamor, P., 2012. Major earthquakes occur regularly on an isolated plate boundary fault. *Science* 336, 1690-1693.
- Cochran, U.A., Clark, K.J., Howarth, J.D., Biasi, G.P., Langridge, R.M., Villamor, P., Berryman, K.R., & Vandergoes, M.J., 2017. A plate boundary earthquake record from a wetland adjacent to the Alpine Fault in New Zealand refines hazard estimates. *Earth and Planetary Science Letters* 464, 175-188.
- De Pascale, G.P., Quigley, M., Davies, T.R.H., 2014. Lidar reveals uniform Alpine Fault offsets and bimodal plate boundary rupture behaviour, New Zealand. *Geology* 45, 411-414.
- Dowrick, D.J., & Rhoades, D.A., 2005. Revised models for attenuation of Modified Mercalli intensity in New Zealand earthquakes. *Bulletin of the New Zealand Society for Earthquake Engineering* 38, 185-241.
- Fry, B., Bannister, S., Beavan, J., Bland, L., Bradley, B., Cox, S., Cousins, J., Gale, N., Hancox, G., Holden, C., Jongens, R., Power, W., Prasetya, G., Reyners, M., Ristau, J., Robinson, R., Samsonov, S., Wilson, K., & the GeoNet team, 2010. The Mw 7.6 Dusky Sound earthquake of 2009: preliminary report. *Bulletin of the New Zealand Society for Earthquake Engineering* 43, 24-40.
- Hamling, I.J., Hreinsdottir, S., Clark, K., Elliot, J., Liang, C., Fielding, E., Litchfield, N., Villamor, P., Wallace, L., Wright, T.J., D'Anastasio, E., Bannister, S., Burbridge, D., Denys, P., Gentle, P., Howarth, J., Mueller, C., Palmer, N., Pearson, C., Power, W., Barnes, P., Barrel, D.J.A., Van Dissen, R., Langridge, R., Little, T., Nicol, A., Pettinga, J., Rowland, J., & Stirling, M., 2017. Complex multifault rupture during the 2016 Mw 7.8 Kaikōura earthquake, New Zealand. *Science* eaam7194, doi: 10.1126/science.aam7194.
- Hancox, G.T., & Perrin, N.D., 1994. Green Lake landslide: a very large ancient rock slide in glaciated terrain, Fiordland, New Zealand. *Institute of Geological and Nuclear Sciences Science Report* 93-18, p. 31.
- Hancox, G.T., & Perrin, N.D., 2009. Green Lake landslide and other giant and very large postglacial landslides in Fiordland, New Zealand. *Quaternary Science Reviews* 28, 1020-1036.
- Hancox, G.T., & Wright, K., 2005. Landslides caused by the February 2004 rainstorms and floods in southern North Island, New Zealand. *Institute of Geological and Nuclear Sciences Science Report* 2004/10, p. 32.
- Hancox, G.T., Cox, S.C., Turnbull I.M., & Crozier, M.J., 2003. Reconnaissance studies of landslides and other ground damage caused by the Mw 7.2 Fiordland earthquake of 22 August 2003. *Institute of Geological and Nuclear Sciences Science Report* 2003/30, p. 32.
- Howarth, J.D., Fitzsimmons, S.J., Norris, R.J., & Jacobsen, G.E., 2012. Lake sediments record cycles of sediment driven by large earthquakes on the Alpine Fault, New Zealand. *Geology* 40, 1091-1094.
- Howarth, J.D., Fitzsimmons, S.J., Norris, R.J., & Jacobsen, G.E., 2014. Lake sediments record high intensity shaking that provides insight into the location and rupture length of large earthquakes on the Alpine Fault, New Zealand. *Earth and Planetary Science Letters* 403, 340-351.
- Korup, O., Clague, J.J., Hermanns, R.L., Hewitt, K., Strom, A.L., & Weidinger, J.T., 2007. Giant landslides, topography, and erosion. *Earth and Planetary Science Letters* 261, 578-589.
- Stirling, M., McVerry, G., Gerstenberger, M., Litchfield, N., Van Dissen, R., & Berryman, K., 2012. National Seismic Hazard Model for New Zealand: 2010 Update. *Bulletin of the Seismological Society of America* 102, 1514-1542.
- Whitehouse, I.E., 1983. Distribution of large rock avalanche deposits in the central Southern Alps, New Zealand. *New Zealand Journal of Geology and Geophysics* 26, 271-279.



Near real-time modelling of landslide dams from the 2016 Kaikōura earthquake

Robinson, Thomas (1), Rosser, Nick (1), Davies, Tim (2), Wilson, Thomas (2), Orchiston, Caroline (3)

- (1) Department of Geography, Durham University, Durham, UK – tom.robinson@durham.ac.uk
 (2) Department of Geological Sciences, University of Canterbury, Christchurch, NZ
 (3) Centre for Sustainability, University of Otago, Dunedin, NZ

Abstract: Following the 2016 Kaikōura earthquake, one of the first ever near real-time coseismic landslide modelling campaigns was undertaken to inform the response to the event. This modelling campaign combined previously published approaches to landslide modelling with simple runout analysis to model the likelihood of landslide dams forming in order 3+ rivers. Despite being undertaken manually, the first outputs of the model were available <24 hours after the earthquake occurred, providing the first region-wide landslide analysis of the event. The results were fed to various emergency and science responders at the time, and helped define initial reconnaissance flight paths across the affected region. Continued development and automation of the model is expected to allow model outputs to be derived faster in future, potentially producing results <30 minutes after an earthquake. This approach may therefore be able to provide an important addition to current near real-time shaking models such as GeoNet's ShakeMap.

Key words: Kaikōura earthquake, landslide hazard, landslide dams, near real-time modelling.

INTRODUCTION

Landslides are one of the most widespread and damaging secondary hazards to result from earthquakes in mountainous regions (Bird & Bommer, 2004), often forming dams that may fail catastrophically and devastate downstream communities. Those dams that fail typically do so soon after formation (Costa & Schuster, 1988), highlighting the need for rapid identification. However, this can be difficult in the steep and remote terrain in which landslide dams typically form (Korup, 2004; 2005), with previous examples in New Zealand remaining unidentified for several weeks (Massey et al., 2013).

Previously, approaches to identifying landslides and landslide dams following an earthquake have relied on either aerial reconnaissance, satellite imagery, or a combination of both (Joyce et al., 2009). However, these approaches can be hindered by cloud cover, satellite return times, helicopter availability, flying conditions, and image processing times amongst other factors, meaning often the assessments come too late to effectively inform emergency response (Robinson et al., 2017; Williams et al., 2017). One way to combat this is via the use of rapid modelling, which is unaffected by such factors.

Despite this, very few attempts to model earthquake-triggered landslides in near real-time have been made, and currently no operational platform exists for such a purpose. Following the 2016 Kaikōura earthquake (Figure 1) we therefore undertook one of the first ever near real-time modelling campaigns in order to inform response to the event. This paper briefly summarises some of the results of that campaign, with a more detailed description of the methods and results intended to follow in a Special Issue on the earthquake in *Bulletin of Seismological Society of America* (Robinson et al., forthcoming).

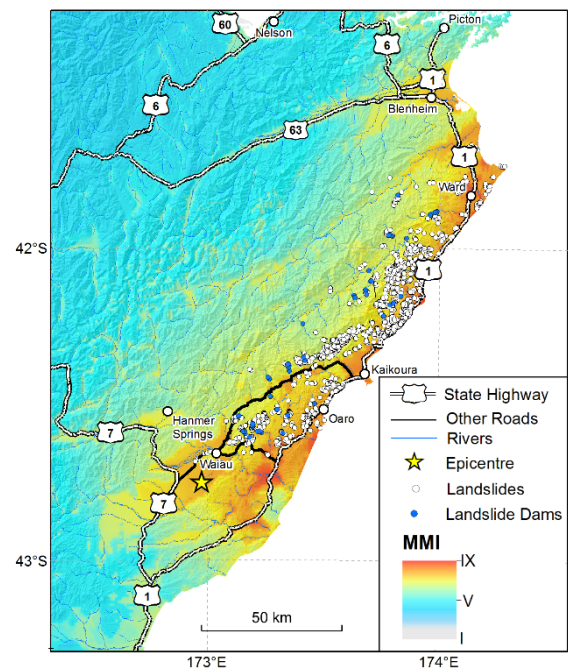


Figure 1: Landslides and landslide dams from the 2016 Kaikōura earthquake in relation to ground shaking. Landslides from Sotiris et al., (2016), landslide dams from ECan (2017).

METHODS AND OBJECTIVES

This study aims to demonstrate the predictive ability of near real-time landslide modelling for informing emergency and science response post-earthquake based on results from the 2016 Kaikōura earthquake. In particular, this study provides results produced at the time of the event on the likelihood of landslide dam locations in order 3 or larger rivers during the earthquake.



Despite few attempts at near real-time landslide modelling, two main approaches exist: Newmark sliding block analysis and empirical analysis. Newmark approaches (e.g. Gallen et al., 2016) combine slope angle, ground shaking, and rock mass strength to estimate slope factor of safety for each pixel in the study area. However, these approaches are hindered by a lack of data on rock mass strength at scales relevant to landsliding. Alternatively, empirical analyses (e.g. Nowicki et al., 2014; Kritikos et al., 2015) use observations of landslides in multiple previous earthquakes to identify pixels with similar preconditions, assuming that landslides occur under similar conditions globally.

Previously, the empirical analysis of Kritikos et al. (2015), which is based on observations from the Northridge, Wenchuan, and Chi-Chi earthquakes, has been shown to accurately model landslides from historic earthquakes in New Zealand (Robinson et al., 2016). This method facilitates rapid modelling of landslide hazard in GIS due to the limited data requirements and pre-existing formulae describing the relationship between landsliding and various preconditioning factors. These factors include:

- i. Slope angle;
- ii. Ground shaking;
- iii. Distance from active faults;
- iv. Distance from rivers; and
- v. Slope position.

Combining the influence of these five factors for a given earthquake provides an analysis of the probability of landslides occurring in any given pixel. Following the Kaikōura earthquake, this method was applied manually in order to identify where landslides were most likely to have occurred (

Figure 2).

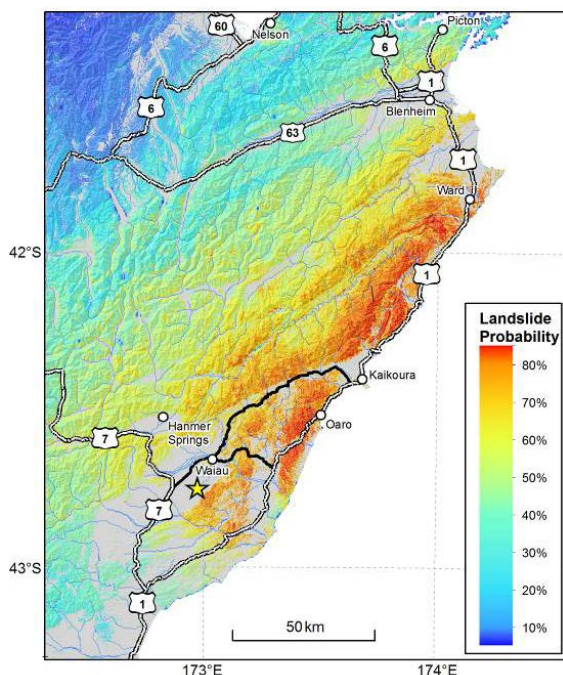


Figure 2: Modelled landslide hazard for the 2016 Kaikōura earthquake based on the method of Kritikos et al. (2015).

To model the likelihood of landslide dam formation during the earthquake, this study undertook an analysis based on the expected mobility of landslides. By assessing the angle between all pixels in the study area and the river network, the required mobility of landslides to reach the corresponding river can be derived. Assuming most landslides will have angles of reach $\geq 30^\circ$ (Hung et al., 2015) identifies those pixels from which landslides are expected to reach the river. Averaging the probability of landslide occurrence (

Figure 2) in the corresponding pixels therefore provides an estimate of the likelihood of one or more landslide dams forming.

At the time of the earthquake, this analysis was undertaken for all order 3+ rivers in the northern South Island. While landslide dams also formed on smaller rivers, confining the analysis to order 3 rivers provided the best compromise between modelling speed and identifying those dams likely to present the highest risk.

RESULTS

The 2016 M_w 7.8 Kaikōura earthquake occurred at 00:02hrs on 14 November New Zealand Standard Time (NZST). At the time, an automated approach to modelling earthquake-triggered landslide hazard was not available. Consequently, consideration was given to whether manual application of the Kritikos et al. (2015) method could be undertaken sufficiently quickly. These were hampered by the modelling team being located in the GMT time zone (13 hours behind NZ at the time). Eighteen hours after the earthquake occurred, it was decided that manual application of the model could still yield useful and useable results, and collection of the necessary data (i.e. digital elevation model, earthquake shaking, river networks etc.) began.

Initial data collection and processing was completed at 21:00 hrs on 14 November NZST, ~21 hrs after the earthquake occurred. Subsequent manual application of the model was undertaken and completed ~30 mins later, yielding the first region-wide analysis of landsliding (Figure 2) from the earthquake <21.5 hrs after the earthquake occurred. At the same time, an analysis of the likelihood of landslide dams was also undertaken and completed (Figure 3).

The landslide dam model results suggested that 261 locations on the river network had $\geq 60\%$ likelihood of landslide dam blockage. The majority of these locations were located on the eastern slopes of the coastal ranges between Waiau and Ward, where both ground shaking (Figure 1) and landslide hazard were high (Figure 2). Of these 429 locations, 90 had likelihoods $>70\%$, of which 41 locations were north of Kaikōura (Figure 3).

At the same time as the modelling was being undertaken, separate efforts to identify landslides and landslide dams from aerial reconnaissance and satellite imagery were also being undertaken. The first publicly available assessment



of landsliding from the earthquake came from Sotiris et al. (2016), who identified 1771 landslides (Figure 1) from satellite images taken after the event. Nevertheless, this mapping was not completed until >5 days after the earthquake, and subsequent analysis has shown the total number of landslides to be at least 5x greater than this initial inventory. Further, this inventory did not contain any details of landslide dams, and consequently the first publically available data on landslide dams did not become available until 18 days after the earthquake, when Environment Canterbury released data from aerial and ground based reconnaissance (ECan, 2017). This identified >190 landslide dams that formed during the earthquake, of which 58 were located on order 3+ rivers (Figure 1).

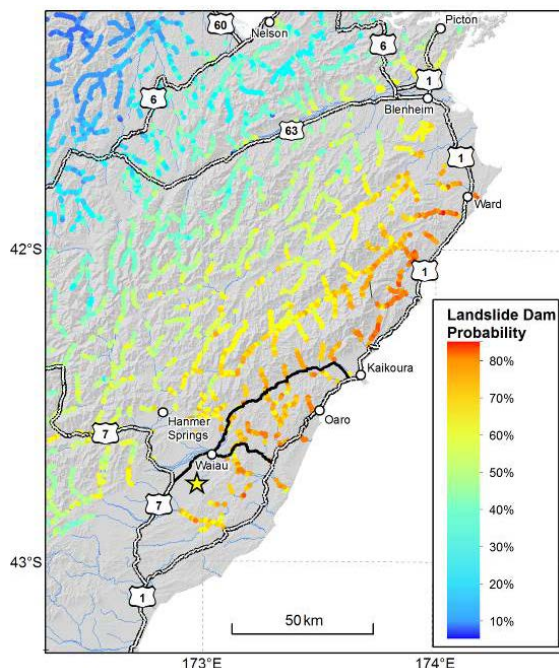


Figure 3: Likelihood of landslide dam formation in order 3+ rivers from the 2016 Kaikōura earthquake. Modelling was undertaken manually and completed <21.5 hrs after the earthquake occurred.

Using this data, we assess the accuracy of the landslide hazard (Figure 2) and landslide dam (Figure 3) models completed within the first 24 hours of the earthquake occurring. This shows that of the 1771 landslides mapped, 1063 (~60%) occurred in pixels where the likelihood of landslides was $\geq 60\%$. However, the total number of pixels in which landslide likelihood was $\geq 60\%$ was >500,000 (~1800 km²), confirming the model was largely over-predicted. Comparatively, of the 58 landslide dams on order 3+ rivers, 52 (~90%) occurred at locations where modelled landslide dam likelihood was $\geq 60\%$, and 10 (~17%) occurred at locations $\geq 70\%$ likelihood.

While both model outputs are therefore able to predict the majority of landslide and landslide dam locations, both are notably over-predicted. This is common to most landslide hazard models and demonstrates the difficulties in predicting landslide occurrence and high resolution (~60 m pixels). Nevertheless, it is notable that in both the landslide hazard and landslide dam model outputs, the area

encompassed by likelihoods $\geq 60\%$ is broadly equivalent to the observed extent of landsliding and landslide dams. Thus, considering the speed with which these models can be produced and the large percentage of true positives that they can capture, these results are potentially useful as a rapid method for delimiting the total area affected by landslides and landslide dams. Compared to more traditional approaches to identify landslides, which can take days or weeks, this may therefore enable better understanding of landslide hazard post-earthquake earlier in the response phase.

DISCUSSION & CONCLUSIONS

This study has described the results of one of the first-ever near real-time earthquake-triggered landslide modelling campaigns. Currently, operational near real-time earthquake modelling is predominantly focussed on either the ground shaking resulting from the earthquake (e.g. the GeoNet Shakemap) or on aggregated earthquake losses (e.g. the USGS PAGER; Wald et al., 2008). Specifically, identifying the impacts resulting from landslides is therefore important for informing emergency response, as this may enable greater understanding of the causes of impacts in different locations.

In particular, the rapid assessment of landslide dams is a crucial component of near real-time modelling of earthquake impacts. The majority of landslide dams that fail do so soon after they form, with >25% failing within 24 hours of formation (Costa & Schuster, 1988). Because landslide dams form in steep and narrow valleys they can be difficult to identify from the ground and may therefore go unnoticed. Any subsequent catastrophic failure of a landslide dam could therefore have potentially devastating consequences for downstream communities. Rapidly identifying where landslide dams may have formed is therefore a crucial component of post-earthquake assessments in mountainous terrain.

While the model outputs described in this study are largely over-predicted, importantly the total spatial extent of landslides and landslide dams was captured. Consequently, such outputs can provide an initial, rapid analysis of locations that require urgent assessment via either ground-based or aerial reconnaissance. These outputs may also therefore help to prioritise those locations in urgent need of such reconnaissance. Presently, most emergency reconnaissance is undertaken based on incoming reports from an affected location. However, in the aftermath of large earthquakes some locations in need of assistance may be cut off and without means of communication, potentially leading to them being overlooked. Following the 2015 Nepal earthquake, it took ~1 week before emergency responders were alerted to potential landslide impacts in Langtang Valley, where a large landslide had destroyed a village and partially blocked the valley, cutting both access and communication (Kargel et al., 2015). Models such as the one described here may reduce the chance of this happening by providing an unbiased assessment of the locations potential in need of aid, allowing emergency responders to prioritise reconnaissance at locations even if communications are not readily available.



Finally, it is important to note that, despite being completed <21.5 hrs after the Kaikōura earthquake, the results of this study could have been completed sooner. Firstly, the lack of an operational automated approach was the main hindrance, as this required modellers to consider manual application of the model and communicate with responders in different time zones. This delay accounted for ~18 hrs (>80%) of the time required to produce the model and could be reduced, or removed entirely with an automated model. Of the remaining 3.5 hrs required to complete the modelling, 3 hrs involved downloading and processing the necessary data. Given that the only data not available prior to the earthquake is the ground shaking models, which are typically available within minutes of an earthquake occurring, this time could be reduced by compiling pre-event repositories of the necessary and available input data. Consequently, if such measures are undertaken, it is conceivable that in future landslide impact models could be completed within 30 mins of an earthquake occurring.

This study has therefore demonstrated that modelling may provide a rapid and accurate approach to understanding landslide impacts following an earthquake, providing results faster than current manual mapping approaches can afford. Using the outputs of these models to inform reconnaissance mapping may subsequently improve these manual mapping speeds and reduce the likelihood of affected locations going unnoticed due to lack of communication as has recently occurred. Producing rapid analysis of the potential locations of landslide dams following an earthquake may enable more rapid identification of such dams and potentially help avoid further losses resulting from catastrophic outburst floods that may occur within 24 hours of the earthquake.

Acknowledgements: This work was partly supported by University of Canterbury and by the DiFeREns2 (2014-2019) COFUND scheme supported by the European Union's Seventh Framework Programme (grant number 609412).

REFERENCES

- Bird, J.F., & Bommer, J.J., 2004). Earthquake losses due to ground failure. *Engineering Geology* 75, 147-179.
- Costa, J.E., & Schuster, R.L., 1988. The formation and failure of natural dams. *Geological Society of America Bulletin* 100, 1054-1068.
- Environment Canterbury (ECAN), 2017. North Canterbury landslide dams following the 7.8 magnitude earthquake on the 14th November 2016. <http://ecan.maps.arcgis.com/apps/Cascade/index.html?appid=50f00d42e29c46b1a61b848440c5295a>. Last accessed: 2 June 2017.
- Gallen, S.F., Clark, M.K., Godt, J.W., Roback, K. & Niemi, N.A., 2016. Application and evaluation of a rapid response earthquake-triggered landslide model to the 25 April 2015 Mw 7.8 Gorkha earthquake, Nepal. *Tectonophysics*.
- Hung, O., Corominas, J., & Eberhardt, E., 2005). Estimating landslide motion mechanism, travel distance and velocity. *Landslide Risk Management*, 99-128.
- Joyce, K., Belliss, S., Samsonov, S., McNeill, S. & Glassey, P., 2009. A review of the status of satellite remote sensing and image processing techniques for mapping natural hazards and disasters. *Progress in Physical Geography* 33, 183-207.
- Kargel, J.S., Leonard, G.J., Shugar, D.H., Haritashya, U.K., Bevington, A., Fielding, E. J., et al., 2016. Geomorphic and geologic controls of geohazards induced by Nepal's 2015 Gorkha earthquake. *Science* 351, aac8353.
- Korup, O., 2004). Geomorphometric characteristics of New Zealand landslide dams. *Engineering Geology* 73, 13-35.
- Korup, O., 2005. Geomorphic hazard assessment of landslide dams in South Westland, New Zealand: fundamental problems and approaches. *Geomorphology* 66, 167-188.
- Kritikos, T., Robinson, T.R. and Davies, T.R., 2015. Regional coseismic landslide hazard assessment without historical landslide inventories: A new approach. *Journal of Geophysical Research-Earth Surface* 120, 711-729.
- Massey, C., McSaveney, M., & Davies, T., 2013). Evolution of an overflow channel across the Young River Landslide dam, New Zealand. In *Landslide Science and Practice*, Springer Berlin Heidelberg, 43-49.
- Nowicki, M.A., Wald, D.J., Hamburger, M.W., Hearne, M. & Thompson, E.M., 2014. Development of a globally applicable model for near real-time prediction of seismically induced landslides. *Engineering Geology* 173, 54-65.
- Robinson, T.R., Davies, T.R.H., Wilson, T.M., & Orchiston, C., 2016. Coseismic landsliding estimates for an Alpine Fault earthquake and the consequences for erosion of the Southern Alps, New Zealand. *Geomorphology*, 263, 71-86.
- Robinson, T.R., Rosser, N.J., Densmore, A.L., Williams, J.G., Kincey, M.E., Benjamin, J., & Bell, H.J.A., 2017. Rapid post-earthquake modelling of coseismic landslide magnitude and distribution for emergency response decision support. *Natural Hazards and Earth Systems Science*.
- Robinson, T.R., Rosser, N.J., Davies, T.R.H., Wilson, T.M., & Orchiston, C., (In Review). Near real-time modelling of landslide impacts to inform rapid response following the 2016 Kaikōura, New Zealand, earthquake. Intended for: *Bulletin of the Seismological Society of America Special Issue: Kaikōura earthquake*.
- Sotiris, V., Papathanassiou, G., & Spyros, P., 2016. Preliminary map of co-seismic landslide for the M 7.8 Kaikōura, New Zealand Earthquake [Data Set]. Zenodo, <http://doi.org/10.5281/zenodo>.
- Wald, D.J., Earle, P.S., Allen, T.I., Jaiswal, K., Porter, K., & Hearne, M., 2008. Development of the US Geological Survey's PAGER system (prompt assessment of global earthquakes for response). In *Proceedings of the 14th World Conference on Earthquake Engineering*.
- Williams, J.G., Rosser, N.J., Kincey, M.E., Benjamin, J., Oven, K.J., Densmore, A.L., Milledge, D.G., & Robinson, T.R., 2017. Satellite-based emergency mapping: Landslides triggered by the 2015 Nepal earthquake. *Natural Hazard and Earth System Sciences Discussions*.



Paleoseismology of the Northern Elsinore fault in Southern California

Rockwell, Thomas K.

Dept. of Geological Sciences, San Diego State University, San Diego, CA 92182. trockwell@mail.sdsu.edu

Abstract: Paleoseismic trenching across the northern Elsinore fault at Glen Ivy Marsh has resolved the ages of the past six to seven surface ruptures, all having occurred in the past 1.2 ka, with the most recent event (MRE) in 1910 (~M6-6.2) laterally displacing an 1890's water flume by ~25 cm. The short recurrence interval suggests the occurrence of moderate-size earthquakes that rupture this short section of fault, which contrasts sharply with the long recurrence interval and larger displacements for the Whittier fault to the northwest and the Temecula Valley-Agua Tibia section to the southeast. 3D excavation of small fluvial channels in Glen Ivy Marsh that only ruptured in the ca 1300 AD earthquake indicate that as much as 87 cm of lateral slip occurred on a secondary fault strand, with additional slip likely also having occurred on the main strand. This indicates that some ruptures were significantly larger than 1910.

Key words: paleoseismology, Elsinore fault, Glen Ivy Marsh, displacement per event.

INTRODUCTION

The Elsinore fault is a major branch of the San Andreas fault system in southern California that extends about 200 km from the Santa Ana River near the southern margin of the LA Basin southeast for 200 km to the Yuha Basin (Figures 1 and 2). Farther south, the Elsinore fault transfers slip to the Laguna Salada and related faults in the Sierra Cucapah and Sierra Mayor in northern Baja California, Mexico, two of which generated M7.2 earthquakes in 1892 and 2010. To the northwest, the Elsinore fault feeds slip directly into the Los Angeles basin via the Whittier fault (Figure 1). The only notable historical earthquake on the Elsinore fault itself is the May, 1910 Glen Ivy earthquake at ~M6-6.2 that produced about 25 cm of right-lateral displacement at Glen Ivy Marsh (Brake, 1987; Rockwell et al., 2016).

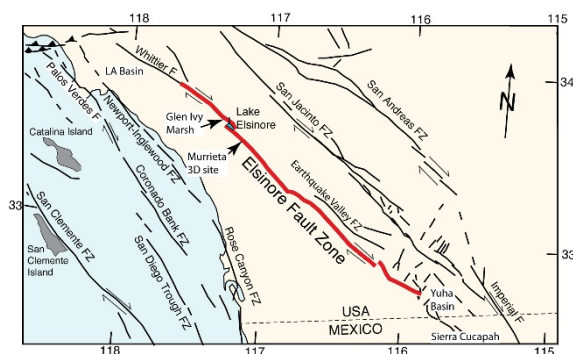


Figure 1. Generalized map of major faults in southern California, with the Elsinore fault in red. Total motion across the entire system is about 50 mm/yr.

Total slip on the northern Elsinore fault is estimated at 9-11 km (Weber, 1977), whereas displacement is only 2.5-3 km along the central Elsinore fault at Granite Mountain near Julian (Magistrale and Rockwell, 1996). Magistrale and Rockwell recognized the double-stranded nature of the central Elsinore fault with the eastern strand being the Earthquake Valley fault (Figure 1), which transfers the balance

of the displacement to the southeast onto the southern San Jacinto fault zone (Gordon and Rockwell, 2015). Estimates of the slip rate range from 2-9 mm/yr with a best estimate of ~5 mm/yr on the northern Elsinore fault (Millman and Rockwell, 1986; Vaughan and Rockwell, 1986; Rockwell et al., 2000), with large uncertainties because age control for two of the studies was based on soil age estimates and the Rockwell et al. study only included slip for the past 2 ka. To the south, Magistrale and Rockwell estimate a rate for the past 900 ka on the central Elsinore fault of about 2.8 mm/yr, and Rockwell et al. (2013) estimate about 2.5 mm/yr for the Earthquake Valley fault based on offset of middle Quaternary deposits that contain the ~800 ka Bishop Tuff. Farther south in the Coyote Mountains, the slip rate very close to the faults' southern terminus was resolved by U-series dating of pedogenic carbonate in offset alluvial fans to be 1.6 ± 0.4 mm/yr (Fletcher et al., 2011). A more recent study several kms to the northwest from the Fletcher et al. study, and using the same methods, resolved a higher rate of 2.4 mm/yr (Rockwell et al., 2017 in review), and they suggest that the full rate in the central part of the range is likely 2.5-3 mm/yr.

In this paper, I present paleoseismic results from Glen Ivy Marsh along the northern Elsinore fault that were completed in the 1980's but that until now, were mostly unpublished. The initial trench results were presented in a guidebook (Rockwell et al., 1986), and extensive subsequent work and dating results are presented here.

PALEOSEISMOLOGY OF GLEN IVY MARSH

Glen Ivy Marsh is a linear sag depression caused by a releasing bend in the Glen Ivy North strand of the Elsinore fault (Figure 2). The Glen Ivy North fault strand is about 15-20 km in length and lies between the Eagle fault strand to the north and the 2.5 km-wide releasing step at Lake Elsinore to the south, where fault slip steps to the Wildomar fault strand. Lateral juxtaposition of Pleistocene alluvial fan deposits from north of the bend provide a trap for sediments shed from the Santa Ana Mountains to the west (Millman and Rockwell, 1986).



Twelve trenches, with numerous secondary cuts, were excavated (Figure 3) to expose the marsh sediments and fault zone. The main trench (MT-1) was excavated as three benches, each 1-1.5 m high, that were cut back as successive slices at 30-50 cm intervals, ultimately exposing over 30 faces. A deep trench was cut down the middle of MT-1 exposing stratigraphy and faulting to 6 m depth. Trenches AT-8 and AT-12 were excavated parallel to the fault zone to connect and correlate all stratigraphic units. Trench AT-12 encountered a concrete flume constructed by hand in the 1890's; the flume was cleaned off and found to be laterally offset about 25 cm, which is attributed to the 1910 Glen Ivy earthquake, estimate at about M6-6.2 (Brake, 1987; Rockwell et al., 2016).

The marsh has accumulated a sequence of well-bedded sand, silt and clayey strata with some pebbly gravel layers, separated by centimeter-thick organic peat-like layers (Figure 4), many of which are dated by ¹⁴C (Table 1). The peats are numbered sequentially from 1 near the surface down to 28/29, and stratigraphic units are designated with letters (following Rockwell et al., 1986). Evidence for past surface ruptures was well-expressed in many exposures as upward terminations of fault splays, liquefaction of fine-grained sand flowing down into the fault zone and capped by bedded sediment, and angular unconformities that indicated a folding event (Figures 4 and 5).

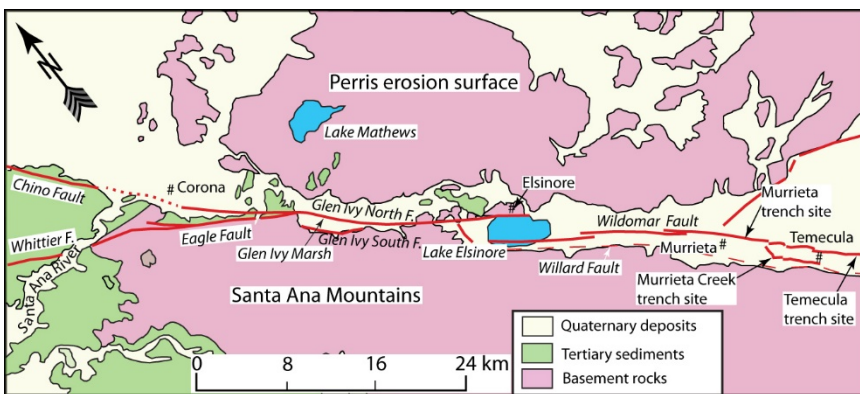


Figure 2. Generalized geologic map of the northern Elsinore fault, with individually named fault strands (derived from the CDMG Santa Ana Geologic Sheet). Trench sites are indicated.

Figure 3. Map of trenches at Glen Ivy Marsh. The main trench (MT-1) was the site of 30 successive cuts at 30-50 cm intervals. Lateral trenches were excavated to connect all stratigraphic units. It was found after excavation of trenches AT-3 to 9 and AT-12 that the upper meter of section was missing from the center of the site, a consequence of a drain ditch from 1977.

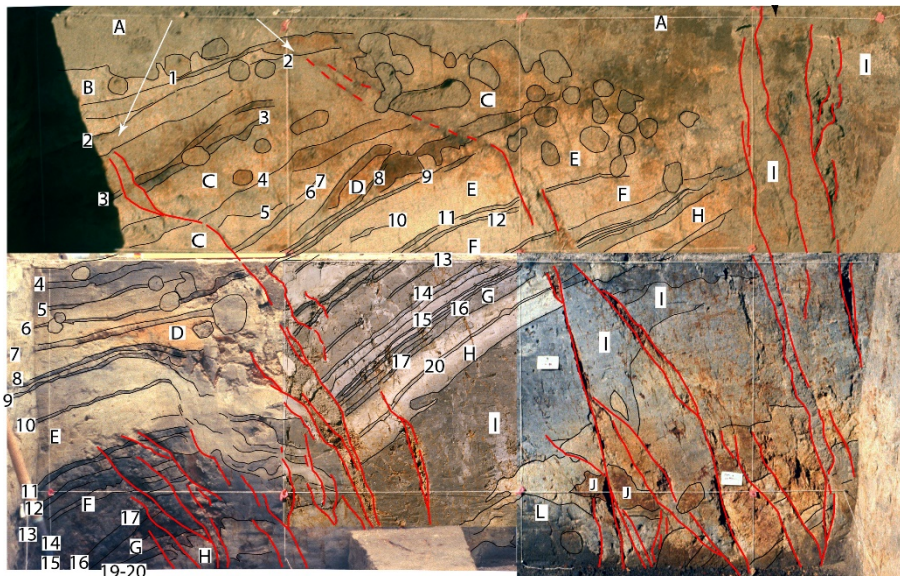
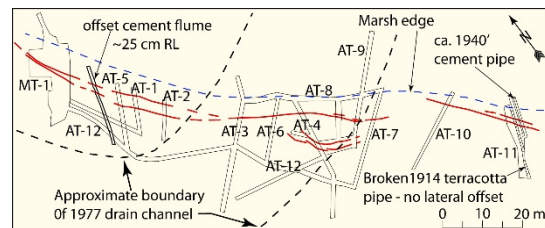


Figure 4. Mosaic of the upper 2+ m of cut 0+90 cm in MT-1 showing evidence for several of the interpreted events. The MRE ruptures to the surface into the topsoil (A) horizon and laterally offsets a concrete flume by about 25 cm (Rockwell et al., 2016). The penultimate event is interpreted to have ruptured to the surface prior or during the formation of the A horizon, as the entire section is strongly tilted which cannot be attributed to the 1910 earthquake. The third event ruptures up through unit C and peat 3 and is capped by peat 2 and unit B in this and many exposures. There is also an angular unconformity between units B and C. A third event is recognized as faulting and liquefaction up through unit E and peats 8 and 9, capped by fine sand of unit D and peats 7 and 6. A 4th event caused rupture up through unit F and peat 11, which is then capped by peat 10 and upper unit E. MT-1 was excavated to 6 m depth.

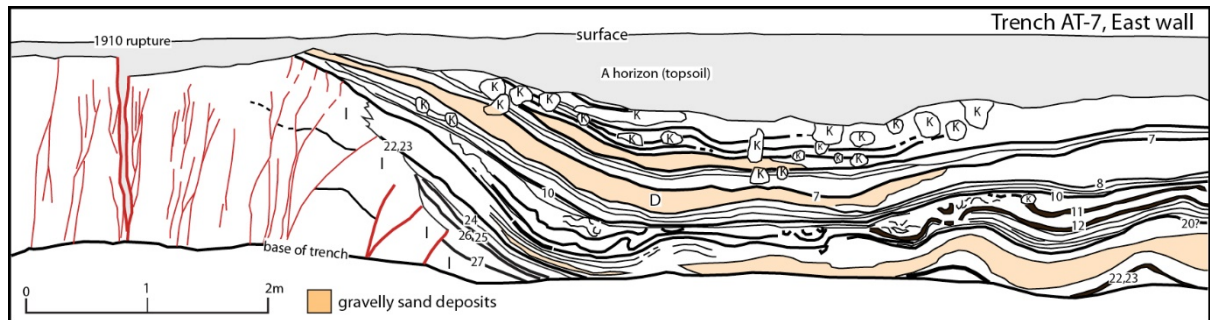


Figure 5. Log of the east Wall, trench AT-7. Note that the Young faulting is north (left) of the area of sag sediment accumulation, so most late Holocene events won't be recognized. Note also the liquefaction and folding of sediments below peat 10, and the angular unconformity between peats 11 and 10, supporting evidence for event 4. Another event is indicated by faulting of peat 27, capped by peat 26.

Evidence for six or seven late Holocene (past 1.2 ka) ruptures was found in the stratigraphy exposed in the trenches, although evidence for some ruptures was obscured by bioturbation, which was locally extensive, or not recorded by periods of non-deposition. A buried soil (unit I in Figures 4, 5 and 7) is developed in mid-Holocene stratigraphy within and east of the fault zone, and a massive clayey section below unit I, is present on the downthrown (SW) side of the fault, probably due to an extended period of bioturbation when the sag depression experienced drier conditions.

during event 4 at about 1350 A.D. An additional 39 cm of offset is accommodated by folding, suggesting that this secondary fault produced at least 87 cm of strike-slip (Brake, 1987). As there was almost certainly additional slip on the main fault, this event is interpreted to have been significantly larger than the 1910 earthquake.

Sample Number	Lab Number	¹³ C-Corrected Age (years BP) AD 1910
		hist. prior - 1810
P2	A4029	220 + 80
P3a	QL4306	358+20
P3b	A4400	490+90
P4a	QL4307	407+34
P4b	A4374	590+90
P7	A4401	380+150
P8a	QL4308	717±21
P8b	A4375	820±90
P8c	A4034	730±100
P9	QL4309	688±20
P10a	QL4310	816±34
P10b	A4370	630±100
P11a	A4369	780±120
P11b	A4033	760±50
P12	QL4311	889±21
P15	A4376	1020+80
P20a	QL4312	931±15
P20b	A4377	910±60
P22a	QL4351	1076±16
P22b	A4378	1010±70
P24	QL4350	1141±15
P26	QL4315	1069±15
P28/29	QL4352	1216±23
Unit A	A4372	5,130±110
Unit B	A4373	9,040±160
Unit C	A4371	10,190±350

Table 1. Radiocarbon dates from Glen Ivy Marsh. Dates were run at the University of Washington (QL) and Arizona (A). Most dates are on bulk peat samples and likely contain a mix of detrital ages.

Figure 5 shows the log from trench AT-7, where the main fault is located along the margin of sedimentation such that discrete ruptures cannot be recognized. Nevertheless, some events caused folding and liquefaction of the bedded stratigraphy, producing angular unconformities and discordant folding.

Figure 6 shows one of the exposures in the area of AT-4 where peat 8 is offset and capped by the upper part of unit D and peat 7. 3D hand excavations exposed the edges of a unit D channel that was offset 48 cm on a secondary fault

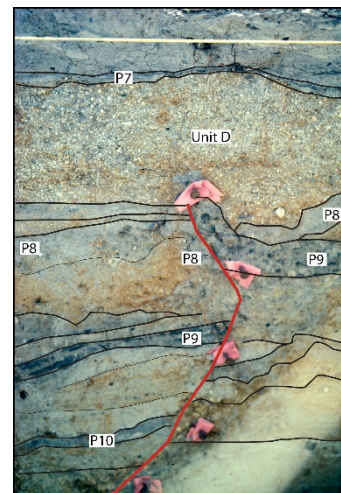


Figure 6. Secondary fault splay produced during the ca 1300 AD earthquake. Faulting up through P8 and into the very base of unit D, capped by unit D and P7. This splay offset a small sand channel by at least 87 cm, when folding is included.

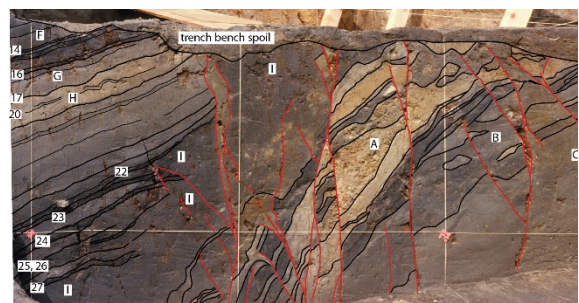


Figure 7. Logged photo of third bench of cut 0+00 (original trench face) in MT-1. Evidence for a surface rupture is juxtaposition of unit I against peats 23 and 24, capped by peat 22.

Rupture event horizons are identified as E1 through E7. E1 is interpreted as the 1910 earthquake as it breaks to the soil surface, producing soil-filled fissures that extend down into the fault zone (Figures 4 and 5). A ca 1890's concrete flume



is laterally offset about 25 cm whereas a 1914 terracotta pipe displays no lateral offset (Brake, 1987; Rockwell et al., 2016). Event E2 is an inferred event to explain the large amount of folding and tilting observed above peats P1 and P2 in the MT1 exposures, which are difficult to explain with only the 1910 earthquake (see Figure 4). A rupture could be hidden in the surface soil because there has been no deposition across the fault for the past few hundred years. The first settlers occupied a site adjacent to the marsh in 1810, so any additional event must predate this date. Alternatively, much of this warping may have resulted from subsidence from groundwater withdrawal, so this remains a questionable interpretation. Event E3 ruptured up through peat P3 in many exposures and is capped by peat P2, and an angular unconformity between peats P2 and P3 is evident in many exposures (see Figure 4). Event E4 ruptured up through peat P8, and is capped by unit D and peat P7 in many exposures (see Figures 4 and 6). Event E5 ruptured up through peat P11, is capped by fine sand strata that contains peat P10, and is associated with liquefaction and folding of strata between peats P11 and P10 (see Figures 4 and 5). Event E6 juxtaposes unit I against peats 23 and 24 and is capped by peat 22 (Figure 7). Finally, event E7 ruptured through unit I and peat 27, and is capped by peat P26 (see figure 5). The radiocarbon dates on individual peat layers are presented in Table 1, and an OxCal model of the event ages is presented in Figure 8.

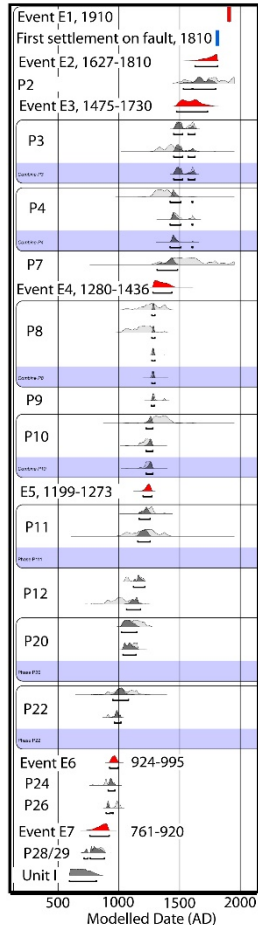


Figure 8. OxCal model of interpreted surface ruptures on the Elsinore fault at Glen Ivy Marsh.

DISCUSSION

The Glen Ivy north strand of the northern Elsinore fault ruptures on average every 180 years, with some earthquakes being of moderate size, such as in 1910, and some being larger, such as in ca 1350. It is likely that the larger events represent “cascade” earthquakes that involved the Elsinore fault to the north and/or south, whereas the smaller, 1910-type events ruptured only the short 15-20 km-long fault between the Lake Elsinore releasing step and the Glen Ivy North releasing bend.

Comparison of the paleoseismic record to the south near Pala suggests that event E2 could correspond to the MRE along the Wildomar fault, as documented at Agua Tibia Mountain (Vaughan et al., 1997). The late Holocene record is mostly missing at the Pala site, but Vaughan et al. (1997) estimate the average recurrence interval to be about 400-600 years based on preservation of the middle to late Holocene earthquake record. The longer average recurrence interval is consistent with the longer Wildomar fault strand of the Elsinore fault zone, about 50 km, which argues for larger earthquakes. Combined with the ~10 m offset of a 1.9 ka fluvial channel at Murrieta (Rockwell et al., 2000) suggests 2-3 m for slip per event on the Wildomar fault. Using the same rationale, and the ~180 year recurrence interval for the Glen Ivy North segment suggests average slip per event of about 90 cm, which is larger than 1910 and likely smaller than the 1350 event. In contrast to the north, the MRE on the Whittier fault predates all of the Glen Ivy events by several hundred years, consistent with its lower slip rate and multimeter slip per event (see Gath et al., this volume).

Acknowledgements: Portions of this work were supported by grants from the US Geological Survey.

REFERENCES

- Brake, J.F., 1987, Analysis of historic and pre-historic slip on the Elsinore fault at Glen Ivy Marsh, Temescal Valley, southern California. Unpub. MS thesis, San Diego State Univ., 116 p.
- Fletcher, K.E.K., Rockwell, T.K., and Sharp, W.D., 2011, Late Quaternary slip rate of the southern Elsinore fault, southern California: Dating offset landforms via $^{230}\text{Th}/\text{U}$ on pedogenic carbonate. *J. Geophysical Research*, 116, F02006, doi:10.1029/2010JF001701.
- Gordon, E.M., T.K. Rockwell, G.H. Girty, and C. Goetz (2015). Geomorphic analysis of late Quaternary activity of the Earthquake Valley and Hot Springs-San Felipe fault zones, and their role in slip transfer between the northern Elsinore and southern San Jacinto faults. In: *Geology of the Coyote Mountains, southern California* (R. Wagner, ed.), San Diego Association of Geologists, Sunbelt Publications, p. 95-108.
- Magistrale, H. and Rockwell, T., 1996, The central and southern Elsinore fault zone, southern California: *Bulletin of the Seismological Society of America*, v. 86, no. 6, pp. 1793-1803.
- Millman, D.E. and Rockwell, T.K., 1986. Neotectonics of the Elsinore fault in Temescal Valley, California, in P.L. Ehlig (ed.), *Neotectonics and faulting in southern California*, Geological Society of America Cordilleran Section fieldtrip guidebook, 159-166.
- Rockwell, T.K., McElwain, R.S., Millman, D.E. and Lamar, D.L., 1986, Recurrent late Holocene faulting on the Glen Ivy North strand of the Elsinore fault at Glen Ivy Marsh: in Guidebook and Volume on Neotectonics and Faulting in Southern California (P.



INQUA Focus Group Earthquake Geology and Seismic Hazards



paleoseismicity.org

- Ehlig, ed.), Cordilleran Section, Geological Society of America, p. 167-176.
- Rockwell, T., Bergmann, M., and Kenney, M., 2000, Holocene slip rate of the Elsinore fault in Temecula Valley, Riverside County, California. In *Geology and Enology of the Temecula Valley* (B. Birnbaum and K. Cato, eds), p. 105-118.
- Rockwell, T.K., K.M. Scharer, T.E. Dawson, 2016, Paleoseismology of the San Andreas Fault Zone. in Anderson, R. L., and Ferriz, H., *Applied Geology in California: Association of Environmental and Engineering Geologists Special Publication 26*, p. 721-756.
- Vaughan, P.R., and Rockwell, T.K., 1986. Alluvial stratigraphy and neotectonics of the Elsinore fault zone at Agua Tibia Mountain, southern California, in P.L. Ehlig (ed.), *Neotectonics and faulting in southern California*, Geological Society of America Cordilleran Section fieldtrip guidebook, 177-191.
- Vaughan, P.R., Thorup, K.M., and Rockwell, T.K., 1999, Paleoseismology of the Elsinore fault at Agua Tibia Mountain, southern California: *Bulletin Seismological Society of America*, v. 89, no. 6, p. 1447-1457.



Earthquake Archaeological Effects (EAEs) in Machupicchu. Preliminary results

Rodríguez-Pascua, M.A.1; Benavente Escobar, C.2; Rosell Guevara, L.N.2; Ttito Mamani, R.V.3; Champi Monterroso, P.3; Astete Victoria, F.3

- (1) Spanish Geological Survey (IGME). Madrid. Spain. ma.rodriguez@igme.es
- (2) Peruvian Geological Survey (INGEMMET). Lima. Peru. cbenavente@ingemmet.gob.pe; lrosell@ingemmet.gob.pe
- (3) National Archaeological Park of Machupicchu. Ministry of Culture. Cusco. Peru. vero20_10@hotmail.com; arqlpiedadz@hotmail.com; fastetemachupicchu@yahoo.es.

Abstract: The National Archaeological Park of Machupicchu (Cusco, Peru) is one of the most important archaeological sites in the world. The relevance of this site makes the necessity of the prevention against natural hazards. Peru is affected by large earthquakes from the Pacific Trench, and there are important active on-shore faults in the Andean Range that could generate destructive earthquakes ($M > 7$). In this study we show the preliminary result of the analysis of Earthquake Archaeological Effects (EAEs) and their differentiation from the effects generated by slope movement (creep) in Machupicchu. This type of study may be useful in the future for the prevention of earthquake effects in the archaeological site.

Key words: Machupicchu, Earthquake Archaeological Effects (EAEs), ancient earthquakes, creep slope movement.

INTRODUCTION

The archaeological site of Machupicchu, located in the Oriental Cordillera in the Andes (Fig. 1), is affected by different geological hazards, mainly landslides and erosional process, controlled and monitored by the National Archaeological Park. Some of these processes affected the archaeological buildings of the Inca culture like displacements in masonry blocks.

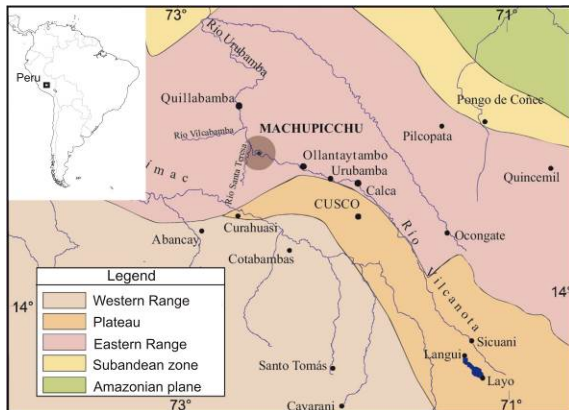


Figure 1: Physiographic setting of the National Archaeological Park of Machupicchu (Cusco, Peru) (modified from Carlotto et al., 2007).

The largest and more destructive earthquakes in Peru are generated by the subduction zone in the Pacific Coast (Perfettini et al., 2010). Also, there are active on-shore faults in the Andes Cordillera that could produce earthquakes with $M > 7$ (Macharé et al., 2009; Benavente et al., 2013). The analysis of Earthquake Archaeological Effects (EAE) affecting the archaeological remains could contribute to identify ancient earthquakes not recorded (Rodríguez-Pascua et al., 2011), and hence increasing the recurrence period of large earthquakes. The combination of EAE analysis with geomorphology and paleoseismology, allow identifying potential on-shore active faults that generated the earthquakes that affected Machupicchu in the past. These

earthquakes can be used in the future as a model to prevent future seismic effects in the archaeological site.

Applying EAE analysis in Archeoseismology, it is possible to discriminate the seismic origin of deformation affecting the architecture of the site from other origin (war, disrepair, etc.). The EAEs observed in masonry walls are (1) dipping broken corners and (2) displacement of masonry blocks (see Rodríguez-Pascua et al., 2011). These effects are “oriented deformations” and mapping each effect, the ground seismic vibration orientation can be depicted (Rodríguez-Pascua et al., 2017). We selected the Temple of Sun and the sector of the Temples to apply the EAE analysis. The Temple of Sun is a semi-circular structure well-oriented for ground shaking and fossilizing the seismic ground motion (Fig.2).



Figure 2: Temple of the Sun. Machupicchu (Cusco, Peru).

DEFORMATION STRUCTURES IN THE INCA BUILDINGS

Different authors described slope movements affecting to Machupicchu (e.g. Bouchard et al., 1992; Carlotto et al., 2007; Kauffmann, 2014). Furthermore, creeping movement slope down is affecting the Inca buildings as well. One example is the Principal Temple, affected by creep (Carlotto et al., 2007) (Fig. 3).



Figure 3: Horizontal displaced masonry blocks associated to creep movement in the Principal Temple.

The earthquakes can generate different deformation structures affecting archaeological sites. In consequence we have collected the data concerning the EAEs (Rodríguez-Pascua et al., 2011) and the geological structural analysis proposed by Giner et al. (2011). This classification was created for use in archaeological sites and historic buildings to distinguish seismic effects from other causes. The geological tool used for this purpose was the analysis of seismic strain structures. All of these deformational structures have been classified and studied according to the geological structural analysis of brittle deformation to estimate the orientation of the maximum horizontal movement of the ground. The initial hypothesis requires that most of the seismic damage must be oriented in relation to the seismic ground movement. Hence, we can compare oriented seismic deformation with others damages. Moreover, we have used the original Hiran Bingham photography's (1912) of Machupicchu in order to observe de EAEs and discriminate posterior effects that could produce the deformations (creep, restoration, tourist facilities, etc.).

Firstly we analysed the displaced masonry blocks (Fig. 4) and the dipping broken corners (Fig. 5), structures generated by horizontal movement of the ground and we can discard other effects like creeping slope down.

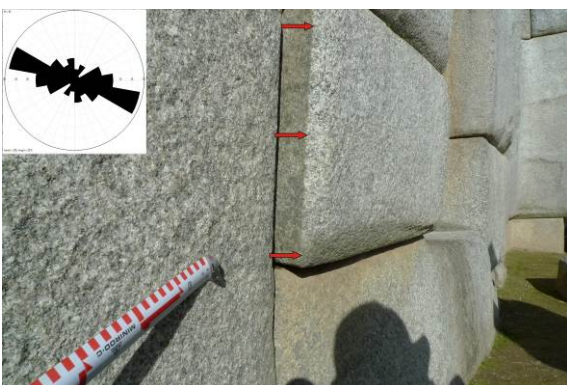


Figure 4: Displaced masonry block in the Temple of the Three Windows. The rose diagram show the medium ground movement of the structural analysis of total displaced masonry blocks data.

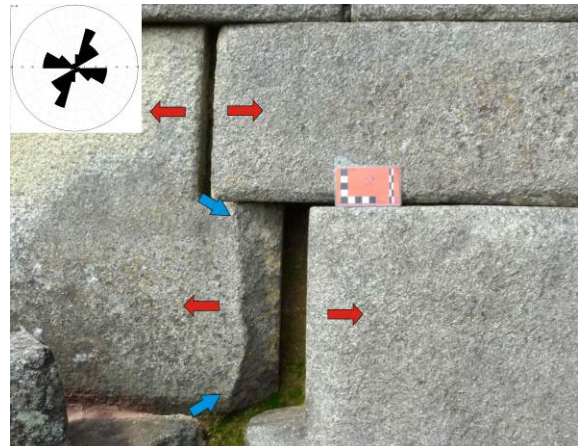


Figure 5: Displaced masonry blocks (red arrows) and dipping broken corner (blue arrows) in the Temple of the Sun (external wall). The rose diagram shows the medium ground movement of the structural analysis of total dipping broken corners data.

DISCUSSION AND CONCLUSIONS

We took 142 measures of deformation structures in in both sectors. The results obtained for the medium direction of ground movement are two: N025°E and N110°E. The direction of maximum slope in these sectors is N060°E. The two directions of ground movement are different with the slope movement and it is possible that could be related with two earthquakes. We plotted the accumulated displacement in masonry blocks in a histogram. Two main direction of ground movement were obtained: N060°-080°E and N100°-120°E (Fig. 6). The first one (N060°-080°E) is the maximum with an accumulated movement of 190 cm, related to slope movements (Fig. 6).

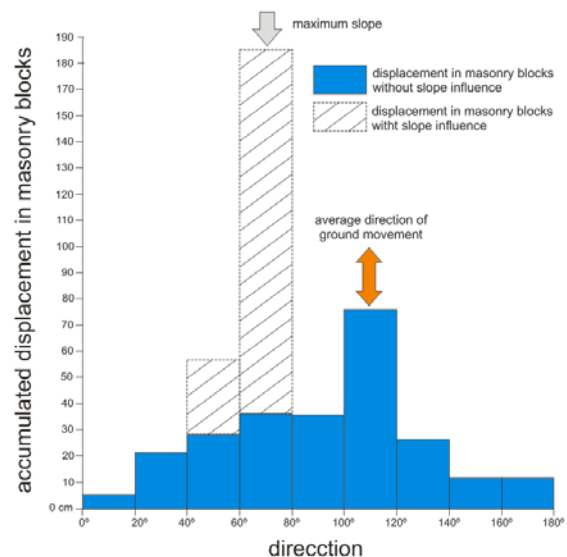


Figure 6: Histogram of the accumulated displacement in masonry blocks in the Temple of the Sun and in the Temples Sector (Principal Temple and Temple of the Three Windows).

The secondary orientation is N100°-120°E, with an accumulated movement of 76 cm (Fig. 6) and parallel to the medium ground movement direction N110°E obtained by the EAEs analysis. The direction of N025°E has a little



displacement of masonry blocks (25 cm), but it is good represented by dipping broken corners. For this reason, our hypothesis is that the directions of ground movements N025°E and N110°E are not related to slope movements and the seismic hypothesis is the most confinable with the present data. The direction N060°-080°E, parallel to the slope, is conditioned by gravity processes with the maximum of accumulated displacements in the archaeological site.

Acknowledgements: To the National Archaeological Park of Machupicchu (Ministry of Culture. Cusco. Peru) for his kindly and strong support during the field work. This work was supported by the Peruvian Project "Cusco-PATA" (Convenio 006-2016 FONDECYT) and by the Spanish Civil Society Rodríguez-Perucha.

REFERENCES

- Benavente, C., Delgado, F., Taipei, E., Audin, L., & Pari, W., 2013. *Neotectónica y peligro sísmico en la región de Cusco*. INGEMMET, Boletín Serie C: Geología Ambiental y Riesgo Geológico, 55. 245 p & 1 map.
- Bouchard, J., Carlotto, V., & Usselman, P., 1992. Machupicchu: Problemas de conservación de un sitio de ceja de selva. *Boletín del Instituto Francés de Estudios Andinos* 21 (3), 905-927.
- Carlotto, V., Cárdenas, J., & Fidel, L., 2007. *La geología en la conservación de Machupicchu*. Patrimonio y Geoturismo 1 (I), INGEMMET. 305P.
- Giner-Robles, J.L., Pérez-López, R., Silva, P.G., Rodríguez-Pascua, M.A., Martín-González, F. and Cabañas, L. (2012). Análisis estructural de danos orientados en el terremoto de Lorca del 11 de mayo de 2011. Aplicaciones en Arqueoseismología. *Boletín Geológico y Minero de España*, 123 (4): 503-513.
- Kauffmann, F., 2014. *Machu Picchu, Inca Treasure*. Gheller Ediciones. Lima. 129p.
- Macharé, J., Benavente, C., & Audin, L., 2009. *Síntesis descriptiva del mapa neotectónico 2008*. INGEMMET, Boletín, Serie C: Geodinámica e Ingeniería Geológica, 40, 103p.
- Perfettini, H., Avouac, J.P., Tavera, H., Kositsky, A., Nocquet, J.M., Bondoux, F., Chlieh, M., Sladen, A., Audin, L., Farber, D.L., and Soler, P., 2010. Seismic and aseismic slip on the Central Peru Megathrust. *Nature*, 465 (6), 78-81.
- Rodríguez-Pascua, M.A., Pérez-López, R., Silva, P.G., Giner-Robles, J.L., Garduño-Monroy, V.H., and Reicherter, K., 2011. A Comprehensive Classification of Earthquake Archaeological Effects (EAE) for Archeoseismology. *Quaternary International*, 242: 20-30.
- Rodríguez-Pascua, M. A., Pérez-López, R., Garduño-Monroy, V.H., Perucha, M.A., Israde-Alcántara, I., 2017. Estimation of the epicentral area of the 1912 Acambay Earthquake (M 6.9, Mexico) determined from the earthquake archaeological effects (EAE) and the ESI07 macroseismic scale. *Quaternary International*, in press: doi.org/10.1016/j.quaint.2017.06.045.



The record of ancient and historic earthquakes in the archaeological site of Idanha-a-Vela (Central Portugal; Iberian Peninsula)

Rodríguez-Pascua, M.A.(1), Giner Robles, J.L.(2), Silva, P.(3), Pérez López, R.(1), Perucha, M.A.(1), Elez, J.(3), Bardaji, T.(4), Roquero, E.(5), Sánchez Ramos, I.(6), Morin de Pablos, J.(7)

- (1) Spanish Geological Survey (IGME). Madrid. Spain. ma.rodriguez@igme.es; r.perez@igme.es; ma.perucha@igme.es.
- (2) Dpto. de Geología y Geoquímica, Universidad Autónoma de Madrid, Cantoblanco, Madrid, Spain. jorge.giner@uam.es.
- (3) Dpto. de Geología, Universidad de Salamanca, Escuela Politécnica Superior, Avila, Spain. pgsilva@usal.es; jelezv@gmail.com.
- (4) U.D.Geología, Universidad de Alcalá, 28871- Alcalá de Henares, Madrid, Spain. teresa.bardaji@uah.es.
- (5) Dpto. de Edafología, Universidad Politécnica de Madrid, Spain. elvira.roquero@upm.es.
- (6) Dpto. de Prehistoria y Arqueología. Fac. de Filosofía y Letras, Universidad Autónoma de Madrid, Spain. isabelm.sanchez@uam.es.
- (7) Dpto. Arq., Pal. y RR. Culturales de AUDEMA. Madrid. Spain. jmorin@audema.com.

Abstract: The western zone of the Iberian Peninsula is of moderate seismicity, but there is important paleoseismic evidence that indicate the occurrence of active faults with stronger seismic potential. Until now, this evidence has not been quantified or summarized in a manner that provides meaningful and useful data for better understanding seismic hazard risk. Here, Earthquake Archaeological Effects (EAEs) were applied to observations from Idanha-a-Vela in order to resolve this question. Results are showing the first archaeoseismic evidence that records almost two earthquakes: one during the end of the Roman period (4th century AD) and the second related to the AD 1755 Lisbon earthquake. The Roman earthquake is the oldest one identified in the historical period, and not documented before. The EAEs associated to this ancient earthquake (4th century AD) show a damage directivity (i.e. direction of ground movement) in a N157°-189°E orientation, compatible with the location of the active fault of Ponsul (10 km south). The EAEs affecting pre-18th century buildings display a larger dispersion in a N150°-240°E orientation, which can be reasonably related to far field effects of the AD 1755 Lisbon earthquake.

Key words: Idanha-a-Vela, Earthquake Archaeological effects, induced effects, Roman period, Lisbon Earthquake.

INTRODUCTION

Idanha-a-Vela is an exceptionally preserved archaeological site located on the western side of the Iberian Peninsula (Portugal). The site is located in the Palaeozoic Iberian Massif, close to one of the most tectonically active structures of Portugal: The Ponsul Fault (Fig. 1) (Cabral, 1995; 2012).

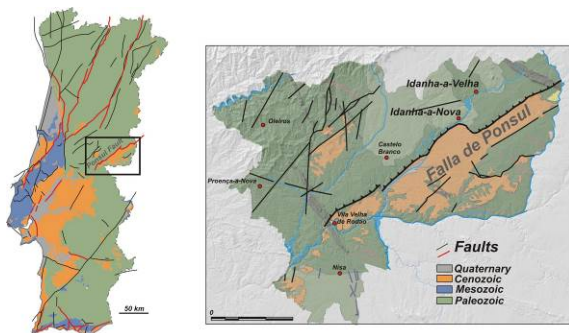


Figure 1: Geological setting of the Idanha-a-Vela archaeological site and the Ponsul Fault.

This site has a continuous archaeological record from the Roman period (1st century AD) until the 20th century. The Roman remains present evidence of a large-scale rebuilding of the city during the 3th century AD (Sanchez Ramos and Morin, 2017). The later cultures common in the Iberian Peninsula (Visigoth, Islamic and Christian) are represented in Idanha-a-Vela as well (Sanchez Ramos and Morin, 2017). The buildings of these different periods have deformational structures. We

applied archaeoseismological techniques in order to study the orientation of the deformation structures and determine their compatibility with the propagation of the seismic waves coming from feasible near-field seismic sources in the zone or far-field ones (i.e. 1755 Lisbon Earthquake).

METHODOLOGY

We have analysed EAEs preserved in the archaeological site from a range of chronologically distinct cultural periods (Roman, Visigoth, Islamic and Christian). Earthquakes are capable of generating different deformation structures that affect archaeological structures, so there is some variation on how these features are interpreted (REF, REF). We have collected EAEs as defined and proposed by Rodríguez-Pascua et al. (2011) and the geological structural analysis proposed by Giner et al., (2011). This specific classification was created for use in archaeological sites and historic buildings to discriminate seismic effects from other causes. The geological tool used for this purpose is the analysis of seismic strain structures conventionally used in structural geology. All of these deformational structures have been classified and studied according to the tenets of geological structural analysis to estimate the orientation of the maximum horizontal movement of the ground. The initial hypothesis requires that most of the seismic damage must be oriented in relation to the seismic ground movement, and this allows us to compare oriented seismic data with non-oriented damage of aseismic origin. This is critical in the effort to distinguish between causal mechanisms.



EARTHQUAKE ARCHAEOLOGICAL EFFECTS (EAEs)

Two primary sets of deformations were identified; the earlier associated to Roman remains, and a more recent set of deformations in later pre-18th century buildings (Rodríguez-Pascua et al., 2017). These two groups of deformations allow us to estimate the dates of the possible causative events.

Roman defensive wall

This defensive wall is intensely deformed in the south sector of the structure. In this zone the original, external stone-cover of the wall is absent, and displaced masonry blocks are present (Fig. 2). This part of the wall was built over unconsolidated Quaternary sediments of the lower terrace level of the Ponsul River.



Figure 2: Displaced masonry blocks in the south sector of the Roman defensive wall.

The western sector of the defensive wall is affected by a visible horizontal folding (Fig. 3), in addition to displaced masonry blocks. The fold axes are oriented N0145°E with a mean wavelength of 15-20 m (Fig. 4).



Figure 3: Folded Roman defensive wall in the west sector of the site.

The elevation of the ground level on the internal side of the wall (within the city walls) is higher than outside (Fig. 5), as a consequence of anthropogenic infilling and levelling of the area with sands, debris and rubble. The deformation produced by the folding of the wall affected the artificial

infilling, triggering collapses of columns in opposite sense in depending if the infilling was affected by push in or pull out the wall (see Fig. 5). The direction of these collapses is perpendicular to the direction of ground movement that generated the folds in the wall, for this reason could be confused with other events. For these deformational structures generated by the space accommodation of other deformations we propose the term “induced effects” (Fig. 5), which could not be confused with other effects. The “induced effects” are not generated directly by the seismic waves, they are generated like a secondary effect related to the development of the main deformations generated by the earthquake. For this reason, these “induced effects” could be oriented in different directions of the EAEs.

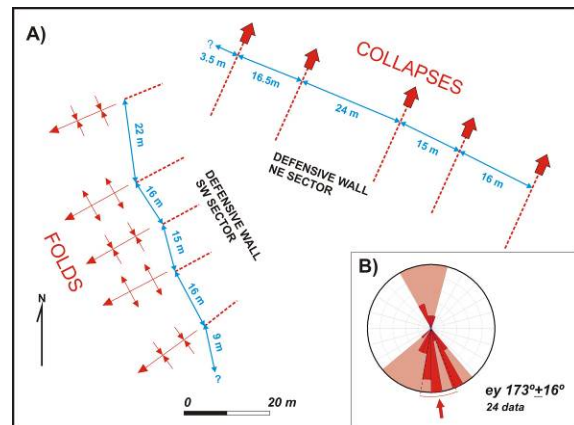


Figure 4: Schematic sketch of the: A) folds and collapses of the Roman defensive wall and B) rose diagram of medium direction of ground movement.

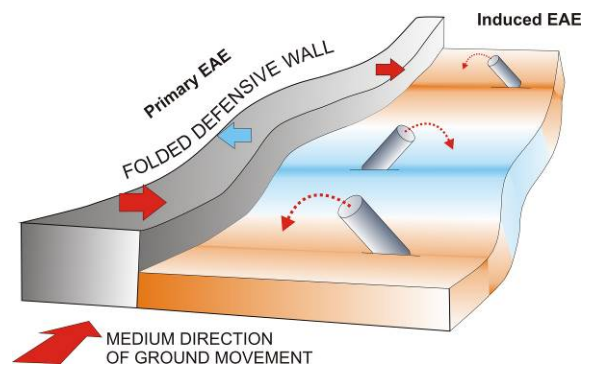


Figure 5: Interpretative sketch of the genesis of “induced effects” of EAES. Note the different ground-level at the external and internal side of the wall (also folded).

The north sector of the defensive wall is generally well preserved, but it has several collapsed sections. There are several collapses in the basement (Fig. 6) separated from each other by 15-20m intervals (Fig. 4A). We took 24 data points from the wall (fold axes and collapse directions sense), the result is that the medium direction of ground movement is N173°E (Fig. 4B).



Figure 6: Collapses in the North sector of the Roman defensive wall.

Episcopal sector

This zone is related to houses and a public building of the Roman period which was transformed into a church during the Visigoth Period (5th- 8th centuries). The houses display tilted walls (Fig. 7), oriented collapses (in the same direction), folded walls, dipping broken corners and “induced effects” (the last ones close to the deformed city wall, like tilted and collapsed walls). All of these EAEs, excluding the “induced effects”, were generated by a ground movement of a mean N-S orientation, compatible with the deformations observed in the Roman remains.



Figure 7: Tilted walls in the Episcopal area close to the west Roman defensive wall.



Figure 8: Displaced masonry blocks in the arches of the Medieval Bridge.

Middle Age (12th-16th c.) Bridge.

The bridge has a Roman foundation, but underwent significant modifications during the Middle Age and the 16th century. The horizontal direction of the bridge is N080°E and is folded in a perpendicular direction. The accommodation of the deformation related to the folds is visible in the arch by displaced masonry blocks (Fig. 8). The medieval renovations indicate that the deformations are not associated to ancient earthquakes and the most probable origin for these features is the 1755 Lisbon earthquake.

Main Church

This building was built between the 17-18th centuries AD. The main façade of the church has an E-W orientation and it is possible to identify several EAEs: displaced masonry blocks, dropped keystones in arches and dipping broken corners (Fig. 9). This is the same case of the middle ages bridge (Fig. 8), in that the orientation of the medium direction of ground movement and date of the built make that the most probable event that affect the church is the 1755 Lisbon earthquake.



Figure 9: Principal façade of the Main Church. Close view of the dropped key stone in the door, displaced masonry blocks (blue arrows) and dipping broken corners (orange arrows).



DISCUSSION AND CONCLUSIONS

The defensive Roman wall and the episcopal building record a robust set of Earthquake Archaeological Effects (EAEs), indicating a uni-directional damage with a mean N-S direction. The obtained damage orientation is congruent with seismic activity in the Ponsul Fault during the late 4th century AD (near field effects; Fig. 10A). This earthquake is not historically documented (there is no entry in conventional seismic catalogues such as REFERENCE) and constitutes the first ancient earthquake reported in Portugal. The most significant EAEs are associated to the defensive city-wall with folds and collapses. The horizontal folding affecting the defensive wall triggered associated deformations (collapsed and tilted structures), that we have labelled as “induced effects”. This is a new term in the classification of Earthquake Archaeological Effects (EAEs) and it has a key meaning. The identification of this new type of EAE may prevent mistakes in the interpretation on the seismic origin of the deformations. In more modern buildings (e.g., Main Church and a medieval bridge) the recorded EAEs display a dominant NE-SW orientation, related in this case to the far-field effects of the well-known AD 1755 Lisbon earthquake (far field effects; Fig. 10B).

Acknowledgements: This work has been funded by the research projects: “Arqueología de los Paisajes urbanos en la Antigüedad tardía en la Península Ibérica (450-850)” (Ref: 2016-T1/HUM-1113) and MINECO-FEDER research projects CGL2015-686 67169-P: QTTECTSPAIN (USAL). This is a contribution of the Spanish Working Group QTTECT-AEQUA.

REFERENCES

- Cabral, J., 1995. *Neotectónica em Portugal Continental*. Memórias do Instituto Geológico e Mineiro, 31, Lisboa: 265 p.
- Cabral, J., 2012. Neotectonics of mainland Portugal: state of the art and future perspectives. *Journal of Iberian Geology*, 38 (1): 71-84.
- Giner-Robles, J.L., Pérez-López, R., Silva, P.G., Rodríguez-Pascua, M.A., Martín-González, F. and Cabañas, L. (2012). Análisis estructural de danos orientados en el terremoto de Lorca del 11 de mayo de 2011. Aplicaciones en Arqueosismología. *Boletín Geológico y Minero de España*, 123 (4): 503-513.
- Rodríguez-Pascua, M.A., Pérez-López, R., Silva, P.G., Giner-Robles, J.L., Garduño-Monroy, V.H., and Reicherter, K., 2011. A Comprehensive Classification of Earthquake Archaeological Effects (EAE) for Archaeoseismology. *Quaternary International*, 242: 20-30.
- Rodríguez-Pascua, M.A., Giner Robles, J.L., Pérez López, R., Perucha, M.A., Silva, P.G., Elez, J., Bardají, T., Roquero, E., Sánchez Ramos, I., and Morín, J., 2017. Evidencias arqueosismológicas en el yacimiento arqueológico de Idanha la Vella (Portugal). In: *Arqueología No Invasiva. Proyecto Idave. Egítania, Idanha-a-Velha. Portugal*. Sánchez Ramos, I., and Morín, J. Editors. AUDEMA. 215 p.
- Sanchez Ramos, I., and Morin, J., 2017. *Arqueología No Invasiva. Proyecto Idave. Egítania, Idanha-a-Velha. Portugal*. Sánchez Ramos, I., and Morín, J. Editors. AUDEMA. 215 p.

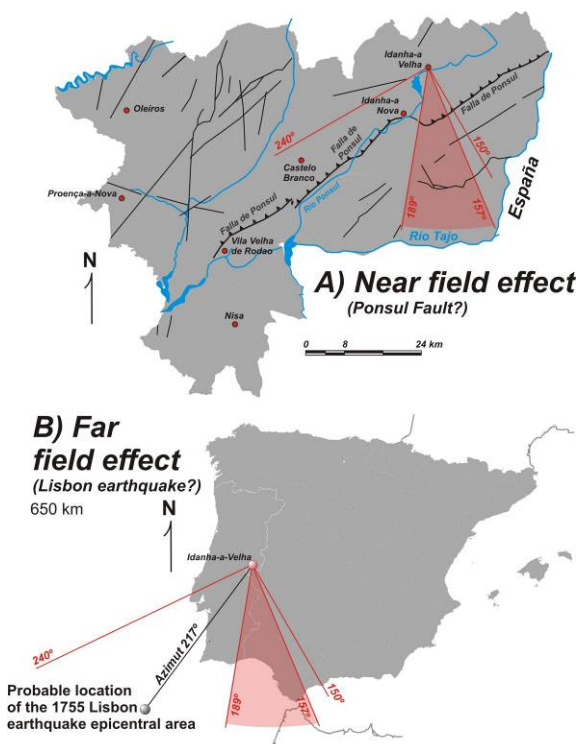


Figure 10: Mapping interpretation of the orientation of mean ground movement for: A) near field effects associate to the Ponsul Fault and B) far-field effects linked to the AD 1755 Lisbon earthquake.



Ground response analysis of the 8 October 2005 Kashmir earthquake (M_w 7.6): implications for historical and paleoearthquake seismic hazard assessment

Sana, Hamid

Department of Neotectonics and Thermochronology, Institute of Rock Structure and Mechanics, Czech Academy of Sciences, Prague 18209, Czech Republic. Email address of corresponding author: sana@irms.cas.cz

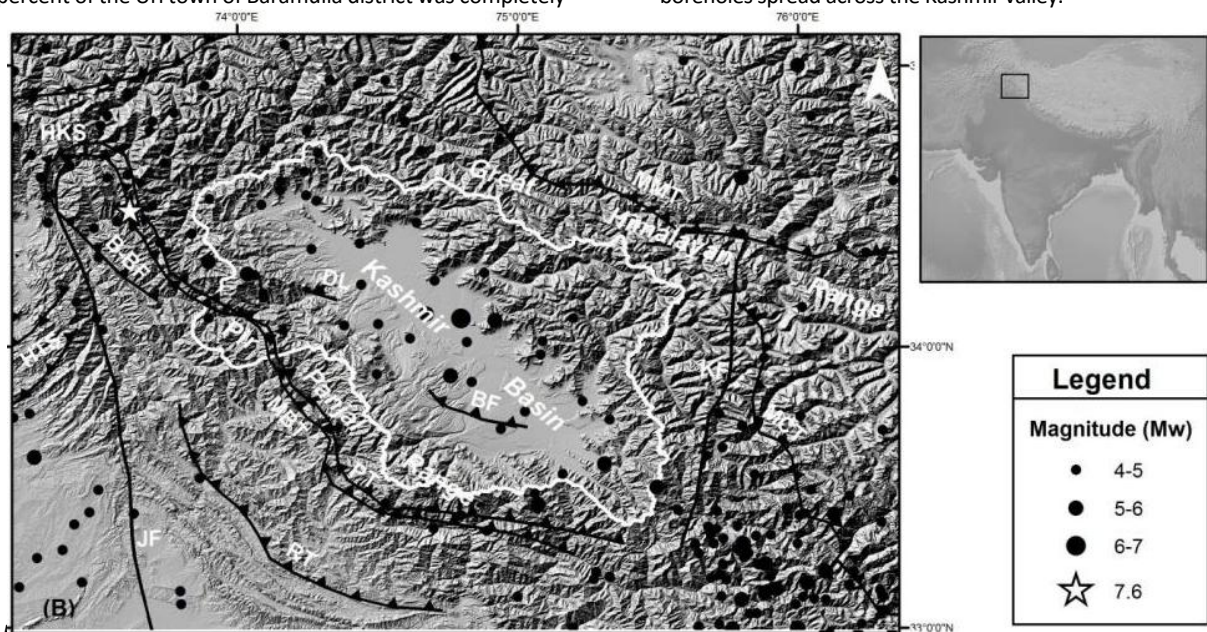
Abstract: The ground response during the 8 October 2005 Kashmir earthquake (M_w 7.6) using geotechnical SPT (N) boreholes spread across the Kashmir basin (NW Himalaya) is presented here. The first step was to develop the shear wave velocity (V_s 30) profile for each borehole, which were later interpolated to develop a V_s 30 map of the basin. The results show that site classes C and D are dominant in the basin according to the NEHRP site classification. The synthetic ground motions from this earthquake were then transmitted through each borehole from the engineering bedrock to the surface. The results demonstrate that the local site conditions amplify the ground motions and result in the unequal distribution of the resultant ground motions at the surface. Hence, for seismic hazard assessment of the Kashmir basin the incorporation of the ground response is required, not only for instrumental earthquakes but also for historical and paleo-earthquakes.

Key words: Kashmir basin, Earthquake, Ground response, Synthetic ground motion, shear wave velocity

INTRODUCTION

The 8 October 2005 Kashmir earthquake (M_w 7.6) was one of the most destructive earthquakes of the recent past. It resulted in massive damage of life and property in Jammu and Kashmir on both sides of the line of control (LOC). About 86,000 people were killed and 69,000 injured as a result of this earthquake. It mostly affected Pakistan-administered Kashmir but significant damage and destruction was caused in the Kashmir valley (Indian administered) as well, especially in the northwestern part. In the NW Kashmir basin Baramulla and Kupwara districts suffered severe damage, 80 percent of the Uri town of Baramulla district was completely

destroyed. At least 32,335 buildings collapsed in the Indian-administered part of Kashmir (Sana and Nath, 2017). The seismotectonic setting of the Kashmir basin is shown in figure 1. Here, the ground response of the Kashmir basin during this large magnitude earthquake is presented by adopting a geotechnical approach. Ground response evaluates the contribution of local site conditions (geology) in enhancing the ground motions during an earthquake. Hence, ground response analysis is an important aspect of the seismic hazard assessment of a region the cities located in the sedimentary basins. In this study, the geotechnical dataset consists of Standard Penetration Test (SPT N) boreholes spread across the Kashmir valley.



Crystalline Thrust (MCT), Main Boundary Thrust (MBT), Kishtwar Fault (KF), Panjal Thrust (PT), Reasi Thrust (RT), Jhelum Fault (JF), Bagh-Balakot Fault (B-BF), Hazara Thrust System (HTS), Balapur Fault (BF), Drangbal-Laridora Fault (DL), Hazara-Kashmir Syntaxis (HKS). The star represents the epicenter of 8 October 2005 Kashmir earthquake (M_w 7.6).



Shear wave velocity (V_{s30}) map of the Kashmir basin

The first and foremost step in ground response analysis is the generation of shear wave velocity profiles, which in this case were generated by developing soil type specific relationships between SPT (N) value and the shear wave velocity (V_{s30}). The distribution of boreholes in the basin is shown in figure 2. Using these relationships shear wave velocity profiles for each borehole were generated and later interpolated in the GIS environment to develop the shear wave velocity map of the Kashmir basin.

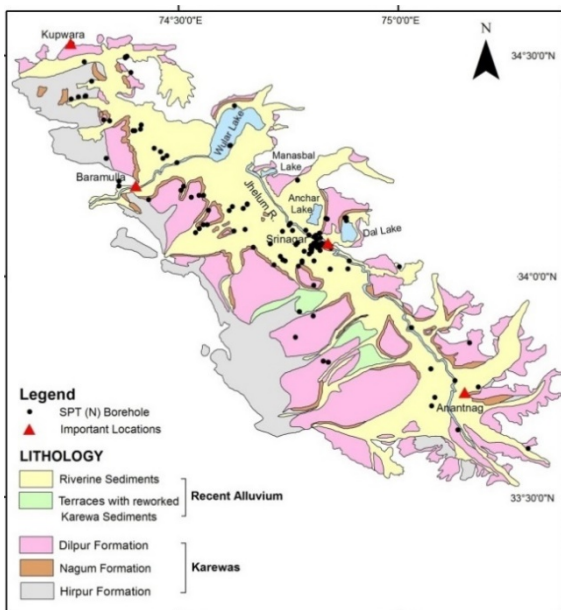


Figure 2: Lithology map of the Kashmir basin with SPT (N) borehole locations.

The National Earthquake Hazards Reduction Program (NEHRP) site classification was used to classify the Kashmir valley alluvium based on shear wave velocity. The NEHRP scheme uses shear wave velocity for site classification to a depth of 30 m (Table 1) for designing earthquake resistant infrastructure (Kramer, 1997). The results show that site classes C and D of the NEHRP classification dominate the Kashmir basin alluvium. The resultant shear wave velocity map of the Kashmir basin classified according to the NEHRP site classification is shown in figure 3.

Table 1: NEHRP site classification scheme (Kramer, 1997).

SITE CLASS	Rock/Soil Type	V_{s30} (m/sec)
A	Hard Rock	>1500
B	Rock	760-1500
C	Dense Soil/Soft Rock	360-760
D	Stiff Soil	180-360
E	Soft Soil	<180

Synthetic ground motions at the engineering bedrock level

Due to the non-availability of the ground motion records of this earthquake, the synthetic ground motions were generated using stochastic finite fault modeling (Motezedin and Atkinson, 2005) at each borehole location at the bedrock level throughout the basin. The synthetic seismograms at the most affected NW towns of Baramulla and Kupwara of the Kashmir basin are shown in figure 4a.

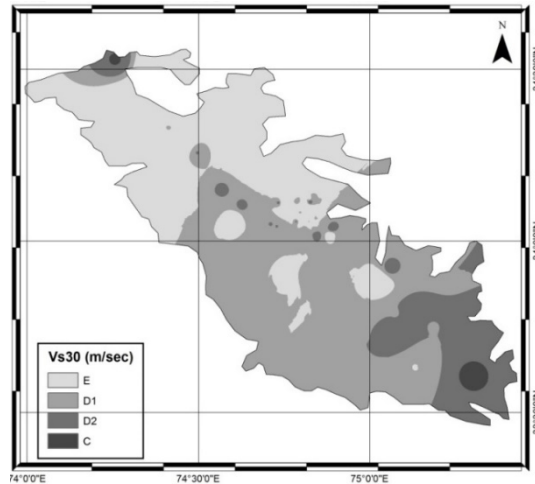


Figure 3: Shear wave velocity (V_{s30}) map of the Kashmir basin, classified according to the NEHRP site classification scheme.

Ground motions at the surface

These ground motions were later transmitted through the boreholes using the equivalent linear approach to evaluate the ground response. The results show that local site conditions play an important role in amplification and unequal distribution of ground motions travelling from the engineering bedrock to the surface. The synthetic seismograms of the 8 October 2005 Kashmir earthquake (M_w 7.6) at the surface in Baramulla and Kupwara in the Kashmir basin are shown in figure 4b.

The map generated from interpolation of all the ground motions (PGA) at every borehole is shown in figure 5.

DISCUSSION

The synthetic seismograms at the NW districts of Baramulla and Kupwara in the Kashmir basin clearly show the amplification of the ground motion travelling from the engineering bedrock to the surface. The synthetic ground motion map also clearly shows the unequal distributions of the peak ground acceleration (PGA) at the surface. The PGA (g) is of the order of 0.77 g in the NW part of the Kashmir basin, the most affected part of the basin during the 8 October 2005 Kashmir earthquake 2005 (M_w 7.6). Whereas, a PGA of $\geq 0.3 g$ is considered destructive to the engineering structures (Christenson, 1994). This encompasses the amount of damage that the NW part of the basin suffered. Thus, the results of this study are in agreement with the observed damage during the earthquake. Furthermore, the amplification and unequal distribution of synthetic ground motions clearly demonstrate the site effects.

The results show that seismic hazard assessment of the Kashmir basin without consideration of site effects is incomplete. Furthermore, apart from the recent instrumental earthquakes, damage during historical earthquakes is also reported in the Kashmir basin (Ahmad et al. 2014). So, the site classification and site effect in the Kashmir basin presented in this study should be taken into consideration while assessing the deterministic hazard scenario due to historical- and paleo-earthquakes.

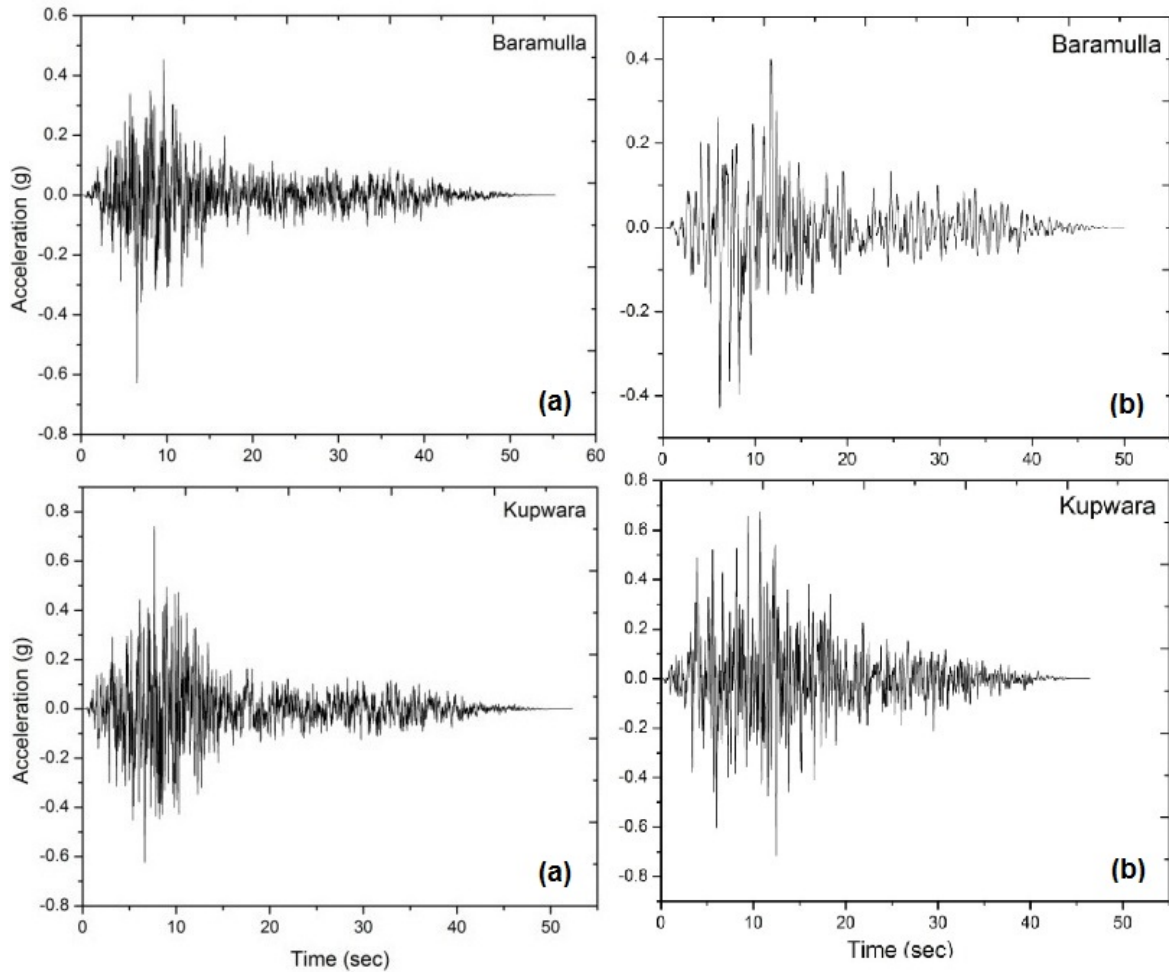


Figure 4: Synthetic ground motions of the 8 October 2005 Kashmir earthquake (Mw 7.6) at Baramulla and Kupwara in the Kashmir basin at the engineering bedrock (a) and at the surface (b).

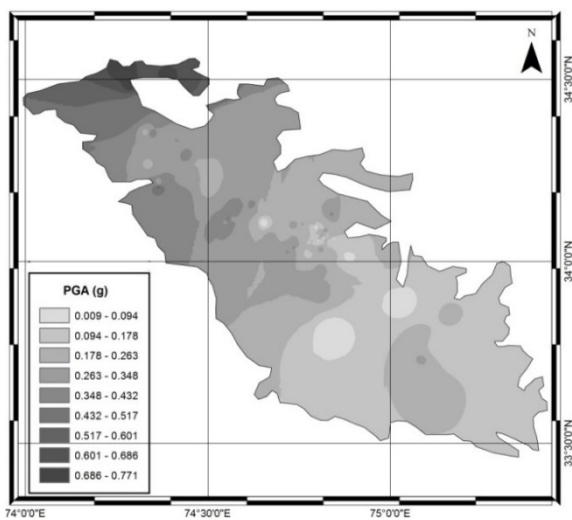


Figure 5: Synthetic ground motion (PGA) map of the Kashmir basin at the ground surface.

Acknowledgements: I'm thankful to CSIR-UGC India for the award of CSIR-UGC (JRF) NET Fellowship. I would also like to thank Institute of Rock Structure and Mechanics, Czech Academy of Sciences, Czech Republic for supporting me through Grant no. 343. I'm also thankful to the support of the long-term conceptual development research organisation RVO: 67985891, Czech Republic.

REFERENCES

- Ahmad, B., Sana, H., & Alam, A., 2014. Macroseismic intensity assessment of 1885 Baramulla Earthquake of northwestern Kashmir Himalaya, using the Environmental Seismic Intensity scale (ESI 2007). *Quaternary International* 321, 59-64.
- Christenson, G.E., 1994. Ground Shaking in Utah. Utah Geological Survey, Public information Series 29, 1-4.
- Kramer, S.L., 1997. *Geotechnical Earthquake Engineering*, Prentice Hall, New Jersey, 653 p.
- Motezedin, D., & Atkinson, G.M., 2005. Stochastic finite-fault modeling based on a dynamic corner frequency. *Bulletin of the Seismological Society of America* 95(3), 995-1010.
- Sana, H., & Nath, S.K., 2017. Seismic Source Zoning and Maximum Credible Earthquake Prognosis of the Greater Kashmir Territory, NW Himalaya. *Journal of Seismology* 21(2), 411-424.



The M7 2016 Kumamoto, Japan, Earthquake: 3D coseismic deformation from differential topography

Scott, Chelsea (1), Arrowsmith, Ramon (2), Lajoie, Lia (3), Nissen, Edwin (4), Maruyama, Tadashi (5), Chiba, Tatsuro (6)

- (1) School of Earth and Space Exploration, Arizona State University, Tempe, Arizona, USA. cpsott1@asu.edu;
- (2) Arizona State University, Arizona, USA;
- (3) Colorado School of Mines, Colorado, USA;
- (4) University of Victoria, Victoria, Canada;
- (5) Geological Survey of Japan, Japan;
- (6) Asia Air Survey Co., Japan.

Abstract: The April 2016 Kumamoto earthquake sequence ruptured the Hinagu and Futagawa faults on the Kyushu Island of southwestern Japan. Our work concentrates on the M7 mainshock, which ruptured 30km of fault length with an oblique strike-slip mechanism and surface slip exceeding 2m. We present 3D near-fault displacements determined from the differencing of high-resolution topography acquired before and after the mainshock. To examine the mechanical properties of the shallow fault zone, we jointly invert the near-field lidar and InSAR displacements to solve for distributed fault slip. Our earthquake source inversion suggests that fault slip is depleted in the upper 100m of the crust relative to 500m depth. A comparison to published field measurements suggests additional slip depletion near the surface. Differential topography and InSAR data resolve slip throughout the seismogenic zone and are indicative of the physical processes that control the transmission of slip from the shallow crust to the surface.

Key words: Earthquake deformation, differential topography, InSAR

INTRODUCTION

Observations of coseismic deformation place valuable constraints on the location of active faults, the distribution of slip in the seismogenic zone, and the mechanical properties of the fault volume. Near-fault displacements from differential topography bridge the observational gap between on-fault field measurements of offset and InSAR displacements that determine the far-field deformation but often lose coherence near the fault. We use near-field displacements to study the behavior of the shallow fault zone and the localization of fault slip. Multiple previous studies including *Rockwell et al.* [2002], *Nissen et al.* [2014] and *Milliner et al.* [2015] show significant distributed surface deformation within ~100 m of the fault. To quantify this near-surface depletion of shallow fault slip, we construct a distributed slip model from near-field differential lidar topography and far-field InSAR displacements. Our results show that differential topography and InSAR datasets place

constraints on fault slip in the upper portion of the seismogenic zone and contribute to a deeper understanding of the mechanical properties of the fault.

The well-documented near-fault surface displacements produced by the April 16 2016 M7 Kumamoto, Japan, earthquake offer unusual insight into the behavior of the shallow fault zone. We present 3D near-fault displacement fields constrained from the differencing of high-resolution topography acquired before and after the mainshock. We examine two approaches for quantifying depth-dependent variations in fault slip. First, we calculate differential displacements at increasing apertures across the fault. Second, we solve for fault geometry and distributed slip in a joint-inversion of the near-field lidar and far-field InSAR displacements. Both approaches suggest that fault slip is depleted in the upper 100 m of the crust relative to 500 m depth. A comparison of the modeled slip to published field

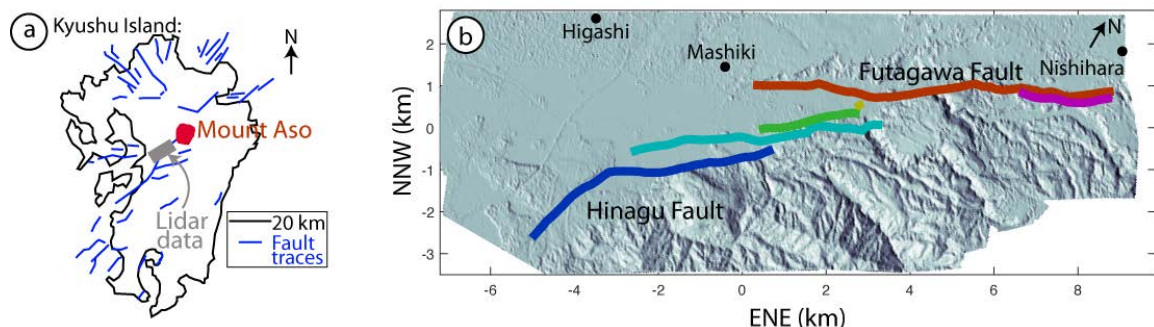


Figure 1: (a) Kyushu island of southwestern Japan. Grey box: location of lidar datasets acquired before and after the mainshock. Blue lines: faults from the Active fault database of Japan [AIST, 2017]. (b) Shaded relief map produced from the lidar elevations. Colored lines indicate fault segments that ruptured in the M7 Kumamoto earthquake, and the color corresponds to the slip profile in Figure 3.



measurements suggests an additional depletion of slip from a 100 m depth to the surface. The high surface strains of 1 to 4% in the ~100 m surrounding the fault suggest that the elastic strength of rocks is exceeded in the fault volume and that the depleted fault slip is accommodated by off-fault folding and fracturing at a finer scale than our analysis.

METHODS

Lidar data: Motivated by the M_w 6.2 foreshock on 14 April 2016, the Asia Air Survey Company acquired the pre-mainshock lidar dataset on 15 April 2016 at the location shown in Figure 1. The post-mainshock dataset was acquired on 23 April 2016 with the same pilot, aircraft, and lidar instrument as the first dataset. The pre- and post-mainshock datasets have shot densities of 2.5 and 3.5 points/m², respectively.

3D deformation: We use a windowed implementation of the piecewise Iterative Closest Point algorithm [ICP; Besl and McKay, 1992; Chen and Medioni, 1992] to determine the 3D surface deformation field produced by the M7 Kumamoto earthquake shown in Figure 2. We calculate the deformation at a set of core points from the optimal

rotation and displacement required to align 50 m windowed subsets of the pre- and post- earthquake point cloud data. We implement the LIBICP software developed by Geiger et al. [2012]. The deformation of the pre-earthquake point cloud dataset (PC_{pre}) that produces the deformed point cloud ($PC_{pre}^{deformed}$) is,

$$PC_{pre}^{deformed} = \begin{pmatrix} 1 & -\gamma & \beta \\ \gamma & 1 & -\alpha \\ -\beta & \alpha & 1 \end{pmatrix} PC_{pre} + \begin{pmatrix} t_x \\ t_y \\ t_z \end{pmatrix}, \tag{1}$$

where α , β and λ , are rotations about the x, y and z axes, and t_x , t_y and t_z are translations in the x, y, and z directions. The solution is penalized for misalignments between $PC_{pre}^{deformed}$ and the post-earthquake point-cloud dataset.

We develop an approach for computing displacement uncertainty, and demonstrate that the performance of the ICP method depends on the local topographic roughness. Errors range from 10 cm over higher relief and forested areas to 25 cm over flatter agricultural lands.

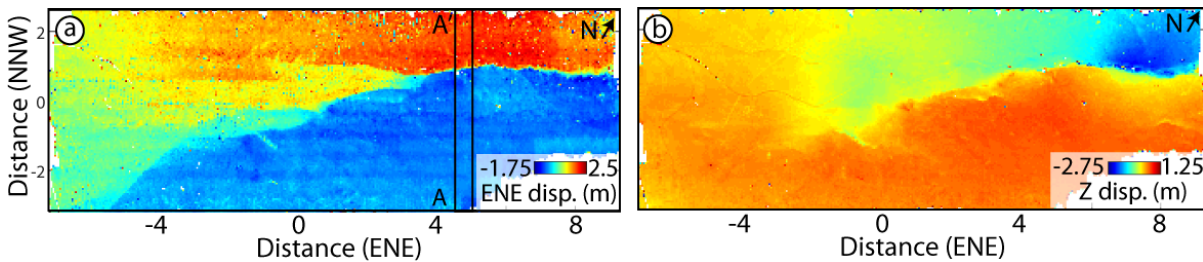


Figure 2: Iterative Closest Point (ICP) results showing (a) the east-northeast and (b) the vertical displacement fields for the 2016 M7 Kumamoto earthquake. The A-A' transect is shown in Figure 4.

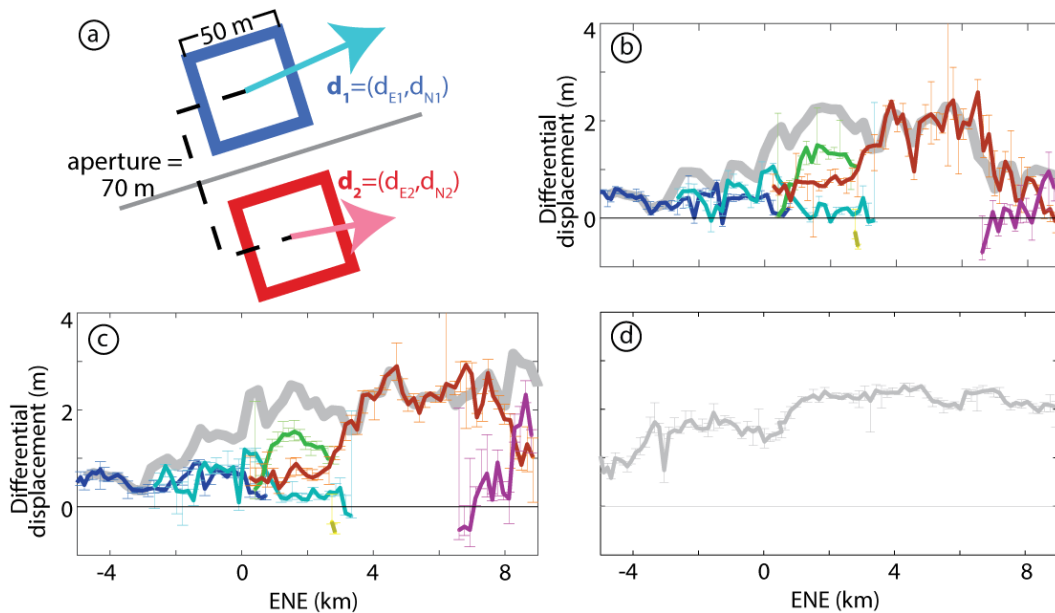


Figure 3: Right-lateral ICP differential displacements. (a) Schematic illustration showing the geometry of the differential displacement calculation over an aperture of 70 m. The grey line is the fault trace. The light blue and pink arrows show the displacement calculated from the pre- and post- earthquake point cloud data in the blue and red boxes, respectively. (b) Differential displacement calculated at an aperture of 70 m as illustrated in (a). The colored lines correspond to individual fault segments shown in Figure 1b. The thick grey line is the summed slip on all fault segments within a moving window. (c) Differential displacements calculated at an aperture of 200 m. (d) Differential displacements calculated at an aperture of 2000 m. This larger aperture calculation represents the summed displacement from all faults.

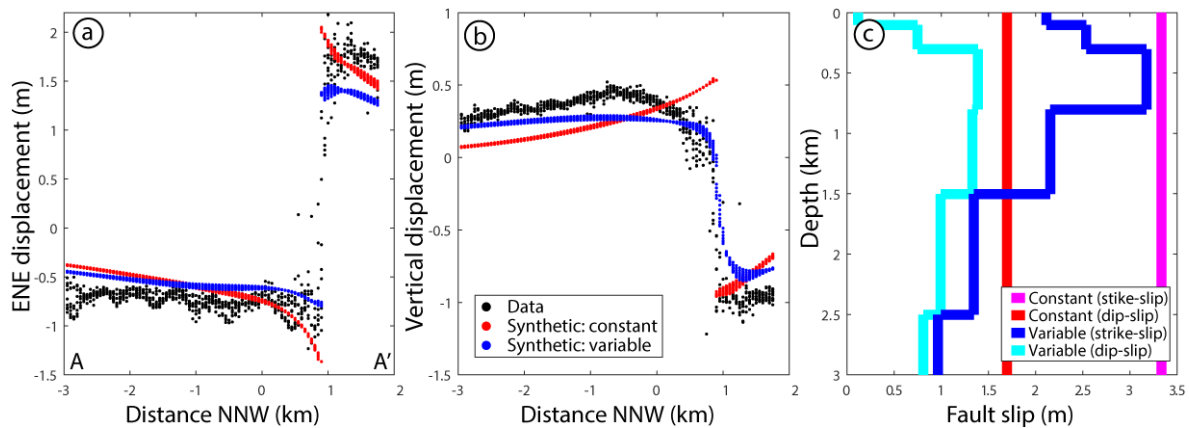


Figure 4: Earthquake source inversion results along the A-A' transect in Figure 2a. (a) ENE displacement showing ICP displacements (black), surface displacements produced by a fault model where slip is constant with depth (red) and varies with depth (blue). (b) Vertical displacement with the same colors as in (a). (c) Depth vs. fault slip: Strike-slip (pink) and dip-slip (red) profiles when slip is constant with depth. Strike-slip (blue) and dip-slip (light blue) when slip varies with depth. Slip continues to decrease with depth for the depth-dependent slip model.

Differential displacement: We calculate displacement discontinuities from ICP displacements at points that lie on opposite sides of the fault as a metric for fault slip as shown in Figure 3a. We align the ICP coordinate system with the fault trace shown in grey. We separate the center of the ICP boxes by the aperture of interest. For a 70 m aperture, the ICP boxes are placed 70 m apart

leaving a 10 m buffer between the edge of the ICP box and the fault trace. We calculate the right-lateral displacement (d_r) by projecting the difference in displacement across the fault along the fault strike:

$$d_r = ((d_{E1}, d_{N1}) - (d_{E2}, d_{N2})) \cdot \langle \text{fault strike} \rangle \quad (2)$$

where d_{E1} and d_{N1} are the east and north displacements, respectively, on the northern side of the fault, d_{E2} and d_{N2} are the displacements on the southern side of the fault, and $\langle \text{fault strike} \rangle$ is a unit vector oriented parallel to the local fault strike.

Joint lidar and InSAR earthquake source inversion: We conduct a joint inversion of our lidar displacements and the InSAR data from Jiang *et al.* [2017] to constrain along-strike and depth-dependent variations in fault slip (Figure 4). We solve for the fault geometry in 500 m segments to capture the sub-kilometer complexity in the fault rupture pattern. Fault slip does not vary with depth in our 'depth-independent slip model.' In the 'depth-dependent slip model,' we solve for distributed slip in fault patches whose dimension increases with depth according to the decreased resolving power of the data [Lohman and Simons, 2005; Barnhart and Lohman, 2010]. For both slip models, we allow the rake to vary spatially and impose smoothing and minimum norm constraints on the fault slip.

DISCUSSION

The 16 April 2016 Kumamoto earthquake propagated from its epicenter near the town of Higashi (Figure 1) to the NNE- striking Hinagua fault [Yagi *et al.*, 2016]. The earthquake then ruptured the NE-striking Futagawa fault,

which hosted the dominant moment release. As shown in the ICP-derived displacement maps in Figure 2, the earthquake accommodated right-lateral and southeast-side-up motion. The Hinagua fault accommodated a maximum right-lateral slip of 0.5 m and negligible vertical slip. East of Mashiki, the earthquake ruptured a northern and southern strand of the Futagawa fault with right-lateral slip on the individual strands varying from 0.5-1.5 m and decimeter-scale vertical slip. When the two strands joined to a single strand, slip exceeded 2 m. The fault bifurcated to the ENE, and the fault stands accommodated 2 m of both right-lateral motion and subsidence distributed over 3 km.

We calculate differential displacement at apertures of 70 m, 200 m, and 2000 m as a measure of fault slip at increasing depths (Figure 3). The differential displacement calculated at an aperture of 70 m reaches a maximum of 2.25 m along the red segment of the Futagawa fault (Figure 1b). The summed displacement curve shows an roughly elliptical slip envelope beginning at the Hinagua fault that continues to grow as slip is transferred to the Futagawa fault. At the 200 m aperture, the differential displacement is equal to or exceeds the 70 m aperture displacement. At the 2000 m aperture, the differential displacement is smoother than at the narrower apertures, suggesting a dampening of the slip heterogeneity present closer to the fault. In the zone of fault bifurcation to the ENE, the differential displacement is 3 m at the 200 m aperture and decreases to 2.25 m at the 2000 m aperture. This suggests a concentration of off-fault deformation at a distance of 100 m to 1 km from the fault, likely indicating elevated fault slip at similar depths.

We compare the lidar and InSAR-derived earthquake source inversion results for the depth-independent and depth-dependent slip models along the segment of the Futagawa fault in the A-A' transect. The ENE lidar displacements show a 2.5 m displacement step along the fault (Figure 4a). The depth-independent slip model does not replicate the concavity of the displacement signal and overpredicts the fault offset by 1 m. The depth-dependent slip model replicates the concavity, yet underpredicts slip



by 0.5 m. The vertical displacement (Figure 4b) shows an on-fault offset of 1 m and additional distributed displacement over 1 km of the footwall. The depth-dependent slip model reproduces the concavity of the displacement signal yet underpredicts the surface slip. We conclude that the depth-dependent slip model replicates both the shape and the magnitude of the displacement signal better than the depth-independent model. The depth-dependent slip model suggests a maximum right-lateral slip of 3 m at 0.4 to 0.8 km depth (Figure 4c) that decays to 2.5 m at 0.1 to 0.4 km depth and to 2 m at the surface. The dip-slip reaches a maximum value of 1.5 m from depths of 0.4 to 1.5 km and decays rapidly near the surface.

CONCLUSION

We use the ICP algorithm to calculate the near-fault 3D coseismic displacements for the 2016 Kumamoto earthquake from pre- and post-earthquake lidar datasets. The displacement field illustrates the development of the rupture and the distribution of both on- and off-fault deformation. We combine near-field lidar and far-field InSAR displacements to solve for distributed fault slip throughout the seismogenic zone. These results show a depletion of fault slip in the upper 100 m of the crust. The high surface strains of 1 to 4% in the ~100 m that surround the fault suggest the depleted fault slip is accommodated as off-fault deformation.

We use high-resolution topography to infer slip at the shallow depths that are commonly elusive to seismic and geodetic datasets. Our observation of depleted slip in the upper 100 m of the crust has implications for the frictional properties of the shallow crust and the interpretation of earthquake behavior from the paleoseismic and geomorphic records. As more earthquakes are observed with lidar data, the earthquake community will be able to better understand the physics of shallow faults and the hazards posed by crustal faults.

Acknowledgements: C. Scott is supported by the US NSF Postdoctoral Fellowship 1625221.

REFERENCES

- Barnhart, W. D., and R. B. Lohman (2010), Automated fault model discretization for inversions for coseismic slip distributions, *J. Geophys. Res.*, *115*(B10), doi:10.1029/2010JB007545.
- Besl, P. J., and N. D. McKay (1992), A method for registration of 3-D shapes, *IEEE Trans. Pattern Anal. Mach. Intell.*, *14*(2), 239–256, doi:10.1109/34.121791.
- Chen, Y., and G. Medioni (1992), Object modelling by registration of multiple range images, *Image Vis. Comput.*, *10*(3), 145–155, doi:10.1016/0262-8856(92)90066-C.
- Geiger, A., P. Lenz, and R. Urtasun (2012), Are we ready for autonomous driving? The KITTI vision benchmark suite, pp. 3354–3361, IEEE.
- Jiang, H., G. Feng, T. Wang, and R. Bürgmann (2017), Toward full exploitation of coherent and incoherent information in Sentinel-1 TOPS data for retrieving surface displacement: Application to the 2016 Kumamoto (Japan) earthquake, *Geophys. Res. Lett.*, doi:10.1002/2016GL072253.
- Lohman, R. B., and M. Simons (2005), Some thoughts on the use of InSAR data to constrain models of surface deformation: Noise structure and data downsampling, *Geochem. Geophys. Geosystems*, *6*(1), doi:10.1029/2004GC000841.
- Milliner, C. W. D., J. F. Dolan, J. Hollingsworth, S. Leprince, F. Ayoub, and C. G. Sammis (2015), Quantifying near-field and off-fault deformation patterns of the 1992 M_w 7.3 Landers earthquake: Deformation of the Landers earthquake, *Geochem. Geophys. Geosystems*, *16*(5), 1577–1598, doi:10.1002/2014GC005693.
- National Institute of Advanced Industrial Science and Technology (AIST; 2017), Active fault database of Japan.
- Nissen, E., T. Maruyama, J.R. Arrowsmith, J. R. Elliott, A. K. Krishnan, M. E. Oskin, and S. Saripalli (2014), Coseismic fault zone deformation revealed with differential lidar: Examples from Japanese □7 intraplate earthquakes, *Earth Planet. Sci. Lett.*, *405*, 244–256, doi:10.1016/j.epsl.2014.08.031.
- Rockwell, T. K., S. Lindvall, T. Dawson, R. Langridge, W. Lettis, and Y. Klinger (2002), Lateral Offsets on Surveyed Cultural Features Resulting from the 1999 Izmit and Duzce Earthquakes, Turkey, *Bull. Seismol. Soc. Am.*, *92*(1), 79–94, doi:10.1785/0120000809.
- Yagi, Y., R. Okuwaki, B. Enescu, A. Kasahara, A. Miyakawa, and M. Otsubo (2016), Rupture process of the 2016 Kumamoto earthquake in relation to the thermal structure around Aso volcano, *Earth Planets Space*, *68*(1), doi:10.1186/s40623-016-0492-3.



Timing of Earthquakes during the past 800 years along the Peninsula Section of the San Andreas Fault Suggests Persistent 1906-like Behavior

Seitz, Gordon

California Geological Survey, 1900 S. Norfolk St., Suite 300, San Mateo, California, USA
Gordon.Seitz@conservation.ca.gov

Abstract: Evidence to support the existence of a distinct Peninsula San Andreas Fault segment has been largely based on fault geometry as opposed to paleoseismology. The presented new paleoseismic record allows an evaluation of the fault based on its earthquake behavior. The only historical earthquake that has clearly ruptured the Peninsular San Andreas Fault section is the 1906 M7.9 San Francisco earthquake. Trench exposures at the new Monte Bello site provide evidence for four events during the past 800 years. Preliminary interpretations of onsite geomorphic channel offsets appear consistent with a slip-predictable model. This new event record correlates well with on and offshore records spanning the North Coast San Andreas Fault, suggesting the Peninsula section of the San Andreas Fault may have only failed in 1906-type earthquakes that include surface rupture of the entire North Coast section of the San Andreas Fault during the past 800 years.

Key words: Peninsula San Andreas Fault Paleoseismology

INTRODUCTION

This investigation was motivated by the San Francisco Peninsula section of the San Andreas Fault significantly lagging behind other fault sections in terms of the existence of robust paleoseismic data. The 1906 M7.9 San Francisco Earthquake was the most recent event that ruptured this fault section, and until this study, it was nearly all that we knew aside from a high slip rate of about 20 mm/y (Blisnuik pers. com., Hall et al, 1999). What was not known is whether 1906-like earthquakes are common or the exception. This sparse paleoseismic data set leads to broad uncertainties in hazard forecasts. Current rupture scenarios are less informed because we simply cannot confidently evaluate the San Andreas Fault earthquake behavior without *additional records of past earthquakes.*

DISCUSSION

The geomorphic channel offsets at the site (fig. 1) are 7 m, 17 m and 67 m. The 7 m offset includes a smaller 3-4 m depression that appears to represent the most recent event, which would result in 4 m of lateral slip remaining for the penultimate event. Seven meters appears too large for the 1906 earthquake given Lawson's (1908) observation of about 1-2 m 2.5 miles north of the site. The 17 m offset results in an additional 10 m for the pre event 2 offset, again this appears large for an individual event, so we speculate that the 10 m offset may have resulted from two or more events, based on the incision and event horizon depths. These channels are only incised about 1.5 m on the alluvial fan that we trenched just 20 m to the north (fig. 1, 2), so a reasonable assumption is that these

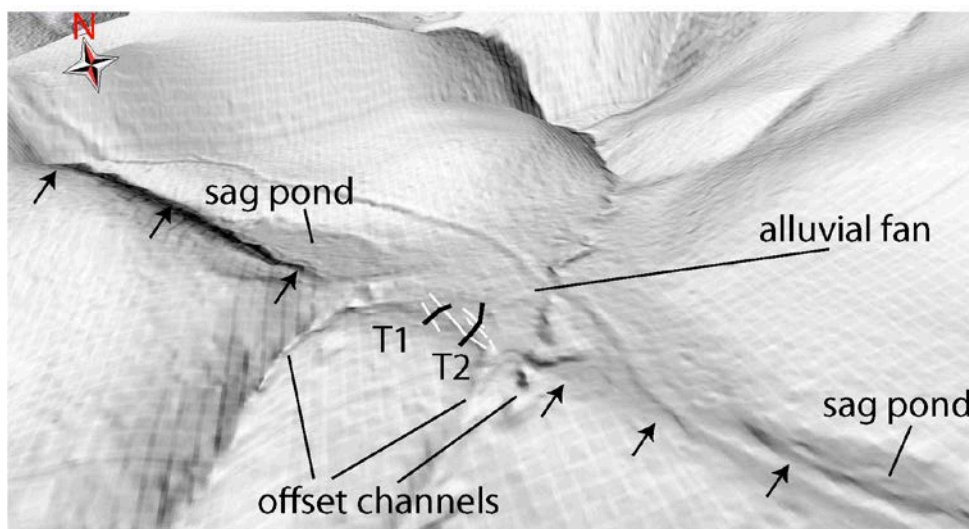


Figure 1: Oblique Lidar Hillshade Image of the San Andreas Fault and the Monte Bello Site. The site is located on an alluvial fan that has formed on a fault-generated sidehill bench. The trenches T1 and T2 cross the fault zone and the primary fault trace which is expressed as an uphill-facing scarp. Arrows indicate the general location of the fault, with detailed fault traces as white lines. Channel offsets are 7 m, 17 m and 67 m and their association with events are addressed in the text. Location: (MB; 37.3077°N, 122.1545°W).



channels have formed during the approximate same time span as the exposed stratigraphy. If this speculation is correct, it results in offsets of 3 m for 1906, 4 m for event 2, and a combined 10 m for events 3 and 4. This scenario is consistent with the slip rate estimates for the fault of about 20mm/year, which should average about 4 m of slip each 200 years. These offsets are all comparable to the 1906 displacements (Prentice and Schwartz, 1991).

The fault is expressed in both the trenches (fig. 3, 4) and the geomorphology as a fault at the base of a low, uphill-facing continuous scarp, and a parallel secondary fault trace located a few meters to the northeast. This secondary fault zone is only fully exposed in T2. The geomorphic channel offsets indicate that most of the lateral displacement occurs along the main fault, however some units, such as the unit 4 gravel, are not exposed on the west side of the secondary fault zone in T2 (fig. 4), suggesting lateral displacements of greater than 1.5 m, the trench width, have taken place. The faulting pattern, as shown on fig. 2, is a rough en echelon left-stepping fault trace, which in places is recognized in the surface geomorphology.

The preliminary chronology at the Monte Bello site has significant individual event age uncertainties (fig. 5), however, the number of four events for the overall time span of 800 years is robust. Paleoseismic records in the Santa Cruz Mountains (Fumal, 2012, Streig et al., 2014, Schwartz et al., 2014, Schwartz et al., 1998) clearly show more frequent

earthquakes, likely due to moderate size earthquakes nucleating near the seismically active creeping portion of the fault. Examples of these moderate size earthquakes include the historical 1838 and 1890 earthquakes (Streig et al., 2014, Schwartz et al., 2014). The event chronology at the Monte Bello site indicates the penultimate event occurred at 1700 AD, and although one cannot completely rule out the historical 1838 earthquake, it appears unlikely. Another observation that supports the notion that each of the Monte Bello site events are large 1906-like events are the large offsets of geomorphic channels discussed previously. It is permissible that the event record correlates completely with the North Coast San Andreas Fault paleoseismic records (Zhang et al., 2006, Schwartz et al., 2014), including the offshore turbidite record (Goldfinger et al., 2007), suggesting these represent long 1906-like ruptures. At this point we cannot prove that each of the past four Monte Bello site events correlates directly with each of the past four North Coast San Andreas Fault events, however we certainly cannot say they do not correlate.

It appears that the interpretation that requires the least amount of assumptions is that the Peninsula section of the San Andreas Fault has exclusively failed in 1906-type earthquakes during the past 800 years, in sync with the North Coast San Andreas Fault; whereas the Santa Cruz Mountains San Andreas Fault section experiences more frequent moderate size earthquakes in addition to large 1906-like earthquakes.

Structure from Motion DEM

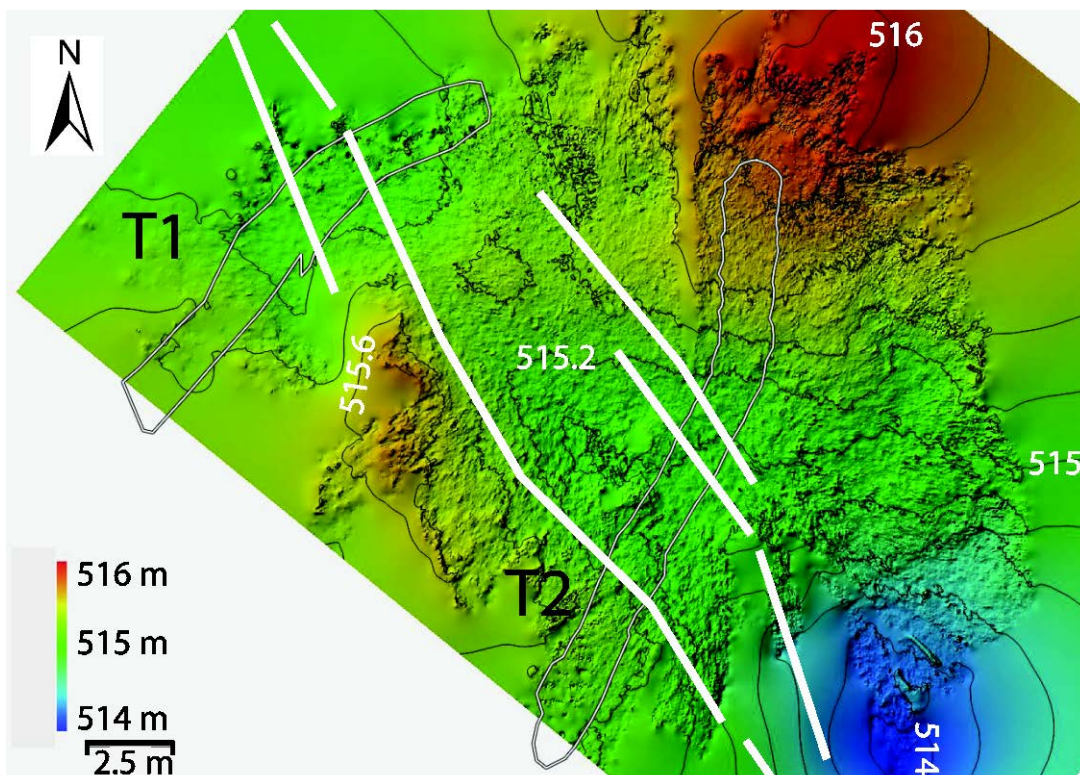


Figure 2: Structure from Motion DEM. This map shows the geomorphology and fault traces from the trench exposures. This DEM was created because the bare earth lidar under the tree cover was lower resolution. The contours are 0.2 m.

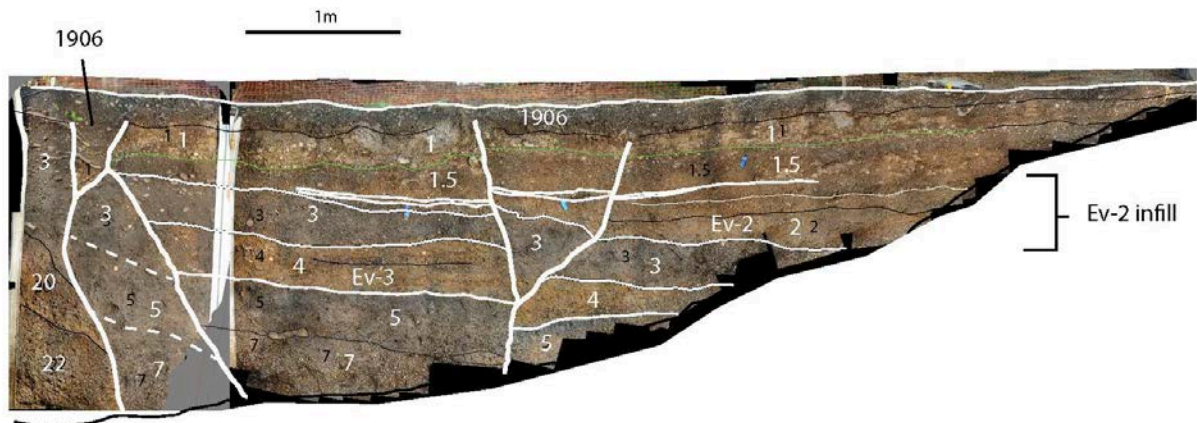


Figure 3: Trench 1 North Wall Exposure. The 1906 M7.9 San Francisco Earthquake was the most recent event that ruptured this fault section and in the exposures it extends into the surface soil. The top of unit 3 makes the penultimate event horizon (Ev-2). On the right fault trace unit 3 was downfaulted during Ev-2, and the post Ev-2 sediments deposited as an infill, units 2, 1.5, and 1, are only displaced by the 1906 event.

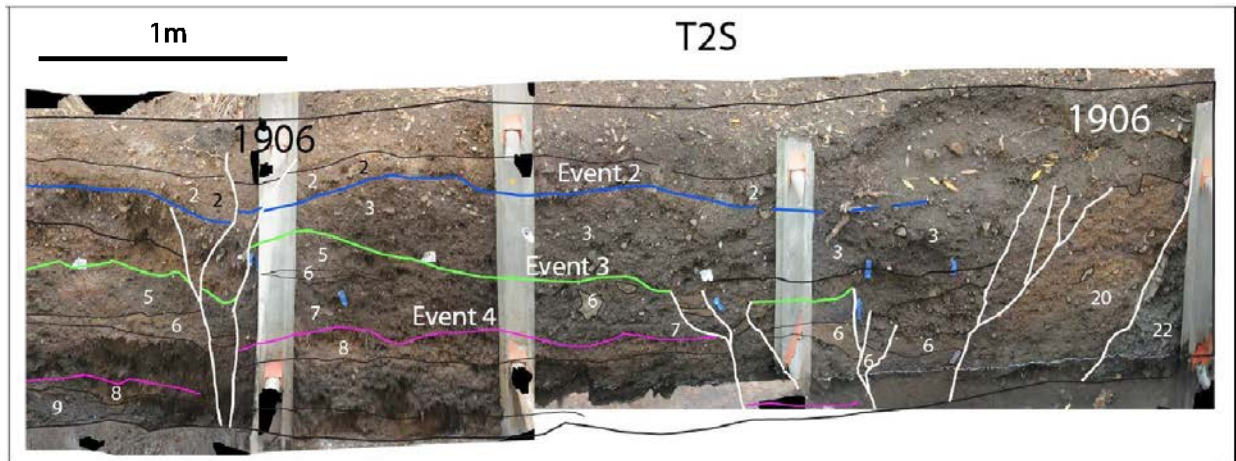


Figure 4: Trench 2 South Wall Exposure. The primary fault trace is on the right side faulting units 3 and 6 against unit 20. A parallel secondary fault trace is shown on the left side. Event horizons are labelled above the units.

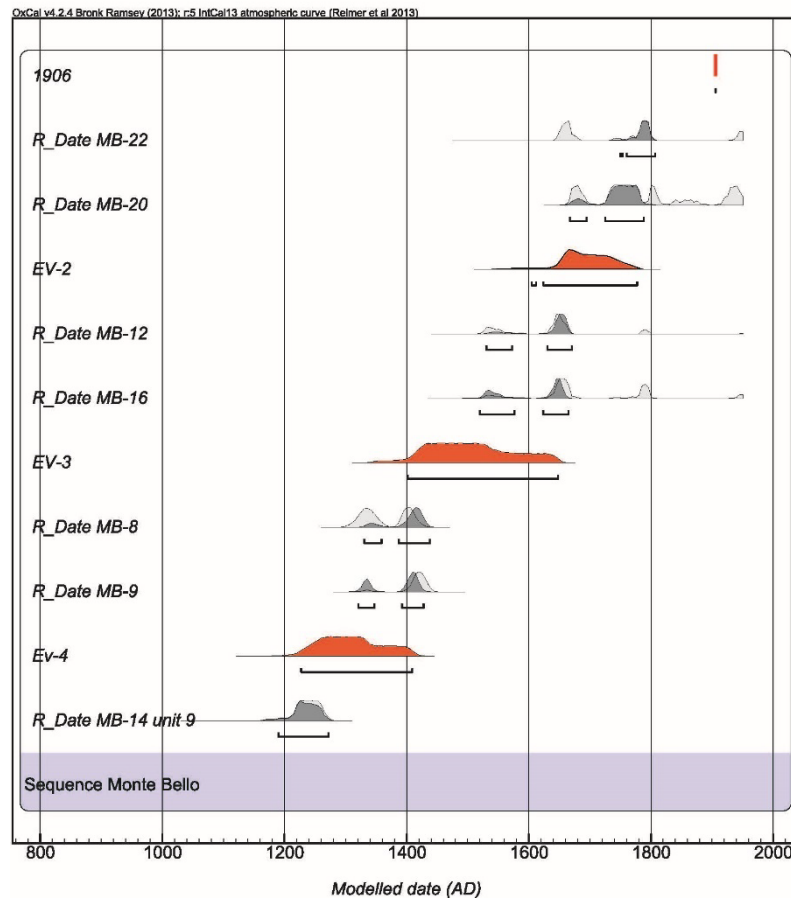


Figure 5: Chronological Age Model with Event Age Estimates. The event ages were modelled using the Oxcal program (Bronk Ramsey, 1994). The constraints that we used are the most recent event is assumed to be 1906, and the stratigraphic order of all samples, event ages were calculated between modelled sample ages. The age distributions are shown as: calibrated in light gray, modelled in dark gray and event age distributions in red.

Acknowledgements: This research was supported by the U.S. Geological Survey (USGS), Department of the Interior, National Earthquake Hazards Reduction Program.

REFERENCES

- Bronk Ramsey, C. (1994), Analysis of Chronological Information and Radiocarbon Calibration: The Program OxCal. *Archaeological Computing Newsletter*, 41, 11-16.
- Fumal, T. E., (2012), Timing of large earthquakes during the past 500 years along the Santa Cruz mountains segment of the San Andreas Fault at Mill Canyon, near Watsonville, California, *Bull. Seismol. Soc. Am.* 102, 1099–1119.
- Goldfinger, C., Morey, A.E., Nelson, C.H., Gutierrez-Pastor, J., Johnson, J.E., Karabanov, E., Chaytor, J., Eriksson, A., Shipboard Scientific Party, (2007), Rupture lengths and temporal history of significant earthquakes on the offshore and north coast segments of the Northern San Andreas Fault based on turbidite stratigraphy, *Earth and Planetary Science Letters*, 254, p.9-27.
- Hall, N.T., Wright, R.H., and Clahan, K.B., (1999), Paleoseismic studies of the San Francisco Peninsula segment of the San Andreas Fault zone near Woodside, California: *J. Geophys. Res.*, v. 104, no. B10, p. 23, 215-23,236.
- Lawson, A. C., (1908), The California Earthquake of April 18, 1906, Report of the State Earthquake Investigation Commission, Vol. 1, Carnegie Inst., Washington, 451 pp.
- Prentice, C.S., and D.P. Schwartz, (1991), Re-evaluation of 1906 surface faulting, geomorphic expression, and seismic hazard along the San Andreas Fault in the southern Santa Cruz mountains, *Bull. Seis. Soc. Amer.*, v. 81, 1424-1479.
- Schwartz, D.P., Lienkaemper, J.J., Hecker, S, Kelson, K. I., Fumal, T.E., Baldwin, J.N., Seitz, G.G., Niemi, T.M., (2014), The Earthquake Cycle in the San Francisco Bay Region: A.D. 1600-2012, *Bull. Seismol. Soc. Am.*, vol. 104, no. 3, p. 1299-1328.
- Schwartz, D.P., Pantosti, D., Okumura, K., Powers, T., and Hamilton, J., (1998), Paleoseismic investigations in the Santa Cruz Mountains: Implications for the recurrence of large magnitude earthquakes on the San Andreas Fault: *J. Geophys. Res.*, v. 103, p. 17,985-18,001.
- Streig, A. R., T. E. Dawson, and R. J. Weldon II, (2014), Paleoseismic evidence of the 1890 and 1838 earthquakes on the Santa Cruz Mountains section of the San Andreas Fault, near Corralitos, CA, *Bull. Seismol. Soc. Am.* 104, 285–300, doi: 10.1785/0120130009
- Zhang, H., Niemi, T., and Fumal T., (2006), A 3000-year record of earthquakes on the northern San Andreas Fault at the Vedanta marsh site, Olema, California: *Seismol. Res. Lett.*, v. 77, p. 176.



Lichenometric analysis of rocky fault scarps: The example of the Sencelles Fault (Balearic Islands, Spain).

P.G. Silva (1), E. Roquero (2), T. Bardají (3), R. Pérez-López (4), M.A. Rodríguez-Pascua (4), J.L. Giner (5), M.A. Perucha (4)

- (1) Dpto. Geología. Escuela Politécnica Superior de Ávila. Universidad Salamanca. 05003-Ávila.Spain. pgsilva@usal.es
- (2) Dpto. Edafología. E.T.S.I. Agrónomos. Universidad Politécnica de Madrid. Madrid, Spain. elvira.roquero@upm.es
- (3) U.D. Geología. Universidad de Alcalá. 28871-Alcalá de Henares (Madrid), Spain. teresa.bardaji@uah.es
- (4) Instituto Geológico y Minero de España (IGME). C/ Ríos Rosas, 23. 28003-Madrid Spain. ma.rodriguez@igme.es , r.perez@igme.es
- (5) Dpto. Geología. Facultad de Ciencias. Universidad Autónoma de Madrid. Cantoblanco. Madrid. Spain. jorge.giner@uam.es

Abstract: The Sencelles fault constitutes the main extensional structure of the Mallorca Island tentatively linked to the AD 1851 Palma earthquake (VII EMS.) The SE termination of the fault is featured by a linear bedrock fault scarp of c. 1 km in length. This rocky scarp display a significant horizontal banding, with up to five bands differentially colonized by lichens. The lichenometric analysis is based on the measurement of 155 specimens of “*Aspicilia calcarea*” (Ar) and “*Aspicilia radiosa*”(Ac) in tombstones (with inscribed dates) of the cemeteries of, Sta. María del Camí, Sta. Eugenia and Sencelles to obtain the lichen growth rates (LGR) for the zone. Lichenometric analyses indicate a strong sensitivity of LGR to location, orientation and position in vertical or horizontal stone surfaces. The obtained LGR for vertical lichen datasets indicate that the second fault ribbon (23-47 cm) can be related to the AD 1851 Earthquake, with exposure dates of AD 1853±18 (Ar) and AD 1855±59 (Ac).

Key words: Sencelles fault, lichenometry, AD 1851 Palma Earthquake, Mallorca, Spain.

INTRODUCTION

The NE-SW Sencelles fault constitutes the main extensional structure of the Mallorca Island (East Spain; Fig. 1). It has been active from the last c. 19 Ma, with a maximum accumulated throw of 750 m constituting the southern border of the Cenozoic Inca basin (Benedicto et al., 1993). Geologic and geomorphologic evidence prove its activity from Late Pliocene to Pleistocene times with a mean throw of c. 100 m for the last c. 3.0 Ma (Silva et al., 2001). This fault (7 km length) is subdivided in two main segments: The Sencelles segment and the Sta. Eugenia segment (Fig. 1). The last segment displays a length of c. 2.8 km between Puig Son Seguí and Sta. Eugenia and was tentatively identified as the suspect seismic source of the AD 1851 (VII EMS) Palma Earthquake (Silva et al., 2001).

The SW termination of the Sencelles Fault is featured by a NE-SW bedrock fault scarp c. 2.8 km long and 3.15 m (maximum) high facing to the NNW (Fig. 1). The scarp is developed on Plio-Pleistocene strongly cemented calcarenites (Benedicto et al., 1993). In this zone scarp height diminishes from 3.15 m in the East to its eventual die-out near the cemetery of Sta. Eugenia. Fault trenching analyses in this zone identified an upper earthquake colluvial wedge comprised by blocks of adjacent stone fences built-up over the bedrock fault scarp, burying artificial fillings containing post AD 1950 car-oil cans of “Ertolil” (Silva et al., 2005). These artificial fillings of the middle 20th century post-date the AD 1851 earthquake along the fault scarp and any other chronological data was available before the preliminary lichenometric analysis reported by Silva et al. (2016). Data reported in this study intend to complement the previous lichen analyses and unravel the geochronology of the bedrock fault scarp and its potential relationships with the AD 1851 earthquake affecting the zone.

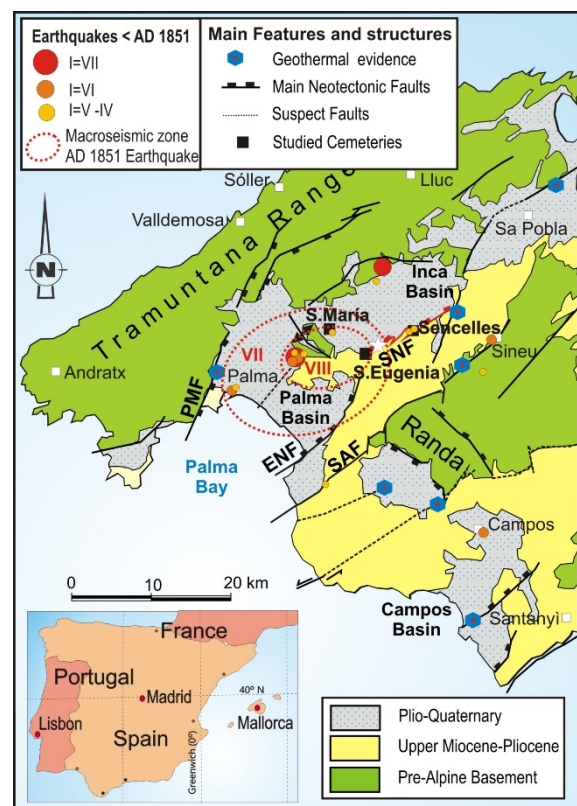


Figure 1. Major geological and seismotectonic features of western zone of Mallorca Island, showing the main neotectonic faults. PMF: Palma Fault; ENF: Cap Enderrocot Fault; SNF: Sencelles Fault; SAF: Sineu-Algaida Fault. After Silva et al. (2016)



LICHENOMETRIC ANALYSIS OF THE FALUT-SCARP

The Sta. Eugenia fault scarp shows evidence of recent reactivation, featured by the development of differentially weathered ribbons (Fig. 2) along the eastern c. 840 m of this fault segment. In fact, these different weathered ribbons are characterized by the colonization of different lichen species and different lichen sizes, which clearly decreases from the top to the base of the scarp free-face. This fault plane banding can be assumed to be produced during recent recurrent displacements of the fault (Silva et al., 2001), which is a typical feature in similar fault-scarps on calcareous materials (Wallace, 1984; Stewart and Hancock, 1989). What is common in these cases is the generation of a coseismic thin reddish pedogenic veneer staining the lower ribbon of the activated fault plane. Recurrent fault displacements generate differentially weathered fault ribbons punctuated by different lichen colonies (in size and specie), recording the maximum slip of the intervening events.

A detailed study of the fault scarp identifies five main ribbons differentially colonized by lichens (Fig.3). Two sites for lichenometric analyses were selected c. 400 m west to the fault-trench site performed by Silva et al. (2005). Fig. 3 shows a synthetic cross-section illustrating the main features in site 2, where the free-face of the scarp is 2.45 m in height. The performed analysis considered the calcareous lichen species *Aspicilia calcarea* (L.) and *Aspicilia (Lobolotalia) radiosa* (Hoffm.), commonly used in lichenometric analyses in SE Spain (i.e. Pérez-López et al., 2012, 2015; Silva et al., 2016). Specimens of the orange crusty lichen *Xanthoria Calcicola* (Hellb.) and large colonies of black crusty lichens (unidentified) are present in the upper oldest ribbons of the fault scarp as well (Figs. 2 and 3). The analysis involved the measurement of the “tallus” (maximum diameter) of 42 individual specimens over the three lower ribbons (the youngest ones). In the two upper ribbons these species appear assembled in colonies of amoeboid geometry no suitable for lichenometric measurements (Fig. 2).



Figure 2. Sencelles fault scarp near Sta. Eugenia displaying the different ribbons of lichens discussed in text.

LICHEN GROWTH RATES (LGR)

In order to obtain the annual growth rate of the lichen species, common procedures to take measurements of the “tallus” diameter on rocky surfaces of know age were developed. For this purpose we selected the cemeteries of Sta. Eugenia and Sencelles (both on the fault trace) as well as Sta. Maria del Camí (6 km ENE to the measured rocky scarp). Measurements were made in both vertical and horizontal tombstone surfaces and funerary monuments with inscribed date (or year) of death. Preliminary approaches for *A. Calcarea* specimens reported for the zone (Silva et al., 2016) strongly suggested a large variability in the size of the tallus and the resulting lichen growth rates (LGR) for horizontal and vertical surfaces among the different analysed cemeteries. These data also indicated that the orientation of tombstones (N-S or E-W) also was sensitive to LGR.

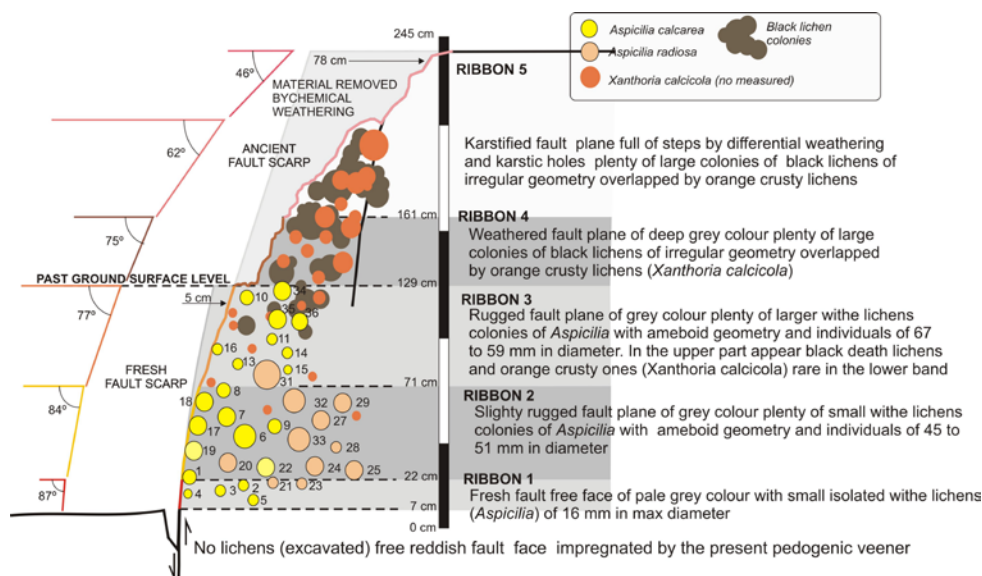


Figure 3. Schematic cross-section of the Sencelles bedrock fault scarp in Site 2. Measured Lichen species are plotted attending to their position in the fault plane. Lichen ribbons, mean angles of the fault plane bands, theoretical width of removed materials and mean computed ages for the three lower ribbons are displayed.



A total, 155 data on lichen size were collected for individual *A. calcarea* (110) and *A. radiosa* (40) specimens in the three studied cemeteries for a time period comprised from AD 1853 to 1992 (c. 140 years) in the range of the elapsed time since the last strong earthquake in the zone (AD 1851). After the preliminary data reported by Silva et al. (2016) for the Sta. Maria and Sta. Eugenia cemeteries, the new data collection in the Sencelles cemetery was focused on populations of *A. radiosa* in vertical surfaces with the same orientation of the fault scarp. The data set from Sta. Eugenia and Sencelles, located on the own fault trace, have been used to evaluate LGR in this work. These produce LGR of 0.15 - 0.21 mm/year for vertical datasets, but of 0.25 – 0.40 mm/year for horizontal datasets depending on the cemetery location and orientation (Silva et al., 2016). These LGR for horizontal surfaces are similar than other obtained by these species in SE Spain (Pérez-López et al., 2012), but vertical LGR to be applied to bedrock fault scarps are firstly reported here. Size measurements were made with digital calipers in order to increase precision and reduce bias. The obtained data sets were grouped by cemetery and by their horizontal and vertical location. The obtained lichen growth rates came from the calculation of the maximum and mean rates from each data set, as well as for the statistical analysis of best-fit regression lines (Fig. 4), following the standards of this type of analyses (i.e. Jomelli et al., 2007).

DISCUSSION: CHRONOLOGY OF THE SCARP

Using mean LGR for vertical datasets of *A. Calcareea*, Silva et al. (2016) obtained the following chronology for the different ribbons of the fault scarp: Ribbon 1 is dated in AD 1953 ± 9 years; Ribbon 2 in AD 1855 ± 59 years and the upper third ribbon (3) in AD 1712 ± 24 years. Data from mean LGR of *A. radiosa* reported here offer similar predicted ages of AD 1958 ± 10 years for Ribbon 1; AD 1853 ± 18.2 years for Ribbon 2; AD 1744 ± 57 years for Ribbon 3

(Figs. 3 and 4). The statistical analysis of selected lichen data sets for vertical surfaces in the cemeteries of Sta. Eugenia and Sencelles indicate that best-fit regression lines ($R^2 > 0.85$) corresponds to linear functions (Fig. 4). 2nd polynomial functions also produce well correlation coefficients, but will predict unrealistic lichen sizes for lichens ages beyond the 18th century, not observed in the nature. The obtained numerical curves are similar to others produced for SE Spain (Pérez-López et al., 2012) and offer computed ages for the youngest ribbons 1 and 2 in the range than those resulting for the evaluation of mean LGR (Fig. 4).

The first basal ribbon (15-13 cm wide) dated in the middle 20th Century can be linked to man-made ground levelling works in the area as observed in the fault-trench excavated in the zone (Silva et al., 2005). The upper levels of this trench displayed old artificial excavations buried by anthropic fillings containing oil-car cans of “Ertoil”, a trademark mark introduced in Spain in the 1950’s decade. The second ribbon (23 – 47 cm wide) throw mean ages (AD 1853 – 1855), congruent with the AD 1851 Palma Earthquake and can be catalogued as a probable ground failure triggered by the earthquake. In this sense, Bouvy (1851) reported the occurrence of “generic” ground failure cases over the macroseismic area (around Sta. Eugenia; Fig. 1) during the main earthquake (VII EMS) and the stronger aftershock (VI EMS) causing the collapse of the St. Marçal Church at Sa Cabaneta (Silva et al., 2001).

Since the maximum width of the ribbon is 47 cm over a length of c. 840 m, this cannot be considered surface-faulting, but some kind of secondary or sympathetic rupture along the fault trace. This, in addition, could be subject of ground-levelling works after the earthquake, since the largest lichen specimens (51 to 45 mm in diameter) are found in the upper 10-15 cm of the ribbon. This can be considered the maximum displacement occurred during the earthquake. On the other hand, some of the oldest funerary monuments in the Sta. Eugenia cemetery show evidences of

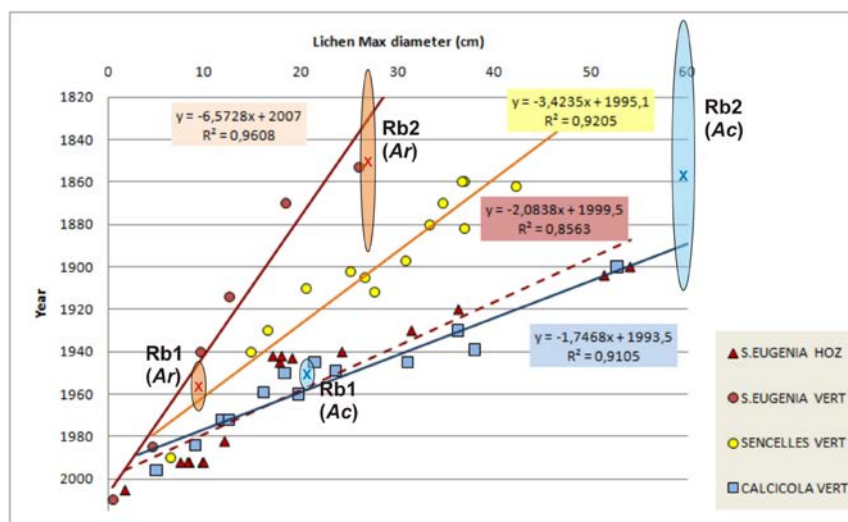


Figure 4. Plot of Lichen tallus (maximum diameters) and resulting growth rates (LGR) LGR regression lines (lineal functions) for vertical lichen datasets (*A. radiosa*) measured in the cemeteries of Sta. Eugenia and Sencelles. Also are represented vertical dataset for *A. Calcicola* (quadrangles) in the zone and horizontal data sets and horizontal dataset of *A. radiosa* for Sta. Eugenia (Silva et al., 2016) for comparison. Colored ellipses in the graphic represents the mean ages of the ribbons 1 (Rb1) and 2 (Rb2) obtained by the calculation of mean values using *A. Calcicola* (Ac) and *A. radiosa* (Ar).



earthquake damage, such as the small mausoleum of “Juan Castell y Los Suyos” AD 1853; Fig. 5), but very probably built soon before the AD 1851 Earthquake. Dropped keystone, penetrative fractures and broken dipping corners are visible at the door of the mausoleum.

The third ribbon (58-55 cm wide) offers a mean age bracketed in AD 1712 and 1744 (Fig. 3). This third ribbon is the oldest historic ribbon of the fault scarp. As discussed by Silva et al. (2016), this ribbon can be tentatively related to previous events occurred in the island (VII – V EMS) between AD 1721 and 1764. However the rugged fault plane represented by this ribbon (Fig. 3), have to be interpreted as secondary ground failures or secondary surface faulting events probably related to some of these moderate 18th century events.



Figure 5. Detail of lichens specimens (*A. radiosa*) and dropped keystone in the Mausoleum of “Juan Castell y los Suyos” dated in AD 1853 and located at the Sta. Eugenia Cemetery.

CONCLUSIONS

The Sencelles bedrock fault scarp is differentially weathered, displaying five different ribbons diversely colonized by lichens. The fault scarp is vertically segmented displaying a basal fresh historical fault-plane (three first ribbons) and an upper deeply weathered and karstified one, probably related to older Holocene events (Fig. 3).

Lichen measurements and analyses in the nearby cemeteries of Sta. Maria, Sta. Eugenia and Sencelles covered a time span between AD 1853 and AD 2005 within the range of the last historical event in the zone (AD 1851; VII EMS). The large amount of measurements developed in the three cemeteries (155 data) on vertical and horizontal surfaces, indicate a strong sensitivity of LGR depending on the Lichen specie cemetery, tombstone orientation and greatly their position (vertical or horizontal). Eventually the most suitable data sets were those corresponding to vertical data sets of *A. radiosa* in the two cemeteries located onto the analyzed fault plane (Fig. 4). The strong sensitivity of (LGR) to particular environmental conditions strongly points to a

necessary revision of regional or general LGR applied to the analyses of rockfalls or seismically induced rockfalls (i.e. Bull, 2003; Pérez-López et al., 2012).

Lichenometric analyses developed on the basal fresh fault-plane suggest and historical age, younger than c. AD 1700. Within this historical scarp, the second lichen ribbon (23-47 cm wide) can be reasonably linked to the AD 1851 Palma earthquake. This vertical displacement of the fault plane can be interpreted as a secondary earthquake effect (secondary or sympathetic rupture) according to the established size of the earthquake (VII EMS). However fault trenching studies in this zone (Silva et al., 2005) display apparent colluvial wedges in the rocky fault plane indicating that the fault produced surface faulting events during the Pleistocene. At present the seismic source of the AD 1851 earthquake remains unclear, but activity of the Palma de Mallorca or Cap de Enderrocat normal faults (PMF and ENF in Fig. 1) bounding the Palma Bay can be considered the more probable ones.

Acknowledgements: Supported by the MINECO-FEDER Spanish Research Projects CGL2015-67169-P (USAL), CGL2015-69919-R (UAH) and EGEO-IGME (Ref:2612). A contribution QTECT-AEQUA.

REFERENCES

- Benedicto, A., Ramos, E., Casas, A. Sabat, E. & Barón, A., 1993. Evolución tecto-sedimentaria de la cubeta neógena de Inca (Mallorca). *Rev. Soc. Geol. España* 6, 167-176.
- Bouvy, P., 1851. Sobre el Terremoto ocurrido en la Isla de Mallorca el 15 de mayo último. *Revista Minera* 2 (26), 375-378.
- Bull, W.B. 2003. Lichenometry dating of coseismic changes to a New Zealand landslide complex. *Annals of Geophysics* 46 (5), 1155 – 1167.
- Jomelli, V., Grancher, D. Naveau, P. Cooley, D. and Brunstein, D. 2007. Assessment study of lichenometric methods for dating surfaces. *Geomorphology*, 86, 131-143.
- Pérez-López, R., Martín, F., Martínez-Díaz, J.J. & Rodríguez-Pascua, M.A., 2012. Datación mediante liqenometría de los desprendimientos rocosos asociados a la sismicidad histórica en Lorca (Murcia, SE España). *Boletín Geológico y Minero* 123 (4), 473-485.
- Silva. P.G., González Hernández, F.M., Goy, J.L., Zazo C. & Carrasco, P., 2001. Paleoseismicity and historical seismicity in the Mallorca Island (Balears, Spain): A preliminary approach. *Acta Geológica Hispánica* 36, 245-266.
- Silva. P.G., Goy, J.L., Zazo C., Giménez, J., Fornós, J., Cabero A., Bardají T., Mateos, R., Hillaire-Marcel, C. & Bassam, G., 2005. *Mallorca Island: Geomorphological evolution and neotectonics*. Field-trip Guide Book (A7). 6th Int. Conference on Geomorphology, IAG-SEG, Zaragoza. 54pp.
- Silva, P.G., Roquero, E., Bardají, T., Pérez-López, R., Rodríguez-Pascua, M.A., Giner-Robles, J.L., & Perucha, M.A. (2016). Geochronology of the Sencelles fault scarp and its relationships with the AD 1851 Mallorca Earthquake (Balears Islands, Spain). *Geo-Temas* 16 (1), 653 -656.
- Stewart, I. & Hancock, P.L. (1991): What is a fault scarp?. *Episodes*, 13 (4): 256-263.
- Wallace, R.E. (1984): Fault scarps formed during the earthquake of October 2, 1951, in Pleasant Valley, Nevada, and some tectonic implications. USGS. Professional Papers, 1274-A: 33pp



The AD 1755 Lisbon Earthquake-Tsunami: Modelling the seismic source from the analysis of environmental and building macroseismic data

P.G. Silva(1), J. Elez(1), J.L. Giner-Robles(2), P.V. Gómez-Diego(1), M.A. Rodríguez-Pascua(3),
E. Roquero(4), A. Martínez-Graña(1), T. Bardají(5)

- (1) Dpto. Geología, Universidad de Salamanca. Ávila – Salamanca, Spain. pgsilva@usal.es, j.elez@usal.es, amgrana@usal.es
- (2) Dpto. Geología y Geoquímica, Universidad Autónoma de Madrid. Cantoblanco, Madrid, Spain. jorge.giner@uam.es
- (3) Instituto Geológico y Minero de España. Ríos Rosas 23. 28003-Madrid. Spain. marodriguez@igme.es
- (4) Dpto. Edafología, Universidad Politécnica de Madrid. 28040-Madrid. Spain. elvira.roquero@upm.es
- (5) U.D. Geología, Universidad de Alcalá, 28871- Alcalá de Henares, Madrid, Spain. teresa.bardaji@uah.es

Abstract: This work presents a macroseismic analysis of the AD 1755 Lisbon Earthquake-Tsunami event by means of the combination of intensity data derived from the EMS-98 scale and the ESI-07 scale (Environmental damage). About 600 records of earthquake environmental effects for the whole Spain have been used to define intensities. The analyses indicate maximum intensities of X EMS-ESI along the Atlantic margin and important amplification (VIII – VII) along the Guadalquivir basin. From the intensity distribution the historic seismic scenarios are explored by means of the development of empirical ShakeMaps. These take into account the three classical seismic sources considered for this earthquake, but the resulting scenario is only possible considering the three seismic sources together. This will imply an NNE-SSW offshore rupture length of 350 km and a rupture area of c. 250,000 km² resulting in an event magnitude 8.6 - 8.9 Mw. The results demonstrate the efficacy of this approach for better identifying and modelling seismic sources.

Key words: Lisbon earthquake-tsunami, Macroseismicity, Intensity distribution, Shakemaps, Seismic source.

INTRODUCTION

The AD 1755 Lisbon earthquake was the strongest seismic event ever reported in Europe, and was extremely destructive throughout Portugal, Spain and Morocco (Martínez Solares 2001). Effects of the seismic shaking was even felt in Northern Germany, the Azores and the Cape Verde Islands. The large size of the earthquake is further attested by the observation of seiches in southern England, the Netherlands and as far as Finland (Reid 1914). The tsunami-waves generated by the earthquake triggered extensive damage along the Atlantic littoral of Portugal, SW Spain and Morocco, and were even detected in the SW England, Mexico and the Antilles (Baptista et al., 2003). In spite of extensive geological evidence of tsunami records has been widely published since the 1990 decade (e.g. Andrade 1992; Costa et al., 2016). However, analyses of onshore secondary geological effects has been more scarce (Martínez Solares, 2001). It is widely agreed upon that the maximum intensities along the SW Iberian Peninsula reached the intensity X during the 1755 Lisbon Earthquake event (e.g. Grandini et al., 2007; Santos & Koshimura, 2015). In the same way most of the authors agree that earthquake magnitude was of c. 8.5 -9.0 Mw and the epicentre occurred few hundred kilometres offshore SW Portugal (Fig. 1).

This work is focused on the analysis of probable seismic sources for the AD1755 Lisbon earthquake based on the development of seismic scenarios (ShakeMaps) simulating the intensity distributions and corresponding ground peak accelerations (PGA) resulting from an ESI-07 and EMS-98 hybrid analyses using the methodology proposed by Silva et al. (2017).

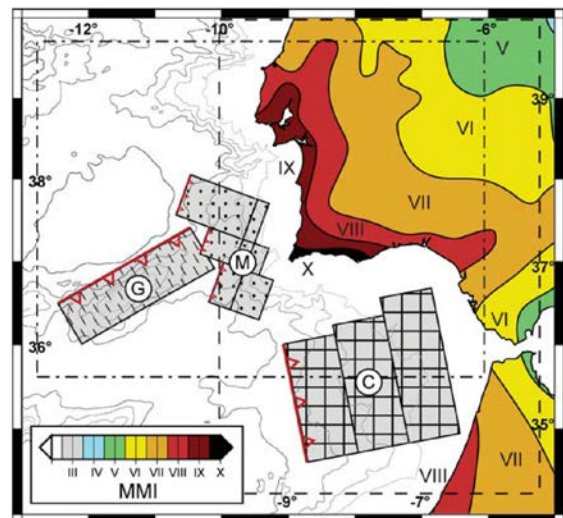


Figure 1: Isoseismal map of the AD 1755 Lisbon earthquake (Modified Mercalli Intensity) and seismic sources considered for this historical event: (G) Goringe Bank; (M) Marques de Pombal – Pereira de Sousa Fault; and (C) Eastwards subduction of the Atlantic delaminated lithosphere beneath the Gulf of Cádiz. From Grandini et al. (2007).

AD 1755 LISBON EARTHQUAKE SEISMIC SOURCES

The Goringe Bank (G), Marques de Pombal Fault and the subduction beneath the Gulf of Cadiz (C) have been considered as the more probable seismic sources for the AD 1755 Lisbon event (Fig. 1; e.g. Zitellini et al., 2001; Baptista et al., 2003; Grandini et al., 2007). This event is considered to be generated around the Goringe Bank (Atlantic Ocean) by the rupture of a reverse fault segment of about 180 – 200 km



length (Marqués de Pombal Fault), with an estimated minimum slip of 10 m, considering the event as a subduction zone-like earthquake (Zitellini et al., 2001).

From the first studies it was clear that any of the abovementioned sources alone had a sufficient potential and dimensions (fault rupture length; area) to generate an earthquake ≥ 8.5 Mw. Baptista et al. (2003) suggest that a composite source considering the G and M individual sources will be suitable to explain the overall L-shaped intensity distribution displayed onshore (Fig. 1). Similar conclusions are indicated by Grandini et al. (2007), which suggest the Gorringe Bank (G) as the most probable seismic source for the studied

event. Most of these studies concluded that a source compatible with an incipient subduction along the western Portuguese margin provides a better fit between onshore intensity and tsunami damage than a source located at Gorringe Banks. More recent studies suggest that the subduction of the Atlantic lithosphere beneath the Gulf of Cadiz and the Gibraltar Arc (C) provides a sufficiently large seismic source capable to explain the size of the AD 1755 Earthquake-Tsunami event (Gutscher et al., 2006; Duarte et al., 2013). These last authors take into account the effects on the Gulf of Cádiz area and the complex tectonics of the zone, normally biased by the Portuguese authors focused on the effects recorded at Portugal.

Scenarios: Lisbon earthquake AD 01/11/1755

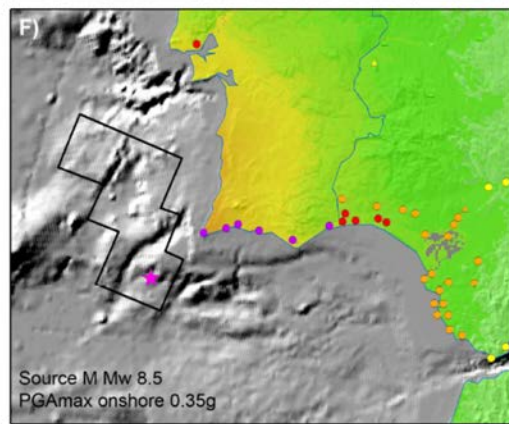
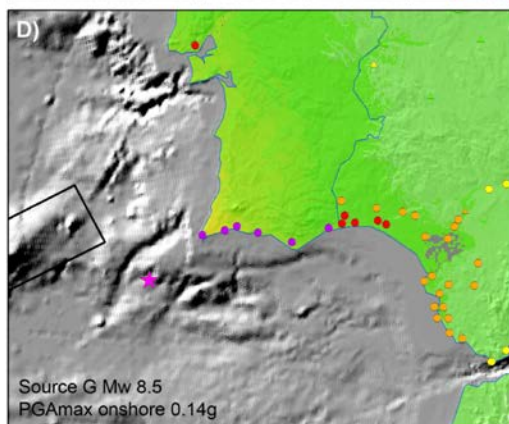
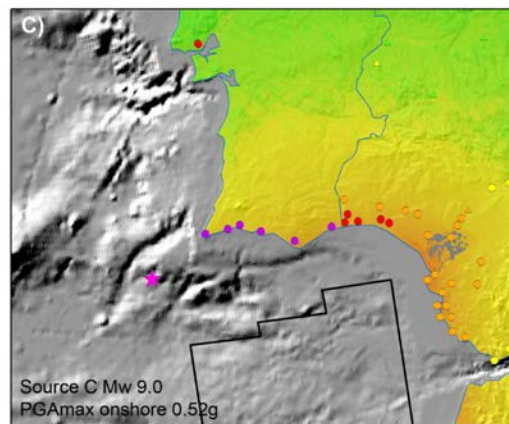
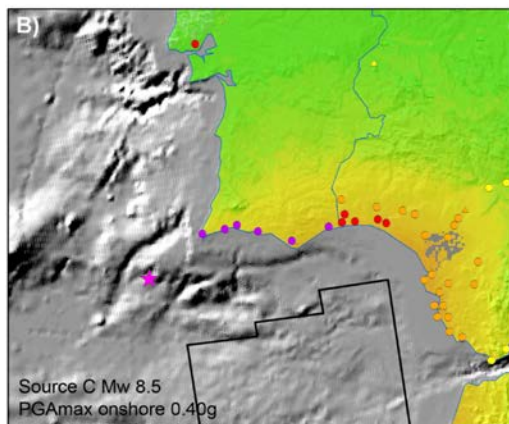
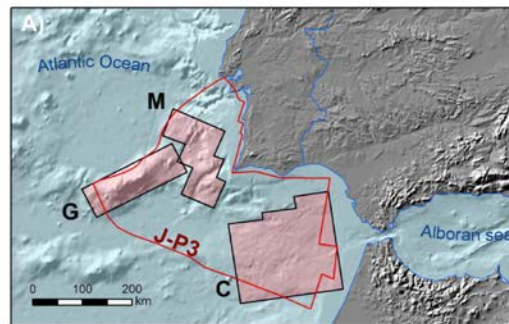
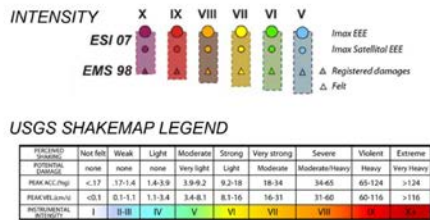


Figure 2: Seismic sources in the SW Atlantic region of the Iberian Peninsula (G, M, C and the combined one proposed in this study: J-P3, colored in red) and resulting hypothetical seismic scenarios (ShakeMaps with PGA values) from the occurrence of earthquake magnitudes 8.5 Mw (B, D & E) in each of the individual case. Only the seismic source C has the sufficient dimensions to generate a 9.0 Mw earthquake illustrated in graph C. Note that in any of the individual cases PGA max values recorded onshore are always down to 0.60 g and not explain intensities X and IX reached in the coast (Fig. 1). Colored dots represent intensity levels reached in each locality by EMS and ESI data (See legend at top). The ShakeMaps have been produced with the methodology of Silva et al (in press) modified from the applied in the USGS ShakeMap Program: On-line Sahke Map Manual http://usgs.github.io/shakemap/manual_index.html



SEISMIC SCENARIOS PRODUCED BY DIFFERENT SEISMIC SOURCES FOR THE AD 1755 EVENT

In spite of the different proposals the seismic source of the AD 1755 Event remains unclear. By means the application of Magnitude – Seismic source dimensions empirical relationships produced for subduction frameworks (i.e. Strasser et al., 2010), each individual seismic source is unable to explain the recorded intensities onshore (Fig. 2). These empirical relationships will imply rupture areas in the order of 500,000 km² and fault rupture lengths around 900 km to produce an ≥ 8.5 Mw earthquake. These values are typical to those linked to large earthquake-tsunami events of 9.0 Mw (i.e. Japan 2011), but all the checked sources for the AD 1755 event (i.e. Grandini et al., 2007) have smaller dimensions (< 40,000 km²). Figure 2 illustrates the resulting seismic scenarios (ShakeMaps) produced for the different seismic sources of the area. Shakemaps have been produced by the methodology proposed by Silva et al. (2017) for historical earthquakes based on the combination of EMS-98 and ESI-07 to the procedures and ground motion prediction equations used in the USGS ShakeMap Program (Wald et al., 2005). In all of the cases tested an 8.5 Mw earthquake is sufficient to simulate the intensities reached onshore (i.e. Fig. 1). The computed PGA values in the coastal sites are down to 0.40 g for source C, implying maximum intensities of VIII (Fig 2B). Sources G (0.14 g) and M (0.35 g) can only generate intensities VII or even VI at coastal sites (Fig. 2D and 2E). Only source C has the minimum dimensions to generate a 9.0 Mw, and the checked seismic scenario (Fig. 2B) would imply the record of PGA max values around 55g (upper range of intensity VIII) in southern Spain. Even in this case, PGA values recorded around Lisbon (0.19 g) will not be beyond intensity V (Fig. 2C), which does not fit with known values.

Taking into account the obtained results for the different seismic sources (Fig. 2), it seems clear that an 8.5 – 9.0 Mw event in the zone will need a seismic source of larger dimensions. Recent tectonic proposals for the SW Iberian Margin indicate the probability of the occurrence of an extensive composite seismic source in (G+M+C) linked to the initial eastwards subduction of the Atlantic lithosphere (Duarte et al., 2013). These authors assume that the Gibraltar Arch is a similar case to those recorded in the Lesser Antilles and Scotia subduction arches in the opposite margin of the Atlantic Ocean, otherwise dominantly a passive continental margin. From these tectonic proposals and regional structural data of the SW Iberian margin a new composite seismic source has been modelled and calculations tested (Fig. 2A). Following Duarte et al (2013) the new extended seismic source will include thrusting along the NE-SW linear structures of the Gorringe Bank (G) and Marques de Pombal Fault (M) and low angle incipient subduction of the Atlantic lithosphere beneath the frontal accretionary wedge of the Gibraltar Arc (C) in the Gulf of Cádiz (Fig. 3).

To check the geodynamic model related to the proposed seismic source the “*ey trajectories*” (maximum horizontal deformation) and the related “*k coefficients*” have been

calculated for the zone. The *s trajectories* of compressive stress (*ey*) come from the analyses of the existing focal solutions in the zone between the years 2000 and 2015 (Fig. 3). They grey dots in the background of figure 3 represent the instrumental seismicity recorded in the zone during the mentioned period. The resulting trajectories are compatible with the proposed subduction, and the *K* factor shows as active compression (reverse and oblique faulting sources), are clearly related to the initiation (G and M sources), and the end (C) of the new proposed seismic source beneath the Gibraltar Arc.

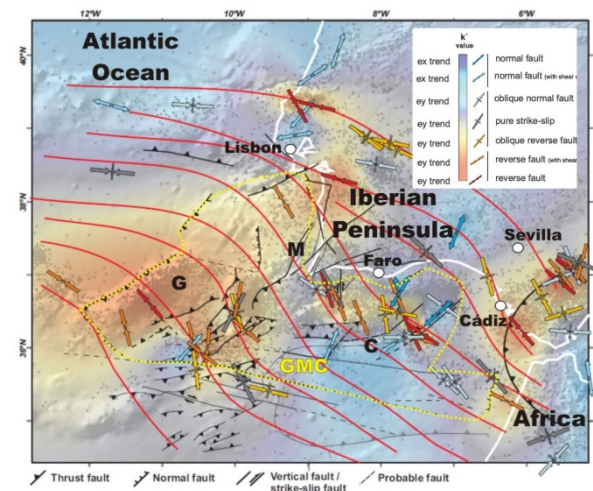


Figure 3: Active structures in the Atlantic margin of the SW Iberian Peninsula and Gulf of Cádiz, location of the three classical seismic sources considered in the zone (G, M and C) and the composite GMC one proposed in this study (dotted yellow line). The proposed source is compatible with the *ey* trends deduced from the analysis of focal solutions in the zone for this study. Structural data compiled from Duarte et al. (2013), Cabral (2012).

The proposed seismic source has a potential rupture area of c. 250,000 km² and a potential fault rupture length of c. 350 – 380 km along the NE-SW faults bounding the Gorringe Bank and northern structures (Fig. 3). However the complete length of the proposed source adjacent to the SW Iberian littoral reaches about 730-750 km. Considering these source parameters, empirical relationships (i.e. Strasser et al., 2010) indicate that the proposed source will trigger an earthquake of maximum magnitude between 8.6 – 8.9 Mw. These values agree with the widely accepted magnitudes proposed for the AD 1755 event. To check the theoretical intensities and PGA values related to this earthquake magnitude in the extended seismic source, a new seismic scenario (Fig. 4) was calculated following the same procedures than for the previous ones (Fig. 2). The results match reasonably with the recorded intensities all along the SW quadrant of the Iberian Peninsula illustrated in the classical isoseismal maps (Fig. 1). Maximum intensities (X) occur in the Algarve littoral with computed PGA values between 1.15g and 0.85g from the St. Vicente Cape to Faro. In the Spanish littoral of the Gulf of Cadiz PGA values diminish from west (Ayamonte; 0,65g) to east (Doñana marshlands; 0.45 g) supporting intensities between IX and VIII along the coast. Towards the Gibraltar Arc, the city of Cadiz (0.34g) is within



the limits of intensity VII-VIII. To the north along the Portuguese coast the PGA values indicate intensity values between X and IX. Lisbon reaches a computed PGA of 0.76g supporting a minimum intensity of IX as in the classical intensity models (Fig. 1). The computed model also describes well the amplification to intensity VIII –VII recorded within the whole Guadalquivir Depression (Fig. 4; Sevilla 0.33g; Córdoba 0.21g) and intensities that occurred in the whole Iberian Peninsula (Fig. 4).

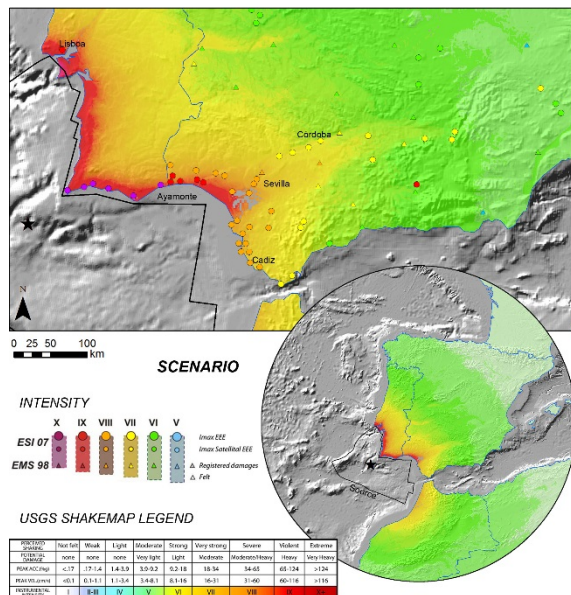


Figure 4: ShakeMap for the AD 1755 Lisbon earthquake produced by the composite seismic source GMC proposed in this study

CONCLUSIONS

This study illustrates that the classically accepted seismic sources for the AD 1755 Lisbon event (Fig. 1: G, M, C) can not explain the intensity distribution caused by this event. Previous works (Baptista et al., 2003; Grandini et al., 2007) are strongly focused in the Portuguese macroseismic data, and their proposed seismic sources (G, M or G+M) are insufficient to explain intensity levels reached in the Guadalquivir basin and even in the Gibraltar Arc. Solutions based on the subduction beneath the Gulf of Cádiz (C) provide very good intensity constraints for the southern Spanish littoral and the Guadalquivir basin but are still insufficient to explain the intensity levels reached around the Lisbon area to the north. All the scenarios have been checked by means of the calculation of corresponding ShakeMaps (Fig. 2). Following the tectonic models of Duarte et al (2013), we propose a composite seismic source including all the three traditionally considered sources (Fig. 3: GMC) in a process of incipient eastwards

subduction of the Atlantic lithosphere beneath de Gibraltar Arc. The seismic scenario proposed (Fig. 4) fulfils the intensity distribution across the whole Iberian Peninsula. This scenario also supports the classical L-shaped geometry of stronger intensity levels (IX – X) between Lisbon and the Doñana Marshlands combining EMS-98 and ESI-07 data.

Acknowledgements: Supported by the MINECO-FEDER Spanish Research Projects CGL2015-67169-P (USAL), CGL2015-69919-R (UAH) and EGEO-IGME (Ref:2612). A contribution QTECT-AEQUA.

REFERENCES

- Andrade, C., 1992. Tsunami generated forms in the Algarve barrier islands (south Portugal), *Science of Tsunami Hazards* 10(1), 21–34.
- Baptista, M. A., Miranda, J. M., Chierici, F. & Zitellini, N., 2003. New study of the 1755 earthquake source based on multi-channel seismic survey data and tsunami modeling. *Natural Hazards and Earth System Science* 3 (5), 333-340.
- Costa, P. J. M., 2016. Imprints of the AD 1755 Tsunami in Algarve (South Portugal) Lowlands and Post-impact Recovery. Tsunamis and Earthquakes in Coastal Environments. Springer International Publishing, 17-30.
- Duarte, J.C., Rosas, F.M., Terrinha, P., Schellart, W.P., Boutelier, D., Gutscher, M.-A. & Ribeiro, A., 2013. Are subduction zones invading the Atlantic? Evidence from the southwest Iberia margin. *Geology* 41 (8), 839 -842.
- Gardin, R., Borges, J.F., Bezzeghoud, M., Caldeira, F. & Carrilho, F., 2007. Simulations of strong ground motion in SW Iberia for the 1969 February 28 (MS= 8.0) and the 1755 November 1 (Mw 8.5) earthquakes—II. Strong ground motion simulations. *Geophysical Journal International* 171(2), 807 – 822
- Gutscher, M.A. Baptista, M.A., Miranda, J.M., 2006. Constraints on a shallow east dipping fault plane source for the 1755 Lisbon earthquake provided by tsunami modeling and seismic intensity (part 2). *Tectonophysics* 426, 153–166.
- Martínez Solares, J.M., 2001. *Los efectos en España del terremoto de Lisboa (1 de noviembre de 1755)*. Monografías IGN, 19. IGN, Madrid (Spain), 756 pp.
- Santos, A., & Koshimura, S., 2015. The Historical Review of the 1755 Lisbon Tsunami. *Journal of Geodesy and Geomatics Engineering*, 1, 38–52.
- Silva, P.G., Elez, J., Giner-Robles, J.L., Rodríguez-Pascua, M.A., Pérez-López, R., Roquero, E., Bardají, T. & Martínez-Graña, A.M., 2017. ESI-07 ShakeMaps for instrumental and historical events in the Betic Cordillera (SE Spain). *Quaternary international* 451, 185 - 208.
- Strasser, F.O., Arango, M.C. & Bommer, J.J. 2010. Scaling of the source dimensions of interface and intraslab subduction-zone earthquakes. *Seismological Research Letters* 81 6, 941–950
- Zitellini, N., Mendes Victor, L. A. & Cordoba, J. D., 2001. Source of 1755 Lisbon Earthquake and tsunami Investigated. *EOS Transactions* 82 (26), 285.
- Wald, D.J., Worden, B.C., Quitoriano, V., Pankow, K.L., 2005. ShakeMap Manual: Technical Manual, User's Guide, and Software Guide. U.S. Geological Survey, p. 132.



Using the X-ray micro-computed tomography to reveal cryptic strain fabric of faulted soft sediment: outlines of a pilot study and preliminary results

Špaček, Petr (1), Herzán, Petr (2), Smékalová, Veronika (3)

- (1) Masaryk University Brno, Czech Republic, spacek@ipe.muni.cz
 (2) SolidVision Ltd. Brno, Czech Republic
 (3) CEITEC, Brno University of Technology, Czech Republic

Abstract: In many exposed faults we fail to determine the slip direction and sense due to the absence of clear macroscopic kinematic indicators. To improve this situation we have been working out a technique employing the X-ray imaging of narrow faults by micro-computed tomography to reveal their cryptic strain fabric. It is expected that a detailed knowledge of 3-D particle orientation will allow resolving the shear kinematics. Here, we give a methodical concept and preliminary results of a pilot study to validate this assumption. The approach tested is potentially suitable for coarser clastic sediments or clasts-in-matrix lithologies representing common examples of faulted rocks in which slickensides typically do not develop.

Key words: fault slip kinematics, strain fabric, X-ray computed tomography

INTRODUCTION

In near-surface conditions the shear deformation of non-consolidated rock is taking place largely by passive rotation of grains. The oblique fabric developed as a result of non-coaxial shearing is often used as an indicator of shear direction and sense. While in clay-rich sediments and fault gouges the magnetic susceptibility tensor may be used as a sensitive proxy of cryptic strain fabric, in coarser materials the visually evaluated orientation of anisometric clasts is used (e.g. Cladouhos 1999, Hayman et al. 2004). With slickensides typically missing in the latter, our poor knowledge of the clast fabric may result in failure to resolve the fault kinematics.

The orientation of clasts is usually studied in 2D sections and even though detailed analyses are possible using optical or electron microscopy, the direct selection of representative section for such study is precluded by the apriori unknown shear geometry. Therefore, 3D analysis of bulk samples is desirable. Here, we introduce a pilot study focused on revealing the 3D orientation of clasts in bulk samples of faulted soft sediments by micro-computed tomography (μ CT).

STARTING IDEAS FOR PILOT STUDY

Assuming that the fault and the associated shear zone developed in the same kinematic regime, the mean orientation of long axes of the freely rotating elongated solid particles within the sheared volume should indicate the fault slip direction, while its sense may be deduced from the imbrication of flat particles or the S-C fabrics, if present. The idealized concept is schematically illustrated in Fig. 1.

The shape-preferred orientation of particles should be resolvable provided that we are able to produce 3D image in which individual particles can be differentiated and to measure the orientation of sufficient number of particles

to perform quantitative statistical analysis. Theoretically, such image may be acquired by μ CT, however, in large rock samples serious limits may be posed by insufficient contrast and resolution.

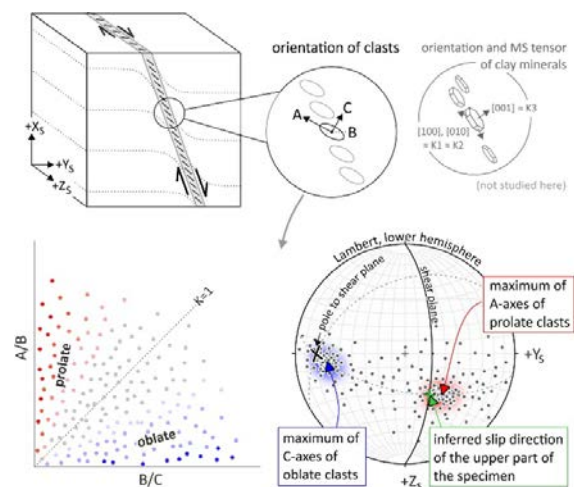


Figure 1: Idealized scheme of geometric relations between fault slip and orientation of particles used for kinematic reconstruction.

The X-ray attenuation is proportional to the mean atomic number of the material (i.e. density as a good proxy). Despite similar densities of minerals constituting the rocks, high porosity in samples is expected to ensure the desired intensity contrast between the image representation of particles and hosting matrix or intergranular voids.

A typical ratio of $\sim 1:1000$ between the horizontal sample dimension and the μ CT image resolution suggests that millimetre-sized or even smaller grains should be well represented in the image of decimetre-sized sample. However, larger samples will have larger effective attenuation which may become a limiting factor.



To verify the applicability of the above given concept to real faulted sediments and to find the optimal instrumentation and methods of 3D image analysis, we started a pilot study whose outlines and preliminary results are given below.

SAMPLES AND CT SCANNING

Three types of faulted soft sediments from southeast Czech Republic have been chosen, each represented by two samples to be tested for the effects on μ CT image quality of the sample lithology, size and instrumentation used:

- 1) Fine quartz sand with layers of fine gravel; the mm-sized quartz pebbles are incorporated in a ~5-9 mm thick shear zone (samples A1, diameter \times height of 100 \times 85 mm, and A2, 120 \times 120 \times 90 mm); sense of shear not resolved;
- 2) Silt with debris of shale from a colluvium/loess sequence hosting broad shear zone (sample B1, 150 \times 120 \times 170 mm, and B2, 50 \times 100 mm); sense of shear in B1 resolved as normal dip-slip;
- 3) Fine sandy gravels with polymict, mostly flat mm-sized pebbles hosting narrow shear zone (samples C1, 220 \times 230 \times 220 mm, and C2, 95 \times 75 mm); sense of shear not resolved.

In all samples bedding is within 30° from horizontal and faults are steep, with dips ranging 70-90°.

After strengthening by diluted glue where necessary, the oriented sediment samples were cut out of the profiles, shaped to approximate near-cylinder shape where possible, and stabilized onto its own gypsum base or into a vertically oriented plastic cylinder to minimize the horizontal diameter. A metal orientation mark with known in-situ dip and azimuth was stuck to each sample to be easily located in the final image.

Three different instruments have been used for μ CT scanning – DeskTom 130 (RX Solutions) at SolidVision (testing on samples A2 and B2), GE Phoenix v|tome|x L240 (GE Sensing & Inspection Technologies) at CEITEC Brno (samples A1, B1, C2) and XT H 450 (Nikon Metrology NV) at ICT Ostrava (large sample C1; currently in progress).

The horizontal sample diameter in the range of 8-30 cm resulted in the image resolution ranging from 70 to 300 μ m.

IMAGE ANALYSIS

16-bit 3D image volumes produced by the scanners were registered to fault-parallel coordinate system and visually evaluated in myVGL software (VolumeGraphics). While for most of samples the detailed analyses are in progress, the sample A1 has been chosen as a testing material for finding optimal algorithms of quantitative analysis. Selected region of interest within this sample was exported as a stack of 2D images and further processed in ImageJ open source program (Fiji distribution; Schindelin et al. 2012). Supervised image segmentation (separation of particles and matrix);

was performed using Trainable Weka Segmentation 3D plugin (Arganda-Carreras et al. 2017) and refined by Distance Transform Watershed algorithm in MorphLibJ plugin (Legland et al. 2016) to produce an image with connected-component labels (i.e., with defined boundaries of each particle). Using the latter plugin, inertia ellipsoid was calculated for each labelled particle, the length and orientation of its principal axes being recorded. These parameters were then taken, after conversion, as input for orientation analysis using the open source toolbox MTEX (Bachmann et al. 2010) in MATLAB program (MathWorks). The correctness of the orientation data is currently being tested and here presented results are preliminary.

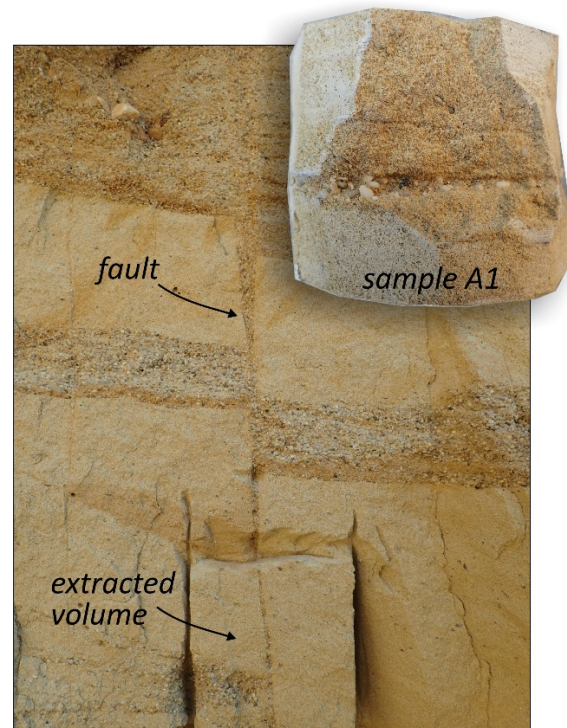


Figure 2: Example of faulted sediment used for a pilot study (Tertiary sand with gravel beds, locality for samples A1 and A2).

PRELIMINARY RESULTS

The image volumes acquired by μ CT scanning of all sediments tested display good enough quality to clearly recognise individual grains and some larger-scale structures in matrix related to tiny changes of porosity or mineralogy (Fig. 3). In samples A1&2, B1&2, and C2 the image resolution results in satisfactory representation of homogeneous particles with minimum dimension of 1 mm or even smaller when sufficient contrast is present. Measurement of the largest sample C1 is still in progress but threshold particle dimension of ca. 2-3 mm is expected.

The images reveal detailed anatomy of faults that can be evaluated visually and quantitatively. Fig. 3 shows some examples: real shape of the shear zone, extent of dilatancy zone, preferred orientation and clustering of particles and their spatial variations. Weak preferred orientation of the long grain axes in the fault plane-parallel sections and the asymmetry in fault-perpendicular sections is visible in all



samples, including those in which they were not resolved macroscopically (A1&2, B1&2; Fig. 3). In samples A and C approximate orientation of shear direction can be deduced based on these observations, while in sample C2 the indication is less clear. It should be noted that while the preferred orientation is often hardly visible in 2D sections of most samples, it is seen much more clearly when 3D image is examined.

The quantitative evaluation performed on sample A1 allows to support statistically (and hence make objective) the observations of weak preferred orientations and to perform more detailed analyses taking into account real grain shapes. Figure 4 illustrates the preliminary analysis of sample A1 based on methodical scheme described above. The grains' preferred orientation exhibits clear orthorhombic symmetry with centroids of smoothed maxima of long (A) and short (C) axes inclined 20-30° to the fault plane and its pole,

respectively. This asymmetry is in accordance with the visual observation and may be interpreted as indication of shear parallel to the $x-x'$ direction (shown in Fig. 4) with the top displaced towards x' . Converted to geographic coordinates this shear sense suggests a nearly pure dip-slip of the SW block, which is consistent with the observed offset of gravel beds (comp. Fig. 2).

CONCLUSIONS

The advantage of adding the third sample dimension to the commonly available 2D views is obvious: the μ CT scans allow to observe and analyse the real orientation and shape of components and structures in geological materials. Preliminary results of our study have shown that good quality images can be acquired even by less costly scanners from relatively large (horizontal diameter of >10 cm) samples of common types of non-consolidated sediments.

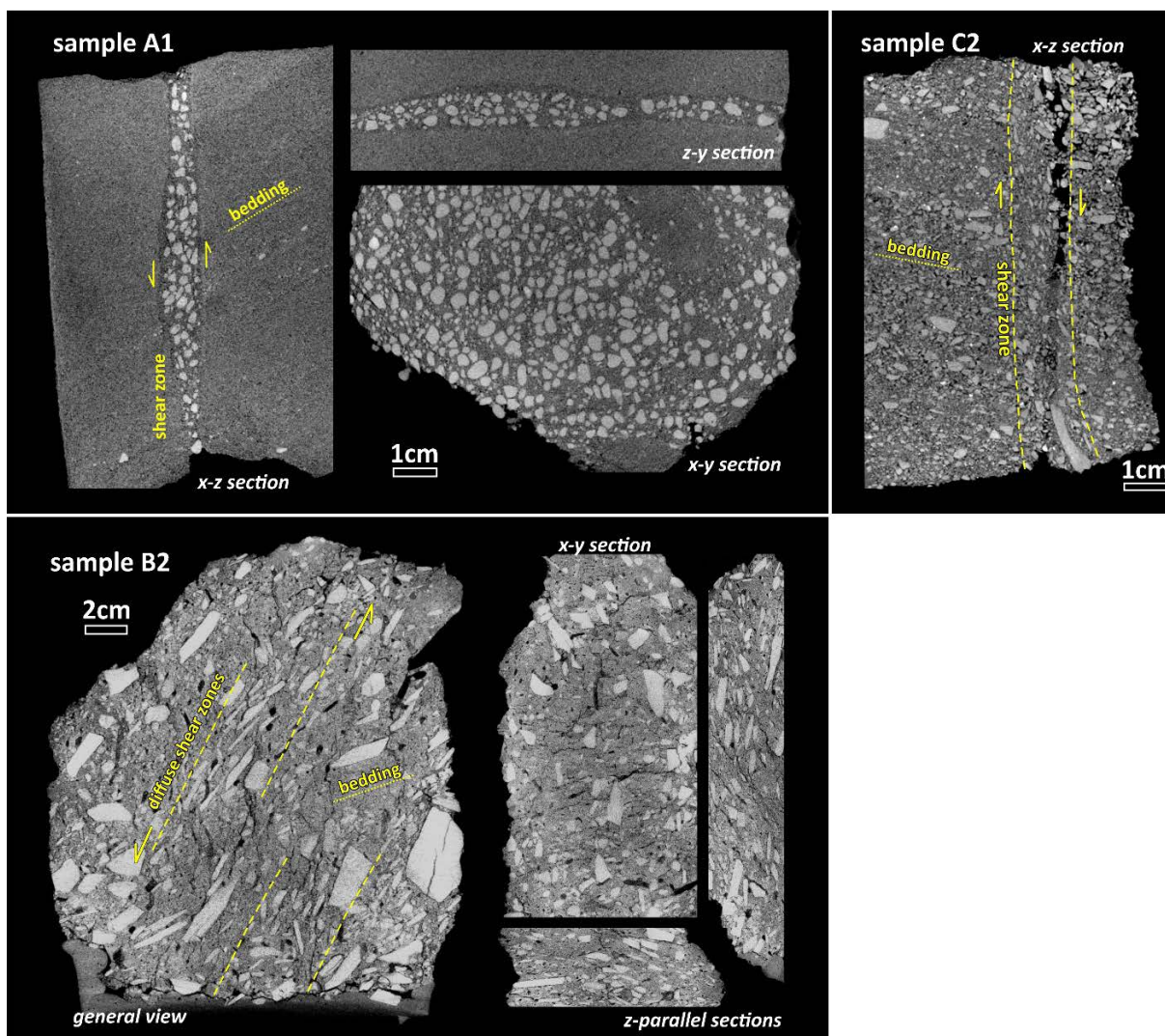


Figure 3: Representative 2D sections from 3d mjuCT scans of samples A1, B2 and C2. Main structural features are highlighted. The orientation of sections is related to x-y-z direction system based on visual evaluation: x denotes the shear direction, z is the direction perpendicular to the fault and y is perpendicular to x and z.

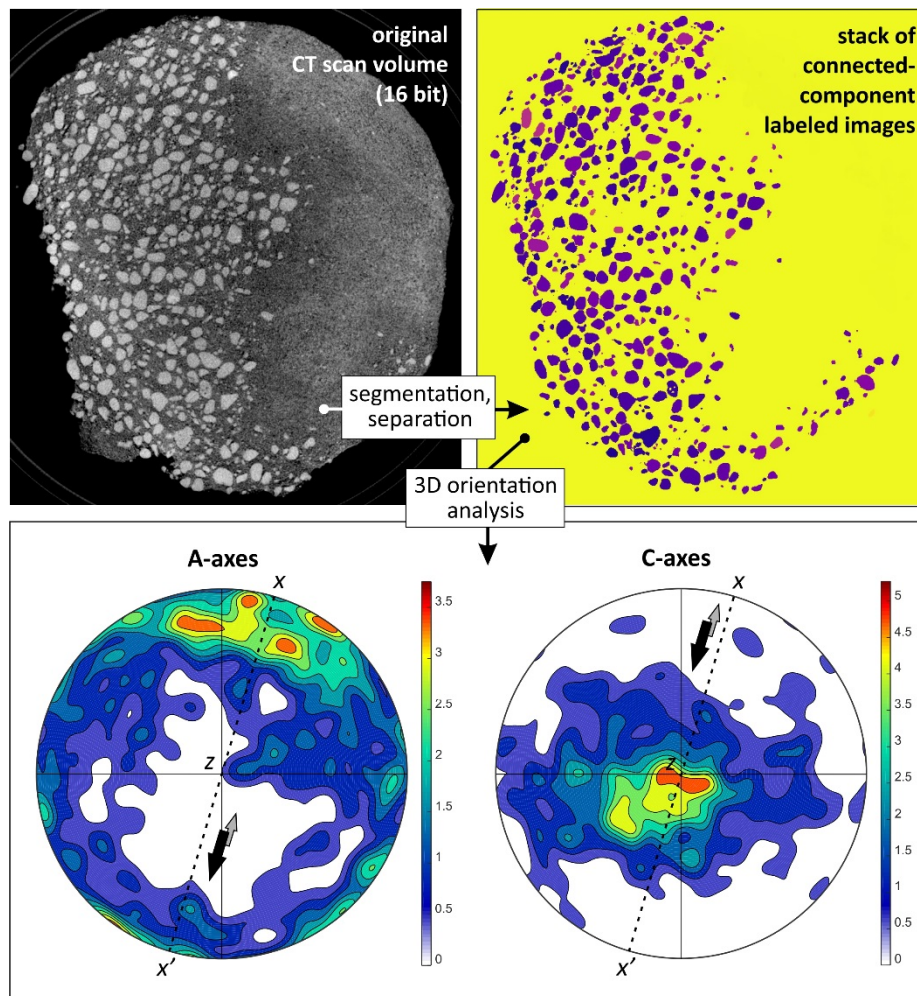


Figure 4: Top: Simplified illustration of main steps in the image processing and analysis to extract the data needed for orientation analysis. Each particle defined by unique label is modeled by an ellipsoid whose shape and orientation is calculated. Bottom: Orientation of long (A) and short (C) axes of particles in the fault shear zone of sample A1. Lambert projection, lower hemisphere, viewed from the pole to shear plane (preliminary results). More than 550 particles were analysed in this sample. The shear sense can be deduced from the asymmetry of centroids of distribution maxima - the black and grey arrows are the interpreted slip directions of the upper and lower parts of the specimen, respectively.

These high contrast and high resolution images not only provide the study material for detailed visual evaluation of 3D sample anatomy but also allow semi-automated separation of individual grains or clasts and subsequent quantitative analysis of large number of particles. Some analytical tools have been tested to show that quantitative analysis of particle orientation may be used as indicator of shear kinematics.

This methodical approach is potentially suitable for coarser clastic sediments or clasts-in-matrix lithologies representing common examples of faulted rocks in which slickensides typically do not develop. Alternatively, internal fabric of any soft sediment can be studied by similar ways to reveal the flow direction related to other processes than faulting, e.g. liquefaction, solifluction or frost-related deformation.

Acknowledgements: SolidVision Ltd. is thanked for providing free μ CT scanning of two samples.

REFERENCES

- Arganda-Carreras, I., Kaynig, V., Rueden, C. et al., 2017. Trainable Weka Segmentation: a machine learning tool for microscopy pixel classification, *Bioinformatics* 33 (15), 2424-2426.
- Bachmann, F. Hiescher R., Schaeben H., 2010. Texture Analysis with MTEX – Free and Open Source Software Toolbox. *Solid State Phenomena* 160, 63-68.
- Cladouhos T.T., 1999. Shape preferred orientations of survivor grains in fault gouge. *J. Struct. Geol.* 21, 419-436.
- Hayman N.W., Housen B.A., Cladouhos T.T., Livi K., 2004. Magnetic and clast fabrics as measurements of grain-scale processes within the Death Valley shallow crustal detachment faults. *J. Geoph. Res.* 109, B05409.
- Legland D., Arganda-Carreras I., Andrey P., 2016. MorphoLibJ: integrated library and plugins for mathematical morphology with ImageJ. *Bioinformatics* 32 (22), 3532–3534.
- Schindelin J. and 15 co-authors, 2012. Fiji: an open-source platform for biological-image analysis. *Nature Methods* 9, 676–682.



Tectono-magmatic domains of the eastern Basin and Range, Utah, determined from paleoseismic investigations of active faults

Stahl, Timothy (1), Niemi, Nathan (2), Bunds, Michael (3), Andreini, Jeremy (3), Wells, Jack (3)

- (1) Department of Geological Sciences, University of Canterbury, Christchurch, New Zealand. timothy.stahl@canterbury.ac.nz
 (2) Department of Earth and Environmental Sciences, University of Michigan, Ann Arbor, Michigan, USA
 (3) Department of Earth Science, Utah Valley University, Orem, Utah, USA

Abstract: Tectonic and magmatic processes accommodate extension at the eastern margin of the Basin and Range province in the Sevier Desert of Utah. Paleoseismic investigations across a transect of active faults, using a range of survey (terrestrial lidar, UAV-photogrammetry, and manual RTK transects) and Quaternary geochronology ($^{40}\text{Ar}/^{39}\text{Ar}$, ^3He and ^{10}Be exposure-ages), reveal the spatiotemporal relationship of faulting to magmatic (e.g., dike intrusion) and tectonic (seismogenic) processes. Based on these data, two primary faulting domains are delineated: (i) Basin and Range normal faults of tectonic origin, and (ii) magma-assisted rifting and dike-induced faults. This framework is consistent with previous elastic-dislocation modelling of continuous GPS velocities across the region that suggests localized, pure shear extension in the eastern Sevier Desert superimposed on the far-field, plate boundary-driven rifting of the Basin and Range. This points towards trans-rift segmentation of the eastern Basin and Range into magma-poor and magma-assisted segments.

Key words: Sevier Desert, tectonic faults, magma-assisted rifting, paleoseismology

INTRODUCTION

Within continental rifts, active faults provide records of the tectonic and magmatic processes that accommodate extension. In magma-starved rifts or rift segments, the accumulation of extensional strain through the seismic cycle leads to the development of seismogenic normal faults. These faults are capable of generating moment magnitude (M_w) 7 or greater earthquakes that rupture the upper crust to the surface (Smith et al., 1996). Over millions of years, hanging wall subsidence and footwall uplift from the cumulative interseismic and coseismic deformation leads to the development of topographic and structural basins and ranges. In magma-assisted rifts, seismogenic faults may form alongside other faults that have formed in

response to local magmatic and volcanic processes (e.g., via dike intrusion). These faults do not typically rupture the full width of the seismogenic crust and therefore have maximum magnitudes limited to c. M_w 5.5 in historical datasets (Smith et al., 1996). Determining which mode of faulting predominates in a region is critical for both assessing regional seismic hazard and understanding the spatiotemporal variability in processes that contribute to lithospheric deformation (Rowland et al., 2010; Villamor et al., 2011; Gómez-Vasconcelos et al., 2017). These issues are salient in the eastern Sevier Desert of Utah (eastern Basin and Range, Fig. 1), where recent seismic hazard assessments have questioned the origin and seismogenic potential of active faults (WGUEP, 2016).

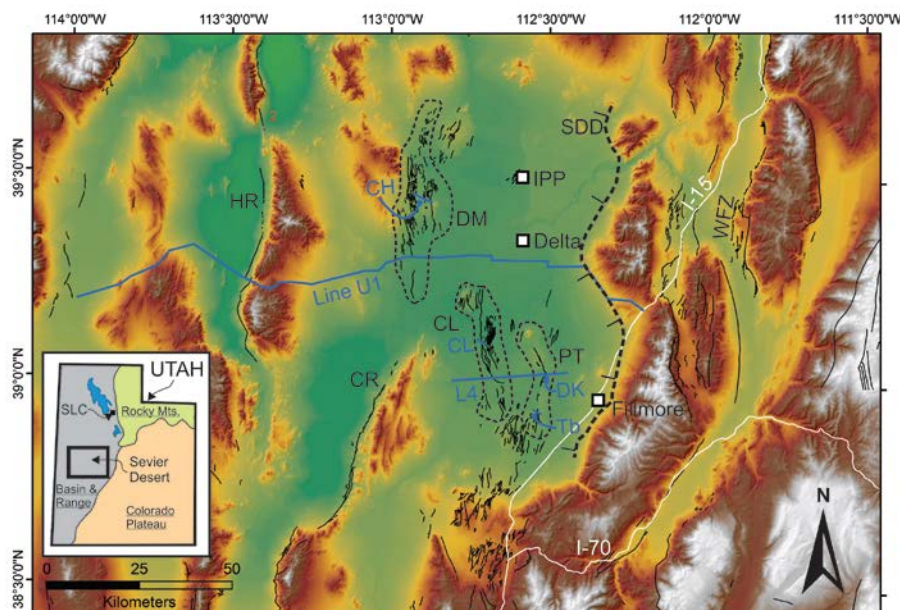


Figure 1: Location map of faults within and proximal to the Sevier Desert, Utah. The inset (modified after McBride et al., 2010) shows the location of the Sevier Desert at the eastern margin of the Basin and Range (gray). Faults discussed in text are HR: House Range; CR: Cricket Range; CL: Clear Lake (includes Deseret); DM: Drum Mountains; PT: Tabernacle-Pavant; SDD: Sevier Desert Detachment; WFZ: Wasatch Fault Zone. Blue lines are the locations of seismic reflection studies of Allmendinger et al. (1983), Crone and Harding (1984), Planke and Smith (1991), and McBride et al. (2015). IPP: Intermountain Power Plant. I-15 and I-70 are major interstate highways.



We present preliminary paleoseismic evidence for five previously mapped fault zones across the Sevier Desert – the House Range, Cricket Mountains, Tabernacle-Pavant, Deseret, and Clear Lake faults— that highlight the varying characteristics and modes of faulting in the tectono-magmatic domains of the eastern Basin and Range (Fig. 1). Terrestrial laser scanning (TLS), UAV-photogrammetry, and manual GPS surveying of fault scarps provide displacement data at key sites along the faults. Age control of faulted landforms and of most recent surface-rupturing events (MREs) is provided by ^{10}Be and ^3He age models of faulted alluvial fans and basalt tension fissures, respectively. Additional age control was provided by $^{40}\text{Ar}/^{39}\text{Ar}$ dating of Pleistocene lava flows.

Western Sevier Desert faults

Time-averaged net slip rates are less than 0.1 mm yr^{-1} over the last c. 20-30 ka on range-bounding normal faults of the western Sevier Desert (House Range and Cricket Mountains faults, Fig. 1). In the House Range, timing of the MRE is constrained to a maximum of c. 15-18.5 ka BP by modelling of ^{10}Be ages on undeformed, post-Provo highstand alluvial fans (Fig 2). Single event displacements (SEDs) of c. 1-2 m on both the House Range and Cricket Mountains faults last occurred during the establishment, or soon after the abandonment, of the Provo shoreline of Lake Bonneville (dated to c. 15-18 ka BP in other closed sub-basins of Lake Bonneville). Transgressive shorelines that formed before the Bonneville highstand (i.e., between c. 20-30 ka BP) are displaced by the same amount as the Provo shoreline, indicating a minimum recurrence interval on the faults of c. 15 ka (Fig. 2). Both the House Range and Cricket Mountains fault traces are confined to $10^1\text{-}10^2 \text{ m}$ zones along the range front and demarcate the boundary between asymmetric gravity anomalies associated with long-term range growth and basin development (Fig. 1).

Eastern Sevier Desert faults

Time-averaged net slip rates of the Tabernacle-Pavant, Clear Lake, and Deseret faults are $0.2\text{-}0.5 \text{ mm yr}^{-1}$. Despite having higher slip rates than faults of the western Sevier Desert, volcanic centers dominate the topographic relief of the eastern Sevier Desert; distributed slip across the $10^3\text{-}10^4 \text{ m}$ -wide zones of antithetic and synthetic faults has resulted in little cumulative topographic relief over the last c. 700 ka (based on $^{40}\text{Ar}/^{39}\text{Ar}$ dating of the Pavant and Deseret lava flows). Additionally, large on-fault vertical displacements are clustered around volcanic centers and taper to negligible values along- and across the faults.

Two vertical displacements of c. 5 m for the Tabernacle-Pavant section of the Tabernacle-Pavant fault, determined using TLS, occurred around the timing of formation of the Provo shoreline at c. 15-18 ka (Fig. 3). Field observations and detailed mapping facilitated by TLS revealed evidence of two Provo-aged shorelines on the hanging wall of the primary west-dipping fault (Fig. 3). There is evidence of rounded basalt boulders, wave-eroded cavities, and tufa development along the two shorelines, and both are clearly defined in the TLS. The lower and upper shorelines are offset from the correlative footwall shoreline by 5 and 10 m, respectively (Fig. 3). This indicates two events took place: the first occurring during initial formation of the Provo shoreline and the second sometime during or after development of the upper shoreline. Cosmogenic ^3He dating of a tension fissure situated within the fold scarp shows evidence for one event occurring at $c. 15.9 \pm 1.8 \text{ ka BP}$ and a second possible event at $13.6 \pm 2.5 \text{ ka BP}$. At present, it cannot be determined whether these ages, from four samples at different locations on the fissure walls, represent one or both of the events observed in the geomorphology (Fig. 3).

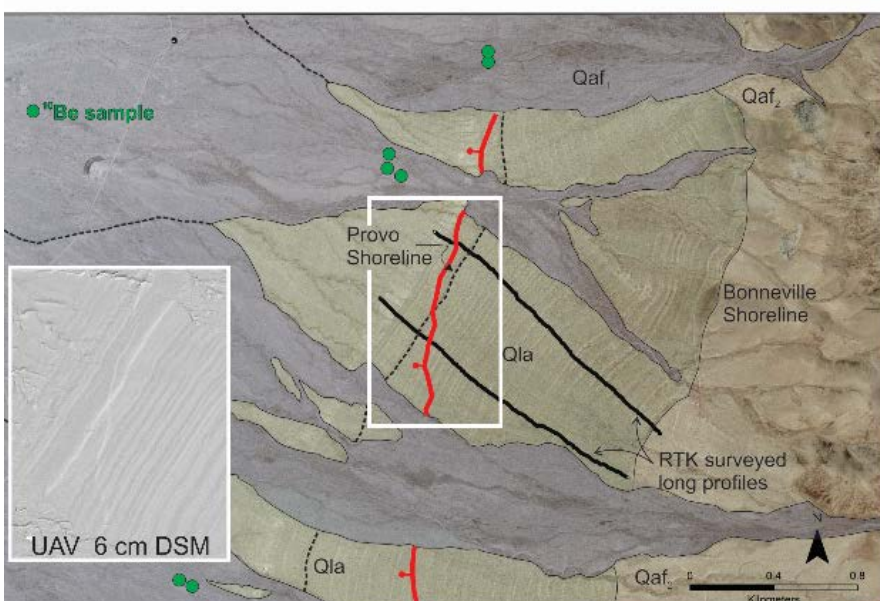


Figure 2: Displaced shorelines of Lake Bonneville along the House Range fault. Inset shows UAV-derived DSM used for detailed mapping and displacement measurements. The Provo shoreline (c. 15-18 ka BP, dashed in the aerial photo) is displaced by the same amount, within uncertainty, as the sequence of transgressive shorelines (c. 20-30 ka BP) located topographically above and below. This is indicative of a single Surface-rupturing earthquake having occurred on the House Range fault in the last 20-30 ka, likely during occupation of the Provo shoreline. Green dots show the locations of ^{10}Be samples which constrain the age of post-Provo alluvial fans to being a maximum of 18.5 ka BP. This is in agreement with geomorphic evidence of rapid Post-provo sediment aggradation (Hintze and Davis, 2003).



Sedimentary evidence from tension fissures further north along the Pavant section of the Tabernacle-Pavant fault indicates that fault-related fissures along these stretches were established prior to the Provo highstand and possibly before Lake Bonneville (20-30 ka BP), with no evidence of recent on-fault displacement. This indicates a remarkably small fault length (c. 5 km) for the observed 5 m vertical SED along the Tabernacle section. Such observations are consistent with dike-induced faulting elsewhere (Rowland et al., 2007) but would be at odds with length-displacement scaling of seismogenic faults in historical earthquakes (e.g., Wells and Coppersmith, 1994).

DISCUSSION

Both western and eastern Sevier Desert faults show evidence for latest Pleistocene to Holocene surface-rupturing events; however, the rates and characteristics of these surface displacements are fundamentally different. On the basis of our observations, and those of Stahl and Niemi (2017), we demarcate two faulting domains across the Sevier Desert:

(i) Seismogenic 'Basin and Range' normal faults of entirely tectonic origin (House Range and Cricket Mountains faults)

These faults accumulate elastic strain over thousand year timescales and rupture the seismogenic part of the crust (c. 10-15 km) in $\geq M_w$ 6-7 earthquakes. They have subdued surface expression on active traces due to the relatively low modern slip rates being nearly matched by the rate of hillslope diffusion and basin deposition. Fault traces are confined to narrow zones along range fronts and delineate the boundaries between topographic and structural relief. Single event displacements (1-2 m) are consistent with average displacements observed along other surface-rupturing normal faults of the Basin and Range.

(ii) Intrabasin normal faults of primarily magmatic origin (Deseret, Clear Lake, and Tabernacle-Pavant faults)

These faults are spatially and temporally associated with volcanic centers and are likely the result of dike intrusion and arrest in the upper crust. Extension rates across the fault zones are similar to that of a tensile dislocation modelled in continuous GPS velocities (Stahl and Niemi, 2017), indicating a local 'active rifting' mechanism acting on the crust in this region. Large on-fault displacements are local and decrease rapidly along and perpendicular to faults. While there is some evidence for accumulated displacements of subsurface units since the Pliocene, there is little net topographic relief controlled by faulting over the last 1 Ma.

Segmentation of continental rifts into magma-poor and magma-assisted segments has typically been considered along the axis of narrow rift zones (e.g., East Africa and Taupo Volcanic Zone). The evidence presented here points towards trans-rift segmentation across the eastern margin of the Basin and Range province. In this particular circumstance, it is likely that the relatively large amount of extension accommodated at this margin margin of the Basin and Range over the course of late Cenozoic rifting has

primed this area for magmatism and dike-induced faulting relative to the interior of the rift.

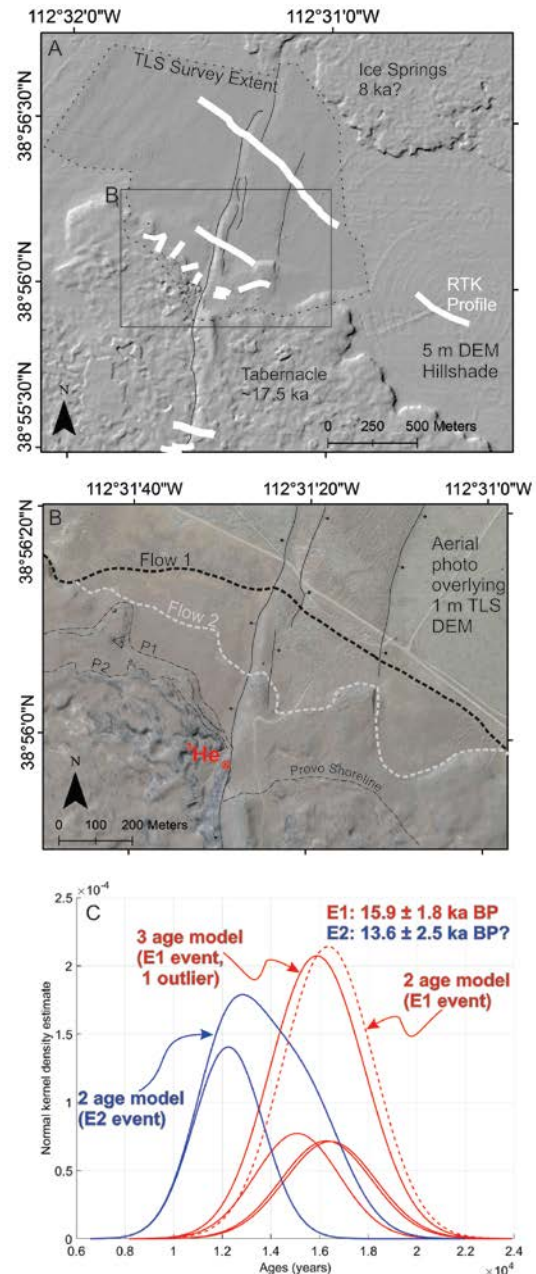


Figure 3: Location of study site, field surveys, and exposure-age dating along the Tabernacle section of the Tabernacle-Pavant fault. (A) 5 m DEM showing the location of the study site situated at the northern edge of the Tabernacle flow and south of the Ice Springs flow. White lines show locations of RTK GPS surveys across faults and the Provo shoreline(s). (B) Mapping on 1 m TLS-derived DEM showing two Provo shorelines on the downthrown side of the major fault and correlation of flow edges across the faults. The location of the tension fissure sampled for ^3He dating of olivine in the basalt is shown in red. The depth of fissure is approximately 10 m and is equal to the vertical displacement on the fault. Samples were taken from the base and top (below 2.5 m of the flow surface) to test for progressive opening of the crack in multiple events. (C) Probability density functions (PDFs) of the exposure-ages of individual samples (smaller PDFs) and summary "camel plots" for different event scenarios (PDF envelopes).



CONCLUSIONS

Faults of the Sevier Desert, Utah can be split into two tectono-magmatic domains: those relating to local stresses induced by dike intrusion and those related to far-field plate boundary stresses. The different domains are characterized by variations in surface expression, slip rate, and SEDs. While rift segmentation along narrow continental rifts is commonly observed (e.g., East African Rift and Taupo Volcanic Zone), we observe segmentation across the eastern margin of the Basin and Range. Detailed mapping, surveying and dating can resolve this pattern of segmentation; future efforts should be directed towards delineating magma-assisted segments from purely tectonic segments across other continental rifts.

Acknowledgements: This research was funded by NSF EAR Postdoctoral Fellowship to Stahl (NSF1451466). The authors wish to thank the numerous lab managers, technicians, and geochronologists who assisted with this work. Amanda Maslyn is gratefully acknowledged for assisting with quartz and olivine mineral separation at the University of Michigan. Field support was provided by the Utah Geological Survey. John Sandru and Chris Crosby of UNAVCO helped organize various aspects of TLS field surveys and processing. Eldon Gath helped improve the quality of this manuscript.

REFERENCES

Crone, A.J. & Harding, S.T. 1984. Relationship of late Quaternary fault scarps to subjacent faults, eastern Great Basin, Utah. *Geology* 12(5): 292-295.

Gómez-Vasconcelos, M. & Villamor, P., Cronin, S., Procter, J., Palmer, A., Townsend, D., Leonard, G. 2017. Crustal extension

in the Tongariro graben, New Zealand: Insights into volcano-tectonic interactions and active deformation in a young continental rift. *Geological Society of America Bulletin* 129(9-10): 1085-1099.

Hintze, L.F., Davis, F.D. 2003. Geology of Millard County, Utah. *Utah Geological Survey Bulletin* 133: 287 p.

Rowland, J. V., Baker, E., Ebinger, C.J., Keir, D., Kidane, T., Biggs, J., Hayward, N., Wright, T.J. 2007. Fault growth at a nascent slow-spreading ridge: 2005 Dabbahu rifting episode, Afar. *Geophysical Journal International* 171: 1226–1246. doi: 10.1111/j.1365-246X.2007.03584.x.

Rowland, J.V., Wilson, C.J., and Gravley, D.M. 2010. Spatial and temporal variations in magma-assisted rifting, Taupo volcanic zone. New Zealand. *Journal of Volcanology and Geothermal Research* 190(1–2): 89–108. doi:10.1016/j.jvolgeores.2009.05.004.

Smith, R. P., Jackson, S. M. & Hackett, W. R. 1996. Paleoseismology and seismic hazards evaluations in extensional volcanic terrains. *Journal of Geophysical Research: Solid Earth* 101: 6277–6292. doi: 10.1029/95jb01393.

Stahl, T., Niemi, N. 2017. Late Quaternary faulting in the Sevier Desert driven by magmatism. *Nature Scientific Reports*: doi:10.1038/srep44372.

Villamor, P., Berryman, K.R., Nairn, I.A., Wilson, K., Litchfield, N., and Ries, W. 2011. Associations between volcanic eruptions from Okataina volcanic center and surface rupture of nearby active faults, Taupo Rift, New Zealand: Insights into the nature of volcanotectonic interactions. *Geological Society of America Bulletin* 123(7-8): 1383–1405. doi:10.1130/B30184.1.

Wells, D.L., Coppersmith, K.J. 1994. New empirical relationships among magnitude, rupture length, rupture width, rupture area, and surface displacement. *Bulletin of the Seismological Society of America* 84(4): 974-1002.

Working Group on Utah Earthquake Probabilities (WGUEP). 2016. Earthquake probabilities for the Wasatch Front region in Utah, Idaho, and Wyoming. *Utah Geological Survey Miscellaneous Publication* 16-3: 164 p., 5 appendices.



Valley evolution of the Biala Łądecka drainage network during late Cenozoic, Lower Silesia, Poland

Stemberk, Jakub (1,2), Štěpančíková, Petra (2), Tábořík, Petr (1,2), Coubal Miroslav (2)

- (1) Department of Physical Geography and Geoecology, Charles University in Prague, Albertov 6, Prague 2, 128 43, Czech Republic. Email: kuba.stemberk@gmail.com
- (2) Institute of Rock Structure and Mechanics, Academy of Sciences of the Czech Republic, Dpt. Engineering Geology, V Holešovičkách 41, Prague 8, 182 09, Czech Republic.
- (3) Institute of Hydrogeology, Engineering Geology and Applied Geophysics, Charles University in Prague, Albertov 6, Prague 2, 128 43, Czech Republic.

Abstract: Biala Łądecka (Biala Kłodzka) river is located in Lower Silesia (Poland) and its valley separates Góry Złote Mts. (Rychlebské hory Mts.) on the NE from Góry Bialskie Mts. on the SW. We conducted geomorphic investigations on the Biala Łądecka river basin, in order to determine if Quaternary tectonic activity at the Bělský fault (or near Marginal Sudetic fault) is contributing to the river's asymmetry. Our research was focused on analysis of selected landforms, DEM parameters, morphometric indexes and their spatial distribution which could potentially indicate recent tectonic activity in the area. At selected places geophysical measures were used to discover proper location and structure of Bělský fault or presence of suggested morpholineaments. Preliminary results suggest a Quaternary tectonic activity for the Bělský fault. Moreover we tried to clarify nowadays stress regime in study area based striae measurement on fault planes and precise monitoring of selected faults using TM-71 device.

Key words: Poland - Czech border, NE Europe, stable continental areas, Biala Łądecka river, Bělský fault, morphometric indexes, DEM analysis, geophysical survey.

INTRODUCTION

The study area covers the upper part of Biala Łądecka drainage and adjacent region which is located partly in Czech Republic, but mainly in Poland (Fig. 1) and belongs to Bohemian Massif as a part of Epihercynian platform. It belongs to eastern part of the Sudety mountain system, specifically Rychlebské hory Mts. on the Czech side, Góry Złote and Góry Bialskie on the Polish side, where the highest peaks of these mountains are located (Smrk 1127 m a.s.l., Czernica 1083 m a.s.l.).

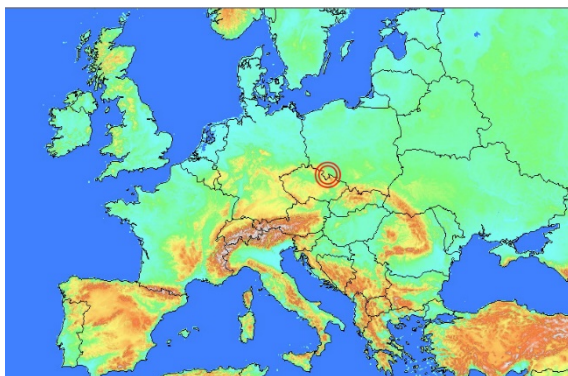


Fig. 1: Location of the study area.

It is represented by tectonically uplifted blocks with well-preserved NNE-SSW trending Variscan structure (the Staré Město unit and Śnieżnik unit) built almost exclusively of Precambrian metamorphic rocks and later granitoids (Kasza 1964, Don 2003). During the Pliocene and Pleistocene faults striking NW-SE to NNW-SSE were reactivated (Grygar and Jelínek, 2003) and movements on these faults influenced now-a-days relief of mountains. However the Bohemian

Massif was in older literature considered as a tectonically inactive area, monitoring of micro-displacements directly on fault planes using TM-71 devices (see lower) or GPS measurements have discovered recent tectonic activity in this part of the Bohemian Massif, (see eg. Cacoň and Dyjor, 1995, Schenk et al. 2003; Kontny 2004, Cacoň et al. 2005).



Fig. 2: Topographic map of the Rychlebské hory Mts. (Góry Złote Mts.) with marking the Bělský fault zone and the Sudetic Marginal Fault. BLV – Biala Łądecka valley, red line delineate the study area.

The main structure in study area is the 100km long Bělský fault (BF), in Poland called Bielawka fault or Trzebieszowice-Biala fault, sometimes Biala fault (BF). It belongs to Elbe Fault System which is the zone of predominantly parallel NW-SE striking faults (eg. Sudetic Marginal Fault, Klepáčovský fault) traceable from the SE North Sea to the front of the Carpathian outer flysch nappes (Schenk et al. 2002). The zone has been active at least since



Late Cretaceous time and underwent various types of movements during its evolution (Danišík et al. 2012). BF continues to SE through in Hrubý Jeseník Mts. and Nížký Jeseník Highland as a step-over fault of the Sudetic Marginal Fault and forms an 8 km wide fault zone with CO₂ mineral springs (eg. in Karlova Studánka, Dolní Moravice, etc.) (Hynie 1963). To the SE also Neogene and Quaternary volcanics (eg. Uhlířský vrch hill, Venušina sopka volcano) are placed in the zone (Buday et al., 1995). Historical (Guterch and Lewandowska-Marciniak 2002) and present seismicity has been documented in this area (eg. Špaček et al. 2006, Zedník et al. 2001). The NW extension of the BF is uncertain; the presence of the 3.83 – 5.46 Ma old volcano and 2 lava flows (Birkemajer 2002) near Łądek Zdroj might be evidence of a fault segment related to the main BF fault.

The aim of this contribution is to show the likely possible young reconfiguration of upper part of Biala Łądecka drainage network caused by BF during the Cenozoic based on geomorphological evidence. Drainage network parameters may contain useful information about present and past tectonic movements (see eg. Burbank and Anderson 2001, Keller and Pinter 2002, etc.). We analyzed the spatial distribution of selected landforms (eg. gullies, springs, swamps, linear shapes of relief, youngest erosion in drainage, etc.) based on detail geomorphological mapping (see Fig. 4). We performed geophysical prospecting in order to properly map the BF fault trace and define the fault structure in detail (see Fig. 3).

ANALYSIS AND DISCUSSION

The analysis of drainage network of upper part of Biala Łądecka river basin discovered extreme asymmetry of the basin (asymmetry factor AF = 31.5%) as visible on Fig. 4. It indicates the influence of tectonic movements on faults in this area during Cenozoic. Recent works about the Sudetic Marginal Fault zone (BF belongs to this zone) in Rychlebské hory Mts. (Góry Złote Mts.) describe that the region have undergone 4-5 stages of uplift since Miocene (Badura et al. 2007), and also horizontal movements are determined on Sudetic Marginal Fault (Štěpančíková 2010, 2017 in prepare). In the BF zone sinistral sense of movement on main faults was suggested (same as on the Sudetic Marginal Fault) base on the valley offset of the Biala Łądecka river and Stříbrný potok brook. (see Fig. 4) Nowadays left lateral displacement of the Biala Łądecka river valley is nearly 2km since upper Pliocene when the valleys have started to downcutting (Ivan 1966). The offset of valley of the Stříbrný potok brook in BF zone is nearly 1.2 km. The rectangular bands in valley direction occur mainly due to presence of lithostratigraphic boundaries and also due to probably horizontal tectonic movements. We observed horizontal displacement on other smaller (younger) creeks, where offset is only several meters.

Unfortunately nowadays valleys are free of any sediment suitable to date, even in many cases streams are flowing directly on bedrock. Holocene and Saal 1 river terraces of Biala Łądecka river are preserved in lower part of the valley.

Longitudinal profiles and SL indexes (Hack 1973) were constructed and calculated for all streams longer than 1 km based on 1m - LIDAR data (see Fig. 5 and Fig. 6. The SL indexes (Hack, 1973) were calculated for 100m long segments each 50 m of the stream following the formula $SL = SL = (\Delta H / \Delta L) L$, where $\Delta H / \Delta L$ is gradient of 100m long segment and L is the distance of midpoint from the stream beginning. The advantage of the SL index is to compare changes in channel slope of streams in different order. Afterwards it is possible to evaluate the relationships among tectonic activity, rock resistance and topography (Keller and Pinter 2002).

Longitudinal profiles of streams are highly unbalanced due to presence of lithostratigraphic boundaries and also presence and movements of verified faults or suggested morpholineaments (see below). Moreover these faults were based on SL indexes marked as active/inactive. The example of longitudinal profile of Bielawka river and its tributaries in combination with SL index position show plots on Fig. 5 and Fig. 6.

Morpholineaments represent the linear elements of the relief, such as linear sections of valleys, linear spatial distribution of selected landforms or linear structures directly visible from DEM. They can be associated with tectonic dislocations or lithostratigraphic boundaries (see e.g. Badura et al. 2003, Štěpančíková 2005). Based on analyse of morpholineaments and linear arrangement of selected geomorphological landforms new traces of suggested faults were delineated, some of them were based on SL indexes marked as active (see Fig. 4). This method seems to be useful to determine fault traces in areas where geological maps or other materials are missing.

We used geophysical survey (ERT transects) to see structure and placement of BF and also to confirm some suggested faults (from morpholineaments). The BF zone is more-or-less parallel faults, express as high conductive ~60-100 m width fault zone nearly vertical filled by weathered or crushed rocks, sometimes followed on the surface by springs or swamps. (see Fig. 3).

To determine the ongoing stress regime in study area we monitored selected faults with TM-71 devices installed directly across a fissure or a fault plane. The TM71 device is based on a mechanical optical principle (Moiré technique) and is able to monitor movements with precision 0.01 mm/year in 3D. This device was installed in several regions with different levels of tectonic activity (for more details see Košťák 1991, Stemberk et al. 2003, etc.). Even though the tectonic activity in study area is low, aseismic tectonic movements ~0,05mm/year were observed. The records of several TM-71 devices from adjacent area will be presented. Measurement of orientation and dip of striae on several rock outcrops were also carry out to support TM71 results.



CONCLUSIONS

Based on detailed geomorphological mapping, DEM analyses, geophysical research and monitoring of nowadays movements on selected faults using TM-71 device we suggest Bělský fault (and also other regional faults in study area) activity during the Quarternary. As a preliminary results we've clarified the stress regime in study area and sense of movement on Bělský fault. All results will be presented, additional research will build off of this work.

Acknowledgements: This work was supported by the Grant Agency of Charles University in Prague (GAUK862213 - Multidisciplinary geophysical survey in investigation of landforms) and by Grant of Ministry of Education, Youth and Sports of the Czech Republic (LH12078 - Assessment of Tectonic Movements on Active Faults, Program KONTAKT II.). Special thanks to support by Strategie AV21, Czech Academy of Sciences.

REFERENCES

- Badura, J., Zuchiewicz, W., Górecki, A., Sroka, W., Przybylski, B., Żyszkowska, M. (2003): Morphotectonic properties of the Sudetic Marginal Fault, SW Poland. *Acta Montana, Serie A 24* (131), p21–49.
- Badura, J., Zuchiewicz, W., Štěpančíková, P., Przybylski, B., Kontny, B., Cacoń, S. (2007): The Sudetic Marginal Fault: A Young Morphotectonic Feature at the NE Margin of the Bohemian Massif, Central Europe. *Acta Geodyn. Geomater.*, 4, p. 1-23.
- Birkenmajer, K., Pécskay, Z., Grabowski, J., Lorenc, M.W., Zagożdżon, P.P. (2002): Radiometric dating of the Tertiary volcanics in Lower Silesia, Poland. II. K–Ar and palaeomagnetic data from Neogene basanites near Łądek Zdrój, Sudetes Mts. *Annales Societatis Geologorum Poloniae* 72, p119–129.
- Buday, T., Ďurica, D., Opletal, M., Šebesta, J. (1995): Význam bělského a klepáčovského zlomového systému a jeho pokračování do Karpat. Uhlí, rudy, geologický průzkum 2 (9), 275–282.
- Burbank, D.W., Anderson, R.S., 2001. *Tectonic Geomorphology*. Blackwell Science, Oxford.
- Cacoń, S., Dyjor, S., 1995. Neotectonic and recent crustal movements as potential hazard to water dams in Lower Silesia, SW Poland. *Folia Quaternaria* 66, p59–72.
- Cacoń, S., Vyskočil, P., Talich, M., Kontny, B., Bosy, J., 2005. Deformation analysis of the Polish Sudetes and Fore–Sudetic block. *Reports on Geodesy* 2 (73), p211–219.
- Danišík, M., Štěpančíková P. and Evans N. (2012): Constraining long-term denudation and faulting history in intraplate regions by multi-system thermochronology - an example of the Sudetic Marginal Fault (Bohemian Massif, Central Europe), *Tectonics* 31, Tc2003, 19pp.
- Don, J., Skácel, J., Gotowała, R. (2003): The boundary zone of the East and West Sudetes on the 1:50 000 scale geological map of the Velké Vrbno, Staré Místo and Sněžník Metamorphic Units. *Geologia Sudetica*, 2003, 35, p25–59.
- Finckh, L. and Götzinger, G. (1931): Erläuterung zur geologischen Karten des Richenstein Gebirges, des Nesselkoppenkammes und des Neisse-Vorlandes, Wien, 108p.
- Grygar R. and Jelínek J. (2003): The Upper Morava and Nysa pull apart grabens the evidence of neotectonic dextral transtension on the Sudetic Fault System. *Acta Montana IRSM AS CR, ser. A*, 24, p51 - 59.
- Gutercz B. and Lewandowska-Marciniak H. (2002): Seismicity and seismic hazard in Poland. *Folia Quat.*, 73, p85-99.
- Hack, J.T., 1973. Stream-profile analysis and stream-gradient index. *Journal of Research of the U.S. Geological Survey*, 1 (4), p421–429.
- Hynie O. (1963): *Hydrogeologie ČSSR II, Minerální vody*. — Nakladatelství Československé akademie věd. Praha.
- Ivan, A. (1966): Geomorfologické poměry severozápadní části Rychlebských hor. Theses, GÚ ČSAV, Brno, 120 p.
- Kasza, L., (1964): Budowa geologiczna górnego dorzecza Białej Łądeckiej. *Geologia Sudetica*, Vol. 1, Krakow.
- Keller, E.A., Pinter, N., (2002): *Active tectonics—Earthquakes, Uplift and Landscape*. Prentice Hall, New Jersey.
- Kontny, B., 2004. Is the Sudetic Marginal Fault still active? Results of the GPS monitoring 1996–2002. *Acta Geodynamica et Geomaterialia* 1, 3 (135), p35–39.
- Košťák, B., 1991. Combined indicator using Moiré technique. *Proc. 3rd Int. Symp. On Field Measurements in Geomechanics*, 9–11 Sept. 1991 Oslo, I, Brookfield, Balkema, Rotterdam, p53–60.
- Schenk, V., Schenková, Z., Cacoń, S., Kontny, B., Bosy, J., Kottnauer, P. (2003): To geodynamic interpretations of GPS data monitorred on the EAST SUDETEN network. *Acta Montana, Serie A, No.24* (131), p87–97.
- Stemberk, J., Košťák, B., Vilímek, V., 2003. 3-D monitoring of active tectonic structures. *Journal of Geodynamics* 36, p103–112.
- Stemberk J., Štěpančíková P. (2003): Tectonic setting and newly organised monitoring of recent deformation in the Rychlebské Hory Mts. *Acta Montana*, 24 (131), p153 – 161.
- Špaček, P., Sýkorová, Z., Pazdírková, J., Švancara, J., Havíř, J. (2006): Present-day seismicity of the south-eastern Elbe Fault system (NE Bohemian Massif). *Studia Geophysica Et Geodaetica* 50, p233–258.
- Štěpančíková, P. (2005): Selected analysis of the morphostructure of the NE part of the Rychlebské hory Mts. (Czech republic). *Acta Geodyn. Geomater.*, 2, p59-67.
- Štěpančíková, P., Hók, J., Nývlt, D., Dohnal, J., Sýkorová, I., Stemberk, J. (2010): Active tectonics research using trenching technique on the south-eastern section of the Sudetic Marginal Fault (NE Bohemian Massif, central, Europe). *Tectonophysics*, 485, p269–282.
- Walczak, W. (1954): Pradolina Nysy i plejstocenijski zmiany hydrograficzne na przedpolu Sudetów wschodnich. *Polska Akademia Nauk, Instytut geografii, Warszawa*.
- Zedník, J., Pospíšil, J., Růžek, B., Horálek, J., Boušková, A., Jedlička, P. (2001): Earthquakes in the Czech Republic and surrounding regions in 1995-1999. *Stud. Geophys. et Geod.*, 45, p267-282.

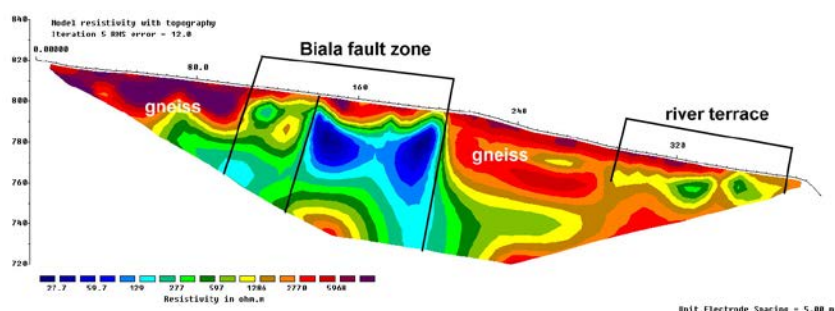
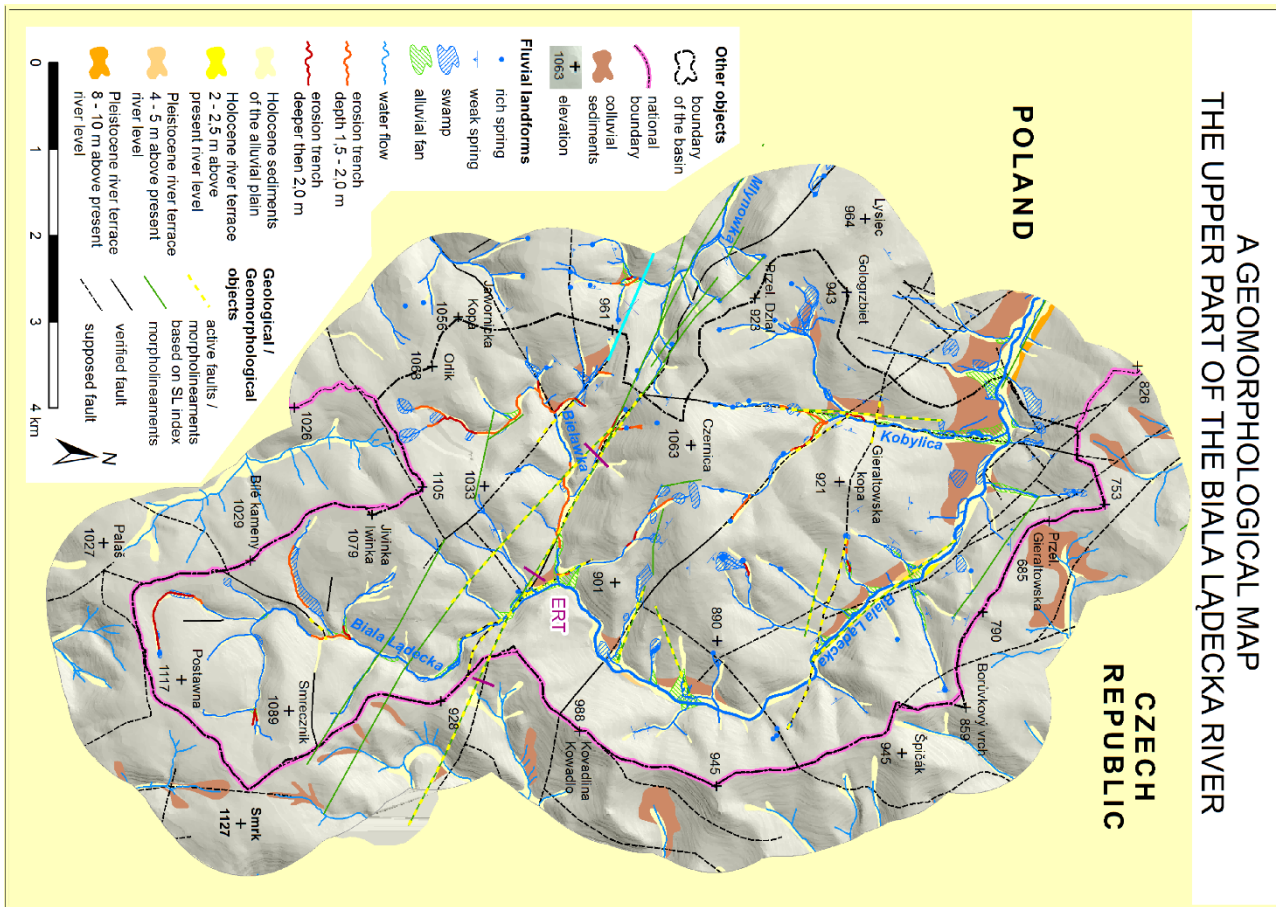
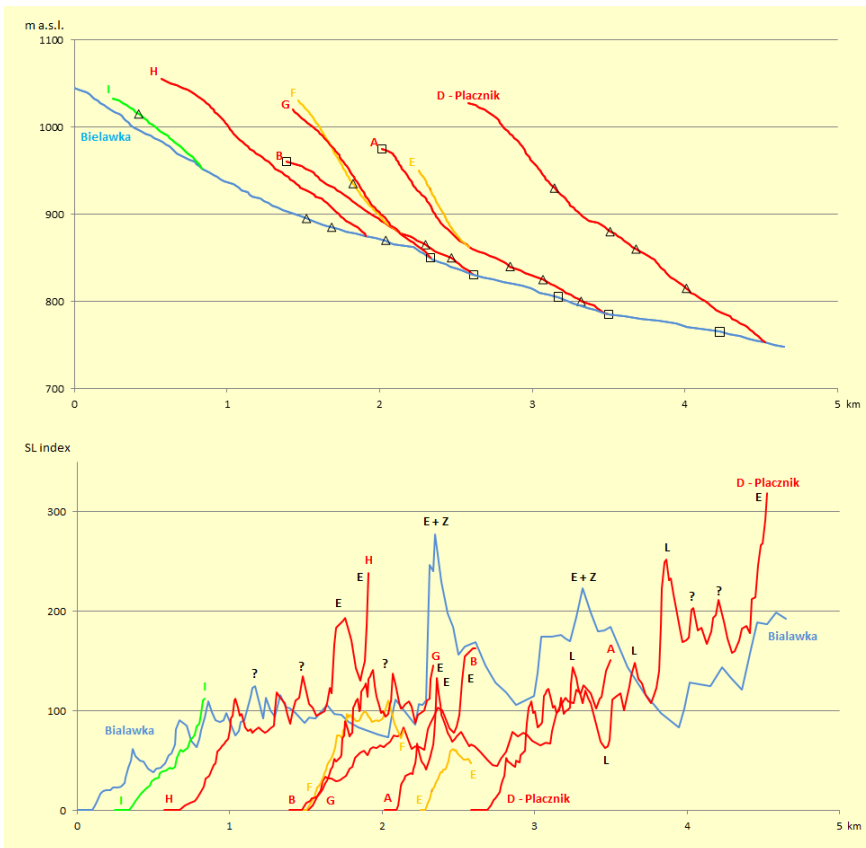


Fig 3: ERT profile cross the Biala fault; location of the profile is mark on Fig 4



A GEOMORPHOLOGICAL MAP
THE UPPER PART OF THE BIALA LADECKA RIVER



↑ Fig. 4: A special geomorphological map.

← Fig. 5: Longitudinal profile of Bielawka brook with all tributaries, triangles identify places where brooks cross the faults; boxes identify places where brooks are following fault.

← Fig. 6: SL index (Hack 1973), reason of peaks: E – erosion, Z – fault, L – lithostratigraphic boundaries; ? – unknown reason.



Late Quaternary activity of slow-slip intraplate Mariánské Lázně fault as revealed by trenching and shallow geophysical survey; Bohemian Massif (Czech Republic, central Europe)

Štěpančíková, Petra (1), Fischer, Tomáš (2), Hartvich, Filip (1), Tábořík, Petr (1, 2), Rockwell, Thomas (3), Stemberk, Jakub (1, 2), Šíroký, Jakub (2), Sana, Hamid (1)

(1) Inst. of Rock Structure and Mechanics, Czech Academy of Sciences, Prague, Czech Rep., stepancikova@irms.cas.cz

(2) Faculty of Science, Charles University, Prague, Czech Rep.

(3) Dpt. of Geological Sciences, San Diego State University, California

Abstract: The NNW-SSE trending Mariánské Lázně Fault (MLF) zone is situated in the western part of the Bohemian Massif (Czech Republic, central Europe) where it intersects NE-trending Cenozoic Eger rift. The northern segment of the MLF controls the morphologically pronounced mountain front of Krušné hory Mts. and eastern limit of Cenozoic Cheb basin, which is famous for earthquake swarms (max. $M_L=4.6$) and CO₂ emanation. We performed 2D and 3D geophysical survey (electric resistivity tomography, ground penetration radar) and 3D trenching to look for large surface-rupturing prehistoric earthquake responsible for pronounced mountain range front. Seven excavated and six hand-dug trenches revealed a complex geology and deformation at the study site probably as a result of right-lateral transpression during Late Quaternary. Two Holocene earthquakes 1150-590 BC and 780-1000 AD were inferred from 14C dating of faulted Holocene colluvium with corresponding magnitudes $M_w=6.7-7.0$. The latter one is the youngest documented surface-rupturing event in central Europe.

Key words: paleoseismic trenching, historic earthquake, Cheb basin, Mariánské Lázně fault, Bohemian Massif

The NNW-SSE trending Mariánské Lázně Fault (MLF) zone is situated in the western part of the Bohemian Massif (Czech Republic, central Europe) and its northern segment controls the eastern limit of Cenozoic Cheb basin. The Cheb basin intersects the NE-trending Cenozoic Eger rift and is typical of present-day earthquake swarms with maximum magnitude $M_w=4.3$, abundant occurrences of mantle-derived carbon-dioxide emanations, and Mid-Pleistocene volcanoes (Fig. 1). In the NW, the MLF governs morphologically pronounced mountain front of the Krušné hory Mts.

The study site Kopanina is situated at the north-eastern limit of the Cheb basin, where the MLF intersects N-S main seismoactive zone of Nový Kostel, which is the most active zone of the West Bohemia/Vogtland region (Fischer et al. 2012). The trace of the studied fault segment is delineated by most recent morphology of the marginal slope of the Krušné hory Mts. and by sites where series of sub-parallel valleys become deeply incised into uplifted block of the Mts (Fig. 2). To study the Quaternary activity of the fault, we combined geophysical survey using ground penetration radar (GPR) and electric resistivity tomography (ERT) with trenching survey. The preliminary results of the first trenching and geophysical campaign were presented by Fischer et al. (2012), Štěpančíková et al. (2015). Here we combine the results from the very first, a 100 m long fault-crossing trench with the following 3D trenching (3 fault-crossing trenches, 3 fault-parallel trenches, 6 small hand-dug trenches) and additional 3D GPR, and 2D and 3D ERT survey.

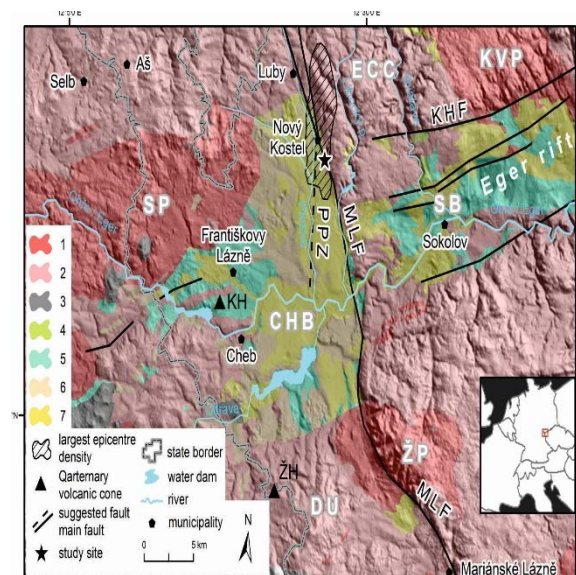


Fig. 1. Geological map of Cheb basin (CHB). Mariánské Lázně Fault (MLF) and Eger Rift (EG) are indicated by black lines. 1 Late Variscan granites and granitoids; 2 Variscan metamorphic units; 3 Volcanics (mainly Oligo-/Miocene); 4 Eocene–Oligocene (Staré Sedlo Formation); 5 Miocene (Cypris Formation); 6 Plio-Pleistocene (Vildštejn Formation); 7 Quaternary; ECC – Erzgebirge (Krušné hory) Crystalline Complex, DU – Dyleň Unit; Variscan granitoids: SP – Smrčiny (Fichtelgebirge) Pluton, KVP – Karlovy Vary Pluton, ŽP – Žandov Pluton; CHB – Cheb basin, SB – Sokolov Basin; KHF – Krušné hory Fault zone, MLF – Mariánské Lázně Fault zone, PPF – Počátky-Plesná Fault zone. Quaternary volcanic cones: KH – Komorní Hůrka volcano, ŽH – Železná Hůrka volcano.



The trenches revealed Cenozoic basin sediments being displaced by repeated movements (7 events/periods) along several faults of the MLF zone of various ages striking 132° to 162° . The succession of sedimentary units of the Cheb basin, consist of the oldest basal Staré Sedlo Formation (upper Eocene to Oligocene) (units group *e*), fluvio-lacustrine Plio-Quaternary Vildstein Formation (units group *f*), and Holocene colluvium (units *h*) (Fig. 3). The oldest units seem to be dragged out, which is suggested by layer inclination observable in the trench as well as in the results of geophysical survey (Fischer et al. 2012). Also the fact that they have been found mostly only in drill holes but they occur on the surface at the study site could be a result of dragging out of the basin infill at its limit. This flexure could be due to normal faulting during Late Oligocene – Early Miocene N-NE-directed extension in the Bohemian Massif (Adamovič and Coubal 1999, Coubal et al. 2015).

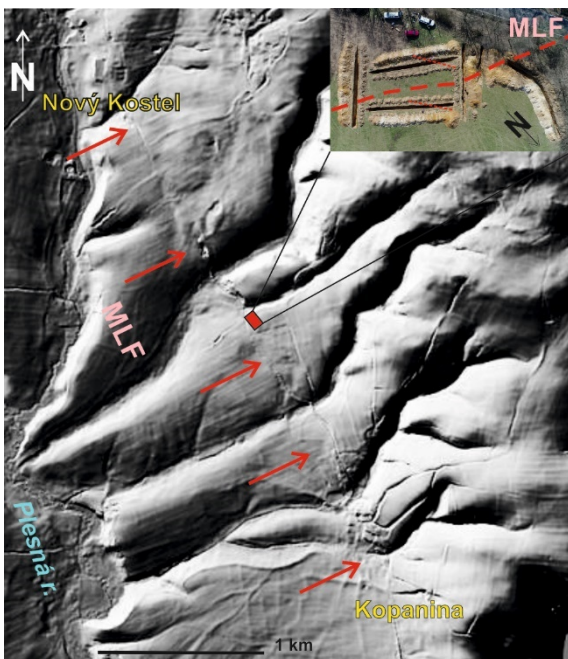


Fig. 2. LiDAR-based DEM of the study site. Red rectangle – trenching site, on the orthophoto in the upper right corner. Red arrows point to MLF, which is highlighted by DEM shows.

The Vildstein Formation in the basin centre has been dated by paleomagnetic and paleobotanic methods as 4.5-1.4 Ma (Bucha et al. 1990, Theodoridis et al. 2017). We dated the younger part of the Formation close to the basin limit by OSL dating, which yielded approx. 173 to 495 ka for different layers. The Formation at the site is displaced by several successive normal faults with probable horizontal component within the 28 m wide zone, which most probably form a single fault at the depth. The Mid-Pleistocene fault activity obviously migrates towards the basin centre, which is probably related to a basin subsidence. The summed displacement per event along these faults reaches up to 30 cm.

The youngest faults striking 132° to 156° displaced also Holocene colluvium at least twice and deformed also the

older *f* units (Fig. 3). The style of deformation with a push-up structure suggests a transpressive regime with prevailing horizontal component of the slip. The older Holocene unit *h1* dated by radiocarbon dating of charcoals as approx. 3300 to 380 BC (modelled cal. years) was displaced by *event 1* and *event 2* with the summed vertical displacement at all faults approx. $49 \text{ cm} \pm 3 \text{ cm}$ per older *event 2*. The younger unit *h2* dated as 360 BC to 1020 AD (modelled cal. years) is vertically displaced by the main fault F1 (132° - 142°) by 39 cm. If we consider the vertical displacements of supposedly strike-slip as minimum value for presumed horizontal slip and consider it as maximum displacement then by using empirical relationships “magnitude versus maximum displacement” (Wells and Coppersmith, 1994) we obtain the minimum magnitude around $M_w=6.5$. In addition, if we consider the length of 11 km of the youngest morphological expression of the MLF as a surface rupture length, by using “magnitude versus surface rupture length” relationship (Wells and Coppersmith, 1994), we obtain at least $M_w=6.3$.

As the above considered displacements are vertical offsets measured in the fault-crossing trenches (trench A and D) and because the deformation style suggests prevailing horizontal slip, the proposed magnitudes might be underestimated. Thus we performed also 3D fault-parallel trenches to trace a horizontally offset feature to obtain the horizontal displacement. We found an offset channel which was dated by radiocarbon dating as 3330 BC to 2140 BC (which would correspond to unit *h1*) and which was right-laterally offset by 1-1.5 m by an oblique fault striking 158° . Occurrence of another oblique faults suggests their en échelon arrangement and could be a result of complex geology within the right-lateral transpression zone. As the channel did not contain a younger unit *h2*, which might have been already eroded, we supposed that it was offset by *event 2* but also displacement during the younger *event 1* cannot be ruled out. Thus, provided that the channel has been offset twice, horizontal slip per event would be around 0.5-0.75 m along this fault. If we sum up this value of 0.5-0.75 m and value for the fault F1 from other fault-crossing trenches we obtain 0.9-1.2 m displacement for *event 1* and 1-1.3 m for *event 2* (including also faults F6 and F7). In such case the corresponding magnitude yields $M_w=6.8 \pm 0.1$ for *event 1* and for *event 2* $M_w=6.8-6.9$ as minimum because we do not know the horizontal offset on the main 132° - 142° striking fault. In an alternative scenario of only one displacing event, we would obtain $M_w=6.8$ to 7.0 for the older Holocene *event 2*.

To refine the age of the Holocene events, we used a chronological model produced in Oxcal programme v4.3.1 (Bronk Ramsey, 2017), using probability distribution of ^{14}C dating results following Lienkaemper and Bronk Ramsey (2009). The modelling yielded *event 2* between 1150 BC and 590 BC and *event 1* occurring between 780 and 1000 AD. To find historic or archeological data supporting the historic surface-rupturing earthquake (*event 1*), the youngest and largest documented in central Europe and in Bohemian Massif, will be a subject of further study.

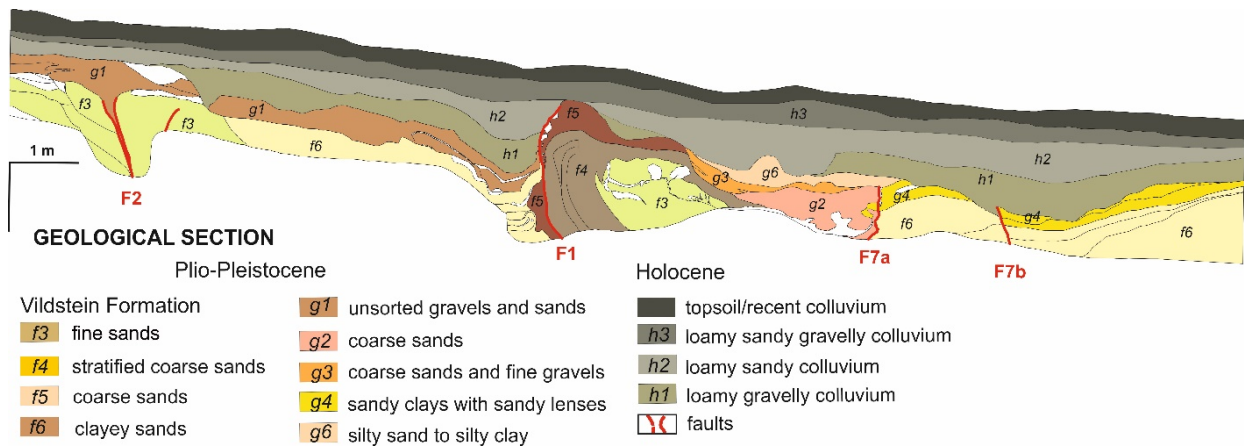


Fig. 3. Log of the NW-facing wall of the trench Kopanina A.

Acknowledgements: The research was supported by Czech Science Foundation project No. 16-10116J.

REFERENCES

Adamovič J. and Coubal M., 1999: Intrusive geometries and Cenozoic stress history of the northern part of the Bohemian Massif. *Geolines*, 9, 5-14.

Bronk Ramsey, C. (2009). Bayesian analysis of radiocarbon dates. *Radiocarbon*, 51(1), 337-360.

Coubal, M., Málek, J., Adamovič, J., Prouza, V., Štěpančíková, P. (2016): Record of post-Late Cretaceous kinematic activity of the Lusatian Fault as revealed from its fault-belt architecture. Pospíšil L. and A. Berková (ed.): 17th Czech-Polish Workshop On Recent Geodynamics of the Sudeten and the Adjacent Areas. Abstracts, Ramzová, Czech Republic, October 20-22, 2016, p.50.

Štěpančíková, P., Tábořík, P., Fischer, T., Hartvich, F., Karousová, M., Stemberk, J., Nováková, L. (2015): Holocene activity of the Mariánské Lázně Fault (Cheb basin, Bohemian Massif): youngest proved surface faulting in central Europe? In: Blumetti AM et al. (eds): Abstracts Volume 6th International INQUA Meeting on Paleoseismology, Active Tectonics and Archaeoseismology 19-24 April 2015, Pescina, Fucino Basin, Italy. *Miscellanea INGV*, n. 27, 478-480. ISSN 2039-6651.

Lienkaemper, J. J., Bronk Ramsey, C. (2009): OxCal: Versatile tool for developing paleoearthquake chronologies — A primer, *Seismological Research Letters*, 80, 431–434, doi: 10.1785/gssrl.80.3.431

Fischer, T., Štěpančíková, P., Karousová, M., Tábořík, P., Flechsig, Ch., M. Gaballah, (2012): Imaging the Mariánské Lázně Fault (Czech Republic) by 3-D ground-penetrating radar and electric resistivity tomography. *Studia Geophysica et Geodaetica*, 56 (4): 1019-1036.

Wells, D.L., Coppersmith, K.J., 1994. Empirical relationships among magnitude, rupture length, rupture area, and surface displacement. *Bulletin of the Seismological Society of America*, 82, 974–1002.



The Hundalee Fault and the M_w7.8 2016 Kaikoura earthquake

Stirling, Mark (1), Barrell, David (2), Williams, Jack (1), Sauer, Katrina (1), Duke, Grace (1), Hao, Ken X (3)

- (1) Department of Geology, University of Otago, Dunedin New Zealand. mark.stirling@otago.ac.nz.
 (2) GNS Science, Dunedin, New Zealand.
 (3) National Research Institute for Earth Science and Disaster Resilience, Tsukuba, Japan

Abstract: The Hundalee Fault is one of the 21 faults that ruptured during the Mw7.8 2016 Kaikoura earthquake. The earthquake produced a minimum 12 km-long surface rupture that comprised discontinuous displacements and slip types. Having recently completed a rupture and slip distribution database for the fault rupture, we are now attempting to understand the rupture in the context of the long-term behaviour of the fault. The ephemeral nature of the surface rupture is suggestive of a structurally immature fault, yet evidence of previous prehistoric earthquakes, large cumulative late-Cenozoic throw, and well developed fault zone rocks are more consistent with a well-established fault. Future work will constrain the paleoseismicity of the fault, and seek to understand the wider tectonic controls on the fault rupture.

Key words: Kaikoura earthquake, surface rupture, maturity

INTRODUCTION

The Hundalee Fault is one of the 21 faults that ruptured during the Mw7.8 2016 Kaikoura earthquake (Fig. 1). The ruptures are located towards the south end of the c. 180 km long rupture zone, and show a combination of strike-slip and reverse displacements. The following is a precis of our observations of the rupture, and discussion of the ruptures in the context of the longer term behaviour of the fault.

FAULT RUPTURES

The general location of the Hundalee Fault ruptures is shown in Figure 1. The Kaikoura earthquake ruptured a minimum of 12 km of the length of the onland northeastern section of the Hundalee Fault. Maximum displacements of c.4 m dextral (with c.2 m reverse slip, north side up) were observed at the coast. Uplift of the coastal platform shows that the rupture also continued offshore, which is consistent with submarine investigations indicating c.2 km of surface rupture between the coast and the rim of the Kaikōura Canyon (Clark et al. in review). The southwestern c.15 km of the fault source did not experience surface-rupture in the Kaikoura earthquake (Fig. 1). The Hundalee Fault is included as a fault source in the 2010 national seismic hazard model (NSHM; Stirling et al. 2012), though no paleoseismic data are available for the fault.

We have recently completed our rupture trace and slip distribution database for the Hundalee Fault, and this will be combined with databases from the other 2016 ruptures at GNS Science. From Figure 2 it can be seen that the Hundalee fault rupture is very discontinuous, especially at the southwestern end. The distribution of slip is also highly irregular, with the maximum (dextral) strike-slip at the coast (Coast SH1 in Fig. 2), but generally

dip slip of widely varying amounts inland (generally 0.5-2m throw). A component of sinistral slip is also observed inland (e.g. Glenstrae area in Fig. 2). In the Birches area (Fig. 2) multiple parallel ruptures are observed in a zone no more than a few hundred metres wide. The rupture is therefore very complex in comparison to 2016 fault ruptures to the north and southwest, which are more continuous and linear (Fig. 1).

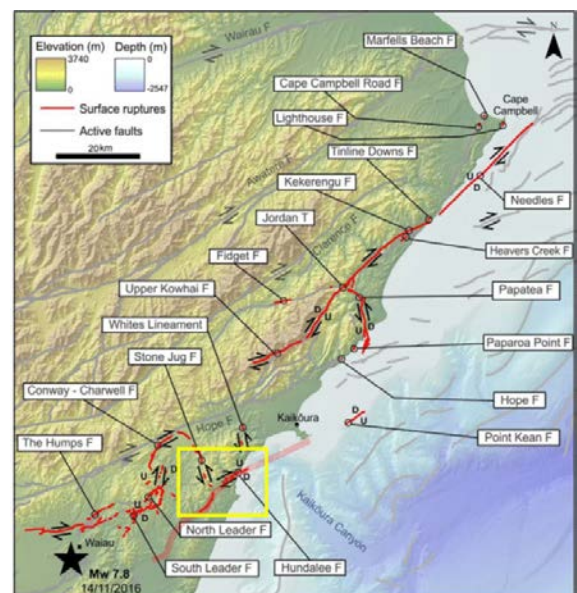


Figure 1: The rupture zone produced by the M7.8 2016 Kaikoura earthquake. The yellow box encloses the Hundalee Fault ruptures, and the area shown in Figure 2. The faint thick red line both inside and outside the yellow box shows the Hundalee Fault source from the NSHM (Stirling et al. 2012). Figure modified from Stirling et al. (2017).

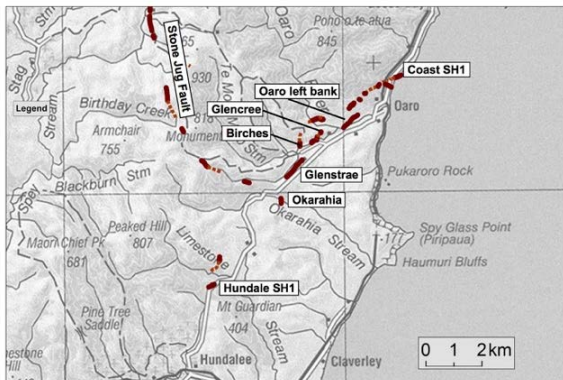


Figure 2: Main surface ruptures of the Hundalee Fault. The Stone Jug Fault ruptures are also shown since these were close to the Hundalee Fault, and were also a focus of our rupture mapping.



Figure 3: Example of a surface rupture of the Hundalee Fault in the Oaro left bank area (see Fig. 2).

FAULT RUPTURES VERSUS LONG TERM BEHAVIOUR

The Hundalee Fault is mapped over a total onland length of c.35 km, and was considered to be a pure reverse fault prior to the Kaikoura earthquake (e.g. Kingsbury et al. 2008). While little was known about the Late Quaternary activity of the fault prior to the earthquake, we see evidence of previous earthquakes at two of the rupture areas in Figure 2 (Coast SH1 and Okarahia; e.g. Fig. 4). The absence of previous scarps at the other sites is possibly due to the landscape being too young to have preserved the scarps of the previous earthquake. Many of the scarps were observed on active floodplains and on hummocky landslide terrain.

The complexity and fragmented nature of the Hundalee Fault ruptures may be suggestive of a fault that is poorly developed and immature. However, this is at odds with the large vertical displacements on the fault during the late Cenozoic. At the coast the fault juxtaposes greywacke basement in the hanging wall against Amuri limestone in the footwall, which represents hundreds of metres or more of late Cenozoic throw across the fault. An exposure of well-developed fault zone rocks in the Birches area (Fig. 2) is characteristic of a fault that has accommodated considerable displacement. Our present challenge is to reconcile how such large displacements

and well-developed fault rocks could develop on a fault that shows such pronounced rupture complexity and fragmentation in the most recent earthquake. This is one of many enigmas that the Kaikoura earthquake has revealed. The complexity of the rupture as a whole in terms of the number of faults involved (21), and the combination of fault slip types and slip rates, were beyond our prior expectations for seismic hazard source modelling in the area. Multi-fault rupture sources had been considered in the 2010 NSHM (Stirling et al. 2012; 2017), but not to the extent seen in the 2016 earthquake. There may be more than simply crustal controls on the earthquake rupture parameters (e.g. Hikurangi subduction interface influences).



Figure 4: Scarp of the Hundalee Fault at the Okarahia area (see Fig. 2). The 2016 rupture has produced the shaded turf roll at the base of the scarp, whereas the rounded scarp above is evidence of a previous, prehistoric earthquake.

CONCLUSIONS

The Hundalee Fault was one of the mapped faults in the northern South Island that ruptured during the Mw7.8 2016 Kaikoura earthquake. It produced a minimum 12 km-long discontinuous rupture zone of widely varying displacements and slip types. The ephemeral nature of the rupture is suggestive of a structurally immature fault, yet evidence of previous prehistoric earthquakes, large cumulative late-Cenozoic throw, and well-developed fault rocks are consistent with a well-established fault. Future work will constrain the paleoseismicity of the fault, and seek to understand the wider tectonic controls on the fault rupture.

Acknowledgements: Many thanks to the land owners who allowed us access to the Hundalee Fault ruptures during the November-December 2016 fieldwork, and to the Otago School of Surveying for letting us use two of their RTK instruments.

REFERENCES

Clark K.J., Nissen E., Howarth J., Hamling I., Mountjoy J., Ries W., Jones K., Goldstein S., Cochran U.A., Villamor P., Hreinsdóttir S., Litchfield N.J., Berryman K.R. and Strong D. (2017). "Highly variable coastal deformation in the 2016 Mw7.8 Kaikōura earthquake reflects rupture complexity along a transpressional plate boundary". *Geophysical Research Letters* (Under Review).



- Kingsbury, P., and Pettinga, J., (2018). Canterbury region earthquake source identification and characterisation. Environment Canterbury Report U088/41. ISBN 978-1-86937-857-8.
- Stirling M., McVerry G., Gerstenberger M., Litchfield N., Van Dissen R., Berryman K., Barnes P., Wallace L., Villamor P., Langridge R., Lamarche G., Nodder S., Reyners M., Bradley B., Rhoades D., Smith W., Nicol A., Pettinga J., Clark K. and Jacobs K. (2012). "National seismic hazard model for New Zealand: 2010 update". *Bulletin of the Seismological Society of America*, 102(4): 1514-1542.
- Stirling M.W., Litchfield N.J., Villamor P., Van Dissen R.J., Nicol A., Pettinga J., Barnes P., Langridge R.M., Little T., Barrell D.J.A., Mountjoy J., Ries W.F., Rowland J., Fenton C., Hamling I., Asher C., Barrier A., Benson A., Bischoff A., Borella J., Carne R., Cochran U.A., Cockroft M., Cox S.C., Duke G., Fenton F., Gasston C., Grimshaw C., Hale D., Hall B., Hao K.X., Hatem A., Hemphill-Haley M., Heron D.W., Howarth J., Juniper Z., Kane T., Kearse J., Khajavi N., Lamarche G., Lawson S., Lukovic B., Madugo C., Manousakis I., McColl S., Noble D., Pedley K., Sauer K., Stahl T., Strong D.T., Townsend D.B., Toy V., Villeneuve M., Wandres A., Williams J., Woelz S. and Zinke R. (2017). "The Mw7.8 2016 Kaikōura earthquake: Surface fault rupture and seismic hazard context". *Bulletin of the New Zealand Society for Earthquake Engineering*, 50(2): 73-84.



Soft sediment deformation structures from a cave as an indicator of tremors in mountains: insights from site effects analysis (Kalacka Cave, Tatra Mts., Carpathians)

Szczygiel, J (1), Mendecki, M (2), Wroblewski, W (2)

- (1) Faculty of Earth Sciences, University of Silesia, Będzińska 60, 41-200 Sosnowiec, Poland; jacek.szczygiel@us.edu.pl
(2) Institute of Geological Sciences, Jagiellonian University, Gronostajowa 3a, 30-387 Kraków, Poland

Abstract: The Kalacka Cave is located in the Bystra Valley in the Tatra Mountains (Central Western Carpathians). The cave is a paleo-phreatic conduit which was drained prior to 160 ka. Cave morphology has been affected by faulting which has dislocated passages. One of the faults is located ca. 15 m west of a sump filled by sandstones and siltstones, within which unusual deformation structures for such a geological environment were found, including: microfaults and folds (disharmonic folds, fault-bend folds, upright anticlines), load structures, and water escape structures (various shapes conduits, clastic dykes). We tried to identify the probable trigger mechanism of the deformation structures based on the geological setting and plausible physical processes within the cave environment. To check the possibility of liquefaction in thin soft-sediment infilling the bedrock we attempted to estimate the site effects and the vulnerability index (K_g) of the cave sediment. Acoustic measurements were used to measure S-wave velocities and densities of the soft sediment and the surrounding rigid rocks and we then estimated the values of the amplification coefficient and resonance frequency that might have occurred in the cave sediment during tremors. The resonance frequency has been calculated at ca. 17.5 Hz pointing at a near, relatively high-frequency shaking source (such as microtremors, rockslides, near earthquakes). Such frequency, combined with $K_g > 5$, makes liquefaction of the cave sediment very likely. Based on the Tatra Mountains geologic setting the most probable trigger mechanism for liquefaction could be a tremor induced by gravity sliding resulting from rock mass relaxation. The mountain ranges were most prone to simultaneous slope destabilization and supersaturation of deposits at the end of the glaciations. The Kalacka Cave are not only a site with a rare structure but also the first location with soft sediment deformation structures triggered by gravity sliding caused by the relaxation.



Electrical resistivity imaging of active faulting - examples from Central Europe

Tábořík, Petr (1,2), Štěpančíková, Petra (1), Stemberk, Jakub (1,2) and Hartvich, Filip (1,2)

(1) Institute of Rock Structure and Mechanics, Czech Academy of Sciences, V Holešovičkách 41, 18209, Prague 8, Czech Republic, Email: petr.taborik@post.cz

(2) Faculty of Science, Charles University, in Prague, Albertov 6, Prague 2, 12843, Czech Republic

Abstract: Different rock properties cause various specific resistivities of rocks. The ability to distinguish between different rock types depends on lithology, intensity of chemical and frost weathering, or mechanical disruptions caused by gravitational slope movements and tectonic processes. Water content and water mineralization are factors with very variable effects on resistivity. The final resistivity model represents a complex value describing the combined effect of all above-mentioned factors. Due to its versatility and relatively easy data processing, electrical resistivity measurements (ERT) can be seen as the leading geophysical method for identifying tectonic features. The method can be used for both (i) large scale surveying of the main fault structures and (ii) detailed investigation of the near-surface manifestations of the fault. Here we present some examples from Central Europe that exhibit typical resistivity images of active faulting.

Key words: active tectonics, depth fault tracking, shallow trenching, electrical resistivity tomography, Central Europe

INTRODUCTION

Resistivity measurements (electrical resistivity tomography – ERT; electrical resistivity imaging - ERI) have become a very effective tool of imaging of the subsurface in the last decades. A fast development of measurement devices and data processing makes geophysical measurements available for many different geoscience applications, including surveys of tectonic features such as faults and their subsurface manifestations. The use of geophysical methods in fault investigation is not a new application (Berge 2014, Nguyen et al. 2005, Suzuki et al. 2000). Several inversion algorithms can now easily be used for data processing and interpretation, e.g. Res2Dinv (Loke, 1997), BERT (Günther et al. 2006), among others.

Different rock properties (namely mineral composition and structure) cause various specific values of resistivity. However, it is not only the geochemical properties of rock that influence the resistivity. Intensive chemical weathering processes can change the specific values of resistivity by several orders. This means that a weathered rock can be represented by completely different values compared with intact rock. Furthermore, mechanical disruption, such as fracturing by frost weathering, gravitational slope movements, or tectonics, can lead to significant changes in rock properties and, thus, in specific rock resistivity. Last but not least another factor affecting the resistivity of the subsurface is water content and water mineralisation. It is obvious that each measurement point represents a complex value describing (besides the mineral composition of the rock) a combined effect of all factors mentioned above. The final resistivity image is thus very complex and it bears information on rock type, its mechanical disruption and chemical alteration as well as on water content in subsurface. The effect of tectonics and related processes (weathering, mechanical disruption or penetration of ground water from the depth) can change the rock

properties significantly. On the other hand, these specific changes are often identified as distinctive and they can be interpreted as results of tectonic processes. Here we present some examples from Central Europe showing typical resistivity manifestation of active faulting (Fig 1.). This paper aims to declare that ERT method is one of the most useful geophysical methods in active tectonic research.

SURVEY SCALE

It is necessary to distinguish different scales and spatial resolutions of fault surveys. Basically, we can distinguish between (i) large scale (both planar and to the depth) surveying of the main fault structures and (ii) detailed investigations of the near-surface manifestations of the faults (e.g. for paleoseismological analysis).

In the first case, we are not focused on details but on main structural or lithological units separated or intersected by the fault line. The geophysical survey is thus not such detailed but it is usually covering quite large areas in order to depict wider zones along the fault. Frequently, fault zones consist of several parallel structures and their widths can reach hundreds of meters. Using ERT imaging, the total length of the measured profile is crucial for the depth range of the measurement. In order to image down to depths of several tens or hundreds of meters, the total lengths of the profiles will need to be in the order of hundreds of meters or even a few kilometres. The final resistivity image then represents the general structure of the investigated area with the possibility of tracking the fault to relatively great depths. Such surveys might be very important for understanding the general geological situation in context of regional seismicity and stress field. Usually, such surveys are combined with seismic reflection surveying. However, the seismic survey is, despite the indisputable ability to describe elastic properties of the rocks, very demanding in terms of time, equipment,

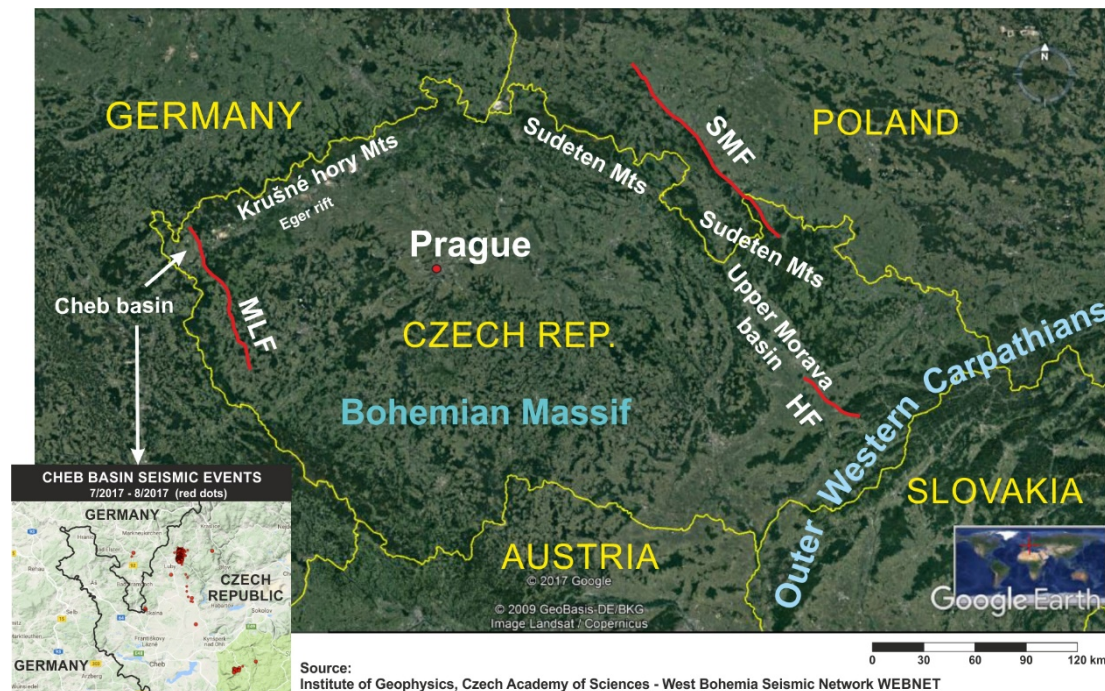


Figure 1: Studied sites fault zones (red line): MLF – Mariánské-Lázně fault; SMF – Sudetic Marginal fault; HF – Holešov fault. Map source: GoogleEarth.

post-processing, and costs. ERT, on the contrary, is a fast method that can deliver satisfactory results. It cannot substitute the seismic survey fully; however, it can be used for a “cheap” pioneer survey or as a complementary measurement for seismics.

The ERT method can be also used for investigating the near-surface structure of faults. The method is broadly exploited in paleoseismological research and often combined with paleoseismological trenching (Berge, 2014). Typically, the ERT survey is used in several research stages: (i) pre-trenching phase (searching for the exact location of the fault); (ii) trenching phase (in order to track particular structures in the close vicinity of the trenches), and (iii) extensive (often in 3-D) survey of the wider fault zone in order to place the known situation from the trenching to the wider context of local geology (with possible interpretation of fault kinematics). Compared with large scale measurements, such surveys are very detailed not only in terms of the measurements, but it also demands a different “scale of interpretation”.

Considering different scales of surveying, the above-mentioned factors, influencing the final resistivity picture, can play quite different roles. Geochemical composition (lithology) will play a significant role in both cases; however, the chemical weathering will play significant role in shallow subsurface rather than in the depth of several hundreds of metres. Also, fracturing due to mechanical weathering or thin disruptions such as crevices will not play a significant role in greater depth. We have to consider the decrease of spatial resolution with depth, which is an inherent property of the method given by the geometry of the measurement (Loke, 1997). With lower resolution we will not be able to detect small subsurface structures. The effect of water saturation can be also different in various depth levels. In

shallow prospection, measurements are often confined to the regions above the groundwater table and most of the water in the subsurface comes from precipitation. Deeper measurements will probably reach the saturated zone. Deep waters are often mineralized, which has a significant effect on the resistivity (mineral water rapidly decreases measured values). All of these aspects need to be considered during the interpretation of ERT measurements.

CASE STUDIES

The above-mentioned 3-stage geophysical survey was applied to all three sites discussed in the following. We started with deep surveys in order to track the faults on a regional scale. Then we conducted more detailed investigation of the trench sites, and finally we employed the very detailed verification of the structures known from trenches.

The first trenching site **Kopanina** is situated in the westernmost part of the Czech Republic in the western part of the Bohemian Massif. Here, the Cenozoic Cheb Basin is controlled by the NW-trending Mariánské Lázně Fault (**MLF**) in the NE, which is a part of the Cheb-Domažlice Graben on its intersection with the NE-trending Eger Rift. The area belongs to the Nový Kostel zone, which is famous for the earthquake swarms and CO₂ emanations. The area represents one of the seismically most active zones in Central Europe.

The trenching survey revealed the eastern limit of the Cheb Basin infill (Oligocene to Holocene) and also repeated movements of the Mariánské-Lázně Fault zone. The youngest documented faulting offsets the radiometrically well dated Holocene colluvium (Fischer et al. 2012, Štěpančíková et al. 2015).



ERT (Fig. 2) was performed at two different scales. The shallow detailed survey up to several tens of meters depth was realized in order (i) to locate the exact position of the MLF for trenching, (ii) to extend information on fault properties (gained directly from the trench walls) laterally and to the depth, and (iii) to trace the faults as well as displaced sedimentary bodies. The deep survey focused on the subsurface image of the MLF fault zone at greater depths. Shallow ERT was combined with other geophysical methods: (i) high-frequency ground penetrating radar (GPR) with a shielded 250 MHz antenna, and (ii) dipole electromagnetic profiling (DEMP) measuring the conductivity of the subsurface (so called conductometry). Together, the geophysical methods revealed the spatial distribution of the well-pronounced sedimentary body, which is sheared by the fault. The results confirmed three main zones: (i) fine-grained sediments of the Vildstein formation of the Cheb basin (lower resistivity values, low intensity of GPR reflections), (ii) a coarse heterogeneous sedimentary body with scattered concretions (higher resistivity values), and (iii) intensively argillaceous weathered crystalline rocks (mica-schists) (very low resistivity values, practically no reflections due to strong signal dispersion). Moreover, the spatial distribution of the coarse sedimentary body suggested right-lateral displacement along the fault line known from the trench most probably due to disruption of the sedimentary body by active faulting (Štěpančíková et al. 2016, Tábořík et al. in prep.).

Deep geophysical survey to the depth of 200 m followed the MLF zone to the depth. The ERT measurement was also supplemented with seismic tomography and a gravity survey. In contrast to detailed ERT measurements with high resolution (1 m electrode spacing), very long ERT (with length of 1 km and electrode separation of 10 m) was performed. The deep ERT survey confirmed a steeply inclined low resistivity fault zone. The results and methodological aspects of combined geophysical measurements, including the importance of integrated interpretation of different geophysical results, are reported in detail by Blecha et al. (in review).

The **Bílá Voda** site is situated in the north-eastern part of the Bohemian Massif. The morphologically well-pronounced NW-trending Sudetic Marginal Fault (**SMF**), controlling the mountain front of the Sudeten Mts, was investigated. Besides other geophysical techniques which were used at the Bílá Voda site within a complex geophysical survey, the ERT served as a main method of geophysical investigation. ERT was used also within several stages of research: (i) pre-trenching geophysical searching for the exact fault location; (ii) detailed geophysical investigation alongside the trenching phase (to trace particular structures in the trenches vicinity), and (iii) extensive 3-D surveying of the wider area in order to distinguish high-conductive Miocene clayey sediments from the offset alluvial fan displayed as high resistivity body.

Due to distinct lithology differences and related varying physical rock properties on both sides of the fault, a strong horizontal gradient in electric resistivity clearly showed the fault position and allowed us to identify more resistive crystalline bedrock juxtaposed against conductive Miocene clayey sands covered by a veneer of the alluvial fan deposits. ERT also revealed the limits of the alluvial fan deposits. It helped in the interpretation of the paleoseismic survey such as sense of the movements. The results, together with interpretations of paleoseismological trenching, were summarized in published papers (Štěpančíková et al. 2011, 2016), and will be summarized by Tábořík et al. (in prep.).

The third site, **Brodek**, is located in the Upper Morava Basin, a region that was tectonically active in the Late Cenozoic, located at the contact of Bohemian Massif and the Western Carpathians. The studied site is situated on the NW-trending Holešov Fault (**HF**), which controls the south-eastern basin margin. It offsets Lower Badenian marine sediments (Middle Miocene) and Plio-Quaternary fluvio-lacustrine sediments (in the NW) against the allochthonous flysch of the Outer Western Carpathians and the underlying Karpatian sediments (Lower Miocene) of the Carpathian Foredeep (to the SW) (Špaček et al. 2015). Similarly to the previous two sites, ERT was used as the leading method within the integrated geophysical survey (consisting of ERT, DEMP and GPR) in a multi-stage measurement. Geophysical measurements allowed us to clearly distinguish between two different sedimentary units and, thus, indicated the position of the studied fault. Based on the ERT results, the most suitable site for trenching was selected. Detailed resistivity sections were then compared to trenching logs and interpreted together with the GPR and DEMP results.

DISCUSSION

Electrical resistivity measurements (ERT) confirmed their ability to serve as the leading method of geophysical surveying. Due to its versatility and relatively easy data processing, the ERT method can be applied successfully in most of the sites in order to identify tectonic features and their areal extent, as well as their depth continuation (up to several hundreds of meters). The method can be used for both (i) large scale surveying of the main fault structures (e.g. Blecha et al., under review) and (ii) detailed investigation of the near-surface manifestations of the fault (e.g. Fischer et al. 2012). However, the correct interpretation of the ERT results can be complicated by several aspects, such as weathering intensity, mechanical disruption of the rock or water content and water mineralization. These factors need to be always considered, however, different factors or their combination will be prevailing in detailed shallow survey, and different prevails within a deep large scale investigation of the whole fault zones.



Kopanina site (MLF)

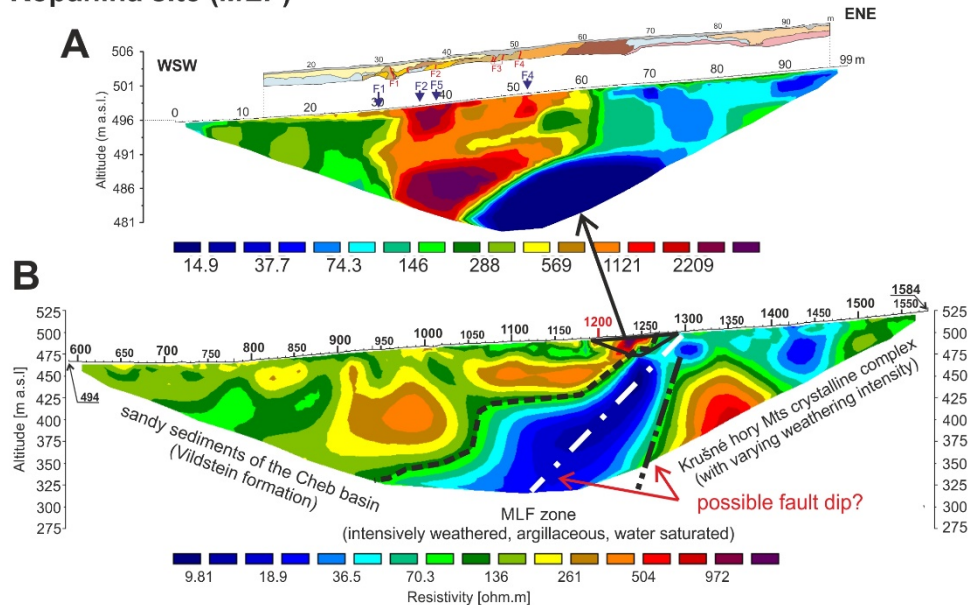


Figure 2: Example of the multi-stage resistivity survey: (A) detailed investigation of the Kopanina trench site (with trench log), (B) deep resistivity survey of the MLF (modified after Fischer et al. 2012 and Blecha et al., under review).

Acknowledgements: The research was supported by Grant Agency of CAS, project No. IAA300120905 and Czech Science Foundation No.P210/12/0573, and No.16-10116J.

REFERENCES

- Berge M. A. (2014): Electrical resistivity tomography investigations on a paleoseismological trenching study. *Journal of Applied Geophysics* 109, 162–174.
- Blecha V., Fischer T., Tábořík P., Vilhelm J., Klanica R., Valenta J. (under review): Geophysical evidence of the Eastern marginal fault of the Cheb basin (Czech Republic). *Studia Geophysica et Geodaetica*.
- Fischer T., Štěpančíková P., Karousová M., Tábořík P., Flechsig C., Gaballah M. (2012): Imaging the Mariánské Lázně Fault (Czech Republic) by 3-D ground-penetrating radar and electric resistivity tomography. *Stud. Geophys. Geod.* 56: 1019-1036.
- Günther T., Rücker C. and Spitzer K. (2006): Three-dimensional modelling and inversion of dc resistivity data incorporating topography – II. Inversion. *Geophysical Journal International*, 166, 506–517.
- Loke, M. H., 1997. Electrical imaging surveys for environmental and engineering studies. A practical guide to 2-D and 3-D surveys. Geotomo software. Accessed on Apr 22, 2017 at <http://www.geotomosoft.com/>
- Nguyen F., Garambois S., Jongmans D., Pirard E., Loke M.H. (2005): Image processing of 2D resistivity data for imaging faults. *Journal of Applied Geophysics*, 57, 260–277.
- Špaček P., Bábek O., Štěpančíková P., Švancara J., Pazdírková J., Sedláček J. (2015): The Nysa-Morava Zone: an active tectonic domain with Late Cenozoic sedimentary grabens in the Western Carpathians' foreland (NE Bohemian Massif). *International Journal of Earth Sciences: Volume 104, Issue 4* (2015), Page 963-990.
- Štěpančíková P., Nývlt D., Hók J., Dohnal J. (2011): Paleoseismic study of the Sudetic Marginal Fault at the locality Bílá Voda (Bohemian Massif). In: *Earthquake geology and geoarchaeology: Science, Society and Critical facilities* (Grützner C., Pérez-López R., Fernández-Steegeer T., Papanikolaou I., Reicherter K., Silva P.G. and Vött A. eds). 2nd INQUA-IGCP-567 International Workshop, Corinth, (Greece). 239-242.
- Štěpančíková P., Tábořík P., Fischer, T., Hartvich, F., Karousová, M., Stemberk, J., Nováková, L. (2015): Holocene activity of the Mariánské Lázně Fault (Cheb basin, Bohemian Massif): youngest proved surface faulting in central Europe? In: Blumetti AM et al. (eds): *Abstracts Volume 6th International INQUA Meeting on Paleoseismology, Active Tectonics and Archaeoseismology 19-24 April 2015, Pescina, Fucino Basin, Italy*. *Miscellanea INGV*, n. 27, 478-480.
- Štěpančíková P., Tábořík P., Hartvich, F., Stemberk J., Fischer T., Karousová M., Vilhelm J., Šíroky J., Špaček P., Blecha V., Pek J., Rockwell T., Havaš M. (2016): Applicability of complex geophysical surveying in paleoseismic studies: three case studies from the Bohemian Massif. In: Calpin J. P., Gruetzner Ch.: *Proceedings of the 7th International INQUA Workshop on Paleoseismology, Active Tectonics and Archaeoseismology PATA Days, 30 May - 3 June 2016, Creston, Colorado, USA*. ISBN 978-0-9974355-2-8.
- Tábořík P., Hartvich F., Štěpančíková P., Stemberk J., Vilhelm J., Pek J., Šálek O. (in preparation): Fault detection and kinematics as revealed by 2-D and 3-D geophysical surveying and trenching (Sudetic Marginal Fault).
- Suzuki K., Toda S., Kusunoki K., Fujimitsu Y., Mogi T., Jomori A. (2000): Case studies of electrical and electromagnetic methods applied to mapping active faults beneath the thick quaternary. *Engineering Geology*, 56, 29–45.



Strike-slip deformation behind the Hellenic subduction: The Amorgos Shear Zone, South Aegean Sea

Tsampouraki-Kraounaki, Konstantina (1), Sakellariou, Dimitris (1)

(1) Inst. Of Oceanography, Hellenic Centre for Marine Research, 47th km Athens-Sounio Ave. 19013 Anavyssos, Greece, tsampourakik@hcmr.gr

Abstract: The "Amorgos Basin" is located in the South Aegean Sea, Greece. Seismic and swath bathymetry data provide information on the kinematics and the deformation which led to its present structure. The "Amorgos Basin" is a group of NE-SW trending, asymmetric sub-basins. Their sedimentary infill displays very similar seismic character, with well-defined unconformities indicating major tectonic events. Tectonic asymmetry has led to enhanced subsidence in the hangingwall and basin inversion in the footwall of the basin bounding faults. The fault network and the style of deformation suggest oblique rifting in NE-SW direction, accommodated by NE-SW trending, strike-slip to oblique faults and E-W trending normal fault overstep. The "Amorgos Basin" constitutes a dextral, oblique to horizontal shear zone, the Amorgos Shear Zone. The normal-faulting focal mechanism proposed for the M:7.8 earthquake of July 1956 southwest of Amorgos Island is not compatible with the kinematic regime of the Amorgos Shear Zone.

Key words: Amorgos Shear Zone, dextral oblique rifting, transtension, basin inversion

INTRODUCTION

The Aegean Sea, in the NE Mediterranean Sea, displays active, complex deformation resulting from the interaction of the NNE-dipping subduction of the East Mediterranean slab along the Hellenic Arc in the south with the westward extrusion of the Anatolia crustal block along the dextral North Anatolian Fault in the north. The latter, along with the Kephallonia Fault in the Ionian coast, clearly delineate the northern boundary of the Aegean extensional domain, while the sinistral fault-zones along the Strabo-Pliny trench system in the eastern part of the Hellenic Arc, clearly define the southeastern boundary of the Aegean microplate. Dextral, NE-SW trending, strike-slip faulting dominates in the northern part of the Aegean Sea. According to the GPS data, the central and western part of the South Aegean Sea behaves more or less as a rigid body and moves fast towards SSW while the Southeastern Aegean moves moderately fast towards SSE, away from the rigid South Aegean (Kahle et al, 1999; McClusky et al. 2000; Kiratzi & Louvari, 2003; Kreemer & Chamot-Rooke, 2004, and references therein).

The so-called "Amorgos Basin" is located in the Southeast Aegean Sea. The largest earthquake in the last century in the Aegean Sea occurred in July 1956 southwest of Amorgos Island with magnitude M:7.8. The proposed focal mechanisms vary between dextral strike slip and dip-slip movement on a NE-SW trending, SE dipping fault (Okal et al, 2009 and references therein). Previous marine research campaigns in the area of the South Aegean Sea (Masclé & Martin, 1990; Piper & Perissoratis, 2003; Piper et al., 2007) have highlighted the significant role of NE-SW trending, strike-slip to oblique-slip fault zones, indicating that a significant part of the extension in the South Aegean Sea is due to transtension.

Here we present new swath bathymetry and seismic profiling data acquired recently in the area of the "Amorgos

basin" and we show that the geological structure, the fault network and kinematics deviate largely from the "pure extension" model. We introduce the term "Amorgos Shear Zone" to highlight the actual structure of a complicate oblique rifting, evolved during Plio-Quaternary as a NE-SW trending dextral-oblique fault-zone.

MATERIALS AND METHODS

This work is based on the: (i) processing and analysis of roughly 5,000 km² of swath bathymetry data between Santorini, Amorgos, Kalymnos, Astypalea and Anafi Islands and the (ii) processing and interpretation of >700 km of seismic profiles (Fig. 1). Both data sets have been obtained during three cruises on board HCMR's R/V Aegaeo in 2006 (THERA-2006), 2016 (EUROFLEETS2 LGT-AMORGOS-56) and 2017 (SE AEGEAN GEODYNAMICS), funded by NSF, Eurofleets2 and HCMR respectively.

RESULTS

Seafloor morphology

The bathymetric data in combination with the interpretation of seismic profiles suggest that "Amorgos Basin" is in fact a series of mostly asymmetric basins separated by uplifted, shallow ridges. Specifically, the bathymetry indicates a group of well-developed, NE-SW trending, "Lazy-S-shaped" basins, named from northeast to southwest as Kinairos (KB, 600m), Amorgos North (ANB, 750m), Astypalea (AsB, 600m), Amorgos South (ASN, 700m) and Anafi (AnB, 600m) Basins. Astypalea Ridge (AsR) separates Kinairos and Amorgos North Basins, from Astypalea Basin. Further on, Anhydros Ridge (AdR), splits towards NE into two branches: the northern one separates Anydhros Basin (AdB) from ANB, while the southern one separates ANB from ASB. Steep, fault-controlled slopes define the northern margins of the basins mainly.

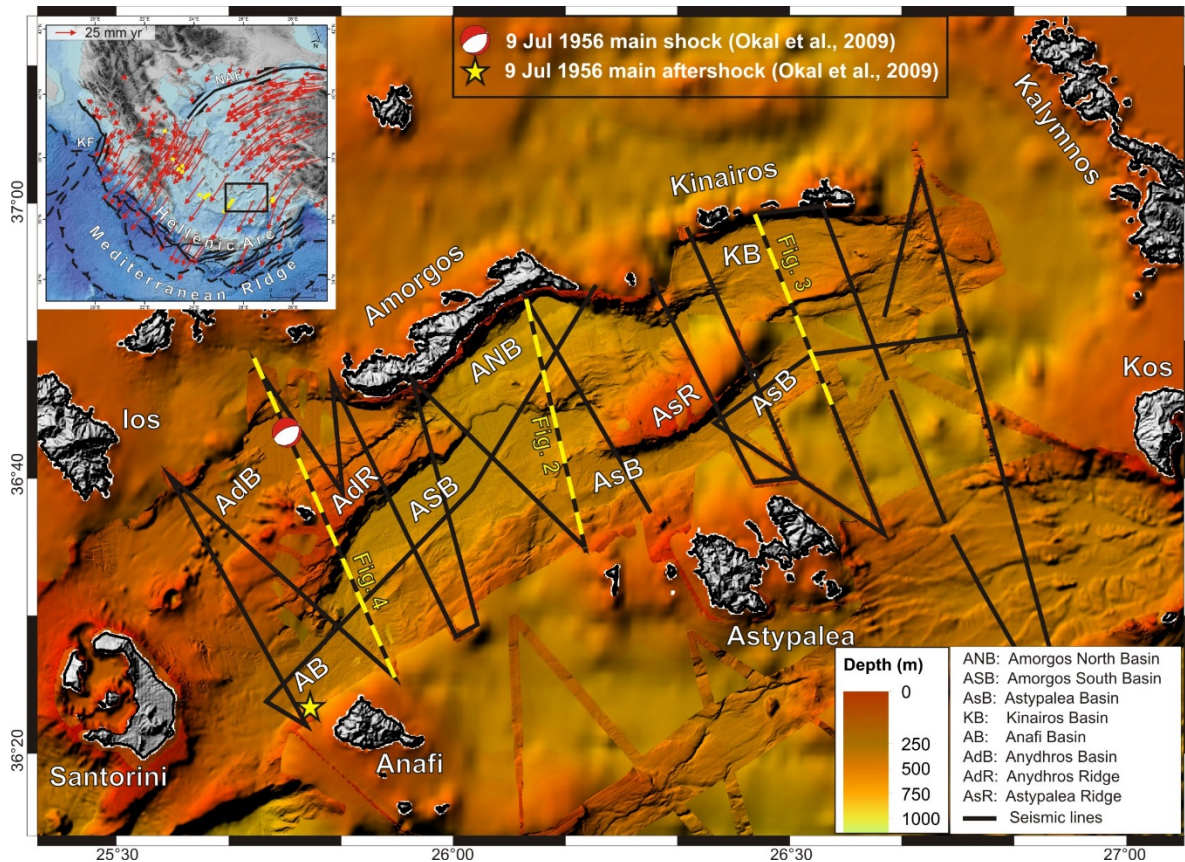


Fig. 1: Swath bathymetry, location of seismic profiles and terminology of the morphological features discussed in this paper. Bathymetry of the surrounding areas is from EMODNET Bathymetry (www.emodnet.eu). Land topography SRTM90. Inset map: Main geotectonic elements of the Aegean, GPS vectors from Kreemer & Chamot-Rooke (2004).

Seismic stratigraphy

The interpretation of seismic profiles confirms the existence of more than one basins at the study area. The uplifted acoustic basement clearly defines the basins margins. The sedimentary infill of the basins displays similarities on the seismic character within the basins. Four clearly recognizable seismic units have been mapped within the sedimentary sequence. At least 3 major unconformities (U1, U2, U3) showing onlap relationship between the strata above and below, mark the interfaces between Units 1, 2, 3 and 4. They are well illustrated in Fig. 2 within Amorgos South and Amorgos North Basins, indicating that major tectonic events affect the entire area and lead to an episodic opening of the basins. Minor unconformities are also recognizable within the stratified basin's infill, by the onlap and/or downlap termination of the seismic layers on the acoustic basement or the underlying strata.

Several units characterized by low amplitude, discontinuous reflectors and slightly chaotic facies can be interpreted as mass transport deposits (MTDs). A thick MTD1 within Unit 2, with thickness exceeding 50 msec close to the basin's margins, with chaotic, undulating reflectors occurs at comparable stratigraphic level within the Kinairos, Amorgos North, Amorgos South and Astypalea Basins, always above unconformity U2.

The Astypalea Ridge and the south-eastern part of Anydhros Ridge are covered by tilted and uplifted sediments of the lowermost parts of the sedimentary sequence of the basins (Units 3 and 4), suggesting basin's inversion (Fig. 2, 3, 4). Unit 1 displays constant thickness across the basins infill, indicating symmetric subsidence during the deposition of the younger strata. Units 2, 3 and 4 show a maximum thickness close to the northern margins, suggesting rapid syndepositional subsidence and tilting of the basins to the north.

Fault network

The steep margins of the basins are controlled by mainly NE-SW trending, SE dipping faults and WSW-ENE to WNW-ESE trending, S-dipping, step-over faults (Fig. 5). Tectonic asymmetry across the basins results in enhanced subsidence in the hangingwall, close to the main, basin bounding faults and uplift and tilting in the footwall (Figs 2, 3, 4). Maximum thickness of the basin's infill is observed close to the main faults. Uplift and tilting of the faults' footwalls leads to basin inversion, with the lower units of the basins infill and their substrate being uplifted and forming shallow ridges (e.g. Astypalea Ridge, Anydhros Ridge). Pop-up structures observed in the basins and on the ridges indicate significant deformation due to horizontal shearing.

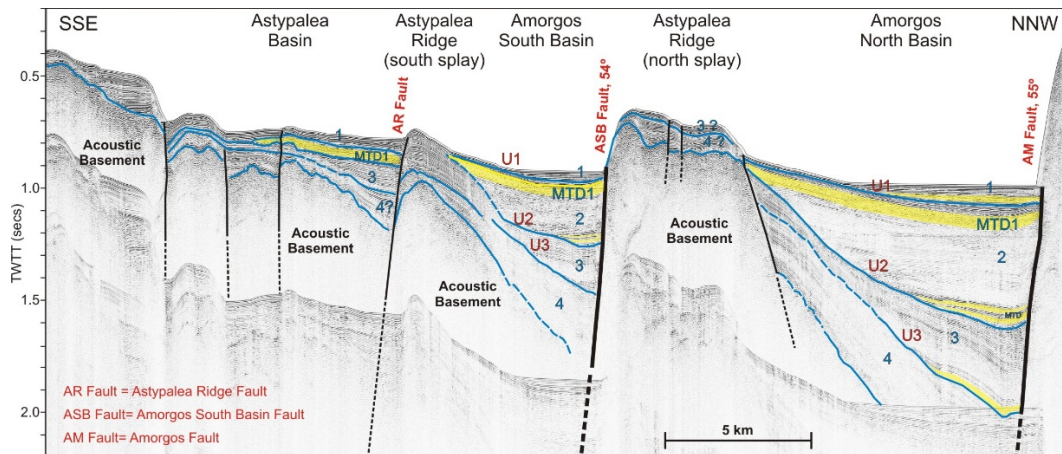


Fig. 2: Seismic profile across Amorgos North, Amorgos South and western part of Astypalea Basins. See Fig. 1 for location.

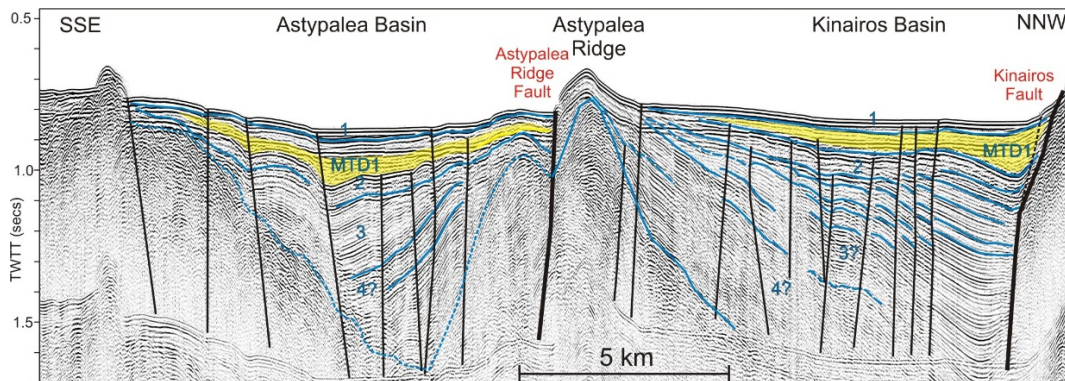


Fig. 3: Seismic profile across Kinairos and Astypalea Basins. See Fig. 1 for location.

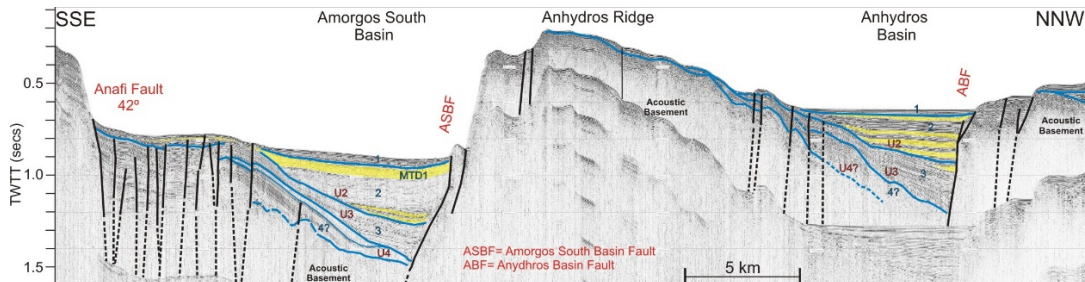


Fig. 4: Seismic profile across Amorgos South and Anafi Basins. See Fig. 1 for location.

CONCLUSIONS - DISCUSSION

The “Amorgos Basin” initiated probably in Early Pliocene as a single basin and evolved into a significantly more complex morphological and tectonic structure with at least six tectonically controlled, asymmetric basins separated by two uplifted and tilted narrow ridges. The basins are Lazy-S- to rhomb- or spindle-shaped, fault bounded depressions displaying very similar seismic stratigraphy with at least three major and several minor unconformities. The spatial distribution and shape of the uplifted and subsided areas, the basin inversion with uplifted and tilted older sediments occurring on the top of the shallow ridges, the enhanced subsidence and the multiple unconformities within the basins, the fault network with NE-SW main faults and W-E transfer zones and the transtensional structures observed strongly

suggest that the initial “Amorgos Basin” has evolved in Late Pliocene to Quaternary into the “Amorgos Shear Zone” with significant dextral horizontal to transtensional deformation (Fig. 5). The fault network and the style of deformation suggest dextral oblique rifting (Withjack & Jamison, 1986) in NE-SW direction. The relative displacement between the opposite sites of the shear zone is directed N25°-30°E, parallel to the observed GPS vectors and roughly 30° oblique to the N50°-55°E rift axis. The oblique rifting is accommodated by NE-SW, dextral strike-slip to oblique faults and E-W normal fault oversteps. This kinematic regime questions the pure normal-faulting mechanism proposed for the M:7.8 July 1956 “Amorgos earthquake” and supports earlier interpretations by Papazachos & Delibassis (1969) and Ritsema (1974) suggesting strike slip motion in NE-SW direction.

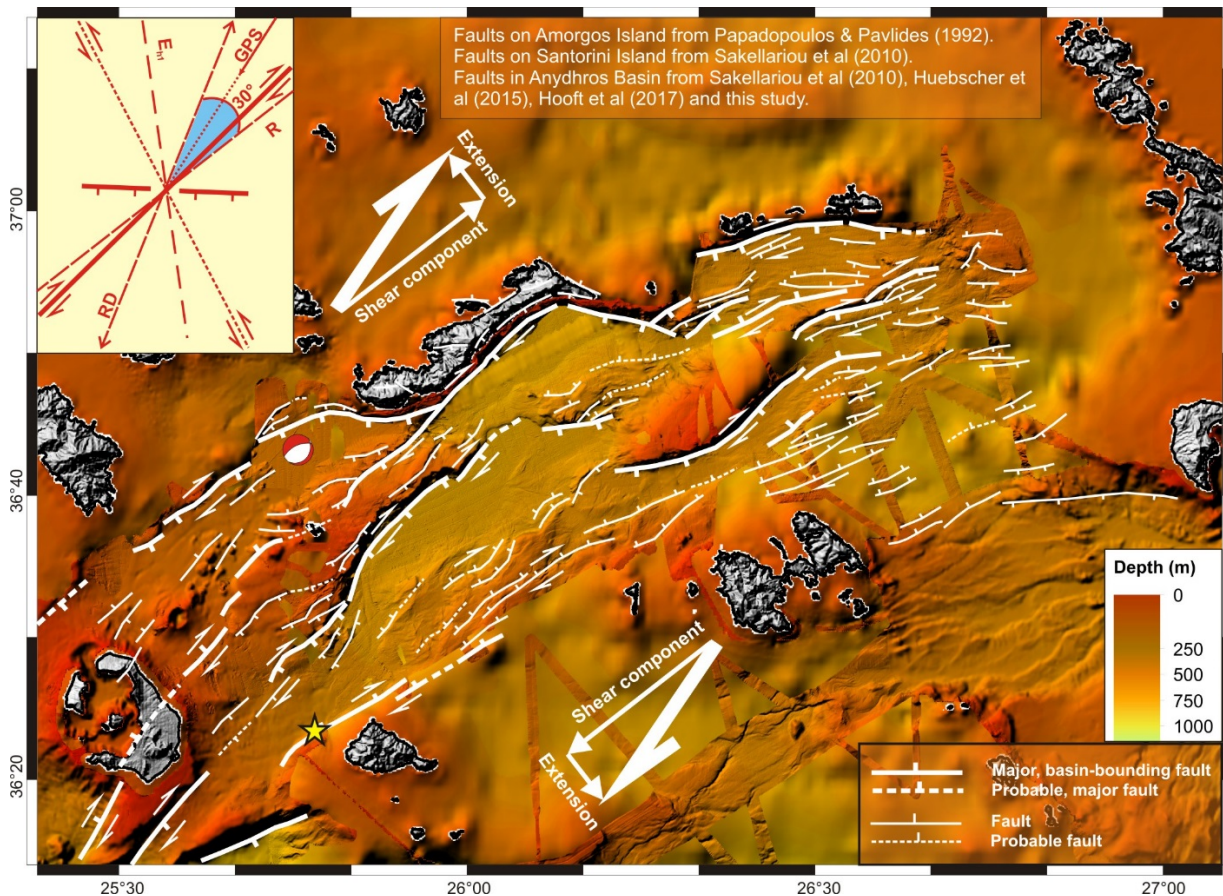


Fig. 5: Fault network in the Amorgos Shear Zone. Large white half-arrows are roughly parallel to the GPS vectors and show the sense of shearing. The inset drawing (modified after Withjack & Jamison, 1986) explains the kinematics of the oblique extension in the Amorgos Shear Zone. R: Rift trend; RD: Relative Displacement direction between opposite sites; E_{H2} : Direction of max. extensional strain; GPS: Mean trend of GPS vectors after Kreemer & Chamot-Rooke (2004).

REFERENCES

- Hooft, E.E.E., Nomikou, P., Toomey, D.R., Lampridou, D., Getz, C., Christophoulou, M.-E., O'Hara, D., Arnoux, G.M., Bodmer, M., Gray, M., Heath, B.A., VanderBeek, B.P., 2017. Backarc tectonism, volcanism, and mass wasting shape seafloor morphology in the Santorini-Christiana-Amorgos region of the Hellenic Volcanic Arc. *Tectonophysics* 712–713, 396–414.
- Hübscher, C., Ruhnau, M., Nomikou, P., 2015. Volcano-tectonic evolution of the polygenetic Kolumbo submarine volcano/Santorini (Aegean Sea). *J. Volc. & Geoth. Res.* 291, 101–111.
- Kahle, H.-G., Cocard, M., Peter, Y., Geiger, A., Reilinger, R., Barka, A. & Veis, G., 2000. GPS-derived strain rate field within the boundary zones of the Eurasian, African, and Arabian plates. *J. Geophys. Res.* 105, 23 353–23 370.
- Kiratzis, A., Louvari, E., 2003. Focal mechanisms of shallow earthquakes in the Aegean Sea and the surrounding lands determined by waveform modelling: a new database. *J. Geodyn.* 36 (1–2), 251–274.
- Kreemer, C. & Chamot-Rooke, N. 2004. Contemporary kinematics of the southern Aegean and the Mediterranean Ridge. *Geoph. J. Int.* 157, 1377–1392.
- Masle, J. & Martin L., 1990. Shallow structure and recent evolution of the Aegean Sea: A synthesis based on continuous reflection profiles. *Marine Geology* 94, 271–299.
- McClusky, S. et al., 2000. Global Positioning System constraints on plate kinematics and dynamics in the eastern Medi-terranean and Caucasus, *J. Geophys. Res.* 105, 5695–5719.
- Okal, E.A., Synolakis, C.E., Uslu, B., Kalligeris, N., Voukouvalas, E., 2009. The 1956 earthquake and tsunami in Amorgos, Greece. *Geoph. J. Int.* 178, 1533–1554.
- Papadopoulos, G.A., Pavlides, S., 1992. The 1956 large shock in the South Aegean: macroseismic field, faulting and neotectonics of the Amorgos Island. *Earth & Plan. Sc. Let.* 113, 383–396.
- Papazachos, B.C., Delibasis, N.D., 1969. Tectonic stress field and seismic faulting in the area of Greece. *Tectonophysics* 7(3), 231–255.
- Piper, D.J.W., Perissoratis, C., 2003. Quaternary neotectonics of the South Aegean arc. *Mar. Geol.* 198 (3–4), 259–288.
- Piper, D., Pe-Piper, G., Perissoratis, C., 2007. Distribution and chronology of submarine volcanic rocks around Santorini and their relationship to faulting. *Geol. Soc. Lond. Spec. Publ.* 291, 99–111.
- Ritsema, A.R., 1974. Earthquake mechanisms of the Balkan region. *Kon. Ned. Meteor. Inst. Repts.* 74(4), 36 pp.
- Sakellariou, D., Sigurdsson, H., Alexandri, M., Carey, S., Rousakis, G., Nomikou, P., Georgiou, P., Ballas, D., 2010. Active tectonics in the Hellenic volcanic arc: The Kolumbo submarine volcanic zone. *Bull. Geol. Soc. Greece* 43 (2), 1056–1063.
- Withjack, M.O., Jamison, W.R., 1986. Deformation produced by oblique rifting. *Tectonophysics*, 126 (1986) 99–124



Predicting rock failure as a function of the total stress state: An example from the western Southern Alps

Upton, Phaedra (1), Koons, Peter (2), Roy, Sam (2)

(1) GNS Science, PO Box 30368, Lower Hutt, New Zealand. p.upton@gns.cri.nz

(2) University of Maine, Orono ME 04469, USA

Abstract: The western Southern Alps of New Zealand are shaped by high rates of relative motion across the Australian/Pacific plate boundary in conjunction with a dynamic climatic regime and consequent rapid rates of erosion. The result is a tightly linked and dynamic landscape of high relief, subject to rapid surface processes that is difficult to capture with traditional flux-based landscape models. To do so, we present a formulation, the Failure Earth Response Model (FERM), which unifies the description of tectonic and geomorphic forcings and responses within a single framework. We explicitly consider the contribution that fault damage and pore pressure fluctuations make toward failure of the rock mass. We use the Waikukupa River area of the Alpine Fault, Westland and surrounding topography as an example. Constrained by field observations, these models allow us to predict where failure, and hence erosion, are likely to occur and under what conditions.

Key words: Alpine Fault, topographic stresses, slope failure

INTRODUCTION

We showcase a new landscape evolution modelling framework, the Failure Earth Response Model (FERM) (Koons et al. 2013). It is based on two basic assumptions about the 3D stress state and material rheology at the Earth's surface: (1) Both geomorphic (e.g., fluvial or glacial incision, landsliding) and tectonic (e.g., faulting) material displacement occur when local resistance is overcome by local forces, and (2) large displacements, whether tectonic or geomorphic in origin, alter Earth material properties resulting in a long term strain memory contained within the topography. The FERM framework provides a context in which we can gather stresses generated by far field tectonic processes, topography and surface processes into a single stress state for every point.

We present the concept of FERM using a generic topography that potentially allows exploration of several individual components of landscape evolution including strain weakened fault rocks, glacial loading and unloading, and fluvial erosion. Here we consider the contribution that fault damage and pore pressure fluctuations make toward failure of the rock mass. We present a test case based on the Waikukupa River area of the Alpine Fault, Westland, New Zealand and surrounding topography

MODELS AND METHODS

We start with a generic model of a valley (Figure 1A). The model contains a series of slopes at angles of 27°, 64° and two at 39° left to right. The material modelled has an elasto-plastic rheology characterised by the properties of tensile strength (σ_t), cohesion (C) and friction angle (ϕ). Failure can occur in a tensile or shear environment and we consider both failure modes.

The model of the Waikukupa region of the Alpine Fault is a 2x2 km² block of the upper crust with a resolution of 10 m and is centred on a point downstream of the SH6 bridge across the Waikukupa River (Figure 2A). The region encompasses the presently active Hare Mare thrust strand of the Alpine Fault and the abandoned Waikukupa thrust strand (Norris and Cooper 1995, Norris and Cooper 1997). Topography is imposed onto the model geometry with elevations in the model domain ranging from near sea-level to 1200 m. The geology is taken from the mapping of Norris and Cooper (1995, 1997) and the friction (ϕ) angle used for the different geological units is shown in Figure 2B. Cohesion (not shown) was estimated using the Hoek-Brown (1980) criterion using field measurements of structural competence and base rock competence.

The four rock units located within the model domain are mylonite, cataclasite, and fault gouge associated with the Alpine Fault, and Western Province greywacke and gravels (Figure 2B). The mylonite is the strongest unit with a massive to blocky structure hosting widely spaced fractures. Fracture surface conditions are very good to good, with predominantly fresh and unweathered surfaces. The cataclasite and gouge units are associated with localized seismogenic cataclasis along the Alpine Fault. These units are much weaker, having a much higher fracture density that increases with proximity to the primary slip surface. Fracture surface quality decreases with proximity to the primary slip surface, and fractures are largely wet, slicken-sided, and coated with clay. The greywacke unit has a somewhat higher fracture density than the mylonite, producing a very blocky rock mass with rough, slightly weathered fracture surfaces. We ran two models, one dry and one wet.

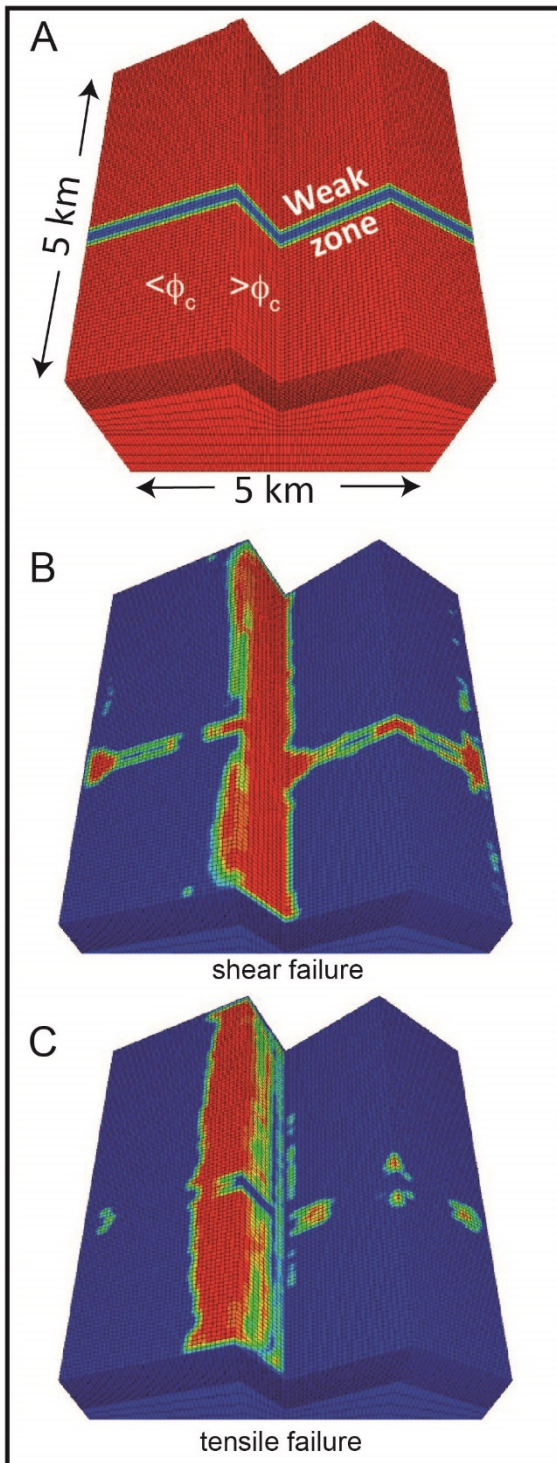


Figure 1: A: Model geometry used to explore slope failure where subjected to only topographic forces. A weak zone ($\phi = 15^\circ$) cuts across stronger material ($\phi = 35^\circ$). B: Location of shear failure throughout the model. Shear failure occurs along the weak zone and on the steepest slope. Blue = no failure, red = failure. C: Location of tensile failure throughout the model. Tensile failure occurs along the ridge, along the backslope behind where shear failure is occurring and next to where shear failure has removed material from the weak zone. Colour scale as for B.

Erosion in the models occurs as a function of rock failure and by assuming a completely supply limited system (Koons et al. 2012). That is, we assume that as soon as material has been detached from the rock mass as a result of the failure of the rock mass, it is transported away from the system, as long as there is a downhill path available to it. The western Southern Alps experience one of the highest rainfalls on Earth, yearly rainfall at Waikukupa is estimated to be about 5 metres per year (NIWA 2004) and it is distributed throughout the year. Thus a supply-limited assumption is reasonable for the Waikukupa region.

RESULTS OF GENERIC MODEL

Taking only topographic stresses into account, shear failure occurs along the weak zone and on the steepest slope (Figure 1B). A small amount of shear failure also occurs at the base of the moderate slope, where the shear stresses are increased by the weight of the slope above pushing against the boundary at the base of the slope. Tensile failure occurs along the steeper of the two ridges. It also occurs adjacent to erosion of the weak zone at the shallower ridge. Here erosion of the weak zone creates extensional stresses in the stronger material due to the removal of buttressing material.

RESULTS OF WAIKUKUPA MODEL

We use the parameter C:Tau to measure how close a packet of rock is to failure. Where C:Tau > 1 the material is not at failure and where C:Tau ≤ 1 the material is at failure. In the dry Waikukupa model (Figure 2), shear failure is more common at the base of the slope and in the very weak material while tensile failure is more likely to occur near the ridge tops. The weight of the hillslopes are adding to the compressional stresses felt by the material at the base of the slopes, decreasing C:Tau by increasing the magnitude of the shear stresses (Figure 2C). Where the ridge tops are not being compressed, the shear stresses are lower and C:Tau is increased. They are instead subjected to extensional stresses making tensile failure more likely.

Our model removes material that is consistently at failure and that has a downhill path for removal from the system. Most of the material removed from the dry model has failed in shear and is located either within the very weak gouge zone or at the base of the cataclastic zone. Much of the exposed cataclastic is close to failure but it is only at the base of the slope that the shear stresses are sufficient to bring it to failure. The pattern of erosion produced is one of gullies forming and slowly propagating upward (Figure 2D).

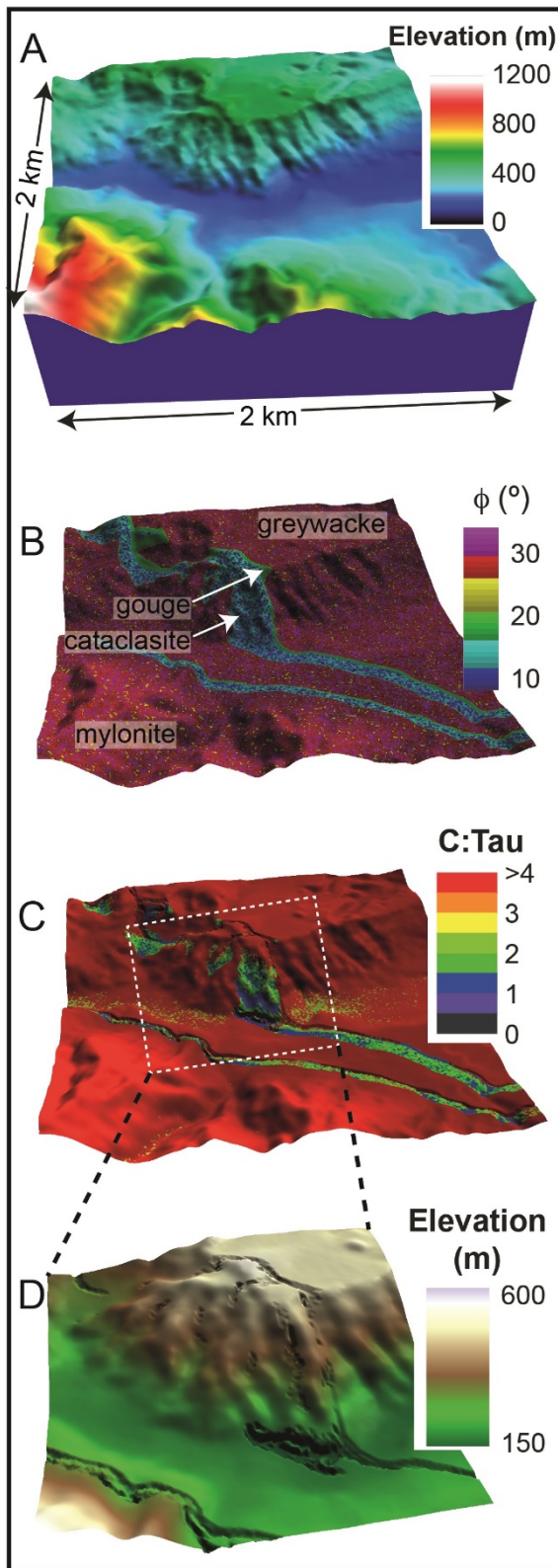


Figure 2: A: Model geometry and elevation contours. B: Rock types in the model and their friction angle – note heterogeneity of material strength. C: The proximity to failure (C: Tau) at the surface of the model. Where C: Tau > 1 the material is not at failure and where C: Tau ≤ 1 the material is at failure. D: Zoom into cataclasite slope showing gullies developing from the bottom of the slope upward. Erosion is also occurring along the Hare Mare creek strand of the Alpine Fault.

Adding a pore pressure ($\lambda = 0.6$) to the models changes the pattern of failure (Figure 3). Within the exposed cataclasites, the pore pressure causes much of the exposed cataclasites to fail in tension. Around the edges of the eroding region, it also brings the material close to shear failure. This is probably due to two factors, the effective stresses lowering the stresses required for failure and also deformation around the edge of the eroding region as material is removed from the adjacent zones. The result is the cataclasites are weakened and large scale mass failure occurs rather than the gullying that occurs when the material is dry (Figure 3B).

DISCUSSION AND CONCLUSIONS

Erosion requires that a rock packet is detached from the Earth's surface. Rock failure requires that local stresses overcome the strength of the rock. The stresses can have many sources, topographic, tectonic, fluvial or glacial. Here we are only considering topographic stresses.

Steep slopes and weak materials both promote failure while shallow slopes and strong rheology inhibit failure. The position of the rock packet on the slope also affects its proximity to failure and likely failure mode. The base of a slope is more likely to fail in shear while higher up the slope, tensile failure is more common.

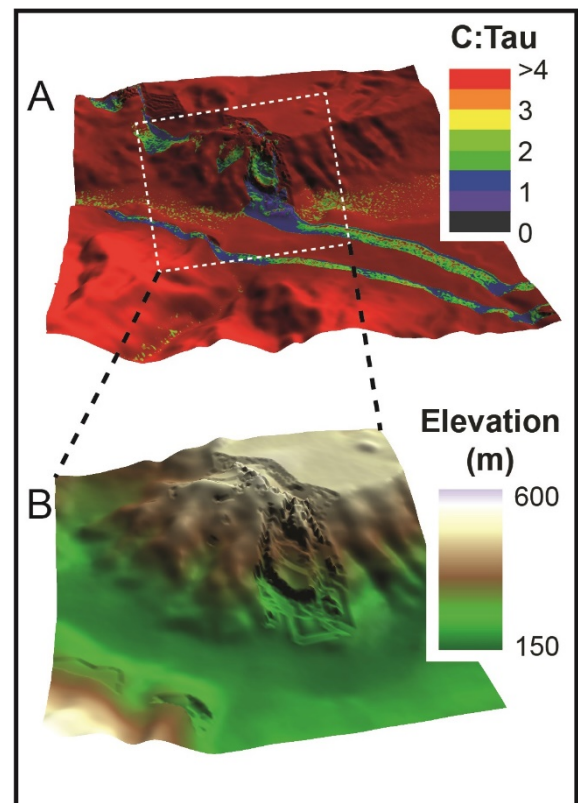


Figure 3: Model with pore pressure included. A: The proximity to failure (C: Tau) at the surface of the model. More of the material at the base of the slope is failing in shear. B: Zoom into cataclasite slope showing that enhanced tensile failure caused by the pore fluid pressure means that much of the slope is at failure and has been eroded.



INQUA Focus Group Earthquake Geology and Seismic Hazards



paleoseismicity.org

Pore pressure fluctuations impact both geodynamic and landscape processes (Terzaghi 1943). Increasing the pore pressure leads to widespread surface failure and erosion of the weaker material, particularly in the exposed cataclasite face. Unlike the dry case, where shear failure and hence erosion is concentrated at the base of the slope and propagates upward, in the wet example, tensile failure and associated erosion starts near the ridges and when combined with the shear failure at the base of the slope, allows the whole slope to fail and erode.

Acknowledgements: The work presented here was supported by the NZ Ministry for Business Innovation and Employment and NSF-EAR-1324637 to P.O. Koons and P. Upton and NSF-EAR-1323137 to G.E. Tucker.

REFERENCES

Hoek E, Brown ET. 1980. *Underground Excavations in Rock*. 1st ed. London: Stephen Austin and Sons Ltd.

Koons PO, Upton P, Barker AD. 2012. The influence of mechanical properties on the link between tectonic and topographic evolution. *Geomorphology*.29:168–180.

Koons PO, Upton P, Roy S, Tucker G. 2013. Linking Earth and Atmosphere at Higher Frequencies with the Failure Earth Response Model. AGU Fall Meeting, 9-13 December, Washington DC.

NIWA. 2004. Mean annual rainfall, 1971-2000.

Norris RJ, Cooper AF. 1995. Origin of small-scale segmentation and transpressional thrusting along the Alpine Fault, New Zealand. *Geological Society of America Bulletin*.107:231-240.

Norris RJ, Cooper AF. 1997. Erosional control on the structural evolution of a transpressional thrust complex on the Alpine Fault, New Zealand. *Journal of Structural Geology*.19:1323-1342.

Terzaghi K. 1943. *Theoretical Soil Mechanics*. New York: John Wiley and Sons.



Integrating faults and past earthquakes into a probabilistic seismic hazard model for peninsular Italy

Valentini, Alessandro (1), Visini, Francesco (2), Pace, Bruno (2)

- (1) DiSPUTer, Università degli Studi “Gabriele D’Annunzio”, Chieti, Italy. alessandro.valentini@unich.it
(2) Istituto Nazionale di Geofisica e Vulcanologia, L’Aquila, Italy.

Abstract: Probabilistic seismic hazard assessments in Italy are mainly based on area source models, in which the seismicity is modelled on a number of seismotectonic zones, and the occurrence of earthquakes is assumed to be uniform. In our model, we used two categories of earthquake sources. The first involves active faults, and fault slip rates were used to quantify the seismic activity rate. The second one involves distributed seismicity, and a smoothed approach and a historical catalogue were used to evaluate seismic activity. Under the assumption that deformation is concentrated along faults, we combined the two earthquake sources and assumed that the smoothed seismic activity in the vicinity of an active fault gradually decreases by a fault-size driven factor. We think our model represents an advance for Italy in terms of input data and method in the field of the fault-based regional seismic hazard modelling.

Key words: Probabilistic Seismic Hazard Analysis, Faults, Earthquakes

INTRODUCTION

We present the results of a new probabilistic seismic hazard (PSH) model for Italy that includes significant advances in the use of integrated active fault and seismological data. The use of active faults as an input for PSH analysis is a consolidated approach in many countries characterized by high strain rates and seismic releases, as shown by, for example, Field et al. (2015) in California and Stirling et al. (2012) in New Zealand. However, in recent years, active fault data have also been successfully integrated into PSH assessments in regions with moderate-to-low strain rates, such as SE Spain (e.g., Garcia-Mayordomo et al., 2007), France (e.g., Scotti et al., 2014), and central Italy (e.g., Peruzza et al., 2011).

In Europe, a working group of the European Seismological Commission, named *Fault2SHA*, is discussing fault-based seismic hazard modelling¹. The working group, born to motivate exchanges between field geologists, fault modellers and seismic hazard practitioners, organized in the last years workshops, conference sessions, special issues, and stimulated collaborations between researchers. The work we are presenting here is born within the activities of the *Fault2SHA* working group.

Combining active faults with background sources is also one of the main issues in this type of approach. Although the methodology remains far from identifying a standard procedure, common approaches combine active faults and background sources by applying a threshold magnitude, generally between 5.5 and 7, above which seismicity is modelled as occurring on faults and below which seismicity is modelled via a smoothed approach (e.g., Akinci et al., 2009), area sources (e.g. the so-called FSBG model in SHARE, Woessner et al., 2015) or a combination of the two (Field et al., 2015; Pace et al., 2006).

Another important issue in the use of active faults in PSHA is given by the choice of the “correct” magnitude-frequency distribution (MFD) to be assigned to the fault sources. Gutenberg-Richter (GR) and Characteristic earthquake models are commonly used and the choice sometimes depends on the knowledge of the fault and on the data availability. Often, the choice of the “appropriate” MFD for each fault source is a difficult task because palaeoseismological studies are scarce and it is often difficult to establish clear relationships between mapped faults and historical seismicity. In this work, we decided to explore the impact on the calculations of these two MFD, a characteristic Gaussian (CHG) model and a Truncated Gutenberg-Richter (TGR) model, in order to explore the epistemic uncertainties, and also to consider a *Mixed model* as a sort of an “expert judgment” model, useful for comparison analysis, in which we assigned one of the two MFDs to each fault source. However, this approach obviously does not solve the issue, and the choice of MFD, still remain an open question in the fault-based PSHA.

However, we think that more efforts have to be directed towards using geological data (e.g. fault sources and palaeoseismological information) in PSH models, in order to obtain more detailed patterns of ground motion, extend the observational time to capture the recurrence of large magnitude events, and to improve the reliability of seismic hazard assessments.

METHOD

Two earthquake-source inputs are considered in this work. The first one is a fault source input that is based on active faults and uses the geometries and slip rates of the known active faults to compute activity rates over a certain range of magnitude. The second is a classical smoothed approach that can take into account rates of expected earthquakes

¹ <https://sites.google.com/site/linkingfaultpsa/home>



from a minimum moment magnitude (M_w) of 4.5 but excludes earthquakes associated with known faults based on a modified earthquake catalogue. Note that our PSH model requires the combination of the two source inputs related to the locations of expected seismicity rates into a single model. Therefore, these two earthquake-source inputs are not independent but complementary, both in magnitude and frequency distribution, and together accounting for all seismicity in Italy.

Fault source inputs are useful for seismic hazard studies, and we compiled a database for Italy via analysis and synthesis of neotectonic and seismotectonic data from approximately 90 published studies on 110 faults across Italy. Based on the compiled database, we explored in detail three main issues associated with defining a fault source input: the slip rate evaluation, the segmentation model and the expected seismicity rate calculation.

Introducing distributed earthquakes into our PSH model is necessary because researchers have not been able to identify a causative source (i.e., a mapped fault) for important earthquakes in the historical catalogue. This lack of correlation between earthquakes and faults may be related to (i) interseismic strain accumulation in areas between major faults, (ii) earthquakes occurring on unknown or blind faults, (iii) earthquakes occurring on unmapped faults characterized by slip rates lower than the erosional processes, and/or (iv) the general lack of surface ruptures associated with faults generating $M_w < 5.5$ earthquakes.

We used the historical catalogue of earthquakes (CPTI15; Rovida et al., 2016) to model the occurrence of moderate-to-large ($M_w \geq 4.5$) earthquakes. The catalogue consists of 4,427 events and covers approximately the last one thousand years from 01/01/1005 to 28/12/2014. Before using the catalogue, we removed all events not considered as mainshock via a declustering filter (Gardner & Knopoff, 1977), resulting in a complete catalogue composed of 1,839 independent events.

To combine the two source inputs, we introduced a distance-dependent linear weighting function, such that the contribution from the distributed sources linearly decreases from 1 to 0 with decreasing distance from the fault. The expected seismicity rates from the distributed sources input start at $M_w = 4.5$, which is lower than the minimum magnitude of the fault sources, and the weighting function acts only in the magnitude range overlapping the MFD of each fault. This weighting function is based on the assumption that faults tend to modify the surrounding deformation field. Our approach allows incompleteness in the fault database to be bypassed, which is advantageous because all fault databases should be considered incomplete. In our approach, the seismicity is modified only in the vicinity of mapped faults. The remaining areas are fully described by the *distributed* input. With this approach, we do not define areas with reliable fault information, and the locations of currently unknown faults can be easily included when they are discovered in the future.

DISCUSSION

To obtain PSH maps we assign the calculated seismicity rates to their pertinent geometries, i.e., individual 3D seismogenic sources for the *fault input* and point sources for the *distributed input*. All the computations are performed using the OpenQuake Engine (Global Earthquake Model, 2016) with a grid spacing of 0.05° in both latitude and longitude. We used this software because it is open source software developed recently by GEM with the purpose of providing seismic hazard and risk assessments. Moreover, it is widely recognized within the scientific community for its potential. The ground motion prediction equations (GMPE) of Akkar et al. (2013), Chiou et al., (2008), Faccioli et al., (2010) and Zhao et al., (2006) are used, as suggested by the SHARE European project (Woessner et al., 2015). In addition, we also used Bindi et al. (2014), a GMPEs calibrated using Italian data. We put together all GMPE in a logic tree with the same weight of 0.2 for each branch. The distances used for each GMPE are the Joyner and Boore distance for Akkar 2013, Bindi 2014 and Chiou 2008 and the closest rupture distance for Faccioli 2010 and Zaho 2006.

To explore the epistemic uncertainty due to the distribution of activity rates over the range of magnitudes in the fault source input, we compared the seismic hazard levels obtained with the TGR and CHG fault source inputs using the TGR and CHG MFDs for all the fault sources. Although both models have the same amount of seismic moment release, the different MFDs generate clear differences. In fact, in the *TGR* model, all faults contribute significantly to the seismic hazard, whereas in the *CHG* model, only a few faults located in the central Apennines and Calabria contribute to the seismic hazard. This difference is due to the different shapes of the MFDs in the two models. The rates of earthquakes with magnitudes between 5.5 and approximately 6, which are likely the main contributors to these levels of seismic hazard, are generally higher in the *TGR* model than in the *CHG* model. At a 2% probability of exceedance in 50 years, all fault sources in the CHG contribute to the seismic hazard, but the absolute values are still generally higher in the *TGR* model.

The *distributed input* depicts a more uniform shape of the seismic hazard than the fault source inputs. A PGA lower value of 0.125 g at a 10% probability of exceedance in 50 years and a lower value of 0.225 g at a 2% probability of exceedance in 50 years envelope a large part of peninsular Italy and Sicily. Two areas with higher seismic hazard levels are located in the central Apennines and North-East Sicily.

The probabilistic seismic hazard maps produced from our model show a hazard pattern similar to that of the current national maps at the national scale, but some significant differences in hazard are present at the regional-to-local scale.



Moreover, the relative contributions of fault source inputs and distributed source inputs have been identified in maps and profiles in three sectors of the study area. These profiles show that: the hazard is generally higher where faults have been used; and for high probabilities of exceedance the contribution of the *distributed* sources equals that of the *fault* input.

Finally, a preferred model, called the *Mixed* model, was obtained by selecting the most appropriate MFD model for each fault.

This new PSH model is not intended to replace, integrate or test the currently official national seismic hazard model for Italy. While some aspects remain to be implemented in our approach (e.g., the integration of reverse/thrust faults in the database, sensitivity tests for the distance-dependent linear weighting function parameters, sensitivity tests for possible different segmentation models, and fault source inputs that account for fault interaction), the proposed model represents an advance in terms of input data (quantity and quality) and methodology based on a decade of research in the field of fault-based approaches to regional seismic hazard modelling.

REFERENCES

- Akinci, A., Galadini, F., Pantosti, D., Petersen, M., Malagnini, L., and Perkins, D., 2009. Effect of Time Dependence on Probabilistic Seismic-Hazard Maps and Deaggregation for the Central Apennines, Italy, *B Seismol Soc Am*, 99, 585-610.
- Akkar, S., Sandikkaya, M.A., Bommer, J.J., 2013. Empirical Ground-Motion Models for Point and Extended-Source Crustal Earthquake Scenarios in Europe and the Middle East, *Bulletin of Earthquake Engineering*, ISSN:1570-761X.
- Bindi, D., Massa, M., Luzi, L., Ameri, G., Pacor, F., Puglia, R., and Augliera, P., 2014. Pan-European ground-motion prediction equations for the average horizontal component of PGA, PGV, and 5%-damped PSA at spectral periods up to 3.0 s using the RESORCE dataset (vol 12, pg 391, 2014), *B Earthq Eng*, 12, 431-448.
- Chiou, B. S. J. and Youngs, R. R., 2008. An NGA model for the average horizontal component of peak ground motion and response spectra, *Earthq Spectra*, 24, 173-215.
- Faccioli, E., Bianchini, A., and Villani, M.: New ground motion prediction equations for $t > 1$ s and their influence on seismic hazard assessment, In: Proceedings of the University of Tokyo symposium on long-period ground motion and urban disaster mitigation, 2010.
- Field, E. H., Biasi, G. P., Bird, P., Dawson, T. E., Felzer, K. R., Jackson, D. D., Johnson, K. M., Jordan, T. H., Madden, C., Michael, A. J., Milner, K. R., Page, M. T., Parsons, T., Powers, P. M., Shaw, B. E., Thatcher, W. R., Weldon, R. J., and Zeng, Y. H., 2015. Long-Term Time-Dependent Probabilities for the Third Uniform California Earthquake Rupture Forecast (UCERF3), *B Seismol Soc Am*, 105, 511-543.
- Garcia-Mayordomo, J., Gaspar-Escribano, J. M., and Benito, B., 2007. Seismic hazard assessment of the Province of Murcia (SE Spain): analysis of source contribution to hazard, *J Seismol*, 11, 453-471.
- Gardner, J. K., Knopoff, L., 1974. Is the sequence of earthquakes in Southern California, with aftershocks removed, Poissonian? *Bulletin of the Seismological Society of America*, 64, 1363-1367.
- GEM: The OpenQuake-engine User Manual. Global Earthquake Model (GEM) Technical Report, doi: 10.13117/GEM.OPENQUAKE.MAN.ENGINE.1.9/01, 189 pages, 2016.
- Pace, B., Peruzza, L., Lavecchia, G., and Boncio, P., 2006. Layered seismogenic source model and probabilistic seismic-hazard analyses in central Italy, *B Seismol Soc Am*, 96, 107-132.
- Peruzza, L., Pace, B., and Visini, F.: Fault-Based Earthquake Rupture Forecast in Central Italy: Remarks after the L'Aquila M-w 6.3 Event, *B Seismol Soc Am*, 101, 404-412, 2011.
- Rovida, A., Locati, M., Camassi, R., Lolli, B., and Gasperini P., 2016. CPTI15, the 2015 version of the Parametric Catalogue of Italian Earthquakes. Istituto Nazionale di Geofisica e Vulcanologia. doi:<http://doi.org/10.6092/INGV.IT-CPTI15>.
- Scotti, O., Clement, C., and Baumont, D., 2014. Seismic hazard for design and verification of nuclear installations in France: regulatory context, debated issues and ongoing developments, *B Geofis Teor Appl*, 55, 135-148.
- Stirling, M., McVerry, G., Gerstenberger, M., Litchfield, N., Van Dissen, R., Berryman, K., Barnes, P., Wallace, L., Villamor, P., Langridge, R., Lamarche, G., Nodder, S., Reyners, M., Bradley, B., Rhoades, D., Smith, W., Nicol, A., Pettinga, J., Clark, K., and Jacobs, K., 2012. National Seismic Hazard Model for New Zealand: 2010 Update, *B Seismol Soc Am*, 102, 1514-1542.
- Woessner, J., Laurentiu, D., Giardini, D., Crowley, H., Cotton, F., Grunthal, G., Valensise, G., Arvidsson, R., Basili, R., Demircioglu, M. B., Hiemer, S., Meletti, C., Musson, R. W., Rovida, A. N., Sesetyan, K., Stucchi, M., and Consortium, S., 2015. The 2013 European Seismic Hazard Model: key components and results, *B Earthq Eng*, 13, 3553-3596.
- Zhao, J. X., Zhang, J., Asano, A., Ohno, Y., Oouchi, T., Takahashi, T., Ogawa, H., Irikura, K., Thio, H. K., Somerville, P. G., Fukushima, Y., and Fukushima, Y.: Attenuation relations of strong ground motion in Japan using site classification based on predominant period, *B Seismol Soc Am*, 96, 898-913, 2006.



Extreme soft-sediment deformation structures as palaeoseismic indicators in slurries from the Late Triassic Ordos Basin (central China)

Van Loon, A.J. (Tom) (1, 2, 3), Yang, Renchao (4, 5), Fan Aiping (4), Han, Zuozhen (4)

- (1) Geocom Consultants, Valle del Portet 17, 03726 Benitachell, SPAIN; E-mail: Geocom.VanLoon@gmail.com
- (2) College of Earth Science and Engineering, Shandong University of Science and Technology, No. 579, Qianwangang Road, 266590 Qingdao, Huangdao District, CHINA
- (3) Institute of Geology, Adam Mickiewicz University, B. Krygowskiego Str. 12, 61-680 Poznan, POLAND
- (4) Shandong Provincial Key Laboratory of Depositional Mineralization & Sedimentary Minerals, Shandong University of Science and Technology, Qingdao 266590, CHINA
- (5) Laboratory for Marine Mineral Resources, Qingdao National Laboratory for Marine Science and Technology, Qingdao 266071, CHINA

Abstract: In contrast to other gravity flows, slurries (highly fluid mixtures of water and finely divided material) do not easily originate in nature by processes other than seismic shocks. They can therefore be considered as good evidence for seismic activity, which may help to recognize palaeoseismicity in the geological record. This requires, however, the recognition of sediments deposited by slurry flows. The often extreme and chaotic soft-sediment deformation structures (commonly much more chaotic than in seismites) are a good indicator, both in the field and in boreholes. Good examples have been found in the Late Triassic Yanchang Formation in the Ordos Basin (central China). Characteristic are the numerous remnants of deformed layers, commonly resembling parts of load casts or even pseudonodules, that show, no orientation that might be expected on the basis of post-depositional loading.

Key words: gravity flows, slurry deposits, soft-sediment deformation structures, Ordos Basin, Yanchang Formation

INTRODUCTION

Fine-grained sediments can, be transported and deposited in turbulent environments, which is in contrast with the traditional view that mud can be deposited only by settling from suspension in a quiet subaqueous environment (Schieber, 1994; Macquaker and Bohacs, 2007; Ichaso and Dalrymple, 2009; Ghadeer and Macquaker, 2011, 2012) or by specific mass-flow types (Plint, 2014; Schieber, 2016).

Even more recent is the progress concerning the transformation of gravity flows into other types, and regarding the co-occurrence of different gravity-flow deposits (Sumner, 2009; Haughton et al., 2009; Talling et al., 2012; Bernhardt et al., 2012; Kane and Pontén, 2012; Yang et al., 2014). Debris flows may be transformed into turbidity currents, commonly in the middle to upper part and in the tail of the flow (Yang et al., 2014). Debris flows, mixing with ambient water and thus becoming dilute, can change into turbidity currents (Sumner, 2009; Bernhardt et al., 2012; Yang et al., 2014), whereas turbidity currents may become transformed into debris flows because due to settling of suspended particles, the concentration of suspended sediments in the bottom of turbidity currents increases. The flow thus can erode the substrate or underwater levees more easily, and the eroded material may then re-enter the flow. When the concentration of muddy debris passes a threshold value, a turbidity current will change into a debris flow (Talling, 2007; Sumner, 2009; Christopher et al., 2009; Bernhardt et al., 2012; Bourget et al., 2012). This leads commonly to the co-occurrences of various types of mass-flow deposits.

SLURRIES AND SLURRY DEPOSITS

A special and relatively rare – type of gravity flow is constituted by slurries, which are highly fluid mixtures of water and finely divided material. Whereas almost all other types of gravity flow are most easily initiated by slope failure, slurries seem – as far as can be deduced from the geological context of their deposits – exclusively (or at least almost exclusively) to be triggered by seismic shocks. This makes them a strong indicator of palaeoseismic activity.

How to distinguish slurry deposits? Just like most autochthonous marine and lacustrine sediments, many mass-flow deposits can be fine-grained (turbidites, mudflow deposits, hyperpynites, etc.). The characteristics of such sediments must therefore be studied in detail. An exceptionally good opportunity is provided by the Ordos Basin in central China (Fig. 1), where slurry deposits occur jointly with other fine-grained mass-flow deposits in the Late Triassic lacustrine Yanchang Formation (Yang et al., 2017a).



Figure 1: Setting of the Ordos Basin (modified from Yang et al., 2017b).



The present contribution is aimed at exploring the depositional processes that built the lacustrine muddy gravity-flow deposits of the Late Triassic lacustrine fine-grained sedimentary system in the southern Ordos Basin (about 15000 km²), so as to find out what triggered the initiation of the mass flows. The results of this study are based on detailed examination of 112 cores and 10 thin sections of muddy rocks

THE ORDOS BASIN

The Ordos Basin is situated on a stable Archean crystalline basement. It underwent a long tectonic-sedimentary evolution from the Palaeozoic to the Cenozoic, and a sedimentary succession accumulated during this time-span with an average thickness of 4-5 km (Yang and Deng, 2013). During the Late Triassic, a palaeocontinent was uplifted in what is now the southern part of the basin. This was due to the collision between the Yangtze Plate and the North China Plate. This palaeocontinent supplied most of the sediment that accumulated in the southern part of the basin (Weislogel et al., 2006; Dong et al., 2012). The North China Plate was extruded by the Yangtze Plate and the Hinggan-Mongolia Plate from the south and north, respectively. This process resulted in subsidence of the Ordos Basin.

The collision and thrusting downwarped the Ordos Basin during the Late Triassic, resulting in steep slopes at both sides: 3.5°-5.5° in the south and 1.5°-2.5° in the north (Deng et al., 2011; Yang and Deng, 2013; Yang et al., 2017b). The rapid subsidence of the basement and the rapid transgression during the early Late Triassic resulted in sediment that was derived mainly from the surrounding palaeocontinents (Fig. 1) (Deng et al., 2011; Yang and Deng, 2013).

THE YANCHANG FORMATION

Various types of lacustrine mudstones, shales and oil shales occur in the fine-grained parts of the Yanchang Formation, but geologists and specialists have focused for a long time on sandstones, because they form economically important reservoirs of hydrocarbons (Deng et al., 2011; Yang and Deng, 2013; Yang et al., 2013). The depositional processes of the mudstones and shales in this formation have not yet raised much attention, and the research of gravity-flow deposits has only just begun (Yang et al., 2017a).

SOFT-SEDIMENT DEFORMATION STRUCTURES

Numerous SSDS are present in the lacustrine mudstones of the Yanchang Formation; they always contain a certain amount of sand and silt. Most of them occur in mass-flow deposits. The most interesting ones are those in the slurry deposits. When water-saturated slope sediments started to move downslope, increasingly more water was included, so that eventually a slurry was formed. The turbulent flow of the slurry led to erosion of the sedimentary bottom and of subaqueous natural levees

that existed alongside the channels in the delta slope; part of these sediments may have been so water-saturated that the individual particles lost the contact with each other, so that they became mixed up with the other sediment particles in the slurry, thus increasing the erosional power of this flow. The increased erosional capability occasionally led to the erosion of more consolidated sediment. These became included in the slurry with its chaotic turbulent character, forming lumps that partly became deformed during transport, either by rolling over the sedimentary bottom, or by the powerful whirls in the slurry. This explains the occurrence in several cores of slurry deposits consisting predominantly of mud, in which deformed lumps of somewhat more sandy material are embedded, sometimes as floating, more or less isolated masses (Fig. 2) sometimes in quantities that are almost equal in volume as the mud matrix (Fig. 3).



Figure 2: Isolated more sandy masses floating in a silty/clayey matrix. The diameter of the coin (for scale) is 20 mm.



Figure 3: High concentration of sandy lumps in the mud matrix of a slurry deposit. The material is distinctly derived from a deformed layer, probably in the form of a load cast that became detached from its parent layer and that was transported and partially destroyed by the slurry flow. Scale in cm.



The farther downslope slurry flows travelled, the less recognizable the individual lumps of eroded more sandy material became: the individual fragments were torn apart, bumped against each other, absorbed water, etc., so that they lost their original shapes and eventually became more or less shapeless masses (Fig. 4).

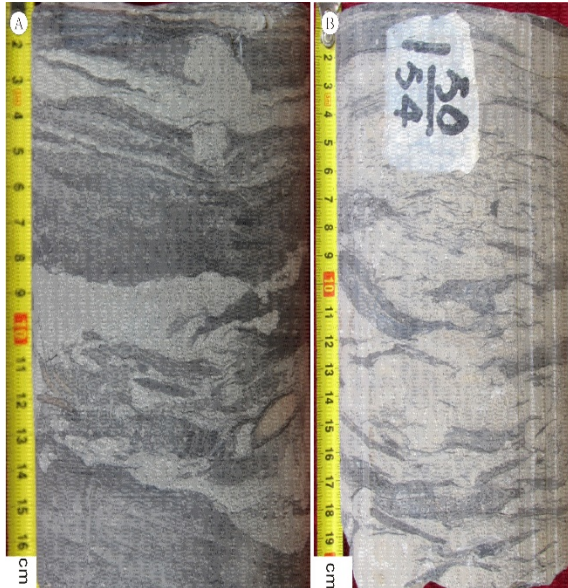


Figure 4: Muddy slurry deposits with fairly shapeless masses of deformed fine-sandy material (after Yang et al., 2016). A: Relatively thick slurry deposit with concentrations of fine-sandy material at several levels. B: Densely packed, more or less bedding-parallel masses of fine-sandy deformed sediment in a relatively thick slurry deposit with a muddy matrix.

CONCLUSIONS

During the Late Triassic, subaqueous gravity flows transported and deposited mainly fine-grained particles such as silt and mud on the slopes of delta fronts and in the deep lacustrine areas of the Ordos Basin. These event deposits occur frequently intercalated between the autochthonous mudstones. Many of the flows had the characteristics of slurries, and their deposits contain abundant soft-sediment deformation structures that reflect these flows and depositional conditions.

The flows were possibly triggered by earthquakes, either or not due to volcanic eruptions. A tectonically active setting, a depositional slope and a high sedimentation rate facilitated the development of soft-sediment deformations on the lacustrine delta fronts. Alternations of water-saturated sands and soft muds with, consequently, reversed density gradients were additional favourable factors for deformation processes, but the most chaotic soft-sediment deformation structures originated by the transport of already deformed unconsolidated sediment lumps in highly turbulent slurries. These chaotic SSDS, when present in slurry deposits, might be considered as strong evidence for seismic activity that affected water-saturated fine-grained sediments on a slope, and thus can help to recognize phases of palaeoseismic events.

Acknowledgements: The study was supported by the National Science Foundation of China (Grants 41372135 and 41672120) and by the SDUST Research Fund (Grant 2015TDJH101).

REFERENCES

- Bernhardt, A., Stright, L., Lowe, D., 2012. Channelized debris-flow deposits and their impact on turbidity currents: the Puchkirchen axial channel belt in the Austrian Molasse Basin. *Sedimentology* 59, 2042-2070.
- Bourget, J., Zaragosi, S., Mulder, T., 2010. Hyperpycnal-fed turbidite lobe architecture and recent sedimentary processes: a case study from the Al Batha turbidite system, Oman margin. *Sedimentary Geology* 229, 144-159.
- Christopher, J.A.-L., Howard, D.J., 2009. Sustained turbidity currents and their interaction with debris-related topography: Labuan Island, offshore NW Borneo, Malaysia. *Sedimentary Geology* 219, 77-96.
- Deng, X., Fu, J., Yao, J., Pang, J. & Sun, B., 2011. Sedimentary facies of the Middle - Upper Triassic Yanchang Formation in Ordos Basin and breakthrough in petroleum exploration. *Journal of Palaeogeography* 13, 443-455. (in Chinese with English abstract)
- Dong, Y., Liu, X., Zhang, G., Chen, Q., Zhang, X., Li, W. & Yang, C., 2012. Triassic diorites and granitoids in the Foping area: Constraints on the conversion from subduction to collision in the Qinling orogen, China. *Journal of Asian Earth Sciences* 47, 123-142.
- Ghadeer, S.G., Macquaker, J.H.S., 2011. Sediment transport processes in an ancient mud-dominated succession: a comparison of processes operating in marine offshore settings and anoxic basinal environments. *Journal of the Geological Society, London* 168, 1121-1132.
- Ghadeer, S.G., Macquaker, J.H.S., 2012. The role of event beds in the preservation of organic carbon in fine-grained sediments: analyses of the sedimentological processes operating during deposition of the Whitby Mudstone Formation (Toarcian, Lower Jurassic), preserved in northeast England. *Marine and Petroleum Geology* 35, 309-320.
- Ichaso, A.A. & Dalrymple, R.W., 2009. Tide- and wave-generated fluid mud deposits in the Tilje Formation (Jurassic), offshore Norway. *Geology* 37, 539-542.
- Kane, I.A., Pontén, A.S.M., 2012. Submarine transitional flow deposits in the Paleogene Gulf of Mexico. *Geology* 40, 1119-1122.
- Macquaker, J.H.S., Bohacs, K.M., 2007. On the accumulation of mud. *Science* 318, 1734-1735.
- Plint, A.G., 2014. Mud dispersal across a Cretaceous prodelta: Storm-generated, wave-enhanced sediment gravity flows inferred from mudstone microtexture and microfacies. *Sedimentology* 61, 609-647.
- Schieber, J., 1994. Evidence for episodic high energy events and shallow water deposition in the Chattanooga Shale, Devonian, central Tennessee, U.S.A. *Sedimentary Geology* 93, 193-208.
- Schieber, J., 2016. Mud re-distribution in epicontinental basins – exploring likely processes. *Marine & Petroleum Geology* 71, 119-133.
- Sumner, E.J., Talling, P.J. & Amy, L.A., 2009. Deposits of flows transitional between turbidity current and debris flow. *Geology* 37, 991-994.
- Talling, P.J., Wynn, R.B., Masson, D.G., Frenz, M., Cronin, B.T., Schiebel, R., Akhmetzhanov, A.M., Dallmeier-Tiessen, S., Benetti, S., Weaver, P.P.E., Georgiopoulou, A., Zühlsdorff, C. & Amy, L.A., 2007. Onset of submarine debris flow deposition far from original giant landslide. *Nature* 450, 541-544.
- Talling, P.J., Masson, D.G., Sumner, E.J., 2012. Subaqueous sediment density flows: depositional processes and deposit types. *Sedimentology* 59, 1937-2003.
- Weislogel, A.L., Graham, S.A., Chang, E.Z., Wooden, J.L., Gehrels, G.E. & Yang, H., 2006. Detrital zircon provenance of the Late Triassic



INQUA Focus Group Earthquake Geology and Seismic Hazards



paleoseismicity.org

- Songpan-Ganzi complex: Sedimentary record of collision of the North and South China blocks. *Geology* 34, 97–100.
- Yang, H. & Deng, X., 2013. Deposition of Yanchang Formation deep-water sandstone under the control of tectonic events, Ordos Basin. *Petroleum Exploration and Development* 40, 513–520.
- Yang, R.C., He, Z.L., Qiu, G.Q., Jin, Z.J., Sun, D.S. & Jin, X.H., 2014. A Late Triassic gravity flow depositional system in the southern Ordos Basin. *Petroleum Exploration and Development* 41, 724–733.
- Yang, R., Van Loon, A.J., Yin, W., Fan, A. & Han Z., 2016. Soft-sediment deformation structures in cores from lacustrine slurry deposits of the Late Triassic Yanchang Fm. (central China). *Geologos* 22, 201-211.
- Yang, R., Fan, A., Han, Z. & Van Loon, A.J., 2017a. *Marine and Petroleum Geology* 85, 194-219.
- Yang, R., Jin, Z., Van Loon, A.J., Han, Z. & Fan, A., 2017b. Climatic and tectonic controls of lacustrine hyperpynite origination in the Late Triassic Ordos Basin, central China: implications for unconventional petroleum development. *American Association of Petroleum Geologists Bulletin* 101, 95-117.



Assessing giant tsunamigenic subduction earthquakes in the Northern Chile Seismic Gap during the last millennia from submarine and archaeological records

Gabriel Vargas Easton (1)*, Diego Salazar (2), Sergio Ruiz (3), Felipe Leyton (4), Rachel Abrahami (1), Jacobus Le Roux (1), Silvio Pantoja (5), Carina Lange (5), Jaime Campos (3)

- (1) Departamento de Geología, Universidad de Chile
 (2) Departamento de Antropología, Universidad de Chile
 (3) Departamento de Geofísica, Universidad de Chile
 (4) Centro Sismológico Nacional, Universidad de Chile
 (5) Departamento de Oceanografía, COPAS, Universidad de Concepción, Chile
 *Corresponding author: gvargas@ing.uchile.cl

Abstract: Coastal and marine records off the hyperarid Atacama Desert provide a new view about the occurrence of large subduction earthquakes in the Central Andes. From high-resolution geochronology of laminated series accumulated on a narrow shelf, we associate anomalous structures such as slumps and discontinuities -overlaid by turbidite deposits-, to the last giant 1877 $M_w \sim 8.8$ tsunamigenic earthquake. Once compared with the reanalysis of historical chronicles and seismological data, we suggest that large magnitude events produce destabilisation at the sea bottom capable to generate slumping or discontinuities. From the ongoing analysis of marine records coupled with observations from coastal archaeological sites, we assess the occurrence of several giant tsunamigenic earthquakes in the last millennia, suggesting that the predecessor of the 1877 episode occurred close to CE 1450. In light of this new paleoseismic evidence it is likely that the last $M_w \sim 8$ earthquakes in 2014 and 2007 along this seismic gap region, seem to be moderate episodes in a larger seismic cycle.

Key words: Northern Chile seismic gap, paleoseismology, 1877 tsunamigenic earthquake, subduction contact, Central Andes

INTRODUCTION

The subduction margin of the Central Andes is characterized by the occurrence of large earthquakes associated with the convergence of the Nazca and South American Plates at about 6.5-7.0 cm/yr (DeMets et al., 1994; Angermann et al., 1999; Béjar-Pizarro et al., 2010). This convergence rate is responsible for causing giant tsunamigenic subduction earthquakes like the 1868 M_w 8.8 and 1877 M_w 8.8 events that affected vast areas along southern Peru and northern Chile (Kausel, 1986; Dorbath et al., 1990; Comte and Pardo, 1991; Fig. 1). In particular, the last giant earthquake in 1877 ruptured ~450-500 km along northern Chile in a region that has been characterized as a mature seismic gap (Kelleher, 1972; Nishenko, 1985; Kausel, 1986; Fig. 2). The earthquake rupture stopped at the Mejillones Peninsula near 23°S, which is a late Cenozoic geomorphologic feature constituted by emerged tectonic blocks limited by Quaternary faults (Armijo and Thiele, 1990; Ortlieb et al., 1996; Delouis et al., 1998; Gonzalez et al., 2003; Vargas et al., 2011). In the last decades, several large earthquakes have struck the hyperarid Atacama Desert significantly impacting the region, like the 1995 M_w 8.1 Antofagasta earthquake, the 2007 M_w 7.7 Tocopilla earthquake, and the 2014 M_w 8.1 Iquique-Pisagua earthquake (Fig. 1). While the 1995 subduction earthquake ruptured along 180 km of the plate interface southward from the Mejillones Peninsula, the 2007 Tocopilla earthquake ruptured ~150 km and ended below this feature (Ruegg et al., 1996; Delouis et al., 1997; Chlieh et al., 2004; Pritchard et al., 2006; Delouis et al.,

2009; Béjar-Pizarro et al., 2010). In addition, the last 2014 M_w 8.1 Pisagua-Iquique earthquake ruptured a moderate portion along the subduction contact, contributing only moderately to the rupture of the large Northern Chile seismic gap region (Ruiz et al., 2014).

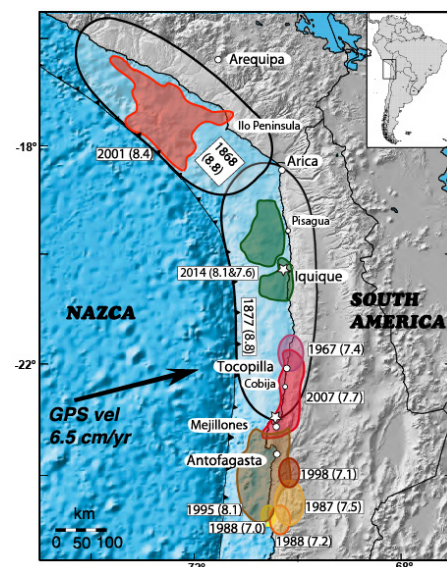


Fig. 1: Regional tectonic setting off Northern Chile, and ruptures areas of the historic earthquakes, including those of the last giant 1868 and 1877 tsunamigenic events. White stars indicate the location of the sediment cores (modified from Béjar-Pizarro et al., 2010 and Ruiz et al., 2014).

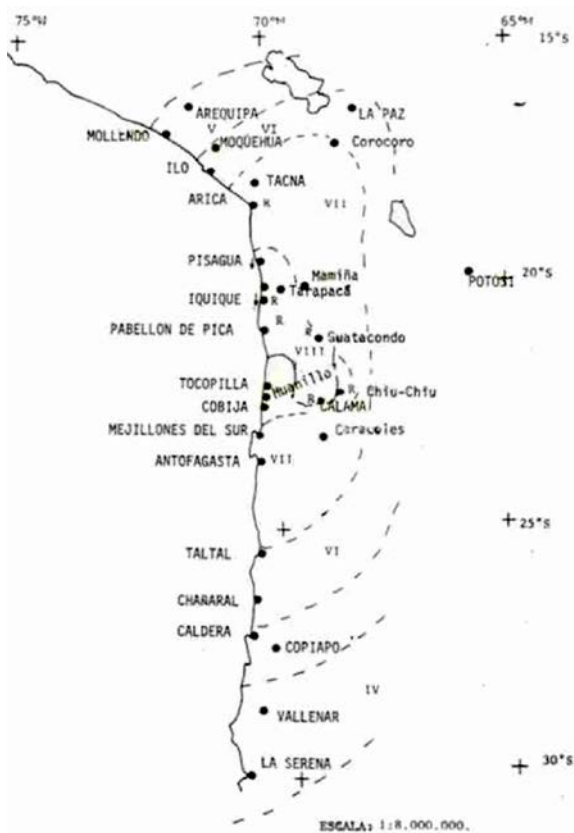


Fig. 2: Isoseismal contour lines inferred from the historical review of damages associated to the large M_w 8.8 1877 tsunamigenic earthquake along the hyperarid Northern Chile (Kausel, 1986). Isoseismal VIII MM indicates the most affected area, defining the most probably rupture length along the subduction contact, between Mejillones del Sur and Pisagua (Kausel, 1986).

PALEOSEISMOLOGY OF GIANT TSUNAMIGENIC EARTHQUAKES

The historical seismic record of the region is only two hundred years long (Comte and Pardo, 1991), which limits our knowledge about earthquake occurrence along this hyperarid subduction margin. From high resolution geochronology based upon Pb-210 an C-14 data and sedimentology in laminated series accumulated on a narrow shelf along the continental margin (Vargas et al., 2004; 2005; 2007), we observed that anomalous structures, such as slumps and discontinuities, are chronologically associated with the occurrence of giant historic earthquakes in the area (e.g. Vargas et al., 2005).

Holocene laminated sediments off Northern Chile result from a combination of variable ocean-climate conditions, which together with hypoxic to anoxic conditions at the sea bottom and geomorphological configurations especially associated to local embayment and basins, favor the accumulation and preservation of organic rests on the shelf (Vargas et al., 2004; Valdés et al., 2004). High primary production rates at the surface of the ocean result in the accumulation of hemipelagic sediments at rates around

10-15 cm/100 years ($32 \text{ mg.cm}^{-2}.\text{y}^{-1}$; Vargas et al., 2004; 2007). Organic-rich laminated sediments at the sea bottom are mostly constituted by diatom and other plankton rests, organic matter and less abundant aeolian lithogenic particles (Vargas et al., 2004; Valdés et al., 2004), from which high-resolution ocean-climate variability can be inferred (Vargas et al., 2004; 2007). Slumps and deformed sediments together with lithogenic-rich lenses interbedded within horizontal laminae have been associated to the occurrence of large subduction earthquakes and tsunamis (Vargas et al., 2005).

The analysis of long (ca. 5.5 m) sediment cores together with high resolution seismic profile data, compared with records from coastal archaeological sites, allow us to infer the occurrence of several giant earthquakes in the last two millennia in this seismic gap region.

The anomalous sedimentary features that we relate to the occurrence of large subduction tsunamigenic earthquakes are systematically characterized by centimeter to decimeter thickness layer of deformed strata with inversed radiocarbon ages, which we interpret as slumps produced by the shaking associated to seismic waves during the mainshock (Fig. 3). These deposits are overlaid by centimeter thickness detritic lenses enriched in lithogenic minerals (Fig. 3). From the analysis of thin sections, Vargas et al. (2005) described one of these detritic layers associated to a discontinuity observed in a sediment core (33C) from Mejillones, evidencing its lenses-shape as well as its mineralogical content, which together with the coarser grain size of lithogenic particles with respect to the adjacent layers, suggest its origin as the result of local reworking from shallower areas in the same shelf basin. Considering the stratigraphic association with the underlying slump deposit (Fig. 3), as well as the limited supply of alluvial sediments to the marine basin in this hyperarid region, mostly associated to localized runoff during alluvial episodes related to El Niño events (Vargas et al., 2006), we interpret that detritic lenses overlying slumps deposits result from turbidites or density currents produced by backwash of tsunami waves immediately after the earthquake occurrence (Figs. 3 and 4).

In addition, we observed that other structures in the sedimentary record are characterized by smoothly deformed sediment that are not associated with inversed radiocarbon ages, neither with detritic overlying deposit, which we interpret as a possible signal of minor events as in the case of the 1768 M_w 7.7, occurred within the seismic gap region, close to the Mejillones basin, which did not produce a tsunami according the historical analysis of Comte and Pardo (1991). Moreover, in the sediment records of cores 33C and F981A (Vargas et al., 2005; 2007), as well as in cores GC3 and GC1, it is not possible to precisely determine any signal associated to the 1995 M_w 8.1 Antofagasta earthquake, whose rupture area encompassed the southern portion of the Mejillones Peninsula (Fig. 1).

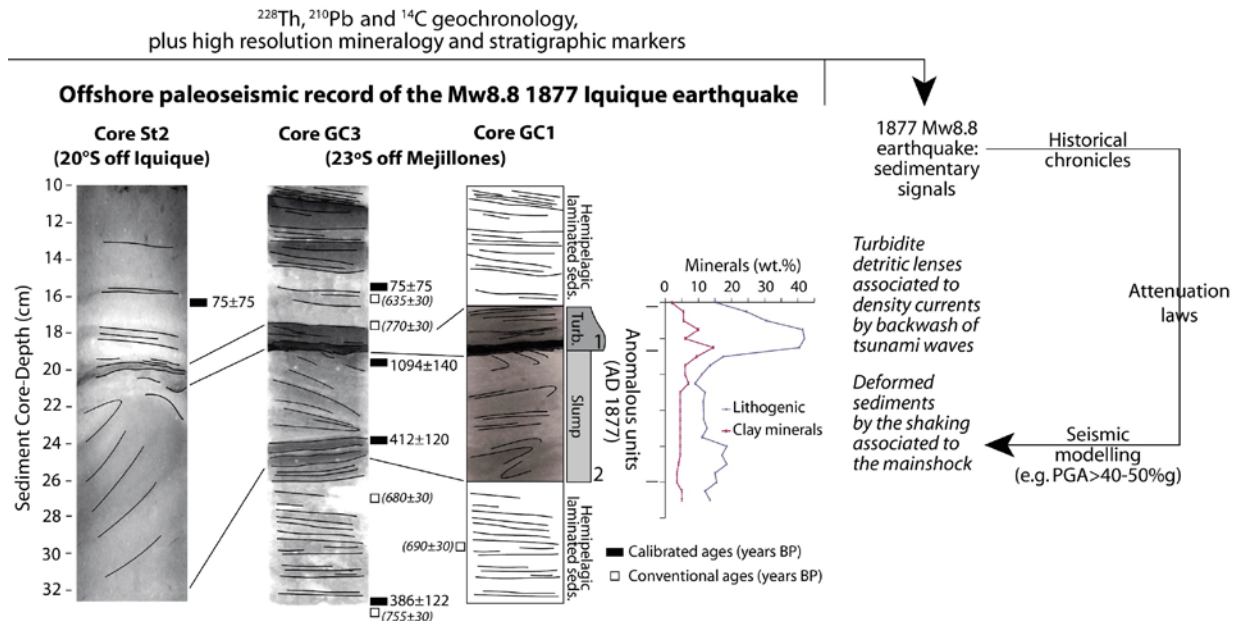


Fig. 3: Interpreted offshore paleoseismological record of the 1877 giant tsunamigenic earthquake off Iquique and Mejillones.

From the observation of anomalous structures similar to the 1877-event record (Fig. 3), in cores GC1 and GC3 from Mejillones basin (23°S), we infer giant tsunamigenic earthquakes during the last ca. 1650 years (Fig. 4). All of these structures are characterized by inversed radiocarbon ages providing additional support for evidencing slump deposits in the sedimentary series. Thus, we inferred predecessors of the 1877-event, which are characterized by a couple of slump deposits overlaid by turbidites in the sedimentary record, close to CE 1450, CE 953 and CE 655, with a possible episode, characterized only by a turbidite, in CE 1046.

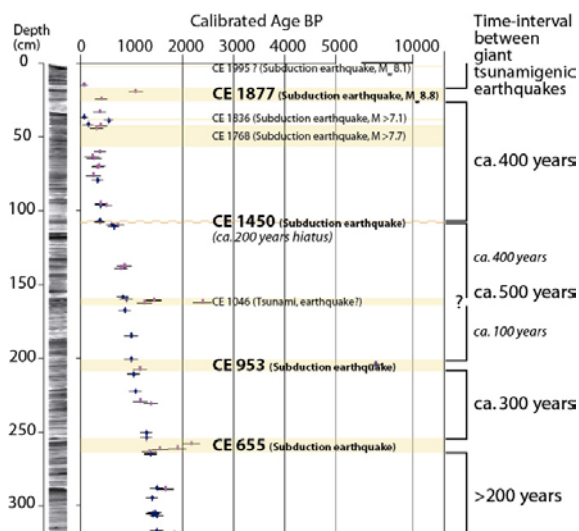


Fig. 4: Radiocarbon ages, stratigraphy and paleoseismic interpretation from sediment core GC3, from Mejillones bay (23°S).

IMPLICATIONS FOR SEISMIC HAZARD ASSESSMENT

The overall data indicate that large earthquakes, similar in magnitude to the 1877-episode, have occurred at a variable

time intervals mostly in the range of 300 to 500 years during the last two millennia, and that the predecessor of this last large event occurred ca. 430 years before.

From the review of historical chronicles compared with the sedimentary record coupled with model results of estimated Peak Ground Acceleration (PGA) values, we suggests that high horizontal PGAs (at least greater than 40-50%g), are needed to produce slumping or discontinuities similar to those associated to the last 1877 event. Minor episodes recorded in the historical chronicles reported by Comte and Pardo (1991) such as those of 1768 and 1836, did not produce significant slumping in the study sites. In addition, we review the historical seismic catalog for Northern Chile interplate thrust-earthquakes from NEIC and Centro Sismológico Nacional (www.sismologia.cl), and we computed the Gutenberg-Richter law after evaluating the appropriate time window for each magnitude range. The Gutenberg-Richter law predicts the behavior of mega-earthquakes (such as 1877 earthquake) with long return periods (~400 years for earthquakes with magnitude ~8.8), similarly to our findings from the paleoseismic record. In contrast, the events ~Mw 8.0 shows a shorter return period of around ~100 years. Ongoing research in needed to test these last hypotheses (the relation of anomalous sedimentary structures with PGA and G-R law) to improve seismic hazard assessment in the region.

CONCLUSION AND PERSPECTIVES

The analysis of marine records coupled with observations from coastal archaeological sites, allow us to infer the occurrence of several giant tsunamigenic earthquakes in the last two millennia, with a variable recurrence in the order of 400 years. Under this scope, the last Mw~8 earthquakes occurred on 2014 and 2007 along this seismic gap region, seem to be moderate episodes into a larger seismic cycle. On-going analyses from archaeological



coastal sites will provide additional key information about the impact of predecessors of the 1877 event on this hyperarid coast as well as on the early inhabitants. We preliminarily dated those predecessors close to CE 1450, CE 953 and CE 655, with a possible event also at CE 1046.

Acknowledgements: This work was funded by Fondecyt project #1161547.

REFERENCES

- Angermann, D., Klotz, J., Reigber, C., 1999. Space-geodetic estimation of the Nazca-South America Euler vector. *Earth and Planetary Science Letters* 171, 329-334.
- Armijo, R., Thiele, R., 1990. Active faulting in northern Chile—ramp stacking and lateral decoupling along a subduction plate boundary. *Earth and Planetary Science Letters* 98, 40–61.
- Béjar-Pizarro, M., Carrizo, D., Socquet, A., Armijo, A., Barrientos, S., Bondoux, F., Bonvalot, S., Campos, J., Comte, D., de Chabalière, J.B., Charade, O., Delorme, A., Gabalda, G., Galetzka, J., Genrich, J., Nercessian, A., Olcay, M., Ortega, F., Ortega, I., Remy, D., Ruegg, J.C., Simons, M., Valderas, C., Vigny, C., 2010. Asperities and barriers on the seismogenic zone in North Chile: state-of-the-art after the 2007 M_w 7.7 Tocopilla earthquake inferred by GPS and InSAR data. *Geophysical Journal International*, doi: 10.1111/j.1365-246X.2010.04748.x.
- Chlieh, M., Chabalière, J.B., Ruegg, J.C., Armijo, R., Dmowska, R., Campos, J., Feigl, K.L., 2004. Crustal deformation and fault slip during the seismic cycle in the North Chile subduction zone, from GPS and InSAR observations. *Geophysics Journal of the Interior* 158, 695–711.
- Comte, D., Pardo, M., 1991. Reappraisal of great historical earthquakes in the northern Chile and southern Peru seismic gap. *Natural Hazards* 4, 23–44.
- DeMets, C., Gordon, R.G., Argus, D.F., Stein, S., 1994. Effect of recent revisions to the geomagnetic reversal timescale on estimates of current plate motions. *Geophysical Research Letters* 21, 2191-2194.
- Delouis, B., Monfret, T., Dorbath, L., Pardo, M., Rivera, L., Comte, D., Haessler, H., Caminade, J.P., Ponce, L., Kausel, E., Cisternas, A., 1997. The M_w =8.0 Antofagasta (Northern Chile) earthquake of 30 July 1995; a precursor to the end of the large 1877 gap. *Bulletin of the Seismological Society of America* 87, 427-445.
- Delouis, B., Philip H., Dorbath L., Cisternas, A., 1998. Recent crustal deformation in the Antofagasta region (northern Chile) and the subduction process. *Geophysics Journal of the Interior* 132, 302-338.
- Delouis, B., Pardo, M., Legrand, D. and Monfret T., 2009. The M_w 7.7 Tocopilla earthquake of 14 November 2007 at the Southern Edge of the Northern Chile seismic gap: rupture in the deep part of the coupled plate interface. *Bulletin of the Seismological Society of America* 99, 87-94.
- Dorbath, L., Cisternas, A., Dorbath, C., 1990. Quantitative assessment of great earthquakes in Peru. *Bulletin of the Seismological Society of America* 80, 551-576.
- González, G., Cembrano, J., Carrizo, D., Macci, A., Schneider, H., 2003. The link between forearc tectonics and Pliocene–Quaternary deformation of the Coastal Cordillera, northern Chile. *Journal of South American Earth Science* 16, 321–342.
- Kausel, 1986. Los terremotos de agosto de 1868 y mayo de 1877 que afectaron el sur del Perú y norte de Chile. *Boletín Academia Chilena de Ciencias*, pp. 8-13.
- Kelleher, J.A., 1972. Rupture zones of large South American earthquakes and some predictions. *Journal of Geophysics Research* 77, 2087-2103.
- Nishenko, S.P., 1985. Seismic potential for large and great interplate earthquakes along the Chilean and southern Peruvian margins of South America: A quantitative reappraisal. *Journal of Geophysical Research* 90, 3589-3615.
- Ortlieb, L., Zazo, C., Goy, J.L., Hillaire-Marcel, C., Ghaleb, B., Cournoyer, L., 1996. Coastal deformation and sea-level changes in the northern Chile subduction area (23°S) during the last 330 ky. *Quaternary Science Review* 15, 819-831.
- Pritchard, M.E., Ji, C., Simons, M., 2006. Distribution of slip from 11 M_w >6 earthquakes in the northern Chile subduction zone. *Journal of Geophysical Research* 111, doi: 10.1029/2005JB004013.
- Ruegg, J.C., Campos, J., Armijo, R., Barrientos, S., Briole, P., Thiele, R., Arancibia, M., Canuta, J., Duquesnoy, T., Chang, M., Lazo, D., Lyon-Caen, H., Ortlieb, L., Rossignol, J.C., Serrurier, L., 1996. The M_w =8.1 Antofagasta earthquake of July 30, 1995: First results from teleseismic and geodetic data. *Geophysical Research Letters* 23, 917-920.
- Ruiz, S., Metois, M., Fuenzalida, A., Ruiz, J., Leyton, F., Grandin, R., Vigny, C., Madariaga, R., Campos, J., 2014. Intense foreshocks and a slow slip event preceded the 2014 Iquique M_w 8.1 earthquake. *Science* 345, 1165, doi: 10.1126/science.1256074.
- Valdés, J., Sifeddine, A., Lallier-Verges, E., Ortlieb, L., 2004. Petrographic and geochemical study of organic matter in surficial laminated sediments from an upwelling system (Mejillones del Sur Bay, Northern Chile). *Organic Geochemistry* 35: 881-894.
- Vargas, G., Ortlieb, L., Pichon, J.J., Bertaux, J., Pujos, M., 2004. Sedimentary facies and high resolution primary production inferences from laminated diatomaceous sediments off northern Chile (23°S). *Marine Geology*, 211: 79-99.
- Vargas, G., Ortlieb, L., Chapron, E., Valdés, J., Marquardt, C., 2005. Paleoseismic inferences from a high resolution marine sedimentary record in northern Chile (23°S). *Tectonophysics*, 399: 381-398.
- Vargas, G., Rutllant, J., Ortlieb, L., 2006. ENSO tropical-extratropical climate teleconnections and mechanisms for Holocene debris flows along the hyperarid coast of western South America (17-24°S). *Earth and Planetary Science Letters*, 249(3-4): 467-483.
- Vargas, G., Pantoja, S., Rutllant, J., Lange, C., Ortlieb, L., 2007. Enhancement of interdecadal ENSO-like coastal upwelling variability in the eastern boundary Peru-Chile Current overrides global warming. *Geophysical Research Letters*, Vol. 34, L13607, doi:10.1029/2006GL028812.
- Vargas, G., Palacios, C., Reich, M., Luo, S., Shen, Ch.-Ch., González, G., Wu, Y.-Ch., 2011. U-series dating of co-seismic gypsum and submarine paleoseismology of active faults in northern Chile. *Tectonophysics*, 497: 34-44.



Complex surface rupture morphology of the western Hope and Kelly faults, New Zealand

Vermeer, Jessica (1), Quigley, Mark (1,2), Pettinga, Jarg (2), Langridge, Rob (3)

- (1) School of Earth Sciences, University of Melbourne, 3010, Victoria, Australia
- (2) Department of Geological Sciences, University of Canterbury, 8011, New Zealand
- (3) Active Landscapes Dept., GNS Science, PO Box 30-368, Lower Hutt, New Zealand

Abstract: We present new lidar-based maps of the western Hope and Kelly Faults where they approach the Alpine Fault in New Zealand’s South Island. These maps form the basis for ongoing field investigations to determine slip rates and earthquake chronologies along the southern margin of the Marlborough Fault system. Surface rupture morphologies are highly complex and influenced by cumulative slip and topography. Preliminary field observations are also presented.

Key words: Hope fault, lidar, rupture morphology, strike-slip, Marlborough

INTRODUCTION

The Marlborough fault system lies between the Alpine fault and Hikurangi subduction zone and transfers motion between them. It consists of five principal faults: the Wairau, Awatere, Clarence, Hope and Kekerengu faults, the latter of which ruptured during the 2016 M_w 7.8 Kaikōura earthquake (Hamling et al., 2017)). The southernmost is the Hope fault, which has the one of the highest slip rates in the Marlborough fault system, 23 ± 4 mm/yr (Langridge et al. 2003). The interaction between

the Alpine fault and the Marlborough system is not well understood, but north of the Kelly and Hope fault intersections, the slip rate on the Alpine fault drops by ~50%, indicating a significant component of slip is transferred into the Marlborough fault system through these faults (Langridge et al. 2010). The aim of this study is to determine slip rates and earthquake chronologies on the Hope Fault and Hura-Newton-Kelly fault system (Figure 1) and thus better understand the transfer of motion from the Alpine fault to the Hope fault, including how these fault systems interact in earthquakes.

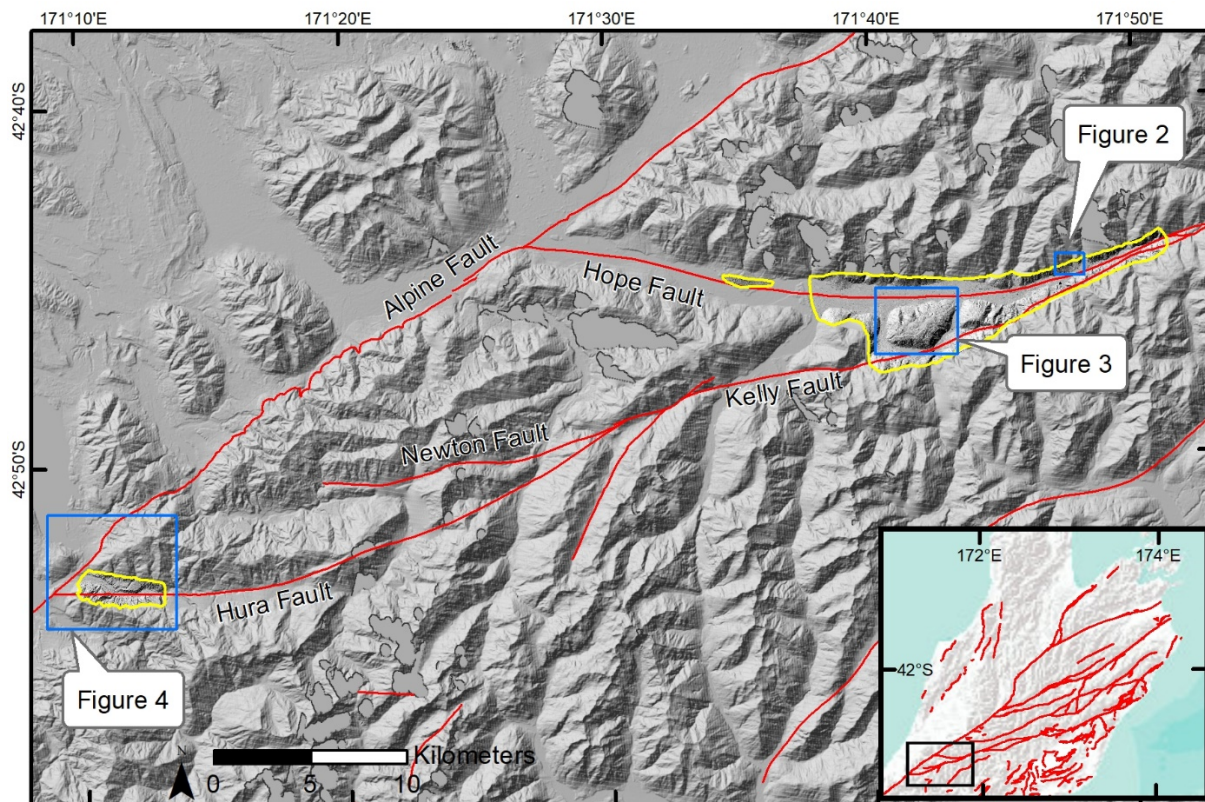


Figure 1: Lidar coverage (yellow outline) and study area. The lidar covers the junction of the Hope and Kelly faults, as well as near the junction of the Hura and Alpine faults. The faults shown are from the New Zealand Active Fault Database (Langridge et al., 2016). The background is derived from a 30 m resolution ALOS DEM.



DISCUSSION

We use lidar to map portions of the western Hope, Kelly, and Hura faults (Figure 1). Previous sources indicate that the trace of the westernmost Hope fault is obscured by the river (Nathan et al., 2002). However, using lidar we are able to trace the Hope fault along the north side of the Taramakau River valley and northern subsidiary faults associated with the Kelly fault along the south side of the valley (Figure 2). The fault is expressed as a series of short strands subparallel to the overall strike of the main fault zone, similar to observations on fault rupture traces in the Darfield earthquake (Quigley et al., 2012) and investigations elsewhere along the Hope Fault (Khajavi et al., 2014).

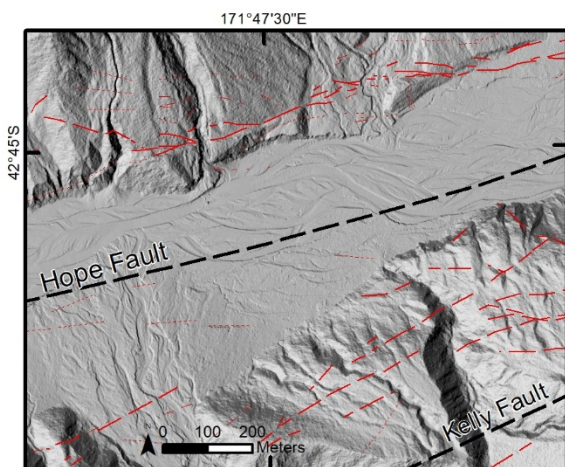


Figure 2: The main trace of the Hope fault is identified on the northern side of the river valley. Debris fans and fluvial terraces are offset and provide geomorphic markers for fault displacement measurements. The trace from the New Zealand Active Fault Database (Langridge et al., 2016) is shown in tick black dashed line, lidar-mapped faults are shown in red lines.

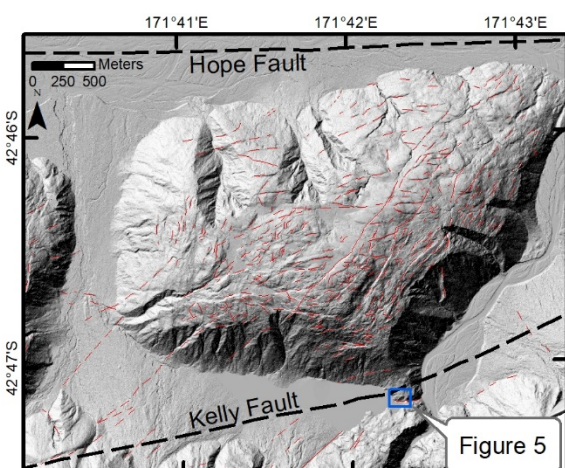


Figure 3: Bedrock between the Hope and Kelly faults is highly fractured, though the northwest trending (probable glacial) striations have only small dextral offsets. The NE and E striking fractures may represent gravitational failure of the bedrock in the form of ridge rents, and/or oblique and extensional faulting in a fold above a thrust fault.

Initial efforts to measure offsets of geomorphic features yield right lateral displacement of stream channels, terraces, and alluvial fans of up to 165 m. Preliminary

mapping has also revealed possible thrust faults and folds, and highly fractured bedrock (Figure 3).

Near the Alpine fault, the Hura fault traces are diffuse, with many short strands at various orientations (Figure 4). There are extensive flights of terraces that may yield uplift chronologies or records of base level dropping. Base level drops may record movement on the adjacent Alpine fault that dam and un-dam, or uplift of the Styx river valley.

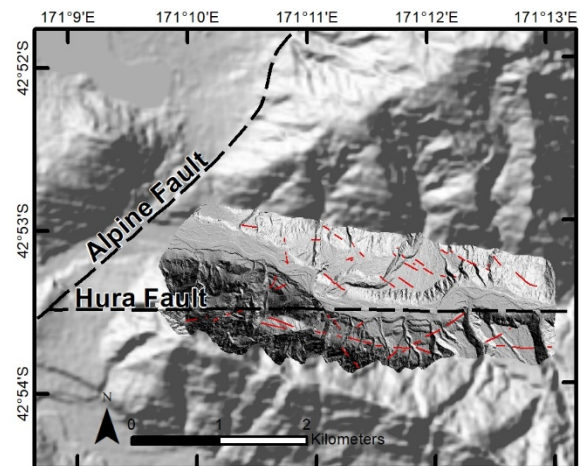


Figure 4: Active faulting and high geomorphic activity near the Alpine fault may yield insights into how the plate motion is being transferred between the Alpine fault and the Marlborough fault system. The faults from the New Zealand Active Fault Database (Langridge et al., 2016) is shown in tick black dashed line, lidar-mapped faults are shown in red lines.

Preliminary field mapping resulted in validation that some of the fault traces visible on the lidar are also exposed in the field as shear zones (Figure 5). Future field work will focus on validating more of these structures. After field mapping the fault traces and geomorphic features, we will choose sites for paleoseismic investigations to investigate the rupture history of the Hope, Kelly, and Hura faults. Field methods may include peat marsh coring and fault trenching. Possible dating methods include radiocarbon, luminescence, and dendrochronology.



Figure 5: Exposed active fault plane on the Kelly Fault where it passes through the eastern Saddle of Lake Kaurapataka (Figure 3). Bedrock is thrust over light grey colored glaciofluvial gravels, implying post LGM displacement. Fault strike/dip = 285 / 40°N.



REFERENCES

- Hamling, I.J. and 28 others, 2017. Complex multifault rupture during the 2016 Mw 7.8 Kaikoura earthquake, New Zealand. *Science*, 356 (6334).
- Khajavi, N., Quigley, M., Langridge, R., 2014. "Influence of Topography and Basement Depth on Surface Rupture Morphology Revealed from LiDAR and Field Mapping, Hope Fault, New Zealand." *Tectonophysics* 630 (C), 265–84.
- Langridge, R.M., Ries, W.F., Litchfield, N.J., Villamor, P., Van Dissen, R.J., Rattenbury, M.S., Barrell, D.J.A., Heron, D.W., Haubrock, S., Townsend, D.B., Lee, J.A., Cox, S., Berryman, K.R., Nicol, A., Stirling, M., 2016. The New Zealand active faults database: NZAFD250. accepted to *New Zealand Journal of Geology and Geophysics* 59 (1).
- Langridge, R., Campbell, J., Hill, N., Pere, V., Pope, J., Pettinga, J., Estrada, B., Berryman, K., 2003. Paleoseismology and Slip Rate of the Conway Segment of the Hope Fault at Greenburn Stream, South Island, New Zealand. *Annals of Geophysics* 46 (5), 1119–40.
- Langridge, R., Villamor, P., Basili, R., Almond, P., Martinez-Diaz, J.J., Canora, C., 2010. Revised Slip Rates for the Alpine Fault at Inchbonnie: Implications for Plate Boundary Kinematics of South Island, New Zealand. *Lithosphere* 2 (3), 139–52.
- Nathan, S., Rattenbury, M.S., Suggate, R.P. (compilers), 2002. Geology of the Greymouth area: scale 1:250,000. Lower Hutt: Institute of Geological & Nuclear Sciences. Institute of Geological & Nuclear Sciences 1:250,000 geological map 12. 58 p. + 1 folded map.
- Quigley, M., Van Dissen, R., Litchfield, N., Villamor, P., Duffy, B., Barrell, D., Noble, D., 2012. Surface rupture during the 2010 Mw 7.1 Darfield (Canterbury) earthquake: Implications for fault rupture dynamics and seismic-hazard analysis. *Geology* 40(1), 55-58.



The 2007 Aysén earthquake sequence: complex faulting and seismic migration in a transpressional fault zone

Angelo Villalobos-Claramunt^{1*}, Gabriel Vargas¹, Andrei Maksymowicz², Sergio Ruiz² and Galderic Lastras³

(1) Departamento de Geología, Facultad de Ciencias Físicas y Matemáticas, Universidad de Chile, Plaza Ercilla 803, Santiago, Chile.

(2) Departamento de Geofísica, Facultad de Ciencias Físicas y Matemáticas, Universidad de Chile, Av. Blanco Encalada 2002, Santiago, Chile.

(3) Geociències Marines, Universitat de Barcelona, Barcelona E-08028, España.

*Mail: angelovillalobos42@ug.uchile.cl

Abstract. The Liquiñe-Ofqui Fault System (LOFS) is an intra-arc fault zone located in the Norpatagonian Andes, where historical neotectonic and seismotectonic activity has been reported. Nevertheless, scarce –conclusive– evidence has been shown demonstrating the relationship between crustal seismicity and active faulting. In the Aysén fjord area a seismic swarm was felt between January 2007 and February 2008. The peak stage of the seismic activity occurred on April 2007 characterized by two main earthquakes, on April 2th, $M_w=6.1$, and on April 21th, $M_w=6.2$. $M_w=6.2$ triggered landslides that induced tsunami waves causing human losses and damage to the local economy. We identified six submerged faults in a transfer zone of the LOFS, from which three structures were directly involved in the seismic swarm, Río Cuervo (RCF), Quitralco (QF) and Punta Cola faults (PCF). Using our data and seismological ones, we propose a seismotectonic model for the occurrence and evolution of the 2007 seismic sequence. Finally, we propose a new 3d geometric model of the LOFS at a crustal scale for this area.

Keywords: Aysén Earthquake, Aysén Fjord, Liquiñe-Ofqui Fault System, seismic sequence, 3d geometric model.

INTRODUCTION

The study area is located near the southern termination of the oblique subduction margin between Nazca and South American plates (Figure 1), whose convergence rate is ~ 6.6 cm/year (Angermann et al., 1999). In this area, the main structural feature in the over-riding plate is the Liquiñe-Ofqui Fault System (LOFS). Its length is $\sim 1,200$ km and extend between 38° to 47° S (e.g. Cembrano et al., 2002, 1996; Lavenu and Cembrano, 1999; Legrand et al., 2011). This fault system is located in the intra-arc, parallel to the continental margin. Prior to this work, few efforts regarding to the identification of active segments have been done and they were mostly focused on the 2007 Aysén seismic swarm itself (2007-AYSS) (e.g. Agurto et al., 2012; Lara et al., 2008; Legrand et al., 2011; Mora et al., 2010; Russo et al., 2011; Vargas et al., 2013). The 2007-AYSS began on January 10th with a small earthquake ($M_L < 3$) at a shallow depth below inner fjord. Many similar events took place on January 14nd, 18nd, 19nd and 21th, until an Moment Magnitude, M_w 5.2 earthquake struck the area on January 23rd, generating a sequence with more than 20 events per hour (Barrientos et al., 2007; Russo et al., 2011). From this initial stage five major events ($M > 5$; USGS NEIC catalog) occurred on January 28nd (M_w 5.2), February 3rd (M_w 5.3), February 23rd (M_w 5.7), April 2nd (M_w 6.1) and finally on April 21th (M_w 6.2) (Figure 1c). These last two events are considered the seismic swarm peak stage (Agurto et al., 2012). To date, there is no certainty as to which structures have been responsible for the seismic activity or the mechanisms in which these events took their course.

In this study, we analyze the seismogenic structures associated with the 2007-AYSS and explain the evolution of the seismic sequence. We use new multi-beam bathymetric

data and high-resolution multi-channel seismic profiles for the inner Aysén Fjord. The results allow us to identify the submerged section of a transfer zone of the LOFS, using the observed and projected geometry. We associate seismic clusters to specific fault planes.

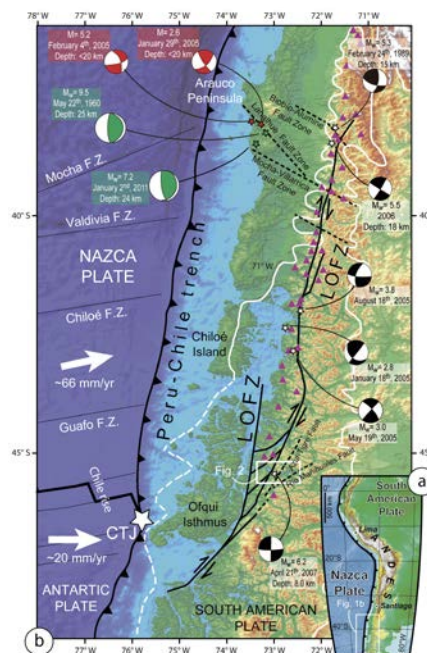


Figure 1. (a) Geotectonic framework of South America showing regional tectonics (b) Regional tectonic context at the triple junction of the Nazca, Antarctic and South American plates. Composite Digital Elevation Model (DEM) of Nazca and South American plates. Regional map showing the location and extent of LOFS (continuous



black lines), transverse fault systems (TFS; segmented black lines) and main volcanoes (purple triangles), (after Hervé, 1994; Moreno and Naranjo, 2003; Rosenau et al., 2006; Cembrano and Lara, 2009). Previously published focal mechanisms of crustal earthquakes are shown for the LOFS (black), TFS (red) and megathrust earthquakes (green and green stars) (Barrientos and Acevedo-Aránguiz, 1992; Cifuentes, 1989; Haberland et al., 2006; Lange et al., 2008; Legrand et al., 2011; Moreno et al., 2009). Convergence velocity vectors after Angermann et al. (1999). White lines show the approximate maximum extends of the Pleistocene ice sheet during the Last Glacial Maximum (modified from Thomson et al., 2010).

DATA AND METHODOLOGIES

To identify submerged continuation of LOFS branches we used high-resolution bathymetry and sub-bottom profiles. The area where data was obtained is located westward of Puerto Aysén, in the inner-fjord (73.13°-72.68°W and 45.32°-45.47°S) (Figure 2). The data set used was obtained in a geophysical campaign of the DETSUFA project that took place between March 4th and 17nd, 2013. The maritime campaign was on board the R/V BIO *Hesperides* of the Spanish Navy.

Additional information concerning location and relocation of hypocenters was compiled bibliographically and correspond to data taken by temporary stations of the Chilean National Seismological Center (CSN; Barrientos et al., 2007; Legrand et al., 2011) and University Of Liverpool (Agurto et al., 2012).

Bathymetry

To make a high-resolution bathymetric map a KONGSBERG SIMRAD multi-beam EM-1002S was used, which was perfect for depth of the inner fjord. This allowed us to obtain a seafloor digital model. Equidistant mode was used for swath bathymetry acquisition. The vessel during the campaign followed parallel lines of navigation, using a mosaic method separated every 150 m. Also thickness of the swaths had the same width which generated a 50% overlap with the only exception of those areas near the coast, places that were not covered for the safety of the mission. XBP probes were used at specific sites to measure changes in sound velocity on water due to ever-changing conditions associated with a restriction of fresh water circulation, tides, and sediments.

Seismic profiles

The sub-bottom seismic profiles were obtained using two BOLT air guns (165 and 175 inches), which were towed behind the vessel stern. The configuration used in the seismic sources was 2,000 psi, a depth of the gun at 3 m and a distance of 15 m over seafloor. The recording system used was DELPH SEISMICPLUS mini-streaming with a recording length of 4 s and a pre-gain of 8 Hz. Raw seismic lines were obtained in SEG-Y format in conjunction with the vessel navigation file.

RESULTS

Bathymetry maps and seismic profiles allow us to identify and describe faults that form LOFS transfer zone in the study area and cut post-glacial sedimentary infill. We

focused our effort on Punta Cola Fault (PCF), Quitralco Fault (QF) and Río Cuervo Fault (RCF) because its participation in the seismic events. Other faults suggested in previous work as lineaments were recognize in our seismic images. These faults are parallel to QF and we named them from west to east, Cuervo Ridge, Río Pescado, Isla Mentirosa and Punta Mano.

Punta Cola Fault

Vargas et al. (2013) described PCF as a ~20 km length dextral-reverse fault. From south to north its on-land style varies from being expressed as a simple fault trace with a N05°E to NS strike, observable for ~8.2 km until it submerge into the fjord. Seismic images completed the remaining submerged ~4.2 km, shown in detail asymmetrical positive flower geometry. This structural feature is not evidenced in surface by any pressure-ridge. On the contrary, the existence of a small depression limited by escarpments masks it. The deformation zone associated with this structure narrows southwards from an average width ~1,080 m to ~242.6 m. Branches tips observed in the northern seismic images reach the surface. In contrast, seismic line n°SL-07 shows fault tips falling at ~0.42 s TWT (?) "depth". In addition to the latter, offset reflectors generates a pop-up within the deformation zone northward and a depression in SL-07. We interpreted this phenomenon because of an area of lesser sliding in the fault plane.

Río Cuervo Fault

RCF extends ~100 km length and was characterized and described in detail by Vargas et al. (2013) using geomorphological segments that ranges ~30-40 km long. There is no direct observation in bathymetric surface of escarpments or surface displacement associated with this fault. Seismic images show it as a vertical fault with at least four parallel branches well distinguished. Estimated deformation zone width ranges ~313-852.8 m, being wider northward. Tip position seen in seismic profiles together with vertical offset of reflectors decreases northward from 0.39 to 0.45 s, never reaching the seafloor.

Quitralco Fault

QF is a NE-SW striking fault with ~70 km length and part of LOFS transfer zone. Westward connects with the western lineament of the system (Canal Costa Fault), ending to the east when connect with PCF (Cembrano et al., 1996; Thomson, 2002; Vargas et al., 2013). In the study area, the fault also interacts with RCF. Such interaction is not evident, but like other faults with similar strike and kinematics, QF has been displaced in right-lateral sense ~636 m (Figure 3). Seismic profiles show QF as a simple trace accompanied by synthetic and antithetic faults. The fault defines two blocks being the western one the hanging wall block. Figure 3 shows fault tip near the seafloor and forming an escarpment. Meanwhile southward its tip location is deepened reaching 0.47 s.

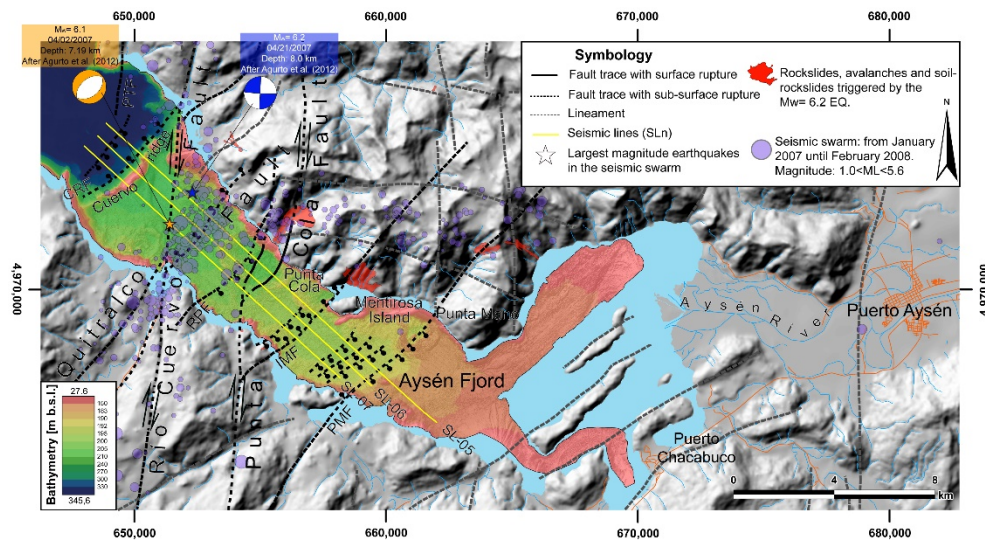


Figure 2. Study area showing the location of the seismic profiles (SL-05, SL-05 and SL-07) obtained from Aysén fjord using two BOLT air-gun devices in the area of the 2007-AYSS. Subaerial and submarine reliefs shown by means of a Digital elevation model based on 1:50,000 topographic sheets from the Chilean Army Geographic Institute (IGM) and bathymetric information obtained using a KONGSBERG SIMRAD multi-beam EM-1002S by DETSUFU project. The figure shows the location of the epicenters of the 2007-AYSS (transparent purple circles) and the focal mechanism solutions for $M_w=6.1$ and $M_w=6.2$ (After Agurto et al., 2012). Seismic profiles are shown in figures 4, 5 and 6. Inset of the Figure 3 is also shown.

DISCUSSION

In order to associate seismic activity with each faults presented here and to propose a geometric model at a crustal scale, we used two seismic catalogs that cover most of the temporal interval of the seismic swarm.

Seismic sequence migration in the fjord area is shown in Figure 2, covering the first four months until the generation of the $M_w=6.2$ earthquake (Figures 3a, 3b, 3c and 3d), to then summarize in Figure 2e the final stage between May 2007 and February 2008. It is noted that the swarm does not present a random distribution but rather form clusters. We made a first order correlation for each cluster to QF, RCF and PCF.

On January 2007 (Figure 3a), two NE-SW clusters of epicenters (a shallow and a deeper one) are located on QF trace. The depth of the earthquakes ranges 6-8.2 km with local magnitudes $2.0 \leq M_L \leq 4.7$. On February 2007 (Figure 3b), seismicity migrates southward with a dispersed distribution and depths that ranges 3.9-8.7 km and magnitudes $1.3 \leq M_L \leq 5.0$. We tentatively associate it with RCF. In intersection area between RCF and QF, seismicity shows a well-defined cluster whose depths ranges 3.3-6.1 km with magnitudes $1.5 \leq M_L \leq 3.2$. To the north following QF, epicenters could correspond to the continuation of the activity during January. Depths range 1.7-7.4 km and magnitudes $1.1 \leq M_L \leq 5.3$. In addition, some epicenters appear near PCF (Depths: 2-3.4 km; $1 \leq M_L \leq 3.1$). During March 2007 (Figure 3c), epicenters were concentrated mainly near QF and ranges 2-6.8 km with magnitudes $1 \leq M_L \leq 4.8$, although a small cluster (Depths: 5-6.4 km; $\sim 1 < M_L \leq 4.1$) in the north of the study area and westward RCF trace is well defined. On April 2007,

earthquakes distribution in QF and RCF was similar as in March. On the other hand, PCF plays a more important role for this study due to the presence of a NW cluster characterized by shallow depths (1.8-3.7 km) near the place where faulting reached the surface.

In the following months, aftershocks of $M_w=6.1$ and $M_w=6.2$ earthquakes continued their nucleation in these three faults reaching greater depths (>10 km). A migration that covers W-E lineation is observable (Figure 3e). This last point was not analyzed due to being outside the objectives and scope of this work.

In order to generate a local 3D model of LOFS on a crustal scale (Figure 4) we plotted all earthquakes in a three-dimensional diagram, we made 3D-surfaces that represent QF, RCF and PCF. The geometry is better constrained in inner-fjord area.

The surface representing PCF has a dip of $88^\circ E$ until the first ~ 1.1 km, subsequently it is curved and then maintained with $53^\circ E$ in the range of ~ 2.8 - ~ 4.1 km, between ~ 5.5 - ~ 7.2 km its angle of $75^\circ E$. At greater depths we interpreted a steepening of the fault passing from 85° between ~ 7.2 - ~ 10.5 km, and finally 90° (>10.5 km). PCF has a vertical geometry where the first ~ 20 km characterized by $\sim 90^\circ$, changing slightly to $85^\circ E$ between ~ 3.1 - ~ 8.0 km, again to reach 90° at depths >8.0 km. Finally, QF has an $88^\circ NW$ dipping plane that maintains the first ~ 3.5 km, 75° between ~ 4.5 - ~ 9.0 km and to depths greater than 90 km it becomes $77^\circ NW$. This model presents similarities with the theoretical model of Thomson (2002) where $\sim NS$ LOFS structures forms a positive flower at crustal scale.

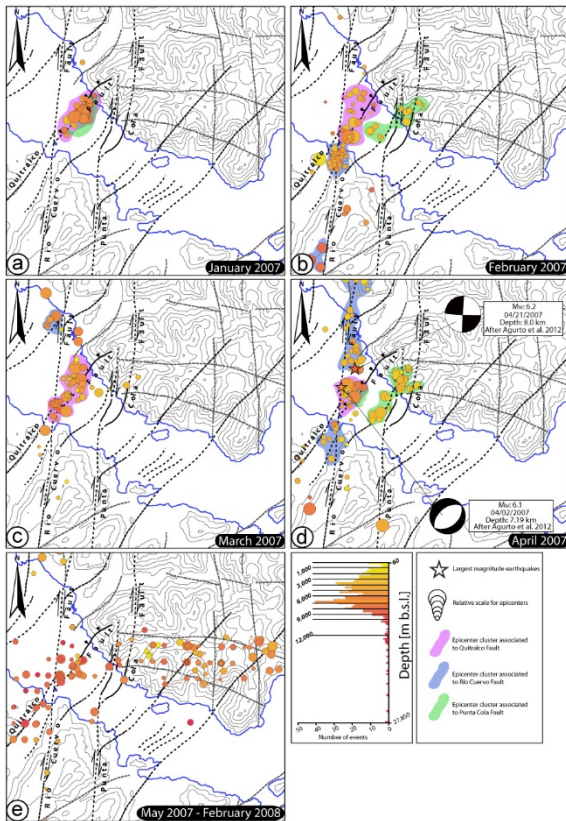


Figure 3. Seismic migration of the 2007-AYSS. Fault map and seismological data (Agurto et al., 2012; Barrientos et al., 2007) were used. A warm color-scale is used to highlight the depth of each event. Epicenters of $M_w = 6.1$ and $M_w = 6.2$ are shown using stars symbols. Epicenter clusters, which we associated to each active fault involved in 2007-AYSS, are colored on purple (QF), blue (RCF) and green (PCF). (a) January, 2007. (b) February, 2008. (c) March, 2007. (d) April, 2007. (e) May, 2007 to February, 2008.

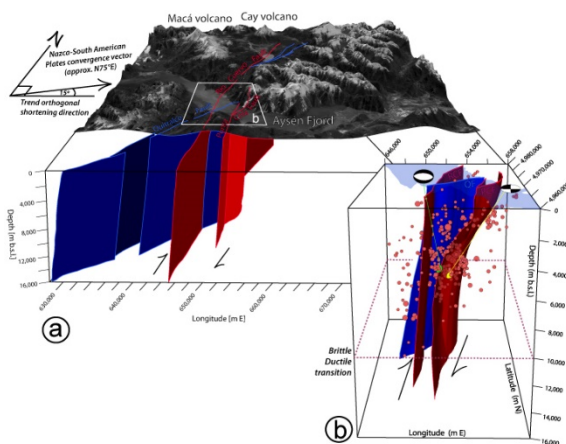


Figure 4. 3D model of the LOFS in the study area. (a) Seismogenic faults projected at the scale of the fjord and its surroundings. A Digital elevation model based on 1:50,000 topographic sheets from the Chilean Army Geographic Institute (IGM) with a SPOT-image in grayscale have been superimposed to the fault model. Red surfaces represent dextral-inverse kinematics, blue surfaces represent normal-dextral kinematics.

Acknowledgements: We thank the research team and the crew of the DEFUTSA campaign to acquire and provide seismic and bathymetric data that made this work possible. Also we thank the support and reiterative help of the CEGA program. Finally, we appreciate the financial support of CONICYT, through its national scholarship PhD program.

REFERENCES

Agurto, H., Rietbrock, A., Barrientos, S., Bataille, K., Legrand, D., 2012. Seismo-tectonic structure of the Aysén Region, Southern Chile, inferred from the 2007 $M_w = 6.2$ Aysén earthquake sequence. *Geophys. J. Int.* 190, 116–130. doi:10.1111/j.1365-246X.2012.05507.x

Angermann, D., Klotz, J., Reigber, C., 1999. Space-geodetic estimation of the Nazca-South America Euler vector. *Earth Planet. Sci. Lett.* 171, 329–334. doi:10.1016/S0012-821X(99)00173-9

Barrientos, S., Bataille, K., Aranda, C., Legrand, D., Baez, J.C., Agurto, H., Pavez, A., Gen-Rich, J., Vigny, C., Bondoux, F., 2007. Complex sequence of earthquakes in Fjorland, Southern Chile, in: *Geosur 2007, International Geological Congress on the Southern Hemisphere*. Santiago de Chile, pp. 19–20.

Cembrano, J., Hervé, F., Lavenu, A., 1996. The Liquiñe-Ofqui fault zone: a long-lived intra-arc fault system in southern Chile. *Tectonophysics* 259, 55–66. doi:10.1016/0040-1951(95)00066-6

Cembrano, J., Lavenu, A., Reynolds, P., Arancibia, G., López, G., Sanhueza, A., 2002. Late Cenozoic transpressional ductile deformation north of the Nazca – South America – Antarctica triple junction. *Tectonophysics* 354, 289–314. doi:10.1016/S0040-1951(02)00388-8

Lara, L.E., Cembrano, J., Lavenu, a., 2008. Quaternary Vertical Displacement along the Liquiñe-Ofqui Fault Zone: Differential Uplift and Coeval Volcanism in the Southern Andes? *Int. Geol. Rev.* 50, 975–993. doi:10.2747/0020-6814.50.11.975

Lavenu, A., Cembrano, J., 1999. Compressional- and transpressional-stress pattern for Pliocene and Quaternary brittle deformation in fore arc and intra-arc zones (Andes of Central and Southern Chile). *J. Struct. Geol.* 21, 1669–1691. doi:10.1016/S0191-8141(99)00111-X

Legrand, D., Barrientos, S., Bataille, K., Cembrano, J., Pavez, A., 2011. The fluid-driven tectonic swarm of Aysen Fjord, Chile (2007) associated with two earthquakes ($M_w = 6.1$ and $M_w = 6.2$) within the Liquiñe-Ofqui Fault Zone. *Cont. Shelf Res.* 31, 154–161. doi:10.1016/j.csr.2010.05.008

Mora, C., Comte, D., Russo, R., Gallego, A., Mocanu, V., 2010. Aysén seismic swarm (January 2007) in southern Chile: Analysis using Joint Hypocenter Determination. *J. Seismol.* 14, 683–691. doi:10.1007/s10950-010-9190-y

Russo, R.M., Gallego, A., Comte, D., Mocanu, V.I., Murdie, R.E., Mora, C., VanDecar, J.C., 2011. Triggered seismic activity in the Liquiñe-Ofqui fault zone, southern Chile, during the 2007 Aysen seismic swarm. *Geophys. J. Int.* 184, 1317–1326. doi:10.1111/j.1365-246X.2010.04908.x

Thomson, S.N., 2002. Late Cenozoic geomorphic and tectonic evolution of the Patagonian Andes Late Cenozoic geomorphic and tectonic evolution of the Patagonian Andes between latitudes 42° S and 46° S : An appraisal based on fission-track results from the transpressional intr. *Geol. Soc. Am. Bull.* 114, 1159–1173. doi:10.1130/0016-7606(2002)114<1159

Vargas, G., Rebolledo, S., Sepúlveda, S., Lahsen, A., Thiele, R., Townley, B., Padilla, C., Rauld, R., Herrera, M.J., Lara, M., 2013. Submarine earthquake rupture, active faulting and volcanism along the major Liquiñe-Ofqui Fault Zone and implications for seismic hazard assessment in the Patagonian Andes. *Andean Geol.* 40, 141–171. doi:10.5027/andgeoV40n1-a07



New seismicity models for updating the national Italian seismic hazard model

Visini, Francesco (1), Pace, Bruno (2), Meletti, Carlo (1), Marzocchi, Warner (1), and MPS16 Working Group

(1) Istituto Nazionale di Geofisica e Vulcanologia, INGV, Centro di Pericolosità Sismica, Italy, francesco.visini@ingv.it

(2) Università degli Studi "G. d'Annunzio", Chieti-Pescara, DiSPUter, Italy.

Abstract: We present the new seismicity models that are used to update the national seismic hazard model for Italy. More than 30 researchers have contributed to the development of 12 seismicity models and to the analysis of their uncertainties. All modelers have worked independently, but they could access to the same common input data that include the most updated information about Italian seismicity (historical and instrumental), seismogenic faults, and deformation. The seismicity models have been built in terms of classic source areas, fault sources and gridded seismicity using different approaches and input data. Eleven seismicity models cover the entire Italian territory and surrounding area, whereas 1 seismicity model has been built ad hoc for the volcanic Mt Etna area. Seismicity rates derived from seismicity models are currently being compared with the past historical seismicity to verify their consistency with the data and the strength and weakness of each one of them. We also compare the relative forecasting performance of each model; this quantitative information, together with the outcome of an experts' elicitation session, is going to be used to weigh each model.

Key words: National Seismic Hazard model, Seismicity models, Italy.

In this work we present the results of the activities of a task (task 3: "seismicity models") of the MPS16 project that aims at producing the new national probabilistic seismic hazard (PSH) model for Italy. In particular, the task 3 activities have been focused on the definition of a set of seismicity models and on the analysis of their uncertainty. More than 30 researchers subdivided in 12 working groups have produced 11 seismicity models covering the entire Italian territory and 1 has been built ad hoc for the volcanic Mt Etna area. We have also modeled the subduction in the Tyrrhenian Sea through an ad hoc model. To avoid underestimation of the ground shaking in border regions, we have also used the seismicity models developed by SHARE (www.share-eu.org) to assess the seismicity rates outside the Italian territory. The 11 national models have been built using different types of sources, methods, and input data. Specifically, 5 models have been based on area sources, using a variety of seismotectonic zonations, and different approaches to estimate the seismicity rates; 2 models have been based on different approaches of smoothed seismicity; 2 models have explicitly used faults as source models together with a background seismicity; and 2 models have been based on geodetic data. In the following we describe in more details the basic features of each single model.

AREA SOURCE MODELS

Model A1: The seismotectonic zonation (SZ hereafter) of A1 has been defined according to the regional seismotectonic settings and past seismicity. The seismotectonic conditions have been considered homogeneous within each area for the purposes of source model development. The availability of new data and geological studies in most of the country allows the definition of a new SZ model with respect to the one used

in the past seismic hazard model for Italy (namely, the seismogenic zonation version 9 -SZ9- in Meletti et al 2008) Meletti et al., 2008). In the zones where new SZ and ZS9 do not show any marked difference in the geographical boundaries and seismotectonic characteristics, we have maintained the regionalization used in ZS9. Individual seismicity rates have been computed for each zone, using the parametric catalogue of Italian earthquakes (CPTI15); for each zone, the seismicity rate has been assessed using two approaches: (i) zones have been grouped into some macro areas to evaluate the b-value, and then it has been used to calculate seismicity rates into the zones according to a Gutenberg-Richter (GR) magnitude-frequency distribution; (ii) using the observed seismicity rates for each zone. As regards the uncertainties, the modelers explore the uncertainty on the maximum magnitude, completeness approaches (historical and statistical), and the different approaches to estimate the seismicity rates described above.

Model A2: Source zones used by A2 are the same of the A4 model described later, but A2 has adopted an original approach to estimate seismicity rates. The most innovative part of the approach consists of the joint estimation of the time completeness and of the seismicity rate of the complete part of the historical catalogue. Specifically, assuming that the main shocks follow a homogeneous Poisson process, the problem consists of analysing the completeness of the earthquake occurrences and calculating the rates for the complete part of the CPTI15 catalogue. The issue has been tackled as a problem of identification, in a Bayesian framework, of the change-point between two Poisson processes. The rate of occurrence of part considered as complete of the data set of events has been then assumed as representative of the long-term seismic rate occurrence. Considering both the



rates and the time when the process changes rate as random variables, the method computes, the entire probability distribution of these variables; hence it provided a potentially more informative result than that of the most-used methods.

Models A3a and A3b: Two models, A3a and A3b, are here described together as they use the same approach to evaluate seismicity rates, but with different definitions of area sources. Both models have been based on a first-order geodynamic subdivision that identifies areas characterized by a common tectonic setting under the current stress regime and plate-tectonic setting. Then, these zones have been split into smaller zones, which have been drawn using two different approaches. At the end the two models depict a different picture of area source geometries. The annual rates in each zone have been estimated using the declustered historical catalogue CPTI15, considering the two completeness studies (historical and statistical). For each zone, the b value and the corner magnitude (M_c) of a Tapered GR (Pareto) distribution (Kagan 2002a) have been estimated with the maximum-likelihood algorithm by Jackson & Kagan (1999). Successively, annual rates of each zone have been partitioned onto the smaller zones. A3a and A3b have considered uncertainties on: completeness magnitude approaches, and partitioning rates approaches (from superzones to zones).

Model A4: Source zones of A4 have been designed using the most recent input data, in a conventional PSHA scheme. The main features of A4 can be summarized as follows. It represents an update of the previous model ZS9 (Meletti et al., 2008), which is the reference source model for the past seismicity hazard model for Italy, MPS04; it includes all recent advances on the understanding of the active tectonics of the Italian territory and on the distribution of seismogenic sources, which are described by the Database of Individual Seismogenic Sources (DISS 3.2.1) and other active fault compilations at the national and regional scales; it accounts for information that are derived from the investigation of the most recent seismic sequences that have struck Italy after the compilation of ZS9, such as the L'Aquila 2009, Emilia 2012, and Amatrice 2016 earthquakes. To estimate the expected seismicity rates, the zones have been grouped into macro areas, according to their tectonic features. Assuming that the distribution of the earthquake magnitudes follows a truncated GR model, the b and a values have been estimated applying the Weichert (1980) approach to each macro area, using CPTI15. Then, the seismicity rate for each zone has been estimated from the rates of the macro areas using different approaches. For A4, the same procedure (Weichert, 1980) has been applied directly also to the zones, but imposing upper and lower bounds for the b -value. As regards the uncertainties, A4 accounts for uncertainties on: completeness studies (historical and statistical); corner magnitude; different approaches in calculating the seismicity rate for each zone from the rates of the macro areas.

FAULT-BASED MODELS

Model F1: it is a fault-based seismicity model that uses exclusively geological information taken from the DISS 3.2.1. Other datasets, such as earthquake catalogues, focal mechanisms, stress orientations, and crustal models have been used to constrain various parameters of the model, but not the seismicity rates. Although the model has been based solely on fault information, an empirical proximity function has been specifically developed to estimate off-fault seismicity rates, i.e. the occurrence of earthquakes of any size away from faults. These characteristics ensured the independence of the seismicity rates predicted by this model from the earthquake catalogue. The basic idea of this model is that potentially seismogenic faults can provide a representation of the seismicity on a time frame much longer than that of any earthquake catalogue. The seismic moment rate \dot{M}_s of a seismogenic fault is derived from the geologic moment rate, by multiplying the shear modulus, fault length and width, slip rate, and a coefficient (often referred to as seismic efficiency) that determines how much of the geologic rate is converted into the seismic rate. Using the moment conservation principle, the seismic moment rate of any seismogenic fault has been converted in the annual earthquake rate of a Tapered GR (Pareto) magnitude-frequency distribution (MFD) using the formulations by Kagan (2002a; 2002b) and assuming a unique Beta (a different representation of the parameter b) equal to 0.667 for all the faults. To evaluate off-fault seismicity rates F1 follows an empirical approach aimed to capture the natural distribution of observed earthquakes around faults and the inherent location uncertainty of both earthquakes and faults. To this aim, an Empirical Proximity Function (EPF), which represents the frequency at which any observed earthquake has occurred at any distance from any mapped fault, has been firstly developed. Then, the earthquakes predicted by the MFD described above are symmetrically spread around the fault according to the EPF. Uncertainties in the slip rate and in the value of the seismic efficiency have been considered in this model.

Model F2: the model combines the seismic rates obtained by three different databases: the database of Italian Seismogenic Sources (DISS 3.2.1), the historical seismic catalogue (CPTI15) and the Instrumental catalogue. As regards the seismogenic sources, F2 has only considered a subset of 126 individual sources. For each individual seismogenic fault, F2 considers the following information: location, dimension, depth, focal mechanism, slip rate and maximum magnitude. The seismic moment rate of each individual source has been computed using the seismic-moment conservation principle (Field et al., 1999) that allows the estimation of the seismic moment rate from long-term slip rate and geometry of the fault source. F2 assumes that the distribution of the on-fault earthquake magnitudes follows a truncated GR model from a threshold magnitude M_w 5.5. The seismic moment rate has been thus partitioned and balanced over this range of magnitudes. F2 estimates the seismicity rate of smaller magnitudes using the smoothed-seismicity approach proposed by Frankel (1995) applied to the historical and



instrumental catalogues in a regular spatial grid. For cells of the grid that overlap the surface projection of an individual fault, the rates of occurrence evaluated by the smoothed seismicity approach from magnitude greater or equal than Mw5.5, have been replaced by the rates estimated for that individual source, taking into account the extension of the overlapping area. F2 considers uncertainties on the completeness studies for the historical catalogue and slip rates of the individual sources.

SMOOTHING SEISMICITY MODELS

Model G1: it is a smoothed seismicity model that has been developed using both fixed and the adaptive smoothing algorithms. Recent developments in adaptive smoothing methods and statistical tests for evaluating and comparing rate models prompt authors of this model to investigate the appropriateness of adaptive smoothing together with the fixed smoothing seismicity models for the new Italian seismic hazard maps. The gridded-seismicity model has been built using on both historical and instrumental earthquakes, assuming that larger earthquakes occur at, or nearby, clusters of past smaller earthquakes. G1 merges two different smoothed seismicity models following the well-known and widely applied fixed (Frankel, 1995) and adaptive smoothing methods. These two models have been merged accounting for the outcomes of likelihood tests. G1 follows the same procedures of previous studies to optimize the correlation distance (fixed smoothing) as well as the neighbouring number (adaptive smoothing); these procedures are based on likelihood scores, which estimate the likelihood that the observed earthquake epicentres from the recent catalogue are derived from the smoothed rate models. G1 considers the uncertainties associated with the weights of each smoothing scheme, and of the completeness of the catalogues.

Model G2: the model follows the Woo (1996) approach and proposes a zone-free method solely based on the use of the earthquake catalogue. Proxy seismogenic sources have been “created” from the epicentral locations of the events that are smoothed according with their fractal distribution in space. The zone-free method by Woo (1996) of the program KERFRAC has been used to compute the probabilistic seismic hazard using a kernel function, which describes the spatial smoothing of seismicity. A grid of point sources (nodes) has been defined around the site of interest and the activity rates of each source have not been computed using a recurrence relationship, such as the GR equation, but they have been calculated from the density and proximity of events lying within that magnitude range. The contribution of each earthquake to the seismicity of the region has been smeared over all grid points falling within an epicentral distance that depends on the magnitude of the event itself. This magnitude-dependent relationship has been defined by a kernel function. Moreover, given the availability of some earthquake-fault associations in the DISS 3.2.1 database, an anisotropic kernel function has been used when there is a connection between faults and earthquakes.

GEODETTIC MODELS

Model G3: this model estimates the seismicity rates over the whole Italian territory using exclusively the GPS velocity field. In particular, G3 has been based on the analysis of 919 GPS derived horizontal velocities, after excluding stations in volcanic areas and velocities that are inconsistent with regional velocity field. The strain rate tensor field has been calculated on a regular $0.1^\circ \times 0.1^\circ$ grid using the VISR software (Shen et al., 2015) taking into account the variable station spacing for the optimal smoothing parameters and finally applying a Gaussian filter of 50 km (6-sigma width) to the scalar strain rate value (maximum absolute eigenvalue of the strain rate tensor). The model converts the strain rate in seismic moment rate and then to earthquake rate under the assumption (Kagan, 2002b; Ward, 1998) that earthquakes magnitudes follow a tapered Gutenberg- Richter distribution, where the b-value and corner magnitude are given. The model explores the uncertainties on the b-value and corner magnitude of the tapered GR relationship, and on values of the thickness of the seismogenic depth.

Model G4: the model follows the approach proposed by Bird & Liu (2007), Bird et al. (2010), and Bird & Kreemer (2015), with some adaptations to Italy. Here for the sake of simplicity we describe only the calculation for a single grid-point falling into one particular finite-element of the long-term deformation model; in this small domain all parameters can be approximated as laterally constant. First of all, a probabilistic method to assign upper crustal earthquakes from the historical catalogue to their presumed causative faults has been used. Then, the so-collected events have been grouped into three sub-catalogues corresponding to the compressional, extensional and strike-slip fault classes. Then, the parameters of their GR magnitude-frequency relations (using maximum-likelihood methods) have been computed. These distributions have been integrated to estimate the long-term seismic moment rate for each class. Hence to evaluate expected rate of seismicity: (1) the principal axes and principal values of the long-term strain-rate tensor have been computed and labelled by using GPS data; (2) based on the orientation and relative magnitude of the principal axes and values and rake of active faults, the given grid point has been characterized by a certain amount of strain-rate and slip-rate of the appropriate kinematic class (normal, reverse, strike-slip); (3) the tectonic moment rate has been computed from the long-term permanent strain-rate and from long-term slip-rates using the coupled thickness, the elastic modulus and the angle for the relevant tectonic class; (4) the tectonic moment rates have been compared and expressed as a fraction of the appropriate sub-catalogue of seismicity; (5) the expected earthquake rate of the given grid point, for earthquakes above the threshold magnitude, has been obtained by multiplying this fraction for the rate(s) obtained from the earthquakes reported in the relevant sub-catalogue; (6) the magnitude -frequency distribution of the expected rates has been obtained by scaling the rate computed in (5) using the beta and corner magnitude previously estimated for the relevant tectonic class.



Mt Etna model

For the volcanic area of Mt. Etna an *ad hoc* seismicity model has been developed. The reason is that the seismicity in volcanic area has specific features, which may be significantly different from the seismicity in tectonic regions, which includes also the use of different frequency-magnitude relationship. This ad hoc model avoids to introduce significant biases in seismic hazard.

Acknowledgements: The financial support of the Centro di Pericolosità Sismica dell'Istituto Nazionale di Geofisica e Vulcanologia in developing these seismicity models for the MPS16-project is gratefully acknowledged. This paper summarises the products of a large team of earthquake geologists, seismologists, and engineering seismologists, reflecting the open and inclusive philosophy behind the approach to PSH modelling that has evolved in Italy in the last years. Numerous researchers deserve acknowledgement for their technical input to this study, for producing the seismicity models, and for contributing to the next PSH model for Italy: Santulin M., Rebez A., Spallarossa D., Barani S., Monaco C., Rotondi R., Varini E., Basili R., Burrato P., Fracassi U., Kastelic V., Tarabusi G., Tiberti M.M., Valensise G., Vannoli P., Azzaro R., Barberi G., D'Amico S., Palano M., Tuvè T., Peruzza L., Gee R., Carafa M.M.C., Bird P., Murru M., Falcone G., Console R., Akinci A., Moschetti M.P., Taroni M., D'Agostino N., Lai C. and Zuccolo E. Finally, we thank M. Stirling for his helpful comments on the manuscript.

REFERENCES

- Bird, P., & Liu, Z., 2007. Seismic Hazard Inferred from Tectonics: California. *Seismological Research Letters* 78, 37-48.
- Bird, P., Kreemer, C., & Holt, W.E., 2010. A Long-term forecast of Shallow Seismicity Based on the Global Strain Rate Map. *Seismological Research Letters* 81, 184-194.
- Bird, P., & Kreemer, C., 2015. Revised Tectonic Forecast of Global Shallow Seismicity Based on Version 2.1 of the Global Strain Rate Map. *Bulletin of the Seismological Society of America* 105, 152-166.
- Cornell, C.A., 1968. Engineering seismic risk analysis. *Bulletin of the Seismological Society of America* 58 (5), 1583-1606.
- Field, E. H., Jackson, D.D. and Dolan, J. F., 1999. A mutually consistent seismic-hazard source model for Southern California. *Bulletin of the Seismological Society of America* 89 (3), 559-578.
- Frankel, A., 1995. Mapping Seismic Hazard in the Central and Eastern United States. *Seismological Research Letters* 66 (4), 8–21.
- Jackson, D.D. & Kagan, Y.Y., 1999. Testable earthquake forecast for 1999. *Seismological research letters* 70 (4), 393-403.
- Kagan, Y.Y., 2002a. Seismic moment distribution revisited: I. statistical results. *Geophysical Journal International* 148, 520-541.
- Kagan, Y.Y., 2002b. Seismic moment distribution revisited: II. Moment conservation principle. *Geophysical Journal International* 149, 731-754.
- Meletti, C., Galadini, F., Valensise, G., Stucchi, M., Basili, R., Barba, S., Vannucci, G. & Boschi, E., 1968. A seismic source zone model for the seismic hazard assessment of the Italian territory. *Tectonophysics* 450, 85-108.
- Shen, Z.K., Wang, M., Zeng, Y., & Wang, F., 2015. Optimal Interpolation of Spatially Discretized Geodetic Data. *Bulletin of the Seismological Society of America* 105, 2117-2127.
- Ward, S.N., 1998. On the consistency of earthquake moment release and space geodetic strain rates: The United States. *Geophysical Journal International* 134 (1), 172–186.
- Weichert, D.H., 1980. Estimation of the earthquake recurrence parameters for unequal observation periods for different magnitudes. *Bulletin of the Seismological Society of America* 70 (4), 1337-1346.
- Woo, G., 1996. Kernel Estimation Methods for Seismic Hazard Area Source Modeling. *Bulletin of the Seismological Society of America* 86 (2), 353-362.



Surface displacement during and after the 2016 Kaikōura earthquake revealed from SAR imagery

Wang, Teng * (1), Wei, Shengji (1), Shi, Xuhua (1), Peng, Dongju (1), Barbot, Sylvain (1)

* wang.teng@ntu.edu.sg

(1) Earth Observatory of Singapore, Nanyang Technological University.

Abstract: Faults overlying the subduction interface play an important role in slip propagation and tsunami generation during megathrust earthquakes. However, the interaction between these shallow faults and subducting plate is poorly understood largely due to the lack of direct observation. The 2016 Kaikōura earthquake, with most surface ruptures onshore, occurred at the southern end of the Hikurangi subduction zone, providing a rare opportunity to study the slip distribution and partitioning amongst the subduction interface and overriding faults. Here, we use satellite radar imagery and GPS records to reveal detailed slip distribution at the surface during and after this extraordinary event. The observation and interpretation of splay faulting should cast light on understanding the connections between the subduction interface and overlying faults during megathrust earthquakes.

Key words: Kaikōura earthquake, SAR, Geodesy, Coseismic, Postseismic.

New Zealand straddles the Australia-Pacific plate boundary with east-facing Hikurangi trench in the north, and west-facing Puysegur trench in the southwest. The 2016 M_w 7.8 Kaikōura earthquake occurred near the southern termination of the Hikurangi subduction system, where a transition from subduction to strike-slip motion dominates the pre-seismic strain accumulation (Wallace et al., 2012). The coastline is very close to the trench (<50km) in the earthquake area and dense onshore dense geodetic measurements provide near-field constraints to study how slip was distributed among the subduction interface and the overlying fault systems during and after the earthquake.

Synthetic aperture radar (SAR) images acquired from the Japanese ALOS-2 and European Sentinel-1A/B satellites allow for identification of surface ruptures and the derivation of three-dimensional (3D) coseismic displacements (Figure 1, Wang et al., submitted). The satellite data also reveal post-seismic deformation on a large-scale in unprecedented spatial resolution (Figure 2). To map the rupture, pixel offsets of SAR images are calculated by tracking the amplitude features between images acquired before and after the earthquake. Pixel offsets measure the surface displacements in independent directions, and therefore are combined to calculate the 3D coseismic displacements. The ALOS-2 ScanSAR interferograms that cover the entire New Zealand region have been processed to image the post-seismic deformation distributed over a large spatial scale.

Based on a coseismic slip model derived from seismic and geodetic observations, we calculate the stress perturbation incurred by the earthquake. We explore a range of possibilities of friction laws and rheology via a linear combination of strain rate in finite volumes and slip velocity on ruptured faults (Moore et al., 2017; Barbot et al., 2017). We obtain the slip distribution that

can best explain our geodetic measurements using outlier-insensitive hierarchical Bayesian model, to better understand different mechanisms behind the localized shallow afterslip and distributed deformation.

Both GPS and InSAR data show that the coseismic and post-seismic deformation related to the Kaikōura earthquake is distributed over an extraordinarily large area, as far as to the north tip of the North Island. Such surface displacement distribution indicates that complex interactions among the subduction interface and the overlying faults plays an important role during and after the earthquake.

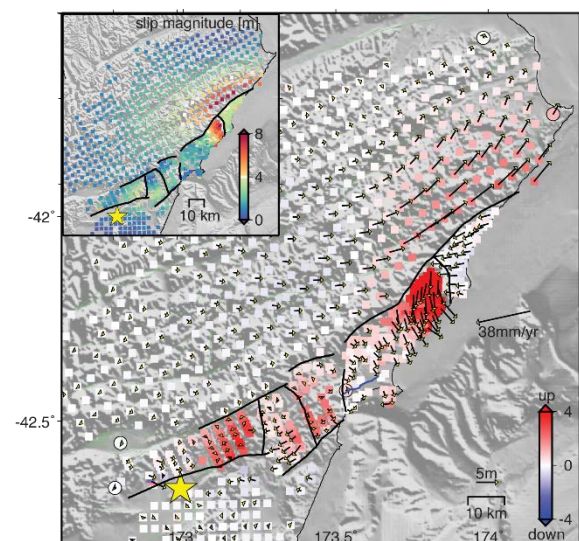


Figure 1: Three-dimensional coseismic displacement derived by combining Sentinel-1A/B and ALOS-2 SAR image offsets and GPS data. Significant surface ruptures are in black. The inset shows the magnitude of total surface displacement.

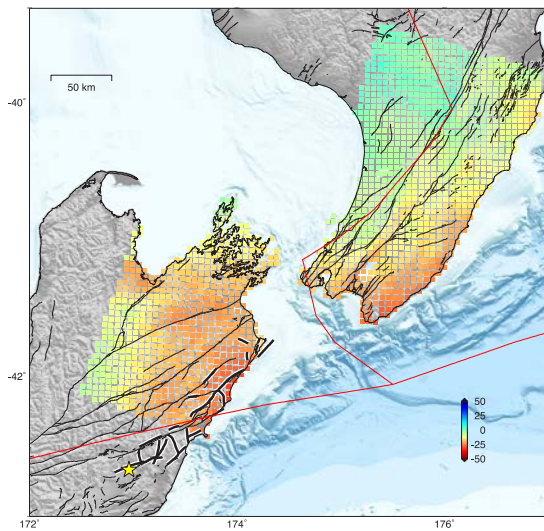


Figure 2: Large scale post-seismic displacement observed from ALOS-2 interferogram.

Acknowledgements: The Sentinel-1A/B images are provided by the European Space Agency. The ALOS-2 images were provided by JAXA under the ALOS-2 RA4 Research Project 1413. We thank GNS for making the 250-m resolution bathymetry, continuous GPS data, active fault maps, strong motion waveform data and field observation reports of earthquake ruptures publicly available. T.W., S.W., X.S., D.P. and S.B. thank the support from the Earth Observatory of Singapore (EOS), Nanyang Technological University through its funding from the National Research Foundation Singapore and the Singapore Ministry of Education under the Research Centers of Excellence initiative. T.W., D.P. and S.B., were also supported by the National Research Foundation of Singapore under the NRF Fellowship scheme (National Research Fellow Award NRF-NRFF2013-04) and Singapore Ministry of Education Academic Research Fund Tier 1 RG181/16. S.W. thanks EOS fund M4430240.B50. X.S. thanks EOS fund M4430214.B50. We thank Y. Wang, J. Moore, M. Hamahashi and P. Tapponnier at EOS for discussions. Data used in this study are stored at the Earth Observatory of Singapore and are freely available upon request.

REFERENCES

- Barbot, S. D., Moore, J. D. P., Lambert, V., Displacements and Stress Associated with Distributed Anelastic Deformation in a Half Space. *Bull. Seismol. Soc. Am.* **107**(2), 10.1785/0120160237 (2017).
- Moore, J. D. P., Hang, Y., Tang, C., Wang, T., Barbot, S., Peng, D., Masuti, S., Dauwels J., Hsu, Y., Lambert, V., Nanjundia, P., Wei, S., Lindsey, E., Feng, L., Shibasaki, B. Imaging the distribution of transient viscosity after the 2016 Mw 7.1 Kumamoto earthquake. *Science* **356**, 163–167 (2017).
- Wallace, L., P. Barnes, and J. Beavan, The kinematics of a transition from subduction to strike-slip: An example from the central New Zealand plate boundary, *Journal of Geophysical Research*, doi:10.1029/2011JB008640. (2012)
- Wang, T., Wei, S., Shi, X., Qiu Q., Li L., Peng, P., Weldon, R., Barbot, S., The 2016 Kaikōura earthquake: Simultaneous rupture of the subduction interface and overlying faults., Submitted to EPSL.



Structure from Motion (SfM) as a tool in Archaeoseismology

Wechsler, Neta (1)

(1) School of Geosciences, Tel-Aviv University, Israel. netawe@post.tau.ac.il

Abstract: Two archaeological sites close to the Dead-Sea Transform fault in northern Israel and known to have suffered earthquake damage are the focus of SfM archaeoseismic damage documentation. In Tiberias a Roman theatre constructed astride a normal fault and consequently deformed during one or more earthquakes is surveyed. A SfM-generated 3D model of the theatre allows precise quantification of the deformation at multiple fault cross sections. In Omrit a Roman temple where the collapse of the façade deformed the pavement is surveyed. Here SfM was used to study the collapse pattern of the façade. In both sites the deformation was documented within 10 minutes. The accuracy of the SfM – generated model is on par with total station measurements. The results are discussed in the context of regional earthquake history.

Key words: Archaeoseismology, Historical Earthquakes, Structure from Motion.

INTRODUCTION

Archaeoseismology, the study of earthquake-caused damage in archaeological sites, is an important source of information for earthquake hazard estimation (Marco, 2008; Stiros, 1996; Galadini et al., 2006). It can add information about time, local intensities and strong ground motions, help define epicentral locations and possibly estimate paleo-magnitudes. Stiros (1996) systematically described the criteria for the identification of earthquakes from archaeological data. Rodríguez-Pascua et al. (2011) detailed a list of earthquake archaeological effects (EAE) based on the seismic deformation of buildings and monuments within urban areas of ancient cities. Hinzen et al. (2011) introduced the concept of quantitative Archaeoseismology, which incorporated high resolution three dimensional (3D) structure mapping and strong ground-motion modeling in order to determine whether other causes rather than seismogenic could have been the cause of damage.

EAE can be documented using many methods, from drawings to laser scanning. In some cases documentation must be performed quickly: if there are plans to excavate further; if the site will be restored, buried or even demolished. One of the new methods of documentation is structure from motion (SfM) – using photographs of the same target from different angles to construct a 3D model (James & Robson, 2012; Westoby et al., 2012). The advantages of using SfM are numerous: it is faster than any other method in the field; it can be very accurate if executed properly, using cheap equipment. Another advantage is that SfM can be used if the site was already demolished and all that is left are photos.

This work presents examples from two archaeological sites where SfM was used to document and quantify earthquake damage to man-made structures. Both sites are located near the Dead-Sea Transform fault in Israel (Fig.1), a known source of powerful earthquakes in historical and recent times (Ambraseys, 2009; Agnon, 2014). The first site is a Roman theatre in Tiberias, constructed astride a normal fault and consequently deformed during one or more

earthquakes. The second site is a Roman temple in Omrit where the Temenus pavement is deformed. In both sites the deformation was documented within 10 minutes, using only a hand-held camera and a scale bar. The photos were processed using Agisoft Photoscan and the resulting point cloud was analyzed with ArcGIS and CloudCompare. For each site the documented archaeoseismic evidence is discussed in the framework of historical earthquake records.

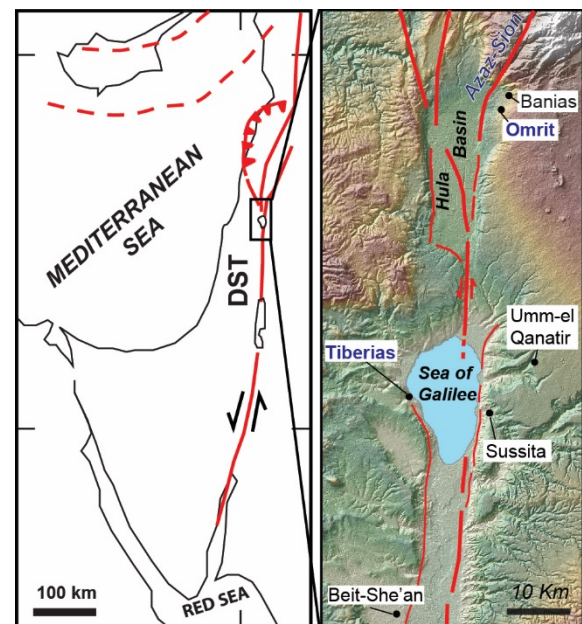


Figure 1: Left: general location map. DST – Dead Sea Transform. Right: close-up on the region around the Sea of Galilee. Locations on the map are discussed in text. Active faults are marked in red.

THE ROMAN THEATRE OF TIBERIAS

The founding of Tiberias in the name of Emperor Tiberius by king Herod in 19 CE led to the establishment of a polis in the Galilee (Atrash, 2010). The city was built on the western shore of the Sea of Galilee and included several monumental structures such as a basilica, a bathhouse, a stadium and a theatre. The theatre is found in the south of the city and was



excavated in 2009 by the Israel Antiquities Authority (Atrash, 2012). It was first erected during the 1st century CE, its eastern flank was damaged and consequently the theatre was renovated in the beginning of the 2nd century CE, as well as during the 4th century CE. The theatre was abandoned around the 6th century CE and filled with soil and rubble, then covered by a Fatimid and Abbasid (750-1099 CE) residential quarter which was placed over it (Atrash, 2012) and was itself abandoned in the 11th century CE.

Several active faults with clear geomorphic expression at the surface were mapped on the western flanks of the Sea of Galilee (Sagy et al., 2016, Ferrario et al., 2014a). One of those normal faults cuts through the theatre at a 140°N

strike and is likely the source of the damage that was described by Ferrario et al. (2014b) – tilting, offset structures with vertical displacement, open cracks and small lateral displacements. While trenching revealed inconclusive faulting evidence, Ferrario et al. (2014b) suggest that the alignment of vertical deformation in the theatre and additional structures in the Polis is in agreement with faulting rather than landslide or liquefaction mass movement related deformation.

For this study a 3D model was created for two locations inside the theatre: the north wall and the benches. The north wall model was made of 20 photos (Fig. 2). The contacts between the masonry basalt blocks are used to

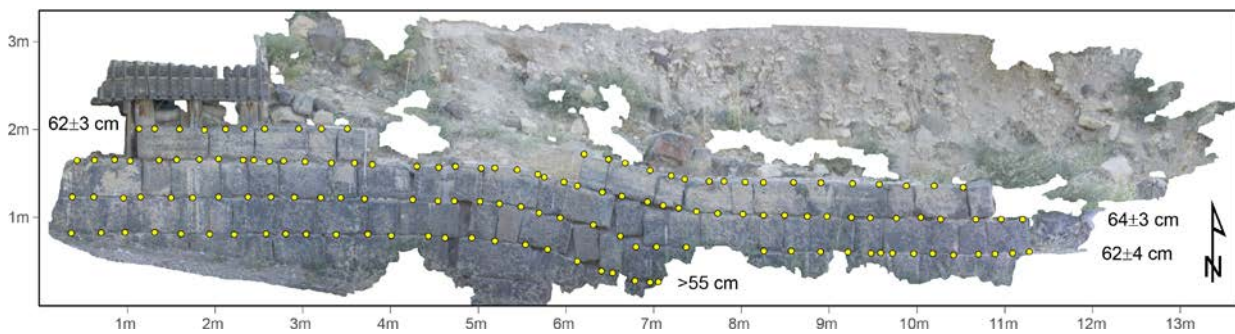


Figure 2: The SfM-derived model of the north wall of the theatre in Tiberias. The yellow dots were picked along previously levelled horizons. For each line, vertical offset and error were estimated using the average vertical location of the picked points E and W of the deformed zone.

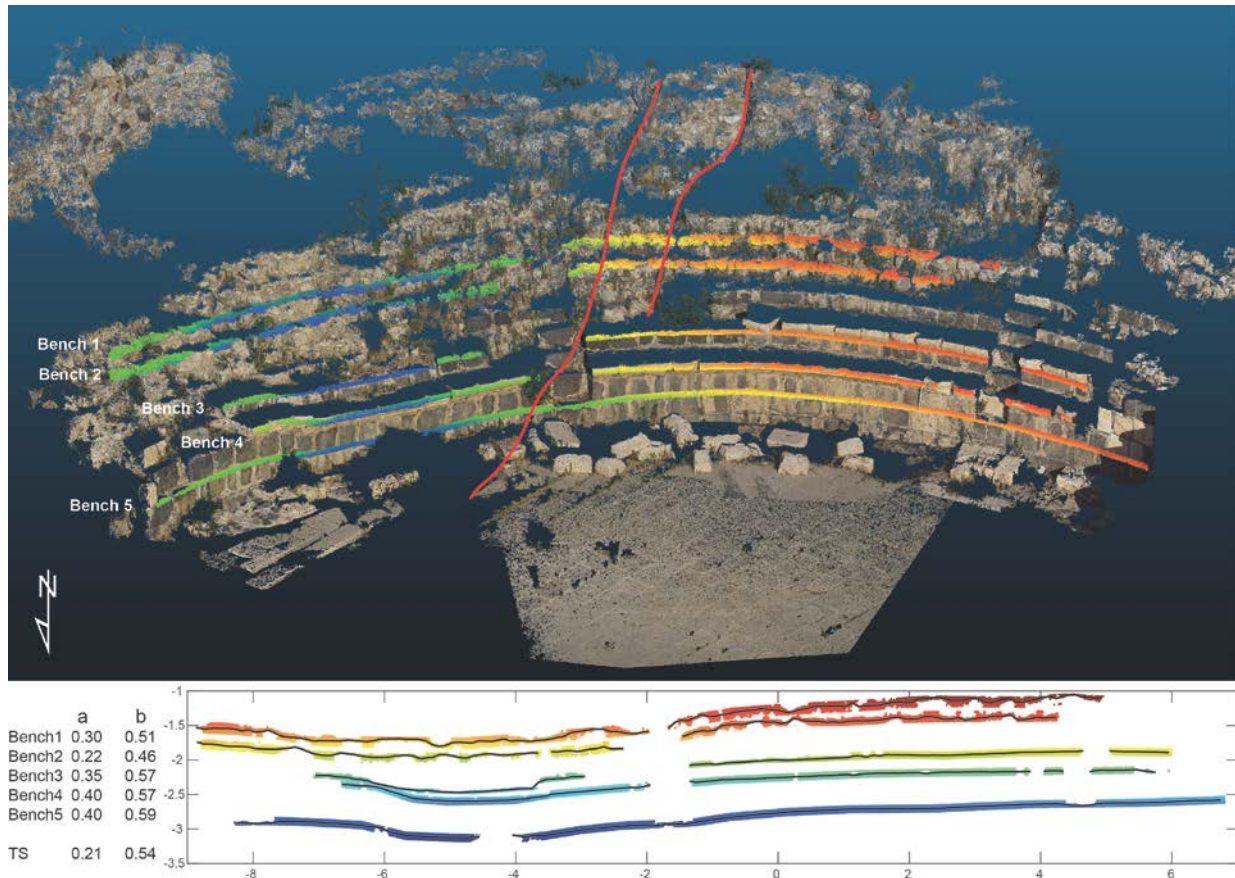


Figure 3: **Top:** The SfM-derived point cloud of the theatre benches. Selected points for displacement measurements are coloured by relative elevation within each bench. The cracks are marked in red. **Bottom:** an E-W projection of the picked points along the benches and calculated vertical offsets. The black line is an average of the points. **a** is the vertical offset between bench levels at the two side of the deformation zone. **b** is the maximum vertical offset. The total station points were measured just below bench 4.



measure lateral and vertical offsets of 4 profiles and the results compared with a Total Station (TS) survey that was previously conducted at the site (Kats, unpublished data). The vertical offset measured from the model is 62-64 cm (down to the east), identical to the offsets measured by the TS. The benches are part of the theatre structure, built in a semi-circle facing NNE. The TS survey included only one row of benches, whereas this study used a 3D point cloud constructed from 20 photos and picked the edges of 5 benches (Fig. 3). A 5 cm buffer both in the horizontal (E-W) and vertical planes was used to overcome uncertainties due to the removal of masonry stones and vegetation obscuration, and the points were projected onto an E-W plane to determine offsets and uncertainties. There are 2 visible cracks that run through the upper bench area, and east of them there is a small graben, about 4-5 m wide, which displaced the benches by 46-59 cm. The E side of the benches is only downthrown by 22-40 cm compared to the W side, and no lateral offsets were detected although offsets smaller than 5 cm would not be measurable. The TS survey measured vertical offset was 54 cm, in excellent agreement with SfM-derived results.

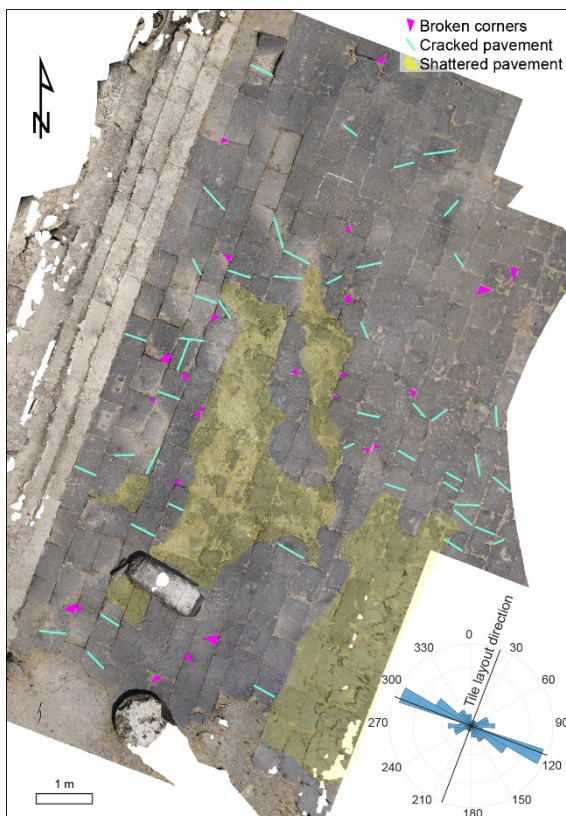


Figure 4: The Temenus pavement at Omrit with mapped damage. Rose diagram shows tile-crossing cracks (light blue) orientations.

Based on the mapped offsets and archaeological evidence, the offset can be a result of one or more damaging earthquakes. The theatre was reconstructed several times yet the exposed damage appears too severe to have been left alone if the theatre was in use, making it reasonable to assume that it can be mostly attributed to the post-abandonment earthquake of 749 CE. The sediment fill above the theatre is also deformed (Fig. 2) but the younger

structures above had no significant vertical offsets, although small cracks were visible in the deformation zone. During the mid-8th century CE there are reports of 2-3 different earthquakes that affected a large area from Egypt to Turkey (Ambraseys, 2005). The earthquake of 749 CE was very strong (estimated M7.0) and caused extensive damage in the region, including the destruction of Tiberias and Beit-She'an (Scythopolis). Many neighboring villages were also abandoned at the same time, such as Sussita and Qanatir (Wechsler et al., 2008, Wechsler & Marco, 2017). There is evidence of surface rupture on the western shore of the Sea of Galilee (Marco et al., 2003) and near Jericho (Reches and Hoexter, 1981) that can be correlated with this earthquake. Based on Wells & Coppersmith (1994) a maximum offset of 64 cm on a normal fault is correlative to a M6.3 earthquake and a 4 km long fault, in agreement with mapped fault extent (Sagy et al. 2016).

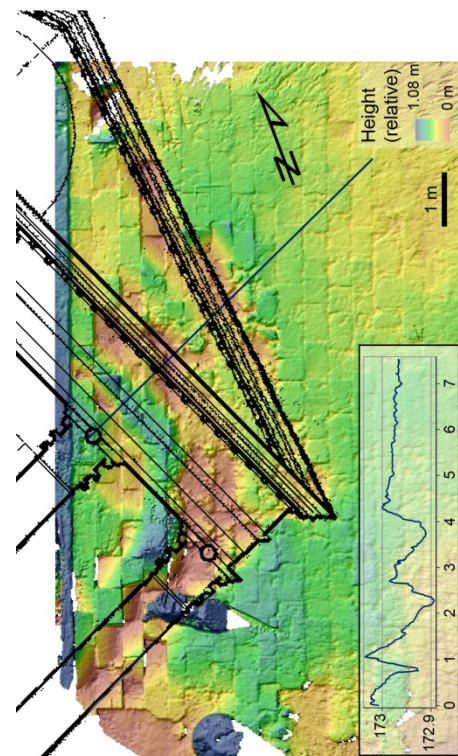


Figure 5: DEM model of the pavement. The blue line marks the location of the height profile (bottom). Reconstructed temple façade from Stoehr (2011).

THE ROMAN TEMPLE COMPLEX AT OMRIT

The archaeological site of Omrit is located in the foothills of the Hermon mountains, on the eastern side of the Hula valley and in close proximity to the Sion-Azaz fault segments of the Dead-Sea fault in northern Israel (Fig. 1). The site has been excavated by the Macalester college since 1999. In it is an extremely well preserved temple complex from Roman times. The temple was built in the beginning of the 1st century CE (probably by King Herod to honor Augustus Caesar), and was later renovated and enlarged at the beginning of the 2nd century. The damage that instigated the renovation of the temple at that time, and again during the late Roman period/early byzantine



period, was suggested to be the result of damaging earthquakes (Stoehr, 2011). Stoehr describes evidence for earthquake damage which includes fallen columns, fissuring of floors, and destruction layers well dated to the 4th century CE. Additional evidence include broken corners in masonry blocks, pop-up arrays of flagstones and shattered pavement in the surrounding Temenos (Fig. 4). Stoehr also describe the later temple as built with earthquake resistant features. However, he is reluctant to attribute the damage to the second temple solely to seismic ground movements, claiming that the pattern of fallen columns does not fit a “sequenced collapse” and suggesting that the observed rubble is the result of purposeful scavenging for reuse of materials. Stoehr claims that the different directions of the depressions in the pavement points away from earthquake activity, because an earthquake will typically topple a colonnade so that the columns are parallel. He suggests that the temple façade has been deliberately toppled by pulling the columns out and causing the architrave to collapse. Based on the above, Stoehr concludes that an earthquake damaged the temple and rendered it nonfunctional without completely leveling it, which then created an opportunity for material removal.

In order to quantify damage to the Temenus pavement, a 3D model was reconstructed using 40 photos. The resulting high resolution orthophoto (0.5 mm per pixel) was used for mapping crack orientations (Fig. 4), and the point cloud was used to construct a 1 cm per pixel DEM model of the pavement (Fig. 5). The crack orientations are almost identical to the pavement layout direction, as many cracks cross the flagstones perpendicularly. Silva et al. (2009) documented similar patterns in the pavement of the forum of Baelo Claudia, attributed to the direction of ground shortening, which cannot be ruled out at Omrit either, given the N-S direction of the neighboring strike-slip fault. The flagstone pop-up and subsidence is on the order of 10 cm, and there is a clear pattern emerging from the geometry of the disturbance. In fact, the pattern fits with a collapse of the temple façade to the NE, based on reconstructed façade drawing (Fig. 5). It would stand to reason that had the façade been intentionally demolished, it would have fallen to the SE, perpendicular to the building front. It is therefore suggested that the pattern of pavement deformation indicates a seismically induced collapse that was probably controlled by the structure of the building as a whole (walls, columns, architrave, ceiling etc.). For example, an inward collapse of the SW walls would have pushed the façade out at an angle. The direction of collapse is not necessarily indicative of the direction of ground motion polarization, as shown by Hinzen (2009) for the case of columns with a roof construction above. A model of the toppled façade can be used to elucidate ground motion intensities at the site and contribute to hazard evaluation along the DST.

Additional evidence for typical archaeoseismic damage at Omrit supports the theory that the temple’s destruction in the 4th century was earthquake-caused. The best candidate is the 363 CE quake, which was widely felt and caused damage from Baniyas in the north to Gaza in the south, and

perhaps even in Petra (Ambraseys, 2009, Russel, 1980). Omrit is a mere 4 km away from Baniyas, which makes it likely to have suffered at least partial destruction.

CONCLUSIONS

Two archaeological sites with suspected seismic damage were documented rapidly and inexpensively yet precisely using SfM. The results of this study’s high-resolution damage mapping can be used for future studies of earthquake hazard in northern Israel, and the method can be utilized in any archaeological setting, even during an excavation, by inexperienced users.

Acknowledgements: Thanks to Oded Katz from the Geological Survey of Israel for the Total Station measurements and to Ronen Gersman for putting up with me and for help in the field.

REFERENCES

- Agnon, A., 2014. 8 Pre-instrumental earthquakes along the Dead Sea transform, in *Dead Sea Transform Fault System: Reviews*, pp. 207–261, (Garfunkel, Z., Ben Avraham, Z. & Kagan, E., eds) Springer.
- Ambraseys, N.N., 2005. The seismic activity in Syria and Palestine during the middle of the 8th century; an amalgamation of historical earthquakes. *J. of seismology*, 9(1), 115-125.
- Ambraseys, N., 2009. *Earthquakes in the Mediterranean and Middle East: A Multidisciplinary Study of Seismicity up to 1900*, Cambridge U. Press.
- Atrash, W., 2010. Tiberias, the Roman Theatre, Preliminary Report. *Excavations and Surveys in Israel*, 122.
- Atrash, W., 2012. The Roman Theater at Tiberias. *Qadmoniot* 144, 79-83.
- Ferrario, M.F., Katz, O., Livio, F., Michetti, A.M., & Amit, R., 2014a. Archaeoseismology and paleoseismology in the area of Tiberias city, Sea of Galilee - preliminary results. *Miscellanea INGV*.
- Ferrario, M.F., Amit, R. & Katz, O., 2014b. Evaluation of earthquake hazard for the city of Tiberias. Israel Geological Survey.
- Galadini, F., Hinzen, K.G., Stiros, S., 2006. Archaeoseismology: methodological issues and procedure. *J. of Seismology* 10, 395-414.
- Hinzen, K.G., Fleischer, C., Reamer, S.K., Schreiber, S., Schütte, S. & Yerli, B., 2011. Quantitative methods in archaeoseismology. *Quaternary International*, 242(1), 31-41.
- Hinzen, K.G., 2009. Sensitivity of earthquake-topped columns to small changes in ground motion and geometry. *Israel J. of Earth Sciences*, 58.
- James, M.R., & Robson, S., 2012. Straightforward reconstruction of 3D surfaces and topography with a camera: accuracy and geoscience application. *J. Geophys. Res.* 117, F03017.
- Marco, S., Hartal, M., Hazan, N., Lev, L., & Stein, M., 2003. Archaeology, history, and geology of the A.D. 749 earthquake, Dead Sea transform. *Geology* 31, 665–668.
- Marco, S., 2008. Recognition of earthquake-related damage in archaeological sites: examples from the Dead Sea fault zone. *Tectonophysics* 453, 148-156.
- Reches, Z., Hoexter, D.F., 1981. Holocene seismic and tectonic activity in the Dead Sea area. *Tectonophysics* 80, 235–254.
- Rodríguez-Pascua, M.A., Pérez-López, R., Giner-Robles, J.L., Silva, P.G., Garduño-Monroy, V.H. and Reicherter, K., 2011. A comprehensive classification of Earthquake Archaeological Effects (EAE) in archaeoseismology: Application to ancient remains of Roman and Mesoamerican cultures. *Quaternary International*, 242(1), 20-30.
- Russell, K.W., 1980. The earthquake of May 19, AD 363. *Bulletin of the American Schools of Oriental Research* 238, 47-64.



INQUA Focus Group Earthquake Geology and Seismic Hazards



paleoseismicity.org

- Sagy, A., Sneh, A., Rosensaft, M. & Bartov, Y., 2016. Map of active faults and potentially active faults for the Israel Standard 413 "design provisions for earthquakes resistance of structures", Update 2016, *Israel Geological Survey*.
- Silva, P.G., Reicherter, K., Grützner, C., Bardají, T., Lario, J., Goy, J.L., Zazo, C. & Becker-Heidmann, P., 2009. Surface and subsurface palaeoseismic records at the ancient Roman city of Baelo Claudia and the Bolonia Bay area, Cádiz (south Spain). *Geological Society, London, Special Publications*, 316(1), 93-121.
- Stiros, S., 1996. Identification of Earthquakes from Archaeological Data: Methodology, Criteria and Limitations. In: *Archeoseismology* (Stiros, S., Jones, R.E. eds). Fitch laboratory occasional paper 7, British School at Athens, Oxford.
- Stoehr, G.W., 2011. The Potential for Earthquake Damage to Temple II Architecture at Roman Omrit, In: *The Roman Temple Complex at Horvat Omrit: An Interim Report* (Overman, J.A. & Schowalter, D.N. eds.). Archaeopress.
- Wechsler, N., Katz, O., Dray, Y. Gonen, I., & Marco, S., 2009, Estimating location and size of historical earthquake by combining archaeology and geology in Um-El-Kanatir, Dead Sea Transform, *Natural Hazards* 50(1), 27-43.
- Wechsler, N. & Marco, M., 2017 in press, Historical earthquakes in northern Israel and their influence on Sussita/Hippos, *Michmanim* 27.
- Wells, DL. & Coppersmith, KJ., 1994, *BSSA* 84(4), 974-1002.
- Westoby, MJ., Brasington, J., Glasser, NF., Hambrey, MJ., & Reynolds, JM., 2012. "Structure-from-Motion" photogrammetry: a low-cost, effective tool for geoscience applications. *Geomorphology* 179, 300-314.



Assessing the “Clustering and Quiescence” earthquake occurrence model for Stable Continental Region faults and the implications for Probabilistic Seismic Hazard Analysis

Whitney, Beau (1, 2) and Hengesh, James (1, 3)

- (1) The University of Western Australia, Centre for Offshore Foundation Systems, Perth. Email: bbwhitney@gmail.com
 (2) Geoter SAS, 3 Rue Jean Monnet, Clapiers, 34830 France
 (3) Interface Geohazard Consulting, 20 Plumeria Pl., Lahaina, HI, 96761 USA: hengesh@igc.com

Abstract: Over the past three decades research focused on earthquakes in Stable Continental Regions has suggested the occurrence of earthquakes on faults typically consists of periods of clustered activity separated by long (10^5 - 10^6 yr) intervals of quiescence. This interpretation is based on paleoseismological data gathered from faults mostly from Australia and the central eastern United States. Understanding earthquake occurrence behaviour is critical for accurately modelling seismic hazard, especially in Stable Continental Regions where seismicity data and fault specific geologic data are often lacking. The question we address is whether the reported clustering behaviour of large earthquakes on faults in Stable Continental Regions is borne out in the paleoseismological and historical record of surface rupturing events. This paper presents a summary and comparison of the data and interpretations that have advanced the clustering and quiescence (C&Q) occurrence model with data on faults that do not demonstrate C&Q behaviour. Although there is some evidence to suggest some faults may exhibit C&Q behaviour, most Stable Continental Region faults do not show evidence of this style of earthquake occurrence. Most faults in Stable Continental Regions with historical or paleoseimological data for surface rupturing events have evidence for only one event. Therefore, individual earthquake recurrence intervals and fault slip rates are unconstrained.

Key words: SCR, earthquake, recurrence, clustering

INTRODUCTION

The current model for earthquake occurrence in Stable Continental Regions (SCR) was first posited by Crone *et al.* (1997) in reference to their earlier paleoseismological work on faults in Australia and the eastern U.S. The authors state:

“Palaeoseismic investigations of recent faulting in stable continental regions of Australia, North America and India show that these faults typically have a long-term behaviour characterized by episodes of activity separated by quiescent intervals of at least 10,000 and commonly 100,000 years or more.”

Subsequently the concepts behind this assertion have established themselves as the working model for how SCR faults behave (e.g., Crone *et al.*, 2003; Estrada *et al.*, 2006; Clark *et al.*, 2011; 2012). In this paper we review the paleoseismic data and interpretations behind the C&Q model and provide an updated list of data on earthquake recurrence from SCRs, including data from Africa. We evaluate these data in order to understand the basis for the C&Q model and if the model is truly representative of SCR fault behaviour.

Background

The surface rupturing 1986 Mw 5.7 Marryat Creek earthquake and 1988 Mw 6.6, 6.3., 6.2, Tennant Creek earthquake sequences that occurred in Australia perplexed the seismic hazard community in that both sequences occurred in areas without previous historical seismicity and neither contained geomorphological

indicators that the faults had hosted previous large magnitude earthquakes. Paleoseismological studies of these faults led to a series of papers by researchers at the USGS that documented the paleo-earthquake history of the faults (e.g., Crone *et al.* 1992; Machette *et al.*, 1993). Years later, Crone *et al.* (1997) synthesized the results of these studies along with other SCR faults and presented a new model for large magnitude earthquake recurrence in SCRs. Data on faults associated with the historical Tennant Creek, Marryat Creek, and Meckering earthquakes in Australia, the Killari event in India, the Ungava event in eastern Canada, and the Meers and Cheraw faults in the U.S. were presented (Table 1).

Table 1. Data cited by Crone *et al.* (1997) for C&Q behaviour.

Fault/EQ	Number of rupture events (age)			
	Tennant Creek	3 (1988)	? (Precambrian>100 ka)	
Marryat Creek	1 (1986)	? (Precambrian>50 ka)		
Meckering	1 (1968)	? (“ancient”)		
Killari	1 (1993)			
Ungava	1 (1989)	1 (<Archean)		
Meers	1 (1 ka)	1 (3 ka)	?	?
Cheraw	1 (8 ka)	1 (12 ka)	1 (25-20 ka)	

In summary, none of the five faults that hosted historical events exhibit evidence for multiple late Quaternary events or earlier clustered activity. In addition, the two faults that had multiple late Quaternary events have no evidence for earlier earthquakes or clustering. Indeed the sparseness of these data (five faults with one event, and two faults with two events) do not strongly support the clustering earthquake occurrence model.

DISCUSSION

Fault recurrence data in SCR

The source data from paleoseismological studies of 31 SCR faults are compiled in Table 2. Equivocality of the event, age, or both is indicated by *italics*. Magnitude values presented in italics are estimated by the report authors using empirical relations, others are from instrumental earthquake records.

We do not include the results of a number of studies of faults within the central European Cenozoic rift system (e.g., Roer and Rhine graben faults), or faults related to the Alpine orogenic belt (e.g., France: Trevaresse), although these structures are within regions mapped as SCR (e.g., Woessner *et al.*, 2015). We believe that their designation as SCR faults should be reconsidered as has been done in SE Asia (Wheeler, 2011) and Western Australia (Whitney, 2015) given consideration for the criteria defining a SCR (Johnston *et al.*,

1994), the slip rates associated with some of these structures, and the mechanisms driving deformation in these regions—compared with SCR faults overall.

Eighteen of the faults compiled in this review have evidence for only one morphogenic earthquake event (60%). Three faults have evidence for one and possibly more events (9%). Six of the faults have evidence for two and possibly more events (19%). Three faults have evidence for three or more events (9%) and one fault has evidence for neotectonic activity but no data on event history (3%).

The equivocal nature of some interpretations (*italicised in Table 2*) reflects the uncertainty from the primary source publications; it does not reflect our judgment. In some instances (e.g., Estrada, 2009), a range of alternative interpretations are provided and in some instances the authors directly speculate (e.g., Crone *et al.*, 1997) about the occurrence and/or timing of events.

Table 2. Historical and paleo-earthquake events on SCR faults. Letter designation next to age corresponds to author in reference list.

Fault/EQ	Number of rupture events and age	Magnitude	Kinematic	Length (km)	Slip Rate (mm/yr)	C&Q evidence
Australia						
Ernabella	1 (2012) ^N	Mw 5.4	Reverse	1.6	-	No
Williamstown-Meadows	1 (between ~61-41 ka) ^O	Mw 6.8	Reverse	38	-	No
Alma fault	1 (<i>Quaternary?</i>) ^O	Mw >7.0	Reverse	93	-	No
Eden Burnside	1 (<120ka) ^O	Mw >7.0	Reverse	53	-	No
Para	1 (<300ka) ^{P,O}	Mw >7.0	Reverse	43	0.2-0.8 mm/yr to 0.04-0.0.16mm/yr	Inconclusive
Tennant Creek	1 (1988) ^{E,Y}	Mw 6.6, 6.3, 6.2	Reverse	32	-	No
Milendella	1 (22-7.5ka) ^F	-	Reverse	54	-	No
Meckering	1 (1968) ^A	Mw 6.5	Reverse	37	-	No
Burra	1 (>83ka) ^H	-	Reverse	57.2	-	No
Mundi Mundi	1 (>59ka) ^H	-	Reverse	160	-	No
Cadoux	1 (1979) ^K	Mw 6.1	Reverse	15	-	No
Calingiri	1 (1970) ^A	Mw 5.7	Reverse	3.5	-	No
Marryat Creek	1 (1986) ^{L,Y}	Mw 5.7	Reverse	13	-	No
Willunga	1 (>32ka) ^F	Mw >7.0	Reverse	45	-	No
Cobble Knickpoint	1 (unknown) ^H	Mw 6.6-7.3	Reverse-oblique	59	0.02-0.03mm/yr to 0.036-0.051 mm/yr	No
Wilkatana North	1 (<12ka) ^H					
Wilkatana South	1 (32-29ka); 1 (67-32ka) ^H					
	1 (<80ka) ^H					
	⇒ these may all be different segments of the same fault.					
Roopena	1 (~27ka); 1 (~100ka); 1 (<i>older</i>) ^C	-	Reverse	29.5	-	Inconclusive
Lort River	1 (~13-7ka); 1 (~35-29ka); 1 (216-120ka) ^P	Mw ~7.0	Reverse	40	~0.1 mm/yr	Possible
Dumbleyung	1 (~9-8ka); 1 (~24-15ka); 1 (~120-24ka) ^P	Mw ~7.0	Reverse	35.7	0.13-0.3 mm/yr	No
Hyden	1 (~30ka); 1 (55-50ka); 1 (<i>Tertiary</i> >1Ma) ^C	-	Reverse	30	-	Inconclusive
	1 (55-50ka); 1 (100-90ka); 1 (>200ka) ^B	Mw ~6.8	Reverse	32	<0.01-0.03 mm/yr	Inconclusive
Lake Edgar	1 (18ka); 1 (28ka); 1 (48-61ka) ^{I,J}	Mw 6.8-7.0	Reverse	46	0.11-0.24 mm/yr	No
Cadell	3 (~70ka-45ka); 3 (~45-20ka); ? (Mio-Plio to Quaternary) ^{M,X}	Mw 7.3-7.5	Reverse	80	0.4-0.5mm/yr to 0.005-.01 mm/yr	Probable
Lake George	See Clark <i>et al.</i> , this volume	Mw 7.4	Reverse	75	See reference	Probable ^P
North America						
Ungava	1 (1989) ^Q	Ms 6.3; mb 6.2	Reverse-sinistral	10	-	No
Cheraw	1 (8ka); 1 (12ka); 1 (25-20ka) ^R	-	Reverse	44	<0.01 mm/yr	No
Meers	1 (1ka); 1 (3ka); ? (>130ka) ^{R,S,W}	-	Reverse-oblique	26-37	-	No
Africa						
Kangoo (S.A.) eastern segment	1 (10ka) ^T ; 1 (~24ka); ? (>350ka) ^U	Mw 6.6-7.4	Normal	42-51 50	See reference	Possible
western segment	1 (4.5ka); 1 (10ka) ^U					
Hebron (Namibia)	? (Quaternary) ^V	-	Normal	300	-	Inconclusive

Our assessment of the evidence for C&Q behaviour is presented in the last column of Table 2. Evidence for C&Q behaviour is assessed based on the data presented in the primary source publications, which considers the number of events, age-control, long-term tectonic geomorphological indicators, etc. Our assessment honours the data as presented, but it may differ from the “preferred interpretation” of some of the primary report authors.

Faults with evidence for the C&Q recurrence model

The Cadell fault in Australia is the only fault identified during this review that exhibits evidence consistent with the C&Q model (Clark *et al.*, 2015; Clark *et al.*, *this volume*). Clark *et al.* (2015) suggest as many as six morphogenic events occurred on the fault between 70-20ka. Based on the interpretation of geophysical data they suggest that previously similar amounts and styles of displacement occurred on the fault sometime between the Miocene and Quaternary.

Several others of the reviewed faults may exhibit C&Q behavior, but the data are inconclusive. For instance, tectonic geomorphologic data may provide information to deduce long-term slip rates that are inconsistent with more recent slip rates derived from paleoseismological studies. However, this observation alone does not constitute C&Q occurrence behavior.

Alternative SCR earthquake occurrence behaviour

The data summarized in this review broadly show a general pattern. Most (60%) of the earthquakes in the historic and paleoseismological record that ruptured SCR faults are one-off events. The apparent one-off behaviour could be attributed to myriad processes beyond the scope of this short summary. However, whether one-offs are indicative of isolated strain or a more complex interplay of processes over broad temporal and spatial scales should continue to be investigated.

The problem of limiting age constraints and vastly different yet accurate interpretations of the same data

A consistent pattern we observed during this review involves an assumption made by most authors that a prior earthquake must have occurred on a given fault. This assumes SCR fault behavior is consistent with plate-boundary style stick-slip seismic cycles albeit at lower rates. However, alternative hypotheses for long-term SCR occurrence have been postulated. Recently, questions have been raised regarding the applicability of the concept of recurrence to SCR earthquakes (Calais *et al.*, 2016; Craig *et al.*, 2016). These authors suggest that SCR seismicity is a product of perturbations to a relic crustal stress state and not directly related to ongoing (long-lived) tectonic loading. Therefore, SCR events are likely transient and need not repeat on an individual structure. Alternatively, the recent onset of fault activation or change in stress state has been suggested for structures in the SCR of western Australia (e.g., Hengesh and Whitney, 2016), thereby limiting the availability of a long-term paleoseismic record or significant tectonic geomorphology to develop (Whitney *et al.*, 2015).

A characteristic of large SCR earthquakes is that they tend to reactivate older structures. These older structures developed prior to the neotectonic period; typically they are Mesozoic, Paleozoic or older features (Clark *et al.*, 2011; 2012). However, the age of the host structure is effectively irrelevant to the earthquake occurrence

behaviour within periods of interest for seismic hazard assessments (10^{-5} yrs).

The assumption that plate boundary style stick-slip earthquake occurrence behaviour is applicable to large earthquakes on SCR faults has contributed to the preferred earthquake occurrence models for many of the faults assessed in this review. A few examples of preferred interpretations indicating this assumption are presented below.

The Tennant Creek earthquakes: Crone *et al.*, (1992) document that the earthquake sequence ruptured a pre-existing fault in Precambrian bedrock. All of the materials overlying the bedrock host the single episode. The oldest faulted sediments overlying the bedrock are ~100 ka. The authors conclude that a previous event must have occurred prior to 100 ka. An equally plausible interpretation given the data is that there was an earthquake sequence in 1988 and one previously, sometime since the Precambrian. The implications of these differences are considerable. One suggests there are multiple events related to the same tectonic regime and suggests evidence exists for long periods of seismic quiescence; one does not.

The Meers fault exhibits data that can be summarized as follows: displacement values measured in materials aged 32 ka and 130 ka are the same. There is no evidence for any rupture prior to the 32 ka event. A plausible interpretation of these data is that the late Quaternary earthquake record preserved on this fault is younger than 32 ka—in actuality younger than mid-Holocene. However, the authors assume that an older event must have occurred and based on a lack of progressive deformation to Quaternary sediments it must have occurred prior to 130 ka (Crone and Luza, 1990).

The difficulty of interpreting SCR fault behaviour is further illustrated by multiple event sequences interpreted on the Cheraw fault. During the assessment of seismic hazard in the central eastern United States (EPRI, 2012), three interpreted events on the Cheraw fault (Crone *et al.*, 1997) were requalified to be maybe 2 or 3 events (0.4 and 0.6 weights on the Probabilistic Seismic Hazard Analysis (PSHA) logic tree, respectively) in part due to communication with the original report author who acknowledged that the evidence for the third event was less definitive.

As pointed out by Calais *et al* (2016) the traditional view is that SCR faults behave in a similar manner to their plate boundary counterparts albeit with loading rates, strain rates, and recurrence an order of magnitude or more, lower. However, examination of these 31 case studies suggests that at most locations only one event has been recorded. There are only 12 cases with multiple events, and even fewer cases where the data are sufficient to defined a clear case of C&Q behaviour.

IMPLICATIONS FOR PSHA

The significance of having a defensible event chronology cannot be understated for regions with such limited seismicity, paleoseismological information, and poorly constrained slip rates and recurrence. Indeed an “extra” event can affect the earthquake recurrence rates by an order of magnitude. Similarly, because of the acceptance of the C&Q earthquake occurrence model some PSHAs model SCR faults

as either being “in cluster” or “out of cluster” (e.g., Bommer *et al.*, 2014). A fault that is “in cluster” can have a slip rate an order of magnitude or more greater than the long term slip rate of the fault. Therefore, assessing whether a fault is “in cluster” or “out of cluster” becomes a critical input for the model. However, identifying whether a fault is in a clustered behaviour mode appears unachievable for most faults given the resolution of the data assessed in this review. Simply, there are not enough data to establish a coefficient of variation for earthquake recurrence on most SCR faults.

This paper provides a condensed summary of the paleoseismological and historical data for large magnitude earthquakes in SCR. Based on the 31 locations presented in the paper, the C&Q model is supported by only a small percentage of the data and there remain large uncertainties in how to characterize earthquake occurrence in SCR regions for hazard assessments. There is some evidence that supports the C&Q model (e.g. Clark *et al.*, 2015), however the data do not exist to favour this over an alternative model for SCR faults.

The standard of practice in PSHA for SCR is to capture the epistemic uncertainty in earthquake occurrence models by considering both the Poisson and C&Q earthquake occurrence models. The applicability of the C&Q model, based on the available data, should be considered when assigning weights to the alternative “style of earthquake occurrence” branches of the logic tree.

Acknowledgements: We thank Dan Clark for fruitful discussions on the topic and an initial review of our manuscript. We thank Tom Rockwell for his review and suggestions for improving our submission.

REFERENCES

- Bommer J. J., Coppersmith K. J., Coppersmith, R. T., Hansen, K. L., Mangongolo, A., Nevelig, J., Rathje, E. M., Roderiquez-Marek, A., Scherbaum, F., Shelembe, R., Stafford, P. J. and Strasser, F. O. (2015). A SSHAC Level 3 Probabilistic Seismic Hazard Analysis for a New-Build Nuclear Site in South Africa. *Earthquake Spectra*, Vol. 31, n° 2, p. 661-698
- Calais E., Camelbeeck T., Stein S., and Craig T. (2016). A new paradigm for large earthquakes in stable continental plate interiors: Large earthquakes in SCR. *Geophysical Research Letters*, In Press, September, DOI: 10.1002/2016GL070815
- ^MClark, D., McPherson, A., Allen, T., De Kool, M. 2014. Coseismic surface deformation caused by the 23 March 2012 M_w 5.4 Ernabella (Pukatja) earthquake, central Australia: implications for fault scaling relations in cratonic settings. *Bulletin for the Seismological Society of America*, 104, 24-39.
- ^OClark, D., McPherson, A. 2011. Large earthquake recurrence in the Adelaide region: a palaeoseismological perspective. *Australian Earthquake Engineering Society Proceedings*, 9 pp.
- ^IClark, D., Cupper, M., Sandiford, M., and Kiernan, K., 2011, Style and timing of late Quaternary faulting on the Lake Edgar fault, southwest Tasmania, Australia: Implications for hazard assessment in intracratonic areas, in Audemard M., F.A., Michetti, A.M., and McCalpin, J.P., eds., *Geological Criteria for Evaluating Seismicity Revisited: Forty Years of Paleoseismic Investigations and the Natural Record of Past Earthquakes*: Geological Society of America Special Paper 479, p. 109–131, doi:10.1130/2011.2479(05).
- Clark, D., McPherson, A., Collins, C.D.N., 2011. Australia’s seismogenic neotectonic record: a case for heterogeneous intraplate deformation. *Geoscience Australia Record 11*.
- Clark, D., McPherson, A., Van Dissen, R., 2012. Long-term behaviour of Australian stable continental region (SCR) faults. *Tectonophysics* 566-567, 1-30.
- ^MClark, D., McPherson, A., Cupper, M., Collins, C. D. N. and Nelson, G. 2015. The Cadell Fault: a record of temporally clustered morphogenic seismicity in a low-strain intraplate region, south-eastern Australia. *Geological Society, London, Special Publications, Vol. 432, 39 p.*
- ^BClark, D., Dentith, M., Wyrwoll, K. H., Yanchou, L., Dent, V., Featherstone, C. 2008. The Hyden fault scarp, Western Australia: paleoseismic evidence for repeated Quaternary displacement in an intracratonic setting. *Australian Journal of Earth Sciences* 55, 379-395.
- ^PClark, D., 2017. personal communication. Discussions, June.
- Craig T. J., Calais E., Fleitout, L., Bollinger, L. and Scotti, O. (2016). Evidence for the release of long-term tectonic strain stored in continental interiors through intraplate earthquakes. *Geophysical Research Letters*, Vol. 43, 12 p.
- ^RCrone, A.J., Luza, K.V., 1990, Style and timing of Holocene surface faulting on the Meers fault, southwestern Oklahoma: *Geological Society of America Bulletin*, v. 102, p. 1-17.
- ^ECrone, A.J., Machette, M.N., Bowman, R.J., 1992, Geologic investigations of the 1988 Tennant Creek, Australia, earthquake: implications for paleoseismicity in stable continental regions: *USGS Bulletin*, p. A1-A51.
- ^QCrone, A.J., Machette, M.N., Bowman, J.R., 1997. Episodic nature of earthquake activity in stable continental regions revealed by palaeoseismicity studies of Australian and North American Quaternary faults. *Australian Journal of Earth Sciences* 44, 203–214.
- ^CCrone, A.J., DeMartini, P.M., Machette, M.N., Okumura, K., Prescott, J.R., 2003, Paleoseismicity of Two Historically Quiescent Faults in Australia: Implications for Fault Behavior in Stable Continental Regions: *Bulletin of the Seismological Society of America*, v. 93, p. 1913-1934.
- EPRI, 2012. *Technical Report: Central and Eastern United States Seismic Source Characterization for Nuclear Facilities*. EPRI, Palo Alto, CA, U.S. DOE, and U.S. NRC: 2012.
- Estrada, B., Clark, D., Wyrwoll, K-H., Dentith, M., 2006, Paleoseismic investigation of a recently identified Quaternary fault in Western Australia; the Dumbleyung Fault, Earthquake engineering in Australia, Conference Proceedings. p. 189-194.
- ^PEstrada, B. 2009. Neotectonic and palaeoseismological studies in the southwest of Western Australia. Ph.D. thesis, The University of Western Australia, Perth (unpubl.).
- ^TGoedhart, M., Booth, P. 2009. The Lake Edgar Fault: an active fault in Southwestern Tasmania, Australia, with repeated displacement in the Quaternary. 11th SAGA Biennial Technical Meeting and Exhibition, Swaziland, 16-18 Sept. p. 510-513.
- Hengesh, J. V., and B. B. Whitney (2016), Transcurrent reactivation of Australia’s western passive margin: An example of intraplate deformation from the central Indo-Australian plate, *Tectonics*, 35, 1066–1089.
- ^AGordon, F. R., and J. D. Lewis, 1980. The Meckering and Calingiri earthquakes October 1968 and March 1970, *Geol. Surv. West. Aust. Bull.*126.
- ^UHanson, K., C. Slack, R. Coppersmith, J. Neveling , L. Glaser, P. Bierman , S. Forman , M. Goedhart , C. Johnson, D. Black . 2014. Paleoseismic Investigations of the Kango Fault, South Africa: Incorporating Temporal and Spatial Temporal Clustering Behavior into a Seismic Source Characterization Model, *Seismological Society of America SLR v 85*, 2.
- Johnston, A.C., Coppersmith, K.J., Kanter, L.R., Cornell, C.A., 1994. The earthquakes of stable continental regions. Electric Power Research Institute Publication TR-102261-V1, Palo Alto, California.
- ^SKelson, K.I., and Swan, F.H., 1990, Paleoseismic history of the Meers fault, southwestern Oklahoma, and its implications for evaluations of earthquake hazards in the central and eastern United States: in Weiss, A.J. (editor), *Proceedings of the Seventeenth Water Reactor Safety Information Meeting, Nuclear Regulatory Commission, NUREG/CP-0105*, pp. 341-365.
- ^KLewis, J.D., Daetwyler, N.A., Bunting, J.A., Moncrieff, J.S., 1981. The Cadoux earthquake. *Western Australia Geological Survey Report 1981/11*.
- ^LMachette, M.N., Crone, A.J., Bowman, R.J., 1993, Geologic investigations of the 1986 Marryat Creek, Australia, earthquake:

- implications for paleoseismicity in stable continental regions: *USGS Bulletin*, v. Report B 2032-B, p. B1-B28.
- ^YMachette, M.N., Crone, A.J., Bowman, J.R., Prescott, J.R., 1991. Surface ruptures and deformation associated with the 1988 Tennant Creek and 1986 Marryat Creek, Australia, intraplate earthquakes. Open-File Report - U. S. Geological Survey OF 91-0582, 27p.
- ^JMcCue, K, Van Dissen, R., Gibson, G., Jensen, V., Boreham, B., 2003. The Lake Edgar Fault: an active fault in Southwestern Tasmania, Australia, with repeated displacement in the Quaternary. *Annals of Geophysics*, 46 n 5, 12 pp
- ^XMcPherson, A., Clark, D., Cupper, M., Collins, C.D.N., Nelson, G., 2012. The Cadell fault: a record of long-term fault behaviour in south-eastern Australia. Second Australian Regolith Geoscientists Association Conference / 22nd Australian Clay Minerals Society Conference, Mildura, Victoria, 10 pp.
- ^HQuigley, M. C., Cupper, M.L., Sandiford, M., 2006. Quaternary faults of south-central Australia: Palaeoseismicity, slip rates and origin, *Australian Journal of Earth Science*. 53, 285–301.
- ^FReid, B., 2007. *A Neotectonic study of the Willunga and Milendella Faults, South Australia*. B.Sc. (Hons) thesis, The University of Melbourne, Melbourne (unpubl.).
- ^WLuza, K., Madole., R., Crone, A. 1987. Investigation of the Meers fault, southwest Oklahoma. *Oklahoma Geological survey special publication 87-1*, 82 pp.
- Wheeler, R. 2011. Reassessment of Stable Continental Regions of Southeast Asia. *Seismological Research Letters Volume 82, Number 6*, 13 pp.
- Whitney, B. B. 2015, Neotectonic deformation in the Western Australia Shear Zone, PhD Dissertation, The University of Western Australia.
- Whitney, B. B., D. Clark, J. V. Hengesh, and P. Bierman (2015), Paleoseismology of the Mount Narryer fault zone, Western Australia: A multistrand intraplate fault system, *Geol. Soc. Am. Bull.*, 128, 684.
- ^VWhite, S., Stollhofen, H., Stanistreet, I., Lorenz, V. 2009. Pleistocene to recent rejuvenation of the Hebron fault, SW Namibia, in: Reicherter, K., Michetti, A.M. and Silva, P. G. (eds) Palaeoseismology: Historical and Prehistorical Records of Earthquake Ground Effects for Seismic Hazard Assessment. *The Geological Society, London, Special Publications*, 316, 293–317. DOI: 10.1144/SP316.18
- Woessner, J., Laurentiu, D., Giardini, D., Crowley, H., Cotton, F., Grunthal, G., Valensise, G., Arvidsson, R., Basili, R., Betul Dermircioglu, M., Hiemer, S., Meletti, C., Musson, R. W., Rovida, A. N., Sesetyan, K. and Stucchi, M. (2015). The 2013 European Seismic Hazard Model : key components and results. *Bulletin of Earthquake Engineering*, Vol.13, n° 12, p. 3553-3596



Testing the shorter and variable recurrence interval hypothesis along the Cholame segment of the San Andreas Fault

Williams, Alana (1), Arrowsmith, J Ramon (1), Rockwell, Thomas (2), Akciz, Sinan (3), Grant-Ludwig, Lisa (4), Gontz, Allen (2)

- (1) School of Earth and Space Exploration, Arizona State University, Tempe, AZ, alana.m.williams@asu.edu
- (2) Department of Geological Sciences, San Diego State University, San Diego, CA, trockwell@mail.sdsu.edu
- (3) College of Natural Sciences and Mathematics, California State University, Fullerton, CA, sakciz@fullerton.edu
- (4) Department of Earth System Science, University of California, Irvine, CA, lgrant@uci.edu

Abstract: Paleoseismic data from the Cholame segment of the San Andreas fault (SAF) are important for testing earthquake recurrence models along the central SAF. Slip per event or paleosurface rupture information coupled with tightly constrained event age control is needed to build a catalog of paleoseismic ruptures between the Parkfield and Carrizo sections of the SAF. We excavated 2 fault-perpendicular and 1 parallel trenches ~20 km southeast of Highway 46 in the Cholame segment. We present evidence for 6 ground rupturing events and 1 post-1857 ground shaking event, spanning a similar timeline with other paleoseismic sites on the southern San Andreas Fault. Further excavation of the Annette site is planned for Fall 2017.

Key Words: paleoseismology, active tectonics, San Andreas, Cholame, earthquake recurrence

INTRODUCTION

The Cholame segment of the southern San Andreas fault (SAF) is significant because it records the interaction between the creeping Parkfield segment to the northwest and the locked Carrizo segment to the southeast. Offset distributions have been reconstructed along this ~75 km long fault reach (Figure 1), but a more complete understanding of past ruptures for the Cholame section has not been forthcoming. Given its central position along the SAF, this lack of information places significant limitations on evaluating seismic hazard. New paleoseismic data on earthquake recurrence will lead to a better understanding of past rupture behavior and earthquake hazard analysis.

Large gaps in the paleoseismic record and various interpretations of past earthquake offset pose challenges to modeling past fault behavior along the Cholame segment of the SAF. Sieh's extensive measurements (1978a) of geomorphic offsets along the Cholame segment of the SAF implied a characteristic slip of 3-4 m during the 1857 rupture and prior events. Re-investigation of surface offsets revised the estimates of 1857 offset along Cholame upward to 4-6 m (Lienkaemper, 2001; Zielke 2010, 2012). Three dimensional reconstruction of an offset gravel sheet at LY4 along the Cholame segment showed 3 m offset in 1857 across a few meter aperture (Young, et al., 2002). Current rupture models for the Cholame segment are constrained locally only by this limited offset information, the regional millennial scale SAF slip rate, and the behavior of the adjacent sections (Parkfield and Carrizo; Field, et al., 2013). Note for example that the paleoseismic record along the Cholame section was insufficient for any maximum likelihood recurrence interval estimation by Biasi for the UCERF3 exercise (Biasi, 2013; UCERF3 Appendix H).

Assuming Cholame should slip at the SAF long term slip rate (~33mm/yr), and the 1857 rupture produced uniform slip of

at least 3 m (Sieh, 1978a; Sieh and Jahns, 1984; Young, et al., 2002; Lienkaemper, 2001; Zielke, et al., 2010; 2012), there is a large slip deficit that could accommodate a M7 rupture along the full length of the segment (Toke & Arrowsmith 2006). More importantly, this ~5 m deficit is too large to be released by creep alone (Lienkaemper, 2001). This prompted the investigation of the LY4 paleoseismic site by

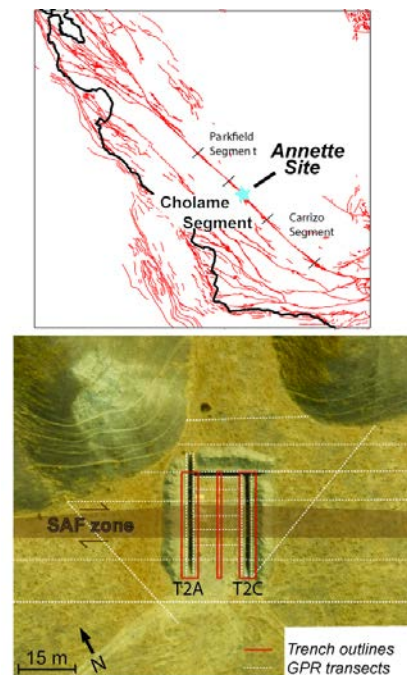


Figure 1: (Above) Map of Annette Site location with reference to the Parkfield and Carrizo segments of the San Andreas Fault. Quaternary faults shown in red. (Below) SfM model taken from balloon photos of the excavation. GPR transects shown in white, plans for further excavation shown by red boxes.



Stone et al. 2002, and Young et al. 2002. While no significant surface slip has been reported along the Cholame section since 1857, subsequent Parkfield events and creep have terminated around Highway 46 (northwest end of Cholame segment), and Young et al., 2002 report possible surface cracking at LY4 (35 km southeast of Highway 46).

This prompted the investigation of the LY4 paleoseismic site by Stone et al. 2002, and Young et al. 2002. While no significant surface slip has been reported along the Cholame section since 1857, subsequent Parkfield events and creep have terminated around Highway 46 (northwest end of Cholame segment), and Young et al., 2002 report possible surface cracking at LY4 (35 km southeast of Highway 46). Young et al.'s measurement of 3.0 ± 0.7 m slip on the 1857 earthquake is much smaller than the offsets measured on the neighboring Carrizo segment, and much larger than the Parkfield segment to the northwest, which suggests differences in fault properties (Sieh, 1978a; Hilley, et al., 2001). Young et al., 2002 interpreted 3 ground rupturing events, one of which was the 1857 event, followed by possible surface cracking. This corresponds with Stone et al.'s (2002) interpretation of 2 to 4 ground rupturing events, and provides a recurrence interval of 290-410 years. This longer recurrence rate differs from the hypothesis of more rapid Cholame recurrence intervals (Sieh and Jahns, 1984; Young et al. 2002) derived from assumed lower slip/event in Cholame than Carrizo and a uniform long-term slip rate along strike. The poorly constrained geochronology at the previous Cholame excavations spurred the 2015 excavations detailed later in this paper.

Slip/event is more variable than previously thought along the south central SAF (Akciz, et al., 2010 and Zielke, et al., 2010). Paleoseismic studies just southeast of the Carrizo segment at Frasier Mountain present evidence for 6 or 7 earthquakes within the last 650 years, indicating a 90-110 year recurrence interval (Scharer et al., 2014). This is consistent with the Bidart

record from Carrizo which implies surface rupture recurrence of 88 ± 41 years (Akciz et al., 2010) (Figure 3). Therefore, revisiting the poor geochronology and possibly incomplete record at Cholame becomes more urgent.

2016 EXCAVATIONS

We present data from 2 fault-perpendicular trenches and 1 fault-parallel trench in the northern Cholame segment, ~36 km north of LY4. Fault zone stratigraphy consists of alternating finely bedded sand, silt, and gravel strata, and bioturbated soil horizons. The strata record evidence for up to 6 earthquakes, of which 4 are of high quality. There is also possible post-1857 deformation, similar to that recognized at the LY4 and Bidart sites (Young, et al., 2002; Akciz, et al., 2010), which may represent a strong ground-shaking event. The events are numbered such that the ground shaking event (E0) and the six interpreted rupture events (E1 through E6) have increasing numbers with increasing age (Figures 2 and 3). Units display fault separations ranging from as much as 60 cm at the base of the exposure to 12 cm near the E1 horizon, with some exhibiting small colluvial wedges and sag deposits within the ~4 m wide fault zone. The oldest event (E6) is indicated deep in the stratigraphy by tilted and faulted sand and silt blocks that are capped by horizontally-bedded sand and onlapping sediments deposited against a paleoscarp, and differential vertical separation of units. E5 shows a much larger vertical separation than overlying strata, and exhibits shear fabric and thickened gravel units across the fault. Evidence for the E4 event horizon is represented by a gradational clayey silt sag deposit capped by discontinuous gravel. The E3 and E2 are the less well-defined event horizons, and are represented by fault strands capped by thinly-bedded silty clay, and bounded by discontinuous burn horizons that allow precise ^{14}C dating. We infer that E1 was the 1857 earthquake. It is represented by several fault splays capped by silty clay sag deposits that fill a depression in the fault zone that would have been produced by the 1857 surface rupture.

T2A SE

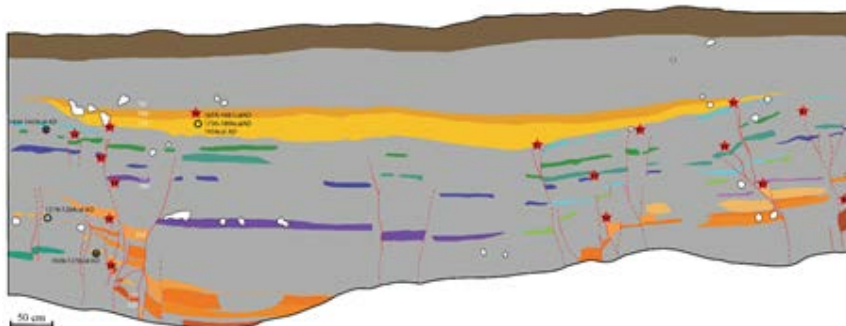
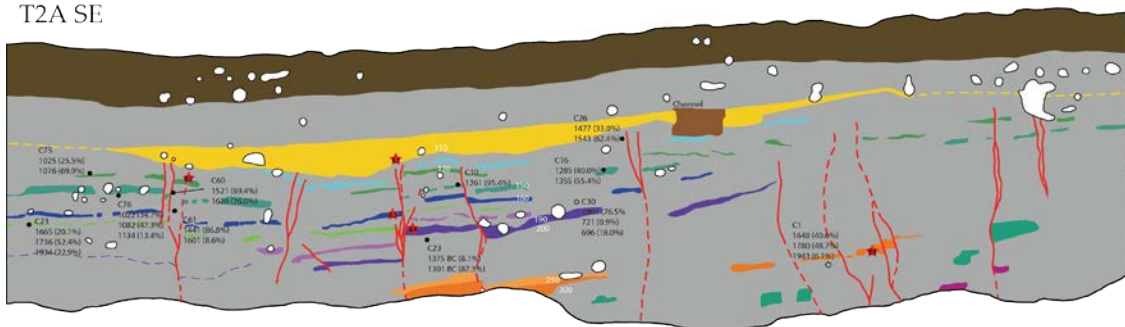


Figure 2: Trench 2A partial panel of the southeast facing wall (above) and 2C partial panel of the northwest facing wall (right). Important units are colored, fault splays are shown in red. Stars indicate event horizons, black circles indicate radiocarbon dates.

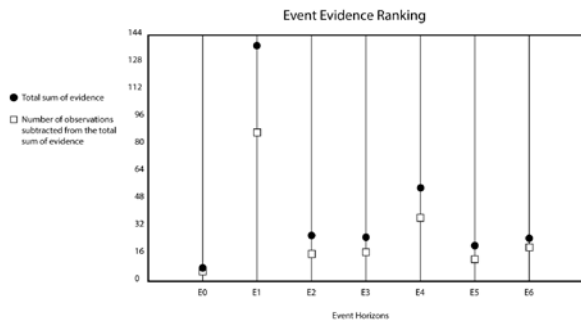


Figure 3 Black circles represent the sum of evidence ranking for each event horizon. Squares show the sum total subtracted by the number of observations. See Table 1 for list of evidence rankings and examples.

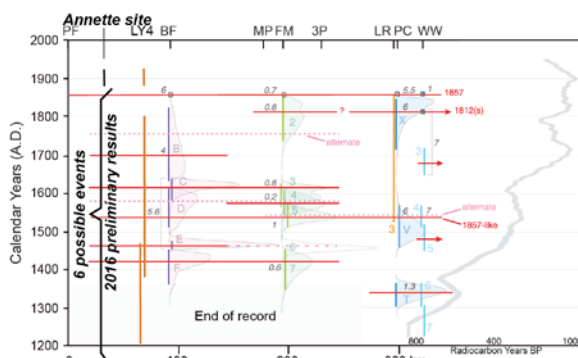


Figure 4: Correlation diagram for SSF paleoearthquakes from Parkfield to Wrightwood showing location of new sites we propose to develop. The black line and bracket indicate our preliminary interpretations from 2016. The orange lines represent the 3 poorly dated events at LY4. The rest of the figure is adapted from Scharer et al. 2015. Paleoseismology are labeled by the letter or number used in the original reference [Weldon et al., 2004; Pruitt et al., 2009; Akçiz et al., 2010; Scharer et al., 2011]. Grey numbers indicate horizontal displacement in meters (and vertical lowering for FM); bracket is used to signify when measurement is the cumulative total over several earthquakes. Solid red lines show possible ruptures based on Scharer's correlation of paleoearthquake ages among sites; lines arbitrarily end midway when no temporally correlative earthquake exists at the neighboring site.

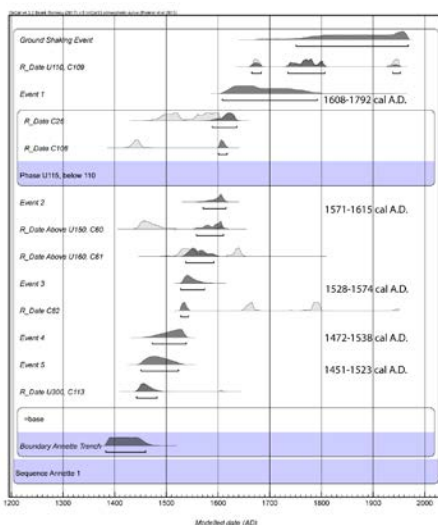


Figure 5: OxCal models for two different potential rupture sequences based on preliminary dates. Sequences vary based on the inclusion or exclusion of radiocarbon that do not fit in the sequence or that may have been bioturbated. Bottom sequence is the current preferred model.

The quality descriptions we have given to events are based on event horizon confidence. We evaluated this by compiling event indicators for E0 through E6 and assigning quality rankings for specific tectonic and geomorphic evidence of ground deformation in the style of Scharer et al. 2007 (Table 1). The likelihood of an event horizon is therefore interpreted by the quality and frequency of the event indicators. However, the total rank sum of an event horizon is not an absolute indication of earthquake horizon certainty. A robust set of low quality event indicators can falsely indicate a higher event certainty compared to a few observations of high quality event indicators at another horizon (Figure 4). E2, E3 and E6 are good examples of this, where E2 and E3 have higher total sums and greater numbers of observations compared to E6, which has just a few high-quality observations.

This site contains abundant detrital charcoal in many of the units and burn horizons at or near event horizons that provide great potential for bracketing the ages of these paleoearthquakes. We sent an initial package of 50 samples to the UC Irvine Keck Radiocarbon Facility and 23 ¹⁴C samples were dateable. They provide tantalizing evidence that the sequence of layers we are investigating at the Annette site spans from 1300 A.D. to 1857. We are confident that the last ground rupturing event in Cholame was the 1857 Fort Tejon earthquake, however the youngest bracketing date was very small, resulting in a large error margin. For this reason E1 is displayed in the models as 1600-1800 cal A.D. Our preliminary interpretations conclude that the timing of the six ground rupturing events correlate with timing of events at the Bidart Fan and Frasier Mountain sites, but extend beyond the oldest records at those sites. The current OxCal sequence (Figure 5) compared with the Scharer et al. diagram suggests that potentially 4 of the 6 events at Annette ruptured with the Carrizo segment, E1, E2, E3, and E4/E5. The similarities in the number and timing of events between the three sites compared with the longer record at the Annette site indicates that the recurrence interval on the Cholame segment may be longer than previously put forward by Sieh and Jahns, 1984, and that Cholame ruptures independently of the Carrizo segment (Figure 4).

2017 EARTHQUAKE GEOLOGY EFFORTS

In 2017, we plan to excavate a new fault perpendicular trench at the Annette site between T2A and T2C down to 11 ft, to collect additional evidence to test the current rupture model. We will also re-excavate T2A down to 16 ft to obtain an older record, and attempt to date the large offset channel surveyed with GPR. Channel age and offset measurement could also provide us with a long-term slip rate of the Cholame segment, which is currently poorly constrained.

CONCLUSION

The timing of rupture events at the Annette site suggests that Cholame ruptures with continuation into the Carrizo segment, as well as independently. The ranking and summation of event evidence ensures a quantitative approach to evaluating and comparing ground ruptures between paleoseismic sites. However, more data is needed to constrain the number of events and the recurrence interval. The Annette site has excellent potential to fill a gap



in the data for current hazard assessment in California, by placing geologic bounds on the character and frequency of multi-segment and multi-fault ruptures along the SAF.

Acknowledgements: We gratefully acknowledge the financial support of the Southern California Earthquake Center, as well as the contributions of Sally Brandscomb, Michael Say, Nick Insera, and Mary Braza.

REFERENCES

- Akciz, S. O., Grant Ludwig, L., Arrowsmith, J R., Zielke, O., Century-long average time intervals between earthquake ruptures of the San Andreas fault in the Carrizo Plain, California, *Geology*, 38, 9, p. 787-790, 2010.
- Field, E. H., Arrowsmith, J R., Biasi, G. P., Bird, P., Dawson, T. E., Felzer, K. R., Jackson, D. D., Johnson, K. M., Jordan, T. H., Madden, C., Michael, A. J., Milner, K. R., Page, M. T., Uniform California Earthquake Rupture Forecast, Version 3 (UCERF3)--The Time-Independent Model, *Bulletin of the Seismological Society of America*, Vol. 104, No. 3, pp. 1122–1180, doi: 10.1785/0120130164, 2014.
- Hilley, G. E., Arrowsmith, J R., and Stone, E. M., Using microseismicity and surface offset data to define fault segment boundaries along low friction faults, with an example from the Cholame-Carrizo segment boundary along the San Andreas Fault, Southern California, *Bulletin of the Seismological Society of America*, 91, 427-440, 2001.
- Lienkaemper, J. (2001). 1857 Slip on the San Andreas Fault Southeast of Cholame, California. *Bulletin of the Seismological Society of America*, 1659-1672.
- Scharer, K., Weldon, R., Biasi, G., Streig, A., & Fumal, T. (2017). Ground-rupturing earthquakes on the northern Big Bend of the San Andreas Fault, California, 800 AD to Present. *Journal of Geophysical Research: Solid Earth*, 122(3), 2193-2218.
- Scharer, K., Weldon, R., Streig, A., & Fumal, T. (2014). Paleoeearthquakes at Frazier Mountain, California delimit extent and frequency of past San Andreas Fault ruptures along 1857 trace. *Geophys. Res. Lett. Geophysical Research Letters*.
- Scharer, K. M., Weldon, R. J., Fumal, T. E., & Biasi, G. P. (2007). Paleoeearthquakes on the southern San Andreas fault, Wrightwood, California, 3000 to 1500 BC: A new method for evaluating paleoseismic evidence and earthquake horizons. *Bulletin of the Seismological Society of America*, 97(4), 1054-1093.
- Sieh, K. E. (1978a). Slip along the San Andreas fault associated with the great 1857 earthquake, *Bulletin of the Seismological Society of America*, 68, 1421–1448.
- Sieh, K. E. (1978b). Central California foreshocks of the great 1857 earthquake. *Bulletin of the Seismological Society of America*, 68(6), 1731-1749.
- Sieh, K., & Jahns, R. (1984). Holocene activity of the San Andreas fault at Wallace Creek, California. *Geol Soc America Bull Geological Society of America Bulletin*, 883-883.
- Stone, E.M., Grant, L., and Arrowsmith, J R., Recent rupture history of the San Andreas Fault southeast of Cholame in the northern Carrizo Plain, California, *Bulletin of the Seismological Society of America*, 92, 983-997, 2002.
- Toke, N., & Arrowsmith, J. (2006). Reassessment of a Slip Budget along the Parkfield Segment of the San Andreas Fault. *Bulletin of the Seismological Society of America*, S339-S348.
- Williams, A., (2015). Exploration of a new paleoseismic site in the Cholame section of the San Andreas fault, CA. Poster presented at the Annual Southern California Earthquake Center Conference, Palm Springs, CA.
- Young, J., Arrowsmith, J., Collini, L., Grant, L., & Gootee, B. (2002). Three-Dimensional Excavation and Recent Rupture History along the Cholame Segment of the San Andreas Fault. *Bulletin of the Seismological Society of America*, 2670-2688.
- Zielke, O., Arrowsmith, J., Ludwig, L., & Akciz, S. (2010). Slip in the 1857 and Earlier Large Earthquakes Along the Carrizo Plain, San Andreas Fault. *Science*, 1119-1122.
- Zielke, O., Arrowsmith, J., Ludwig, L., & Akciz, S. (2012). High-Resolution Topography-Derived Offsets along the 1857 Fort Tejon Earthquake Rupture Trace, San Andreas Fault. *Bulletin of the Seismological Society of America*, 1135-1154.

EQ ID	Event Rating	Location	Trench Evidence
E0 Total	16		
	16	T2C-NW-P9 through T2C-NW-P6	Liquefaction features in Unit 110 (4) across four panels
E1 Total	45		
	6	T2A-NW-P4	Truncated units (2), fracturing (1), Units 110 and 100 sag across fault (3)
	8	T2A-NW-P5	Vertical separation of units (4), fissure beneath Unit 110 (4)
	13	T2A-NW-P6	Decreasing vertical separation upsection (2), fissure below Unit 110 (4), disrupted Unit 115 (3), shear fabric (4)
	2	T2C-NW-P4	Truncated silt units (2)
	3	T2C-NW-P5	Shear fabric along truncated layers (3)
	10	T2C-NW-P7	Aligned clasts (2), disrupted grass burn layer beneath Unit 110 (3), truncated silt units (2), vertical separation decreasing upsection (3)
	3	T2C-NW-P9	Silt units display decreasing vertical throw upsection (3)
E2 Total	12		
	2	T2A-NW-P4	Decreased vertical separation between Unit 150 and 120 (2)
	3	T2C-NW-P5	Decreasing vertical separation of units capped by conformable grassy burn layer beneath Unit 115 (3)
	7	T2C-NW-P5	Block from Unit 130 draped across fault (4), fracture capped by grassy burn layer and continuous gravels (3)
E3 Total	6		
	3	T2C-NW-P5	Fault strand capped by Unit 150 (3)
	3	T2C-NW-P5	Silty fissure fill beneath Unit 150 truncated silts (3)
E4 Total	34		
	12	T2A-NW-P4	Unit 190 sag deposit thickens across fault (4), Unit 270 offset 47 cm (2), color change in soil Unit 200 (2), increased thickness in soil Unit 200 (4)
	8	T2A-NW-P6	Unit 190 sag deposit draped across fault (4), Unit 200 soil thickens across fault (4)
	6	T2C-NW-P5	Disrupted and tilted blocks draped across fault stratigraphically equivalent with Unit 190 (4), apparent diagonal offset decreasing upsection (2)
	8	T2C-NW-P9	Draped gravels in Unit 250 vertically separated 44 cm (4), Unit 190 sag deposit is draped across fault (4)
E5 Total	15		
	5	T2A-NW-P4	Shear fabric (1), Unit 270 vertical separation of ~50 cm is 2x greater than Unit 190 vertical separation (4)
	10	T2C-NW-P9	Draped gravels in Unit 250 thicken across fault (4), truncated silt units (2), onlapping sediments offset ~35 cm (4)
E6 Total	17		
	11	T2A-NW-P4	Truncated and rotated gravels beneath draped sag deposit Unit 270 (4), Unit 270 thickens across fault (4), soil color change across fault (3)
	8	T2C-NW-P9	Rotated Unit 290 block in fault zone capped by horizontal silt and sand layers (4), onlapping sands and silts deposited against paleoscarp (4)

Table 1 Event evidence rankings for horizons in Partial trench logs T2A SE and T2C NW. Ratings as follows: 4 = excellent, 3 = moderate, 2 = fair, 1 = poor, following methodology suggested by Scharer et al., 2007. Ranking can vary between sites, these sums rate the likelihood that the evidence is indicative of a paleosurface when the rupture occurred at this site.

LIST OF PARTICIPANTS

LAST NAME	FIRST NAME	ORGANISATION	COUNTRY
ABRAHAMI	Rachel	University of Chile	Chile
AKCIZ	Sinan	California State University Fullerton	USA
ALEXOUDI	Vassiliki	National and Kapodistrian University Of Athens	Greece
ALMOND	Peter	Lincoln University	New Zealand
ANTONIOU	Varvara	National and Kapodistrian University of Athens	Greece
ARAYA	Jose	University of Chile	Chile
AZUMA	Takashi	Geological Survey of Japan/AIST	Japan
BAIZE	Stephane	Institut Radioprotection et Surete Nucleaire	Germany
BARDAJÍ	Teresa	Universidad de Alcalá	France
BARRELL	David	GNS Science	Spain
BASTIN	Sarah	QuakeCoRE, University of Canterbury	New Zealand
BELZYT	Szymon	Uniwersytet im. Adama Mickiewicza w Poznaniu	Poland
BERRYMAN	Kelvin	GNS Science	New Zealand
BRONIKOWSKA	Malgorzata	Adam Mickiewicz University in Poznań	Poland
BROOKS	Greg	Geological Survey of Canada	Canada
BROUGH	Thomas	University of Canterbury	New Zealand
BUSHELL	Tabitha	University of Canterbury	New Zealand
CHO	Sung-il	Korea Hydro & Nuclear Power company	South Korea
CHOI	Jin-Hyuck	Korea Institute of Geoscience and Mineral Resources	South Korea
CHOI	Sung-ja	Korean Institute of Geoscience and Mineral Resources	South Korea
CINTI	Francesca Romana	Istituto Nazionale di Geofisica e Vulcanologia	Italy
CIVICO	Riccardo	Istituto Nazionale di Geofisica e Vulcanologia	Italy
CLARK	Kate	GNS Science	New Zealand
CLARK	Dan	Geoscience Australia	Australia
COCHRAN	Ursula	GNS Science	New Zealand
CODY	Emma	Massey University	New Zealand
DAWSON	Timothy	California Geological Survey	USA
DE PASCALE	Gregory	University of Chile	Chile
DUFFY	Brendan	The University of Melbourne	Australia
EGGER	Anne	Central Washington University	USA
ELLIOTT	Austin	University of Oxford	United Kingdom
ELLIS	Susan	GNS Science	New Zealand
FRECHEN	Manfred	Leibniz Institute for Applied Geophysics	Germany
GARCIA	Victor Hugo	CAPES Foundation (Brazil) - CONICET (Argentina)	Germany
GATH	Eldon	Earth Consultants International	USA
GIHM	Yong Sik	Korea Institute of Geoscience and Mineral Resources	South Korea
GIONA BUCCI	Monica	Lincoln University	New Zealand
GONZÁLEZ-ALFARO	José	Universidad de Chile	Chile
GOORABI	Abolghasem	University of Tehran	Iran
GRAMPA	Alexia	National and Kapodistrian University of Athens	Greece
GRUETZNER	Christoph	Friedrich Schiller University Jena	Germany
HOWARTH	Jamie	Victoria University of Wellington	New Zealand
HUANG	Xuemeng	Institute of Crustal Dynamics, China Earthquake Administration	China
HUOT	Sebastien	Illinois State Geological Survey	USA
HYLAND	Natalie	University of Canterbury	New Zealand

LAST NAME	FIRST NAME	ORGANISATION	COUNTRY
ISHIMURA	Daisuke	Tokyo Metropolitan University	Japan
JIN	Kwangmin	Korea Institute of Geoscience and Mineral Resources	South Korea
JONES	Katie	GNS Science	New Zealand
KEARSE	Jesse	Victoria University of Wellington	New Zealand
KEITARO	Komura	Chiba University	Japan
KHAJAVI	Narges	University of Canterbury	New Zealand
KIM	Taehyung	Pukyong National University	South Korea
KIM	Hak-Sung	Korea Hydro & Nuclear Power Co., Ltd.	South Korea
KIM	Young-Seog	Pukyong National University	South Korea
KLEBER	Emily	Utah Geological Survey	USA
KLINGER	Yann	Institut de Physique du Globe Paris - CNRS	France
KOEHLER	Rich	University of Nevada Reno	USA
KÖKÜM	Mehmet	Firat University-Turkey	Turkey
LANDGRAF	Angela	University of Potsdam	Germany
LANGRIDGE	Robert	GNS Science	New Zealand
LARIO	Javier	Universidad Nacional de Educación a Distancia	Spain
LEE	Seung Ryeol	Korea Institute of Geoscience and Mineral Resources	South Korea
LEKKAS	Efthymios	National and Kapodistrian University of Athens	Greece
LEON	Tomas	Universidad de Chile	Chile
LITCHFIELD	Nicola	GNS Science	New Zealand
LITTLE	Timothy	Victoria University of Wellington	New Zealand
LIVIO	Franz	Università degli Studi dell'Insubria	Italy
MACKEY	Ben	Otago Regional Council	New Zealand
MARLIYANI	Gayatri	Universitas Gadjah Mada	Indonesia
MASSEY	Chris	GNS Science	New Zealand
MAVROULIS	Spyridon	National and Kapodistrian University of Athens	Greece
MELETTI	Carlo	Istituto Nazionale di Geofisica e Vulcanologia	Italy
MENDECKI	Maciej	University of Silesia in Katowice	Poland
MIYASHITA	Yukari	Geological Survey of Japan, AIST	Japan
MIYAUCHI	Takahiro	Chiba University	Japan
MONICA	Giona Bucci	Lincoln University	New Zealand
MOORE	James	Earth Observatory of Singapore	Singapore
NAIK	Sambit Prasanajit	Pukyong National University	South Korea
NIEMI	Tina	University of Missouri-Kansas City	USA
NINIS	Dee	Victoria University of Wellington	New Zealand
NISHIMURA	Yuichi	Hokkaido University	Japan
NISSEN	Edwin	University of Victoria	Canada
OKUMURA	Reiko	Higashiroshima City	Japan
OKUMURA	Koji	Hiroshima University	Japan
ORCHISTON	Caroline	University of Otago	New Zealand
PACE	Bruno	DiSPUter-Università "G. d'Annunzio" Chieti-Pescara, Italy	Italy
PANTOSTI	Daniela	Istituto Nazionale di Geofisica e Vulcanologia	Italy
PATON	Brian	Marlborough Civil Defence Emergency Management	New Zealand
PATTON	Jason	Humboldt State University	USA
PATYNIAK	Magda	University of Potsdam	Germany
PEDLEY	Kate	University of Canterbury	New Zealand
PEREA MANERA	Hector	Scripps Institution of Oceanography, University of California, San Diego/Institut de Ciències del Mar, Consejo Superior de Investigaciones Científicas	USA
PETER	Almond	Lincoln University	New Zealand
PISARSKA-JAMROZY	Malgorzata	Adam Mickiewicz University in Poznań	Poland

LAST NAME	FIRST NAME	ORGANISATION	COUNTRY
PUCCI	stefano	Istituto Nazionale di Geofisica e Vulcanologia	Italy
QUIGLEY	Mark	University of Melbourne	Australia
REICHERTER	Klaus	RWTH Aachen University	Germany
REN	Junjie	Institute of Crustal Dynamics, China Earthquake Administration	China
RIES	William	GNS Science	New Zealand
ROBINSON	Tom	Durham University	United Kingdom
ROCKWELL	Thomas	San Diego State University	USA
RODRÍGUEZ-PASCUA	Miguel Angel	Geological Survey of Spain	Spain
ROQUERO	Elvira	Universidad de Alcalá	Spain
ROTEVATN	Atle	University of Bergen	Norway
SANA	Hamid	Institute of Rock Structure and Mechanics, Czech Academy of Sciences	Czech Republic
SCHOENFELD	Marion	Environment Canterbury Regional Council	New Zealand
SCOTT	Chelsea	Arizona State University	USA
SEITZ	Gordon	California Geological Survey	USA
SILVA	Pablo G.	Universidad de Salamanca	Spain
SIMPSON	Ian	GNS Science	New Zealand
SINTUBIN	Manuel	KU Leuven	Belgium
SPACEK	Petr	Masaryk University Brno	Czech Republic
STAHL	Timothy	University of Canterbury	New Zealand
STEMBERK	Jakub	Institute of Rock Structure and Mechanics, Czech Academy of Sciences	Czech Republic
ŠTĚPANČÍKOVÁ	Petra	Institute of Rock Structure and Mechanics, Czech Academy of Sciences	Czech Republic
STIRLING	Mark	University of Otago	New Zealand
SZCZYGIEL	Jacek	University of Silesia in Katowice	Poland
TABORIK	Petr	Institute of Rock Structure and Mechanics, Czech Academy of Sciences	Czech Republic
UPTON	Phaedra	GNS Science	New Zealand
VAN DISSEN	Russ	GNS Science	New Zealand
VAN ECHELPOEL	Erna	Tractebel	Belgium
VAN LOON	Antonius (Tom)	Adam Mickiewicz University, Poznan	Poland
VARGAS	Gabriel	University of Chile	Chile
VERMEER	Jessica	University of Melbourne	Australia
VILLALOBOS	Angelo	University of Chile	Chile
VILLAMOR	Pilar	GNS Science	New Zealand
VISINI	Francesco	Istituto Nazionale di Geofisica e Vulcanologia	Italy
WANG	Teng	Earth Observatory of Singapore (EOS), Nanyang Technological University	Singapore
WECHSLER	Neta	Tel Aviv University	Israel
WILLIAMS	Alana	Arizona State University	USA
WILLIAMS	Jack	University of Otago	New Zealand

PROCEEDINGS VOLUMES OF PATA DAYS

VOL. 8:

Proceedings of the 8th International INQUA Meeting on Paleoseismology, Active Tectonics and Archeoseismology. Handbook and Programme. (Clark KJ, Upton P, Langridge R, Kelly K, Hammond K.), 13-16 November 2017. Lower Hutt (NZ): GNS Science. 441 p. (GNS Science miscellaneous series 110). doi:10.21420/G2H061

VOL. 7:

Proceeding of the 7th International INQUA Meeting on Paleoseismology, Active Tectonics and Archeoseismology (J.P. McCalpin & C. Gruetzner, eds.). ISBN 978-0-9974355-2-8, 2016. Published digitally by the Crestone Science Center, Crestone, CO 81131 USA, Guidebook No. 12; 7th International INQUA Meeting on Paleoseismology, Active Tectonics and Archeoseismology, Crestone (USA).

VOL. 6:

Abstracts Volume, 6th International INQUA Meeting on Paleoseismology, Active Tectonics and Archeoseismology (Blumetti, A.M., Cinti, F.R., De Martini, P.M., Galadini, F., Guerrieri, L., Michetti, A.M., Pantosti, D. and Vittori, E., eds.), 19-24 April 2015, Pescina, Fucino Basin, Italy: Miscellanea INGV, Anno 2015 Numero 27, ISSN 2039-6651, printed in Italy by Istituto Nazionale di Geofisica e Vulcanologia, Rome, Italy, 545 p.

VOL. 5:

Proceeding of the 5th International INQUA Meeting on Paleoseismology, Active Tectonics and Archeoseismology (C. Gruetzner, J.-H. Choi, P. Edwards & Y.-S. Kim, eds.). ISBN 9791195344109 93450. Printed in Korea, 2014. 5th International INQUA Meeting on Paleoseismology, Active Tectonics and Archeoseismology, Busan (Korea).

VOL. 4:

Seismic Hazard, Critical Facilities and Slow Active Faults (C. Gruetzner, A. Rudersdorf, R. Pérez-López & K. Reicherter, eds.). ISBN 978-3-00-0427-96-1. Printed in Germany, 2013. 4th International INQUA Meeting on Paleoseismology, Active Tectonics and Archeoseismology, Aachen (Germany).

VOL. 3:

Earthquake Geology and Archeoseismology: Society and Seismic Hazard (R. Pérez-López, P.G. Silva, M.A. Rodríguez Pascua, V.H. Garduño Monroy, G. Suarez & K. Reicherter, eds.) Printed in Mexico, 2012. 3rd INQUA-IGCP 567 International Workshop on Earthquake Geology, Paleoseismology and Archeoseismology, Morelia (Mexico).

VOL. 2:

Earthquake Geology and Archeoseismology: Society and Seismic Hazard (C. Gruetzner, R. Pérez-López, T. Fernández-Steeger, I. Papanikolaou, K. Reicherter, P.G. Silva & A. Vott, eds.). ISBN: 978-960-466-093-3. Printed in Greece, 2011. 2nd INQUA-IGCP 567 International Workshop, Corinth (Greece).

VOL. 1:

Archeoseismology and Paleoseismology in the Alpine-Himalayan Collisional Zone (R. Pérez-López, C. Gruetzner, J. Lario, K. Reicherter & P.G. Silva, eds.). ISBN: 978-84-7484-217-3. Printed in Spain, 2009. 1st INQUA-IGCP 567 International Workshop, Baelo Claudia, Cadiz (Spain).